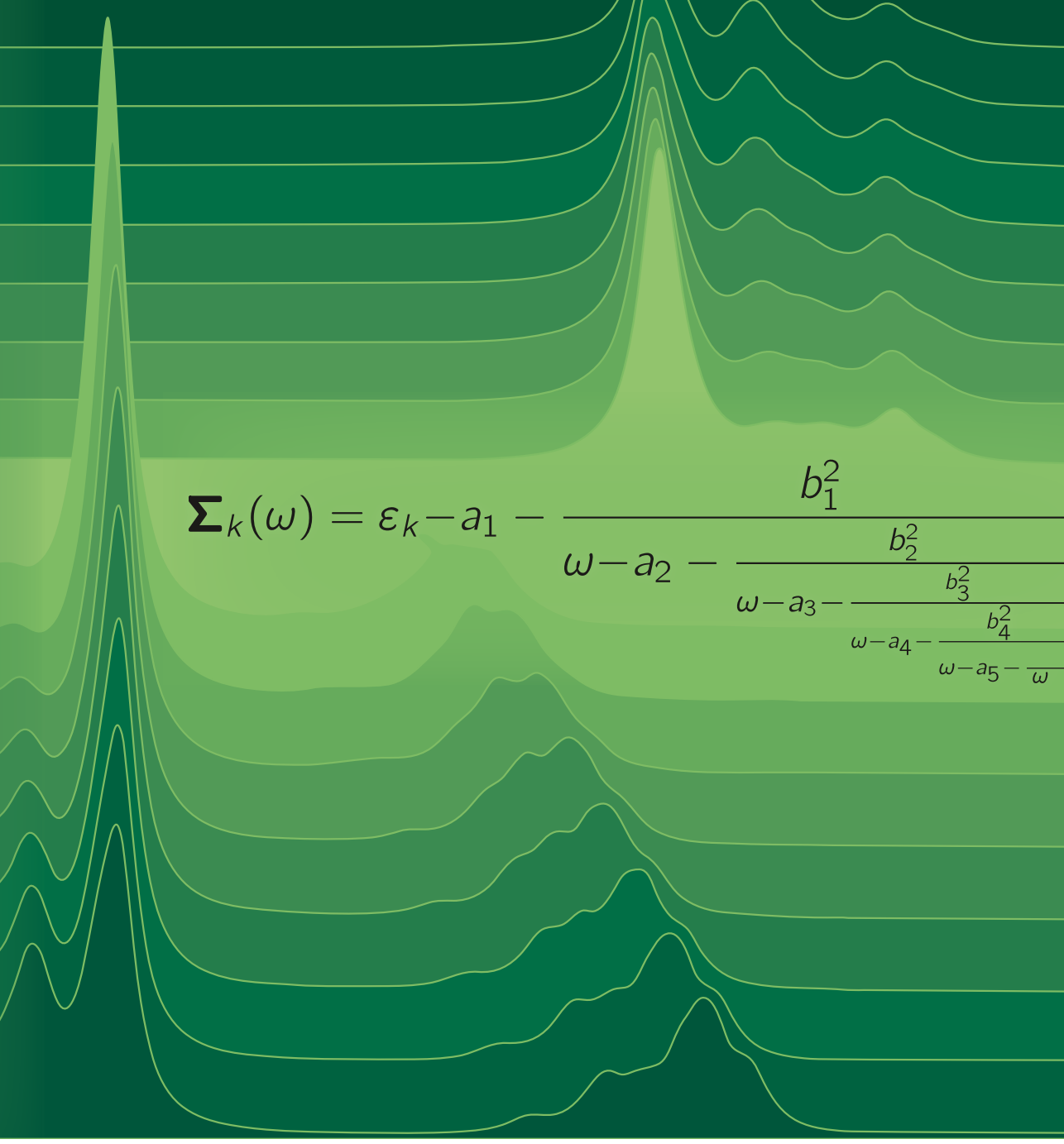

Topology, Entanglement, and Strong Correlations

Eva Pavarini and Erik Koch (Eds.)

JÜLICH
Forschungszentrum

Schriften des Forschungszentrums Jülich
Reihe Modeling and Simulation Band / Volume 10

Forschungszentrum Jülich GmbH
Institute for Advanced Simulation

Lecture Notes of the Autumn School on Correlated Electrons 2020

Eva Pavarini and Erik Koch (Eds.)

Topology, Entanglement, and Strong Correlations

Autumn School organized by
the Institute for Advanced Simulation
at Forschungszentrum Jülich
21 – 25 September 2020

Schriften des Forschungszentrums Jülich
Modeling and Simulation Band / Volume 10

ISSN 2192-8525 ISBN 978-3-95806-466-9

Bibliographic information published by the Deutsche Nationalbibliothek.
Die Deutsche Nationalbibliothek lists this publication in the Deutsche Nationalbibliografie; detailed bibliographic data are available in the Internet at http://dnb.d-nb.de.

Publisher:	Forschungszentrum Jülich GmbH Institute for Advanced Simulation
Cover Design:	Grafische Medien, Forschungszentrum Jülich GmbH
Printer:	Schloemer & Partner GmbH, Düren
Copyright:	Forschungszentrum Jülich 2020
Distributor:	Forschungszentrum Jülich Zentralbibliothek, Verlag 52425 Jülich Phone +49 (0)2461 61-5368 · Fax +49 (0)2461 61-6103 e-mail: zb-publikation@fz-juelich.de www.fz-juelich.de/zb

Schriften des Forschungszentrums Jülich
Reihe Modeling and Simulation, Band / Volume 10

ISSN 2192-8525
ISBN 978-3-95806-466-9

Vollständig frei verfügbar über das Publikationsportal des Forschungszentrums Jülich (JuSER) unter www.fz-juelich.de/zb/openaccess

Contents

Preface

Topology and entanglement are key concepts in many-body physics. Understanding the associated emergent phenomena beyond toy models – in the world of real strongly-correlated materials – requires the mastery of a wealth of different methods. These encompass analytical tools such as group theory, first principles techniques based on density-functional theory, materials-specific model-building schemes, as well as advanced modern numerical approaches for solving realistic many-body models.

This year's school provides an overview of the state-of-the art of these methods, their successes and their limitations. After introducing the basics, lectures will present the core concepts of topology and entanglement in many-body systems. To make contact to real materials, strategies for building materials specific models and techniques for their solution will be introduced. Among the latter, the school will cover quantum Monte Carlo methods, construction and optimization of correlated wave-functions, recursion and renormalization group techniques, as well as dynamical mean-field theory. More advanced lectures will give a pedagogical overview on topological materials and their physics: topological metals, semimetals, and superconductors. Towards the end of the school entanglement in quantum dynamics and perspectives in quantum computation will be discussed.

The goal of the school is to introduce advanced graduate students and up to these modern approaches for the realistic modeling of strongly correlated materials.

A school of this size and scope requires backing from many sources. This is even more true this year. As everywhere, the Corona pandemics provided scores of new challenges. Plans had to be changed and real facilities had to be replaced with virtual ones. We are very grateful for all the practical and financial support we have received. The Institute for Advanced Simulation at the Forschungszentrum Jülich and the Jülich Supercomputer Centre provided the major part of the funding and were vital for the organization and re-organization of the school as well as for the production of this book. The Institute for Complex Adaptive Matter (ICAM) supplied additional funds and ideas for successful online formats.

The nature of a school makes it desirable to have the lecture notes available when the lectures are given. This way students get the chance to work through the lectures thoroughly while their memory is still fresh. We are therefore extremely grateful to the lecturers that, despite tight deadlines, provided their manuscripts in time for the production of this book. We are confident that the lecture notes collected here will not only serve the participants of the school but will also be useful for other students entering the exciting field of strongly correlated materials.

We are grateful to Mrs. H. Lexis of the Verlag des Forschungszentrum Jülich and to Mrs. D. Mans of the Grafische Betriebe for providing their expert support in producing the present volume on a tight schedule. We heartily thank our students and postdocs who helped with proofreading the manuscripts, often on quite short notice: Elaheh Adibi, Julian Mußhoff, Neda Samani, and Xue-Jing Zhang.

Finally, our special thanks go to Dipl.-Ing. R. Hölzle for his invaluable advice on the innumerable questions concerning the organization of such an endeavor, and to Mrs. L. Snyders for expertly handling all practical issues.

Eva Pavarini and Erik Koch

August 2020

1 Density Functional Theory for the Correlated

Robert O. Jones
Peter-Grünberg-Institut
Forschungszentrum Jülich

Contents

E. Pavarini and E. Koch (eds.)
Topology, Entanglement, and Strong Correlations
Modeling and Simulation Vol. 10
Forschungszentrum Jülich, 2020, ISBN 978-3-95806-466-9
http://www.cond-mat.de/events/correl20

1 Introduction

A practical definition of "strongly correlated" systems covers those that are not described well by electron density functional (DF) theory. Most seminars and many publications on the subject mention in the first sentence the widespread use of density functional (DF) theory in materials, often quoting Walter Kohn: "For periodic solids it is sometimes referred to as the standard model" [1]. The second sentence, however, lists the systems where DF results with standard approximations are disastrous (a "metallic" transition metal oxide insulator, almost anything to do with rare earth or actinide elements, ...), emphasizing the importance of describing such "strongly correlated" materials correctly [2].[1] DF theory is nevertheless an essential part of this school. It is used widely in materials science and chemistry and provides useful results for countless systems for which the exact wave function cannot be computed. The organizers have asked me to provide you with a feel for the areas where physical insight can be obtained and *why* approximations used in DF calculations can give sensible answers far from their regions of obvious validity.

The origins of DF theory go back to the early years of quantum mechanics in the late 1920s. Thomas [3] and Fermi [4] recognized the electron density as a basic variable, and Dirac [5] showed already in 1930 that the state of an atom can be determined completely within Hartree-Fock theory by its one-particle density matrix; it is not necessary to specify the wave function. We follow here the history of density-related methods to the single-particle equations of Kohn and Sham in 1965 and beyond. In its modern form, the DF formalism shows that ground state properties of a system of electrons in an external field can be determined from a knowledge of the *density distribution* $n(r)$ alone. Much of the work in materials science and chemistry focuses on the *structure* and cohesive energies and a property for which DF calculations are particularly valuable: the total energy E of a system of electrons in the presence of ions located at $R_{\rm I}$.

Accurate calculations of the entire energy surface $E(R_{\rm I})$ are possible only for systems with very few atoms, and this function generally has vast numbers of maxima and minima at unknown locations. The lowest energy, however, corresponds to the ground state *structure*, and paths between minima are essential to our studies of chemical reactions, including their activation barriers. When I read the autobiography of Francis Crick [6], I was taken by his observation

> "If you want to study *function*, study *structure*."

and have used it ever since. This relationship may be self-evident to molecular biologists and most chemists, but it is also true in many other areas. The DF approach allows us to calculate $E(R_{\rm I})$, and hence the structure and many related properties, without using experimental input. If you are more interested in "real materials" than in mathematical models, this is a crucial advantage for strongly correlated materials as well.

[1] An example can be found in the Preface of the 2012 Autumn School: "Density functional theory (DFT) is considered the Standard Model of solid state physics. The state-of-the-art approximations to DFT, the local-density approximation (LDA) or its simple extensions, fail, however, even qualitatively, for strongly correlated systems."

Olle Gunnarsson and I reviewed the density functional formalism, its history, and its prospects in 1989 [7], and I returned to the subject and its literature again recently [8]. I have drawn on this article for some of the present content, and I refer you to it for a much wider discussion and more extensive literature. The focus here is on *electron* density functional theory, and I comment in [8] on DF methods in classical systems and nuclei. My final remarks in [8] discussed the concern that prominent DF practitioners express about the future of the field, and I return to this point below. A second review article covers my view of the fascinating history of the chemical "bond", starting from the first use of this word in the mid nineteenth century [9]. This is perhaps peripheral to the main interests of the "strongly correlated" community, but the reader will be surprised at how much he or she did not know. Have you ever really thought about why atoms usually like being close together and not infinitely far apart?
In my lecture at the Autumn School 2020, I plan to cover much of the ground presented in these notes. Participants at the school, however, should not be surprised if I make some less than standard remarks about DF theory and its relationship to other areas of many-electron physics and chemistry, as well as on some of the personalities involved.

2 The electron density as basic variable

The books by Gino Segrè [10] and Graham Farmelo [11] give fascinating accounts of the very rapid development of quantum mechanics in the years following 1925. Methods for finding approximate solutions of the Schrödinger equation followed soon after it was published in 1926 and have had a profound effect on chemistry and condensed matter physics ever since.
The "Hartree approximation" to the many-electron wave function is a product of single-particle functions,

$$\Psi(\mathbf{r}_1, \mathbf{r}_2, ...) = \psi_1(\mathbf{r}_1) \cdots \psi_N(\mathbf{r}_N) \tag{1}$$

where each $\psi_i(\mathbf{r}_i)$ satisfies a one-electron Schrödinger equation with a potential term arising from the average field of the other electrons. Hartree [12] indeed introduced the idea of a "self-consistent field", with specific reference to the core and valence electrons, but his papers do not mention the approximation (1). However, Slater [13] and Fock [14] recognized immediately that the product wave function (1) in conjunction with the variational principle led to a generalization of the method that would apply to systems more complex than atoms. They showed that replacing (1) by a determinant of such functions [13, 14] led to equations that were not much more complicated than those of Hartree, while satisfying the Pauli exclusion principle. These determinantal functions, which had been used in discussions of atoms [15] and ferromagnetism [16], are known today as "Slater determinants", and the resulting "Hartree-Fock equations" have formed the basis of most discussions of atomic and molecular structure since.
In 1929 Dirac wrote [17]:

> "The general theory of quantum mechanics is now almost complete, ... The underlying physical laws necessary for the mathematical theory of a large part of physics and the whole of chemistry are thus completely known, and the difficulty is only that the exact application

> of these laws leads to equations much too complicated to be soluble. It therefore becomes desirable that approximate practical methods of applying quantum mechanics should be developed, which can lead to an explanation of the main features of complex atomic systems without too much computation."

I cannot think of a better short description of density functional theory than an "approximate practical method of applying quantum mechanics" to explain "complex atomic systems". I and many others ignored the point "without too much computation."

Dirac [17] also sought to improve the model of Thomas [3] and Fermi [4] for calculating atomic properties based purely on the electron density $n(r)$. In the first "density functional theory", Thomas and Fermi assumed that the electrons form a homogeneous electron gas satisfying Fermi statistics and the kinetic energy has a simple dependence on the density $n(r)$. The TF equations are:

$$\frac{5}{3}C_k n(\mathbf{r})^{\frac{2}{3}} + e^2 \int d\mathbf{r}' \, \frac{n(\mathbf{r}')}{|\mathbf{r}-\mathbf{r}'|} + V_{\rm ext}(\mathbf{r}) + \lambda = 0, \tag{2}$$

where $C_k = 3\hbar^2(3\pi^2)^{\frac{2}{3}}/(10m)$, $V_{\rm ext}$ is the external potential, and λ is the Lagrange multiplier related to the constraint of constant particle number. Dirac noted the necessity of incorporating "exchange" phenomena, as in the Hartree-Fock approach [17], and he included these effects in the "Thomas atom" [5] by means of the potential

$$V_{\rm x}^{\rm Dirac} = -\left(\frac{1}{\pi}\right)\left(3\pi^2 n(\mathbf{r})\right)^{\frac{1}{3}} . \tag{3}$$

This term was derived for a homogeneous gas of density n and should be valid for weak spatial variations of $n(\mathbf{r})$.[2] The modified TF equation is often referred to as the "Thomas-Fermi-Dirac" equation.

The Thomas-Fermi method and its extensions give rough descriptions of the charge density and the electrostatic potential of atoms, and its mathematical properties have attracted considerable attention [18, 19]. However, it has severe deficiencies. The charge density is infinite at the nucleus and decays as r^{-6}, not exponentially, far from it. Teller [20] and others also showed that TF theory does not bind atoms to form molecules or solids, which rules out its use in chemistry or materials science. There is also no shell structure in the TF atom, so that the periodic variation of many properties with changing atomic number Z cannot be reproduced, no ferromagnetism [7], and atoms *shrink* with increasing Z (as $Z^{-1/3}$) [21]. Nevertheless, it may be useful in the context of very dense matter [8].

One point made by Dirac [5], however, has been emphasized by many advocates of the DF method over the years, even if we were unaware of his words of over 80 years ago:

> "Each three-dimensional wave function will give rise to a certain electric density. This electric density is really a matrix, like all dynamical variables in the quantum theory. By adding the electric densities from all the wave functions we can obtain the total electric density for the atom. If we adopt the equations of the self-consistent field as amended for

[2] The exchange energy in a homogeneous (spin-polarized!) electron gas had been derived by Bloch [16] in 1929.

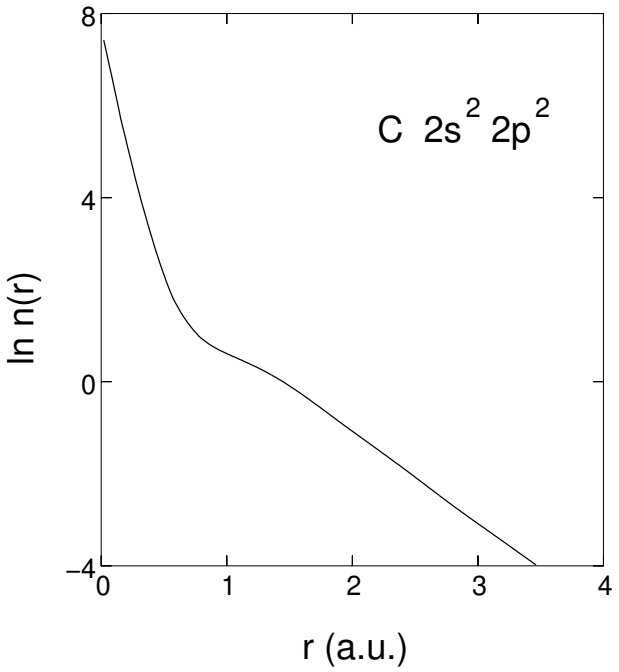

Fig. 1: *Logarithm of spherical average of density in ground state of C atom as a function of the distance from the nucleus (atomic units) [7].*

> exchange, then this total electric density (the matrix) has one important property, namely, if the value of the total electric density at any time is given, then its value at any later time is determined by the equations of motion. This means that *the whole state of the atom is completely determined by this electric density; it is not necessary to specify the individual three-dimensional wave functions that make up the total electric density.* Thus one can deal with any number of electrons by working with just one matrix density function."

The italics are in the original. The derivation is based on the "self-consistent field" or Hartree-Fock approximation, and the "matrix density function" is known today as the one-particle density matrix, but the observation that the density follows the equations of motion is much in the spirit of Ehrenfest's theorem [22], which has wider validity. Ehrenfest had proved in 1927 what I have seen referred to as the "time-dependent Hellmann-Feynman theorem", namely that the acceleration of a quantum wave packet that does not spread satisfied Newton's equations of motion.

The central role played by the density means that we must know what it looks like in real systems. Figure 1 shows that the spherically averaged *density* in the ground state of the carbon atom falls monotonically from the nucleus and does not show the radial oscillations that occur if we plot $r^2 n(r)$. The charge density in small molecules is also rather featureless, with maxima at the nuclei, saddle points along the bonds, and a generally monotonic decay from both. The electron density in molecules and solids also shows relatively small departures from the overlapped densities of the constituent atoms. Energy differences, including binding, ionization, and cohesive energies, are the focus of much DF work and result from subtle changes in relatively featureless density distributions. It is amazing that this is sufficient to determine ground state properties.

3 An "approximate practical method"

The basis of a quantum theory of atoms, molecules, and solids was in place at the beginning of the 1930's. Linear combinations of atomic orbitals formed molecular orbitals, from which determinantal functions could be constructed, and linear combinations of determinants ("configuration interaction") would provide approximations to the complete wave function. Dirac had noted already, however, that this procedure could not be implemented in practice, so that approximations are essential. Furthermore, numerical techniques for solving the Schrödinger equation in extended systems were still to be developed.

Wigner and Seitz [23] developed a method for treating the self-consistent problems in crystals, and the "Wigner-Seitz cell" is known to all condensed matter physicists. The first application to metallic sodium used a pseudopotential for the Na ion, and calculations of the lattice constant, cohesive energy, and compressibility gave satisfactory results. Of particular interest for our purposes, however, is the calculation of the probability of finding electrons with parallel spins a distance r apart (Fig. 2). This function obtains its half-value for $r = 1.79\,d'$ or $0.460\,d$ for a body-centered cubic lattice with cube edge d, which is close to the radius of the "Wigner-Seitz sphere" $(\frac{3}{8\pi})^{\frac{1}{3}}\,d = 0.492\,d$. The exclusion principle means then that two electrons with parallel pins will very rarely be at the same ion. This argument does not depend significantly on the potential and should apply to a Fermi gas subject to periodic boundary conditions [23]. The corresponding curves for spin up and spin down electrons, as well as for both spins combined, were discussed in the 1934 review article of Slater [24].

The picture that results is simple and appealing: the exclusion principle means that an electron with a given spin produces a surrounding region where there is a deficiency of charge of the same spin. This region contains one unit charge and is referred to as the "Fermi" [23] or "exchange" hole [25]. In the Hartree-Fock scheme, the exchange hole is different for each electronic function, but Slater [25] developed a simplified "exchange potential" that depended only on the density

$$V_{\rm x}^{\rm Slater} = -\left(\frac{3}{2\pi}\right)\left(3\pi^2 n(r)\right)^{\frac{1}{3}}\,. \tag{4}$$

The Slater approximation (4) was proposed at the time that electronic computers were becoming available for electronic structure calculations and proved to be very useful in practice. Methods for solving the Schrödinger equation had been developed—but not implemented—somewhat earlier, including the augmented plane wave (APW) [26] and Korringa-Kohn-Rostoker approaches [27, 28].

The exchange potential of Slater (4) is 3/2 times that derived by Dirac and Bloch (3) for a homogeneous electron gas, but Slater [29] pointed out that an effective potential proportional to the cube root of the density could be obtained by arguments based on the exchange hole that do not depend on the free electron gas arguments used in the original derivation [25]. The exchange hole discussed above for a spin up electron contains a single electron. If we assume

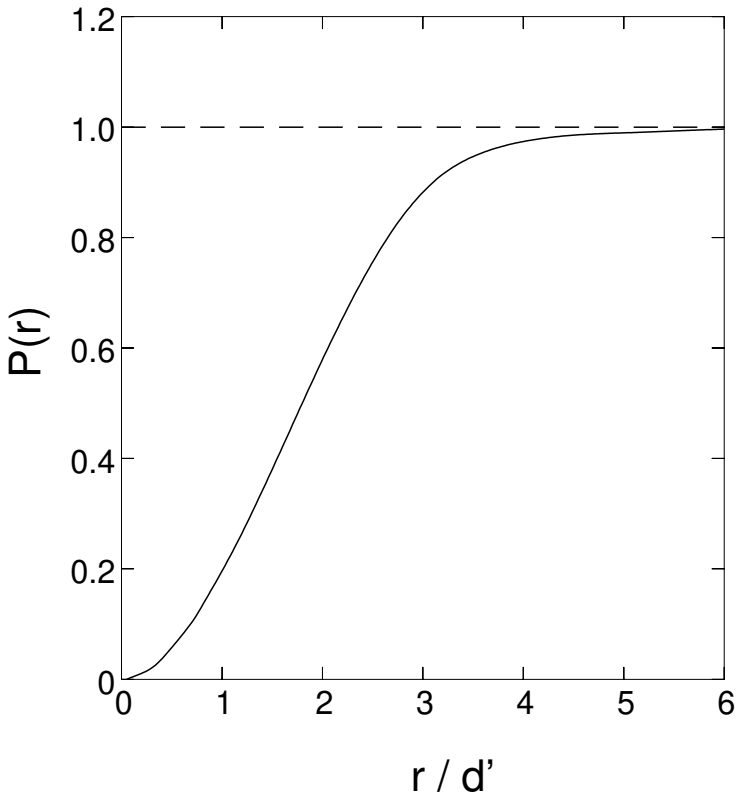

Fig. 2: *Probability that electrons in Na metal with parallel spins are r/d' apart ($d'^3 = V_0/(3\pi^2)$, where V_0 is the atomic volume). After Wigner and Seitz [23].*

that it can be approximated by a sphere of radius $R_\uparrow$, then

$$\left(\frac{4\pi}{3}\right) R_\uparrow^3 n_\uparrow = 1 \;\; ; \;\; R_\uparrow = \left(\frac{3}{4\pi n_\uparrow}\right)^{\frac{1}{3}} \tag{5}$$

where $n_\uparrow$ is the density of spin up electrons. Since the electrostatic potential at the center of such a spherical charge is proportional to $1/R_\uparrow$, the exchange potential will be proportional to $n_\uparrow^{\frac{1}{3}}$. This argument was used by Slater to counter a misconception (unfortunately still widespread) that local density approximations based on the homogeneous electron gas are only appropriate if the electron density is nearly homogeneous.

In 1954, Gáspár [30] questioned the prefactor of the effective exchange potential (Eq. 4). If one varies the spin orbitals to minimize the total energy in the Thomas-Fermi-Dirac form, one obtains a coefficient just $\frac{2}{3}$ as large. Gáspár applied this approximation to the Cu^+ ion and found good agreement with Hartree-Fock eigenfunctions and eigenvalues. Slater noted that Gáspár's method was "more reasonable than mine" [31], but the larger value was used in most calculations in the following years.

4 Electron density functional formalism

The variational principle on the energy was the basis of the derivation of the density functional formalism given by Hohenberg and Kohn (HK) [32]. First, they showed that there is a one-to-one relationship between the external potential $V_{\rm ext}(\mathbf{r})$ and the (nondegenerate) ground state (GS) wave function Ψ, and then that there is a one-to-one relationship between Ψ and the ground state density $n(\mathbf{r})$ of an N-electron system,

$$n(\mathbf{r}) = N \int d\mathbf{r}_2..d\mathbf{r}_N \, \Psi^*(\mathbf{r}, \mathbf{r}_2, ..\mathbf{r}_N) \, \Psi(\mathbf{r}, \mathbf{r}_2, ..\mathbf{r}_N) \, , \tag{6}$$

where the spin coordinates are not shown explicitly. Knowledge of the density then determines the external potential to within a constant, so that all terms in the Hamiltonian are known. Since the Hamiltonian operator determines completely all states of the system, $n(\mathbf{r})$ determines excited states as well as the ground state.

These ideas can be applied to the total energy using the variational principle. For this purpose, HK defined the functional $F[n(\mathbf{r})]$, which is "universal" in the sense that it is valid for any external potential $V_{\rm ext}$,

$$F[n] = \big\langle \Psi_n \big| T + V_{\rm ee} \big| \Psi_n \big\rangle, \tag{7}$$

and showed that the energy functional $E[n, V_{\rm ext}]$ satisfies a variational principle

$$E_{\rm GS} = \min_{n(\mathbf{r})} \, E[n, V_{\rm ext}], \tag{8}$$

where

$$E[n, V_{\rm ext}] = \int d\mathbf{r} \; V_{\rm ext}(\mathbf{r}) \; n(\mathbf{r}) + F[n] \, . \tag{9}$$

The minimization is performed in HK over all non-degenerate densities that can be derived from the ground state of some external potential ("V-representable"). Levy [33] generalized this to a minimization over all densities, including degeneracies.

4.1 Single-particle description of a many-electron system.

The task of finding good approximations to the energy functional $E[n]$ is simplified greatly if we use the decomposition introduced by Kohn and Sham [34],

$$E[n] = T_0[n] + \int d\mathbf{r} \; n(\mathbf{r}) \Big(V_{\rm ext}(\mathbf{r}) + \frac{1}{2} \Phi(\mathbf{r}) \Big) + E_{\rm xc}[n]. \tag{10}$$

T_0 is the kinetic energy that a system with density n would have if there were no electron-electron interactions, Φ is the classical Coulomb potential for electrons, and $E_{\rm xc}$ *defines* the exchange-correlation energy. T_0 is not the true kinetic energy T, but it is of comparable magnitude and is treated here without approximation. This removes many of the deficiencies of the Thomas-Fermi approach, such as the lack of a shell structure of atoms or the absence of chemical bonding in molecules and solids. In the expression (10) all terms other than the exchange-correlation energy $E_{\rm xc}$ can be evaluated exactly, so that approximations for this term are crucial in density functional applications.

The variational principle applied to (10) yields

$$\frac{\delta E[n]}{\delta n(\mathbf{r})} = \frac{\delta T_0}{\delta n(\mathbf{r})} + V_{\rm ext}(\mathbf{r}) + \Phi(\mathbf{r}) + \frac{\delta E_{\rm xc}[n]}{\delta n(\mathbf{r})} = \mu, \tag{11}$$

where μ is the Lagrange multiplier associated with the requirement of constant particle number. If we compare this with the corresponding equation for a system with an effective potential $V(\mathbf{r})$ but *without* electron-electron interactions,

$$\frac{\delta E[n]}{\delta n(\mathbf{r})} = \frac{\delta T_0}{\delta n(\mathbf{r})} + V(\mathbf{r}) = \mu, \tag{12}$$

we see that the mathematical problems are identical, provided that

$$V(\mathbf{r}) = V_{\rm ext}(\mathbf{r}) + \Phi(\mathbf{r}) + \frac{\delta E_{\rm xc}[n]}{\delta n(\mathbf{r})}. \tag{13}$$

The solution of Eq. (12) can be found by solving the Schrödinger equation for *non-interacting* particles,

$$\left(-\frac{1}{2}\nabla^2 + V(\mathbf{r}) \right) \psi_i(\mathbf{r}) = \epsilon_i \psi_i(\mathbf{r}), \tag{14}$$

yielding

$$n(\mathbf{r}) = \sum_{i=1}^{N} |\psi_i(\mathbf{r})|^2 \tag{15}$$

The condition (13) can be satisfied in a self-consistent procedure.

The solution of this system of equations leads to the energy and density of the lowest state, and all quantities derivable from them. The formalism can be generalized to the lowest state with a given symmetry [35]. Instead of seeking these quantities by determining the wave function of the system of interacting electrons, the DF method reduces the problem to the solution of a single-particle equation of Hartree form. In contrast to the Hartree-Fock potential,

$$V_{\rm HF}\ \psi(\mathbf{r}) = \int d\mathbf{r}'\ V_{\rm HF}(\mathbf{r}, \mathbf{r}')\psi(\mathbf{r}'), \tag{16}$$

the effective potential, $V(\mathbf{r})$ is a *local* (i.e. multiplicative) operator.

The numerical advantages of solving the Kohn-Sham equations [34] are obvious. Efficient methods exist for solving single-particle Schrödinger-like equations with a local effective potential, and there is no restriction to small systems. With a local approximation to $E_{\rm xc}$, the equations can be solved as readily as the Hartree equations. Unlike the Thomas-Fermi method, where the large kinetic energy term is approximated, the valence kinetic energy and the core-valence and valence-valence electrostatic interactions are treated exactly. However, $E_{\rm xc}$ is the difference between the *exact* energy and terms we can evaluate exactly, and approximations are unavoidable.

4.2 Exchange-correlation energy $E_{\rm xc}$ and the xc-hole

Kohn and Sham [34] proposed using the "local density (LD) approximation"

$$E_{\rm xc}^{\rm LD} = \int d\mathbf{r}\; n(\mathbf{r})\; \varepsilon_{\rm xc}[n(\mathbf{r})], \tag{17}$$

where $\varepsilon_{\rm xc}[n]$ is the exchange and correlation energy per particle of a homogeneous electron gas with density n. This approximation is exact in the limits of slowly varying densities and very high densities. The authors noted that this approximation "has no validity" at the "surface" of atoms and in the overlap regions of molecules and concluded [34]:

> "We do not expect an accurate description of chemical bonding."

The generalization to spin-polarized systems is

$$E_{\rm xc}^{\rm LSD} = \int d\mathbf{r}\; n(\mathbf{r})\; \varepsilon_{\rm xc}[n_\uparrow(\mathbf{r}), n_\downarrow(\mathbf{r})], \tag{18}$$

where $\varepsilon_{\rm xc}[n_\uparrow, n_\downarrow]$ is the exchange and correlation energy per particle of a homogeneous, spin-polarized electron gas with spin-up and spin-down densities $n_\uparrow$ and $n_\downarrow$, respectively.[3] The "Xα" approximation

$$E_{\rm x}^{\rm X\alpha} = -\frac{3}{2}\alpha C \int d\mathbf{r}\; \Big((n_\uparrow(\mathbf{r}))^{4/3} + (n_\downarrow(\mathbf{r}))^{4/3} \Big), \tag{19}$$

where $C = 3(3/4\pi)^{1/3}$ was used in numerous calculations in the late 1960s and 1970s. The α-dependence of energy differences for a given atom or molecule is weak for values near $2/3$, the value of Bloch [16], Dirac [5], Gáspár [30] and Kohn and Sham [34]. We have noted that the electron density in molecules and solids is generally far from that of a homogeneous electron gas, and the validity of calculations based on properties of a gas of constant density has often been questioned. We now discuss some general properties of $E_{\rm xc}$ using arguments closely related to the "exchange hole" picture of Wigner and Seitz [23] and Slater [25, 29].

The crucial simplification in the density functional scheme is the relationship between the interacting system, whose energy and density we seek, and the fictitious, non-interacting system for which we solve Eq. (14), (15). This can be studied by considering the interaction $\lambda/|\mathbf{r}-\mathbf{r}'|$ and varying λ from 0 (non-interacting system) to 1 (physical system). This is done in the presence of an external potential V_λ [35], such that the ground state of the Hamiltonian

$$H_\lambda = -\frac{1}{2}\nabla^2 + V_{\rm ext}(\mathbf{r}) + V_\lambda + \lambda V_{\rm ee} \tag{20}$$

has density $n(\mathbf{r})$ for all λ. The exchange-correlation energy of the interacting system can then be expressed as an integral over the coupling constant λ [36]

$$E_{\rm xc} = \frac{1}{2}\int d\mathbf{r}\; n(\mathbf{r}) \int d\mathbf{r}'\; \frac{1}{|\mathbf{r}-\mathbf{r}'|} n_{\rm xc}(\mathbf{r}, \mathbf{r}'-\mathbf{r}), \tag{21}$$

[3] The calculation by Bloch [16] in 1929 of ferromagnetism in a free-electron model of a metal was the first where the exchange energy was expressed as the sum of terms proportional to $n_\uparrow^{4/3}$ and $n_\downarrow^{4/3}$.

with

$$n_{\rm xc}(\mathbf{r},\mathbf{r}'-\mathbf{r}) \equiv n(\mathbf{r}') \int_0^1 d\lambda \left(g(\mathbf{r},\mathbf{r}',\lambda) - 1 \right). \tag{22}$$

The function $g(\mathbf{r},\mathbf{r}',\lambda)$ is the pair correlation function of the system with density $n(\mathbf{r})$ and Coulomb interaction $\lambda V_{\rm ee}$. The exchange-correlation hole $n_{\rm xc}$ describes the fact that an electron at point $\mathbf{r}$ reduces the probability of finding one at $\mathbf{r}'$, and $E_{\rm xc}$ is simply the energy resulting from the interaction between an electron and its exchange-correlation hole. This is a straightforward generalization of the work of Wigner and Seitz [23] and Slater [25] discussed above.
Second, the isotropic nature of the Coulomb interaction $V_{\rm ee}$ has important consequences. A variable substitution $\mathbf{R} \equiv \mathbf{r}'-\mathbf{r}$ in (21) yields

$$E_{\rm xc} = \frac{1}{2} \int d\mathbf{r}\, n(\mathbf{r}) \int_0^\infty dR\, R^2\, \frac{1}{R} \int d\Omega\, n_{\rm xc}(\mathbf{r},\mathbf{R}). \tag{23}$$

Equation (23) shows that the xc-energy depends only on the spherical average of $n_{\rm xc}(\mathbf{r},\mathbf{R})$, so that approximations for $E_{\rm xc}$ can still give an *exact* value, even if the description of the non-spherical parts of $n_{\rm xc}$ is arbitrarily inaccurate. Third, the definition of the pair-correlation function leads to a sum-rule requiring that the xc-hole contains one electron, i.e., for all $\mathbf{r}$,

$$\int d\mathbf{r}'\, n_{\rm xc}(\mathbf{r},\mathbf{r}'-\mathbf{r}) = -1. \tag{24}$$

This means that we can consider $-n_{\rm xc}(\mathbf{r},\mathbf{r}'-\mathbf{r})$ as a normalized weight factor and define the radius of the xc-hole locally for a particular value of $\mathbf{r}$,

$$\left\langle \frac{1}{\mathbf{R}} \right\rangle_{\mathbf{r}} = -\int d\mathbf{R}\, \frac{n_{\rm xc}(\mathbf{r},\mathbf{R})}{|\mathbf{R}|}. \tag{25}$$

This leads to

$$E_{\rm xc} = -\frac{1}{2} \int d\mathbf{r}\, n(\mathbf{r}) \left\langle \frac{1}{\mathbf{R}} \right\rangle_{\mathbf{r}}. \tag{26}$$

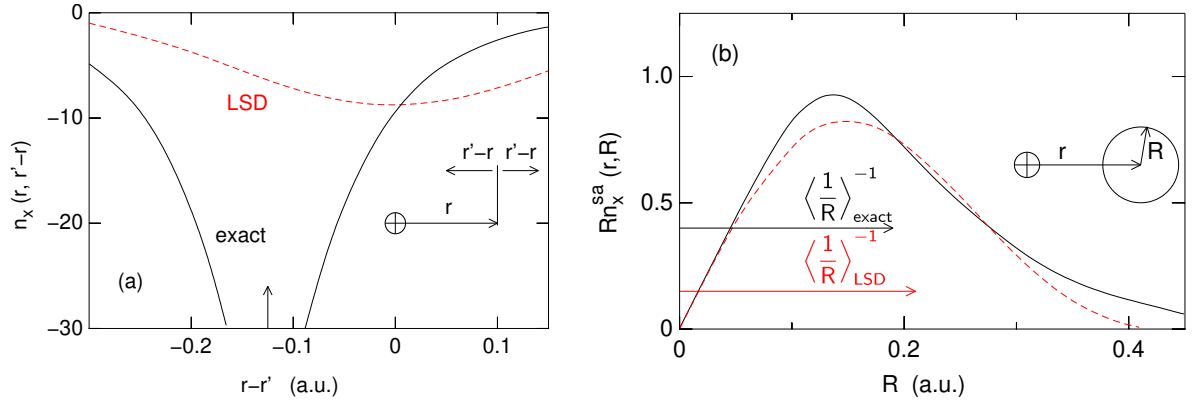

Fig. 3: *Magnitude of exact (solid) and LSD (red, dashed) exchange holes $n_{\rm xc}(\mathbf{r},\mathbf{r}'-\mathbf{r})$ for spin up electrons in an N atom for $\mathbf{r} = 0.13$ a.u. (a) Hole along line through nucleus (arrow) and electron ($\mathbf{r}-\mathbf{r}' = 0$). (b) spherical averages of holes, and $\langle 1/\mathbf{R} \rangle$ [Eq. (25)] [7].*

Provided Equation (24) is satisfied, $E_{\rm xc}$ is determined by the first moment of a function whose second moment we know exactly and depends only weakly on the details of $n_{\rm xc}$ [35]. Provided that the spherical average of the exchange-correlation hole is correct, approximations to $E_{\rm xc}$ can then lead to good total energies, even if other details are described very poorly. This is shown by the example in Figure 3, where the exchange hole in a nitrogen atom is shown for a representative value of $\mathbf{r}$ for both the local density and exact (Hartree-Fock) cases. The holes are qualitatively different: The LD hole is spherically symmetric and centered on the electron, while the exact hole has a large weight at the nucleus and is very asymmetric. Nevertheless, the spherical averages are very similar, and the exchange energies differ by only around 10%.

5 DF theory to 1990

5.1 Condensed matter

Condensed matter physicists were generally pleased to have justification for the "local density" calculations they had been performing for years, and numerous electronic structure theorists moved seamlessly from performing "Xα" or "Hartree-Fock-Slater" calculations into the density functional world (the names of some program packages also changed seamlessly). However, Fig. 4 shows that there was remarkably little impact of DF calculations prior to 1990. Volker Heine, a prominent condensed matter theorist, looked back on the 1960's in this way [37]:

> "Of course at the beginning of the 1960s the big event was the Kohn Hohenberg Sham reformulation of quantum mechanics in terms of density functional theory (DFT). Well, we recognize it now as a big event, but it did not seem so at the time. That was the second big mistake of my life, not to see its importance, but then neither did the authors judging from the talks they gave, nor anyone else. Did you ever wonder why they never did any calculations with it?"

There were also prominent critics of density functional and related computational techniques, and one of the best known solid state theoreticians, Philip Anderson, made devastating comments in 1980 [38]:

> "There is a school which essentially accepts the idea that nothing further is to be learned in terms of genuine fundamentals and all that is left for us to do is calculate. [...] One is left, in order to explain any phenomenon occurring in ordinary matter, only with the problem of doing sufficiently accurate calculations. This is then the idea that I call "The Great Solid State Physics Dream Machine" ... This attitude is closely associated with work in a second field called quantum chemistry."

Anderson associated the "Dream Machine" with the name of John Slater and described the DF method as a "simplified rather mechanical kind of apparatus" that "shows disturbing signs of become a victim of the 'Dream Machine' syndrome" [38]. While noting that DF calculations can be valuable in some contexts, he continued:

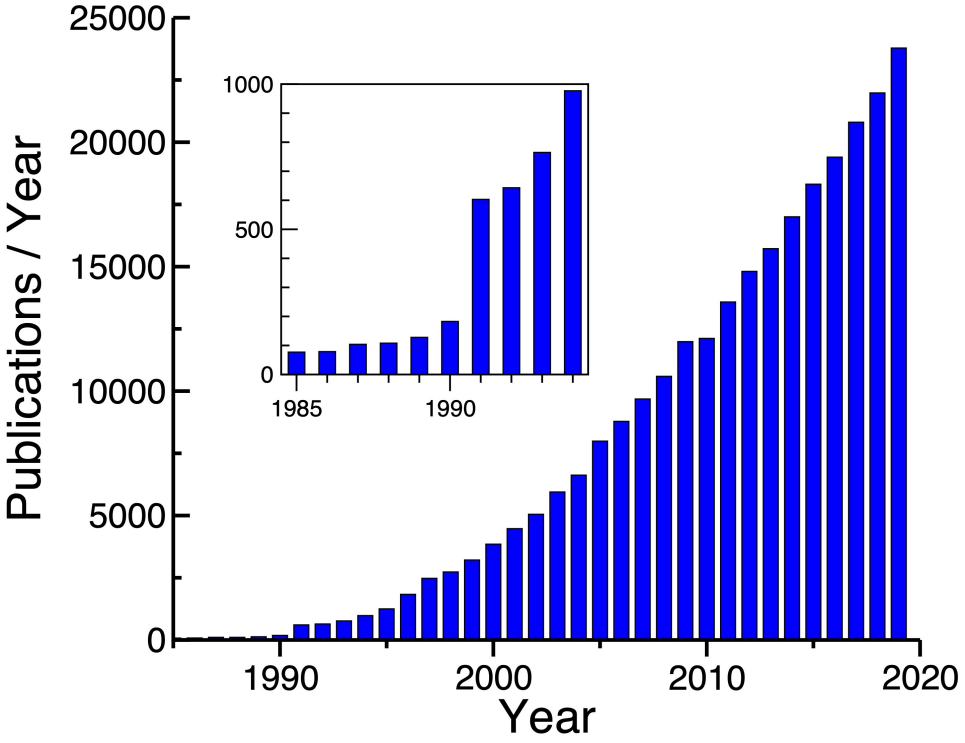

Fig. 4: *Number of publications per year (1980-2019) on topics "density functional" or "DFT", according to Web of Knowledge (June 2020). The inset shows data near 1990 on an expanded scale [39].*

> " . . . a great deal of the physics is concealed inside the machinery of the technique, and that very often once one has the answers that these techniques provide, one is not exactly clear what the source of these answers is. In other words the better the machinery, the more likely it is to conceal the workings of nature, in the sense that it simply gives you the experimental answer without telling you why the experimental answer is true."

These are harsh words, and some DF practitioners are still angry about the damage that they caused. They did, however, apply to some electronic structure calculations at the time, and I return to them in Sec. 7. The increasing availability of computing resources made possible calculations that had previously been inaccessible, and not all users of the method were critical of the approximations involved.

5.2 Chemistry

It took many years for DF calculations to be taken seriously by most chemists, and the reasons were often convincing: (1) Unlike the TF theory, the Kohn-Sham expression for the energy is not really a "functional" of the density, since the kinetic energy term is treated exactly and is defined by an effective potential that leads to the density, (2) the original functional of Hohenberg and Kohn is not even *defined* for all n, because not all densities can be derived from the ground state of some single-particle potential [33, 40], (3) approximations to the exchange-correlation

energy are unavoidable, and their usefulness can be assessed only by trying them out, and (4) there is no *systematic* (perhaps better described as "mechanical") way to approach the exact solution of the Schrödinger equation and, of course, the exact energy.

This last point was (and is) emphasized by many. In principle, the Hartree-Fock method could be extended to multiple determinants ("configuration interaction") and, coupled with a large basis set, lead to the exact wave function and all properties obtainable from it. This is an attractive proposition, and the dramatic improvements in computing power (three orders of magnitude per decade) might make the reservations of Dirac [17] less formidable. It was often emphasized that solutions of the Schrödinger equation led to the "right answer for the right reason." Nevertheless, obtaining numerically exact total energies from calculations of the wave function remains a major challenge to this day, and it is not surprising that several groups looked at alternatives.

Hartree-Fock-Slater calculations (Xα calculations with $\alpha = 0.7$) on small molecules were carried out from the early 1970's, particularly by Evert Jan Baerends and collaborators in Amsterdam, and some of the first DF calculations on small molecules were performed by Olle Gunnarsson [35]. John Harris and I had not expected that the local density approximations would give reasonable results for molecules, but we (with Olle) developed a full-potential LMTO code for small molecules and clusters [41]. These calculations led to good geometries and reasonable binding energies in most cases. In spite of the shortcomings of the local density description of $E_{\rm xc}$, it became possible to perform calculations without adjustable parameters on families of molecules and small clusters that had previously been inaccessible. I was unprepared for so many unexpected and exciting results, my own examples including the trends in the binding energies of group 2 dimers [42, 43] and the structures of small phosphorus clusters [44]. Most condensed matter physicists were neither surprised nor interested, but theoretical chemists remained sceptical or critical, or they ignored these developments entirely. This situation continued throughout the 1980s and into the 1990s.

The Seventh International Congress of Quantum Chemistry in Menton, France, from 2–5 July 1991, marked a major turning point in the fortunes of DF methods in chemistry. Density-related methods were discussed in detail, and communication between their proponents and the sceptics improved. Becke described his development of a non-local exchange functional that promised improvements over local approximations [45], and this approximation was tested for the atomization energies of small molecules immediately after the meeting. Many—including the authors— were surprised by the results [46]:

> "In summary, these initial results indicate that DFT is a promising means of obtaining quantum mechanical atomization energies; here, the DFT methods B-VWN and B-LYP outperformed correlated ab initio methods, which are computationally more expensive."

and [47]

> "The density functional vibration frequencies compare favorably with the ab initio results, while for atomization energies two of the DFT methods give excellent agreement with experiment and are clearly superior to all other methods considered."

The ab initio methods mentioned were Hartree-Fock, second order Møller-Plesset (MP2), and quadratic configuration interaction with single and double substitutions (QCISD). In addition to the growing body of results on molecules and clusters that were beyond the scope of calculations of correlated wave functions, this change in attitude by one of the most prominent theoretical chemists led to a dramatically new attitude towards the DF method in chemistry.

5.3 Situation in 1990

The number of citations to density functional theory and related topics was very small prior to 1990 and exploded thereafter (see Figure 4). However, work was already in place by 1990 that has proved to be crucial to the ultimate acceptance of the method, and I now outline some of it. More details can be found elsewhere [8, 48].

The generalizations to finite temperatures and to spin systems were carried out soon after the original work of Hohenberg and Kohn [32]. The former was provided by Mermin [49], who showed that, in a grand canonical ensemble at given temperature T and chemical potential μ, the equilibrium density is determined by the external potential $V_{\rm ext}$, and the equilibrium density minimizes the grand potential. Single-particle equations can be derived for a fictitious system with kinetic energy T_0 and entropy S_0, with $E_{\rm xc}$ replaced by the exchange-correlation contribution to the free energy.

The extension to spin systems [50] or an external magnetic field requires the introduction of the spin indices α of the one-electron operators $\psi_\alpha(\mathbf{r})$ and replacing $V_{\rm ext}$ by $V_{\rm ext}^{\alpha\beta}(\mathbf{r})$, and the charge density $n(\mathbf{r})$ by the density matrix $\rho_{\alpha\beta}(\mathbf{r}) = \langle\Psi|\psi_\beta^+(\mathbf{r})\psi_\alpha(\mathbf{r})|\Psi\rangle$. All ground state properties are functionals of $\rho_{\alpha\beta}$, and E is stationary with respect to variations in $\rho_{\alpha\beta}$. The expression for the energy $E_{\rm xc}$ is analogous to Equations (21), (22). A current- and spin density functional theory of electronic systems in strong magnetic fields was formulated by Vignale and Rasolt [51]. Time-dependent density functional theory, which has proved to be invaluable in discussing excited states, was described by Runge and Gross [52].

Most of the early DF calculations on small clusters and molecules used the LD and/or LSD approximations. Although the results were generally encouraging, it was soon clear that local density calculations can lead to unacceptable errors. Examples were the exchange energy difference between states with different nodal structures [53], including the s-p promotion energies in first-row atoms, particularly O and F. Dispersion forces—the weak, non-local interactions between closed shells systems—are a particular problem for such approximations. The long-range interaction between separated atoms or molecules is absent, and yet the LD approximation *overestimates* the binding energy in many such systems, e.g. He_2 [42]. It is not surprising that new approximations were developed, and corrections involving density gradients were soon available for the correlation [54, 55] and exchange energies [45]. The semi-empirical exchange energy approximation of Becke [45] had the correct asymptotic behavior for atoms.

The combination of DF calculations with molecular dynamics (Car-Parrinello method) [56] made simulations of bulk systems at elevated temperatures possible, and simulated annealing techniques could be used to study the energy surfaces of molecules and clusters. My 1991

article [57] showed that unexpected structures could result. An essential part of DF work prior to 1990 was, of course, the gradual generation of a data base of results for molecules and clusters.

6 1990–present

There have been over 200,000 publications on the topics "density functional" and "DFT" between 1990 and June 2020 (Figure 4), and I leave detailed surveys of this vast literature to others. I mention here some aspects that should be of general interest and give an example of the possibilities provided by the combination of DF calculations with molecular dynamics.

6.1 Progress and problems

One of the first signs of growing acceptance of DF methods in chemistry was the incorporation of such calculations into popular ab initio program packages, with GAUSSIAN leading the way. It seems that Michael Frisch, first author of that package, was a willing convert. At the end of a talk at the ACS National Meeting in San Francisco (13 April 1997) on "Ab initio calculations of vibrational circular dichroism and infrared spectra using SCF, MP2, and density functional theories for a series of molecules," an unknown (to me) member of the audience asked:

> "What about Hartree-Fock?"

Michael Frisch answered:

> "It does not matter what you want to calculate, and it does not matter what functional you use; density functional results are always better than Hartree-Fock."

The availability of such codes and the possibility of comparing the results of different types of calculation were important to establishing the credentials of DF calculations in chemistry.
There has been progress in all the above areas. Time-dependent DF theory has become a standard way to calculate excited states and is an option in most DF program packages. The combination of density functional calculations with molecular dynamics is likewise a part of many such packages. The combination of DF calculations for a chemically active region with classical molecular dynamics for the surrounds (the "QM/MM approach") [58] has found applications in many systems in biology, organic and solid state chemistry [59]. Classical force fields that lead to simulations with near-DF accuracy can be developed by a neural network or machine-learning representation of the results of (very many) DF calculations on small systems [60], and this has been an active field of research recently [61, 62]. Reviews of orbital-dependent functionals and constrained DF theory are provided in [8].
These and other developments are very welcome, but the most contentious issue has been the development of approximations to the exchange-correlation energy that overcome the weaknesses of the local density approximations. The LD [Eq. (17)] and LSD [Eq. (18)] approximations lead to overbinding of many molecules, poor exchange energy differences if the nodal structures of

the orbitals change, and the Kohn-Sham eigenvalues often underestimate measured optical band gaps significantly. Nevertheless, calculations that used them provided insight into many physical problems, and the reasons for the errors (and ways to assess their magnitude) became clear. However, if insight is not enough and reliable *numbers* are needed, improved approximations are necessary.

The first generalized gradient approximations [45, 54, 55] did lead to better results, and hybrid functionals including exact exchange were introduced by Becke in 1993 [63]. This form of E_{x} has three parameters, and its combination with E_{c} of Lee, Yang, and Parr [55] (B3LYP) remains one of the most common approximations used in chemical applications [64]. Many other empirical and hybrid functionals have been developed since, with parameters usually fit to thermochemical data for particular groups of molecules. The use of experimental data for fitting functional forms is understandable [65]. The additional parameters led to improvement over the LD and LSD results, and the use of "training sets" of atomic and molecular systems to optimize the parameters improved the calculated results for particular sets of molecules [66].

An alternative path has been followed by others, particular Perdew and collaborators, who developed a sequence ("Jacob's ladder") of approximations without experimental input, where each "rung" built on the experience of lower level and satisfies particular physical constraints. The gradient corrected form of Perdew, Burke, and Ernzerhof [67] (PBE) incorporates the LSD form below it, and the "meta-GGA" form of Tao, Perdew, Staroverov, and Scuseria (TPSS) [68], where $n_{\uparrow}$ and $n_{\downarrow}$ are joined by their gradients and the kinetic energy density of the occupied Kohn-Sham orbitals, built on both. The agreement with experiment improves (and the complexity of the calculations increases) as one climbs the "ladder" [69].

It should be emphasized that the Jacob's ladder approach is systematic and not empirical [70]. Starting with a proof of the existence of a functional, we can derive formally exact relationships that we can develop into constraints on approximate forms. If these forms are flexible enough, we can fit their free parameters to appropriate norms of energies or densities. These should not include binding energies, which are always susceptible to error cancellation between exchange and correlation. A recent member of the family is the "SCAN" (strongly constrained and appropriately normed) semilocal functional of Sun et al. [71]. Medvedev et al. [70] note that many (empirically fitted) functionals developed since the year 2000 lead to improved energies but *densities* that are more removed from the exact results.

Two areas have remained particular challenges for DF calculations. The first are the weak dispersion or van der Waals forces mentioned above, where there has been substantial progress during recent years. The development of a functional that changes seamlessly on going from weakly interacting units to a combined system has been a goal of many, and one successful project has been that of Langreth and coworkers [72]. Their functional incorporates results for electron gas slabs and the electron gas itself, is free of experimental input, and has been implemented in several program packages. An empirical correction to DF results has been made by Grimme [73], an alternative has been suggested by Tkatchenko and Scheffler [74].

"Strongly correlated" systems often involve transition element or rare earth atoms, and the potential energy can dominate over the kinetic energy. Local density approximations can give

qualitatively incorrect descriptions of these materials, and the use of model Hamiltonians has been a popular way to avoid them. A common approach has been to add an on-site Coulomb repulsion ("Hubbard U") in the "LSD+U" scheme [75]. The parameter U can be estimated within a DF framework [76] or fit to experiment.

There are developments in the quantum Monte Carlo (QMC) studies of *interacting* electron systems that are relevant for DF work. The full configuration interaction (FCI) implementation of QMC uses Monte Carlo sampling of Slater determinants and circumvents the Fermion sign problem. It has been applied to the homogeneous electron gas [77] and to simple solids [78]. For a recent application to the solid phases of hydrogen under pressure, see [79]. Condensed matter scientists have much experience with periodic boundary conditions and plane wave orbital expansions, and this has aided the implementation of the method in extended systems. Another example is the reformulation of the constrained search approach in DF theory [33, 40] in terms of the density *and* the $(N-1)$-conditional probability density, which can be treated by ground state path integral QMC [80]. It remains to be seen whether the computational demands usually associated with QMC can be reduced.

The terms "ab initio" and "first principles" are used differently in the "chemical" and "materials" worlds. For most chemists, the expressions means solutions of the Schrödinger equation for the system of interacting electrons (e.g. by QMC), for materials scientists it can be a DF calculation without (or even with) adjustable parameters. I carry out "density functional" calculations and describe them as such, and I am happy to use the term "ab initio" for solutions of the Schrödinger equation, as done by chemists.

6.2 An application

In 1871, Charles Darwin saw the formation of protein molecules under extreme—prebiotic—conditions as a possible path of evolution of life on Earth [81]:

> " ...But if (and what a big if) we could conceive in some warm little pond with all sorts of ammonia and phosphoric salts,—light, heat, electricity, &c present, that a protein compound was chemically formed, ready to undergo still more complex changes, at the present day such matter would be instantly devoured, or absorbed, which would not have been the case before living creatures were formed."

DF simulations can be used to test whether biological molecules can be produced by chemical processes that do not require biological synthesis machines like ribosomes. Schreiner et al. [82] studied possible reactions of N-carboxy anhydrides (a form of activated amino acids) in water under high pressures and temperatures in the presence of pyrites, FeS_2 (the controversial "iron-sulfur world" of Wächtershäuser [83]). The presence of an FeS_2 surface changes the free energetics of the steps of the carbonyl sulfide (COS)-mediated polymerization of glycine carried out under different thermodynamic conditions (Fig. 5), and it stabilizes the peptide product against hydrolysis.

The reactions studied are just a few of many possible scenarios for the production of molecules that are essential to life on Earth, but they demonstrate the value of simulations under conditions

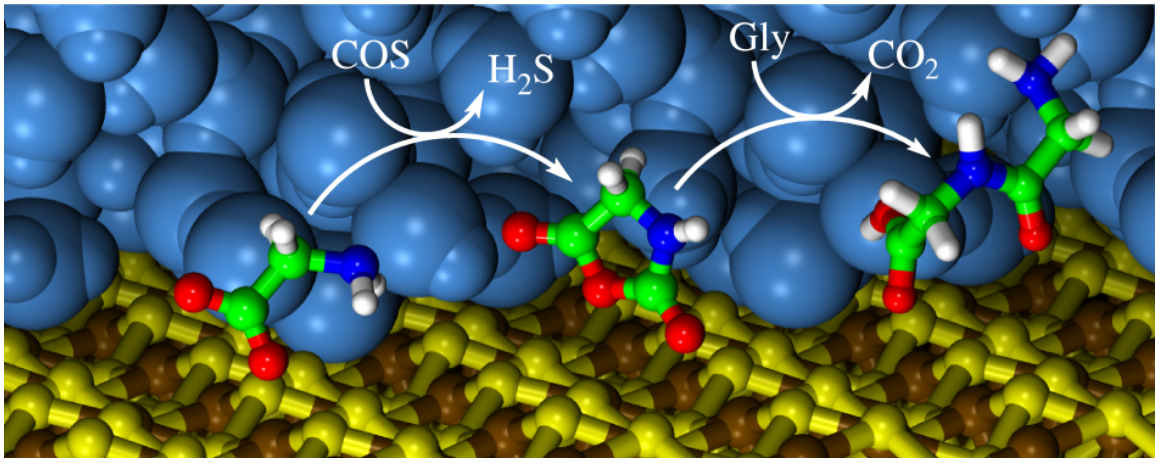

Fig. 5: *(Schematic) Glycine (left), activated glycine (center), and the glycine-glycine dipeptide (right) between an FeS_2 surface (below) and water (blue). COS: carbonyl sulfide.*

that are difficult to attain experimentally. They also show that simulations without adjustable parameters can be performed on biological systems that were absolutely out of the question with earlier generations of computers. Of course, there are many such systems for which the simulation sample sizes currently accessible with DF methods are simply inadequate. Classical force fields with appropriately chosen parameters are likely to remain the method of choice for such systems for some time yet.

7 Summary. Quo vadis?

The astonishing growth of density functional calculations since 1990 resulted in the award of the 1998 Nobel Prize for Chemistry to Walter Kohn. Although he noted that "very deep problems" remain, Philip Anderson felt that this award may indicate that [2]

> "the labours and controversies [...] in understanding the chemical binding in materials had finally come to a resolution in favor of 'LDA' and the modern computer".

The LD and LSD approximations have well documented drawbacks, and the resulting *numbers* (binding energies, band gaps, ...) should be treated with caution. However, the approximations satisfy important physical criteria, such as the sum-rule on the exchange-correlation hole, and our long experience with them helps us to judge when the results may be wrong and by how much. The bonding *patterns* are correct in most cases, which is no doubt one reason why LD approximations and their modifications are still used. They make possible the simultaneous study of numerous related systems, such as families of molecules or materials, with the computational resources needed to determine the wave function of a single much smaller system.
Figure 4 shows that density functional theory will be with us for the foreseeable future, and we can be sure that some exciting results lie ahead. Why then should two of the most cited workers in the field have serious reservations about the future of DF theory? Kieron Burke [64] wrote that "it is clearly both the best of times and the worst of times for DFT" and wondered whether

it is time for a "paradigm shift". A newcomer to the field might indeed despair of understanding why one of the countless approximations for $E_{\rm xc}$, even those with a sound physical basis, should be favored over another, or the real physical reasons behind a particular result.

The concerns of Axel Becke [84] are just as real. It is obvious that great progress has been made in applying DF methods to systems that seemed beyond us only 10 or 15 years ago, and the use of Hartree-Fock-like exchange in many modern functionals has helped communication between the different fields where DF methods are used. However, Becke (and many others, including me) have focused for years on the "Kohn-Sham" version of DF theory ("occupied orbitals only"), which is a major reason for the popularity of the method. Should we move our focus away from the relatively featureless electron density with its small and subtle changes? Can the combination with density matrix functional methods lead to a new breakthrough? Will the inherent accuracy of wave function-based methods prove to be decisive as computational resources expand?[4] Many years ago, a colleague predicted that DF methods would ultimately lose out to solutions of the Schrödinger equation as computer power increased. He was not impressed by my view that DF calculations would always be far ahead in the size of system we could calculate (I think I said 5–10 years, but it is more), and he moved on. I stayed.

The comments by Burke and Becke were made some years ago, but not everyone noticed them. The number of DF applications continues to rise (Fig. 4), and there are developments in important areas, such as functionals for use with "orbital-free" calculations [85] or understanding range-separated hybrid functionals [86]. Nevertheless, there is still much debate and little consensus on the "best" functional approximations, and the search for schemes that produce better *numbers* automatically continues. Comparisons of the results of calculations with those of other approximations and with experiment abound. Are DF calculations in chemistry and materials science now following the "Dream Machine" scenario foreseen for the solid state world by Anderson in 1980 [38]?

Density functional theory deserves better than to be a background justification for empirical curve fitting, which implies a lack of confidence in the theory, or the development of a chain of approximations seeking the "right" numbers, with less concern for their physical origin. Its long and fascinating history involves some of the best known names in physics. It may not provide precise answers to some questions using simple descriptions of the exchange-correlation energy, but its ability to outperform methods that seek exact solutions of the Schrödinger equation is not threatened. We shall continue to obtain insight into all sorts of problems that we cannot imagine today.

[4] The fundamental limitations of wave function based methods are discussed by [1]. He noted that "in chemistry DFT complements traditional wave function based methods particularly for systems with very many atoms ($\geq$ 10)."

References

[1] W. Kohn, Rev. Mod. Phys. **71**, 1253 (1999)

[2] P.W. Anderson: *More and different. Notes from a thoughtful curmudgeon* (World Scientific, Singapore, 2011)

[3] L.H. Thomas, Proc. Camb. Phil. Soc. **23**, 542 (1927)

[4] E. Fermi, Z. Physik **48**, 73 (1928)

[5] P.A.M. Dirac, Proc. Camb. Phil. Soc. **26**, 376 (1930)

[6] F.H.C. Crick: *What mad pursuit* (Penguin, London, 1988), p. 150

[7] R.O. Jones, O. Gunnarsson, Rev. Mod. Phys. **61**, 689 (1989)

[8] R.O. Jones, Rev. Mod. Phys. **87**, 897 (2015)

[9] R.O. Jones, J. Phys.: Condens. Matter **30**, 153001 (2018)

[10] G. Segrè: *Faust in Copenhagen: A struggle for the soul of physics* (Jonathan Cape, London, 2007)

[11] G. Farmelo: *The Strangest Man. The Hidden Life of Paul Dirac, Quantum Genius* (Faber and Faber, London, 2009)

[12] D.R. Hartree, Proc. Camb. Phil. Soc. **24**, 89,111 (1928)

[13] J.C. Slater, Phys. Rev. **35**, 210 (1930)

[14] V. Fock, Z. Physik **61**, 126 (1930)

[15] J. C. Slater, Phys. Rev. **34**, 1293 (1929)

[16] F. Bloch, Z. Physik **57**, 545 (1929)

[17] P.A.M. Dirac, Proc. Roy. Soc. (London) A **123**, 714 (1929)

[18] E.H. Lieb, Rev. Mod. Phys. **53**, 601 (1981)

[19] L. Spruch, Rev. Mod. Phys. **63**, 151 (1991)

[20] E. Teller, Rev. Mod. Phys. **34**, 627 (1962)

[21] E.H. Lieb, B. Simon, Phys. Rev. Lett. **31**, 681 (1973)

[22] P. Ehrenfest, Z. Physik A **45**, 455 (1927)

[23] E. Wigner, F. Seitz, Phys. Rev. **43**, 804 (1933); Phys. Rev. **46**, 509 (1934)

[24] J.C. Slater, Rev. Mod. Phys. **6**, 209 (1934)

[25] J.C. Slater, Phys. Rev. **81**, 385 (1951)

[26] J.C. Slater, Phys. Rev. **51**, 846 (1937)

[27] J. Korringa, Physica **13**, 392 (1947)

[28] W. Kohn, N. Rostoker, Phys. Rev. **94**, 111 (1954)

[29] J.C. Slater, Phys. Rev. **165**, 658 (1968)

[30] R. Gáspár, Acta Phys. Hung. **3**, 263 (1954)

[31] J.C. Slater, in *The World of Quantum Chemistry*, R. Daudel, B. Pullman (eds.), (D. Reidel, Dordrecht, 1974), pp. 3–15

[32] P. Hohenberg, W. Kohn, Phys.Rev. **136**, B864 (1964)

[33] M. Levy, Proc. Nat. Acad. Sci. (USA), **76**, 6062 (1979)

[34] W. Kohn, L.J. Sham, Phys. Rev. **140**, A1133 (1965)

[35] O. Gunnarsson, B.I. Lundqvist, Phys. Rev. B **13**, 4274 (1976)

[36] J. Harris, R.O. Jones, J. Phys. F **4**, 1170 (1974)

[37] V. Heine, in Ψ_k *Newsletter*, Ab Initio (from Electronic Structure) Calculations of Complex Processes in Materials, *50*, 7–19 (April 2002)
`www.psi-k.org/newsletters/News_50/newsletter_50.pdf`

[38] P.W. Anderson, La Recherche **11**, 98 (1980). The English language version of this article was never published. The quote is from the English preprint I have.

[39] Many thanks to Phivos Mavropoulos, private communication

[40] See also E.H. Lieb, Int. J. Quantum Chem. **24**, 243 (1983)

[41] O. Gunnarsson, J. Harris, R.O. Jones, J. Chem. Phys. **67**, 3970 (1977)

[42] R.O. Jones, J. Chem. Phys. **71**, 1300 (1979)

[43] R.O. Jones in *Strongly Correlated Systems*, Springer Series in Solid-State Sciences 171, A. Avella, F. Mancini (eds.) (Springer-Verlag, Berlin Heidelberg, 2012), pp. 1-28

[44] R.O. Jones, D. Hohl, J. Chem. Phys. **92**, 6710 (1990)

[45] A.D. Becke, Phys. Rev. A **38**, 3098 (1988)

[46] B.G. Johnson, P.M.W. Gill, J.A. Pople, J. Chem. Phys. **97**, 7846 (1992)

[47] B.G. Johnson, P.M.W. Gill, J.A. Pople, J. Chem. Phys. **98**, 5612 (1993)

[48] See, for example, R.M. Dreizler, E.K.U. Gross: *Density Functional Theory* (Springer-Verlag, Berlin Heidelberg, 1990)

[49] N.D. Mermin, Phys. Rev. **137**, A1441 (1965)

[50] U. von Barth, L. Hedin, J. Phys. C: Solid State Phys. **5**, 1629 (1972)

[51] G. Vignale, M. Rasolt, Phys. Rev. B **37**, 10685 (1978)

[52] E. Runge, E.K.U. Gross, Phys. Rev. Lett. **52**, 997 (1984)

[53] O. Gunnarsson, R.O. Jones, Phys. Rev. B **31**, 7588 (1985)

[54] J.P. Perdew, Phys. Rev. B **33**, 8822 (1986)

[55] C.T. Lee, W.T. Yang, R.G. Parr, Phys. Rev. B **37**, 785 (1988)

[56] R. Car, M. Parrinello, Phys. Rev. Lett. **55**, 2471 (1985)

[57] R.O. Jones, Angew. Chemie **103**, 647 (1991); Angew. Chemie Int. Ed. **30**, 630 (1991)

[58] See, for example, P. Carloni, U. Röthlisberger, M. Parrinello, Acc. Chem. Res. **35**, 455 (2002)

[59] H. Lin, D.G. Truhlar, Theor. Chem. Acc. **117**, 185 (2007)

[60] J. Behler, M. Parrinello, Phys. Rev. Lett. **97**, 146401 (2007)

[61] G.C. Sosso, M. Salvalaglio, J. Behler, M. Bernasconi, and M. Parrinello, J. Phys. Chem. C **119**, 6428 (2015)

[62] F.C. Mocanu, K. Konstantinou, T.H. Lee, N. Bernstein, V.L. Deringer, G. Csányi, and S.R. Elliott, J. Phys. Chem. B **122**, 8998 (2018)

[63] A.D. Becke, J. Chem. Phys. **98**, 5648 (1993)

[64] K. Burke, J. Chem. Phys. **136**, 150901 (2012)

[65] A.D. Boese, N.C. Handy, J. Chem. Phys. **114**, 5497 (2001)

[66] Y. Zhao, D.G. Truhlar, Acc. Chem. Res. **41**, 157 (2008), and references therein

[67] J.P. Perdew, K. Burke, M. Ernzerhof, Phys. Rev. Lett. **77**, 3865 (1996)

[68] J. Tao, J.P. Perdew, V.N. Staroverov, G.E. Scuseria, Phys. Rev. Lett. **91**, 146401 (2003)

[69] See, for example, F. Furche, J.P. Perdew, J. Chem. Phys. **124**, 044103 (2006)

[70] M.G. Medvedev, I.S. Bushmarinov, J. Sun, J.P. Perdew, and K.A. Lyssenko, Science **355**, 49 (2017)

[71] J. Sun, A. Ruzsinszky, and J.P. Perdew, Phys. Rev. Lett. **115**, 036401 (2015)

[72] M. Dion, H. Rydberg, E. Schröder, D.C. Langreth, B.I. Lundqvist, Phys. Rev. Lett. **92**, 246401 (2004)

[73] S. Grimme, J. Comput. Chem. **27**, 1787 (2006)

[74] A. Tkatchenko, M. Scheffler, Phys. Rev. Lett. **102**, 073005 (2009)

[75] V.I. Anisimov, F. Aryasetiawan, A.I. Lichtenstein, J. Phys.: Condens. Matter **9**, 767 (1997)

[76] M. Cococcioni, S. de Gironcoli, Phys. Rev. B **71**, 035105 (2005), and references therein

[77] J.J. Shepherd, G.H. Booth, A. Alavi, J. Chem. Phys. **136**, 244101 (2012)

[78] G.H. Booth, A. Grüneis, G. Kresse, A. Alavi, Nature **453**, 365 (2013)

[79] L. Liao, X.-Z. Li, A. Alavi, and A. Grüneis, NPJ Comput. Mater. **5**, 110 (2019)

[80] L. Delle Site, L.M. Ghiringhelli, D.M. Ceperley, Int. J. Quantum Chem. **113**, 155 (2013)

[81] C. Darwin in *The Life and Letters of Charles Darwin*, Vol. 3, edited by F. Darwin (John Murray, London), p. 18

[82] E. Schreiner, N.N. Nair, C. Wittekindt, and D. Marx, J. Am. Chem. Soc. **133**, 8216 (2011), and references therein

[83] G. Wächtershäuser, Microbiol. Rev. **52**, 452 (1988)

[84] A.D. Becke, J. Chem. Phys. **140**, 18A301 (2014)

[85] K. Luo, V.V. Karasiev, and S.B. Trickey, Phys. Rev. B **98**, 041111 (2018)

[86] T. Aschebrock and S. Kümmel, J. Chem. Phys. **151**, 154108 (2019)

2 Variational Wave Functions for Molecules and Solids

W.M.C. Foulkes
Department of Physics
Imperial College London

Contents

E. Pavarini and E. Koch (eds.)
Topology, Entanglement, and Strong Correlations
Modeling and Simulation Vol. 10
Forschungszentrum Jülich, 2020, ISBN 978-3-95806-466-9
http://www.cond-mat.de/events/correl20

1 Introduction

Chemists and condensed matter physicists are lucky to have a reliable "grand unified theory" — the many-electron Schrödinger equation — capable of describing almost every phenomenon we encounter. If only we were able to solve it! Finding the exact solution is believed to be "NP hard" in general [1], implying that the computational cost almost certainly scales exponentially with N. Until we have access to a working quantum computer, the best we can do is seek good approximate solutions computable at a cost that rises less than exponentially with system size.

Another problem is that our approximate solutions have to be surprisingly accurate to be useful. The energy scale of room-temperature phenomena is $k_B T \approx 0.025\,\text{eV}$ per electron, and the energy differences between competing solid phases can be as small as 0.01 eV per atom [2]. Quantum chemists say that 1 kcal mol^{-1} ($\approx 0.043\,\text{eV}$) is "chemical accuracy" and that methods with errors much larger than this are not good enough to provide quantitative predictions of room temperature chemistry. Yet the natural energy scale built in to the many-electron Schrödinger equation is 1 Hartree ($\approx 27.2\,\text{eV}$) per electron,[1] which is about 630 times larger. The total energy of a medium-sized atom can be hundreds of Hartrees, so we need to be able to calculate energies to at least five significant figures. Describing low-temperature many-body phenomena such as magnetism, superconductivity, heavy fermions, and spin liquids requires another couple of orders of magnitude. Single-precision arithmetic (accurate to about seven significant figures) is not good enough.

Thinking about a simple non-interacting electron gas shows that calculating the properties of solids to very high precision also requires very large simulations. Suppose that you want to reach an accuracy of 0.1 eV per electron in an electron gas with Fermi energy $E_F = 10\,\text{eV} \approx 0.37$ Hartrees. Since

$$E = \frac{1}{2}k^2, \qquad \left[E = \frac{\hbar^2 k^2}{2m} \text{ in MKS units}\right] \tag{1}$$

the energy ratio $E/E_F = 0.01$ implies a wave vector ratio $k/k_F = 0.1$. The Fermi wave vector $k_F = \sqrt{2E_F} \approx 0.86\,a_0^{-1}$, so the wave vector k associated with an accuracy of 0.1 eV is $0.086\,a_0^{-1}$. The corresponding length scale is $2\pi/k \approx 73\,a_0$. Given that the electron density $n = k_F^3/(3\pi^2)$ is around $0.021\,a_0^{-3}$, you need to solve the Schrödinger equation for a simulation cell containing of order $n\lambda^3 \approx 8{,}000$ electrons, which is rarely possible in interacting systems. A great deal of effort has gone into understanding and correcting the finite-size errors that arise when smaller simulation cells are used [3].

The obvious conclusion is that attempting to study chemical reactions by starting from the many-electron Schrödinger equation is a fool's errand; it would be much better to work with

[1] This chapter uses dimensionless equations involving only the numerical values of physical quantities. The numerical values are as measured in Hartree atomic units, where Planck's constant $h = 2\pi$ (so $\hbar = 1$), the permittivity of free space $\epsilon_0 = 1/4\pi$ (so $4\pi\epsilon_0 = 1$), the electron mass $m = 1$, and the elementary charge $e = 1$. Distances are made dimensionless by dividing by the Hartree atomic unit of length, $a_0 = 4\pi\epsilon_0\hbar^2/(me^2) \approx 0.529 \cdot 10^{-10}$ m, which is also known as the Bohr radius. Energies are made dimensionless by dividing by the Hartree atomic unit of energy, $\hbar^2/(ma_0^2) = e^2/(4\pi\epsilon_0 a_0) \approx 27.2\,\text{eV}$.

a low-energy effective theory. Most of the strongly correlated phenomena of interest in many-body physics take place at energy scales smaller than 0.025 eV and are indeed treated using low-energy theories (even the Hubbard model, which ignores all but a few bands near the Fermi level, is a low-energy theory by electronic structure standards), but we have at present no reliable low-energy theory of chemical bond breaking and formation. The pseudo-potential approximation allows the core electrons to be eliminated from the Schrödinger equation with only a small loss in accuracy, but that is as far as we can go. If we want to use quantum theory to understand the mechanical properties of solids or follow chemical reactions in real time, the only option is to solve the Schrödinger equation to extraordinarily high precision.

How might we accomplish this? The most widely used electronic structure method is density functional theory (DFT) [4–6], which is reasonably accurate and can, with enough effort, be scaled to thousands of electrons. Although the Hohenberg-Kohn theorem shows that DFT is in principle capable of producing exact ground-state energies and electron densities, this guarantee is of little value in practice because we do not know the exact exchange-correlation functional. DFT calculations for weakly correlated Fermi liquids give excellent qualitative results and reasonably good quantitative results, but current exchange-correlation functionals are far from capable of delivering chemical accuracy consistently. DFT's main contribution to the study of strong-correlation effects has been as a useful framework on which to build more sophisticated approaches. Dynamical mean-field theory, the GW approximation, and the Bethe-Salpeter equation [7] are examples of these.

Guessing the form of the many-electron wave function has proved to be a surprisingly successful approach to complicated many-electron problems. The Bethe Ansatz [8] for one-dimensional systems, the BCS theory of superconductivity [9], and Laughlin's treatment of the fractional quantum Hall effect [10] are all good examples. When seeking ground states, a common approach is to guess a trial wave function Ψ with a number of adjustable parameters and vary the parameters until the energy expectation value,

$$E[\Psi] = \frac{\langle \Psi | \hat{H} | \Psi \rangle}{\langle \Psi | \Psi \rangle}, \tag{2}$$

is minimized. According to the variational principle, this is the best you can do given the constraints imposed by the assumed functional form.

The greatest successes of guessing the wave function have been in many-body theory, but this article is about approximate wave functions used in electronic structure theory and quantum chemistry. The aim here is to guess the ground-state wave function accurately enough to identify the most stable molecular and crystal structures, study chemical and biochemical reactions, and follow atomic rearrangements in solids, such as those associated with fracture processes or the motion of dislocations. It is rare to achieve chemical accuracy in systems larger than small molecules, but it is possible to outperform DFT in most cases. For the most part we will work in the Schrödinger picture, using trial wave functions of the form $\Psi(x_1, x_2, \ldots, x_N)$, where $x_i = (\mathbf{r}_i, \sigma_i)$ is shorthand for the combined spatial and spin coordinates of electron i.

Before we can use the variational principle to optimize the parameters of a trial wave function, we need to be able to work out the energy expectation value $E[\Psi]$. This is not an easy task when

the number of electrons N is 10, never mind when it is 100 or 1000. In the variational quantum Monte Carlo (VMC) method [11, 7], the energy expectation value is rewritten as

$$E[\Psi] = \int \left(\frac{\hat{H}\Psi(x_1, \ldots, x_N)}{\Psi(x_1, \ldots, x_N)} \right) \left(\frac{|\Psi(x_1, \ldots, x_N)|^2}{\int |\Psi|^2 \, dx_1 \ldots dx_N} \right) dx_1 \ldots dx_N, \tag{3}$$

where integrals over x are understood to include a spin sum:

$$\int dx' = \sum_{\sigma'} \iiint d^3r'. \tag{4}$$

The $\hat{H}\Psi/\Psi$ term is called the *local energy*, and the $|\Psi|^2/\int|\Psi|^2$ term, which is positive and integrates to one, is interpreted as a probability density in coordinate space. Points in this space are specified by giving $3N$ position variables and N binary spin variables.

As long as it is possible to evaluate the local energy, one can obtain statistical estimates of the value of $E[\Psi]$ using Monte Carlo integration. The Metropolis algorithm [7,11] is used to sample random coordinate-space points from the probability density $|\Psi|^2/\int|\Psi|^2$, and the values of the local energy at the sampled points are averaged. Neither the Metropolis algorithm (which uses only ratios of the probability density at different points) nor the evaluation of the local energy require knowledge of the normalization of the wave function, so wave functions used in VMC simulations do not need to be normalized. Other more sophisticated and accurate quantum Monte Carlo (QMC) methods, including diffusion quantum Monte Carlo (DMC) [11, 7] and auxiliary-field QMC [12], are also used to simulate molecules and solids and produce much more accurate results, but all require trial wave functions as a starting point.

To whittle down the amount of material, I have had to leave out several important types of trial wave function: the subject is larger than is apparent from this article. I have omitted all discussion of pairing wave functions such as the BCS wave function [9], geminals [13] and Pfaffians [14]. Until recently I would have said that attempts to use pairing wave functions to describe non-superconducting electrons had produced disappointing results, but a new preprint [15] has changed my mind. I have also omitted the family of trial wave functions that developed from the density matrix renormalization group [16] and includes matrix product states and tensor network states [17]. These are very important in low-dimensional model systems and becoming more important in quantum chemistry.

2 Slater determinants

Non-interacting electrons

Let us start by thinking about a molecule or periodically-repeated simulation cell containing N *non-interacting* electrons. The many-electron Hamiltonian is

$$\hat{H} = \sum_{i=1}^{N} \left(-\frac{1}{2}\nabla_{\mathbf{r}_i}^2 + V(x_i) \right) = \sum_{i=1}^{N} \hat{h}(x_i), \tag{5}$$

where $\hat{h}(x_i) = -\frac{1}{2}\nabla^2_{\mathbf{r}_i} + V(x_i)$ acts on the coordinates of electron i only. In the simplest plausible model of a molecule or solid, the effective potential might look like this:

$$V(x) = V_{\text{nuc}}(\mathbf{r}) + V_{\text{Hartree}}(\mathbf{r}) = -\sum_I \frac{Z_I}{|\mathbf{r} - \mathbf{d}_I|} + \int \frac{n(x')}{|\mathbf{r} - \mathbf{r}'|}\, dx', \tag{6}$$

where Z_I is the atomic number of the (fixed, classical) nucleus at position $\mathbf{d}_I$, and $n(x) = n(\mathbf{r}, \sigma)$ is the number density of spin σ electrons at point $\mathbf{r}$. In Hartree-Fock theory [18, 5, 7], $V(x)$ also contains a non-local spin-dependent exchange potential. In the Kohn-Sham equations of density functional theory (DFT) [4–6], it contains a local exchange-correlation potential.
The many-electron Schrödinger equation for the N non-interacting electrons,

$$\hat{H}\Psi(x_1, x_2, \ldots, x_N) = E\,\Psi(x_1, x_2, \ldots, x_N), \tag{7}$$

is a separable partial differential equation with solutions of the form

$$\Psi(x_1, x_2, \ldots, x_N) = \varphi_1(x_1)\,\varphi_2(x_2) \ldots \varphi_N(x_N). \tag{8}$$

(Such solutions are not totally antisymmetric, but let us ignore this problem for the time being.) Substituting the trial solution into the Schrödinger equation gives

$$(\hat{h}\,\varphi_1)\,\varphi_2 \ldots \varphi_N + \varphi_1(\hat{h}\,\varphi_2) \ldots \varphi_N + \ldots + \varphi_1\,\varphi_2 \ldots (\hat{h}\,\varphi_N) = E\,\varphi_1\,\varphi_2 \ldots \varphi_N. \tag{9}$$

If we now divide by $\varphi_1\varphi_2 \ldots \varphi_N$ we get,

$$\frac{\hat{h}(x_1)\,\varphi_1(x_1)}{\varphi_1(x_1)} + \frac{\hat{h}(x_2)\,\varphi_2(x_2)}{\varphi_2(x_2)} + \ldots + \frac{\hat{h}(x_N)\,\varphi_N(x_N)}{\varphi_N(x_N)} = E. \tag{10}$$

The first term depends only on x_1, the second only on x_2, and so on, but the sum must be the constant E. This is only possible if each and every term is constant:

$$\hat{h}_1\varphi_1 = \varepsilon_1\varphi_1, \quad \hat{h}_2\varphi_2 = \varepsilon_2\varphi_2, \quad \ldots, \quad \hat{h}_N\varphi_N = \varepsilon_N\varphi_N, \tag{11}$$

with

$$E = \varepsilon_1 + \varepsilon_2 + \ldots + \varepsilon_N. \tag{12}$$

Functions such as $\varphi_i(x)$, obtained by solving a one-electron Schrödinger equation of the form $\hat{h}\varphi_i = \varepsilon_i\varphi_i$, are called *one-electron orbitals* or *one-electron energy eigenfunctions*.
Although Ψ is not antisymmetric, we can easily construct an antisymmetric linear combination of solutions with the N electrons distributed among the N one-electron orbitals in different ways

$$\Psi(x_1, x_2, \ldots, x_N) = \frac{1}{\sqrt{N!}} \sum_P (-1)^{\zeta_P} \varphi_{P1}(x_1)\varphi_{P2}(x_2) \ldots \varphi_{PN}(x_N). \tag{13}$$

Every term in the linear combination is an eigenfunction of $\hat{H}$ with the same eigenvalue E, so the linear combination is also an eigenfunction with eigenvalue E.

- The list $P1,\ P2,\ \ldots,\ PN$ is a permutation P of the list $1,\ 2,\ \ldots,\ N$. The sum is over all permutations, with ζ_P the total number of pair interchanges needed to build the permutation P. The value of $(-1)^{\zeta_P}$ is $+1$ when P is an even permutation and -1 when P is an odd permutation.

- The $1/\sqrt{N!}$ is a normalizing factor.

- When $N = 2$,

$$\Psi(x_1, x_2) = \frac{1}{\sqrt{2}}\left[\varphi_1(x_1)\varphi_2(x_2) - \varphi_2(x_1)\varphi_1(x_2)\right] = \frac{1}{\sqrt{2}}\begin{vmatrix} \varphi_1(x_1) & \varphi_1(x_2) \\ \varphi_2(x_1) & \varphi_2(x_2) \end{vmatrix}. \tag{14}$$

- Generally,

$$\Psi(x_1, x_2, \ldots, x_N) = \frac{1}{\sqrt{N!}}\begin{vmatrix} \varphi_1(x_1) & \varphi_1(x_2) & . & . & . & \varphi_1(x_N) \\ \varphi_2(x_1) & \varphi_2(x_2) & . & . & . & \varphi_2(x_N) \\ . & . & & & & . \\ . & . & & & & . \\ \varphi_N(x_1) & \varphi_N(x_2) & . & . & . & \varphi_N(x_N) \end{vmatrix}. \tag{15}$$

  Wave functions of this type are called Slater determinants. (For bosons we can use analogous symmetrized sums of products called permanents.)

- If two or more of $\varphi_1,\ \varphi_2,\ \ldots,\ \varphi_N$ are the same, two or more rows of the determinant are the same and the wave function is zero; this is how the Pauli exclusion principle follows from the antisymmetry. If two electrons of the same spin approach the same point in space, even when all of the φ_i are different, two columns of the determinant become the same and the wave function is again zero. The antisymmetry built in to the Slater determinant helps to keep spin-parallel electrons apart.

- If we add a component of φ_2 to φ_1,

$$\tilde{\varphi}_1(x) = \varphi_1(x) + c\,\varphi_2(x), \tag{16}$$

  the Slater determinant is unchanged:

$$\begin{aligned}\tilde{D}(x_1, x_2, \ldots, x_N) &= \frac{1}{\sqrt{N!}}\begin{vmatrix} \tilde{\varphi}_1(x_1) & \tilde{\varphi}_1(x_2) & \ldots & \tilde{\varphi}_1(x_N) \\ \varphi_2(x_1) & \varphi_2(x_2) & \ldots & \varphi_2(x_N) \\ \ldots & \ldots & \ldots & \ldots \\ \ldots & \ldots & \ldots & \ldots \\ \varphi_N(x_1) & \varphi_N(x_2) & \ldots & \varphi_N(x_N) \end{vmatrix} \\ &= \frac{1}{\sqrt{N!}}\begin{vmatrix} \varphi_1(x_1) & \varphi_1(x_2) & \ldots & \varphi_1(x_N) \\ \varphi_2(x_1) & \varphi_2(x_2) & \ldots & \varphi_2(x_N) \\ \ldots & \ldots & \ldots & \ldots \\ \ldots & \ldots & \ldots & \ldots \\ \varphi_N(x_1) & \varphi_N(x_2) & \ldots & \varphi_N(x_N) \end{vmatrix} + \frac{1}{\sqrt{N!}}\begin{vmatrix} c\varphi_2(x_1) & c\varphi_2(x_2) & \ldots & c\varphi_2(x_N) \\ \varphi_2(x_1) & \varphi_2(x_2) & \ldots & \varphi_2(x_N) \\ \ldots & \ldots & \ldots & \ldots \\ \ldots & \ldots & \ldots & \ldots \\ \varphi_N(x_1) & \varphi_N(x_2) & \ldots & \varphi_N(x_N) \end{vmatrix} \\ &= D(x_1, x_2, \ldots, x_N). \end{aligned} \tag{17}$$

  This shows that no generality is lost by assuming that the one-electron orbitals are orthonormal.

Interacting electrons

In the interacting N-electron Schrödinger equation, the one-electron operator $V(x)$ (which depends on the electron density in DFT and the one-electron density matrix in Hartree-Fock theory) is replaced by the electron-electron interaction

$$\left(\sum_{i=1}^{N}\left(-\frac{1}{2}\nabla_i^2+V_{\text{nuc}}(\mathbf{r}_i)\right)+\frac{1}{2}\sum_{i=1}^{N}\sum_{\substack{j=1\\(j\neq i)}}^{N}\frac{1}{|\mathbf{r}_i-\mathbf{r}_j|}\right)\Psi(x_1,x_2,\ldots,x_N)=E\,\Psi(x_1,x_2,\ldots,x_N). \tag{18}$$

I have assumed for simplicity that spin-orbit interactions can be neglected, so the Hamiltonian is independent of spin. Reintroducing the electron-electron interaction may look like a small change but it has large consequences: the Schrödinger equation is no longer separable and the many-electron wave functions are no longer Slater determinants. Unlike the non-interacting Schrödinger equation, the interacting version cannot be solved exactly for systems of more than a few electrons, even using the world's most powerful computers.

Slater determinants as basis functions

Although Slater determinants are not exact solutions of the many-electron Schrödinger equation with interactions, we can still use them as *basis functions*. Suppose that $\varphi_1(x)$, $\varphi_2(x)$, ... are a complete orthonormal basis for the one-particle Hilbert space. A common way to choose the $\varphi_i(x)$ is to solve a one-electron or mean-field Schrödinger equation, usually obtained from density functional or Hartree-Fock theory, and use the resulting one-electron orbitals.
Given a complete basis for the one-electron Hilbert space, the set of all products of the form

$$\varphi_{i_1}(x_1)\,\varphi_{i_2}(x_2)\ldots\varphi_{i_N}(x_N) \tag{19}$$

is a complete basis for the N-particle Hilbert space. If the N particles are electrons or other fermions, only antisymmetrized products are required and we can express the wave function as a linear combination of Slater determinants

$$\Psi(x_1,x_2,\ldots,x_N)=\sum_{\mathbf{i}}C_{\mathbf{i}}\,D_{\mathbf{i}}(x_1,x_2,\ldots,x_N), \tag{20}$$

where the sum is over all distinct determinants, the vector index $\mathbf{i}=(i_1,i_2,\ldots,i_N)$ identifies the N one-electron basis function φ_{i_1}, φ_{i_2}, ..., φ_{i_N}, appearing in determinant $D_{\mathbf{i}}$, and the $C_{\mathbf{i}}$ are expansion coefficients. Interchanging any two basis functions leaves $D_{\mathbf{i}}$ unaltered (bar a sign), so we can restrict the summation to vector indices $\mathbf{i}$ for which $i_1<i_2<\ldots<i_N$.[2]
Another way to index Slater determinants is to use the occupation number representation, in which every determinant is defined by a list of binary numbers, one for each one-electron basis

[2]It is interesting to think about how this works in an infinite system. Even if the set of one-electron basis functions is countable, the set of all ordered subsets of the set of one-electron basis functions is not, implying that we cannot index the determinants using natural numbers. Perhaps attempting to describe large systems using wave functions is not such a good idea?

function. If basis function φ_i appears in the determinant (is "occupied"), the i'th binary number is set to 1; otherwise, it is set to 0.
Slater determinants are the "building blocks" of many-fermion physics, including most of the approximate many-electron wave functions we will be looking at.

Slater determinants and second quantization

The properties of Slater determinants underlie the properties of the creation and annihilation operators, $\hat{c}_p^\dagger$ and $\hat{c}_p$, which are defined by their actions in the determinantal basis:

$$\hat{c}_p^\dagger |D_{i_1,i_2,\ldots,i_N}\rangle = |D_{p,i_1,i_2,\ldots,i_N}\rangle, \qquad \hat{c}_p |D_{p,i_1,i_2,\ldots,i_N}\rangle = |D_{i_1,i_2,\ldots,i_N}\rangle. \tag{21}$$

If the determinant $|D_{i_1,i_2,\ldots,i_N}\rangle$ already contains orbital φ_p, acting with $\hat{c}_p^\dagger$ produces a determinant $|D_{p,i_1,i_2,\ldots,i_N}\rangle$ with two identical rows. The result is therefore equal to zero. Similarly, if $|D_{i_1,i_2,\ldots,i_N}\rangle$ does not contain φ_p, then $\hat{c}_p$ finds nothing to annihilate and $\hat{c}_p|D_{i_1,i_2,\ldots,i_N}\rangle = 0$. Whenever you are working with creation and annihilation operators, you are in fact manipulating Slater determinants.
The fermion anti-commutation relations follow from the antisymmetry of the determinantal basis. For example, given any determinant containing φ_q in the k^{th} row but not containing φ_p, where $p \neq q$, we have

$$\begin{aligned}\hat{c}_p^\dagger \hat{c}_q |D_{i_1,\ldots,i_{k-1},q,i_{k+1},\ldots,i_N}\rangle &= (-1)^{k-1} \hat{c}_p^\dagger \hat{c}_q |D_{q,i_1,\ldots,i_{k-1},i_{k+1},\ldots,i_N}\rangle \\ &= (-1)^{k-1} |D_{p,i_1,\ldots,i_{k-1},i_{k+1},\ldots,i_N}\rangle \end{aligned} \tag{22}$$

and

$$\begin{aligned}\hat{c}_q \hat{c}_p^\dagger |D_{i_1,\ldots,i_{k-1},q,i_{k+1},\ldots,i_N}\rangle &= \hat{c}_q |D_{p,i_1,\ldots,i_{k-1},q,i_{k+1},\ldots,i_N}\rangle \\ &= (-1)^k \hat{c}_q |D_{q,p,i_1,\ldots,i_{k-1},i_{k+1},\ldots,i_N}\rangle \\ &= (-1)^k |D_{p,i_1,\ldots,i_{k-1},i_{k+1},\ldots,i_N}\rangle, \end{aligned} \tag{23}$$

implying that

$$\left(\hat{c}_p^\dagger \hat{c}_q + \hat{c}_q \hat{c}_p^\dagger\right) |D_{i_1,\ldots,i_{k-1},q,i_{k+1},\ldots,i_N}\rangle = 0. \tag{24}$$

If $D_{i_1,\ldots,i_N}$ already contains φ_p or does not contain φ_q, the operators $\hat{c}_p^\dagger \hat{c}_q$ and $\hat{c}_q \hat{c}_p^\dagger$ annihilate it and Eq. (24) still holds. Since the basis of Slater determinants is complete, it follows that

$$\hat{c}_p^\dagger \hat{c}_q + \hat{c}_q \hat{c}_p^\dagger = 0, \qquad p \neq q. \tag{25}$$

If you have never worked through a detailed explanation of how the properties of fermion creation and annihilation operators arise from the properties of the Slater determinants on which they act, try Chapter 1 of Negele and Orland [19] for a physicist's perspective or Chapter 1 of Helgaker, Jorgensen and Olsen [20] for a chemist's perspective.

Exchange and correlation

If we write the full many-electron Hamiltonian,

$$\hat{H} = \sum_{i=1}^{N} \left(-\frac{1}{2}\nabla_i^2 + V_{\text{nuc}}(\mathbf{r}_i) \right) + \frac{1}{2} \sum_{i=1}^{N} \sum_{\substack{j=1 \\ (j\neq i)}}^{N} \frac{1}{|\mathbf{r}_i - \mathbf{r}_j|}, \tag{26}$$

in the form

$$\hat{H} = \sum_{i=1}^{N} \hat{h}(x_i) + \frac{1}{2} \sum_{i=1}^{N} \sum_{\substack{j=1 \\ (j\neq i)}}^{N} \hat{v}(x_i, x_j), \tag{27}$$

and evaluate its expectation value $E = \langle D|\hat{H}|D\rangle$ in a normalized Slater determinant D of orthonormal one-electron functions φ_i, it is in principle straightforward, although in practice tedious [7, 18, 20], to show that

$$E = \sum_{i=1}^{N} \langle \varphi_i|\hat{h}|\varphi_i\rangle + \frac{1}{2} \sum_{i=1}^{N} \sum_{\substack{j=1 \\ (j\neq i)}}^{N} \big(\langle \varphi_i\varphi_j|\hat{v}|\varphi_i\varphi_j\rangle - \langle \varphi_j\varphi_i|\hat{v}|\varphi_i\varphi_j\rangle \big), \tag{28}$$

where

$$\langle \varphi_i|\hat{h}|\varphi_j\rangle = \int \varphi_i^*(x)\, \hat{h}(x)\, \varphi_j(x)\, dx, \tag{29}$$

$$\langle \varphi_i\varphi_j|\hat{v}|\varphi_k\varphi_l\rangle = \iint \varphi_i^*(x)\varphi_j^*(x')\, \hat{v}(x,x')\, \varphi_k(x)\varphi_l(x')\, dx\, dx'. \tag{30}$$

In the case of Coulomb interactions, when $\hat{v}(x,x') = 1/|\mathbf{r} - \mathbf{r}'|$, the first contribution to the electron-electron interaction energy is

$$\frac{1}{2} \iint \frac{\sum_i |\varphi_i(x)|^2 \sum_{j(\neq i)} |\varphi_j(x')|^2}{|\mathbf{r} - \mathbf{r}'|}\, dx dx'. \tag{31}$$

This is known as the Hartree energy and is equal to the sum of the classical Coulomb interaction energies of the charge densities associated with the one-electron orbitals appearing in the determinant. We could have guessed it would appear. The second contribution to the interaction energy, which is known as the *exchange* energy because the order of the orbitals in the bra is reversed relative to their order in the ket, describes how the Pauli principle affects the electron-electron interactions. The antisymmetry built into the Slater determinant prevents spin-parallel electrons from getting close to each other, and this decreases the positive (*i.e.*, repulsive) Coulomb energy of the electrons. The exchange term is therefore negative.

If the spins in a solid line up, so that there are more electrons of one spin than the other, the exchange energy (which acts only between electrons of the same spin) becomes more negative and the total electron-electron interaction energy (which is positive) is lowered. At the same time, the one-electron contribution to the total energy rises because electrons have been promoted from lower-energy occupied minority-spin orbitals to higher-energy unoccupied majority-spin

orbitals. In some solids, the lowering of the Coulomb energy wins and the spins polarize spontaneously. This is more likely when the hopping kinetic energy is small because the atoms are far apart and the energy bands are narrow. Exchange interactions are the primary cause of magnetism.

Real electrons are also kept apart by the repulsive Coulomb interactions between them. This effect, called *correlation*, is not included in a simple Slater determinant wave function. The Hartree energy of the Slater determinant is low when the electronic charge distribution is smooth, which helps to keep electrons away from regions in which there are lots of other electrons *on average*, but does not keep individual pairs of electrons apart. In a real solid, electrons are kept apart both by the Pauli principle (exchange), which is included in the Slater determinant, and by the Coulomb interaction (correlation), which is not.

One way to understand exchange and correlation is in terms of the pair density $n(\mathbf{r},\sigma;\mathbf{r}',\sigma')$, defined such that $n(\mathbf{r},\sigma;\mathbf{r}',\sigma')\,d^3r d^3r'$ is proportional to the probability of finding a spin σ electron in the volume element d^3r at $\mathbf{r}$ and a (different) spin σ' electron in the volume element d^3r' at $\mathbf{r}'$. The closely related pair-correlation function, $g(\mathbf{r},\sigma;\mathbf{r}',\sigma')$, is defined by

$$n(\mathbf{r},\sigma;\mathbf{r}',\sigma') = n(\mathbf{r},\sigma)g(\mathbf{r},\sigma;\mathbf{r}',\sigma')n(\mathbf{r}',\sigma'). \tag{32}$$

If the volume elements d^3r and d^3r' are far apart, the numbers of electrons in d^3r and d^3r' are statistically independent; one therefore expects $\lim_{|\mathbf{r}'-\mathbf{r}|\to\infty} g(\mathbf{r},\sigma;\mathbf{r}',\sigma') = 1$.

Figure 1 shows the pair-correlation functions of pairs of spin-parallel and spin-antiparallel electrons in a uniform electron gas, calculated assuming that the wave function is a Slater determinant of plane waves. The way in which antisymmetry keeps pairs of spin-parallel electrons apart is clear, as is the failure of pairs of spin-antiparallel electrons to avoid each other. Antisymmetry alone is not sufficient to correlate (in the statistical sense) the positions of spin-antiparallel electrons.

Basic notions of probability theory tell us that

$$n(\mathbf{r},\sigma;\mathbf{r}',\sigma')\,d^3r d^3r' = n(\mathbf{r},\sigma|\mathbf{r}',\sigma')\,d^3r \times n(\mathbf{r}',\sigma')\,d^3r', \tag{33}$$

where $n(\mathbf{r},\sigma|\mathbf{r}',\sigma')\,d^3r$ is proportional to the conditional probability of finding a spin σ electron in d^3r given that there is a spin σ' electron in d^3r'. Since there are $N-1$ electrons in the system, excluding the one frozen at $\mathbf{r}'$, the conditional density satisfies the sum rule

$$\sum_\sigma \int n(\mathbf{r},\sigma|\mathbf{r}',\sigma')\,d^3r = N-1. \tag{34}$$

Describing statistical correlations in terms of conditional probabilities is very natural, but it is often easier to think about the exchange-correlation hole, $n_{\rm xc}(\mathbf{r},\sigma|\mathbf{r}',\sigma')$, defined by

$$n(\mathbf{r},\sigma|\mathbf{r}',\sigma') = n(\mathbf{r},\sigma) + n_{\rm xc}(\mathbf{r},\sigma|\mathbf{r}',\sigma'). \tag{35}$$

The density of spin σ electrons at $\mathbf{r}$ would be $n(\mathbf{r},\sigma)$ in the absence of the frozen spin σ' electron at $\mathbf{r}'$, so the exchange-correlation hole provides a very direct picture of the change (normally a

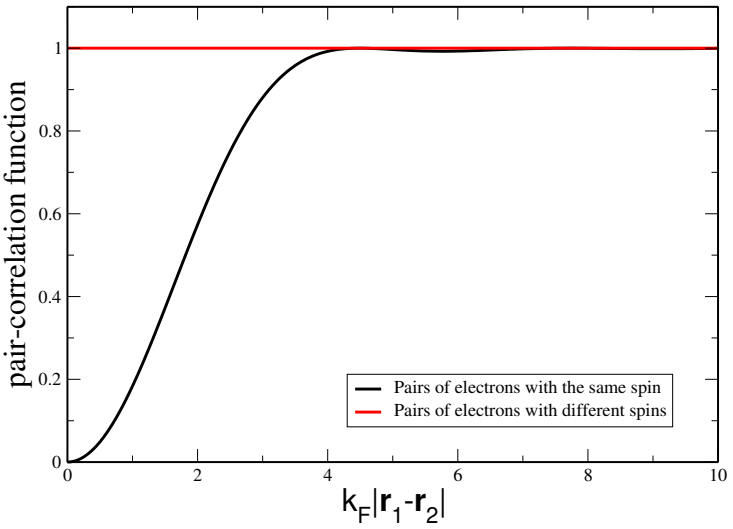

Fig. 1: *Pair-correlation functions of pairs of spin-parallel and spin-antiparallel electrons in a uniform electron gas, calculated assuming that the wave function is a single Slater determinant of plane waves. The antisymmetry of the wave function helps to keep pairs of spin-parallel electrons apart but does not affect the pair-correlation function of pairs of spin-antiparallel electrons.*

reduction) in electron density caused by the presence of the frozen electron. It follows from the definition of the exchange-correlation hole and the conditional-probability sum rule that

$$\sum_{\sigma} \int n_{\mathrm{xc}}(\mathbf{r}, \sigma | \mathbf{r}', \sigma') \, d^3r = -1. \tag{36}$$

Every electron of charge $-e$ is thus surrounded by a hole of charge $+e$. If the hole is close to the electron, which is not always the case, the entire *quasi-particle* — the electron plus its hole — is charge neutral and might be expected to have only short-ranged interactions. This helps explain why the models of non-interacting electrons used in undergraduate solid-state physics courses work so well.

Figure 2 shows two views of the spin-summed exchange-correlation hole, $\sum_{\sigma} n_{\mathrm{xc}}(\mathbf{r}, \sigma | \mathbf{r}', \sigma')$, around a single electron frozen at the point $\mathbf{r}'$ in the middle of a bond in silicon [21]. The graphs were calculated using the VMC method and a Slater-Jastrow wave function (see later), which includes both exchange and correlation effects.

3 The Hartree-Fock approximation

Although the many-electron eigenfunctions of real molecules and solids can in principle be written as linear combinations of (huge numbers of) Slater determinants, we will see later that the number of determinants required rises exponentially with the number of electrons. This forces us to try something less ambitious. In the Hartree-Fock approximation, the variational principle is used to find the *single* Slater determinant that best approximates the many-electron ground state [18, 20, 6]. It turns out that the one-electron orbitals appearing in the best possible

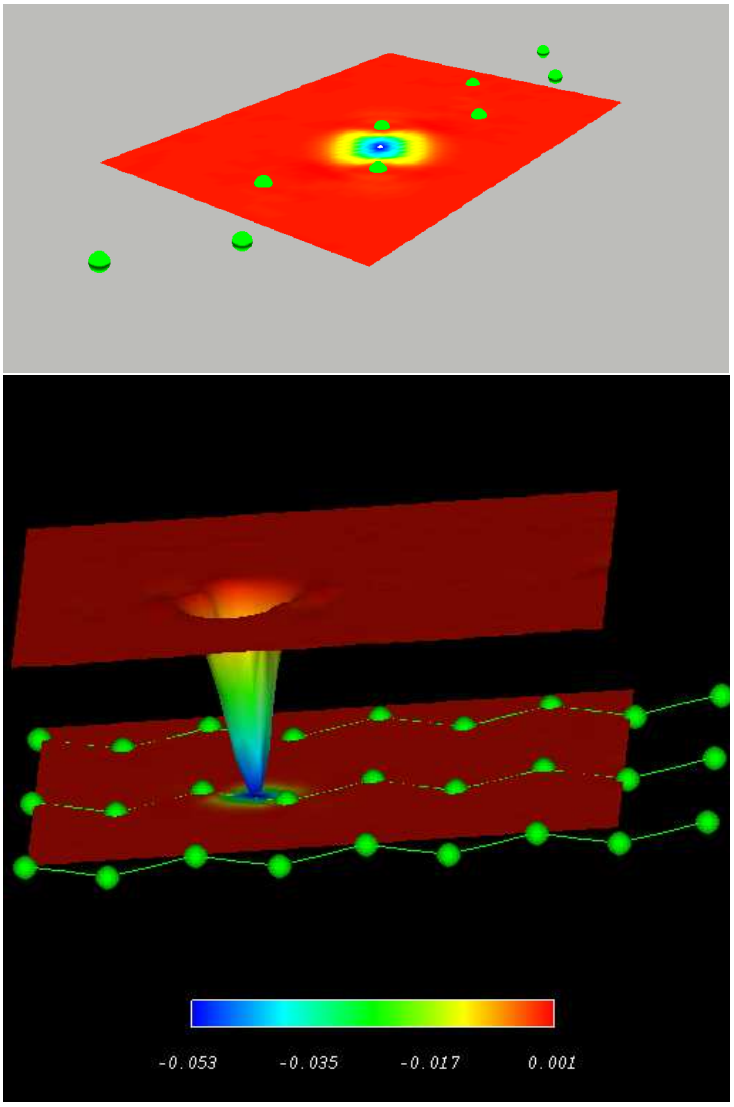

Fig. 2: *Two views of the exchange-correlation hole around an electron in the middle of a bond in silicon. The zig-zag chains of atoms lie in the Si (110) plane. From Ref. [21].*

single determinant obey a mean-field Schrödinger-like equation,

$$\hat{h}(x)\,\varphi_n(x) + \sum_{\substack{j=1\\(j\neq n)}}^{N} \int dx'\,\varphi_j^*(x')\,\hat{v}(x,x')\,\varphi_j(x')\varphi_n(x) - \sum_{\substack{j=1\\(j\neq n)}}^{N} \int dx'\,\varphi_j^*(x')\,\hat{v}(x,x')\,\varphi_n(x')\varphi_j(x) = \lambda_n\,\varphi_n(x), \tag{37}$$

known as the Hartree-Fock equation. The electron-electron interactions have been replaced by an effective potential with two contributions: the first summation describes the action of the Hartree potential on orbital $\varphi_n(x)$ and the second the action of the exchange potential. Notice that the exchange potential is actually an integral operator. The $j{=}n$ terms in both summations cancel if they are included, so the form of the Hartree-Fock differential equation is

independent of n. Another partial explanation for the success of one-electron concepts such as band-structures, atomic orbitals, and π and σ bonds, in interacting systems where these ideas appear to make little sense, is that the Hartree-Fock approximation is often reasonably accurate. Other mean-field-like methods, such as DFT, work better than Hartree-Fock for many purposes, but the wave function in DFT is an artificial construct introduced to help calculate the kinetic energy of a fictitious system of non-interacting electrons with the same position-dependent number density as the interacting system and has little to do with the true many-electron wave function [4–6]. Our aim here is to devise approximate many-electron wave functions for atoms, molecules and solids, so Hartree-Fock theory is a better starting point.

The Hartree-Fock Hamiltonian depends on the one-electron orbitals obtained by solving the Hartree-Fock equation, so we have a chicken and egg problem: we cannot find the orbitals until we know the Hamiltonian; but we cannot work out the Hamiltonian until we know the orbitals. As usual in mean-field theories, we have to iterate until the inputs and outputs of the mean-field equation are consistent with each other:

1. Guess the set of one-electron orbitals φ_j ($j = 1, \ldots, N$) and construct the corresponding Hartree-Fock Hamiltonian.

2. Solve the Hartree-Fock equation to find a new set of one-electron orbitals. (This is quite tricky because the exchange term is an integral operator with a Coulomb kernel that diverges as $|\mathbf{r} - \mathbf{r}'| \to 0$, but it can be done.)

3. Use the new set of one-electron orbitals to construct a new Hartree-Fock Hamiltonian.

4. Repeat steps 2 and 3 until the set of one-electron orbitals no longer changes from cycle to cycle.

There is no guarantee that iterative algorithms of this type are stable, and clever tricks are sometimes required to make them converge, but self-consistent solutions can be found within a reasonable amount of computer time for systems of up to a few hundred electrons.

Until about 20 years ago, Hartree-Fock theory was widely used to study molecules, even though it is far from being able to reach chemical accuracy. DFT has now become dominant, partly because DFT calculations are easier to do and normally more accurate, and partly because our imperfect knowledge of the exchange-correlation functional leaves more scope for tweaking the calculations to make them give the right answers! A common tweak is to mix fractions of the Hartree-Fock exchange energy into the DFT exchange-correlation functional, making DFT calculations more similar to Hartree-Fock calculations. “Hybrid” density functionals including a portion of exact exchange are not consistently able to achieve chemical accuracy, but are often accurate enough to provide useful results. Hartree-Fock methods were not much used in solids until fairly recently because the calculations were difficult; their main use now is in wide band-gap insulators, where the results are not too bad. For metals, Hartree-Fock is something of a disaster, but hybrid exchange-correlation functionals including screened exchange interactions are popular and successful.

4 Configuration expansions

Configuration-interaction methods

We saw in Sec. 2 that any many-electron wave function can be expressed as a linear combination of Slater determinants (also known as configurations):

$$\Psi(x_1, x_2, \ldots, x_N) = \sum_{\mathbf{i}} C_{\mathbf{i}}\, D_{\mathbf{i}}(x_1, x_2, \ldots, x_N). \tag{38}$$

This expansion underlies most of the approximate wave functions used in traditional quantum chemistry. In the full-configuration-interaction (FCI) method [20], the sum over determinants is made finite by choosing a finite set of M ($\geq N$) one-electron basis functions (normally Hartree-Fock or DFT one-electron orbitals) and approximating Ψ as a linear combination of the ${}^M\mathrm{C}_N$ distinct N-electron Slater determinants that can be built using them. The vector of expansion coefficients that minimizes the energy expectation value,

$$E = \frac{\langle\Psi|\hat{H}|\Psi\rangle}{\langle\Psi|\Psi\rangle} = \frac{\sum_{\mathbf{i},\mathbf{j}} C^*_{\mathbf{i}} \langle D_{\mathbf{i}}\,|\hat{H}|D_{\mathbf{j}}\rangle C_{\mathbf{j}}}{\sum_{\mathbf{k}} C^*_{\mathbf{k}} C_{\mathbf{k}}}, \tag{39}$$

is easily shown to be the lowest eigenvector of the matrix eigenvalue problem

$$\sum_{\mathbf{j}} H_{\mathbf{ij}} C_{\mathbf{j}} = E C_{\mathbf{i}}, \tag{40}$$

where $H_{\mathbf{ij}} = \langle D_{\mathbf{i}}|\hat{H}|D_{\mathbf{j}}\rangle$ is an ${}^M\mathrm{C}_N \times {}^M\mathrm{C}_N$ matrix. The use of the variational principle is exactly as in one-electron quantum theory, but the basis functions are many-electron Slater determinants rather than one-electron orbitals and it is more difficult to work out the Hamiltonian matrix elements.

Unfortunately, the number of determinants required to approximate the ground state to a given accuracy rises exponentially with the system size, making FCI calculations impractical for anything but the smallest molecules. Suppose (very optimistically) that you can obtain a reasonably good description of the ground state of a single helium atom using a one-electron basis set containing $1s$ and $2s$ orbitals only. Since every atom holds four spin-orbitals ($1s\uparrow$, $1s\downarrow$, $2s\uparrow$, $2s\downarrow$), the FCI basis for a system of $N/2$ helium atoms and N electrons contains

$${}^M\mathrm{C}_N = {}^{2N}\mathrm{C}_N = \frac{(2N)!}{N!\,N!} \tag{41}$$

determinants. Using Stirling's approximation, $\ln(n!) \approx n\ln n - n$ for large n, gives

$${}^{2N}\mathrm{C}_N \approx e^{(2\ln 2)N}, \tag{42}$$

which rises exponentially with N. Even in this minimal and inaccurate basis set, calculating the many-electron ground state of a system of 5 helium atoms and 10 electrons requires finding the lowest eigenvector of a matrix with more than a million rows and columns. Dealing with 10 helium atoms requires a Hamiltonian matrix with over 10^{12} rows and columns and 10^{24}

elements. The size of the matrix can often be reduced using symmetry arguments, and the $H_{\mathbf{ij}}$ matrix is sparse because applying the Hamiltonian to a determinant changes at most two of the one-electron orbitals, but increasing the system size soon makes the state vector too large to store and manipulate.

It seems reasonable to hope that most of the Slater determinants in the vast FCI basis set are unnecessary and can be neglected. Even when the He atoms are far enough apart to be independent, however, simple truncation schemes do not work well.

The exact (within the FCI basis) $S_z = 0$ ground state of a single He atom is a linear combination of four determinants,

$$\Psi(x,x') = C_1 \begin{vmatrix} \varphi_{1s}(\mathbf{r})\chi_\uparrow(\sigma) & \varphi_{1s}(\mathbf{r}')\chi_\uparrow(\sigma') \\ \varphi_{1s}(\mathbf{r})\chi_\downarrow(\sigma) & \varphi_{1s}(\mathbf{r}')\chi_\downarrow(\sigma') \end{vmatrix} + C_2 \begin{vmatrix} \varphi_{2s}(\mathbf{r})\chi_\uparrow(\sigma) & \varphi_{2s}(\mathbf{r}')\chi_\uparrow(\sigma') \\ \varphi_{2s}(\mathbf{r})\chi_\downarrow(\sigma) & \varphi_{2s}(\mathbf{r}')\chi_\downarrow(\sigma') \end{vmatrix}$$
$$+ C_3 \begin{vmatrix} \varphi_{1s}(\mathbf{r})\chi_\uparrow(\sigma) & \varphi_{1s}(\mathbf{r}')\chi_\uparrow(\sigma') \\ \varphi_{2s}(\mathbf{r})\chi_\downarrow(\sigma) & \varphi_{2s}(\mathbf{r}')\chi_\downarrow(\sigma') \end{vmatrix} + C_4 \begin{vmatrix} \varphi_{1s}(\mathbf{r})\chi_\downarrow(\sigma) & \varphi_{1s}(\mathbf{r}')\chi_\downarrow(\sigma') \\ \varphi_{2s}(\mathbf{r})\chi_\uparrow(\sigma) & \varphi_{2s}(\mathbf{r}')\chi_\uparrow(\sigma') \end{vmatrix}, \qquad (43)$$

where $\chi_\uparrow(\sigma) = \delta_{\sigma,\uparrow}$ and $\chi_\downarrow(\sigma) = \delta_{\sigma,\downarrow}$ are the usual up-spin and down-spin S_z eigenstates. The exact (within the basis) ground state of a system of 10 well separated He atoms is an antisymmetrized product of the ground states of each individual atom:

$$\Psi(x_1, x_2, \ldots, x_{20}) = \mathcal{N}\hat{\mathcal{A}}\big[\Psi_1(x_1,x_2)\Psi_2(x_3,x_4)\ldots,\Psi_{10}(x_{19},x_{20})\big]$$
$$= \frac{\mathcal{N}}{N!}\sum_P (-1)^{\zeta_P}\Psi_1(x_{P1},x_{P2})\Psi_2(x_{P3},x_{P4})\ldots\Psi_{10}(x_{P19},x_{P20}), \qquad (44)$$

where $\hat{\mathcal{A}}$ is the antisymmetrization operator and $\mathcal{N}$ is a normalizing constant. The atomic ground states $\Psi_1(x_1,x_2)$, $\Psi_2(x_3,x_4)$, …, $\Psi_{10}(x_{19},x_{20})$ are all of the same form but translated with respect to one another because they are centered on different atoms. Every atom has a finite probability, $p_{\text{excited}} = |C_2|^2 + |C_3|^2 + |C_4|^2$, of being found in an excited configuration in which at least one of the two electrons is occupying a $2s$ orbital. If the states of all 10 atoms were measured repeatedly, the average number found in excited configurations would be $10p_{\text{excited}}$. If the number of He atoms in the system were doubled, the expected number found in excited configurations would also double.

Suppose that you try to describe the $S_z = 0$ ground state of the system of 10 isolated He atoms using an FCI singles and doubles basis set, consisting of the Hartree-Fock ground-state determinant, in which all 20 electrons are occupying $1s$ orbitals, plus the 14,250 distinct $S_z = 0$ determinants with one or two of the twenty electrons occupying $2s$ orbitals. Three of the 118 determinants occurring in the $S_z = 0$ FCI singles and doubles basis set for a system of three He atoms are illustrated in Fig. 3. In one of these configurations an electron has been transferred from one atom to another; this excitation is very unlikely to happen when the atoms are far apart but might become more important as they approach each other.

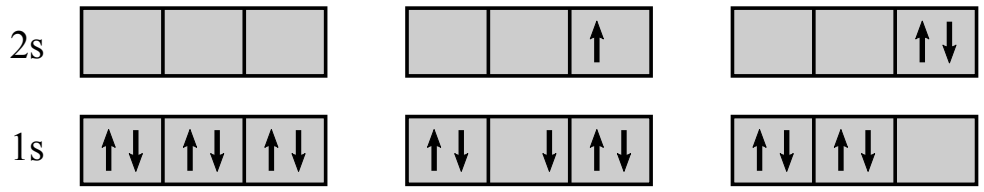

Fig. 3: *Three of the 118 $S_z = 0$ configurations appearing in the FCI singles and doubles wave function for three He atoms. Only the $1s$ and $2s$ orbitals on each atom are included in the one-electron basis set. The configuration on the left is the Hartree-Fock ground state; the one in the middle contains a single electron-hole excitation; and the one on the right contains two excitations.*

No configuration within the singles and doubles basis set contains more than two excited electrons, so no more than two of the 10 He atoms can be found in (charge neutral) excited configurations at any one time. If the expected number of excited atoms ($10p_{\text{excited}}$) is substantially less than 2 that might be sufficient, but what happens as the system size is increased? For large enough systems (and large enough is often very small), the expected number of atoms in excited configurations will exceed 2 and the basis set will be inadequate.

All naive attempts to truncate the FCI basis set introduce analogues of this problem, the most obvious symptom of which is that the calculated energy of a system of N well-separated atoms is greater than N times the energy of one atom. (Remember that FCI is a variational method, so lower energies are better energies.) In the language of quantum chemistry, the truncated FCI method is not size consistent; in the language of condensed matter physics, the results are not extensive. The problem gets worse as the number of atoms increases, with the fraction of the correlation energy recovered reducing to zero as the system size tends to infinity. If you try to fix the problem by increasing the maximum number of excited electrons in proportion to the system size, the truncated FCI method becomes exponentially scaling.

Even when the FCI eigenvalue problem is too large to solve using the conventional methods of linear algebra, molecules with up to a few tens of electrons can often be treated using the FCI QMC method [22,23], in which the contributions to the numerator and denominator of Eq. (39) are sampled stochastically without ever storing the complete eigenvector. This approach has also been used to study very small solid-state simulation cells subject to periodic boundary conditions [24]. Unfortunately, the fermion sign problem [25] imposes another limitation on the number of electrons and the maximum system size remains disappointingly small. Another way to increase the system size is to use one of several selected-CI approaches [26–29], which iteratively identify determinants that make important contributions to the ground state, neglecting the rest. The selection can reduce the rate at which the basis set increases with system size, but selected-CI methods remain exponentially scaling.

To summarize, although FCI methods can produce extraordinarily accurate results for light atoms and small molecules, they are of little value for large molecules or solids.

Coupled-cluster methods

The coupled-cluster method [20, 30] offers a better way of truncating the FCI Hilbert space. To motivate the idea, consider two well-separated He atoms, A and B, at positions $\mathbf{d}_A$ and $\mathbf{d}_B$. The four-electron Hamiltonian is

$$\hat{H} = \sum_{i=1}^{4} \left(-\frac{1}{2}\nabla_{\mathbf{r}_i}^2 + V_{\text{nuc}}(\mathbf{r}_i - \mathbf{d}_A) + V_{\text{nuc}}(\mathbf{r}_i - \mathbf{d}_B) \right) + \frac{1}{2} \sum_{i=1}^{4} \sum_{\substack{j=1 \\ (j \neq i)}}^{4} \frac{1}{|\mathbf{r}_i - \mathbf{r}_j|}. \tag{45}$$

What happens when we apply this Hamiltonian to the product $\Psi_A(x_1, x_2)\Psi_B(x_3, x_4)$ of the two atomic ground states? (The product is not a valid four-electron wave function because it is not antisymmetric on exchange of electrons between atoms, but we will antisymmetrize it later on.) If the two atoms are far enough apart, all interactions involving pairs of charged particles on different atoms can be neglected and we get

$$\begin{aligned} \hat{H}\Psi_A(x_1, x_2)\Psi_B(x_3, x_4) &\approx \left[\hat{H}_A(x_1, x_2) + \hat{H}_B(x_3, x_4) \right] \Psi_A(x_1, x_2)\Psi_B(x_3, x_4) \\ &= 2E_{\text{atom}}\, \Psi_A(x_1, x_2)\Psi_B(x_3, x_4), \end{aligned} \tag{46}$$

where H_A and H_B are the two-electron Hamiltonians for the two separate atoms. Applying the antisymmetrization operator $\hat{\mathcal{A}}$ to both sides of this equation gives

$$\hat{\mathcal{A}}\hat{H}\Psi_A(x_1, x_2)\Psi_B(x_3, x_4) \approx 2E_{\text{atom}}\, \hat{\mathcal{A}}\Psi_A(x_1, x_2)\Psi_B(x_3, x_4). \tag{47}$$

The Hamiltonian is totally symmetric on exchange of particles, so it commutes with $\hat{\mathcal{A}}$ to leave

$$\hat{H} \left[\hat{\mathcal{A}}\Psi_A(x_1, x_2)\Psi_B(x_3, x_4) \right] \approx 2E_{\text{atom}} \left[\hat{\mathcal{A}}\Psi_A(x_1, x_2)\Psi_B(x_3, x_4) \right]. \tag{48}$$

We have reached the obvious result: the energy of two well-separated atoms is the sum of the atomic energies and the wave function is an antisymmetrized product of the atomic wave functions.

Within an FCI expansion, the ground states on atoms A and B can be expanded in Slater determinants constructed using orbitals on those two atoms:

$$\Psi_A(x_1, x_2) = \sum_{\mathbf{i}_A} C_{\mathbf{i}_A} D_{\mathbf{i}_A}(x_1, x_2), \qquad \Psi_B(x_3, x_4) = \sum_{\mathbf{i}_B} C_{\mathbf{i}_B} D_{\mathbf{i}_B}(x_3, x_4), \tag{49}$$

where $\mathbf{i}_A$ lists the occupied orbitals on atom A and $\mathbf{i}_B$ lists the occupied orbitals on atom B. Applying the antisymmetrization operator to a product of two Slater determinants, $D_{\mathbf{i}_A}(x_1, x_2)$ $D_{\mathbf{i}_B}(x_3, x_4)$, produces a single larger determinant containing all of the orbitals involved, so

$$\Psi_{AB}(x_1, x_2, x_3, x_4) = \sum_{\mathbf{i}_A, \mathbf{i}_B} C_{\mathbf{i}_A} C_{\mathbf{i}_B} D_{\mathbf{i}_A, \mathbf{i}_B}(x_1, x_2, x_3, x_4). \tag{50}$$

An analogous result holds for any system consisting of well-separated fragments.

An easier way to reach the same conclusions is to use second-quantized notation, where

$$\hat{H} = \sum_{i,j} \hat{c}_i^\dagger h_{ij} \hat{c}_j + \frac{1}{2} \sum_{i,j,k,l} \hat{c}_i^\dagger \hat{c}_j^\dagger V_{ijkl} \hat{c}_l \hat{c}_k, \tag{51}$$

with

$$\begin{aligned} h_{ij} &= \int \varphi_i^*(x) \left(-\frac{1}{2}\nabla^2 + V_{\text{nuc}}(\mathbf{r}-\mathbf{d}_A) + V_{\text{nuc}}(\mathbf{r}-\mathbf{d}_B) \right) \varphi_j(x)\, dx, \\ V_{ijkl} &= \iint \varphi_i^*(x)\varphi_j^*(x') \frac{1}{|\mathbf{r}-\mathbf{r}'|} \varphi_k(x)\varphi_l(x')\, dx\, dx'. \end{aligned} \tag{52}$$

When the two atoms are far enough apart, h_{ij} is negligible unless φ_i and φ_j are on the same atom and V_{ijkl} is negligible unless φ_i, φ_j, φ_k, and φ_l are all on the same atom. Furthermore, if φ_i and φ_j are both on atom A, the $V_{\text{nuc}}(\mathbf{r}-\mathbf{d}_B)$ contribution to h_{ij} is negligible and vice versa. Under these assumptions,

$$\hat{H} \approx \hat{H}_A + \hat{H}_B. \tag{53}$$

Let us write the two-electron ground states of atoms A and B, treated separately, as

$$|\Psi_A\rangle = \hat{\Psi}_A^\dagger |\text{VAC}\rangle, \qquad\qquad |\Psi_B\rangle = \hat{\Psi}_B^\dagger |\text{VAC}\rangle. \tag{54}$$

For the $S_z = 0$ ground state of Eq. (44), for example, we would have

$$\begin{aligned} \hat{\Psi}_A^\dagger &= C_1\, \hat{c}_{A,1s,\uparrow}^\dagger \hat{c}_{A,1s,\downarrow}^\dagger + C_2\, \hat{c}_{A,2s,\uparrow}^\dagger \hat{c}_{A,2s,\downarrow}^\dagger + C_3\, \hat{c}_{A,1s,\uparrow}^\dagger \hat{c}_{A,2s,\downarrow}^\dagger + C_4\, \hat{c}_{A,1s,\downarrow}^\dagger \hat{c}_{A,2s,\uparrow}^\dagger, \\ \hat{\Psi}_B^\dagger &= C_1\, \hat{c}_{B,1s,\uparrow}^\dagger \hat{c}_{B,1s,\downarrow}^\dagger + C_2\, \hat{c}_{B,2s,\uparrow}^\dagger \hat{c}_{B,2s,\downarrow}^\dagger + C_3\, \hat{c}_{B,1s,\uparrow}^\dagger \hat{c}_{B,2s,\downarrow}^\dagger + C_4\, \hat{c}_{B,1s,\downarrow}^\dagger \hat{c}_{B,2s,\uparrow}^\dagger. \end{aligned} \tag{55}$$

Since $\hat{H}_A$ commutes with $\hat{\Psi}_B^\dagger$, $\hat{H}_B$ commutes with $\hat{\Psi}_A^\dagger$, and $\hat{\Psi}_A^\dagger$ commutes with $\hat{\Psi}_B^\dagger$ (they would anti-commute if $\hat{\Psi}_A^\dagger$ and $\hat{\Psi}_B^\dagger$ both created odd numbers of electrons, but the argument below is easily generalized to the anti-commuting case), we find that $\hat{\Psi}_A^\dagger \hat{\Psi}_B^\dagger |\text{VAC}\rangle$ is the approximate four-electron ground state:

$$\begin{aligned} \hat{H}\hat{\Psi}_A^\dagger \hat{\Psi}_B^\dagger |\text{VAC}\rangle &\approx (\hat{H}_A + \hat{H}_B)\hat{\Psi}_A^\dagger \hat{\Psi}_B^\dagger |\text{VAC}\rangle \\ &= \hat{\Psi}_B^\dagger \hat{H}_A \hat{\Psi}_A^\dagger |\text{VAC}\rangle + \hat{\Psi}_A^\dagger \hat{H}_B \hat{\Psi}_B^\dagger |\text{VAC}\rangle \\ &= \hat{\Psi}_B^\dagger E_{\text{atom}}\, \hat{\Psi}_A^\dagger |\text{VAC}\rangle + \hat{\Psi}_A^\dagger E_{\text{atom}}\, \hat{\Psi}_B^\dagger |\text{VAC}\rangle = 2E_{\text{atom}}\, \hat{\Psi}_A^\dagger \hat{\Psi}_B^\dagger |\text{VAC}\rangle. \end{aligned} \tag{56}$$

The problem with the FCI singles and doubles wave function is that it neglects the contributions made by strings of four creation operators, two on atom A and two on atom B, appearing in $\hat{\Psi}_A^\dagger \hat{\Psi}_B^\dagger$. The coupled-cluster trial wave function adopts a product form from the beginning, cleverly ensuring that $\hat{\Psi}_{AB}^\dagger$ reduces to $\hat{\Psi}_A^\dagger \hat{\Psi}_B^\dagger$ when fragments A and B are far enough apart.

Instead of creating states from the vacuum, it is convenient to start from a single N-electron determinant, D_0, normally taken to be the Hartree-Fock ground state. Once D_0 has been chosen, we can separate the orbitals (and corresponding creation and annihilation operators) into two types: the N orbitals appearing in D_0 are denoted φ_i; and the $M-N$ orbitals not appearing in D_0 (known as "virtuals") are denoted φ_a. The choice of suffix (i, j, k, ... for occupied orbitals;

a, b, c, ... for unoccupied orbitals) indicates the type of any given orbital, creation operator, or annihilation operator.

Any determinant in the FCI basis set may be created from D_0 by making a number (ranging from 1 to N) of electron-hole excitations of the form $\hat{X}_i^a = \hat{c}_a^\dagger \hat{c}_i$. The excitation operator $\hat{X}_i^a$ replaces the orbital φ_i appearing in D_0 by the previously unoccupied orbital φ_a. We can also define operators that create multiple electron-hole pairs, such as the double excitation $\hat{X}_{ij}^{ab} = \hat{c}_a^\dagger \hat{c}_b^\dagger \hat{c}_i \hat{c}_j = -\hat{c}_a^\dagger \hat{c}_i \hat{c}_b^\dagger \hat{c}_j = -\hat{X}_i^a \hat{X}_j^b$. Because the excitation operators are constructed using annihilation operators for orbitals in D_0 and creation operators for orbitals not in D_0, creation and annihilation operators for the same orbital never occur. The excitation operators therefore commute with one another. No orbital in D_0 can be annihilated more than once and no orbital not in D_0 can be created more than once, so products of excitation operators are often zero. For example, $\hat{X}_i^a \hat{X}_i^a = 0$.

In the coupled-cluster method, the many-electron wave function is written in the product form

$$|\Psi\rangle = \left[\prod_{a,i} \left(1 + t_i^a \hat{X}_i^a\right) \right] \left[\prod_{b>a,j>i} \left(1 + t_{ij}^{ab} \hat{X}_{ij}^{ab}\right) \right] \ldots |D_0\rangle, \tag{57}$$

where the coupled-cluster amplitudes t_i^a and t_{ij}^{ab}, ..., are variational parameters. If the system consists of two well-separated fragments, A and B, all amplitudes involving orbitals on both fragments will be zero. After moving the terms involving fragment A to the front of the product of operators, the coupled-cluster wave function takes the separable form $\hat{\Psi}_A^\dagger \hat{\Psi}_B^\dagger |D_0\rangle$, where $\hat{\Psi}_A^\dagger$ and $\hat{\Psi}_B^\dagger$ are just as they would be for an isolated fragment. The coupled-cluster approach is therefore size consistent.

The product of any excitation operator $\hat{X}$ with itself is zero, so

$$1 + t\hat{X} = 1 + t\hat{X} + \frac{1}{2!}\left(t\hat{X}\right)^2 + \ldots = e^{t\hat{X}}. \tag{58}$$

This allows us to rewrite the coupled-cluster Ansatz in the more commonly encountered exponential form

$$\begin{aligned} |\Psi\rangle &= \left[\prod_{a,i} e^{t_i^a \hat{X}_i^a} \right] \left[\prod_{b>a,j>i} e^{t_{ij}^{ab} \hat{X}_{ij}^{ab}} \right] \ldots |D_0\rangle \\ &= \exp\left(\sum_{a,i} t_i^a \hat{X}_i^a + \sum_{a>b,i>j} t_{ij}^{ab} \hat{X}_{ij}^{ab} + \ldots \right) |D_0\rangle = \exp\left(\hat{T}\right) |D_0\rangle. \end{aligned} \tag{59}$$

Truncating the exponent at the single excitation level, including only the $\sum_{i,a} t_i^a \hat{X}_i^a$ term, leads to the coupled-cluster singles (CCS) method; truncating at double excitations yields the coupled-cluster singles and doubles (CCSD) method; and so on. Regardless of the truncation level, the expectation value of the energy of n well-separated molecules is n times the expectation value of the energy of one molecule. The exponential form ensures that the wave function always includes determinants (but not *all* determinants) with up to N electron-hole pair excitations. When the maximum excitation level reaches N, the coupled-cluster method becomes equivalent to FCI.

method	$R = R_{\text{ref}}$	$R = 2R_{\text{ref}}$
HF	0.217822	0.363954
CCSD	0.003744	0.022032
CCSDT	0.000493	−0.001405
CCSDTQ	0.000019	−0.000446

Table 1: *Difference between the energy of a water molecule calculated using the coupled-cluster method and the FCI energy in the same basis set. The convergence is very rapid at the equilibrium bond length, $R_{ref} = 1.84345a_0$, but slower when the bond length is doubled. The bond angle is fixed at 110.565^o and energies are in Hartree atomic units. Note that the coupled-cluster energy may lie below the FCI energy. Coupled-cluster results are not necessarily variational. Data from Ref. [31].*

Table 1 shows how the calculated energy of a water molecule converges as a function of the excitation level. The convergence is very rapid at the equilibrium bond length of $1.184345\,a_0$ but slower when the bond length is doubled. Despite running into difficulties if there are multiple very different determinants with similar energies, as is often the case when bonds are being broken, the CCSD method hits a sweet spot between the demands of computational efficiency and accuracy. Adding the effect of triples perturbatively yields the CCSD(T) method, often known as the "gold standard" of quantum chemistry, which frequently produces excellent results. Straightforward implementations of the CCSD and CCSD(T) methods scale steeply with system size, the effort being proportional to N^6 for CCSD and N^7 for CCSD(T), but correlations are local and it is possible to do better than this. Coupled-cluster methods are even beginning to become useful in solids.

It would be nice if it were possible to treat the CC wave function variationally, evaluating the corresponding energy expectation value and adjusting the amplitudes to minimize the total energy. Unfortunately, however, the presence of arbitrary numbers of electron-hole pairs (at all truncation levels) makes the computational effort scale factorially with system size. To motivate a more practical approach, let us suppose for the time being that the cluster operator $\hat{T}$ has not been truncated and that $|\Psi\rangle = e^{\hat{T}}|D_0\rangle$ is the exact ground-state wave function:

$$\left(\hat{H} - E_0\right) e^{\hat{T}}|D_0\rangle = 0. \tag{60}$$

Multiplying by $e^{-\hat{T}}$ gives

$$\left(e^{-\hat{T}}\hat{H}e^{\hat{T}} - E_0\right)|D_0\rangle = 0. \tag{61}$$

We can therefore view the coupled-cluster method as a search for the operator $e^{\hat{T}}$ that makes the reference determinant $|D_0\rangle$ the ground state of the similarity-transformed Hamiltonian $\hat{H}_T = e^{-\hat{T}}\hat{H}e^{\hat{T}}$. Note that $\hat{H}_T$ is not Hermitian, so its left and right eigenstates need not be the same; $|D_0\rangle$ is a right eigenstate.

In the CCSD method, we replace the cluster operator by a truncated approximation,

$$\hat{T} \approx \sum_{a,i} t_i^a \hat{X}_i^a + \sum_{a>b,i>j} t_{ij}^{ab} \hat{X}_{ij}^{ab}, \tag{62}$$

so that Eq. (61) is only approximately correct. To make it as correct as possible, we insist that it is satisfied in the subspace consisting of $|D_0\rangle$ and the determinants

$$|D_i^a\rangle = \hat{X}_i^a |D_0\rangle = \hat{c}_a^\dagger \hat{c}_i |D_0\rangle, \tag{63}$$
$$|D_{ij}^{ab}\rangle = \hat{X}_{ij}^{ab} |D_0\rangle = \hat{c}_a^\dagger \hat{c}_b^\dagger \hat{c}_i \hat{c}_j |D_0\rangle. \tag{64}$$

(Since $e^{\hat{T}}$ also contains products of excitation operators, this does not ensure that Eq. (61) is satisfied exactly.) The result is the CCSD equations:

$$\langle D_0|\hat{H}_T - E_0|D_0\rangle = \langle D_0|\hat{H}_T|D_0\rangle - E_0 = 0, \tag{65}$$
$$\langle D_i^a|\hat{H}_T - E_0|D_0\rangle = \langle D_i^a|\hat{H}_T|D_0\rangle = 0, \tag{66}$$
$$\langle D_{ij}^{ab}|\hat{H}_T - E_0|D_0\rangle = \langle D_{ij}^{ab}|\hat{H}_T|D_0\rangle = 0, \quad a>b,\ i>j. \tag{67}$$

The second and third lines provide exactly as many equations as there are amplitudes, allowing us to find the t_i^a and t_{ij}^{ab}. The first line then determines the approximate ground-state energy. Furthermore, because the determinants appearing in the bras contain no more than two electron-hole pairs, the matrix elements can all be evaluated with an effort that scales as a power of the system size.

5 Slater-Jastrow wave functions

Cusps

Quantum chemists often find it useful to divide correlation effects into two separate types. The division is not clear or absolute, but helpful nevertheless. *Static correlation* arises when the ground state contains substantial components of several significantly different determinants with similar energy expectation values. For small molecules, static correlation can in principle be dealt with by including all of the important determinants in the basis set, although the number required may grow exponentially with system size. Configuration-expansion methods such as single-reference CCSD, that make excitations from a single determinant, often find strong static correlations difficult to deal with. *Dynamic correlation* arises from the Coulomb repulsions between nearby electrons. An important contribution is made by the non-analytic cusps in the many-electron wave function at points where pairs of electrons coalesce [32, 33].

The simplest case of a wave function cusp occurs when an electron approaches a nucleus; a good example is provided by the $1s$ energy eigenfunction of a hydrogen atom, $\varphi_{1s}(r) = \frac{1}{\sqrt{\pi}} e^{-r}$. The electron-nucleus cusps can easily be built into the one-electron orbitals (although not when the orbitals are expanded in a smooth analytic basis set of Gaussians or plane waves, as is often done for computational reasons). The electron-electron cusps are difficult to represent in a basis

of Slater determinants and cause FCI expansions to converge very slowly. This is the problem that Slater-Jastrow wave functions solve.

The forms of the cusps can be understood in general [32, 33]. Consider what happens when particles 1 and 2, with masses m_1 and m_2 and charges Z_1 and Z_2, approach each other. Transforming into center-of-mass and difference coordinates, $\mathbf{r}_{\rm cm} = (m_1\mathbf{r}_1 + m_2\mathbf{r}_2)/(m_1{+}m_2)$ and $\mathbf{r} = \mathbf{r}_1{-}\mathbf{r}_2$, the N-particle Schrödinger equation becomes

$$\left(-\frac{1}{2\mu}\nabla^2_{\mathbf{r}} - \frac{1}{2M}\nabla^2_{\mathbf{r}_{\rm cm}} - \sum_{i=3}^{N}\frac{1}{2m_i}\nabla^2_{\mathbf{r}_i} + \frac{1}{2}\sum_{i=1}^{N}\sum_{\substack{j=1\\(j\neq i)}}^{N}\frac{Z_iZ_j}{r_{ij}}\right)\Psi(\mathbf{r},\mathbf{r}_{\rm cm},\sigma_1,\sigma_2,x_3,\ldots,x_N)$$
$$= E\Psi(\mathbf{r},\mathbf{r}_{\rm cm},\sigma_1,\sigma_2,x_3,\ldots,x_N), \quad (68)$$

where $\mu = m_1m_2/(m_1{+}m_2)$ is the reduced mass and $M = m_1{+}m_2$ is the total mass of the two particles involved. As $\mathbf{r}_1 \to \mathbf{r}_2$ with $\mathbf{r}_{\rm cm}$, $\mathbf{r}_3$, $\mathbf{r}_4$, …, $\mathbf{r}_N$ held fixed, the Z_1Z_2/r divergence in the potential energy must be cancelled by a corresponding divergence in the $\nabla^2_{\mathbf{r}}$ part of the kinetic energy. In other words, we require

$$\frac{1}{\Psi(\mathbf{r})}\left(-\frac{1}{2\mu}\nabla^2_{\mathbf{r}} + \frac{Z_1Z_2}{r}\right)\Psi(\mathbf{r}) \quad (69)$$

to remain finite as $r \to 0$, where $\Psi(\mathbf{r})$ is shorthand for $\Psi(\mathbf{r},\mathbf{r}_{\rm cm},\sigma_1,\sigma_2,x_3,\ldots,x_N)$.

Near the origin, we can use the familiar representation of $\Psi(\mathbf{r})$ as a linear combination of spherical harmonics and radial functions,

$$\begin{aligned}\Psi(\mathbf{r}) &= \sum_{l=0}^{\infty}\sum_{m=-l}^{l} c_{l,m}Y_{l,m}(\vartheta,\varphi)r^lR_l(r)\\ &= \sum_{l=0}^{\infty}\sum_{m=-l}^{l} c_{l,m}Y_{l,m}(\vartheta,\varphi)r^l\left(1 + b_1^{(l)}r + b_2^{(l)}r^2 + \cdots\right), \end{aligned} \quad (70)$$

where the $c_{l,m}$ and $b_i^{(l)}$ are expansion coefficients that depend on $\mathbf{r}_{\rm cm}$, σ_1, σ_2, x_3, …, x_N. Starting from this representation, a few lines of algebra show that

$$\begin{aligned}\frac{1}{\Psi}\left(-\frac{1}{2\mu}\nabla^2_{\mathbf{r}} + \frac{Z_1Z_2}{r}\right)\Psi &= \frac{1}{\Psi}\sum_{l,m}c_{l,m}Y_{l,m}\left(-\frac{1}{2\mu r^2}\frac{\partial}{\partial r}\frac{1}{r}\frac{\partial}{\partial r} + \frac{l(l{+}1)}{2\mu r^2} + \frac{Z_1Z_2}{r}\right)R_l\\ &= \frac{\sum_{l,m}c_{l,m}Y_{l,m}\left(\left(Z_1Z_2 - \dfrac{l{+}1}{\mu}\,b_1^{(l)}\right)r^{l-1} + \cdots\right)}{\sum_{l,m}c_{l,m}Y_{l,m}\,(r^l + \cdots)}. \end{aligned} \quad (71)$$

The largest terms in the denominator at small r are the ones corresponding to the smallest angular momentum for which $c_{l,m}$ is non-zero. Denoting this angular momentum by l_0, we see the right-hand side of Eq. (71) diverges as $r \to 0$ unless

$$Z_1Z_2 - \frac{l_0{+}1}{\mu}\,b_1^{(l_0)} = 0. \quad (72)$$

We can therefore express $\Psi(\mathbf{r})$ for small r as

$$\Psi(\mathbf{r}) = r^{l_0}\sum_{m=-l_0}^{l_0} c_{l_0,m}Y_{l_0,m}\left(1+\frac{\mu Z_1 Z_2}{l_0+1}r\right) + r^{l_0+1}\sum_{m=-(l_0+1)}^{l_0+1} c_{l_0+1,m}Y_{l_0+1,m} + \mathcal{O}(r^{l_0+2}). \qquad (73)$$

Any wave function that describes particles interacting via Coulomb forces must be of this form. We are interested in three specific cases of this general result.

Electron-nucleus cusps: When an electron (mass $m = 1$, charge -1) approaches a nucleus (mass M, charge $+Z$), symmetry imposes no restrictions on the value of l and one generally expects $l_0 = 0$. Equation (73) then reduces to

$$\Psi(\mathbf{r}) = c_{0,0}Y_{0,0}\big(1-Zr\big) + r\sum_{m=-1}^{1} c_{1,m}Y_{1,m} + \mathcal{O}(r^2), \qquad (74)$$

where we have noted that $M \gg 1$ and hence that $\mu \approx 1$. Since

$$Y_{1,-1} \propto \frac{x-iy}{r} \qquad Y_{1,0} \propto \frac{z}{r}, \qquad Y_{1,1} \propto \frac{x+iy}{r},$$

we can rewrite Eq. (74) as

$$\Psi(\mathbf{r}) = a_{\text{en}}\big(1-Zr\big) + \mathbf{b}_{\text{en}}\cdot\mathbf{r} + \mathcal{O}(r^2), \qquad (75)$$

where $a_{\text{en}} = c_{0,0}Y_{0,0}$ and the $\mathbf{r}$-independent vector $\mathbf{b}_{\text{en}}$ depends on $c_{1,-1}$, $c_{1,0}$ and $c_{1,1}$. The $-Zr$ contribution to the first term provides the cusp at the origin.

Electron-electron cusps, antiparallel spins: If a spin-up electron meets a spin-down electron, the wave function has singlet and triplet components in general. As long as the singlet component is non-zero, the spatial wave function need not be antisymmetric on exchange of $\mathbf{r}_1$ and $\mathbf{r}_2$ and l_0 is again 0 in the general case. Proceeding as for the electron-nucleus cusp, setting $\mu = 1/2$ and $Z = -1$, yields:

$$\Psi(\mathbf{r}) = a_{ee}^{\uparrow\downarrow}\left(1+\frac{1}{2}r\right) + \mathbf{b}_{\text{ee}}^{\uparrow\downarrow}\cdot\mathbf{r} + \mathcal{O}(r^2). \qquad (76)$$

Electron-electron cusps, parallel spins: If two electrons of the same spin meet, the spin wave function must be a triplet, implying that the spatial wave function must be antisymmetric. Only terms with odd values of l can appear in Eq. (70) and one expects l_0 to be 1 in the general case. The $l = 2$ term vanishes because it is even, so Eq. (73) becomes:

$$\begin{aligned}\Psi(\mathbf{r}) &= r\sum_{m=-1}^{1} c_{1,m}Y_{1,m}\left(1+\frac{1}{4}r\right) + \mathcal{O}(r^3)\\ &= \big(\mathbf{b}_{\text{ee}}^{\uparrow\uparrow}\cdot\mathbf{r}\big)\left(1+\frac{1}{4}r\right) + \mathcal{O}(r^3). \qquad (77)\end{aligned}$$

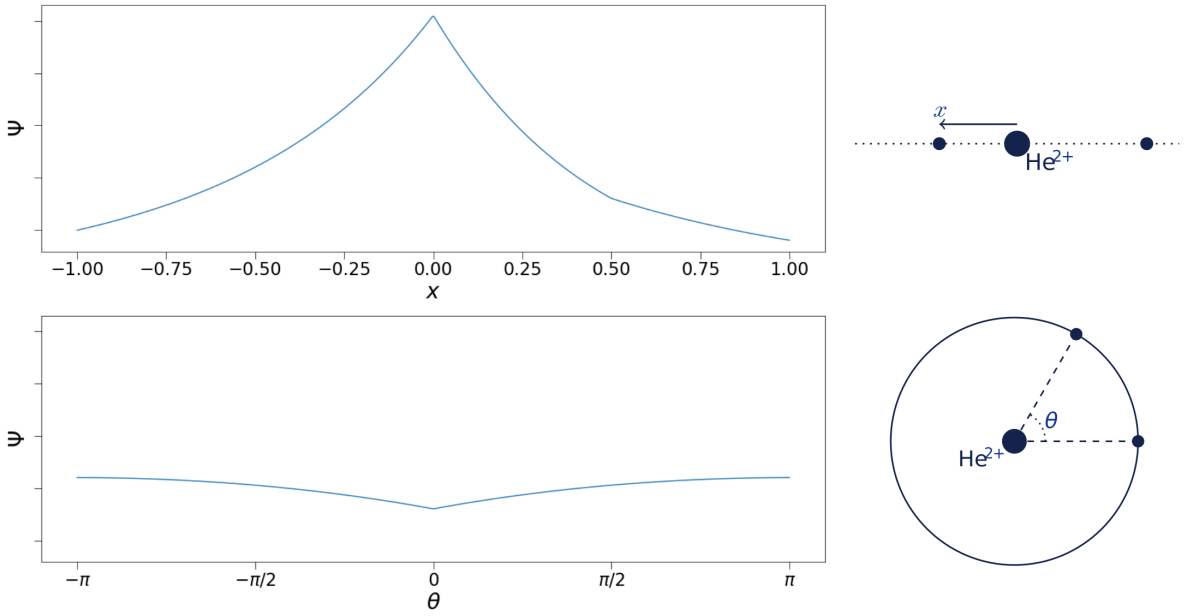

Fig. 4: *The cusps in the S=0 ground-state wave function of He, as learnt by a deep neural network. The cusps were not built in to the wave function in advance but discovered by the network in its attempts to minimize the total energy. According to Eqs. (75) and (76), the coefficients of the nuclear-electron and antiparallel electron-electron cusp terms should be -2 and 0.5; the learnt values were $-1.9979(4)$ and 0.4934(1). From Ref. [34].*

Figure 4 shows the electron-electron and electron-nucleus cusps for a helium atom. The wave function was represented as a deep neural network [34] (see later), the parameters of which were adjusted to minimize the variational ground-state energy. No attempt was made to force the network to generate the correct cusps; it discovered them spontaneously in its attempts to minimize the total energy. Its success in doing so confirms that the cusps have a significant effect on the total energy and adds weight to the assertion that it is a bad idea to use trial wave functions without cusps.

The Jastrow factor

We have explained that Slater determinants behave smoothly as electrons approach each other and cannot easily represent the electron-electron cusps. This failure increases the energy expectation value and slows down the convergence of configuration expansions. Cusp-related errors often limit the accuracy of otherwise well-converged FCI and coupled-cluster calculations.
A good way to add cusps to a Slater determinant is to use a Jastrow factor [35, 11, 7]. The determinant $D(x_1, x_2, \ldots, x_N)$ is replaced by a Slater-Jastrow wave function,

$$\Psi_{\rm SJ}(x_1, x_2, \ldots, x_N) = e^{J(x_1,x_2,\ldots,x_N)} D(x_1, x_2, \ldots, x_N), \tag{78}$$

where J is a totally symmetric function of the electron coordinates. The Jastrow factor affects the normalization in a manner that is not easy to calculate, so we have made no attempt to normalize $\Psi_{\rm SJ}$. Fortunately, QMC methods do not require normalized trial wave functions.

The simplest approximation assumes that

$$J(x_1, x_2, \ldots, x_N) = -\frac{1}{2}\sum_{i=1}^{N}\sum_{\substack{j=1\\(j\neq i)}}^{N} u(x_i, x_j) \tag{79}$$

is a sum of two-electron terms. In a typical example, $u(x_i, x_j)$ increases in value as $|\mathbf{r}_i - \mathbf{r}_j|$ decreases, suppressing the value of the wave function when pairs of electrons approach each other. The determinant incorporates the antisymmetry that helps to keep like-spin electrons apart; the Jastrow factor adds a partial description of the correlations caused by the repulsive Coulomb interactions, which keep both like- and unlike-spin electrons apart.

By making sure that $u(x_i, x_j)$ has the right behavior as $|\mathbf{r}_i - \mathbf{r}_j| \to 0$, we can also use the Jastrow factor to make Ψ_{SJ} satisfy the cusp conditions. As in our previous discussion of cusps, we express Ψ_{SJ} as a function of $\mathbf{r}, \mathbf{r}_{\text{cm}}, \sigma_1, \sigma_2, x_3, \ldots, x_N$, where $\mathbf{r} = \mathbf{r}_1 - \mathbf{r}_2$ and $\mathbf{r}_{\text{cm}} = \frac{1}{2}(\mathbf{r}_1 + \mathbf{r}_2)$. We then consider how the wave function depends on $\mathbf{r}$ at fixed σ_1, σ_2, x_3, …, x_N. Writing $\Psi(\mathbf{r}, \mathbf{r}_{\text{cm}}, \sigma_1, \sigma_2, x_3, \ldots, x_N)$ as $\Psi(\mathbf{r})$ to simplify the notation, we have $\Psi_{\text{SJ}}(\mathbf{r}) = e^{-u(\mathbf{r})}D(\mathbf{r})$.

Antiparallel spins: The antiparallel cusp condition,

$$\Psi(\mathbf{r}) = a_{ee}^{\uparrow\downarrow}\left(1 + \frac{1}{2}r\right) + \mathbf{b}_{\text{ee}}^{\uparrow\downarrow}\cdot\mathbf{r} + \mathcal{O}(r^2), \tag{80}$$

can be imposed using a spherical Jastrow function, $u(\mathbf{r}) \to u(r)$.

Expanding $u(r)$ and $D(\mathbf{r})$ about the origin,

$$u(r) = u(0) + u'(0)r + \ldots, \quad \text{and} \qquad D(\mathbf{r}) = D(\mathbf{0}) + \mathbf{r}\cdot\boldsymbol{\nabla}_{\mathbf{r}}D\big|_{\mathbf{r}=\mathbf{0}} + \ldots, \tag{81}$$

we get

$$\begin{aligned}\Psi_{\text{SJ}}(\mathbf{r}) = e^{-u(r)}D(\mathbf{r}) &= \Big(1 - u'(0)r + \ldots\Big)e^{-u(0)}\Big(D(\mathbf{0}) + \mathbf{r}\cdot\boldsymbol{\nabla}_{\mathbf{r}}D\big|_{\mathbf{r}=\mathbf{0}} + \ldots\Big)\\ &= a_{\text{ee}}^{\uparrow\downarrow}\big(1 - u'(0)r\big) + \mathbf{b}_{\text{ee}}^{\uparrow\downarrow}\cdot\mathbf{r} + \mathcal{O}(r^2),\end{aligned} \tag{82}$$

where $a_{\text{ee}}^{\uparrow\downarrow} = e^{-u(0)}D(\mathbf{0})$ and $\mathbf{b}_{\text{ee}}^{\uparrow\downarrow} = e^{-u(0)}\,\boldsymbol{\nabla}_{\mathbf{r}}D\big|_{\mathbf{r}=0}$.

In order to satisfy the spin-antiparallel cusp condition, all we require is that

$$\left.\frac{\partial u}{\partial r}\right|_{r=0} = -\frac{1}{2}. \tag{83}$$

Parallel spins: The parallel cusp condition,

$$\Psi(\mathbf{r}) = \big(\mathbf{b}_{\text{ee}}^{\uparrow\uparrow}\cdot\mathbf{r}\big)\left(1 + \frac{1}{4}r\right) + \mathcal{O}(r^3), \tag{84}$$

can also be imposed using a spherical Jastrow function. $D(\mathbf{0})$ is now zero, so (82) becomes

$$\Psi_{\text{SJ}}(\mathbf{r}) = \Big(1 - u'(0)r + \cdots\Big)e^{-u(0)}\Big(\mathbf{r}\cdot\boldsymbol{\nabla}_{\mathbf{r}}D\big|_{\mathbf{r}=\mathbf{0}} + \cdots\Big) = \big(\mathbf{b}_{\text{ee}}^{\uparrow\uparrow}\cdot\mathbf{r}\big)\big(1 - u'(0)r\big) + \mathcal{O}(r^3), \tag{85}$$

with $\mathbf{b}_{\text{ee}}^{\uparrow\uparrow} = e^{-u(0)}\,\boldsymbol{\nabla}_{\mathbf{r}}D\big|_{\mathbf{r}=\mathbf{0}}$. This has the correct cusp if

$$\left.\frac{\partial u}{\partial r}\right|_{r=0} = -\frac{1}{4}. \tag{86}$$

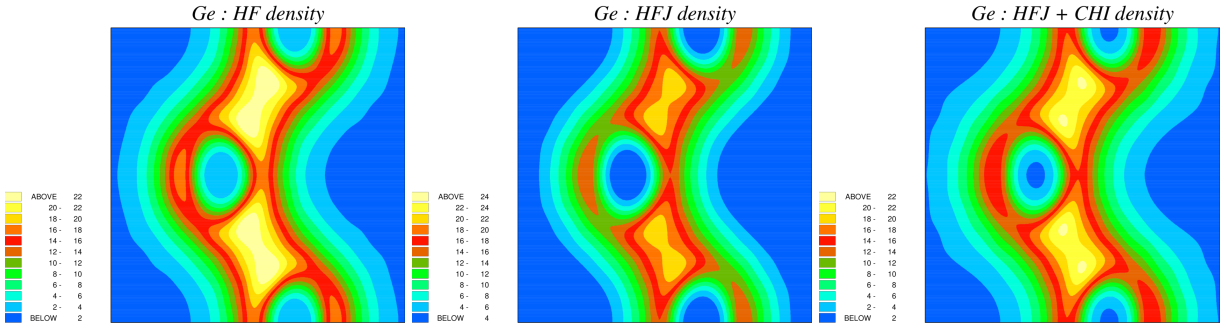

Fig. 5: *The left-hand figure shows the pseudo-valence electron density of germanium as calculated using a determinant of DFT orbitals. The middle figure shows the effect of introducing a Jastrow factor containing spherical two-electron $u(|\mathbf{r}_i-\mathbf{r}_j|)$ terms. The cusps (which cannot be seen here) are improved and the energy expectation value is lowered, but the electron density is changed significantly. The right-hand figure shows the effect of including one-electron $\chi(\mathbf{r}_i)$ terms in addition to the spherical $u(|\mathbf{r}_i-\mathbf{r}_j|)$ terms. The cusps remain correct but the density is pushed back towards the original HF density, which was quite accurate.*

Writing the spherical Jastrow function $u(x_1,x_2) = u(\mathbf{r}_1,\sigma_1,\mathbf{r}_2,\sigma_2)$ as $u_{\sigma_1\sigma_2}(r)$, we can summarize these results as follows:

$$\left.\frac{\partial u_{\sigma_1\sigma_2}(r)}{\partial r}\right|_{r=0} = \begin{cases} -\frac{1}{2}\,, & \sigma_1 = -\,\sigma_2, \\ -\frac{1}{4}\,, & \sigma_1 = \;\;\sigma_2. \end{cases} \tag{87}$$

If the one-electron orbitals are expanded in a basis of smooth functions such as plane waves or Gaussians, it is often best to incorporate the electron-nucleus cusps into the Jastrow factor too. This requires adding terms dependent on $|\mathbf{r}_i-\mathbf{d}_I|$ to J, where $\mathbf{d}_I$ is the position of nucleus I.
The large-r behavior of $u(r)$ in solids can be derived within the random phase approximation [35]. The result is that $u(r) \sim 1/\omega_p\, r$ as $r \to \infty$, where n is the average electron density and $\omega_p = \sqrt{4\pi n}$ is the plasma frequency of a uniform electron gas of that density.
The Jastrow function does not have to be pairwise or spherical. We can, for example, add any smooth function of $\mathbf{r}$ to the spherical pairwise term $u(r)$ without affecting the cusps. We can also add to J a totally symmetric one-electron contribution of the form $\sum_i \chi(x_i)$, which can provide a convenient way to optimize the electron spin density $n(x) = n(\mathbf{r},\sigma)$. An example is shown in Fig. 5. Finally, we can add terms that depend on the positions of more than two charged particles. The usual practice in QMC simulations [36] is to choose a fairly general parametrized Jastrow factor incorporating the cusps and adjust the parameters to minimize the energy expectation value.
Although one-determinant Slater-Jastrow wave functions do not achieve chemical accuracy, they are easy to use and often account for 80–90% or more of the correlation energy missed by Hartree-Fock theory. The $\mathcal{O}(N^3)$ system-size scaling of Slater-Jastrow based variational QMC simulations is favorable enough that they can be used to study periodic supercells containing of order 1000 electrons.
When studying small molecules, it is straightforward to carry out Slater-Jastrow QMC simulations with large linear combinations of Slater determinants, all multiplied by a Jastrow factor,

thus accounting for static correlation as well as dynamic correlation. Dealing with static correlation in solids is an unsolved problem in general, as the number of configurations required rises exponentially with system size, but one-determinant Slater-Jastrow VMC calculations are often used and often produce surprisingly good results. Jastrow factors are not so easy to combine with conventional quantum chemical methods such as coupled cluster, but alternative "R12" approaches are available [37].

6 Beyond Slater determinants

Attempting to describe the wave functions of solids as linear combinations of Slater determinants, with or without a Jastrow factor, is a futile task because the number of determinants required rises exponentially with system size. As a result, the vast majority of solid-state QMC simulations have used single-determinant trial wave functions. Single-determinant VMC results are not very much more accurate than DFT, but DMC simulations [11, 7] with one-determinant Slater-Jastrow trial wave functions have produced much of the most accurate data available for weakly correlated bulk solids, including the electron gas data used to parametrize the local density approximation. Until recently, it has been difficult to ascertain the quality of DMC results for solids because experiments are of limited accuracy and no better methods were known, but auxiliary-field QMC (which also requires a trial wave function) is now producing slightly better results for some molecules and solids and coupled-cluster approaches are making progress.

Given the limitations of multi-determinant expansions, it is no surprise that efforts have been made to find better starting points. An old idea that still has value is the backflow transformation introduced by Richard Feynman in 1954 [38]. Feynman's approach was inspired by the way a classical fluid flows around an obstruction and his application was to liquid ^{4}He, but the idea is general enough to work for electrons too. It was first used in a QMC simulation of the interacting electron gas in 1994 [39].

In a backflow wave function, the electron positions in the Slater determinant are replaced by "quasi-particle" coordinates that depend on the positions of other nearby electrons

$$\mathbf{q}_i = \mathbf{r}_i + \boldsymbol{\xi}_i(x_1, x_2, \ldots, x_N) = \mathbf{r}_i + \sum_{j\ (\neq i)} \eta_{ij}\mathbf{r}_{ij}, \tag{88}$$

where $\mathbf{r}_{ij} = \mathbf{r}_i - \mathbf{r}_j$ and η_{ij} depends on $r_{ij} = |\mathbf{r}_i - \mathbf{r}_j|$ and on the relative spins of electrons i and j. The Slater matrix is otherwise unchanged, but every entry in every row and column now depends on the coordinates of every electron, which slows down QMC calculations by a factor of N. Although the backflow wave function is still a determinant, it is *not* a Slater determinant and cannot be expanded as a linear combination of a small number of Slater determinants; it is something new.

One advantage of the use of parametrized backflow transformations is that they provide a convenient way to adjust the *nodal surface* of the trial wave function. Given a choice of the spin coordinates $(\sigma_1, \sigma_2, \ldots, \sigma_N)$, the nodal surface is the $(3N-1)$-dimensional surface in the $3N$-dimensional space of positions $(\mathbf{r}_1, \mathbf{r}_2, \ldots, \mathbf{r}_N)$ on which the wave function is zero. It matters

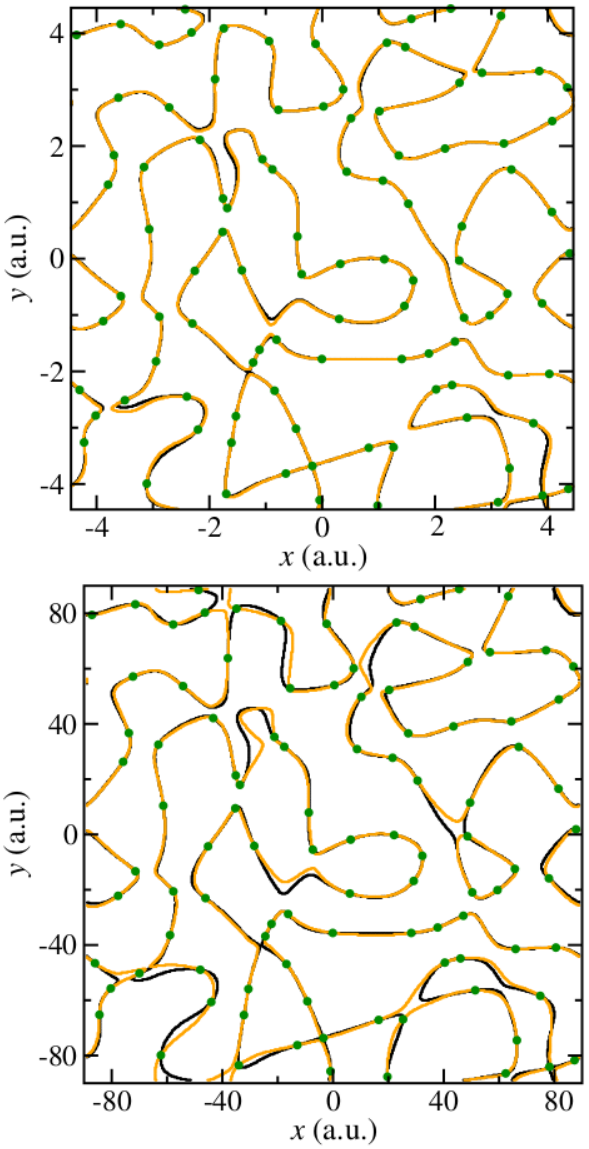

Fig. 6: *Nodes encountered when moving one of the electrons in a two-dimensional homogeneous gas of 101 like-spin electrons. The positions of the other 100 electrons, indicated by the green circles, are held fixed. The Hartree-Fock and backflow nodes are in black and orange, respectively. The top panel shows results for a weakly correlated electron gas with density parameter $r_s = 0.5$; the bottom panel shows results for a less dense and more strongly correlated electron gas with $r_s = 10$. From Ref. [40].*

because the quality of the nodal surface is the only factor that limits the quality of DMC results: if the nodal surface is exact, DMC gives the exact ground-state energy. Figure 6 shows how the nodes of an optimized backflow wave function differ from those of the Hartree-Fock determinant [40]. The differences are subtle but improve the quality of the results substantially. As far as can be ascertained, energies calculated using backflow DMC simulations of electron gases at densities comparable to those found in most solids are almost exact. Results for light atoms, where we know the ground-state energy almost exactly, are somewhat less impressive but Fig. 7 shows that backflow remains useful, reducing the error in the total energy of a Slater-Jastrow wave function by more than 50%.

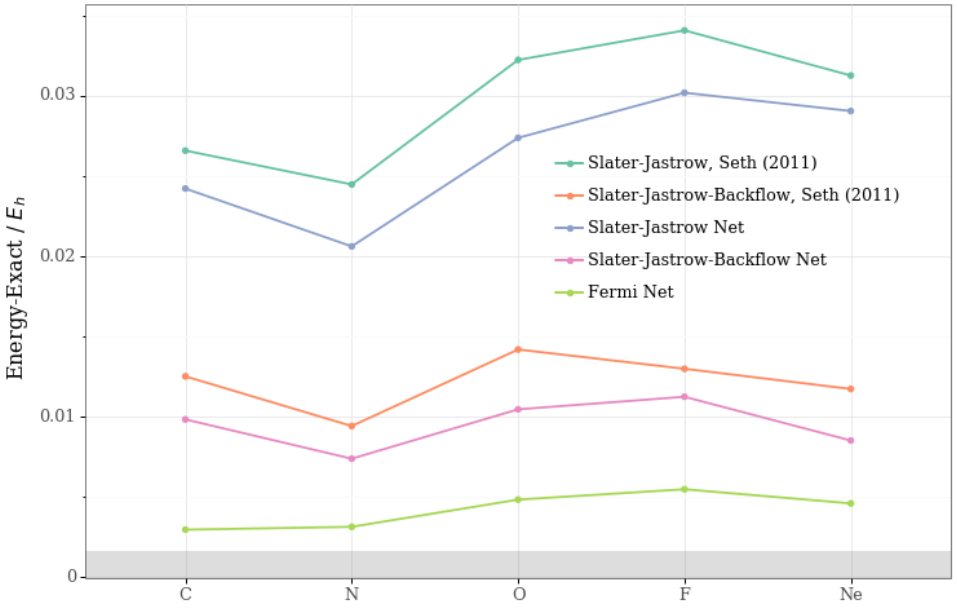

Fig. 7: *Errors in the energies of various atoms as calculated using a variety of different one-determinant VMC trial wave functions. Hartree atomic units are used. The data used to plot the cyan and orange lines comes from Ref. [41]; the other three lines show data from Ref. [34].*

Backflow is a good idea but we can take it much further [34]. Nothing requires the orbitals in a Slater determinant to be functions of the coordinates of a single electron only, nor need they be functions of a single three-dimensional (plus spin) quasi-particle coordinate, as in a backflow wave function. The only requirement is that interchanging any two coordinates, x_i and x_j, exchanges the corresponding columns of the determinant and thus changes the sign of the wave function. This freedom allows us to replace the one-electron orbitals $\varphi_i(x_j)$ by multi-electron functions of the form

$$\varphi_i(x_j; x_1, \ldots, x_{j-1}, x_{j+1}, \ldots, x_N) = \varphi_i(x_j; \{x_{/j}\}), \tag{89}$$

where $x_{/j}$ is shorthand for all of the coordinates except x_j. As long as $\varphi_i(x_j; \{x_{/j}\})$ is invariant under any change in the order of the arguments after x_j, the resulting wave function,

$$D = \begin{vmatrix} \varphi_1(x_1, \{x_{/1}\}) & \varphi_1(x_2, \{x_{/2}\}) & \ldots & \varphi_1(x_N, \{x_{/N}\}) \\ \varphi_2(x_1, \{x_{/1}\}) & \varphi_2(x_2, \{x_{/2}\}) & \ldots & \varphi_2(x_N, \{x_{/N}\}) \\ . & . & \ldots & . \\ . & . & \ldots & . \\ \varphi_N(x_1, \{x_{/1}\}) & \varphi_N(x_2, \{x_{/2}\}) & \ldots & \varphi_N(x_N, \{x_{/N}\}) \end{vmatrix}, \tag{90}$$

is totally antisymmetric.

Surprisingly, it can be shown that *any* totally antisymmetric wave function can be represented as a *single* generalized determinant of this type [34]. The proof does not explain how to construct the generalized determinant we need, but the fact that it exists is reassuring: the exponential wall that makes expanding many-electron wave functions in conventional Slater determinants so difficult might not apply when generalized determinants are used. The NP hardness of the

many-electron problem is bound to rear its ugly head somewhere, but it is going to take a different form and the exponential rise in difficulty with system size might be less steep.

Trial wave functions of the type introduced in Eq. (90) are so general that it is hard to see how to parametrize them. This is a common problem with trial wave function construction: the more general the functional form, the more parameters you need and the less you know about which ones to choose. Until a few years ago, this would have ruled out using generalized determinants, but recent progress in machine learning [42, 43] has made it much easier to find parametrized representations of extremely complicated functions without having to choose the functional form or parameters explicitly. Deep neural networks [44] are general function approximators, able in principle to represent any function in any number of dimensions. Furthermore, via the magic of automatic differentiation and back propagation, optimizing the parameters that define a neural network is remarkably efficient.

In Ref. [34], generalized determinants were represented using a new neural network architecture, the *Fermi Net*, designed to guarantee the necessary exchange symmetries but otherwise being very general. The method used was VMC, conventional in all respects except for the wave function. The Fermi Net *was* the wave function and was used to calculate the value and first and second derivatives of the wave function at arbitrary points in coordinate space. This is all that is required to implement the Metropolis algorithm and allow the calculation of the local energy. The parameters of the network were adjusted to minimize the energy expectation value, exactly as prescribed by the variational principle. Learning from the variational principle differs from the more frequently encountered concept of learning from data; the Fermi-Net optimization generates its own input on the fly and can never run out of training data.

Using neural networks to represent wave functions is a fashionable idea and several other approaches are being explored [45–47]. Here I concentrates on Fermi Net because I played a minor role in helping to develop it and because it is in some way the most accurate approach proposed so far. The field is so young, however, that I would not be surprised to see better approaches come along soon.

The Fermi Net takes electron spins σ_i, positions $\mathbf{r}_i$, the vectors between electrons $\mathbf{r}_i - \mathbf{r}_j$, and electron-nucleus vectors $\mathbf{r}_i - \mathbf{d}_I$ as input. The network is only capable of representing smooth analytic functions of position (this is on purpose; the VMC method runs into difficulties if the gradient or value of the trial wave function is discontinuous), so it is unable to represent the cusps exactly. To circumvent this problem, the distances $|\mathbf{r}_i - \mathbf{r}_j|$ and $|\mathbf{r}_i - \mathbf{d}_I|$ are also provided as inputs. The distance function $|\mathbf{r}|$ has its own cusp at the origin, enabling the network to represent the electron-electron and electron-nucleus cusps as smooth functions of the interparticle distances. As was shown in Fig. 4, it accomplishes this very effectively. Note that the Fermi-Net wave function takes positions as input and returns values of the wave function as output. No one-electron or many-electron basis set is required.

Although this approach to machine learning wave functions has only been applied to atoms and small molecules to date, the results have been spectacularly good. Fermi-Net wave functions are clearly much better than any other known type of VMC trial wave function used in such systems.

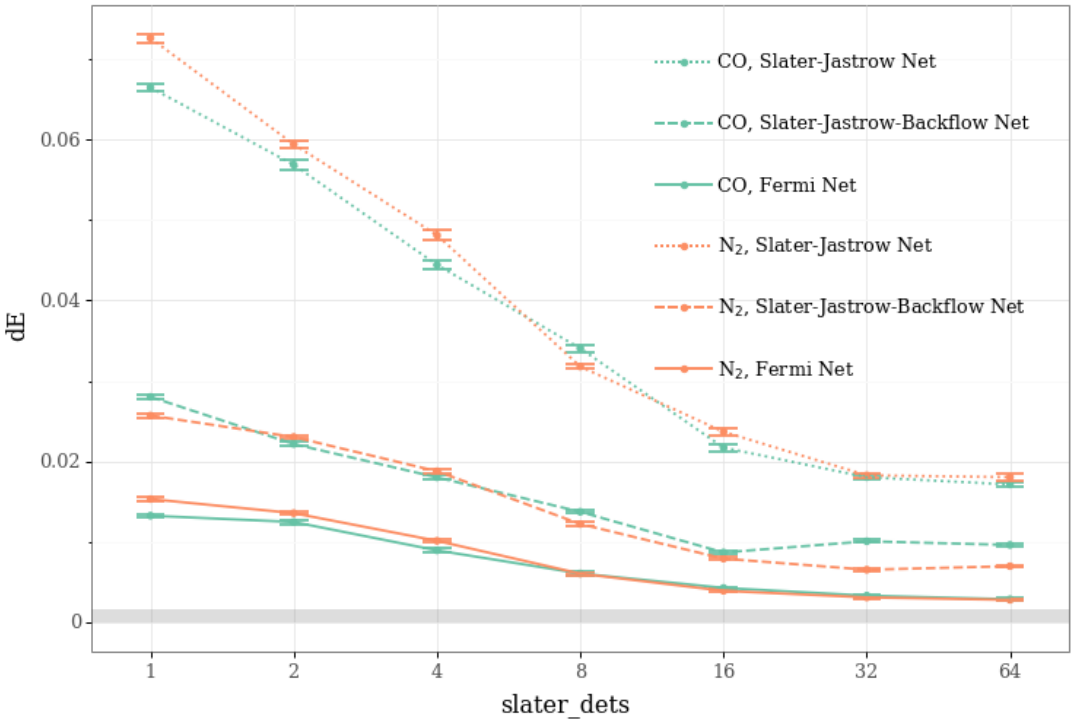

Fig. 8: *Convergence with the number of determinants of the total energy (in Hartrees) of the CO and N_2 molecules. The Slater-Jastrow, Slater-Jastrow-backflow, and Fermi-Net wave functions were all represented as neural networks. From Ref. [34].*

Figure 7 compares the accuracies of several different one-determinant VMC methods. The dark blue and cyan lines show results obtained with a single-determinant Slater-Jastrow wave function. They differ only because the dark blue results were generated using a neural-network representation of the Slater-Jastrow wave function whereas the cyan line used an explicitly parametrized functional form [41]. The generality and freedom inherent in the neural network allows it to slightly outperform the conventional implementation. The orange and pink lines are related in the same way. Both show results for a single-determinant Slater-Jastrow-backflow wave function, but the orange line used a conventional representation and the pink line a neural network representation. The green line shows the Fermi-Net results. Even though only one determinant was used, they are quite close to chemical accuracy indicated by the grey bar.

Figure 8 illustrates the convergence of the total energy of two molecules, CO and N_2, as a function of the number of determinants used. All results were obtained using neural-network wave functions of the corresponding type, so these are fair comparisons. The results obtained with 16 Fermi-Net determinants are close to chemical accuracy. From now on, all of the calculations reported used 16 Fermi-Net determinants and a neural network with approximately 700,000 variational parameters. This may sound extreme, but the number of amplitudes required for comparably accurate CCSD(T) calculations is even larger.

Figure 9 shows results for various molecules with up to 30 electrons. All of the methods investigated are less accurate for larger systems, but the Fermi Net is again the best and the growth of the Fermi Net errors with system size appears to be more systematic.

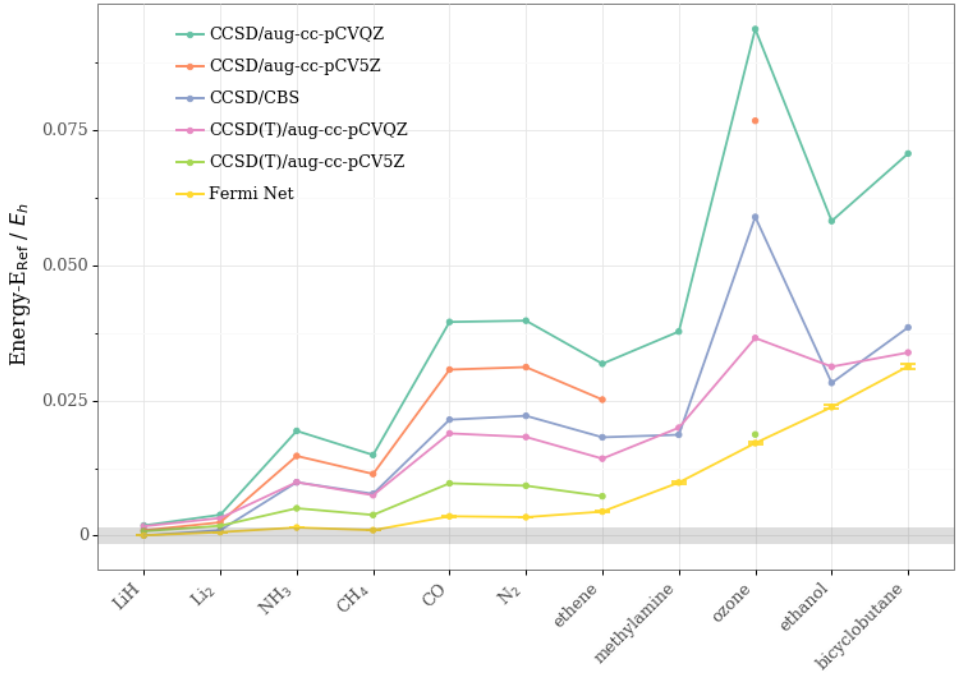

Fig. 9: *Errors in the total energies (in Hartrees) of various molecules with up to 30 electrons calculated using Fermi Net, CCSD, and CCSD(T). High-quality QZ and 5Z basis sets were used for the coupled-cluster calculations. From Ref. [34].*

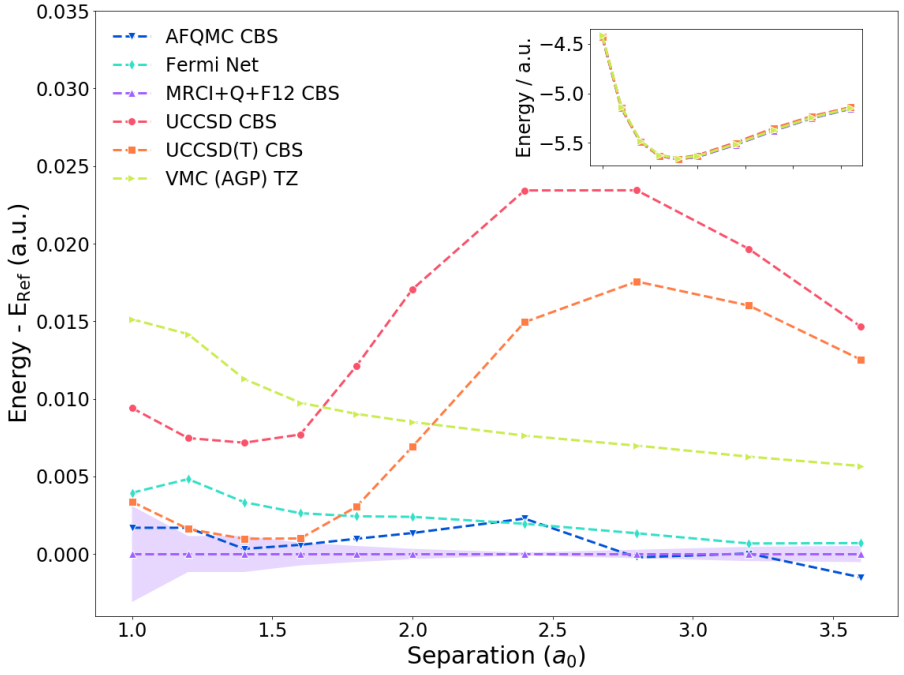

Fig. 10: *Energy (in Hartrees) of the H_{10} chain calculated using a wide variety of different methods for a range of inter-atomic distances (in Bohr radii). All energies are measured relative to the MRCI + Q + F12 CBS energy. The mauve shaded region indicates the estimated uncertainty in the reference result. Fermi Net results from Ref. [34]; all other results from Ref. [48].*

The H_{10} chain was the subject of an important recent benchmark paper [48] comparing practically every accurate method known at the time. Figure 10 shows the total energy as a function of the inter-atomic spacing. At each spacing, all energies are measured relative to a reference obtained by extrapolating the MRCI + Q + F12 result to the complete basis set (CBS) limit. The mauve shaded region indicates the estimated uncertainty in the reference energy. All of the data except for the Fermi-Net results came from Ref. [48]. Despite the newness and conceptual simplicity of our neural-net based approach, it comfortably outperforms most of its rivals.

References

[1] M. Troyer and U.J. Wiese, Phys. Rev. Lett. **94**, 170201 (2005)

[2] S. Azadi, B. Monserrat, W.M.C. Foulkes, and R.J. Needs, Phys. Rev. Lett. **112**, 165501 (2014)

[3] N.D. Drummond, R.J. Needs, A. Sorouri, and W.M.C. Foulkes, Phys. Rev. B **78**, 125106 (2008)

[4] R.G. Parr and W. Yang: *Density-Functional Theory of Atoms and Molecules* (Oxford University Press, 1989)

[5] J. Kohanoff: *Electronic Structure Calculations for Solids and Molecules: Theory and Computational Methods* (Cambridge University Press, 2006)

[6] R.M. Martin: *Electronic Structure: Basic Theory and Practical Methods* (Cambridge University Press, 2008)

[7] R.M. Martin, L. Reining, and D.M. Ceperley: *Interacting Electrons: Theory and Computational Approaches* (Cambridge University Press, 2016)

[8] X.W. Guan, M.T. Batchelor, and C. Lee, Rev. Mod. Phys. **85**, 1633 (2013)

[9] J. Bardeen, L.N. Cooper, and J.R. Schrieffer, Phys. Rev. **108**, 1175 (1957)

[10] R.B. Laughlin in R.E. Prange and S.M. Girvin (eds.): *The Quantum Hall Effect* (Springer, New York, 1990), chap. 7, p. 233.

[11] W.M.C. Foulkes, L. Mitas, R.J. Needs, and G. Rajagopal, Rev. Mod. Phys. **73**, 33 (2001)

[12] S. Zhang in E. Pavarini, E. Koch, and S. Zhang (eds.): *Many-Body Methods for Real Materials* (Forschungszentrum Jülich, 2019), Ch. 6 `www.cond-mat.de/events/correl19/manuscripts/correl19.pdf`

[13] M. Casula and S. Sorella, J. Chem. Phys. **119**, 6500 (2003)

[14] M. Bajdich, L. Mitas, L.K. Wagner, and K.E. Schmidt, Phys. Rev. B **77**, 115112 (2008)

[15] C. Genovese, T. Shirakawa, K. Nakano, and S. Sorella, arXiv:2002.03347 (2020)

[16] U. Schollwöck, Rev. Mod. Phys. **77**, 259 (2005)

[17] R. Orús, Ann. Phys. **349**, 117 (2014)

[18] N. Ashcroft and N.D. Mermin: *Solid State Physics* (Brooks Cole, 1976)

[19] J.W. Negele and H. Orland: *Quntum Many-Particle Systems* (Perseus, 1998)

[20] T. Helgaker, P. Jorgensen, and J. Olsen: *Molecule Electronic-Structure Theory* (Wiley, 2014)

[21] R.Q. Hood, M.Y. Chou, A.J. Williamson, G. Rajagopal, R.J. Needs, and W.M.C. Foulkes, Phys. Rev. Lett. **78**, 3350 (1997)

[22] G.H. Booth, A.J.W. Thom, and A. Alavi, J. Chem. Phys. **131**, 054106 (2009)

[23] D. Cleland, G.H. Booth, and A. Alavi, J. Chem. Phys. **132**, 041103 (2010)

[24] G.H. Booth, A. Grüneis, G. Kresse, and A. Alavi, Nature **493**, 365 (2013)

[25] J.S. Spencer, N.S. Blunt, and W.M.C. Foulkes, J. Chem. Phys. **136**, 054110 (2012)

[26] E. Giner, A. Scemama, and M. Caffarel, Can. J. Chem. **91**, 879 (2013)

[27] F.A. Evangelista, J. Chem. Phys. **140**, 124114 (2014)

[28] N.M. Tubman, J. Lee, T.Y. Takeshita, M. Head-Gordon, and K.B. Whaley, J. Chem. Phys. **145**, 044112 (2016)

[29] A.A. Holmes, N.M. Tubman, and C.J. Umrigar, J. Chem. Theory Comput. **12**, 3674 (2016)

[30] I. Shavitt and R.J. Bartlett: *Many-Body Methods in Chemistry and Physics: MBPT and Coupled-Cluster Theory* (Cambridge University Press, 2009)

[31] W. Klopper and D.P. Tew: *Coupled cluster theory: Fundamentals* (2006) `www.ipc.kit.edu/theochem/download/Kapitel3.pdf`

[32] T. Kato, Commun. Pure Appl. Math. **10**, 151 (1957)

[33] R.T. Pack and W.B. Brown, J. Chem. Phys. **45**, 556 (1966)

[34] D. Pfau, J.S. Spencer, A.G.d.G. Matthews, and W.M.C. Foulkes, arXiv:1909.02487 (2019)

[35] D.M. Ceperley, Phys. Rev. B **18**, 3126 (1978)

[36] P. López-Ríos, P. Seth, N.D. Drummond, and R.J. Needs, Phys. Rev. E **86**, 036703 (2012)

[37] W. Klopper, F.R. Manby, S. Ten-No, and E.F. Valeev, Int. Rev. Phys. Chem. **25**, 427 (2007)

[38] R.P. Feynman, Phys. Rev. **94**, 262 (1954)

[39] Y. Kwon, D.M. Ceperley, and R.M. Martin, Phys. Rev. B **48**, 12037 (1993)

[40] P. López Ríos, A. Ma, N.D. Drummond, M.D. Towler, and R.J. Needs, Phys. Rev. E **74**, 066701 (2006)

[41] P. Seth, P. López-Ríos, and R.J. Needs, J. Chem. Phys. **134**, 084105 (2011)

[42] A. Krizhevsky, I. Sutskever, and G.E. Hinton: In *NIPS* (2012), Vol. 25, pp. 1097–1105

[43] D. Silver, A. Huang, C.J. Maddison, A. Guez, L. Sifre, G. Van Den Driessche, J. Schrittwieser, I. Antonoglou, V. Panneershelvam, M. Lanctot et al., Nature **529**, 485 (2016)

[44] I. Goodfellow, Y. Bengio, and A. Courville: *Deep Learning* (MIT Press, 2017)

[45] D. Luo and B.K. Clark, Phys. Rev. Lett. **122**, 226401 (2019)

[46] J. Hermann, Z. Schätzle, and F. Noé, arXiv:1909.08423 (2019)

[47] K. Choo, A. Mezzacapo, and G. Carleo, Nat. Commun. **11**, 2368 (2020)

[48] M. Motta, D.M. Ceperley, G.K.L. Chan, J.A. Gomez, E. Gull, S. Guo, C.A. Jiménez-Hoyos, T.N. Lan, J. Li, F. Ma, A.J. Millis, N.V. Prokof'ev, U. Ray, G.E. Scuseria, S. Sorella, E.M. Stoudenmire, Q. Sun, I.S. Tupitsyn, S.R. White, D. Zgid, and S. Zhang, Phys. Rev. X **7**, 031059 (2017)

3 From Electrons to Interatomic Potentials for Materials Simulations

Ralf Drautz
ICAMS
Ruhr-Universität Bochum

Contents

E. Pavarini and E. Koch (eds.)
Topology, Entanglement, and Strong Correlations
Modeling and Simulation Vol. 10
Forschungszentrum Jülich, 2020, ISBN 978-3-95806-466-9
http://www.cond-mat.de/events/correl20

1 Interatomic potentials for materials simulation

The computation of phase diagrams or mechanical properties of materials needs millions of force evaluations for thousands of atoms, requirements which make these simulations unfeasible with density functional theory (DFT). For many problems in materials science, chemistry, or physics it is essential to simplify the description of the interatomic interaction in order that large and long time atomistic simulations become possible.

The development of interatomic potentials is not a new field. Potentials became important when the first computers were available to carry out atomistic simulations. Until about the 1980's the development of interatomic potentials was largely empirical. The electrons were regarded as a glue that mediates the interaction of the atomic cores and the mathematical modeling of the glue was based on intuition and trial and error. Interatomic potentials for materials that are the focus of this chapter were developed along different strategies than force fields for biology and polymer science. Guidance for the development of interatomic potentials for materials was then obtained from DFT or tight-binding electronic structure methods. The assumption of a constant semi-infinite recursion chain (discussed in Sec. 3.1) leads to the second-moment potentials [1–3]. The square-root embedding function of the Finnis-Sinclair potential [4],

$$E_i = \sqrt{\rho_i} + \frac{1}{2}\sum_j V(r_{ji})\,, \tag{1}$$

is explained from the root mean square width of the second moment (see Sec. 3.4), where $\rho_i = \sum_j \phi(r_{ji})$ is the local density of atomic sites and where ϕ and V are pairwise functions of the interatomic distance between atoms i and j. The observation that the atomic energy is a non-linear function of the charge density [5, 6] also motivated the embedded atom method [7], where instead of the square-root function of the Finnis-Sinclair potential a general, quasi-concave embedding function is used. While the Finnis-Sinclair and embedded atom method potentials compute the densities as a pairwise sum over neighbors, Tersoff included an angularly dependent three-body term for modeling directional bond formation in semiconductors [8, 9], so that the energy is written as a non-linear function that depends on a three-body contribution $\rho_i = \sum_{jk} \phi(\boldsymbol{r}_{ji}, \boldsymbol{r}_{ki})$. Later angular terms were also introduced in the modified embedded atom method [10].

Since then many different potentials were developed, with more complex many-body contributions and improved descriptions of bond formation. From the many developments I will present two strategies:

1. the derivation of interatomic potentials from a systematic coarse graining of the electronic structure,

2. the development of general parametrizations of the many-atom interactions for interpolating reference data.

The bond-order potentials (BOPs) are derived by first simplifying DFT to the tight-binding (TB) approximation. Then local, approximate solutions of the TB models are developed from which

expressions for the effective interaction between atoms are obtained. In this way the analytic BOPs provide a rigorous derivation of interatomic potentials for semiconductors [11, 12] and metals [13, 14], where the BOPs for metals will be discussed in this chapter. At their lowest order of approximation the BOPs recover the Tersoff [8, 9] and Finnis-Sinclair [4] potentials, respectively.

In contrast, the development of more formal, general parametrizations is often based on large numbers of DFT data that enable the application of methods from statistical learning for interpolating the reference data. This has led to the development of machine-learning interatomic potentials, such as neural networks potentials [15] or Gaussian process regression for the Gaussian approximation potentials [16]. The field is very active with many recent developments [17–36]. The machine-learning potentials reproduce DFT reference data sets with excellent accuracy. As machine-learning potentials are not derived or motivated by physical or chemical intuition, the excellent accuracy of the machine-learning potentials comes at the cost of interpretability. Machine-learning potentials employ a descriptor that quantifies the local atomic environment. The atomic energy or other atomic properties are then learned as a non-trivial function of the descriptor by training with reference data. The atomic cluster expansion (ACE) provides a formally complete descriptor of the local atomic environment [34,37] and may be used to compare and re-expand different machine-learning interatomic potentials.

In section 2, I will discuss the derivation of the TB approximation from DFT. In Sec. 3 the moments theorem will be introduced. Several local expansions that implicitly or explicitly exploit the moments theorem will then be summarized, before the analytic BOPs will be introduced. In Sec. 4, I will discuss the ACE for the many-atom expansion of the interatomic interaction.

2 Coarse graining the electronic structure for interatomic potentials

The TB approximation is obtained from a second-order expansion of the DFT functional. I will first discuss the second-order expansion of the DFT energy and then introduce the TB approximation. This section follows closely the review in Ref. [38]. It builds on many earlier developments. Here I highlight a few references only, some of which were key for the development of modern TB, others which provide excellent reviews [39–47].

2.1 Second-order expansion of the density functional

The contributions to the Hohenberg-Kohn-Sham DFT energy functional [48, 49] are given by

$$E = T_S + E_H + E_{XC} + E_{ext}\,, \tag{2}$$

with T_S the kinetic energy of the non-interacting electrons, E_H the Hartree energy, E_{XC} the exchange-correlation energy and E_{ext} the interaction of the electrons with the nuclei. The Coulomb interaction between the cores of the nuclei still needs to be added for the computation of total energies. Next, the eigenstates ψ_n are expanded in basis functions φ_i. In general

the basis functions are non-orthogonal,

$$S_{ij} = \langle \varphi_i | \varphi_j \rangle \quad \text{and} \quad \delta_{ij} = \langle \varphi^i | \varphi_j \rangle \quad \text{with} \quad |\varphi^i\rangle = \sum_j S^{-1}_{ij} |\varphi_j\rangle \,, \tag{3}$$

with the overlap matrix S. The basis function indices may be raised with the inverse of the overlap matrix and lowered with the overlap matrix, which enables a more compact notation in the following. The eigenstates are then written as

$$|\psi_n\rangle = \sum_i c^{i(n)} |\varphi_i\rangle \,, \quad \text{and} \quad c^{i(n)} = \sum_j S^{-1}_{ij} c^{(n)}_j \,, \tag{4}$$

with expansion coefficients $c^{i(n)}$. The matrix elements of the density matrix are given by

$$\rho^{ij} = \langle \varphi^i | \hat{\rho} | \varphi^j \rangle = \sum_n f_n \langle \varphi^i | \psi_n \rangle \langle \psi_n | \phi^j \rangle = \sum_n f_n c^{i(n)} (c^{j(n)})^* \,, \tag{5}$$

with the occupation numbers f_n of the eigenstates ψ_n. Here I take $f_n = 1$ for occupied states below the Fermi level and $f_n = 0$ for empty states above the Fermi energy. The charge density is expressed as

$$\rho(\boldsymbol{r}) = \sum_{ij} \rho^{ij} \varphi_i(\boldsymbol{r}) \varphi^*_j(\boldsymbol{r}) \,. \tag{6}$$

If expressed in eigenstates, the density matrix is diagonal

$$\rho_{nn'} = f_n \delta_{nn'} \,. \tag{7}$$

The DFT energy can be categorized in first-, second-, and higher-order contributions in terms of the density matrix. The kinetic energy of non-interacting electrons is linear in the density matrix,

$$T_S = \sum_n f_n \langle \psi_n | \hat{T} | \psi_n \rangle = \boldsymbol{T\rho} \,, \tag{8}$$

where here and in the following the trace is implicitly included in the matrix products,

$$\boldsymbol{T\rho} = \sum_{ij} T_{ij} \rho^{ji} \,. \tag{9}$$

The matrix elements of $\boldsymbol{T}$ are given by

$$T_{ij} = \langle \varphi_i | \hat{T} | \varphi_j \rangle \,. \tag{10}$$

The external energy that contains the interaction of the electrons with the ionic cores is also written as a first-order term

$$E_{ext} = \int V^{ext}(\boldsymbol{r}) \rho(\boldsymbol{r}) \, d\boldsymbol{r} = \boldsymbol{V}^{ext} \boldsymbol{\rho} \,, \tag{11}$$

with

$$V^{ext}_{ij} = \int \varphi^*_i(\boldsymbol{r}) V_{ext}(\boldsymbol{r}) \varphi_j(\boldsymbol{r}) \, d\boldsymbol{r} \,. \tag{12}$$

The Hartree energy E_H is of second order in the density matrix $\boldsymbol{\rho}$ or the density ρ,

$$E_H = \frac{1}{2}\int \frac{\rho(\boldsymbol{r})\rho(\boldsymbol{r}')}{|\boldsymbol{r}-\boldsymbol{r}'|} d\boldsymbol{r}\, d\boldsymbol{r}' = \sum_{ijkl} \frac{1}{2} J^H_{ijkl}\, \rho^{ij}\rho^{kl} = \frac{1}{2}\boldsymbol{J}^H\boldsymbol{\rho}\boldsymbol{\rho}\,, \tag{13}$$

with the Coulomb integral

$$J^H_{ijkl} = \frac{1}{2}\int \frac{\varphi_i^*(\boldsymbol{r})\varphi_j(\boldsymbol{r})\,\varphi_k^*(\boldsymbol{r}')\varphi_l(\boldsymbol{r}')}{|\boldsymbol{r}-\boldsymbol{r}'|} d\boldsymbol{r}\, d\boldsymbol{r}'\,. \tag{14}$$

The exchange-correlation energy E_{XC} is in general parametrized as a non-linear functional of the density ρ and gradients of the density and therefore the only contribution to the DFT energy that contains terms beyond second order. Here I just write a formal series expansion as

$$E_{XC} = \boldsymbol{V}^{XC}\boldsymbol{\rho} + \frac{1}{2}\boldsymbol{J}^{XC}\boldsymbol{\rho}\boldsymbol{\rho} + \frac{1}{6}\boldsymbol{K}^{XC}\boldsymbol{\rho}\boldsymbol{\rho}\boldsymbol{\rho} + \cdots\,. \tag{15}$$

As the exchange correlation energy summarizes corrections due to many-electron interactions, it is relatively short ranged. For example, while $\boldsymbol{J}^H$ decays as $1/r$ for large separations between the orbitals, we expect that the term $\boldsymbol{J}^{XC}$ is limited to distances of the order of the interatomic separation.
By grouping terms of the same order,

$$\boldsymbol{V} = \boldsymbol{T} + \boldsymbol{V}^{ext} + \boldsymbol{V}^{XC}\,, \quad \boldsymbol{J} = \boldsymbol{J}^H + \boldsymbol{J}^{XC}\,, \quad \boldsymbol{K} = \boldsymbol{K}^{XC}\,, \tag{16}$$

the DFT energy is written as a polynomial expansion in the density matrix

$$E = \boldsymbol{V}\boldsymbol{\rho} + \frac{1}{2}\boldsymbol{J}\boldsymbol{\rho}\boldsymbol{\rho} + \frac{1}{6}\boldsymbol{K}\boldsymbol{\rho}\boldsymbol{\rho}\boldsymbol{\rho} + \cdots\,. \tag{17}$$

2.1.1 Hamiltonian and band energy

The elements of the Hamiltonian matrix are obtained from the derivative of the energy with respect to the density matrix

$$\boldsymbol{H} = \frac{\partial E}{\partial \boldsymbol{\rho}} = \boldsymbol{V} + \boldsymbol{J}\boldsymbol{\rho} + \frac{1}{2}\boldsymbol{K}\boldsymbol{\rho}\boldsymbol{\rho} + \cdots\,. \tag{18}$$

The energy may then be represented as the band energy $E_{band} = \boldsymbol{H}\boldsymbol{\rho}$ and a double-counting contribution,

$$E = \boldsymbol{H}\boldsymbol{\rho} - \frac{1}{2}\boldsymbol{J}\boldsymbol{\rho}\boldsymbol{\rho} - \frac{1}{3}\boldsymbol{K}\boldsymbol{\rho}\boldsymbol{\rho}\boldsymbol{\rho} - \cdots\,. \tag{19}$$

The band energy may be decomposed into contributions from different orbitals simply as

$$E_{band,i} = \sum_j H_{ij}\rho^{ij} \quad \text{and} \quad E_{band} = \sum_i E_{band,i}\,. \tag{20}$$

This is called the *intersite* representation of the band energy as it involves two orbitals i and j. By making use of $\sum_j H_{ij}c^{j(n)} = E_n c_i^{(n)}$, where E_n is the eigenvalue of eigenstate ψ_n, and

inserting in the band energy, one arrives at $E_{band} = \sum_i \sum_n f_n E_n c_i^{(n)} (c^{i(n)})^*$. It is customary to define the local and global density of states

$$n_i(E) = \sum_n c_i^{(n)} (c^{i(n)})^* \, \delta(E_n - E) \,, \quad \text{and} \quad n(E) = \sum_i n_i(E) = \sum_n \delta(E_n - E) \,, \tag{21}$$

such that

$$E_{band,i} = \int^{E_F} E \, n_i(E) \, dE \quad \text{and} \quad E_{band} = \int^{E_F} E \, n(E) \, dE \,, \tag{22}$$

with the Fermi energy E_F. This is called the *onsite* representation of the band energy as it involves only one orbital i.

2.1.2 Perturbation expansion

Often one is interested in the response of a material to a perturbation. Then instead of expanding the DFT energy about $\rho = 0$, one would like to discuss the energy associated to the deviation of the density from a particular density $\rho^{(0)}(\boldsymbol{r})$ [39, 40]. I re-expand the series Eq. (17) about a reference density matrix $\boldsymbol{\rho}^{(0)}$ such that

$$\boldsymbol{\rho} = \boldsymbol{\rho}^{(0)} + \delta\boldsymbol{\rho} \,. \tag{23}$$

From Eq. (17) one then obtains

$$E = E^{(0)} + \boldsymbol{H}^{(0)} \delta\boldsymbol{\rho} + \frac{1}{2} \boldsymbol{J}' \delta\boldsymbol{\rho} \, \delta\boldsymbol{\rho} + \frac{1}{6} \boldsymbol{K}' \delta\boldsymbol{\rho} \, \delta\boldsymbol{\rho} \, \delta\boldsymbol{\rho} + \cdots \,, \tag{24}$$

where $\boldsymbol{J}'$ and $\boldsymbol{K}'$ refer to the second and third-order expansion coefficients about $\boldsymbol{\rho}^{(0)}$. The Hamiltonian is given by

$$\boldsymbol{H} = \boldsymbol{H}^{(0)} + \boldsymbol{J}' \delta\boldsymbol{\rho} + \frac{1}{2} \boldsymbol{K}' \delta\boldsymbol{\rho} \delta\boldsymbol{\rho} + \cdots \,, \quad \text{with} \quad \boldsymbol{H}^{(0)} = \boldsymbol{V} + \boldsymbol{J}\boldsymbol{\rho}^{(0)} + \frac{1}{2} \boldsymbol{K} \boldsymbol{\rho}^{(0)} \boldsymbol{\rho}^{(0)} + \cdots \,. \tag{25}$$

2.2 Tight-binding approximation

In the TB approximation one takes the view that bond formation takes place when atomic-like orbitals overlap. In practice this means that one builds TB models on a minimal basis of atomic-like orbitals. The one-electron eigenstates are expanded as linear combinations of atomic-orbital type (LCAO) basis functions. Orbital $|i\alpha\rangle$ is located on atom i and has a well defined angular momentum character, so that α comprises $\alpha = n, l, m$. The basis functions are written as

$$\varphi_{i\alpha}(\boldsymbol{r}) = R_{nl}(|\boldsymbol{r} - \boldsymbol{r}_i|) \, Y_l^m(\theta, \phi) \,, \tag{26}$$

where the radial functions R_{nl} depend only on the distance to the position $\boldsymbol{r}_i$ of atom i and Y_l^m are spherical harmonics or real linear combinations of spherical harmonics. Differently from an LCAO basis that is used in DFT, where often several radial basis functions are employed for a given angular momentum, in TB one typically uses only one radial function for each angular momentum and only includes orbitals that are dictated by the chemistry of the problem at hand.

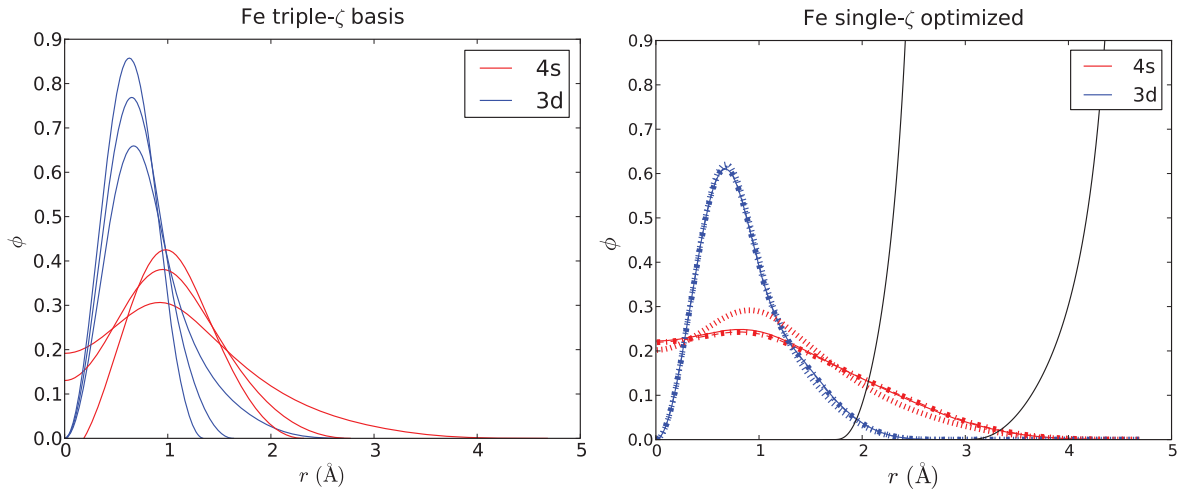

Fig. 1: *Derivation of a single s and a single d radial function for Fe (right) from multiple s and d basis functions (left). Taken from Ref. [50].*

For example, for carbon or silicon four orbitals are used, one s orbital and three p orbitals. This makes the TB approximation a chemically and physically intuitive method for analyzing bond formation in materials.

The TB approximation builds on the perturbation expansion of the Hohenberg-Kohn-Sham functional discussed in the previous section. The reference charge density $\boldsymbol{\rho}^{(0)}$ and the reference Hamiltonian $\boldsymbol{H}^{(0)}$ in Eq. (24) are formally obtained by placing charge neutral, non-magnetic atoms on positions for which the calculation is carried out and then overlapping the charge densities of the atoms. The expansion of the energy Eq. (24) is typically terminated after second order, which implies that the Hamiltonian Eq. (25) is a linear function of the density matrix. As argued before, this should be a good approximation to DFT as only the exchange-correlation energy includes contributions that are of higher than third order and these contributions are partly taken into account in Eq. (24).

The radial functions of the TB orbitals must be modified from the radial functions of a free atom in order that a good representation of the original DFT eigenfunctions may be achieved. In a solid the atomic charge densities contract when the charge densities of neighboring atoms are overlapped and therefore the radial function of the TB orbitals must also contract. Optimal radial functions may be obtained by downfolding from DFT eigenstates [50,51]. Fig. 1 illustrates the downfolding of several radial functions onto a single radial function in Fe.

2.2.1 Parametrized Hamiltonian

Often the Slater-Koster two-center approximation is used to parametrize the Hamiltonian matrix $\boldsymbol{H}^{(0)}$. The matrix element $\langle i\alpha|\hat{H}|j\beta\rangle$ is assumed to depend only on the position of atoms i and j and the orbitals α and β. Clearly, this is a crude approximation and in general the matrix element $\langle i\alpha|\hat{H}|j\beta\rangle$ will depend on other close-by atoms [52], but it is often surprising how much can be achieved with the simple two-center approximation. Fig. 2 shows the Hamiltonian matrix elements for Fe that were obtained from the DFT eigenstates.

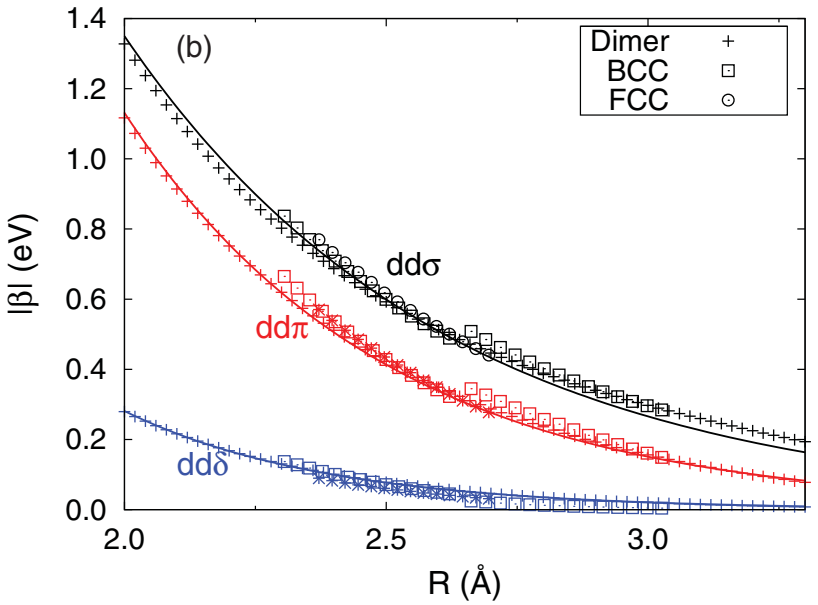

Fig. 2: *Hamiltonian matrix elements for a d-valent orthogonal TB model of Fe in different crystal structures. The solid lines show a fit to an exponential function. Taken from Ref. [50].*

2.2.2 Charge transfer

In TB one frequently assumes that only the diagonal elements of $\delta\boldsymbol{\rho}$ contribute to the second-order term $\frac{1}{2}\boldsymbol{J}\delta\boldsymbol{\rho}\delta\boldsymbol{\rho}$. The diagonal elements are the charges in each orbital

$$q_{i\alpha} = N_{i\alpha} - N_{i\alpha}^{(0)} \,, \tag{27}$$

that correspond to Mulliken charges in a non-orthogonal basis. The index 0 indicates the population of orbital $|i\alpha\rangle$ in a non-magnetic free atom. This approximation has important implications for the structure of the TB model. From Eq. (24) and Eq. (25) the energy is given by

$$E = E^{(0)} + \sum_{i\alpha j\beta} H_{i\alpha j\beta}^{(0)} n_{j\beta i\alpha} + \sum_{i\alpha j\beta} \frac{1}{2} J_{i\alpha j\beta} q_{j\beta} q_{i\alpha} \,, \tag{28}$$

and the Hamiltonian as

$$H_{i\alpha j\beta} = H_{i\alpha j\beta}^{(0)} + J_{i\alpha k\gamma}\, q_{k\gamma} S_{i\alpha j\beta} \,. \tag{29}$$

The modification of $\boldsymbol{H}$ may thus be written as

$$\left(E_{i\alpha} - E_{i\alpha}^{(0)}\right) S_{i\alpha j\beta} \qquad \text{with} \qquad E_{i\alpha} - E_{i\alpha}^{(0)} = J_{i\alpha k\gamma}\, q_{k\gamma} \,. \tag{30}$$

Charge transfer modifies the onsite matrix elements $E_{i\alpha}$ but leaves the rest of the Hamiltonian unchanged from its reference state $H_{i\alpha j\beta}^{(0)}$. Sometimes multipole expansions are used for non-spherical charges with an explicit parametrization of the angular contributions of $\boldsymbol{J}$ in the above equations.

Often, in an even simpler approximation, only the total charge on each atom $q_i = \sum_\alpha q_{i\alpha}$ is considered and the second-order term takes the form $\sum_{ij} \frac{1}{2} J_{ij} q_i q_j$. Then from Eq. (29) all onsite levels on an atom are shifted in parallel upon charge transfer. In literature it is sometimes incorrectly assumed that this automatically corresponds to a point charge approximation.

2.3 Bond formation in the tight-binding approximation

Following Eq. (28) two different types of bond formation are represented in a TB model, the formation of covalent bonds through the modification of the off-diagonal elements of the density matrix $\delta\rho_{i\alpha j\beta}$ with $i\alpha \neq j\beta$ and ionic interactions driven by charge transfer through the modification of the diagonal elements of the density matrix $\delta\rho_{i\alpha i\alpha} = q_{i\alpha}$. I will discuss the decomposition of the TB energy in physically and chemically intuitive and transparent contributions in the following.

2.3.1 Bond energy

The bond energy summarizes the energy that is stored in the bonds between different atoms

$$E_{bond} = \sum_{i\alpha j\beta} \big(H_{i\alpha j\beta} - E_{i\alpha} S_{i\alpha j\beta}\big) n_{j\beta i\alpha} = E_{band} - \sum_{i\alpha} E_{i\alpha} N_{i\alpha} \,. \tag{31}$$

Differently from the band energy, the bond energy is invariant with respect to a shift of the energy scale. Using Eq. (29) the bond energy is closely related to the linear term in the TB energy

$$\boldsymbol{H}^{(0)}\boldsymbol{n} = E_{bond} + \sum_{i\alpha} E^{(0)}_{i\alpha} N_{i\alpha} \,. \tag{32}$$

Equivalent to the intersite representation of the bond energy above is the onsite representation,

$$E_{bond} = \sum_{i\alpha} \int_{-\infty}^{E_F} \big(E - E_{i\alpha}\big) n_{i\alpha}(E)\, dE \,. \tag{33}$$

The population of the density of states below $E_{i\alpha}$ leads to a negative contribution to the bond energy, i.e., corresponding to the filling of bonding states. Once states above $E_{i\alpha}$ have to be populated, the bond energy decreases, corresponding to a filling of anti-bonding states. The integral over the complete band is zero, $0 = E_{bond} = \sum_{i\alpha} \int_{-\infty}^{\infty} \big(E - E_{i\alpha}\big) n_{i\alpha}(E)\, dE$, which helps to show that the bond energy is always smaller or equal to zero,

$$E_{bond} \leq 0 \,. \tag{34}$$

2.3.2 Promotion energy

When bonds are formed, the onsite levels are re-populated. In the free atom the number of electrons per orbital is denoted by $N^{(0)}_{i\alpha}$. For charge neutral atoms the promotion energy is then written as

$$E_{prom} = \sum_{i\alpha} E^{(0)}_{i\alpha} \big(N_{i\alpha} - N^{(0)}_{i\alpha}\big) \,. \tag{35}$$

In contrast to the bond energy, the promotion energy is strictly positive as the electrons in the free atom occupy the energetically lowest orbitals.

2.3.3 Free atom energy

For the evaluation of the binding energy the energies of the free atoms are subtracted

$$E_B = E^{TB} - E^{TB}_{free\ atoms}\,. \tag{36}$$

From Eq. (28) the TB energy of non-magnetic, charge neutral free atoms is given by

$$E^{TB}_{free\ atoms} = \sum_{i\alpha} E^{(at)}_{i\alpha} N^{(0)}_{i\alpha} - \frac{1}{2}\sum_{i\alpha\beta} J_{i\alpha i\beta} N^{(0)}_{i\alpha} N^{(0)}_{i\beta}\,, \tag{37}$$

where $E^{(at)}_{i\alpha}$ are the eigenstates of the free atom i and the population of the atomic orbitals is equal to the population in the reference state, $N^{(0)}_{i\alpha}$.

2.3.4 Preparation energy

The preparation energy takes into account modifications of the onsite levels when the free atoms are brought together and their charge density is overlapped to the reference charge density $\boldsymbol{\rho}^{(0)}$,

$$E_{prep} = \sum_{i\alpha} \left(E^{(0)}_{i\alpha} - E^{(at)}_{i\alpha}\right) N^{(0)}_{i\alpha}\,. \tag{38}$$

2.3.5 Charge transfer

Charge transfer leads to two further contributions to the energy and a somewhat modified expression for the promotion energy above. Because of the onsite level difference between atoms there is an energy linear in charge, and further the second-order contribution to the TB energy Eq. (28). The two terms are denoted as an electrostatic interaction of charges on different atoms

$$E_{es} = \frac{1}{2}\sum_{ij}^{i\neq j} J_{ij} q_i q_j\,, \tag{39}$$

and an ionic onsite contribution for charging each atom

$$E_{ion} = \bar{E}_i q_i + \frac{1}{2}\sum_i J_{ii} q_i^2\,. \tag{40}$$

The energy $\bar{E}_i$ is obtained as a weighted average of the reference onsite levels on atom i and corresponds to the electronegativity of the atom. The parameter J_{ii} further determines resistance against charge transfer from the charge neutral state.

2.3.6 Repulsive energy

The repulsive energy summarizes all terms that do not explicitly depend on the modification of the density matrix $\delta\boldsymbol{n}$. For this reason E_{prep} is also absorbed in the repulsive energy

$$E_{rep} = -\frac{1}{2}\sum_{i\alpha j\beta}^{j\neq j} J_{i\alpha j\beta} N^{(0)}_{i\alpha} N^{(0)}_{j\beta} + E_{nuc} + E_{prep}\,, \tag{41}$$

where E_{nuc} corresponds to the Coulomb repulsion of the bare atomic cores.

2.3.7 Summary of the energy in the tight-binding approximation

In summary, the second-order expansion of DFT, Eq. (24), cast in a TB binding energy is re-written in the form

$$E_B = E_{bond} + E_{prom} + E_{ion} + E_{es} + E_{rep}\,. \tag{42}$$

The TB expansion suggests a representation of bond formation in the steps summarized in the following table. Typically, the steps 1–3 are repulsive, while step 4 is attractive and drives bond formation.

1	E_{rep}	$\rightarrow$ overlap atomic charge densities
2	E_{ion}	$\rightarrow$ charge atoms
3	E_{prom}	$\rightarrow$ re-populate atomic energy levels
4	$E_{bond} + E_{es}$	$\rightarrow$ chemical and electrostatic interactions

3 The moments theorem and local expansions

For the derivation of interatomic potentials I next turn to local solutions of the TB model. In particular, the moments theorem will allow us to relate the local electronic structure to the local atomic environment, which is critical for analyzing the interaction between atoms.
The moments of the local density of states may be defined as

$$\mu_{i\alpha}^{(N)} = \int E^N n_{i\alpha}(E)\, dE\,. \tag{43}$$

The moments may be used to characterize the density of states. The zeroth moment is just the norm, $\mu_{i\alpha}^{(0)} = 1$. The first moment gives the center of the density of states. From the second moment the root mean square width of the density of states may be obtained and from the third moment its skewness. The fourth moment characterizes the bimodality of the local density of states, etc. If all moments are known, then the density of states may be reconstructed and therefore may be viewed as a function of its moments,

$$n_{i\alpha}(E) = n_{i\alpha}(E, \mu_{i\alpha}^{(0)}, \mu_{i\alpha}^{(1)}, \mu_{i\alpha}^{(2)}, \dots)\,. \tag{44}$$

The idea of reconstructing the density of states from its moments (or equivalent information) is the basis for the different methods that will be discussed in the following. In order that such a reconstruction can be efficient, the moments of the density of states need to be accessible. Here the moments theorem that I will briefly derive in the following provides the critical link. I assume for ease of notation that the basis functions are orthonormal

$$\langle i\alpha | j\beta \rangle = \delta_{ij}\delta_{\alpha\beta}\,. \tag{45}$$

By using the definition of the density of states from Eq. (21) the moments may be rewritten as

$$\begin{aligned}\mu_{i\alpha}^{(N)} &= \int E^N n_{i\alpha}(E)\, dE = \sum_n E_n^N \langle i\alpha|n\rangle\langle n|i\alpha\rangle \int \delta\big(E_n - E\big)\, dE \\ &= \sum_n \langle i\alpha|\hat{H}^N|n\rangle\langle n|i\alpha\rangle = \langle i\alpha|\hat{H}^N|i\alpha\rangle\,, \end{aligned} \tag{46}$$

where I used the completeness of the eigenstates $\hat{1} = \sum_n |n\rangle\langle n|$. A further manipulation enables a geometric interpretation

$$\begin{aligned}\mu_{i\alpha}^{(N)} = \langle i\alpha|\hat{H}^N|i\alpha\rangle &= \sum_{j\beta k\gamma\ldots} \langle i\alpha|\hat{H}|j\beta\rangle\langle j\beta|\hat{H}|k\gamma\rangle\langle k\gamma|\hat{H}\ldots\hat{H}|i\alpha\rangle \\ &= \sum_{j\beta k\gamma\ldots} H_{i\alpha j\beta} H_{j\beta k\gamma} H_{k\gamma\ldots}\ldots H_{\ldots i\alpha}\,, \end{aligned} \tag{47}$$

with a complete basis $\hat{1} = \sum_{i\alpha} |i\alpha\rangle\langle i\alpha|$. The last identity tells us that the N^{th} moment may be obtained from the product of N Hamiltonian matrix elements. The N^{th} moment may therefore be described as the sum of all self-returning hopping path of length N that start and end on the same basis function.

Along the same lines it is straightforward to show that the moments of the spectrally resolved density matrix

$$n_{i\alpha j\beta}(E) = \frac{d\rho_{i\alpha j\beta}}{dE}\,, \quad \text{or} \quad \rho_{i\alpha j\beta} = \int^{E_F} n_{i\alpha j\beta}(E)\, dE\,, \tag{48}$$

may be obtained as

$$\xi_{i\alpha j\beta}^{(N)} = \int E^N n_{i\alpha j\beta}(E)\, dE = \langle i\alpha|\hat{H}^N|j\beta\rangle\,. \tag{49}$$

The N^{th} moment $\xi_{i\alpha j\beta}^{(N)}$ of the spectrally resolved density matrix is thus given by all interference paths of N products of the Hamiltonian matrix that start and end on orbitals $|i\alpha\rangle$ and $|j\beta\rangle$, respectively.

As the Hamiltonian matrix elements depend on the positions of the atoms, the moments theorem relates the atomic structure to the electronic structure. For the reconstruction of the local density of states, the lowest moments contribute basic information on the width and shape of the density of states, while higher moments may be used to reconstruct increasingly finer details. This is intuitive: the matrix elements $H_{i\alpha j\beta}$ decay roughly exponentially with distance between the atoms i and j, which means that the low moments only sample the local environment of an atom and higher moments incorporate information of an increasingly distant neighborhood of orbital $|i\alpha\rangle$.

In the following I will discuss methods for the reconstruction of the band energy from the atomically local neighborhood. These methods were developed originally for linear-scaling DFT or TB. The methods have different starting points, but implicitly or explicitly they all correspond to a reconstruction of the density of states from its moments. For the analytic bond-order potentials we use the moments to derive a hierarchical analytic expansion of the interatomic interaction.

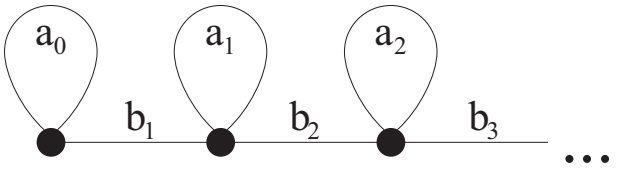

Fig. 3: *Illustration of the semi-infinite recursion chain Hamiltonian.*

3.1 Recursion and numerical bond-order potentials

In the recursion method the Hamiltonian matrix is transformed to tridiagonal form, from which the Green function may be obtained as a continued fraction [53, 54]. Given a starting orbital $|u_0\rangle = |i\alpha\rangle$ first a basis transformation is carried out,

$$b_{n+1}|u_{n+1}\rangle = \big(\hat{H} - a_n\big)|u_n\rangle - b_n|u_{n-1}\rangle\,, \tag{50}$$

with

$$b_n = \langle u_n|\hat{H}|u_{n-1}\rangle\,, \quad \text{and} \quad a_n = \langle u_n|\hat{H}|u_n\rangle\,. \tag{51}$$

The recursion is initialized with $b_0 = 0$ and leads to orbitals $|u_n\rangle$ that have remarkable properties: the resulting Hamiltonian matrix is tridiagonal, i.e., it only has entries on the diagonal and next to the diagonal,

$$\langle u_n|\hat{H}|u_m\rangle = \begin{pmatrix} a_0 & b_1 & 0 & 0 & 0 & 0 & \dots \\ b_1 & a_1 & b_2 & 0 & 0 & 0 & \dots \\ 0 & b_2 & a_2 & b_3 & 0 & 0 & \dots \\ 0 & 0 & b_3 & a_3 & b_4 & 0 & \dots \\ 0 & 0 & 0 & b_4 & a_4 & b_5 & \dots \\ 0 & 0 & 0 & 0 & b_5 & a_6 & \ddots \\ \vdots & \vdots & \vdots & \vdots & \vdots & \ddots & \ddots \end{pmatrix}, \quad \text{and} \quad \langle u_n|u_m\rangle = \delta_{nm}\,. \tag{52}$$

The tridiagonal Hamiltonian may be viewed as semi-infinite, one-dimensional chain and is illustrated in Fig. 3. The recursion also shows that every Hamiltonian may be represented as a one-dimensional semi-infinite chain with nearest-neighbor interactions.

The moments of the density of states Eq. (43) may be obtained from self-returning paths along the tridiagonal Hamiltonian matrix as

$$\begin{aligned} \mu_{i\alpha}^{(0)} &= 1\,, \\ \mu_{i\alpha}^{(1)} &= a_0\,, \\ \mu_{i\alpha}^{(2)} &= a_0^2 + b_1^2\,, \\ \mu_{i\alpha}^{(3)} &= a_0^3 + (a_0 + a_1)b_1^2\,, \\ \mu_{i\alpha}^{(4)} &= a_0^4 + b_1^4 + (a_0^2 + a_1^2 + a_0 a_1 + b_2^2)b_1^2\,, \\ &\vdots \end{aligned}$$

3.1.1 Green function expansion

The Green function is defined as

$$\hat{G} = \left(E\hat{1} - \hat{H}\right)^{-1} . \tag{53}$$

The matrix elements of the Green function in eigenstates are given by

$$\langle\psi_n|\hat{G}|\psi_m\rangle = \frac{\delta_{nm}}{E - E_n} . \tag{54}$$

This is easily verified by inserting the identify $\hat{1} = \sum_{n'} |\psi_{n'}\rangle\langle\psi_{n'}|$ into

$$\begin{aligned}\delta_{n,m} = \langle\psi_n|\psi_m\rangle &= \langle\psi_n|(E\hat{1}-\hat{H})\hat{G}|\psi_m\rangle \\ &= \sum_{n'}\langle\psi_n|E\hat{1}-\hat{H}|\psi_{n'}\rangle\langle\psi_{n'}|\hat{G}|\psi_m\rangle = \frac{E - E_n}{E - E_m}\,\delta_{nm} .\end{aligned} \tag{55}$$

The Green function matrix elements in basis functions are given by

$$G_{i\alpha j\beta}(E) = \sum_{nm}\langle i\alpha|\psi_n\rangle\langle\psi_n|\hat{G}|\psi_m\rangle\langle\psi_m|j\beta\rangle = \sum_n \frac{\langle i\alpha|\psi_n\rangle\langle\psi_n|j\beta\rangle}{E - E_n} . \tag{56}$$

With the help of the recursion chain Eq. (50) the diagonal elements of the Green function matrix may be expressed in the form of a continued fraction [53],

$$G_{i\alpha i\alpha}(E) = G_{00}(E) = \cfrac{1}{E - a_0 - \cfrac{b_1^2}{E - a_1 - \cfrac{b_2^2}{E - a_2 - \cfrac{b_3^2}{E - a_3 - \cfrac{b_4^2}{E - a_4 - \cfrac{b_5^2}{\ddots}}}}}} . \tag{57}$$

Next the Green function is related to the density matrix by making use of the identity

$$-\frac{1}{\pi}\,\mathrm{Im}\int \frac{1}{E - E_n}\,dE = \int \delta(E-E_n)\,dE , \tag{58}$$

so that comparing to Eq. (21) and Eq. (48) results in the identities

$$n_{i\alpha}(E) = -\frac{1}{\pi}\,\mathrm{Im}\,G_{i\alpha i\alpha}(E) \quad \text{and} \quad n_{i\alpha j\beta}(E) = -\frac{1}{\pi}\,\mathrm{Im}\,G_{i\alpha j\beta}(E) . \tag{59}$$

The Green function may therefore be used for the computation of the band or bond energy. This is used in the numerical bond-order potentials (BOPs) that will be introduced next.

3.1.2 Numerical bond-order potentials

We are interested in the local calculation of the band energy or, for the TB approximation, the bond energy associated to orbital $|i\alpha\rangle$. This is achieved by terminating the recursion expansion of the Green function after a few recursion levels n: The recursion coefficients a_m and b_m for $m > n$ are replaced by a constant terminator

$$a_m = a_\infty\,, \quad b_m = b_\infty \quad \text{for } m > n\,. \tag{60}$$

The terminator in the Green function may be summed analytically and leads to termination of the continued fraction at level n by

$$E - a_{n-1} - T(E)\,, \tag{61}$$

with

$$T(E) = \frac{1}{2}\left(E - a_\infty - \sqrt{(E-a_\infty)^2 - 4b_\infty^2}\right) \tag{62}$$

obtained from the functional equation $T(E) = b_\infty^2/(E - a_\infty - T(E))$ for the ininite continued fraction with constant coefficients.

The corresponding density of states is different from zero only in the interval between $a_\infty - 2b_\infty$ and $a_\infty + 2b_\infty$. A local expansion of the bond energy is now obtained as

$$E_{bond,i\alpha} = -\frac{1}{\pi}\,\mathrm{Im}\int^{E_F} \cfrac{E - E_{i\alpha}}{E - a_0 - \cfrac{b_1^2}{E - a_1 - \cfrac{b_2^2}{\ddots - \cfrac{\ddots}{E - a_{n-1} - T(E)}}}}\,. \tag{63}$$

The integration of the Green function is carried out numerically, therefore the name numerical BOPs.

For the evaluation of forces the off-diagonal elements of the Green function are also required. These are obtained by defining

$$|u_0\rangle = \frac{1}{\sqrt{2}}\Big(|i\alpha\rangle + e^{i\vartheta}|j\beta\rangle\Big)\,, \tag{64}$$

with $\vartheta = \cos^{-1}\lambda$ and therefore

$$G_{00} = \lambda G_{i\alpha j\beta} + \frac{1}{2}\big(G_{i\alpha i\alpha} + G_{j\beta j\beta}\big)\,. \tag{65}$$

A particular termination of the expansion ensures that the onsite and intersite representation of the bond energy are identical [55]. Details of the numerical BOPs are available in Refs. [56–58].

3.2 Kernel polynomial method

In the Kernel Polynomial Method (KPM) [59–61] the density of states is represented as

$$n_{i\alpha}(\varepsilon) = \int K(\varepsilon,\varepsilon')\, n_{i\alpha}(\varepsilon')\, d\varepsilon' \,, \tag{66}$$

where the energy has been rescaled as

$$\varepsilon = \frac{E - a_\infty}{2b_\infty} \,. \tag{67}$$

It is clear that this identity only holds if the kernel fulfills $K(\varepsilon,\varepsilon') = \delta(\varepsilon-\varepsilon')$. In order to achieve an approximate, local representation of $n_{i\alpha}(\varepsilon)$ the kernel is expanded in Chebyshev polynomials of the first kind

$$K(\varepsilon,\varepsilon') = \frac{1}{\pi}\frac{1}{\sqrt{1-\varepsilon^2}}\left(g_T^{(0)} + 2\sum_{n=1}^{n_{max}} g_T^{(n)} T_n(\varepsilon) T_n(\varepsilon') \right) . \tag{68}$$

The factors $g_T^{(n)}$ are chosen in such a way that for every n_{max} the kernel is positive, $K(\varepsilon,\varepsilon') \geq 0$, while it is also as narrow as possible for an efficient convergence to the Dirac delta function when n_{max} is increased. Typically $g_T^{(n)}$ smoothly decays as a function of n from $g_T^{(0)} = 1$ to $g_T^{(n_{max})} = 0$. Fig. 4 illustrates different damping factors.
By inserting the expansion for the Kernel in Eq. (66), an expansion for the density of states is obtained as

$$n_{i\alpha}(\varepsilon) = \frac{1}{\pi}\frac{1}{\sqrt{1-\varepsilon^2}}\left(g_T^{(0)} + 2\sum_{n=1}^{n_{max}} g_T^{(n)} T_n(\varepsilon) \mu_n^T \right) , \tag{69}$$

with the Chebyshev moments

$$\mu_n^T = \int_{-1}^{1} T_n(\varepsilon)\, n_{i\alpha}(\varepsilon)\, d\varepsilon \,. \tag{70}$$

As the Chebyshev polynomials may just be written in powers of ε, the Chebyshev moments are linear combinations of the moments of the density of states, Eq. (21).
The damping factors $g_T^{(n)}$ that ensure a positive expansion of the density of states remove much of the contribution of higher moments. One way to avoid this is to add higher moments that are generated based on a maximum entropy principle [63].

3.3 Fermi operator expansion

In DFT it is customary to introduce an electronic temperature. This is done in part for practical reasons, as temperature dampens details of the Fermi surface in a metal and leads to faster convergence of the k-space integration over the Brillouin zone as a function of the k-mesh density. For the Fermi operator expansion the electronic temperature provides the starting point for the expansion. With temperature, the band energy and the number of electrons are computed as

$$E_{band} = \int \varepsilon\, f(\varepsilon,\mu)\, n(\varepsilon)\, d\varepsilon \quad \text{and} \quad N = \int f(\varepsilon,\mu)\, n(\varepsilon)\, d\varepsilon \tag{71}$$

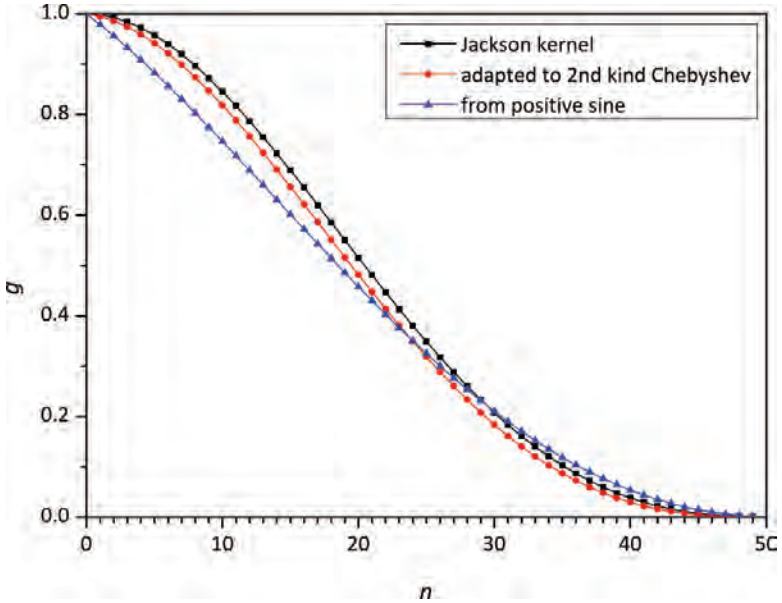

Fig. 4: *Damping factors used in the KPM (Jackson kernel) and analytic BOPs for* $n_{exp} = 50$. *Taken from Ref. [62].*

with the energy scale Eq. (67), where μ is the electron chemical potential and

$$f(\varepsilon,\mu) = \frac{1}{1+\exp\left(\frac{\varepsilon-\mu}{k_B T}\right)}\,, \tag{72}$$

the temperature dependent Fermi-Dirac distribution function and $n(\varepsilon)$ the density of states. At $T = 0$ K the smearing is zero and $f(\varepsilon,\mu)$ corresponds to the Heaviside step function $\Theta(\varepsilon,\varepsilon_F)$ which is one below the Fermi energy ε_F and zero above. In the Fermi operator expansion (FOE) method [64, 65] the density matrix is locally approximated by writing it as

$$\rho_{i\alpha j\beta} = \int f(\varepsilon,\mu)\, n_{i\alpha j\beta}(\varepsilon) d\varepsilon\,, \tag{73}$$

and then expanding f in a polynomial

$$f(\varepsilon,\mu) = \sum_k c_k \varepsilon^k\,. \tag{74}$$

By making use of Eq. (49) the density matrix is written as

$$\rho_{i\alpha j\beta} = \sum_k c_k\, \xi^{(k)}_{i\alpha j\beta}\,, \quad \text{and} \quad E_{band} = \sum_{i\alpha j\beta}\sum_k c_k\, \xi^{(k)}_{i\alpha j\beta} H_{j\beta i\alpha} = \sum_{i\alpha}\sum_k c_k \mu^{(k+1)}_{i\alpha}\,. \tag{75}$$

In practice the Fermi-Dirac distribution function is expanded in Chebyshev polynomials

$$f(\varepsilon) = \frac{1}{\pi\sqrt{1-\varepsilon^2}}\left(\mu_0^T + 2\sum_{n=1}^{n_{max}} \mu_n^T T_n(\varepsilon)\right). \tag{76}$$

with the Chebyshev moments μ_n^T, Eq. (70), and the band energy accordingly. Another representation of the Fermi operator expansion, the rational representation, may be related to the recursion expansion.

3.4 Analytic bond-order potentials

The analytic BOPs combine the recursion expansion and the KPM. I start from a scaled energy Eq. (67) that allows us to work with Chebyshev polynomials that are defined on the interval $[-1,1]$. The analytic BOPs use the Chebyshev polynomials of the second kind as the they are orthogonal with respect to the square root function

$$\frac{2}{\pi}\int_{-1}^{+1} U_n(\varepsilon)\, U_m(\varepsilon)\, \sqrt{1-\varepsilon^2}\, d\varepsilon = \delta_{nm}\,. \tag{77}$$

The square root function is also the density of states of the semi-infinite recursion chain when all matrix elements are identical $a_0 = a_1 = \cdots = a_\infty$ and $b_1 = b_2 = \cdots = b_\infty$. If the reference energy is shifted to $a_0 = 0$, then $b_1^2 = \mu_{i\alpha}^{(2)}$. As $b_1 = b_\infty$ determines the width of the density of states, the bond energy scales as $\sqrt{\mu_{i\alpha}^{(2)}}$ and the Finnis-Sinclair potential, Eq. (1), is immediately obtained. Therefore, by choosing the Chebyshev polynomials of the second kind, the analytic BOPs incorporate the Finnis-Sinclair potential at the lowest order of approximation.
The Chebyshev polynomials of the second kind fulfill the recursion relation

$$U_{n+1}(\varepsilon) = 2\varepsilon\, U_n(\varepsilon) - U_{n-1}(\varepsilon)\,, \tag{78}$$

with $U_0 = 1$ and $U_1 = 2\varepsilon$.
The expansion coefficients for the density of states are obtained by projection,

$$\sigma_{i\alpha}^{(n)} = \int_{-1}^{+1} U_n(\varepsilon)\, n_{i\alpha}(\varepsilon)\, d\varepsilon\,, \tag{79}$$

and the density of states is expressed as

$$n_{i\alpha}(\varepsilon) = \frac{2}{\pi}\sum_n \sqrt{1-\varepsilon^2}\, \sigma_{i\alpha}^{(n)}\, U_n(\varepsilon)\,. \tag{80}$$

The expansion coefficients $\sigma_{i\alpha}^{(n)}$ are computed using the moments theorem Eq. (43) as

$$\sigma_{i\alpha}^{(n)} = \langle i\alpha | U_n(\hat{h}) | i\alpha \rangle\,, \tag{81}$$

with the scaled Hamiltonian

$$\hat{h} = \frac{\hat{H} - a_\infty}{2b_\infty}\,. \tag{82}$$

In practice n_{max} expansion coefficients are computed, which corresponds to evaluating n_{max} moments of the density of states. Thus the expansion Eq. (80) becomes

$$n_{i\alpha}(\varepsilon) = \sum_{n=0}^{n_{max}} \sqrt{1-\varepsilon^2}\, \sigma_{i\alpha}^{(n)} U_n(\varepsilon)\,, \tag{83}$$

or using $\varepsilon = -\cos\phi$,

$$n_{i\alpha}(\varepsilon) = \sum_{n=0}^{n_{max}} \sigma_{i\alpha}^{(n)} \sin(n+1)\phi\,. \tag{84}$$

If a Fourier series expansion is abruptly terminated because only the first n_{max} expansion coefficients are taken into account, this may lead to significant oscillations that are known as Gibbs ringing. In particular, these oscillations may be so large that the expansion of the density of states Eq. (84) may become negative.
The Gibbs ringing may be removed and a strictly positive expansion of the density of states may be enforced by damping the expansion coefficients,

$$n_{i\alpha}(\varepsilon) = \sum_{n=0}^{n_{max}} g_n \, \sigma_{i\alpha}^{(n)} \sin(n{+}1)\phi \, . \tag{85}$$

The damping factors g_n are similar to the damping factors in KPM and decrease monotonically from $g_0 = 1$ to $g_{n_{max}} = 0$ [62, 66], see Fig. 4. They damp oscillations and avoid Gibbs ringing and potentially negative values of the density of states. As the damping factors decrease to zero for n_{max}, they remove most of the contribution from higher moments. Therefore more moments need to be calculated, i.e., n_{max} needs to be increased. As the calculation of the moments is the most time consuming part in the energy and force evaluation, one would like to keep n_{max} as small as possible.
This may be resolved by terminating the expansion Eq. (85). One first evaluates moments up to n_{max} from the Hamiltonian using the moments theorem. Further moments from $n_{max}{+}1$ up to $n_{exp} \gg n_{max}$ are then computed using an estimated model Hamiltonian that has the form of a semi-infinite chain with nearest neighbor bonds only [62]. Because of the simple structure of the semi-infinite chain, only very few matrix elements need to be multiplied and therefore the computation of the moments along the chain is very fast. The resulting expansion takes the form

$$n_{i\alpha}(\varepsilon) = \sum_{n=0}^{n_{max}} g_n \, \sigma_{i\alpha}^{(n)} \sin(n{+}1)\phi + \sum_{n=n_{max}+1}^{n_{exp}} g_n \, \sigma_{i\alpha}^{(n)} \sin(n{+}1)\phi \, . \tag{86}$$

The damping factors decay monotonically from $g_0{=}1$ to $g_{n_{exp}}{=}0$. For $n_{exp}{\gg}n_{max}$ the damping factors for the first few moments are close to one and the contributions of the corresponding moments are hardly affected. This means that the expansion as a function of n_{max} converges quickly to the tight-binding reference. In practice one uses $n_{exp} \approx 20{\times}n_{max}$. This leads to a good quality of the reconstructed DOS already at a small number of calculated moments.
The density of states Eq. (86) may be integrated analytically,

$$E_{bond,i\alpha} = 2b_\infty \sum_{n=0}^{n_{exp}} g_n \, \sigma_{i\alpha}^{(n)} \Big(\hat{\chi}_{n+2}(\phi_F) - \gamma_0 \hat{\chi}_{n+1}(\phi_F) + \hat{\chi}_n(\phi_F) \Big) \, , \tag{87}$$

with $\gamma_0 = (E_{i\alpha}{-}a_\infty)/b_\infty$ and $\hat{\chi}_0 = 0$,

$$\hat{\chi}_1 = 1 - \frac{\phi_F}{\pi} + \frac{1}{2\pi} \sin(2\phi_F) \, . \tag{88}$$

The response functions take the form

$$\hat{\chi}_n(\phi_F) = \frac{1}{\pi} \left(\frac{\sin(n{+}1)\phi_F}{n{+}1} - \frac{\sin(n{-}1)\phi_F}{n{-}1} \right) . \tag{89}$$

Finally, the number of electrons in orbital $N_{i\alpha}$ is obtained as

$$N_{i\alpha} = \sum_{n=0}^{n_{exp}} g_n \, \sigma_{i\alpha}^{(n)} \, \hat{\chi}_{n+1}(\phi_F) \, , \tag{90}$$

with the Fermi phase $\varepsilon_F = -\cos\phi_F$. For the gradients of the bond energy $E_{bond,i\alpha}$ and the number of electrons $N_{i\alpha}$ efficient analytic expressions may be obtained [14, 62]. The analytic BOPs have been extended further to include non-collinear magnetism [14, 67]. The analytic BOPs scale-linearly with the number of atoms. An efficient and parallel implementation is available [68] that enables simulations with millions of atoms.

3.5 Examples for the analytic bond-order potentials

3.5.1 Bond order

The density matrix is also called the bond order, a factor of two is usually between the two quantities in non-magnetic systems. I transform the orbitals $|i\alpha\rangle$ and $|j\beta\rangle$ in a new basis of bonding and anti-bonding dimer states to analyze bond formation

$$|+\rangle = \frac{1}{\sqrt{2}}\Big(|i\alpha\rangle + |j\beta\rangle\Big) \quad \text{bonding state} \, , \tag{91}$$

$$|-\rangle = \frac{1}{\sqrt{2}}\Big(|i\alpha\rangle - |j\beta\rangle\Big) \quad \text{anti-bonding state} \, . \tag{92}$$

The density matrix may then be obtained from the difference of the number of electrons in bonding and anti-bonding states

$$\rho_{i\alpha j\beta} = \langle i\alpha|\hat{\rho}|j\beta\rangle = \frac{1}{2}\big(N_+ - N_-\big) \, , \tag{93}$$

with $N_+ = \langle +|\hat{\rho}|+\rangle$ and $N_- = \langle -|\hat{\rho}|-\rangle$ and $N_{i\alpha i\alpha} + N_{j\beta j\beta} = (N_+ + N_-)$ the number of electrons in the bond. If we assume a non-magnetic calculation and take into account spin degeneracy, then $0 \leq N_{i\alpha i\alpha} \leq 2$ and the same for $N_{j\beta j\beta}$. This allows one to put limits on the density matrix

$$|\rho_{i\alpha j\beta}| \leq N_{i\alpha j\beta} \quad \text{and} \quad |\rho_{i\alpha j\beta}| \leq 2 - N_{i\alpha j\beta} \, , \tag{94}$$

with $N_{i\alpha j\beta} = (N_{i\alpha i\alpha} + N_{j\beta j\beta})/2$. Fig. 5 shows the density matrix for close packed transition metals as a function of band filling.

3.5.2 Structural stability

The analytic BOPs may be employed for the analysis of the structural stability of different phases. To this end one compares the structures at the same repulsive energy, following the structural energy difference theorem [44]. Fig. 6 shows the structural energy differences for a number of close packed phases.

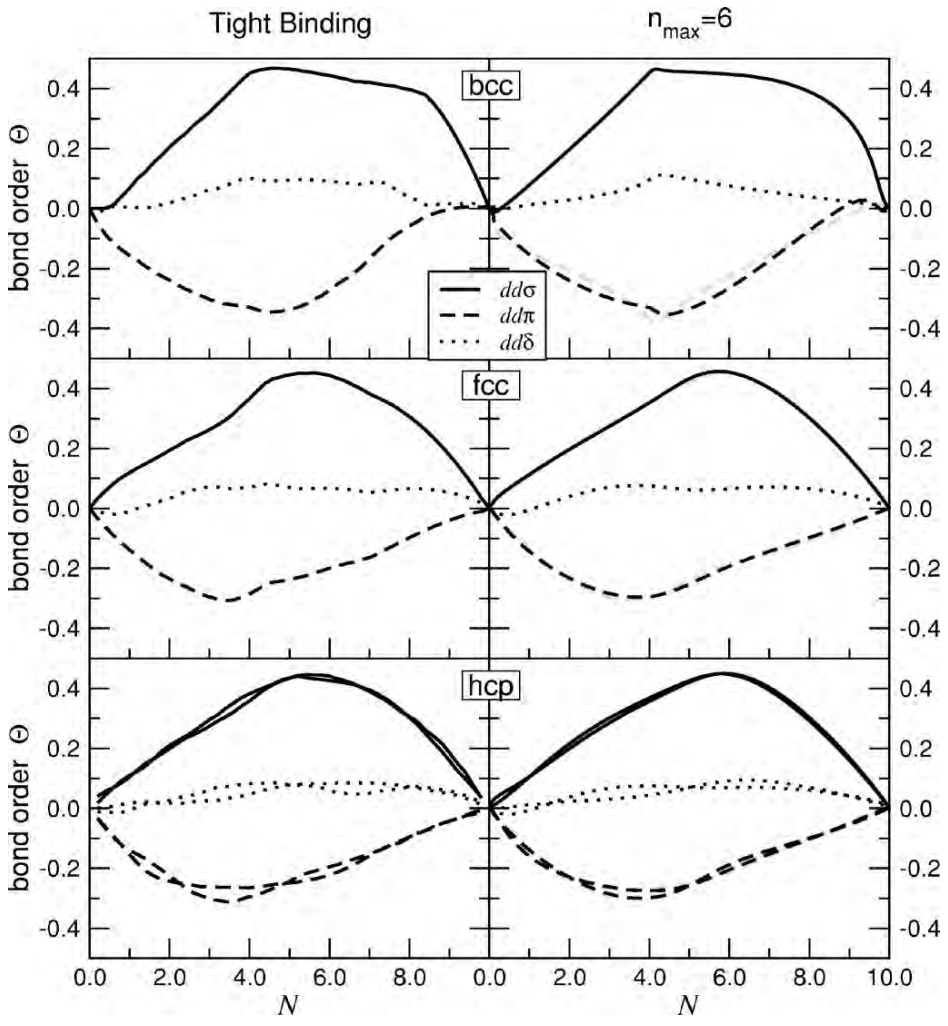

Fig. 5: *Bond order as a function of band filling for close-packed transition metals. The TB approximation is compared to BOPs. Taken from Ref. [13].*

3.5.3 Ti phase diagram

Fig. 7 shows the free energy differences between competing phases in Ti. The phase diagram predicted from analytic BOPs is in very good agreement with experiment and DFT, despite the fact that the energy differences between the competing phases are of the order of only a few meV.

3.5.4 Parametrization

For the parametrization of the analytic BOPs, first the Hamiltonian matrix elements are obtained from downfolding on DFT wavefunctions [50, 51], see Figs. 1 and 2. The Hamiltonian is then parametrized and together with the repulsive energy fitted to reproduce DFT reference data. Software that largely automatizes the parametrization procedure is available [68, 71].

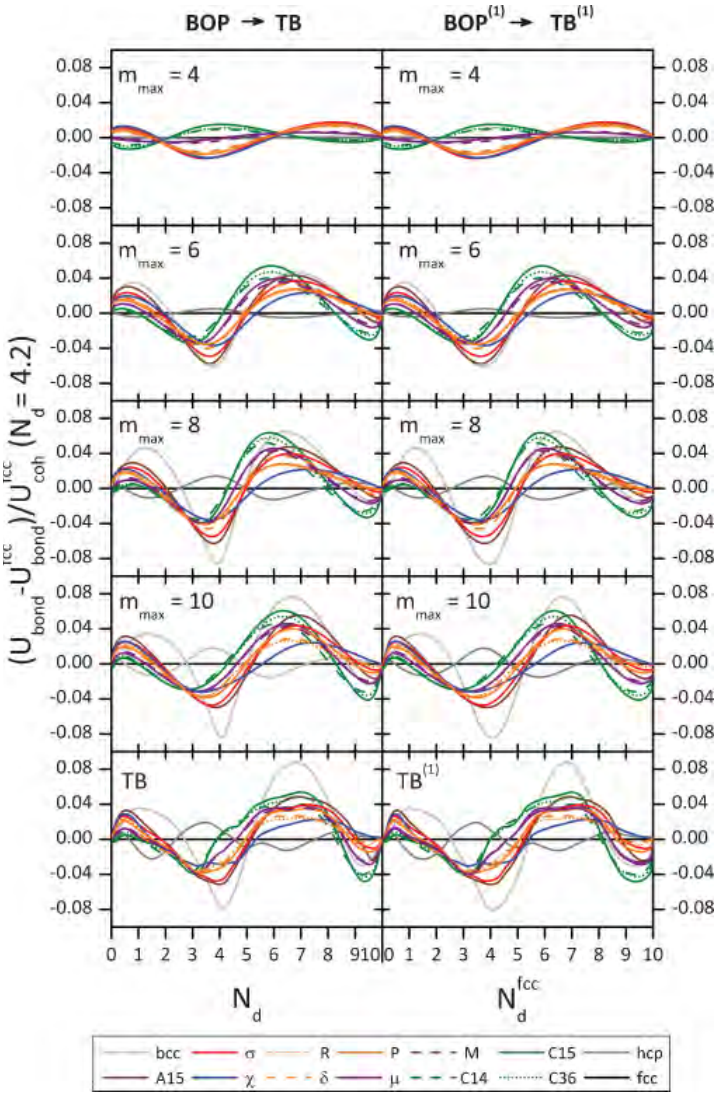

Fig. 6: *Structural energy differences for a number of close-packed phases (left panel).* m_{max} *indicates the moment at which the expansion was terminated, the lowest panels show the TB reference. The right panel shows a first order expansion. For details Ref. [69], from which this figure was also taken.*

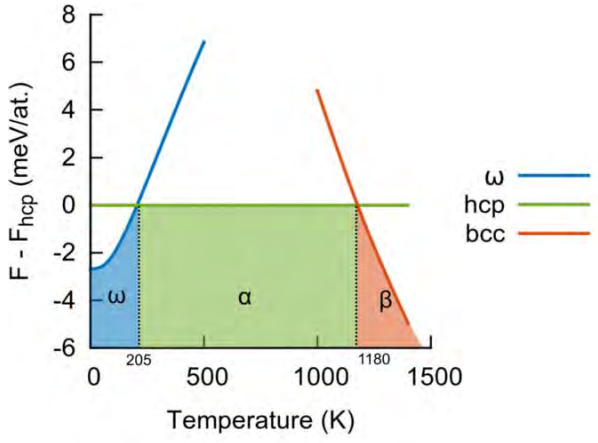

Fig. 7: *Free energy differences as computed for Ti with analytic BOPs. Taken from Ref. [70].*

4 Many atom expansions

In the first part of this chapter I discussed the derivation of simplified electronic structure models from DFT. A local expansion of the TB energy then led to explicit interatomic potentials. While a lot of insight can be gained from the analysis of bond formation in the BOPs and robust parametrizations may be achieved with few parameters, the accuracy and transferability of the BOPs are also limited by the coarse-graining approximations from DFT to TB and BOP.

In the past years an important focus in the field of atomistic modeling was the parametrization of DFT reference data with very high accuracy, i.e., errors of less than a few meV. The TB and BOP expansions introduced in the previous sections are not competitive here, as the approximations made down the coarse-graining hierarchy from DFT to TB to BOPs introduce errors that are larger than a few meV. As I will discuss in the following, one can develop models that incorporate some of the spirit of TB for obtaining meV accurate parametrizations of DFT reference data.

For the parametrization of large DFT datasets with very high accuracy typically methods that are rooted in machine-learning are employed, for example, neural network potentials that are based on neural networks [15] or Gaussian process regression in the Gaussian approximation potentials [16]. All machine-learning methods have in common that the target property, for example, the atomic energy, is obtained as a complex, non-linear function of some mathematical descriptions of the local atomic environment. The detailed mathematical structure of the descriptors are mostly obtained by intuition. One may view the empirical mathematical structure of the descriptors as the Achilles' heel of machine-learning interatomic potentials and a formally complete descriptor of the local atomic environment is desirable. The atomic cluster expansion [34, 37] achieves a formally complete description of the local atomic environment and will be introduced in the following.

4.1 Atomic cluster expansion

The atomic cluster expansion (ACE) provides a complete descriptor for the local environment of an atom [34, 37]. Each atom i has a configuration that in the simplest case of an elemental material and excluding charge transfer or magnetism is fully characterized by the distance vectors to all neighboring atoms j, $\boldsymbol{r}_{ji} = \boldsymbol{r}_i - \boldsymbol{r}_j$, and where $\boldsymbol{r}_i$ and $\boldsymbol{r}_j$ are the positions of the atoms i and j, respectively. The collection of all the distance vectors is the configuration

$$\boldsymbol{\sigma} = (\boldsymbol{r}_{1i}, \boldsymbol{r}_{2i}, \boldsymbol{r}_{3i}, \dots)\,. \tag{95}$$

A scalar product between functions $f(\boldsymbol{\sigma})$ and $g(\boldsymbol{\sigma})$ is defined as

$$\langle f | g \rangle = \int d\boldsymbol{\sigma}\; f^*(\boldsymbol{\sigma})\, g(\boldsymbol{\sigma})\, \omega(\boldsymbol{\sigma})\,, \tag{96}$$

where $\omega(\boldsymbol{\sigma})$ is a weight function. Next complete basis functions that depend only on a single bond are introduced

$$\langle \phi_v(\sigma) | \phi_u(\sigma) \rangle = \delta_{vu} \,, \tag{97}$$

$$\sum_v [\phi_v(\boldsymbol{r})]^* \phi_v(\boldsymbol{r}') = \delta(\boldsymbol{r} - \boldsymbol{r}') \,. \tag{98}$$

For establishing a hierarchical expansion furthermore $\phi_0 = 1$, which may be understood as an atom without properties, i.e., the vacuum state.
A cluster α with K elements contains K atoms $\alpha = (j_1, j_2, \ldots, j_K)$, where the order of entries in α does not matter and indices are pairwise different $i \neq j_1 \neq j_2 \neq j_K$. The vector $\nu = (v_0; v_1, v_2, \ldots, v_K)$ contains the list of single-atom basis functions in the cluster, and only single-atom basis functions with $v > 0$ are considered in ν. A cluster basis function is then given by

$$\Phi_{\alpha\nu} = \phi_{v_1}(\boldsymbol{r}_{j_1 i}) \, \phi_{v_2}(\boldsymbol{r}_{j_2 i}) \ldots \phi_{v_K}(\boldsymbol{r}_{j_K i}) \,. \tag{99}$$

The orthogonality and completeness of the single-atom basis functions transfers to the cluster basis functions

$$\langle \Phi_{\alpha\nu} | \Phi_{\beta\mu} \rangle = \delta_{\alpha\beta} \delta_{\nu\mu} \,, \tag{100}$$

$$1 + \sum_{\gamma \subseteq \alpha} \sum_{\nu} [\Phi_{\gamma\nu}(\boldsymbol{\sigma})]^* \Phi_{\gamma\nu}(\boldsymbol{\sigma}') = \delta(\boldsymbol{\sigma} - \boldsymbol{\sigma}') \,, \tag{101}$$

where α is an arbitrary cluster and the right-hand side of the completeness relation is the product of the relevant right-hand sides of Eq. (98). The expansion of an element of the energy of atom i may therefore be written in the form

$$E_i = J_0 + \sum_{\alpha\nu} J_{\alpha\nu} \Phi_{\alpha\nu}(\boldsymbol{\sigma}) \,, \tag{102}$$

and the expansion coefficients $J_{\alpha\nu}$ obtained by projection

$$J_{\alpha\nu} = \langle \Phi_{\alpha\nu} | G(\boldsymbol{\sigma}) \rangle \,. \tag{103}$$

Writing the expansion Eq. (102) explicitly in single-atom basis functions leads to

$$\begin{aligned} E_i = & \sum_{j}^{i \neq j} \sum_{v_1} J_{v_1} \phi_{v_1}(\boldsymbol{r}_{ji}) + \frac{1}{2} \sum_{j_1 j_2}^{i \neq j_1 \neq j_2} \sum_{v_1 v_2} J_{v_1 v_2} \phi_{v_1}(\boldsymbol{r}_{j_1 i}) \phi_{v_2}(\boldsymbol{r}_{j_2 i}) \\ & + \frac{1}{3!} \sum_{j_1 j_2 j_3}^{i \neq j_1 \neq j_2 \ldots} \sum_{v_1 v_2 v_3} J_{v_1 v_2 v_3} \phi_{v_1}(\boldsymbol{r}_{j_1 i}) \phi_{v_2}(\boldsymbol{r}_{j_2 i}) \phi_{v_3}(\boldsymbol{r}_{j_3 i}) + \ldots \,. \end{aligned} \tag{104}$$

This may be rewritten in a slightly different way with unrestricted sums and updated expansion coefficients

$$\begin{aligned} E_i = & \sum_{j} \sum_{v_1} c_{v_1} \phi_v(\boldsymbol{r}_{ji}) + \frac{1}{2} \sum_{j_1 j_2} \sum_{v_1 v_2} c_{v_1 v_2} \phi_{v_1}(\boldsymbol{r}_{j_1 i}) \phi_{v_2}(\boldsymbol{r}_{j_2 i}) \\ & + \frac{1}{3!} \sum_{j_1 j_2 j_3} \sum_{v_1 v_2 v_3} c_{v_1 v_2 v_3} \phi_{v_1}(\boldsymbol{r}_{j_1 i}) \phi_{v_2}(\boldsymbol{r}_{j_2 i}) \phi_{v_3}(\boldsymbol{r}_{j_3 i}) + \ldots \,, \end{aligned} \tag{105}$$

where only i is excluded from the summations over $j_1, j_2, \ldots$. The expansion Eq. (105) is identical to Eq. (104), with expansion coefficients c_ν that are different from the expansion coefficients J_ν in Eq. (104). The expansion coefficients c_ν are simple functions of J_ν that may be obtained by taking into account that products of basis functions of the same argument may be expanded into linear combinations of single basis functions, for example, $\phi_{v_1}(\boldsymbol{r}_{ji})\,\phi_{v_2}(\boldsymbol{r}_{ji}) = \sum_v a_v \phi_v(\boldsymbol{r}_{ji})$, *etc.*, such that the self-interactions are removed by an appropriate modification of a lower-order expansion coefficient. The relation between J_ν and c_ν is also outlined in Ref. [72]. I next introduce the atomic density

$$\rho_i(\sigma) = \sum_j^{j\neq i} \delta(\sigma - \sigma_j)\,, \tag{106}$$

and the atomic base that is obtained as

$$A_v = \langle \rho_i | \phi_v \rangle = \sum_j^{j\neq i} \phi_v(\boldsymbol{r}_j)\,. \tag{107}$$

This allows us to rewrite the expansion Eq. (105) in the form

$$E_i = \sum_\nu c_\nu \boldsymbol{A}_\nu \quad \text{with} \quad \boldsymbol{A}_\nu = A_{v_1} A_{v_2} A_{v_3} \ldots \tag{108}$$

where the index ν collects the required indices $v_1, v_2, v_3, \ldots$ from Eq. (105).
By construction the expansion is invariant with respect to permutation of identical atoms. The change from Eq. (104) to Eq. (105) further means that the atomic expectation values of the many-atom correlation functions $\Phi_{\alpha\nu}$ may be expressed exactly by products of expectation values of single-bond basis functions. This enables a very efficient implementation as the effort for evaluating the many-atom correlation functions scales linearly with the number of neighbors irrespective of the order of the correlation functions.
The expansion Eq. (107) is general, which also means that in general it is not invariant under rotation. Rotationally invariant expansions may be obtained as outlined in the following. First, the single-bond basis functions are chosen as basis functions of the irreducible representations of the rotation group. In practice, this corresponds to linear combination of atomic orbitals (LCAO) basis functions as in TB, Eq. (26),

$$\phi_{inlm}(\boldsymbol{r}) = R_{nl}(|\boldsymbol{r} - \boldsymbol{r}_i|) Y_l^m(\theta, \phi)\,. \tag{109}$$

Rotationally invariant products are obtained with the help of generalized Clebsch Gordan coefficients

$$B_\nu = \sum_{\boldsymbol{m}} \begin{pmatrix} \boldsymbol{l} \\ \boldsymbol{L} \end{pmatrix}_N A_{n_1 l_1 m_1} A_{n_2 l_2 m_3} A_{n_3 l_2 m_3} \ldots\,, \tag{110}$$

with $\boldsymbol{l} = (l_1, l_2, l_3, \ldots)$, $\boldsymbol{m} = (m_1, m_2, m_3, \ldots)$ and $\boldsymbol{L}$ are intermediate angular momenta that arise from products of the spherical harmonics [34, 37, 72–74]. The expansion for the energy may then be represented as

$$E_i = \sum_\nu c_\nu \boldsymbol{B}_\nu\,. \tag{111}$$

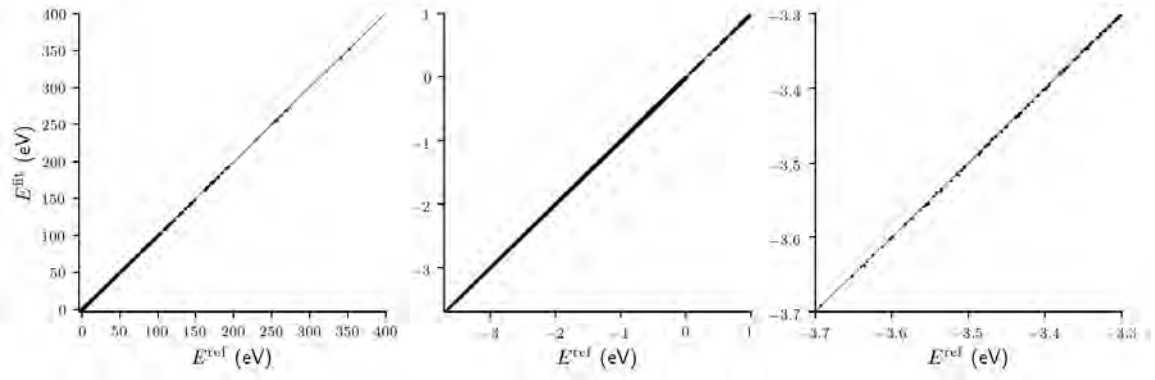

Fig. 8: *Comparison of predictions from ACE to DFT reference. The energies are compared over three orders of magnitude. The graph shows many thousand data points and outliers are visible in particular. Taken from Ref. [34].*

4.2 Relation to other descriptors

The completeness of the ACE allows one to make contact with other frequently used descriptors. Here I list a few popular descriptors and machine-learning potentials that may be rewritten in the form of an ACE [34, 37]:

- Steinhardt parameters: the Steinhardt parameters [75] are frequently employed for structure classification.
- Symmetry functions: neural network potentials use 2-body and 3-body functions, called symmetry functions, as descriptors for the atomic environment [15].
- Smooth overlap of atomic positions (SOAP): the SOAP descriptor [76] is employed, for example with the Gaussian approximation potential (GAP) [16]. A tensorial version of SOAP is also available [27].
- Spectral neighbor analysis potential (SNAP): the SNAP employs the SOAP descriptor with hyperspherical harmonics [21].
- Moment tensor potentials (MTP): the MTPs [22] provide an expansion of the interatomic energy in terms of Cartesian tensors.

4.3 Parametrization

Compared to TB and BOP models, the ACE provides less physical insight but greater flexibility for the accurate parametrization of arbitrary interatomic interactions. This means that a larger number of reference data needs to be available for fitting the ACE expansion coefficients c_ν. Fig. 8 shows the comparison of the ACE predictions for copper compared to DFT reference data. More than 50000 DFT total energy calculations were used for the parametrization of the ACE. The reference data set comprises many different bulk crystal structures, with and without defects, at various volumes and deformations in addition to small clusters with 2 to 25 Cu atoms.

Knowledge and insight gained from TB and BOP can be used for the parametrization of ACE. For the Cu example, the ACE was built on the Finnis Sinclair potential Eq. (1). However, instead of computing the density ρ_i and the repulsion $\sum_j V_{ij}/2$ from pairwise functions, density and repulsion were represented by a general ACE expansion. The non-linear square-root embedding function helps to converge the ACE faster as compared to a linear expansion as the non-linear dependence of the bond energy on coordination is immediately taken into account. Furthermore, the radial functions R_{nl} may be related to the minimal basis radial functions of TB models.

5 Summary and conclusions

This chapter exemplifies two strategies for obtaining interatomic potentials in materials science. The derivation of BOPs from DFT encompasses a systematic coarse-graining of the electronic structure that provides insight into bond formation and is amenable to physical and chemical interpretation. In contrast, ACE is a formal many-atom expansion that is flexible to model bond formation accurately but with many fitting parameters, so that large numbers of DFT reference data are required.

The TB approximation is obtained from DFT as a second-order expansion with respect to the density matrix of overlapping spherical atomic charge densities. A physically transparent mechanism of bond formation is obtained by grouping the terms in the expansion in bond energy and electrostatic interactions that drive the formation of covalent, polar and ionic bonds, the charging of the atoms and the promotion of electrons out of their atomic state, and a repulsive energy that keeps the atoms apart.

The moments theorem allows one to relate the atomic structure to the electronic structure. I introduced several methods that implicitly or explicitly make use of the moments theorem to reconstruct the bond energy from the local atomic environment. The recursion method first transforms the Hamiltonian to tridiagonal form, which enables a continued fraction representation of the Green function. The numerical BOPs make use of the recursion method for a local construction of the bond energy. The KPM expands the kernel into Chebyshev polynomials for a local expansion of the bond energy. Closely related is the FOE that starts from the expansion of a temperature dependent electronic broadening function. Finally, the analytic BOPs provide explicit analytic expressions for energies and forces that may also be used to analyze bond strengths and structural stability. The analytic BOPs reproduce the DFT energies very well and enable the simulations of phase diagrams in good agreement with experiment. Software for simulations with millions and for the efficient parametrization of new models is available.

The ACE provides a formal many-atom expansion that enables parametrizations with arbitrary accuracy given that sufficient reference data is available. The completeness of the ACE also means that other descriptors and machine-learning potentials may be represented in the form of an ACE. The parametrization of the ACE was discussed briefly and illustrated for copper.

Acknowledgments

I thank Isabel Pietka for carefully reading the manuscript and helpful comments and corrections.

References

[1] J. Friedel in J.M. Ziman (Ed.): *Electrons* (Pergamon, London, 1969), *Physics of Metals*, Vol. 1

[2] F. Ducastelle, J. Phys. (Paris) **31**, 1055 (1970)

[3] R.P. Gupta, Phys. Rev. B **23**, 6265 (1981)

[4] M.W. Finnis and J.E. Sinclair, Philos. Mag. A **50**, 45 (1984)

[5] J.K. Nørskov and N.D. Lang, Phys. Rev. B **21**, 2131 (1980)

[6] M.J. Puska, R.M. Nieminen, and M. Manninen, Phys. Rev. B **24**, 3037 (1981)

[7] M.S. Daw and M.I. Baskes, Phys. Rev. B **29**, 6443 (1984)

[8] J. Tersoff, Phys. Rev. Lett. **56**, 632 (1986)

[9] J. Tersoff, Phys. Rev. B **38**, 9902 (1988)

[10] M.I. Baskes, Phys. Rev. B **46**, 2727 (1992)

[11] D.G. Pettifor and I.I. Oleinik, Phys. Rev. Lett. **84**, 4124 (2000)

[12] D.G. Pettifor and I.I. Oleinik, Phys. Rev. B **65**, 172103 (2002)

[13] R. Drautz and D.G. Pettifor, Phys. Rev. B **74**, 174117 (2006)

[14] R. Drautz and D.G. Pettifor, Phys. Rev. B **84**, 214114 (2011)

[15] J. Behler and M. Parrinello, Phys. Rev. Lett. **98**, 146401 (2007)

[16] A.P. Bartók, M.C. Payne, R. Kondor, and G. Csányi, Phys. Rev. Lett. **104**, 136403 (2010)

[17] S. Manzhos and T. Carrington, Jr., J. Chem. Phys. **125**, 084109 (2006)

[18] M. Rupp, A. Tkatchenko, K.-R. Müller, and O.A. von Lilienfeld, Phys. Rev. Lett **108**, 058301 (2012)

[19] Z. Li, J.R. Kermode, and A. DeVita, Phys. Rev. Lett. **114**, 096405 (2015)

[20] J. Behler, Int. J. Quantum Chem. **115**, 1032 (2015)

[21] A. Thompson, L. Swiler, C. Trott, S. Foiles, and G. Tucker, J. Comp. Phys. **285**, 316 (2015)

[22] A.V. Shapeev, Multiscale Model. Simul. **14**, 1153 (2016)

[23] N. Artrith, A. Urban, and G. Ceder, Phys. Rev. B **96**, 014112 (2017)

[24] A. Takahashi, A. Seko, and I. Tanaka, Phys. Rev. Materials **1**, 063801 (2017)

[25] T.D. Huan, R. Batra, J. Chapman, S. Krishnan, L. Chen, and R. Ramprasad, NPJ Comput. Mater. **3**, 37 (2017)

[26] S. Chmiela, A. Tkatchenko, H.E. Sauceda, I. Poltavsky, K.T. Schütt, and K.-R. Müller, Science Advances **3**, e1603015 (2017)

[27] A. Grisafi, D.M. Wilkins, G. Csányi, and M. Ceriotti, Phys. Rev. Lett. **120**, 036002 (2018)

[28] M.A. Wood and A.P. Thompson, J. Chem. Phys. **148**, 241721 (2018)

[29] T.T. Nguyen, E. Székely, G. Imbalzano, J. Behler, G. Csányi, M. Ceriotti, A.W. Götz, and F. Paesani, J. Chem. Phys. **148**, 241725 (2018)

[30] D. Dragoni, T.D. Daff, G. Csányi, and N. Marzari, Phys. Rev. Materials **2**, 013808 (2018)

[31] T. Bereau, R.A. DiStasio Jr., A. Tkatchenko, and O.A. von Lilienfeld, J. Chem. Phys. **148**, 241706 (2018)

[32] A. Kamath, R.A. Vargas-Hernández, R.V. Krems, T. Carrington Jr., and S. Manzhos, J. Chem. Phys. **148**, 241702 (2018)

[33] M. Rupp, O.A. von Lilienfeld, and K. Burke, J. Chem. Phys. **148**, 241401 (2018)

[34] R. Drautz, Phys. Rev. B **99**, 014104 (2019)

[35] M.J. Willatt, F. Musil, and M. Ceriotti, J. Chem. Phys. **150**, 154110 (2019)

[36] C. van der Oord, G. Dusson, G. Csányi, and C. Ortner, Mach. Learn.: Sci. Technol. **1**, 015004 (2020)

[37] R. Drautz, Phys. Rev. B **102**, 024102 (2020)

[38] R. Drautz, T. Hammerschmidt, M. Cak, and D.G. Pettifor, Modelling Simul. Mater. Sci. Eng. **23**, 074004 (2015)

[39] J. Harris, Phys. Rev. B **31**, 1770 (1985)

[40] W.M.C. Foulkes and R. Haydock, Phys. Rev. B **39**, 12520 (1989)

[41] A.P. Sutton, M.W. Finnis, D.G. Pettifor, and Y. Ohta, J. Phys. C **21**, 35 (1988)

[42] M. Elstner, D. Porezag, G. Jungnickel, J. Elsner, M. Haugk, T. Frauenheim, S. Suhai, and G. Seifert, Phys. Rev. B **58**, 7260 (1998)

[43] M.W. Finnis: *Interatomic Forces in Condensed Matter* (Oxford University Press, 2003)

[44] D.G. Pettifor: *Bonding and Structure in Molecules and Solids* (Oxford University Press, 1995)

[45] A. Sutton: *Electronic Structure of materials* (Clarendon Press, Oxford, 1993)

[46] A.T. Paxton in [77], p. 145

[47] T. Hammerschmidt and R. Drautz in [77], p. 229

[48] P. Hohenberg and W. Kohn, Phys. Rev. **136**, B864 (1964)

[49] W. Kohn and L.J. Sham, Phys. Rev. **140**, A1133 (1965)

[50] G.K.H. Madsen, E.J. McEniry, and R. Drautz, Phys. Rev. B **83**, 184119 (2011)

[51] A. Urban, M. Reese, M. Mrovec, C. Elsässer, and B. Meyer,
Phys. Rev. B **84**, 155119 (2011)

[52] E.J. McEniry, R. Drautz, and G.K.H. Madsen,
J. Phys.: Condens. Matter **25**, 115502 (2013)

[53] C. Lanczos, J. Res. Natl. Bur. Stand. **45**, 225 (1950)

[54] R. Haydock in H. Ehrenreich, F. Seitz, and D. Turnbull (eds.)
Solid State Physics (Academic Press, New York, 1980) Vol. 35, p. 215

[55] M. Aoki, Phys. Rev. Lett. **71**, 3842 (1993)

[56] A.P. Horsfield, A.M. Bratkovsky, D.G. Pettifor, and M. Aoki, Phys. Rev. B **53**, 1656 (1996)

[57] A.P. Horsfield, A.M. Bratkovsky, M. Fearn, D.G. Pettifor, and M. Aoki,
Phys. Rev. B **53**, 12694 (1996)

[58] M. Aoki, D. Nguyen-Manh, D.G. Pettifor, and V. Vitek, Prog. Mat. Sci. **52**, 154 (2007)

[59] R.N. Silver, H. Röder, A.F. Voter, and J.D. Kress, J. Comp. Phys. **124**, 115 (1996)

[60] A.F. Voter, J.D. Kress, and R.N. Silver, Phys. Rev. B **53**, 12733 (1996)

[61] A. Weiße, G. Wellein, A. Alvermann, and H. Fehske, Rev. Mod. Phys. **78**, 275 (2006)

[62] B. Seiser, D.G. Pettifor, and R. Drautz, Phys. Rev. B **87**, 094105 (2013)

[63] R.N. Silver and H. Röder, Phys. Rev. E **56**, 4822 (1997)

[64] S. Goedecker and M. Teter, Phys. Rev. B **51**, 9455 (1995)

[65] S. Goedecker, Rev. Mod. Phys. **71**, 1085 (1999)

[66] R.N. Silver and H. Röder, Int. J. Mod. Phys. C **5**, 735 (1994)

[67] M.E. Ford, D.G. Pettifor, and R. Drautz, J. Phys.: Condens. Matter **27**, 086002 (2015)

[68] T. Hammerschmidt, B. Seiser, M.E. Ford, A.N. Ladines, S. Schreiber, N. Wang, J. Jenke, Y. Lysogorskiy, C. Teijeiro, M. Mrovec, M. Cak, E.R. Margine, D.G. Pettifor, and R. Drautz, Comput. Phys. Commun. **235**, 221 (2019)

[69] B. Seiser, T. Hammerschmidt, A.N. Kolmogorov, R. Drautz, and D.G. Pettifor, Phys. Rev. B **83**, 224116 (2011)

[70] A. Ferrari, M. Schröder, Y. Lysogorskiy, J. Rogal, M. Mrovec, and R. Drautz, Modelling Simul. Mater. Sci. Eng. **27**, 085008 (2019)

[71] A. Ladines, T. Hammerschmidt, and R. Drautz, Comp. Mater. Sci. **173**, 109455 (2020)

[72] G. Dusson, M. Bachmayr, G. Csányi, R. Drautz, S. Etter, C. van der Oord, and C. Ortner, in preparation (2020)

[73] A.P. Yutsis, I.B. Levinson, and V.V. Vanagas: *The Theory of Angular Momentum* (Israel Program for Scientific Translations, Jerusalem, 1962)

[74] D.M. Brink and G.R. Satchler: *Angular Momentum* (Clarendon Press, Oxford, 1968)

[75] P.J. Steinhardt, D.R. Nelson, and M. Ronchetti, Phys. Rev. B **28**, 784 (1983)

[76] A.P. Bartók, R. Kondor, and G. Csányi, Phys. Rev. B **87**, 184115 (2013)

[77] J. Grotendorst, N. Attig, S. Blügel, and D. Marx (Eds.): *Multiscale Simulation Methods in Molecular Sciences* NIC Series Vol. 42 (Forschungszentrum Jülich, 2009)

4 Effective Hamiltonians in Chemistry

Frank Neese, Lucas Lang, Vijay Gopal Chilkuri
Max-Planck-Institut für Kohlenforschung
Mülheim an der Ruhr

Contents

E. Pavarini and E. Koch (eds.)
Topology, Entanglement, and Strong Correlations
Modeling and Simulation Vol. 10
Forschungszentrum Jülich, 2020, ISBN 978-3-95806-466-9
http://www.cond-mat.de/events/correl20

1 Introduction

1.1 Why effective Hamiltonians?

Effective Hamiltonians (EHs) occupy an important place in quantum chemistry. EHs serve a multitude of different purposes. On the one hand, they are vital in the formulation of new approximate methods that lead to new computationally efficient tools. On the other hand, they allow one to recast highly complex problems that are difficult to understand into seemingly simpler problems that are amenable to human analysis. In this latter application, they unfold their full power by creating models that can be used to highlight the physical essence of the problem at hand. In many cases, the emerging model Hamiltonians are of low dimension and can be solved by hand or with very little computational effort. The crucial step is that the matrix elements of the EH can be recast in terms of effective parameters. The latter are adjustable and can, for example, be fitted to experiments or higher-level calculations. The benefit of EH theory is here that: a) the model Hamiltonians are derived from more complete Hamiltonians; hence the theory provides explicit and concrete expressions that allow the calculation of the model parameters and b) being derived from first principles, these model Hamiltonians are solidly grounded in fundamental physics. Thus, the effective Hamiltonians derived in this way do not just represent a curve fitting exercise of uncertain physical content and interpretation as would be the case for model Hamiltonians that are only based on physical intuition or conjecture.

The effective Hamiltonian concept can even be taken a step further and effective Hamiltonians can be derived from more elaborate effective Hamiltonians that themselves are derived from first-principles physics. The important point is that there is an unbroken chain of logic that leads by pure deduction from first physical principles to a simple, intuitively appealing, and physically sound model that can be used to interpret the results of measurements or even the behavior of entire classes of substances or materials. The benefit of having model Hamiltonians derived in this way can hardly be overemphasized since the theory does not only provide a concrete and unambiguous way to compute the model parameters, but it also makes it clear under which conditions the model Hamiltonian is valid and when it is expected to break down. A concrete example for such a situation that will be discussed in more detail in section 3.2 is the spin Hamiltonian (SH) used to interpret magnetic measurements (electron paramagnetic resonance, EPR or nuclear magnetic resonance, NMR) on molecules or solids. The SH is derived conveniently from the time-independent relativistic many-particle Schrödinger equation (technically the Dirac-Coulomb-Breit (DCB) Hamiltonian). It leads to a low-dimensional model Hamiltonian that contains the SH parameters as adjustable parameters. These are the g-matrix, the hyperfine coupling (HFC) matrix, the zero-field splitting (ZFS, in physics often referred to as the magnetic anisotropy), the quadrupole splitting, the chemical shift and the nuclear spin-spin coupling. For interacting magnetic systems, the familiar Heisenberg exchange Hamiltonian is obtained from the theory.

However, once there are enough spins in a given system (for example in clusters containing a dozen to a few dozen open-shell transition metal ions), even the SH dimensions become

unmanageable and can reach dimensions of hundreds of millions. Quite frequently, one is only interested in the lowest few eigenstates of such a system that are thermally accessible over a given temperature range. In this case, one wants to describe these few magnetic sublevels with an effective Hamiltonian that can be derived from the enormous SH of the entire system. The parameters that enter this secondary SH are then functions of all the spins and SH parameters of the full system. A very simple concrete example would be an $S = 5/2$ system with strong ZFS (relative to external magnetic fields). Such a system contains $2S+1 = 6$ magnetic sublevels that, by means of Kramers degeneracy, form three so-called "Kramers doublets". The latter can each be described by an effective Hamiltonian with spin $S = 1/2$. Hence, three pseudo $S = 1/2$ systems substitute for the entire $S = 5/2$ system. We refer to the specialist literature for further details [1, 2].
In this chapter, we will provide an introduction into the theory of effective Hamiltonians. We will cover formal aspects in section 2 before proceeding to actual chemical applications in section 3 that will discuss both computational tools for the calculation of static ("strong" in physics language) and dynamic electron correlation as well as EHs derived to parameterize and understand magnetic properties. An example for the combination of both strategies will conclude our chapter.

1.2 An introduction into quantum-chemical notation

Since we will present the material covered in this chapter mostly from a quantum chemistry point of view, it is convenient to briefly discuss the point of departure of the theory and introduce the necessary notation along the way.

1.2.1 One-particle and many-particle Hamiltonians

We start from the nonrelativistic many-particle Hamiltonian in the Born-Oppenheimer (BO) approximation (clamped nuclei), which is simply given by

$$\hat{H}_{\mathrm{BO}} = \sum_i \hat{h}(\mathbf{x}_i) + \tfrac{1}{2} \sum_{i \neq j} \frac{1}{|\mathbf{r}_i - \mathbf{r}_j|} + \tfrac{1}{2} \sum_{A \neq B} \frac{Z_A Z_B}{|\mathbf{R}_A - \mathbf{R}_B|} \tag{1}$$

with the one-electron part of the Hamiltonian given by the sum of the kinetic energy and nucleus-electron attraction terms,

$$\hat{h}(\mathbf{x}_i) = -\tfrac{1}{2}\nabla_i^2 - \sum_A \frac{Z_A}{|\mathbf{R}_A - \mathbf{r}_i|}. \tag{2}$$

Here, we consider a system consisting of N electrons and M nuclei. The electrons are described by the coordinates $\mathbf{x}_i = (\mathbf{r}_i, \sigma_i)$, where $\mathbf{r}_i$ is the set of three position variables for the i'th electron and σ_i represents its spin degree of freedom (spin-up, α, $\uparrow$ or spin-down, β, $\downarrow$). The nuclei are assumed to be at rest at positions $\mathbf{R}_A$ and have nuclear charges Z_A (for the A'th nucleus). Hartree atomic units ($4\pi\varepsilon_0 = \hbar = e = m_e = 1$) [3] are used throughout.

In this chapter, we will remain within the confines of the time-independent Schrödinger equation

$$\hat{H}_{\text{BO}}\Psi_I(\mathbf{x}|\mathbf{R}) = E_I(\mathbf{R})\Psi_I(\mathbf{x}|\mathbf{R}), \tag{3}$$

where $\mathbf{x}$ and $\mathbf{R}$ denote the collection of all electronic and nuclear degrees of freedom respectively and the notation $\Psi(\mathbf{x}|\mathbf{R})$ indicates that the many particle wavefunction depends explicitly on the electron coordinates and parametrically on the nuclear coordinates. In order to be concise, we will follow the convention of using uppercase letters and indices for many-electron quantities and lowercase letters, symbols, and indices for one-electron quantities. Thus, $I = 0, ..., \infty$ enumerates the possible electronic eigenstates of the BO Hamiltonian.

While conceptionally simple, the BO Schrödinger equation cannot be solved analytically even for a two-electron system such as the helium atom. However, very powerful approximations have been developed over the course of the last century. Many of them begin with a model of effective independent particles (Hartree-Fock method, HF). In the HF method one replaces the many-particle equation by an effective one-particle equation of the form

$$\hat{F}(\{\psi\})\psi_i(\mathbf{x}) = \varepsilon_i\psi_i(\mathbf{x}). \tag{4}$$

The HF equations are readily derived from the BO Schrödinger equation and the variational principle [3]. The effective one-particle operator $\hat{F}$ depends on its own solutions (the set of one-particle functions $\{\psi\}$) and yields the orbital energies ε_i and orbitals $\psi_i(\mathbf{x})$. Given the dependence of $\hat{F}$ on its own solutions, the HF equations must be solved by iteration starting from a set of trial orbitals. We will write down an explicit form of the Fock operator after introducing second-quantized notation (see Eq. (13) below).

In general, the HF equations do not only have N solutions, but an infinite number of solutions. The lowest N orbitals are referred to as "occupied orbitals" of the system and they are usually denoted with the indices i, j, k, l. The remaining orbitals are the leftover solutions of the variational principle and are referred to as unoccupied or "virtual" orbitals with indices customarily denoted by a, b, c, d. This corresponds to the particle-hole convention frequently encountered in physics. General orbitals are given the indices p, q, r, s.

The set of occupied orbitals $\{\psi\}$ are the building blocks of the HF wavefunction, which is an antisymmetrized product ("Slater determinant")

$$\Psi_{\text{HF}}(\mathbf{x}_1 \dots \mathbf{x}_N) = \frac{1}{\sqrt{N!}} \begin{vmatrix} \psi_1(\mathbf{x}_1) & \psi_2(\mathbf{x}_1) & \cdots & \psi_N(\mathbf{x}_1) \\ \psi_1(\mathbf{x}_2) & \psi_2(\mathbf{x}_2) & \cdots & \psi_N(\mathbf{x}_2) \\ \vdots & \vdots & \ddots & \vdots \\ \psi_1(\mathbf{x}_N) & \psi_2(\mathbf{x}_N) & \cdots & \psi_N(\mathbf{x}_N) \end{vmatrix} \equiv |\psi_1 ... \psi_N|. \tag{5}$$

Occasionally, an overbar is used in order to indicate occupation of an orbital with a spin down electron, while no overbar indicates a spin-up electron, e.g. $|\psi_1\bar{\psi}_1 ... \bar{\psi}_i ... \psi_j ... \psi_N|$. The HF wavefunction is a mean-field approximation to the mind-boggling complexity of the exact ground state many-particle wavefunction.

It is our experience that much confusion arises from not properly differentiating between the many-particle and single-particle levels. Hence, in this chapter, we will make a dedicated effort

to be clear at which level we are arguing. We note in passing that only the eigenspectrum of the many-particle Hamiltonian (and the associated properties of the many-particle wavefunctions) are directly related to observable quantities. The orbitals and orbital energies are not observables and they are not related to observable quantities. For the purpose of the theory, they are simply auxiliary quantities used to construct better and better approximations to the many-particle wavefunction(s) of the system. In chemistry, the term "state" is reserved for the many-particle eigenfunctions of the Schrödinger equation (or approximations thereof). Orbitals are not referred to as "states". Hence, in chemical language, there also can be no notion of "occupied states" or "unoccupied states".

1.2.2 Electron correlation and the correlation energy

While the HF method yields a fairly good approximation to the total energy of the system (about 99.8% correct), the remaining 0.2% error are very large on the chemical energy scale. For a somewhat larger system the error can easily reach 10 E_h which translates to more than 270 eV. Hence, in absolute terms, the error of the HF approximation is very large and one needs to proceed beyond the HF approximation. By definition, the difference between the exact energy and the HF energy is referred to as the "correlation energy"

$$E_\mathrm{corr} = E_\mathrm{exact} - E_\mathrm{HF}. \tag{6}$$

By definition, the correlation energy is always negative. If the system is conceptionally well-described by a single Slater determinant, then all of the correlation energy is referred to as "dynamic" correlation energy. The physical picture being that the instantaneous electron-electron interaction provides a correction to the mean-field HF method. If, however, the system is not well described by a single Slater determinant, the energy gained by choosing a qualitatively correct "ansatz" is referred to as "static" correlation energy. An example would be the H_2 molecule towards its dissociation limit that requires two Slater determinants for a qualitatively correct description. From this description, it is already evident that the distinction between static and dynamic correlation is vague, ill-defined, and not unique. We will not dwell on the subject here. The shortcomings of the HF model are conceptually readily remedied. To this end, we will make use of second-quantization notation and introduce the electron replacement operators

$$a_p^q = a_q^\dagger a_p, \tag{7}$$

where $a_q^\dagger$ and a_p are the familiar fermion creation and annihilation operators, respectively. Since most of the presented theory as well as the BO Hamiltonian do not explicitly contain spin operators, it is convenient to define the spin-traced excitation operators (also called "generators of the unitary group")

$$E_p^q = a_{\bar{p}}^{\bar{q}} + a_p^q. \tag{8}$$

The operator E_p^q is a singlet excitation operator, i.e., it does not change the total spin of the state on which it acts.

Obviously, these operators refer to a specific one-particle basis. This is usually taken to be the set of HF orbitals. The HF orbitals themselves can not, however, be exactly calculated in practice. In quantum chemistry, it is common to expand them into a fixed, finite set of atom-centered basis functions $\{\varphi\}$ as

$$\psi_i(\mathbf{x}) = \sum_\mu c_{\mu i}\varphi_\mu(\mathbf{x}). \tag{9}$$

The actual functional form of the basis function is usually taken to be of the Gaussian type but details would lead too far astray here.
In terms of the second-quantized operators, the BO Hamiltonian reads

$$\hat{H}_{\text{BO}} = \sum_{p,q} h_{pq}E^p_q + \tfrac{1}{2}\sum_{p,q,r,s} g^{qs}_{pr}(E^p_qE^r_s - E^p_s\delta_{qr}). \tag{10}$$

Since the BO Hamiltonian can be written entirely in terms of singlet excitation operators, it is clear that it conserves the total spin S. In Eq. (10), the nuclear repulsion term has been dropped for convenience. Furthermore, the one- and two-electron integrals have been introduced:

$$h_{pq} = \left\langle \psi_p|\hat{h}|\psi_q \right\rangle, \tag{11}$$

$$g^{qs}_{pr} = \left(\psi_p\psi_q|\psi_r\psi_s\right) \equiv \left\langle \psi_p\psi_r|\psi_q\psi_s \right\rangle. \tag{12}$$

In chemistry the round bracket notation $(11|22)$ is more common, while in physics the bracket notation $\langle 12|12\rangle$ is usually preferred ('1' and '2' refer to the coordinates of electrons 1 and 2, respectively). The second-quantized BO operator is only equivalent to its first-quantized counterpart in the limit that the one-particle basis is mathematically complete. This is never the case in practice and consequently, the second-quantized BO Hamiltonian can be regarded as the projection of the BO Schrödinger equation onto the finite one-particle basis.
With the definition of the one- and two-electron integrals, we can give an explicit form of the Fock operator. It is represented by the matrix

$$F_{pq} = h_{pq} + \sum_k \underbrace{\left[\left\langle \psi_p\psi_k|\psi_q\psi_k \right\rangle - \left\langle \psi_p\psi_k|\psi_k\psi_q \right\rangle\right]}_{\equiv\langle pk||qk\rangle}, \tag{13}$$

where the antisymmetrized two-electron repulsion integral $\langle pk||qk\rangle$ has been introduced. The negative term in the sum over k is the "exchange" term. It arises from the electrostatic repulsion of the electrons among each other in conjunction with the antisymmetry requirements of the fermionic many-particle wavefunction. It does not represent an "exchange force".
Given the second-quantized notation, it is straightforward to write down an expansion of the many-particle ground-state wavefunction:

$$|\Psi_0\rangle = |\Psi_{\text{HF}}\rangle + \sum_{i,a} C^a_i\left|\Phi^a_i\right\rangle + \left(\tfrac{1}{2!}\right)^2\sum_{i,j,a,b} C^{ab}_{ij}\left|\Phi^{ab}_{ij}\right\rangle + \left(\tfrac{1}{3!}\right)^2\sum_{i,j,k,a,b,c} C^{abc}_{ijk}\left|\Phi^{abc}_{ijk}\right\rangle + \ldots \tag{14}$$

Here, the building blocks $|\Phi^{a\cdots}_{i\cdots}\rangle$ are determinants in which one-, two-, three- ... up to N orbitals have been replaced in the HF determinant, e.g.

$$\left|\Phi^a_i\right\rangle = a^a_i\left|\Psi_{\text{HF}}\right\rangle \tag{15}$$

etc. In the language of second quantization, the HF determinant acts as the "Fermi vacuum". The coefficients C_i^a ... are wavefunction parameters that must be determined in one way or another. If this is done variationally, one refers to the method as "configuration interaction" (CI). If perturbation theory is used, "many body perturbation theory" (MBPT) arises. If CI is done with all possible Slater determinants, the method of Full CI (FCI) arises. It represents the exact solution of the Schrödinger equation in the chosen finite basis. Since the number of possible Slater determinants grows factorially, this method is restricted to very small systems. However, it serves as an invaluable benchmark for approximate methods.
Truncated CI expansion have the very undesirable property of not being size-consistent, i.e., the energy of two non-interacting systems is not the sum of the energy of the individual systems calculated in the same approximation. Hence, truncated CI has essentially been abandoned. The method of coupled-cluster (CC) theory does not suffer from this shortcoming. Here, one uses an exponential ansatz

$$|\Psi_0\rangle = \exp(\hat{T})\,|\Psi_{\text{HF}}\rangle \tag{16}$$

with the cluster operator being the sum of one-, two-, ... particle excitation operators,

$$\hat{T} = \hat{T}_1 + \hat{T}_2 + ... = \sum_{i,a} t_i^a a_i^a + \tfrac{1}{4} \sum_{i,j,a,b} t_{ij}^{ab} a_j^b a_i^a + ... \tag{17}$$

CC theory is nonlinear and therefore more complex than CI. However, it is size-consistent and extensive at any truncation level of the cluster operator and consequently the method of choice. Truncated MBPT is also size-consistent and frequently used in chemistry.

1.2.3 Relativistic and external field terms

In order to relate to the material presented in section 3, we need to briefly mention extensions to the BO Hamiltonian. Next to many other terms, these corrections arise either from relativity or the presence of external electric or magnetic fields.
All relativistic terms can be derived from the DCB Hamiltonian and are usually grouped into spin-free ("scalar") and spin-dependent terms. Among the numerous terms that arise, the most important relativistic term for our discussion is the spin-orbit coupling (SOC). The SOC is in general a complex two-electron operator. Here, we represent it in a spin-orbit mean-field (SOMF) approximation [4, 5] that can be written in the form

$$\hat{H}_{\text{SOC}} \approx \sum_i \mathbf{h}_i^{\text{SOC}}\,\hat{\mathbf{s}}_i. \tag{18}$$

Here, $\hat{\mathbf{s}}_i$ is the spin of the i'th electron and $\mathbf{h}^{\text{SOC}}$ is an effective SOC operator with purely imaginary matrix elements.
Since the BO Hamiltonian is spin-free, it commutes with the total spin $\hat{\mathbf{S}} = \sum_i \hat{\mathbf{s}}_i$ and consequently, the eigenfunctions of the BO Hamiltonian can be labeled according to two additional quantum numbers S (the total spin) and $M = S, S-1, ..., -S$ (the projection of the total spin onto the z axis). At the level of the BO Hamiltonian all M-components ("magnetic sublevels")

of a given S and electronic state I are exactly degenerate (they form a "spin multiplet"). This degeneracy is lifted by the SOC which mixes states of different S and M. It is essential to properly differentiate between the total spin $\hat{\mathbf{S}}$ and the individual spins $\hat{\mathbf{s}}_i$ when discussing magnetic properties.
Other contributions to the Hamiltonian will be briefly visited in section 3.2.

2 Theory of effective Hamiltonians

2.1 Effective Hamiltonians via similarity transformation

Let H be the "complete" Hamiltonian describing a quantum system, e.g. the BO or DCB Hamiltonians introduced above. Its eigenvalues and eigenstates fulfill the time-independent Schrödinger equation

$$H|\Psi_I\rangle = E_I|\Psi_I\rangle. \tag{19}$$

As already mentioned in the introduction, it can be inconvenient to work with this Hamiltonian if it has a large number of eigenstates and eigenvalues, since usually one is only interested in the low-energy part of the spectrum. One can then define an "exact" effective Hamiltonian that acts in a subspace of reduced dimensionality and reproduces the exact eigenvalues for a limited number of eigenstates of H,

$$H^{\text{eff}}|\tilde{\Psi}_I\rangle = E_I|\tilde{\Psi}_I\rangle. \tag{20}$$

The eigenstates $|\tilde{\Psi}_I\rangle$ need not be identical to the true eigenstates $|\Psi_I\rangle$. However, they are usually required to provide a qualitatively correct physical description of the true eigenstates.
One can formulate effective Hamiltonian theory very generally on the basis of similarity transformations. This was done by Shavitt and Redmon [6] and we follow their treatment in the following. The theory was also summarized in a recent dissertation [7]. Let $\mathcal{H}$ be the complete Hilbert space on which H acts. A given basis of this Hilbert space is then divided into two orthogonal subsets: The "model space" $\mathcal{H}_0$ with projector $P = \sum_{I\in\text{model}} |\Phi_I\rangle\langle\Phi_I|$ and the complementary or outer space $\mathcal{H}_{\text{outer}}$ with projector $Q = 1-P = \sum_{K\in\text{outer}} |\Phi_K\rangle\langle\Phi_K|$. In the following, we use indices $I, J, ...$ to refer to states in the model space and indices $K, L, ...$ to refer to states in the outer space. The model space will be the space on which the effective Hamiltonian acts. Once the model space is chosen, an arbitrary operator A can be decomposed as [6]

$$A = A_D + A_X, \tag{21}$$

where

$$A_D = PAP + QAQ \tag{22}$$

is called its block diagonal part and

$$A_X = PAQ + QAP \tag{23}$$

is called its block off-diagonal part. The essence of effective Hamiltonian theory can now be described as finding a so-called decoupling operator U such that the similarity-transformed

Hamiltonian

$$\tilde{H} = U^{-1} H U \tag{24}$$

is block-diagonal [6]. The effective Hamiltonian is then defined as the model-space part of the similarity-transformed Hamiltonian, i.e.

$$H^{\text{eff}} = P\tilde{H}P. \tag{25}$$

If one assumes that the energies E_I and model-space states $|\tilde{\Psi}_I\rangle$ fulfill the eigenvalue equation (20), it is easy to show that

$$HU|\tilde{\Psi}_I\rangle = U\tilde{H}|\tilde{\Psi}_I\rangle = E_I U|\tilde{\Psi}_I\rangle. \tag{26}$$

This shows that $|\Psi_I\rangle = U|\tilde{\Psi}_I\rangle$ are exact eigenfunctions and the E_I the corresponding exact eigenenergies of the full Hamiltonian H. The requirements formulated so far still leave many different possible choices for the decoupling operator U.

2.2 Choice of the decoupling operator: Bloch and van Vleck

We already mentioned that the eigenstates of the effective Hamiltonian are usually required to give a qualitatively correct description of the true eigenstates.
One common choice that fulfills this requirement consists in setting $U_D = 1$ [6], where U_D is defined as the block diagonal part (see Eq. (22)) of the decoupling operator U. This leads to

$$|\tilde{\Psi}_I\rangle = P|\Psi_I\rangle, \tag{27}$$

i.e., the eigenstates of the effective Hamiltonian are orthogonal projections of the exact eigenstates on the model space. For this choice, the effective Hamiltonian, which is named after Bloch [8], can be written

$$H^{\text{eff}} = PH\Omega, \tag{28}$$

where the so-called wave operator Ω is defined as

$$\Omega = UP. \tag{29}$$

The wave operator is a solution of the equation

$$\Omega H \Omega = H\Omega, \tag{30}$$

which is a nonperturbative version [9] of the so-called generalized Bloch equation [10]. Since its eigenstates are – as projections on the model space – in general not orthogonal, the Bloch effective Hamiltonian is in general not Hermitian.
Another choice for U is given by the canonical Van Vleck approach [6], where the decoupling operator is defined as

$$U = \exp(G) \tag{31}$$

with G being an anti-Hermitian ($G^\dagger = -G$) and block off-diagonal ($G_D = 0$) operator. Since G is anti-Hermitian, U is unitary with this choice ($U^\dagger U = 1$). Hence, the eigenstates of the effective Hamiltonian are orthogonal,

$$\langle \tilde{\Psi}_I | \tilde{\Psi}_J \rangle = \langle \tilde{\Psi}_I | U^\dagger U | \tilde{\Psi}_J \rangle = \langle \Psi_I | \Psi_J \rangle = \delta_{IJ}. \tag{32}$$

This also means that the effective Hamiltonian in the canonical Van Vleck approach is Hermitian. One can show that the eigenstates of the Bloch (label B) and the canonical van Vleck (label C) effective Hamiltonians are related by symmetric orthonormalization [6],

$$|\tilde{\Psi}_I^{\mathrm{C}}\rangle = \sum_J |\tilde{\Psi}_J^{\mathrm{B}}\rangle S_{JI}^{-1/2}. \tag{33}$$

Here, $S_{JI} = \langle \tilde{\Psi}_J^{\mathrm{B}} | \tilde{\Psi}_I^{\mathrm{B}} \rangle$ is the positive-definite overlap matrix of the Bloch eigenstates. It should be mentioned that the canonical van Vleck effective Hamiltonian turns out to be identical to the effective Hamiltonian introduced by des Cloizeaux [11], as discussed by Klein [12] and Brandow [13, 14].

If the eigenstates and eigenvalues of the effective Hamiltonians are known, it is possible to write them via a spectral decomposition. The Bloch effective Hamiltonian can be written as

$$H_{\mathrm{B}}^{\mathrm{eff}} = \sum_I |\tilde{\Psi}_I^{\mathrm{B}}\rangle E_I \langle \tilde{\Psi}_I^{\mathrm{D}}|, \tag{34}$$

where

$$|\tilde{\Psi}_I^{\mathrm{D}}\rangle = \sum_J |\tilde{\Psi}_J^{\mathrm{B}}\rangle S_{JI}^{-1} \tag{35}$$

defines the state that is dual (also called contravariant) to the state $|\tilde{\Psi}_I^{\mathrm{B}}\rangle$. The dual states are the unique set of states that are biorthogonal to the original set of Bloch eigenstates,

$$\langle \tilde{\Psi}_I^{\mathrm{D}} | \tilde{\Psi}_J^{\mathrm{B}} \rangle = \delta_{IJ}. \tag{36}$$

The canonical van Vleck / des Cloizeaux effective Hamiltonian can be written as

$$H_{\mathrm{C}}^{\mathrm{eff}} = \sum_I |\tilde{\Psi}_I^{\mathrm{C}}\rangle E_I \langle \tilde{\Psi}_I^{\mathrm{C}}|. \tag{37}$$

The quality of the chosen model space can be quantitatively defined by the norm of the projected states $|\tilde{\Psi}_I^{\mathrm{B}}\rangle$, which is given by the diagonal of the overlap matrix S_{II}. The closer these norms are to 1, the less severe is the non-Hermiticity of the Bloch effective Hamiltonian and the smaller is the difference between the Bloch and canonical van Vleck effective Hamiltonian.

2.3 Partitioning method

Another approach to the construction of effective Hamiltonians, called the partitioning method, was introduced by Löwdin [15–17]. It starts by dividing the Hilbert space into a model space

A (corresponding to $\mathcal{H}_0$ from above) and a remainder B (corresponding to $\mathcal{H}_{\text{outer}}$ from above). The time-independent Schrödinger equation can then be written in block matrix form as

$$\begin{pmatrix} \mathbf{H}_{AA} & \mathbf{H}_{AB} \\ \mathbf{H}_{BA} & \mathbf{H}_{BB} \end{pmatrix} \begin{pmatrix} \mathbf{C}_A \\ \mathbf{C}_B \end{pmatrix} = E \begin{pmatrix} \mathbf{C}_A \\ \mathbf{C}_B \end{pmatrix}. \tag{38}$$

This can be rewritten in terms of two coupled equations

$$\mathbf{H}_{AA}\mathbf{C}_A + \mathbf{H}_{AB}\mathbf{C}_B = E\mathbf{C}_A, \tag{39}$$

$$\mathbf{H}_{BA}\mathbf{C}_A + \mathbf{H}_{BB}\mathbf{C}_B = E\mathbf{C}_B. \tag{40}$$

From Eq. (40) one can obtain

$$\mathbf{C}_B = (E - \mathbf{H}_{BB})^{-1}\mathbf{H}_{BA}\mathbf{C}_A, \tag{41}$$

which can be inserted into Eq. (39) to eliminate $\mathbf{C}_B$ and obtain

$$\mathbf{H}^{\text{eff}}_{AA}(E)\mathbf{C}_A = E\mathbf{C}_A. \tag{42}$$

The energy-dependent A-space effective Hamiltonian is given by

$$\mathbf{H}^{\text{eff}}_{AA}(E) = \mathbf{H}_{AA} + \mathbf{H}_{AB}(E - \mathbf{H}_{BB})^{-1}\mathbf{H}_{BA}. \tag{43}$$

One can see that the effective Hamiltonian consists of the A block of the original Hamiltonian "dressed" with the matrix $\mathbf{H}_{AB}(E - \mathbf{H}_{BB})^{-1}\mathbf{H}_{BA}$. The inverse $(E - \mathbf{H}_{BB})^{-1}$ exists if E does not overlap with the spectrum of $\mathbf{H}_{BB}$. Diagonalization of the effective Hamiltonian Eq. (43) gives $\mathbf{C}_A$, the projection of the exact eigenstate with energy E on the model space. A drawback is that the effective Hamiltonian is a function of the exact energy E, which is unknown unless one solves the full problem first.

2.4 Intermediate effective Hamiltonians

In section 2.2 we made the assumption that there is a one-to-one mapping between eigenstates $|\tilde{\Psi}_I\rangle$ of the effective Hamiltonian in the model space and the same number of exact eigenstates $|\Psi_I\rangle$. Sometimes this identification is ambiguous or not even possible. For example, the qualitatively correct description of the electronic ground state of the Be atom requires two electron configurations. Apart from the dominant $(1s)^2(2s)^2$ configuration, also $(1s)^2(2p)^2$ is needed [18]. This means that at least these two configurations should be included in the model space. However, it is not possible to identify a bound excited state of the Be atom that has $(1s)^2(2p)^2$ as its dominant configuration [19]. In such a case, the effective Hamiltonian is not well-defined and its perturbative expansion (see the next section) will often diverge.
To solve this problem, Malrieu and coworkers have introduced the concept of intermediate effective Hamiltonians (IEH) [20]. One defines an IEH H^{int} by the requirement that the equation

$$H^{\text{int}}P|\Psi_I\rangle = E_I P|\Psi_I\rangle \tag{44}$$

from Bloch effective Hamiltonian theory is only fulfilled for a number N_m of exact eigenstates $|\Psi_I\rangle$ that is *smaller* than the dimension of the model space. The whole model space is divided into the "main model space" containing N_m determinants that dominate the states of interest and the "intermediate space" containing all remaining determinants. They explicitly contribute to the solutions of interest and act as a "buffer space" between the main model space and the outer space. Eq. (44) apparently does not define the IEH uniquely; hence there is a large variety of different intermediate Hamiltonians.
If the IEH gives only a single exact energy and projection of an exact eigenstate, it is called a state-specific intermediate Hamiltonian. An example of this is the partitioning technique effective Hamiltonian (Eq. (43)) introduced in the last section [19].

2.5 Perturbative expansion of effective Hamiltonians

The definitions of the effective Hamiltonians given in the previous sections all require that the solution of the full problem is known first, i.e., they do not provide a computational simplification. Perturbation theory provides a means to construct these effective Hamiltonians without prior knowledge of the exact solutions. Here, the Hamiltonian is separated into a zeroth-order Hamiltonian and a perturbation,

$$H = H_0 + V. \tag{45}$$

The eigenvalues and eigenstates of the zeroth-order Hamiltonian must be known,

$$H_0|\Psi_I^{(0)}\rangle = E_I^{(0)}|\Psi_I^{(0)}\rangle, \tag{46}$$

and V is supposed to be small compared to H_0.
The derivation of the final equations would go beyond the scope of the present chapter. Therefore, we just present the results together with the relevant literature references. We also restrict ourselves to expansions up to second order, which are most relevant in practice.

2.5.1 Quasidegenerate perturbation theory

The expansion of the Bloch effective Hamiltonian in orders of the perturbation operator V (also known as quasidegenerate perturbation theory, QDPT) gives up to second order [6]

$$\langle\Psi_I^{(0)}|H_{\mathrm{B}}^{\mathrm{eff}(0-2)}|\Psi_J^{(0)}\rangle = H_{IJ} + \sum_K \frac{\langle\Psi_I^{(0)}|H|\Psi_K^{(0)}\rangle\langle\Psi_K^{(0)}|H|\Psi_J^{(0)}\rangle}{E_J^{(0)} - E_K^{(0)}}. \tag{47}$$

This effective Hamiltonian is the "bare" Hamiltonian within the model space plus a "dressing", a form that was already observed for the partitioning technique effective Hamiltonian above. From the presence of the index J in the denominator, it becomes apparent that the effective Hamiltonian is not Hermitian. Up to second order (but not at higher orders), it turns out that the canonical Van Vleck / des Cloizeaux effective Hamiltonian is simply the Hermitization of the corresponding Bloch second-order effective Hamiltonian [6],

$$\mathbf{H}_{\mathrm{C}}^{\mathrm{eff}(0-2)} = \frac{1}{2}\left(\mathbf{H}_{\mathrm{B}}^{\mathrm{eff}(0-2)} + \mathbf{H}_{\mathrm{B}}^{\mathrm{eff}(0-2)^\dagger}\right). \tag{48}$$

If all states in the model space have the same 0th order energy $E_I^{(0)} = E^{(0)}$, the 2nd order Bloch and canonical van Vleck effective Hamiltonians are identical and given by

$$H_{IJ}^{\text{eff}(0-2)} = H_{IJ} + \sum_K \frac{\langle\Psi_I^{(0)}|H|\Psi_K^{(0)}\rangle\langle\Psi_K^{(0)}|H|\Psi_J^{(0)}\rangle}{E^{(0)} - E_K^{(0)}}. \tag{49}$$

This is the common degenerate perturbation theory (DPT) expression up to second order. For a one-dimensional model space (where the effective Hamiltonian is equal to the energy), this reduces to the well-known nondegenerate Rayleigh-Schrödinger perturbation theory formula.

2.5.2 Expansion of the partitioning technique effective Hamiltonian

One can show that [17]

$$\begin{aligned}\big(E-\mathbf{H}_{BB}\big)^{-1} = \big(E-\mathbf{H}_{BB}^{(0)}\big)^{-1} + \big(E-\mathbf{H}_{BB}^{(0)}\big)^{-1}\mathbf{V}_{BB}\big(E-\mathbf{H}_{BB}^{(0)}\big)^{-1} \\ + \big(E-\mathbf{H}_{BB}^{(0)}\big)^{-1}\mathbf{V}_{BB}\big(E-\mathbf{H}_{BB}^{(0)}\big)^{-1}\mathbf{V}_{BB}\big(E-\mathbf{H}_{BB}^{(0)}\big)^{-1} + \ldots\end{aligned} \tag{50}$$

If this is inserted into Eq. (43), one obtains the well-known Brillouin-Wigner (BW) perturbation series. Truncated at the 2nd order, the BW effective Hamiltonian is

$$\mathbf{H}_{AA}^{\text{eff}}(E) \approx \mathbf{H}_{AA} + \mathbf{H}_{AB}\big(E-\mathbf{H}_{BB}^{(0)}\big)^{-1}\mathbf{H}_{BA}. \tag{51}$$

In a basis of eigenstates $|\Psi_I^{(0)}\rangle \in A$ and $|\Psi_K^{(0)}\rangle \in B$ of the 0th order Hamiltonian, one can use $\langle\Psi_K^{(0)}|H_{BB}^{(0)}|\Psi_L^{(0)}\rangle = E_K^{(0)}\delta_{KL}$ to write the effective Hamiltonian as

$$H_{IJ}^{\text{eff}}(E) \approx H_{IJ} + \sum_{K\in B} \frac{\langle\Psi_I^{(0)}|H|\Psi_K^{(0)}\rangle\langle\Psi_K^{(0)}|H|\Psi_J^{(0)}\rangle}{E - E_K^{(0)}}. \tag{52}$$

If a good approximation $E^{(0)}$ to the exact energy E is known, this can be simplified to an energy-independent effective Hamiltonian

$$H_{IJ}^{\text{eff}} \approx H_{IJ} + \sum_{K\in B} \frac{\langle\Psi_I^{(0)}|H|\Psi_K^{(0)}\rangle\langle\Psi_K^{(0)}|H|\Psi_J^{(0)}\rangle}{E^{(0)} - E_K^{(0)}} \tag{53}$$

that is equivalent to the so-called "shifted B_k" [21] method. If there is a one-to-one map between the states spanning the model space A and the same number of exact eigenstates of the Hamiltonian, then the same model space can be used for all of them, but the state-specific effective Hamiltonians Eq. (53) are in general different for each of those states. However, in the special case that the same $E^{(0)}$ is a reasonable zeroth-order energy for all the states in the model space, Eq. (53) can be considered as an effective Hamiltonian delivering all energies and projections on the model space simultaneously. One can see that this is identical to the DPT expression discussed in the previous section.

2.5.3 Generalized degenerate perturbation theory

We finally mention the perturbative expansion of the first state-specific intermediate Hamiltonian introduced by Malrieu *et al.* in their seminal paper [20]. It is called generalized degenerate perturbation theory (GDPT). Up to second order, the intermediate Hamiltonian is given by

$$H_{IJ}^{\text{int}(0-2)} = H_{IJ} + \sum_K \frac{\langle \Psi_I^{(0)} | H | \Psi_K^{(0)} \rangle \langle \Psi_K^{(0)} | H | \Psi_J^{(0)} \rangle}{E^{(0)} - E_K^{(0)}}. \tag{54}$$

This is equivalent to the shifted-B_k effective Hamiltonian (see Eq. (53)) as was already recognized by Malrieu and coworkers [20]. This expression also forms the basis for the recently introduced dynamic correlation dressed complete active space method (DCD-CAS(2)) [22, 23]. The results of this section show that often one can end up with similar or even identical final expression using quite different starting points.

3 Examples for effective Hamiltonians

3.1 The Heisenberg exchange

The Heisenberg-Dirac-van Vleck (HDvV) Hamiltonian [24–26] is a model Hamiltonian which is one of the simplest and most widely used Effective Hamiltonian. The Heisenberg Hamiltonian is a model that can describe interactions between unpaired electrons (belonging to metal atoms or organic radicals) localized on spatially separated atomic centers or groups of atoms constituting a molecule. Such a model is of considerable importance not only in the understanding of the electronic structure and properties of single molecule magnets (SMMs) but also for the design of molecules capable of showing a high-spin ground state. The Heisenberg-Dirac-van Vleck Hamiltonian reads

$$\hat{H}_{\text{Heisenberg}} = -2J_{ab}\hat{\mathbf{S}}_a \cdot \hat{\mathbf{S}}_b. \tag{55}$$

It is an effective Hamiltonian that works in the basis of spin states of the interacting sites and contains the adjustable parameter J_{ab} that is determined by fitting magnetization data (or other magnetic measurements). The task at hand is to elucidate how this parameter can be understood and also quantitatively calculated in terms of first-principles electronic structure theory.

3.1.1 Partitioning of the Hamiltonian and definition of Model space

Consider the simplest valence space made up of two electrons of opposite spin on centers A and B that are spatially separated. The Hilbert space of these two electrons in two orbitals is spanned by the Slater determinants

$$\left\{ |a\bar{b}\rangle\,,\ |\bar{a}b\rangle\,,\ |a\bar{a}\rangle\,,\ |b\bar{b}\rangle \right\},$$

where a and b refer to the valence local orbitals on centers A and B with a and $\bar{a}$ denoting the orbital at A occupied by an α or a β electron respectively. The determinants of the type

$\left\{|a\bar{b}\rangle \text{ and } |\bar{a}b\rangle\right\}$ belong to a configuration with one electron per center. These configurations are referred to as 'Neutral' configurations. On the other hand the centers with two (zero) electrons on a site are known as 'Ionic' configurations. The Ionic configurations can be expected to be high in energy as the two electrons occupy orbitals that are spatially closer and therefore suffer greater Coulomb repulsion compared to the Neutral configuration where they are spatially separated. Therefore, in local orbital basis, the low energy spectrum will be dominated by states made up dominantly of the Neutral configurations which will be well separated from states made up of Ionic configurations. The task of the Heisenberg Hamiltonian is then to describe the ground state of such systems in terms of the Neutral determinants only taking into account the effect of the Ionic states in an effective manner.
The full Hamiltonian in terms of the four determinants can be written as

$$\begin{array}{c} |a\bar{b}\rangle \\ |\bar{a}b\rangle \\ |a\bar{a}\rangle \\ |b\bar{b}\rangle \end{array} \begin{bmatrix} 0 & K_{ab} & t_{ab} & t_{ab} \\ K_{ab} & 0 & t_{ab} & t_{ab} \\ t_{ab} & t_{ab} & U & K_{ab} \\ t_{ab} & t_{ab} & K_{ab} & U \end{bmatrix}, \tag{56}$$

where we have taken the energy of the Neutral determinants as origin of energy. The matrix-elements of the Hamiltonian are as follows: the t_{ab} is the matrix-element $\langle a\bar{b}|\mathbf{H}|b\bar{b}\rangle$ and describes the movement of the electrons from site A to B, the direct exchange integral between orbitals a and b is represented by $K_{ab} = (ab|ba)$, and finally the Coulomb integral (electron-electron repulsion) on orbitals a and b is given by $U = (aa|aa) = (bb|bb)$.
The low energy spectrum of this Hamiltonian, i.e., one singlet and one triplet state, is dominated by the Neutral determinants whereas the higher energy states are dominated by the Ionic determinants. This intuition leads to a natural partition of the Hamiltonian given above into a model space and an outer space. The model space here is made of the two Neutral determinants whereas the outer space constitutes the two ionic determinants. The two determinants in the model space give rise to a singlet state and a triplet configuration which can be written as

$$|T_0\rangle = \frac{1}{\sqrt{2}}\left(|a\bar{b}\rangle + |\bar{a}b\rangle\right), \tag{57}$$

$$|S_N\rangle = \frac{1}{\sqrt{2}}\left(|a\bar{b}\rangle - |\bar{a}b\rangle\right), \tag{58}$$

where T_0 signifies the $M_S = 0$ component of the triplet state and the S_N signifies that the singlet is made up of neutral determinants. Note that both the singlet and triplet configurations are of gerade(g) symmetry. The outer space is made up of purely singlet configurations composed of ionic configurations which can be written in g and u symmetry combinations such as

$$|S_I^g\rangle = \frac{1}{\sqrt{2}}\left(a\bar{a} - b\bar{b}\right), \tag{59}$$

$$|S_I^u\rangle = \frac{1}{\sqrt{2}}\left(a\bar{a} + b\bar{b}\right). \tag{60}$$

In this basis, the above Hamiltonian given in Eq. (56) is transformed as follows

$$\begin{array}{c} |T_0\rangle \\ |S_N\rangle \\ |S_I^g\rangle \\ |S_I^u\rangle \end{array} \left[\begin{array}{cc|cc} -K_{ab} & 0 & 0 & 0 \\ 0 & K_{ab} & 2t_{ab} & 0 \\ \hline 0 & 2t_{ab} & U+K_{ab} & 0 \\ 0 & 0 & 0 & U+K_{ab} \end{array}\right]. \tag{61}$$

Here, we have also partitioned the Hamiltonian into a model space which is the upper left block and the outer space which is the lower right one. Notice that the neutral singlet S_N only interacts with the ionic singlet of the same spatial symmetry i.e., S_I^g. There are a few important points that one realizes from the above form of the Hamiltonian which are as follows:

- Naturally, the triplet state T_0 does not interact with any of the other three states and therefore it does not change in energy. However, the energy of the triplet state is already lower than the singlet state by $2K_{ab}$ which means that in the absence of the interaction with the outer space (for, e.g., due to symmetry reasons), the ground state naturally tends towards a triplet state. This implies that the system can behave as a ferromagnet due the orthogonality of a and b orbitals which can be artificially or physically enforced.
- The singlet state, on the other hand, interacts with the ionic singlet state of gerade g symmetry. Therefore it is influenced by the outer space configurations. This always results in the stabilization of the lowest singlet state. In the case of large interaction between a and b given by $\langle a\bar{b}|\mathbf{H}|b\bar{b}\rangle$, this might invert the energetic ordering of the triplet and singlet states leading to a low spin singlet ground state and an antiferromagnetic coupling.

3.1.2 Derivation of the Effective Spin Hamiltonian via QDPT

Here we shall describe how the Heisenberg Hamiltonian given in Eq. (55) can be derived by using QDPT, as described in 2.5.1, and applied to the partitioned Hamiltonian given in Eq. (61). In order to see the expression for the "effective" interaction J_{ab}, it is instructive to investigate the g symmetry block of the Hamiltonian given in Eq. (62) [27],

$$\begin{array}{c} |T_0\rangle \\ |S_N\rangle \\ |S_I^g\rangle \end{array} \left[\begin{array}{cc|c} -K_{ab} & 0 & 0 \\ 0 & K_{ab} & 2t_{ab} \\ \hline 0 & 2t_{ab} & U+K_{ab} \end{array}\right]. \tag{62}$$

In order to derive the Heisenberg Hamiltonian, we first begin by defining the basis representations of the model space. The model space of the Heisenberg Hamiltonian contains only neutral configurations, i.e., configurations which show only isotropic spin-spin interaction. Therefore, we can adopt a more compact notation which only takes into account the spin degrees of freedom of the electron occupying orbitals a and b such as

$$\left\{|\tfrac{1}{2}, M_{s_a}\rangle\right\} = \left\{|\uparrow\rangle_a, |\downarrow\rangle_a\right\}, \tag{63}$$

$$\left\{|\tfrac{1}{2}, M_{s_b}\rangle\right\} = \left\{|\uparrow\rangle_b, |\downarrow\rangle_b\right\}. \tag{64}$$

Subsequently, the operators $\hat{\mathbf{S}}_a, \hat{\mathbf{S}}_b$ can be defined as

$$\hat{\mathbf{S}}_a = \hat{\mathbf{S}}_a^+ + \hat{\mathbf{S}}_a^- + \hat{\mathbf{S}}_a^z, \tag{65}$$

$$\hat{\mathbf{S}}_b = \hat{\mathbf{S}}_b^+ + \hat{\mathbf{S}}_b^- + \hat{\mathbf{S}}_b^z, \tag{66}$$

where the operators $\hat{\mathbf{S}}^+, \hat{\mathbf{S}}^-$ are the spin ladder operators and the $\hat{\mathbf{S}}^z$ gives the z component of the spin $\mathbf{S}$. Here, $\hat{\mathbf{S}}_\mathbf{a}$ and $\hat{\mathbf{S}}_\mathbf{b}$ operators act on model space representations $|\frac{1}{2}, M_{s_a}\rangle$ and $|\frac{1}{2}, M_{s_b}\rangle$ respectively.

Given this basis of the model space, operators and the Hamiltonian defined in Eq. (55), the matrix form of the model Hamiltonian can be written as

$$\begin{array}{c} \\ |\uparrow,\downarrow\rangle \\ |\downarrow,\uparrow\rangle \end{array} \begin{array}{c} \begin{array}{cc} \quad & \quad \end{array} \\ \begin{bmatrix} J_{ab} & -J_{ab} \\ -J_{ab} & J_{ab} \end{bmatrix} \end{array} \tag{67}$$

with $\uparrow$ and $\downarrow$ representing the $M_s = \frac{1}{2}$ and $M_s = -\frac{1}{2}$ components of $S = \frac{1}{2}$ respectively. The value of J_{ab} can then be derived from QDPT based upon Eq. (62) at second order and takes the following form

$$2J_{ab} = 2K_{ab} - \frac{4t_{ab}^2}{U}. \tag{68}$$

Therefore, using the above expression for J_{ab}, the Heisenberg Hamiltonian can finally be derived as given in Eq. (55). Note that the operators $\hat{\mathbf{S}}_a$ and $\hat{\mathbf{S}}_b$ in Eq. (55) only describe the isotropic spin-spin interaction between the two electron spins assuming they are fixed on centers A and B respectively.

3.1.3 Physical interpretation of J_{ab}

Using the above derivation, one can analyze the physics described by the Heisenberg exchange J_{ab}, which is an effective parameter. As shown in Eq. (68), J_{ab} contains the effect of both the direct exchange K_{ab} and what is known as the kinetic exchange effect represented by the second term of Eq. (68):

$$\text{Direct Exchange:} \quad 2J_{ab}^{\text{direct}} = 2K_{ab}, \tag{69}$$

$$\text{Kinetic Exchange:} \quad 2J_{ab}^{\text{kinetic}} = -\frac{4t_{ab}^2}{U}. \tag{70}$$

Therefore, the nature of the exchange between sites A and B will be described by these two factors. The direct exchange K_{ab} has the effect of making J_{ab} more positive, i.e., stabilizing the high-spin state (triplet), whereas the kinetic exchange terms leads to a more negative J_{ab} and therefore stabilizes the low-spin state (singlet).

This also suggests how one can control and predict the nature of coupling by looking at the geometry (and hence the symmetry) of a given molecule. As described in the previous section if one orients the two magnetic orbitals a and b, such that their interaction is 0 due to symmetry, the term $\langle a\bar{b}|\mathbf{H}|b\bar{b}\rangle$ vanishes and the coupling is only due to the direct exchange K_{ab} which is always positive leading to a ferromagnetic coupling. In this manner, we can also predict new materials with the desired coupling and ground state. The "effective" Hamiltonian parameter

J_{ab} therefore results from a competition between these two contributions and shows how one can compress information efficiently without any loss in the described physics. Herein lies the power of effective and model Hamiltonian.

Here we have derived the Heisenberg Hamiltonian for the simplest case of two electrons in two valence orbitals. The Heisenberg Hamiltonian can of course be applied to multi-center molecules with more than one electron per center in which case the general form of the Hamiltonian is similar to Eq. (55) with summation over all nearest neighbors $\langle ab \rangle$. Note that in the case of a large number of interacting centers, a first principles treatment of the resulting molecular system becomes complicated due to the presence of a large number of open-shell electrons coupling to give a low-spin ground state. However, the physics of the problem remains largely the same.

A final point concerns the physics contained in the coupling term J_{ab} which is simple enough to describe in the case of two electrons. Such systems can be realized in Copper dimers and have been extensively studied by first principles calculations [28–30]. The detailed physical effects contained in J_{ab} turn out to be quite more complicated in reality and have been a subject of study for a long time [27].

3.2 The spin Hamiltonian in EPR and NMR spectroscopy

The spin Hamiltonian (SH) is a major asset in the analysis of magnetic resonance experiments. The massive simplification that the SH offers, is that it only contains the effective electron spin ($\hat{\mathbf{S}}$), the nuclear spins ($\hat{\mathbf{I}}$), and external magnetic fields ($\mathbf{B}$) but makes no explicit reference to electronic coordinates, molecular geometry, or any of the intricacies that render the application of the exact (relativistic) many particle Hamiltonian so difficult. The price to pay for this enormous simplification is that the SH contains adjustable parameters that are usually fitted to the results of magnetic measurements. A fairly standard SH may be written:

$$\hat{H}_{spin} = \beta \mathbf{B} \mathbf{g} \hat{\mathbf{S}} + \hat{\mathbf{I}} \mathbf{A} \hat{\mathbf{S}} + \hat{\mathbf{S}} \mathbf{D} \hat{\mathbf{S}} + \hat{\mathbf{I}} \mathbf{Q} \hat{\mathbf{I}} + ... \tag{71}$$

(β is the Bohr magneton). The individual terms are:

- $\beta \mathbf{B} \mathbf{g} \hat{\mathbf{S}}$ is the molecular Zeeman term that describes the interaction of the electron spin with an external magnetic field $\mathbf{B}$.
- $\hat{\mathbf{I}} \mathbf{A} \hat{\mathbf{S}}$ represents the hyperfine interaction that describes the interaction of an electron spin with the nuclear spin of a given nucleus.
- $\hat{\mathbf{S}} \mathbf{D} \hat{\mathbf{S}}$ is the zero-field splitting (ZFS) that describes the interaction of the unpaired electrons among themselves.
- $\hat{\mathbf{I}} \mathbf{Q} \hat{\mathbf{I}}$ is the quadrupole splitting that describes the interaction of the electric field gradient with the quadrupole moment of a nucleus.

All quantities $\mathbf{g}$, $\mathbf{A}$, $\mathbf{D}$ and $\mathbf{Q}$ are 3×3 tensors. Their elements are the adjustable parameters mentioned above. The SH acts on the space of spin functions

$$|SMIM_I\rangle = |SM\rangle \otimes |IM_I\rangle \tag{72}$$

that has the (small) dimension of $(2S+1)\,(2I+1)$. The matrix elements of the SH are straightforward to calculate using standard angular momentum operator algebra. The corresponding eigenvalue problems are of low dimension and can usually be solved with paper and pencil or very quickly numerically with a computer. The effective Hamiltonian approach enters the stage upon asking the question: "how are the SH parameters related to the actual electronic structure of my system?" Or, in other words, how do they relate to the (relativistic) eigenfunctions of the molecular Schrödinger equation. Below, we will derive the equation for $\mathbf{g}$ as an illustration of how the general argument proceeds.

The most straightforward connection is based on exploiting the partitioning method of section 2.3; see Eqs. (42), (43), and (53). To proceed from these equations, we need to define the nature of the 'A' and 'B' spaces and how we define the full Hamiltonian. Let us assume that we have solved the non-relativistic (BO) Schrödinger equation exactly, such that we know the entire spectrum of eigenstates:

$$\hat{H}_{\text{BO}} \left|\Psi_I^{SM}\right\rangle = E_I \left|\Psi_I^{SM}\right\rangle . \tag{73}$$

Of course, this is entirely impractical, but we will still proceed along these lines for the sake of the conceptual argument. Since the BO Hamiltonian is spin-free, the total spin of the system and its projection on the z-axis are good quantum numbers and hence, we can label the eigenstates as $\left|\Psi_I^{SM}\right\rangle$. At the level of the BO Hamiltonian, these states are $(2S+1)$-fold degenerate. This degeneracy is then lifted by relativistic effects and external magnetic fields. If we are interested in the splittings of the 'magnetic sublevels' $M = S, S-1, ..., -S$ of the electronic ground state then it follows naturally to define the 'A' set as the $2S+1$ states belonging to the ground state multiplet (we assume that there are no other degeneracies than the spin degeneracies). The 'B' set then consists of the infinite number of excited states. The splittings induced by external magnetic fields and relativistic effects are relatively small – usually (but not always) on the order of only 1 cm^{-1} (roughly $5 \cdot 10^{-6}$ atomic units). On the other hand, the excited states are often $>$ 5000–10000 cm^{-1} above the ground state. Hence, it is sensible to replace the unknown energy E in the effective Hamiltonian Eq. (43) by E_0, the energy of the ground state multiplet. Second, we need to define the full Hamiltonian operator. Since we are only interested in $\mathbf{g}$, we only need to consider two additional terms. One is the molecular Zeeman operator

$$\hat{H}_{\text{Ze}} = \beta \mathbf{B} \sum_i \left(g_e \hat{\mathbf{s}}_i + \hat{\mathbf{l}}_i\right). \tag{74}$$

This operator consists of the spin-Zeeman ($g_e = 2.002319...$ is the free electron g-value) and orbital Zeeman operator. Note carefully that $\hat{\mathbf{s}}_i$ is the spin of the i'th electron, rather than the total spin $\hat{\mathbf{S}} = \sum_i \hat{\mathbf{s}}_i$. The angular momentum operator $\hat{\mathbf{l}}_i$ is referred to the global origin. The second term we need is the spin-orbit coupling (SOC) operator. In principle, this is a two-electron operator, but it can be reasonably well approximated by an effective one-electron

operator as given by Eq. (18). The operator $\mathbf{h}_i^{\text{SOC}}$ can take many different forms like the SOMF operator mentioned in the introduction. One crude approximation is the effective nuclear charge Hamiltonian that has the form

$$\mathbf{h}_i^{\text{SOC,ENC}} = \frac{\alpha^2}{2} \sum_A \frac{Z_A^{\text{eff}}}{|\mathbf{R}_A - \mathbf{r}_i|^3} \hat{\mathbf{l}}_i^A, \tag{75}$$

where α is the fine structure constant, the sum A is over all nuclei in the system at positions $\mathbf{R}_A$ with effective charges Z_A^{eff}. $\hat{\mathbf{l}}_i^A$ is the angular momentum operator of the i'th electron relative to the A'th nucleus. We now have to insert the full Hamiltonian

$$\hat{H} = \hat{H}_{\text{BO}} + \hat{H}_{\text{Ze}} + \hat{H}_{\text{SOC}} \tag{76}$$

and wavefunctions $\left|\Psi_I^{SM}\right\rangle$ into the effective Hamiltonian and pick out terms that are bilinear in $\mathbf{B}$ and $\hat{\mathbf{S}}$ since those will define the g-tensor. The effective Hamiltonian is given by (see Eq. (53))

$$\left\langle \Psi_0^{SM} \middle| \hat{H}_{\text{eff}} \middle| \Psi_0^{SM'} \right\rangle = \left\langle \Psi_0^{SM} \middle| \hat{H} \middle| \Psi_0^{SM'} \right\rangle - \sum_{I>0} \Delta_I^{-1} \left\langle \Psi_0^{SM} \middle| \hat{H} \middle| \Psi_I^{S'M''} \right\rangle \left\langle \Psi_I^{S'M''} \middle| \hat{H} \middle| \Psi_0^{SM'} \right\rangle, \tag{77}$$

where $\Delta_I = E_I - E_0$ is the energy difference between the I'th multiplet and the ground state at the level of the BO Hamiltonian. A little reflection will quickly reveal that:

- The only first-order term (first term on the right-hand side of Eq. (77)) comes from the spin-Zeeman term and equals the free electron g-value.
- In the infinite sum over excited states, only those terms with $S' = S$ can contribute since the orbital Zeeman operator is spin-independent and the spin-Zeeman operator does not couple the ground and excited states.
- Contributions to the g-tensor will only arise from cross terms between $\hat{H}_{\text{Ze}}$ and $\hat{H}_{\text{SOC}}$ since these are the only ones that have the correct bilinear structure in $\mathbf{B}$ and $\hat{\mathbf{S}}$

Thus, the relevant part of the effective Hamiltonian becomes

$$\begin{aligned} \left\langle \Psi_0^{SM} \middle| \hat{H}_{\text{eff}} \middle| \Psi_0^{SM'} \right\rangle &= \beta \mathbf{B} g_e \cdot \left\langle \Psi_0^{SM} \middle| \mathbf{S} \middle| \Psi_0^{SM'} \right\rangle \\ &- \beta \mathbf{B} \sum_{I>0} \Delta_I^{-1} \left\{ \left\langle \Psi_0^{SM} \middle| \sum_i \hat{\mathbf{h}}_i^{\text{SOC}} \hat{\mathbf{s}}_i \middle| \Psi_I^{S'M''} \right\rangle \left\langle \Psi_I^{S'M''} \middle| \sum_i \hat{\mathbf{l}}_i \middle| \Psi_0^{SM'} \right\rangle + \text{c.c.} \right\}. \end{aligned} \tag{78}$$

This is to be compared to the matrix element of the SH (focusing on the z-component)

$$\left\langle SS \middle| \beta B_z g_{zz} \hat{S}_z \middle| SS \right\rangle = \beta B_z g_{zz} S, \tag{79}$$

from which it readily follows that

$$g_{zz} = g_e - \frac{1}{S} \sum_{I>0(S'=S)} \Delta_I^{-1} \left\{ \left\langle \Psi_0^{SS} \middle| \sum_i \hat{h}_i^{\text{SOC},z} \hat{s}_i^z \middle| \Psi_I^{SS} \right\rangle \left\langle \Psi_I^{SS} \middle| \sum_i \hat{l}_i^z \middle| \Psi_0^{SS} \right\rangle + \text{c.c.} \right\}. \tag{80}$$

The generalization to all components of the g-tensor is straightforward with the aid of the Wigner-Eckart theorem, but the details would lead too far astray here. We note in passing that $\mathbf{g}$ is not symmetric. However, $\mathbf{g}^T\mathbf{g}$ behaves like a proper symmetric second-rank tensor and hence, in the EPR community it is common practice to refer to it as the g-tensor. Along the same lines, all parts of the SH can be derived.

3.3 The size-consistent self-consistent configuration interaction method

In this section, we will demonstrate that effective (in this case intermediate) Hamiltonian approaches are not only useful to derive effective, parameterized models, but that they can also pave the way for new and accurate electronic structure methods. The method that we have chosen to highlight in this respect is the 'size-consistent-self-consistent configuration interaction' (SC^2-CI) method of Malrieu and coworkers [31, 32]. It is an elegant way to derive a size-consistent electron correlation theory that is similar in spirit to the older coupled-electron pair approaches (CEPA) and might be viewed as a step towards full coupled cluster theory with single- and double excitations (CCSD). Let us re-iterate the principle of CI: we start from a reference determinant $|\Phi_0\rangle$ and expand the many-particle wavefunction in terms of excited determinants in which one-, two-, ... occupied spin-orbitals have been replaced by virtual orbitals,

$$|\Psi\rangle = |\Phi_0\rangle + \sum_{ia} C_a^i \left|\Phi_i^a\right\rangle + \tfrac{1}{4}\sum_{ijab} C_{ab}^{ij} \left|\Phi_{ij}^{ab}\right\rangle + \left|\Psi_{\text{higher}}\right\rangle, \tag{81}$$

where $\left|\Psi_{\text{higher}}\right\rangle$ collectively denotes triple-, quadruple- and higher substitutions. As explained in the introduction, in untruncated form, this ansatz leads to an exact solution of the many particle Schrödinger equation in the chosen one-particle basis. However, it is well-known that the most important substitutions in this expansion are the doubly excited determinants. Hence, it is tempting to truncate the ansatz to single- and double substitutions, thus defining the $|\Psi_{\text{CISD}}\rangle$ wavefunction by setting $\left|\Psi_{\text{higher}}\right\rangle = 0$. This is still a somewhat computationally manageable theory, since the number of single and double substitutions 'only' grows as the fourth power of system size and the solution of the CISD equations features $O(N^6)$ scaling.

3.3.1 A model system

In order to see what is wrong with this method, consider first a single H_2 molecule in a minimal basis set consisting only of the bonding σ and anti-bonding σ^* orbital. Neglecting the single substitutions, we only have two determinants: $|\Phi_0\rangle = |\sigma\bar{\sigma}|, |\Phi_{\text{D}}\rangle = |\sigma^*\bar{\sigma}^*|$. In this basis, the CID matrix becomes

$$\mathbf{H}_A = \begin{array}{c} \\ \sigma^*\bar{\sigma}^* \end{array} \begin{array}{c} \begin{array}{cc} \sigma & \bar{\sigma} \end{array} \\ \begin{bmatrix} 0 & K \\ K & \Delta \end{bmatrix} \end{array}, \tag{82}$$

where $\Delta = \langle\Phi_{\text{D}}|H|\Phi_{\text{D}}\rangle - \langle\Phi_0|H|\Phi_0\rangle$ and $K = \langle\sigma\ \bar{\sigma}||\sigma^*\bar{\sigma}^*\rangle$. The solution of the eigenvalue equation gives the correlation energy as

$$E_{\text{corr}} = \tfrac{1}{2}\left(\Delta - \sqrt{\Delta^2{+}4K^2}\right), \tag{83}$$

which is the exact solution. Now, consider adding a second H_2 molecule at infinite distance. In this case our many particle basis consists of the three determinants

$$|\Phi_0\rangle\,, \left|\Phi_{\mathrm{D}}^{A}\right\rangle\,, \left|\Phi_{\mathrm{D}}^{B}\right\rangle\,, \tag{84}$$

where superscripts in 'Φ_{D}^{A}' and 'Φ_{D}^{B}' denote locally excited H_2 molecules. This leads us to the Hamiltonian

$$\mathbf{H}_{A+B}^{\mathrm{D}} = \begin{array}{c} |\Phi_0^A\rangle\,|\Phi_0^B\rangle \\ |\Phi_{\mathrm{D}}^A\rangle\,|\Phi_0^B\rangle \\ |\Phi_0^A\rangle\,|\Phi_{\mathrm{D}}^B\rangle \end{array} \begin{bmatrix} 0 & K & K \\ K & \Delta & 0 \\ K & 0 & \Delta \end{bmatrix} \tag{85}$$

and hence the correlation energy

$$E_{\mathrm{corr}} = \tfrac{1}{2}\left(\Delta - \sqrt{\Delta^2+8K^2}\right), \tag{86}$$

which is clearly wrong, because for non-interacting H_2 molecules, the correlation energy should be exactly twice the monomer correlation energy. This severe shortcoming is known as a lack of 'size-consistency'. Electron correlation methods that are not size-consistent are next to useless in practice since they will give inconsistent results as a function of system size. Now, let us try to remedy the situation by including further (higher) substitutions. The first that comes to mind is the simultaneous pair substitution $\left|\Phi_{\mathrm{Q}}\right\rangle = \left|\Phi_{\mathrm{D}}^{AB}\right\rangle$, which gives the Hamiltonian including quadruple substitutions $|\Phi_{\mathrm{Q}}\rangle$:

$$\mathbf{H}_{A+B}^{\mathrm{DQ}} = \begin{array}{c} |\Phi_0^A\rangle\,|\Phi_0^B\rangle \\ |\Phi_{\mathrm{D}}^A\rangle\,|\Phi_0^B\rangle \\ |\Phi_0^A\rangle\,|\Phi_{\mathrm{D}}^B\rangle \\ |\Phi_{\mathrm{D}}^A\rangle\,|\Phi_{\mathrm{D}}^B\rangle \end{array} \begin{bmatrix} 0 & K & K & 0 \\ K & \Delta & 0 & K \\ K & 0 & \Delta & K \\ 0 & K & K & 2\Delta \end{bmatrix}. \tag{87}$$

Diagonalizing this Hamiltonian gives us the ground state energy for the $A + B$ system as

$$E_{\mathrm{corr}}^{A+B} = \left(\Delta - \sqrt{\Delta^2+4K^2}\right), \tag{88}$$

which is the expected value, i.e., $E_{\mathrm{corr}}^{A+B} = 2E_{\mathrm{corr}}^{A}$. It is an elementary, yet rewarding mathematical excise to demonstrate that the inclusion of the quadruple substitutions indeed restores the size consistency of the calculation. What can we learn from this model system? First of all, that truncated CI is not size-consistent and that it is essential to remedy this shortcoming. Second, that the inclusion of higher substitutions restores this size consistency. This was a trivial exercise in this model system. However, in a real system the number of triple-, quadruple- and even higher substitutions becomes overwhelming very quickly. Hence, it is necessary to develop approximations that approximately include the effect of the higher substitutions without explicitly including them.

This is precisely the idea of the SC^2-CI method: we use the concept and language of intermediate Hamiltonians to divide the many particle space into three subspaces:

- The main model space that consists of only the reference determinant.
- The intermediate or "buffer" space that consists of the single- and double substitutions.
- The "outer space" consisting of the triple and quadruple substitutions.

Clearly, the task at hand is to incorporate the effect of the higher substitutions in an approximate manner. The task at had is thus to derive an effective Hamiltonian that incorporates these effects. This will come in the form of a "dressed" CISD Hamiltonian matrix, the diagonalization of which yields a size-consistent result that approximately incorporates the effects of the triple and quadruple substitutions.

3.3.2 The model problem treated via intermediate Hamiltonian theory

Before we show the connection between intermediate Hamiltonian theory and the SC^2-CI equations, it is instructive to analyze the wavefunction of the above $A + B$ model system with quadruply excited configurations. The Hamiltonian for $A + B$ given above has the ground state wavefunction

$$|\Psi\rangle = C_0 \, |\Phi_0^A\rangle \, |\Phi_0^B\rangle - C_{\mathrm{D}_A} \, |\Phi_{\mathrm{D}}^A\rangle \, |\Phi_0^B\rangle - C_{\mathrm{D}_B} \, |\Phi_0^A\rangle \, |\Phi_{\mathrm{D}}^B\rangle + C_{\mathrm{Q}} \, |\Phi_{\mathrm{D}}^A\rangle \, |\Phi_{\mathrm{D}}^B\rangle \, . \tag{89}$$

It can be readily derived that the explicit form of this wavefunction is

$$|\Psi\rangle = \frac{X^2}{(1+X^2)} \left(|\Phi_0^A\rangle \, |\Phi_0^B\rangle - \frac{1}{X} \, |\Phi_{\mathrm{D}}^A\rangle \, |\Phi_0^B\rangle - \frac{1}{X} \, |\Phi_0^A\rangle \, |\Phi_{\mathrm{D}}^B\rangle + \frac{1}{X^2} \, |\Phi_{\mathrm{D}}^A\rangle \, |\Phi_{\mathrm{D}}^B\rangle \right) \tag{90}$$

with $X = (2K + \sqrt{4K^2+\Delta^2})/\Delta$. The products of the monomer wavefunctions occurring in this equation should be understood as being properly antisymmetrized. Importantly, it follows from Eq. (90) that the coefficient of the quadruply-excited configuration C_{Q} is exactly a product of the coefficient of the two doubly-excited ones C_{D_A} and C_{D_B}. This suggests a path towards a simplification that includes the higher order excitations without explicitly including them and hence towards the SC^2-CI formulation.
First, we begin by writing the CIDQ problem with a linearly parametrized function given in Eq. (89). The eigenvalue equation then is written as

$$\mathbf{H} \, |\Psi\rangle = E \, |\Psi\rangle \, , \tag{91}$$

$$\mathbf{H} \, |\Psi_{\mathrm{HF}}\rangle + \mathbf{H} \, |\Psi_{\mathrm{D}}\rangle + \mathbf{H} \, |\Psi_{\mathrm{Q}}\rangle = E\big(|\Psi_{\mathrm{HF}}\rangle + |\Psi_{\mathrm{D}}\rangle + |\Psi_{Q}\rangle\big). \tag{92}$$

Here, the functions $|\Psi_{\mathrm{HF}}\rangle$, $|\Psi_{\mathrm{D}}\rangle$, and $|\Phi_{\mathrm{Q}}\rangle$ denote the reference, doubles, and quadruples component of the wavefunction respectively such as

$$|\Psi_{\mathrm{HF}}\rangle = C_{\mathrm{HF}} \, |\Phi_0^A \Phi_0^B\rangle \, , \tag{93}$$

$$|\Psi_{\mathrm{D}}\rangle = C_{\mathrm{D}_B} \, |\Phi_0^A \Phi_{\mathrm{D}}^B\rangle + C_{\mathrm{D}_A} \, |\Phi_{\mathrm{D}}^A \Phi_0^B\rangle = C_{\mathrm{D}_B} \, |\Psi_{\mathrm{D}_B}\rangle + C_{\mathrm{D}_A} \, |\Psi_{\mathrm{D}_A}\rangle \, , \tag{94}$$

$$|\Psi_{\mathrm{Q}}\rangle = \ C_{\mathrm{Q}} \, |\Phi_{\mathrm{D}}^A \Phi_{\mathrm{D}}^B\rangle = C_{\mathrm{Q}} \, |\Psi_{\mathrm{Q}_{AB}}\rangle \, . \tag{95}$$

The correlation energy E_{corr} is given by

$$\sum_{D\in \text{D}_A,\text{D}_B} C_D^2 E_{\text{corr}} = \langle \Psi_{\text{D}} | \mathbf{H} | \Psi_{\text{HF}} \rangle + \langle \Psi_{\text{D}} | \mathbf{H} | \Psi_{\text{D}} \rangle + \langle \Psi_{\text{D}} | \mathbf{H} | \Psi_{\text{Q}} \rangle \,. \tag{96}$$

From Eq. (96) it becomes clear that the task here is to avoid the last term $\langle \Psi_{\text{D}} | \mathbf{H} | \Psi_{\text{Q}} \rangle$ and at the same time obtaining a size-consistent solution. Here, we can leverage the understanding from the above discussion and make the following assumptions:

- The coefficients of quadruply excited configurations can be seen as products of doubly excited coefficients.

$$C_{\text{Q}} = C_{\text{D}_A} C_{\text{D}_B} \implies |\Psi_{\text{Q}}\rangle = \frac{1}{2} \sum_{\text{D}_X} \sum_{\text{D}_Y \neq \text{D}_X} C_{\text{D}_X} C_{\text{D}_Y} \, |\Psi_{\text{D}_X}\rangle \,.$$

- The matrix-elements between the doubles and quadruples $\langle \Psi_{\text{D}_X} | \mathbf{H} | \Psi_{\text{Q}_{AB}} \rangle$ have the same magnitude as that between the Φ_{HF} and doubles, i.e.

$$\langle \Phi_{\text{D}_X} | \mathbf{H} | \Phi_{\text{D}_X} \Phi_{\text{D}_Y} \rangle = \langle \Phi_{\text{HF}} | \mathbf{H} | \Psi_{\text{D}_Y} \rangle \,. \tag{97}$$

These two assumptions are exact in the case of two non-interacting molecules A and B. With these two assumptions, we can then simplify the expression for the correlation energy Eq. (96) such that

$$\langle \Psi_{\text{D}_X} | \mathbf{H} | \Psi_{\text{Q}} \rangle = \frac{1}{2} \sum_{\text{D}_Z} \sum_{\text{D}_Y \neq \text{D}_Z} C_{\text{D}_Z} C_{\text{D}_Y} \langle \Psi_{\text{D}_X} | \mathbf{H} | \Phi_{\text{D}_Z} \Phi_{\text{D}_Y} \rangle = \frac{1}{2} C_{\text{D}_X} \sum_{\text{D}_Y} C_{\text{D}_Y} \langle \Psi_{\text{D}_X} | \mathbf{H} | \Phi_{\text{D}_X} \Phi_{\text{D}_Y} \rangle \,, \tag{98}$$

$$\langle \Psi_{\text{D}_X} | \mathbf{H} | \Phi_{\text{D}_X} \Phi_{\text{D}_Y} \rangle = \langle \Psi_{\text{HF}} | \mathbf{H} | \Psi_{\text{D}_Y} \rangle \,, \implies \langle \Psi_{\text{D}_X} | \mathbf{H} | \Psi_{\text{Q}} \rangle = C_{\text{D}_X} E_{\text{corr}}.$$

Using this result and substituting it in Eq. (91) we finally get the coupled electron pair approximation of type 0 (CEPA-0) equations which are given by

$$C_{\text{D}_X} E = \langle \Psi_X | \mathbf{H} | \Psi_{\text{HF}} \rangle + \langle \Psi_X | \mathbf{H} | \Psi_{\text{D}} \rangle + C_{\text{D}_X} E_{\text{corr}}, \tag{99}$$

$$C_{\text{D}_X} E_{\text{HF}} = \langle \Psi_X | \mathbf{H} | \Psi_{\text{HF}} \rangle + \langle \Psi_X | \mathbf{H} | \Psi_{\text{D}} \rangle \,. \tag{100}$$

Hence, we recover a size-consistent form of CID without actually physically including the quadruply excited configurations.

Now looking at Eq. (99) one can show that it can also be written in an equivalent form in terms of a modification of the doubles part of the Hamiltonian. In fact, one can show that in our model system $\mathbf{H}^{\text{D}}_{A+B}$ above, if one replaces the diagonal energies of the doubly excited configurations Δ with an equivalent 'dressed' diagonal energy $\tilde{\Delta}$ given by

$$\tilde{\Delta} = \Delta + \frac{1}{2}\left(\Delta - \sqrt{\Delta^2 + 4K^2}\right) = \Delta + E^A_{\text{corr}} = \Delta + \frac{1}{2} E^{A+B}_{\text{corr}} \tag{101}$$

then the CID matrix looks like an intermediate effective Hamiltonian obtained by a diagonal 'dressing' of the intermediate space of the CID Hamiltonian

$$\tilde{\mathbf{H}}^{\mathrm{D}}_{A+B} = \begin{matrix} |\Phi^A_0\rangle\,|\Phi^B_0\rangle \\ |\Phi^A_{\mathrm{D}}\rangle\,|\Phi^B_0\rangle \\ |\Phi^A_0\rangle\,|\Phi^B_{\mathrm{D}}\rangle \end{matrix} \begin{bmatrix} 0 & K & K \\ K & \tilde{\Delta} & 0 \\ K & 0 & \tilde{\Delta} \end{bmatrix}. \tag{102}$$

This diagonally dressed Hamiltonian is exactly equivalent to the CEPA-0 equations and gives the expected correct Energy, i.e.,

$$\tilde{\mathbf{H}}^{\mathrm{D}}_{A+B}\,|\Psi\rangle = \tilde{E}^{\mathrm{D}}_{A+B}|\Psi\rangle, \tag{103}$$

$$\tilde{E}^{\mathrm{D}}_{A+B} = E^{\mathrm{DQ}}_{A+B} = \left(\Delta - \sqrt{\Delta^2{+}4K^2}\right) = 2E_A. \tag{104}$$

Therefore, a size-consistent CID Hamiltonian can be thought of as an intermediate Hamiltonian with a single configuration $|\Psi_{\mathrm{HF}}\rangle$ in the model space with all the doubles $|\Psi_{\mathrm{D}}\rangle$ being treated in the intermediate space and with the quadruples being the out-of-space configurations. Hence, in this sense, a size-consistent SC^2-CI consists of a state-specific (i.e., dependent on the specific model space $|\Psi_{\mathrm{HF}}\rangle$) dressing of the intermediate space configurations.

3.3.3 General case using intermediate effective Hamiltonians

In the previous section, we highlighted the basic idea of the role of intermediate Hamiltonian theory in the derivation of the SC^2-CI equations for a model system. Here we derive the equations for SC^2-CI in the general case following along the same steps as described above. In the general case, the model space will consist of the 0'th order wavefunction Ψ_0 and all the doubly excited configurations with respect to Ψ_0 given by Ψ_{D} make up the buffer space. The outer space will be made up of the quadruply excited configurations. This results in the same Schrödinger equation as before

$$\hat{H}\,|\Psi_0\rangle + \hat{H}\,|\Psi_{\mathrm{D}}\rangle + \hat{H}\,|\Psi_{\mathrm{Q}}\rangle = E\big(|\Psi_0\rangle + |\Psi_{\mathrm{D}}\rangle + |\Psi_{\mathrm{Q}}\rangle\big). \tag{105}$$

The goal here is to devise a diagonal dressing $\langle\Psi_{\mathrm{D}_X}|\tilde{\mathbf{V}}|\Psi_{\mathrm{D}_X}\rangle$ such that the intermediate Hamiltonian $\tilde{\mathbf{H}}$ given in Eq. (107) is size-consistent. This dressing is defined by the following equations

$$\tilde{\mathbf{H}} = \mathbf{P}\cdot\mathbf{H}\cdot\mathbf{P} + \tilde{\mathbf{V}}, \tag{106}$$

$$\sum_{\mathrm{D}_I} \tilde{C}_I\,\langle\Psi_X|\tilde{\mathbf{H}}|\Psi_{\mathrm{D}_I}\rangle = E\tilde{C}_X, \tag{107}$$

$$\sum_{\mathrm{D}_I} \tilde{C}_I\,\langle\Psi_X|\mathbf{H}|\Psi_{\mathrm{D}_I}\rangle + \sum_{Q_J} \tilde{C}_J\,\langle\Psi_X|\mathbf{H}|\Psi_{Q_J}\rangle = E\tilde{C}_X. \tag{108}$$

For this we proceed similarly to the previous case with the same two assumptions as before but we shall be careful about the indices here. The main task is the derivation of the last term on the LHS of Eq. (108). Using the assumption that the coefficients of the quadruples can be

expressed as products of the coefficients of the doubles (Eq. (98)), we can simplify the dressing $\langle\Psi_{\mathrm{D}_X}|\tilde{\mathbf{V}}|\Psi_{\mathrm{D}_X}\rangle$ as shown below

$$\langle\Psi_{\mathrm{D}_X}|\mathbf{H}|\Psi_Q\rangle = \frac{1}{2}\sum_{\mathrm{D}_Z}\sum_{\mathrm{D}_Y} C_{\mathrm{D}_Z}C_{\mathrm{D}_Y}\,\langle\Psi_{\mathrm{D}_X}|\mathbf{H}|\Phi_Z^{\mathrm{D}}\Phi_Y^{\mathrm{D}}\rangle\,, \tag{109}$$

$$\langle\Psi_{\mathrm{D}_X}|\mathbf{H}|\Psi_Q\rangle = C_{\mathrm{D}_X}\sum_{\mathrm{D}_Y\in\mathcal{D}_{\mathrm{D}_X}} C_{\mathrm{D}_Y}\,\langle\Psi_0|\mathbf{H}|\Psi_{\mathrm{D}_Y}\rangle\,, \tag{110}$$

$$\langle\Psi_{\mathrm{D}_X}|\mathbf{H}|\Psi_Q\rangle = C_{\mathrm{D}_X}\,\langle\Psi_{\mathrm{D}_X}|\tilde{\mathbf{V}}|\Psi_{\mathrm{D}_X}\rangle\,, \tag{111}$$

$$\langle\Psi_{\mathrm{D}_X}|\tilde{\mathbf{V}}|\Psi_{\mathrm{D}_X}\rangle = \sum_{\mathrm{D}_Y} C_{\mathrm{D}_Y}\,\langle\Psi_0|\mathbf{H}|\Psi_{\mathrm{D}_Y}\rangle - \sum_{Y\notin\mathcal{D}_{\mathrm{D}_X}} C_{\mathrm{D}_Y}\,\langle\Psi_{\mathrm{D}_X}|\mathbf{H}|\Psi_{\mathrm{D}_Y}\rangle\,, \tag{112}$$

$$\langle\Psi_{\mathrm{D}_X}|\tilde{\mathbf{V}}|\Psi_{\mathrm{D}_X}\rangle = E_{corr} - \sum_{\mathrm{D}_Y\notin\mathcal{D}_{\mathrm{D}_X}} C_{\mathrm{D}_Y}\,\langle\Psi_{\mathrm{D}_X}|\mathbf{H}|\Psi_{\mathrm{D}_Y}\rangle\,. \tag{113}$$

Here 'D_X' and 'D_Y' collectively denote a 4-tuple of indices (i,j,a,b) that denote double substitutions from occupied orbitals i and j to virtual orbitals a and b. Importantly, the summation over D_Y in the above equations is over those doubles that are 'disconnected' $\mathrm{D}_Y \in \mathcal{D}_{\mathrm{D}_X}$ with respect to the doubly excited configuration Ψ_{D_X}. The 'disconnected' refers to two tuples (i,j,a,b) and (k,l,c,d) where no index in the first tuple is identical to any index in the second tuple. This is a direct consequence of the Pauli exclusion principle since the quadruply substituted determinant is written as a product of doubly substituted. Hence, after performing a given double substitution, the second double substitution will only lead to a non-zero result if the spin-orbital that is depopulated by the second substitution is not already empty or the virtual orbital that is populated by the substitution is not already populated. This is only the case if no index is repeated. Substitutions that violate this requirement are known as 'exclusion principle violating' (EPV) terms. Therefore, the final expression of the dressing with the correct consideration of the EPV terms is as follows:

$$\langle\Psi_{\mathrm{D}_X}|\mathbf{H}|\Psi_0\rangle + \langle\Psi_{\mathrm{D}_X}|\mathbf{H}|\Psi_{\mathrm{D}}\rangle + \tilde{C}_{\mathrm{D}_X}\left(E_{corr} - \Delta_{\mathrm{D}_X}^{\mathrm{EPV}}\right) = \tilde{C}_{\mathrm{D}_X}\left(E_{\mathrm{HF}} + E_{\mathrm{corr}}\right). \tag{114}$$

The last thing to do is to derive the expression for the EPV terms of the diagonal dressing $\Delta_{\mathrm{D}_X}^{\mathrm{EPV}}$. Note that now the dressing becomes dependent on the doubly excited configuration Ψ_{D_X} which makes the result dependent on orbitals i,j,a,b which are the four orbitals involved in the double substitution $|\Psi_{\mathrm{D}_X}\rangle = E_i^a E_j^b\,|\Psi_0\rangle$. The expression for the EPV term may be written as

$$\Delta_X^{\mathrm{EPV}} = \sum_{klcd\in ijab} C_{\mathrm{D}_Y}\,\langle\Psi_0|\mathbf{H}E_k^c E_l^d|\Psi_0\rangle\,. \tag{115}$$

The EPV terms enumerated by considering the number of ways, in which one-, two-, three- or all four indices in the two tuples can coincide. There are four total different type of tuples k,l,c,d which satisfy the rule $k,l,c,d \in i,j,a,b$ depending on one, two, three or four indices in common. The intermediate quantities required for these cases are as follows:

- One common occupied index i (analogously for virtual)

$$e_1(i) = \sum_{kcd}\langle\Psi_0|\mathbf{H}E_k^d E_i^c|\Psi_0\rangle\,, \tag{116}$$

- one occupied pair (i,j) common (analogous for virtual pairs)

$$e_2(i,j) = \sum_{cd} \langle \Psi_0 | \mathbf{H} E_j^d E_i^c | \Psi_0 \rangle \,, \tag{117}$$

- a triple of indices identical (i,j,a) common (analogous of i,a,b)

$$e_3(i,j,a) = \sum_{c} \langle \Psi_0 | \mathbf{H} E_j^c E_i^a | \Psi_0 \rangle \,, \tag{118}$$

- all four indices common

$$e_4(i,j,a,b) = \langle \Psi_0 | \mathbf{H} E_j^b E_i^a | \Psi_0 \rangle \,. \tag{119}$$

Using these intermediate quantities, we can finally write general equations for the full SC^2-CISD as follows [31, 32]

$$\begin{aligned} \Delta_{\mathrm{D}_X}^{\mathrm{EPV}} = \quad & e_1(i) + e_1(j) + e_1(a) + e_1(b) \\ & + e_2(i,j) + e_2(i,a) + e_2(i,b) + e_2(j,a) + e_2(j,b) + e_2(a,b) \\ & + e_3(i,j,a) - e_3(i,j,b) - e_3(i,a,b) - e_3(j,a,b) \\ & + e_4(i,j,a,b). \end{aligned} \tag{120}$$

Thus, we have the general SC^2-CISD equations which include the correct contributions resulting from a careful consideration of the spurious EPV terms.

3.3.4 Further generalization and connection to Coupled Cluster Theory

The SC^2-CI represents a logical progression from the highly flawed CISD method towards a more accurate and size-consistent theory. It exactly restores size consistency by taking care of all EPV terms. However, it still has one significant shortcoming: the lack of unitary non-invariance. The Hartree-Fock wavefunction and even the CISD wavefunction is invariant under unitary transformations of the occupied or virtual orbitals among themselves. The SC^2-CI, owing to the way the higher substitutions are incorporated, does not have this property. Again, this is quite problematic for chemical applications of this theory. However, if one takes inspiration from this development, it is not difficult to envision how one can work around this problem. In fact, with some contemplation, one could arrive at the conclusion that the essential feature is to approximate higher substitutions as products of lower substitutions. Thus triples are products of singles- and doubles, quadruples arise from products of doubles with other doubles etc. The easiest way to formalize this, is to define the n-fold substitution operators $\hat{T}_n$:

$$\hat{T}_1 = \sum_{ia} t_a^i a_a^\dagger a_i \quad \hat{T}_2 = \tfrac{1}{4} \sum_{ijab} t_{ab}^{ij} a_a^\dagger a_i a_b^\dagger a_j \quad \ldots \tag{121}$$

Here, the t-amplitudes take the place of the CI coefficients. Thus, triple substitutions would be approximated as $\hat{T}_1 \hat{T}_2$, quadruples as $\hat{T}_2^2$ and so on. Importantly, these higher excitation do

not lead to additional wavefunction parameters. The singles and doubles amplitudes is all that is required. The simplest such theory is the QCISD theory of Pople and coworkers. It may be thought of as the simplest way to restore size consistency and unitary invariance in CISD. However, this is not how it historically came about. In fact, one can generalize the idea of using products of excitation operators in a beautiful way by using the coupled cluster ansatz briefly mentioned in the introduction, in which the many-particle wavefunction is written as an exponential

$$|\Psi\rangle = \exp(\hat{T})\,|\Phi_0\rangle\,,\ \text{with}\ \hat{T} = \hat{T}_1 + \hat{T}_2 + ... \tag{122}$$

Expanding the exponential leads to

$$\exp(\hat{T}) = \hat{1} + \hat{T} + \tfrac{1}{2}\hat{T}^2 + ... = \hat{1} + \hat{T}_1 + \hat{T}_2 + \tfrac{1}{2}\hat{T}_1^2 + \hat{T}_1\hat{T}_2 + \tfrac{1}{2}\hat{T}_2^2 + ... \tag{123}$$

Thus, all products of excitations are automatically included. It can readily be shown that the theory remains size consistent at any truncation level of the cluster operator. There would be much more to say about coupled cluster theory. However, here we only wanted to illustrate that physical reasoning based on effective Hamiltonians can lead in a natural way to its formulation. Today, coupled cluster theory is a mainstay of quantum chemistry and perhaps the most advanced and most successful wavefunction-based electronic structure method in existence.

3.4 Ab initio ligand field theory

3.4.1 Ligand field theory

The analysis of experimental results like optical absorption spectra shows that the low-energy states of many mononuclear transition metal complexes can be qualitatively understood as linear combinations of a certain set of Slater determinants. They all share the same doubly occupied MOs (ligand orbitals and core orbitals on the metal) and have different occupations of a set of 5 MOs that resemble the d orbitals of free transition metal atoms or ions. For simplicity, these MOs are also called d orbitals with the understanding that they are partially delocalized onto the ligands. Ligand field theory (LFT) is a parametrization of an effective Hamiltonian that describes this manifold of 'ligand field states' in terms of intuitively appealing parameters.
The form of the model can be derived as follows [33]: Within the Slater determinant basis introduced above, one can replace the BO Hamiltonian H (apart from a constant energy shift) by the effective Hamiltonian

$$H^{\text{eff}} = \sum_{i\in d} F_i^{\text{core}} + \sum_{i<j\in d} \frac{1}{r_{ij}}, \tag{124}$$

where

$$F^{\text{core}} = h + \sum_i (2J_i - K_i). \tag{125}$$

Note that the i in Eq. (124) denotes electrons in d orbitals, while i in Eq. (125) denotes doubly occupied orbitals. J_i and K_i in Eq. (125) are Coulomb and exchange operators. This means

that this effective Hamiltonian describes the movement of the d electrons in the mean field of the closed-shell core and ligand orbitals.

For constructing the matrix representation of the effective Hamiltonian Eq. (124) in the basis of all Slater determinants introduced above, one needs all one-electron integrals $F^{\text{core}}_{pq} = \langle d_p | F^{\text{core}} | d_q \rangle$ and two-electron integrals $(d_p d_q | d_r d_s)$. Since the core Fock operator is Hermitian, there are a total of 15 parameters arising from the one-electron integrals. Furthermore, there are (considering permutational symmetry) 120 independent two-electron integrals.

In the simplest ligand field model, one makes the assumption that the d orbitals have full spherical symmetry (i.e., they transform like the spherical harmonics belonging to quantum number $l = 2$). In this case, there are only 3 independent parameters in terms of which one can express all two-electron integrals. These parameters are either the Slater-Condon parameters F_0, F_2, F_4 or the Racah parameters A, B, C [33]. In ligand field theory, one usually denotes the one-electron part of the effective Hamiltonian as the one-electron ligand field matrix h^{LFT}_{pq} instead of a "core Fock operator". In high-symmetry situations, the number of parameters is highly reduced. For example, in tetrahedral or octahedral complexes, h^{LFT}_{pq} is fully determined (apart from an irrelevant constant energy shift) by a single number: the ligand field splitting Δ (often also denoted by $10Dq$), which is the orbital energy difference between the $e_{(g)}$ and the $t_{2(g)}$ orbital sets.

Traditionally, the parameters of the model are fitted to experimental data like electronic excitation energies, thermochemical data, EPR spectra, or magnetization data. Particularly in low-symmetry situations (where all elements of h^{LFT}_{pq} appear as distinct parameters), this fit is often underdetermined. Furthermore, one is fitting quantities that depend nonlinearly on the ligand field parameters. This means that there can be many local minima in parameter space and the fit is not unique. Therefore, the extracted ligand field parameters are not well-defined and can possibly lack physical meaning.

One should also note that since the Slater determinant basis used in the definition of the ligand field model is far from being complete, it describes the true spectrum only approximately if Eqs. (124) and (125) are understood literally. Fitting to experimental data (or to ab initio effective Hamiltonians as described below) can go beyond this simple picture and lead to parameters that for example include the effect of electron correlation. They can be considered as "renormalized parameters" [34].

3.4.2 Ab initio ligand field theory

The ab initio ligand field theory (AILFT) approach is based on the observation that the matrix elements of the ligand field effective Hamiltonian are linear functions of the parameters of the model [35]. When combining all the parameters in a single vector $\mathbf{p}$, one can write this as

$$H^{\text{LFT}}_{IJ}(\mathbf{p}) = \sum_k H^{\text{LFT},k}_{IJ} p_k. \tag{126}$$

Combining I and J into a single compound index (such that the effective Hamiltonian becomes a vector), this can also be written in matrix-vector form,

$$\mathbf{H}^{\text{LFT}}(\mathbf{p}) = \mathbf{A}\mathbf{p}, \tag{127}$$

where the matrix $\mathbf{A}$ is defined as $A_{IJ,k} = H_{IJ}^{\text{LFT},k}$.
The basic idea of AILFT is now to construct an ab initio effective Hamiltonian $\mathbf{H}^{\text{eff}}$ that describes the same part of the electronic spectrum as the LFT model Hamiltonian. One then optimizes the parameters $\mathbf{p}$ such that the model Hamiltonian resembles the ab initio effective Hamiltonian as much as possible. This can be achieved by minimizing the sum of squared deviations of all matrix elements, i.e., $\sum_{IJ}\left(H_{IJ}^{\text{eff}} - H_{IJ}^{\text{LFT}}(\mathbf{p})\right) \stackrel{!}{=} \min$ (least-squares fitting). Since the matrix elements are linear functions of the parameters, this problem has a unique solution that is given by [36, 37]

$$\mathbf{p} = \mathbf{A}^{+}\mathbf{H}^{\text{eff}}, \tag{128}$$

where $\mathbf{A}^{+}$ is the Moore-Penrose pseudoinverse of $\mathbf{A}$. If the number of effective Hamiltonian matrix elements is larger than the number of parameters (which is usually the case), the pseudoinverse can be written as $\mathbf{A}^{+}{=}(\mathbf{A}^{T}\mathbf{A})^{-1}\mathbf{A}^{T}$. Inserting this into Eq. (128), one arrives at

$$\mathbf{p} = (\mathbf{A}^{\text{LFT}})^{-1}\mathbf{b}^{\text{LFT}}, \tag{129}$$

$$A_{kl}^{\text{LFT}} = \sum_{IJ} H_{IJ}^{\text{LFT},k} H_{IJ}^{\text{LFT},l}, \tag{130}$$

$$b_{k}^{\text{LFT}} = \sum_{IJ} H_{IJ}^{\text{LFT},k} H_{IJ}^{\text{eff}}. \tag{131}$$

These are the equations derived in the original description of the AILFT approach [35]. This ab initio approach for obtaining ligand field parameters is distinguished from traditional approaches by the fact that the model is linear (i.e., the fit is unique) and that the system is not underdetermined. This is because the full effective Hamiltonian provides much more information than just the energies.
The most straightforward ab initio effective Hamiltonian that can be used in the AILFT context is the CASCI Hamiltonian, where the metal d orbitals are chosen as active orbitals. In terms of its spectral resolution, it can be written as

$$\mathbf{H}_{\text{CASCI}} = \mathbf{C}_{\text{CASCI}}\mathbf{E}_{\text{CASCI}}\mathbf{C}_{\text{CASCI}}^{T}, \tag{132}$$

where $\mathbf{C}_{\text{CASCI}}$ is the matrix of CASCI coefficients and $\mathbf{E}$ is the diagonal matrix of energies. The problem in this case is that dynamic correlation, which is important for quantitative results, is missing. A straightforward way to incorporate dynamic correlation on top of a CASSCF calculation is 2nd order multireference perturbation theory (MRPT). Popular variants of MRPT are CASPT2 [38, 39] and NEVPT2 [40–42]. The standard version of these methods is state-specific, i.e., they are performed for each CASSCF root individually. A variant of AILFT based on state-specific NEVPT2 was introduced in which the ab initio effective Hamiltonian is in analogy to Eq. (132) defined as

$$\mathbf{H}_{\text{NEVPT2}}^{\text{eff}} = \mathbf{C}_{\text{CASCI}}\mathbf{E}_{\text{NEVPT2}}\mathbf{C}_{\text{CASCI}}^{T}. \tag{133}$$

By definition, this effective Hamiltonian has again simply the CASCI wavefunctions as eigenstates, while its energies include dynamic correlation at 2nd order in perturbation theory. A downside of this approach is that often large root-mean-square deviations (RMSDs) between the NEVPT2 energies and the energies of the fitted LFT model were observed, indicating that the LFT model is not well suited to parametrize the NEVPT2 effective Hamiltonian of Eq. (133). In contrast to this, there are also so-called multistate methods that can describe the dynamic-correlation-induced mixing of states in the model space. Recently, new versions of AILFT based on two such methods, the DCD-CAS(2) method [22, 23] and a Hermitian version of quasidegenerate NEVPT2 (HQD-NEVPT2) [43], were implemented and tested. It turns out that the possibility of state mixing can lead to better fits and lower RMSDs than at the NEVPT2 level. This leads to ligand field models that are closer to the physical picture provided by the ab initio calculations.

LFT has the advantage that it allows for the rationalization of complicated properties like excitation energies, EPR spectra, magnetization curves, and many other experimental results in terms of parameters whose behavior can be intuitively understood. In particular, the reduction of the size of the Racah parameters can be interpreted as a manifestation of the "nephelauxetic effect", i.e., the expansion of the size of the d orbitals due to covalency. A popular tool for analysis of the one-electron ligand-field matrix is the angular overlap model (AOM) [44,45]. In this case, the model parameters are e_σ and e_π, which are measures for the strength of σ and π bonding between the metal center and the ligand.

AILFT has been used in many studies over the last few years to rationalize the spectra and other properties of transition metal complexes. For example, it was used in the analysis of the magnetostructural correlations in pseudotetrahedral cobalt(II) complexes [46], the analysis of the ligand field of the azido ligand [47], and for the rationalization of experimental results on a cobalt single ion magnet [48]. Furthermore, AILFT was used to gain understanding of periodic trends in lanthanide [49, 50] and actinide [50] ions and complexes.

For further information on AILFT, we refer to two recent review articles [51, 52].

4 Conclusions

We hope that in this chapter, we have provided a useful entry point into the fascinating world of effective Hamiltonians. We have briefly touched upon many and diverse aspects of the subject. However, the serious student will need to consult the cited literature in order to work out any of the topics in full detail. Nevertheless, we hope that it came across that effective Hamiltonians are an incredibly versatile and powerful concept. They help us to conceptualize difficult electronic structure problems, they help us to connect in a clear and concise way to experimental reality and they may inspire us to develop more accurate electronic structure theories – to reiterate only a few possible applications. Clearly, the avenues that can be explored are nearly endless. Consequently, we hope that future generations of theoreticians will embrace effective Hamiltonians in their research and make ample use of the creative possibilities that their offer.

References

[1] F. Neese and E.I. Solomon: In J.S. Miller and M. Drillon (Eds.) *Magnetism: Molecules to Materials IV* (Wiley-VCH, Weinheim, 2003), book section 9, pp. 345–466

[2] R. McWeeny: *Methods of Molecular Quantum Mechanics* (Academic Press, 1992)

[3] A. Szabo and N.S. Ostlund: *Modern Quantum Chemistry: Introduction to Advanced Electronic Structure Theory* (Dover Publications, Mineola, 1996)

[4] B.A. Heß, C.M. Marian, U. Wahlgren, and O. Gropen, Chem. Phys. Lett. **251**, 365 (1996)

[5] F. Neese, J. Chem. Phys. **122**, 034107 (2005)

[6] I. Shavitt and L.T. Redmon, J. Chem. Phys. **73**, 5711 (1980)

[7] L. Lang: *Development of New Multistate Multireference Perturbation Theory Methods and Their Application*. Ph.D. thesis, Rheinische Friedrich-Wilhelms-Universität Bonn (2020)

[8] C. Bloch, Nucl. Phys. **6**, 329 (1958)

[9] P. Durand, Phys. Rev. A **28**, 3184 (1983)

[10] I. Lindgren, J. Phys. B: At. Mol. Phys. **7**, 2441 (1974)

[11] J. des Cloizeaux, Nucl. Phys. **20**, 321 (1960)

[12] D.J. Klein, J. Chem. Phys. **61**, 786 (1974)

[13] B.H. Brandow: In B.R. Barrett (Ed.) *Effective Interactions and Operators in Nuclei* (Springer, Berlin, 1975), *Lecture Notes in Physics*, Vol. 40, pp. 1–24

[14] B.H. Brandow, Int. J. Quantum Chem. **15**, 207 (1979)

[15] P.-O. Löwdin, J. Chem. Phys. **19**, 1396 (1951)

[16] P.-O. Löwdin, J. Mol. Spectrosc. **10**, 12 (1963)

[17] P.-O. Löwdin, J. Mol. Spectrosc. **13**, 326 (1964)

[18] J. Heully and J. Daudey, J. Chem. Phys. **88**, 1046 (1988)

[19] J.-L. Heully and J.-P. Malrieu, Chem. Phys. **356**, 76 (2009)

[20] J.P. Malrieu, P. Durand, and J.P. Daudey, J. Phys. A: Math. Gen. **18**, 809 (1985)

[21] L.E. Nitzsche and E.R. Davidson, J. Chem. Phys. **68**, 3103 (1978)

[22] S. Pathak, L. Lang, and F. Neese, J. Chem. Phys. **147**, 234109 (2017)

[23] L. Lang and F. Neese, J. Chem. Phys. **150**, 104104 (2019)

[24] P.A.M. Dirac, Proc. R. Soc. London, Ser. A **112**, 661 (1926)

[25] W. Heisenberg, Z. Phys. **49**, 619 (1928)

[26] W. Heisenberg, Rev. Mod. Phys. **7**, 167 (1935)

[27] J.-P. Malrieu, R. Caballol, C.J. Calzado, C. de Graaf, and N. Guihéry, Chem. Rev. **114**, 429 (2014)

[28] C. Calzado, J. Cabrero, J.-P. Malrieu, and R. Caballol, J. Chem. Phys. **116**, 2728 (2002)

[29] C. Calzado, J. Cabrero, J.-P. Malrieu, and R. Caballol, J. Chem. Phys. **116**, 3985 (2002)

[30] C. Calzado, C. Angeli, D. Taratiel, R. Caballol, and J.-P. Malrieu, J. Chem. Phys. **131**, 44327 (2009)

[31] J.-P. Daudey, J.-L. Heully, and J.-P. Malrieu, J. Chem. Phys. **99**, 1240 (1993)

[32] N. Ben-Amor and D. Maynau, Chem. Phys. Lett. **286**, 211 (1998)

[33] J.S. Griffith: *The theory of transition-metal ions* (Cambridge University Press, 1971)

[34] M. Gerloch, J.H. Harding, and R.G. Woolley: *The context and application of ligand field theory* (Springer, Berlin Heidelberg, 1981), *Structure and Bonding*, Vol. 46, pp. 1–46

[35] M. Atanasov, D. Ganyushin, K. Sivalingam, and F. Neese: *A Modern First-Principles View on Ligand Field Theory Through the Eyes of Correlated Multireference Wavefunctions* (Springer, Berlin Heidelberg, 2012), pp. 149–220. Structure and Bonding

[36] R. Penrose, Math. Proc. Cambridge Philos. Soc. **52**, 17 (1956)

[37] L. Lang, M. Atanasov, and F. Neese, J. Phys. Chem. A **124**, 1025 (2020)

[38] K. Andersson, P.A. Malmqvist, B.O. Roos, A.J. Sadlej, and K. Wolinski, J. Phys. Chem. **94**, 5483 (1990)

[39] K. Andersson, P.-Å. Malmqvist, and B.O. Roos, J. Chem. Phys. **96**, 1218 (1992)

[40] C. Angeli, R. Cimiraglia, S. Evangelisti, T. Leininger, and J.-P. Malrieu, J. Chem. Phys. **114**, 10252 (2001)

[41] C. Angeli, R. Cimiraglia, and J.-P. Malrieu, Chem. Phys. Lett. **350**, 297 (2001)

[42] C. Angeli, R. Cimiraglia, and J.-P. Malrieu, J. Chem. Phys. **117**, 9138 (2002)

[43] L. Lang, K. Sivalingam, and F. Neese, J. Chem. Phys. **152**, 014109 (2020)

[44] C.E. Schäffer and C K. Jørgensen, Mol. Phys. **9**, 401 (1965)

[45] C.E. Schäffer: *A perturbation representation of weak covalent bonding* (Springer Berlin Heidelberg, 1968), pp. 68–95

[46] E.A. Suturina, D. Maganas, E. Bill, M. Atanasov, and F. Neese, Inorg. Chem. **54**, 9948 (2015)

[47] D. Schweinfurth, M.G. Sommer, M. Atanasov, S. Demeshko, S. Hohloch, F. Meyer, F. Neese, and B. Sarkar, J. Am. Chem. Soc. **137**, 1993 (2015)

[48] Y. Rechkemmer, F.D. Breitgoff, M. van der Meer, M. Atanasov, M. Hakl, M. Orlita, P. Neugebauer, F. Neese, B. Sarkar, and J. van Slageren, Nat. Commun. **7**, 10467 (2016)

[49] D. Aravena, M. Atanasov, and F. Neese, Inorg. Chem. **55**, 4457 (2016)

[50] J. Jung, M. Atanasov, and F. Neese, Inorg. Chem. **56**, 8802 (2017)

[51] M. Atanasov, D. Aravena, E. Suturina, E. Bill, D. Maganas, and F. Neese, Coord. Chem. Rev. **289-290**, 177 (2015)

[52] S.K. Singh, J. Eng, M. Atanasov, and F. Neese, Coord. Chem. Rev. **344**, 2 (2017)

5 Multiplets and Spin-Orbit Coupling

Erik Koch
Jülich Supercomputer Centre
Forschungszentrum Jülich

Contents

E. Pavarini and E. Koch (eds.)
Topology, Entanglement, and Strong Correlations
Modeling and Simulation Vol. 10
Forschungszentrum Jülich, 2020, ISBN 978-3-95806-466-9
http://www.cond-mat.de/events/correl20

1 Atomic configurations

Given their modest size and symmetry, atoms are among the simplest many-electron problems. On the other hand, they are of outstanding importance as the building blocks of all matter, with their level structure determining the to a large extent the electronic structure in the condensed state. Their symmetry, combined with the early availability of high-accuracy spectral data, made it possible to analyze the electronic structure of atoms and ions already before the Schrödinger equation was known [1]. Knowing the (non-relativistic) Hamiltonian for an N-electron ion of charge $Z-N$ (in atomic units, see App. A)

$$H = \sum_{i=1}^{N} \left(-\frac{1}{2}\Delta_i - \frac{Z}{|\vec{r}_i|} \right) + \sum_{i<j} \frac{1}{|\vec{r}_i - \vec{r}_j|} \tag{1}$$

does, however, not mean that we can determine its ground state exactly. To get an impression of the complexity of the problem presented by a system of many interacting electrons, we may consider a simple iron atom, Fe, with $N = Z = 26$ electrons. Its wave-function is a function of $3{\times}26$ coordinates. Writing a numerical approximation to it, even on a coarse discretization grid of 10 grid-points per coordinate would require us to store 10^{76} amplitudes, for which we would need a classical memory device containing more atoms than exist in the visible universe—a practical impossibility. We thus need "approximate practical methods" [2] to deal with the problem.

The approximate practical approach for dealing with the atomic many-body problem consists of treating the electron-electron repulsion in two steps. First, equation (1) is solved in the central-field approximation. This provides us with orbitals $\varphi_{n,l,m,\sigma}(\vec{r}) = u_{n,l}(r)/r\, Y_{l,m}(\vartheta,\varphi)\, \chi_\sigma$. If we were to stop at the mean-field level, we might look for unrestricted mean-field solutions that break the spherical and spin symmetry to lower the mean-field energy. When we continue the calculation by reintroducing the electron-electron interaction, we stay with the symmetry-restricted mean-field solutions, as the many-body treatment otherwise would have to restore the broken symmetries.

Filling the central-field orbitals by the Aufbauprinzip already gives the structure or the periodic table: orbitals are filled—roughly—with increasing quantum numbers $n{+}l$ and for given $n{+}l$ with increasing principle quantum number n:

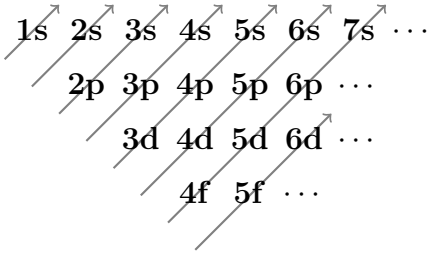

The reordering of the atomic shells relative to the hydrogen levels is a result of the mean-field: inner electrons screen the nuclear charge, so that electrons further away from the nucleus see only a small effective charge. Since $u_{n,l}(r{\to}0) \sim r^{l+1}$ orbitals with higher angular momentum l have a lower probability of coming close to the nucleus, so their energy tends to go up.

In the central-field approximation the orbital energy only depends on the quantum numbers n and l, but not on m and σ. Thus, when a shell (n,l) is filled with less than $2(2l+1)$ electrons, there will be many different ways of distributing the electrons over spin-orbitals, all of the same energy. Thus open shells are highly degenerate.

This degeneracy is lifted when we re-introduce the electron-electron interaction in degenerate perturbation theory, or, when including more than the degenerate orbitals, in a variational way. The actual perturbation is the two-body interaction minus the mean-field (double-counting correction)

$$\sum_i V_{MF}(\vec{r}_i) := \left\langle \frac{1}{2} \sum_{j \neq i} \frac{1}{|\vec{r}_i - \vec{r}_j|} \right\rangle. \tag{2}$$

When the mean-field density is close to the true density as, e.g., in a density-functional calculation, the long-range Hartree potential is already properly included V_{MF}, so that the perturbation becomes short-ranged—of the order of the exchange-correlation hole. This perturbation arising from the electron-electron repulsion splits a configuration l^N of N electrons in an (n,l)-shell into multiplet terms. They are characterized by their total orbital momentum L and spin S quantum numbers and are in general still highly degenerate. The total spin is usually given by its multiplicity $2S+1$ so that the multiplet term is written as ${}^{2S+1}L$. When the relativistic spin-orbit coupling is included in a second step of degenerate perturbation theory, these terms split into multiplet levels, which are characterized by the additional total angular momentum as ${}^{2S+1}L_J$. This two-step degenerate perturbation approach is called LS or Russell-Saunders coupling and works well when the splitting due to spin-orbit coupling is much smaller than that due to the electron-electron repulsion.

Doing perturbation theory in the opposite order, i.e., calculating the splitting of the open shell l^N under spin-orbit interaction and then doing perturbation theory for the electron-electron repulsion on the degenerate spin-orbit levels is called jj coupling. It is appropriate in extremely heavy atoms, where the spin-orbit splitting dominates the multiplet splitting. In practice this is not realized for stable atoms. In heavy atoms the spin-orbit interaction can, however, become sufficiently strong that LS coupling breaks down and one has to treat electron-electron repulsion and spin-orbit coupling on the same footing, i.e., in a single step of degenerate perturbation theory. This is called intermediate coupling.

In the following we will start by analyzing the two-body electron-electron repulsion that makes the N-electron atom a many-body problem. We will see that the multiplet terms are almost completely determined by symmetry—which was instrumental in making the analysis of spectra before the introduction of the Schrödinger equation possible. We will then turn to the construction of the electron-electron Hamiltonian bring it into matrix form and investigate its properties, in particular under an electron-hole transformation. This will involve a number of technical concepts, in particular the addition theorem for spherical harmonics and its implications as well as Gaunt coefficients, which are explained in separate appendices. Finally, we will briefly discuss the much simpler one-body spin-orbit interaction and its interplay with the electron-electron repulsion. For an introduction to multiplets with a focus of different aspects of the theory, see also the excellent lecture of Robert Eder on multiplets in transition metal ions in [3].

2 Multiplets

We start by considering the splitting of an open shell of N electrons in orbitals $\varphi_{n,l,m,\sigma}$ of angular momentum l. There are $2(2l+1)$ such spin-orbitals and, by the antisymmetry of the N-electron wave function, $\binom{2(2l+1)}{N}$ degenerate states in the shell l^N. The computational approach of dealing with the electron-electron repulsion is to write $H_{ee}\sum_{i<j}1/|\vec{r}_i-\vec{r}_j|$ in second quantization in the N-electron space spanned by the spin-orbitals and diagonalize the resulting $\binom{4l+2}{N}$-dimensional matrix numerically. The techniques for this exact diagonalization are explained in [4]. As a result we will find a highly degenerate spectrum.

The degeneracies are the consequence of the symmetries of the perturbation: H_{ee} is invariant under inversions and simultaneous rotations of all electrons, as well as independent of spin. This means, in particular, that it commutes with the total spin $\vec{S}=\sum_i\vec{S}_i$ operator and total orbital momentum $\vec{L}=\sum_i\vec{L}_i$, where $\vec{L}_i=\vec{r}_i\times\vec{p}_i$. Thus, there will be simultaneous eigenstates of H_{ee}, $\vec{L}$, and $\vec{S}$. The symmetry-based approach to calculating multiplet terms and their energies is thus based on constructing the eigenstates $|L,M;\,S,\Sigma\rangle$ of the total angular momenta, spanning the multiplet term ${}^{2S+1}L$. When the terms are unique, the $|L,M;\,S,\Sigma\rangle$ are automatically eigenstates of H_{ee}. When there is more than one term with quantum numbers L and S, H_{ee} needs only be diagonalized on this small space. Written in multiplet states, H_{ee} is thus block diagonal, with most blocks being one-dimensional.

Constructing eigenstates of L and S can, however, be quite tedious: the resulting states when adding more that two angular momenta depend on the order in which the momenta are added, and the resulting states need to be antisymmetrized. The traditional approach [5–10] proceeds by constructing the multiplet states for the l^N shell from the states for the simpler l^{N-1}-shell by adding the angular momentum of the additional electron and antisymmetrizing the resulting function. To ease this task, there are tables of coefficients of fractional parentage [10]:

> Fractional parentage coefficients were introduced by Racah [7] to facilitate computation of matrix elements for complicated configurations. They are important because all antisymmetric states of N electrons can be expressed as linear combinations of the states obtained by angular-momentum coupling one additional electron to the antisymmetric states of $N-1$ electrons. The coefficients of these linear combinations are the fractional parentage coefficients.

The problem simplifies drastically when we work in a formalism that only allows us to express physical quantities, i.e., when working in second quantization [11]: all states must be antisymmetric and all operators must be symmetric: total orbital momentum can be represented, while unphysical operators acting on only a single electron cannot (if such an operator would be physical, we could use it to distinguish the electron it acts on from the others...). The procedure starts by identifying the state with maximum M and Σ (i.e., that vanishes under L_+ and S_+ so that it is a states with $L=M$ and $S=\Sigma$). Using ladder operators L_- and S_- then produces the other states of multiplet ${}^{2S+1}L$, after which the procedure is repeated with the remaining states.

2.1 Constructing multiplet states

The key tools for constructing multiplet state are the ladder operators of total orbital momentum

$$\hat{L}_\pm = \sum_{l,m,\sigma} \sqrt{(l\pm m+1)(l\mp m)}\, c^\dagger_{l,m-1,\sigma}\, c_{l,m,\sigma}$$

and total spin

$$\hat{S}_+ = \sum_{l,m} c^\dagger_{l,m,\uparrow}\, c_{l,m,\downarrow} \quad \text{and} \quad \hat{S}_- = \sum_{l,m} c^\dagger_{l,m,\downarrow}\, c_{l,m,\uparrow}.$$

In addition we have to fix some order of the orbitals in our basis determinants, which we choose to be sorted according to their eigenvalues m, σ: operators with spin $\uparrow$ to the left of $\downarrow$ and, for given spin, m to the left of m' when $m > m'$.

2.1.1 Multiplet terms of p^2

To see how multiplets are identified and their states are constructed in practice, we look at the simple case of two electrons in a p shell. To start, we arrange the $\binom{6}{2} = 15$ basis determinants according to their eigenvalues of L_z and S_z:

		Σ		
		1	0	-1
M	2		$p^\dagger{}_{1\uparrow} p^\dagger{}_{1\downarrow}\|0\rangle$	
	1	$p^\dagger_{1\uparrow} p^\dagger{}_{0\uparrow}\|0\rangle$	$p^\dagger{}_{1\uparrow} p^\dagger{}_{0\downarrow}\|0\rangle$ $p^\dagger{}_{0\uparrow} p^\dagger{}_{1\downarrow}\|0\rangle$	$p^\dagger_{1\downarrow} p^\dagger{}_{0\downarrow}\|0\rangle$
	0	$p^\dagger_{1\uparrow} p^\dagger_{-1\uparrow}\|0\rangle$	$p^\dagger{}_{1\uparrow} p^\dagger_{-1\downarrow}\|0\rangle$ $p^\dagger{}_{0\uparrow} p^\dagger{}_{0\downarrow}\|0\rangle$ $p^\dagger_{-1\uparrow} p^\dagger{}_{1\downarrow}\|0\rangle$	$p^\dagger_{1\downarrow} p^\dagger_{-1\downarrow}\|0\rangle$
	-1	$p^\dagger_{0\uparrow} p^\dagger_{-1\uparrow}\|0\rangle$	$p^\dagger{}_{0\uparrow} p^\dagger_{-1\downarrow}\|0\rangle$ $p^\dagger_{-1\uparrow} p^\dagger{}_{0\downarrow}\|0\rangle$	$p^\dagger_{0\downarrow} p^\dagger_{-1\downarrow}\|0\rangle$
	-2		$p^\dagger_{-1\uparrow} p^\dagger_{-1\downarrow}\|0\rangle$	

For the states with $\Sigma = 1$ both electron spins are up, so that applying S_+ produces zero. From the relation $\vec{J}^2 = J_z^2 - J_z + J_- J_+$ for general angular momenta $\vec{J}$, it then follows that these states are eigenstates of $\vec{S}^2$ with $S = 1$. Similarly, when a state vanishes under L_+ it is an eigenstate of $\vec{L}^2$. We can thus identify a state $|L, M;\, S, \Sigma\rangle$

$$|1, 1;\, 1, 1\rangle = p^\dagger_{1\uparrow} p^\dagger_{0\uparrow}|0\rangle \tag{3}$$

from which we can construct more eigenstates $|1, 1;\, 1, \Sigma\rangle$ by applying $S_- = \sum_m p^\dagger_{m\downarrow} p_{m\uparrow}$, using $[S_-,\, p^\dagger_{m\sigma}] = \delta_{\sigma,\uparrow}\, p^\dagger_{m\downarrow}$. For example

$$\sqrt{2}\,|1, 1;\, 1, 0\rangle = S_-\,|1, 1;\, 1, 1\rangle = \left(-p^\dagger_{0\uparrow} p^\dagger_{1\downarrow} + p^\dagger_{1\uparrow} p^\dagger_{0\downarrow}\right)|0\rangle,$$

where in the last term we have brought the operators in the order required by our choice of basis. Note how the factor on the left just ensures normalization of the state on the right.

Also using L_-, we can construct all nine states $|1, M;\, 1, \Sigma\rangle$ of the ${}^3P$ multiplet term

$\boxed{{}^3P}$		Σ		
		1	0	-1
	1	$p^\dagger_{1\uparrow}p^\dagger{}_{0\uparrow}\|0\rangle$	$\frac{1}{\sqrt{2}}\big(p^\dagger{}_{1\uparrow}p^\dagger{}_{0\downarrow} - p^\dagger{}_{0\uparrow}p^\dagger{}_{1\downarrow}\big)\|0\rangle$	$p^\dagger_{1\downarrow}p^\dagger{}_{0\downarrow}\|0\rangle$
M	0	$p^\dagger_{1\uparrow}p^\dagger_{-1\uparrow}\|0\rangle$	$\frac{1}{\sqrt{2}}\big(p^\dagger{}_{1\uparrow}p^\dagger_{-1\downarrow} - p^\dagger_{-1\uparrow}p^\dagger{}_{1\downarrow}\big)\|0\rangle$	$p^\dagger_{1\downarrow}p^\dagger_{-1\downarrow}\|0\rangle$
	-1	$p^\dagger_{0\uparrow}p^\dagger_{-1\uparrow}\|0\rangle$	$\frac{1}{\sqrt{2}}\big(p^\dagger{}_{0\uparrow}p^\dagger_{-1\downarrow} - p^\dagger_{-1\uparrow}p^\dagger{}_{0\downarrow}\big)\|0\rangle$	$p^\dagger_{0\downarrow}p^\dagger_{-1\downarrow}\|0\rangle$

Similarly, we see that

$$|2, 2;\, 0, 0\rangle = p^\dagger_{1\uparrow}p^\dagger_{1\downarrow}|0\rangle \tag{4}$$

from which by repeated application of $L_- = \sqrt{2}\sum_\sigma \big(p^\dagger_{0\sigma}p_{1\sigma} + p^\dagger_{-1\sigma}p_{0\sigma}\big)$ we can construct all five states of the ${}^1D$ term

$\boxed{{}^1D$		$\Sigma = 0$
	2	$p^\dagger_{1\uparrow}p^\dagger_{1\downarrow}\,\|0\rangle$
	1	$\frac{1}{\sqrt{2}}\big(p^\dagger_{1\uparrow}p^\dagger_{0\downarrow} + p^\dagger_{0\uparrow}p^\dagger_{1\downarrow}\big)\|0\rangle$
M	0	$\frac{1}{\sqrt{6}}\big(p^\dagger_{1\uparrow}p^\dagger_{-1\downarrow} + 2p^\dagger_{0\uparrow}p^\dagger_{0\downarrow} + p^\dagger_{-1\uparrow}p^\dagger_{1\downarrow}\big)\|0\rangle$
	-1	$\frac{1}{\sqrt{2}}\big(p^\dagger_{0\uparrow}p^\dagger_{-1\downarrow} + p^\dagger_{-1\uparrow}p^\dagger_{0\downarrow}\big)\|0\rangle$
	-2	$p^\dagger_{-1\uparrow}p^\dagger_{-1\downarrow}\,\|0\rangle$

The remaining state in the 3-dimensional eigenspace $M{=}0$, $\Sigma{=}0$ must be a singlet state ${}^1S$. We can construct it by finding the state orthogonal to $|1, 0;\, 1, 0\rangle$ and $|2, 0;\, 0, 0\rangle$:

$$\boxed{{}^1S} \qquad |0, 0;\, 0, 0\rangle = \frac{1}{\sqrt{3}}\big(-p^\dagger_{1\uparrow}p^\dagger_{-1\downarrow} + p^\dagger_{0\uparrow}p^\dagger_{0\downarrow} - p^\dagger_{-1\uparrow}p^\dagger_{1\downarrow}\big)|0\rangle\,. \tag{5}$$

The procedure is quite remarkable. Simply counting the number of basis determinants with given M and Σ we could identify states of maximum L_z and S_z eigenvalues and see that p^2 splits into ${}^3P$, ${}^1D$, and ${}^1S$. Constructing the multiplet states explicitly then involved merely ladder-operator algebra. For the ${}^3P$ and ${}^1D$ multiplets the starting state $|L, L;\, S, S\rangle$ turned out to be just a Slater determinant. Only the singlet state had to be constructed by orthogonalizing to the already constructed states.

The p^2-shell is, of course, quite a simple case. Adding two angular momenta is a unique procedure. Already for three angular momenta this is no longer true: Adding two spins gives a triplet $S{=}1$ and one singlet $S{=}0$ state. Adding another spin to the triplet gives a quadruplet $S{=}\frac{3}{2}$ and a doublet $S{=}\frac{1}{2}$, adding the third spin to the singlet gives another doublet. While the triplet is unique, the choice of the basis in the two-doublet space is arbitrary. It is usually resolved by specifying in which order the spins are added: $(\vec{S}_1{+}\vec{S}_2){+}\vec{S}_3$ results in doublet states different from those obtained by adding, e.g., $\vec{S}_1{+}(\vec{S}_2{+}\vec{S}_3)$. For shells of more than two electrons we might therefore expect that there will be multiplets that appear several times. Because of the antisymmetry constraint this does, however, not happen in any of the p-shells. The first time we see multiple multiplets is for d^3, which we study next.

2.1.2 Multiplet states of d^3

The d^3-shell has considerably more states than p^2. We can reduce the discussion from $\binom{10}{3} = 120$ down to the 35 basis states with $M \geq 0$ and $\Sigma \geq 0$, since the space spanned by these contains all states that vanish under L_+ and S_+.

		Σ	
		$\frac{3}{2}$	$\frac{1}{2}$
M	5		$d^\dagger_{2\uparrow}d^\dagger{}_{1\uparrow}d^\dagger{}_{2\downarrow}\|0\rangle$
	4		$d^\dagger_{2\uparrow}d^\dagger{}_{1\uparrow}d^\dagger{}_{1\downarrow}\|0\rangle$ $\quad$ $d^\dagger_{2\uparrow}d^\dagger{}_{0\uparrow}d^\dagger{}_{2\downarrow}\|0\rangle$
	3	$d^\dagger_{2\uparrow}d^\dagger_{1\uparrow}d^\dagger{}_{0\uparrow}\|0\rangle$	$d^\dagger_{2\uparrow}d^\dagger{}_{1\uparrow}d^\dagger{}_{0\downarrow}\|0\rangle$ $\quad$ $d^\dagger_{2\uparrow}d^\dagger_{-1\uparrow}d^\dagger{}_{2\downarrow}\|0\rangle$ $d^\dagger_{2\uparrow}d^\dagger{}_{0\uparrow}d^\dagger{}_{1\downarrow}\|0\rangle$ $\quad$ $d^\dagger_{1\uparrow}d^\dagger{}_{0\uparrow}d^\dagger{}_{2\downarrow}\|0\rangle$
	2	$d^\dagger_{2\uparrow}d^\dagger_{1\uparrow}d^\dagger_{-1\uparrow}\|0\rangle$	$d^\dagger_{2\uparrow}d^\dagger{}_{1\uparrow}d^\dagger_{-1\downarrow}\|0\rangle$ $\quad$ $d^\dagger_{1\uparrow}d^\dagger{}_{0\uparrow}d^\dagger{}_{1\downarrow}\|0\rangle$ $d^\dagger_{2\uparrow}d^\dagger{}_{0\uparrow}d^\dagger{}_{0\downarrow}\|0\rangle$ $\quad$ $d^\dagger_{2\uparrow}d^\dagger_{-2\uparrow}d^\dagger{}_{2\downarrow}\|0\rangle$ $d^\dagger_{2\uparrow}d^\dagger_{-1\uparrow}d^\dagger{}_{1\downarrow}\|0\rangle$ $\quad$ $d^\dagger_{1\uparrow}d^\dagger_{-1\uparrow}d^\dagger{}_{2\downarrow}\|0\rangle$
	1	$d^\dagger_{2\uparrow}d^\dagger_{1\uparrow}d^\dagger_{-2\uparrow}\|0\rangle$ $d^\dagger_{2\uparrow}d^\dagger_{0\uparrow}d^\dagger_{-1\uparrow}\|0\rangle$	$d^\dagger_{2\uparrow}d^\dagger{}_{1\uparrow}d^\dagger_{-2\downarrow}\|0\rangle$ $\quad$ $d^\dagger_{2\uparrow}d^\dagger_{-2\uparrow}d^\dagger{}_{1\downarrow}\|0\rangle$ $d^\dagger_{2\uparrow}d^\dagger{}_{0\uparrow}d^\dagger_{-1\downarrow}\|0\rangle$ $\quad$ $d^\dagger_{1\uparrow}d^\dagger_{-1\uparrow}d^\dagger{}_{1\downarrow}\|0\rangle$ $d^\dagger_{2\uparrow}d^\dagger_{-1\uparrow}d^\dagger{}_{0\downarrow}\|0\rangle$ $\quad$ $d^\dagger_{1\uparrow}d^\dagger_{-2\uparrow}d^\dagger{}_{2\downarrow}\|0\rangle$ $d^\dagger_{1\uparrow}d^\dagger{}_{0\uparrow}d^\dagger{}_{0\downarrow}\|0\rangle$ $\quad$ $d^\dagger_{0\uparrow}d^\dagger_{-1\uparrow}d^\dagger{}_{2\downarrow}\|0\rangle$
	0	$d^\dagger_{2\uparrow}d^\dagger_{0\uparrow}d^\dagger_{-2\uparrow}\|0\rangle$ $d^\dagger_{1\uparrow}d^\dagger_{0\uparrow}d^\dagger_{-1\uparrow}\|0\rangle$	$d^\dagger_{2\uparrow}d^\dagger{}_{0\uparrow}d^\dagger_{-2\downarrow}\|0\rangle$ $\quad$ $d^\dagger_{1\uparrow}d^\dagger_{-1\uparrow}d^\dagger{}_{0\downarrow}\|0\rangle$ $d^\dagger_{2\uparrow}d^\dagger_{-1\uparrow}d^\dagger_{-1\downarrow}\|0\rangle$ $\quad$ $d^\dagger_{1\uparrow}d^\dagger_{-2\uparrow}d^\dagger{}_{1\downarrow}\|0\rangle$ $d^\dagger_{1\uparrow}d^\dagger{}_{0\uparrow}d^\dagger_{-1\downarrow}\|0\rangle$ $\quad$ $d^\dagger_{0\uparrow}d^\dagger_{-1\uparrow}d^\dagger{}_{1\downarrow}\|0\rangle$ $d^\dagger_{2\uparrow}d^\dagger_{-2\uparrow}d^\dagger{}_{0\downarrow}\|0\rangle$ $\quad$ $d^\dagger_{0\uparrow}d^\dagger_{-2\uparrow}d^\dagger{}_{2\downarrow}\|0\rangle$

From $|3,3;\,\frac{3}{2},\frac{3}{2}\rangle = d^\dagger_{2\uparrow}d^\dagger_{1\uparrow}d^\dagger_{0\uparrow}|0\rangle$ we can construct the twenty states in ${}^4F$.
Using $L_- = \sum_\sigma \left(2d^\dagger_{-2\sigma}d_{-1\sigma} + \sqrt{6}\, d^\dagger_{-1\sigma}d_{0\sigma} + \sqrt{6}\, d^\dagger_{0\sigma}d_{1\sigma} + 2d^\dagger_{1\sigma}d_{2\sigma}\right)$ and remembering that L_- on the left-hand side ensures normalization we obtain

$$
\begin{aligned}
|3,3;\,\tfrac{3}{2},\tfrac{3}{2}\rangle &= d^\dagger_{2\uparrow}d^\dagger_{1\uparrow}d^\dagger_{0\uparrow}\,|0\rangle \\
|3,2;\,\tfrac{3}{2},\tfrac{3}{2}\rangle &= d^\dagger_{2\uparrow}d^\dagger_{1\uparrow}d^\dagger_{-1\uparrow}\,|0\rangle \\
|3,1;\,\tfrac{3}{2},\tfrac{3}{2}\rangle &= \tfrac{1}{\sqrt{5}}\left(\sqrt{3}\, d^\dagger_{2\uparrow}d^\dagger_{0\uparrow}d^\dagger_{-1\uparrow} + \sqrt{2}\, d^\dagger_{2\uparrow}d^\dagger_{1\uparrow}d^\dagger_{-2\uparrow}\right)|0\rangle \\
|3,0;\,\tfrac{3}{2},\tfrac{3}{2}\rangle &= \tfrac{1}{\sqrt{5}}\left(d^\dagger_{1\uparrow}d^\dagger_{0\uparrow}d^\dagger_{-1\uparrow} + 2\, d^\dagger_{2\uparrow}d^\dagger_{0\uparrow}d^\dagger_{-2\uparrow}\right)|0\rangle
\end{aligned}
$$

The state $|\Psi_\perp\rangle$ orthogonal to $|3,1\;\frac{3}{2},\frac{3}{2}\rangle$ in the two-dimensional eigenspace must vanish under L_+, since it is orthogonal also to $L_-L_+|3,1;\,\frac{3}{2},\frac{3}{2}\rangle$ so that $0 = \langle L_+\Psi_\perp|3,2;\,\frac{3}{2},\frac{3}{2}\rangle$. It is thus

$$
|1,1;\,\tfrac{3}{2},\tfrac{3}{2}\rangle = \frac{1}{\sqrt{5}}\left(\sqrt{2}\, d^\dagger_{2\uparrow}d^\dagger_{0\uparrow}d^\dagger_{-1\uparrow} - \sqrt{3}\, d^\dagger_{2\uparrow}d^\dagger_{1\uparrow}d^\dagger_{-2\uparrow}\right)|0\rangle
$$

from which we can construct the twelve states of ${}^4P$.

Starting from $|5,5;\,\frac{1}{2},\frac{1}{2}\rangle = d^\dagger_{2\uparrow}d^\dagger_{1\uparrow}d^\dagger_{2\downarrow}|0\rangle$ we obtain the twenty-two ${}^2H$ states, e.g.,

$$\begin{aligned}
|5,5;\tfrac{1}{2},\tfrac{1}{2}\rangle &= d^\dagger_{2\uparrow}d^\dagger_{1\uparrow}d^\dagger_{2\downarrow}\,|0\rangle\\
|5,4;\tfrac{1}{2},\tfrac{1}{2}\rangle &= \tfrac{1}{\sqrt{5}}\big(\sqrt{3}\,d^\dagger_{2\uparrow}d^\dagger_{0\uparrow}d^\dagger_{2\downarrow} + \sqrt{2}\,d^\dagger_{2\uparrow}d^\dagger_{1\uparrow}d^\dagger_{1\downarrow}\big)|0\rangle\\
|5,3;\tfrac{1}{2},\tfrac{1}{2}\rangle &= \tfrac{1}{\sqrt{15}}\big(\sqrt{2}\,d^\dagger_{1\uparrow}d^\dagger_{0\uparrow}d^\dagger_{2\downarrow} + \sqrt{3}\,d^\dagger_{2\uparrow}d^\dagger_{-1\uparrow}d^\dagger_{2\downarrow} + \sqrt{8}\,d^\dagger_{2\uparrow}d^\dagger_{0\uparrow}d^\dagger_{1\downarrow} + \sqrt{2}\,d^\dagger_{2\uparrow}d^\dagger_{1\uparrow}d^\dagger_{0\downarrow}\big)|0\rangle\\
&\;\;\vdots
\end{aligned}$$

There remains one state orthogonal to $|5,4;\,\frac{1}{2},\frac{1}{2}\rangle$ in the eigenspace for $M{=}4$, $\Sigma{=}\frac{1}{2}$

$$|4,4;\,\tfrac{1}{2},\tfrac{1}{2}\rangle = \frac{1}{\sqrt{5}}\big(\sqrt{2}\,d^\dagger_{2\uparrow}d^\dagger_{d\uparrow}d^\dagger_{0\downarrow}2 - \sqrt{3}\,d^\dagger_{2\uparrow}d^\dagger_{1\uparrow}d^\dagger_{1\downarrow}\big)|0\rangle$$

from which we can construct the eighteen states in ${}^2G$. Similarly, in the four-dimensional eigenspace of $M{=}3$, $\Sigma{=}\frac{1}{2}$ there remains one state orthogonal to the already constructed states $|5,3;\,\frac{1}{2},\frac{1}{2}\rangle$, $|4,3;\,\frac{1}{2},\frac{1}{2}\rangle$, and $|3,3;\,\frac{3}{2},\frac{1}{2}\rangle \propto S_-|3,3;\,\frac{3}{2},\frac{3}{2}\rangle$

$$|3,3;\,\tfrac{1}{2},\tfrac{1}{2}\rangle = \frac{1}{\sqrt{12}}\big(2\,d^\dagger_{1\uparrow}d^\dagger_{0\uparrow}d^\dagger_{2\downarrow} - \sqrt{6}\,d^\dagger_{2\uparrow}d^\dagger_{-1\uparrow}d^\dagger_{2\downarrow} + d^\dagger_{2\uparrow}d^\dagger_{0\uparrow}d^\dagger_{1\downarrow} - d^\dagger_{2\uparrow}d^\dagger_{1\uparrow}d^\dagger_{0\downarrow}\big)|0\rangle$$

from which we obtain the fourteen ${}^2F$ states.

In the next step we encounter a new situation: the eigenspace of $M{=}2$, $\Sigma{=}\frac{1}{2}$ is six-dimensional, but so far we could only construct four states out of it: $|5,2;\,\frac{1}{2},\frac{1}{2}\rangle$, $|4,2;\,\frac{1}{2},\frac{1}{2}\rangle$, $|3,2;\,\frac{1}{2},\frac{1}{2}\rangle$, and $|3,2;\,\frac{3}{2},\frac{1}{2}\rangle$. Any state out of the remaining two-dimensional orthogonal space will vanish under L_+ and S_+, i.e., it will be an eigenfunction of the type $|2,2;\,\frac{1}{2},\frac{1}{2}\rangle$, so that there will be two ${}^2D$ multiplets. This ambiguity is, of course, lifted in a natural way by diagonalizing the Hamiltonian on the two dimensional space and using the resulting energy eigenstates to construct the two multiplets. If we insist on defining states independently of the Hamiltonian, we need to define a recipe for lifting the ambiguity. This route has been taken by Racah by introducing the concept of seniority [8]. Before discussing this, we finish the determination of the multiplets of a d^3-shell by noting that after constructing the two ${}^2D$ multiplet states, there is still one undetermined state in the $M{=}1$, $\Sigma{=}\frac{1}{2}$ eigenstate, which gives rise to a ${}^2P$ multiplet.

Thus the 120-fold degenerate d^3-shell splits into ${}^4F$, ${}^4P$, ${}^2H$, ${}^2G$, ${}^2F$, $2{\times}{}^2D$, and ${}^2P$.

2.1.3 Seniority and Kramers pairs

The key to understanding seniority are the Kramers pair creators

$$K^\dagger_l := \frac{1}{\sqrt{2l{+}1}}\sum_{m=-l}^{l}(-1)^m\,l^\dagger_{m\uparrow}l^\dagger_{-m\downarrow} \tag{6}$$

which create electron-pairs in a singlet state (note the analogy to Cooper pairs), i.e., $[\vec{L},\,K^\dagger_l] = 0 = [\vec{S},\,K^\dagger_l]$. For the z-components this is straightforward

$$\begin{aligned}
\big[L_z,\,l^\dagger_{m\uparrow}l^\dagger_{-m\downarrow}\big] &= \big[L_z,\,l^\dagger_{m\uparrow}\big]l^\dagger_{-m\downarrow} + l^\dagger_{m\uparrow}\big[L_z,\,l^\dagger_{-m\downarrow}\big] = (m{-}m)\,l^\dagger_{m\uparrow}l^\dagger_{-m\downarrow} = 0\\
\big[S_z,\,l^\dagger_{m\uparrow}l^\dagger_{-m\downarrow}\big] &= \big[S_z,\,l^\dagger_{m\uparrow}\big]\,l^\dagger_{-m\downarrow} + l^\dagger_{m\uparrow}\big[S_z,\,l^\dagger_{-m\downarrow}\big] = \big(\tfrac{1}{2}{-}\tfrac{1}{2}\big)\;l^\dagger_{m\uparrow}l^\dagger_{-m\downarrow} = 0
\end{aligned}$$

For the other components, we use the ladder operators. The principle is most easily seen for the simple case of $l = 1$:

$$\begin{aligned}\big[L_+,\, -p^\dagger_{1\uparrow}p^\dagger_{-1\downarrow} + p^\dagger_{0\uparrow}p^\dagger_{0\downarrow} - p^\dagger_{-1\uparrow}p^\dagger_{1\downarrow}\big] &= -\sqrt{2}p^\dagger_{1\uparrow}p^\dagger_{0\downarrow} + \sqrt{2}p^\dagger_{1\uparrow}p^\dagger_{0\downarrow} + \sqrt{2}p^\dagger_{0\uparrow}p^\dagger_{1\downarrow} - \sqrt{2}p^\dagger_{0\uparrow}p^\dagger_{1\downarrow} = 0\\ \big[S_+,\, -p^\dagger_{1\uparrow}p^\dagger_{-1\downarrow} + p^\dagger_{0\uparrow}p^\dagger_{0\downarrow} - p^\dagger_{-1\uparrow}p^\dagger_{1\downarrow}\big] &= -p^\dagger_{1\uparrow}p^\dagger_{-1\downarrow} + 0 - p^\dagger_{-1\uparrow}p^\dagger_{1\downarrow} = 0\end{aligned}$$

This means that $K^\dagger$ adds two electrons to a state without changing its angular momentum. The simplest example is the singlet state of p^2 in equation (5): $K^\dagger_1|0\rangle \propto |0,0;\,0,0\rangle$. For d^3 we can obtain a ^2D state by adding a Kramers pair to a ^2D state in d^1, e.g.,

$$|2,2;\,\tfrac{1}{2},\tfrac{1}{2}\rangle_{d^1} = d^\dagger_{2\uparrow}|0\rangle, \tag{7}$$

which after normalization gives the state

$$|2,2;\,\tfrac{1}{2},\tfrac{1}{2}\rangle_1 = \frac{1}{2}\big(-d^\dagger_{2\uparrow}d^\dagger_{1\uparrow}d^\dagger_{-1\downarrow} + d^\dagger_{2\uparrow}d^\dagger_{0\uparrow}d^\dagger_{0\downarrow} - d^\dagger_{2\uparrow}d^\dagger_{-1\uparrow}d^\dagger_{1\downarrow} + d^\dagger_{2\uparrow}d^\dagger_{-2\uparrow}d^\dagger_{2\downarrow}\big)|0\rangle. \tag{8}$$

The corresponding ^2D multiplet in d^3 is assigned seniority 1 as it originates from the multiplet in the d^1 shell. The second ^2D multiplet in d^3, which can now be uniquely constructed from the remaining (orthogonal) state in the eigenspace of $M{=}2$, $\Sigma{=}\frac{1}{2}$, is assigned the seniority 3

$$\begin{aligned}&|2,2;\,\tfrac{1}{2},\tfrac{1}{2}\rangle_3 = \qquad\qquad (9)\\ &\frac{1}{\sqrt{84}}\big(3d^\dagger_{2\uparrow}d^\dagger_{1\uparrow}d^\dagger_{-1\downarrow} - 3d^\dagger_{2\uparrow}d^\dagger_{0\uparrow}d^\dagger_{0\downarrow} - d^\dagger_{2\uparrow}d^\dagger_{-1\uparrow}d^\dagger_{1\downarrow} + 5d^\dagger_{2\uparrow}d^\dagger_{-2\uparrow}d^\dagger_{2\downarrow} + \sqrt{24}d^\dagger_{1\uparrow}d^\dagger_{0\uparrow}d^\dagger_{-1\downarrow} - 4d^\dagger_{1\uparrow}d^\dagger_{-1\uparrow}d^\dagger_{2\downarrow}\big)|0\rangle.\end{aligned}$$

This approach works for all d shells and the grand-parentage relations can be read off table 1. It also shows that there are far to few grandparents to define unique multiplets in f systems. The situation becomes quite involved, quoting [10], page v:

> Because more than one multiplet of a given L, S may occur, some further differentiation of the multiplets is required. For this purpose we have followed consistently the classification scheme of Racah [8] wherein additional quantum numbers, usually not of physical significance, are introduced by reference to the properties of certain mathematical groups. Specifically, the groups used are those denoted by R_5 in the case of the configuration d^n and by R_7 and G_2 for the configurations f^n. The so-called seniority quantum number is consistent with this scheme. Even with these additional quantum numbers, some duplications occur for f^n configurations, which were resolved arbitrarily by Racah in his work on the electrostatic energy of f^n configurations [8].

In practice it is more economical to directly work with energy eigenstates. For this we need, of course, the representation of the electron-electron interaction in our basis of spherically symmetric orbitals. Before turning our attention to the Hamiltonian, however, let us briefly discuss the particle-hole transformation between configurations l^N and $l^{2(2l+1)-N}$ which is apparent from the table of multiplets.

s^0, s^2	^1S						
s^1		^2S					
p^0, p^6	^1S						
p^1, p^5		^2P					
p^2, p^4	$^1S\ ^1D$		^3P				
p^3		$^2P\ ^2D$		^4S			
d^0, d^6	^1S						
d^1, d^9		^2D					
d^2, d^8	$^1S\ ^1D\ ^1G$		$^3P\ ^3F$				
d^3, d^7		$^{2\times}_{2}P\ ^2D\ ^2F\ ^2G\ ^2H$		$^4P\ ^4F$			
d^4, d^6	$^{2\times}_{1}S\ ^{2\times}_{1}D\ ^1F\ ^{2\times}_{1}G\ ^1I$		$^{2\times}_{3}P\ ^3D\ ^{2\times}_{3}F\ ^3G\ ^3H$		^5D		
d^5		$^{3\times}_{2}S\ ^{2\times}_{2}P\ ^{2\times}_{2}D\ ^2F\ ^2G\ ^2H\ ^2I$		$^4P\ ^4D\ ^4F\ ^4G$		^6S	
f^0, f^{14}	^1S						
f^1, f^{13}		^2F					
f^2, f^{12}	$^1S\ ^1D\ ^1G\ ^1I$		$^3P\ ^3F\ ^3H$				
f^3, f^{11}		$^{2\times}_{2}P\ ^{2\times}_{2}D\ ^{2\times}_{2}F\ ^{2\times}_{2}G\ ^2H\ ^2I\ ^2K\ ^2L$		$^4S\ ^4D\ ^4F\ ^4G\ ^4I$			
f^4, f^{10}	$^{2\times}_{1}S\ ^{4\times}_{1}D\ ^1F\ ^{4\times}_{1}G\ ^{2\times}_{1}H\ ^{3\times}_{1}I\ ^1K\ ^{2\times}_{1}L\ ^1N$		$^{3\times}_{3}P\ ^{2\times}_{3}D\ ^{4\times}_{3}F\ ^{3\times}_{3}G\ ^{4\times}_{3}H\ ^{2\times}_{3}I\ ^{2\times}_{3}K\ ^3L\ ^3M$		$^5S\ ^5D\ ^5F\ ^5G\ ^5I$		
f^5, f^9		$^{4\times}_{2}P\ ^{5\times}_{2}D\ ^{7\times}_{2}F\ ^{6\times}_{2}G\ ^{7\times}_{2}H\ ^{5\times}_{2}I\ ^{5\times}_{2}K\ ^{3\times}_{2}L\ ^{2\times}_{2}M\ ^2N\ ^2O$		$^{2\times}_{4}S\ ^{3\times}_{4}P\ ^{4\times}_{4}D\ ^{4\times}_{4}F\ ^{3\times}_{4}G\ ^{3\times}_{4}H\ ^{2\times}_{4}I\ ^4K\ ^4L\ ^4M$		$^6P\ ^6F\ ^6H$	
f^6, f^8	$^{4\times}_{1}S\ ^{6\times}_{1}P\ ^{4\times}_{1}D\ ^{8\times}_{1}F\ ^{4\times}_{1}G\ ^{7\times}_{1}H\ ^{3\times}_{1}I\ ^{4\times}_{1}K\ ^{2\times}_{1}L\ ^{2\times}_{1}M\ ^1N\ ^1Q$		$^{6\times}_{3}P\ ^{5\times}_{3}D\ ^{9\times}_{3}F\ ^{7\times}_{3}G\ ^{9\times}_{3}H\ ^{6\times}_{3}I\ ^{6\times}_{3}K\ ^{3\times}_{3}L\ ^{3\times}_{3}M\ ^3N\ ^3O$		$^{3\times}_{5}S\ ^{2\times}_{5}P\ ^{3\times}_{5}D\ ^{3\times}_{5}F\ ^{2\times}_{5}G\ ^5H\ ^5I\ ^5K\ ^5L$		^7F
f^5		$^{2\times}_{2}S\ ^{5\times}_{2}P\ ^{7\times}_{2}D\ ^{10\times}_{2}F\ ^{10\times}_{2}G\ ^{9\times}_{2}H\ ^{9\times}_{2}I\ ^{7\times}_{2}K\ ^{5\times}_{2}L\ ^{4\times}_{2}M\ ^{2\times}_{2}N\ ^2O\ ^2Q$		$^{2\times}_{4}S\ ^{2\times}_{4}P\ ^{6\times}_{4}D\ ^{5\times}_{4}F\ ^{7\times}_{4}G\ ^{5\times}_{4}H\ ^{5\times}_{4}I\ ^{3\times}_{4}K\ ^{3\times}_{4}L\ ^4M\ ^4N$		$^6P\ ^6D\ ^6F\ ^6G\ ^6H\ ^6I$	^8S

Table 1: *Multiplet terms of l^N shells. The last entry in each row is the Hund's rule ground state.*

2.1.4 Electron-hole symmetry

Because of the Pauli principle, $\left(c^\dagger\right)^2 = 0$, the state of a filled shell

$$|n,l\rangle := \prod_{m=l}^{-l} c^\dagger_{n,l,m,\uparrow} \prod_{m=l}^{-l} c^\dagger_{n,l,m,\downarrow}|0\rangle =: \prod_{m,\sigma} c^\dagger_{n,l,m,\sigma}|0\rangle \tag{10}$$

behaves as vacuum state for the creators $c^\dagger_{n,m,l,\sigma}$, while the annihilators create holes in the shell, e.g., $s_{0\uparrow}|n,0\rangle = s_{0\uparrow}\, s^\dagger_{0\uparrow} s^\dagger_{0\downarrow}|0\rangle = s^\dagger_{0,\downarrow}|0\rangle$ or $p_{1\downarrow}|n,1\rangle = -p^\dagger_{1\uparrow} p^\dagger_{0,\uparrow} p^\dagger_{-1\uparrow} p^\dagger_{0,\downarrow} p^\dagger_{-1\downarrow}|0\rangle$, or in general

$$c_{n,l,m,\sigma}|n,l\rangle = (-1)^{l-m+1/2-\sigma} \prod_{m',\sigma'} \left(c^\dagger_{n,l,m',\sigma'}\right)^{1-\delta_{m,m'}\delta_{\sigma,\sigma'}}|0\rangle. \tag{11}$$

Applying a lexicographically ordered product of operators $\tilde{h}^\dagger_{n,l,m,\sigma} := (-1)^{l-m+1/2-\sigma} c_{n,l,m,\sigma}$ specified by occupation numbers $n_{n,l,m,\sigma} \in \{0,1\}$ on $|n,l\rangle$ thus simply creates the corresponding holes in the shell

$$\prod_{m,\sigma} \left(\tilde{h}^\dagger_{n,l,m,\sigma}\right)^{n_{m\sigma}}|n,l\rangle = \prod_{m,\sigma} \left(c^\dagger_{n,l,m,\sigma}\right)^{1-n_{m\sigma}}|0\rangle. \tag{12}$$

For more than half-filling, this is an economical way of representing the $2(2l{+}1){-}N$-electron states as N-hole states. To work in this hole-representation, we also have to express the observables in the new operators, e.g.,

$$L_z = \sum m\, c^\dagger_{n,l,m,\sigma} c_{n,l,m,\sigma} = -\sum m\, \tilde{h}^\dagger_{n,l,m,\sigma} \tilde{h}_{n,l,m,\sigma} \tag{13}$$

and likewise for S_z. We can make the operators have the same form in electron- and hole-representation by defining

$$h^\dagger_{n,l,-m,-\sigma} := \tilde{h}^\dagger_{n,l,m,\sigma} = (-1)^{l-m+1/2-\sigma} c_{n,l,m,\sigma} \tag{14}$$

so that

$$L_z = \sum m\, c^\dagger_{n,l,m,\sigma} c_{n,l,m,\sigma} = \sum m\, h^\dagger_{n,l,m,\sigma} h_{n,l,m,\sigma} \tag{15}$$

$$S_z = \sum \sigma\; c^\dagger_{n,l,m,\sigma} c_{n,l,m,\sigma} = \sum \sigma\; h^\dagger_{n,l,m,\sigma} h_{n,l,m,\sigma} \tag{16}$$

while

$$\begin{aligned} L_\pm &= \sum_{n,l,m,\sigma} \sqrt{(l{\pm}m{+}1)(l{\mp}m)}\, c^\dagger_{n,l,m\pm1,\sigma}\, c_{n,l,m,\sigma} \\ &= \sum_{n,l,m,\sigma} \sqrt{(l{\pm}m{+}1)(l{\mp}m)}\, h^\dagger_{n,l,-m,-\sigma}\, h_{n,l,-m\mp1,-\sigma} \\ &= \sum_{n,l,m',\sigma'} \sqrt{(l{\mp}m')(l{\pm}m'{+}1)}\, h^\dagger_{n,l,m'\pm1,\sigma'}\, h_{n,l,m',\sigma'} \end{aligned} \tag{17}$$

and similarly for $S_\pm$. Thus $\vec{L}$ and $\vec{S}$ operate in the same way on N-electron basis states $\prod \left(c^\dagger_{n,l,m,\sigma}\right)^{n_{m\sigma}}|0\rangle$ as they do on the corresponding N-hole basis $\prod \left(h^\dagger_{n,l,-m,-\sigma}\right)^{n_{m\sigma}}|n,l\rangle$. We

can thus translate any N-electron state constructed in the previous sections into an N-hole state with the same quantum numbers by simply replacing the basis states. The corresponding $2(2l+1)-N$-electron state is then obtained from the relation (12), where we have to remember to invert the ordering of the N-hole operators, which just gives an overall sign of $(-1)^{N-1}$.
As an example we consider the p^2 singlet (5)

$$|0,0;\,0,0\rangle_2 = \frac{1}{\sqrt{3}}\big(-p^\dagger_{1\uparrow}p^\dagger_{-1\downarrow} + p^\dagger_{0\uparrow}p^\dagger_{0\downarrow} - p^\dagger_{-1\uparrow}p^\dagger_{1\downarrow}\big)|0\rangle\,.$$

Replacing $p^\dagger_{m\sigma} \to h^\dagger_{-m,-\sigma}$ and $|0\rangle \to |n,2\rangle$, the corresponding 2-hole/4-electron state is

$$\begin{aligned}|0,0;\,0,0\rangle_4 &= \frac{1}{\sqrt{3}}\big(-h^\dagger_{-1\downarrow}h^\dagger_{1\uparrow} + h^\dagger_{0\downarrow}h^\dagger_{0\uparrow} - h^\dagger_{1\downarrow}h^\dagger_{-1\uparrow}\big)|n,2\rangle \\ &= -\frac{1}{\sqrt{3}}\big(-p^\dagger_{0\uparrow}p^\dagger_{-1\uparrow}p^\dagger_{1\downarrow}p^\dagger_{0\downarrow} + p^\dagger_{1\uparrow}p^\dagger_{-1\uparrow}p^\dagger_{1\downarrow}p^\dagger_{-1\downarrow} - p^\dagger_{1\uparrow}p^\dagger_{0\uparrow}p^\dagger_{0\downarrow}p^\dagger_{-1\downarrow}\big)|0\rangle,\end{aligned}$$

Using the Kramers pair (6) it is easily verified that this is indeed the p^4 singlet $\propto \big(K^\dagger_1\big)^2|0\rangle$.

2.2 Hamiltonian matrix elements

So far we have merely used the symmetries of the Hamiltonian to construct its eigenstates. For d- and f-shells we saw, however, that certain multiplet terms can appear several times. In these cases we might use, e.g., seniority to get a unique prescription for constructing the states in those terms. The seniority states are, however, in general no longer eigenstates of the Hamiltonian. To proceed further we need to look at the Hamiltonian in more detail.
As we are working in the spherical mean-field basis, the spin-orbitals

$$\varphi_{n,l,m,\sigma}(\vec{r}) = \frac{u_{n,l}(r)}{r}\,Y_{l,m}(\vartheta,\varphi)\;\chi_\sigma \tag{18}$$

diagonalize $H_{\mathit{eff}} = -\nabla^2/2 - Z/|\vec{r}| + V_{MF}(r)$ and we consider the operator

$$\Delta H = \sum_{i<j}\frac{1}{|\vec{r}_i-\vec{r}_j|} - \sum_i V_{MF}(|\vec{r}_i|) \tag{19}$$

In second quantization the spherical mean-field has matrix elements

$$\langle n,l,m,\sigma|V_{MF}|n',l',m',\sigma'\rangle = \delta_{l,l'}\,\delta_{m,m'}\,\delta_{\sigma,\sigma'}\int dr\,\overline{u_{n,l}(r)}\,V_{MF}(r)\,u_{n',l}(r)\,. \tag{20}$$

For an l^N-shell spanned by N spin-orbitals with the same quantum numbers n and l the spherical mean-field is thus proportional to the identity, giving a mere shift of the entire shell. We can therefore neglect it when we are only interested in the splitting of the shell. The matrix elements of the electron-electron repulsion are, obviously, more interesting. Abbreviating the quantum numbers of a spin-orbital as $\alpha := n_\alpha, l_\alpha, m_\alpha, \sigma_\alpha$ and using the expansion of the Coulomb

repulsion in products of spherical harmonics (85) we get

$$\begin{aligned}\Big\langle \alpha,\beta\Big|\frac{1}{|\vec r-\vec r\,'|}\Big|\gamma,\delta\Big\rangle &= \int d^3r\, d^3r'\, \overline{\varphi_\alpha(\vec r)}\,\overline{\varphi_\beta(\vec r\,')}\,\frac{1}{|\vec r-\vec r\,'|}\,\varphi_\gamma(\vec r\,')\varphi_\delta(\vec r)\;\delta_{\sigma_\alpha,\sigma_\delta}\,\delta_{\sigma_\beta,\sigma_\gamma}\\ &= \sum_k F^{(k)}_{\alpha,\beta,\gamma,\delta}\,\frac{4\pi}{2k+1}\sum_{\mu=-k}^{k}\langle Y_\alpha|Y_{k,\mu}\,Y_\delta\rangle\,\langle Y_\beta Y_{k,\mu}|Y_\gamma\rangle\;\delta_{\sigma_\alpha,\sigma_\delta}\,\delta_{\sigma_\beta,\sigma_\gamma}\end{aligned} \tag{21}$$

with the Slater integrals

$$F^{(k)}_{\alpha,\beta,\gamma,\delta} := \int_0^\infty dr\,\overline{u_\alpha(r)}\,u_\delta(r)\int_0^\infty dr'\,\overline{u_\beta(r')}\,u_\gamma(r')\;\frac{\min(r,r')^k}{\max(r,r')^{k+1}}. \tag{22}$$

For a shell with fixed n and l they simplify to

$$F^{(k)}_{n,l} := \int_0^\infty dr\,\big|u_{n,l}(r)\big|^2\left(\frac{1}{r^{k+1}}\int_0^r dr'\,r'^k\,\big|u_{n,l}(r')\big|^2 + r^k\int_r^\infty dr'\,\frac{\big|u_{n,l}(r')\big|^2}{r'^{k+1}}\right) \tag{23}$$

with $F^{(0)}_{n,l} > F^{(2)}_{n,l} > \cdots > 0$. In practice the ratios of the Slater integrals turn out to be quite close to those obtained for hydrogen orbitals, e.g., $F^{(4)}_{3,2}/F^{(2)}_{3,2} \approx 15/23$. The μ sum-rule for the Gaunt coefficients (App. D) implies $m_\delta - m_\alpha = \mu = m_\beta - m_\gamma$, so that also using the l sum-rule and the notation (94) we can write the electron-electron repulsion in an l^N shell as

$$H_{ee} = \frac{1}{2}\sum_{m\sigma,m'\sigma'}\sum_{k=0,2,\ldots,2l} F^{(k)}_{n,l}\sum_{\Delta m=-k}^{k}(-1)^{\Delta m}c^{(k,l,l)}_{m+\Delta m,m}c^{(k,l,l)}_{m'-\Delta m,m'}\;l^\dagger_{m+\Delta m,\sigma}\,l^\dagger_{m'-\Delta m,\sigma'}\,l_{m',\sigma'}\,l_{m,\sigma} \tag{24}$$

The direct terms, $\Delta m = 0$, have a simple classical interpretation: expanding the charge density of orbital $\varphi_{n,l,m}(\vec r\,)$ using (90) into multipole components, we see that the diagonal matrix elements of the Hamiltonian $U^{(k)}_{m.m'} := F^{(k)}_{n,l}c^{(k,l,l)}_{m,m}c^{(k,l,l)}_{m',m'}$ are nothing but electrostatic interaction energies: k=0 the monopole-monopole interaction, k=2 dipole-dipole, etc. For $\sigma = \sigma'$ there are additional density-density terms when $\Delta m = m'-m$, with, using (95), matrix elements $J^{(k)}_{m,m'} := F^{(k)}_{n,l}\big(c^{(k,l,l)}_{m,m'}\big)^2$. The diagonal part of (24) can then be written as

$$H_{diag} = \frac{1}{2}\sum_{m,\sigma,m',\sigma'}\sum_k \big(U^{(k)}_{m,m'} - \delta_{\sigma,\sigma'}J^{(k)}_{m,m'}\big)\big(n_{m'\sigma'} - \delta_{m,m'}\delta_{\sigma,\sigma'}\big)n_{m\sigma}. \tag{25}$$

Exchange terms appear only for equal spins, and the subtraction of the self interaction is already ensured by the matrix elements, since $U^{(k)}_{m,m} = J^{(k)}_{m,m}$.
The $k = 0$ contribution to H_{ee} is easily evaluated using $c^{(0,l,l)}_{m,m'} = \delta_{m,m'}$

$$H^{(k=0)}_{ee} = \frac{F^{(0)}_{n,l}}{2}\sum_{m,\sigma,m'\sigma'}\big(1-\delta_{\sigma,\sigma'}\delta_{m,m'}\big)n_{m'\sigma'}n_{m\sigma}. \tag{26}$$

We see that any state with N electrons $H^{(0)}_{ee}$ contributes $F^{(0)}_{n,l}\,N(N-1)/2$ to the energy; i.e., the monopole-monopole interaction gives the charging energy of the shell but does not contribute to the splitting.

Because of the spin-independence of the electron-electron repulsion, H_{ee} is block-diagonal in the spin-indices. In the $\uparrow\downarrow$-sector we have, e.g., for a p-shell, using $c^{(2,1,1)}_{m,m'}$ from App. D

$$H^{(k=2)}_{S_z=0} = \begin{pmatrix} p_{-1\uparrow}p_{-1\downarrow} \\ p_{-1\uparrow}p_{\ 0\downarrow} \\ p_{-1\uparrow}p_{\ 1\downarrow} \\ p_{\ 0\uparrow}p_{-1\downarrow} \\ p_{\ 0\uparrow}p_{\ 0\downarrow} \\ p_{\ 0\uparrow}p_{\ 1\downarrow} \\ p_{\ 1\uparrow}p_{-1\downarrow} \\ p_{\ 1\uparrow}p_{\ 0\downarrow} \\ p_{\ 1\uparrow}p_{\ 1\downarrow} \end{pmatrix}^\dagger \frac{F^{(2)}_{n,1}}{5^2} \begin{pmatrix} 1 & & & & & & & & \\ & -2 & & 3 & & & & & \\ & & 1 & & -3 & & 6 & & \\ & 3 & & -2 & & & & & \\ & & -3 & & 4 & & -3 & & \\ & & & & & -2 & & 3 & \\ & & 6 & & -3 & & 1 & & \\ & & & & & 3 & & -2 & \\ & & & & & & & & 1 \end{pmatrix} \begin{pmatrix} p_{-1\uparrow}p_{-1\downarrow} \\ p_{-1\uparrow}p_{\ 0\downarrow} \\ p_{-1\uparrow}p_{\ 1\downarrow} \\ p_{\ 0\uparrow}p_{-1\downarrow} \\ p_{\ 0\uparrow}p_{\ 0\downarrow} \\ p_{\ 0\uparrow}p_{\ 1\downarrow} \\ p_{\ 1\uparrow}p_{-1\downarrow} \\ p_{\ 1\uparrow}p_{\ 0\downarrow} \\ p_{\ 1\uparrow}p_{\ 1\downarrow} \end{pmatrix} \tag{27}$$

where we have ordered the operators in the same way as in the basis states. In the particular ordering we chose, terms with Δm appear on the $2l$ Δm-th side diagonal. Note how fixing the order of the operators ($\sigma=\downarrow$ and $\sigma'=\uparrow$) not only removes the prefactor $1/2$ but also makes the matrix of coefficients a two-electron *matrix* $\boldsymbol{H}^{(k)}_{\uparrow\downarrow}$ rather than a tensor in orbital space (App. B). The average direct interaction is defined via the trace of this $(2l{+}1)^2$-dimensional sector of the two-body matrix, which is invariant under basis changes that respect the spin symmetry,

$$U^{(k)}_{avg} := \sum_k \frac{\operatorname{Tr} \boldsymbol{H}^{(k)}_{\uparrow\downarrow}}{(2l{+}1)^2} = \frac{1}{(2l{+}1)^2} \sum_{m,m'} U^{(k)}_{m,m'} = \sum_k F^{(k)}_{n,l} \left(\frac{\operatorname{Tr} \boldsymbol{c}^{(k,l,l)}}{2l{+}1} \right)^2 = F^{(0)}_{n,l}\, \delta_{k,0} \tag{28}$$

where we used (84) in evaluating $\operatorname{Tr} \boldsymbol{c}^{(k,l,l)} = \delta_{k,0}$. We define the sum $U_{avg} := \sum_k U^{(k)}_{avg} = F^{(0)}_{n,l}$. The $\uparrow\uparrow$- and $\downarrow\downarrow$-sectors have identical matrices $\boldsymbol{H}^{(k)}_{\uparrow\uparrow} = \boldsymbol{H}^{(k)}_{\downarrow\downarrow}$ of dimension $(2l{+}1)2l/2$, e.g.,

$$H^{(k=2)}_{S_z=+1} = \begin{pmatrix} p_{0\uparrow}p_{-1\uparrow} \\ p_{1\uparrow}p_{-1\uparrow} \\ p_{1\uparrow}p_{\ 0\uparrow} \end{pmatrix}^\dagger \frac{F^{(2)}_{n,1}}{5^2} \begin{pmatrix} -5 & & \\ & -5 & \\ & & -5 \end{pmatrix} \begin{pmatrix} p_{0\uparrow}p_{-1\uparrow} \\ p_{1\uparrow}p_{-1\uparrow} \\ p_{1\uparrow}p_{\ 0\uparrow} \end{pmatrix}. \tag{29}$$

Since the matrix elements are spin-independent, these matrices are closely related to $\boldsymbol{H}^{(k)}_{\uparrow\downarrow}$: Defining the rectangular matrix $M_{(\tilde{m}'>\tilde{m}),\,(m',m)} = \big(\delta_{\tilde{m}',m'}\delta_{\tilde{m},m} - \delta_{\tilde{m}',m}\delta_{\tilde{m},m'}\big)/\sqrt{2}$, e.g., for $l{=}1$

$$\boldsymbol{M} := \frac{1}{\sqrt{2}} \begin{pmatrix} 0 & 1 & 0 & -1 & 0 & 0 & 0 & 0 & 0 \\ 0 & 0 & 1 & 0 & 0 & 0 & -1 & 0 & 0 \\ 0 & 0 & 0 & 0 & 0 & 1 & 0 & -1 & 0 \end{pmatrix} \tag{30}$$

which maps $\uparrow\downarrow$-states into the corresponding ordered $\uparrow\uparrow$ basis states, we get

$$\boldsymbol{H}^{(k)}_{\uparrow\uparrow} = \boldsymbol{M}\boldsymbol{H}^{(k)}_{\uparrow\downarrow}\boldsymbol{M}^\dagger = \boldsymbol{H}^{(k)}_{\downarrow\downarrow}. \tag{31}$$

The average exchange interaction is defined similar to (28) in a basis-independent way via

$$U^{(k)}_{avg} - J^{(k)}_{avg} := \sum_k \frac{\operatorname{Tr} \boldsymbol{H}^{(k)}_{\uparrow\uparrow} + \operatorname{Tr} \boldsymbol{H}^{(k)}_{\downarrow\downarrow}}{(2l{+}1)2l} = \frac{1}{2l(2l{+}1)} \sum_{m,m'} \big(U^{(k)}_{m,m'} - J^{(k)}_{m,m'}\big) \tag{32}$$

so that

$$J^{(k)}_{avg} = \frac{1}{2l(2l+1)} \sum_{m,m'} J^{(k)}_{m,m'} - \frac{1}{2l} U^{(k)}_{avg} = \frac{1}{2l} \sum_{k=2}^{2l} F^{(k)}_{n,l}\, c^{(k,l,l)}_{0,0} \tag{33}$$

by using addition theorem (83) and multipole expansion (85) to rewrite the angular integrals

$$\sum_k \sum_{m,m'} J^{(k)}_{m,m'} = \int d^3r\, d^3r' \frac{\left|u_{n,l}(r)\right|^2}{r^2} \frac{\left|u_{n,l}(r')\right|^2}{r'^2} \Big| \underbrace{\sum_m \overline{Y_{l,m}(\vartheta,\varphi)} Y_{l,m}(\vartheta',\varphi')}_{\sqrt{(2l+1)/4\pi}\, Y_{l,0}(\arccos(\hat{r}\cdot\hat{r}'),0)} \Big|^2 \underbrace{\frac{1}{|\vec{r}-\vec{r}\,'|}}_{\sum_k \frac{r_<^k}{r_>^{k+1}} P_k(\hat{r}\cdot\hat{r}')} .$$

The average exchange for the different shells is thus, using the (99) from App. D, given by

$$J_{avg} = \sum_k J^{(k)}_{avg} = \begin{cases} \dfrac{1}{5}\, F^{(2)}_{n,1} & p\text{-shell} \\ \dfrac{1}{14}\, F^{(2)}_{n,2} + \dfrac{1}{14}\, F^{(4)}_{n,2} & d\text{-shell} \\ \dfrac{2}{45}\, F^{(2)}_{n,3} + \dfrac{1}{33}\, F^{(4)}_{n,3} + \dfrac{50}{3^2{\cdot}11{\cdot}13}\, F^{(6)}_{n,3} & f\text{-shell} \end{cases} \tag{34}$$

2.2.1 Electron-hole symmetry

We have already seen that the eigenstates of the total angular momenta for a shell with N electrons and N holes are related by the simple transformation (14). Replacing the electron operators in (24) by the corresponding hole operators, renaming indices $\tilde{m} = -m - \Delta m$ and $\tilde{m}' = -m' + \Delta m$, and using the symmetries (95) and (96) of the Gaunt coefficients, we obtain

$$\begin{aligned} H_{ee} &= \frac{1}{2} \sum_{\tilde{m}\tilde{\sigma},\tilde{m}'\tilde{\sigma}'} \sum_k F^{(k)}_{n,l} \sum_{\Delta m=-k}^{k} (-1)^{\Delta m} c^{(k,l,l)}_{-\tilde{m},-\tilde{m}-\Delta m} c^{(k,l,l)}_{-\tilde{m}',-\tilde{m}'+\Delta m} h_{\tilde{m},\tilde{\sigma}}\, h_{\tilde{m}',\tilde{\sigma}'}\, h^\dagger_{\tilde{m}'-\Delta m,\tilde{\sigma}'}\, h^\dagger_{\tilde{m}+\Delta m,\tilde{\sigma}} \\ &= \frac{1}{2} \sum_{\tilde{m}\tilde{\sigma},\tilde{m}'\tilde{\sigma}'} \sum_k F^{(k)}_{n,l} \sum_{\Delta m=-k}^{k} (-1)^{\Delta m} c^{(k,l,l)}_{\tilde{m}+\Delta m,\tilde{m}} c^{(k,l,l)}_{\tilde{m}'-\Delta m,\tilde{m}'} \Big(h^\dagger_{\tilde{m}+\Delta m,\tilde{\sigma}}\, h^\dagger_{\tilde{m}'-\Delta m,\tilde{\sigma}'}\, h_{\tilde{m}',\tilde{\sigma}'}\, h_{\tilde{m},\tilde{\sigma}} \\ &\qquad + \big(\delta_{\Delta m,0} - \delta_{\tilde{m},\tilde{m}-\Delta m}\, \delta_{\tilde{\sigma},\tilde{\sigma}'}\big)\big(1 - n^h_{\tilde{m},\tilde{\sigma}} - n^h_{\tilde{m}',\tilde{\sigma}'}\big)\Big). \end{aligned} \tag{35}$$

The two-body part has the same form as when written in electron operators. The additional terms arising from normal-ordering the hole operators give the difference between the N-electron and the N-hole states, the superscript on the density operators is a reminder that they give the hole occupations. These terms involve only diagonal matrix elements such that we can write them in a concise form using the basis-independent averages (28) and (34), giving the relation between the energy of a state with N electrons and the conjugate $K{-}N$-electron state, where $K = 2(2l{+}1)$ is the number of spin-orbitals in the shell:

$$E(K{-}N) = E(N) + \left(\frac{K{-}1}{2} U_{avg} - \frac{K{-}2}{4} J_{avg} \right) \big((K{-}N) - N \big). \tag{36}$$

2.2.2 Racah parameters

For expressing energies in a compact way several conventions have been introduced. Condon and Shortley (table 1^6 of [12]) introduced parameters that include the least common prefactors of the Gaunt matrices (p. 30 in App. D) in the Slater integrals

$$
\begin{aligned}
p\text{-shell:}\quad & F_0 := F^{(0)}_{n,1} \\
& F_2 := F^{(2)}_{n,1}/5^2 \\
d\text{-shell:}\quad & F_0 := F^{(0)}_{n,2} \\
& F_2 := F^{(2)}_{n,2}/7^2 \\
& F_4 := F^{(4)}_{n,2}/(3{\cdot}7)^2 \\
f\text{-shell:}\quad & F_0 := F^{(0)}_{n,3} \\
& F_2 := F^{(2)}_{n,3}/(3{\cdot}5)^2 \\
& F_4 := F^{(4)}_{n,3}/(3{\cdot}11)^2 \\
& F_6 := F^{(6)}_{n,3}\big(5/(3{\cdot}11{\cdot}13)\big)^2
\end{aligned}
$$

so that, e.g., the diagonal terms in (25)

$$
U^{(k)}_{m,m'}/F_k = c^{(k,l,l)}_{m,m} c^{(k,l,l)}_{m',m'} \qquad \text{and} \quad J^{(k)}_{m,m'}/F_k = \big(c^{(k,l,l)}_{m,m'}\big)^2 \tag{37}
$$

in the basis of spherical harmonics become integer matrices (App. D):

p-shell:

$$
\boldsymbol{U}^{(2)} = F_2 \begin{pmatrix} 1 & -2 & 1 \\ -2 & 4 & -2 \\ 1 & -2 & 1 \end{pmatrix} \qquad \boldsymbol{J}^{(2)} = F_2 \begin{pmatrix} 1 & 3 & 6 \\ 3 & 4 & 3 \\ 6 & 3 & 1 \end{pmatrix} \tag{38}
$$

d-shell:

$$
\begin{aligned}
\boldsymbol{U}^{(2)} &= F_2 \begin{pmatrix} 4 & -2 & -4 & -2 & 4 \\ -2 & 1 & 2 & 1 & -2 \\ -4 & 2 & 4 & 2 & -4 \\ -2 & 1 & 2 & 1 & -2 \\ 4 & -2 & -4 & -2 & 4 \end{pmatrix} \qquad \boldsymbol{J}^{(2)} = F_2 \begin{pmatrix} 4 & 6 & 4 & 0 & 0 \\ 6 & 1 & 1 & 6 & 0 \\ 4 & 1 & 4 & 1 & 4 \\ 0 & 6 & 1 & 1 & 6 \\ 0 & 0 & 4 & 6 & 4 \end{pmatrix} \\
\boldsymbol{U}^{(4)} &= F_4 \begin{pmatrix} 1 & -4 & 6 & -4 & 1 \\ -4 & 16 & -24 & 16 & -4 \\ 6 & -24 & 36 & -24 & 6 \\ -4 & 16 & -24 & 16 & -4 \\ 1 & -4 & 6 & -4 & 1 \end{pmatrix} \qquad \boldsymbol{J}^{(4)} = F_4 \begin{pmatrix} 1 & 5 & 15 & 35 & 70 \\ 5 & 16 & 30 & 40 & 35 \\ 15 & 30 & 36 & 30 & 15 \\ 35 & 40 & 30 & 16 & 5 \\ 70 & 35 & 15 & 5 & 1 \end{pmatrix}
\end{aligned} \tag{39}
$$

f-shell:

$$\frac{\boldsymbol{U}^{(2)}}{F_2} = \begin{pmatrix} 25 & 0 & -15 & -20 & -15 & 0 & 25 \\ 0 & 0 & 0 & 0 & 0 & 0 & 0 \\ -15 & 0 & 9 & 12 & 9 & 0 & -15 \\ -20 & 0 & 12 & 16 & 12 & 0 & -20 \\ -15 & 0 & 9 & 12 & 9 & 0 & -15 \\ 0 & 0 & 0 & 0 & 0 & 0 & 0 \\ 25 & 0 & -15 & -20 & -15 & 0 & 25 \end{pmatrix} \quad \frac{\boldsymbol{J}^{(2)}}{F_2} = \begin{pmatrix} 25 & 25 & 10 & 0 & 0 & 0 & 0 \\ 25 & 0 & 15 & 20 & 0 & 0 & 0 \\ 10 & 15 & 9 & 2 & 24 & 0 & 0 \\ 0 & 20 & 2 & 16 & 2 & 20 & 0 \\ 0 & 0 & 24 & 2 & 9 & 15 & 10 \\ 0 & 0 & 0 & 20 & 15 & 0 & 25 \\ 0 & 0 & 0 & 0 & 10 & 25 & 25 \end{pmatrix}$$

$$\frac{\boldsymbol{U}^{(4)}}{F_4} = \begin{pmatrix} 9 & -21 & 3 & 18 & 3 & -21 & 9 \\ -21 & 49 & -7 & -42 & -7 & 49 & -21 \\ 3 & -7 & 1 & 6 & 1 & -7 & 3 \\ 18 & -42 & 6 & 36 & 6 & -42 & 18 \\ 3 & -7 & 1 & 6 & 1 & -7 & 3 \\ -21 & 49 & -7 & -42 & -7 & 49 & -21 \\ 9 & -21 & 3 & 18 & 3 & -21 & 9 \end{pmatrix} \quad \frac{\boldsymbol{J}^{(4)}}{F_4} = \begin{pmatrix} 9 & 30 & 54 & 63 & 42 & 0 & 0 \\ 30 & 49 & 32 & 3 & 14 & 70 & 0 \\ 54 & 32 & 1 & 15 & 40 & 14 & 42 \\ 63 & 3 & 15 & 36 & 15 & 3 & 63 \\ 42 & 14 & 40 & 15 & 1 & 32 & 54 \\ 0 & 70 & 14 & 3 & 32 & 49 & 30 \\ 0 & 0 & 42 & 63 & 54 & 30 & 9 \end{pmatrix}$$

$$\frac{\boldsymbol{U}^{(6)}}{F_6} = \begin{pmatrix} 1 & -6 & 15 & -20 & 15 & -6 & 1 \\ -6 & 36 & -90 & 120 & -90 & 36 & -6 \\ 15 & -90 & 225 & -300 & 225 & -90 & 15 \\ -20 & 120 & -300 & 400 & -300 & 120 & -20 \\ 15 & -90 & 225 & -300 & 225 & -90 & 15 \\ -6 & 36 & -90 & 120 & -90 & 36 & -6 \\ 1 & -6 & 15 & -20 & 15 & -6 & 1 \end{pmatrix} \quad \frac{\boldsymbol{J}^{(6)}}{F_6} = \begin{pmatrix} 1 & 7 & 28 & 84 & 210 & 462 & 924 \\ 7 & 36 & 105 & 224 & 378 & 504 & 462 \\ 28 & 105 & 225 & 350 & 420 & 378 & 210 \\ 84 & 224 & 350 & 400 & 350 & 224 & 84 \\ 210 & 378 & 420 & 350 & 225 & 105 & 28 \\ 462 & 504 & 378 & 224 & 105 & 36 & 7 \\ 924 & 462 & 210 & 84 & 28 & 7 & 1 \end{pmatrix} \tag{40}$$

In addition, Racah introduced sets of parameters

d-shell: [6], Eq. (77)

$$\begin{aligned} A &:= F_0 - 7^2 F_4 \\ B &:= F_2 - 5\, F_4 \\ C &:= 5{\cdot}7\, F_4 \end{aligned} \tag{41}$$

f-shell [8], Eq. (66)

$$\begin{aligned} E^0 &:= F_0 - 2{\cdot}5 F_2 - 3{\cdot}11 F_4 - 2{\cdot}11{\cdot}13 F_6 \\ 9E^1 &:= 2{\cdot}5{\cdot}7\, F_2 + 3{\cdot}7{\cdot}11 F_4 + 2{\cdot}7{\cdot}11{\cdot}13 F_6 \\ 9E^2 &:= F_2 - 3\, F_4 + 7\, F_6 \\ 3E^3 &:= 5\, F_2 + 2{\cdot}3\, F_4 - 7{\cdot}13 F_6 \end{aligned} \tag{42}$$

which are "different from those adopted empirically" in [6], Eq. (96)

$$\begin{aligned} A &:= F_0 - 3{\cdot}7\, F_4 - 2^2{\cdot}3^2{\cdot}13\, F_6 \\ 5\,B &:= 5\, F_2 + 2{\cdot}3\, F_4 - 7{\cdot}13\, F_6 \\ 5\,C &:= 7\, F_4 + 2{\cdot}3{\cdot}7\, F_6 \\ D &:= 2{\cdot}3{\cdot}7{\cdot}11\, F_6 \end{aligned} \tag{43}$$

2.2.3 Hund's rules

Quite remarkably, Friedrich Hund was able formulate rules for determining the multiplet term of lowest energy even before the many-body Schrödinger equation was known. Using addition of angular momenta and Pauli principle to analyze spectral data, he found that [1]

1. The lowest term has maximum multiplicity, i.e., maximum total spin S
2. For given multiplicity, the lowest term has largest total orbital momentum L

We can understand these two rules heuristically: 1. Because of the Pauli principle electrons of the same spin have a lower probability of close encounters, reducing their repulsion due to the exchange hole. 2. An electron configuration of larger total orbital momentum must have the electrons contribute in a more coordinated way to the angular momentum, helping them avoid each other.
Because the Hund's rule states are defined by maximum S and, given S, maximum L, they must vanish under application of the ladder operators S_+ and L_+. Hence at least some states of the Hund's rule term must be Slater determinants. They are easily constructed. Using the occupation number representation in our chosen sorting of the basis

$$|n_{l\uparrow}, n_{l-1\uparrow}, \cdots, n_{-l\uparrow}, n_{l\downarrow}, \ldots, n_{-l\downarrow}\rangle := \left(l^\dagger_{l,\uparrow}\right)^{n_{l\uparrow}} \cdots \left(l^\dagger_{-l,\uparrow}\right)^{n_{-l\uparrow}} \left(l^\dagger_{l,\downarrow}\right)^{n_{l\downarrow}} \cdots \left(l^\dagger_{-l,\downarrow}\right)^{n_{-l\downarrow}} |0\rangle \quad (44)$$

the Hund's rule determinant with maximum Σ and M for N electrons are given by filling the orbitals from left to right, i.e., setting the first N occupations to one. For the p-shell this gives Φ_{p^1}=$|100000\rangle$, Φ_{p^2}=$|110000\rangle$, Φ_{p^3}=$|111000\rangle$, Φ_{p^4}=$|111100\rangle$, and Φ_{p^5}=$|111110\rangle$. The total spin and angular momentum of the Hund's term are

$$S_{Hund}(l^N) = \tilde{N}/2\,,\ L_{Hund}(l^N) = \big((2l{+}1){-}\tilde{N}\big)\tilde{N}/2 \quad \text{with } \tilde{N} = (2l{+}1){-}\big|(2l{+}1){-}N\big|. \quad (45)$$

To find the energy of Hund's determinants we only need the diagonal elements of the Hamiltonian (25) that are collected in the $\boldsymbol{U}$ and $\boldsymbol{J}$ matrices

$$E_{Hund} = \langle \Phi_{Hund}|H_{ee}|\Phi_{Hund}\rangle = \sum_{m\sigma<m'\sigma':occ} \big(U_{m,m'} - \delta_{\sigma,\sigma'}J_{m,m'}\big), \quad (46)$$

where the sum is over the ordered pairs of occupied orbitals. For shells with less than two electrons there are obviously no pairs of occupied orbitals, so that the energy vanishes. For higher fillings we get, using the matrix elements given in Sec. 2.2.2, e.g.,

$$E_{Hund}(p^2) = F_0 - 5F_2 \quad E_{Hund}(p^3) = 3F_0 - 15F_2$$

$$E_{Hund}(d^2) = F_0 - 8F_2 - 9F_4 \quad E_{Hund}(d^3) = 3F_0 - 15F_2 - 72F_4$$

$$E_{Hund}(d^4) = 6F_0 - 21F_2 - 189F_4 \quad E_{Hund}(d^5) = 10F_0 - 35F_2 - 315F_4$$

For $N > 2l{+}1$ there are also pairs of opposite spin, for which the exchange term does not contribute. They are most easily calculated using the electron-hole relation (36).

2.2.4 Moments and spectral variance

The Slater-Condon integrals give no direct measure of the size of the multiplet splitting: with identical parameters the splitting changes, e.g., substantially with the number of electrons N in the shell. A measure of the width of the spectrum is its variance $\langle E^2\rangle - \langle E\rangle^2$, with the average defined by

$$\big\langle f(E)\big\rangle := \frac{1}{\dim_H}\sum_n f(E_n)\,, \tag{47}$$

where $\dim_H = \binom{K}{N}$ is the dimension of the Hilbert space. Quite remarkably, we can determine these moments from the representation of the Hamiltonian in terms of a two-body matrix $\boldsymbol{H}$ with blocks given by, e.g., (27) and (29), obtaining information about the N-electron spectrum without having to do any many-body calculations.

By the invariance of the trace, the average energy $\langle E\rangle$ involves only the diagonal terms in the N-electron Hamiltonian. For a density-density term $n_{m\sigma}n_{m'\sigma'}$ to contribute, the two orbitals must be occupied. In the Slater determinant basis for N electrons in $K = 2(2l{+}1)$ spin-orbitals this fixes two electrons in two orbitals, so that for any $m,\sigma > m',\sigma'$ there are $\binom{K-2}{N-2}$ such configurations, hence

$$\binom{K}{N}\langle E\rangle := \sum_n E_n = \mathrm{Tr}_N\, H_{ee} = \binom{K-2}{N-2}\,\mathrm{Tr}\,\boldsymbol{H} \tag{48}$$

which simplifies with $\binom{n}{k} = \frac{n}{k}\binom{n-1}{k-1}$ to

$$\langle E\rangle = \frac{N(N{-}1)}{K(K{-}1)}\,\mathrm{Tr}\,\boldsymbol{H}. \tag{49}$$

Since U_{avg} and J_{avg} are defined via the traces of the blocks $\boldsymbol{H}_{\uparrow\downarrow}$ and $\boldsymbol{H}_{\uparrow\uparrow} = \boldsymbol{H}_{\downarrow\downarrow}$, we can write

$$\mathrm{Tr}\,\boldsymbol{H} = (2l{+}1)^2U_{avg} + 2\cdot(2l{+}1)2l/2\big(U_{avg} - J_{avg}\big) = (2l{+}1)\big((4l{+}1)U_{avg} - 2lJ_{avg}\big), \tag{50}$$

so that the center of gravity of the multiplet terms of l^N is

$$\big\langle E(l^N)\big\rangle = \frac{N(N{-}1)}{2}\left(U_{avg} - \frac{2l}{4l{+}1}J_{avg}\right). \tag{51}$$

To calculate the second moment, we split the N-electron Hamiltonian into its diagonal, and the parts that create single and double excitations: $H_{ee} = H_{diag}{+}H_{single}{+}H_{double}$. To contribute to the trace of H_{ee}^2 calculated in the Slater determinant basis, every excitation must be undone, i.e.,

$$\binom{K}{N}\langle E^2\rangle = \mathrm{Tr}_N\, H_{diag}^2 + \mathrm{Tr}_N\, H_{single}^2 + \mathrm{Tr}_N\, H_{double}^2. \tag{52}$$

The traces over the N-electron space can, again, be reduced to traces over two-electron matrices $\boldsymbol{H} = \boldsymbol{H}_{diag} + \boldsymbol{H}_{single} + \boldsymbol{H}_{double}$. A double excitation involves two electrons moving from occupied to unoccupied orbitals, so that the reduction to $\mathrm{Tr}\,\boldsymbol{H}_{double}^2$ involves a combinatorial factor $\binom{K-4}{N-2}$

$$\mathrm{Tr}_N\, H_{double}^2 = \binom{K-4}{N-2}\sum_{\substack{\alpha<\beta,\,\gamma>\delta\\ \{\alpha,\beta\}\cap\{\gamma,\delta\}=\emptyset}}\big|H_{(\alpha\beta)(\gamma\delta)}\big|^2 = \binom{K-4}{N-2}\,\mathrm{Tr}\,\boldsymbol{H}_{double}^2. \tag{53}$$

Single excitations are one-body-like, so it is convenient to define the single-electron part of $\boldsymbol{H}$ by collecting all the matrix elements contributing to the same excitation $\alpha \leftarrow \beta$, e.g., $c^\dagger_\alpha n_\gamma c_\beta$

$$\big(\boldsymbol{H}_1\big)_{\alpha,\beta} := \sum_{\alpha,\beta<\gamma} H_{(\alpha\gamma)(\gamma\beta)} - \sum_{\alpha<\gamma<\beta} H_{(\alpha\gamma)(\beta\gamma)} - \sum_{\beta<\gamma<\alpha} H_{(\gamma\alpha)(\gamma\beta)} + \sum_{\gamma<\alpha,\beta} H_{(\gamma\alpha)(\beta\gamma)} = \sum_{\gamma} H_{(\alpha\gamma)(\gamma\beta)}, \quad (54)$$

where the last sum has no ordering but we know that sorting the indices $(\alpha\gamma)$ and $(\gamma\beta)$ gives the appropriate signs. For $\alpha \neq \beta$, $\boldsymbol{H}_1$ contains all single excitations, so

$$\begin{aligned}\mathrm{Tr}_N\, H^2_{single} &= \binom{K-3}{N-2} \sum_{\alpha\neq\beta,\gamma} \big|H_{(\alpha\gamma)(\gamma\beta)}\big|^2 + \binom{K-4}{N-3} \sum_{\alpha\neq\beta,\gamma\neq\tilde\gamma} H_{(\alpha\gamma)(\gamma\beta)} H_{(\beta\tilde\gamma)(\tilde\gamma\alpha)} \\ &= \binom{K-4}{N-2} \mathrm{Tr}\, \boldsymbol{H}^2_{single} + \binom{K-4}{N-3} \sum_{\alpha\neq\beta,\gamma,\tilde\gamma} H_{(\alpha\gamma)(\gamma\beta)} H_{(\beta\tilde\gamma)(\tilde\gamma\alpha)} \end{aligned} \quad (55)$$

where we used $\binom{n}{k} = \binom{n-1}{k} + \binom{n-1}{k-1}$ to split the first term and add part of it to the second to eliminate the constraint $\gamma \neq \tilde\gamma$. For the diagonal contribution we get three terms, depending on how many orbitals are involved in the density-density operators

$$\begin{aligned}&\mathrm{Tr}_N H^2_{diag} = \quad (56)\\ &= \binom{K-2}{N-2} \sum_{\alpha<\beta} H^2_{(\alpha\beta)(\beta\alpha)} + \binom{K-3}{N-3} \sum_{\substack{\alpha<\beta;,\tilde\alpha<\tilde\beta \\ |\{\alpha,\beta\}\cap\{\tilde\alpha,\tilde\beta\}|=1}} H_{(\alpha\beta)(\beta\alpha)} H_{(\tilde\alpha\tilde\beta)(\tilde\beta\tilde\alpha)} + \binom{K-4}{N-4} \sum_{\substack{\alpha<\beta;,\tilde\alpha<\tilde\beta \\ |\{\alpha,\beta\}\cap\{\tilde\alpha,\tilde\beta\}|=0}} H_{(\alpha\beta)(\beta\alpha)} H_{(\tilde\alpha\tilde\beta)(\tilde\beta\tilde\alpha)} \\ &= \binom{K-4}{N-2} \mathrm{Tr}\, \boldsymbol{H}^2_{diag} + \binom{K-4}{N-3} \Big(2\sum_{\alpha<\beta} H^2_{(\alpha\beta)(\beta\alpha)} + \sum_{\substack{\alpha<\beta;,\tilde\alpha<\tilde\beta \\ |\{\alpha,\beta\}\cap\{\tilde\alpha,\tilde\beta\}|=1}} H_{(\alpha\beta)(\beta\alpha)} H_{(\tilde\alpha\tilde\beta)(\tilde\beta\tilde\alpha)} \Big) + \binom{K-4}{N-4} \big(\mathrm{Tr}\, \boldsymbol{H}_{diag}\big)^2 \end{aligned}$$

where the first and second term were split as above. Writing the middle terms as unsorted sums over orbitals and combining them with the corresponding single-excitation term, we get

$$\mathrm{Tr}_N\, H^2 = \binom{K-4}{N-2} \mathrm{Tr}\, \boldsymbol{H}^2 + \binom{K-4}{N-3} \mathrm{Tr}\, \boldsymbol{H}_1^2 + \binom{K-4}{N-4} \big(\mathrm{Tr}\, \boldsymbol{H}\big)^2, \quad (57)$$

This expression holds for a general two-body operator [13]. For the electron-electron interaction H_{ee} it simplifies further, since there are no single excitations (they would change the L_z eigenvalue), so that we obtain for the N-dependence of the splitting

$$\mathrm{var}_l(N) := \frac{\langle E^2\rangle - \langle E\rangle^2}{N(N-1)(4l+2-N)(4l+1-N)} \quad (58)$$

$$\mathrm{var}_p(N) = \frac{9}{20} {F_2}^2 \quad (59)$$

$$\mathrm{var}_d(N) = \frac{5\cdot 13}{2} \left(\frac{F_2}{9}\right)^2 + \frac{5}{8} \left(\frac{F_2}{9} - 5F_4\right)^2 \quad (60)$$

$$\mathrm{var}_f(N) = 3\cdot 5\cdot 7 \left(\frac{{F_2}^2}{11\cdot 13} + \frac{5{F_4}^2}{2^2\cdot 13} + \big(7F_6\big)^2\right) + \frac{5}{2} \left(11\frac{F_2}{13} + 9\frac{F_4}{13} - 7F_6\right)^2. \quad (61)$$

3 Spin-orbit coupling

We started our discussion with the non-relativistic N-electron Hamiltonian (1). It only operates on the electron coordinates. In the non-relativistic theory, spin is added to the wave function in an ad-hoc way. An electron spin is, in fact, required by relativity, and has, through the Pauli principle, a major effect on the "non-relativistic" electronic structure. Relativistic corrections to the Hamiltonian, on the other hand, tend to be quite weak, as they scale with powers of the inverse speed of light, $1/c \approx 1/137$ in atomic units. The most prominent relativistic effect splitting the levels in an open shell is the coupling of the orbital- with its spin-moment, the spin-orbit coupling

$$H_{SO} = \sum_i \xi(r_i)\, \vec{L}_i \cdot \vec{S}_i \quad \text{with} \quad \xi(r) = \frac{1}{2c^2\, r} \frac{dV_{MF}(r)}{dr}\,. \tag{62}$$

It is a one-body interaction, that is easily diagonalized by a Clebsch-Gordan transformation from our spin-orbitals $\varphi_{n,l,m,\sigma}$ to orbitals of given total angular momentum $\vec{J}_i = \vec{L}_i + \vec{S}_i$, giving two sets of orbitals with total angular momentum quantum numbers $j{=}l{\pm}1/2$ and $\mu{=}-j\ldots j$:

$$j^\dagger_{n,l\pm\frac{1}{2},\mu;\, l;\frac{1}{2}} := \sqrt{\frac{l\mp\mu+\frac{1}{2}}{2l+1}}\, c^\dagger_{n,l,\mu+\frac{1}{2},\downarrow} \pm \sqrt{\frac{l\pm\mu+\frac{1}{2}}{2l+1}}\, c^\dagger_{l,\mu-\frac{1}{2},\uparrow}\,. \tag{63}$$

In this basis we can easily calculate the variance of the spin-orbit-split spectrum:

$$\frac{\mathrm{var}_l^{SO}(N)}{N((4l{+}2){-}N)} = \frac{l(l{+}1)}{4(4l{+}1)} \int_0^\infty dr\, |u_{n,l}(r)|^2\, \xi(r). \tag{64}$$

The variance does, however, not show a simple quadratic dependence on N since, unlike the Slater integrals, the spin-orbit matrix elements increase strongly within a period. In fact, assuming a hydrogen-like system, they scale, for given quantum numbers n and l, as Z^4.

For light atoms the splitting is much smaller than the multiplet splitting, so that it can be treated by perturbation theory, splitting the multiplet terms ${}^{2S+1}L$ into multiplet levels ${}^{2S+1}L_J$ characterized by their total angular momentum J. By the third of Hund's rules, the lowest level is the one with $J = |L{-}S|$ when the shell is less than half-filled, while it has $J = L{+}S$ for $N > 2l{+}1$ (H_{SO} changes sign under the electron-hole transformation (14)). This two-step perturbation approach is called LS or Russell-Saunders coupling. The opposite approach, called jj coupling, of first doing perturbation theory in H_{SO} and then in H_{ee} is only of theoretical interest, since the spin-orbit coupling only becomes dominant for atoms that are so heavy that they are unstable.

Still, as H_{SO} does not commute with $\vec{L}$ and $\vec{S}$ individually, it couples different multiplet terms. For heavy atoms, where the spin-orbit splitting can become appreciable compared to the multiplet splitting, we have to treat H_{ee} and H_{SO} on the same footing, i.e., to diagonalize their sum on the states of an open shell. This approach is called intermediate coupling. Since the Hamiltonian in intermediate coupling has a significantly lower symmetry, the levels can no longer be (almost) uniquely characterized by angular momentum quantum numbers, so that the approach is more numerical in nature. Nevertheless, often the Russell-Saunders levels can give a good indication of the character of the intermediate-coupling levels.

4 Conclusions

We have seen that the description of even a single atom or ion poses a complex many-body problem. Atoms are round [14], so the algebra of angular momenta is key to understanding the structure of their electronic states: Arguments based on angular momenta together with the Pauli exclusion principle allowed Friedrich Hund to formulate rules for the ground-state multiplets even before the Schrödinger equation was known.

Starting from the N-electron Schrödinger equation, we saw that switching from a wave function picture to the representation of many-body states in second quantization provided a crucial simplification by allowing us to represent only physical states and observables, making the construction of the multiplet states of the electron-electron interaction a problem of simple operator algebra. Writing the two-body interaction not as a tensor but as a matrix in 2-electron space makes it easy to perform basis transformations, define basis independent quantities like U_{avg} and J_{avg} from its trace, and even calculate the moments of the N-electron Hamiltonian entirely in terms of a small 2-body matrix. Finally we saw how simple it is in second quantization to relate states with the same number of electrons and holes.

A relativistic effect modifying the multiplet terms originates from the coupling of the orbital momentum with the electron spin. It is a single-body effect that is usually weak, so that it can be well described in degenerate perturbation theory on the multiplet terms. This is the LS- or Russell-Saunders coupling. The opposite procedure of first diagonalizing the spin-orbit Hamiltonian and then introducing the electron-electron repulsion on the degenerate spin-orbit terms, called jj coupling, is only of theoretical interest. For heavy atoms the spin-orbit splitting can, however, become large enough that H_{SO} has to be treated on the same footing as H_{ee}, which is the intermediate coupling scheme.

A systematic study of the interaction parameters including practical parametrizations can be found in [13]. Of particular practical relevance is the analysis of the relative importance of the electron-electron interaction versus the spin-orbit coupling across the periodic table, based on the ratio of the variance of the splitting induced by the respective interaction.

Our main interest in atoms is, of course, as the building block of matter. It is quite remarkable that a large part of their electronic structure survives in the solid, where atomic levels broaden into bands so that an understanding of the constituent atoms allows us to gain deep insights into the electronic structure of the resulting material [14].

Putting an atom in a crystal environment, of course does change its level structure. Particularly interesting is the effect of the potential created by the neighboring ions, which lifts the degeneracy of the levels in an atomic shell already on the single-electron level. Filling those crystal-field levels, following the Aufbauprinzip, results in low-spin states, competing with Hund's first rule, which favors high spin. A nice discussion of this can be found in [3].

To try out the methods explained in this chapter, you may perform practical calculations at

`https://www.cond-mat.de/sims/multiplet/`

A Atomic units

Practical electronic structure calculations are usually done in atomic units, a.u. for short. While the idea behind the atomic units is remarkably simple, in practice there is often some confusion when trying to convert to SI units. We therefore give a brief explanation.

The motivation for introducing atomic units is to simplify the equations. For example, in SI units the Hamiltonian of a hydrogen atom is

$$H = -\frac{\hbar^2}{2m_e}\nabla^2 - \frac{e^2}{4\pi\epsilon_0\, r}\ . \tag{65}$$

When we implement such an equation in a computer program, we need to enter the numerical values of all the fundamental constants. We can avoid this by inventing a system of units in which the *numerical values* of the electron mass m_e, the elementary charge e, the Planck-constant $\hbar$, and the dielectric constant $4\pi\epsilon_0$ are all equal to one. In these units the above equation can be programmed as

$$H = -\frac{1}{2}\nabla^2 - \frac{1}{r}\ . \tag{66}$$

This immediately tells us: 1 a.u. mass $= m_e$ and 1 a.u. charge $= e$. To complete the set of basis units we still need the atomic unit of length, which we call a_0, and of time, t_0. To find the values of a_0 and t_0 we write $\hbar$ and $4\pi\epsilon_0$ (using simple dimensional analysis) in atomic units: $\hbar = 1\, m_e a_0^2/t_0$ and $4\pi\epsilon_0 = 1\, t_0^2 e^2/(m_e a_0^3)$. Solving this system of equations, we find

1 a.u. length	$= a_0 =$	$4\pi\epsilon_0\hbar^2/m_e e^2$	$\approx 5.2918\cdot 10^{-11}$	m
1 a.u. mass	$= m_e =$		$\approx 9.1095\cdot 10^{-31}$	kg
1 a.u. time	$= t_0 =$	$(4\pi\epsilon_0)^2\hbar^3/m_e e^4$	$\approx 2.4189\cdot 10^{-17}$	s
1 a.u. charge	$= e =$		$\approx 1.6022\cdot 10^{-19}$	C

The atomic unit of length, a_0, is the Bohr radius. As the dimension of energy is mass times length squared divided by time squared, its atomic unit is $m_e a_0^2/t_0^2 = m_e e^4/(4\pi\epsilon_0)^2\hbar^2$. Because of its importance the atomic unit of energy has a name, the Hartree. One Hartree is minus twice the ground-state energy of the hydrogen atom, about 27.211 eV.

It would be tempting to try to set the numerical value of all fundamental constants to unity. But this must obviously fail, as the system of equations to solve becomes overdetermined when we try to prescribe the numerical values of constants that are not linearly independent in the space of basis units. Thus, we cannot, e.g., choose also the speed of light to have value one, as would be practical for relativistic calculations. Instead, in atomic units it is given by $c\, t_0/a_0 = 4\pi\varepsilon_0\hbar c/e^2 = 1/\alpha$, where α is the fine structure constant. Thus $c = \alpha^{-1}$ a.u. ≈ 137 a.u. The Bohr magneton is $\mu_B = 1/2$ a.u. The Boltzmann constant k_B, on the other hand, is independent of the previous constants. Setting its value to one fixes the unit of temperature to 1 a.u. temperature $= m_e e^4/(4\pi\epsilon_0)^2\hbar^2 k_B = Ha/k_B \approx 3.158\cdot 10^5$ K.

B Second quantization

The formalism of second quantization for electrons is the generalization of the Dirac formalism of single-electron quantum mechanics to many-electron system. The key idea is to eliminate the coordinates of the wave function and absorb them in the representation of the operators instead. Wave functions are then written in terms of Dirac states using the Dirac delta function: $\varphi_n(x) = \langle x|n\rangle$. In second quantization, field operators $\hat\Psi(x)$ take the role of $\langle x|$, so that $\varphi_n(x) = \langle 0|\hat\Psi(x)\, c_n^\dagger|0\rangle$, where the orbital is represented by

$$c_n^\dagger := \int dx\, \varphi_n(x)\, \hat\Psi^\dagger(x)\,, \tag{67}$$

$|0\rangle$ is the zero-electron (vacuum) state defined by

$$\hat\Psi(x)|0\rangle = 0 \quad \text{and} \quad \langle 0|0\rangle = 1\,, \tag{68}$$

and the field operators are defined to fulfill the anticommutation relations $\big(\{a,\, b\} := ab + ba\big)$

$$\big\{\hat\Psi(x),\, \hat\Psi(x')\big\} = 0 \quad \text{and} \quad \big\{\hat\Psi(x),\, \hat\Psi^\dagger(x')\big\} = \delta(x{-}x')\,. \tag{69}$$

From the adjoint of the first anticommutator follows, in particular, that $\big(\hat\Psi(x)^\dagger\big)^2 = 0$, which is the Pauli exclusion principle in second quantization. These relations define the formalism completely.
The representation of single-electron functions generalizes to N-electron Slater determinants

$$\Phi_{\alpha_1\dots\alpha_N}(x_1\dots x_N) = \frac{1}{\sqrt{N!}}\begin{vmatrix} \varphi_{\alpha_1}(x_1)\cdots\varphi_{\alpha_N}(x_1) \\ \vdots \qquad\qquad \vdots \\ \varphi_{\alpha_1}(x_N)\cdots\varphi_{\alpha_N}(x_N)\end{vmatrix} = \frac{1}{\sqrt{N!}}\big\langle 0\big|\hat\Psi(x_1)\cdots\hat\Psi(x_N)\; c_{\alpha_N}^\dagger\cdots c_{\alpha_1}^\dagger\big|0\big\rangle. \tag{70}$$

Their overlap is

$$\begin{aligned}\int dx_1\cdots dx_N\, \overline{\Phi_{\alpha_1\dots\alpha_N}(x_1\dots x_N)}\, \Phi_{\beta_1\dots\beta_N}(x_1\dots x_N) \\ = \langle 0|c_{\alpha_1}\cdots c_{\alpha_N}\, c_{\beta_N}^\dagger\cdots c_{\beta_1}^\dagger|0\rangle = \begin{vmatrix} \langle\alpha_1|\beta_1\rangle\cdots\langle\alpha_1|\beta_N\rangle \\ \vdots \qquad\qquad \vdots \\ \langle\alpha_N|\beta_1\rangle\cdots\langle\alpha_N|\beta_N\rangle\end{vmatrix}\end{aligned} \tag{71}$$

so that N-electron Slater determinants constructed from a complete orthonormal set of single-electron orbitals form an orthonormal basis of the N-electron Hilbert space, when only Slater determinants with some given ordering of the orbitals, e.g., $\alpha_1 < \alpha_2 < \ldots < \alpha_N$, are chosen.
The key point of (70) is that the second quantized form allows us to split the coordinates form the orbital content. The latter is the generalization of the Dirac state. Introducing the occupation number representation with $n_i \in \{0, 1\}$ to make the chosen sorting of the orbitals and the corresponding operators manifest, a Slater state is written as

$$|n_1, n_2, \ldots\rangle := \prod_i \big(c_{n_i}^\dagger\big)^{n_i}|0\rangle. \tag{72}$$

The coordinates are then included in with the operators, giving the operators in second quantization. For a one-electron observable $\sum_{i=1}^{N} M_1(x_i)$ we find (see [4] for the derivations)

$$\hat{M}_1 = \int dx\, \hat{\Psi}(x)^\dagger\, M(x)\, \hat{\Psi}(x)\,, \tag{73}$$

for a two-electron operator $\sum_{i<j} M_2(x_i, x_j)$ we get

$$\hat{M}_2 = \frac{1}{2} \int dx \int dx'\, \hat{\Psi}(x)^\dagger \hat{\Psi}(x')^\dagger\, M(x,x')\, \hat{\Psi}(x') \hat{\Psi}(x)\,. \tag{74}$$

Quite remarkably, while the operators in first quantization contain an explicit N-dependence, the form of the same operator in second quantization is independent of the particle number. This makes second quantization so suitable for working in Fock space, as, e.g., in BCS theory. Another crucial advantage of working in the second-quantization formalism is that it only allows us to express physical, i.e., antisymmetric, wave functions and physical operators, i.e., those that act on all electrons in the same way (e.g., total angular momenta, but not angular momenta acting on an individual electron, which would violate the indistinguishability of electrons [4]). Given a complete orthonormal orbital basis $\{\varphi_n\}$, we can invert (67) to write the field-operators $\hat{\Psi}^\dagger$ as a linear combination of the orbital operators $c_n^\dagger$. Inserting this into (73), we get

$$\hat{M}_1 = \sum_{\alpha\beta} \langle \alpha | M_1 | \beta \rangle\, c_\alpha^\dagger c_\beta \tag{75}$$

where the $\langle \alpha | M | \beta \rangle$ are the matrix elements of the one-body operator in the orbital basis. Similarly, we obtain

$$\hat{M}_2 = \frac{1}{2} \sum_{\alpha\beta\gamma\delta} \langle \alpha\beta | M_2 | \gamma\delta \rangle\, c_\alpha^\dagger c_\beta^\dagger c_\gamma c_\delta \tag{76}$$

with the four-index tensor

$$\langle \alpha\beta | M_2 | \gamma\delta \rangle \;:=\; \int dx \int dx'\, \overline{\varphi_\alpha(x) \varphi_\beta(x')}\, M(x,x')\, \varphi_\gamma(x') \varphi_\delta(x). \tag{77}$$

Realizing that exchanging the two creation or annihilation operators in (76) connects the same many-body states, we can collect all four such terms by imposing an ordering on the operators:

$$\hat{M}_2 = \sum_{\alpha<\beta;\gamma>\delta} \big(\underbrace{\langle \alpha\beta | M_2 | \gamma\delta \rangle - \langle \alpha\beta | M_2 | \delta\gamma \rangle}_{=: M_{(\alpha\beta)(\gamma\delta)}} \big) c_\alpha^\dagger c_\beta^\dagger c_\gamma c_\delta\,. \tag{78}$$

Instead of a tensor, the $M_{(\alpha\beta)(\gamma\delta)}$ form a matrix in the two-electron-like space spanned by sorted pairs of operators. This makes them quite convenient to handle. Changes in the orbital basis like $c_\alpha^\dagger = \sum_n c_n^\dagger U_{n,\alpha}$ described by a unitary single-electron matrix $\boldsymbol{U}$ are then easily written as unitary transformation in two-electron space

$$c_\alpha^\dagger c_\beta^\dagger = \sum_{n,m} c_n^\dagger c_m^\dagger U_{n,\alpha} U_{m,\beta} = \sum_{n<m} c_n^\dagger c_m^\dagger \big(U_{n,\alpha} U_{m,\beta} - U_{m,\alpha} U_{n,\beta} \big) \tag{79}$$

which effects the basis change in the two-electron matrix $M_{(\alpha\beta)(\gamma\delta)}$.

C Addition theorem for spherical harmonics

Using the completeness of the spherical harmonics, we can expand any function of a single coordinate $f(\vec{r})=\sum_{m,l} a_{l,m}(r)\, Y_{l,m}(\vartheta,\varphi)$. Similarly, we can expand functions of two coordinates

$$f(\vec{r},\vec{r}\,') = \sum_{l,m} a_{l,m}(r,\, r',\vartheta',\varphi')\, Y_{l,m}(\vartheta,\varphi) = \sum_{l,m} \Big(\sum_{l',m'} a_{\substack{l,m,\\ l',m'}}(r,r')\, Y_{l',m'}(\vartheta',\varphi') \Big) Y_{l,m}(\vartheta,\varphi).$$

The expansion simplifies considerably when the function is invariant under simultaneous rotations of $\vec{r}$ and $\vec{r}\,'$, i.e., when $\big(\vec{L}+\vec{L}'\big)s(\vec{r},\vec{r}\,')=0$. This is, e.g., the case for any function that depends only on the scalar products of $\vec{r}$ and $\vec{r}\,'$, e.g.,

$$iL_x\, s(\vec{r}\cdot\vec{r}\,') = \left(r_y\frac{\partial}{\partial r_z} - r_z\frac{\partial}{\partial r_y}\right) s(r_x r_{x'} + r_y r_{y'} + r_z r_{z'}) = s'(\vec{r}\cdot\vec{r}\,')\big(r_y r_{z'} - r_z r_{y'}\big) = -iL'_x s(\vec{r}\cdot\vec{r}\,').$$

Then $s(\vec{r},\vec{r}\,')$ must be an eigenfunction of $\big(\vec{L}+\vec{L}'\big)^2$ with eigenvalue 0. From adding angular momenta we know that the products may only contain an $l_{tot}=0$ contribution when $l=l'$. In addition, $\big(L_z+L'_z\big)s(\vec{r},\vec{r}\,')=0$, i.e., $m'=-m$, so that

$$s(\vec{r},\vec{r}\,') = \sum_{l,m} a_{l,m}(r,r')\, Y_{l,-m}(\vartheta',\varphi')\, Y_{l,m}(\vartheta,\varphi)\,.$$

Using $\big(\vec{L}+\vec{L}'\big)^2 = \vec{L}^2 + \vec{L}'^2 + 2L_zL'_z + L_+L'_- + L_-L'_+$ with $L_\pm Y_{l,m} = \sqrt{(l\pm m+1)(l\mp m)}\, Y_{l,m\pm1}$ we obtain a homogeneous linear system of equations

$$\begin{aligned} 0 &= \big(\vec{L}+\vec{L}'\big)^2\, s(\vec{r},\vec{r}\,') \\ &= \sum_{l,m} \Big(a_{l,m}\big(2l(l+1)-2m^2\big) + a_{l,m-1}(l+m)(l-m+1) + a_{l,m+1}(l-m)(l+m+1) \Big) Y'_{l,-m} Y_{l,m} \end{aligned}$$

with the non-trivial solution $a_{l,m}(r,r') = (-1)^m a_l(r,r')$. Hence

$$s(\vec{r},\vec{r}\,') = \sum_{l=0}^{\infty} a_l(r,r') \sum_{m=-l}^{l} (-1)^m Y_{l,-m}(\vartheta',\varphi')\, Y_{l,m}(\vartheta,\varphi) \tag{80}$$

$$= \sum_{l=0}^{\infty} a_l(r,r') \sum_{m=-l}^{l} \overline{Y_{l,m}(\vartheta',\varphi')}\, Y_{l,m}(\vartheta,\varphi) \tag{81}$$

where (80) is reminiscent of a Kramers pair singlet (6). The expansion coefficients are easily calculated when choosing coordinates such that $\vec{r}\,' = r'\hat{z}$, i.e., $\vartheta'=0$

$$a_l(r,r') = \int_0^{2\pi} d\varphi \int_{-1}^{1} d\cos\vartheta\, \overline{Y_{l,0}(\vartheta,\varphi)} \sqrt{\frac{4\pi}{2l+1}}\, s(\vec{r},r'\hat{z}) \tag{82}$$

For $s(\vec{r},\vec{r}\,') = P_l(\hat{r}\cdot\hat{r}')$ we find the addition theorem for spherical harmonics

$$P_l(\hat{r}\cdot\hat{r}') = \sqrt{\frac{4\pi}{2l+1}} Y_{l,0}(\arccos(\hat{r}\cdot\hat{r}'),0) = \frac{4\pi}{2l+1} \sum_{m=-l}^{l} \overline{Y_{l,m}(\vartheta',\varphi')}\, Y_{l,m}(\vartheta,\varphi)\,. \tag{83}$$

Setting $\hat{r}' = \hat{r}$, it follows as a corollary that the charge density of closed shells is spherical

$$\sum_{m=-l}^{l} \left|Y_{l,m}(\vartheta,\varphi)\right|^2 = \frac{2l+1}{4\pi}\,. \tag{84}$$

For the electron-electron repulsion we obtain the multipole expansion

$$\frac{1}{|\vec{r}-\vec{r}\,'|} = \frac{1}{\sqrt{r^2-2\vec{r}\cdot\vec{r}\,'+r'^2}} = \sum_{l=0}^{\infty} \frac{r_<^l}{r_>^{l+1}}\, P_l(\hat{r}\cdot\hat{r}') = \sum_{l=0}^{\infty} \frac{r_<^l}{r_>^{l+1}} \frac{4\pi}{2l+1} \sum_{m=-l}^{l} \overline{Y_{l,m}(\vartheta',\varphi')}\, Y_{l,m}(\vartheta,\varphi), \tag{85}$$

where the choice $r_< := \min(r,r')$ and $r_> := \max(r,r')$ makes the power series converge. The series is obtained from the generating function of the Legendre polynomials

$$\frac{1}{\sqrt{1-2xt+t^2}} = \sum_{n=0}^{\infty} P_n(x)\, t^n\,. \tag{86}$$

To convince ourselves that the $P_n(x)$ are indeed the Legendre polynomials, we expand the left-hand side in powers of t and find $P_0(x) = 1$ and $P_1(x) = x$. Taking the derivative of (86) with respect to t gives

$$\frac{x-t}{\left(1-2xt+t^2\right)^{3/2}} = \sum_{n=1}^{\infty} n\, P_n(x)\, t^{n-1}.$$

multiplying by $1-2xt+t^2$, inserting (86) on the left-hand side, and comparing coefficients for $n{>}0$, gives the recursion relation for the Legendre polynomials

$$(n{+}1)P_{n+1}(x) = (2n{+}1)x\, P_n(x) - n\, P_{n-1}(x)\,. \tag{87}$$

Likewise, a plane wave can be expanded into spherical plane waves

$$e^{i\vec{k}\cdot\vec{r}} = 4\pi \sum_{l=0}^{\infty} i^l\, j_l(kr) \sum_{m=-l}^{l} \overline{Y_{l,m}(\vartheta',\varphi')}\, Y_{l,m}(\vartheta,\varphi), \tag{88}$$

using the integral representation of the spherical Bessel functions

$$a_l(r,k) = 2\pi \int_{-1}^{1} dx\, P_l(x)\, e^{ikr\,x} = 4\pi\, i^l\, j_l(kr). \tag{89}$$

D Gaunt coefficients

Gaunt coefficients appear when expanding products of spherical harmonics

$$Y_{l,m}(\vartheta,\varphi)\,Y_{l',m'}(\vartheta,\varphi) = \sum_{k=0}^{\infty}\sum_{\mu=-k}^{k} \left\langle Y_{k,\mu}\middle| Y_{l,m}Y_{l',m'}\right\rangle Y_{k,\mu}(\vartheta,\varphi)\,. \tag{90}$$

Because of the product rule, the angular momentum operators act on the product of the spherical harmonics the same way as they act on independent angular momenta, e.g.,

$$L_+\,Y_{l,m}\,Y_{l',m'} = \big(L_+\,Y_{l,m}\big)Y_{l',m'} + Y_{l,m}\,\big(L_+\,Y_{l',m'}\big)\,. \tag{91}$$

Thus, for fixed l, l', and k, the integrals of three spherical harmonics $\left\langle Y_{k,\mu}\middle| Y_{l,m}Y_{l',m'}\right\rangle$ fulfill the same recursion relation as the Clebsch-Gordan coefficients $\langle k,\mu;\ l;\ l'|l,m;\ l',m'\rangle$ (Wigner-Eckart theorem). In particular, evaluating $\left\langle Y_{k,\mu}\middle| L_z|Y_{l,m}Y_{l',m'}\right\rangle$ shows that the integrals vanish for $\mu \neq m{+}m'$ and consequently are real. More generally, the products $Y_{l,m}\,Y_{l',m'}$ behaves as if we were adding two angular momenta l and l', so that the $\left\langle Y_{k,m+m'}\middle| Y_{l,m}Y_{l',m'}\right\rangle$ vanish for $k < |l{-}l'|$ and $k > l{+}l'$. The difference to adding angular momenta is that the products of spherical harmonics are not orthonormal (e.g., $\langle Y_{0,0}Y_{0,0}|Y_{l,m}Y_{l,-m}\rangle = (-1)^m/4\pi$), so that the space spanned by the $Y_{l,m}Y_{l',m'}$ for fixed l and l' may be smaller than $(2l{+}1){\times}(2l'{+}1)$. In fact, from the inversion symmetry $Y_{l,m}(\pi{-}\vartheta,\varphi{+}\pi) = (-1)^l\,Y_{l,m}(\vartheta,\varphi)$ of the spherical harmonics we see by changing the variables of integration that

$$\left\langle Y_{k,\mu}\middle| Y_{l,m}Y_{l',m'}\right\rangle = (-1)^{k+l+l'}\left\langle Y_{k,\mu}\middle| Y_{l,m}Y_{l',m'}\right\rangle \tag{92}$$

so that the coefficients also vanish when $k{+}l{+}l'$ is odd, and (90) consequently simplifies to

$$Y_{l,m}(\vartheta,\varphi)\,Y_{l',m'}(\vartheta,\varphi) = \sum_{k=|l-l'|,\,|l-l'|+2,\ldots,\,l+l'} \left\langle Y_{k,m+m'}\middle| Y_{l,m}Y_{l',m'}\right\rangle Y_{k,m+m'}(\vartheta,\varphi)\,. \tag{93}$$

Using $\overline{Y_{l,m}} = (-1)^m\,Y_{l,-m}$ we can write the Gaunt coefficients in a form more convenient for the use in the electron-electron repulsion part of the Hamiltonian

$$c^{(k,l,l')}_{m,m'} := \sqrt{\frac{4\pi}{2k{+}1}}\left\langle Y_{l,m}\middle| Y_{k,m-m'}Y_{l',m'}\right\rangle = (-1)^{m'}\sqrt{\frac{4\pi}{2k{+}1}}\left\langle Y_{k,m'-m}\middle| Y_{l,-m}Y_{l',m'}\right\rangle. \tag{94}$$

They can be readily written as matrices $\boldsymbol{c}^{(k,l,l')}$ with indices m and m', where matrix elements with $|m{-}m'| = |\mu| > k$ (on the μth side-diagonal) vanish so that $\boldsymbol{c}^{(k,l,l')}$ is a $2k{+}1$-diagonal $(2l{+}1)\times(2l'{+}1)$ matrix, in particular $c^{(k=0,l,l')}_{m,m'} = \delta_{l,l'}\,\delta_{m,m'}$. Matrices with exchanged $l{\leftrightarrow}l'$ are related by

$$c^{(k,l,l')}_{m,m'} = (-1)^{m+m'}\,c^{(k,l',l)}_{-m',-m} \quad\text{and}\quad c^{(k,l,l')}_{m,m'} = (-1)^{m-m'}\,c^{(k,l',l)}_{m',m} \tag{95}$$

where in the last relation we used that the Gaunt coefficients are real. Combining the two transformations gives the inversion symmetry of each $\boldsymbol{c}^{k,l,l'}$ matrix

$$c^{(k,l,l')}_{m,m'} = c^{(k,l,l')}_{-m,-m'}\,. \tag{96}$$

For the special case $l'{=}l$ eq. (95) give the symmetries of $\boldsymbol{c}^{(k,l,l)}$ under reflection along the anti-diagonal and the diagonal, respectively.
Using

$$L_\pm Y_{l,m} = \sqrt{(l{\pm}m{+}1)(l{\mp}m)}\, Y_{l,m\pm1}\,,$$

the elements of the matrix $\boldsymbol{c}^{(k,l,l')}$ are related via $\big\langle Y_{l,m}|L_\pm\, Y_{k,m-m'\mp1}Y_{l',m'}\big\rangle$ by

$$\sqrt{(l{\mp}m{+}1)(l{\pm}m)}c^{(k,l,l')}_{m\mp1,m'} = \sqrt{(k{\pm}(m{-}m')(k{\mp}(m{-}m'){+}1)}c^{(k,l,l')}_{m,m'} + \sqrt{(l'{\pm}m'{+}1)(l'{\mp}m')}c^{(k,l,l')}_{m,m'\pm1} \tag{97}$$

which relates matrix elements according to the patterns $\begin{smallmatrix}\bullet\\ \bullet\!\!-\!\!\bullet\end{smallmatrix}$ for L_+ and $\begin{smallmatrix}\bullet\!\!-\!\!\bullet\\ \bullet\end{smallmatrix}$ for L_-. With one of the prefactors vanishing, these relations become simple two-point recursions along the border of the matrix ($m' = \pm l'$ for the L_+ or $m = \pm l$ for the L_- formula), as well as along the outermost side-diagonals ($m{-}m' = k{+}1$ for L_+ or $m{-}m' = -k{-}1$ for L_-).
Filling the matrix $\boldsymbol{c}^{(k,l,l')}$ according to (97) starting, e.g., from $c^{(k,l,l')}_{-l,-l'} = 1$, using the L_+ recursion to fill the top row and then the L_- recursion to fill the subsequent rows from right to left, we get the matrix of Clebsch-Gordan coefficients

$$\langle k, m{+}m';\, l; l'|l, m;\, l', m'\rangle = (-1)^{m'}\, \bar{c}^{(k,l,l')}_{-m,m'}$$

by normalizing any of the (side)diagonals of $\boldsymbol{c}$ to get $\bar{\boldsymbol{c}}$ (since the μ-th side diagonal holds the expansion coefficients of $|k, \mu;\, l;\, l'\rangle$).
To obtain the Gaunt matrices, we still need the reduced matrix element. A simple approach for small values of l and l' is to use

$$Y_{l,0}(\vartheta,\varphi) = \sqrt{\frac{2l{+}1}{4\pi}}\, P_l(\cos\vartheta)$$

and calculate $c^{(k,l,l')}_{0,0}$ by explicit integration over the corresponding Legendre polynomials, e.g.,

$$c^{(k,l,l)}_{0,0} = \sqrt{\frac{4\pi}{2k{+}1}}\big\langle Y_{l,0}\big|Y_{k,0}\, Y_{l,0}\big\rangle = \frac{2l{+}1}{2}\int_{-1}^{1} dx\, P_l(x)^2\, P_k(x) \tag{98}$$

Using the recursion relation for the Legendre polynomials (87) with starting points $P_0(x) = 1$ and $P_1(x) = x$, we get by explicit integration over the product of polynomials

l	1	2		3		
k	2	2	4	2	4	6
$c^{(k,l,l)}_{0,0}$	$\frac{2}{5}$	$\frac{2}{7}$	$\frac{2}{7}$	$\frac{2^2}{3\cdot5}$	$\frac{2}{11}$	$\frac{2^2\cdot5^2}{3\cdot11\cdot13}$

(99)

from which we obtain the Gaunt matrices for p-, d-, and f-shells listed below. There are, of course, more refined methods that remain fast and accurate also for large angular momenta [13].

p-shell:

$$c^{(2,1,1)}_{m,m'} = \frac{1}{5}\begin{pmatrix} -1 & \sqrt{3} & -\sqrt{6} \\ -\sqrt{3} & 2 & -\sqrt{3} \\ -\sqrt{6} & \sqrt{3} & -1 \end{pmatrix}$$

d-shell:

$$c^{(2,2,2)}_{m,m'} = \frac{1}{7}\begin{pmatrix} -2 & \sqrt{6} & -2 & 0 & 0 \\ -\sqrt{6} & 1 & 1 & -\sqrt{6} & 0 \\ -2 & -1 & 2 & -1 & -2 \\ 0 & -\sqrt{6} & 1 & 1 & -\sqrt{6} \\ 0 & 0 & -2 & \sqrt{6} & -2 \end{pmatrix}$$

$$c^{(4,2,2)}_{m,m'} = \frac{1}{3{\cdot}7}\begin{pmatrix} 1 & -\sqrt{5} & \sqrt{15} & -\sqrt{35} & \sqrt{70} \\ \sqrt{5} & -4 & \sqrt{30} & -\sqrt{40} & \sqrt{35} \\ \sqrt{15} & -\sqrt{30} & 6 & -\sqrt{30} & \sqrt{15} \\ \sqrt{35} & -\sqrt{40} & \sqrt{30} & -4 & \sqrt{5} \\ \sqrt{70} & -\sqrt{35} & \sqrt{15} & -\sqrt{5} & 1 \end{pmatrix}$$

f-shell:

$$c^{(2,3,3)}_{m,m'} = \frac{1}{3{\cdot}5}\begin{pmatrix} -5 & 5 & -\sqrt{10} & 0 & 0 & 0 & 0 \\ -5 & 0 & \sqrt{15} & -\sqrt{20} & 0 & 0 & 0 \\ -\sqrt{10} & -\sqrt{15} & 3 & \sqrt{2} & -\sqrt{24} & 0 & 0 \\ 0 & -\sqrt{20} & -\sqrt{2} & 4 & -\sqrt{2} & -\sqrt{20} & 0 \\ 0 & 0 & -\sqrt{24} & \sqrt{2} & 3 & -\sqrt{15} & -\sqrt{10} \\ 0 & 0 & 0 & -\sqrt{20} & \sqrt{15} & 0 & -5 \\ 0 & 0 & 0 & 0 & -\sqrt{10} & 5 & -5 \end{pmatrix}$$

$$c^{(4,3,3)}_{m,m'} = \frac{1}{3{\cdot}11}\begin{pmatrix} 3 & -\sqrt{30} & \sqrt{54} & -\sqrt{63} & \sqrt{42} & 0 & 0 \\ \sqrt{30} & -7 & \sqrt{32} & -\sqrt{3} & -\sqrt{14} & \sqrt{70} & 0 \\ \sqrt{54} & -\sqrt{32} & 1 & \sqrt{15} & -\sqrt{40} & \sqrt{14} & \sqrt{42} \\ \sqrt{63} & -\sqrt{3} & -\sqrt{15} & 6 & -\sqrt{15} & -\sqrt{3} & \sqrt{63} \\ \sqrt{42} & \sqrt{14} & -\sqrt{40} & \sqrt{15} & 1 & -\sqrt{32} & \sqrt{54} \\ 0 & \sqrt{70} & -\sqrt{14} & -\sqrt{3} & \sqrt{32} & -7 & \sqrt{30} \\ 0 & 0 & \sqrt{42} & -\sqrt{63} & \sqrt{54} & -\sqrt{30} & 3 \end{pmatrix}$$

$$c^{(6,3,3)}_{m,m'} = \frac{5}{3{\cdot}11{\cdot}13}\begin{pmatrix} -1 & \sqrt{7} & -\sqrt{28} & \sqrt{84} & -\sqrt{210} & \sqrt{462} & -\sqrt{924} \\ -\sqrt{7} & 6 & -\sqrt{105} & \sqrt{224} & -\sqrt{378} & \sqrt{504} & -\sqrt{462} \\ -\sqrt{28} & \sqrt{105} & -15 & \sqrt{350} & -\sqrt{420} & \sqrt{378} & -\sqrt{210} \\ -\sqrt{84} & \sqrt{224} & -\sqrt{350} & 20 & -\sqrt{350} & \sqrt{224} & -\sqrt{84} \\ -\sqrt{210} & \sqrt{378} & -\sqrt{420} & \sqrt{350} & -15 & \sqrt{105} & -\sqrt{28} \\ -\sqrt{462} & \sqrt{504} & -\sqrt{378} & \sqrt{224} & -\sqrt{105} & 6 & -\sqrt{7} \\ -\sqrt{924} & \sqrt{462} & -\sqrt{210} & \sqrt{84} & -\sqrt{28} & \sqrt{7} & -1 \end{pmatrix}$$

References

[1] F. Hund, Z. Phys. **33**, 345 (1925)

[2] P.M.A. Dirac, Proc. Roy. Soc. **123**, 714 (1929)

[3] R. Eder: *Multiplets in Transition Metal Ions*, in
E. Pavarini, E. Koch, F. Anders, and M. Jarrell (eds):
Correlated Electrons: From Models to Materials
Modeling and Simulation Vol. 2 (Forschungszentrum Jülich, 2012)

[4] E. Koch: *Exact Diagonalization and Lanczos Method*, in
E. Pavarini, E. Koch, and S. Zhang (eds.): *Many-Body Methods for Real Materials*
Modeling and Simulation Vol. 9 (Forschungszentrum Jülich, 2019)

[5] G.Racah, Phys. Rev. **61**, 186 (1942)

[6] G. Racah, Phys. Rev. **62**, 438 (1942)

[7] G. Racah, Phys. Rev. **63**, 367 (1943)

[8] G. Racah, Phys. Rev. **76**, 1352 (1949)

[9] B.R. Judd: *Operator Techniques in Atomic Spectroscopy*
(Princeton University Press, 1998)

[10] C.W. Nielson and G.F. Koster: *Spectroscopic Coefficients for the p^n, d^n, and f^n Configurations* (MIT Press, 1963)

[11] J. Avery: *Creation and Annihilation Operators* (McGraw-Hill, 1976)

[12] E.U. Condon and G.H. Shortley: *The Theory of Atomic Spectra*
(Cambridge University Press, 1935)

[13] Q. Zhang: *Building Effective Models for Correlated Electron Systems*
(PhD Thesis, RWTH Aachen University, 2020)

[14] O.K. Andersen: *From Materials to Models: Deriving Insight from Bands*, in
E. Pavarini, E. Koch, A. Lichtenstein, and D. Vollhardt (eds.):
DMFT: From Infinite Dimensions to Real Materials
Modeling and Simulation, Vol. 8 (Forschungszentrum Jülich, 2018)

6 The Physics of Doped Mott Insulators

Robert Eder
Institute for Quantum Materials and Technologies
Karlsruhe Institute of Technology

Contents

E. Pavarini and E. Koch (eds.)
Topology, Entanglement, and Strong Correlations
Modeling and Simulation Vol. 10
Forschungszentrum Jülich, 2020, ISBN 978-3-95806-466-9
http://www.cond-mat.de/events/correl20

1 Introduction

Following the discovery of copper oxide superconductors with their spectacularly high superconducting transition temperatures by Bednorz and Müller [1], the problem of the doped Mott insulator has become a central issue in solid state physics. Still, after more than 30 years of research and thousands of papers devoted to this subject, there is no generally accepted theory for this problem. So what exactly do we mean by 'doped Mott insulator' and why is this problem so hard to solve?

Let us consider a two-dimensional square lattice with lattice constant $a = 1$, which consists of $N = L^2$ sites and impose periodic boundary conditions with period L along both the x- and y-direction. We denote the number of electrons with spin σ by N_σ, the total number of electrons by $N_e = N_\uparrow + N_\downarrow$. Also, we denote densities per site by n, for example $n_e = N_e/N$. To explain the idea of a Mott-insulator it would be neither necessary that the system is two-dimensional, nor that we have a square lattice, but this is the suitable geometry to describe the CuO_2 planes in copper oxide superconductors. We assume that there is one s-like atomic orbital $|\phi_i\rangle$ centered at each lattice site i. Orbitals on different sites are assumed to be orthogonal, $\langle\phi_i|\phi_j\rangle = \delta_{i,j}$, but there may be nonvanishing matrix elements of the Hamiltonian – that means the kinetic and potential energy – between them, $\langle\phi_i|H|\phi_j\rangle = -t_{i,j}$. We assume that the orbital $|\phi\rangle$ is the same for each lattice site, whence the matrix element $\langle\phi_i|\phi_j\rangle$ depends only on the distance between i and j: $t_{i,j} = t_{\mathbf{R}_i - \mathbf{R}_j}$. We also assume that the atomic orbital $|\phi_i\rangle$ decays exponentially, $\langle\mathbf{r}|\phi_i\rangle \propto e^{-|\mathbf{r}-\mathbf{R}_i|/\zeta}$, so we expect $t_{\mathbf{R}} \propto e^{-|\mathbf{R}|/\zeta}$ and $t_{i,j}$ will differ appreciably from zero only for close neighbors. Introducing operators $c^\dagger_{i,\sigma}$ which create an electron of z-spin σ in orbital $|\phi_i\rangle$ the Hamiltonian reads

$$H_0 = -\sum_{i,j} t_{i,j} \sum_\sigma c^\dagger_{i,\sigma} c_{j,\sigma} = \sum_{\mathbf{k}} \sum_\sigma \varepsilon_{\mathbf{k}}\, c^\dagger_{\mathbf{k},\sigma} c_{\mathbf{k},\sigma}.$$

The second expression for H_0 is obtained by Fourier transformation

$$c^\dagger_{\mathbf{k},\sigma} = \frac{1}{\sqrt{N}} \sum_j e^{i\mathbf{k}\cdot\mathbf{R}_j}\, c^\dagger_{j,\sigma} \quad\Rightarrow\quad \varepsilon_{\mathbf{k}} = -\frac{1}{N}\sum_{i,j} t_{i,j}\, e^{i\mathbf{k}\cdot(\mathbf{R}_i - \mathbf{R}_j)} = -\sum_{\mathbf{R}} t_{\mathbf{R}}\, e^{i\mathbf{k}\cdot\mathbf{R}}. \tag{1}$$

Here $\mathbf{k} = \left(\frac{2n\pi}{L}, \frac{2m\pi}{L}\right)$ with $-L/2 < m, n \le L/2$ is a wave vector in the first Brillouin zone. Unless otherwise stated we will from now on assume that $t_{i,j}$ is different from zero only for nearest neighbors i and j and denote its value by t, whence $\varepsilon_{\mathbf{k}} = -2t\big(\cos(k_x) + \cos(k_y)\big)$. The number of wave vectors $\mathbf{k}$ equals N and the ground state for N electrons is obtained by 'filling the band from below', that means occupying those $N/2$ wave vectors $\mathbf{k}$ which minimize the sum $\sum_{\mathbf{k}} \varepsilon_{\mathbf{k}}$ with two electrons of opposite spin. The band therefore is half-filled, the Fermi surface covers precisely half of the Brillouin zone and we have a metal.

In the discussion so far we have ignored the Coulomb interaction between the electrons. Recalling that the atomic orbital $\langle\mathbf{r}|\phi_i\rangle \propto e^{-|\mathbf{r}-\mathbf{R}_i|/\zeta}$, we expect that if the orbital is occupied by two electrons of opposite spin, the electrostatic energy is $U \propto e^2/\zeta$, whereas it is $\propto e^2/a$ if the electrons are in orbitals on different sites. If we take the limit of a 'small atomic orbital',

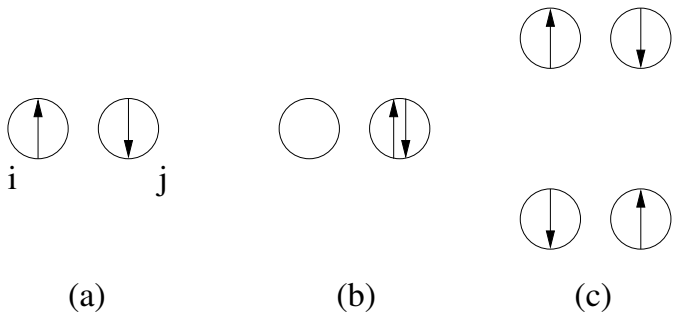

Fig. 1: *An exchange process in a Mott insulator.*

$\zeta \to 0$, we find $U/t \to \infty$ – accordingly we neglect the Coulomb repulsion $\propto e^2/a$ between electrons in different orbitals. Taking the extreme limit $U/t = \infty$ and returning to the problem of finding the ground state with N electrons we find that there is precisely one electron in each of the N orbitals (putting two electrons into the same orbital increases the energy by the large amount U). The electrons thus are 'frozen in' and cannot react to an applied electric field, so that the system is an insulator. This is the prototype of a *Mott insulator*: a system which would be a metal in the band picture, but is an insulator due to the strong Coulomb repulsion between electrons in 'small' atomic orbitals. It should be noted that for noninteracting electrons ($U = 0$) and $t = 0$ the electrons would be unable to move as well and the system would be an insulator. However, any arbitrarily small value of t would immediately lead to the formation of a band and a Fermi surface, whereas in the presence of a large U switching on $t \ll U$ would not change the insulating nature of the ground state.

The discussion above already shows one of the reasons why the problem of the Mott-insulator is so difficult. Whereas the ground state for $U = 0$ is unique and easy to write down – the filled Fermi sea – a well-defined ground state for $U/t = \infty$ does not even exist: namely in this limit each site is occupied by one electron, which can have a spin of $\sigma = \pm\frac{1}{2}$. The way in which the spins are distributed over the sites is not determined, however, and for $N_\uparrow = N_\downarrow = N/2$ the number of ways to distribute the $\uparrow$-spins (which automatically fixes the $\downarrow$-spins) is

$$n_d = \binom{N}{N_\uparrow} \approx \sqrt{\frac{2}{\pi N}}\, 2^N,$$

where the Stirling formula has been used. This shows the enormous degree of degeneracy.

If we reduce U/t from infinity to a large but finite value, the spins on the individual sites start to 'communicate' with each other via the process shown in Figure 1. An electron from site i may hop to a neighbor j and form an intermediate state with an empty orbital at i and a doubly occupied orbital at j, see Fig. 1(b). Since the energy of this intermediate state is U, it will be short lived and one of the two electrons in j will hop to the empty site i, resulting in one of the two states in Fig. 1(c). The upper state is identical to the initial state, Fig. 1(a), but there is a gain in kinetic energy of order t^2/U due to the back-and-forth hopping of the electron. Since this back-and-forth hopping is possible only if the spins at i and j are antiparallel to each other, it is energetically favorable if spins on nearest neighbors are antiparallel. In the lower of

the two states in Fig. 1(c) both spins have flipped their direction as compared to Fig. 1(a), so that the spins in the Mott insulator are not static, but have a dynamics of their own. A more quantitative treatment shows that the 'virtual' hopping processes in Fig. 1 can be described by the *Heisenberg antiferromagnet*

$$H_{HAF} = J \sum_{\langle i,j \rangle} \mathbf{S}_i \cdot \mathbf{S}_j = J \sum_{\langle i,j \rangle} \left(S_i^z S_j^z + \frac{1}{2} \left(S_i^+ S_j^- + S_i^- S_j^+ \right) \right). \tag{2}$$

Here $J = 4t^2/U$, $\sum_{\langle i,j \rangle}$ denotes a sum over all $2N$ nearest neighbor pairs, and $\mathbf{S}_i$ is the operator of electron spin at site i, and the spin raising and lowering operators $S^{\pm} = S_x \pm iS_y$ have been introduced to rewrite the term $S_{i,x}S_{j,x} + S_{i,y}S_{j,y}$. Although the electrons in a Mott insulator are localized, their spins therefore acquire a 'life of their own', that means a nontrivial ground state and a spectrum of *spin-excitations*. This problem is even compounded by doping the system, that means removing electrons and thus create mobile vacancies. The appropriate model to describe this is the famous t-J *model*

$$H_{t-J} = -t \sum_{\langle i,j \rangle} \sum_{\sigma} \left(\hat{c}_{i,\sigma}^{\dagger} \hat{c}_{j,\sigma} + H.c. \right) + J \sum_{\langle i,j \rangle} \mathbf{S}_i \cdot \mathbf{S}_j, \tag{3}$$

where the *Hubbard operator* $\hat{c}_{i,\sigma}^{\dagger} = c_{i,\sigma}^{\dagger}(1 - n_{i,\bar{\sigma}})$ creates an electron only on an empty site. The t-J model was originally derived rigorously as the strong coupling version of the Hubbard model by Chao, Spałek, and Oleś [2], and later shown to be the proper theoretical description of the CuO_2 planes in cuprate superconductors by Zhang and Rice [3]. For application to the CuO_2 planes, the appropriate parameter values are $t \approx 350\,\text{meV}$ and $J \approx 140\,\text{meV}$, so $J/t = 0.4$. The Hilbert space of the t-J model consists of states where each site is occupied either by a vacancy or a spin. The first term exchanges a vacancy and a spin on nearest neighbors, the second term is the Heisenberg exchange between spins. We therefore expect that the system continues to have spin excitations, but by their very motion through the 'spin background' the vacancies interact with these, which will modify both, the motion of the holes and the dynamics of the spins.

2 Planar model at half-filling

2.1 Magnons

To illustrate these somewhat vague remarks we now discuss the reasonably well understood case of the undoped Heisenberg antiferromagnet, $N_e = N$, and the motion of a single vacancy in a Heisenberg antiferromagnet, $N_e = N-1$. We consider the Hamiltonian Eq. (2) for one electron per site. If only the terms $\propto S_i^z S_j^z$ were present, the ground state of (2) would be the *Néel state*, shown in Figure 2(a). In this state, the square lattice is divided into two *sublattices* whereby all sites of the A-sublattice are occupied by an $\uparrow$-electron, those of the B-sublattice by a $\downarrow$-electron (we assume that the A-sublattice is the one containing the site $(0,0)$). The energy of this state is $2N\left(-\frac{J}{4}\right) = -NJ/2$. The Néel state, however, is not an eigenstate of the full Hamiltonian (2): acting, e.g., with one of the products $\frac{J}{2} S_i^- S_j^+$ contained in the second term

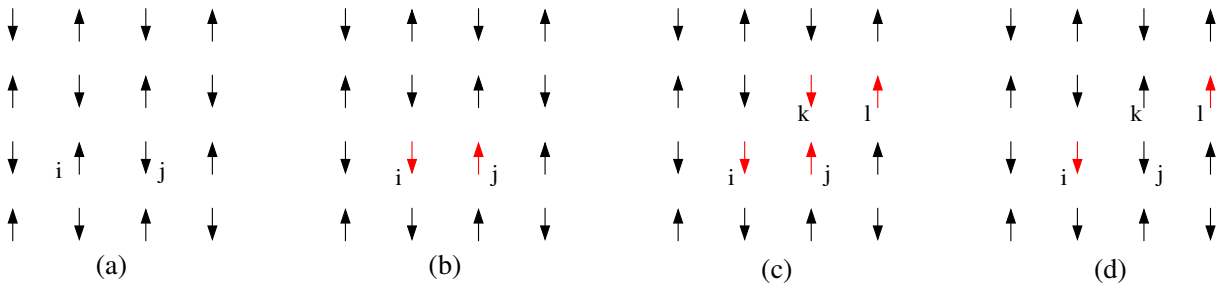

Fig. 2: *The Néel state (a) is* not *the ground state of the Heisenberg antiferromagnet. By acting, e.g., with the term* $\frac{J}{2}\, S_i^- S_j^+$ *in (2) the state (b) is generated, which is orthogonal to the Néel state. Acting further with* $\frac{J}{2}\, S_k^- S_l^+$ *produces (c) and then acting with* $\frac{J}{2}\, S_j^- S_k^+$ *gives (d).*

in (2), the spins at the sites i and j are inverted, resulting in the state shown in Figure 2(b) which is orthogonal to the Néel state. Interestingly, the inverted spins have very much the character of particles in that they can propagate: first, the term $\frac{J}{2}\, S_k^- S_l^+$ appends two additional inverted spins – see Figure 2(c) – and then the term $\frac{J}{2}\, S_j^- S_k^+$ removes two inverted spins, to produce the state in Figure 2(d). The net result of this two-step process is that one of the inverted spins seems to have moved from site j to site l. The particle-like nature of the inverted spins has led to the name *magnons* for them. One can then envisage how this will go on: magnons are created in pairs at various places in the system, then separate and propagate independently by the append-and-remove process, but when two magnons meet they can also 'pair-annihilate' each other by the inverse process Figure 2(b)→(a). There are then two possible outcomes of this scenario: the density of magnons may reach an equilibrium value, where pair-creation and pair annihilations balance each other, so that the underlying antiferromagnetic order persists and we have a Néel state hosting a 'gas of magnons' – or the process may go on until the ordered state is wiped out and we get an entirely new state without order. It turns out that in dimensions $D \geq 2$ the first scenario is realized, and the resulting gas of magnons in antiferromagnetic Mott insulators can be described very well by *linear spin wave theory*. This is frequently derived by means of the Holstein-Primakoff transformation [4] but for the extreme quantum limit of spin $1/2$, which we are considering here, a simpler and more transparent derivation is possible.

We interpret the Néel state in Figure 2(a) as the vacuum state $|0\rangle$ for magnons and model an inverted spin at the site i of the A sublattice by the presence of a Boson, created by $a_i^\dagger$. Similarly, an inverted spin on the site j of the B sublattice is modeled by the presence of a Boson created by $b_j^\dagger$. The state in Figure 2(b) thus would be represented as $a_i^\dagger b_j^\dagger |0\rangle$. We use Bosons to represent the magnons because spin-flip operators such as S_i^+ and S_j^- commute for different sites i and j and these are the operators which create or annihilate the magnons. Since any given spin can be inverted only once, a state like $(a_i^\dagger)^2|0\rangle$ is meaningless. Accordingly, we have to impose the constraint that at most one Boson can occupy a given site. This is equivalent to an infinitely strong on-site repulsion between the magnons and we call this the *hard-core constraint*. An inverted spin on either sublattice is parallel to its $z = 4$ nearest neighbors and the energy changes from $-J/4$ to $+J/4$ for each of these z bonds. Accordingly, we ascribe an energy of formation of $zJ/2$ to each Boson. The spin-flip part creates or annihilates pairs of magnons on

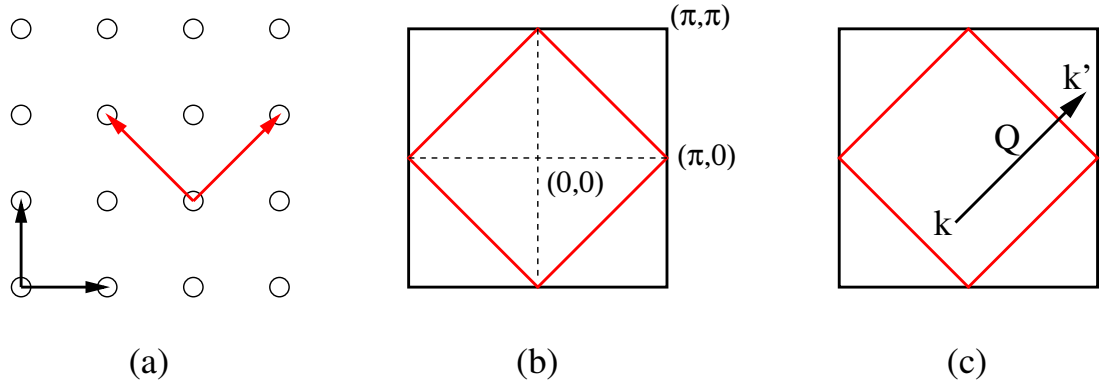

Fig. 3: *(a) The ordered moments in the Néel state make the two sublattices inequivalent, so that the new lattice vectors connect only the sites of one sublattice. The new unit cell is rotated by 45^o and has twice the size of the original one. (b) Accordingly, the new Brillouin zone is rotated by 45^o as well and has half the size of the original one. (c) Every vector* $\mathbf{k}'$ *outside the antiferromagnetic Brillouin zone can be written as* $\mathbf{k}' = \mathbf{k} + \mathbf{Q}$ *with a* $\mathbf{k}$ *inside the zone.*

nearest neighbors, with the matrix element being $J/2$, so that the Hamiltonian for the magnons becomes

$$H_{SW} = \frac{zJ}{2}\left(\sum_{i\in A} a_i^\dagger\, a_i + \sum_{i\in B} b_i^\dagger\, b_i\right) + \frac{J}{2}\sum_{i\in A}\sum_{\mathbf{n}}\left(a_i^\dagger\, b_{i+\mathbf{n}}^\dagger + b_{i+\mathbf{n}}\, a_i\right). \tag{4}$$

Here $\mathbf{n}$ are the z vectors which connect a given site with its z nearest neighbors. In fact, we have made a slight mistake in writing down (4): when two inverted spins reside on nearest neighbors, the number of frustrated bonds is $2z-1$ rather than $2z$. This could be incorporated into H_{SW} as an attractive interaction between magnons on nearest neighbors, but here we ignore this.
The Hamiltonian (4) is a quadratic form but we recall that the Bosons are not free particles, but have to obey the hard-core constraint. However, for the moment we ignore this and treat the Bosons as if they were free particles – we will return to this issue later on. Fourier transforming (4) then gives

$$H_{SW} = \frac{zJ}{2}\sum_{\mathbf{k}}\left(a_{\mathbf{k}}^\dagger a_{\mathbf{k}} + b_{\mathbf{k}}^\dagger b_{\mathbf{k}} + \gamma_{\mathbf{k}}\left(a_{\mathbf{k}}^\dagger b_{-\mathbf{k}}^\dagger + b_{-\mathbf{k}} a_{\mathbf{k}}\right)\right) \tag{5}$$

with

$$a_{\mathbf{k}}^\dagger = \sqrt{\frac{2}{N}}\sum_{j\in A} e^{i\boldsymbol{k}\cdot\boldsymbol{R}_j} a_j^\dagger \quad \text{and} \qquad \gamma_{\mathbf{k}} = \frac{1}{z}\sum_{\mathbf{n}} e^{i\mathbf{k}\cdot\mathbf{n}} = \frac{1}{4}\big(2\cos(k_x) + 2\cos(k_y)\big).$$

Here $\mathbf{k}$ is a wave vector in the antiferromagnetic Brillouin zone (AFBZ), see Figure 3. We can solve (5) by a *Bosonic Bogoliubov transformation*, i.e., we make the ansatz

$$\begin{array}{rcl} \alpha_{\mathbf{k}}^\dagger &=& u_{\mathbf{k}}\;\; a_{\mathbf{k}}^\dagger + v_{\mathbf{k}}\, b_{-\mathbf{k}}, \\ \beta_{-\mathbf{k}}^\dagger &=& u_{\mathbf{k}}\, b_{-\mathbf{k}}^\dagger + v_{\mathbf{k}}\;\; a_{\mathbf{k}}, \end{array} \quad \Rightarrow \quad \begin{array}{rcl} a_{\mathbf{k}}^\dagger &=& u_{\mathbf{k}}\,\alpha_{\mathbf{k}}^\dagger - v_{\mathbf{k}}\,\beta_{-\mathbf{k}}, \\ b_{-\mathbf{k}} &=& -v_{\mathbf{k}}\;\alpha_{\mathbf{k}}^\dagger + u_{\mathbf{k}}\,\beta_{-\mathbf{k}}. \end{array} \tag{6}$$

Demanding that $[\alpha_{\mathbf{k}}, \alpha_{\mathbf{k}}^\dagger] = [\beta_{\mathbf{k}}, \beta_{\mathbf{k}}^\dagger] = 1$ gives the condition $u_{\mathbf{k}}^2 - v_{\mathbf{k}}^2 = 1$, which actually has been used to revert the equations on the left hand side of (6) to obtain the right-hand side. Next,

we demand that when expressed in terms of the $\alpha_{\mathbf{k}}^\dagger$ and $\beta_{\mathbf{k}}^\dagger$ the Hamiltonian takes the form

$$H = \sum_{\mathbf{k}} \omega_{\mathbf{k}} \left(\alpha_{\mathbf{k}}^\dagger \alpha_{\mathbf{k}} + \beta_{\mathbf{k}}^\dagger \beta_{\mathbf{k}} \right) + \text{const.}$$

It follows that $[H, \alpha_{\mathbf{k}}^\dagger] = \omega_{\mathbf{k}} \alpha_{\mathbf{k}}^\dagger$. We now insert the *ansatz* (6) into this equation, use the Bosonic commutation relations for $a^\dagger$ and $b^\dagger$, and equate the coefficients of $a_{\mathbf{k}}^\dagger$ and $b_{-\mathbf{k}}$ on both sides of the resulting equation. This leads to the following non-Hermitean eigenvalue problem

$$\begin{pmatrix} \frac{zJ}{2} & -\gamma_{\mathbf{k}} \\ \gamma_{\mathbf{k}}^* & -\frac{zJ}{2} \end{pmatrix} \begin{pmatrix} u_{\mathbf{k}} \\ v_{\mathbf{k}} \end{pmatrix} = \omega_{\mathbf{k}} \begin{pmatrix} u_{\mathbf{k}} \\ v_{\mathbf{k}} \end{pmatrix}. \tag{7}$$

The eigenvalues and eigenvectors of (7) are easily calculated and one finds

$$\omega_{\mathbf{k}} = \frac{zJ}{2} \sqrt{1-\gamma_{\mathbf{k}}^2}, \quad \text{and} \qquad u_{\mathbf{k}} = \sqrt{\frac{1+\nu_{\mathbf{k}}}{2\nu_{\mathbf{k}}}}\,, \quad v_{\mathbf{k}} = \sqrt{\frac{1-\nu_{\mathbf{k}}}{2\nu_{\mathbf{k}}}}, \tag{8}$$

where $\nu_{\mathbf{k}} = \sqrt{1-\gamma_{\mathbf{k}}^2}$. In particular, for $\mathbf{k} \to 0$ we find $\gamma_{\mathbf{k}} \to 1 - (k_x^2+k_y^2)/4 = 1-\mathbf{k}^2/4$ so that $\nu_{\mathbf{k}} \to |\mathbf{k}|/\sqrt{2}$ and $\omega_{\mathbf{k}} \to J\sqrt{2}|\mathbf{k}|$. This shows that the spin waves reach zero frequency at $\mathbf{k} = (0,0)$ and have a cone-shaped dispersion in the neighborhood.

Spin waves can be observed experimentally by inelastic neutron scattering (INS) which, as scattering experiments usually do [5], ultimately measures a dynamical correlation function, in the case of INS the *dynamical spin correlation function* $S(\mathbf{k},\omega)$. Denoting the eigenstates of the system under consideration by $|\nu\rangle$ (with ν=0 the ground state) then at zero temperature it is given by

$$S(\mathbf{k},\omega) = \sum_{\nu} \left| \langle \nu | S_{\mathbf{k}}^+ | 0 \rangle \right|^2 \delta\big(\omega - (E_\nu - E_0)\big), \quad \text{with} \qquad S_{\mathbf{k}}^+ = \frac{1}{\sqrt{N}} \sum_i e^{i\mathbf{k}\cdot\mathbf{R}_i}\, S_i^+.$$

This expression describes the following scattering process: initially, the sample is in its ground state $|0\rangle$ with energy E_0 and $S_z = 0$. A neutron enters the sample with wave vector $\mathbf{K}$, kinetic energy T, and spin $\uparrow$. Its magnetic moment interacts with that of the spin density of a $\downarrow$-electron in some atomic wave function $|\phi_i\rangle$, so that both, the electron and the neutron, flip their spins. The sample remains in an excited state $|\nu\rangle$ with momentum $\mathbf{k}$, energy E_ν and $S_z = 1$, whereas the neutron leaves the sample with wave vector $\mathbf{K} - \mathbf{k}$, energy $T - (E_\nu - E_0)$ and spin $\downarrow$. In our case, the $|\nu\rangle$ are the eigenstates of the spin wave Hamiltonian, so we need to translate the spin operator $S_{\mathbf{k}}^+$ into 'spin wave language'. The operator S_i^+ raises the spin at site i, so if i belongs to the B-sublattice S_i^+ creates a magnon, $S_i^+ = b_i^\dagger$, whereas if i belongs to the A-sublattice S_i^+ annihilates a magnon, $S_i^+ = a_i$. Accordingly we have

$$S_{\mathbf{k}}^+ = \frac{1}{\sqrt{N}} \sum_{i\in A} e^{i\mathbf{k}\cdot\mathbf{R}_i}\, a_i + \frac{1}{\sqrt{N}} \sum_{i\in B} e^{i\mathbf{k}\cdot\mathbf{R}_i}\, b_i^\dagger = \frac{1}{\sqrt{2}} \big(a_{-\mathbf{k}} + b_{\mathbf{k}}^\dagger\big) = \frac{1}{\sqrt{2}} \big(u_{\mathbf{k}} - v_{\mathbf{k}}\big) \big(\alpha_{-\mathbf{k}} + \beta_{\mathbf{k}}^\dagger\big),$$

where the inverse transformation in (6) was used in the last step as well as $u_{-\mathbf{k}} = u_{\mathbf{k}}$ and $v_{-\mathbf{k}} = v_{\mathbf{k}}$. When acting onto the magnon vacuum $|0\rangle$, the term $\propto \alpha_{-\mathbf{k}}$ gives nothing, whereas the term $\propto \beta_{\mathbf{k}}^\dagger$ creates a single magnon. The possible final states $|\nu\rangle$ thus are $\beta_{\mathbf{k}}^\dagger |0\rangle$ with energy

$E_\nu = E_0 + \omega_{\mathbf{k}}$. However, using this expression for all momenta in the Brillouin zone, we would be making a mistake: namely the momenta $\mathbf{k}$ of the magnons in (6) are restricted to the AFBZ whereas the momentum transfer $\mathbf{k}$ in the scattering experiment can be anywhere in the whole Brillouin zone. This is easily remedied, however, if we note that each momentum $\mathbf{k}'$ outside the AFBZ can be written as $\mathbf{k} + \mathbf{Q}$, with $\mathbf{Q} = (\pi, \pi)$ and $\mathbf{k}$ within the AFBZ, see Figure 3(c). Since $e^{i\mathbf{Q}\cdot\mathbf{R}_i} = 1$ for all sites of the A-sublattice (remember that the A-sublattice was the one containing $(0,0)$) and $e^{i\mathbf{Q}\cdot\mathbf{R}_i} = -1$ for all states of the B-sublattice, we have $S^+_{\mathbf{k}+\mathbf{Q}} = (a_{-\mathbf{k}} - b^\dagger_{\mathbf{k}})/\sqrt{2} = (u_{\mathbf{k}} + v_{\mathbf{k}})(\alpha_{-\mathbf{k}} - \beta^\dagger_{\mathbf{k}})/\sqrt{2}$. Inserting everything we find

$$S(\mathbf{k},\omega) = \frac{1}{2}\big(u_{\mathbf{k}} - v_{\mathbf{k}}\big)^2\, \delta(\omega - \omega_\nu), \qquad S(\mathbf{k}+\mathbf{Q},\omega) = \frac{1}{2}\big(u_{\mathbf{k}} + v_{\mathbf{k}}\big)^2\, \delta(\omega - \omega_\nu).$$

Let us assume that the momentum transfer is $\boldsymbol{k} = \mathbf{Q} + \delta\mathbf{k}$ or $\boldsymbol{k} = \delta\mathbf{k}$, with a small $\delta\mathbf{k}$. In both cases, $\omega_{\boldsymbol{k}} \to J\sqrt{2}|\delta\mathbf{k}|$, whereas the square of the scattering matrix element

$$\big|\langle\nu|S^+_{\mathbf{k}}|0\rangle\big|^2 = \frac{1}{2}\big(u_{\delta\mathbf{k}} \pm v_{\delta\mathbf{k}}\big)^2 = \frac{1}{2}\,\frac{1 \pm |\gamma_{\delta\mathbf{k}}|}{\sqrt{1-\gamma^2_{\delta\mathbf{k}}}} \to \begin{cases} \dfrac{\sqrt{2}}{|\delta\mathbf{k}|} & , + \\[2ex] \dfrac{|\delta\mathbf{k}|}{4\sqrt{2}} & , - \end{cases}$$

The matrix element, which gives the peak-intensity in the inelastic neutron spectrum, thus approaches zero for momentum transfer 0, but diverges for momentum transfer $\mathbf{Q}$. A comparison to an actual INS experiment is shown in Figure 4. It is quite obvious that the agreement with experiment is excellent, both with respect to the spin wave dispersion and the $\mathbf{k}$-dependence of the peak intensity, and in fact spin wave theory is a highly successful description of the properties of antiferromagnetic Mott insulators. The bandwidth of $\omega_{\mathbf{k}}$ is roughly $300\,\text{meV}$ and from (8) one can see that spin wave theory predicts a bandwidth of $2J$, so $J \approx 150\,\text{meV}$. This is slightly larger than the value given above, but to get a really good fit the authors of Ref. [6] actually have included an additional ring exchange term whereas their nearest neighbor $J = 138m\,\text{meV}$.
To conclude this section, we return to the issue of the hard-core constraint which the $a^\dagger$ and $b^\dagger$ Bosons had to obey and which we had simply ignored. To address this question, we calculate the density of these Bosons, i. e.,

$$n_a \;=\; \frac{2}{N}\sum_{\mathbf{k}} \big\langle a^\dagger_{\mathbf{k}} a_{\mathbf{k}}\big\rangle = \frac{2}{N}\sum_{\mathbf{k}} v^2_{\mathbf{k}} = \frac{2}{N}\sum_{\mathbf{k}} \frac{1-\nu_{\mathbf{k}}}{2\nu_{\mathbf{k}}}.$$

Numerical evaluation for a 2D square lattice gives $n_a = 0.19$. The probability that two of the Bosons occupy the same site and violate the constraint therefore is $\approx n_a^2 = 0.04 \ll 1$ and our assumption of relaxing the constraint is justified a posteriori.
Summarizing the discussion so far we have seen that in a Mott-insulator the sites carry a spin of $\pm\frac{1}{2}$. These spins can communicate with each other by means of virtual charge fluctuations and this is described by the Heisenberg antiferromagnet. In dimensions $D \geq 2$ this leads to antiferromagnetic order in the ground state and a new type of excitations, magnons or spin waves, which correspond to spins standing opposite to the antiferromagnetic order.

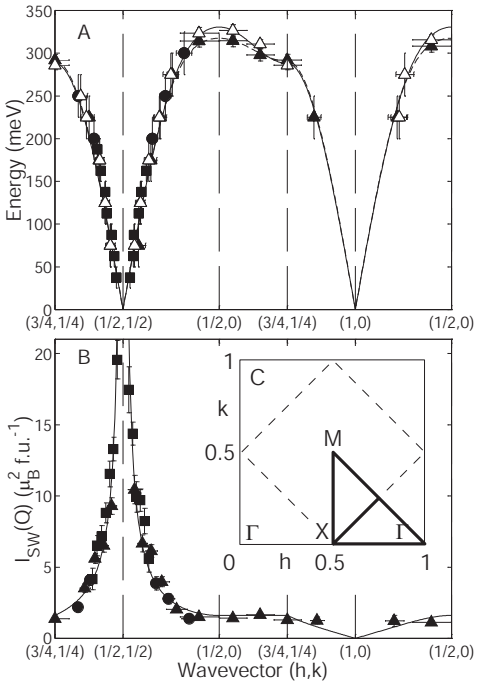

Fig. 4: *Comparison of spin wave theory to INS results for La_2CuO_4. The top part shows the dispersion of the frequency $\omega_{\mathbf{k}}$ of the spin waves, the bottom part the* **k***-dependence of the peak intensity $\propto (u_{\mathbf{k}} \pm v_{\mathbf{k}})^2$. In this Figure, wave vectors* **k** *are given in units of $2\pi/a$, so that the authors' $(1,0)$ is our $(0,0)$ (but measured in the 2nd zone to avoid looking into the incoming beam) whereas $(\frac{1}{2},\frac{1}{2})$ is our (π,π). The dots are experimental data, the lines the prediction of spin wave theory. Note the cone-shaped dispersion around $(0,0)$ and (π,π) and the divergence/vanishing of the spectral weight at these points. Reprinted with permission from [6], Copyright 2001 by the American Physical Society.*

2.2 One hole in an antiferromagnet

Let us next consider the first step of 'doping the system' and consider the case of a single vacancy in a system described by the t-J model, Eq. (3). A single hole will not change the magnetic order due to interaction of the remaining $N-1$ spins, so we assume antiferromagnetic order and decompose the t-J Hamiltonian Eq. (3) as $H = H_t + H_I + H_\perp$ whereby

$$H_t = -t \sum_{\langle i,j \rangle} \sum_{\sigma} \left(\hat{c}^\dagger_{i,\sigma} \hat{c}_{j,\sigma} + H.c \right), \quad H_I = J \sum_{\langle i,j \rangle} S^z_i S^z_j, \quad H_\perp = \frac{J}{2} \sum_{\langle i,j \rangle} \left(S^+_i S^-_j + H.c. \right),$$

and choose $H_0 = H_t + H_I$ as our unperturbed Hamiltonian. As already stated, in the absence of any hole the ground state of H_0 is the Néel state with energy $E_N = -NJ/2$. If now an electron is removed from site i belonging to the $\uparrow$-sublattice – see Figure 5(a). This raises the exchange energy by $zJ/4$, because z bonds change their energy from $-J/4$ to 0. We choose the exchange energy of the resulting state, $E_N + zJ/4$, as the zero of energy. Then, the hopping term in (3) can become active and the spin from a neighboring site i_1 is transferred to i, resulting in the state in Figure 5(b). Since the shifted spin has 'switched sublattices', however, it now is opposite to the antiferromagnetic order. In fact, this inverted spin at site i is nothing but a magnon as

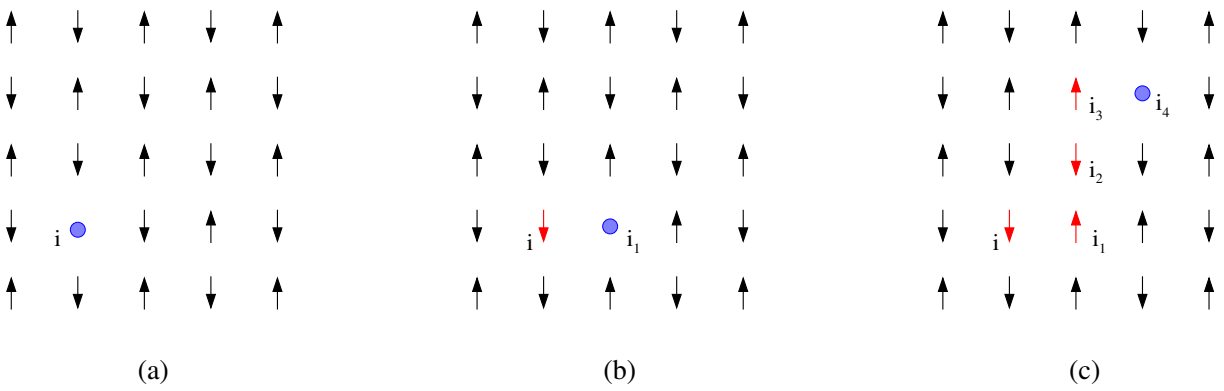

Fig. 5: *A hole hopping in the Néel state creates a 'string' of misaligned spins.*

discussed in the preceding section, so that the hopping vacancy 'radiates off' magnons [7, 8]. Since the displaced spin at site i is parallel to $z-1$ neighbors, the exchange energy increases by $(z-1)J/2$. And this continues as the vacancy moves through the Néel state, see Figure 5(c): in each step another spin is shifted to the opposite sublattice, so that the vacancy leaves behind a trace of misaligned spins and the exchange energy increases roughly linearly with the distance travelled by the hole. We call a state which is created by the motion of a vacancy in the Néel state a 'string state' and denote it by $|i_0, i_1, \ldots, i_\nu\rangle$. Here i_0 is the site where the hole was created, $i_1, i_2, i_{\nu-1}$ are the sites visited by the hole, whereas i_ν is the site where the vacancy is located. We call ν the length of the string, for example Figure 5(c) shows a string of length 4. There are z different string states with $\nu = 1$, whereas in any subsequent hop starting from a string state of length ν, $z-1$ new string states of length $\nu+1$ are generated. The number of different strings of length ν therefore is $n_\nu = z(z-1)^{\nu-1}$ for $\nu \geq 1$ whereas $n_0 = 1$. Since each displaced spin is parallel to $z-2$ neighbors – see Figure 5 – the magnetic energy increases by $J(z-2)/2$ per displaced spin, except for the first hop away from i where it increases by $J(z-1)/2$. Accordingly, the exchange energy for a string of length $\nu > 0$ his

$$I_\nu = \frac{(z-1)J}{2} + (\nu-1)\,\frac{(z-2)J}{2} = \frac{J}{2}\big((z-1) + (\nu-1)(z-2)\big), \tag{9}$$

and $I_0 = 0$. It may happen that the path which the hole has taken is folded or self-intersecting in which case (9) clearly is not correct. However it will be correct for 'most' possible paths of the hole, in particular it is correct for $\nu \leq 2$ so that we will use this expression. Neglecting the possibility of self-intersection or folding of the string is an approximation known as *Bethe-lattice*. Since the magnetic energy increases linearly with the number of hops the hole has taken, we conclude that under the action of H_0 the hole is self-trapped. To describe the resulting localized state we make the following *ansatz*

$$|\Phi_i\rangle = \sum_{\nu=0}^{\infty} \alpha_\nu \sum_{i_1, i_2, \ldots, i_\nu} |i, i_1, i_2, \ldots, i_\nu\rangle, \tag{10}$$

where it is understood that the second sum runs only over those ν-tuples of sites which correspond to a true string starting at i. Since we assume that the magnetic energy is the same for all

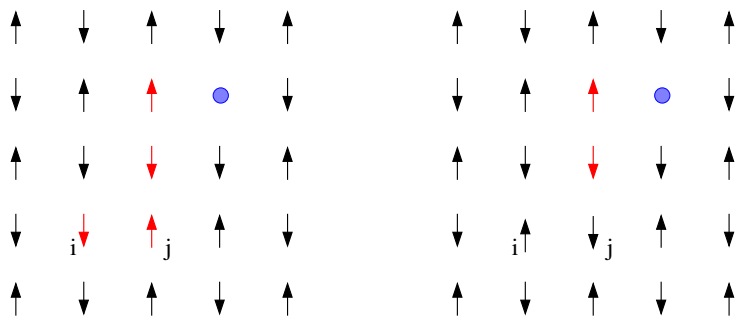

Fig. 6: *By acting with the term* $\frac{J}{2}\, S_i^+ S_j^-$ *the first two defects created by the hole can be 'healed' and the starting point of the string be shifted to a neighbor.*

strings of length ν, the coefficient α_ν depends only on the length of the string. The coefficients α_ν in (10) are to be determined by minimizing the expectation value of H_0. The norm and magnetic energy are

$$\langle \Phi_i | \Phi_i \rangle = \sum_{\nu=0}^{\infty} n_\nu \alpha_\nu^2 \quad = \sum_{\nu=0}^{\infty} \beta_\nu^2, \tag{11}$$

$$\langle \Phi_i | H_I | \Phi_i \rangle = \sum_{\nu=0}^{\infty} n_\nu I_\nu \alpha_\nu^2 = \sum_{\nu=0}^{\infty} I_\nu \beta_\nu^2, \tag{12}$$

where we have introduced $\beta_\nu = \alpha_\nu / \sqrt{n_\nu}$. To obtain the expectation value of the kinetic energy we consider a string state of length $\nu \geq 1$ which has the coefficient α_ν. By acting with the hopping term we obtain $z-1$ strings of length $\nu+1$, with coefficient $\alpha_{\nu+1}$, and 1 string of length $\nu-1$, with coefficient $\alpha_{\nu-1}$. For $\nu = 0$ we obtain z strings of length 1. In this way we find

$$\langle \Phi_i | H_t | \Phi_i \rangle = t \Big(z\alpha_0\alpha_1 + \sum_{\nu=1}^{\infty} n_\nu \alpha_\nu \big(\alpha_{\nu-1} + (z-1)\alpha_{\nu+1} \big) \Big) = 2t \sum_{\nu=0}^{\infty} n_{\nu+1} \alpha_\nu \alpha_{\nu+1} = 2 \sum_{\nu=0}^{\infty} \tilde{t}_\nu \, \beta_\nu \beta_{\nu+1}, \tag{13}$$

where $\tilde{t}_0 = \sqrt{z}\, t$ and $\tilde{t}_\nu = \sqrt{z-1}\, t$ for $\nu > 0$. The prefactor on the right-hand side is t instead of $-t$ as one might have expected from (3) because the hopping term has to be rearranged as $-t\, \hat{c}^\dagger_{i,\sigma} \hat{c}_{j,\sigma} = t\, \hat{c}_{j,\sigma} \hat{c}^\dagger_{i,\sigma}$ to describe the hopping of a hole. As already stated, the β_ν now are determined from the requirement that the expectation value $E_{loc} = \langle \Phi_i | H_0 | \Phi_i \rangle / \langle \Phi_i | \Phi_i \rangle$ be stationary under variation of each β_ν

$$\begin{aligned} \frac{\partial E_{loc}}{\partial \beta_\nu} &= \frac{1}{\langle \Phi_i | \Phi_i \rangle^2} \left[\frac{\partial \langle \Phi_i | H_0 | \Phi_i \rangle}{\partial \beta_\nu} \langle \Phi_i | \Phi_i \rangle - \langle \Phi_i | H_0 | \Phi_i \rangle \frac{\partial \langle \Phi_i | \Phi_i \rangle}{\partial \beta_\nu} \right] \\ &= \frac{1}{\langle \Phi_i | \Phi_i \rangle} \left[\frac{\partial \langle \Phi_i | H_0 | \Phi_i \rangle}{\partial \beta_\nu} - E_{loc} \frac{\partial \langle \Phi_i | \Phi_i \rangle}{\partial \beta_\nu} \right] = 0. \end{aligned}$$

Setting the square bracket equal to zero and using Eqs. (11), (12), and (13) we obtain [9]

$$\big(\tilde{t}_\nu \beta_{\nu+1} + \tilde{t}_{\nu-1} \beta_{\nu-1} \big) + I_\nu \beta_\nu = E_{loc} \beta_\nu,$$

with the boundary condition $\beta_{-1} = 0$. This results in a tridiagonal Hamilton matrix for the β_ν and after cutting off at a sufficiently large ν, E_{loc} and the βs can be obtained by a simple numerical matrix diagonalization.

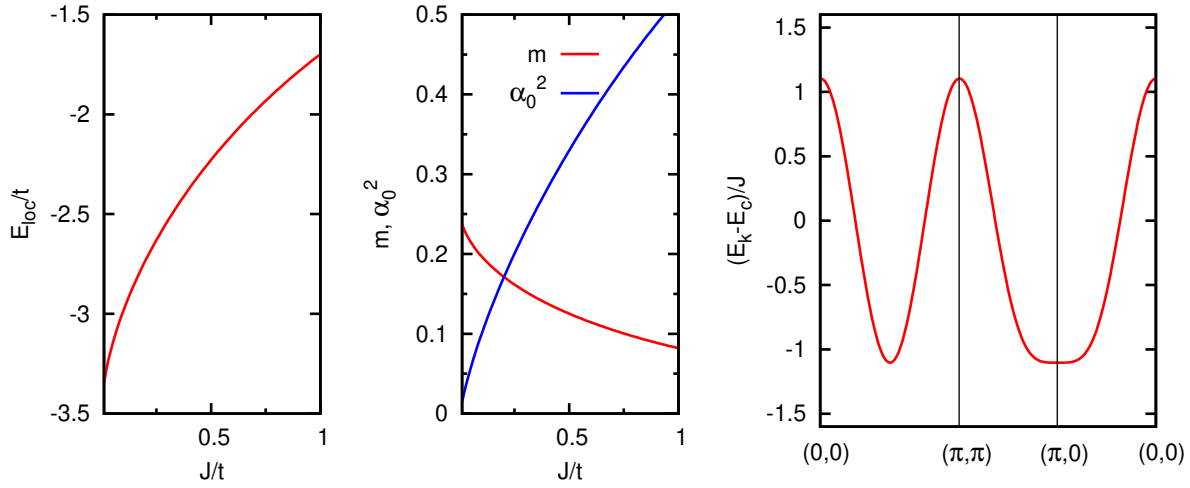

Fig. 7: *Left: Energy of the self-trapped state E_{loc} versus J/t. Center: Matrix element m due to string truncation and renormalization factor α_0^2 for the t' and t'' hopping terms versus J/t. Right: Band structure $E_{\boldsymbol{k}}$ for $J/t = 0.4$.*

So far it seems that the hole in the Néel state is localized. It is easy to see, however, that the term $H_\perp$ which we have neglected so far can assist the trapped hole in escaping from the string potential, see Figure 6. Namely by acting on the first two sites of a string, the spins which were inverted by the hole are inverted a second time and thus fit with the Néel order again: $H_\perp|i, i_1, i_2, i_3, \ldots, i_\nu\rangle = \frac{J}{2}\ |i_2, i_3, \ldots, i_\nu\rangle$. The initial site of the string thus is shifted to a $(2,0)$- or $(1,1)$-like neighbor while simultaneously the length ν is decreased by two. The term $H_\perp$ may also append two new defects to a string, $H_\perp|i_2, i_3, \ldots, i_\nu\rangle = \frac{J}{2}\ |i, i_1, i_2, i_3, \ldots, i_\nu\rangle$ thus increasing the length by 2 and again shifting the starting point to a $(2,0)$- or $(1,1)$-like neighbor. Using again the Bethe lattice approximation we find the matrix element

$$\langle\Phi_{i+2\hat{x}}|H_\perp|\Phi_i\rangle = J\sum_{\nu=0}^{\infty}(z-1)^\nu\ \alpha_\nu\alpha_{\nu+2} = \frac{J}{z}\left(\sqrt{\frac{z}{z-1}}\,\beta_0\beta_2 + \sum_{\nu=1}^{\infty}\beta_\nu\beta_{\nu+2}\right) = J\cdot m,$$

whereas $\langle\Phi_{i+\hat{x}+\hat{y}}|H_\perp|\Phi_i\rangle = 2J\cdot m$ because a string to a $(1,1)$-like neighbor can pass either trough $(1,0)$ or $(0,1)$ and the contributions from these two different paths are additive.
When the full Hamiltonian $H_0 + H_\perp$ is taken into account the hole therefore can propagate through the entire lattice and we describe this by the Bloch state

$$|\Phi_{\mathbf{k}}\rangle \ = \ \sqrt{\frac{2}{N}}\sum_{j\in A} e^{-i\mathbf{k}\cdot\mathbf{R}_j}\ |\Phi_i\rangle. \tag{14}$$

This is reminiscent of an LCAO wave function such as (1), but the role of the atomic orbital $|\phi_i\rangle$ here is played by the self-trapped function $|\Phi_i\rangle$. Since the matrix element of $H_\perp$ between $(1,1)$-like neighbors is twice that between $(2,0)$-like neighbors we obtain the dispersion

$$\begin{aligned} E_{\mathbf{k}} &= E_{loc} + 2Jm\cdot 4\cos(k_x)\cos(k_y) + Jm\cdot 2\big(\cos(2k_x)+\cos(2k_y)\big) \\ &= E_{loc} - 4Jm + 4Jm\big(\cos(k_x)+\cos(k_y)\big)^2 \end{aligned} \tag{15}$$

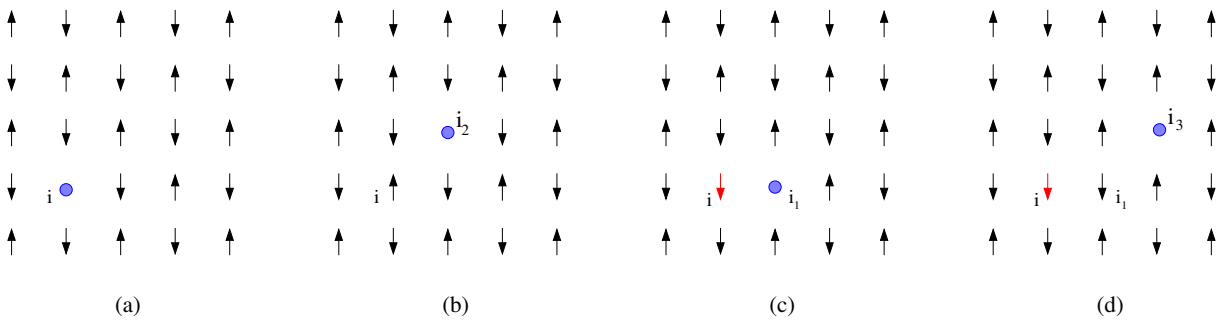

Fig. 8: *Hopping processes involving a term $\propto t'$ that connects $(1,1)$-like neighbors.*

This expression shows several remarkable features which reflect the unusual nature of hole motion. First, there is the constant term $E_{loc} \propto t$. As we have seen, in the absence of the spin-flip term $H_\perp$, the hole is self-trapped in a linearly ascending 'effective potential' due to magnetic frustration. The hole executes a rapid zig-zag motion on a timescale $\tau_{loc} \propto t^{-1}$, and E_{loc} is the gain of kinetic energy due to this zig-zag motion. Figure 7 shows that $E_{loc} \approx -2.4\,t$ at $J/t = 0.4$, which is an appreciable fraction of $-4t$, the lowest possible kinetic energy which a freely propagating electron can have in an empty $2D$ lattice. On the longer time scale $\tau_{deloc} \propto J^{-1}$, the spin-flip term shifts the center of the zig-zag motion to a 2^{nd} or 3^{rd} nearest neighbor, and the zig-zag motion starts anew. It follows that the bandwidth for coherent motion is *not* proportional to the hopping integral t, but to the smaller exchange constant J. The total bandwidth is $16Jm$ and since m is around 0.14 for $J/t = 0.4$ – see Figure 7 – the bandwidth is roughly $2J$. With $J = 140$ meV as appropriate for cuprates, we expect $W \approx 300$ meV, almost a factor of 10 smaller than the width of the free tight-binding dispersion, which is $8t \approx 2.8$ eV. $E_{\mathbf{k}}$ has a degenerate minimum along $(\pi, 0) \to (0, \pi)$ and symmetry equivalent lines, its maxima are at $(0, 0)$ and (π, π). It has 'antiferromagnetic symmetry', $E_{\mathbf{k}+\mathbf{Q}} = E_{\mathbf{k}}$, which is to be expected since we are considering hole motion in an antiferromagnetic background.

In order to compare our theory to experiment we need to take into account that in the actual CuO_2-planes there are appreciable additional hopping integrals t' between $(1,1)$-like and t'' between $(2,0)$-like neighbors. Since these terms connect pairs of neighbors which are on the same sublattice, they do not create frustration and it might seem that they immediately dominate the hole motion. However, this is not the case and the reason can be seen in the next Figure. Fig. 8(a) shows a 'string of length 0', that means a hole at site i and the hopping term $\propto t'$ can transport the hole to the $(1,1)$-like neighbor i_2 without creating a magnon. On the other hand, 8(c) shows a 'string of length 1', that means a hole which has executed one nearest neighbor hopping process and is now at site i_1, with a single magnon at site i. Again, the t'-term can transport the hole to the $(1,1)$-like neighbor i_3, but it cannot transport the magnon along with the hole. Therefore, the hopping terms $\propto t', t''$ can transport only the 'bare hole', and since this has the coefficient α_0 in the self-trapped states $|\Phi_i\rangle$, these terms are renormalized by a factor α_0^2. Accordingly, they give the following contribution to the hole dispersion relation

$$E_{lr}(\mathbf{k}) = 4t'\alpha_0^2 \cos(k_x)\cos(k_y) + 2t''\alpha_0^2\big(\cos(2k_x) + \cos(2k_y)\big)$$

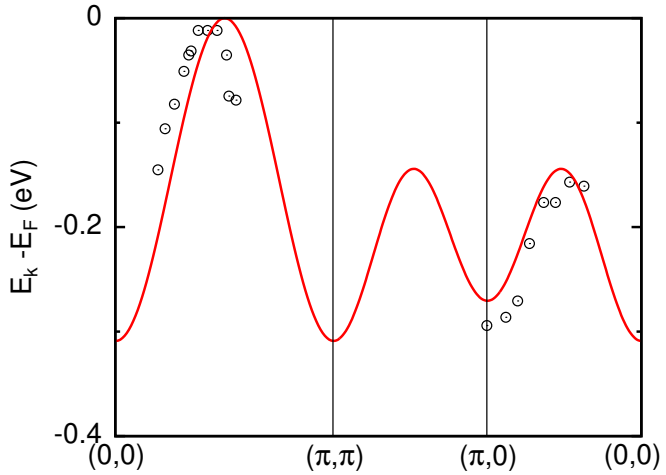

Fig. 9: *The band structure for the t-J model with additional hopping terms compared to the experimental valence band structure for the antiferromagnetic insulator $Sr_2CuO_2Cl_2$ [10]. Parameter values are $t = 350\,meV$, $J = 140\,meV$, $t' = -120\,meV$, and $t'' = 60\,meV$.*

which has to be added to (15). Note again the opposite sign of the hopping terms as compared to the original Hamiltonian (3) because the Fermion operators have to be exchanged to transport a hole. Figure 9 shows a comparison of the modified hole dispersion and the experimental band structure obtained by Angle Resolved Photoemission Spectroscopy (ARPES) on the insulating CuO-compound $Sr_2CuO_2Cl_2$ [10]. The band structure for a hole has to be turned upside down to compare to ARPES because the minimum of the hole-bandstructure is the maximum of the electron-band structure. The agreement is reasonable whereby it has to be kept in mind that in a wide area around (π, π) and also close to $(0, 0)$ the band structure cannot be observed because the band has vanishing spectral weight in ARPES. In any way, the drastic reduction of the bandwidth can be seen clearly.

Looking back, the above discussion illustrates the general remarks in the introduction. In a Mott insulator each site carries a spin and spins on neighboring sites are coupled by the exchange term. This leads to a tendency for neighboring spins to be antiparallel and the appearance of spin excitations, which in the antiferromagnetic phase take the form of spin waves. Doped holes then have to move through this 'spin background' and by their very motion constantly interact with the magnetic excitations. As we have seen this leads to a drastic modification of the hole motion and band structure. And in fact, this also goes the other way round: since the holes are constantly 'stirring' the spins, these react and change their arrangement so as to make hole motion easier and allow for a gain kinetic energy. In cuprate superconductors the antiferromagnetic state which could be described by the above theory breaks down for hole concentrations of only a few per cent. Even in the resulting disordered state, the spin exchange term in the t-J Hamiltonian still favors antiparallel orientation of spins on nearest neighbors and in fact neutron scattering experiments show that there it still has *short range antiferromagnetic order* that means the spin correlation function $\langle \boldsymbol{S}_i \cdot \boldsymbol{S}_{i+\boldsymbol{R}} \rangle \propto e^{i\boldsymbol{Q}\cdot\boldsymbol{R}}\, e^{-|\boldsymbol{R}|/\zeta}$. This is reminiscent of the density correction function in a molten crystal, where locally the correlations between atoms resemble that of the original solid but there is no more long range crystalline order. Accordingly, such a state is called a 'spin liquid' and this is what we want to discuss next.

3 Spin liquids

3.1 Dimer basis

As a prelude we follow Sachdev and Bhatt [11] as well as Gopalan, Rice, and Sigrist [12] and consider a *dimer* of two sites, labeled 1 and 2, and assume that both of them are occupied by one electron each, with their spins coupled by the exchange term $H = J\ \mathbf{S}_1 \cdot \mathbf{S}_2$. According to the rules for addition of angular momenta, the two spins of $\frac{1}{2}$ can be coupled to the total spin $S = 1$ (spin triplet) or $S = 0$ (spin singlet). The singlet and the three components of the triplet are eigenstates of the square of the operator of total spin $\mathbf{S} = \mathbf{S}_1 + \mathbf{S}_2$ with eigenvalue $S(S+1)$: $\mathbf{S}^2 = \mathbf{S}_1^2 + 2\mathbf{S}_1 \cdot \mathbf{S}_2 + \mathbf{S}_2^2 = S(S+1)$, and using that $\mathbf{S}_1^2 = \mathbf{S}_2^2 = \frac{1}{2}\left(\frac{1}{2}+1\right) = \frac{3}{4}$ we find $\mathbf{S}_1 \cdot \mathbf{S}_2 = \frac{1}{2}(S(S+1) - \frac{3}{2})$. Accordingly, $\mathbf{S}_1 \cdot \mathbf{S}_2$ gives $-\frac{3}{4}$ when acting on the singlet and $\frac{1}{4}$ for a triplet. Due to the limited size of the Hilbert space of the dimer, constructing states with definite total spin thus is equivalent to diagonalizing the exchange term, and we find the eigenenergies $-3J/4$ for the singlet, and $J/4$ for the three components of the triplet. The eigenstates themselves can be found by using the standard technique for adding angular momenta and are given by [11, 12]

$$\begin{aligned}
|s\rangle &= \frac{1}{\sqrt{2}} \left(c^\dagger_{1,\uparrow} c^\dagger_{2,\downarrow} - c^\dagger_{1,\downarrow} c^\dagger_{2,\uparrow} \right) |0\rangle, \\
|t_x\rangle &= \frac{1}{\sqrt{2}} \left(c^\dagger_{1,\downarrow} c^\dagger_{2,\downarrow} - c^\dagger_{1,\uparrow} c^\dagger_{2,\uparrow} \right) |0\rangle, \\
|t_y\rangle &= \frac{i}{\sqrt{2}} \left(c^\dagger_{1,\uparrow} c^\dagger_{2,\uparrow} + c^\dagger_{1,\downarrow} c^\dagger_{2,\downarrow} \right) |0\rangle, \\
|t_z\rangle &= \frac{1}{\sqrt{2}} \left(c^\dagger_{1,\uparrow} c^\dagger_{2,\downarrow} + c^\dagger_{1,\downarrow} c^\dagger_{2,\uparrow} \right) |0\rangle. \qquad (16)
\end{aligned}$$

with $|s\rangle$ the singlet and $|t_x\rangle$, $|t_y\rangle$, and $|t_z\rangle$ the three components of the triplet. Thereby the three $|t_\alpha\rangle$ in (16) are *not* eigenstates of the total z-spin – rather they are linear combinations of these eigenstates which obey $S_\alpha |t_\beta\rangle = i\varepsilon_{\alpha\beta\gamma}\ |t_\gamma\rangle$, for example:

$$\begin{aligned}
S_x |t_y\rangle &= \frac{1}{2} \sum_{i=1}^{2} (S_i^- + S_i^+)\ \frac{i}{\sqrt{2}}\ \left(c^\dagger_{1,\uparrow} c^\dagger_{2,\uparrow} + c^\dagger_{1,\downarrow} c^\dagger_{2,\downarrow} \right) \\
&= \frac{i}{2\sqrt{2}} \left(c^\dagger_{1,\downarrow} c^\dagger_{2,\uparrow} + c^\dagger_{1,\uparrow} c^\dagger_{2,\downarrow} + c^\dagger_{1,\uparrow} c^\dagger_{2,\downarrow} + c^\dagger_{1,\downarrow} c^\dagger_{2,\uparrow} \right) = i |t_z\rangle.
\end{aligned}$$

This means that the three states $|t_\alpha\rangle$ transform like a vector under spin rotations which will be convenient later on. We also note that under the exchange of the two sites, $1 \leftrightarrow 2$, we have $|s\rangle \to |s\rangle$ but $|t_\alpha\rangle \to -|t_\alpha\rangle$. Let us now return to the problem of describing a 'spin liquid' and first consider the undoped Heisenberg antiferromagnet on a 2D square lattice with N sites. A state which on one hand is disordered and on the other hand is an exact spin singlet can be obtained in the following way: let the N sites be partitioned into $N/2$ dimers, whereby each dimer comprises two nearest neighbor sites, see Figure 10 (a), and assume moreover that the two spins in each dimer are coupled to form a singlet. This state is a product state

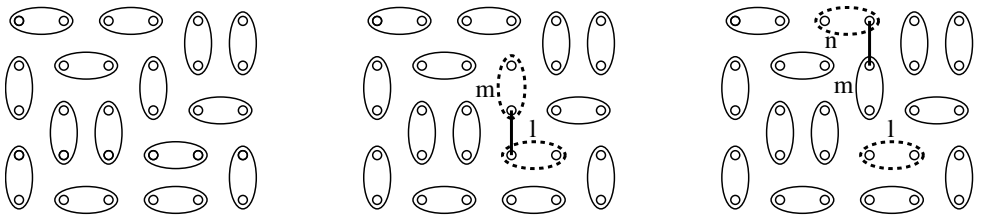

(a) (b) (c)

Fig. 10: *(a) A dimer covering of the plane – spins on sites covered by an ellipse are coupled to a singlet. (b) By acting with the exchange along the bond connecting the dimers l and m both dimers are excited into the triplet state. (c) By acting with the exchange along the bond connecting the dimers m and n bond m is de-excited to the singlet whereas dimer n is excited to the triplet – the triplet has propagated.*

$$|\Psi_0\rangle = \prod_{(i,j)\in D} \frac{1}{\sqrt{2}} \left(c^\dagger_{i,\uparrow} c^\dagger_{j,\downarrow} - c^\dagger_{i,\downarrow} c^\dagger_{j,\uparrow} \right)$$

where D is the set of $N/2$ pairs (i,j) of nearest neighbor sites corresponding to the given dimer covering. $|\Psi_0\rangle$ is an eigenstate of the 'depleted Hamiltonian' $H_d = J \sum_{(i,j)\in D} \mathbf{S}_i \cdot \mathbf{S}_j$ with eigenvalue $E_{d,0} = (N/2) \cdot (-3J/4)$. Since $\langle \mathbf{S}_i \cdot \mathbf{S}_j \rangle = 0$ if i and j belong to different dimers – as will be shown in a moment – this is also the expectation value of the full Hamiltonian in the state $|\Psi_0\rangle$. Next, let us consider what happens if we act onto $|\Psi_0\rangle$ with the exchange along a bond *not included* in the set D, that means a bond connecting spins in different dimers – such as the bond indicated in Figure 10(b). Due to the product nature of $|\Psi_0\rangle$ it is sufficient to discuss what happens when the spin operator acts on a singlet, e.g.,

$$S_{1,x}|s\rangle = \frac{1}{2}\left(S^-_1 + S^+_1\right) \frac{1}{\sqrt{2}} \left(c^\dagger_{1,\uparrow} c^\dagger_{2,\downarrow} - c^\dagger_{1,\downarrow} c^\dagger_{2,\uparrow} \right) |0\rangle = \frac{1}{2\sqrt{2}} \left(c^\dagger_{1,\downarrow} c^\dagger_{2,\downarrow} - c^\dagger_{1,\uparrow} c^\dagger_{2,\uparrow} \right) |0\rangle. \quad (17)$$

Comparing with (16), the expression on the right-hand side is seen to be $\frac{1}{2}|t_x\rangle$. Next, we exchange $1 \leftrightarrow 2$ on both sides of (17), whence $S_{1,x} \to S_{2,x}$, $|s\rangle \to |s\rangle$, and $|t_x\rangle \to -|t_x\rangle$, and obtain $S_{2,x}|s\rangle = -\frac{1}{2}|t_x\rangle$. Since the triplets where constructed to transform like a vector, this holds true for the other Cartesian components as well: $S_{1,\alpha}|s\rangle = \pm\frac{1}{2}|t_\alpha\rangle$, $\alpha \in \{x,y,z\}$. Acting with the term $J\mathbf{S}_i \cdot \mathbf{S}_j$ along a bond which connects sites i and j in different dimers therefore simultaneously excites both dimers to the triplet state, with a prefactor of $\pm J/2$ (the prefactor will be discussed more precisely below). The new state is again an eigenstate of H_d, with eigenvalue $E_{d,0} + 2J$ and obviously is orthogonal to $|\Psi_0\rangle$ – which also proves that the expectation value $\langle \mathbf{S}_i \cdot \mathbf{S}_j \rangle$ vanishes if the sites i and j belong to different dimers. Next, we consider what happens when the exchange term acts along the bond indicated in Figure 10(c). We already know that bond n will be excited to the triplet state but we need to study what happens when the spin operator acts on the triplet in bond m:

$$S_{1,x}|t_x\rangle = \frac{1}{2}\left(S^+_1 + S^-_1\right) \frac{1}{\sqrt{2}} \left(c^\dagger_{1,\downarrow} c^\dagger_{2,\downarrow} - c^\dagger_{1,\uparrow} c^\dagger_{2,\uparrow} \right) |0\rangle = \frac{1}{2\sqrt{2}} \left(c^\dagger_{1,\uparrow} c^\dagger_{2,\downarrow} - c^\dagger_{1,\downarrow} c^\dagger_{2,\uparrow} \right) |0\rangle, \quad (18)$$

which is nothing but $\frac{1}{2}|s\rangle$. Therefore, acting with the exchange term along the bond indicated in Figure 10(c), the dimer m is de-excited to the singlet state according to (18), whereas the

dimer n is excited to the triplet state according to (17). Comparing now with Figure 2 we see a quite analogous pattern arising: both, the Néel state and the dimer state $|\Psi_0\rangle$ are the ground state of a part of the Hamiltonian, namely the longitudinal part $J\sum_{\langle i,j\rangle} S_{i,z}S_{j,z}$ in the case of the Néel state and the depleted Hamiltonian H_d for the dimer state. Switching on the remainder of the Hamiltonian then creates 'fluctuations': these were the inverted spins or magnons in the case of the Néel state, and the excited dimers in the case of the singlet soup. The fluctuations increase the energy: by $zJ/2$ for a magnon, and by J for a triplet. After having been created these fluctuations then propagate through the lattice. This suggests that we proceed as in the case of spin wave theory and interpret the triplets as effective Bosonic particles (we use Bosons because a triplet is composed of two electrons). To be more quantitative, we need to introduce some conventions: We assume that the bonds are labeled by a number $n \in \{1,\ldots,N/2\}$. Since the triplet has negative parity under the exchange of sites, $1 \leftrightarrow 2$, we need to specify which of the sites i and j in a given dimer corresponds to the site 1 in Eq. (16) and which one to the site 2. We adopt the convention that for a bond in x-direction (y-direction) the left (lower) site always corresponds to the site 1. We call the site which corresponds to 1 the 1-site of the dimer and the site which corresponds to 2 the 2-site of the dimer. For each site i we define $\lambda_i = 1$ if it is the 1-site of its respective dimer, and -1 if it is the 2-site. Then, if a given dimer m is occupied by a singlet, we consider it as occupied by a Bosonic particle, created by $s^\dagger_m$, whereas if the dimer is in one of the three triplet states we consider it as occupied by a Boson, created by $t^\dagger_{m,\alpha}$ with $\alpha \in \{x,y,z\}$. We have already seen that the three triplet states transform like a vector under spin rotations and it follows that the corresponding creation operators form a *vector operator* $[S_\alpha, t^\dagger_\beta] = i\varepsilon_{\alpha\beta\gamma}t^\dagger_\gamma$, and by Hermitean conjugation it is found that the annihilation operator $\mathbf{t}_m$ is a vector operator as well. By calculating the action of the spin operator on triplet states we then find the representation of the spin operator

$$\mathbf{S}_j \to \frac{\lambda_j}{2}\left(s^\dagger\mathbf{t} + \mathbf{t}^\dagger s\right) - \frac{i}{2}\,\mathbf{t}^\dagger \times \mathbf{t}.$$

The x-component of the correspondence $\mathbf{S}_j \to \frac{\lambda_j}{2}\left(s^\dagger\mathbf{t} + \mathbf{t}^\dagger s\right)$ was demonstrated in (17) and (18). We recall that we found $S_{1,x}|s\rangle = \frac{1}{2}|t_x\rangle$ whereas $S_{2,x}|s\rangle = -\frac{1}{2}|t_x\rangle$ and the factor of λ_i keeps track of this sign. From the discussion after (17) we see that such a sign – and hence a factor of λ_i – will occur whenever the Hamiltonian induces a transition between states which have opposite parity under $1 \leftrightarrow 2$. The overall form of the terms on the right-hand side follows from the fact that $\mathbf{S}$ is a Hermitean vector operator, so the right-hand side has to be one as well. Indeed, it is easy to verify that the right-hand side is Hermitean, and the vector product $\mathbf{t}^\dagger \times \mathbf{t}$ is the only way to contract two vector operators into a single one. By forming the scalar product, we can now write the exchange term along a bond connecting the sites i and j such that site i belongs to dimer m, site j to dimer n

$$\begin{aligned} J\,\mathbf{S}_i\cdot\mathbf{S}_j \to{}& \frac{J\lambda_i\lambda_j}{4}\left(s^\dagger_m\mathbf{t}_m + \mathbf{t}^\dagger_m s_m\right)\left(s^\dagger_n\mathbf{t}_n + \mathbf{t}^\dagger_n s_n\right) - \frac{J}{4}\,(\mathbf{t}^\dagger_n\times\mathbf{t}_n)\cdot(\mathbf{t}^\dagger_m\times\mathbf{t}_m) \\ &- \frac{iJ}{4}\Big(\lambda_i\left(s^\dagger_m\mathbf{t}_m + \mathbf{t}^\dagger_m s_m\right)\cdot(\mathbf{t}^\dagger_n\times\mathbf{t}_n) + \lambda_j\left(s^\dagger_n\mathbf{t}_n + \mathbf{t}^\dagger_n s_n\right)\cdot(\mathbf{t}^\dagger_m\times\mathbf{t}_m)\Big), \end{aligned} \tag{19}$$

The right-hand side comprises all possible ways to construct a spin scalar from the vectors $\mathbf{t}$ and $\mathbf{t}^\dagger$ and only the numerical prefactors need to be determined. Lastly, using the identity $\varepsilon_{\alpha\beta\gamma}\varepsilon_{\alpha\mu\nu} = \delta_{\beta\mu}\delta_{\gamma\nu} - \delta_{\beta\nu}\delta_{\gamma\mu}$ the double-cross product in (19) can be written as

$$-\frac{J}{4}\,(\mathbf{t}_n^\dagger \times \mathbf{t}_n)\cdot(\mathbf{t}_m^\dagger \times \mathbf{t}_m) = \frac{J}{4}\sum_{\alpha\neq\beta}\left(t_{m,\alpha}^\dagger t_{n,\alpha}\, t_{n,\beta}^\dagger t_{m,\beta} - t_{m,\alpha}^\dagger t_{n,\alpha}^\dagger\, t_{n,\beta} t_{m,\beta}\right). \tag{20}$$

3.2 Spin ladders

Before proceeding with our discussion of the planar model, we make a short digression to *spin ladders* [12, 13]. As one might have expected, these consist of two parallel spin chains – the 'legs' of the ladder – which are coupled by an exchange along the 'rungs' of the ladder, see Figure 11. Such systems can actually be realized in suitably designed copper oxide compounds such as $SrCu_2O_3$ [14]. Here we consider such a ladder with N_r rungs and periodic boundary conditions in x-direction, the exchange constants along the rungs, J_1, and along the legs, J_2, may be different and we assume $J_1 > J_2$. This selects the 'natural' dimer covering in Figure 11(b), because singlets along the rungs give a lower energy than those along the legs. We define the coordinate axes as indicated, whence our convention for assigning the 1-site and 2-site in a dimer gives the λ's as in the Figure. Any two successive rungs m and $m{+}1$ are connected by two bonds, and one of them connects the two 1-sites, the other one the two 2-sites, so that the products $\lambda_i\lambda_j$ in the first term in (19) all are equal to 1. On the other hand, the terms of 3^{rd} order in triplets in the second line of (19) contain only one factor of λ and therefore cancel between the two bonds connecting the rungs m and $m{+}1$. The Hamiltonian becomes [12]

$$\begin{aligned} H = J_1 \sum_m \mathbf{t}_m^\dagger\cdot\mathbf{t}_m + \frac{J_2}{2}\sum_m\left[\left(\mathbf{t}_m^\dagger\cdot\mathbf{t}_{m+1}^\dagger s_m s_{m+1} + H.c\right) + \left(\mathbf{t}_{m+1}^\dagger\cdot\mathbf{t}_m s_{m+1} s_m^\dagger + H.c\right)\right] \\ + \frac{J_2}{2}\sum_{\alpha\neq\beta}\left(t_{m,\alpha}^\dagger t_{m+1,\alpha}\, t_{m+1,\beta}^\dagger t_{m,\beta} - t_{m,\alpha}^\dagger t_{m+1,\alpha}^\dagger\, t_{m+1,\beta} t_{m,\beta}\right) - \frac{3J_1 N_r}{4}. \end{aligned} \tag{21}$$

The first term describes the increase in energy due to replacing a singlet by a triplet and the particles have to obey the constraint $s_m^\dagger s_m + \mathbf{t}_m^\dagger\cdot\mathbf{t}_m = 1$ separately for each rung m. Except for the first one, all terms in this Hamiltonian are 4^{th} order in the Boson operators, so to make any progress we need to make approximations. As a first step, we assume that the singlet Bosons are condensed into the state with momentum $k{=}0$. This implies that all singlet operators $s_m^\dagger$, s_m can be replaced by a real number s, the singlet condensation amplitude. Next, we replace the constraint on particle number for each rung by a single constraint for all rungs

$$N_r s^2 + \sum_m \mathbf{t}_m^\dagger\cdot\mathbf{t}_m - N_r = 0. \tag{22}$$

It needs to be stressed that this approximation is both drastic and questionable: once the $s_m^\dagger$, s_m are replaced by a mere number, the Hamiltonian contains terms such as $\frac{J_2 s^2}{2}\,\mathbf{t}_{m+1}^\dagger\cdot\mathbf{t}_m$, i.e., a free hopping term for the triplets. On the other hand, the original constraint $s_m^\dagger s_m + \mathbf{t}_m^\dagger\cdot\mathbf{t}_m = 1$ implies that at most one triplet can be on any rung – so that the triplets also have to obey a

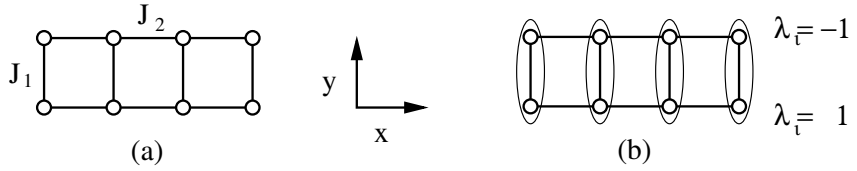

Fig. 11: *A spin ladder.*

hard-core constraint as the magnons. Physically, condensation of the singlets means that they form a kind of inert background and have no excitation spectrum of their own. If this is correct, one might hope that the approximation still is reasonable as long as the density of triplets is low – we made a similar argument for the magnons in linear spin wave theory. Lastly, the terms which are of 4^{th} order in triplet operators are treated in mean-field approximation:

$$\begin{aligned} H_4 &= \frac{J_2}{3}\Big[\Big(\mathbf{t}^\dagger_{m+1}\cdot\mathbf{t}_m\,\langle\mathbf{t}^\dagger_m\cdot\mathbf{t}_{m+1}\rangle - \mathbf{t}^\dagger_m\cdot\mathbf{t}^\dagger_{m+1}\,\langle\mathbf{t}_{m+1}\cdot\mathbf{t}_m\rangle\Big) + H.c.\Big] - A \\ &= J_2\Big[\Big(\,\eta\,\mathbf{t}^\dagger_{m+1}\cdot\mathbf{t}_m - \zeta\,\mathbf{t}^\dagger_m\cdot\mathbf{t}^\dagger_{m+1}\Big) + H.c.\Big] - A. \end{aligned}$$

Here we have introduced the mean-field parameters $\eta = \langle t^\dagger_{m,\alpha}t_{m+1,\alpha}\rangle$ and $\zeta = \langle t_{m+1,\alpha}t_{m,\alpha}\rangle$, which are the same for all α due to spin rotation symmetry, and $A = 3J_2(\eta^2-\zeta^2)$. Lastly, we multiply the constraint (22) by a Lagrange multiplier μ and subtract it from the Hamiltonian. The Hamiltonian is now in a quadratic form and after Fourier transformation becomes

$$\begin{aligned} H_{MF} &= \sum_k \varepsilon_k\,\mathbf{t}^\dagger_k\cdot\mathbf{t}_k + \frac{1}{2}\sum_k \Delta_k\big(\mathbf{t}^\dagger_k\cdot\mathbf{t}^\dagger_{-k} + H.c\big) - n_rA - \mu N_r(s^2{-}1) \\ &= \sum_{k>0}\Big(\varepsilon_k\,(\mathbf{t}^\dagger_k\cdot\mathbf{t}_k + \mathbf{t}^\dagger_{-k}\cdot\mathbf{t}_{-k}) + \Delta_k\,(\mathbf{t}^\dagger_k\cdot\mathbf{t}^\dagger_{-k} + \mathbf{t}_{-k}\cdot\mathbf{t}_k)\Big) - N_rA - \mu N_r(s^2{-}1), \\ \varepsilon_k &= J_1 + J_2\big(s^2{+}2\eta\big)\cos(k) - \mu, \qquad \Delta_k = J_2\big(s^2{-}2\zeta\big)\cos(k). \end{aligned} \tag{23}$$

Note that the Lagrange multiplier μ appears in both, the additive constant and the term ε_k where it may be viewed to act as an additive renormalization $J_1 \to J_1{-}\mu$ of the energy of formation of a triplet. Each of the blocks for a given $k > 0$ can be diagonalized by the ansatz

$$\begin{array}{rcl} \boldsymbol{\tau}^\dagger_k &=& u_k\mathbf{t}^\dagger_k + v_k\mathbf{t}_{-k} \\ \boldsymbol{\tau}_{-k} &=& v_k\mathbf{t}^\dagger_k + u_k\mathbf{t}_{-k} \end{array} \quad\Rightarrow\quad \begin{array}{rcl} \mathbf{t}^\dagger_k &=& u_k\boldsymbol{\tau}^\dagger_k - v_k\boldsymbol{\tau}_{-k} \\ \mathbf{t}_{-k} &=& -v_k\boldsymbol{\tau}^\dagger_k + u_k\boldsymbol{\tau}_{-k} \end{array} \tag{24}$$

where again $u_k^2{-}v_k^2 = 1$. The requirement $[H,\tau^\dagger_{k,\nu}] = \omega_k\tau^\dagger_{k,\nu}$ again leads to a $2{\times}2$ eigenvalue problem and we obtain

$$\omega_k \;=\; \sqrt{\varepsilon_k^2 - \Delta_k^2}, \qquad u_k = \frac{\Delta_k}{\sqrt{2\omega_k(\varepsilon_k-\omega_k)}}, \qquad v_k = \sqrt{\frac{\varepsilon_k-\omega_k}{2\omega_k}}. \tag{25}$$

Reinserting (24) into H_{MF} one finds after a somewhat lengthy calculation that

$$H_{MF} = \sum_{k>0}\Big(\omega_k(\boldsymbol{\tau}^\dagger_k\cdot\boldsymbol{\tau}_k + \boldsymbol{\tau}^\dagger_{-k}\cdot\boldsymbol{\tau}_{-k}) + 3(\omega_k-\varepsilon_k)\Big) - 3N_rJ_2(\eta^2-\zeta^2) - \mu N_r(s^2-1).$$

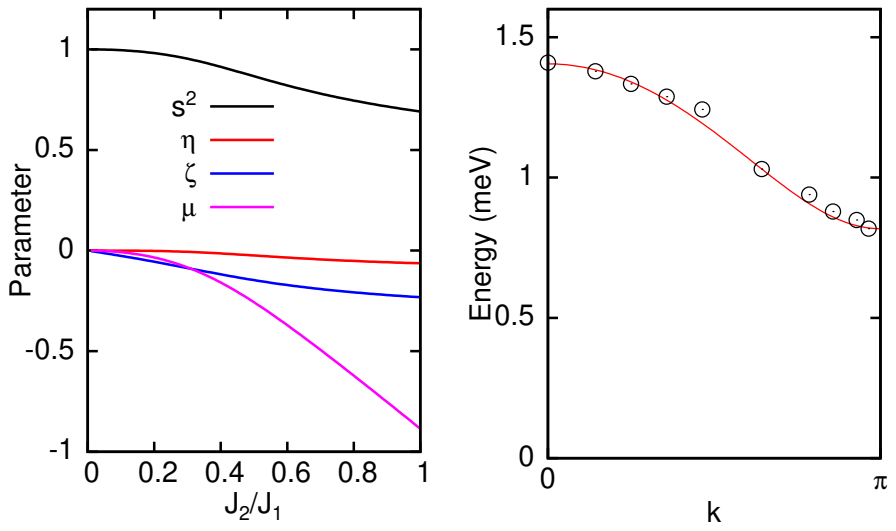

Fig. 12: *Left: mean-field parameters obtained by self-consistent solution of the system of equations (26) as functions of J_2/J_1 [13]. Right: triplet dispersion ω_k in (25) calculated self-consistently for $J_1 = 1.09\,meV$ and $J_2 = 0.30\,meV$ compared to the experimental dispersion for the spin ladder compound $(C_5D_{12}N)_2CuBr_4$ [16].*

It remains to determine the singlet condensation amplitude s, the mean-field parameters η and ζ, and the Lagrange multiplier μ. We consider s, η and ζ as freely adjustable parameters in the Hamiltonian, whence a well-known theorem from thermodynamics [15] tells us that these parameters will adjust themselves such as to minimize the Helmholtz Free Energy $F = U - T{\cdot}S$ of the system. The same holds true for the Lagrange multiplier μ. We restrict ourselves to the case of zero temperature, where $F = U$, the expectation value of H_{MF} in its ground state. The ground state is the vacuum for the $\boldsymbol{\tau}^\dagger$-Bosons, so we can drop the terms $(\boldsymbol{\tau}_k^\dagger \cdot \boldsymbol{\tau}_k + \boldsymbol{\tau}_{-k}^\dagger \cdot \boldsymbol{\tau}_{-k})$ and find

$$U = \frac{3}{2}\sum_k (\omega_k - \varepsilon_k) - 3N_r J_2(\eta^2 - \zeta^2) - \mu N_r(s^2 - 1).$$

Setting the derivatives with respect to the four parameters equal to zero we find

$$\begin{aligned} s^2 &= 1 - \frac{3}{N}\sum_k \frac{\varepsilon_k - \omega_k}{2\omega_k}, & \mu &= \frac{3J_2}{N}\sum_k \frac{\varepsilon_k - \omega_k - \omega_k}{2\omega_k}\cos(k), \\ \eta &= \frac{1}{N}\sum_k \frac{\varepsilon_k - \omega_k}{2\omega_k}\cos(k), & \zeta &= -\frac{1}{N}\sum_k \frac{\Delta_k}{2\omega_k}\cos(k). \end{aligned} \tag{26}$$

This set of self-consistency equations can be solved numerically and the results are shown in Figure 12. We note that s^2 is close to unity, and Eq. (22) then tells us that the density of triplets is low so that the majority of rungs is in the singlet state. The Lagrange multiplier μ is large and negative. As stated above, μ may be considered as an additive correction to the triplet energy $J_{1,eff} = J_1 + |\mu|$. Apparently J_1 is enhanced considerably: due to the hard-core constraint, presence of a triplet on rung m blocks this rung, that means no other triplets can be created on this rung and no other triplet can hop to this rung. It follows that there will be a loss of kinetic energy $\propto J_2$ of the triplets, and this has to be added to the energy cost J_1 for adding a triplet to the system. Consistent with this interpretation, this correction becomes

more important for larger J_2. Finally, the mean-field parameters η and ζ are rather small and could be neglected – this is a consequence of the low density of triplets, $1-s^2$. Figure 12 also shows a comparison of the mean-field dispersion ω_k to the experimental dispersion obtained by INS for the compound $(C_5D_{12}N)_2CuBr_4$, in which the Cu^{2+} ions indeed form spin ladders [16]. With the choice $J_1 = 1.09\,\text{meV}$ and $J_2 = 0.30\,\text{meV}$ the mean-field theory gives quite a good description of experiment, but it should be noted that for other compounds where J_2/J_1 is closer to one the agreement is less satisfactory.

3.3 Planar system

We now return to the planar system and first restrict ourselves to a pure spin system without holes. As we have seen above, the ground state of the half-filled system has antiferromagnetic order and is well described by spin wave theory, so considering the planar Heisenberg model without antiferromagnetic order is strictly speaking unphysical. However, we continue the discussion of the singlet soup because we want to construct a theory for a disordered spin state and its excitations, so as to set the stage for adding the mobile holes. In exactly the same way as for spin ladders we can use the expressions (19) for the Heisenberg exchange to rewrite the Heisenberg Hamiltonian *exactly* in terms of the singlets and triplets for any given dimer covering of the plane such as in Figure 10(a). On the other hand we do not gain very much in this way, because even writing down a dimer covering for a macroscopic system is not feasible, let alone solve the corresponding Hamiltonian. One might consider choosing a particular 'simple' dimer covering, such as periodically repeating the spin ladder in Figure 11 in y-direction. However, since one is forced to make approximations, the special symmetry of the covering will make itself felt in the approximate solutions as an artificial supercell structure, leading to a reduction of the Brillouin zone and an unphysical backfolding of bands.

On the other hand, rewriting the Hamiltonian in terms of the singlet and triplet Bosons provides an exact representation of the Heisenberg model for *any* dimer covering of the plane. This means that, for example, the result for the spin correlation function $\langle \mathbf{S}_j(t) \cdot \mathbf{S}_i \rangle$ cannot depend on the specific dimer covering in which the calculation is carried out. Put another way, the way in which a spin excitation propagates through the network of dimers from site $i \to j$ during the time t does not depend at all on the geometry of the particular dimer covering. This suggests to construct a translationally invariant approximate Hamiltonian by *averaging* the dimer Hamiltonian over all possible coverings.This means that now *every* bond in the lattice may be occupied by a Boson and the averaged Hamiltonian for two bonds m and n connected by the exchange term is $\bar{h}_{m,n} = \zeta\, h_{m,n}$ with $h_{m,n}$ given in (19) and

$$\zeta = \frac{N_{m,n}}{N_d}. \tag{27}$$

Here $N_{m,n}$ is the number of dimer coverings which contain the bonds n and m whereas N_d is the total number of dimer coverings. The resulting Hamiltonian obviously is translationally invariant and isotropic. We estimate ζ by a crude approximation: consider two adjacent bonds

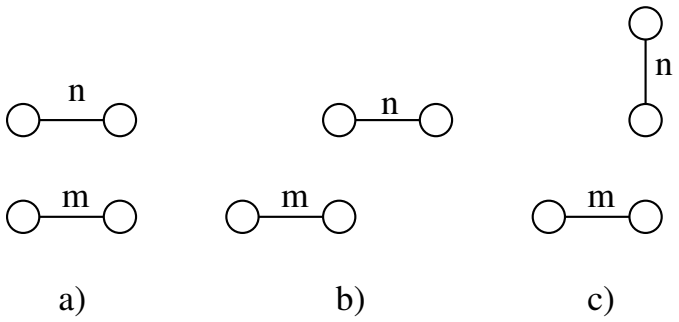

Fig. 13: *Estimation of the renormalization factor ζ.*

as in Figure 13. By symmetry the bond m is covered by a dimer in exactly $1/4$ of all dimer coverings and we restrict ourselves to these. Assuming for simplicity that the number of coverings containing one of the three possible orientations of the adjacent bond n are equal, we estimate $\zeta = 1/12$. From now on, we proceed in the same way as in the case of spin ladders. As a first step we assume that the singlets are condensed and replace all operators $s_m^\dagger$, s_m in (19) by a real number s. To keep things simple we, moreover, discard the interaction terms in (19), that means the terms of 3^{rd} or 4^{th} order in the triplet operators. The terms of 4^{th} order could again be treated in mean-field approximation but as we have seen in the discussion of spin ladders the corresponding mean-field parameters η and ζ were quite small. With these simplifications the Hamiltonian becomes

$$H = \tilde{J} \sum_m \mathbf{t}_m^\dagger \cdot \mathbf{t}_m^\dagger + \frac{\zeta s^2}{4} \sum_{m,n} \sum_{\substack{i \in m \\ j \in n}} J_{i,j}\, \lambda_i\, \lambda_j \Big(\mathbf{t}_m^\dagger \cdot \mathbf{t}_n^\dagger + \mathbf{t}_n \cdot \mathbf{t}_m + \mathbf{t}_m^\dagger \cdot \mathbf{t}_n + \mathbf{t}_n^\dagger \cdot \mathbf{t}_m \Big). \qquad (28)$$

The sum runs over all $2N$ bonds in the averaged system, $J_{i,j} = J$ when i and j are nearest neighbors and zero otherwise. The first term describes the change in energy when a singlet on bond m is replaced by a triplet, and initially we set $\tilde{J} = J$. The second term describes the propagation of the triplets. Being a quadratic form, (28) is readily diagonalized by Fourier transform – we only need to specify a convention for the position of a bond: if bond m connects the sites i and j we define $\mathbf{R}_m = (\mathbf{R}_i + \mathbf{R}_j)/2$. Moreover we have to keep in mind that we have two species of bonds, namely bonds in x-directions and bonds in y-direction. We specify this by an additional subscript for the Fourier transformed operators, e.g., $\mathbf{t}_{\mathbf{k},\mu}^\dagger$ with $\mu \in \{x, y\}$. The products $\lambda_i \lambda_j$ are given in Figure 14 from which we readily can read off

$$H = \sum_{\mathbf{k}} \sum_{\mu,\mu' \in \{x,y\}} \left(\mathbf{t}_{\mathbf{k},\mu}^\dagger \left(\tilde{J} \delta_{\mu\mu'} + \varepsilon_{\mu,\mu'}(\mathbf{k}) \right) \mathbf{t}_{\mathbf{k},\mu'} + \frac{1}{2} \left(\mathbf{t}_{\mathbf{k},\mu}^\dagger\, \varepsilon_{\mu,\mu'}(\mathbf{k})\, \mathbf{t}_{-\mathbf{k},\mu'}^\dagger + H.c. \right) \right)$$

with

$$\begin{aligned} \varepsilon_{x,x}(\mathbf{k}) &= \zeta s^2 J \left(\cos(k_y) - \frac{1}{2}\cos(2k_x) - \cos(k_x)\cos(k_y) \right), \\ \varepsilon_{x,y}(\mathbf{k}) &= \zeta s^2 J \left(\sin\Big(\frac{3k_x}{2}\Big) \sin\Big(\frac{k_y}{2}\Big) + \sin\Big(\frac{k_x}{2}\Big) \sin\Big(\frac{3k_y}{2}\Big) \right), \end{aligned}$$

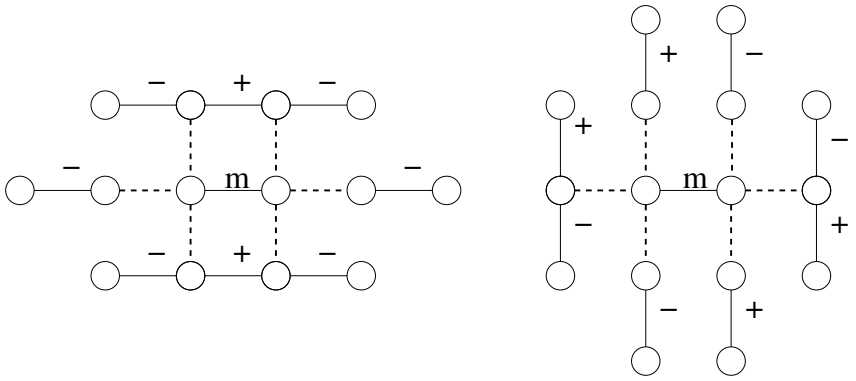

Fig. 14: *The factors of $\lambda_i\lambda_j$ for all bonds connected to the bond m by a nearest neighbor bond. In a) both bonds are along the x-direction so that these pairs contribute to $\varepsilon_{x,x}$ whereas in b) one bond is along y-direction so that these pairs contribute to $\varepsilon_{x,y}$. In a) both bonds connecting parallel bonds have $\lambda_i\lambda_j = 1$.*

$\varepsilon_{y,x} = \varepsilon_{x,y}$, and $\varepsilon_{y,y}$ is obtained from $\varepsilon_{x,x}$ by $k_x \leftrightarrow k_y$. To diagonalize H we repeat the procedure for spin ladders and make the *ansatz* (with $\nu \in \{1,2\}$)

$$\begin{aligned} \boldsymbol{\tau}^\dagger_{\nu,\mathbf{k}} &= \sum_{\mu\in\{x,y\}} \left(u_{\nu,\mathbf{k},\mu}\, \mathbf{t}^\dagger_{\mathbf{k},\mu} + v_{\nu,\mathbf{k},\mu}\, \mathbf{t}_{-\mathbf{k},\mu} \right), \\ \boldsymbol{\tau}_{\nu,-\mathbf{k}} &= \sum_{\mu\in\{x,y\}} \left(v^*_{\nu,\mathbf{k},\mu}\, \mathbf{t}^\dagger_{\mathbf{k},\mu} + u^*_{\nu,\mathbf{k},\mu}\, \mathbf{t}_{-\mathbf{k},\mu} \right), \end{aligned} \tag{29}$$

Demanding $[H,\, \boldsymbol{\tau}^\dagger_{\nu,\mathbf{k}}] = \omega_{\nu,\mathbf{k}} \boldsymbol{\tau}^\dagger_{\nu,\mathbf{k}}$ gives the non-Hermitean 4×4 eigenvalue problem

$$\begin{pmatrix} \tilde{J}+\varepsilon_{\mathbf{k}} & -\varepsilon_{\mathbf{k}} \\ \varepsilon^*_{-\mathbf{k}} & -\tilde{J}-\varepsilon^*_{-\mathbf{k}} \end{pmatrix} \begin{pmatrix} u_{\nu,\boldsymbol{k}} \\ v_{\nu,\boldsymbol{k}} \end{pmatrix} = \omega_{\nu,\mathbf{k}} \begin{pmatrix} u_{\nu,\boldsymbol{k}} \\ v_{\nu,\boldsymbol{k}} \end{pmatrix}. \tag{30}$$

For a matrix like the one on the left hand side it is easy to show that if (u, v) is an eigenvector with eigenvalue ω, then (v^*, u^*) is an eigenvector with eigenvalue $-\omega$ so that the eigenvalues come in pairs of $\pm\omega$. We multiply (30) by $\omega_{\nu,\mathbf{k}}$ and replace products such as $\omega_{\nu,\mathbf{k}} u_{\nu,\boldsymbol{k}}$ or $\omega_{\nu,\mathbf{k}} v_{\nu,\boldsymbol{k}}$ on the left hand side of the resulting equations by the expressions given by the original version of (30). Since the commutator $[\tilde{J}+\varepsilon_{\mathbf{k}},\, \varepsilon_{\mathbf{k}}] = 0$ we obtain

$$\left(\tilde{J}^2 + 2\tilde{J}\varepsilon_{\mathbf{k}}\right) u_{\nu,\boldsymbol{k}} = \omega^2_{\nu,\mathbf{k}}\, u_{\nu,\boldsymbol{k}},$$

and the same equation for $v_{\nu,\boldsymbol{k}}$. It follows that $\omega_{\nu,\mathbf{k}} = \sqrt{\tilde{J}^2 + 2\tilde{J}\lambda_{\nu,\mathbf{k}}}$, where $\lambda_{\nu,\mathbf{k}}$ are the eigenvalues of the Hermitean 2×2 matrix $\varepsilon_{\mathbf{k}}$, and both, $u_{\nu,\boldsymbol{k}}$ and $v_{\nu,\boldsymbol{k}}$, must be the corresponding eigenvector, albeit multiplied by different prefactors. The eigenvalues of $\varepsilon_{\mathbf{k}}$ are $\lambda_{1,\mathbf{k}} = -\zeta s^2 J/2$ and $\lambda_{2,\mathbf{k}} = \zeta s^2 J(3/2 + 2\gamma_{\mathbf{k}} - 4\gamma^2_{\mathbf{k}})$, with $\gamma_{\mathbf{k}}$ given in (5).

In principle we should now repeat the self-consistency procedure for spin ladders but for the sake of simplicity we switch to a more phenomenological description, using the discussion of spin ladders as a guideline. There we saw that the energy needed to convert a singlet into a

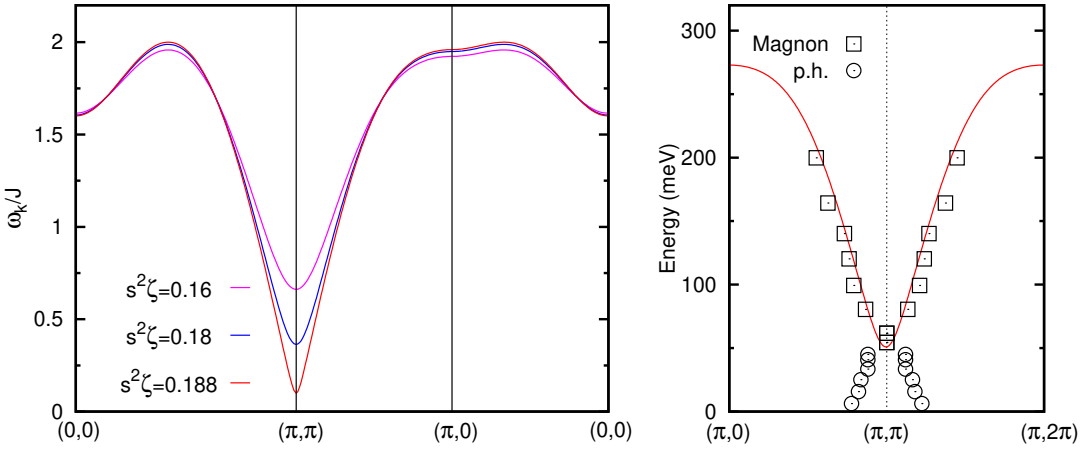

Fig. 15: *Left: Spin excitation dispersion relation $\omega_{\mathbf{k}}$ using the parameter values $\tilde{J} = 1.7\,J$ and different $s^2\zeta$. Right: $\omega_{\mathbf{k}}$ calculated for $\tilde{J} = 1.7\,J$, $s^2\zeta = 0.16$ and $J = 140\,meV$ compared to the hourglass dispersion measured in $La_{1.875}Ba_{0.125}CuO_4$ [17]. The data points labeled 'Magnon' correspond to the triplet dispersion, the points labeled 'p.h.' correspond to particle-hole excitations which are absent in our theory.*

triplet was increased to $J_1+|\mu|$ – see (23) – whereby $|\mu|$ could be quite appreciable for $J_2 \to J_1$, see Figure 12. We had interpreted this as an additional cost in kinetic energy because a triplet would block a given rung. Clearly the same would happen also for the planar system, and accordingly we assume that the prefactor of the first term in (28) is $\tilde{J} > J$ which we take as a first adjustable parameter. Next, we will not attempt to calculate the singlet condensation amplitude s but consider the product $s^2\zeta$ as a single adjustable parameter. We recall that ζ was determined somewhat vaguely anyway. Our theory now has two adjustable parameters, which we use to fix two physical quantities, the total bandwidth of the spin excitations, and the spin gap (to be explained below). Lastly, we recall that we have two eigenvalues $\lambda_{\nu,\mathbf{k}}$ for each wave vector $\mathbf{k}$, whereby $\lambda_{1,\mathbf{k}}$ has the peculiar feature of being independent of $\mathbf{k}$. A more detailed analysis shows [18], that the band derived from the dispersionless eigenvalue also has zero spectral weight in the spin correlation function. This suggests, that this band is an artifact of the enlargement of the basis by doubling the number of bonds. We therefore drop this dispersionless band and retain only the band of spin excitations resulting from $\lambda_{2,\mathbf{k}}$. Figure 15 then shows the resulting triplet dispersion $\omega_{\mathbf{k}}$. The parameter $\tilde{J}$ has been adjusted to set the total bandwidth to $2J$, the bandwidth for antiferromagnetic spin waves. $\omega_{\mathbf{k}}$ has its minimum at (π,π) and the energy at this wave vector is frequently called the spin gap, Δ_S. With increasing value of $s^2\zeta$, Δ_S closes rapidly and one can envisage how for $\Delta_S \to 0$ the cone-shaped dispersion of antiferromagnetic spin waves at (π,π) is recovered. Experimentally, INS on many cuprate compounds shows an 'hourglass' dispersion around (π,π) – an example is shown in Figure 15. This is frequently interpreted [19] as a magnon-like collective mode above the neck of the hour-glass co-existing with particle-hole excitations of the Fermi gas of free carriers below the neck. The part above the neck of the hourglass thus should correspond to our triplet band and the comparison in Figure 15 shows reasonable agreement.

3.4 Doped holes

Having developed a description for a disordered spin system we are finally ready to include doped holes into our theory. To that end we introduce dimers which contain a single electron or no electron at all. We again consider a dimer with sites 1 and 2, but now assume that the dimer contains one electron with spin σ. This means that instead of the exchange term now the hopping term is active: $H_t = -t \sum_\sigma \left(\hat{c}^\dagger_{1,\sigma}\hat{c}_{2,\sigma} + H.c.\right)$ and there are two eigenstates of H_t

$$|f_{\pm,\sigma}\rangle = \frac{1}{\sqrt{2}}\Big(\hat{c}^\dagger_{1,\sigma} \pm \hat{c}^\dagger_{2,\sigma}\Big)|0\rangle, \tag{31}$$

which obviously obey $H_t|f_{\pm,\sigma}\rangle = \mp t|f_{\pm,\sigma}\rangle$. To extend our theory to doped system, we introduce a new type of effective particle to represent dimers occupied by one electron. Namely if dimer m is in one of the states $|f_{\pm,\sigma}\rangle$ we consider it as occupied by a Fermion, created by $f^\dagger_{m,\pm,\sigma}$. We choose a Fermion, because the number of electrons in such a dimer is one. We also introduce one more Boson, created by $e^\dagger$, to represent an empty dimer. In order to include these particles we need to transcribe the electron creation and annihilation operators $\hat{c}^\dagger_{i,\sigma}$ and $\hat{c}_{i,\sigma}$. The two spin components of any Fermion creation operator can be combined into a two-component vector or spinor $\mathbf{a}^\dagger = \left(a^\dagger_\uparrow, a^\dagger_\downarrow\right)^T$. The spin components of any Fermion annihilation operator also can be combined into a spinor $\mathbf{a} = \left(a_\uparrow, a_\downarrow\right)^T$ but under spin rotations this type of spinor transforms as $i\tau_y\mathbf{a}^\dagger$ [20]. Using this notation we can write (with $j \in \{1,2\}$)

$$\mathbf{c}_j \to :\ \frac{1}{2}\big(s\, i\tau_y + \lambda_j \mathbf{t}\cdot\boldsymbol{\tau} i\tau_y\big)\left(\mathbf{f}^\dagger_+ - \lambda_j \mathbf{f}^\dagger_-\right) + \frac{1}{\sqrt{2}}\, e^\dagger\left(\mathbf{f}_+ + \lambda_j \mathbf{f}_-\right)\ : \tag{32}$$

where $: \cdots :$ denotes normal ordering. As was the case for the triplets, the overall form of the terms on the right-hand side can be guessed by making use of the transformation properties under spin rotations. Namely the 'spinor product' $\mathbf{t}\cdot\boldsymbol{\tau}\mathbf{a}$ is the way to construct a new spinor from a vector operator $\mathbf{t}$ and given spinor $\mathbf{a}$. The factors of λ_j again are associated with states of opposite parity under $1 \leftrightarrow 2$. From now on we omit the terms involving the $e^\dagger$-Bosons because for low hole concentration the probability to find two holes in the same dimer will be small. We rewrite the hopping term, again along a bond connecting the sites i and j such that site i belongs to dimer m, site j to dimer n:

$$\begin{aligned} -t\sum_\sigma \hat{c}^\dagger_{i,\sigma}\hat{c}_{j,\sigma} \to\ & \frac{t}{4}\Big((s^\dagger_m s_n\ + \lambda_i\lambda_j \mathbf{t}^\dagger_m\cdot\mathbf{t}_n)\Big(\sum_\sigma f^\dagger_{n,j,\sigma} f_{m,i,\sigma}\Big) \\ & - \big(\lambda_i \mathbf{t}^\dagger_m s_n + \lambda_j s^\dagger_m \mathbf{t}_n\big)\cdot\mathbf{v}_{(n,j),(m,i)} - i\lambda_i\lambda_j\big(\mathbf{t}^\dagger_m\times\mathbf{t}_n\big)\cdot\mathbf{v}_{(n,j),(m,i)}\Big), \end{aligned} \tag{33}$$

where the combination $f_{m,i,\sigma} = f_{m,+,\sigma} - \lambda_i\, f_{m,-,\sigma}$ and the vector

$$\mathbf{v}_{(n,j),(m,i)} = \sum_{\sigma,\sigma'} f^\dagger_{n,j,\sigma}\,\boldsymbol{\tau}_{\sigma,\sigma'}\, f_{m,i,\sigma'}$$

obeys $[S_\alpha,\, v_\beta] = i\varepsilon_{\alpha\beta\gamma}\, v_\gamma$. Again, the right-hand side is a linear combination of all possible ways to construct a spinor from another spinor and one or two vector operators. Next, we make

analogous approximations as in the case of the triplet Hamiltonian. We average the Hamiltonian over dimer coverings, again introducing the factors of ζ. We discard the terms in the second line of (33) which describe the emission/absorption of a triplet by a Fermion or the scattering of a Fermion from a triplet. The terms in the first line of (33) are treated in mean-field approximation, that means we replace the singlet operators $s_m^\dagger$, s_m by the real number s, the singlet condensation amplitude. A full mean-field decomposition would also produce expectation values such as $\langle \mathbf{t}_m^\dagger \cdot \mathbf{t}_m \rangle$, but such expectation values were discarded above and we do the same here. All in all we obtain in this way

$$H_F = -t \sum_{m,\sigma} \left(f^\dagger_{m,+,\sigma} f_{m,+,\sigma} - f^\dagger_{m,-,\sigma} f_{m,-,\sigma} \right) + \frac{s^2 \zeta t}{4} \sum_{m,n} \sum_{\substack{i \in m \\ j \in n}} \sum_{\sigma} f^\dagger_{n,j,\sigma} f_{m,i,\sigma}, \qquad (34)$$

where the sums over m and n run over all $2N$ bonds in the system.
We now arrive at the crucial point which distinguishes the present theory from most others: how do we count the electrons? Obviously, each $f^\dagger_{m,\pm,\sigma}$-Fermion contains one hole and has a z-spin of σ. Accordingly, in a given dimer covering the number of Fermions must be equal to the number of doped holes, $N_h = N - N_e$

$$N_h = \sum_{m,\sigma} \left(f^\dagger_{m,+,\sigma} f_{m,+,\sigma} + f^\dagger_{m,-,\sigma} f_{m,-,\sigma} \right), \qquad (35)$$

where the sum is over the $N/2$ dimers. We have obtained an approximate theory by averaging over dimer coverings, so that each of the $2N$ bonds in the plane can be occupied by a Boson or Fermion. The physically relevant quantity, however, is the *density of holes per site*, whereas the number of dimers looses its significance due to the averaging approximation. We therefore retain the condition (35), but with the sum over m now over all $2N$ bonds in the system. This condition implies, that the bands obtained by diagonalizing (34) have to be filled from below with N_h *holes*, and since the $f^\dagger_{m,\pm,\sigma}$-Fermions have a spin of $\frac{1}{2}$, the Fermi surface covers a fraction of $n_h/2$ of the Brillouin zone. As the Mott-insulator is approached, $n_e \to 1$ or $n_h \to 0$, the volume of the Fermi surface approaches zero.
We continue with the discussion of the band structure. We are interested mainly in the lowermost bands – these are the ones which will accommodate the doped holes – so for simplicity we drop the $f^\dagger_{m,-,\sigma}$-Fermions, because their energy is $2t$ above that of the $f^\dagger_{m,+,\sigma}$-Fermions, whereas the dispersive terms are $\propto s^2\zeta t \approx 0.2t$. With this last approximation Fourier transformation gives $H_F = \sum_{\mathbf{k},\sigma} v^\dagger_{\mathbf{k},\sigma} \tilde{H}_{\mathbf{k}} v_{\mathbf{k},\sigma}$ with the vector $v_{\mathbf{k},\sigma} = (f_{\boldsymbol{k},x,+,\sigma}, f_{\boldsymbol{k},y,+,\sigma})^T$. The $\mathbf{k}$-dependence of the 2×2 matrix $\tilde{H}_{\mathbf{k}}$ can again be read off from Figure 14, but with all $\lambda = 1$. We obtain

$$\tilde{H}_{x,x} = -t + s^2\zeta t \left(\cos(k_y) + \cos(k_x)\cos(k_y) + \frac{1}{2}\cos(2k_x) \right)$$
$$\tilde{H}_{x,y} = s^2\zeta t \left(\cos\Big(\frac{3k_x}{2}\Big)\cos\Big(\frac{k_y}{2}\Big) + \cos\Big(\frac{k_x}{2}\Big)\cos\Big(\frac{3k_y}{2}\Big) \right),$$

$\tilde{H}_{y,x} = \tilde{H}_{x,y}$ and $\tilde{H}_{y,y}$ is obtained from $\tilde{H}_{x,x}$ by $k_x \leftrightarrow k_y$. The eigenvalues of $\tilde{H}_{\mathbf{k}}$ are $\varepsilon_{1,\mathbf{k}} = -t + s^2\zeta t/2$ and $\varepsilon_{2,\mathbf{k}} = -t + s^2\zeta t(-3/2 + 2\gamma_{\mathbf{k}} + 4\gamma_{\mathbf{k}}^2)$. More detailed investigation shows [18]

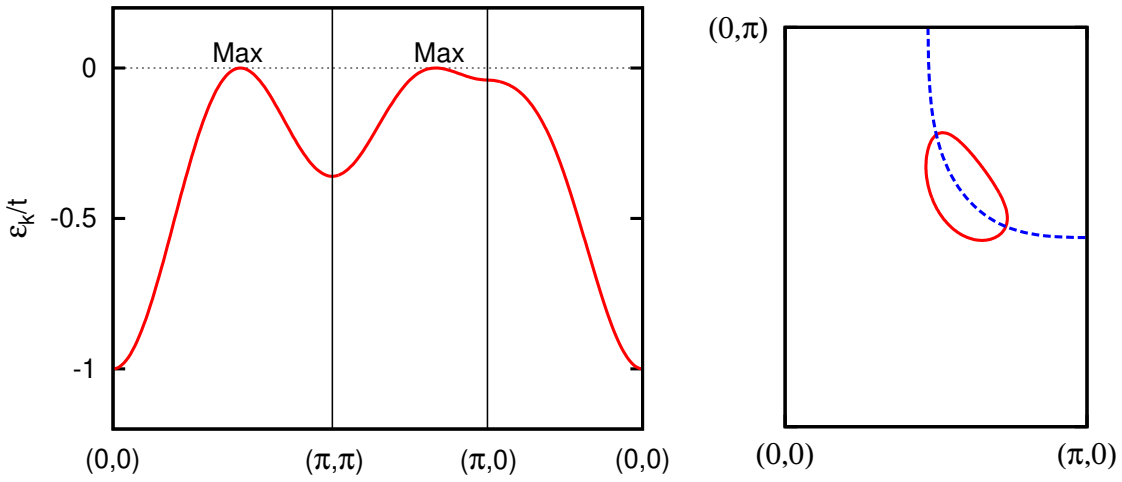

Fig. 16: *Left: Dispersion dispersion relation $-\varepsilon_{2,\boldsymbol{k}}$ for $s^2\zeta = 0.16$. Holes would occupy the maxima of this band – indicated in the Figure – so that the zero of energy corresponds roughly to the Fermi energy for small doping. Right: Adding additional hopping terms between $(1,1)$ and $(2,0)$-like neighbors lifts the degeneracy of the band maximum (indicated in blue) and the Fermi surface takes the form of a hole pocket (indicated in red) [18]. The values are $t' = -0.2t$, $t'' = 0.1t$ and the hole concentration $\delta = 1-n_e = 0.1$.*

that the dispersionless band $\varepsilon_{1,\mathbf{k}}$ has zero weight in the electron spectral function, so again we interpret this as an artifact of the enlargement of the basis states and discard it. As we have seen above the band structure resulting from (34) has to be filled with holes from below, that means at $T = 0$ the condition for the Fermi energy E_F is

$$n_h = \frac{2}{N}\sum_{\boldsymbol{k}} \Theta\big(\varepsilon_{2,\mathbf{k}} - E_F\big).$$

Figure 16 shows $-\varepsilon_{2,\mathbf{k}}$, that means the band is again turned upside down as it would be seen in ARPES. The maxima therefore correspond to the minima of $\varepsilon_{2,\mathbf{k}}$, and this is the location in $\mathbf{k}$-space where the doped holes would accumulate. $\varepsilon_{2,\mathbf{k}}$ depends on $\mathbf{k}$ only via $\gamma_{\mathbf{k}}$, so that lines of constant $\gamma_{\mathbf{k}}$ automatically are lines of constant $\varepsilon_{2,\mathbf{k}}$, in particular the maximum of the inverted dispersion is a roughly circular contour around (π,π). The Fermi surface therefore would be a ring with a width $\propto n_h$, which does not agree with ARPES results. This is a drawback of the present approximation and it is likely that even a small perturbation would lift the degeneracy of the maximum and lead to a unique maximum around which the Fermi surface would be centered. One such perturbation could be the additional hopping terms $\propto t', t''$ discussed above and inclusion of the terms indeed lifts the degeneracy and leads to a Fermi surface which takes the form of a hole pocket centered along the $(1,1)$ direction, see Fig. 16. Comparing to experiment, the pocket is shifted towards (π,π) – one might speculate that including the coupling between holes and triplets, described by the omitted terms in (33) might improve this, but at present this is speculation.

4 Summary and outlook

As explained in the introduction, the hallmark of a Mott insulator is the breakdown of the Fermi surface due to the effectively enhanced Coulomb repulsion in 'small' atomic orbitals: if the number of electrons is equal to the number of sites, N, the electrons are caught in a 'traffic jam' and form a spin system instead of a half-filled band with a Fermi surface. The spins interact via virtual hopping processes of electrons as described by the Heisenberg exchange, which leads to antiferromagnetic correlations and spin excitations.

In the description of the *doped* Mott insulator given in the preceding sections, the electrons continue to form a mere spin system: the majority of electrons are coupled to inert ('condensed') singlets, a few singlets are excited to the triplet state, so that most electrons still contribute only their spin degrees of freedom. This is not surprising, because for a low density of vacancies, most electrons still are completely surrounded by other electrons and thus 'stuck'. Instead, the true mobile Fermions in the system are the $f^\dagger$-particles, which may be viewed as tightly bound states of a spinless hole and one spin, and their number equals the doped holes. Since the $f^\dagger$-particles have a spin of $\frac{1}{2}$, their Fermi surface covers a fraction $n_h/2$ of the Brillouin zone, where $n_h = 1-n_e$ is the concentration of *holes*. We recall that for free electrons the fraction of the Brillouin zone covered by the Fermi surface is $n_e/2$, which differs drastically from $n_h/2$.

On the other hand, the state where the electrons are 'jammed' and form an inert background can persist only over a limited range of the hole concentration n_h. A crude estimate for the range of stability of this phase can be obtained by noting that once the hole concentration reaches $1/z = 0.25$, on average each electron will find an empty site on one of its z neighbors to which it can hop without creating a double occupancy. With increasing n_h it therefore will become energetically favorable for the electrons to form the all-electron Fermi surface of the free electron gas, although the strong scattering will lead to correlation narrowing of the quasiparticle band and strong incoherent weight in the single-particle spectral function. In fact, in the limit $n_e \to 0$ it is known [5] that one recovers a Fermi surface with volume $n_e/2$ but enhanced effective mass.

Accordingly, at some critical hole concentration $n_{h,c}$ we expect a phase transition from the doped Mott-insulator with a hole-like Fermi surface of fractional volume $n_h/2$ described by the above theory, to a renormalized all-electron Fermi liquid with an electron-like Fermi surface of fractional volume $n_e/2$. And, in fact, the experimental situation has pretty much converged to this scenario: a transition between two nonmagnetic Fermi liquids of spin-$\frac{1}{2}$ particles without any obvious order but different Fermi surface volume, which occurs at a hole concentration $n_{h,c} \approx 0.22$. This is discussed in detail in Ref. [18]. Assuming that this $T = 0$ phase transition 'shrouds itself in superconductivity' as quantum phase transitions often do, one arrives at the phase diagram in Figure 17. In fact, unlike many other quantum phase transitions, the transition in the cuprates appears to be between two phases which are homogeneous, isotropic and nonmagnetic and differ only in the Fermi surface volume, so that there is no obvious order parameter. This would be consistent with the above scenario. The detailed description of this transition and how it can give rise to the spectacularly high superconducting transition temperatures is probably the key problem in understanding cuprate superconductors.

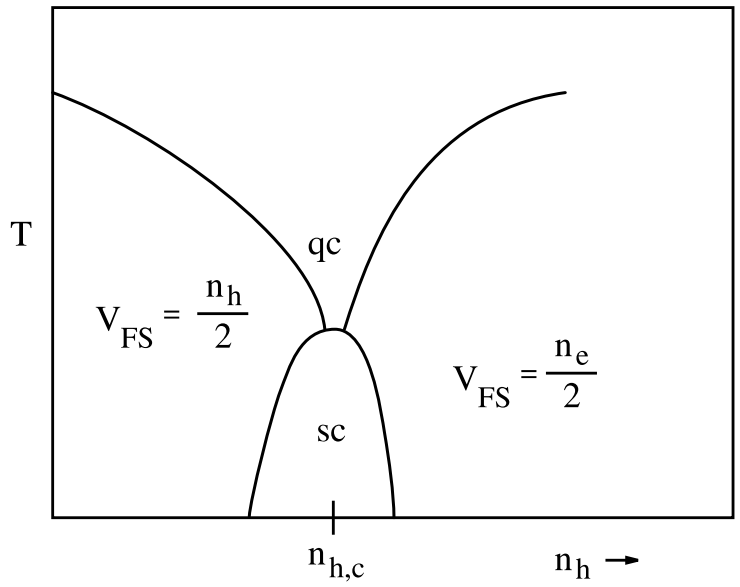

Fig. 17: *Schematic phase diagram for the cuprate superconductors. There is a quantum critical point at the hole concentration $n_{h,c} \approx 0.22$ which at $T = 0$ corresponds to a transition between two Fermi liquids of different fractional Fermi surface volume V_{FS}. The transition gives rise to a superconducting dome (sc) in the phase diagram, and a quantum critical region with non-Fermi liquid behavior above it (qc).*

References

[1] J.G. Bednorz and K.A. Müller, Z. Phys. B **64**, 189 (1986)

[2] K.A. Chao, J. Spałek, A.M. Oleś, J. Phys. C10, L **271** (1977)

[3] F.C. Zhang, T.M. Rice, Phys. Rev. B **37**, 3759 (1988)

[4] P.W. Anderson, Phys. Rev. **86**, 694 (1952)

[5] A.L. Fetter and J.D. Walecka, *Quantum Theory of Many-Particle Systems* (McGraw-Hill, San Francisco, 1971)

[6] R. Coldea, S.M. Hayden, G. Aeppli, T.G. Perring, C.D. Frost, T.E. Mason, S.-W. Cheong, and Z. Fisk, Phys. Rev. Lett. **86**, 5377 (2001)

[7] L.N. Bulaevskii, E.L. Nagaev, and D.L. Khomskii, Sov. Phys. JETP. **27**, 836 (1968)

[8] S.A. Trugman, Phys. Rev. 37, 1597 (1988); *ibid* Phys. Rev. B **41**, 892 (1990)

[9] R. Eder and K.W. Becker, Z. Phys. B **78**, 219 (1990)

[10] S. LaRosa, I. Vobornik, F. Zwick, H. Berger, M. Grioni, G. Margaritondo, R.J. Kelley, M. Onellion, and A. Chubukov Phys. Rev. B **56**, R525(R) (1997)

[11] S. Sachdev and R.N. Bhatt, Phys. Rev. B **41**, 9323 (1990)

[12] S. Gopalan, T.M. Rice, and M. Sigrist, Phys. Rev. B **49**, 8901 (1994)

[13] B. Normand and Ch. Rüegg, Phys. Rev. B **83**, 054415 (2011)

[14] E. Dagotto and T.M. Rice, Science **27**, 618 (1996)

[15] H.B. Callen, *Thermodynamics and an Introduction to Thermostatistics* (Wiley, 1985)

[16] A.T. Savici, G.E. Granroth, C.L. Broholm, D.M. Pajerowski, C.M. Brown, D.R. Talham, M.W. Meisel, K.P. Schmidt, G.S. Uhrig, and S.E. Nagler, Phys. Rev. B, **80**, 094411 (2009)

[17] J.M. Tranquada, H. Woo, T.G. Perring, H. Goka, G.D. Gu, G. Xu, M. Fujita, and K. Yamada, Nature **429**, 534 (2004)

[18] R. Eder, Phys. Rev. B **100**, 085133 (2019)

[19] M. Fujita, H. Hiraka, M. Matsuda, M. Matsuura, J.M. Tranquada, S. Wakimoto, G. Xu, and K. Yamada, J. Phys. Soc. Jpn. **81**, 011007 (2012)

[20] L.D. Landau and E.M. Lifshitz: *Lehrbuch der Theoretischen Physik* (Akademie Verlag Berlin, 1988)

7 Mott Physics in Correlated Nanosystems: Localization-Delocalization Transition by the Exact Diagonalization Ab Initio Method

Józef Spałek
Institute of Theoretical Physics
Jagiellonian University, Kraków

Contents

E. Pavarini and E. Koch (eds.)
Topology, Entanglement, and Strong Correlations
Modeling and Simulation Vol. 10
Forschungszentrum Jülich, 2020, ISBN 978-3-95806-466-9
http://www.cond-mat.de/events/correl20

1 Introduction & motivation: Localized versus itinerant

The textbook division of the electronic states in quantum matter ranges between the two principal categories: *(i)* localized (bound, atomic) states and *(ii)* extended (delocalized, band, Fermi-liquid, free-particle-like) states. The two classes of states are depicted schematically in Fig. 1. While the question of existence of space-bound states in solids are described and characterized experimentally to a very good accuracy [1], the transformation of those atomic states into emerging delocalized states in solid state physics (or in general, in condensed matter physics) is still under debate. The classical textbooks on the latter subject with a successful implementation of wave mechanics to molecular and metallic systems start with the Bloch theorem establishing the periodic nature of the single-electron states in solids under the influence of the corresponding translation-symmetric single-particle potential. The first success of the methods of the LCAO, Hückel, etc. approaches was quite impressive given a total negligence of the interparticle interactions. Those interactions are not only of Coulomb type, but also of the, e.g., van der Waals type which appear in molecular or solid-state systems.

The question of including interparticle interactions in the context of periodic solid-state systems was posed qualitatively by Nevill Mott (for review see [2,3]). Mott based his argument on earlier experimental observations: for example, cobalt oxide, CoO, according to the elementary Wilson classification of electronic states, should be regarded as a metallic system, since it possesses an odd number of valence electrons. Quite to the contrary, it was recognized as one of the best insulators known then. The argument was that probably the repulsive electron-electron interaction is responsible for a destruction of coherent periodic Bloch states, as it favors separating the particles from each other as far as possible, i.e., fixing them on the atomic states they originate from. Additionally, Mott argued later that the transition between atomic-type and itinerant (Bloch-type) states should be discontinuous (first-order), since the Coulomb interaction is long-range, so the transition must take place from zero-concentration limit (insulating ground state) to the metallic state of sizable electron concentration, to warrant screening of the increasing - energy Coulomb interaction. In such a situation, those insulators should not only be clear-cut from metals with odd number of valence electrons, but also from the full-band Wilson-type insulators. In that, two features of such Mott (or Mott-Hubbard) systems should be singled out. First, as they contain unpaired spins, their magnetic ordering is tightly connected with them, usually of antiferromagnetic type as was discussed clearly by Anderson, see eg., [4] and Goodenough [5]. Second, the Mott localization should be common to any condensed matter system, such as quark-gluon plasma [6] or even cold-atom bosonic systems, and should appear if only the repulsive interparticle interaction is strong compared to their bare band (kinetic) energy. This shows a universal character of the related physics, particularly to those system in which such a matter-insulator (localization-delocalization) transition is observed. A textbook example of an electronic system with such a transitions is the vanadium sesquioxide doped with chromium, $(V_{1-x}Cr_x)_2O_3$ (see Fig. 2 and [7])

The aim of this chapter is to characterize first briefly the most striking properties of Mott-Hubbard systems of macroscopic size and then turn to the question of the localization in cor-

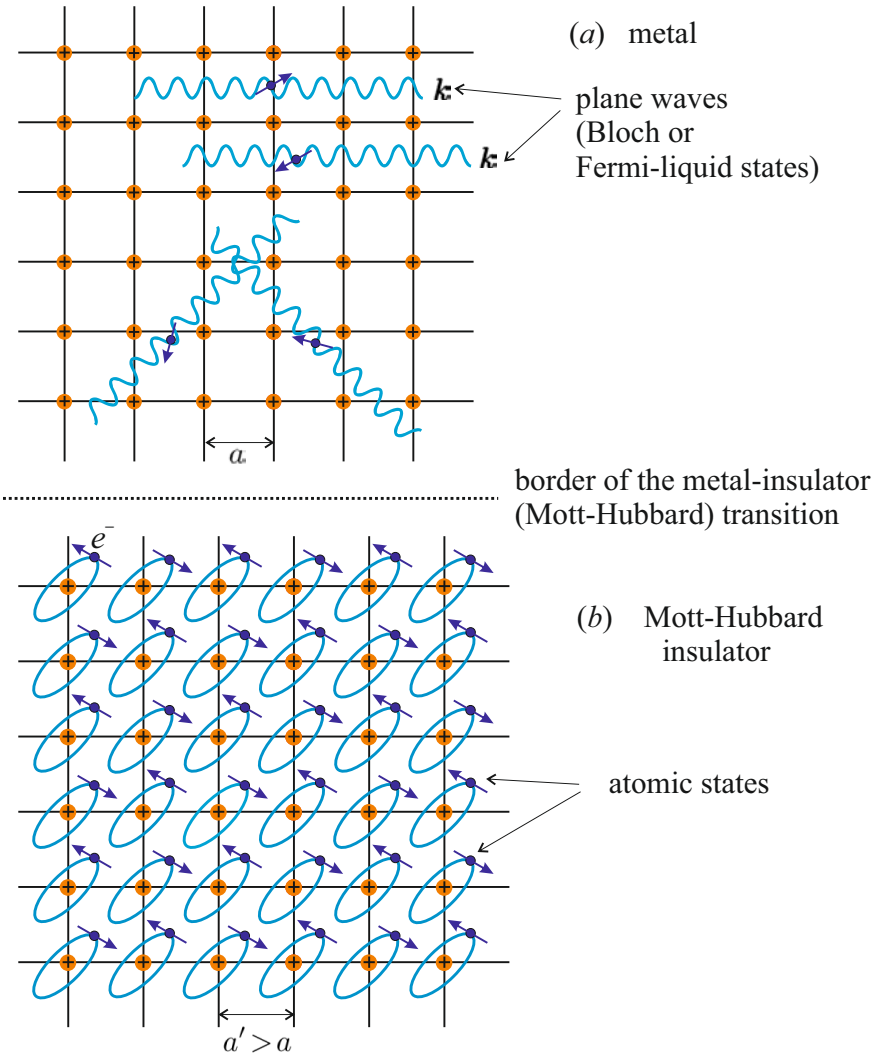

Fig. 1: *Schematic representation of metallic (Fermi-liquid) (a) and Mott-Hubbard insulating (localized) states (b). Note that in the state (a) electrons derive from the parent atoms, which form a background lattice of cations (red solid points). The spins of unpaired electrons form as a rule an antiferromagnetic lattice.*

related nanosystems. The atomicity and itineracy of the valence electrons in the latter case can then be seen clearly on example of exact results, at least for model systems. This analysis should provide us with additional arguments for the universality of the Mott phenomenon within the physics of quantum condensed matter.

2 Essence of Mott-Hubbard localization: A physical picture

In this section we define the concept of almost an localized Fermi liquid and the thermodynamic character of the Mott-Hubbard transition for electrons in a single narrow band. This picture is based on the Hubbard model and its direct variational analysis.

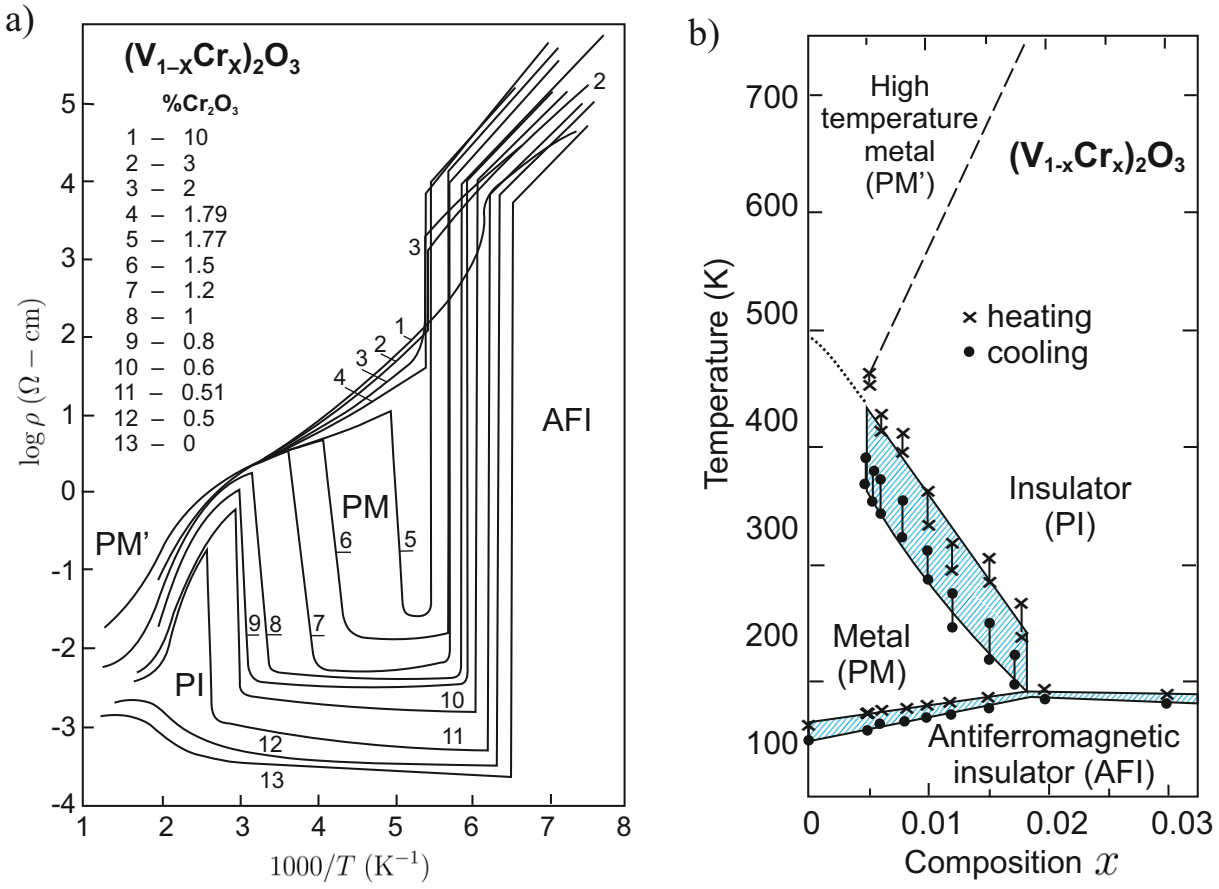

Fig. 2: *a) Temperature dependence of the electrical resistivity (in logarithmic scale) vs.* $1/T$ *for Cr-doped* V_2O_3*. A very sharp transition from antiferromagnetic insulating (AFI) to paramagnetic metallic (PM) phase is followed by a reverse PM* $\rightarrow$ *PI at higher temperature, which in turn is followed by PI* $\rightarrow$ *PM' crossover transition to a reentrant metallic (PM') phase at still higher temperatures; b) Phase diagram for the same system in the* T*-*x *plane; the hatched area depicts the hysteretic behavior accompanying the discontinuous transitions (taken from Ref. [7, 8], with small modifications. Both AFI* $\rightarrow$ *PM and PM* $\rightarrow$ *PI represent examples of the Mott-Hubbard transition (see main text).*

2.1 Definitions

The ground-state energy of a periodic system of fermions can be described by starting from the system of atomic configurations and, subsequently, adding other dynamic interactions which appear in the emerging condensed state. Namely, its energy per atomic state can be simply expressed in the form of [9]

$$\frac{E_G}{N} = \varepsilon_a + \langle T \rangle + \langle V \rangle + \langle V_{12} \rangle \equiv E_1 + E_2, \tag{1}$$

where ε_a is the single particle energy in an atomic (*Wannier*) state, $\langle T \rangle$ and $\langle V \rangle$ are the average kinetic and potential energies in, whereas $\langle V_{12} \rangle$ is the expectation value of the two-particle interaction. The single-particle part E_1 comprises the first three terms, and $E_2 \equiv \langle V_{12} \rangle$. In such a periodic system near the delocalization-localization transition, we usually assume that

$\varepsilon_a = 0$; i.e., it is regarded as a constant (reference) value which is often disregarded unless stated explicitly (see next sections). In this manner, the remaining terms characterize solely the energy contributions of relevant fermions in the condensed state with respect to that in the atomic state. Note also that usually $E_1 < 0$. Next, one can define two physically distinct regimes:

1° $|E_1| \gtrsim E_2$: Fermi-liquid (metallic) regime, ranging from a simple-metal region ($|E_1| \gg E_2$), through the Fermi-liquid regime, to the delocalization-localization threshold $|E_1| \approx E_2$;

2° $|E_1| \ll E_2$: strong-correlation (Mott-Hubbard) regime.

Let us characterize briefly each of them and introduce the states in these regimes. Connected with this we start from an atomic (Wannier) representation of the involved states and interactions, in the situation *1°*. The starting point is described then by either a gas of fermions or a Landau Fermi liquid, and associated with both of them momentum representation and the Fermi-Dirac statistics (distribution) in its canonical form. In discussing the correlated system, we start as a rule from the Wannier representation (see below). This means that, in general, we can start from two *complementary* representations of the single-particle quantum-mechanical states, i.e., either from the Bloch representation, in which the momentum uncertainty is zero, or from the Wannier representation, in which the proper quantum number characterizing the state is a fixed lattice position, at which the wave function is centered. The above division into the two asymptotic regimes $|E_1| \gg E_2$ and $|E_1| \ll E_2$ is illustrated in Fig. 1, where the *complementary* nature of the single-particle states is represented for the example of a solid with metallic (delocalized) states of electrons (a) or correlated (atomic, Mott) states (b) for the case with one relevant valence electron per parent atom. Additionally, we have marked a dividing line (*the Mott-Hubbard boundary*) between the two macrostates. The momentum representation is described by set of the Bloch functions $\{\Psi_{\mathbf{p}\sigma}(\mathbf{r})\}$ with (quasi)momentum $\mathbf{p} = \hbar\mathbf{k}$ and spin quantum number $\sigma = \pm 1 \equiv \uparrow, \downarrow$, whereas the position representation is expressed by the corresponding set of Wannier states $\{w_{i\sigma}(\mathbf{r})\}$. These two representations are equivalent in the sense that they are related by the lattice Fourier transformation. However, in the situation depicted in Fig. 1, when we have a sharp boundary (usually *first-order phase-transition line*) between the states shown in (a) and (b), this equivalence is broken and, in effect, the unitary symmetry U(N) does not apply. The macroscopic state (a) near the transition is represented, strictly speaking, by a modified Landau-Fermi liquid (the so-called *almost localized Fermi liquid*, ALFL), whereas the Mott-insulating state is well accounted for as a localized-spin (Heisenberg) antiferromagnet. From the above qualitative picture one can infer that with approaching the *metal* $\rightarrow$ *insulator boundary*, i.e., with the formation of a localized-spin state, the kinetic energy of the *renormalized-by-interaction* particle progressive motion throughout the system is drastically reduced and, as a result, it reduces to zero in the localized (insulating) state. Effectively, one can say that then the Landau quasiparticle effective mass $m^* \rightarrow \infty$. This feature illustrates the situation that strong enough interactions (called in this context *strong correlations*) limit the stability of the Landau-Fermi quasiparticle picture, as is exemplified explicitly by the appearance of the Mott-Hubbard phase transition. Also, a proper quantitative description of the transition

requires a model with a simultaneous generation of the effective exchange interactions (*kinetic exchange* [10] in the one-band case or superexchange in the multi-orbital situation). In the subsequent Sections 2 and 3 we provide a quantitative analysis of these statements. The starting point of these considerations is the parametrized microscopic Hamiltonian provided below. We limit our discussion to the Hubbard model as an illustration of the more complicated analysis of nanophysical systems in Sections 4 and 5.

2.2 Correlated (nano)materials

The following are examples of bulk systems belonging to *1°* or *2°*

1° Mott-Hubbard systems: $((V_{1-x}Cr_x)_2O_3$ [7]), $NiS_{2-x}Se_x$ [11], organic metals [12];

2° Mott (antiferromagnetic) insulators: NiO, CoO, La_2CuO_4, $YBa_2Cu_3O_7$ etc., strongly correlated metals, high temperature superconductors: $La_{2-x}Sr_xCuO_4$, $YBa_2Cu_3O_{7-\delta}$, heavy fermion systems: $CeAl_3$, $CeCu_2Si_2$, UBe_{13}, $CeCoIn_5$, etc.

These are the most typical systems and can be regarded as almost localized Fermi-liquids. There are also systems with quantum phase transitions and non-Landau (non-Fermi) liquid states, but those are regarded as a separate class as then the quantum fluctuations are as important on the correlations. Those systems are not tackled in detail here.
At this point we would like to say a few words about the correlated nanosystems. The atomic (bound) states are localized by definition. The basic question is what happens when we form, e.g., a nanochain or nanoring. How can such a small system become a nanometal (e.g., a monoatomic quantum wire), when we vary the interatomic distance? In other words, at what point does the set of discrete atomic states form a nanoliquid? We address this type of questions after analyzing first the nature of the delocalization in bulk systems.

2.3 From Landau-Fermi liquid to Mott-Hubbard insulator through an almost localized Fermi liquid

The Landau theory of Fermi liquids represents a standard reference point in the theory of interacting fermions (for recent references see [13–15]). Here we characterize only briefly their characteristics, particularly those which appear or are relevant to theory of correlated systems.
The principal assumption of the theory is that we are interested in the changes of *ideal-Fermi-gas-properties*, which are induced by the inter-particle interactions and associated with thermal excitations at low temperatures. In other words, we express the change of the total energy of the system due to the appearing interaction in the Landau form

$$\delta E \simeq \sum_{\boldsymbol{k}\sigma} \varepsilon_{\boldsymbol{k}\sigma}\, \delta n_{\boldsymbol{k}\sigma} + \frac{1}{2} \sum_{\boldsymbol{k}\boldsymbol{k}'} f^{\sigma\sigma'}_{\boldsymbol{k}\boldsymbol{k}'}\, \delta n_{\boldsymbol{k}\sigma}\, \delta n_{\boldsymbol{k}'\sigma'} \equiv \sum_{\boldsymbol{k}\sigma} E_{\boldsymbol{k}\sigma} \delta n_{\boldsymbol{k}\sigma}, \tag{2}$$

where $\varepsilon_{\boldsymbol{k}\sigma}$ is the single-particle energy (with respect to the chemical potential μ) and $f^{\sigma\sigma'}_{\boldsymbol{k}\boldsymbol{k}'}$ (generally spin-dependent) is the effective interaction between those particles; it has the form of

spin-dependent density-density interactions. Explicitly, the bare-particle energy in the Zeeman field H_a is $\varepsilon_{\boldsymbol{k}\sigma} \equiv \varepsilon_{\boldsymbol{k}} - g\mu_B H_a\sigma - \mu$ and in the isotopic liquid (not generally true for fermions in lattice systems) we have that $f^{\sigma\sigma'}_{\boldsymbol{k}\boldsymbol{k}'} = f^s_{\boldsymbol{k}\boldsymbol{k}'}(\boldsymbol{k}\cdot\boldsymbol{k}'/k_F^2) + \sigma\sigma' f^a(\boldsymbol{k}\cdot\boldsymbol{k}'/k_F^2)$, where k_F is the Fermi wave vector and $f^{s,a}$ express spin-independent and spin-dependent parts, respectively. The next assumption is that we take into account the interaction-induced scattering processes for particles at the Fermi surface, i.e, put that $\boldsymbol{k}\cdot\boldsymbol{k}'/k_F^2 = \cos\theta_{\boldsymbol{k}\boldsymbol{k}'}$ and subsequently we can express the interaction parameters in terms of a Legendre polynomial expansion

$$f^{(s,a)}(\cos\theta) = \sum_{l=0}^{\infty} f_l^{(s,a)} P_l(\cos\theta). \tag{3}$$

There are three basic assumptions in the Landau formulation of the Fermi-liquid theory. First, the interparticle scattering is important only very near or, strictly speaking, at the Fermi surface due to the Pauli principle, i.e., the circumstance that particles can scatter only from occupied states $|\boldsymbol{k}\sigma\rangle$ into unoccupied ones. Second, a well defined Fermi surface remains intact even if the scattering processes are included (this is *the Luttinger theorem* proved later on the grounds of perturbation expansion and assuming validity the Dyson theorem, which is not always valid for correlated systems). Third, there is a *one-to-one* correspondence between the initial (bare energy states, $\varepsilon_{\boldsymbol{k}\sigma}$) and the effective (*quasiparticle*) states with energies $E_{\boldsymbol{k}\sigma} \equiv \varepsilon_{\boldsymbol{k}\sigma} + \frac{1}{2}\sum_{\boldsymbol{k}'\sigma'} f^{\sigma\sigma'}_{\boldsymbol{k}\boldsymbol{k}'}\delta n_{\boldsymbol{k}'\sigma'}$. Moreover, the Fermi energy value $E_F \equiv \mu$ at $T = 0$ can be regarded as the reference energy for both the *bare-* and *quasi-particle* states. Effectively, this means that the interaction processes, practically active only at the Fermi surface, do not influence the Fermi surface volume. Finally, from the third assumption it follows that the statistical distribution for the quasiparticles can be taken in the form of the Fermi-Dirac distribution for those states, i.e., $f(E_{k\sigma}) = [\exp(\beta E_{k\sigma}) + 1]^{-1}$.

The additional ingenious feature of the theory is the circumstance that the principal properties of a Fermi liquid, such as liquid ^{3}He, can be expressed solely by the first three parameters of expansion (3): f_0^s, f_1^s, and f_0^a, what makes this theory, even though phenomenological in its nature, fully testable in its original form, at least for the isotropic quantum liquid ^{3}He. What is more important, the assumption about the Fermi-Dirac distribution applicability has been tested on two systems: experimentally, for liquid ^{3}He (cf. Fig. 3ab) and theoretically by considering the evolution of the statistical distribution function, calculated exactly for model nano-chains and nano-rings of hydrogen atoms, as a function of interatomic distance [16,17] (see later here).

Nevertheless, as shown in Fig. 3a and b, the effective-mass concept (m_3^*) for ^{3}He atoms breaks down and consequently, the linear specific heat γ ceases to exist at the liquid-solid transition (cf. Fig. 3b). These effects cannot be accounted for within the Landau-Fermi liquid theory. We discuss that question next within the Hubbard model by introducing first the concept of *an almost localized Fermi liquid* and, as a consequence, a discontinuous delocalization-localization (metal-insulator) phase transition. These aspects are regarded as the fundamental features of correlations.

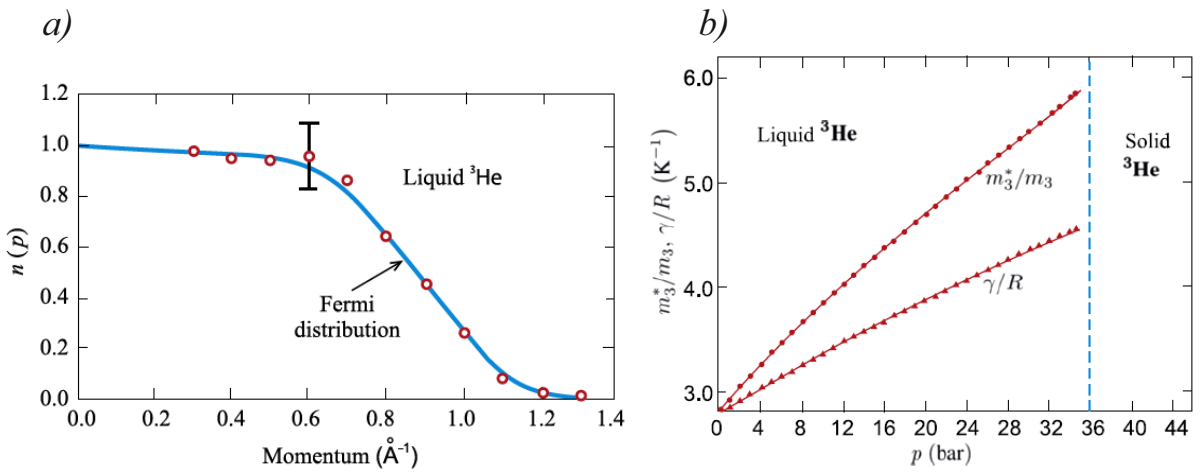

Fig. 3: *Principal characteristics of liquid ^{3}He as a Fermi liquid: a) the Fermi-Dirac distribution measured by neutron scattering at ambient pressure and temperature $T = 0.37$ K [18]; b) the linear-specific-heat coefficient γ in units of gas constant R and inferred from it effective atom mass enhancement m_3^*/m_3, both as a function of external pressure [19]. The vertical dashed line marks the liquid-solid transition, regarded in this case as a discontinuous Mott transition to the localized state of whole atoms. The spin $1/2$ is attached to the nuclei for this case of two-electrons atoms in $1s^2$ configuration.*

2.4 The concept of almost localized Fermi liquid (ALFL)

One can notice from Fig. 3b that the Fermi-liquid state characterized there by the linear specific-heat coefficient (in units of gas constant R), γ/R and the resulting effective-mass enhancement m_3^*/m_3 of the ^{3}He atom in this milieu, both loose their meaning at *the liquid-solid transition*, which takes place at the relatively low external pressure $\simeq$ 36 bar. At this point the atoms freeze into well-defined crystal positions and their individual quantum mechanical states are characterized from now on by a set of Wannier functions $\{w(\mathbf{r}\cdot\mathbf{r}_i)\}$ centered at well-defined lattice sites $\{\mathbf{r}_i\}$. It must be underlined that in this case there is no external single-particle potential trapping the particles, as it is the case for electrons in solids. Such a solidification is regarded thus as an example of a spontaneous breakdown of translational symmetry, albeit in a discontinuous manner. Our task in this section is to briefly discuss the delocalization states in the metallic liquid of electrons close to the transition to the localized state, and next, explain its first-order phase-transition nature.

We model the system by starting from the Hubbard Hamiltonian (4) and calculate first the system ground-state energy per atomic site $\langle\mathcal{H}\rangle/N$. The interaction between correlated particles in the simplest form is given by the single-band Hubbard model [20, 21] with $\varepsilon_a = 0$ (i.e., $t_{ii} = 0$; hence the primed summation in the first term),

$$\tilde{\mathcal{H}} = \sum_{ij\sigma}{}' t_{ij}\,\hat{a}^\dagger_{i\sigma}\,\hat{a}_{j\sigma} + U\sum_i \hat{n}_{i\uparrow}\,\hat{n}_{i\downarrow}, \tag{4}$$

in which $t_{ij} \equiv \langle w_i|\mathcal{H}_1|w_j\rangle < 0$ represents the single-particle parameter phrased as *the hopping parameter*, (and with the bandwidth of bare states $W \equiv 2z\big|\sum_{j(i)} t_{ij}\big|$,where $j(i)$ means the

summation over neighboring sites to i), and U is the magnitude of intraatomic interactions the so-called *Hubbard term*. For strongly correlated electrons we can rephrase the conditions *1°* and *2°*. Namely, situations with $W \gtrsim U$ or $W \simeq U$ represent the systems below and at the Mott-Hubbard transition, respectively, whereas the $W \ll U$ case represents the strong-correlation limit *2°*. Note again that the primed summation in (4) excludes the $i = j$ term $\sum_{i\sigma} t_{ij}\hat{n}_{i\sigma} = t_0 N_e$, when the system is transitionally invariant ($t_{ii} = t_0\ \forall i$); then, $N_e = \sum_{i\sigma} \hat{n}_{i\sigma}$ is the total number of particles of N atomic sites ($n \equiv N_e/N$ is the so-called band filling). If we regard that the reference atomic energy of each of the electrons does not change near the metal-insulator transition ($W \simeq U$), then to N_0 can be thought of an irrelevant constant term (reference energy) and disregarded. This assumption must be revised (see later) as one includes an ab initio calculations, i.e., when the parameters are also calculated explicitly. But, first we analyze the situation as a function of U/W for the half-filled ($n = 1$) situation.

When approaching the localization-delocalization transition we expect that the single-particle and interaction parts become of comparable amplitude. Due to this circumstance, we assume that the hopping probability $\langle \hat{a}^\dagger_{i\sigma}\, \hat{a}_{j\sigma}\rangle$ is renormalized by the interaction to the form $\langle \hat{a}^\dagger_{i\sigma}\, \hat{a}_{j\sigma}\rangle \equiv q\langle \hat{a}^\dagger_{i\sigma}\, \hat{a}_{j\sigma}\rangle_0$, where $\langle \hat{a}^\dagger_{i\sigma}\, \hat{a}_{j\sigma}\rangle_0$ is the hopping probability for noninteracting *(uncorrelated)* particles and q is the so-called renormalization (band narrowing) factor: $q \to 1$ when $U \to 0$ and $q \to 0$ when $U \to U_C$, where U_C is the critical interaction value for the transition to the localized state to the take place. Explicitly, we can write down the system internal energy in the form (for $U \leqslant U_C$) [22, 23]

$$\frac{E_G}{N} = \frac{1}{N}\sum_{\boldsymbol{k}\sigma} E_{\boldsymbol{k}}\, f(E_{\boldsymbol{k}}) + U d^2, \tag{5}$$

where $E_{\boldsymbol{k}} \equiv q\varepsilon_{\boldsymbol{k}}$, $d^2 \equiv \langle \hat{n}_{i\uparrow}\, \hat{n}_{i\downarrow}\rangle$, and $f(E_{\boldsymbol{k}})$ in the Fermi-Dirac function for renormalized particles regarded still as quasiparticles. In this expression d^2 is regarded as a variational parameter to be calculated self-consistently. Therefore, the whole problem reduces to determining microscopically $q \equiv q(d^2)$. This can be carried out by considering Gutzwiller's variational approach [24], but also from physical considerations [25]. It turns out that for the half-filled ($n = 1$) state (i.e., with one particle per atomic site) and for systems with electron-hole symmetry this factor can be calculated in the elementary manner [25] which yields the simple result $q(d^2) = 8d^2(1-2d^2)$. Additionally, we have that for a constant density of states, the chemical potential can be set $\mu \equiv 0$ and thus for $H_a = 0$ we have

$$\bar{\varepsilon} \equiv \frac{1}{N}\sum_{\boldsymbol{k}\sigma} (E_{\boldsymbol{k}}/q) = -\frac{W}{4}, \tag{6}$$

where $E_{\boldsymbol{k}}/q \equiv \varepsilon_{\boldsymbol{k}}$ represents, as before, the single particle energy of bare particles at the temperature $T = 0$; also, the effective-mass renormalization is $m^* = m_B/q$, where m_B is the bare band mass.

By minimizing energy (6) with respect to d^2 we obtain both the physical ground-state energy and the quasiparticle energy spectrum $\{E_{\boldsymbol{k}}\}$. This in turn, allows us to calculate concrete ground-

state and thermodynamic properties. Explicitly [23, 26, 27],

$$d^2 = \frac{1}{4}\left(1 - \frac{U}{U_C}\right), \tag{7}$$

$$\frac{E_G}{N} = \frac{1}{4}\left(1 - \frac{U}{U_C}\right)^2 \bar{\varepsilon}\,, \tag{8}$$

$$\frac{m^*}{m_0} = \frac{1}{1 - \left(\frac{U}{U_C}\right)^2} \qquad \equiv \frac{1}{q_0} \equiv 1 + \frac{1}{3}F_1^s\,, \tag{9}$$

$$\gamma = \gamma_0 \frac{m^*}{m_0} = \gamma_0 \frac{1}{q_0} \qquad \equiv \gamma_0 \left(1 + \frac{1}{3}F_1^s\right), \tag{10}$$

$$\chi = \chi_0 \frac{1}{q_0 \left[1 - \rho_0(\mu)\, U \cdot \frac{1+U/2U_c}{(1+U/U_c)^2}\right]} \qquad \equiv \chi_0 \frac{m_0}{(m^*)\,(1+F_a^0)}\,, \tag{11}$$

$$\frac{\chi}{\gamma} = \frac{\chi_0}{\gamma_0} \frac{1}{1 - \rho_0(\mu)\, U \cdot \frac{1+U/2U_c}{(1+U/U_c)^2}}\,, \tag{12}$$

with $U_C \equiv 8|\bar{\varepsilon}| = 2W$ (the second value is for constant density of states). Additionally, to calculate the magnetic susceptibility χ, the full Gutzwiller approach have been used [24]. When $U \to U_C \to 0$, $d^2 \to 0$, the ground-state energy $E_G \to 0$, the effective mass $m^* \to \infty$, and the magnetic susceptibility to linear specific heat coefficient $\chi/\gamma \to 4$. We see that at the transition, the interaction (> 0) and the single particle (< 0) parts compensate each other, the mass for translational motion throughout the system diverges, and the magnetic susceptibility is roughly proportional to γ. The $U = U_C$ point thus represents the dividing line between the itinerant and atomic states of the matter and the freezing of particles into a lattice breaks the whole system translational invariance (at least, in liquid ^{3}He case). A full microscopic approach requires the explicit determination of the parameters U and $\bar{\varepsilon}$ as a function of pressure. Low-temperature corrections to eq. (7)–(12) have been detailed elsewhere [23, 15]. The expression appearing on the right of the $\equiv$ sign give the results from Landau theory.

One may say that the picture formed by the expressions (7)–(12) represents, as in any Fermi-liquid theory, a basic quasiparticle picture, with the additional boundary of its applicability for $U < U_C$. In fact, this picture can be mapped into the Landau-Fermi-liquid parametrization of the physical properties at $T = 0$ [28]. The question remains what are the collective spin- and charge-excitation spectra in the present case. This subject is a matter of our present studies and will not be detailed here [29, 30].

2.5 Delocalization-localization (Mott-Hubbard) transition

As has been mentioned in the preceding section, the delocalization-localization transition at $T = 0$ takes place at $U = U_C \approx W$. The question is when this transition will appear at arbitrary $T \geqslant 0$. This question is a nontrivial one, since near the transition, the renormalized single-particle and interaction energy not only almost compensate each other, but also each of the two terms vanishes separately. In such a situation, small perturbations such as the thermal

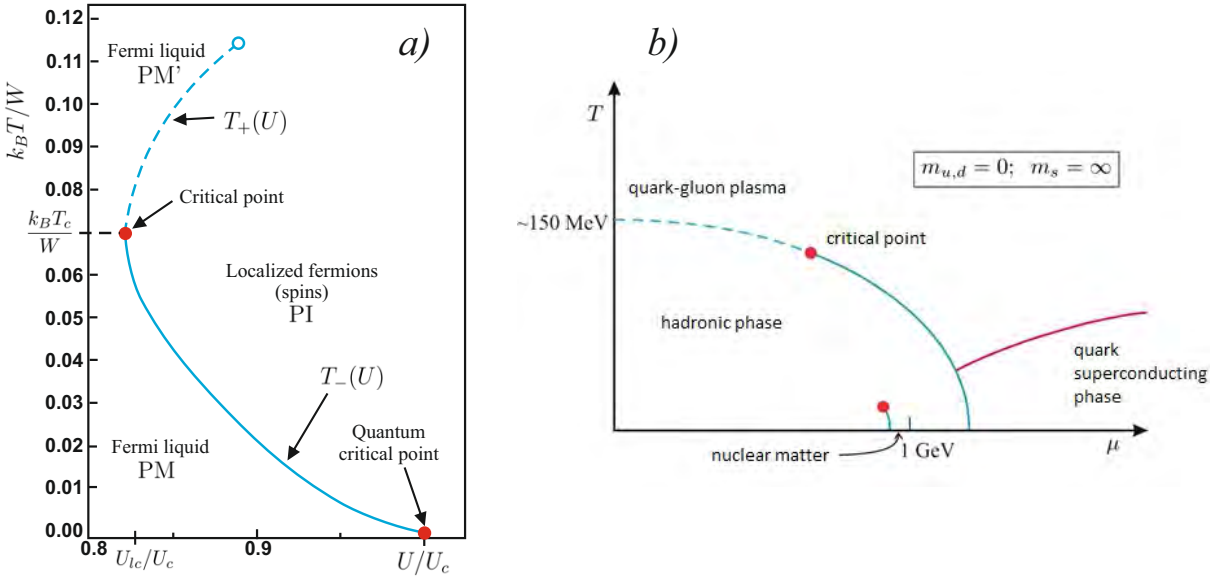

Fig. 4: *a) Phase diagram at $T \neq 0$ for almost localized fermions in the temperature T versus relative interaction magnitude U/U_C plane. Note the presence of two critical points: classical at $T = T_c$ and quantum at $T = 0$. This phase diagram does not include the magnetic phases (see below [22]); b) an analogous phase diagram for nuclear matter [31]. In both cases, the dashed lines represent extrapolations to the high-temperature regime.*

or atomic disorder, applied magnetic field, or even the onset of magnetic order may balance out two quantum-mechanical contributions towards either insulating (localized) or itinerant (ALFL, metallic) state. We discuss the effect of nonzero temperature.

Starting from the internal energy (3) we define the free energy functional of the itinerant correlated system [22, 23] as follows

$$\frac{\mathcal{F}}{N} = \frac{1}{N}\sum_{\boldsymbol{k}\sigma} E_{\boldsymbol{k}}\, f_{\boldsymbol{k}\sigma} + Ud^2 + \frac{k_BT}{N}\sum_{\boldsymbol{k}\sigma}\big(f_{\boldsymbol{k}\sigma}\ln f_{\boldsymbol{k}\sigma} + (1-f_{\boldsymbol{k}\sigma})\ln(1-f_{\boldsymbol{k}\sigma})\big), \tag{13}$$

where $f_{\boldsymbol{k}\sigma}$ is the Fermi-Dirac function for quasiparticles with energies $E_{\boldsymbol{k}\sigma}$ and the last term is the entropy in the given, not necessarily, the equilibrium state, which we determine subsequently by minimizing $\mathcal{F}$. This expression allows also for developing the low-temperature (Sommerfeld-type) expansion defined as the regime with $k_BT/qW \ll 1$. In effect, the first non-trivial terms in the paramagnetic state have the form

$$\frac{\mathcal{F}}{N} = -q\frac{W}{4} + Ud^2 - \frac{\gamma_0 T^2}{q} + \mathcal{O}(T^4). \tag{14}$$

After a minimizing the functional $\mathcal{F}$ with respect to the d^2, we obtain the physical free energy $\mathcal{F}$ of ALFL. A detailed analysis of the low-T expansion is provided in [23], where the Gutzwiller-Brinkman-Rice approach is generalized to $T > 0$. Note that the expressions describe the free energy functional for an almost localized Fermi liquid to be minimized with respect to d^2. As before, we assume that $\mu \equiv 0$, which means that electron-hole symmetry holds. The next step is to introduce the concept of discontinuous phase transitions in the context of this fermion

itinerant state instability. We regard the ALFL as a well-defined phase in the thermodynamic sense and the lattice of localized electrons (spins) as the other. Then, the discontinuous phase boundary between them is determined from the coexistence condition $F = F_I$, where F_I is the free energy of the insulating state and has a very simple form if the spins are disordered

$$\frac{F_I}{N} = -k_B T \ln 2, \tag{15}$$

where $k_B \ln 2$ is the entropy of $S = 1/2$ spins. From the coexistence condition, we obtain two transition temperatures

$$k_B T_{\pm} = \frac{3q_0}{2\pi^2} W \left\{ \ln 2 \pm \left[(\ln 2)^2 - \frac{\pi^2}{3} \left(1 - \frac{U}{U_C} \right)^2 \Big/ q_0 \right]^{1/2} \right\}. \tag{16}$$

The two solutions coalesce at $T_+ \equiv T_- = T_c$ for $U = U_{lc}$, i.e., for the lowest critical value of the interaction for the transition to take place, which is determined from the condition

$$\frac{U_{lc}}{U_C} = 1 - \frac{\sqrt{3} \ln 2}{\pi}. \tag{17}$$

The corresponding classical critical transition temperature at which the transition takes a continuous form and at $U = U_{lc}$ is

$$k_B T_c = \frac{3 \ln 2}{2\pi^2} W \left[1 - \left(\frac{U_{lc}}{U_C} \right)^2 \right]. \tag{18}$$

For $U \leqslant U_{lc}$ the metallic (Fermi liquid) state is stable at all T. In effect, the regime of the transition accuracy is determined by conditions $U_{lc} \leqslant U \leqslant U_C$. Disregarding the magnetic phases one then has the following overall phase sequence. For $T < T_-$ the system is a paramagnetic metal (PM). For $U_{lc} < U < U_C$ and $T_- < T < T_+$ the system is a paramagnetic insulator (a lattice of fluctuating spins $S{=}1/2$). For $T > T_+$ re-entrant metallic behavior is observed (a crossover transition). Such a sequence is indeed observed for V_2O_3 doped with Cr [7] and for liquid ^{3}He (cf. Figs 2. and 3b). The most important factor is the sequence of transformations between localized and itinerant (liquid) states of the valence electrons as a function of temperature and interaction, as shown schematically in Fig. 4a. For comparison, an analogous phase diagram appears for the quark-gluon plasma, this time calculated as a function of the chemical potential (cf. Fig. 4b).

The physical reason for switching between the states M and I is illustrated in Fig. 5 Namely, at temperature close to $T = 0$ the entropy of the disordered localized moments is large ($+k_B \ln 2$ per carrier), whereas for the Fermi liquid, it decreases linearly with T to zero. Hence, at $T = T_-$ the entropy part of the free energy for localized particles outweighs that of the Fermi liquid (ALFL), even though at $T = 0$, the opposite is true. However, as the temperature is raised, the Fermi liquid entropy grows and asymptotically at high temperature approaches the value $2k_B \ln 2$ per carrier. Thus, the detailed shape of the phase boundary is determined by the interplay between the competing energy and entropy contributions, as is the case for classical

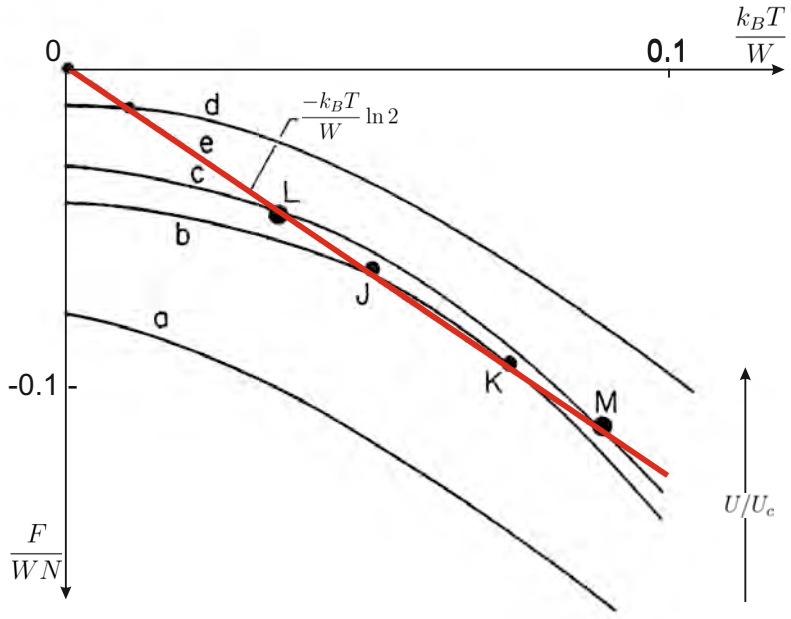

Fig. 5: *Temperature dependence of the free energy per particle (F/WN) in the Fermi-liquid (parabolas a-d) and in the Mott-Hubbard localized state (straight line e). The crossing points LM and JK represent, respectively, M $\rightarrow$ I and I $\rightarrow$ M' transitions. In the low-temperature analysis the I $\rightarrow$ M' transition is weakly discontinuous.*

continuous phase transition. In summary, the continuous evolution of the system at $T = 0$ in approaching U_C from below should be contrasted with the discontinuous nature of the transformation for $T > 0$. Thus, the point $U = U_C$ for $T = 0$ is indeed a quantum critical point, at least within this analysis in which $d^2 = \langle n_{i\uparrow} n_{i\downarrow} \rangle$ plays the role of the order parameter in the expression for the Ginzburg-Landau functional (18) for almost localized correlated fermions and when the antiferromagnetic order is absent.

At the end of this section, we would like to quote our results on metal-insulator transition including simultaneous presence of antiferromagnetism which with the increasing interaction magnitude evolves from band (*Slater-type*, AFS) to the localized spin (Mott, AFI) antiferromagnetism. The part of the phase diagram depicted in Fig. 4a appears only above the Néel temperature, where the antiferromagnetic states (AFS, AFI) cease to exist, here, in a discontinuous manner. The situation is shown in Fig. 6. In the inset we quote the experimental results Fig. 2b obtained for $(V_{1-x}Cr_x)_2O_3$, with the doping x as the horizontal axis. The agreement is qualitatively good, which is rewarding since a very simple model was considered. This means that the inter-particle configurations are the crucial factor to a large extent an independent of the electronic (band) structure.

The presence of the proposed classical critical point (CP) in Figs. 4a and 6 have been also beautifully confirmed much later [32]. It has a mean-field character, exactly the type predicted by our mean-field-like approach [33, 22, 23], which represented the very first realistic attempt to extend theory of metal-insulator transition of the Mott-Hubbard type at $T > 0$. Our results were confirmed much later [34] within the dynamic mean-field approach (DMFT).

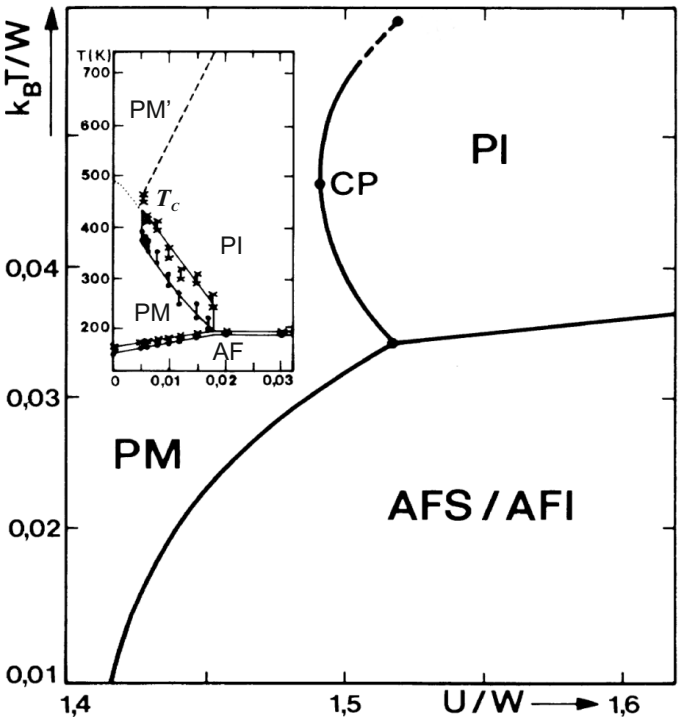

Fig. 6: *Phase diagram of the type presented in Fig. 4, with inclusion of antiferromagnetic Slater (AFS) and Mott (AFI) phases. Note that $W = U_C/2$. Inset: experimentally observed [7] phase diagram in the T-x plane for $(V_{1-x}Cr_x)_2O_3$. After Ref. [22]. The quantum critical point appearing in Fig. 4a is wiped out by the presence of antiferromagnetic order.*

3 Exact diagonalization – *ab initio* approach (EDABI) to correlated systems with simple examples

3.1 The method

The notion of a simultaneous determination of the single-particle wave-function ($1^{\rm st}$ quantization aspect), combined with a precise account of inter-particle correlations ($2^{\rm nd}$ quantization aspect) arose in the author's thinking about many-particle systems because of the following circumstances. In the proper particle language in quantum mechanics ($2^{\rm nd}$ quantization representation) the physical particle is represented by the field operator $\hat{\Psi}_\sigma(\mathbf{r})$ which has the form

$$\hat{\Psi}_\sigma(\mathbf{r}) \equiv \sum \varphi_{i\sigma}(\mathbf{r})\, \hat{a}_{i\sigma}, \tag{19}$$

where the set $\{\varphi_{i\sigma}(\mathbf{r})\}$ represents a complete set of single particle wave-functions (not necessarily orthogonal with the corresponding set of quantum numbers $\{i\sigma\}$ (here the spin quantum number $\sigma = \pm 1$ has been singled out explicitly to underline its fermionic nature (the argument holds equally well for bosons). The explicit $2^{\rm nd}$ quantized form of the Hamiltonian is [35]

$$\hat{\mathcal{H}} = \sum_\sigma \int d^3r\, \hat{\Psi}^\dagger_\sigma(\mathbf{r}) \mathcal{H}_1(\mathbf{r}) \hat{\Psi}_\sigma(\mathbf{r}) + \frac{1}{2}\sum_{\sigma\sigma'} \int d^3r\, d^3r'\, \hat{\Psi}^\dagger_\sigma(\mathbf{r}) \hat{\Psi}^\dagger_{\sigma'}(\boldsymbol{r'}) V(\mathbf{r}-\boldsymbol{r'}) \hat{\Psi}^\dagger_{\sigma'}(\boldsymbol{r'}) \hat{\Psi}_\sigma(\mathbf{r}). \tag{20}$$

In this expression $\mathcal{H}_1(\mathbf{r})$ represents the Hamiltonian for a single particle in wave mechanics, whereas $V(\mathbf{r}-\boldsymbol{r'})$ is the interaction for a single pair of particles. $\hat{\Psi}^\dagger_\sigma(\mathbf{r})\Psi_\sigma(\mathbf{r})$ is the particle

density operator, whereas $\hat{\Psi}^{\dagger}_{\sigma}(\mathbf{r})$ represents creation operator of a physical particle in the system at point $\mathbf{r}$ and with spin σ. This is the reason why we call the 2^{nd} quantization representation the particle language form of quantum approach.

In the situation when both $\mathcal{H}_1(\mathbf{r})$ and $V(\mathbf{r}-\boldsymbol{r'})$ are not explicitly spin independent, the Hamiltonian (20) can be brought to the following form

$$\hat{\mathcal{H}} = \sum_{ij\sigma} t_{ij} \hat{a}^{\dagger}_{i\sigma}\, \hat{a}_{j\sigma} + \frac{1}{2} \sum_{\substack{ijkl \\ \sigma\sigma'}} V_{ijkl}\, \hat{a}^{\dagger}_{i\sigma}\, \hat{a}^{\dagger}_{j\sigma'}\, \hat{a}_{l\sigma'}\, \hat{a}_{k\sigma}, \tag{21}$$

where

$$t_{ij} \equiv \langle \varphi_{i\sigma} | \mathcal{H}_1 | \varphi_{j\sigma} \rangle \quad \text{and} \quad V_{ijkl} = \langle \varphi_i \varphi_j | V | \varphi_k \varphi_l \rangle. \tag{22}$$

In this situation $\varphi_{i\sigma}(\mathbf{r}) = \varphi_i(\mathbf{r})\chi_{\sigma}$, we have the spin-independent hopping matrix elements t_{ij}, as well as the spinless interaction parameters V_{ijkl}. The dynamical system behavior is determined by the corresponding operator parts of (21), the matrix elements (22) contain the arbitrary (expect complete) set of the wave functions.

In canonical modeling of the properties with the help of (21) one takes into account only the first few terms of the first part of $\hat{\mathcal{H}}_1(\mathbf{r})$ (the hopping part) and the quantities $t_{0=t_{ii}}, t_{\langle i,j \rangle} = t$ are regarded as parameters of the model. Likewise, one takes only a few dominant terms in the interaction part and the corresponding V_{ijkl} elements are treated also as free parameters. If one selects the Wannier basis, i.e., $\varphi_i(\mathbf{r}) \equiv w_i(\mathbf{r}) = w(\mathbf{r}-\mathbf{r}_i)$, then we can select the hoping parameters $t_0, t = t_{\langle i,j \rangle}$, and $t'' \equiv t_{\langle\langle i,j \rangle\rangle}$, corresponding to the atomic reference energy and hoping amplitudes of particles between nearest and next-nearest neighbors, respectively.

The parametrized model created in the above way contains, as a rule, an incomplete quantum mechanical basis, as in general the set $\{w_i(\mathbf{r})\} = \{w_{in}(\mathbf{r})\}$, where n is the type of atomic orbital and in effect the multi-orbital (multi-band) system is derived. Hence, the results may depend on the type of orbital-based model we start with. But even if this general situation is not the case, the general question is how to determine the wave functions contained in the matrix elements (22)? One way is to start from a set of orthogonalized atomic orbitals, e.g., hydrogen-like Slater orbitals, as we discuss it below. However, the question still remains, particularly if the selected basis is not complete, whether such a basis should not be optimized in some way. This question is of crucial importance in the case of correlated systems when the two terms in (21) provide contributions of the same magnitude (see the preceding section). In particular, in the limit of strong correlations the interaction part even dominates over the single-particle contribution.

In such a situation our proposal now is as follows. Because of the interaction predominance we first diagonalize the parametrized Hamiltonian (21) in the Fock space and only subsequently minimize the ground state energy $E \equiv \langle \hat{\mathcal{H}} \rangle / N$ obtained in such a manner with respect to $i\sigma$. We developed the whole EDABI method for the Wannier functions $\{w_i\}$ by treating this energy as a functional of $\{\varphi_{i\sigma}\}$. In other words, we determine the single-particle renormalized wave-functions, now adjusted in the correlated state, by solving the effective wave equation obtained from the variational principle for the functional of the form

$$E\{w_i(\mathbf{r})\} \equiv E_G\{w_i(\mathbf{r})\} - \mu N - \sum_{i \geqslant j} \lambda_{ij} \left(\int d^3\mathbf{r}\, w^*_i(\mathbf{r})\, w_j(\mathbf{r}) - \delta_{ij} \right), \tag{23}$$

where

$$N = \sum_{\sigma} \int d^3\mathbf{r} \left\langle \hat{\Psi}^{\dagger}_{\sigma}(\mathbf{r}) \hat{\Psi}_{\sigma}(\mathbf{r}) \right\rangle = \sum_{ij\sigma} \int d^3\mathbf{r}\, w^*_i(\mathbf{r})\, w_j(\mathbf{r}) \left\langle \hat{a}^{\dagger}_{i\sigma} \hat{a}_{j\sigma} \right\rangle, \tag{24}$$

and $N_e = N$ is the number of particles in the system, whereas λ_{ij} are the Lagrange multipliers, to keep the single-particle basis orthonormal.

The general form of this equation in the stationary case and in the ground-ensemble formalism is

$$\frac{\delta(E_G - \mu N)}{\delta w^*_i(\mathbf{r})} - \nabla \frac{\delta(E_G - \mu N)}{\delta(\nabla w^*_i(\mathbf{r}))} - \sum_{i \geqslant j} \lambda_{ij}\, w_j(\mathbf{r}) = 0. \tag{25}$$

We make a fundamental postulate concerning this equation: As this equation does not contain explicitly the (anti)commutation relations between the creation and operators, it is equally valid for both fermions and bosons and determines a rigorous, within the class of the states included in the definition of $\hat{\Psi}_{\sigma}(\mathbf{r})$, the renormalized wave equation for a single-particle wavefunction in the ground state, in the milieu of remaining $(N-1)$ particles.

In this expressions the Lagrange multipliers λ_{ij} plays the role of single-particle energy in the correlated state. Note also that the variational derivatives are taken also with respect to the averages $\left\langle \hat{a}^{\dagger}_{i\sigma} \hat{a}_{j\sigma} \right\rangle$ and $\left\langle \hat{a}^{\dagger}_{i\sigma} \hat{a}^{\dagger}_{j\sigma'} \hat{a}_{l\sigma'} \hat{a}_{k\sigma} \right\rangle$, so is not just the optimization of parameters t_{ij} and V_{ijkl}. Parenthetically, the same type of formal wave-function determination (together with its normalization) has been proposed by Schrödinger in his pioneering work on wave mechanics (Schrödinger, 1926). Also, the optimized quantity is the system energy, not the Lagrangian, which represents the classical system Hamiltonian (its expectation value).

Finally, a general N-particles state $|\Phi_N\rangle$ in the Fock space can be defined through the corresponding N-particle wavefunction $\Psi_{\alpha}(\mathbf{r}_1, \ldots, \mathbf{r}_N)$ in the Hilbert space as [36]

$$|\Phi_N\rangle = \frac{1}{\sqrt{N!}} \int d^3\mathbf{r}_1 \ldots \mathbf{r}_N\, \Psi_N(\mathbf{r}_1, \ldots, \mathbf{r}_N)\, \hat{\Psi}^{\dagger}_{\sigma_1}(\mathbf{r}_1) \cdots \hat{\Psi}^{\dagger}_{\sigma_N} \mathbf{r}_N) |0\rangle, \tag{26}$$

where $|0\rangle$ is the vacuum state. One can reverse this relation and a simple algebra yields the following expression for the wavefunction $\Psi_{\alpha}(\mathbf{r}_1, \ldots, \mathbf{r}_N)$ in the terms of $|\Phi_N\rangle$

$$\Psi_{\alpha}(\mathbf{r}_1, \ldots, \mathbf{r}_N) = \frac{1}{\sqrt{N!}} \langle 0 | \hat{\Psi}_{\sigma_1}(\mathbf{r}_1) \cdots \hat{\Psi}_{\sigma_N}(\mathbf{r}_N) | \Phi_N \rangle, \tag{27}$$

with $\alpha \equiv \{\sigma_1, \ldots, \sigma_N\}$. In other words, to obtain the wavefunction in the coordinate representation, we not only annihilate N particles from the Fock state $|\Phi_N\rangle$, but also project out the thus obtained result onto the Fock vacuum state and normalize it by the factor $(N!)^{-1/2}$. Usually, the formula (27) is not used; as we proceed from the first to second quantization. Now, the crucial point is based on the observation that if we substitute in the field operator $\hat{\Psi}(\mathbf{r})$ the renormalized wavefunctions obtained from equation (24), then we should automatically obtain the renormalized field operator and, as a consequence, the renormalized multiparticle wavefunction $\Psi_{\alpha}(\mathbf{r}_1, \ldots, \mathbf{r}_N)$ from relation (27). This last step of inserting the renormalized field operator completes the procedure of a formal treatment of the many-particle system, which avoids writing down explicitly the N-particle Schrödinger equation. The approach is summarized in Fig. 7.

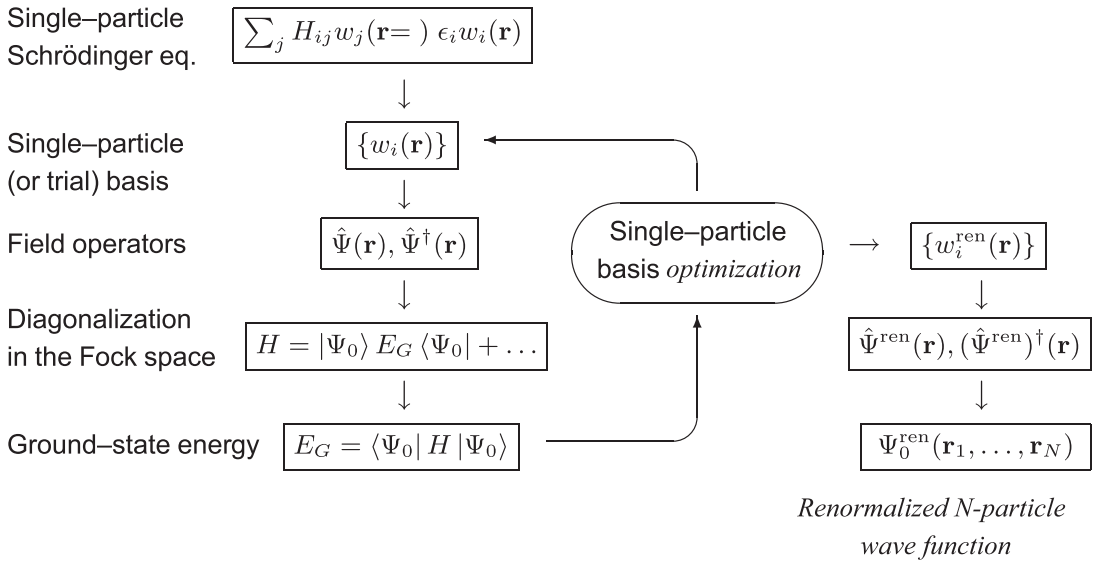

Fig. 7: *Flowchart describing the scheme of the EDABI method. For details see main text. When selecting the single-particle set, the top-most block should be disregarded. The renormalized many-particle wave function $\Psi_0^{ren}(\boldsymbol{r}_1, \ldots, \boldsymbol{r}_N)$ is explicitly constructed for few-particle systems in the next section.*

This scheme provides an exact renormalized single-particle wavefunction from equation (24) and the exact N-particle wavefunction, provided we have diagonalized the second-quantized model Hamiltonian for the problem at hand.

3.1.1 Supplement: Finite basis approximation from the field operator: difference with the multiconfiguration interaction (MCI) approach

The field operator $\hat{\Psi}(\mathbf{r})$ defined in terms of the sum over a complete basis $\{w_i(\mathbf{r})\}$ contains an infinite number of single-particle states. We assume that, in general, we represent the field operator by M wavefunctions $\{w_i(\mathbf{r})\}$. Explicitly,

$$\hat{\Psi}(\mathbf{r}) \equiv \sum_{i=1}^{\infty} w_i(\mathbf{r})\, \hat{a}_i \simeq \sum_{i=1}^{M} w_i(\mathbf{r})\, \hat{a}_i, \tag{28}$$

with i representing a complete set of quantum numbers and M being a finite number. This approximation represents one of the most fundamental features of constructing theoretical models. The neglected states usually represent highly exited (and thus negligible) states of the system. We can then write the approximate N-particle wavefunction ($N \leqslant M$) in the following manner

$$\Psi_\alpha(\mathbf{r}_1, \ldots, \mathbf{r}_n) = \frac{1}{\sqrt{N!}} \sum_{i_1,\ldots,i_N=1}^{M} \langle 0|\hat{a}_{i_N} \ldots \hat{a}_{i_1}|\Phi_N\rangle\, w_{i_1}(\mathbf{r}_1) \ldots w_{i_N}(\mathbf{r}_N) \tag{29}$$

Recognizing that within the occupation-number space spanned on the states $\{|i_k\rangle\}_{k=1\ldots M}$ we have the N-particle state in the Fock space of the form

$$|\Phi_N\rangle = \frac{1}{\sqrt{N!}} \sum_{j_1,\ldots,j_N=1}^{M} C_{j_1\ldots j_N} \hat{a}_{j_1}^\dagger \ldots \hat{a}_{j_N}^\dagger |0\rangle, \tag{30}$$

where $C_{j_1\ldots j_N}$ represents the coefficients of the expansion to be determined from a diagonalization procedure. Substituting (30) into (29) we obtain

$$\Psi_\alpha(\mathbf{r}_1\ldots,\mathbf{r}_n)=\frac{1}{\sqrt{N!}}\sum_{i_1,\ldots,i_N=1}^{M}\sum_{j_1,\ldots,j_N=1}^{M}\langle 0|\hat{a}_{i_1}\ldots\hat{a}_{i_N}\hat{a}^\dagger_{j_1}\ldots\hat{a}^\dagger_{j_N}|0\rangle C_{j_1\ldots j_N}w_{i_1}(\mathbf{r}_1)\ldots w_{i_N}(\mathbf{r}_N). \tag{31}$$

The expression provides $N!$ nonzero terms each equal to $(-1)^P$, where P represents the sign of the permutation of quantum numbers $(j_1\ldots j_N)$ with respect to a selected collection $(i_1\ldots i_N)$. In other words, we can write that

$$\Psi_\alpha(\mathbf{r}_1\ldots,\mathbf{r}_n)=\frac{1}{\sqrt{N!}}\sum_{i_1,\ldots,i_N=1}^{M}C_{i_1\ldots i_N}(A,S)w_{i_1}(\mathbf{r}_1)\ldots w_{i_N}(\mathbf{r}_N). \tag{32}$$

We have the same expansion coefficients for both the wavefunction in the Fock space $|\Phi_N\rangle$ and that in the Hilbert space $\Psi_\alpha(\mathbf{r}_1,\ldots,\mathbf{r}_n)$! Therefore, the above expression represents the multiconfigurational-interaction wavefunction of N particles distributed among M states with the corresponding weights $C_{i_1\ldots i_N}$ for each configuration, and (A,S) represents respectively the antisymmetrization (Slater determinant) or the symmetrization (simple product function $w_{i_1}(\mathbf{r}_1)\ldots w_{i_N}(\mathbf{r}_N)$ for the fermions and bosons, respectively. Whereas the MCI used in quantum chemistry [...] is based on variational optimizations of the coefficients $C_{i_1\ldots i_N}$, here the coefficients C are determined from diagonalization in the Fock space, spanned by M states in Hilbert space. The presence of wave equation (24) thus supplements the usual MCI approach. Next, we discuss selected elementary examples from atomic and molecular physics before turning to modeling extended correlated systems.

3.2 Elementary examples from atomic physics

One of the principal attractive features of EDABI method is the ability to construct atomic orbitals with a precise account for inter-electronic interactions. Here this program is illustrated on example of lightest atomic systems, as well as by an elementary example of the wave equation for renormalized wave functions.

3.2.1 A didactic example: He and Li atom

We start by selecting as $\{w_i(\mathbf{r})\}$ just two $1s$-type Slater orbitals for the He atom $\Phi_\sigma(\mathbf{r})=(\alpha^3/\pi)^{1/2}\exp(-\alpha r)\chi_\sigma$, where α is the effective inverse radius of the states. In other words, the simplest trial field operator is of the form

$$\hat{\Phi}(\mathbf{r})=\Phi_\uparrow(\mathbf{r})\hat{a}_\uparrow+\Phi_\downarrow(\mathbf{r})\hat{a}_\downarrow, \tag{33}$$

where a_σ is the annihilation operator of particle in the state $\Phi_\sigma(\mathbf{r})$. The Hamiltonian in second quantization for this two-element basis has then the form

$$H=\varepsilon_a(\hat{n}_\uparrow+\hat{n}_\downarrow)+U\hat{n}_\uparrow\hat{n}_\downarrow, \tag{34}$$

where $\hat{n}_\sigma = \hat{a}^\dagger_\sigma \hat{a}_\sigma$, whereas

$$\varepsilon_a = \langle \Phi_\sigma | H_1 | \Phi_\sigma \rangle, \tag{35}$$

and

$$U = \langle \Phi_\sigma \Phi_{\overline{\sigma}} | V | \Phi_{\overline{\sigma}} \Phi_\sigma \rangle \tag{36}$$

are the matrix elements of the single-particle part defined as

$$H_1 = -\frac{\hbar^2}{2m}\nabla_1^2 - \frac{\hbar^2}{2m}\nabla_2^2 - \frac{2e^2}{\kappa_0 r_1} - \frac{2e^2}{\kappa_0 r_2} \overset{a.u.}{\equiv} -\nabla_1^2 - \nabla_2^2 - \frac{4}{r_1} - \frac{4}{r_2} \tag{37}$$

and of the Coulomb interaction

$$V = \frac{e^2}{\kappa_0 \, |\mathbf{r_1} - \mathbf{r_2}|} \overset{a.u.}{\equiv} \frac{2}{|\mathbf{r_1} - \mathbf{r_2}|}, \tag{38}$$

with the corresponding definitions in atomic units after the second equality sign. The only eigenvalue of (34) is obtained for the state $\hat{a}^\dagger_\uparrow \hat{a}^\dagger_\downarrow |0\rangle$ and is $E = 2\varepsilon_a + U$. This total energy is then minimized with respect to α to obtain the well-known Bethe and Salpeter variational estimate of both α and the ground state energy E_G, as discussed before. However, we may look at the problem differently. The true wavefunction is obtained from the Euler equation for the functional $E = E\{\Psi_\sigma\}$ under the proviso that the wave function is normalized. This means that we minimize the functional

$$E\{\Phi_\sigma(\mathbf{r})\} = \sum_\sigma \int d^3r \Phi^*_\sigma(\mathbf{r}) H_1(\mathbf{r}) \Phi_\sigma(\mathbf{r}) + \frac{1}{2}\sum_\sigma \int d^3r d^3r' |\Phi_\sigma(\mathbf{r})|^2 V_{12}(\mathbf{r}-\mathbf{r}') |\Phi_{\overline{\sigma}}(\mathbf{r})|^2. \tag{39}$$

In effect, the renormalized wave equation takes the form of the unrestricted Hartree equations for $\Phi_\sigma(\mathbf{r})$

$$\left(\nabla^2 - \frac{2e^2}{\kappa_0 r}\right)\Phi_\sigma(\mathbf{r}) + \Phi_\sigma(\mathbf{r}) \int d^2r' \frac{e^2}{\kappa_0 |\mathbf{r}-\mathbf{r}'|} |\Phi_{\overline{\sigma}}(\mathbf{r}')|^2 = \lambda \Phi_\sigma(\mathbf{r}). \tag{40}$$

Thus, we can see that taking in the simplest case just two spin $1s$-type orbitals we obtain either the well-known Bethe-Salpeter variational estimate for α and E_G for He atom: $\alpha = 27/(16a_0)$ and $E_G = -5.695$ Ry, where $a_0 \simeq 0.53$ Å is the $1s$ Bohr orbit radius. We see that the He atom is the smallest in the Universe!

The proposed expression (33) for the field operator is the simplest one, but it leads to nontrivial results even though the trial atomic basis $\{\Phi_\sigma(\mathbf{r})\}$ is far from being complete in the quantum-mechanical sense. However, we can improve systematically on the basis by selecting a richer basis than that in (33). The further step in this direction is discussed next. Namely, we can expand the field operator in the basis involving the higher order irreducible representations of the rotation group with n=2, which in the variational scheme involve including, apart from the $\Psi_{1s}(\mathbf{r})$ orbital, also the higher $\Psi_{2s}(\mathbf{r})$ and $\Psi_{2pm}(\mathbf{r})$ orbitals, with $m = \pm 1, 0$ (i.e., the next shell); all of them involving the adjustment of the corresponding orbital characteristics α_i, $i = 1s, 2s$ and $2pm$. The field operator is then

$$\hat{\Psi}(\mathbf{r}) = \sum_\sigma \left(w_{1s}(\mathbf{r}) \chi_{1\sigma} \hat{a}_{1\sigma} + w_{2s}(\mathbf{r}) \chi_{2\sigma} \hat{a}_{2\sigma} + \sum_{m=-1}^{+1} w_{2pm}(\mathbf{r}) \chi_{m\sigma} \hat{a}_{2pm\sigma} \right) \equiv \sum_{i\sigma} w_i(\mathbf{r}) \chi_{i\sigma} \hat{a}_{i\sigma}, \tag{41}$$

Table 1: *Optimized Bohr-orbit radii $a_i = \alpha_i^{-1}$ of $1s$, 2s, and $2p$ orbitals (in units of a_0), the overlap S between renormalized $1s$ and 2s states, and the ground state energy for the lightest atoms and ions (five Slater orbitals taken).*

	a_{1s}	a_{2s}	a_{2p}	S	E_G (Ry)
H	1	2	2	0	-1
H^-	0.9696	1.6485	1.017	-0.1	-1.0487
He	0.4274	0.5731	0.4068	-0.272	-5.79404
He^-	1.831	1.1416	0.4354	-0.781	-5.10058
Li	0.3725	1.066	0.2521	0.15	-14.8334
Be^+	0.2708	0.683	0.1829	0.109	-28.5286

where the $w_i(\mathbf{r})$ are orthogonalized orbitals obtained from the nonorthogonal atomic[1] basis $\{\Psi_i(\mathbf{r})\}$ in a standard manner. The Fock space spanned by $2{+}2{+}6{=}10$ trial spin orbitals contains $D{=}\binom{2M}{N_e}$ dimensions, where $M{=}5$ and $N{=}N_e{=}2,3$ is the number of electrons for He and Li, respectively. This means that $D{=}45$ and 120 in those two cases and we have to diagonalize the Hamiltonian matrices of that size to determine the ground and the lowest excited states.

One should note that we construct and subsequently diagonalize the $\langle i|\hat{\mathcal{H}}|j\rangle$ matrix in the Fock space for (fixed) parameters ε_a, t_{ij}, and V_{kl}. After the diagonalization has been carried out, we readjust the wave function and start the whole procedure again until the absolute minimum is reached (cf. Fig. 7).

By diagonalizing the corresponding Hamiltonian matrices and subsequently, minimizing the lowest eigenvalue with respect to the parameters α_i – the inverse radial extensions of the corresponding wave functions, we obtain the results presented in Table 1 (the values a_{2pm} are all equal within the numerical accuracy $\sim 10^{-6}$). For example, the ground state energy of He is $E_G = -5.794$ Ry, which is close to the accepted "exact" value -5.8074 Ry, given the simplicity of our approach. Further improvement is feasible by either including the $n{=}3$ states or by resorting to a Gaussian trial basis. These are not analyzed here.

First, we can represent the ground-state two-particle spin-singlet wavefunction for the He atom taking $\hat{\Psi}(\mathbf{r})$ in the form (41), which has the following form [37]

$$
\begin{aligned}
|\Psi_0^{\mathrm{He}}\rangle \simeq \Big(& -0.799211\, \hat{a}^\dagger_{1s\downarrow}\hat{a}^\dagger_{1s\uparrow} + 0.411751\, \hat{a}^\dagger_{1s\downarrow}\hat{a}^\dagger_{2s\uparrow} - 0.411751\, \hat{a}^\dagger_{1s\uparrow}\hat{a}^\dagger_{2s\downarrow} \\
& - 0.135451\, a^\dagger_{2s\downarrow}\hat{a}^\dagger_{2s\uparrow} + 0.0357708\, \hat{a}^\dagger_{2p0\downarrow}\hat{a}^\dagger_{2p0\uparrow} + 0.0357641\, \hat{a}^\dagger_{2p1\downarrow}\hat{a}^\dagger_{2p-1\uparrow} \\
& - 0.0357641\, \hat{a}^\dagger_{2p1\uparrow}\hat{a}^\dagger_{2p-1\downarrow}\Big)|0\rangle.
\end{aligned}
\tag{42}
$$

[1]Note that the atomic orbitals $1s$ and $2s$ are not orthogonal to each other for arbitrary values of their spatial extents $1/\alpha_i$. The $2p$ orbitals are orthogonal to each other and to s orbitals, since they contain a nontrivial angular dependence expressed via spherical harmonics $Y_l^m(\theta,\varphi)$.

Similarly, the $S^z = +1/2$ state for Li atom is of the form

$$
\begin{aligned}
|\Psi_0^{Li}\rangle \simeq \Big(\quad & 0.997499\, \hat{a}^\dagger_{1s\downarrow}\hat{a}^\dagger_{1s\uparrow}\hat{a}^\dagger_{2s\uparrow} - 0.0570249\, \hat{a}^\dagger_{1s\uparrow}\hat{a}^\dagger_{2s\downarrow}\hat{a}^\dagger_{2s\uparrow} \\
& + 0.0039591\, \hat{a}^\dagger_{1s\uparrow}\hat{a}^\dagger_{2p0\downarrow}\hat{a}^\dagger_{2p0\uparrow} + 0.00395902\, \hat{a}^\dagger_{1s\uparrow}\hat{a}^\dagger_{2p1\downarrow}\hat{a}^\dagger_{2p-1\uparrow} \\
& - 0.00395894\, \hat{a}^\dagger_{1s\uparrow}\hat{a}^\dagger_{2p1\uparrow}\hat{a}^\dagger_{2p-1\downarrow} - 0.023783\, \hat{a}^\dagger_{2s\uparrow}\hat{a}^\dagger_{2p0\downarrow}\hat{a}^\dagger_{2p0\uparrow} \\
& - 0.0237806\, \hat{a}^\dagger_{2s\uparrow}\hat{a}^\dagger_{2p1\downarrow}\hat{a}^\dagger_{2p-1\uparrow} + 0.0237806\, \hat{a}^\dagger_{2s\uparrow}\hat{a}^\dagger_{2p1\uparrow}\hat{a}^\dagger_{2p-1\downarrow}\Big)|0\rangle.
\end{aligned}
\tag{43}
$$

We see that the probability of encountering the configuration $1s^2$ in He is less than $2/3$, whereas the corresponding configuration $1s^2 2s$ for Li almost coincides with that for the hydrogen-like picture. The reason for the difference is that the overlap integral between $1s$ and $2s$ states $S = \langle 1s|2s\rangle$ in the former case is large and the virtual transitions $1s \rightleftharpoons 2s$ do not involve a substantial change of the Coulomb energy. Those wave functions can be used to evaluate any ground-state characteristic by calculating $\langle \Psi_G|\hat{O}|\Psi_G\rangle$ for $\hat{O}$ represented in the 2^{nd} quantized form. For example, the atom dipole moment operator is $\hat{\mathbf{d}} = e\int d^3r\, \hat{\Psi}^\dagger(\mathbf{r})\, \mathbf{x}\, \hat{\Psi}(\mathbf{r})$, etc.
The second feature is connected with determination of the microscopic parameters V_{ijkl} in our Hamiltonian, since their knowledge is crucial for atomic cluster calculations, as well as the determination of physical properties of extended systems as a function of the lattice parameter. Namely, we can rewrite the Hamiltonian for the case of a single atom within the basis (41) as

$$
\begin{aligned}
\mathcal{H} = & \sum_{i\sigma} \varepsilon_i \hat{n}_{i\sigma} + t\sum_{\sigma}\left(\hat{a}^\dagger_{2\sigma}\hat{a}_{1\sigma} + \hat{a}^\dagger_{1\sigma}\hat{a}_{2\sigma}\right) + \sum_{i=1}^{5} U_i \hat{n}_{i\uparrow}\hat{n}_{i\downarrow} + \frac{1}{2}\sum_{i\neq j} K_{ij}\hat{n}_i\hat{n}_j \\
& -\frac{1}{2}\sum_{i\neq j} J_{ij}\left(\mathbf{S_i}\cdot\mathbf{S_j} - \frac{1}{2}\hat{n}_i\hat{n}_j\right) + \sum_{i\neq j} J_{ij}\hat{a}^\dagger_{i\uparrow}\hat{a}^\dagger_{i\downarrow}\hat{a}_{j\downarrow}\hat{a}_{j\uparrow} + \sum_{i\neq j\sigma} V_{ij}\hat{n}_{i\bar{\sigma}}\hat{a}^\dagger_{i\sigma}\hat{a}_{j\sigma}.
\end{aligned}
\tag{44}
$$

t is the hopping integral between $1s$ and $2s$ states, U_i are the intraorbital Coulomb interactions, K_{ij} are their interorbital correspondents, V_{ij} is the so-called correlated hopping integral, and J_{ij} is the direct exchange integral, for states i and $j = 1, \ldots, 5$. The principal parameters for the atoms and selected ions are provided in Table 2. We can draw the following interpretation from this analysis. The calculated energy difference ΔE for He between the ground-state singlet and the first excited triplet is $-2.3707 - (-5.794) \simeq 3.423$ Ry (the singlet $1s_\uparrow 2s_\downarrow$ is still 1 Ry higher). The corresponding energy of the Coulomb interaction in the $1s^2$ configuration is $U_1 = 3.278$ Ry, a value comparable to ΔE. Additionally, the Coulomb interaction in $1s_\uparrow 2s_\downarrow$ state is ≈ 1.5 Ry, a substantially lower value. The relative energetics tells us why we have a substantial admixture of the excited $1s_\uparrow 2s_\downarrow$ state to the singlet $1s^2$. In other words, a substantial Coulomb interaction ruins the hydrogen-like scheme, although the actual values could be improved further by enriching the trial basis.

One may ask how the renormalized wave equation would look in the present situation. The answer to this question is already not brief for the basis containing M=5 starting states $\{w_i(\mathbf{r})\}$ and will not be tackled here.

Table 2: *Microscopic parameters (in Ry) of the selected atoms and ions all quantities are calculated for the orthogonalized atomic states. t is the $1s$-$2s$ hopping magnitude, U_i is the intraorbital Coulomb interaction ($i = 1s(1), 2s(2), m = 0(3)$, and $m = \pm 1(p)$), whereas K_{ij} and J_{ij} are the interorbital Coulomb and exchange interaction parameters.*

	t	U_1	U_2	U_3	U_p	K_{12}	K_{13}	K_{23}	J_{12}	J_{13}	J_{23}
H^-	0.057	1.333	0.369	0.77	0.728	0.519	0.878	0.457	0.061	0.138	0.035
He	1.186	3.278	1.086	1.924	1.821	1.527	2.192	1.289	0.212	0.348	0.115
He^-	-1.1414	1.232	0.764	1.798	1.701	0.929	1.421	1.041	0.269	0.28	0.102
Li	-0.654	3.267	0.533	3.105	2.938	0.749	3.021	0.743	0.06	0.606	0.014
Be^+	-0.929	4.509	0.869	4.279	4.049	1.191	4.168	1.175	0.105	0.837	0.025

3.3 H_2 molecule and H_2^- ion

In this Subsection we consider H_2 molecule. For the illustration of the method we have plotted in Fig. 8 the level scheme for the H_2 and H_2^- systems. We consider first the situation with only one $1s$-like orbital per atom. For H_2 we have $\binom{4}{2} = 6$ two-particle states. For that purpose, we start with the parametrized Hamiltonian (44), where subscripts i and j label now the two atomic sites and hence $U_1 = U_2 = U$, $K_{12} = K$, $J_{12} = J$, $V_{12} = V$, and $\varepsilon_1 = \varepsilon_2 = \varepsilon_a$. Note that the Hamiltonian (44) in the two-site (H_2) case contains all possible intersite interactions.
The lowest eigenstate for H_2 is the spin-singlet state

$$E_G \equiv \lambda_5 = 2\varepsilon_a + \frac{1}{2}(U+K) + J - \frac{1}{2}\Big((U-K)^2 + 16(t+V)^2\Big)^{1/2}, \tag{45}$$

and the corresponding singlet ground state in the Fock space has the form

$$|G\rangle = \frac{1}{\sqrt{2D(D-U+K)}}\left(\frac{4(t+V)}{\sqrt{2}}\big(\hat{a}^\dagger_{1\uparrow}\hat{a}^\dagger_{2\downarrow} - \hat{a}^\dagger_{1\downarrow}\hat{a}^\dagger_{2\uparrow}\big) - \frac{(D-U+K)}{\sqrt{2}}\big(\hat{a}^\dagger_{1\uparrow}\hat{a}^\dagger_{2\downarrow} + \hat{a}^\dagger_{1\downarrow}\hat{a}^\dagger_{2\uparrow}\big)\right)|0\rangle, \tag{46}$$

where

$$D \equiv \big((U-K)^2 + 16(t+V)^2\big)^{1/2}.$$

The lowest spin-singlet eigenstate has an admixture of the ionic state $\big(\hat{a}^\dagger_{1\uparrow}\hat{a}^\dagger_{2\downarrow} + \hat{a}^\dagger_{1\downarrow}\hat{a}^\dagger_{2\uparrow}\big)/\sqrt{2}$. Therefore, to see the difference with either the Hartree-Fock or Heitler-London approach to H_2 is that we construct the two-particle wavefunction for the ground state according to the prescription

$$\Phi_0(\mathbf{r}_1, \mathbf{r}_2) \equiv \frac{1}{\sqrt{2}}\langle 0|\hat{\Psi}(\mathbf{r}_1)\hat{\Psi}(\mathbf{r}_2)|G\rangle. \tag{47}$$

Taking $\hat{\Psi}(\mathbf{r}) = \sum_{i=1}^{2}\sum_{\sigma=\uparrow}^{\downarrow}\Phi_i(\mathbf{r})\chi_\sigma(\mathbf{r})$, we obtain that

$$\Phi_0(\mathbf{r}_1, \mathbf{r}_2) = \frac{2(t+V)}{\sqrt{2D(D-U+K)}}\Phi_c(\mathbf{r}_1, \mathbf{r}_2) - \frac{1}{2}\sqrt{\frac{D-U+K}{2D}}\Phi_i(\mathbf{r}_1, \mathbf{r}_2), \tag{48}$$

where the covalent part is

$$\Phi_c(\mathbf{r}_1, \mathbf{r}_2) = \big(w_1(\mathbf{r}_1)w_2(\mathbf{r}_2) + w_1(\mathbf{r}_2)w_2(\mathbf{r}_1)\big)\big(\chi_\uparrow(\mathbf{r}_1)\chi_\downarrow(\mathbf{r}_2) - \chi_\downarrow(\mathbf{r}_1)\chi_\uparrow(\mathbf{r}_2)\big), \tag{49}$$

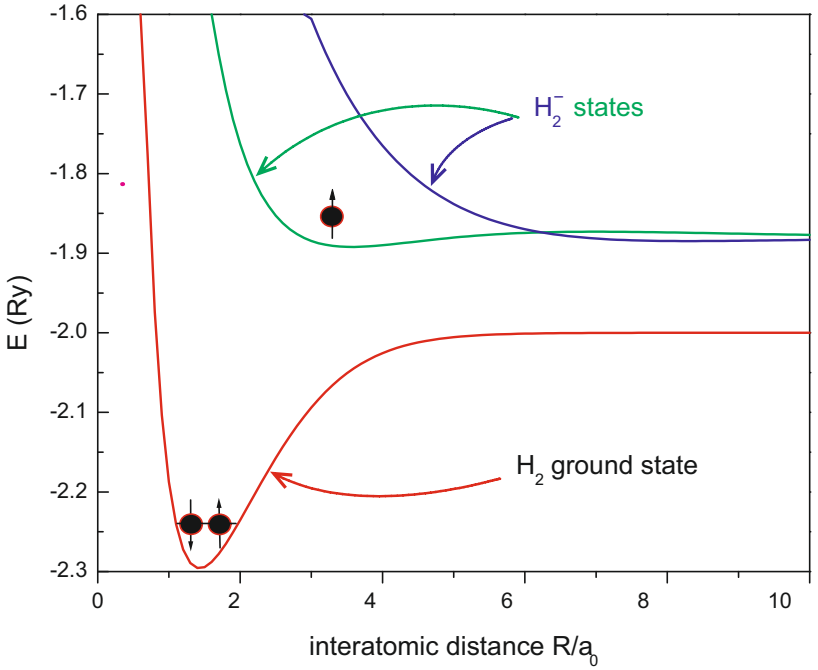

Fig. 8: *Level scheme of the H_2 ground state and the lowest H_2^- states as a function of the interatomic distance R.*

whereas the ionic part takes the form

$$\Phi_i(\mathbf{r}_1,\mathbf{r}_2) = \big(w_1(\mathbf{r}_1)w_1(\mathbf{r}_2) + w_2(\mathbf{r}_1)w_2(\mathbf{r}_2)\big)\big(\chi_\uparrow(\mathbf{r}_1)\chi_\downarrow(\mathbf{r}_2) - \chi_\downarrow(\mathbf{r}_1)\chi_\uparrow(\mathbf{r}_2)\big). \tag{50}$$

The ratio of the coefficients before $\Phi_c(\mathbf{r}_1,\mathbf{r}_2)$ and $\Phi_i(\mathbf{r}_1,\mathbf{r}_2)$ can be termed as the *many-body covalency* γ_{mb}. This value should be distinguished from the usual *single-particle covalency* γ appearing in the definition of the orthogonalized atomic orbital $w_i(\mathbf{r})$

$$w_i(\mathbf{r}) = \beta\big(\Phi_i(\mathbf{r}) - \gamma\Phi_j(\mathbf{r})\big), \tag{51}$$

with $j \neq i$. The two quantities are drawn in Fig. 9. The many-body covalency γ_{mb} represents a true degree of multiparticle configurational mixing.

In Table 3 we list the energies and the values of the microscopic parameters for H_2 system with optimized orbitals. One should notice a drastic difference for the so-called *correlated hopping* matrix element V in the two cases. The same holds true for the direct exchange integral J (ferromagnetic). This exchange integral is always decisively smaller than that for the antiferromagnetic kinetic exchange, $J_{kex} \equiv 4(t+V)^2/(U-K)$.

3.3.1 Hydrogen clusters H_N

As the next application we consider hydrogen-cluster H_N systems. We take the atomic-like $1s$ orbitals $\{\Phi_i(\mathbf{r})\}$ of an adjustable size $a \equiv \alpha^{-1}$, composing the orthogonalized atomic (Wannier) functions $\{w_i(\mathbf{r})\}_{i=1,\ldots,N}$. The cluster of N atoms with N electrons contains $\binom{2N}{N}$ states and the second-quantized Hamiltonian is of the form (44), with three- and four-site terms added. The three- and four-site interaction terms are difficult to calculate in the Slater basis (see below). Therefore, we have made an ansatz [38] namely, we impose the condition on the trial Wannier

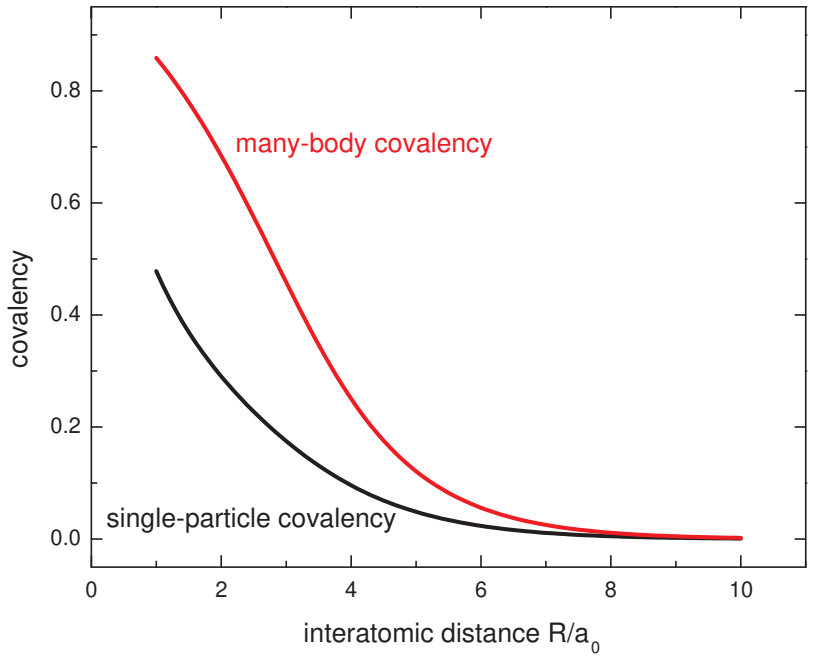

Fig. 9: *The single-particle (γ) and many-body (γ_{mb}) covalency factors for the H_2 wave functions. For details see main text. Note that the many-body covalency is stronger than its single-particle correspondent (orbital mixing).*

function that the three- and four-site matrix elements V_{ijkl} vanish. This allows for an explicit expression of the three- and four-site matrix elements V'_{ijkl} in the atomic representation via the corresponding one- and two-site elements. In Fig. 10 we present the results for the ground- and excited-states energies for the square configuration, $N = 4$ atoms. The states are grouped into manifolds, which are characterized by the number, 0, 1, and 2, of double occupancies, appearing in the system. The horizontal lines mark the ground state, states with one and two double electron occupancies in the atomic limit (i.e., for large interatomic distance). The manifolds thus correspond to the *Hubbard subbands* introduced for strongly correlated solids [21]. As far as we are aware of, our results are the first manifestation of the energy manifold evolution into well separated subbands with the increasing interatomic distance. The first two subbands correspond to HOMO and LUMO levels determined in quantum-chemical calculations. In. Fig. 11 we draw the renormalized Wannier function profiles for the $N = 6$ atoms. Note the small negative values on the nearest-neighbor sites to assure the orthogonality of the functions centered on different sites. In the same manner, the electron density profiles can be obtained as a function of intraatomic distances.

On these examples one can see that both the *ab initio* electronic-structure calculations can be carried out with a simultaneous precise evaluation of microscopic parameters characterizing the particle dynamics and interactions between them. No double counting of the interaction appears at all in either aspect of the calculations. The accuracy of calculating the atomic or molecular structure in the ground state can be reached with accuracy of the order of 1% relatively easy. In the next two sections extend the method to characterize the Mott physics in nanoscopic one- and two-dimensional systems.

Table 3: *Ground-state energy and microscopic parameters (in Ry) for H_2. The last column represents the kinetic-exchange integral characterizing the intersite antiferromagnetic exchange.*

R/a	E_G/N	ε_a	t	U	K	V [mRy]	J [mRy]	$\frac{4(t+V)^2}{U-K}$[mRy]
1.0	-1.0937	-1.6555	-1.1719	1.8582	1.1334	-13.5502	26.2545	7755.52
1.5	-1.1472	-1.7528	-0.6784	1.6265	0.9331	-11.6875	21.2529	2747.41
2.0	-1.1177	-1.722	-0.4274	1.4747	0.7925	-11.5774	16.9218	1130.19
2.5	-1.0787	-1.6598	-0.2833	1.3769	0.6887	-12.0544	13.1498	507.209
3.0	-1.0469	-1.5947	-0.1932	1.3171	0.6077	-12.594	9.8153	238.939
3.5	-1.0254	-1.5347	-0.1333	1.2835	0.5414	-12.8122	6.9224	115.143
4.0	-1.0127	-1.4816	-0.0919	1.2663	0.4854	-12.441	4.5736	55.8193
4.5	-1.006	-1.4355	-0.0629	1.2579	0.4377	-11.4414	2.8367	26.9722
5.0	-1.0028	-1.3957	-0.0426	1.2539	0.3970	-9.9894	1.6652	12.9352
5.5	-1.0012	-1.3616	-0.0286	1.2519	0.3623	-8.3378	0.9334	6.1455
6.0	-1.0005	-1.3324	-0.01905	1.251	0.3327	-6.7029	0.5033	2.8902
6.5	-1.00024	-1.3073	-0.0126	1.2505	0.3075	-5.2242	0.2626	1.3452
7.0	-1.0001	-1.2855	-0.0083	1.2503	0.2856	-3.9685	0.1333	0.6197
7.5	-1.00004	-1.2666	-0.0054	1.2501	0.2666	-2.9509	0.066	0.2826
8.0	-1.00002	-1.25	-0.0035	1.25006	0.25	-2.1551	0.032	0.1277
8.5	-1.00001	-1.2353	-0.0023	1.25003	0.2353	-1.5501	0.01523	0.0572
9.0	-1.	-1.2222	-0.0015	1.25001	0.2222	-1.1005	0.0071	0.0254
9.5	-1.	-1.2105	-0.0009	1.25001	0.2105	-0.7725	0.0033	0.0112
10.0	-1.	-1.2	-0.0006	1.25	0.2	-0.5371	0.0015	0.0049

4 Mott-Hubbard physics for nanochains: Exact analysis with EDABI

Here we analyze the electronic system properties for a system composed of $N = 6 \div 14$ hydrogen atoms in a linear chain or a ring and draw some universal conclusions about "the Mottness". We start with a bit simplified Hamiltonian, but containing the same principal physics. Namely,

$$\hat{\mathcal{H}} = \varepsilon_a \sum_{i\sigma} \hat{n}_i + t \sum_{i\sigma} \left(\hat{a}^\dagger_{i\sigma}\, \hat{a}_{i\sigma} + H.c. \right) + U \sum_i \hat{n}_{i\uparrow}\, \hat{n}_{i\downarrow} + \sum_{i<j} \mathcal{K}_{ij} \hat{n}_i\, \hat{n}_i + \sum_{i<j} V_{ion}(\mathbf{r}_j - \mathbf{r}_i). \quad (52)$$

The first term represents the atomic energy (we include it explicitly, since ε_a changes with the varying lattice constant). The second describes the kinetic energy of the system with nearest-neighbor hopping t. Next two terms express the intra- and interatomic Coulomb interaction. The last term is the Coulomb repulsion between the ions located at positions $\{\mathbf{r}_i\}$, included for the same reasons as the atomic energy ε_a. V_{ion} is the proton-proton classical repulsion term.
Here we recall only the definitions of single- and two-particle parameters t_{ij} and V_{ijkl}, which are

$$\varepsilon_a = t_{ii} = \langle w_i | T | w_i \rangle, \qquad t = t_{i,i+1} = \langle w_i | T | w_{i+1} \rangle, \quad (53)$$

and

$$U = V_{iiii} = \langle w_i w_i | V | w_i w_i \rangle\,, \qquad K_{ij} = V_{ijij} = \langle w_i w_j | V | w_i w_j \rangle\,. \quad (54)$$

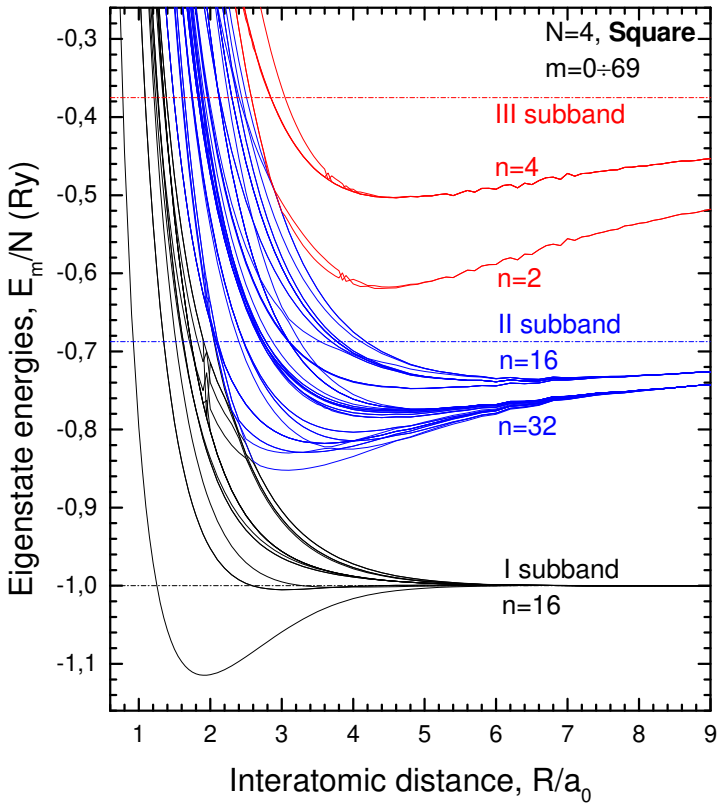

Fig. 10: *Ground- and excited-states energies for the H_4 square configuration as a function of the interatomic distance. The position of subsequent Hubbard subbands (distant by U) are marked. The lowest two are HOMO-LUMO split energy levels.*

The operator T represents the full single-particle lattice potential, i.e.,

$$T(\mathbf{r}) = -\frac{\hbar^2}{2m}\nabla^2 - \sum_j \frac{e^2}{|\mathbf{r}-\mathbf{r}_j|} \stackrel{\text{a.u.}}{=} -\nabla^2 - \sum_j \frac{2}{|\mathbf{r}-\mathbf{r}_j|}, \tag{55}$$

where a.u. means the expression in atomic units. $V = e^2/|\mathbf{r}_1-\mathbf{r}_2|$ is the usual Coulomb potential (we do not include any screening by, e.g., core electrons as we want to discuss the model situation, but in a rigorous manner). Analogously, the Coulomb repulsion between ions is $V_{\text{ion}} = V(\mathbf{r}_1-\mathbf{r}_2)$.
The interatomic Coulomb term in the Hamiltonian can be represented as

$$\begin{aligned}\sum_{i<j} K_{ij} n_i n_j &= \sum_{i<j} K_{ij}(n_i-1)(n_j-1) - \sum_{i<j} K_{ij} + 2N_e \frac{1}{N}\sum_{i<j} K_{ij} \\ &= H_K + N_e \frac{1}{N}\sum_{i<j} K_{ij} + (N_e-N)\frac{1}{N}\sum_{i<j} K_{ij},\end{aligned} \tag{56}$$

where we use the relation $N_e = \sum_i n_i$ and introduce the symbol H_K for the longer-range Coulomb interaction. Substituting (56) into (52) and representing the ionic repulsion in the form

$$\sum_{i<j} \frac{2}{R_{ij}} = N_e \frac{1}{N}\sum_{i<j} \frac{2}{R_{ij}} - (N_e-N)\frac{1}{N}\sum_{i<j} \frac{2}{R_{ij}}$$

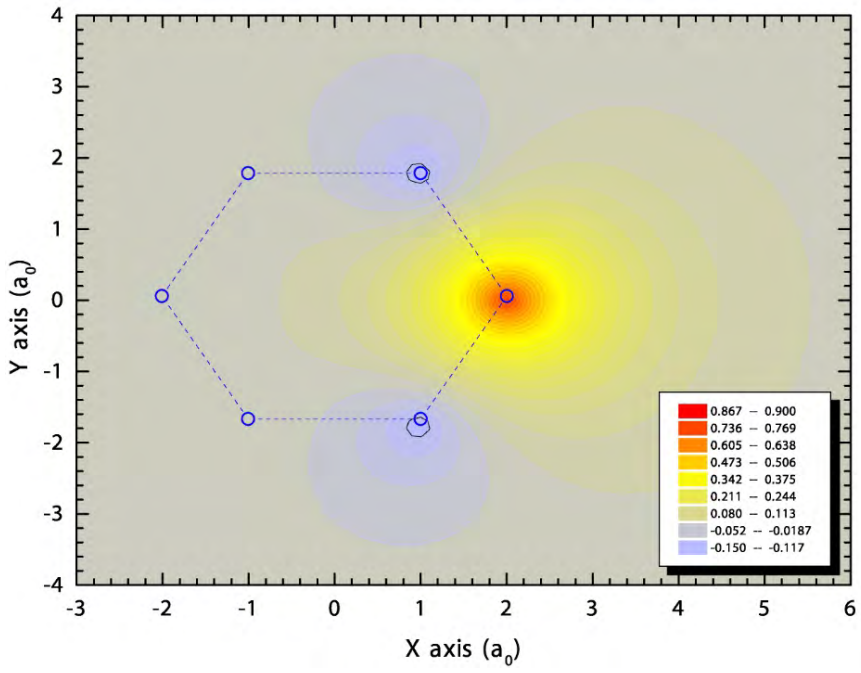

Fig. 11: *Single Wannier function for the H_6 configuration for the ground state and at the optimal interatomic distance. Note the negative values at the nearest neighboring sites, as well as its anisotropic character due to the 6-fold symmetry.*

(in Rydbergs), where $R_{ij} = |\mathbf{r}_j - \mathbf{r}_i|$, we obtain that

$$H = N_e \varepsilon_a^{\mathit{eff}} + H_t + H_U + H_K + (N_e - N)\frac{1}{N}\sum_{i<j}\left(K_{ij} - \frac{2}{R_{ij}}\right), \tag{57}$$

where the kinetic energy and intraatomic Coulomb interaction terms are H_t and H_U, and the *effective atomic energy* is defined (in Ry) as

$$\varepsilon_a^{\mathit{eff}} \equiv \varepsilon_a + \frac{1}{N}\sum_{i<j}\left(K_{ij} + \frac{2}{R_{ij}}\right). \tag{58}$$

The effective atomic energy contains the electron attraction to the ions, as well as the mean-field part of their repulsion (K_{ij}), and the ion-ion interaction. Such a definition preserves correctly the atomic limit, when the distant atoms should be regarded as neutral objects. In practice, the above form is calculated numerically with the help of Richardson extrapolation for $N \to \infty$. One can find it converges exponentially with N, whereas *bare* ε_a is divergent harmonically, due to $\sim 1/r$ Coulomb wells in the single-particle potential (55).

The last term in the Hamiltonian (57) vanishes for the half-filled band case $N_e = N$. It also does not affect the system charge gap (as it depends linearly on N_e), and the correlation functions away from half filling. Therefore, we can write down the system Hamiltonian in the more compact form

$$H = \varepsilon_a^{\mathit{eff}} \sum_i n_i + t\sum_{i\sigma}\left(a_{i\sigma}^\dagger a_{i+1\sigma} + \text{H.c.}\right) + U\sum_i n_{i\uparrow}n_{i\downarrow} + \sum_{i<j} K_{ij}\delta n_i \delta n_j, \tag{59}$$

where $\delta n_i \equiv n_i - 1$. Thus, all the *mean-field* Coulomb terms are collected into $\varepsilon_a^{\mathit{eff}}$.

Table 4: *Wannier-basis parameters for 1D chain calculated in the Gaussian STO-3G basis, with adjustable size, as a function of lattice parameter a (a_0 is the Bohr radius). The values of the optimal inverse orbital size $\alpha_{\min}$ are also provided.*

a/a_0	$\alpha_{\min}a_0$	β	γ	$\langle w_i\|w_{i+2}\rangle$	Δ
1.5	1.363	1.41984	0.32800	0.21689	0.34735
2.0	1.220	1.23731	0.26301	0.10590	0.50525
2.5	1.122	1.14133	0.20965	0.05725	0.63980
3.0	1.062	1.08190	0.16246	0.03089	0.75691
3.5	1.031	1.04394	0.12013	0.01573	0.85349
4.0	1.013	1.02216	0.08568	0.00768	0.92009
4.5	1.007	1.01010	0.05795	0.00343	0.96170
5.0	1.004	1.00429	0.03779	0.00144	0.98327
6.0	1.001	1.00063	0.01451	0.00021	0.99749
7.0	1.000	1.00007	0.00483	$2.3{\cdot}10^{-5}$	0.99972
8.0	1.000	1.00001	0.00139	$1.9{\cdot}10^{-6}$	0.99998
10.0	1.000	1	$7.3{\cdot}10^{-5}$	$5.3{\cdot}10^{-9}$	1

In the framework of the *tight-binding approximation* (TBA) one can postulate Wannier functions in a simple form, which is validated by an exponential drop of Wannier functions. The orthogonality relation $\langle w_i|w_{i\pm1}\rangle = 0$ and the normalization condition $\langle w_i|w_i\rangle = 1$ leads to coefficients of the expansion

$$\gamma = \frac{S_1}{(1{+}S_2) + \sqrt{(1{+}S_2)^2 - S_1(3S_1{+}S_3)}}, \tag{60}$$

and

$$\beta = \left(1 - 4\gamma S_1 + 2\gamma^2(1{+}S_2)\right)^{-1/2}, \tag{61}$$

where we define the overlap integral of atomic functions $S_m = \langle \Psi_i|\Psi_{i+m}\rangle$ (the normalization $S_0 = \langle \Psi_i|\Psi_i\rangle = 1$ is assumed). The above expressions are well-defined if the quantity under the square root of Eq. (60)

$$\Delta \equiv (1{+}S_2)^2 - S_1(3S_1{+}S_3) > 0, \tag{62}$$

(cf. Table 4). The actual limit of TBA comes with nonzero overlap integral of Wannier functions, when including the second-neighbor contribution (see Table 4), i.e.,

$$\langle w_i|w_{i+2}\rangle = \beta^2\gamma^2.$$

The above non-orthogonality may strongly affect the second neighbor hopping, as a zero-overlap is crucial for the convergence of hopping integral on a lattice providing the single-particle potential of the form (55). However, as the only term involving second neighbors in our Hamiltonian (59) is the interatomic Coulomb repulsion K_2, the presented TBA approach seems sufficient for the purpose (for details see [16]).

We already mentioned, that the atomic energy ε_a is divergent with the lattice size N and define the convergent effective quantity $\varepsilon_a^{\mathit{eff}}$ (58).

Table 5: *Microscopic parameters (in Ry) of the 1D chain, calculated in the Gaussian STO-3G basis. Corresponding values of the optimal inverse orbital size $\alpha_{\min}$ are provided in Table 4. The Richardson extrapolation to $N \to \infty$ was used.*

R/a_0	ε_a^{eff}	t	U	V [mRy]	J [mRy]	K_1	K_2	K_3
1.5	0.0997	-0.8309	2.054	-43.93	30.92	1.165	0.667	0.447
2.0	-0.5495	-0.4423	1.733	-23.81	21.06	0.911	0.501	0.334
2.5	-0.7973	-0.2644	1.531	-14.95	15.13	0.750	0.401	0.267
3.0	-0.9015	-0.1708	1.407	-10.99	10.91	0.639	0.334	0.222
3.5	-0.9483	-0.1156	1.335	-9.41	75.6	0.557	0.286	0.191
4.0	-0.9705	-0.0796	1.291	-8.74	4.93	0.493	0.250	0.167
4.5	-0.9815	-0.0549	1.270	-8.10	2.92	0.442	0.222	0.148
5.0	-0.9869	-0.0374	1.258	-7.07	1.57	0.399	0.200	0.133
6.0	-0.9908	-0.01676	1.249	-4.29	0.34	0.333	0.167	0.111
7.0	-0.9915	-0.00710	1.247	-1.96	0.05	0.286	0.146	0.095
8.0	-0.9917	-0.0027	1.247	-0.70	$5{\cdot}10^{-3}$	0.250	0.125	0.083
10.0	-0.9917	$-2.5{\cdot}10^{-3}$	1.247	-0.05	$2{\cdot}10^{-5}$	0.200	0.100	0.067

The values of the model parameters, corresponding to the lattice spacing $a/a_0 = 1.5 \div 10$, are presented in Table 5. The data correspond to the optimal values of the inverse orbital size $\alpha_{\min}$ as displayed in Table 4. We also provide there the values of the *correlated hopping* V and the *Heisenberg-exchange integral* J to show that one could indeed disregard the corresponding terms in the Hamiltonian (59).

One can note that the values of t calculated in the Gaussian STO-3G basis (listed in Table 5) differ from those obtained in the Slater basis by less then 0.5% when using the same values of the inverse orbital size α. However, the differences grow significantly, if α is optimized independently for the Slater basis and the three- and four-site terms are not included in the atomic basis.

4.1 Results

We now consider a nanoscopic linear chain of $N = 6 \div 14$ atoms, each containing a single valence electron (hydrogen-like atoms), including *all* long-range Coulomb interactions (3- and 4-site terms are also included in the adjustable Gaussian STO-3G basis).

4.1.1 Crossover from metallic to Mott-Hubbard regime

The Hamiltonian (59) is diagonalized in the Fock space with the help of the Lanczos method. As the microscopic parameters ε_a^{eff}, t, U, and K_{ij} are calculated numerically in the Gaussian STO-3G basis, the inverse orbital size α of the $1s$-like state is subsequently optimized to obtain the ground state energy E_G as a function of the interatomic distance a.

Their effects on convergence of the results for the ground-state energy E_G and the optimal inverse orbital size $\alpha_{\min}$ are shown in Figure 12 for $N = 6 \div 10$ atoms. These results were used to extrapolate the value of the variational parameter $\alpha_{\min}$ to larger N to speed up the computations. Figure 12 illustrates also the *Mott-Hubbard localization criterion.* Namely, for the interatomic distance $a \approx 3\ a_0$ the energy of the *ideal metallic* state (M), determined as

$$E_G^{\rm M} = \varepsilon_a^{\mathit{eff}} - \frac{4}{\pi}\,|t| + \frac{1}{N}\sum_{i<j} K_{ij}\langle \delta n_i \delta n_j\rangle, \tag{63}$$

where the density correlation function $\langle \delta n_i \delta n_j\rangle$, taken for the 1D electron-gas on the lattice

$$\langle \delta n_i \delta n_j\rangle = -2\frac{\sin^2(\pi\,|i-j|\,/2)}{(\pi\,|i-j|)^2} \tag{64}$$

(for the *half-filled* band), crosses over to that representing the *Mott insulating* state (INS), with

$$E_G^{\rm INS} = \varepsilon_a^{\mathit{eff}}. \tag{65}$$

One usually adds the second-order perturbation correction to the energy of the insulating state (65) in the well-known form [39]

$$\frac{4t^2}{U-K_1}\Big(\langle \mathbf{S}_i\cdot\mathbf{S}_{i+1}\rangle - \frac{1}{4}\Big), \tag{66}$$

the Bethe-Ansatz result is $\langle \mathbf{S}_i\cdot\mathbf{S}_{i+1}\rangle - 1/4 = -\ln 2$ for the quantum Heisenberg antiferromagnet. Here we only compare the two simplest approaches, leading to the energies (63) and (65). The critical value of a is very close to obtained for the $1s$ Slater-type orbitals. The validity of the above Mott-Hubbard criterion for this one-dimensional system is quantitative, as the energy of the antiferromagnetic (so *Slater-type*) Hartree-Fock solution (HF) is lower than those of the paramagnetic M and INS states. Therefore, a detailed verification of this criterion would be estimating the charge-energy gap and transport properties of this correlated system directly.

4.1.2 Evolution of Fermi-Dirac distribution into continuous spread of localized states

We consider now on the principal and exact results for model linear chains of hydrogen atoms. Those results can be viewed as concerning quantum monoatomic nano-wires composed of elements with one valence electron, and the inner-shell electrons treated as part of ionic case. Before presenting the physical properties we characterize briefly the methodology of our approach. First, the single-particle basis is selected in such a way that each of the starting atomic wave function (Slater orbital) is composed of three Gaussians STO-3G of adjustable size. Out of them one constructs the Wannier basis with the help of which we determine the trial values of the microscopic parameters of Hamiltonian (59). Second, in accordance with the scheme presented in Fig. 7, we diagonalize the Hamiltonian in the Fock space for $N \leqslant 14$ atoms using the Lanczos algorithm. At the end, we optimize the orbital size α^{-1} and thus the results can be presented as a function of interatomic distance, which mimics the gradual transformation of collective (itinerant) states at small distances into a set of atomic states, emplifying the Mott-Hubbard insulator.

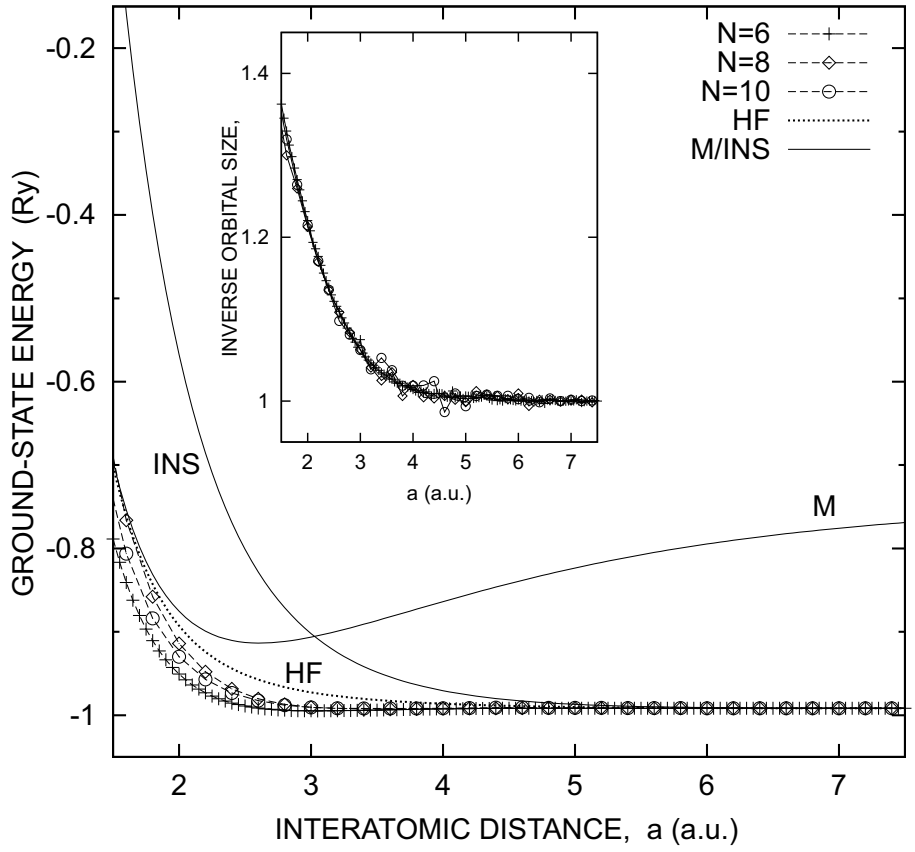

Fig. 12: *The ground state energy per atom for the linear chain of* $N = 6 \div 10$ *atoms with periodic boundary conditions. The Gaussian-type orbitals (STO-3G basis) with their adjustable inverse size* α^{-1} *have been used. The energies of the* ideal *metallic (M),* ideal *insulating (INS), and Hartree-Fock (HF) solutions for an* infinite *system are shown for comparison. The* inset *provides the optimal inverse orbital size* $\alpha_{\min}$.

Few words about the modified boundary conditions should be added. We take periodic conditions for the systems with $N = 4n{+}2$ atoms and antiperiodic for $N = 4n{+}4$. In the case of odd N the phase is defined with value between the above two cases, where the wavefunction phase changes φ by 2π and π, respectively). In Fig. 13 we present the statistical distribution function $n_{k\sigma}$ for $N = 6 \div 14$ atoms in the chain. This is one of our principal results. The solid state lines represent a singular polynomial fit [40]

$$n_{k\sigma} = n_F + A\,|k_F{-}k|^{\Theta}\,\mathrm{sgn}\,(k{-}k_F)\,, \tag{67}$$

with a non-universal (interaction dependent) exponent Θ ranging from 0.4 (for $a = 2a_0$) to $\Theta \simeq 1.5$ for $a \gtrsim 4a_0$. Also, a finite jump of Δn_F is observed at the Fermi momentum providing a quasi-particle type normalization factor Z_{k_F}.

The situation of this nano-Fermi liquid can be characterized equally well a by Tomonaga-Luttinger-model (TLM) scaling [16] of this nanoliquid as depicted is Fig. 14. In conclusion, although the two types of fitting procedures work almost equally well, the intermediate character of the nanoliquid between the Fermi and T-L limits has the value of its own.

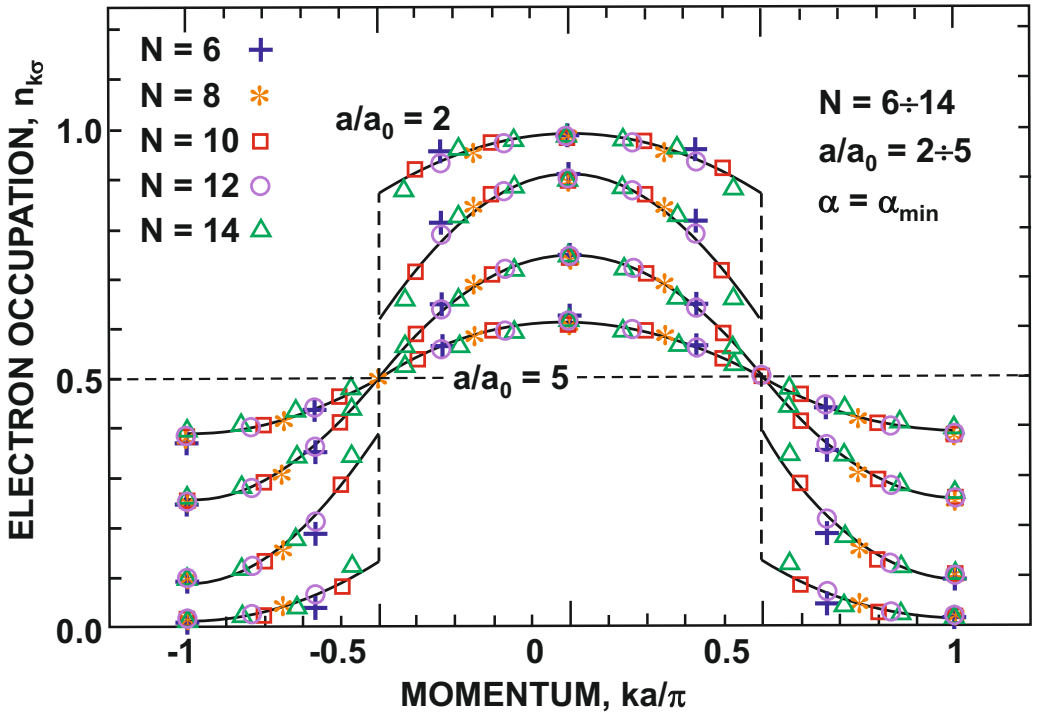

Fig. 13: *Momentum distribution for nanochains of interacting N hydrogen atoms. The distribution is smeared out with increasing lattice constant a and reaches its average $\simeq 0.5$ for the critical distance $a \simeq 5a_0$. The threshold value of a signals a crossover transformation to the localized state.*

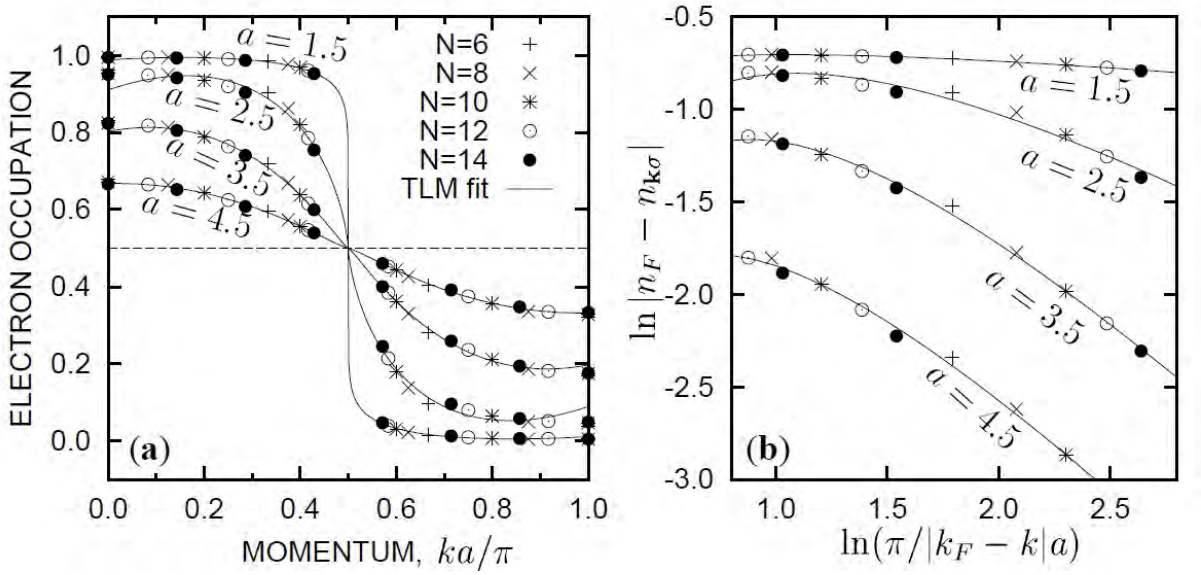

Fig. 14: *Tomonaga-Luttinger-liquid scaling for* half-filled *nano-chains of $N = 6 \div 14$ atoms with* long-range *Coulomb interactions: (a) momentum distribution in linear and (b) in log-log scale: continuous lines represent the fitted singular expansion in powers of* $\ln(\pi/|k_F - k|a)$.

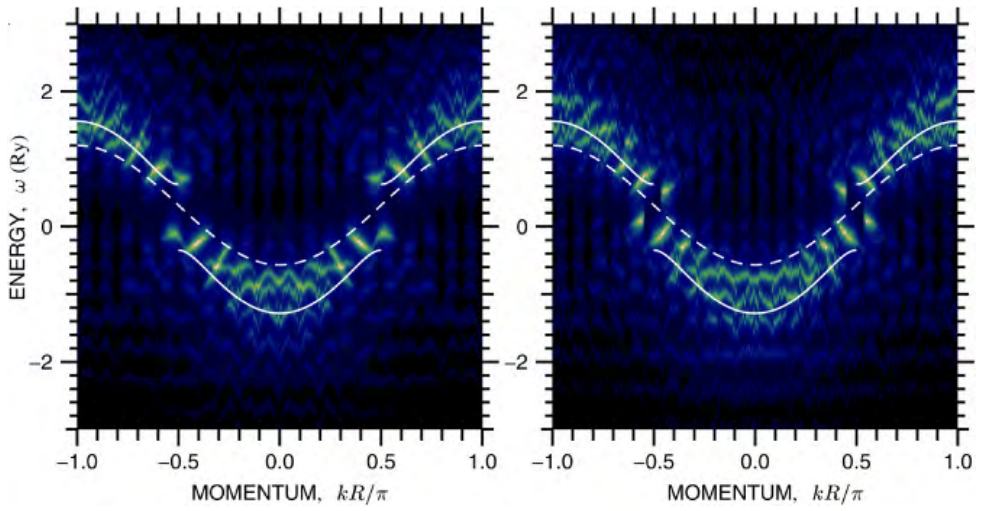

Fig. 15: *Exemplary electronic structure of electrons in a nanochain of $N = 10$ (left panel) and $N = 11$ (right panel) atoms as a representation of spectral-density-peak positions. The solid lines represent the Hartree-Fock results, the dashed lines the result for noninteracting electrons.*

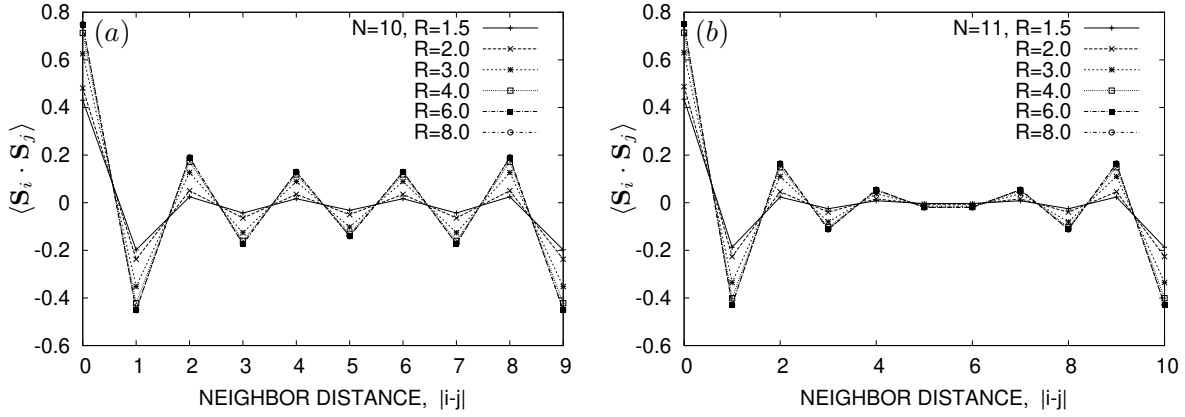

Fig. 16: *Parity effect on spin ordering: spin-spin correlations for nanochains of $N = 10$ (a) and $N = 11$ (b) atoms. The values of the interatomic distance R are specified in atomic units ($a_0 = 0.529$ Å).*

A direct demonstration of the emerging electronic structure is exemplified in Fig. 15, which was obtained by calculating from the definition of the spectral density for N=10 (left panel) and N=11 (right panel). The main novel feature is the splitting accusing at the nominal Fermi-momentum points. The solid line is the calculated electronic structure in the Hartree-Fock approximation and the dashed line is the band structure for noninteracting electrons with t values obtained from EDABI. The striking feature of this electronic structure is the splitting occurring at k_F=$\pm\pi/a$ signaling the onset of the antiferromagnetic superstructure appearing even for this very small system in the ground state. An explanation of this surprising feature emerges directly from the calculation of the spin-spin correlation function $\langle \boldsymbol{S}_i \cdot \boldsymbol{S}_j \rangle$, as illustrated in Fig. 16. We see that the correlations persist throughout the whole system length. In such circumstance the system behaves as if it possessed a long-range order, a truly collective behavior of a system with N_e∼10 electrons, but with long-range interaction (Coulomb interaction) included.

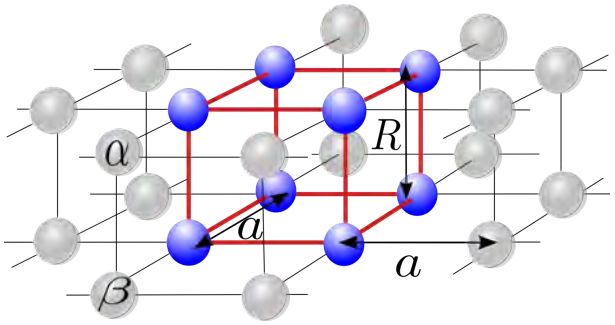

Fig. 17: *Schematic representation of stacked vertically H_2 molecular $2D$ layer forming a square lattice. The bond length and the intermolecular distance are marked by R and a, respectively. There are eight atoms in the supercell (dark blue spheres). The supercell is repeated periodically to conform periodic boundary conditions (PBC). Shaded spheres indicate atoms which are continuations resulting from the PBC implementation. The indices α, β distinguish the component atoms of each molecule.*

5 Recent developments

Here we would like to mention an application of the EDABI method to the problem of metallization of molecular hydrogen. First, the insulator-metal transition (hydrogen metallization of the insulating molecular hydrogen into metal) is a discontinuous transition from a diamagnet into a paramagnet, so this transition should be describable in our local language. Second, we have extended the cluster EDABI analysis to a bulk system, both in one- and two-dimensions. Here we present only the results for the latter situation.

In Fig. 17 we the present schematically the H_2 molecules stacked vertically and forming a square lattice, which is divided into super-cells specified explicitly there. The extent Hubbard Hamiltonian of a single supercell is diagonalized exactly, and repeated periodically, with the intermolecular Coulomb interaction between the cells included (for details see [41]). The system enthalpy is calculated as a function of pressure and the relevant renormalized Wannier functions $\{w_i^u(\mathbf{r})\}$, with $\mu = 1, 2$ characterizing the adjusted wave functions of the individual $1s$ atomic states in the molecule, are determined in the whole procedure. As a result, the phase diagram in the pressure-enthalphy plane is determined and comprises molecular-molecular and molecular-atomic solid discontinuous phase transitions. This phase diagram is drawn in Fig. 18. Those results may serve as a starting point to a more comprehensive analysis of the complex phase diagram of solid hydrogen. The molecular to atomic solid transition can be characterized as an example of a Mott-Hubbard transition, albeit from molecular solid to metal [41]. In brief, this example also shows that the EDABI method may be applied to real systems and to the localization-delocalization transition of a nonstandard nature. As the most recent example of an EDABI application we display the total energy of LiH and LiH $\cdot$ H_2 clusters (M. Hendzel, private communication) within an extended basis involving starting $1s$, $2s$, and $2p$ orbitals of variable size. The values are close to the experimental values for those systems: -16.1611 and -17.8942 Ry, respectively. We should see progress along these lines in the near future.

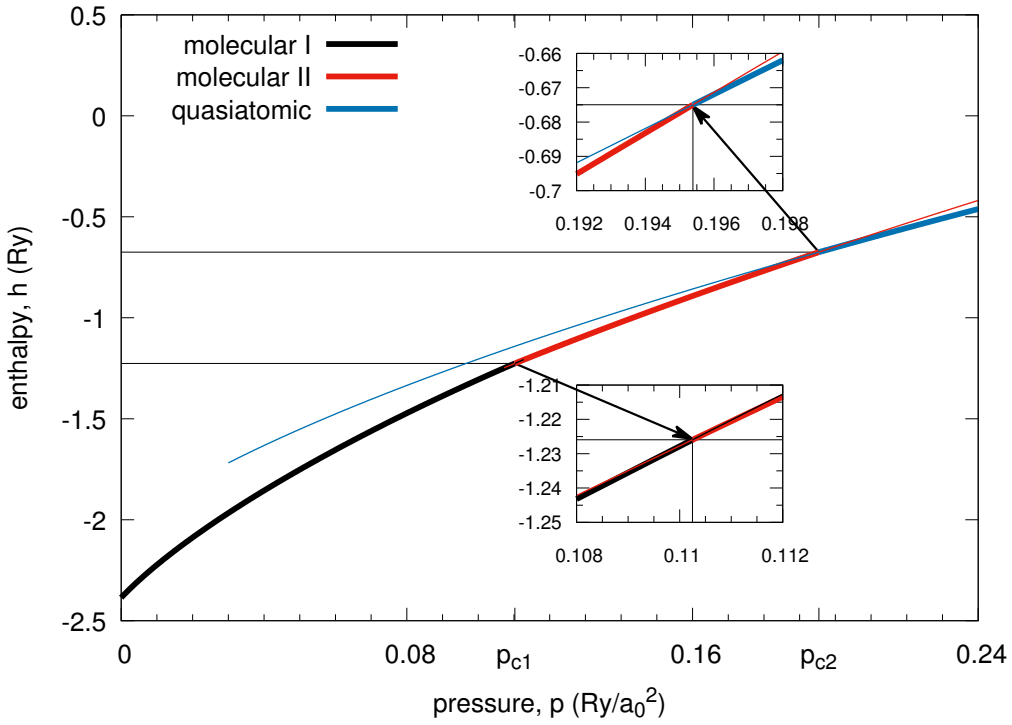

Fig. 18: *Enthalpy (per molecule) versus pressure. At lower pressure, two molecular phases are stable; the transition to the* quasiatomic *phase occurs at* $p_{c2} \sim 0.1954\ Ry/a_0^2$*, as marked.* $E_B(p{=}0) = -2.3858\ Ry$*,* $R_{eff}(p{=}0) = 1.4031\ a_0$*,* $a(p{=}0) = 4.3371\ a_0$*. Thin lines extrapolate the enthalpies of the particular phases beyond the regime of their stability. Insets show some detail of the transitions.*

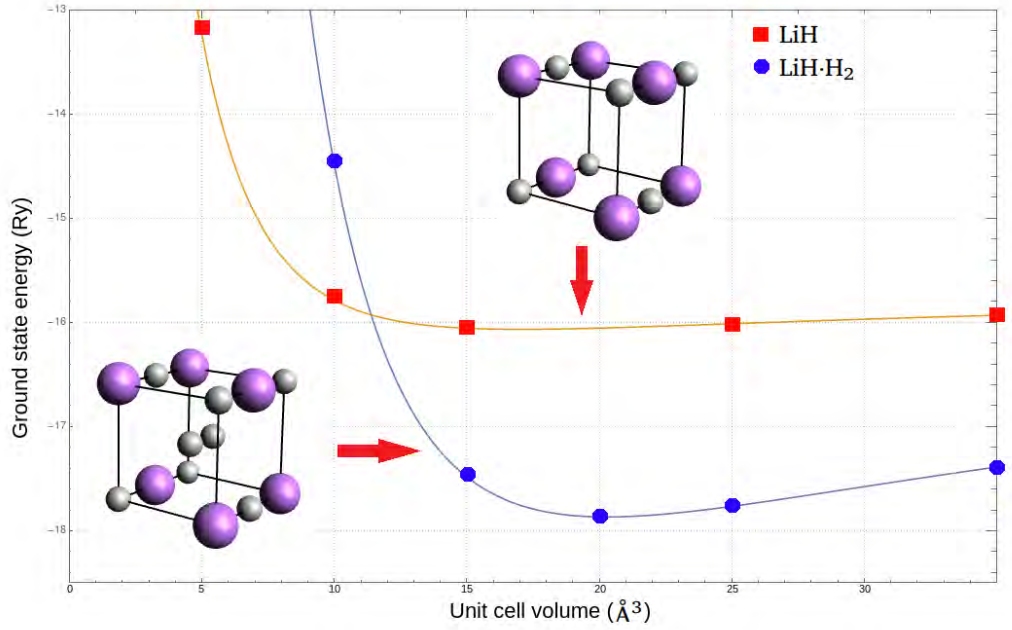

Fig. 19: *Total energy for LiH (squares) and* $LiH \cdot H_2$ *clusters as a function of unit cell volume as obtained from EDABI [M. Hendzel, unpublished].*

6 Conclusions

The **E**xact **D**iagonalization ***Ab* I***nito* (EDABI) method has been developing slowly and so far is useful mainly in describing in a precise manner model systems. Its principle aim has been to determine properties of correlated systems by incorporating also the calculations of model parameters, such as the Hubbard U, the hopping integrals t_{ij}, etc., into the general scheme of electronic structure calculations. It is particularly well suited for a description of nanosystems, in which a crossover from atomic to itinerant character of electronic states occurs as a sign of the Mott-Hubbard behavior. The studied evolution with the lattice parameter emulates the pressure dependence of the basic quantum properties and correlation functions. On the examples discussed in sections 4 and 5 collective (bulk) properties are exhibited in a direct manner. Future studies should show to what extent the results can be analyzed experimentally. Finally, we summarize the fundamental features of the EDABI method:

1° The $1^{\rm st}$ and $2^{\rm nd}$ quantization aspects of the collective (nano)systems are tackled in a consistent manner, i.e., without encountering the problem of double counting interactions, as is the case in the present versions of DFT+U and DFT+DMFT treatments.

2° In the approach we first diagonalize the second-quantized Hamiltonian for selected trial single-particle wavefunction basis and optimize it subsequently in the correlated state. In other words, the usual quantum-mechanical procedure of determining their e.g., the system energy is carried out in a reverse order (the correlations are as crucial as the single-particle wave function evaluation).

3° The method allows to analyze within a single scheme atomic, molecular, and extended systems via studies of nanoscopic systems of the increasing size.

Progress in calculating precisely properties of collective systems composed of more complex atoms will be effective within is method only with the implementation of computing capabilities, perhaps coming with the advent advanced quantum computing.

Acknowledgments

I am grateful to my former students: Adam Rycerz, Edward M. Görlich, Roman Zahorbeński, and Andrzej Kądzielawa, as well as to Dr. Andrzej Biborski, for permission to use some of the numerical results from their Ph.D. Theses and material from joint publications. I would like to thank Dr. Danuta Goc-Jagło and Dr. Maciej Fidrysiak for their technical help with formatting the text and figures. Mr Maciej Hendzel provided Fig. 19 from his unpublished M.Sc. Thesis. The work here was financed through the Grant OPUS No.UMO-2018/29/B/ST3/02646 from Narodowe Centrum Nauki (NCN).

References

[1] J.S. Griffith: *The Theory of Transition-Metal Ions* (Cambridge University Press, 1971)

[2] N.F. Mott: *Metal-Insulator Transitions* (Taylor & Francis, London, 1990)

[3] F. Gebhard: *The Mott Metal-Insulator Transition: Models and Methods* (Springer, Heidelberg, 1997)

[4] P.W. Anderson, Phys. Rev. **115**, 2 (1959)

[5] J.B. Goodenough, Prog. Sol. State Chem. **5**, 145 (1971)

[6] P.W. Anderson, Solid State Physics, **14**, 99–214 (1963)

[7] H. Kuwamoto, J.M. Honig, and J. Appel, Phys. Rev. B **22**, 2626 (1980)

[8] J. Spałek and P. Gopalan, Proc. Indian Natl. Sci. Acad. **64**, 2823 (1986)

[9] J. Spałek, Eur. J. Phys. **21**, 511 (2000)

[10] E. Koch in E. Pavarini, E. Koch, F. Anders, and M. Jarrell (eds.): *Correlated Electrons: From Models to Materials*, Modeling and Simulation Vol. 2 (Forschungszentrum Jülich, 2012) `http://www.cond-mat.de/events/correl12`

[11] J.M. Honig and J. Spałek, Chem. Mater. **10**, 2910 (1998)

[12] K. Kanoda and R. Kato, Ann. Rev. Condens. Matter Physics **2**, 167 (2011)

[13] G. Baym and C. Pethick: *Landau Fermi-Liquid Theory* (Wiley–VCH, 1991)

[14] V. Tripathi: *Landau Fermi Liquids and Beyond* (CRC Press, Boca Raton, 2018)

[15] J. Spałek, J. Sol. St. Chem. **88**, 70 (1990)

[16] A. Rycerz: *Physical properties and quantum phase transitions in strongly correlated electron systems from a combined exact diagonalization ab-initio approach* Ph.D. Thesis, Jagiellonian University, Kraków (2003)

[17] J. Spałek, E.M. Görlich, A. Rycerz, and R. Zahorbeński, J. Phys.: Condens. Matter **19**, 255212 (2007)

[18] H.A. Mook, Phys. Rev. Lett. **55**, 2452 (1985)

[19] D.S. Greywall, Phys. Rev. B **33**, 7520 (1986)

[20] J. Hubbard, Proc. Roy. Soc. (London) A. **276**, 238 (1963)

[21] J. Hubbard, Proc. Roy. Soc. (London) A **281**, 401 (1964)

[22] J. Spałek, A. Datta, and J.M. Honig, Phys. Rev. Lett. **59**, 728 (1987)

[23] J. Spałek, M. Kokowski, and J.M. Honig, Phys. Rev. B **39**, 4175 (1989)

[24] W.F. Brinkman and T.M. Rice, Phys. Rev. B **2**, 4302 (1970)

[25] J. Spałek, A.M. Oleś, and J.M. Honig, Phys. Rev. B **28**, 6802 (1983)

[26] J. Spałek in *Encyclopedia of Condensed Matter Physics* (Elsevier, 2005), pp. 125–135

[27] J. Spałek in *Reference Module in Materials Science and Materials Engineering* (Elsevier, Oxford, 2016)

[28] D. Vollhardt, Rev. Mod. Phys. **56**, 99 (1984)

[29] M. Fidrysiak and J. Spałek: *Robust Spin and Charge Excitations Throughout High-T_c-cuprate Phase Diagram From Incipient Mottness* (2019)

[30] M. Fidrysiak and J. Spałek, Phys. Rev. B **95** (2017)

[31] K. Rajagopal, Nucl. Phys. A **661**, 150 (1999)

[32] P. Limelette, A. Georges, D. Jérome, P. Wzietek, P. Metcalf, and J.M. Honig, Science **302**, 89 (2003)

[33] J. Spałek, A. Datta, and J.M. Honig, Phys. Rev. B **33**, 4891 (1986)

[34] A. Georges, G. Kotliar, W. Krauth, and M.J. Rozenberg, Rev. Mod. Phys. **68**, 13 (1996)

[35] A.L. Fetter and J.D. Walecka: *Quantum Theory of Many-Particle Systems* (Dover Publications, Minmeda, 2003) Ch. 1 & 2

[36] B. Robertson, Am. J. Phys. **41**, 678 (1973)

[37] R. Zahorbeński: *Properties of nanoclusters and the electron tunneling effects from a combined exact diagonalization- ab initio approach* Ph.D. Thesis, Jagiellonian University, Kraków (2004)

[38] E. Görlich: *Properties of molecules and nanoscopic systems from a combined exact diagonalization- ab initio approach* Ph.D. Thesis, Jagiellonian University, Kraków (2003)

[39] J. Spałek, A.M. Oleś, and K.A. Chao, Phys. Stat. Sol. (b) **108**, 329 (1981)

[40] J. Solyom, Adv. Phys. **28**, 201 (1979)

[41] A. Biborski, A.P. Kadzielawa, and J. Spałek, Phys. Rev. B **96**, 085101 (2017)

8 LDA+DMFT: Linear Response Functions

Eva Pavarini
Institute for Advanced Simulation
Forschungszentrum Jülich

Contents

E. Pavarini and E. Koch (eds.)
Topology, Entanglement, and Strong Correlations
Modeling and Simulation Vol. 10
Forschungszentrum Jülich, 2020, ISBN 978-3-95806-466-9
http://www.cond-mat.de/events/correl20

1 Introduction

The electronic many-body problem, in the non-relativistic limit and in the Born-Oppenheimer approximation, is described by the Hamiltonian

$$\hat{H}_e = -\frac{1}{2}\sum_i \nabla_i^2 - \sum_i \sum_\alpha \frac{Z_\alpha}{|\boldsymbol{r}_i - \boldsymbol{R}_\alpha|} + \sum_{i>j} \frac{1}{|\boldsymbol{r}_i - \boldsymbol{r}_j|} + \sum_{\alpha>\alpha'} \frac{Z_\alpha Z_{\alpha'}}{|\boldsymbol{R}_\alpha - \boldsymbol{R}_{\alpha'}|}, \tag{1}$$

where $\{\boldsymbol{r}_i\}$ are electron coordinates, $\{\boldsymbol{R}_\alpha\}$ nuclear coordinates and Z_α the nuclear charges. Using a complete one-electron basis, for example the basis $\{\phi_a(\boldsymbol{r})\}$, where $\{a\}$ are the quantum numbers, we can write this Hamiltonian in second quantization as

$$\hat{H}_e = \underbrace{-\sum_{ab} t_{ab} c_a^\dagger c_b}_{\hat{H}_0} + \underbrace{\frac{1}{2}\sum_{aa'bb'} U_{aa'bb'}\; c_a^\dagger c_{a'}^\dagger c_{b'} c_b}_{\hat{H}_U}.$$

Here the hopping integrals are given by

$$t_{ab} = -\int d\mathbf{r}\; \overline{\phi_a}(\boldsymbol{r}) \Big(-\frac{1}{2}\nabla^2 \underbrace{- \sum_\alpha \frac{Z_\alpha}{|\boldsymbol{r} - \boldsymbol{R}_\alpha|}}_{v_{\rm en}(\boldsymbol{r})} \Big) \phi_b(\boldsymbol{r}),$$

while the elements of the Coulomb tensor are

$$U_{aa'bb'} = \int d\mathbf{r}_2 \int d\mathbf{r}_2\; \overline{\phi_a}(\boldsymbol{r}_1)\, \overline{\phi_{a'}}(\boldsymbol{r}_2)\; \frac{1}{|\boldsymbol{r}_1 - \boldsymbol{r}_2|}\; \phi_{b'}(\boldsymbol{r}_2)\, \phi_b(\boldsymbol{r}_1).$$

In principle, all complete one-electron bases are equivalent. In practice, since, in the general case, we cannot solve the N-electron problem exactly, some bases are better than others. One possible choice for the basis are the Kohn-Sham orbitals, $\{\phi_a^{\rm KS}(\boldsymbol{r})\}$, obtained, e.g., in the local density approximation (LDA).[1] In this case, it is useful to replace the electron-nuclei interaction $v_{\rm en}(\boldsymbol{r})$ with the DFT potential $v_R(\boldsymbol{r})$, which includes in addition the Hartree term $v_{\rm H}(\boldsymbol{r})$ and the (approximate) exchange-correlation potential $v_{\rm xc}(\boldsymbol{r})$

$$v_{\rm R}(\boldsymbol{r}) = v_{\rm en}(\boldsymbol{r}) + \underbrace{\int d\mathbf{r}'\; \frac{n(\boldsymbol{r}')}{|\boldsymbol{r} - \boldsymbol{r}'|}}_{v_{\rm H}(\boldsymbol{r})} + v_{\rm xc}(\boldsymbol{r}),$$

so that

$$\tilde{t}_{ab} = -\int d\mathbf{r}\; \overline{\phi_a^{\rm KS}}(\boldsymbol{r}) \Big(-\frac{1}{2}\nabla^2 + v_{\rm R}(\boldsymbol{r}) \Big) \phi_b^{\rm KS}(\boldsymbol{r}). \tag{2}$$

To avoid double counting (DC), we have however to subtract from $\hat{H}_U$ the term $\hat{H}_{\rm DC}$, which describes the Coulomb terms already included in the hopping integrals

$$\hat{H}_e = \underbrace{-\sum_{ab} \tilde{t}_{ab}\, c_a^\dagger c_b}_{\hat{H}_0 = \hat{H}_e^{\rm LDA}} + \underbrace{\frac{1}{2}\sum_{aba'b'} \tilde{U}_{aa'bb'}\; c_a^\dagger c_{a'}^\dagger c_{b'} c_b - \hat{H}_{\rm DC}}_{\Delta \hat{H}_U}.$$

[1] For the purpose of many-body calculations the differences between LDA, GGA, or their plain extensions are in practice negligible; for simplicity, in the rest of the lecture, we thus adopt LDA as representative functional.

For weakly-correlated systems, in the Kohn-Sham basis, the effects included in $\Delta\hat{H}_U$ can, in first approximation, either be neglected or treated as a perturbation. This implies that $\hat{H}_e^{\rm LDA} \sim \hat{H}_{\rm eff}$, where $\hat{H}_{\rm eff}$ is the effective model which provides a good description of the system (at least) at low energy, and which describes emergent effective "elementary particles" and their interactions. Hypothetically, one could imagine that $\hat{H}_{\rm eff}$ is obtained via a canonical transformation, so that $\hat{H}_{\rm eff} \sim \hat{S}^{-1}\hat{H}_e\,\hat{S}$, although the exact form of the operator $\hat{S}$ is unknown.

A defining feature of strong-correlation effects is that they cannot be described via a single-electron Hamiltonian, however. A model of form $\hat{H}_e^{\rm LDA}$ does not capture the Mott metal-insulator transition, no matter what the specific values of the parameters $\tilde{t}_{ab}$ are.[2] Thus for strongly-correlated materials the low-energy effective model must have a different form. For Mott systems a canonical Hamiltonian is the Hubbard model

$$\hat{H} = -\sum_{\sigma}\sum_{ii'} t^{i,i'} c^{\dagger}_{i\sigma} c_{i'\sigma} + U\sum_{i} \hat{n}_{i\uparrow}\hat{n}_{i\downarrow}, \tag{3}$$

which includes, in addition to a single-electron term, the on-site Coulomb repulsion. This Hamiltonian captures the essence of the Mott transition. At half filling, for $U = 0$ it describes a paramagnetic metal, and for $t^{i,i'}(1-\delta_{i,i'})=0$ an insulating set of paramagnetic atoms. Unfortunately, differently from Hamiltonians of type $\hat{H}_e^{\rm LDA}$, Hubbard-like models cannot be solved exactly in the general case. Remarkably, till 30 years ago, no method for describing the complete phase diagram of (3) in one coherent framework, including the paramagnetic insulating phase, was actually known. This changed between 1989 and 1992, when the dynamical mean-field theory (DMFT) was developed [1–4]. The key idea of DMFT consists in mapping the Hubbard model onto a self-consistent *auxiliary quantum-impurity problem*, which can be solved exactly. The mapping is based on the *local dynamical self-energy approximation*, very good for realistic three-dimensional lattices—and becoming exact in the infinite coordination limit [1, 2].

DMFT was initially applied only to simple cases, due to limitations in model building, computational power, and numerical methods for solving the auxiliary impurity problem (the quantum-impurity solvers). In the last twenty years remarkable progress lifted many of these limitations. First, reliable schemes to build realistic low-energy materials-specific Hubbard-like models have been devised, in particular using Kohn-Sham localized Wannier functions. This is astonishing, given that we do not know the exact operator $\hat{S}$ which gives the effective low-energy Hamiltonian, and thus a truly systematic derivation is not possible. Second, key advances in quantum-impurity solvers and increasingly more powerful supercomputers made it possible to study always more complex many-body Hamiltonians. The approach which emerged, consisting in solving within DMFT materials-specific many-body Hamiltonians constructed via LDA, is known as the LDA+DMFT method [5–7]. This technique (and its extensions) is now the state-of-the-art for describing strongly-correlated materials. In this lecture I will outline the basic ideas on which the method is based, its successes and its limitations. This manuscripts extends the one of last year's school—in which more details on the model building aspects can be found—to the calculation of linear response functions.

[2] One can obtain an insulator by reducing the symmetry, e.g, by increasing the size of the primitive cell. This Slater-type insulator has however different properties than a Mott-type insulator.

2 From DMFT to LDA+DMFT

We will start by introducing the basics of DMFT. First we will consider a case for which analytic calculations can be performed, the two-site Hubbard Hamiltonian. This is a toy model, useful to illustrate how the method works, but for which, as we will see, DMFT is not a good approximation. Indeed, the Hubbard dimer is the worst case for DMFT, since the coordination number is the lowest possible. Next we will extend the formalism to the one-band and then to the multi-orbital Hubbard Hamiltonian. For three-dimensional lattices the coordination number is typically large and thus DMFT is an excellent approximation. Finally, we will discuss modern schemes to construct materials-specific many-body models. They are based on Kohn-Sham Wannier orbitals, calculated, e.g, using the LDA functional. The solution of such models via DMFT defines the LDA+DMFT method.

2.1 DMFT for a toy model: The Hubbard dimer

The two-site Hubbard model is given by

$$\hat{H} = \varepsilon_d \sum_{i\sigma} \hat{n}_{i\sigma} - t \sum_{\sigma} \left(c^\dagger_{1\sigma} c_{2\sigma} + c^\dagger_{2\sigma} c_{1\sigma} \right) + U \sum_i \hat{n}_{i\uparrow} \hat{n}_{i\downarrow},$$

with $i = 1, 2$. The ground state for $N = 2$ electrons (half filling) is the singlet[3]

$$|G\rangle_H = \frac{a_2(t,U)}{\sqrt{2}} \left(c^\dagger_{1\uparrow} c^\dagger_{2\downarrow} - c^\dagger_{1\downarrow} c^\dagger_{2\uparrow} \right) |0\rangle + \frac{a_1(t,U)}{\sqrt{2}} \left(c^\dagger_{1\uparrow} c^\dagger_{1\downarrow} + c^\dagger_{2\uparrow} c^\dagger_{2\downarrow} \right) |0\rangle \tag{4}$$

with

$$a_1^2(t,U) = \frac{1}{\Delta(t,U)} \frac{\Delta(t,U) - U}{2}, \qquad a_2^2(t,U) = \frac{4t^2}{\Delta(t,U)} \frac{2}{\Delta(t,U) - U},$$

and

$$\Delta(t,U) = \sqrt{U^2 + 16t^2}.$$

The energy of this state is

$$E_0(2) = 2\varepsilon_d + \frac{1}{2}\big(U - \Delta(t,U)\big).$$

In the $T \to 0$ limit, using the Lehmann representation (see Appendix B), one can show that the local Matsubara Green function for spin σ takes then the form

$$G^\sigma_{i,i}(i\nu_n) = \frac{1}{4} \Bigg(\frac{1 + w(t,U)}{i\nu_n - (E_0(2) - \varepsilon_d + t - \mu)} + \frac{1 - w(t,U)}{i\nu_n - \big(E_0(2) - \varepsilon_d - t - \mu\big)} + \frac{1 - w(t,U)}{i\nu_n - \big(-E_0(2) + U + 3\varepsilon_d + t - \mu\big)} + \frac{1 + w(t,U)}{i\nu_n - \big(-E_0(2) + U + 3\varepsilon_d - t - \mu\big)} \Bigg),$$

[3] Eigenstates and eigenvalues of the Hubbard dimer for arbitrary filling can be found in Appendix A.1.

where $\nu_n = \pi(2n+1)/\beta$ are fermionic Matsubara frequencies, $\mu = \varepsilon_d + U/2$ is the chemical potential, and the weight is $w(t,U) = 2a_1(t,U)a_2(t,U)$. The local Green function can be rewritten as the average of the Green function for the bonding ($k = 0$) and the anti-bonding state ($k = \pi$), i.e.,

$$G^\sigma_{i,i}(i\nu_n) = \frac{1}{2}\Bigg(\underbrace{\frac{1}{i\nu_n + \mu - \varepsilon_d + t - \Sigma^\sigma(0,i\nu_n)}}_{G^\sigma(0,i\nu_n)} + \underbrace{\frac{1}{i\nu_n + \mu - \varepsilon_d - t - \Sigma^\sigma(\pi,i\nu_n)}}_{G^\sigma(\pi,i\nu_n)} \Bigg).$$

The self-energy is given by

$$\Sigma^\sigma(k,i\nu_n) = \frac{U}{2} + \frac{U^2}{4}\frac{1}{i\nu_n + \mu - \varepsilon_d - \frac{U}{2} - \ e^{ik}\ 3t}.$$

The self-energies $\Sigma^\sigma(0,i\nu_n)$ and $\Sigma^\sigma(\pi,i\nu_n)$ differ due to the phase $e^{ik} = \pm 1$ in their denominators. The local self-energy is, by definition, the average of the two

$$\Sigma^\sigma_l(i\nu_n) = \frac{1}{2}\Big(\Sigma^\sigma(\pi,i\nu_n) + \Sigma^\sigma(0,i\nu_n) \Big) = \frac{U}{2} + \frac{U^2}{4}\ \frac{i\nu_n + \mu - \varepsilon_d - \frac{U}{2}}{(i\nu_n + \mu - \varepsilon_d - \frac{U}{2})^2 - (3t)^2}.$$

The difference

$$\Delta\Sigma^\sigma_l(i\nu_n) = \frac{1}{2}\Big(\Sigma^\sigma(\pi,i\nu_n) - \Sigma^\sigma(0,i\nu_n) \Big) = \frac{U^2}{4}\ \frac{3t}{(i\nu_n + \mu - \varepsilon_d - \frac{U}{2})^2 - (3t)^2},$$

thus measures the importance of non-local effects; it would be zero if the self-energy was independent of $\boldsymbol{k}$. Next we define the hybridization function

$$F^\sigma(i\nu_n) = \frac{\big(t + \Delta\Sigma^\sigma_l(i\nu_n)\big)^2}{i\nu_n + \mu - \varepsilon_d - \Sigma^\sigma_l(i\nu_n)}$$

which for $U = 0$ becomes

$$F^\sigma_0(i\nu_n) = \frac{t^2}{i\nu_n}.$$

By using these definitions, we can rewrite the local Green function as

$$G^\sigma_{i,i}(i\nu_n) = \frac{1}{i\nu_n + \mu - \varepsilon_d - F^\sigma(i\nu_n) - \Sigma^\sigma_l(i\nu_n)}. \tag{5}$$

It is important to point out that, as one may see from the formulas above, the local Green function and the local self-energy satisfy the following *local Dyson equation*

$$\Sigma^\sigma_l(i\nu_n) = \frac{1}{\mathfrak{G}^\sigma_{i,i}(i\nu_n)} - \frac{1}{G^\sigma_{i,i}(i\nu_n)},$$

where $\mathfrak{G}^\sigma_{i,i}(i\nu_n)$ is given by

$$\mathfrak{G}^\sigma_{i,i}(i\nu_n) = \frac{1}{i\nu_n + \mu - \varepsilon_d - F^\sigma(i\nu_n)}.$$

Thus, one could think of mapping the Hubbard dimer into an auxiliary quantum-impurity model, chosen such that, within certain approximations, the impurity Green function is as close as possible to the local Green function of the original problem. How can we do this? Let us adopt as auxiliary model the Anderson molecule

$$\hat{H}^{\rm A} = \varepsilon_s \sum_\sigma \hat{n}_{s\sigma} - t \sum_\sigma \left(c^\dagger_{d\sigma} c_{s\sigma} + c^\dagger_{s\sigma} c_{d\sigma} \right) + \varepsilon_d \sum_\sigma \hat{n}_{d\sigma} + U \hat{n}_{d\uparrow} \hat{n}_{d\downarrow}. \tag{6}$$

The first constraint would be that Hamiltonian (6) has a ground state with the same occupations of the 2-site Hubbard model, i.e., at half filling, $n_d = n_s = 1$. Such a *self-consistency condition* is satisfied if $\varepsilon_s = \mu = \varepsilon_d + U/2$. This can be understood by comparing the Hamiltonian matrices of the two models in the Hilbert space with $N = 2$ electrons. To this end, we first order the two-electron states of the Hubbard dimer as

$$|1\rangle = c^\dagger_{1\uparrow} c^\dagger_{2\uparrow} |0\rangle, \qquad |4\rangle = \tfrac{1}{\sqrt{2}} (c^\dagger_{1\uparrow} c^\dagger_{2\downarrow} - c^\dagger_{1\downarrow} c^\dagger_{2\uparrow}) |0\rangle,$$

$$|2\rangle = c^\dagger_{1\downarrow} c^\dagger_{2\downarrow} |0\rangle, \qquad |5\rangle = c^\dagger_{1\uparrow} c^\dagger_{1\downarrow} |0\rangle,$$

$$|3\rangle = \tfrac{1}{\sqrt{2}} (c^\dagger_{1\uparrow} c^\dagger_{2\downarrow} + c^\dagger_{1\downarrow} c^\dagger_{2\uparrow}) |0\rangle, \qquad |6\rangle = c^\dagger_{2\uparrow} c^\dagger_{2\downarrow} |0\rangle.$$

In this basis the Hamiltonian of the Hubbard dimer has the matrix form

$$\hat{H}_2(\varepsilon_d, U, t) = \begin{pmatrix} 2\varepsilon_d & 0 & 0 & 0 & 0 & 0 \\ 0 & 2\varepsilon_d & 0 & 0 & 0 & 0 \\ 0 & 0 & 2\varepsilon_d & 0 & 0 & 0 \\ 0 & 0 & 0 & 2\varepsilon_d & -\sqrt{2}t & -\sqrt{2}t \\ 0 & 0 & 0 & -\sqrt{2}t & 2\varepsilon_d{+}U & 0 \\ 0 & 0 & 0 & -\sqrt{2}t & 0 & 2\varepsilon_d{+}U \end{pmatrix}.$$

The ground state, the singlet given in Eq. (4), can be obtained by diagonalizing the lower $3{\times}3$ block. For the Anderson molecule, ordering the basis in the same way ($1 \to d, 2 \to s$), this Hamiltonian becomes

$$\hat{H}^A_2(\varepsilon_d, U, t; \varepsilon_s) = \begin{pmatrix} \varepsilon_d{+}\varepsilon_s & 0 & 0 & 0 & 0 & 0 \\ 0 & \varepsilon_d{+}\varepsilon_s & 0 & 0 & 0 & 0 \\ 0 & 0 & \varepsilon_d{+}\varepsilon_s & 0 & 0 & 0 \\ 0 & 0 & 0 & \varepsilon_d{+}\varepsilon_s & -\sqrt{2}t & -\sqrt{2}t \\ 0 & 0 & 0 & -\sqrt{2}t & 2\varepsilon_d{+}U & 0 \\ 0 & 0 & 0 & -\sqrt{2}t & 0 & 2\varepsilon_s \end{pmatrix}.$$

Comparing the lower $3{\times}3$ block of $\hat{H}^A_2(\varepsilon_d, U, t; \varepsilon_s)$ with the corresponding block of $\hat{H}_2(\varepsilon_d, U, t)$ we can see that, unless $\varepsilon_s = \mu = \varepsilon_d + U/2$, the two ionic states $|5\rangle$ and $|6\rangle$ have different energies; hence, for $\varepsilon_s \neq \mu$, the two sites are differently occupied in the ground state.

By setting $\varepsilon_s = \mu$ we find that $\hat{H}_2^A(\varepsilon_d, U, t; \mu) = \hat{H}_2(\varepsilon_d + \frac{U}{4}, \frac{U}{2}, t)$. The $N = 2$ ground state of $\hat{H}_2^A(\varepsilon_d, U, t; \mu)$ has thus the form of the ground-state for the Hubbard dimer

$$|G\rangle_A = \frac{a_2(t, U/2)}{\sqrt{2}} \left(c_{d\uparrow}^\dagger c_{s\downarrow}^\dagger - c_{d\downarrow}^\dagger c_{s\uparrow}^\dagger \right) |0\rangle + \frac{a_1(t, U/2)}{\sqrt{2}} \left(c_{d\uparrow}^\dagger c_{d\downarrow}^\dagger + c_{s\uparrow}^\dagger c_{s\downarrow}^\dagger \right) |0\rangle,$$

and the condition $n_s = n_d = 1$ is satisfied. Since $\varepsilon_s \neq \varepsilon_d$, however, the eigenstates of $\hat{H}^{\mathrm{A}}$ for one electron ($N = 1$) or one hole ($N = 3$) are not the bonding and antibonding states.[4] The impurity Green function is then given by

$$G_{d,d}^\sigma(i\nu_n) = \frac{1}{4} \Bigg(\frac{1 + w'(t,U)}{i\nu_n - (E_0(2) - E_-(1) - \mu)} + \frac{1 - w'(t,U)}{i\nu_n - (E_0(2) - E_+(1) - \mu)} \\ \frac{1 + w'(t,U)}{i\nu_n - (E_-(3) - E_0(2) - \mu)} + \frac{1 - w'(t,U)}{i\nu_n - (E_+(3) - E_0(2) - \mu)} \Bigg),$$

where

$$E_0(2) - E_\pm(1) - \mu = -\Big(E_\pm(3) - E_0(2) - \mu \Big) = -\frac{1}{4} \Big(2\Delta(t, U/2) \pm \Delta(t, U) \Big),$$

and

$$w'(t, U) = \frac{1}{2} \frac{32t^2 - U^2}{\Delta(t, U)\Delta(t, U/2)}.$$

After some rearrangement we obtain a much simpler expression

$$G_{d,d}^\sigma(i\nu_n) = \frac{1}{i\nu_n + \mu - \varepsilon_d - \mathcal{F}_0^\sigma(i\nu_n) - \Sigma_A^\sigma(i\nu_n)}.$$

The impurity self-energy equals the local self-energy of the Hubbard dimer

$$\Sigma_A^\sigma(i\nu_n) = \frac{U}{2} + \frac{U^2}{4} \frac{i\nu_n}{(i\nu_n)^2 - (3t)^2}.$$

The hybridization function is given by

$$\mathcal{F}_0^\sigma(i\nu_n) = \frac{t^2}{i\nu_n}.$$

For $U = 0$, $G_{d,d}^\sigma(i\nu_n)$ equals the non-interacting impurity Green function

$$G_{d,d}^{0\sigma}(i\nu_n) = \frac{1}{i\nu_n + \mu - \varepsilon_d - \mathcal{F}_0^\sigma(i\nu_n)}.$$

The impurity Green function thus satisfies the *impurity Dyson equation*

$$\Sigma_A^\sigma(i\nu_n) = \frac{1}{G_{d,d}^{0\sigma}(i\nu_n)} - \frac{1}{G_{d,d}^\sigma(i\nu_n)}.$$

[4] The complete list of eigenvalues and eigenvectors of the Anderson molecule for $\varepsilon_s = \varepsilon_d + U/2$ and arbitrary electron number N can be found in Appendix A.2.

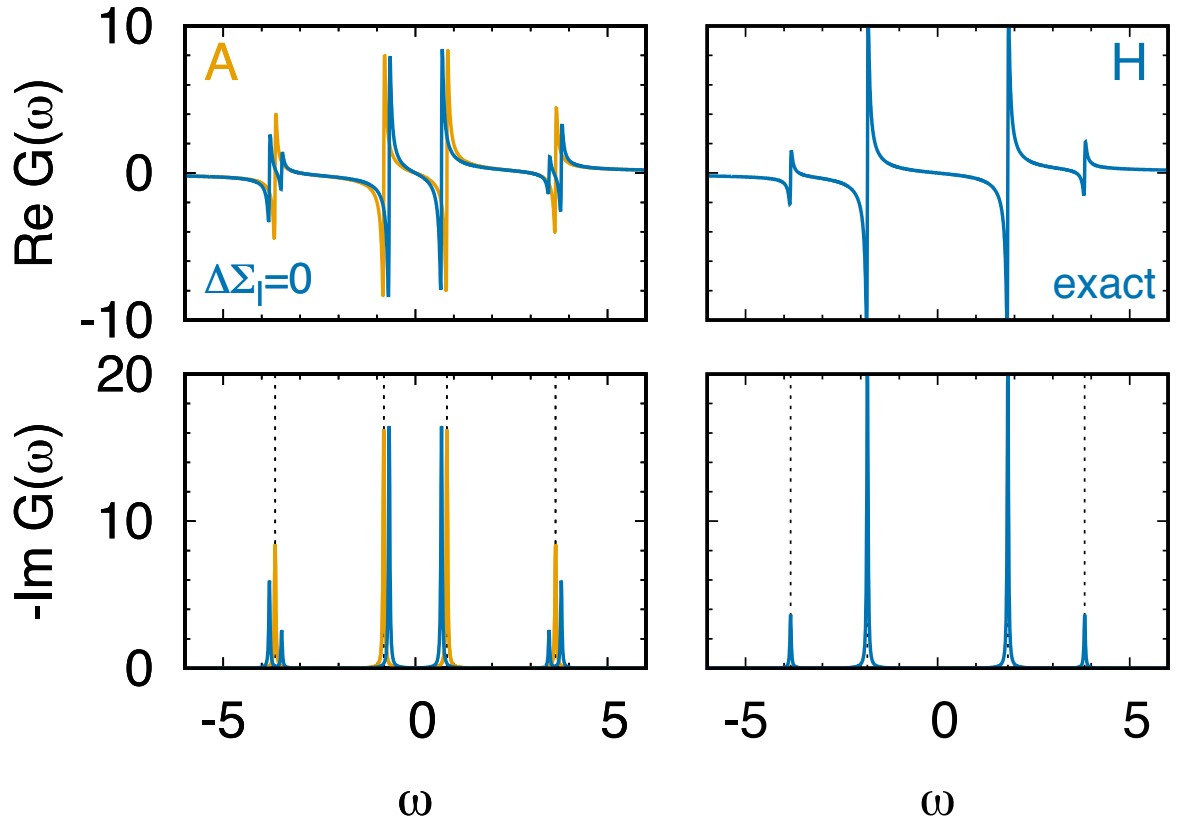

Fig. 1: *Green functions of the Hubbard dimer ($t = 1, U = 4$) and the Anderson molecule ($\varepsilon_s = \varepsilon_d + U/2$) in the zero temperature limit. Left panels, blue: Hubbard dimer with local self-energy only, i.e., with $\Delta\Sigma_l^\sigma(\omega) = 0$. Left panels, orange: Anderson molecule. Right panels: Exact Green function of the Hubbard dimer. Dashed lines: Poles of the Green function of the Anderson molecule (left) or Hubbard dimer (right).*

In Fig. 1 we show the impurity Green function of the Anderson molecule (orange, left panels) and the local Green function of the 2-site Hubbard model, in the local self-energy approximation (blue, left panels) and exact (blue, right panels). Comparing left and right panels we can see that setting $\Delta\Sigma_l^\sigma(\omega) = 0$ yields large errors. The left panels demonstrate, however, that the spectral function of the Anderson molecule is quite similar to the one of the Hubbard dimer with $\Delta\Sigma_l^\sigma(\omega) = 0$. The small remaining deviations come from the fact that, for the Hubbard dimer, in the impurity Dyson equation, the non-interacting impurity Green function is replaced by $\mathfrak{G}_{i,i}^\sigma(i\nu_n)$ in the local self-energy approximation, i.e., with the *bath* Green function

$$\mathcal{G}_{i,i}^\sigma(i\nu_n) = \frac{1}{i\nu_n + \mu - \varepsilon_d - \mathcal{F}_l^\sigma(i\nu_n)},$$

where

$$\mathcal{F}_l^\sigma(i\nu_n) = \frac{t^2}{i\nu_n + \mu - \varepsilon_d - \Sigma_A^\sigma(i\nu_n)}.$$

We are now in the position of explaining how DMFT works for the Hamiltonian of the Hubbard dimer, choosing the Anderson molecule Hamiltonian (6) as the auxiliary quantum-impurity model. The procedure can be split in the following steps

1. Build the initial quantum-impurity model with $G^{0\sigma}_{d,d}(i\nu_n) = G^{0\sigma}_{i,i}(i\nu_n)$. The initial bath is thus defined by energy $\varepsilon_s = \varepsilon_d$ and hopping t.

2. Calculate the local Green function $G^{\sigma}_{d,d}(i\nu_n)$ for the auxiliary model.

3. Use the local Dyson equation to calculate the impurity self-energy

$$\Sigma^{\sigma}_{A}(i\nu_n) = \frac{1}{G^{0\sigma}_{d,d}(i\nu_n)} - \frac{1}{G^{\sigma}_{d,d}(i\nu_n)}.$$

4. Calculate the local Green function of the Hubbard dimer setting the self-energy equal to the one of the quantum-impurity model

$$G^{\sigma}_{i,i}(i\nu_n) \sim \frac{1}{2}\left(\frac{1}{i\nu_n + \mu - \varepsilon_d + t - \Sigma^{\sigma}_{A}(i\nu_n)} + \frac{1}{i\nu_n + \mu - \varepsilon_d - t - \Sigma^{\sigma}_{A}(i\nu_n)}\right).$$

5. Calculate a new bath Green function $\mathcal{G}^{\sigma}_{i,i}(i\nu_n)$ from the local Dyson equation

$$\mathcal{G}^{\sigma}_{i,i}(i\nu_n) = \frac{1}{\Sigma^{\sigma}_{A}(i\nu_n) + 1/G^{\sigma}_{i,i}(i\nu_n)}.$$

6. Build a new $G^{0\sigma}_{d,d}(i\nu_n)$ from $\mathcal{G}^{\sigma}_{i,i}(i\nu_n)$.

7. Restart from the second step.

8. Iterate till self-consistency, i.e., here till $n^{\sigma}_{d} = n^{\sigma}_{i}$ and $\Sigma^{\sigma}_{A}(i\nu_n)$ does not change any more.

The Anderson molecule satisfies the self-consistency requirements for $\varepsilon_s = \mu$. The remaining difference between $G^{\sigma}_{d,d}(i\nu_n)$, the impurity Green function, and $G^{\sigma}_{i,i}(i\nu_n)$, the local Green function of the Hubbard dimer in the local self-energy approximation, arises from the difference in the associated hybridization functions

$$\Delta\mathcal{F}_l(i\nu_n) = \mathcal{F}^{\sigma}_{l}(i\nu_n) - \mathcal{F}^{\sigma}_{0}(i\nu_n) = t^2p^2\left(-\frac{2}{i\nu_n} + \frac{1}{i\nu_n - \varepsilon_a} + \frac{1}{i\nu_n + \varepsilon_a}\right)$$

where $p^2 = U^2/8\varepsilon_a^2$ and $\varepsilon_a = \sqrt{9t^2 + U^2/4}$. If we use the Anderson molecule as quantum-impurity model we neglect $\Delta\mathcal{F}_l(i\nu_n)$; the error made is small, as shown in the left panels of Fig. 1. To further improve we would have to modify the auxiliary model adding more bath sites. Remaining with the Anderson molecule, let us compare in more detail its spectral function with the exact spectral function of the Hubbard dimer. Fig. 2 shows that the evolution as a function of U is different for the two Hamiltonians. Anticipating the discussion of later sections, if we compare to the spectral function of the actual lattice Hubbard model, we could say that the Anderson molecule partially captures the behavior of the central "quasi-particle" or "Kondo"

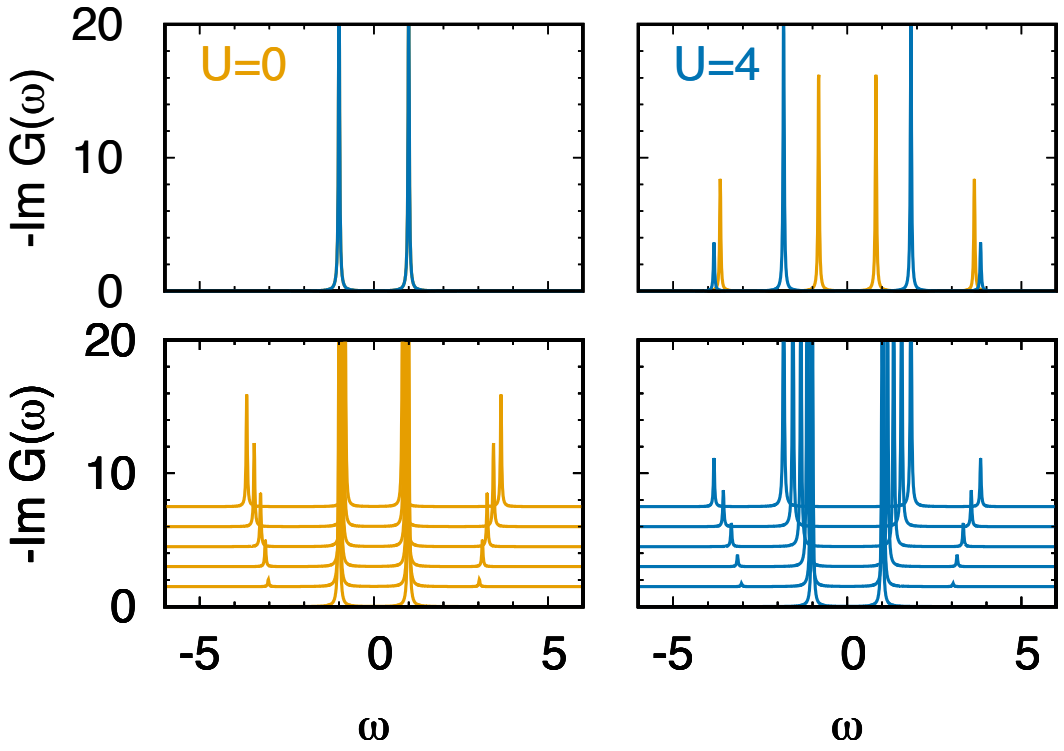

Fig. 2: *Imaginary part of the Green function of the Anderson molecule (orange) and Hubbard dimer (blue) in the zero temperature limit. For the Hubbard dimer the exact Green functions are used, as in the right panels of Fig. 1. Parameters:* $t = 1$, $\varepsilon_s = \mu$. *Top:* $U = 0$ *(left) and* $U = 4t$ *(right). Bottom: Evolution with increasing* U *from* 0 *to* $4t$ *in equal steps.*

peak with increasing U, although the Kondo effect itself is unrealistically described; as a matter of fact, the Kondo energy gain (the "Kondo temperature") is perturbative ($\propto t^2/U$) in the case of the Anderson molecule, while it is exponentially small for a Kondo impurity in a metallic bath. On the other hand, the Hubbard dimer captures well the Hubbard bands and the gap in the large-U limit. The example of the Anderson molecule also points to the possible shortcomings of DMFT calculations for the lattice Hubbard model (3) in which the quantum-impurity model is solved via exact diagonalization, however using a single bath site or very few; this might perhaps be sufficient in the limit of large gap,[5] but is bound to eventually fail approaching the metallic regime. Indeed, this failure is one of the reasons why the solution of the Kondo problem required the development of—at the time new—non-perturbative techniques such as the numerical renormalization group. Finally, the example of the Hubbard dimer shows that DMFT is not a good approximation for molecular complexes with two (or few) correlated sites. This is because in such systems the coordination number is the lowest possible, the worst case for dynamical mean-field theory. In three dimensional crystals, instead, the coordination number is typically large enough to make DMFT an excellent approximation.

[5]For a discussion of bath parametrization in exact diagonalization and the actual convergence with the number of bath sites for the lattice Hubbard model see Ref. [8].

2.2 Non-local Coulomb interaction

In Sec. 2.1 we have seen that the local Coulomb interaction gives rise, *alone*, to non-local self-energy terms, which can be very important. What is, instead, the effect of the non-local part of the Coulomb interaction? For a Hubbard dimer, extending the Coulomb interaction to first neighbors leads to the Hamiltonian

$$\begin{aligned}\hat{H} =&\varepsilon_d \sum_{i\sigma} \hat{n}_{i\sigma} - t \sum_{\sigma} \left(c^\dagger_{1\sigma} c_{2\sigma} + c^\dagger_{2\sigma} c_{1\sigma} \right) + U \sum_{i=1,2} \hat{n}_{i\uparrow} \hat{n}_{i\downarrow} \\ &+ \sum_{\sigma\sigma'} \left(V - 2J_V - J_V\, \delta_{\sigma\sigma'} \right) \hat{n}_{1\sigma} \hat{n}_{2\sigma'} - J_V \sum_{i\neq i'} \left(c^\dagger_{i\uparrow} c_{i\downarrow} c^\dagger_{i'\downarrow} c_{i'\uparrow} + c^\dagger_{i'\uparrow} c^\dagger_{i'\downarrow} c_{i\uparrow} c_{i\downarrow} \right),\end{aligned}$$

where the parameters in the last two terms are the intersite direct (V) and exchange (J_V) Coulomb interaction. For two electrons the Hamiltonian, in a matrix form, becomes

$$\hat{H}_2^{\mathrm{NL}} = \begin{pmatrix} 2\varepsilon_d{+}V{-}3J_V & 0 & 0 & 0 & 0 & 0 \\ 0 & 2\varepsilon_d{+}V{-}3J_V & 0 & 0 & 0 & 0 \\ 0 & 0 & 2\varepsilon_d{+}V{-}3J_V & 0 & 0 & 0 \\ 0 & 0 & 0 & 2\varepsilon_d{+}V{-}J_V & -\sqrt{2}t & -\sqrt{2}t \\ 0 & 0 & 0 & -\sqrt{2}t & 2\varepsilon_d{+}U & -J_V \\ 0 & 0 & 0 & -\sqrt{2}t & -J_V & 2\varepsilon_d{+}U \end{pmatrix}.$$

Since $J_V > 0$, the effect of J_V is to lower the energy of triplet states with respect singlet states. This might change the nature of the ground state. If, however, J_V is sufficiently small, the ground state remains a singlet. Setting for simplicity $J_V = 0$, we can notice that $\hat{H}_2^{\mathrm{NL}}$ equals $\hat{H}_2(\varepsilon'_d, U', t)$, the corresponding $N{=}2$-electron Hamiltonian of the $J_V{=}V{=}0$ Hubbard dimer, with parameters $\varepsilon'_d = \varepsilon_d + V/2$ and $U'{=}U{-}V$. The $N{=}2$ ground state is thus still given by Eq. (4), provided, however, that we replace U with U' in the coefficients. Eventually, in the limiting case $U{=}V$, $\hat{H}_2^{\mathrm{NL}}$ equals the corresponding Hamiltonian of an effective non-correlated dimer. What happens away from half filling? For $N{=}1$ electrons, eigenvectors and eigenvalues are the same as in the $V{=}0$ case; for $N{=}3$ electrons all energies are shifted by $2V$. This leads to further differences in the local Green function with respect to the $V{=}0$ case—in addition to those arising from replacing U with U'; to some extent, these additional changes can be interpreted as a hopping enhancement from t to $t + V/2$. Putting all these results together, we could thus say that, in first approximation, the (positive) intersite coupling V effectively reduces the strength of correlations.

In conclusion, *strong-correlation* effects typically appear when the *local term of the electron-electron repulsion dominates*, i.e., when it is much larger than long-range terms. Instead, a hypothetical system in which the Coulomb interaction strength is independent on the distance between sites (here $U{=}V$) is likely to be already well described via an *effective weakly correlated model*. Of course, in real materials, the effects of long-range Coulomb repulsion can be much more complicated than in the two-site model just discussed, but the general considerations made here remain true even in realistic cases.

2.3 Quantum-impurity solvers: Continuous-time quantum Monte Carlo

For the case of the Anderson molecule exact diagonalization is the simplest quantum-impurity solver and the one that provides most insights. Methods based on quantum Monte Carlo (QMC) sampling are often, however, the only option for realistic multi-orbital and/or multi-site models. Here we explain how to obtain the impurity Green function of the Anderson molecule via hybridization-expansion continuous-time QMC [9], a very successful QMC-based quantum-impurity solver. In this approach, the first step consists in splitting the Hamiltonian into bath ($\hat{H}_{\rm bath}$), hybridization ($\hat{H}_{\rm hyb}$), and local ($\hat{H}_{\rm loc}$) terms

$$\hat{H}^{\rm A} = \underbrace{\varepsilon_s \sum_\sigma \hat{n}_{s\sigma}}_{\hat{H}_{\rm bath}} \underbrace{-t \sum_\sigma \left(c^\dagger_{d\sigma} c_{s\sigma} + c^\dagger_{s\sigma} c_{d\sigma} \right)}_{\hat{H}_{\rm hyb}} + \underbrace{\varepsilon_d \sum_\sigma \hat{n}_{d\sigma} + U \hat{n}_{d\uparrow} \hat{n}_{d\downarrow}}_{\hat{H}_{\rm loc}} .$$

Next, we write the partition function Z as a perturbation series in the hybridization. To this end, we define $\hat{H}_0 = \hat{H}_{\rm bath} + \hat{H}_{\rm loc}$ and rewrite the partition function as

$$Z = {\rm Tr} \left(e^{-\beta(\hat{H}_0 - \mu \hat{N})} \hat{V}(\beta) \right)$$

where the operator $\hat{V}(\beta)$ is given by

$$\hat{V}(\beta) = e^{\beta(\hat{H}_0 - \mu\hat{N})} e^{-\beta(\hat{H}_0 + \hat{H}_{\rm hyb} - \mu\hat{N})} = \sum_m \underbrace{\int_0^\beta d\tau_1 \cdots \int_{\tau_{m-1}}^\beta d\tau_m}_{\int d\boldsymbol{\tau}^m} \underbrace{(-1)^m \prod_{l=m}^1 \hat{H}_{\rm hyb}(\tau_l)}_{\hat{O}^m(\boldsymbol{\tau})},$$

and

$$\hat{H}_{\rm hyb}(\tau_l) = e^{\tau_l(\hat{H}_0 - \mu\hat{N})} \hat{H}_{\rm hyb} e^{-\tau_l(\hat{H}_0 - \mu\hat{N})} = -t \sum_\sigma \left(c^\dagger_{d\sigma_l}(\tau_l) c_{s\sigma_l}(\tau_l) + c^\dagger_{s\sigma_l}(\tau_l) c_{d\sigma_l}(\tau_l) \right).$$

In this expansion, the only terms that contribute to the trace are even order ones ($m = 2k$) and they are products of impurity (d) and bath (s) creator-annihilator pairs. We can thus rewrite

$$\int d\boldsymbol{\tau}^{2k} \longrightarrow \int d\boldsymbol{\tau}^k \int d\bar{\boldsymbol{\tau}}^k \qquad\qquad \hat{O}^{2k}(\boldsymbol{\tau}) \longrightarrow \sum_{\boldsymbol{\sigma},\bar{\boldsymbol{\sigma}}} \hat{O}^{2k}_{\boldsymbol{\sigma},\bar{\boldsymbol{\sigma}}}(\boldsymbol{\tau}, \bar{\boldsymbol{\tau}})$$

where

$$\hat{O}^{2k}_{\boldsymbol{\sigma},\bar{\boldsymbol{\sigma}}}(\boldsymbol{\tau}, \bar{\boldsymbol{\tau}}) = (t)^{2k} \prod_{i=1}^k \left(c^\dagger_{d\bar{\sigma}_i}(\bar{\tau}_i) c_{s\bar{\sigma}_i}(\bar{\tau}_i) c^\dagger_{s\sigma_i}(\tau_i) c_{d\sigma_i}(\tau_i) \right).$$

The vector $\boldsymbol{\sigma} = (\sigma_1, \sigma_2, ..., \sigma_k)$ gives the spins $\{\sigma_i\}$ associated with the k impurity annihilators at imaginary times $\{\tau_i\}$, while $\bar{\boldsymbol{\sigma}} = (\bar{\sigma}_1, \bar{\sigma}_2, ..., \bar{\sigma}_k)$ gives the spins $\{\bar{\sigma}_i\}$ associated with the k impurity creators at imaginary times $\{\bar{\tau}_i\}$. It follows that the local and bath traces can be

decoupled and the partition function can be rewritten as

$$\frac{Z}{Z_{\rm bath}} = \sum_k \int^k d\boldsymbol{\tau} \int^k d\bar{\boldsymbol{\tau}} \sum_{\boldsymbol{\sigma},\bar{\boldsymbol{\sigma}}} d^k_{\bar{\boldsymbol{\sigma}},\boldsymbol{\sigma}}(\boldsymbol{\tau},\bar{\boldsymbol{\tau}}) t^k_{\boldsymbol{\sigma},\bar{\boldsymbol{\sigma}}}(\boldsymbol{\tau},\bar{\boldsymbol{\tau}})$$

$$d^k_{\bar{\boldsymbol{\sigma}},\boldsymbol{\sigma}}(\boldsymbol{\tau},\bar{\boldsymbol{\tau}}) = (t)^{2k}\ {\rm Tr}_{\rm bath}\left(e^{-\beta(\hat{H}_{\rm bath}-\mu\hat{N}_s)}\mathcal{T}\Pi^1_{i=k} c^\dagger_{s\sigma_i}(\tau_i) c_{s\bar{\sigma}_i}(\bar{\tau}_i)\right)/Z_{\rm bath}$$

$$t^k_{\boldsymbol{\sigma},\bar{\boldsymbol{\sigma}}}(\boldsymbol{\tau},\bar{\boldsymbol{\tau}}) = {\rm Tr}_{\rm loc}\left(e^{-\beta(\hat{H}_{\rm loc}-\mu\hat{N}_d)}\mathcal{T}\Pi^1_{i=k} c_{d\sigma_i}(\tau_i) c^\dagger_{d\bar{\sigma}_i}(\bar{\tau}_i)\right),$$

where $Z_{\rm bath} = 1 + 2e^{-\beta(\varepsilon_s-\mu)} + e^{-2\beta(\varepsilon_s-\mu)}$ and

$$c_{d\sigma}(\tau) = e^{\tau(\hat{H}_{\rm loc}-\mu\hat{N}_d)} c_{d\sigma} e^{-\tau(\hat{H}_{\rm loc}-\mu\hat{N}_d)}, \qquad c_{s\sigma}(\tau) = e^{\tau(\hat{H}_{\rm bath}-\mu\hat{N}_s)} c_{s\sigma} e^{-\tau(\hat{H}_{\rm bath}-\mu\hat{N}_s)}.$$

The trace involving only bath operators is simple to calculate, since $\hat{H}_{\rm bath}$ describes an independent-electron problem, for which Wick's theorem holds. It is given by the determinant

$$d^k_{\bar{\boldsymbol{\sigma}},\boldsymbol{\sigma}}(\boldsymbol{\tau},\bar{\boldsymbol{\tau}}) = \det\left(\mathcal{F}^k_{\bar{\boldsymbol{\sigma}},\boldsymbol{\sigma}}(\boldsymbol{\tau},\bar{\boldsymbol{\tau}})\right)$$

of the $k\times k$ non-interacting hybridization-function matrix, with elements

$$\left(\mathcal{F}^k_{\bar{\boldsymbol{\sigma}},\boldsymbol{\sigma}}(\boldsymbol{\tau},\bar{\boldsymbol{\tau}})\right)_{i',i} = \mathcal{F}^0_{\bar{\sigma}_{i'},\sigma_i}(\bar{\tau}_{i'}-\tau_i)$$

where

$$\mathcal{F}^0_{\bar{\sigma},\sigma}(\tau) = \delta_{\bar{\sigma},\sigma}\frac{t^2}{1+e^{-\beta(\varepsilon_s-\mu)}} \times \begin{cases} -e^{-\tau(\varepsilon_s-\mu)} & \tau > 0, \\ +e^{-(\beta+\tau)(\varepsilon_s-\mu)} & \tau < 0. \end{cases}$$

This is the imaginary time Fourier transform of the hybridization function introduced previously

$$\mathcal{F}^0_{\bar{\sigma},\sigma}(i\nu_n) = \frac{t^2}{i\nu_n - (\varepsilon_s-\mu)}\,\delta_{\bar{\sigma},\sigma}.$$

The calculation of the local trace is in general more complicated. In the case discussed here, the Hamiltonian does not flip spins. Thus only terms with an equal number of creation and annihilation operators *per spin* contribute to the local trace, and we can express the partition function in expansion orders per spin, k_σ. This yields [10]

$$\frac{Z}{Z_{\rm bath}} = \left(\prod_\sigma \sum_{k_\sigma=0}^\infty \int^{k_\sigma} d\boldsymbol{\tau}_\sigma \int^{k_\sigma} d\bar{\boldsymbol{\tau}}_\sigma\right) d^k_{\bar{\boldsymbol{\sigma}},\boldsymbol{\sigma}}(\boldsymbol{\tau},\bar{\boldsymbol{\tau}}) t^k_{\boldsymbol{\sigma},\bar{\boldsymbol{\sigma}}}(\boldsymbol{\tau},\bar{\boldsymbol{\tau}})$$

where the vectors $\boldsymbol{\sigma} = (\boldsymbol{\sigma}_\uparrow, \boldsymbol{\sigma}_\downarrow)$ and $\bar{\boldsymbol{\sigma}} = (\bar{\boldsymbol{\sigma}}_\uparrow, \bar{\boldsymbol{\sigma}}_\downarrow)$ have $(k_\uparrow, k_\downarrow)$ components, and for each k_σ component $\sigma_i = \bar{\sigma}_i = \sigma$. Thus

$$t^k_{\boldsymbol{\sigma},\bar{\boldsymbol{\sigma}}}(\boldsymbol{\tau},\bar{\boldsymbol{\tau}}) = {\rm Tr}_{\rm loc}\left(e^{-\beta(\hat{H}_{\rm loc}-\mu\hat{N}_d)}\,\mathcal{T}\prod\nolimits_\sigma \prod\nolimits^1_{i=k_\sigma} c_{d\sigma}(\tau_{\sigma_i}) c^\dagger_{d\sigma}(\bar{\tau}_{\bar{\sigma}_i})\right).$$

The latter can be calculated analytically. To do this, first we parametrize all configurations for a given spin via a timeline $[0,\beta)$ plus a number of creator/annihilator pairs which define segments

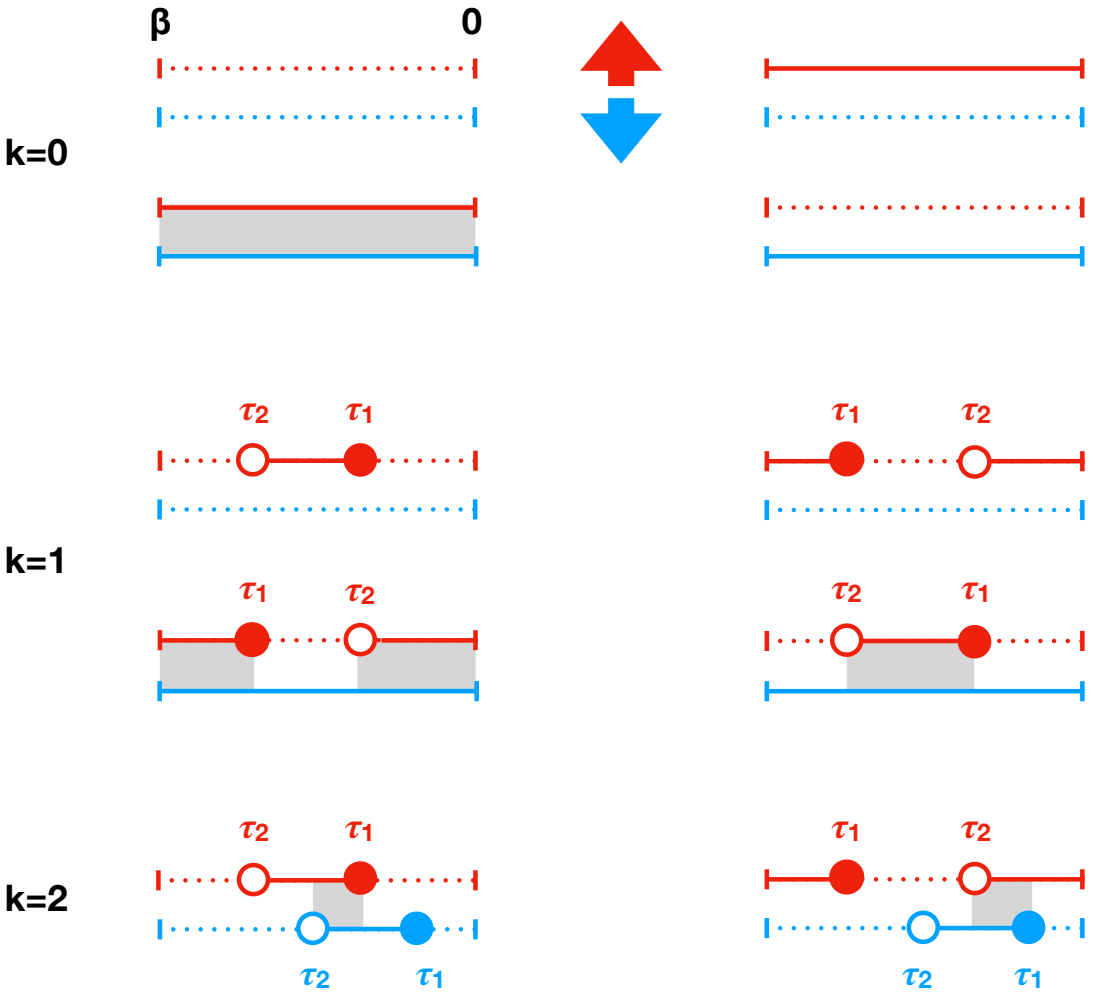

Fig. 3: *Representative configurations contributing to the local trace at zeroth, first and second order. The timelines for spin up are red and those for spin down are blue. The filled circles correspond to the insertion of a creator (time τ_1), and the empty circles to the insertion of an annihilator (time τ_2). Dotted lines represent the vacuum state for a given spin, full lines the occupied state. The grey boxes indicate the regions in which $l_{\uparrow,\downarrow} \neq 0$.*

on the timeline. At zeroth order two possible configurations exist per spin, an empty timeline, which corresponds to the vacuum state $|0\rangle$, and a full timeline, which corresponds to the state $c^\dagger_{d\sigma}|0\rangle$. A given configuration yields at order $k = k_\uparrow + k_\downarrow$

$$t^k_{\sigma,\bar{\sigma}}(\boldsymbol{\tau},\bar{\boldsymbol{\tau}}) = \left(\prod_\sigma s^{k_\sigma}_\sigma\right) e^{-\sum_{\sigma\sigma'}((\varepsilon_d-\mu)\delta_{\sigma\sigma'}+\frac{U}{2}(1-\delta_{\sigma,\sigma'}))l_{\sigma,\sigma'}}$$

where $l_{\sigma,\sigma'}$ is the length of the overlap of the τ segments for spins σ and σ', respectively, while $s_\sigma = \mathrm{sign}(\tau_{\sigma_1} - \bar{\tau}_{\sigma_1})$ is the fermionic sign. Possible configurations at order $k = 0, 1, 2$ are shown in Fig. 3. At order $k = 0$, summing up the contribution of the four configurations shown in Fig. 3 yields the local partition function $Z_{\mathrm{loc}} = 1 + 2e^{-\beta(\varepsilon_d-\mu)} + e^{-\beta(2(\varepsilon_d-\mu)+U)}$. Order $k = 1$

is already more complicated. The bath trace in this case is

$$d^1_{\bar\sigma\sigma}(\tau_1,\tau_2) = \mathcal{F}^0_{\bar\sigma\sigma}(\tau_1,\tau_2) = -\frac{t^2}{2}\delta_{\sigma,\bar\sigma}\ \mathrm{sign}(\tau_1-\tau_2).$$

The local trace is instead given by

$$t^1_{\sigma\bar\sigma}(\tau_2,\tau_1) = \mathrm{Tr}_{\rm loc}\Big(e^{-\beta(\hat H_{\rm loc}-\mu\hat N_d)}\mathcal{T}c_{d\sigma}(\tau_2)c^\dagger_{d\sigma}(\tau_1)\Big). \tag{7}$$

We can now calculate the contribution at half filling of the four $k=1$ configurations shown in Fig. 3. In the case $k_\uparrow = 1$ and $k_\downarrow = 0$ we have

$$t^1_{\uparrow\uparrow}(\tau_2,\tau_1) = \begin{cases} e^{-(\tau_2-\tau_1)(\varepsilon_d-\mu)} & = e^{+\tau_{21}U/2} \\ -e^{-\beta(2(\varepsilon_d-\mu)+U)+(\tau_1-\tau_2)(\varepsilon_d-\mu+U)} & = -e^{-\tau_{21}U/2} \\ -e^{-(\beta-(\tau_1-\tau_2))(\varepsilon_d-\mu)} & = -e^{(\beta+\tau_{21})U/2} \\ e^{-(\tau_2-\tau_1)(\varepsilon_d-\mu+U)-\beta(\varepsilon_d-\mu)} & = e^{(\beta-\tau_{21})U/2} \end{cases}$$

where $\tau_{21} = \tau_2 - \tau_1$ and $\mu = \varepsilon_d + U/2$. Similar results can be obtained for $k_\uparrow = 0$ and $k_\downarrow = 1$. Summing up all terms up to order one we find

$$\begin{aligned}\frac{Z}{Z_{\rm bath}} &\sim Z_{\rm loc} + \sum_\sigma \int_0^\beta d\tau_2 \int_0^\beta d\tau_1\, d^1_{\sigma\sigma}(\tau_1,\tau_2)t^1_{\sigma\sigma}(\tau_2,\tau_1) \\ &\sim Z_{\rm loc}\left(1 - \frac{1-e^{\frac{\beta U}{2}}}{1+e^{\frac{\beta U}{2}}}\frac{2t^2}{U}\beta\right).\end{aligned}$$

The exact formula of the partition function can be obtained from the eigenvalues and eigenvectors in the Appendix A.2; its Taylor expansion in powers of t/U yields, at second order, the expression above. Eq. (7) shows in addition that, for $k=1$, the local trace is proportional to the local Green function, $G^\sigma_{d,d}(\tau)$. Indeed, $G^\sigma_{d,d}(\tau)$ can be calculated using the configurations just described—provided that we start from $k=1$ and we divide by the hybridization function. More specifically, for $k=1$ and $\tau > 0$ we have

$$G^\sigma_{d,d}(\tau) \sim -\frac{1}{\beta}\int_0^\beta\int_0^\beta \underbrace{d\tau_2 d\tau_1\ d^1_{\sigma\sigma}(\tau_1,\tau_2)t^1_{\sigma\sigma}(\tau_2,\tau_1)}_{w^1}\ \delta\big(\tau-(\tau_2-\tau_1)\big)\ \frac{1}{\mathcal{F}^0_{\sigma\sigma}(\tau_1-\tau_2)}.$$

Taking all k values into account, the partition function can be expressed as the sum over all configurations $\{c\}$, i.e., in short

$$Z = \sum_c w_c = \sum_c |w_c|\ \mathrm{sign}\ w_c.$$

In a compact form, we can write $w_c = d\boldsymbol{\tau}_c\ d_c\ t_c$ where $d\boldsymbol{\tau}_c = \prod_\sigma \prod_i^{k_\sigma} d\tau_{\sigma_i} d\bar\tau_{\bar\sigma_i}$, and d_c and t_c are the bath and local traces for the configuration c. This expression of the partition function

shows that we can interpret $|w_c|$ as the sampling weight of configuration c. A generic observable $\hat{O}$ can then be obtained as the Monte Carlo average on a finite number of configurations N_c

$$\langle \hat{O} \rangle = \frac{\sum_c \langle \hat{O} \rangle_c |w_c| \,\mathrm{sign}\, w_c}{\sum_c |w_c| \,\mathrm{sign}\, w_c} = \frac{\sum_c \mathrm{sign}\, w_c \langle \hat{O} \rangle_c \, |w_c| / \sum_c |w_c|}{\sum_c \mathrm{sign}\, w_c \, |w_c| / \sum_c |w_c|} \approx \frac{\frac{1}{N_c} \sum_c^{N_c} \langle \hat{O} \rangle_c \mathrm{sign}\, w_c}{\frac{1}{N_c} \sum_c \mathrm{sign}\, w_c}.$$

The term $\frac{1}{N_c} \sum_c \mathrm{sign}\, w_c$ in the denominator is the average fermionic sign. When this is small, much longer runs are required to obtain data of the same quality; eventually the computational time can become so long that the calculation is in practice impossible—in these cases we have a sign problem. In practice, the QMC simulation starts from a random configuration c. Next we propose an update $c \to c'$. Within the Metropolis algorithm, the acceptance ratio is

$$R_{c \to c'} = \min\left(1, \frac{p_{c' \to c}}{p_{c \to c'}} \frac{|w_{c'}|}{|w_c|}\right)$$

where $p_{c \to c'}$ is the proposal probability for the update $c \to c'$. In the approach described here, known as *segment solver*, the basic updates are addition and removal of segments, antisegments (segments winding over the borders of the timeline, see Fig. 3), or complete lines. As example, let us consider the insertion of a segment for spin σ. A segment is made by a creator and an annihilator. The creator is inserted at time $\tau_{\rm in}$; the move is rejected if $\tau_{\rm in}$ is in a region where a segment exists. If created, the segment can have at most length $l_{\rm max}$, given by the distance between $\tau_{\rm in}$ and the time at which the next creator is, hence

$$p_{c \to c'} = \frac{d\bar{\tau}}{\beta} \frac{d\tau}{l_{\rm max}} \,.$$

The proposal probability of the reverse move (removing a segment) is instead given by the inverse of the number of existing segments

$$p_{c' \to c} = \frac{1}{k_\sigma + 1}$$

The acceptance ratio for the insertion of a segment becomes then

$$R_{c \to c'} = \min\left(1, \frac{\beta l_{max}}{k_\sigma + 1} \left| \frac{d_{c'}}{d_c} \frac{t_{c'}}{t_c} \right| \right).$$

For the impurity Green function, here the most important observable, the direct average yields

$$\langle \hat{O} \rangle_c = \langle G^\sigma_{d,d} \rangle_c = \sum_{\sigma'} \sum_{i=1}^{k_\sigma} \sum_{j=1}^{k_\sigma} \Delta(\tau, \tau_{\sigma' j} - \bar{\tau}_{\sigma' j}) \left(M^{k'_\sigma}\right)_{\sigma' j, \sigma' i} \delta_{\sigma, \sigma_{\sigma' j}} \delta_{\sigma, \bar{\sigma}_{\sigma' i}}$$

where $M^k = \left(\mathcal{F}^k\right)^{-1}$ is the inverse of the hybridization matrix and

$$\Delta(\tau, \tau') = -\frac{1}{\beta} \begin{cases} \delta(\tau - \tau') & \tau' > 0 \\ -\delta(\tau - (\tau' + \beta)) & \tau' < 0 \end{cases} .$$

2.4 DMFT for the one-band Hubbard model

The Hubbard Hamiltonian (3) is in principle the simplest model for the description of the Mott metal-insulator transition. In the tight-binding approximation it becomes

$$\hat{H} = \varepsilon_d \sum_{\sigma i} \hat{n}_{i\sigma} - t \sum_{\sigma \langle ii' \rangle} c^\dagger_{i\sigma} c_{i'\sigma} + U \sum_i \hat{n}_{i\uparrow} \hat{n}_{i\downarrow}, \tag{8}$$

where $\langle ii' \rangle$ is a sum over first neighbors. As discussed in the introduction, for $U = 0$, at half-filling, this Hamiltonian describes a metallic band. For $t = 0$ it describes an insulating collection of disconnected atoms. Somewhere in between, at a critical value of t/U, a metal to insulator transition must occur. In this section we will discuss the DMFT solution of (8) and the picture of the metal-insulator transition emerging from it. The first step consists in mapping the original many-body Hamiltonian into an effective quantum-impurity model, such as the Anderson Hamiltonian

$$\hat{H}^A = \underbrace{\sum_{\boldsymbol{k}\sigma} \varepsilon^s_{\boldsymbol{k}} \hat{n}_{\boldsymbol{k}\sigma}}_{\hat{H}_{\rm bath}} + \underbrace{\sum_{\boldsymbol{k}\sigma} \left(V^s_{\boldsymbol{k}} c^\dagger_{\boldsymbol{k}\sigma} c_{d\sigma} + \text{h.c.} \right)}_{\hat{H}_{\rm hyb}} + \underbrace{\varepsilon_d \sum_\sigma \hat{n}_{d\sigma} + U \hat{n}_{d\uparrow} \hat{n}_{d\downarrow}}_{\hat{H}_{\rm imp}}.$$

In this model the on-site Coulomb repulsion U appears only in the impurity Hamiltonian, $\hat{H}_{\rm imp}$, while the terms $\hat{H}_{\rm bath}$ and $\hat{H}_{\rm hyb}$, describe, respectively, the bath and the bath-impurity hybridization. In the next step, the quantum-impurity model is solved. Differently from the case of the Anderson molecule, this cannot be done analytically. It requires non-perturbative numerical methods, such as exact diagonalization, the numerical renormalization group, or QMC. Here we describe the DMFT self-consistency loop for a QMC quantum-impurity solver. Solving the quantum-impurity model yields the impurity Green function $G^\sigma_{d,d}(i\nu_n)$. From the impurity Dyson equation we can calculate the impurity self-energy

$$\Sigma^\sigma_A(i\nu_n) = \left(G^{0\sigma}_{d,d}(i\nu_n) \right)^{-1} - \left(G^\sigma_{d,d}(i\nu_n) \right)^{-1}.$$

Next, we adopt the local approximation, i.e., we assume that the self-energy of the Hubbard model equals the impurity self-energy. Then, the local Green function is given by

$$G^\sigma_{i_c,i_c}(i\nu_n) = \frac{1}{N_{\boldsymbol{k}}} \sum_{\boldsymbol{k}} \frac{1}{i\nu_n + \mu - \varepsilon_{\boldsymbol{k}} - \Sigma^\sigma_A(i\nu_n)},$$

where $N_{\boldsymbol{k}}$ is the number of $\boldsymbol{k}$ points. The local Dyson equation is used once more, this time to calculate the bath Green function $\mathcal{G}^\sigma(i\nu_n)$, which in turn defines a new quantum-impurity model. This procedure is repeated until self-consistency is reached, i.e., the number of electrons is correct and the self-energy does not change anymore (within a given numerical accuracy). In this situation we have

$$G^\sigma_{i_c,i_c}(i\nu_n) \sim G^\sigma_{d,d}(i\nu_n).$$

It is important to underline that self-consistency is key to the success of DMFT in describing the metal-to-insulator transition. This can, perhaps, be best understood looking at the effects of

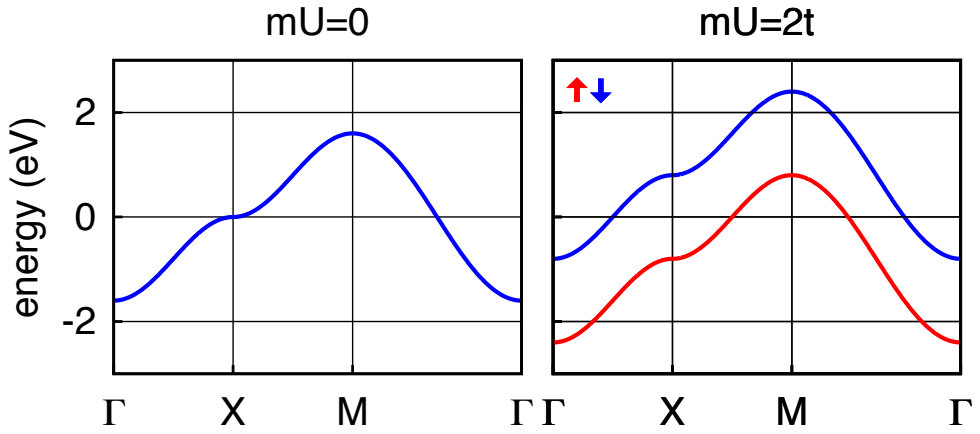

Fig. 4: *The metal-insulator transition in ferromagnetic Hartree-Fock. The calculation is for a square lattice tight-binding model with dispersion* $\varepsilon_{\boldsymbol{k}} = -2t(\cos k_x + \cos k_y)$.

self-consistency in a simpler approach, the static mean-field Hartree-Fock method.[6] The latter consists in replacing the Coulomb interaction with the one-electron operator

$$U\hat{n}_{i\uparrow}\hat{n}_{i\downarrow} \to U(\hat{n}_{i\uparrow}\bar{n}_{i\downarrow} + \bar{n}_{i\uparrow}\hat{n}_{i\downarrow} - \bar{n}_{i\uparrow}\bar{n}_{i\downarrow}),$$

where $\bar{n}_{i\sigma}$ is the expectation value of $\hat{n}_{i\sigma}$. Choosing the same primitive cell as in dynamical mean-field theory ($\bar{n}_{i\sigma} = \bar{n}_\sigma$), the Hartree-Fock self-energy matrix is given by

$$\Sigma^\sigma_{i,i'}(i\nu_n) = U\Big(\frac{n}{2} - \sigma m\Big)\delta_{i,i'},$$

where $\sigma = +1$ for spin up and $\sigma = -1$ for spin down and $m = (\bar{n}_\uparrow - \bar{n}_\downarrow)/2$. The approximation is then identical to replacing the Hubbard Hamiltonian with

$$\hat{H}_{\rm HF} = \sum_{\boldsymbol{k}\sigma}\left[\varepsilon_{\boldsymbol{k}} + U\left(\frac{1}{2} - \sigma m\right)\right]\hat{n}_{\boldsymbol{k}\sigma}. \tag{9}$$

This shows that $h_{\rm eff} = 2Um$ plays the role of an effective magnetic field (Weiss field). The self-consistency criterion is

$$\bar{n}_\sigma = \bar{n}_{i\sigma} = \langle\hat{n}_{i\sigma}\rangle_{\rm HF},$$

where the expectation value $\langle\hat{n}_{i\sigma}\rangle_{\rm HF}$ is calculated using the Hamiltonian $\hat{H}_{\rm HF}$, which in turn depends on $\bar{n}_\sigma$ via m. This gives the self-consistency equation

$$m = \frac{1}{2}\frac{1}{N_{\boldsymbol{k}}}\sum_{\boldsymbol{k}\sigma}\frac{\sigma e^{-\beta(\varepsilon_{\boldsymbol{k}}+U(\frac{1}{2}-\sigma m)-\mu)}}{1+e^{-\beta(\varepsilon_{\boldsymbol{k}}+U(\frac{1}{2}-\sigma m)-\mu)}}.$$

If we set $m = 0$ the equation is satisfied; for such a trivial solution the static mean-field correction in Eq. (9) merely redefines the chemical potential and has therefore no effect. For sufficiently large U, however, a non-trivial solution ($m \neq 0$) can be found. If $m \neq 0$ the spin up and spin down bands split, and eventually a gap can open. This is shown in Fig. 4. The static mean-field correction in Eq. (9) equals the contribution of the Hartree diagram to the self-energy, $\Sigma^\sigma_{\rm H}(i\nu_n) = U\bar{n}_{-\sigma}$. In many-body perturbation theory, however, $\bar{n}_\sigma = 1/2$, i.e., $m = 0$.

[6] Keeping in mind that many self-consistent solutions obtained with the Hartree-Fock method are spurious.

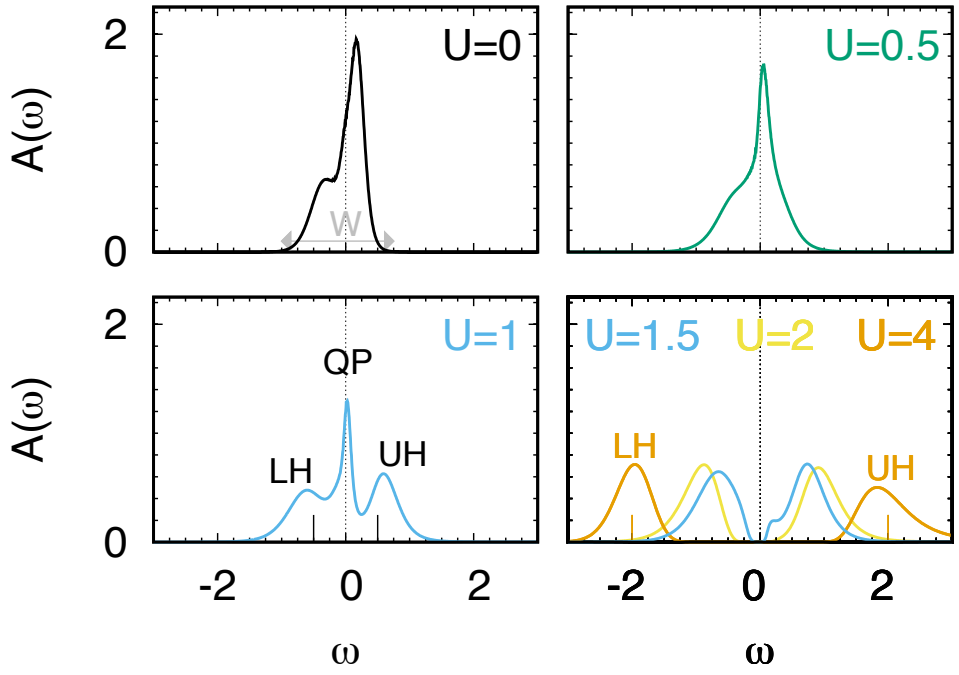

Fig. 5: *$VOMoO_4$: LDA+DMFT spectral function at finite temperature for $0 \leq U \leq 4$. Energies are in eV and spectral functions in states/spin/eV. The calculations have been done using a continuous-time hybridization-expansion QMC solver [10]. A detailed LDA+DMFT study of the electronic and magnetic properties $VOMoO_4$ can be found in Ref. [11].*

In the self-consistent static mean-field approximation, instead, m can differ from zero, and a phenomenon not described by the mere Hartree diagram can be captured, ferromagnetism in a correlated metal. If mU is larger than the bandwidth, the system can even become an insulator. In DMFT the role of the Weiss field is played by the bath Green function $\mathcal{G}^{\sigma}_{i,i}(i\nu_n)$. The emerging picture of the Mott transition is described in Fig. 5 for a representative single-band material. In the $U = 0$ limit, the spectral function $A_0(\omega)$ is metallic at half filling (top left panel). For finite U, if we set $\Sigma^{\sigma}_A(\omega) = 0$ as initial guess, the DMFT self-consistency loop starts with $A(\omega) = A_0(\omega)$. For small U/t, the *converged* spectral function $A(\omega)$ is still similar to $A_0(\omega)$. This can be seen comparing the $U = 0.5$ and $U = 0$ panels in Fig. 5. Further increasing U/t, sizable spectral weight is transferred from the zero-energy quasi-particle peak to the lower (LH) and upper (UH) Hubbard bands, centered at $\omega \sim \pm U/2$. This can be observed in the $U = 1$ panel of Fig. 5. The system is still metallic, but with strongly renormalized masses and short lifetimes, reflected in the narrow quasi-particle (QP) peak. Finally, for U larger than a critical value ($U \geq 1.5$ in the figure) a gap opens and the system becomes a Mott insulator. When this happens the self-energy diverges at low frequency, where

$$\Sigma^{\sigma}_A(\omega+i0^+) \sim \frac{U}{2} + \frac{A}{\omega + i0^+}.$$

In the large U/t limit the gap increases linearly with the Coulomb repulsion, i.e., $E_g(1) \sim U - W$, where W is the bandwidth.

2.5 DMFT for multi-orbital models

The multi-orbital Hubbard-like Hamiltonian has the form

$$\hat{H} = \hat{H}_0 + \hat{H}_U$$
$$\hat{H}_0 = -\sum_{ii'}\sum_{\sigma}\sum_{mm'} t^{i,i'}_{m\sigma,m'\sigma'}\, c^{\dagger}_{im\sigma} c_{i'm'\sigma'}$$
$$\hat{H}_U = \frac{1}{2}\sum_{i}\sum_{\sigma\sigma'}\sum_{mm'}\sum_{pp'} U_{mpm'p'}\, c^{\dagger}_{im\sigma} c^{\dagger}_{ip\sigma'} c_{ip'\sigma'} c_{im'\sigma},$$

where m, m' and p, p' are different orbitals and the Coulomb tensor is local. The DMFT approach can be extended to solve models of this form, mapping them to multi-orbital quantum-impurity models. The main changes with respect to the formalism introduced in the previous section are then the following

$$\varepsilon_{\boldsymbol{k}} \to (H_{\boldsymbol{k}})_{m\sigma,m'\sigma'} \qquad (i\nu_n + \mu) \to (i\nu_n + \mu)\,\hat{1}_{m\sigma,m'\sigma'}$$
$$t^{i,i'} \to t^{i,i'}_{m\sigma,m'\sigma'} \qquad \varepsilon_d \to \varepsilon^{i,i'}_{m\sigma,m'\sigma'} = -t^{i,i}_{m\sigma,m'\sigma'}$$

where $\hat{1}$ is the identity matrix. As a consequence, the local Green function, the bath Green function, the hybridization function and the self-energy also become matrices

$$\mathcal{G}^{\sigma}(i\nu_n) \to \mathcal{G}^{\sigma,\sigma'}_{m,m'}(i\nu_n) \qquad G^{\sigma}(i\nu_n) \to G^{\sigma,\sigma'}_{m,m'}(i\nu_n) \qquad \Sigma^{\sigma}(i\nu_n) \to \Sigma^{\sigma,\sigma'}_{m,m'}(i\nu_n).$$

The corresponding generalization of the self-consistency loop is shown schematically in Fig. 6. Although the extension of DMFT to Hubbard models with many orbitals might appear straightforward, in practice it is not. The bottleneck is the solution of the generalized multi-orbital quantum-impurity problem. The most flexible solvers available so far are all based on QMC. Despite being flexible, QMC-based approaches have limitations. These can be classified in two types. First, with increasing the number of degrees of freedom, calculations become very quickly computationally too expensive—how quickly depends on the specific QMC algorithm used and the actual implementation. Thus, going beyond a rather small number of orbitals and reaching the zero-temperature limit is unfeasible in practice. The second type of limitation is more severe. Increasing the number of degrees of freedom leads, eventually, to the infamous sign problem; when this happens, QMC calculations cannot be performed at all. In order to deal with limitations of the first type, it is crucial to restrict QMC calculations to the essential degrees of freedom; furthermore, we should exploit symmetries, develop fast algorithms and use the power of massively parallel supercomputers to reduce the actual computational time. For the second type of problems not a lot can be done; nevertheless, it has been shown that a severe sign problem might appear earlier with some basis choices than with others [10]. Although eventually we cannot escape it, this suggests that the model set up can be used as a tool to expand the moderate sign-problem zone. For what concerns symmetries, in the paramagnetic case and in absence of spin-orbit interaction or external fields, an obvious symmetry to exploit

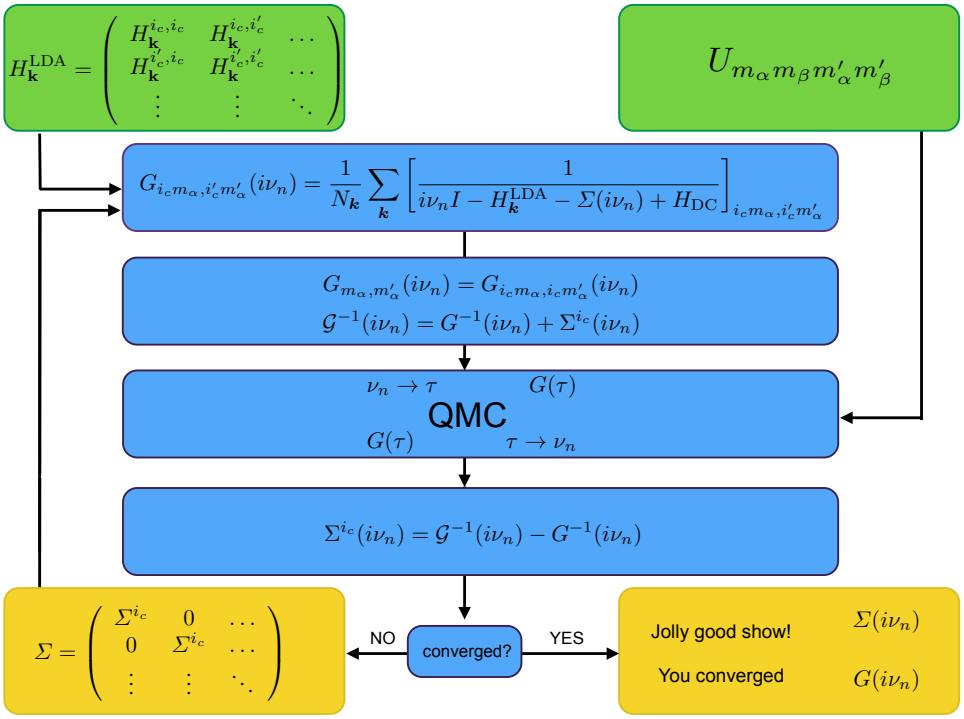

Fig. 6: *LDA+DMFT self-consistency loop. The one-electron Hamiltonian is built in the basis of Bloch states obtained from localized Wannier functions, for example in the local-density approximation (LDA); this gives* $H_{\boldsymbol{k}}^{\mathrm{LDA}}$*. The set* $\{i_c\}$ *labels the equivalent correlated sites inside the unit cell. The local Green-function matrix is at first calculated using an initial guess for the self-energy matrix. The bath Green-function matrix is then obtained via the Dyson equation and used to construct an effective quantum-impurity model. The latter is solved via a quantum-impurity solver, here quantum Monte Carlo (QMC). This yields the impurity Green-function matrix. Through the Dyson equation the self-energy is then obtained, and the procedure is repeated until self-consistency is reached.*

is the rotational invariance of spins, from which follows

$$X_{m,m'}^{\sigma,\sigma'}(i\nu_n) = \delta_{\sigma,\sigma'}\, X_{m,m'}(i\nu_n),$$

where $X = \mathcal{G}, G, \Sigma$. In addition, if we use a basis of real functions, the local Green-function matrices are real and symmetric in imaginary time τ, hence

$$X_{m,m'}^{\sigma,\sigma'}(i\nu_n) = \delta_{\sigma,\sigma'}\, X_{m,m'}(i\nu_n) = \delta_{\sigma,\sigma'}\, X_{m',m}(i\nu_n).$$

Finally, often the unit cell contains several equivalent correlated sites, indicated as $\{i_c\}$ in Fig. 6. In order to avoid expensive cluster calculations, we can use space-group symmetries to construct the matrices $\mathcal{G}, G, \Sigma$ at a given site i'_c from the corresponding matrices at an equivalent site, e.g., $i_c = 1$. Space-group symmetries also tell us if some matrix elements are zero. For example, for a model with only t_{2g} (or only e_g) states, in cubic symmetry, in the paramagnetic case and in absence of spin-orbit interaction or external fields, we have

$$X_{m,m'}^{\sigma,\sigma'}(i\nu_n) = \delta_{\sigma,\sigma'}\, X_{m,m}(i\nu_n)\, \delta_{m,m'}.$$

2.6 LDA+DMFT: Model building

How do we build realistic Hubbard-like models for correlated materials? The state-of-the art approach relies on constructing, for a given system, *materials-specific* Kohn-Sham Wannier functions $\phi^{\rm KS}_{im\sigma}(\boldsymbol{r})$. These can be obtained via electronic structure calculations based on density-functional theory [5–7], e.g., in the LDA approximation.[7] After we have built the complete one-electron basis, the first steps in model-building are those already described in the introduction. We recall here the essential points and then discuss the next stage. The many-body Hamiltonian can be expressed as $\hat{H} = \hat{H}_0 + \hat{H}_U - \hat{H}_{\rm DC}$, with

$$\hat{H}_0 = \hat{H}^{\rm LDA} = -\sum_{\sigma}\sum_{ii'}\sum_{mm'} t^{i,i'}_{m,m'} c^{\dagger}_{im\sigma} c_{i'm'\sigma},$$

$$\hat{H}_U = \frac{1}{2}\sum_{ii'jj'}\sum_{\sigma\sigma'}\sum_{mm'pp'} U^{iji'j'}_{mp\,m'p'} c^{\dagger}_{im\sigma} c^{\dagger}_{jp\sigma'} c_{j'p'\sigma'} c_{i'm'\sigma}.$$

The double-counting correction $\hat{H}_{\rm DC}$ arises from the fact that the hopping integrals are calculated replacing the electron-nuclei interaction $v_{\rm en}(\boldsymbol{r})$ with the self-consistent DFT reference potential

$$v_{\rm R}(\boldsymbol{r}) = v_{\rm en}(\boldsymbol{r}) + \underbrace{\int d\boldsymbol{r}'\, \frac{1}{|\boldsymbol{r}-\boldsymbol{r}'|}}_{v_{\rm H}(\boldsymbol{r})} + v_{\rm xc}(\boldsymbol{r}),$$

which includes the long-range Hartree term $v_{\rm H}(\boldsymbol{r})$ and the exchange-correlation contribution $v_{\rm xc}(\boldsymbol{r})$. To avoid to count these terms twice, we thus subtract from $\hat{H}_U$ the effects already included in $\hat{H}_0$

$$\hat{H}_U \to \Delta\hat{H}_U = \hat{H}_U - \hat{H}_{\rm DC}.$$

Unfortunately we do not know which important correlation effects are indeed included in $\hat{H}_0$ via $v_{\rm R}(\boldsymbol{r})$, and therefore the exact expression of $\Delta\hat{H}_U$ is also unknown. The remarkable successes of the LDA suggest, however, that in many materials the LDA is overall a good approximation, and therefore, in those systems at least, the term $\Delta\hat{H}_U$ can be completely neglected. What about strongly-correlated materials? Even in correlated systems, most likely the LDA works rather well for the delocalized electrons or in describing the average or the long-range Coulomb effects. Thus one can think of separating the electrons into *uncorrelated* and *correlated*; only for the latter we do take the correction $\Delta\hat{H}_U$ into account explicitly, assuming furthermore that $\Delta\hat{H}_U$ is local or almost local [5], since we know that it is the local term which is responsible for most non-trivial many-body effects. Typically, correlated electrons are those that partially retain their atomic character, e.g., those that originate from localized d and f shells; for convenience, here we assume that in a given system they stem from a single atomic shell l (e.g., d for

[7] Using GGA or similar functionals in place of LDA yields minor differences in the many-body Hamiltonian; instead, using LDA+U or similar approximations yields Hartree-Fock-like effects that would have to be subtracted via the double-counting correction.

transition-metal oxides or f for heavy-fermion systems) and label their states with the atomic quantum numbers l and $m = -l, \ldots, l$ of that shell. Thus

$$U^{iji'j'}_{mp\,m'p'} \sim \begin{cases} U^l_{mp\,m'p'} & iji'j' = iiii \quad \wedge \quad mp, m'p' \in l \\ 0 & iji'j' \neq iiii \quad \vee \quad mp, m'p' \notin l. \end{cases}$$

Within this approximation $\Delta\hat{H}_U$ is replaced by $\Delta\hat{H}^l_U = \hat{H}^l_U - \hat{H}^l_{\rm DC}$, where $\hat{H}^l_{\rm DC}$ is, e.g., given by the static mean-field contribution of $\hat{H}^l_U$. There is a drawback in this procedure, however. By splitting electrons into correlated and uncorrelated we implicitly assume that the main effect of the latter is the renormalization or *screening* of parameters for the former, in particular of the Coulomb interaction. The computation of screening effects remains, unfortunately, a challenge. The calculation of exact screening would require the solution of the original many-body problem, taking all degrees of freedom into account, an impossible task. Commonly-used approximate schemes are the constrained LDA approximation (cLDA) and the constrained random-phase approximation (RPA) [5–7]. Both methods give reasonable estimates of screened Coulomb parameters for DMFT calculations. Typically cRPA calculations include more screening channels and are performed for less localized bases than cLDA calculations; thus cRPA parameters turn out to be often smaller than cLDA ones. To some extent, the difference can be taken as an estimate of the error bar.

After we have selected the electrons for which we think it is necessary to include explicitly the Hubbard correction, we have to build the final Hamiltonian for DMFT calculations. To this end, it is often convenient to integrate out or *downfold*, in part or completely, the weakly correlated states. There are different degrees of downfolding. The two opposite extreme limits are (i) *no downfolding*, i.e., keep explicitly in the Hamiltonian all weakly-correlated states (ii) *massive downfolding*, i.e., downfold all weakly correlated states. If we perform massive downfolding, e.g., downfold to the d (or e_g or t_{2g}) bands at the Fermi level, the Hamiltonian relevant for DMFT takes a simpler form. The LDA part is limited to the selected orbitals or bands, which, in the ideal case, are decoupled from the rest

$$\hat{H}^{\rm LDA} = -\sum_{\sigma} \sum_{ii'} \sum_{m_\alpha m'_\alpha} t^{i,i'}_{m_\alpha, m'_\alpha}\, c^\dagger_{im_\alpha\sigma}\, c_{i'm'_\alpha\sigma}.$$

The local *screened* Coulomb interaction for this set of orbitals is the on-site tensor

$$\hat{H}^l_U = \frac{1}{2} \sum_{i} \sum_{\sigma\sigma'} \sum_{m_\alpha m'_\alpha} \sum_{m_\beta m'_\beta} U_{m_\alpha m_\beta m'_\alpha m'_\beta}\, c^\dagger_{im_\alpha\sigma} c^\dagger_{im_\beta\sigma'} c_{im'_\beta\sigma'} c_{im'_\alpha\sigma}.$$

It is important to point out that the level of downfolding does not modify the hardness of the quantum-impurity problem. If, for example, in studying a transition-metal oxide, we plan to treat only $3d$ bands as correlated, it does not matter if we perform calculations with a Hamiltonian containing also, e.g., O p states, or we rather downfold all states but the $3d$ and work with a set of Wannier basis spanning the $3d$-like bands only. The number of correlated orbitals in the quantum-impurity problem is the same.[8]

[8] The choice might influence how severe the QMC sign problem is, however.

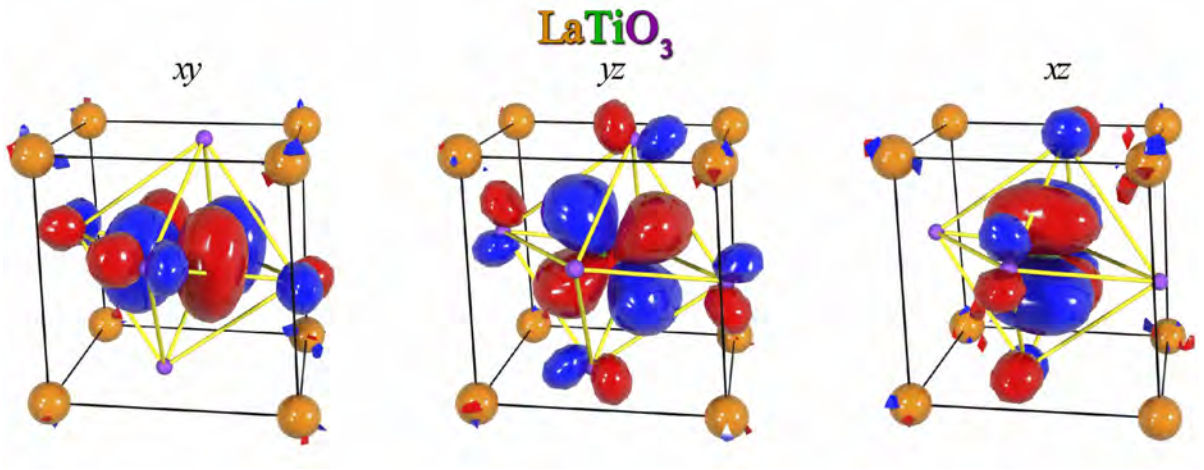

Fig. 7: *NMTO Wannier-like orbitals for t_{2g} states in $LaTiO_3$ obtained via massive downfolding to the t_{2g} bands. The t_{2g}-like orbitals have O p tails at the neighboring O sites reflecting the distortions of the lattice. The figure has been taken from Ref. [12].*

One advantage of massive downfolding is that the double-counting correction typically becomes a shift of the chemical potential, and it is therefore not necessary to calculate it explicitly. A second important advantage is that the interpretation of the final results is simpler. Instead, a disadvantage is that the basis functions are less localized, and therefore the approximation of the Coulomb interaction to a local operator might be less justified, and in some cases it might be necessary to include non-local Coulomb terms. The effect of downfolding on the localization of Wannier functions is illustrated for example in Fig. 7. Finally, another disadvantage of massive downfolding is that the energy window in which the model is valid is more narrow.

All advantages and disadvantages considered, what is then the best way of performing DMFT calculations? There is no universal answer to this question; it depends on the problem we are trying to solve and the system we are studying. Independently of the degree of downfolding we choose, it is important to point out that a clear advantage of Wannier functions in general is that they carry information about the lattice, bonding, chemistry, and distortions. This can be seen once more in Fig. 7, where orbitals are tilted and deformed by the actual structure and chemistry of the compound. Indeed, one might naively think of using an "universal" basis, for example atomic functions, the same for all systems, and thus calculating the hopping integrals using simply the electron-nuclear interaction $v_{en}(\boldsymbol{r})$. Besides the complications arising from the lack of orthogonality, such a basis has no built-in materials-specific information, except lattice positions. It is therefore a worse starting point for describing the electronic structure, even in the absence of correlations: larger basis sets are required to reach the same accuracy. From the point of view of LDA+DMFT, an advantage of an universal basis would be that it is free from double-counting corrections; on the other hand, however, exactly because we do not use the LDA potential and LDA orbitals to calculate the hopping integrals, we also cannot count on the successes of LDA in the description of average and long-range Coulomb effects. The hopping integrals would not even include the long-range Hartree term. For these

reasons *ab-initio* Wannier functions remain so far the basis of choice. They can be built via the Nth-Order Muffin-Tin Orbital (NMTO) method [12], the maximal-localization scheme [13], or projectors. Fig. 7 shows examples of NMTO-based Wannier functions. No matter what construction procedure is used, a common characteristic of *ab-initio* Wannier functions is that they are site-centered and localized.[9] A question naturally arises: How crucial is it to use localized functions as one-electron basis? This is an important point, since we have seen that strong-correlation effects arise in systems in which the on-site Coulomb interaction is much larger than longer-range terms. Let us consider therefore two opposite extreme limits. The first is the case in which the basis functions are independent of the lattice position (i.e., they are totally delocalized). For such a basis choice the Coulomb interaction parameters would be the same for every pair of lattice sites, no matter how distant. Thus a Hubbard-like model would be hard to justify. In the second extreme case, we adopt a hypothetical basis so localized that $\psi_{im\sigma}(\boldsymbol{r})\overline{\psi_{i'm'\sigma'}}(\boldsymbol{r}) \sim \delta_{i,i'}\,\delta(\boldsymbol{r}-\boldsymbol{T}_i)$. Even for such a basis choice, the unscreened Coulomb interaction is *not* local, but given by

$$U^{iji'j'}_{mp\,m'p'} \propto \frac{\delta_{i,i'}\delta_{j,j'}}{|\boldsymbol{T}_i-\boldsymbol{T}_j|},$$

hence it decays slowly with distance, although the (divergent) on-site term dominates. More generally, we can conclude that by increasing the localization of the basis we enhance the importance of the on-site Coulomb repulsion with respect to long-range terms; this better justifies Hubbard-like models—although we have to remember that most of the long-range part of the Coulomb interaction is in any case subtracted via the double-counting correction $\hat{H}_{\rm DC}$. The extreme case of the $\delta(\boldsymbol{r}-\boldsymbol{T}_i)$ functions also illustrates, however, how far we can go. A major problem with the extremely localized basis discussed above is that it would make it impossible to properly describe bonding, since the hopping integrals would be zero. Although such a basis is, of course, never used to build many-body models, there is a tempting approximation that has similar flaws. If one uses DFT-based electronic-structure techniques that tile the space in interstitial and non-overlapping atomic spheres (e.g., the LAPW method), it is tempting to use as basis for correlated electrons the atomic functions *defined inside the atomic spheres*. These functions are, by construction, much more localized than Wannier orbitals (even when no downfolding is performed in the Wannier construction). However, they *do not form a complete basis set* in the space of square-integrable functions. This is obvious because such a basis does not even span the LDA bands; to reproduce the bands we need, in addition, functions defined in the interstitial region. This is illustrated in Fig. 8 for a simple example of two quantum well potentials.[10] We therefore cannot use it to write the many-body Hamiltonian in the usual form $\hat{H}_0 + \hat{H}_U$. In conclusion, a basis which, as *ab-initio* Wannier functions, is complete and indeed spans the bands, is better justified, although we somewhat lose in localization.

[9] Differences in localizations between the various construction procedures are actually small for the purpose of many-body calculations, provided that the same bands are spanned in the same way.

[10] Another, but less severe, problem of atomic sphere truncations is that the results will depend on the sphere size, in particular when atomic spheres are small.

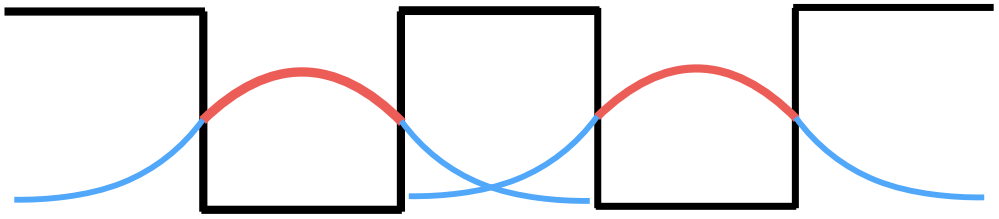

Fig. 8: *The problem of two quantum wells. The figure shows (schematically) for each well the wavefunction of a bound state. If we consider only the part of the wavefunction inside its own well (red in the figure), the differential overlap (and hence the hopping integral) between functions centered on different wells would be zero.*

3 Linear response functions

Linear response functions are key to understand many experimental results. In this section we explain how to calculate them within the LDA+DMFT approach. First we introduce the generalized susceptibility, which yields the linear response to a given external perturbation. Next we present the method used to calculate it and discuss the approximations adopted. Last we analyze in detail the case of the magnetic susceptibility for the one-band Hubbard model.

3.1 The generalized susceptibility

Let us start by introducing the site susceptibility in imaginary time. This is given by

$$\chi_{\hat{P}^i_\nu\,\hat{O}^{i'}_{\nu'}}(\boldsymbol{\tau}) = \left\langle \mathcal{T}\Delta\hat{P}^i_\nu(\tau_1,\tau_2)\Delta\hat{O}^{i'}_{\nu'}(\tau_3,\tau_4)\right\rangle_0, \tag{10}$$

where $\boldsymbol{\tau} = (\tau_1,\tau_2,\tau_3,\tau_4)$. The site operators are defined via the equations

$$\hat{P}^i_\nu(\tau_1,\tau_2) = \sum_{\boldsymbol{\alpha}} p^\nu_{\boldsymbol{\alpha}}\; c^\dagger_{i\alpha'}(\tau_2)c_{i\alpha}(\tau_1), \qquad \Delta\hat{P}^i_\nu(\tau_1,\tau_2) = \hat{P}^i_\nu(\tau_1,\tau_2) - \langle\hat{P}^i_\nu(\tau_1,\tau_2)\rangle$$
$$\hat{O}^{i'}_{\nu'}(\tau_3,\tau_4) = \sum_{\boldsymbol{\gamma}} o^{\nu'}_{\boldsymbol{\gamma}}\; c^\dagger_{i'\gamma'}(\tau_4)c_{i'\gamma}(\tau_3), \qquad \Delta\hat{O}^{i'}_{\nu'}(\tau_3,\tau_4) = \hat{O}^{i'}_{\nu'}(\tau_3,\tau_4) - \langle\hat{O}^{i'}_{\nu'}(\tau_3,\tau_4)\rangle.$$

The labels $\boldsymbol{\alpha} = (\alpha,\alpha')$, $\boldsymbol{\gamma} = (\gamma,\gamma')$ are collective flavors. For the multi-band Hubbard model they may include spin (σ) and orbital (m) quantum number, plus a fractional lattice vector identifying a correlated basis atom in the unit cell (i_c). The weight factors $o^\nu_{\boldsymbol{\alpha}}$ and $p^{\nu'}_{\boldsymbol{\gamma}}$, in general complex numbers, identify the type of response. We can then rewrite Eq. (10) as

$$\chi_{\hat{P}^i_\nu\,\hat{O}^{i'}_{\nu'}}(\boldsymbol{\tau}) = \sum_{\boldsymbol{\alpha\gamma}} p^\nu_{\boldsymbol{\alpha}} o^{\nu'}_{\boldsymbol{\gamma}}\; \chi_{i\boldsymbol{\alpha},i'\boldsymbol{\gamma}}(\boldsymbol{\tau}),$$

with

$$\chi_{i\boldsymbol{\alpha},i'\boldsymbol{\gamma}}(\boldsymbol{\tau}) = \left\langle \mathcal{T}c_{i\alpha}(\tau_1)c^\dagger_{i\alpha'}(\tau_2)c_{i'\gamma}(\tau_3)c^\dagger_{i'\gamma'}(\tau_4)\right\rangle - G_{i\alpha,i\alpha'}(\tau_1,\tau_2)G_{i'\gamma,i'\gamma'}(\tau_3,\tau_4). \tag{11}$$

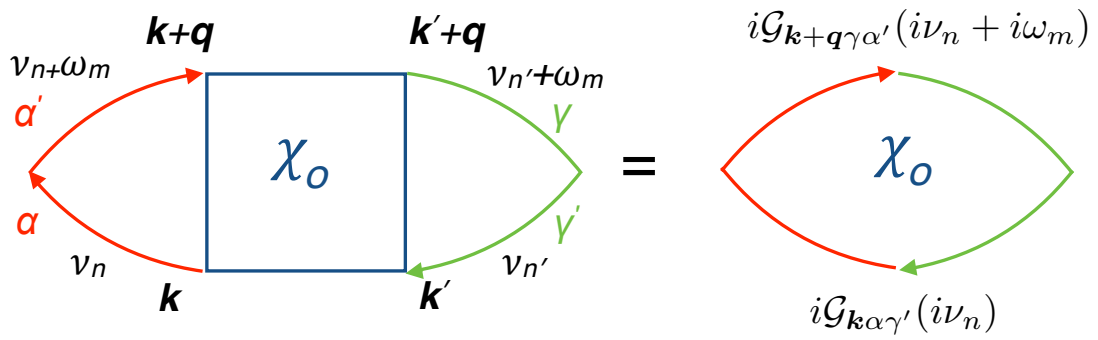

Fig. 9: *Diagram contributing to the linear susceptibility for a non-interacting system. The red lines indicates that the creator/annihilator is originally from the operator $\hat{P}_{\nu'}$ and the green lines indicate that the creator/annihilator is from the operator $\hat{O}_{\nu}$. The corresponding frequencies and momenta are explicitly assigned.*

Performing the Fourier transform from imaginary time to Matsubara frequencies we obtain

$$\chi_{i\boldsymbol{\alpha},i'\boldsymbol{\gamma}}(\boldsymbol{\nu}) = \frac{1}{16}\iiint d\boldsymbol{\tau}\; e^{i\boldsymbol{\nu}\cdot\boldsymbol{\tau}}\chi_{i\boldsymbol{\alpha},i'\boldsymbol{\gamma}}(\boldsymbol{\tau}), \tag{12}$$

where $\boldsymbol{\nu} = (\nu_1, -\nu_2, \nu_3, -\nu_4)$. Due to the conservation of energy, only three of the four ν_i frequencies are independent. Hence, for convenience we set $\nu_1 = \nu_n$, $\nu_2 = \nu_n + \omega_m$, $\nu_3 = \nu_{n'} + \omega_m$, and $\nu_4 = \nu_{n'}$. Next we perform the Fourier transform from site to momentum space. Due to the conservation of lattice momentum, only three of the four $\boldsymbol{k}_i$-vectors are independent. After redefining $\boldsymbol{k}_1 = \boldsymbol{k}$, $\boldsymbol{k}_2 = \boldsymbol{k}+\boldsymbol{q}$, $\boldsymbol{k}_3 = \boldsymbol{k}'+\boldsymbol{q}$ and $\boldsymbol{k}_4 = \boldsymbol{k}'$, we find the expression

$$\chi_{\hat{P}_\nu\,\hat{O}_{\nu'}}(\boldsymbol{q};\boldsymbol{\nu}) = \sum_{\boldsymbol{\alpha}\boldsymbol{\gamma}} p^{\nu}_{\boldsymbol{\alpha}} o^{\nu'}_{\boldsymbol{\gamma}} \sum_{ii'} e^{i(\boldsymbol{T}_i - \boldsymbol{T}_{i'})\cdot\boldsymbol{q}}\chi_{i\boldsymbol{\alpha},i'\boldsymbol{\gamma}}(\boldsymbol{\nu}) = \sum_{\boldsymbol{\alpha}\boldsymbol{\gamma}} p^{\nu}_{\boldsymbol{\alpha}} o^{\nu'}_{\boldsymbol{\gamma}} \underbrace{\frac{1}{N_{\boldsymbol{k}}^2}\sum_{\boldsymbol{k}\boldsymbol{k}'}[\chi(\boldsymbol{q};i\omega_m)]_{\boldsymbol{k}\nu_n\boldsymbol{\alpha},\boldsymbol{k}'\nu_{n'}\boldsymbol{\gamma}}}_{[\chi(\boldsymbol{q};\omega_m)]_{\nu_n\boldsymbol{\alpha},\nu_{n'}\boldsymbol{\gamma}}}.$$

In this expression, by summing over $\boldsymbol{k}$ and $\boldsymbol{k}'$ we obtained $[\chi(\boldsymbol{q};\omega_m)]_{\nu_n\boldsymbol{\alpha},\nu_{n'}\boldsymbol{\gamma}}$. The physical linear response function is given by the sum over the fermionic Matsubara frequencies

$$\chi_{\hat{P}_\nu\,\hat{O}_{\nu'}}(\boldsymbol{q};i\omega_m) = \sum_{\boldsymbol{\alpha}\boldsymbol{\gamma}} p^{\nu}_{\boldsymbol{\alpha}} o^{\nu'}_{\boldsymbol{\gamma}}\,\frac{1}{\beta^2}\sum_{nn'}\Big[\chi(\boldsymbol{q};\omega_m)\Big]_{\nu_n\boldsymbol{\alpha},\nu_{n'}\boldsymbol{\gamma}}. \tag{13}$$

In the case, e.g., of the magnetic susceptibility, the operators $\hat{P}^i_\nu$ and $\hat{O}^{i'}_{\nu'}$ are the three components of the magnetization operator. In the single-orbital limit ($\alpha = \alpha' = \sigma$ and $\gamma = \gamma' = \sigma'$), we thus have, e.g.,

$$o^z_{\boldsymbol{\alpha}} = -g\mu_B\langle\sigma|\hat{\sigma}_z|\sigma\rangle, \qquad p^z_{\boldsymbol{\alpha}} = -g\mu_B\langle\sigma'|\hat{\sigma}_z|\sigma'\rangle.$$

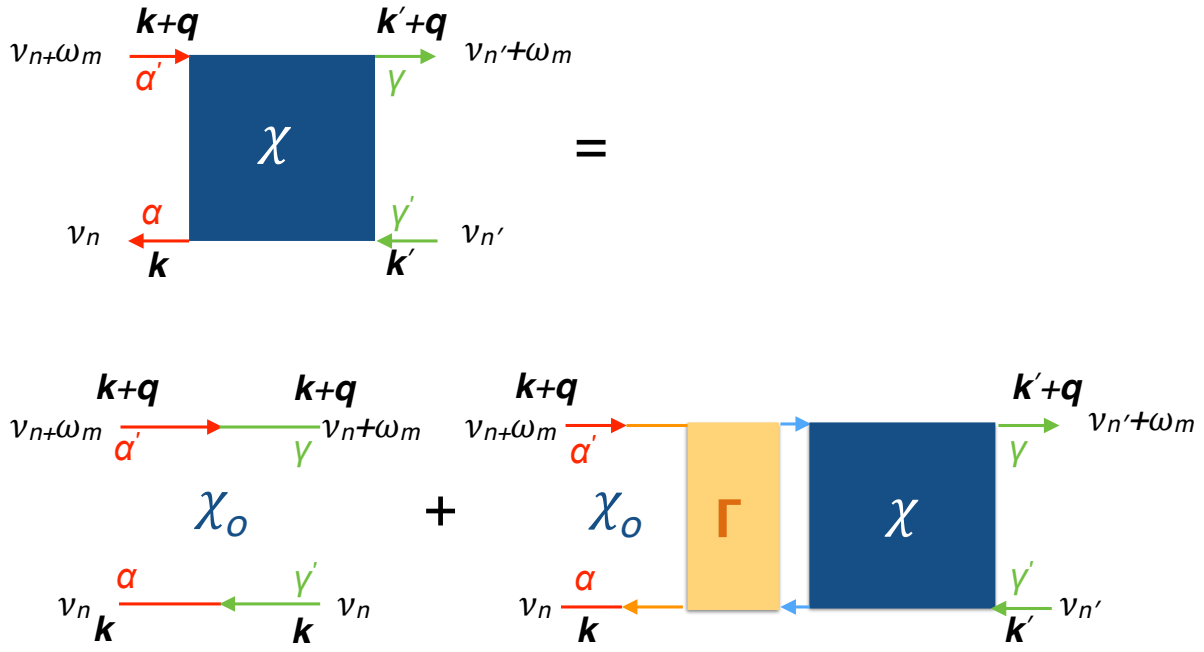

Fig. 10: *Diagrammatic representation of the Bethe-Salpeter equation for the linear susceptibility. The red lines indicates a creator/annihilator stemming from the operator $\hat{P}_\nu$ and the green lines from the operator $\hat{O}_{\nu'}$. The box labeled with Γ is the vertex function, the one labeled with χ the full susceptibility, and χ_0 is the pair-bubble term.*

3.2 DMFT and Bethe-Salpeter equation

To calculate the generalized interacting linear response function introduced in the previous section we can use, in principle, standard many-body perturbation techniques. Let us consider a system described by the multi-band Hubbard model $\hat{H}_0 + \hat{H}_U$, where $\hat{H}_0$ is the non-interacting part. We can formally construct a perturbation series for $\chi_{\hat{P}_\nu \hat{O}_{\nu'}}(\boldsymbol{q}; i\omega_m)$ in the interaction $\hat{H}_U$. The zero-order contribution is the linear response function for $\hat{H}_0$. Thus, due to Wick's theorem

$$\Big[\chi_0(\boldsymbol{q}; i\omega_m)\Big]_{\nu_n \boldsymbol{\alpha}, \nu_{n'} \boldsymbol{\gamma}} = \frac{1}{N_{\boldsymbol{k}}^2} \sum_{\boldsymbol{k}\boldsymbol{k}'} \underbrace{\Big[-\beta N_{\boldsymbol{k}} \mathcal{G}_{\boldsymbol{k}\alpha\gamma'}(i\nu_n)\, \mathcal{G}_{\boldsymbol{k}'+\boldsymbol{q}\alpha'\gamma}(i\nu_{n'}+i\omega_m)\, \delta_{n,n'} \delta_{\boldsymbol{k},\boldsymbol{k}'} \Big]}_{\Big[\chi_0(\boldsymbol{q};i\omega_m)\Big]_{\boldsymbol{k}\nu_n\boldsymbol{\alpha},\boldsymbol{k}'\nu_{n'}\boldsymbol{\gamma}}} . \quad (14)$$

The Feynman diagram corresponding to $[\chi_0(\boldsymbol{q}; \omega_m)]_{\boldsymbol{k}\nu_n\boldsymbol{\alpha},\boldsymbol{k}'\nu_{n'}\boldsymbol{\gamma}}$ is shown in Fig. 9. Once we switch-on the interaction, many-body perturbation theory leads to the Bethe-Salpeter (BS) equation, pictorially shown in Fig. 10. The susceptibility can then be expressed as follows

$$\Big[\chi(\boldsymbol{q}; i\omega_m)\Big]_{\nu_n \boldsymbol{\alpha}, \nu_{n'} \boldsymbol{\gamma}} = \frac{1}{N_{\boldsymbol{k}}^2} \sum_{\boldsymbol{k}\boldsymbol{k}'} \Big[\chi_0(\boldsymbol{q}; i\omega_m) + \frac{1}{N_{\boldsymbol{k}}^2} \chi_0(\boldsymbol{q}; i\omega_m) \Gamma(\boldsymbol{q}; i\omega_m) \chi(\boldsymbol{q}; i\omega_m)\Big]_{\boldsymbol{k}\nu_n\boldsymbol{\alpha},\nu_{n'}\boldsymbol{k}'\boldsymbol{\gamma}} .$$

For systems for which the dynamical mean-field is a good approximation, however, it is more convenient to construct a diagrammatic series starting from the DMFT linear response function

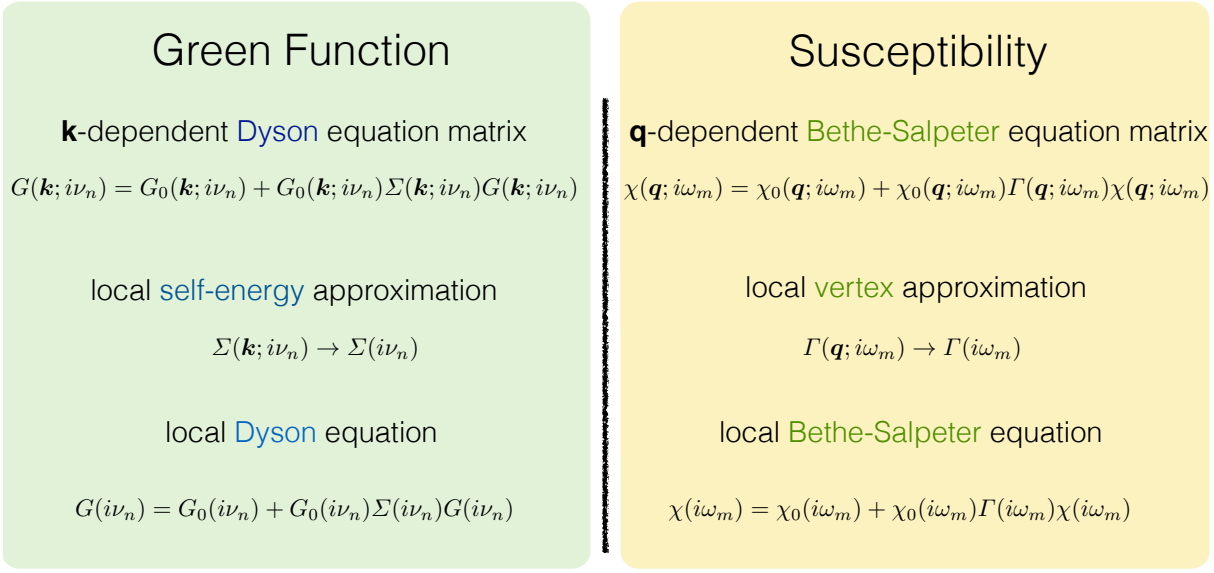

Fig. 11: *Analogies between the calculation of the Green function $G(\boldsymbol{k};i\nu_n)$ in the local-self-energy approximation (left) and the calculation of the response function $\chi(\boldsymbol{q};i\omega_m)$ in the local vertex approximation (right). Each term in the general Bethe-Salpeter equation can be viewed as a square matrix of dimension $N_{\boldsymbol{k}}N_nN_\alpha$, where $N_{\boldsymbol{k}}$ is the number of $\boldsymbol{k}$ points, N_n the number of fermionic Matsubara frequencies, N_α the number of flavors.*

rather than from the non-interacting term. If we do so, $\chi_0(\boldsymbol{q};\omega_m)$ is still given by Eq. (14), but with $\mathcal{G}$ replaced by the DMFT Green function matrices. Hence

$$[\chi_0(\boldsymbol{q};i\omega_m)]_{\nu_n\boldsymbol{\alpha},\nu_{n'}\boldsymbol{\gamma}} = -\beta\delta_{nn'}\frac{1}{N_{\boldsymbol{k}}}\sum_{\boldsymbol{k}} G_{\alpha\gamma'}(\boldsymbol{k};i\nu_n)\, G_{\alpha'\gamma}(\boldsymbol{k}+\boldsymbol{q};i\nu_n+i\omega_m).$$

There is, however, a catch: the vertex $\Gamma(\boldsymbol{q};i\omega_m)$ is unknown. In the infinite dimension limit it has been shown that the vertex can be replaced by a local quantity [4, 14]. Assuming that, in the spirit of the dynamical mean-field approximation, for a real 3-dimensional system we can do the same, we set

$$\Gamma(\boldsymbol{q};i\omega_m) \longrightarrow \Gamma(i\omega_m).$$

Thus, dropping for simplicity the flavor indices, after performing the $\boldsymbol{k}$ sums, the Bethe-Salpeter equation becomes

$$\chi(\boldsymbol{q};i\omega_m) = \chi_0(\boldsymbol{q};i\omega_m) + \chi_0(\boldsymbol{q};i\omega_m)\Gamma(i\omega_m)\chi(\boldsymbol{q};i\omega_m).$$

By solving it we find, formally

$$\chi^{-1}(\boldsymbol{q};i\omega_m) = \chi_0^{-1}(\boldsymbol{q};i\omega_m) - \Gamma(i\omega_m). \tag{15}$$

To actually obtain $\chi(\boldsymbol{q};i\omega_m)$ from this equation we need to calculate first the local vertex. The latter can be obtained using a further approximation, i.e., assuming that (15) is also satisfied if

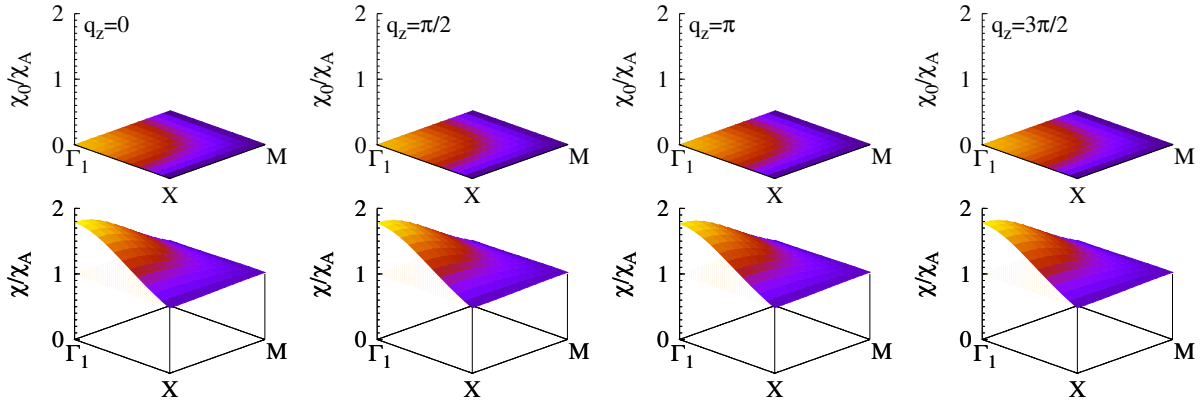

Fig. 12: *$VOMoO_4$: Static magnetic susceptibility $\chi(\mathbf{q};0)/\chi_A(0)$ in the q_x, q_y plane for representative q_z values, $T \sim 380$ K and $U = 5$ eV. The normalization $\chi_A(0) \sim \mu^2_{\rm eff}/k_BT$ is the atomic susceptibility in the large βU limit. Top panels: $\Gamma = 0$. Bottom panels: $\Gamma \neq 0$. Special points: $\Gamma_1 = (2\pi, 0)$, X= $(\pi, 0)$ and M= (π, π). Rearranged from Ref. [11].*

we replace the $\boldsymbol{q}$-dependent susceptibilities with their local counterparts, defined as

$$\chi_0(i\omega_m) = \frac{1}{N_{\boldsymbol{q}}} \sum_{\boldsymbol{q}} \chi_0(\boldsymbol{q}; i\omega_m),$$
$$\chi(i\omega_m) = \frac{1}{N_{\boldsymbol{q}}} \sum_{\boldsymbol{q}} \chi(\boldsymbol{q}; i\omega_m).$$

The first term is calculated directly from the DMFT Green function $\chi_0(\boldsymbol{q}; i\omega_m)$. The second term, $\chi(i\omega_m)$, is obtained via the quantum-impurity solver in the final iteration of the DMFT self-consistency loop. By inverting the local BS equation we have

$$\Gamma(i\omega_m) = \chi_0^{-1}(i\omega_m) - \chi^{-1}(i\omega_m). \tag{16}$$

Replacing $\Gamma(i\omega_m)$ into Eq. (15) yields the $\boldsymbol{q}$-dependent susceptibility. It has to be noticed that, although the two equations (15) and (16) look innocent, solving them numerically is a delicate task because the local susceptibility is in general not diagonal in n, n' and does not decay very fast with the frequencies. There are, however, various ways to reduce the computational costs, e.g., via extrapolations [11] or using compact representations based on auxiliary polynomials [15, 16]. The method just illustrated for the calculation of linear response functions in the local vertex approximation bears resemblance with the approach adopted for the calculation of the Green functions in the local self-energy approximation. These analogies are schematically pointed out in Fig. 11. Instead, in Fig. 12 we show as an example the case of the static magnetic susceptibility for a one-band system, the $S = 1/2$ frustrated Mott insulator $VOMoO_4$. The figure shows both the "bubble" term $\chi_0(\boldsymbol{q}; i\omega_m)$ (top panels) and the full susceptibility $\chi(\boldsymbol{q}; i\omega_m)$ (bottom panels). The two differ sizably in absolute value. In addition, as we will discuss later, the $\chi_0(\boldsymbol{q}; i\omega_m)$ term alone is very weakly dependent on the temperature. The expected Curie-Weiss-like behavior is only recovered when $\Gamma(i\omega_m)$ is taken into account.

3.3 The local susceptibility: Legendre representation

The core of the approach described in the previous section is the calculation of the local susceptibility tensor, $\chi_{\boldsymbol{\alpha\gamma}}(\boldsymbol{\tau})$. In DMFT all local observables $\langle\hat{O}\rangle$ are obtained via the quantum-impurity solver, for example the continuous-time hybridization expansion QMC technique presented in Section 2.3. Susceptibilities, however, require sizably longer computational time than Green-function matrices. Thus, instead of calculating directly $\chi_{\boldsymbol{\alpha\gamma}}(\boldsymbol{\tau})$, it is convenient to express the tensor elements in a basis of orthogonal functions $f_l^m(\tau)$, chosen such that the representation is as compact as possible. A successful choice [15, 16] is

$$f_l^m(\tau) = e^{-i\phi_m(\tau)} \begin{cases} \sqrt{2l+1}\; p_l(x(\tau)), & \tau > 0 \\ -(-1)^m\sqrt{2l+1}\; p_l(x(\tau+\beta)), & \tau < 0 \end{cases}$$

where $p_l(x(\tau))$ is a Legendre polynomial of degree l, with $x(\tau) = 2\tau/\beta - 1$; here the factor $(-1)^m$ in the second row ensures anti-periodicity for all values of m, which is the index for the bosonic Matsubara frequency ω_m. Via the orthogonality properties of the polynomials we obtain

$$\chi_{\boldsymbol{\alpha\gamma}}(i\omega_m) = \frac{1}{\beta^2}\sum_{ll'} f_l^{-m}(0^+)\; \chi^{l,l'}_{\boldsymbol{\alpha\gamma}}(i\omega_m)\; f_{l'}^{-m}(0^+). \tag{17}$$

The expansion coefficients in Eq. (17) take the form

$$\chi^{l,l'}_{\boldsymbol{\alpha\gamma}}(i\omega_m) = \int_0^\beta d\tau_{23}\int_0^\beta d\tau_{12}\int_0^\beta d\tau_{34}\; e^{-i\omega_m\tau_{23}} f_l^m(\tau_{12})\chi^{\alpha\alpha'}_{\gamma\gamma'}(\tau_{14},\tau_{24},\tau_{34},0) f_{l'}^m(\tau_{34}), \tag{18}$$

where $\tau_{ij} = \tau_i - \tau_j$, with $\tau_{14} = \tau_{12}+\tau_{23}+\tau_{34}$, and $\tau_{24} = \tau_{23}+\tau_{34}$. The phase defining the gauge is $\phi_m(\tau) = \omega_m\tau/2$ and does not depend on l. As we have seen, in quantum Monte Carlo the observables are obtained as the average over the visited configurations c. Splitting (18) into two terms [16] we have

$$\left\langle \chi^{l,l'}_{\boldsymbol{\alpha\gamma}}(i\omega_m)\right\rangle_c = \left\langle \mathcal{C}^{l,l'}_{\boldsymbol{\alpha\gamma}}(i\omega_m)\right\rangle_c - \beta\delta_{m,0}\left\langle G^l_{\boldsymbol{\alpha}}\right\rangle_c\left\langle G^{l'}_{\boldsymbol{\gamma}}\right\rangle_c.$$

The first term can be expressed as

$$\left\langle C^{l,l'}_{\boldsymbol{\alpha\gamma}}(i\omega_m)\right\rangle_c = \frac{1}{\beta}\sum_{bb'dd'}^{N_B}\sum_{i,j}^{k_b,k_d}\sum_{i',j'}^{k_{b'},k_{d'}} f_l^m(\tau_{dj}-\bar\tau_{bi}) f_{l'}^m(\tau_{d'j'}-\bar\tau_{b'i'}) c^{db,d'b'}_{ji,j'i'}(i\omega_m)\delta_{\boldsymbol{\alpha},(\alpha_{dj},\bar\alpha_{bi})}\delta_{\boldsymbol{\gamma},(\alpha_{d'j'},\bar\alpha_{b'i'})}$$

where

$$c^{db,d'b'}_{ji,j'i'}(i\omega_m) = (w^{db}_{ji}w^{d'b'}_{j'i'} - w^{d'b}_{j'i}w^{db'}_{ji'})\, e^{-i\omega_m(\bar\tau_{bi}-\tau_{d'j'})}.$$

Here the imaginary times τ_{bi} and $\bar\tau_{bi}$ all vary in the interval $[0,\beta)$. The letters b and d label the N_B flavors decoupled by symmetry, e.g., $\{\uparrow,\downarrow\}$. Finally, $w^{db}_{ji} = \delta_{b,d}\mathcal{M}^{k_b}_{bj,bi}$, where the matrix $\mathcal{M}^{k_b} = [\mathcal{F}_0^{k_b}]^{-1}$ is the inverse of the hybridization function matrix $\mathcal{F}_0^{k_b}$ for expansion order k_b. The Green functions in the second term are instead given by

$$\left\langle G^l_{\boldsymbol{\alpha}}\right\rangle_c = -\frac{1}{\beta}\sum_{b}^{N_B}\sum_{ij}^{k_b} f_l^0(\tau_{bj}-\bar\tau_{bi})\, w^{bb}_{ji}\,\delta_{\boldsymbol{\alpha},(\alpha_{bj},\bar\alpha_{bi})}.$$

3.4 Magnetic susceptibility for the single-band Hubbard model

The magnetic susceptibility is the linear response to an external magnetic field. The associated site susceptibility is

$$\chi^{i,i'}_{zz}(\boldsymbol{\tau}) = \left\langle \mathcal{T}\hat{M}^i_z(\tau)\hat{M}^{i'}_z(0)\right\rangle_0 - \left\langle \hat{M}^i_z\right\rangle_0\left\langle \hat{M}^{i'}_z\right\rangle_0,$$

where $\hat{M}^i_z = -g\mu_B\hat{S}^i_z$ is the magnetization for lattice site i. Its Fourier transform is

$$\begin{aligned}\chi_{zz}(\boldsymbol{q}; i\omega_m) &= \sum_{ii'} e^{i\boldsymbol{q}\cdot(\boldsymbol{T}_i-\boldsymbol{T}_{i'})}\int d\tau\; e^{i\omega_m\tau}\chi^{i,i'}_{zz}(\tau)\\ &= \left\langle \hat{M}_z(\boldsymbol{q};\omega_m)\hat{M}_z(-\boldsymbol{q};0)\right\rangle_0 - \left\langle \hat{M}_z(\boldsymbol{q})\right\rangle_0\left\langle \hat{M}_z(-\boldsymbol{q})\right\rangle_0, \end{aligned} \tag{19}$$

where ω_m is a bosonic Matsubara frequency. For the one-band Hubbard model, the magnetization operator can be expressed in the basis of Bloch functions as

$$\hat{M}_z(\boldsymbol{q}) = -\frac{g\mu_B}{2}\sum_{\boldsymbol{k}}\sum_{\sigma}\sigma c^\dagger_{\boldsymbol{k}+\boldsymbol{q}\sigma}c_{\boldsymbol{k}\sigma}, \tag{20}$$

where $\sigma = 1$ for spin up and $\sigma = -1$ for spin down. To obtain the magnetic response function we thus have to calculate the imaginary-time tensor with elements

$$\begin{aligned}\left[\chi(\boldsymbol{q};\boldsymbol{\tau})\right]_{\boldsymbol{k}\sigma,\boldsymbol{k}'\sigma'} &= \left\langle \mathcal{T}c_{\boldsymbol{k}\sigma}(\tau_1)c^\dagger_{\boldsymbol{k}+\boldsymbol{q}\sigma}(\tau_2)c_{\boldsymbol{k}'+\boldsymbol{q}\sigma'}(\tau_3)c^\dagger_{\boldsymbol{k}'\sigma'}(\tau_4)\right\rangle_0\\ &\quad - \left\langle \mathcal{T}c_{\boldsymbol{k}\sigma}(\tau_1)c^\dagger_{\boldsymbol{k}+\boldsymbol{q}\sigma}(\tau_2)\right\rangle_0\left\langle \mathcal{T}c_{\boldsymbol{k}'+\boldsymbol{q}\sigma'}(\tau_3)c^\dagger_{\boldsymbol{k}'\sigma'}(\tau_4)\right\rangle_0. \end{aligned} \tag{21}$$

The associated imaginary-time magnetic susceptibility is then given by

$$\chi_{zz}(\boldsymbol{q};\boldsymbol{\tau}) = (g\mu_B)^2\frac{1}{4}\sum_{\sigma\sigma'}\sigma\sigma'\underbrace{\frac{1}{\beta}\frac{1}{N^2_{\boldsymbol{k}}}\sum_{\boldsymbol{k}\boldsymbol{k}'}\left[\chi(\boldsymbol{q};\boldsymbol{\tau})\right]_{\boldsymbol{k}\sigma,\boldsymbol{k}'\sigma'}}_{\chi_{\sigma\sigma\sigma'\sigma'}(\boldsymbol{q};\boldsymbol{\tau})}. \tag{22}$$

After we Fourier transform with respect to imaginary time and sum over the fermionic Matsubara frequencies, we have

$$\chi_{zz}(\boldsymbol{q}; i\omega_m) = (g\mu_B)^2\frac{1}{4}\sum_{\sigma\sigma'}\sigma\sigma'\frac{1}{\beta^2}\sum_{nn'}\chi^{n,n'}_{\sigma\sigma\sigma'\sigma'}(\boldsymbol{q}; i\omega_m), \tag{23}$$

where

$$\chi^{n,n'}_{\sigma\sigma\sigma'\sigma'}(\boldsymbol{q}; i\omega_m) = \frac{1}{16}\iiint d\boldsymbol{\tau}\; e^{i\boldsymbol{\nu}\cdot\boldsymbol{\tau}}\chi_{\sigma\sigma\sigma'\sigma'}(\boldsymbol{q};\boldsymbol{\tau}). \tag{24}$$

For $\omega_n = 0$ we obtain the static magnetic susceptibility.

3.4.1 Non-interacting limit

In the non-interacting limit we can use Wick's theorem to simplify Eq. (21). It follows that the elements of the two-particle Green function tensor vanish if $\boldsymbol{k} \neq \boldsymbol{k}'$. In the paramagnetic case, Eq. (22) then becomes

$$\chi_{zz}(\boldsymbol{q};\boldsymbol{\tau}) = -(g\mu_B)^2 \frac{1}{4}\frac{1}{\beta}\frac{1}{N_{\boldsymbol{k}}}\sum_{\boldsymbol{k}}\sum_{\sigma}\mathcal{G}_{\boldsymbol{k}\sigma}(\tau_{14})\mathcal{G}_{\boldsymbol{k}+\boldsymbol{q}\sigma}(-\tau_{23}).$$

For the frequency-dependent magnetic susceptibility Eq. (23) we have instead

$$\chi_{zz}(\boldsymbol{q};i\omega_m) = (g\mu_B)^2 \frac{1}{4}\frac{1}{\beta^2}\sum_{nn'}\sum_{\sigma}\chi^{n,n'}_{\sigma\sigma\sigma\sigma}(\boldsymbol{q};i\omega_m),$$

where

$$\sum_{\sigma}\chi^{n,n'}_{\sigma\sigma\sigma\sigma}(\boldsymbol{q};i\omega_m) = -\beta\frac{1}{N_{\boldsymbol{k}}}\sum_{\boldsymbol{k}}\sum_{\sigma}\mathcal{G}_{\boldsymbol{k}\sigma}(i\nu_n)\,\mathcal{G}_{\boldsymbol{k}+\boldsymbol{q}\sigma}(i\nu_n+i\omega_m)\,\delta_{n,n'}. \tag{25}$$

The actual dynamical susceptibility is then given by

$$\chi_{zz}(\boldsymbol{q};i\omega_m) = -\,(g\mu_B)^2\,\frac{1}{4}\frac{1}{N_{\boldsymbol{k}}}\sum_{\boldsymbol{k}}\sum_{\sigma}\frac{n_\sigma(\varepsilon_{\boldsymbol{k}+\boldsymbol{q}}) - n_\sigma(\varepsilon_{\boldsymbol{k}})}{\varepsilon_{\boldsymbol{k}+\boldsymbol{q}} - \varepsilon_{\boldsymbol{k}} + i\omega_m}.$$

In the $\boldsymbol{q}\to 0$ and $T\to 0$ limit, setting $\omega_m = 0$ we recover the static Pauli susceptibility

$$\chi_{zz}(\boldsymbol{0};0) = \frac{1}{4}\,(g\mu_B)^2\,\rho(\varepsilon_F),$$

$$\rho(\varepsilon_F) = -\sum_{\sigma}\frac{1}{N_{\boldsymbol{k}}}\sum_{\boldsymbol{k}}\left.\frac{dn_\sigma(\varepsilon_{\boldsymbol{k}})}{d\varepsilon_{\boldsymbol{k}}}\right|_{T=0}.$$

Figure 13 shows (at half filling) the non-interacting spin susceptibility in the x-y plane for a d-dimensional hypercubic lattice with dispersion

$$\varepsilon_{\boldsymbol{k}} = -2t\sum_{n=1}^{d}\cos k_d.$$

In $d = 1$ and for $T\to 0$, $\chi_{zz}(\boldsymbol{q};0)$ diverges at the antiferromagnetic vector $\boldsymbol{q}_C = (\pi/a, 0, 0)$; in two dimensions this happens at $\boldsymbol{q}_C$=$(\pi/a, \pi/a, 0)$; in three dimensions at $\boldsymbol{q}_C$=$(\pi/a, \pi/a, \pi/a)$, not shown in the figure. These are perfect nesting vectors, for which

$$\varepsilon_{\boldsymbol{k}+\boldsymbol{q}_C} = -\varepsilon_{\boldsymbol{k}},$$

so that

$$\chi_0(\boldsymbol{q}_C;0) \propto \frac{1}{4}\int_{-\infty}^{\varepsilon_F} d\varepsilon\,\frac{\rho(\varepsilon)}{\varepsilon}.$$

Under these conditions an arbitrarily small U can cause a magnetic transition with magnetic vector $\boldsymbol{q}_C$, e.g., via a Stoner-like mechanism.

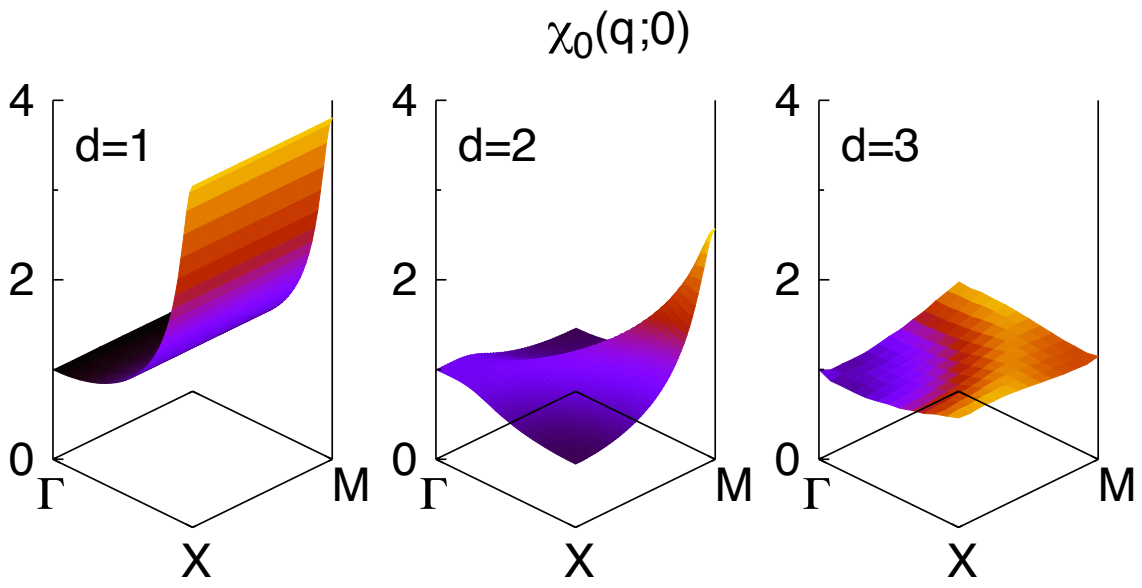

Fig. 13: *The ratio $\chi_0(\boldsymbol{q};0)/\chi_0(\boldsymbol{0};0)$ in the x-y plane for a hypercubic lattice with $t = 0.4$ eV ($T \sim 230$ K) at half filling. From left to right: one, two, and three dimensions.*

3.4.2 Atomic limit

Let us now consider the opposite extreme, the atomic limit. First we adopt a simple approach, i.e., we directly calculate the right-hand side of Eq. (19) by summing up the contributions of the atomic states, $|0\rangle$, $c^\dagger_\uparrow|0\rangle$, $c^\dagger_\downarrow|0\rangle$, $c^\dagger_\uparrow c^\dagger_\downarrow|0\rangle$; since all atoms are decoupled, only on-site terms $i = i'$ contribute. At half filling we thus have

$$\chi_{zz}(\boldsymbol{q}; i\omega_m) = (g\mu_B)^2 \frac{1}{4k_BT} \frac{e^{\beta U/2}}{1+e^{\beta U/2}} \delta_{\omega_m,0}. \tag{26}$$

The same expression can be obtained following the general procedure outlined in the previous pages, i.e., starting from the two-particle Green function tensor $\chi_{\sigma\sigma\sigma'\sigma'}(\boldsymbol{q};\boldsymbol{\tau})$, defined in Eq. (22) for the single-band Hubbard model. In the atomic limit, it is convenient to work in real space, since

$$\chi_{\sigma\sigma\sigma'\sigma'}(\boldsymbol{q};\boldsymbol{\tau}) = \frac{1}{\beta} \sum_i \chi_{i\sigma\sigma,i\sigma'\sigma'}(\boldsymbol{\tau}).$$

Thanks to the symmetries of the tensor in imaginary time, it is sufficient to calculate $\chi_{i\sigma\sigma,i\sigma'\sigma'}(\boldsymbol{\tau})$ for positive times $0 < \tau_{j4} < \beta$, where $\tau_{j4} = \tau_j - \tau_4$ with $j = 1, 2, 3$. Due to the time ordering operator we have, however, to consider separately six different imaginary-time sectors. In the Appendix one can find a list of all these sectors and their contributions. For simplicity, we discuss here explicitly only the case $\tau_{14} > \tau_{24} > \tau_{34} > 0$ and label the corresponding $\boldsymbol{\tau}$-vector as $\boldsymbol{\tau}^+$. Calculating the trace we obtain

$$\chi_{i\sigma\sigma,i\sigma'\sigma'}(\boldsymbol{\tau}^+) = \frac{e^{\tau_{12}U/2+\tau_{34}U/2} + \delta_{\sigma\sigma'} e^{(\beta-\tau_{12})U/2-\tau_{34}U/2}}{2(1+e^{\beta U/2})} - G^\sigma_{i,i}(\tau_{12})\, G^{\sigma'}_{i,i}(\tau_{34}).$$

In the paramagnetic case the mean-field terms $G^{\sigma}_{i,i}(\tau_{12})\, G^{\sigma'}_{i,i}(\tau_{34})$ cancel out in the actual magnetic linear response function, so here we do not give their form explicitly. For a single atom, the contribution of the $\boldsymbol{\tau}^+$ sector to the imaginary-time magnetic susceptibility is

$$\chi_{zz}(\boldsymbol{\tau}^+) = (g\mu_B)^2 \frac{1}{4}\frac{1}{\beta}\sum_{\sigma\sigma'}\sigma\sigma'\chi_{i\sigma\sigma,i\sigma'\sigma'}(\boldsymbol{\tau}^+) = \frac{(g\mu_B)^2}{4\beta}\frac{1}{(1+e^{\beta U/2})}e^{(\beta-\tau_{12}-\tau_{34})U/2}.$$

Summing up the contributions of all imaginary-time sectors and performing the Fourier transform we obtain $\chi^{n,n'}_{\sigma\sigma\sigma'\sigma'}(i\omega_n)$, defined in Eq. (24). For $U \neq 0$ this tensor is non-diagonal in the fermionic Matsubara frequencies. For $\omega_n = 0$ we have [11]

$$\begin{aligned}\sum_{\sigma\sigma'}\sigma\sigma'\,\chi^{n,n'}_{i\sigma\sigma,i\sigma'\sigma'}(0) =& M_{n'}\frac{dM_n}{dy} + M_n\frac{dM_{n'}}{dy} - \beta n(y)\left[\delta_{n,n'}+\delta_{n,-n'}\right]\frac{dM_n}{dy} + \beta n(-y) M_n M_{n'} \\ & -\frac{1}{y}\left\{M_{n'} - \beta\left[n(y)\delta_{n,-n'} - n(-y)\delta_{n,n'}\right]\right\}M_n \end{aligned} \tag{27}$$

where

$$M_n = \frac{1}{i\nu_n - y} - \frac{1}{i\nu_n + y}. \tag{28}$$

We can now calculate the magnetic susceptibility via Eq. (23), recovering the expected result, Eq. (26). The resulting atomic magnetic susceptibility is thus proportional to $1/k_BT$, i.e., has a Curie-like behavior; furthermore it is zero at finite frequency. The temperature dependence can be remarkably different from the $U = 0$ limit. Indeed, if the density of states is flat around the Fermi level, as it is often the case in three-dimensional lattices, the non-interacting Pauli susceptibility $\chi_{zz}(\mathbf{0}; 0)$ is weakly temperature dependent. A strong temperature dependence can be found, however, if, e.g., a logarithmic van-Hove singularity is at the Fermi level, as in the example discussed in the previous subsection for the square lattice at half filling.

3.4.3 DMFT: $\boldsymbol{\chi_0(\mathrm{q};\omega)}$ and the Bethe-Salpeter equation

In order to calculate the magnetic susceptibility with DMFT, we first need $\chi_0(\mathbf{q};\omega)$. Here for simplicity we consider only the two-dimensional case with $\varepsilon_{\boldsymbol{k}} = -2t(\cos k_x + \cos k_y)$. In the atomic limit we can rewrite the local Green function as

$$G^{\sigma}_{i,i}(i\nu_n) = \frac{1}{i\nu_n + \mu - \varepsilon_d - \Sigma^{\sigma}_l(i\nu_n)},$$

where the local self-energy is given by

$$\Sigma^{\sigma}_l(i\nu_n) = \frac{U}{2} + \frac{U^2}{4}\frac{1}{i\nu_n + \mu - \varepsilon_d - \frac{U}{2}}, \tag{29}$$

and $\mu = \varepsilon_d + \frac{U}{2}$ at half filling. In the Mott insulating regime, i.e., for small but finite t/U, we can assume that the local self-energy has the same form (29), with $U^2/4$ replaced by a quantity which plays the role of a dimensionless *order parameter* [17] for the insulating phase

$$\frac{1}{r_U}\frac{4}{U^2} = \int_{-\infty}^{+\infty} d\varepsilon\, \frac{\rho(\varepsilon)}{\varepsilon^2}. \tag{30}$$

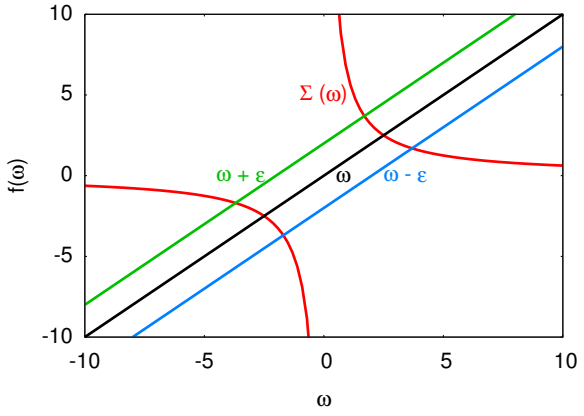

Fig. 14: *Graphical solution of the equation* $\omega - \varepsilon_{\boldsymbol{k}} = \Sigma_l^\sigma(\omega)$ *yielding the poles* $E_{\boldsymbol{k}}^+$ *and* $E_{\boldsymbol{k}}^-$ *of the Green function defined in Eq. (31).*

Here $\rho(\varepsilon)$ is the density of states per spin. The integral in Eq. (30) diverges in the metallic phase. The Green function can then be rewritten as

$$G_{\sigma\sigma}(\boldsymbol{k}; i\nu_n) = \frac{1}{i\nu_n - \Sigma_l^\sigma(i\nu_n) - \varepsilon_{\boldsymbol{k}}} = \frac{1}{E_{\boldsymbol{k}}^+ - E_{\boldsymbol{k}}^-}\left[\frac{E_{\boldsymbol{k}}^+}{i\nu_n - E_{\boldsymbol{k}}^+} - \frac{E_{\boldsymbol{k}}^-}{i\nu_n - E_{\boldsymbol{k}}^-}\right] \tag{31}$$

where $E_{\boldsymbol{k}}^+$ and $E_{\boldsymbol{k}}^-$ are the two roots of the equation $\omega - \Sigma_l^\sigma(\omega) - \varepsilon_{\boldsymbol{k}} = 0$,

$$E_{\boldsymbol{k}}^\pm = \frac{1}{2}\varepsilon_{\boldsymbol{k}} \pm \frac{1}{2}\sqrt{\varepsilon_{\boldsymbol{k}}^2 + r_U\, U^2}.$$

By performing the Matsubara sums, one finds

$$\begin{aligned}\chi_{zz}^0(\boldsymbol{q}; 0) &= (g\mu_B)^2 \frac{1}{4}\sum_\sigma \frac{1}{\beta^2}\sum_n \chi_{\sigma\sigma\sigma\sigma}^{n,n}(0) \\ &= (g\mu_B)^2 \frac{1}{2}\frac{1}{N_{\boldsymbol{k}}}\sum_{\boldsymbol{k}}\Big[\underbrace{-I_{\boldsymbol{k},\boldsymbol{q}}^{++} - I_{\boldsymbol{k},\boldsymbol{q}}^{--}}_{A_{\boldsymbol{k},\boldsymbol{q}}} + \underbrace{I_{\boldsymbol{k},\boldsymbol{q}}^{+-} + I_{\boldsymbol{k},\boldsymbol{q}}^{-+}}_{B_{\boldsymbol{k},\boldsymbol{q}}},\Big]\end{aligned}$$

where, setting $\alpha = \pm$ and $\gamma = \pm$,

$$I_{\boldsymbol{k},\boldsymbol{q}}^{\alpha\gamma} = \frac{E_{\boldsymbol{k}}^\alpha\, E_{\boldsymbol{k}+\boldsymbol{q}}^\gamma}{\big(E_{\boldsymbol{k}}^+ - E_{\boldsymbol{k}}^-\big)\big(E_{\boldsymbol{k}+\boldsymbol{q}}^+ - E_{\boldsymbol{k}+\boldsymbol{q}}^-\big)}\frac{n(E_{\boldsymbol{k}}^\alpha) - n(E_{\boldsymbol{k}+\boldsymbol{q}}^\gamma)}{E_{\boldsymbol{k}}^\alpha - E_{\boldsymbol{k}+\boldsymbol{q}}^\gamma}.$$

In the $\boldsymbol{q} \to \boldsymbol{0}$ limit

$$\begin{aligned}A_{\boldsymbol{k},\boldsymbol{0}} &= \beta\,\left[\frac{(E_{\boldsymbol{k}}^+)^2}{\varepsilon_{\boldsymbol{k}}^2 + r_U\, U^2}\, n(E_{\boldsymbol{k}}^+)\big(1 - n(E_{\boldsymbol{k}}^+)\big) + \frac{(E_{\boldsymbol{k}}^-)^2}{\varepsilon_{\boldsymbol{k}}^2 + r_U\, U^2}\, n(E_{\boldsymbol{k}}^-)\big(1 - n(E_{\boldsymbol{k}}^-)\big)\right] \\ B_{\boldsymbol{k},\boldsymbol{0}} &= \frac{r_U\, U^2}{2(\varepsilon_{\boldsymbol{k}}^2 + r_U\, U^2)^{3/2}}\left(n(E_{\boldsymbol{k}}^-) - n(E_{\boldsymbol{k}}^+)\right).\end{aligned}$$

In the large βU limit, the $A_{\boldsymbol{k},\boldsymbol{0}}$ term, proportional to the density of states at the Fermi level, vanishes exponentially; the $B_{\boldsymbol{k},\boldsymbol{0}}$ term yields the dominant contribution. Hence

$$\chi_{zz}^0(\boldsymbol{0}; 0) \sim (g\mu_B)^2 \frac{1}{4}\frac{1}{N_{\boldsymbol{k}}}\sum_{\boldsymbol{k}} \frac{r_U\, U^2}{(\varepsilon_{\boldsymbol{k}}^2 + r_U\, U^2)^{3/2}} \sim (g\mu_B)^2 \frac{1}{4\sqrt{r_U}\, U}\left[1 - \frac{3}{2}\frac{1}{N_{\boldsymbol{k}}}\sum_{\boldsymbol{k}} \frac{\varepsilon_{\boldsymbol{k}}^2}{r_U\, U^2} + \dots\right].$$

The right-hand side is equal to the atomic term $\chi^0_{zz}(0)$ minus a correction of order t^2/U^3. As we can see, $\chi^0_{zz}(\mathbf{0};0)$ is small and weakly dependent on the temperature. In the Mott-insulating regime, due to the superexchange interaction, the two-dimensional Hubbard model exhibits an antiferromagnetic instability at $\boldsymbol{q}_C = (\pi/a, \pi/a, 0)$. Let us then calculate $\chi^0_{zz}(\boldsymbol{q}_C;0)$ and compare it with $\chi^0_{zz}(\mathbf{0};0)$. Since, as we have seen, $\varepsilon_{\boldsymbol{k}+\boldsymbol{q}_C} = -\varepsilon_{\boldsymbol{k}}$, we find

$$A_{\boldsymbol{k},\boldsymbol{q}_C} = \frac{1}{2}\frac{r_U\,U^2}{\varepsilon^2_{\boldsymbol{k}} + r_U\,U^2}\frac{n(E^+_{\boldsymbol{k}}-\varepsilon_{\boldsymbol{k}}) - n(E^+_{\boldsymbol{k}})}{\varepsilon_{\boldsymbol{k}}}$$

$$B_{\boldsymbol{k},\boldsymbol{q}_C} = \frac{1}{2}\frac{\varepsilon^2_{\boldsymbol{k}}}{\varepsilon^2_{\boldsymbol{k}} + r_U\,U^2}\frac{n(E^+_{\boldsymbol{k}}-\varepsilon_{\boldsymbol{k}}) - n(E^+_{\boldsymbol{k}})}{\varepsilon_{\boldsymbol{k}}} - \frac{1}{2}\frac{1}{\sqrt{\varepsilon^2_{\boldsymbol{k}} + r_U\,U^2}}\left(n(E^+_{\boldsymbol{k}}) - n(E^-_{\boldsymbol{k}})\right),$$

and therefore

$$\chi_0(\boldsymbol{q}_C;0) \sim (g\mu_B)^2\frac{1}{4\sqrt{r_U}U}\left(1 - \frac{1}{2}\frac{1}{N_{\boldsymbol{k}}}\sum_{\boldsymbol{k}}\frac{\varepsilon^2_{\boldsymbol{k}}}{r_U U^2}\right).$$

Thus $\chi_0(\boldsymbol{q};0)$ is indeed larger at $\boldsymbol{q} = \boldsymbol{q}_C$ than at $\boldsymbol{q} = \mathbf{0}$; it is however weakly temperature dependent and does not exhibit Curie-Weiss instabilities. The calculation presented above can be generalized to any $\boldsymbol{q}$ vector [11], obtaining the expression

$$\chi_0(\boldsymbol{q};0) \sim (g\mu_B)^2\frac{1}{4\sqrt{r_U}U}\left(1 - \frac{1}{2}\frac{J_{\mathbf{0}}}{\sqrt{r_U}U} - \frac{1}{4}\frac{J_{\boldsymbol{q}}}{\sqrt{r_U}U}\right), \tag{32}$$

where $J_{\boldsymbol{q}} = J\big(\cos q_x + \cos q_y\big)$, and the super-exchange coupling is $J = 4t^2/U$. To make progress we now need the local vertex. This requires, as we have seen, the solution of the self-consistent quantum-impurity model via the quantum-impurity solver. Here, for the purpose of illustrating how the approach works, we approximate the local susceptibility with the atomic susceptibility in the large βU limit. Furthermore we work with the susceptibilities obtained *after* the Matsubara sums have been performed. Thus

$$\chi^0_{zz}(0) \sim (g\mu_B)^2\frac{1}{4\sqrt{r_U}U}, \qquad \chi_{zz}(0) \sim \frac{1}{4k_BT}.$$

The local vertex is then approximately given by

$$\Gamma \sim \frac{1}{\chi^0_{zz}(0)} - \frac{1}{\chi_{zz}(0)} \sim \frac{1}{(g\mu_B)^2}\left[4\sqrt{r_U}U\left(1 + \frac{1}{2}\frac{J_{\mathbf{0}}}{\sqrt{r_U}U}\right) - 4k_BT\right].$$

The last step consists in solving the Bethe-Salpeter equation

$$\chi_{zz}(\boldsymbol{q};0) = \frac{1}{(\chi^0_{zz}(\boldsymbol{q};0))^{-1} - \Gamma} \sim \frac{(g\mu_B)^2}{4}\frac{1}{k_BT + J_{\boldsymbol{q}}/4} = \frac{(g\mu_B)^2}{4k_B}\,\frac{1}{T - T_{\boldsymbol{q}}}.$$

This shows that including the local vertex correction we recover the Curie-Weiss behavior, as expected for a system described by local spins coupled by a Heisenberg-like exchange; we also correctly find the antiferromagnetic instability, since $\boldsymbol{q}_C$ is the vector for which the critical temperature $T_{\boldsymbol{q}}$ is the largest. In conclusion, we have seen that $\Gamma(i\omega_m)$ is essential to properly describe the magnetic response function of strongly-correlated systems. This can be seen in Fig. 12 for the Mott insulator $VOMoO_4$. In the figure we can compare the very weak linear magnetic response $\chi_0(\boldsymbol{q};0)$ (upper panels) with the LDA+DMFT result $\chi(\boldsymbol{q};0)$ (lower panels). The latter is not only strongly enhanced with respect to $\chi_0(\boldsymbol{q};0)$, but also exhibits the expected Curie-Weiss like behavior, as can be seen in Fig. 15 for $\boldsymbol{q} = \mathbf{0}$.

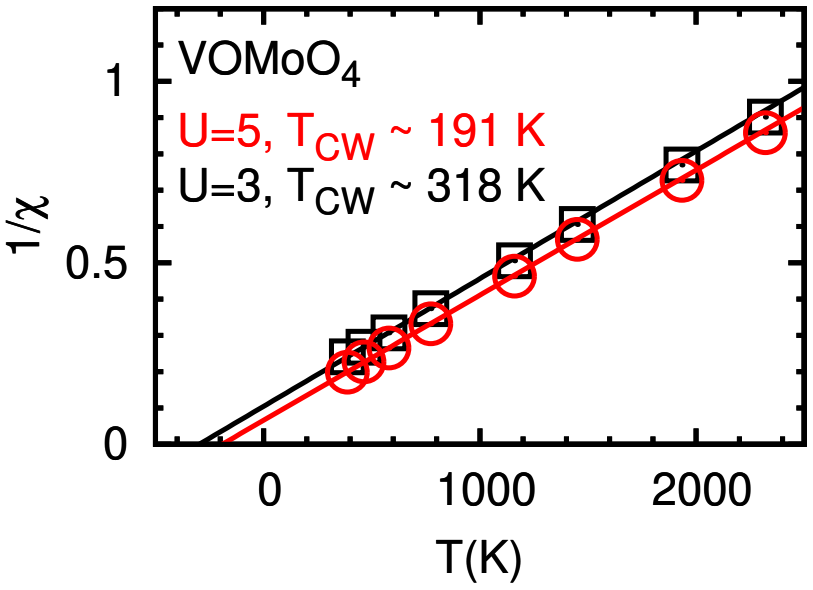

Fig. 15: *$VOMoO_4$: The Curie-Weiss behavior of the uniform magnetic susceptibility at half filling, obtained with the LDA+DMFT approach. Rearranged from Ref. [11].*

4 Conclusion

The LDA+DMFT approach and its extension has proved very successful for describing correlated materials. It has shown us that materials details do matter, contrarily to what often was assumed in the past; for example a crystal field much smaller than the bandwidth can favor the Mott metal-insulator transition [18]. The method is becoming progressively more and more versatile. It is now possible, e.g., to study multi-orbital Hubbard-like models including the full Coulomb vertex and the spin-orbit interaction. Successful extension schemes, e.g., cluster methods, account, at least in part, for the $\boldsymbol{q}$-dependence of the self-energy. In this lecture, we have seen how to use the LDA+DMFT approach to calculate not only Green and spectral functions but also linear-response functions. In the scheme presented, the local susceptibility is obtained via the quantum-impurity solver at the end of the self-consistency loop; the $\boldsymbol{q}$-dependent susceptibility is, instead, calculated solving in addition the Bethe-Salpeter equation in the local-vertex approximation. As representative case we have studied the magnetic susceptibility of the one-band Hubbard model at half filling. The extension of the LDA+DMFT approach to the calculation of generalized susceptibilities makes it possible to put the method and the approximations adopted to more stringent tests. This is key for further advancing the theoretical tools for the description of strong correlation effects in real materials.

Appendix

A Eigenstates of two-site models

A.1 Hubbard dimer

The Hamiltonian of the Hubbard dimer is given by

$$\hat{H} = \varepsilon_d \sum_{\sigma} \sum_{i=1,2} \hat{n}_{i\sigma} - t \sum_{\sigma} \left(c^{\dagger}_{1\sigma} c_{2\sigma} + c^{\dagger}_{2\sigma} c_{1\sigma} \right) + U \sum_{i=1,2} \hat{n}_{i\uparrow} \hat{n}_{i\downarrow}.$$

It commutes with the number of electron operator $\hat{N}$, with the total spin $\hat{S}$ and with $\hat{S}_z$. Thus we can express the many-body states in the atomic limit as

$\lvert N, S, S_z \rangle$			N	S	$E(N,S)$
$\lvert 0,0,0 \rangle$	$=$	$\lvert 0 \rangle$	0	0	0
$\lvert 1,1/2,\sigma \rangle_1$	$=$	$c^{\dagger}_{1\sigma} \lvert 0 \rangle$	1	$1/2$	ε_d
$\lvert 1,1/2,\sigma \rangle_2$	$=$	$c^{\dagger}_{2\sigma} \lvert 0 \rangle$	1	$1/2$	ε_d
$\lvert 2,1,1 \rangle$	$=$	$c^{\dagger}_{2\uparrow} c^{\dagger}_{1\uparrow} \lvert 0 \rangle$	2	1	$2\varepsilon_d$
$\lvert 2,1,-1 \rangle$	$=$	$c^{\dagger}_{2\downarrow} c^{\dagger}_{1\downarrow} \lvert 0 \rangle$	2	1	$2\varepsilon_d$
$\lvert 2,1,0 \rangle$	$=$	$\frac{1}{\sqrt{2}} \left(c^{\dagger}_{1\uparrow} c^{\dagger}_{2\downarrow} + c^{\dagger}_{1\downarrow} c^{\dagger}_{2\uparrow} \right) \lvert 0 \rangle$	2	1	$2\varepsilon_d$
$\lvert 2,0,0 \rangle_0$	$=$	$\frac{1}{\sqrt{2}} \left(c^{\dagger}_{1\uparrow} c^{\dagger}_{2\downarrow} - c^{\dagger}_{1\downarrow} c^{\dagger}_{2\uparrow} \right) \lvert 0 \rangle$	2	0	$2\varepsilon_d$
$\lvert 2,0,0 \rangle_1$	$=$	$c^{\dagger}_{1\uparrow} c^{\dagger}_{1\downarrow} \lvert 0 \rangle$	2	0	$2\varepsilon_d + U$
$\lvert 2,0,0 \rangle_2$	$=$	$c^{\dagger}_{2\uparrow} c^{\dagger}_{2\downarrow} \lvert 0 \rangle$	2	0	$2\varepsilon_d + U$
$\lvert 3,1/2,\sigma \rangle_1$	$=$	$c^{\dagger}_{1\sigma} c^{\dagger}_{2\uparrow} c^{\dagger}_{2\downarrow} \lvert 0 \rangle$	3	$1/2$	$3\varepsilon_d + U$
$\lvert 3,1/2,\sigma \rangle_2$	$=$	$c^{\dagger}_{2\sigma} c^{\dagger}_{1\uparrow} c^{\dagger}_{1\downarrow} \lvert 0 \rangle$	3	$1/2$	$3\varepsilon_d + U$
$\lvert 4,0,0 \rangle$	$=$	$c^{\dagger}_{1\uparrow} c^{\dagger}_{1\downarrow} c^{\dagger}_{2\uparrow} c^{\dagger}_{2\downarrow} \lvert 0 \rangle$	4	0	$4\varepsilon_d + 2U$

Let us order the $N = 1$ states as in the table above, first the spin up and then spin down block. For finite t the Hamiltonian matrix for $N = 1$ electrons takes then the form

$$\hat{H}_1 = \begin{pmatrix} \varepsilon_d & -t & 0 & 0 \\ -t & \varepsilon_d & 0 & 0 \\ 0 & 0 & \varepsilon_d & -t \\ 0 & 0 & -t & \varepsilon_d \end{pmatrix}.$$

This matrix can be easily diagonalized and yields the *bonding* $(-)$ and *antibonding* $(+)$ states

$\|1,S,S_z\rangle_\alpha$	$E_\alpha(1,S)$	$d_\alpha(1,S)$
$\|1,1/2,\sigma\rangle_+ = \frac{1}{\sqrt{2}}\big(\|1,1/2,\sigma\rangle_1 - \|1,1/2,\sigma\rangle_2\big)$	$\varepsilon_d + t$	2
$\|1,1/2,\sigma\rangle_- = \frac{1}{\sqrt{2}}\big(\|1,1/2,\sigma\rangle_1 + \|1,1/2,\sigma\rangle_2\big)$	$\varepsilon_d - t$	2

where $d_\alpha(N)$ is the spin degeneracy of the α manifold.
For $N = 2$ electrons (half filling), the hopping integrals only couple the three $S = 0$ states, and therefore the Hamiltonian matrix is given by

$$\hat{H}_2 = \begin{pmatrix} 2\varepsilon_d & 0 & 0 & 0 & 0 & 0 \\ 0 & 2\varepsilon_d & 0 & 0 & 0 & 0 \\ 0 & 0 & 2\varepsilon_d & 0 & 0 & 0 \\ 0 & 0 & 0 & 2\varepsilon_d & -\sqrt{2}t & -\sqrt{2}t \\ 0 & 0 & 0 & -\sqrt{2}t & 2\varepsilon_d + U & 0 \\ 0 & 0 & 0 & -\sqrt{2}t & 0 & 2\varepsilon_d + U \end{pmatrix}.$$

The eigenvalues and the corresponding eigenvectors are

$\|2,S,S_z\rangle_\alpha$	$E_\alpha(2,S)$	$d_\alpha(2,S)$
$\|2,0,0\rangle_+ = a_1\|2,0,0\rangle_0 - \frac{a_2}{\sqrt{2}}\big(\|2,0,0\rangle_1 + \|2,0,0\rangle_2\big)$	$2\varepsilon_d + \frac{1}{2}\left(U + \Delta(t,U)\right)$	1
$\|2,0,0\rangle_o = \frac{1}{\sqrt{2}}\big(\|2,0,0\rangle_1 - \|2,0,0\rangle_2\big)$	$2\varepsilon_d + U$	1
$\|2,1,m\rangle_o = \|2,1,m\rangle$	$2\varepsilon_d$	3
$\|2,0,0\rangle_- = a_2\|2,0,0\rangle_0 + \frac{a_1}{\sqrt{2}}\big(\|2,0,0\rangle_1 + \|2,0,0\rangle_2\big)$	$2\varepsilon_d + \frac{1}{2}\left(U - \Delta(t,U)\right)$	1

where

$$\Delta(t,U) = \sqrt{U^2 + 16t^2},$$

and

$$a_1^2 = a_1^2(t,U) = \frac{1}{\Delta(t,U)}\frac{\Delta(t,U) - U}{2} \qquad a_2^2 = a_2^2(t,U) = \frac{4t^2}{\Delta(t,U)}\frac{2}{(\Delta(t,U) - U)},$$

so that $a_1 a_2 = 2t/\Delta(t,U)$. For $U = 0$ we have $a_1 = a_2 = 1/\sqrt{2}$, and the two states $|2,0,0\rangle_-$ and $|2,0,0\rangle_+$ become, respectively, the state with two electrons in the bonding orbital and the state with two electrons in the antibonding orbital; they have energy $E_\pm(2,0) = 2\varepsilon_d \pm 2t$; the remaining states have energy $2\varepsilon_d$ and are non-bonding. For $t > 0$, the ground state is unique and it is always the singlet $|2,0,0\rangle_-$; in the large U limit its energy is

$$E_-(2,0) \sim 2\varepsilon_d - 4t^2/U.$$

In this limit the energy difference between the first excited state, a triplet state, and the singlet ground state is thus equal to the Heisenberg antiferromagnetic coupling

$$E_o(2,1) - E_-(2,0) \sim 4t^2/U = \Gamma.$$

Finally, for $N = 3$ electrons, eigenstates and eigenvectors are

$\lvert 3, S, S_z\rangle_\alpha$		$E_\alpha(3)$	$d_\alpha(3,S)$
$\lvert 3, 1/2, \sigma\rangle_+$	$= \frac{1}{\sqrt{2}}\big(\lvert 1, 1/2, \sigma\rangle_1 + \lvert 1, 1/2, \sigma\rangle_2\big)$	$3\varepsilon_d + U + t$	2
$\lvert 3, 1/2, \sigma\rangle_-$	$= \frac{1}{\sqrt{2}}\big(\lvert 1, 1/2, \sigma\rangle_1 - \lvert 1, 1/2, \sigma\rangle_2\big)$	$3\varepsilon_d + U - t$	2

If we exchange holes and electrons, the $N = 3$ case is identical to the $N = 1$ electron case. This is due to the particle-hole symmetry of the model.

A.2 Anderson molecule

The Hamiltonian of the Anderson molecule is given by

$$\hat{H} = \varepsilon_s \sum_\sigma \hat{n}_{2\sigma} - t \sum_\sigma \left(c^\dagger_{1\sigma} c_{2\sigma} + c^\dagger_{2\sigma} c_{1\sigma}\right) + \varepsilon_d \sum_\sigma \hat{n}_{1\sigma} + U \hat{n}_{1\uparrow} \hat{n}_{1\downarrow}.$$

In the atomic limit, its eigenstates states can be classified as

$\lvert N, S, S_z\rangle$			N	S	$E(N,S)$
$\lvert 0, 0, 0\rangle$	$=$	$\lvert 0\rangle$	0	0	0
$\lvert 1, 1/2, \sigma\rangle_1$	$=$	$c^\dagger_{1\sigma}\lvert 0\rangle$	1	1/2	ε_d
$\lvert 1, 1/2, \sigma\rangle_2$	$=$	$c^\dagger_{2\sigma}\lvert 0\rangle$	1	1/2	ε_s
$\lvert 2, 1, 1\rangle$	$=$	$c^\dagger_{2\uparrow} c^\dagger_{1\uparrow}\lvert 0\rangle$	2	1	$\varepsilon_d + \varepsilon_s$
$\lvert 2, 1, -1\rangle$	$=$	$c^\dagger_{2\downarrow} c^\dagger_{1\downarrow}\lvert 0\rangle$	2	1	$\varepsilon_d + \varepsilon_s$
$\lvert 2, 1, 0\rangle$	$=$	$\frac{1}{\sqrt{2}}\left(c^\dagger_{1\uparrow} c^\dagger_{2\downarrow} + c^\dagger_{1\downarrow} c^\dagger_{2\uparrow}\right)\lvert 0\rangle$	2	1	$\varepsilon_d + \varepsilon_s$
$\lvert 2, 0, 0\rangle_0$	$=$	$\frac{1}{\sqrt{2}}\left(c^\dagger_{1\uparrow} c^\dagger_{2\downarrow} - c^\dagger_{1\downarrow} c^\dagger_{2\uparrow}\right)\lvert 0\rangle$	2	0	$\varepsilon_d + \varepsilon_s$
$\lvert 2, 0, 0\rangle_1$	$=$	$c^\dagger_{1\uparrow} c^\dagger_{1\downarrow}\lvert 0\rangle$	2	0	$2\varepsilon_d + U$
$\lvert 2, 0, 0\rangle_2$	$=$	$c^\dagger_{2\uparrow} c^\dagger_{2\downarrow}\lvert 0\rangle$	2	0	$2\varepsilon_s$
$\lvert 3, 1/2, \sigma\rangle_1$	$=$	$c^\dagger_{1\sigma} c^\dagger_{2\uparrow} c^\dagger_{2\downarrow}\lvert 0\rangle$	3	1/2	$\varepsilon_d + 2\varepsilon_s$
$\lvert 3, 1/2, \sigma\rangle_2$	$=$	$c^\dagger_{2\sigma} c^\dagger_{1\uparrow} c^\dagger_{1\downarrow}\lvert 0\rangle$	3	1/2	$2\varepsilon_d + \varepsilon_s + U$
$\lvert 4, 0, 0\rangle$	$=$	$c^\dagger_{1\uparrow} c^\dagger_{1\downarrow} c^\dagger_{2\uparrow} c^\dagger_{2\downarrow}\lvert 0\rangle$	4	0	$2\varepsilon_d + 2\varepsilon_s + U$

For $N = 1$ electrons the Hamiltonian can be written in the matrix form

$$\hat{H}_1 = \begin{pmatrix} \varepsilon_d & -t & 0 & 0 \\ -t & \varepsilon_s & 0 & 0 \\ 0 & 0 & \varepsilon_d & -t \\ 0 & 0 & -t & \varepsilon_s \end{pmatrix}.$$

The eigenstates are thus

$\|1, S, S_z\rangle_\alpha$	$E_\alpha(1, S)$	$d_\alpha(1, S)$
$\|1, 1/2, \sigma\rangle_+ = \alpha_1 \|1, 1/2, \sigma\rangle_1 - \alpha_2 \|1, 1/2, \sigma\rangle_2$	$\frac{1}{2}\big(\varepsilon_d + \varepsilon_s + \sqrt{(\varepsilon_d - \varepsilon_s)^2 + 4t^2}\big)$	2
$\|1, 1/2, \sigma\rangle_- = \alpha_2 \|1, 1/2, \sigma\rangle_1 + \alpha_1 \|1, 1/2, \sigma\rangle_2$	$\frac{1}{2}\big(\varepsilon_d + \varepsilon_s - \sqrt{(\varepsilon_d - \varepsilon_s)^2 + 4t^2}\big)$	2

where $d_\alpha(N)$ is the spin degeneracy of the α manifold. For $\varepsilon_s = \varepsilon_d + U/2$ the eigenvalues are

$$E_\pm(1, S) = \varepsilon_d + \frac{1}{4}\big(U \pm \Delta(t, U)\big),$$

while the coefficients are $\alpha_1 = a_1(t, U)$ and $\alpha_2 = a_2(t, U)$.
For N=2 electrons, the hopping integrals only couple the S=0 states. The Hamiltonian is

$$\hat{H}_2 = \begin{pmatrix} \varepsilon_d{+}\varepsilon_s & 0 & 0 & 0 & 0 & 0 \\ 0 & \varepsilon_d{+}\varepsilon_s & 0 & 0 & 0 & 0 \\ 0 & 0 & \varepsilon_d{+}\varepsilon_s & 0 & 0 & 0 \\ 0 & 0 & 0 & \varepsilon_d{+}\varepsilon_s & -\sqrt{2}t & -\sqrt{2}t \\ 0 & 0 & 0 & -\sqrt{2}t & 2\varepsilon_d{+}U & 0 \\ 0 & 0 & 0 & -\sqrt{2}t & 0 & 2\varepsilon_s \end{pmatrix}$$

For $\varepsilon_s = \varepsilon_d + U/2$ the eigenvalues and the corresponding eigenvectors are

$\|2, S, S_z\rangle_\alpha$	$E_\alpha(2, S)$	$d_\alpha(2, S)$
$\|2, 0, 0\rangle_+ = b_1 \|2, 0, 0\rangle_0 - \frac{b_2}{\sqrt{2}}\big(\|2, 0, 0\rangle_1 + \|2, 0, 0\rangle_2\big)$	$2\varepsilon_d + \frac{U}{2} + \frac{1}{4}\big(U + 2\Delta(t, \frac{U}{2})\big)$	1
$\|2, 0, 0\rangle_o = \frac{1}{\sqrt{2}}\big(\|2, 0, 0\rangle_1 - \|2, 0, 0\rangle_2\big)$	$2\varepsilon_d + U$	1
$\|2, 1, m\rangle_o = \|2, 1, m\rangle$	$2\varepsilon_d + \frac{U}{2}$	3
$\|2, 0, 0\rangle_- = b_2 \|2, 0, 0\rangle_0 + \frac{b_1}{\sqrt{2}}\big(\|2, 0, 0\rangle_1 + \|2, 0, 0\rangle_2\big)$	$2\varepsilon_d + \frac{U}{2} + \frac{1}{4}\big(U - 2\Delta(t, \frac{U}{2})\big)$	1

where $b_1 = a_1(t, U/2)$ and $b_2 = a_2(t, U/2)$. These states have the same form as in the case of the Hubbard dimer; the ground state energy and the weight of doubly occupied states in $|2, 0, 0\rangle_-$ differ, however. Finally, for $N = 3$ electrons, the eigenstates are

$\|3, S, S_z\rangle_\alpha$	$E_\alpha(3, S)$	$d_\alpha(3, S)$
$\|3, 1/2, \sigma\rangle_+ = \alpha_2 \|1, 1/2, \sigma\rangle_1 + \alpha_1 \|1, 1/2, \sigma\rangle_2$	$3\varepsilon_d + U + \frac{1}{4}\big(U + \Delta(t, U)\big)$	2
$\|3, 1/2, \sigma\rangle_- = \alpha_1 \|1, 1/2, \sigma\rangle_1 - \alpha_2 \|1, 1/2, \sigma\rangle_2$	$3\varepsilon_d + U + \frac{1}{4}\big(U - \Delta(t, U)\big)$	2

B Lehmann representation of the local Green function

For a single-orbital model, the local Matsubara Green function for a given site i is defined as

$$G^{\sigma}_{i,i}(i\nu_n) = -\int_0^{\beta} d\tau e^{i\nu_n\tau}\big\langle \mathcal{T} c_{i\sigma}(\tau)c^{\dagger}_{i\sigma}(0)\big\rangle,$$

where $\mathcal{T}$ is the time-ordering operator, $\beta = 1/k_BT$, and ν_n a fermionic Matsubara frequency. Let us assume we know all eigenstates $|N_l\rangle$ and their energy $E_l(N)$, for arbitrary number of electrons N. Thus, formally

$$G^{\sigma}_{i,i}(i\nu_n) = -\frac{1}{Z}\sum_{Nl}\int_0^{\beta} d\tau e^{i\nu_n\tau}e^{-\Delta E_l(N)\beta}\big\langle N_l\big|c_{i\sigma}(\tau)c^{\dagger}_{i\sigma}(0)\big|N_l\big\rangle,$$

where $Z = \sum_{Nl} e^{-\Delta E_l(N)\beta}$ is the partition function, $\Delta E_l(N) = E_l(N) - \mu N$ with μ the chemical potential, and $c^{\dagger}_{i\sigma}(0) = c^{\dagger}_{i\sigma}$. We now insert a complete set of states, obtaining

$$\begin{aligned} G^{\sigma}_{i,i}(i\nu_n) &= -\frac{1}{Z}\sum_{ll'NN'}\int_0^{\beta} d\tau e^{i\nu_n\tau}e^{-\Delta E_l(N)\beta}\big\langle N_l\big|c_{i\sigma}(\tau)|N'_{l'}\big\rangle\big\langle N'_{l'}\big|c^{\dagger}_{i\sigma}\big|N_l\big\rangle \\ &= -\frac{1}{Z}\sum_{ll'NN'}\int_0^{\beta} d\tau e^{-\Delta E_l(N)\beta}e^{(i\nu_n+\Delta E_l(N)-\Delta E_{l'}(N'))\tau}\big|\langle N'_{l'}|c^{\dagger}_{i\sigma}|N_l\rangle\big|^2 \\ &= \frac{1}{Z}\sum_{ll'NN'}\frac{e^{-\Delta E_{l'}(N')\beta}+e^{-\Delta E_l(N)\beta}}{i\nu_n+\Delta E_l(N)-\Delta E_{l'}(N')}\big|\langle N'_{l'}|c^{\dagger}_{i\sigma}|N_l\rangle\big|^2. \end{aligned}$$

Due to the weight $\big|\langle N'_{l'}|c^{\dagger}_{i\sigma}(0)|N_l\rangle\big|^2$ only the terms for which $N' = N+1$ contribute. Thus, after exchanging the labels $l'N' \leftrightarrow lN$ in the first addend, we obtain the Lehmann representation

$$G^{\sigma}_{i,i}(i\nu_n)=\sum_{ll'N}\frac{e^{-\beta\Delta E_l(N)}}{Z}\left(\frac{\big|\langle(N-1)_{l'}|c_{i\sigma}|N_l\rangle\big|^2}{i\nu_n-\Delta E_l(N)+\Delta E_{l'}(N-1)}+\frac{\big|\langle(N+1)_{l'}|c^{\dagger}_{i\sigma}|N_l\rangle\big|^2}{i\nu_n-\Delta E_{l'}(N+1)+\Delta E_l(N)}\right).$$

Let us consider as example the atomic limit of the Hubbard model at half filling. In this case all sites are decoupled; there are four eigenstates per site, the vacuum $|0\rangle$, with $\Delta E(0) = 0$, the doublet $|1_\sigma\rangle = c^{\dagger}_{i\sigma}|0\rangle$, with $\Delta E_\sigma(1) = -U/2$, and the doubly-occupied singlet $|2\rangle = c^{\dagger}_{i\uparrow}c^{\dagger}_{i\downarrow}|0\rangle$, with $\Delta E(2) = 0$. Furthermore, $Z = 2(1 + e^{\beta U/2})$ and

$$\big|\langle(N-1)_{l'}|c_{i\sigma}|N_l\rangle\big|^2=\begin{cases}1 & \text{if } |N_l\rangle=|2\rangle\vee|1_\sigma\rangle\\ 0 & \text{otherwise}\end{cases}\qquad \big|\langle(N+1)_{l'}|c^{\dagger}_{i\sigma}|N_l\rangle\big|^2=\begin{cases}1 & \text{if } |N_l\rangle=|0\rangle\vee|1_{-\sigma}\rangle\\ 0 & \text{otherwise}\end{cases}$$

Thus, after summing up the four non-zero contributions, we find

$$G^{\sigma}_{i,i}(\nu_n) = \frac{1}{2}\left(\frac{1}{i\nu_n+U/2}+\frac{1}{i\nu_n-U/2}\right).$$

C Atomic magnetic susceptibility

Let us consider an idealized single-level atom described by the Hamiltonian

$$\hat{H} = \varepsilon_d\big(\hat{n}_\uparrow + \hat{n}_\downarrow\big) + U n_\uparrow n_\downarrow.$$

The eigenstates of this system, $|\Psi_i^N\rangle$, as well as their expectation values at half filling are

$\lvert\Psi_i^N\rangle$	N	$\Delta E_i = \big\langle\Psi_i^N\big\lvert\hat{H}-\mu\hat{N}\big\rvert\Psi_i^N\big\rangle$
$\lvert 0\rangle$	0	0
$c_\sigma^\dagger\lvert 0\rangle$	1	$-\frac{U}{2}$
$c_\uparrow^\dagger c_\downarrow^\dagger\lvert 0\rangle$	2	0

The magnetic susceptibility in Matsubara space is given by

$$\Big[\chi_{zz}(i\omega_m)\Big]_{nn'} = \beta\frac{1}{4}(g\mu_B)^2\sum_P \mathrm{sign}(P) f_P$$

$$f_P(i\omega_{P_1}, i\omega_{P_2}, i\omega_{P_3}) = \int_0^\beta d\tau_{14}\int_0^{\tau_{14}} d\tau_{24}\int_0^{\tau_{24}} d\tau_{34}\; e^{i\omega_{P_1}\tau_{14}+i\omega_{P_2}\tau_{24}+i\omega_{P_3}\tau_{34}} f_P(\tau_{14},\tau_{24},\tau_{34})$$

where $P = A, B, \ldots$ are the six possible permutations of the indices (123) and

$$\begin{aligned} f_P(\tau_{14},\tau_{24},\tau_{34}) &= \frac{1}{Z}\sum_{\sigma\sigma'}\sigma\sigma'\mathrm{Tr}\; e^{-\beta(\hat{H}-\mu\hat{N})}\Big[\hat{o}_{P_1}(\tau_{14})\hat{o}_{P_2}(\tau_{24})\hat{o}_{P_3}(\tau_{34})c_{\sigma'}^\dagger\Big] \\ &= \frac{1}{Z}\sum_{\sigma\sigma'}\sigma\sigma'\sum_{ijkl} e^{-\beta\Delta E_i}\langle i|\hat{o}_{P_1}|j\rangle\langle j|\hat{o}_{P_2}|k\rangle\langle k|\hat{o}_{P_3}|l\rangle\langle l|c_{\sigma'}^\dagger|i\rangle \\ &\quad\times\left[e^{\Delta E_{ij}\tau_{14}+\Delta E_{jk}\tau_{24}+\Delta E_{kl}\tau_{34}}\right], \end{aligned}$$

where $\Delta E_{ij} = \Delta E_i - \Delta E_j$. For the identity permutation the operators are $\hat{o}_{P_1} = c_\sigma$, $\hat{o}_{P_2} = c_\sigma^\dagger$, and $\hat{o}_{P_3} = c_{\sigma'}$ and the frequencies are $\omega_1 = \nu_n$, $\omega_2 = -\omega_m - \nu_n$, $\omega_3 = \omega_m + \nu_{n'}$. This expression can be used to calculate the magnetic susceptibility of any one-band system whose eigenvalues and eigenvectors are known, e.g., via exact diagonalization. In the case of our idealized atom

$$f_E(\tau_{14},\tau_{24},\tau_{34}) = \frac{1}{(1+e^{\beta U/2})}\; e^{\beta U/2}\; e^{-(\tau_{12}+\tau_{34})U/2} = \frac{1}{(1+e^{\beta U/2})}\; g_E(\tau_{14},\tau_{24},\tau_{34}).$$

The frequencies and functions $f_P(\tau_{14},\tau_{24},\tau_{34})$ for all permutations are given in the table below

	ω_{P_1}	ω_{P_2}	ω_{P_3}	$g_P(\tau_{14},\tau_{24},\tau_{34})$	$\mathrm{sign}(P)$
$E(123)$	ν_n	$-\omega_m-\nu_n$	$\omega_m+\nu_{n'}$	$e^{\beta U/2}\, e^{-(\tau_{12}+\tau_{34})U/2}$	$+$
$A(231)$	$-\omega_m-\nu_n$	$\omega_m+\nu_{n'}$	ν_n	$e^{\beta U/2}\, e^{-(\tau_{12}+\tau_{34})U/2}$	$+$
$B(312)$	$\omega_m+\nu_{n'}$	ν_n	$-\omega_m-\nu_n$	$-e^{+(\tau_{12}+\tau_{34})U/2}$	$+$
$C(213)$	$-\omega_m-\nu_n$	ν_n	$\omega_m+\nu_{n'}$	$-e^{\beta U/2}e^{-(\tau_{12}+\tau_{34})U/2}$	$-$
$D(132)$	ν_n	$\omega_m+\nu_{n'}$	$-\omega_m-\nu_n$	$e^{+(\tau_{12}+\tau_{34})U/2}$	$-$
$F(321)$	$\omega_m+\nu_{n'}$	$-\omega_m-\nu_n$	ν_n	$e^{+(\tau_{12}+\tau_{34})U/2}$	$-$

The missing ingredient is the integral

$$
\begin{aligned}
I_P(x,-x,x;i\omega_{P_1},i\omega_{P_2},i\omega_{P_3}) &= \int_0^\beta d\tau_{14}\int_0^{\tau_{14}} d\tau_{24}\int_0^{\tau_{24}} d\tau_{34}\, e^{i\omega_{P_1}\tau_{14}+i\omega_{P_2}\tau_{24}+i\omega_{P_3}\tau_{34}} e^{x(\tau_{14}-\tau_{24}+\tau_{34})} \\
&= +\int_0^\beta d\tau_{14}\int_0^{\tau_{14}} d\tau\int_0^{\tau_{14}-\tau} d\tau'\, e^{(i\omega_{P_1}+i\omega_{P_2}+i\omega_{P_3}+x)\tau_{14}-i(\omega_{P_2}+\omega_{P_3})\tau} e^{-(i\omega_{P_3}+x)\tau'} \\
&= +\frac{1}{i\omega_{P_3}+x}\frac{1}{-i\omega_{P_2}+x}\left[\frac{1}{i\omega_{P_1}+x}\,\frac{1}{n(x)}+\beta\delta_{\omega_{P_1}+\omega_{P_2}}\right] \\
&\quad +\frac{1}{i\omega_{P_3}+x}\frac{1-\delta_{\omega_{P_2}+\omega_{P_3}}}{i(\omega_{P_2}+\omega_{P_3})}\left[\frac{1}{i\omega_{P_1}+x}-\frac{1}{i(\omega_{P_1}+\omega_{P_2}+\omega_{P_3})+x}\right]\frac{1}{n(x)} \\
&\quad +\delta_{\omega_{P_2}+\omega_{P_3}}\frac{1}{i\omega_{P_3}+x}\left\{\left[\frac{1}{(i\omega_{P_1}+x)}\right]^2\frac{1}{n(x)}-\beta\left[\frac{1}{(i\omega_{P_1}+x)}\right]\frac{1-n(x)}{n(x)}\right\}.
\end{aligned}
$$

where $x = \pm U/2$, depending on the permutation. Summing up all terms we obtain the final expression for $\omega_m = 0$. Setting $y = U/2$ we have in total [11]

$$
\begin{aligned}
\sum_{\sigma\sigma'}\sigma\sigma'\,\chi^{n,n'}_{i\sigma\sigma,i\sigma'\sigma'}(0) =& M_{n'}\frac{dM_n}{dy}+M_n\frac{dM_{n'}}{dy}-\beta n(y)\left[\delta_{n,n'}+\delta_{n,-n'}\right]\frac{dM_n}{dy}+\beta n(-y)M_nM_{n'} \\
&-\frac{1}{y}\left\{M_{n'}-\beta\left[n(y)\delta_{n,-n'}-n(-y)\delta_{n,n'}\right]\right\}M_n
\end{aligned}
\tag{33}
$$

where

$$
M_n = \frac{1}{i\nu_n - y}-\frac{1}{i\nu_n+y}. \tag{34}
$$

The finite frequency term (not given here) vanishes once we sum over n, n'.

References

[1] W. Metzner and D. Vollhardt, Phys. Rev. Lett. **62**, 324 (1989)

[2] E. Müller-Hartmann, Z. Phys. B **74**, 507 (1989); Z. Phys. B **76**, 211 (1989); Int. J. Mod. Phys. B **3**, 2169 (1989)

[3] A. Georges and G. Kotliar, Phys. Rev. B **45**, 6479 (1992)

[4] M. Jarrell, Phys. Rev. Lett. **69**, 168 (1992)

[5] E. Pavarini, E. Koch, D. Vollhardt, A. Lichtenstein (Eds.): *The LDA+DMFT approach to strongly-correlated materials*, Reihe Modeling and Simulation, Vol. 1 (Forschungszentrum Jülich, 2011) http://www.cond-mat.de/events/correl11

[6] E. Pavarini, E. Koch, A. Lichtenstein, D. Vollhardt (Eds.): *DMFT at 25: Infinite Dimensions*, Reihe Modeling and Simulation, Vol. 4 (Forschungszentrum Jülich, 2014) http://www.cond-mat.de/events/correl14

[7] E. Pavarini, E. Koch, A. Lichtenstein, D. Vollhardt (Eds.): *DMFT: From Infinite Dimensions to Real Materials*, Reihe Modeling and Simulation, Vol. 8 (Forschungszentrum Jülich, 2018) http://www.cond-mat.de/events/correl18

[8] E. Koch, G. Sangiovanni, and O. Gunnarsson, Phys. Rev. B **78**, 115102 (2008)

[9] E. Gull, A.J. Millis, A.I. Lichtenstein, A.N. Rubtsov, M. Troyer, and P. Werner, Rev. Mod. Phys. **83**, 349 (2011)

[10] A. Flesch, E. Gorelov, E. Koch, E. Pavarini, Phys. Rev. B **87**, 195141 (2013)

[11] A. Kiani and E. Pavarini, Phys. Rev. B **94**, 075112 (2016)

[12] E. Pavarini, A. Yamasaki, J. Nuss, and O.K. Andersen, New. J. Phys **7**, 188 (2005)

[13] N. Marzari, A.A. Mostofi, J.R. Yates, I. Souza, and D. Vanderbilt, Rev. Mod. Phys. **84**, 1419 (2012)

[14] V. Slatić and B. Horvatić, Sol. Stat. Comm. **75**, 263 (1990)

[15] L. Boehnke, H. Hafermann, M. Ferrero, F. Lechermann and O. Parcollet, Phys. Rev. B **84**, 075145 (2011)

[16] J. Musshoff, G. Zhang, E. Koch, and E. Pavarini, Phys. Rev. B **100**, 045116 (2019)

[17] A. Georges, G. Kotliar, W. Krauth and M.J. Rozenberg, Rev. Mod. Phys. **68**, 13 (1996)

[18] E. Pavarini, S. Biermann, A. Poteryaev, A.I. Lichtenstein, A. Georges, and O.K. Andersen, Phys. Rev. Lett. **92**, 176403 (2004)

9 Correlated Matter: DMFT and Beyond

Alexander Lichtenstein
I. Institut für Theoretische Physik
Universität Hamburg

Contents

E. Pavarini and E. Koch (eds.)
Topology, Entanglement, and Strong Correlations
Modeling and Simulation Vol. 10
Forschungszentrum Jülich, 2020, ISBN 978-3-95806-466-9
http://www.cond-mat.de/events/correl20

1 Introduction: Reference systems

In this lecture we give an introduction to the theoretical description of strongly correlated materials based on non-local extensions of the dynamical mean-field theory (DMFT). This scheme combines the numerically exact DMFT solution of the effective impurity problem with an analytical non-local perturbation scheme. The frequency dependent effective impurity DMFT problem nowadays can be efficiently solved within the continuous time quantum Monte Carlo (CT-QMC) scheme [1]. Therefore the perturbation theory needs to be formulated in the action path-integral formalism. We give a brief introduction to the path integral over fermionic Grassmann fields and formulate a general scheme for the expansion around the DMFT solution using a special dual-space transformation. We discuss here a general way to include nonlocal correlations beyond the DMFT, based on the generalized Hubbard model [2] and describe the dual-fermion formalism [3].

Consider the noninteracting, "kinetic" part H_t of the Hubbard model first [4]. This is fixed by specifying the hopping-matrix elements t_{ij} between sites i and j. In the absence of the local Hubbard-interaction term, H_t is easily diagonalized. For a Hubbard model on a lattice, diagonalization is achieved by Fourier transformation of the hopping parameters to $\mathbf{k}$-space, and one has the normal "band structure" for a single-orbital model, particularly the simple $\varepsilon_{\mathbf{k}} = t_{\mathbf{k}}$ with band-width W. If, on the other hand, only the local part of the Hamiltonian is kept, i.e., the Hubbard interaction H_U with interaction strength U and the local term of H_t is fixed by the on-site energy ε_0, the diagonalization of the Hamiltonian is again trivial and reduces to the diagonalization of a single "Hubbard atom".

The great success of the DMFT approach is related to it numerically interpolating between these two limits [5]. For the Hubbard model on an infinite-dimensional Bethe lattice at half-filling the DMFT gives the exact description of the Mott-transition [6] between the weak-coupling ($U/W \ll 1$) metallic state and the strong-coupling ($U/W \gg 1$) insulating paramagnetic state [7]. In a nutshell, DMFT maps the correlated Hubbard lattice problem onto the self-consistent solution of an effective Anderson impurity problem with a single interacting Hubbard atom (interaction strength U) in a non-interacting fermionic bath (which mimics the rest of the crystal).

Now we can think of how to incorporate nonlocal correlations beyond the DMFT: since the Hubbard and the Anderson-impurity model share the same interaction part, one can think of the Hubbard model as the impurity model plus a residual term $\propto (t_{\mathbf{k}} - \Delta_\nu)$ and treat this *perturbatively*. Since this term is frequency dependent, we need a novel perturbation theory based on the action formalism. One may view this idea as a generalization of the Kohn-Sham idea in density functional theory (DFT) [8] of an optimal reference system, but with a crucial difference. Here, not an interacting homogeneous electron gas, but an effective impurity model, tailored to the problem of strong correlations, serves as the reference system, see Fig. 1. Since in zeroth order of this perturbative expansion, i.e., on the level of the DMFT problem, we already have an interacting problem and since the perturbation is momentum and frequency dependent, one is forced to replace the Hamiltonians by actions within the path-integral formalism. Note that the fermion path-integral can also be used to formulate the DMFT itself [5, 9]. Now, the separation

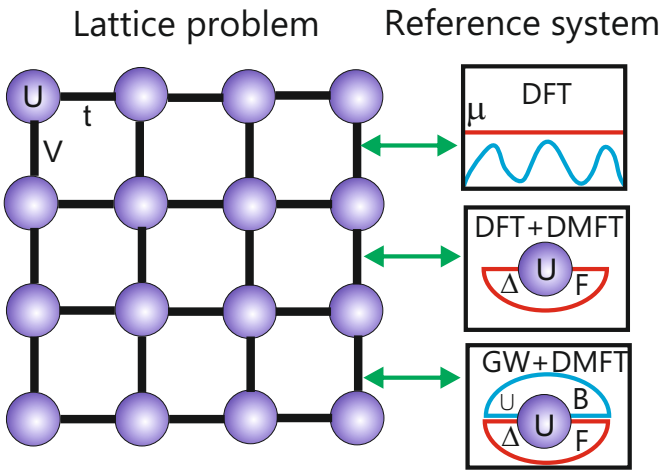

Fig. 1: *Schematic representation of the reference systems in many-body approaches to lattice-fermion models: (i) Density-functional theory (DFT) with the interacting homogeneous electron gas as a reference system, defined by a constant external potential μ. (ii) Dynamical mean-field theory (DMFT) with an effective impurity problem as a reference system, defined by fermionic bath, specified by the hybridization function Δ. (iii) GW+DMFT with a correlated atom in a fermionic (Δ) and a bosonic bath (Λ) due to effects of the frequency-dependent screening of long-range Coulomb (V) interactions.*

of the local and nonlocal terms is achieved by a Hubbard-Stratonovich transformation applied to the single-particle $(t_{\mathbf{k}}-\Delta_\nu)$-term [3]. This provides us with a new action. Moreover, it is formally possible to integrate-out the original local degrees of freedom and in this way generated an effective action in the transformed, so-called dual-fermion representation [3]. Note that integrating out the local degrees of freedom is not only a formal step but can be achieved in practice, by solving the impurity problem within the numerically exact CT-QMC method.

The dual action consists of a bare dual propagator (non-local part of the DMFT Green function) $\tilde{G}^0_{\mathbf{k},\nu}$ and a local but frequency-dependent effective potential related to scattering processes of two, three, and more dual particles on the impurity site. The simplest two-particle dual potential coincides with the fully connected part of the screened impurity interaction vertex $\gamma^\omega_{\nu\nu'}$, which can be calculated with the impurity CT-QMC solver as a function of bosonic (ω) and fermionic (ν,ν') Matsubara frequencies. Normally, correlations between three particles on the DMFT impurity site are much weaker than two-particle correlations and can be ignored. The same applies to higher-order terms. One can think of the dual-fermion formalism as an expansion in the order of local multi-particle correlation functions. This means that "bare" interactions between dual fermions are related with the connected part of the screened impurity vertex. Standard diagrammatic techniques can be applied for calculations of the bold dual propagator $\tilde{G}_{\mathbf{k},\nu}$, which allows to obtain the nonlocal self-energy for the original fermions [3] and to describe nonlocal correlations beyond the DMFT.

The dual-fermion approach is not necessarily bound to a specific starting point. However, the DMFT starting point is very efficient. Namely, it corresponds to the elimination of all local diagrams for any n-particle correlation of dual fermions when using the DMFT self-consistency equation. In the dual space, this simply reduces to $\sum_{\mathbf{k}} \tilde{G}^0_{\mathbf{k},\nu} = 0$ and means that, on average

over the whole Brillouin zone, Δ_ν optimally approximates the electron spectrum $\varepsilon_{\mathbf{k}}$, including its local correlation effects. Therefore, the noninteracting dual fermions correspond to strongly correlated DMFT quasiparticles, and the remaining nonlocal effects can be quite small and reasonably described by perturbative summations of dual diagrams. This also explains the notion "dual fermions".

2 Functional approach

We introduce a general functional approach which will cover the density functional (DFT), dynamical mean-field, (DMFT) and Baym-Kadanoff (BK) theories [9]. Let us start from the full many-body Hamiltonian describing electrons moving in the periodic external potential of ions $V(\mathbf{r})$ with chemical potential μ and interacting via Coulomb law: $U(\mathbf{r}-\mathbf{r}') = 1/|\mathbf{r}-\mathbf{r}'|$. We use the atomic units $\hbar = m = e = 1$. In the field-operator representation the Hamiltonian has the form

$$H = \sum_\sigma \int d\mathbf{r}\, \hat\psi^\dagger_\sigma(\mathbf{r}) \left(-\frac{\nabla^2}{2} + V(\mathbf{r}) - \mu \right) \hat\psi_\sigma(\mathbf{r}) + \frac{1}{2} \sum_{\sigma\sigma'} \int d\mathbf{r} \int d\mathbf{r}' \hat\psi^\dagger_\sigma(\mathbf{r}) \hat\psi^\dagger_{\sigma'}(\mathbf{r}')\, U(\mathbf{r}-\mathbf{r}')\, \hat\psi_{\sigma'}(\mathbf{r}') \hat\psi_\sigma(\mathbf{r}) \tag{1}$$

We can always use a single-particle orthonormal basis set in solids $\varphi_n(\mathbf{r})$, for example Wannier orbitals with full set of quantum numbers, e.g., site, orbital and spin index: $n = (i, m, \sigma)$ and expand the fields in creation and annihilation operators

$$\hat\psi(\mathbf{r}) = \sum_n \varphi_n(\mathbf{r})\, \hat c_n \qquad \hat\psi^\dagger(\mathbf{r}) = \sum_n \varphi^*_n(\mathbf{r})\, \hat c^\dagger_n. \tag{2}$$

Going from fermionic operators to the Grassmann variables $\{c^*_n, c_n\}$ we can write the functional integral representation for partition function of the many-body Hamiltonian in the imaginary time domain using the Euclidean action S

$$Z = \int \mathcal{D}[c^*, c]\, e^{-S}\,, \qquad S = \sum_{12} c^*_1 (\partial_\tau + t_{12}) c_2 + \frac{1}{2} \sum_{1234} c^*_1 c^*_2\, U_{1234}\, c_4 c_3, \tag{3}$$

where the one- and two-electron matrix elements are defined as

$$t_{12} = \int d\mathbf{r}\, \varphi^*_1(\mathbf{r}) \left(-\frac{1}{2}\nabla^2 + V(\mathbf{r}) - \mu \right) \varphi_2(\mathbf{r}) \tag{4}$$

$$U_{1234} = \int d\mathbf{r} \int d\mathbf{r}'\, \varphi^*_1(\mathbf{r}) \varphi^*_2(\mathbf{r}')\, U(\mathbf{r}-\mathbf{r}')\, \varphi_3(\mathbf{r}) \varphi_4(\mathbf{r}').$$

and we use the following short definition of the sum

$$\sum_1 \cdots \equiv \sum_{im} \int d\tau\, \cdots \tag{5}$$

The one-electron Green function is defined via a simple non-zero correlation function for fermions

$$G_{12} = -\left\langle c_1 c^*_2 \right\rangle_S = -\frac{1}{Z} \int \mathcal{D}[c^*, c]\, c_1 c^*_2\, \exp(-S). \tag{6}$$

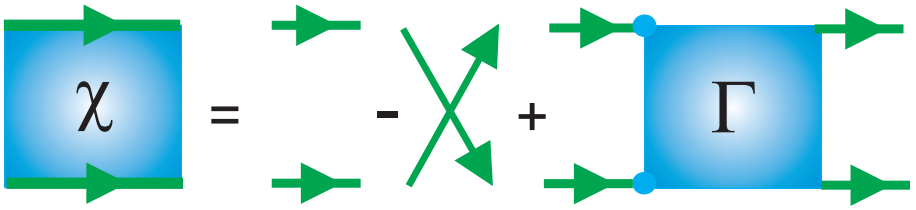

Fig. 2: *Representation of the full two-particle Green function in terms of trivial products of single-particle Green function and the full vertex function Γ.*

The main problem of strongly interacting electronic systems are related to the fact that the higher-order correlation functions do not separate into products of lower order correlation function. For example the two-particle Green function or generalized susceptibility (X) is defined in the following form [10]

$$X_{1234} = \left\langle c_1 c_2 c_3^* c_4^* \right\rangle_S = \frac{1}{Z} \int \mathcal{D}[c^*, c]\, c_1 c_2 c_3^* c_4^* \, \exp(-S), \tag{7}$$

and can be expressed graphically through the Green functions and the full vertex function Γ_{1234} [10, 11] (see Fig. 2)

$$X_{1234} = G_{14}G_{23} - G_{13}G_{24} + \sum_{1'2'3'4'} G_{11'}G_{22'}\Gamma_{1'2'3'4'}G_{3'3}G_{4'4} \tag{8}$$

In the case of non-interacting electron systems, the high-order correlations X are reduced to the antisymmetrized product of lower-order correlations G, which correspond to the first two terms (Hartree- and Fock-like) with the vertex function Γ in Eq. (8) equal to zero. In strongly correlated electron systems the last part with the vertex is dominant and even diverges close to the electronic phase transitions.

The Baym-Kadanoff functional [12] gives the one-particle Green function and the total free energy at its stationary point. In order to construct the exact functional of the Green function (Baym-Kadanoff) we modify the action by introducing the source term J

$$S[J] = S + \sum_{12} c_1^* J_{12} c_2. \tag{9}$$

The partition function Z, or equivalently the free energy of the system, F, becomes a functional of the auxiliary source field

$$Z[J] = e^{-F[J]} = \int \mathcal{D}[c^*, c]\, e^{-S'[J]}. \tag{10}$$

Variation of this source function gives all correlation functions, for example the Green function

$$G_{12} = \left. \frac{\delta F[J]}{\delta J_{21}} \right|_{J=0}. \tag{11}$$

If we use the definition of the generalized susceptibility as a second variation of the $F[J]$ functional instead of $Z[J]$ we will get only the connected part of the X-function, which is represented by the last term in Eq. (8).

The Baym-Kadanoff functional can be obtained by the Legendre transform from variable J to G

$$F[G] = F[J] - \mathrm{Tr}(JG), \tag{12}$$

We can use the standard decomposition of the free energy F into the single-particle part and the correlated part

$$F[G] = \mathrm{Tr}\ln G - \mathrm{Tr}\,(\Sigma G) + \Phi[G], \tag{13}$$

were Σ_{12} is the single particle self-energy and $\Phi[G]$ is the correlated part of the Baym-Kadanoff functional and is equal to the sum of all two-particle irreducible diagrams. At the stationary point this functional gives the free energy of the system. In practice, $\Phi[G]$ is not known for interacting electron systems, which is similar to the problem in density functional theory. Moreover, this general functional approach reduces to DFT, if one uses only the diagonal part in space-time of the Green function, which corresponds to the one-electron density

$$n_1 = G_{12}\,\delta_{12} = \langle c_1^* c_1 \rangle_S, \tag{14}$$

with the Kohn-Sham potential $V_{KS} = V_{ext}+V_H+V_{xc}$ playing the role of the "constrained field". Here V_{ext} is the external potential and V_H the Hartree potential. In principle the exchange-correlation potential V_{xc} is known only for the homogeneous electron gas, therefore in all practical applications one uses a so-called local density approximation to DFT. In this case the DFT functional defined as

$$F_{DFT}[n] = T_0[n] + V_{ext}[n] + V_H[n] + V_{xc}[n] \tag{15}$$

where T_0 is kinetic energy of non-interacting systems. Finally, if we define the total electron density as

$$n(\mathbf{r}) = \sum_i \varphi_i^*(\mathbf{r})\varphi_i(\mathbf{r})$$

the local density approximation to the DFT reads

$$T_0[n] + V_{ext}[n] = \sum_i \int d\mathbf{r}\,\varphi_i^*(\mathbf{r})\left(-\frac{1}{2}\nabla^2 + V_{ext}(\mathbf{r}) - \mu\right)\varphi_i(\mathbf{r}) \tag{16}$$

$$V_H[n] = \frac{1}{2}\int d\mathbf{r}\,n(\mathbf{r})\,U(\mathbf{r}-\mathbf{r}')\,n(\mathbf{r}') \tag{17}$$

$$V_{xc}[n] = \int d\mathbf{r}\,n(\mathbf{r})\varepsilon(n(\mathbf{r})) \tag{18}$$

where $\varepsilon(n)$ is the exchange-correlation density for the homogeneous electron gas, which can be calculated within a QMC-scheme [13].

In the DFT scheme we lose information about the non-equal time Green function, which gives the single particle excitation spectrum as well as the k-dependence of the spectral function, and restrict ourselves to only the ground state energy of the many-electron system. Moreover, we also lose also information about all collective excitations in solids, such as plasmons or

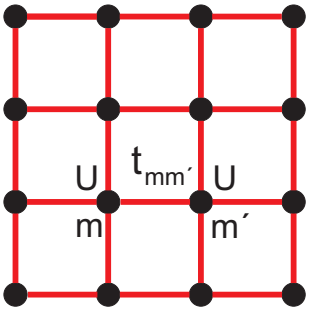

Fig. 3: *Generic Hubbard lattice for correlated lattice fermions with the local Coulomb interaction U and hopping parameters t: m can label different orbitals or lattice sites.*

magnons, which can be obtained from a generalized susceptibility or from the second variation of the free-energy.

One can probably find the Baym-Kadanoff interacting potential $\Phi[G]$ for simple lattice models using quantum Monte Carlo (QMC). Unfortunately due to the sign problem in lattice simulations this numerically exact solution of the electronic correlations is not feasible. On the other hand, one can obtain the solution of a local interacting quantum problem in a general fermionic bath, using the QMC scheme, which has no sign problem if it is diagonal in spin and orbital space. Therefore, a reasonable approach to strongly correlated systems is to keep only the local part of the many-body fluctuations. In such a Dynamical Mean-Field Theory (DMFT) one can obtain numerically the correlated part of the local functional. In this scheme we only use the local part of many electron vertex and obtain, in a self-consistent way, an effective functional of the local Green function. In the following section we discuss the general dual fermion (DF) transformations [3] which help us to separate the local fluctuations in many-body system and show a perturbative way to go beyond the DMFT approximations.

3 Dual fermion approach with a general reference system

We start with a general lattice fermion model with the local Hubbard-like interaction vertex U. Generalization to the multi-orbital case is straightforward [14]. All equations will be written in matrix form, giving an idea of how to rewrite the dual fermion (DF) formula to the multi-orbital or multi-site case. The general strategy is related with the formally exact separation of the local and non-local correlation effects. We introduce auxiliary dual fermionic fields which will couple local correlated impurities or clusters back to the original lattice [3].

Using the path-integral formalism (Appendix A) the partition function of a general fermionic lattice system (Fig. 3) can be written in following form as a functional integral over Grassmann variables $[c^*, c]$

$$Z = \int \mathcal{D}[c^*, c] \, \exp\left(-S_L[c^*, c]\right).$$

The original lattice action of interacting lattice fermions, similar to Eq. (3), can be written in Matsubara space as a sum of the lattice one-electron contributions with the Fourier transformed

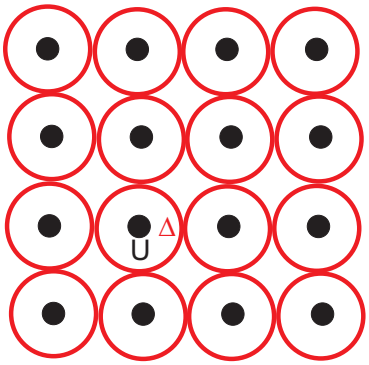

Fig. 4: *Schematic view on the real-space DMFT reference system.*

hopping $t_{\mathbf{k}}$ (or energy spectrum in the single-orbital case) and the local interaction part U

$$S_L[c^*,c] = -\sum_{\mathbf{k}\nu\sigma} c^*_{\mathbf{k}\nu\sigma}\big(i\nu{+}\mu{-}t_{\mathbf{k}}\big)\, c_{\mathbf{k}\nu\sigma} + \sum_i \int_0^\beta d\tau\, U\, n^*_{i\tau\uparrow} n_{i\tau\downarrow}\,. \tag{19}$$

In the following, $\nu = (2n{+}1)\pi/\beta, (\omega = 2n\pi/\beta), n = 0, \pm 1, \ldots$ are the fermionic (bosonic) Matsubara frequencies, β is the inverse temperature, $\tau \in [0,\beta)$ the imaginary time, and μ the chemical potential. The index i labels the lattice sites, m refers to different orbitals, σ is the spin projection and the $\mathbf{k}$-vectors are quasimomenta. In order to keep the notation simple, it is useful to introduce the combined index $|1\rangle \equiv |i,m,\sigma,\tau\rangle$ and assume summation over repeated indices. Translational invariance is assumed for simplicity in the following, although a real space formulation is straightforward. The local part of the action, S_U, may contain any type of local multi orbital interaction.

In order to formulate an expansion around the best possible reference action, Fig. 4, a quantum impurity (cluster) problem is introduced by a general frequency-dependent hybridization function Δ_ν and the same local interaction

$$S_\Delta[c^*_i,c_i] = -\sum_{\nu,\sigma} c^*_{i\nu\sigma}\big(i\nu{+}\mu{-}\Delta_\nu\big)c_{i\nu\sigma} + \sum_\nu U n^*_{i\nu\uparrow} n_{i\nu\downarrow}\,, \tag{20}$$

where Δ_ν is the effective hybridization matrix describing the coupling of the impurity to an auxiliary fermionic bath. The main motivation for rewriting the lattice action in terms of a quantum impurity model is that such a reference system can be solved numerically exactly for an arbitrary hybridization function using the CT-QMC methods [1]. Using the locality of the hybridization function Δ_ν, the lattice action Eq. (19) can be rewritten exactly in terms of individual impurity models and the effective one-electron coupling $(\Delta_\nu{-}t_{\mathbf{k}})$ between different impurities, Fig. 5,

$$S_L[c^*,c] = \sum_i S_\Delta[c^*_i,c_i] - \sum_{\mathbf{k}\nu\sigma} c^*_{\mathbf{k}\nu\sigma}\big(\Delta_\nu{-}t_{\mathbf{k}}\big)c_{\mathbf{k}\nu\sigma}\,. \tag{21}$$

We will find the condition for the optimal choice of the hybridization function later. Although we can solve the individual impurity model exactly, the effect of spatial correlations due to

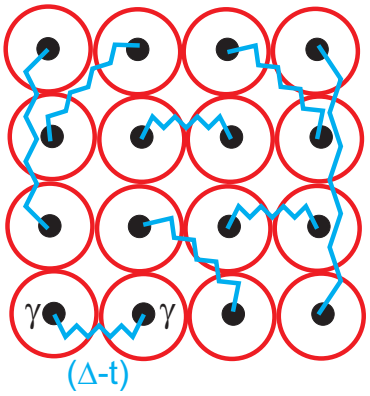

Fig. 5: *Schematic view on the non-local DF perturbation beyond a DMFT solution.*

the second term in Eq. (21) is very hard to treat, even perturbatively, since the impurity action is non-Gaussian and on cannot use of the Wick theorem. The main idea of the dual fermion transformation is to change of variables from strongly correlated fermions (c^*, c) to weakly correlated "dual" Grassmann fields (d^*, d) in the path-integral representation for the partition function of Eq. (3), followed by a simple perturbation treatment. The new variables were introduced through the following Hubbard-Stratonovich(HS)-transformation with the matrix $\widetilde{\Delta}_{\mathbf{k}\nu} = (\Delta_\nu - t_\mathbf{k})$

$$e^{c_1^*\,\widetilde{\Delta}_{12}\,c_2} = \det\widetilde{\Delta}\int\mathcal{D}\,[d^*,d]\;e^{-d_1^*\widetilde{\Delta}_{12}^{-1}d_2 - d_1^*c_1 - c_1^*d_1}. \tag{22}$$

We can immediately seen that using this HS-transformation we "localize" the $[c_i^*, c_j]$ fermions: while on the left-hand side they are still "hopping" through the lattice, on the right-hand side they are localized on one site $[c_i^*, c_i]$.
With this reference system the lattice partition function becomes

$$\frac{Z}{Z_d} = \int\mathcal{D}[c^*,c,d^*,d]\exp\bigl(-S[c^*,c,d^*,d]\bigr) \tag{23}$$

with $Z_d = \det\widetilde{\Delta}$. The lattice action transforms to

$$S[c^*,c,d^*,d] = \sum_i S_\Delta^i + \sum_{\mathbf{k},\nu,\sigma} d_{\mathbf{k}\nu\sigma}^*\bigl(\Delta_\nu - t_k\bigr)^{-1} d_{\mathbf{k}\nu\sigma}\,. \tag{24}$$

Hence the coupling between sites is transferred to a local coupling to the auxiliary fermions

$$S_\Delta^i[c_i^*,c_i,d_i^*,d_i] = S_\Delta[c_i^*,c_i] + \sum_{\nu,\sigma}\bigl(d_{i\nu\sigma}^*\;c_{i\nu\sigma} + c_{i\nu\sigma}^*\;d_{i\nu\sigma}\bigr) \tag{25}$$

For the last term we use the invariance of the trace so that the sum over all states labeled by $\mathbf{k}$ could be replaced by the equivalent summation over all sites by a change of basis in the second term. The crucial point is that the coupling to the auxiliary fermions is purely local and S_Δ^i decomposes into a sum of local terms. The lattice fermions can therefore be integrated out from S_Δ^i for each site i separately. This completes the change of variables

$$\frac{1}{Z_\Delta}\int\mathcal{D}[c^*,c]\exp\bigl(-S_\Delta^i[,c_i^*,c_i,d_i^*d_i]\bigr) = \exp\biggl(-\sum_{\nu\,\sigma} d_{i\nu\sigma}^*\;g_\nu d_{i\nu\sigma} - V_i[d_i^*d_i]\biggr), \tag{26}$$

where Z_Δ is the partition function of the impurity action Eq. (20) and g_ν is the exact impurity Green function

$$g_{12} = -\langle c_1 c_2^* \rangle_\Delta = \frac{1}{Z_\Delta} \int \mathcal{D}[c^*, c]\, c_1 c_2^*\, e^{-S_\Delta[c^*,c]}. \tag{27}$$

The above equation may be viewed as the defining equation for the dual potential $V[d^*, d]$. The choice of matrices in Eq. (22) ensures a particularly simple form of this potential. An explicit expression is found by expanding both sides of Eq. (26) and equating the resulting expressions by order. Formally this can be done up to all orders and in this sense the transformation to the dual fermions is exact. For most applications, the dual potential is approximated by the first non-trivial interaction vertex

$$V[d^*, d] = \frac{1}{4} \sum_{1234} \gamma_{1234}\, d_1^* d_2^* d_4 d_3\,, \tag{28}$$

where for the local vertex the combined index $1 \equiv \{m\nu\sigma\}$ comprises orbital degrees of freedom (or cluster sites), frequency, and spin. γ is the exact, fully antisymmetric, reducible two-particle vertex of the local quantum impurity problem. With the present choice of normalization in the HS-transformation we did not "amputate" the impurity "legs" or g_{12} Greens function which will be very useful choice for CT-QMC calculations of local vertex for multi-orbital case. It is given then by connected part of the local two-particle correlations function

$$\gamma_{1234} = \chi_{1234} - \chi^0_{1234} \tag{29}$$

with the two-particle Green function of the local impurity (reference system) being defined as

$$\chi_{1234} = \langle c_1 c_2 c_3^* c_4^* \rangle_\Delta = \frac{1}{Z_\Delta} \int \mathcal{D}[c^*, c]\, c_1 c_2 c_3^* c_4^*\, e^{-S_\Delta[c^*,c]}\,. \tag{30}$$

The disconnected part of a generalized susceptibility reads

$$\chi^0_{1234} = g_{14} g_{23} - g_{13} g_{24}\,. \tag{31}$$

The single- and two-particle Green functions can be calculated using the CT-QMC Monte Carlo algorithms [1]. After integrating-out the lattice fermions, the dual action depends on the new variables only and for the one-orbital paramagnetic case reads

$$\tilde{S}[d^*, d] = -\sum_{\mathbf{k}\,\nu\sigma} d^*_{\mathbf{k}\nu\sigma}\, \tilde{G}^{-1}_{0\mathbf{k}\nu}\, d_{\mathbf{k}\nu\sigma} + \sum_i V_i[d_i^*, d_i] \tag{32}$$

while the bare dual Green function is has the form

$$\tilde{G}^0_{\mathbf{k}\nu} = \Big(\big(t_{\mathbf{k}} - \Delta_\nu\big)^{-1} - g_\nu \Big)^{-1}. \tag{33}$$

This formula involves only the local Green function g_ν of the impurity model. It is important to note, that the HS-transformation to dual fermion variables, allows us to "perform the analytical amputation" of impurity "legs" which causes enormous problems in the multi-orbital CT-QMC

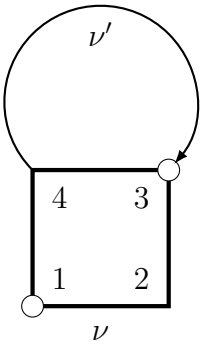

Fig. 6: *Feynman diagram for the 1st-order dual fermion perturbation for the self-energy $\widetilde{\Sigma}$: a line represents the non-local $\widetilde{G}_{43}$ and a box is the local γ_{1234}.*

formalism. Transformation to the original DF-normalization where both dual G_d and real Green function have the same dimension unit reads

$$G_d = g\,\widetilde{G}\,g = G_{DMFT} - g \qquad G_{DMFT} = \left(g_\nu + \Delta_\nu - t_{\mathbf{k}}\right)^{-1}. \tag{34}$$

The Dual Fermion transformation allows us to use arbitrary reference systems and transform the strongly correlated lattice fermion problem to an effective action of weakly coupled dual quasiparticles. This is related with the fact that the bare dual Green function Eq. (34) related with the small non-local part of the DMFT lattice Green function and the main two-particle part of the bare interaction among dual fermions Eq. (28) is exactly equal to the fully screened impurity vertex of the reference system. The rest of the dual fermion problem is related with an optimal perturbation scheme for such an effective action Eq. (32).

4 Superperturbation in dual space

For the general multi-orbital multi-site dual fermion perturbation technique we use the particle-hole notation for local vertex and write the exact spin and imaginary-time structure of generalized connected susceptibility [3, 15]

$$\gamma^{\sigma\sigma'}_{1234}(\tau_1,\tau_2,\tau_3,\tau_4) = -\left\langle c_{1\sigma} c^*_{2\sigma} c_{3\sigma'} c^*_{4\sigma'}\right\rangle_{\Delta} + g^{\sigma}_{12} g^{\sigma'}_{34} - g^{\sigma}_{14} g^{\sigma}_{32}\delta_{\sigma\sigma'}\,.$$

Then the bare vertex of the dual-fermion perturbation is related with the full impurity vertex, which in Matsubara space depends on two fermionic, (ν,ν'), and one bosonic, (ω), frequencies. We also symmetrize the vertex for the charge density d- and spin s-channels

$$\gamma^{d/m}_{1234}(\nu,\nu',\omega) = \gamma^{\uparrow\uparrow}_{1234}(\nu,\nu',\omega) \pm \gamma^{\uparrow\downarrow}_{1234}(\nu,\nu',\omega).$$

Now we can write the first-order, local in site (i), DF-correction to the dual self-energy (Fig. 6)

$$\widetilde{\Sigma}^{(1)i}_{12}(\nu) = \sum_{\nu',3,4} \gamma^{d}_{1234}(\nu,\nu',0)\,\widetilde{G}^{ii}_{43}(\nu') \tag{35}$$

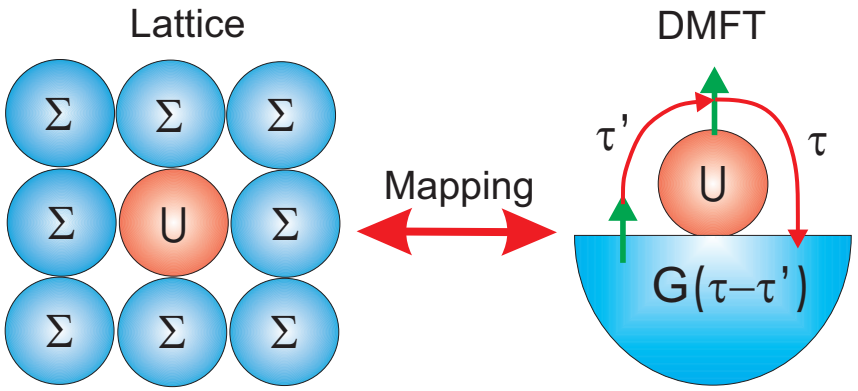

Fig. 7: *Schematic representation of the DMFT reference system for correlated lattice models.*

We now can use the freedom to chose the hybridization function Δ_ν in order to eliminate the main first-oder dual fermion correction Eq. (35). Since the vertex function γ_{1234} is purely local, it is enough to ensure that the local part of dual Green function vanishes $\widetilde{G}_{loc}{=}0$. This is exactly equivalent to the DMFT self-consistency condition for the hybridization function Δ_ν (Fig. 7)

$$\sum_{\mathbf{k}} \left(g_\nu^{-1} + \Delta_\nu - t_{\mathbf{k}} \right)^{-1} = g_\nu \,. \tag{36}$$

The effective impurity model, Eq. (20), which is fully determined by the local hybridization function Δ_ν on the fermionic Matsubara frequencies $i\nu_n$ is solved using the numerically exact CT-QMC scheme [1] from which the exact local Green function g_ν is obtained. The self-consistency DMFT condition for the hybridization function equates the local part of the lattice Green function and with that of the impurity, which shows that DMFT minimizes, in local sense, the distance $|t_{\mathbf{k}}{-}\Delta_\nu|$. It is worthwhile to point here that the "free" or non-interacting dual fermions are equivalent to the full solution of the DMFT problem. This is why dual fermions are only "weakly interacting" so that this perturbation scheme can be very efficient, provided a good reference system.

The second order Feynman diagram for DF-perturbation (Fig. 8) in real space ($\mathbf{R_{ij}}$) has density- and spin-channel contributions with corresponding constants ($c_d = -1/4$ and $c_m = -3/4$)

$$\widetilde{\Sigma}_{12}^{(2)ij}(\nu) = \sum_{\nu'\omega} \sum_{3\text{-}8} \sum_{\alpha=d,m} c_\alpha \gamma_{1345}^{\alpha,i}(\nu,\nu',\omega)\, \widetilde{G}_{36}^{ij}(\nu+\omega) \widetilde{G}_{74}^{ji}(\nu'+\omega)\, \widetilde{G}_{58}^{ij}(\nu')\, \gamma_{8762}^{\alpha,j}(\nu',\nu,\omega).$$

Using the exact relation between dual Green function and real Green function (Appendix B), we can express the total lattice self-energy as the sum of the reference contribution Σ^0 (e.g. the impurity) and corrections Σ', which are related with the dual self-energy $\widetilde{\Sigma}$

$$\Sigma_{\mathbf{k}\nu} = \Sigma^0_\nu + \Sigma'_{\mathbf{k}\nu} \tag{37}$$

$$\Sigma'_{\mathbf{k}\nu} = g_\nu^{-1} - \left(g_\nu + \widetilde{\Sigma}_{\mathbf{k}\nu} \right)^{-1}. \tag{38}$$

We point out that this expression is related with the exact transformation between dual- and real-space and has nothing to do with a correction for missing tree-particle vertices [2].

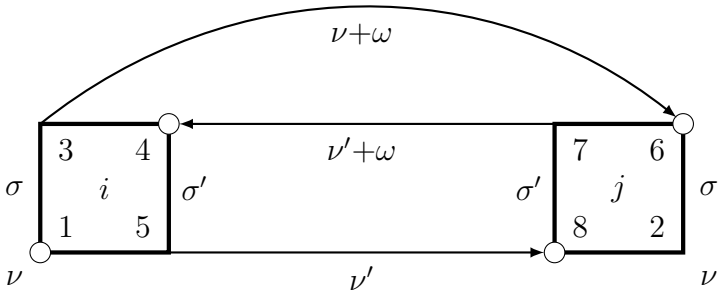

Fig. 8: *Feynman diagram for the 2nd-order dual fermion perturbation for the self-energy* $\widetilde{\Sigma}$.

What is much more important for numerical calculations, is that starting from the full DF-Green function, $\tilde{G}^{-1}_{\mathbf{k}\nu} = \tilde{G}^{-1}_{0\mathbf{k}\nu} - \widetilde{\Sigma}_{\mathbf{k}\nu}$, and exact the relation of Appendix B, Eq. (55), we can directly write an expression for the lattice Green function including only the reference impurity Green function and the dual self-energy [2]

$$G_{\mathbf{k}\nu} = \left(\left(g_\nu + \widetilde{\Sigma}_{\mathbf{k}\nu} \right)^{-1} - \widetilde{\Delta}_{\mathbf{k}\nu} \right)^{-1}. \tag{39}$$

This formula is perfectly suitable for the CT-QMC calculations for realistic multi-orbital correlated matter, where from the noisy Monte-Carlo data one needs only local one- and two-particle Green functions, without knowledge of a local self-energy and an "amputated" vertex function. In principle, one can go beyond second-order perturbation theory and include dual ladder diagrams [15], dual parquet diagrams [16], or even try to sum up all dual diagrams with the two-particle vertex γ_{1234} stochastically, using a diagrammatic Monte Carlo in dual space [17, 18]. We can also make the diagrammatic series self-consistent, using the "bold" line and update the bare dual Green function with the dual self-energy. Finally, one can also "upgrade" the reference system, which is not anymore "best" for dual fermion theory, but only for the DMFT approach with non-interacting dual fermions.

5 Numerical examples

As the first example of the DF-perturbation, we discuss the simple, but non-trivial case of a "two-site" model (Fig. 9) with one correlated site with Hubbard interaction U and one single electron site or a "bath" with the energy level ε coupled by the hybridization V. The reference system is described by the following parameters: $U{=}2$, $\varepsilon_0{=}0$ and $V_0{=}0.5$. The system, calculated by first-order DF-perturbation, has the same interaction U and ε, but 50% larger hybridization $V{=}1.5V_0$. We use an exact-diagonalization solver and find not only the local Green function at the correlated site G_0 for the reference system, but also the exact G for the target system with an effective broadening corresponding to the first Matsubara frequency. One can also use the Lehmann representation not only for the single-particle Green function, but also for two-particle correlators [19] and moreover integrated over the Matsubara frequency for simplest diagram Eq. (35) analytically [20]. For the dual-fermion calculation we use the Matsubara superperturbation first-order correction for inverse temperature $\beta{=}5$ and the Padé analytical

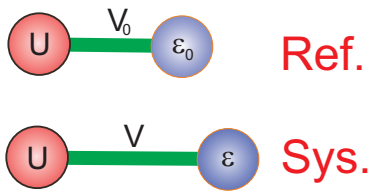

Fig. 9: *Schematic representation of dual-fermion superperturbation test for a two-site model.*

continuation to the real axes [5]. Results of the first-order DF superperturbation are shown in Fig. 10 together with reference and target DOS. We can conclude that even the first-oder DF-correction gives the Green function in very good agreement with the exact one.
The real test for correlated fermions corresponds to a half-filled two-dimensional Hubbard model on the square lattice with a 2×2 plaquette as the reference system (Fig. 11). We used the 2×2 supercell scheme with 4 atoms in the unit cell in oder to describe the lattice on the left-hand side of Fig. 11 with the following 4×4 hopping matrix with the nearest neighbor hopping t and next nearest neighbor hopping p

$$t_{\mathbf{k}} = \begin{pmatrix} \varepsilon & tK^{0+} & pL^{-+} & tK^{-0} \\ tK^{0-} & \varepsilon & tK^{-0} & pL^{--} \\ pL^{+-} & tK^{+0} & \varepsilon & tK^{0-} \\ tK^{+0} & pL^{++} & tK^{0+} & \varepsilon \end{pmatrix}$$

where the functions $K^{mn}_{\mathbf{k}}$ and $L^{mn}_{\mathbf{k}}$ with $[m(n)] = -(1), 0, +(1)$ are defined as

$$\begin{aligned} K^{mn}_{\mathbf{k}} &= 1 + e^{i(mk_x+nk_y)} \\ L^{mn}_{\mathbf{k}} &= 1 + e^{i(mk_x+nk_y)} + e^{imk_x} + e^{ink_y} \end{aligned}$$

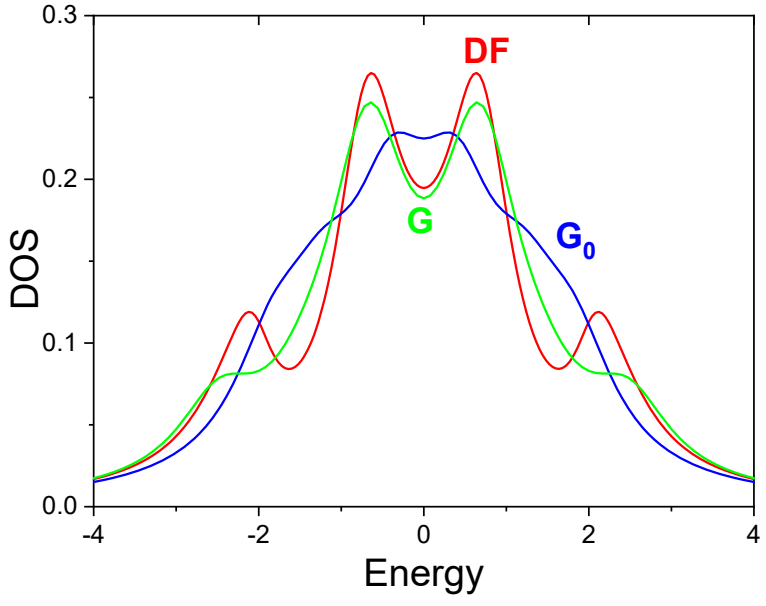

Fig. 10: *Density of states for the dual-fermion first-order scheme together with the reference and target Green function for the two-site model.*

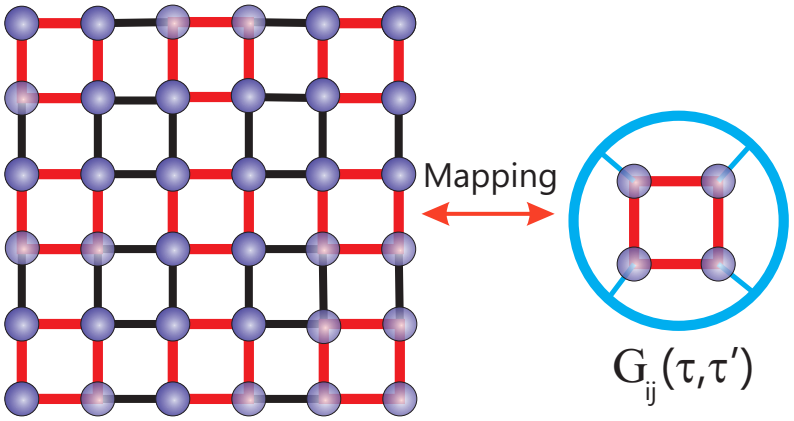

Fig. 11: *Schematic representation of a plaquette cluster-reference system for the square lattice.*

The standard reference system (Fig. 11) corresponds to the Green function, averaged over the supercell Brillouin zone, which is equivalent to the self-consistent cluster-DMFT scheme [21]. Another possibility for the reference system is related with the $\mathbf{k} = 0$ Green function, which corresponds to the decoupled lattice of plaquettes with periodic boundary condition

$$\Delta_0 = t_{\mathbf{k}=0} = \begin{pmatrix} \varepsilon & 2t & 4p & 2t \\ 2t & \varepsilon & 2t & 4p \\ 4p & 2t & \varepsilon & 2t \\ 2t & 4p & 2t & \varepsilon \end{pmatrix}. \tag{40}$$

Note that the spectrum of this hopping Hamiltonian Eq. (40) is equal to the original cubic tight-binding model

$$\varepsilon_{\mathbf{k}} = 2t\big(\cos k_x + \cos k_y\big) + 4p \cos k_x \cos k_y$$

in the 4 $\mathbf{k}$-points: $\Gamma{=}(0,0)$, $X{=}(\pi,0)$, $Y{=}(0,\pi)$ and $M{=}(\pi,\pi)$ which corresponds to the $2{\times}2$ grid in the original Brillouin zone. In this sense, we can view the dual fermion perturbation from the plaquette reference system [21] as a DF-multigrid interpolation from the $2{\times}2$ $\mathbf{k}$-mesh in the original cubic lattice to, e.g., $64{\times}64$ $\mathbf{k}$-points (for this case one needs to use the $32{\times}32$ mesh in our supercell). This is exactly the task for the present numerical test.
In order to calculate the bare dual Green function we use a slightly modified version of Eq. (33) (since $\Delta_{\mathbf{k}} = \Delta_0 - t_{\mathbf{k}} = 0$, for some $\mathbf{k}$-points, e.g. for $\mathbf{k} = 0$)

$$\widetilde{G}^0_{\mathbf{k},\nu} \;=\; \Delta_{\mathbf{k}}\big(1 - g_\nu \Delta_{\mathbf{k}}\big)^{-1}.$$

With this choice of reference system, one can again stay only with the exact diagonalization scheme to calculate the dual Green function and the plaquette vertex function. We choose the strong-coupling parameters with $U{=}W{=}8$, $t{=}-1$, $p{=}0$ and the temperature $T{=}1/3$ for which there is a diagrammatic QMC results [18]. In the Fig. 12 we plot the density of states (DOS) for three different Green functions: ED for the reference plaquette, cluster perturbation (CP) which corresponds to Eq. (39) with $\widetilde{\Sigma}_{\mathbf{k}\nu}{=}0$, and the results for the second-order plaquette dual-fermion. We use Padé-analytical continuation from the Matsubara to the real energy axis [5].

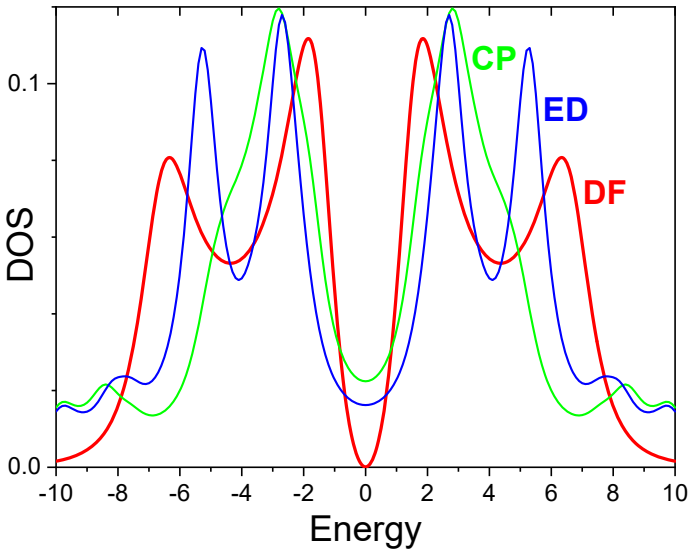

Fig. 12: *Density of states for dual fermion perturbation from plaquette for $U{=}W{=}8$ (DF-red) in comparison with exact diagonalization for periodic plaquette (ED-blue) and cluster perturbation theory (CP-green).*

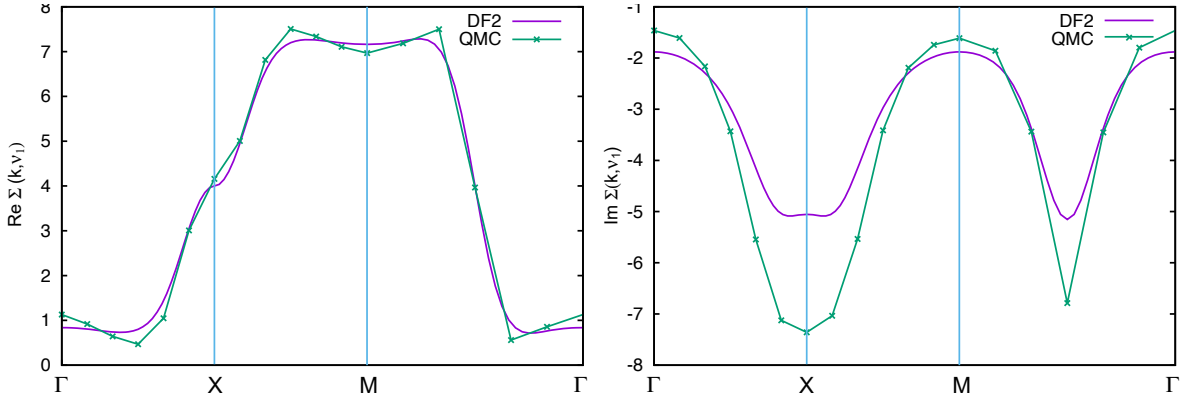

Fig. 13: *Real (left) and imaginary (right) part of the self-energy for the DF plaquette scheme in comparison with diagrammatic-QMC results [18] at the first Matsubara frequency.*

We conclude that the DOS for dual fermion theory differs strongly from the results of the simple perturbation (CP) and the original reference system (ED), and has a broad four-peaks structure, characteristic for the lattice QMC results [22].

Fig. 13 shows the DF-plaquette second-order lattice self-energy Eq. (38) for the standard $\mathbf{k}$-dependent path Γ-X-M-Γ in the two-dimensional Brillouin zone, together with numerically exact lattice diagrammatic QMC [18]. The almost perfect agreement for the real-part of the self-energy $\Sigma(\mathbf{k}, \nu{=}\pi T)$ underlines the strength of the dual-fermion superperturbation technique starting from a "reasonable" plaquette reference system.

Finally, we plot in Fig. 14 the full Brillouin zone $64{\times}64$ $\mathbf{k}$-mesh of the real and imaginary part of DF-plaquette self-energy periodize to original square lattice, in order to have an impression of the complex behavior for strongly correlated lattice fermion systems.

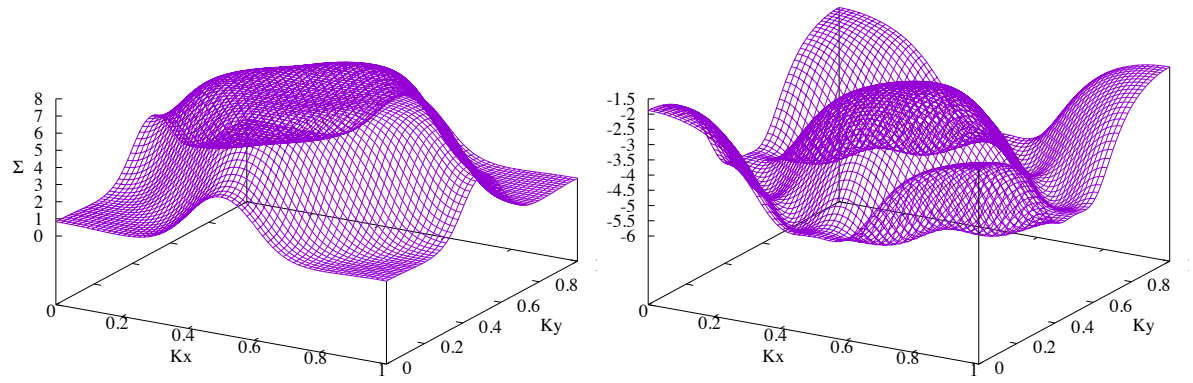

Fig. 14: *Full Brillouin zone* 64×64 **k**-*mesh for the real (left) and imaginary (right) part of the DF plaquette self-energy at the first Matsubara frequency.*

6 Conclusion: Recent developments

We discussed the path-integral expansion for correlated lattice systems beyond the local DMFT approximation using transformations to dual variables. We would like to mention other recent developments in this field. Very important generalization of the dual variable approach are related with the dual-boson approach [23, 2], which properly includes effects of non-local interactions. This scheme allows the very efficient treatment of charge [24] and spin [25] collective fluctuations, and their effects on electronic spectrum and vice versa. Careful analyses of the two-particle divergence using dual variables [26] and fast calculations of the polarization function in correlated solids [27] show the strength of proper path-integral perturbation starting from the best local approximation. The efficient version of dual perturbation based on partial bosonization [28] has a strong potential for development of the realistic GW-like scheme with proper charge- and spin-fluctuations.

Acknowledgments

The author would like to thank for very fruitful discussions with Mikhail Katsnelson, Alexey Rubtsov, Sergey Brener, Evgeny Stepanov, Friedrich Krien, Erik van Loon, Sergey Iskakov, and George Rohringer. Supports by the Cluster of Excellence “Advanced Imaging of Matter” (EXC 2056) of the Deutsche Forschungsgemeinschaft, Project No. ID390715994 and by the European Research Council via Synergy Grant 854843 - FASTCORR are greatly acknowledged.

Appendices

A Path-integrals for fermions

We first introduce a formalism of the path integral over fermionic fields [11]. Let us consider a simple case of a single quantum state $|i\rangle$ occupied by fermionic particles [29]. Due to the Pauli principle the many-body Hilbert space is spanned by only two orthonormal states $|0\rangle$ and $|1\rangle$. In the second quantization scheme for fermions with annihilation $\hat{c}_i$ and creations $\hat{c}_i^\dagger$ operators with anticommutation relations $\{\hat{c}_i, \hat{c}_j^\dagger\} = \delta_{ij}$ we have the following simple rules

$$\hat{c}_i\,|1\rangle = |0\rangle \quad \hat{c}_i\,|0\rangle = 0 \quad \text{and} \quad \hat{c}_i^\dagger\,|0\rangle = |1\rangle \quad \hat{c}_i^\dagger\,|1\rangle = 0\,. \tag{41}$$

Moreover, the density operator and the Pauli principle have the form

$$\hat{c}_i^\dagger \hat{c}_i\,|n\rangle = n_i\,|n\rangle \quad \text{and} \quad \hat{c}_i^2 = (\hat{c}_i^\dagger)^2 = 0\,.$$

The central object here are the so-called fermionic coherent states $|c\rangle$, which are eigenstates of annihilation operator $\hat{c}_i$ with eigenvalue c_i

$$\hat{c}_i\,|c\rangle = c_i\,|c\rangle\,. \tag{42}$$

It is worthwhile to note that such a left-eigenbasis has only annihilation operators, due to the fact that they are bounded from the below and one can rewrite one of equations from Eq. (41) in the following "eigenvalue" form

$$\hat{c}_i\,|0\rangle = 0\,|0\rangle\,.$$

Due to the anti-commutation relations for the fermionic operators the eigenvalues of coherent states c_i are so-called Grassmann numbers with the multiplication rules [30]

$$c_i c_j = -c_j c_i \quad \text{and} \quad c_i^2 = 0\,. \tag{43}$$

It is convenient to assume that the Grassmann numbers also anti-commute with the fermionic operators

$$\{c, \hat{c}\} = \{c, \hat{c}^\dagger\} = 0\,.$$

An arbitrary function of one Grassmann variable can be represented by only the first two Taylor coefficients

$$f(c) = f_0 + f_1 c\,. \tag{44}$$

One can prove the following general many-body representation of coherent states

$$|c\rangle = e^{-\sum_i c_i \hat{c}_i^\dagger}\,|0\rangle\,. \tag{45}$$

Let us show this for the simple case of one fermionic state

$$\hat{c}\,|c\rangle = \hat{c}\big(1 - c\hat{c}^\dagger\big)\,|0\rangle = \hat{c}\big(\,|0\rangle - c\,|1\rangle\,\big) = -\hat{c}c\,|1\rangle = c\,|0\rangle = c\,|c\rangle\,. \tag{46}$$

One can also define a "left" coherent state $\langle c|$ as the left-eigenstates of creation operators $\hat{c}_i^\dagger$

$$\langle c|\, \hat{c}_i^\dagger = \langle c|\, c_i^* .$$

Note that new eigenvalue c_i^* is just another Grassmann number, not the complex conjugate of c_i. The left coherent state can be obtained similar to Eq. (45)

$$\langle c| = \langle 0|\, e^{-\sum_i \hat{c}_i c_i^*} .$$

A general function of two Grassmann variables can, analogously to Eq. (44), be represented by only four Taylor coefficients

$$f(c^*, c) = f_{00} + f_{10} c^* + f_{01} c + f_{11} c^* c \,. \tag{47}$$

Using this expansion we can define a derivative of Grassmann variables in the natural way

$$\frac{\partial c_i}{\partial c_j} = \delta_{ij} \,.$$

One needs to be careful with "right-order" of such a derivative and remember the anti-commutation rules, i.e.,

$$\frac{\partial}{\partial c_2} c_1 c_2 = -c_1 \,.$$

For the case of the general two-variable function in Eq. (47) we have

$$\frac{\partial}{\partial c^*}\frac{\partial}{\partial c} f(c^*, c) = \frac{\partial}{\partial c^*}\big(f_{01} - f_{11} c^*\big) = -f_{11} = -\frac{\partial}{\partial c}\frac{\partial}{\partial c^*} f(c^*, c).$$

One also needs a formal definition of the integration over Grassmann variables, and the natural way consists of the following rules [30]

$$\int 1\, dc = 0 \quad \text{and} \quad \int c\, dc = 1 \,,$$

which just shows that the integration over a Grassmann variable is equivalent to differentiation

$$\int \cdots dc \to \frac{\partial}{\partial c} \cdots$$

The coherent states are not orthonormal and the overlap of any two such states is equal to

$$\langle c|c\rangle = e^{\sum_i c_i^* c_i}$$

which is easy to see for the case of one particle

$$\langle c|c\rangle = \big(\langle 0| - \langle 1|\, c^*\big)\big(|0\rangle - c\,|1\rangle\big) = 1 + c^* c = e^{c^* c}.$$

An important property of coherent states is the resolution of unity

$$\int dc^* \int dc\, e^{-\sum_i c_i^* c_i}\, |c\rangle\langle c| = \hat{1} = \iint dc^* dc\, \frac{|c\rangle\,\langle c|}{\langle c|c\rangle}.$$

For simplicity we demonstrate this relation only for one fermion state

$$\iint dc^* dc\, e^{-c^* c}\, |c\rangle\langle c| = \iint dc^* dc (1 - c^* c)\big(|0\rangle - c\,|1\rangle\big)\big(\langle 0| - \langle 1|\, c^*\big) =$$
$$= -\iint dc^* dc\; c^* c\,\big(|0\rangle\langle 0| + |1\rangle\langle 1|\big) = \sum_n |n\rangle\langle n| = \hat{1}\,.$$

Matrix elements of normally ordered operators are very easy to calculate in the coherent basis by operating with $\hat{c}^\dagger$ on the states to the right and $\hat{c}$ to the left:

$$\langle c^*|\, \hat{H}(\hat{c}^\dagger, \hat{c})\, |c\rangle = H(c^*, c)\, \langle c^*|c\rangle\,. = H(c^*, c)\, e^{\sum_i c_i^* c_i} \tag{48}$$

Within the manifold of coherent states we can map the fermionic operators to the Grassmann variables $(\hat{c}_i^\dagger, \hat{c}_i) \to (c_i^*, c_i)$.
Finally, we prove the so-called "trace-formula" for arbitrary fermionic operators in normal order (in one-fermion notation)

$$\mathrm{Tr}\,\hat{O} = \sum_{n=0,1} \langle n|\, \hat{O}\, |n\rangle = \sum_{n=0,1} \iint dc^* dc\, e^{-c^* c}\, \langle n|\, c\rangle\langle c|\, \hat{O}\, |n\rangle =$$
$$= \iint dc^* dc\, e^{-c^* c} \sum_{n=0,1} \langle -c|\, \hat{O}\, |n\rangle\langle n|\, c\rangle = \iint dc^* dc\, e^{-c^* c}\, \langle -c|\, \hat{O}\, |c\rangle\,.$$

The fermionic "minus" sign in the left coherent states come from the commutation of the (c^*) and (c) coherent state in such a transformation: $\langle n|c\rangle\, \langle c|n\rangle = \langle -c|n\rangle\, \langle n|c\rangle$. One has to use the standard Grassmann rules: $c_i^* c_j = -c_j c_i^*$ and $|-c\rangle = |0\rangle + c\,|1\rangle$.
We are ready now to write the partition function for the grand-canonical quantum ensemble with $H = \hat{H} - \mu\hat{N}$ and inverse temperature β. One has to use the N-slices Trotter decomposition for the partition function in $[0, \beta)$ with imaginary time $\tau_n = n\Delta\tau = n\beta/N$ $(n = 1, ..., N)$, and insert N times the resolution of unity as follows

$$Z = \mathrm{Tr}\, e^{-\beta H} = \iint dc^* dc\, e^{-c^* c} \big\langle -c\big| e^{-\beta H} \big| c\big\rangle$$
$$= \int \Pi_{n=1}^N dc_n^* dc_n\, e^{-\sum_n c_n^* c_n}\, \langle c_N|\, e^{-\Delta\tau H}\, |c_{N-1}\rangle\, \langle c_{N-1}|\, e^{-\Delta\tau H}\, |c_{N-2}\rangle\, ...\, \langle c_1|\, e^{-\Delta\tau H}\, |c_0\rangle$$
$$= \int \Pi_{n=1}^N dc_n^* dc_n\, e^{-\Delta\tau \sum_{n=1}^N [c_n^*(c_n - c_{n-1})/\Delta\tau + H(c_n^*, c_{n-1})]}$$

In the continuum limit $(N \to \infty)$

$$\Delta\tau \sum_{n=1}^N \cdots \to \int_0^\beta d\tau \cdots\,, \qquad \frac{c_n - c_{n-1}}{\Delta\tau} \to \partial_\tau \quad \text{and} \quad \Pi_{n=0}^{N-1} dc_n^* dc_n \to \mathcal{D}\,[c^*, c]$$

with antiperiodic boundary conditions for fermionic Grassmann variables in imaginary time $c(\tau)$ and $c^*(\tau)$

$$c(\beta) = -c(0), \qquad c^*(\beta) = -c^*(0)$$

we end up in the standard path-integral formulation of the partition function

$$Z = \int \mathcal{D}\left[c^*, c\right] e^{-\int_0^\beta d\tau [c^*(\tau)\partial_\tau c(\tau) + H(c^*(\tau), c(\tau))]} \,. \tag{49}$$

It is useful to mention the general form of the Gaussian path-integral for a non-interacting "quadratic" fermionic action, which is equivalent to the Hubbard-Stratonovich transformation used in the dual-fermion derivation Eq. (22). For an arbitrary matrix M_{ij} and Grassmann vectors J_i^* and J_i one can calculate analytically the following integral

$$Z_0\left[J^*, J\right] = \int \mathcal{D}\left[c^* c\right] e^{-\sum_{i,j=1}^N c_i^* M_{ij} c_j - \sum_{i=1}^N \left(c_i^* J_i + J_i^* c_i\right)} = \det M \; e^{\sum_{i,j=1}^N J_i^* (M^{-1})_{ij} J_j} \,. \tag{50}$$

To prove this relation one need first to change variables in order to eliminate J_i^* and J_i and expand the exponential function (only N-th oder is non-zero)

$$e^{-\sum_{i,j=1}^N c_i^* M_{ij} c_j} = \frac{1}{N!}\left(-\sum_{i,j=1}^N c_i^* M_{ij} c_j\right)^N .$$

Finally, different permutations of c_i^* and c_j and integration over Grassmann variables will give $\det M$. As a small exercise we will check such integrals for the first two many-particle dimensions. For N=1 it is trivial

$$\int \mathcal{D}\left[c^* c\right] e^{-c_1^* M_{11} c_1} = \int \mathcal{D}\left[c^* c\right] \left(-c_1^* M_{11} c_1\right) = M_{11} = \det M$$

and for N=2 we have

$$\int \mathcal{D}\left[c^* c\right] e^{-c_1^* M_{11} c_1 - c_1^* M_{12} c_1 - c_2^* M_{21} c_1 - c_2^* M_{22} c_2} =$$

$$= \frac{1}{2!}\int \mathcal{D}\left[c^* c\right] \left(-c_1^* M_{11} c_1 - c_1^* M_{12} c_1 - c_2^* M_{21} c_1 - c_2^* M_{22} c_2\right)^2 = M_{11} M_{22} - M_{12} M_{21} = \det M.$$

For a change of variables in the path integral one uses the following transformation with unit Jacobian: $c \to c + M^{-1} J$ and

$$c^* M c + c^* J + J^* c = \left(c^* + J^* M^{-1}\right) M \left(c + M^{-1} J\right) - J^* M^{-1} J \,.$$

Using the Gaussian path-integral it is very easy to calculate any correlation function for a non-interaction action (Wick-theorem)

$$\begin{aligned} \left\langle c_i c_j^* \right\rangle_0 &= -\frac{1}{Z_0} \frac{\delta^2 Z_0\left[J^*, J\right]}{\delta J_i^* \, \delta J_j}\bigg|_{J=0} = M_{ij}^{-1} \\ \left\langle c_i c_j c_k^* c_l^* \right\rangle_0 &= \frac{1}{Z_0} \frac{\delta^4 Z_0\left[J^*, J\right]}{\delta J_i^* \delta J_j^* \delta J_l \delta J_k}\bigg|_{J=0} = M_{il}^{-1} M_{jk}^{-1} - M_{ik}^{-1} M_{jl}^{-1}. \end{aligned}$$

Corresponding bosonic path-integrals can be formulated in a similar way with complex variables and periodic boundary conditions on imaginary time. The Gaussian path-integral over bosonic fields is equal to inverse of the M-matrix determinant [11].

B Exact relations between Green functions

After appropriate diagrammatic results for the dual self-energy and the dual Green function have been obtained, they have to be transformed back to the corresponding physical quantities in terms of real lattice fermions. The fact that dual fermions are introduced through the exact Hubbard-Stratonovich transformation, Eq. (22), allows to establish exact identities between dual and lattice Greens function [3, 15].
The relations between the n-particle cumulants of dual and lattice fermions can be established using the cumulant (linked cluster) technique. To this end one may consider two different, equivalent representations of the following generating functional

$$e^{F[J^*J,L^*L]} = \mathcal{Z}_d \int \mathcal{D}[c^*c, d^*d]\, e^{-S[c^*c,d^*,d]+J_1^*c_1+c_2^*J_2+L_1^*d_1+d_2^*L_2}\,. \tag{51}$$

Integrating-out the lattice fermions from this functional similar to (26) (this can be done with the sources J and J^* set to zero) yields

$$e^{F[L^*,L]} = \tilde{\mathcal{Z}}_d \int \mathcal{D}[d^*, d]\, e^{-S_{\rm d}[d^*,fd+L_1^*d_1+d_2^*L_2} \tag{52}$$

with $\tilde{\mathcal{Z}}_d = \mathcal{Z}/\tilde{\mathcal{Z}}$. The dual Green function and the two-particle correlator related with non-local susceptibilities are obtained from (52) by suitable functional derivatives, e.g.,

$$\tilde{G}_{12} = -\frac{\delta^2 F}{\delta L_2 \delta L_1^*}\bigg|_{L^*=L=0} \tag{53}$$

where $G \otimes G$ is the antisymmetrized direct product of Green functions, so that the angular bracket is the connected part of the dual two-particle Green function. Conversely, integrating out the dual fermions from Eq. (51) using the HS-transformation, one obtains an alternative representation, which more clearly reveals the connection of the functional derivatives with respect to the sources J, J^*, and L, L^*. The result is

$$\begin{aligned} F[J^*J, L^*L] &= L_1^*(\Delta - t)_{12}L_2 \\ &+ \ln \int \mathcal{D}[c^*, c] \exp\Big(-S[c^*, c] + J_1^*c_1 + c_2^*J_2 + L_1^*(\Delta{-}t)_{12}c_2 + c_1^*(\Delta{-}t)_{12}L_2\Big). \end{aligned} \tag{54}$$

In analogy to (53), the cumulants in terms of lattice fermions are obviously obtained by functional derivative with respect to the sources J and J^* with L and L^* set to zero. Applying the derivatives with respect to L, L^* to (54) with $J = J^* = 0$ and comparing to (53), e.g., yields the identity

$$\tilde{G}_{12} = -(\Delta{-}t)_{12} + (\Delta{-}t)_{11'}G_{1'2'}(\Delta{-}t)_{2'2}. \tag{55}$$

Solving for G provides the rule how to transform the dual Green function to the physical quantity in terms of lattice fermions.

References

[1] E. Gull, A. Millis, A. Lichtenstein, A. Rubtsov, M. Troyer, and P. Werner, Rev. Mod. Phys. **83**, 349 (2011)

[2] G. Rohringer, H. Hafermann, A. Toschi, A.A. Katanin, A.E. Antipov, M.I. Katsnelson, A.I. Lichtenstein, A.N. Rubtsov, and K. Held Rev. Mod. Phys. **90**, 025003 (2018)

[3] A.N. Rubtsov, M.I. Katsnelson, and A.I. Lichtenstein, Phys. Rev. B **77**, 033101 (2008)

[4] F. Lechermann, A.I. Lichtenstein, and M. Potthoff, Eur. Phys. J. Special Topics **226**, 2591 (2017)

[5] A. Georges, G. Kotliar, W. Krauth, and M.J. Rozenberg, Rev. Mod. Phys. **68**, 13 (1996)

[6] N.F. Mott: *Metal-Insulator Transitions*, 2nd ed. (Taylor and Francis, 1990)

[7] A. Georges and G. Kotliar, Phys. Rev. B **45**, 6479 (1992)

[8] P. Hohenberg and W. Kohn, Phys. Rev. **136**, 864 (1964)

[9] G. Kotliar, S.Y. Savrasov, K. Haule, V.S. Oudovenko, O. Parcollet, and C.A. Marianetti, Rev. Mod. Phys. **78**, 865 (2006)

[10] A.A. Abrikosow, L.P. Gorkov, and I.E. Dzyaloshinski: *Methods of Quantum Field Theory in Statistical Physics* (Prentice-Hall, New Jersey, 1964)

[11] J.W. Negele, and H. Orland: *Quantum Many-Particle Systems* (Addison-Wesley, New York, 1988)

[12] G. Baym and L.P. Kadanoff, Phys. Rev. **124**, 287 (1961)

[13] D.M. Ceperley and B.J. Alder, Phys. Rev. Lett. **45**, 566 (1980)

[14] H. Hafermann, F. Lechermann, A.N. Rubtsov, M.I. Katsnelson, A. Georges, and A.I. Lichtenstein, Lecture Notes in Physics **843**, 145 (2012)

[15] H. Hafermann: *Numerical Approaches to Spatial Correlations in Strongly Interacting Fermion Systems* (Cuvillier Verlag, Göttingen, Singapore, 2010)

[16] F. Krien and A. Valli Phys. Rev. B **100**, 245147 (2019)

[17] S. Iskakov, A.E. Antipov, and E. Gull, Phys. Rev. B **94**, 035102 (2016)

[18] J. Gukelberger, E. Kozik, and H. Hafermann, Phys. Rev. B **96**, 035152 (2017)

[19] H. Hafermann, Ch. Jung, S. Brener, M.I. Katsnelson, A.N. Rubtsov, and A.I. Lichtenstein, Europhys. Lett. **85**, 27007 (2009)

[20] X. Dai, K. Haule, and G. Kotliar, Phys. Rev. B **72**, 045111 (2005)

[21] A.I. Lichtenstein and M.I. Katsnelson, Phys. Rev. B **62**, R9283 (2000)

[22] D. Rost, E.V. Gorelik, F. Assaad, and N. Blümer, Phys. Rev. B **86**, 155109 (2012)

[23] A.N. Rubtsov, M.I. Katsnelson, and A.I. Lichtenstein, Ann. Phys. **327**, 1320 (2012)

[24] E.G.C.P. van Loon, H. Hafermann, A.I. Lichtenstein, A.N Rubtsov, and M.I. Katsnelson, Phys. Rev. Lett. **113**, 246407 (2014)

[25] E.A. Stepanov, L. Peters, I.S. Krivenko, A.I. Lichtenstein, M.I. Katsnelson, and A.N Rubtsov, npj Quantum Materials **3**, 54 (2018)

[26] F. Krien, E.G.C.P. van Loon, M.I. Katsnelson, A.I. Lichtenstein, and M. Capone, Phys. Rev. B **99**, 245128 (2019)

[27] F. Krien, Phys. Rev. B **99**, 235106 (2019)

[28] E.A. Stepanov, V. Harkov, and A.I. Lichtenstein, Phys. Rev. B **100**, 205115 (2019)

[29] A. Kamenev: *Field Theory of Non-Equilibrium Systems* (Cambridge University Press, 2011)

[30] F.A. Berezin: *Method of Second Quantization* (Academic Press, New York, 1966)

10 Geometry and Topology in Many-Body Physics

Raffaele Resta
Istituto Officina dei Materiali IOM-CNR, Trieste, Italy
and Donostia International Physics Center,
San Sebastián, Spain

Contents

E. Pavarini and E. Koch (eds.)
Topology, Entanglement, and Strong Correlations
Modeling and Simulation Vol. 10
Forschungszentrum Jülich, 2020, ISBN 978-3-95806-466-9
http://www.cond-mat.de/events/correl20

1 Introduction

Some intensive observables of the electronic ground state in condensed matter have a geometrical or even topological nature. In crystalline systems at the noninteracting (or mean-field) level the term "geometrical" refers to the geometry of the occupied manifold of the state vectors, parametrized by the Bloch vector $\mathbf{k}$ in reciprocal space. A state-of-the-art account about several of such observables can be found in the recent outstanding book by D. Vanderbilt [1].

In the present Review I present, instead, the known geometrical observables beyond band-structure theory, in order to deal with the general case of disordered and/or correlated many-electron systems. The term "geometrical" refers therefore to a Hilbert space (defined below in Sect. 3) different from the Bloch space.

It is now clear that the geometrical observables come in two very different classes. The observables of class (i) only make sense for insulators, and are defined modulo 2π (in dimensionless units), while the observables of class (ii) are defined for both insulators and metals, and are single-valued.

As for class (i), two observables are known: electrical polarization and the "axion" term in magnetoelectric response [1]. For both observables the modulo 2π ambiguity is fixed only after the termination of the insulating sample is specified. Furthermore in the presence of some protecting symmetry only the values zero or π (mod 2π) are allowed: the observable becomes then a topological $\mathbb{Z}_2$ index. So far, the expression of the axion term is only known within band-structure theory: therefore in the present Review I only discuss electrical polarization, whose many-body expression was first obtained in 1998 [2]. The geometrical nature of polarization is thoroughly investigated in Sect. 4, while in Sect. 5 it is shown that $1d$ polarization in inversion-symmetric systems is a $\mathbb{Z}_2$ invariant.

After discussing polarization, I will address four observables of class (ii); they do not include the case of orbital magnetization, whose geometrical expression is known since 2006 at the band-structure level [3], but which to date lacks a corresponding many-body formulation. Of these four observables two are time-reversal (T) even and two are T-odd; the latter are nonzero only if the material breaks T-symmetry. The T-even are the Drude weight and the Souza-Wilkens-Martin sum rule; the T-odd ones are the anomalous Hall conductivity and the magnetic circular dichroism sum rule. It may appear surprising that I include spectral sum rules in the class of ground-state observables: this is because, owing to a fluctuation-dissipation theorem, a frequency-integrated dynamical probe becomes effectively a static one. The corresponding physical property cannot be actually measured with a static probe, but is nonetheless a genuine ground-state property. All of the four single-valued observables—despite being ground-state properties—have to do with the conductivity tensor $\sigma_{\alpha\beta}(\omega)$; therefore, before addressing them, in Sect. 6, I display the full many-body Kubo formulæ. They comprise four terms: real and imaginary, symmetric (longitudinal) and antisymmetric (transverse).

The content of Sects. 7 and 8 is a thorough discussion of the four class-(ii) geometrical observables and of their consequences, in particular for the theory of the insulating state. A synoptic view of all five observables object of this Review is provided in the concluding Sect. 9. Some boring derivations are confined to the Appendix.

2 What does it mean "geometrical" in quantum mechanics?

The founding concept in geometry is distance. Let $|\Psi_1\rangle$ and $|\Psi_2\rangle$ be two quantum states in the same Hilbert space: it is expedient to adopt for their pseudodistance the expression

$$\mathcal{D}_{12}^2 = -\ln|\langle\Psi_1|\Psi_2\rangle|^2. \tag{1}$$

It is "pseudo" because it violates one of the distance axioms in calculus textbooks; such violation does not make any harm in the present context.
Eq. (1) vanishes when the states $|\Psi_1\rangle$ and $|\Psi_2\rangle$ coincide, while it diverges when the states $|\Psi_1\rangle$ and $|\Psi_2\rangle$ are orthogonal. The states $|\Psi_1\rangle$ and $|\Psi_2\rangle$ are defined up to an arbitrary phase factor: fixing this factor amounts to a gauge choice. Eq. (1) is clearly gauge-invariant.
The distance in Eq. (1) can equivalently be rewritten as

$$\mathcal{D}_{12}^2 = -\ln\langle\Psi_1|\Psi_2\rangle - \ln\langle\Psi_2|\Psi_1\rangle, \tag{2}$$

where the two terms are not separately gauge-invariant. While the distance is obviously real, each of the two terms in Eq. (2) is in general a complex number. If we write

$$\langle\Psi_1|\Psi_2\rangle = \big|\langle\Psi_1|\Psi_2\rangle\big|\ \mathrm{e}^{i\varphi_{21}}, \tag{3}$$

then the imaginary part of each of the two terms in Eq. (2) assumes a transparent meaning:

$$-\ \mathrm{Im}\ \ln\ \langle\Psi_1|\Psi_2\rangle = \varphi_{12}, \qquad \varphi_{21} = -\varphi_{12}. \tag{4}$$

Besides the metric, an additional geometrical concept is therefore needed: the connection, which fixes the relative phases between two states in the Hilbert space.
The connection is arbitrary and cannot have any physical meaning by itself. Nonetheless, after the 1984 groundbreaking paper by Michael Berry [4], several physical observables are expressed in terms of the connection and related quantities. When the state vector is a differentiable function of some parameter $\boldsymbol{\kappa}$, then the differential phase and the differential distance define the Berry connection and the quantum metric, respectively:

$$\varphi_{\boldsymbol{\kappa},\boldsymbol{\kappa}+d\boldsymbol{\kappa}} = \mathcal{A}_\alpha(\boldsymbol{\kappa})d\kappa_\alpha, \qquad D^2_{\boldsymbol{\kappa},\boldsymbol{\kappa}+d\boldsymbol{\kappa}} = g_{\alpha\beta}(\boldsymbol{\kappa})d\kappa_\alpha d\kappa_\beta, \tag{5}$$

$$\mathcal{A}_\alpha(\boldsymbol{\kappa}) = i\langle\Psi_{\boldsymbol{\kappa}}|\partial_{\kappa_\alpha}\Psi_{\boldsymbol{\kappa}}\rangle, \qquad g_{\alpha\beta}(\boldsymbol{\kappa}) = \ \mathrm{Re}\ \langle\partial_{\kappa_\alpha}\Psi_{\boldsymbol{\kappa}}|\partial_{\kappa_\beta}\Psi_{\boldsymbol{\kappa}}\rangle - \langle\partial_{\kappa_\alpha}\Psi_{\boldsymbol{\kappa}}|\Psi_{\boldsymbol{\kappa}}\rangle\langle\Psi_{\boldsymbol{\kappa}}|\partial_{\kappa_\beta}\Psi_{\boldsymbol{\kappa}}\rangle; \tag{6}$$

summation over repeated Cartesian indices is understood (here and throughout). The Berry curvature is defined as the curl of the connection

$$\Omega_{\alpha\beta}(\boldsymbol{\kappa})d\kappa_\alpha d\kappa_\beta = [\partial_{\kappa_\alpha}\mathcal{A}_\beta(\boldsymbol{\kappa}) - \partial_{\kappa_\beta}\mathcal{A}_\alpha(\boldsymbol{\kappa})]d\kappa_\alpha d\kappa_\beta = -2\,\mathrm{Im}\langle\partial_{k_\alpha}\Psi_{\boldsymbol{\kappa}}|\partial_{k_\beta}\Psi_{\boldsymbol{\kappa}}\rangle d\kappa_\alpha d\kappa_\beta. \tag{7}$$

The connection is a 1-form and is gauge-dependent; the metric and the curvature are 2-forms and are gauge-invariant. The above fundamental quantities are defined in terms of the state vectors solely; we will also address a 2-form which involves the Hamiltonian as well. Suppose that H is the Hamiltonian and E_0 its ground eigenvalue: we will consider

$$\mathcal{G} = \langle\Psi|(H - E_0)|\Psi\rangle, \tag{8}$$

which vanishes for $|\Psi\rangle = |\Psi_0\rangle$; an essential feature of $\mathcal{G}$ is that it is invariant by translation of the energy zero. The geometrical quantity of interest is the gauge-invariant 2-form which is obtained by varying $|\Psi\rangle$ in the neighborhood of $|\Psi_0\rangle$.

3 Many-body geometry

We address here the geometry of the many-body state vectors by generalizing the Hilbert space defined by W. Kohn in a milestone paper published in 1964 [5], well before any geometrical or topological concepts entered condensed matter physics.
For the sake of simplicity we deal with the case where a purely orbital Hamiltonian can be established. Following Kohn, we consider a system of N interacting d-dimensional electrons in a cubic box of volume L^d, and the family of many-body Hamiltonians parametrized by the parameter $\boldsymbol{\kappa}$

$$\hat{H}_{\boldsymbol{\kappa}} = \frac{1}{2m} \sum_{i=1}^{N} \Big[\mathbf{p}_i + \frac{e}{c} \mathbf{A}(\mathbf{r}_i) + \hbar \boldsymbol{\kappa} \Big]^2 + \hat{V}, \tag{9}$$

where $\hat{V}$ includes one-body and two-body potentials. We assume the system to be macroscopically homogeneous; the eigenstates $|\Psi_{n\boldsymbol{\kappa}}\rangle$ are normalized to one in the hypercube of volume L^{Nd}. The vector potential $\mathbf{A}(\mathbf{r})$ summarizes all T-breaking terms as, e.g., those due to spin-orbit coupling to a background of local moments. The vector $\boldsymbol{\kappa}$, having the dimensions of an inverse length, is called "flux" or "twist" and amounts to a gauge transformation. In order to simplify the notation we will set $\hat{H}_0 \equiv \hat{H}$, $|\Psi_{n0}\rangle \equiv |\Psi_n\rangle$, and $E_{n0} \equiv E_n$.
Bulk properties of condensed matter are obtained from the thermodynamic limit: $N \to \infty$, $L \to \infty$, N/L^d constant. All of the observables discussed here include $\boldsymbol{\kappa}$-derivatives of the state vectors $|\Psi_{n\boldsymbol{\kappa}}\rangle$: it is important to stress that the differentiation is performed first, and the thermodynamic limit afterwards. This ensures that a given eigenstate is followed adiabatically while the flux is turned on. Kohn's Hamiltonian can be adopted within two different boundary conditions, thus defining two different Hilbert spaces.

3.1 Open-boundary-conditions Hilbert space

Within the so-called "open" boundary conditions (OBCs) one assumes that the cubic box confines the electrons in an infinite potential well; we will indicate as $|\tilde{\Psi}_{n\boldsymbol{\kappa}}\rangle$ the OBCs eigenstates, square-integrable over $\mathbb{R}^{Nd}$. Within OBCs the effect of the gauge is easily "gauged away": the energy eigenvalues E_n are gauge-independent, while the eigenstates are $|\tilde{\Psi}_{n\boldsymbol{\kappa}}\rangle = \mathrm{e}^{-i\boldsymbol{\kappa}\cdot\hat{\mathbf{r}}} |\tilde{\Psi}_n\rangle$, where $\hat{\mathbf{r}} = \sum_i \mathbf{r}_i$ is the many-body position (multiplicative) operator, which is well defined on this Hilbert space.

3.2 Periodic-boundary-conditions Hilbert space

Within Born-von-Kármán periodic boundary conditions (PBCs) one assumes that the many-body wavefunctions are periodic with period L over each electron coordinate $\mathbf{r}_i$ independently, whose Cartesian components $r_{i,\alpha}$ are then equivalent to the angles $2\pi r_{i,\alpha}/L$. The potential $\hat{V}$ and the vector potential $\mathbf{A}(\mathbf{r})$ enjoy the same periodicity: this means that the macroscopic $\boldsymbol{\mathcal{E}}$ and $\mathbf{B}$ fields vanish. It is worth observing that the position $\hat{\mathbf{r}}$ is *not* a legitimate operator in this Hilbert space: it maps a vector of the space into something which does not belong to the space [2].

As said above, setting $\boldsymbol{\kappa} \neq 0$ amounts to a gauge transformation; since PBCs violate gauge-invariance, the eigenvectors $|\Psi_{n\boldsymbol{\kappa}}\rangle$ and the eigenvalues $E_{n\boldsymbol{\kappa}}$ have a nontrivial $\boldsymbol{\kappa}$-dependence [5]. The macroscopic ground-state current density is

$$\mathbf{j}_{\boldsymbol{\kappa}} = -\frac{e}{\hbar L^d}\langle\Psi_{0\boldsymbol{\kappa}}|\partial_{\boldsymbol{\kappa}}\hat{H}_{\boldsymbol{\kappa}}|\Psi_{0\boldsymbol{\kappa}}\rangle = -\frac{e}{\hbar L^d}\partial_{\boldsymbol{\kappa}}E_{0\boldsymbol{\kappa}} \ ; \tag{10}$$

it vanishes at any $\boldsymbol{\kappa}$ in insulators;[1] within OBCs it vanishes even in metals.
An important comment is in order. Here we follow Kohn, by keeping the boundary conditions fixed and "twisting" the Hamiltonian; other authors [6] have addressed the many-body geometry by keeping the Hamiltonian fixed, and "twisting" the boundary conditions. The equivalence between the two approaches is rather straightforward.

4 Macroscopic electrical polarization

Macroscopic electrical polarization only makes sense for insulators which are charge-neutral on average, and is comprised of an electronic (quantum) term and a nuclear (classical) term. Each of the terms separately depends on the choice of the coordinate origin, while their sum is translationally invariant; we also assume that the system is T-invariant, such that all $\boldsymbol{\kappa} = 0$ wavefunctions are real.

4.1 Bounded samples within open boundary conditions

We consider, for the time being, the electronic term only. Within OBCs the observable has a pretty trivial definition:

$$\mathbf{P}^{(\mathrm{el})} = -\frac{e}{L^d}\langle\tilde{\Psi}_0|\,\hat{\mathbf{r}}\,|\tilde{\Psi}_0\rangle. \tag{11}$$

I am going to transform Eq. (11) into a geometric form: using $|\tilde{\Psi}_{0\boldsymbol{\kappa}}\rangle = \mathrm{e}^{-i\boldsymbol{\kappa}\cdot\hat{\mathbf{r}}}|\tilde{\Psi}_0\rangle$, one gets

$$\mathbf{P}^{(\mathrm{el})} = \frac{ie}{L^d}\langle\tilde{\Psi}_0|\partial_{\boldsymbol{\kappa}}\tilde{\Psi}_0\rangle = -\frac{e}{L^d}\,\tilde{\boldsymbol{\mathcal{A}}}(0). \tag{12}$$

The Berry connection is gauge dependent and cannot express a physical observable per se; we have in fact arrived at Eq. (12) by enforcing a specific gauge. The most general $\boldsymbol{\kappa}$-dependence of the state vector is $|\tilde{\Psi}_{0\boldsymbol{\kappa}}\rangle = \mathrm{e}^{-i\vartheta(\boldsymbol{\kappa},\hat{\mathbf{r}})}|\tilde{\Psi}_0\rangle$, where $\vartheta(\boldsymbol{\kappa},\hat{\mathbf{r}}) = \boldsymbol{\kappa}\cdot\hat{\mathbf{r}}+\phi(\boldsymbol{\kappa})$ where the gauge function $\phi(\boldsymbol{\kappa})$ is arbitrary; Eq. (12) makes sense only if we impose a gauge which makes $\vartheta(\boldsymbol{\kappa},\hat{\mathbf{r}})$ odd in $\hat{\mathbf{r}}$ at any $\boldsymbol{\kappa}$.

4.2 Unbounded samples within periodic boundary conditions

We may try to adopt within PBCs the same definition as in Eq. (12)

$$\mathbf{P}^{(\mathrm{el})} = \frac{ie}{L^d}\langle\Psi_0|\partial_{\boldsymbol{\kappa}}\Psi_0\rangle = -\frac{e}{L^d}\,\boldsymbol{\mathcal{A}}(0), \tag{13}$$

[1] A mobility gap implies that no infinitesimal perturbation to the Hamiltonian can induce a macroscopic current.

an obviously gauge-dependent expression. If, for instance, we evaluate the $\boldsymbol{\kappa}$-derivative by means of perturbation theory

$$|\partial_{\boldsymbol{\kappa}}\Psi_0\rangle = \sum_{n\neq 0} |\Psi_n\rangle \frac{\langle\Psi_n|\partial_{\boldsymbol{\kappa}}\hat{H}|\Psi_0\rangle}{E_0 - E_n}, \tag{14}$$

we get $\langle\Psi_0|\partial_{\boldsymbol{\kappa}}\Psi_0\rangle = 0$. In fact the parallel-transport gauge is implicit in the standard perturbation formula. In order to fix the gauge in a similar way as we did in the OBCs case, we realize that $\mathrm{e}^{-i\boldsymbol{\kappa}\cdot\hat{\mathbf{r}}}|\Psi_0\rangle$ in general does not belong to the Hilbert space, bar in the cases where the $\boldsymbol{\kappa}$ components are integer multiples of $2\pi/L$. It is easy to verify that in such cases $\mathrm{e}^{-i\boldsymbol{\kappa}\cdot\hat{\mathbf{r}}}|\Psi_0\rangle$ is the ground eigenstate of $\hat{H}_{\boldsymbol{\kappa}}$ with eigenvalue E_0. We choose a $\boldsymbol{\kappa}$ in this set:

$$\boldsymbol{\kappa}_1 = (2\pi/L, 0, 0). \tag{15}$$

Since the connection is by definition the differential phase, Eqs. (4) and (5) yield, to leading order,

$$\mathcal{A}_x(0)\frac{2\pi}{L} \simeq -\mathrm{Im\ ln}\ \langle\Psi_0|\Psi_{0\boldsymbol{\kappa}_1}\rangle; \tag{16}$$

Eq. (13) then yields

$$P_x^{(\mathrm{el})} = \frac{e}{2\pi L^{d-1}}\mathrm{Im\ ln}\ \langle\Psi_0|\Psi_{0\boldsymbol{\kappa}_1}\rangle. \tag{17}$$

The state $|\Psi_{0\boldsymbol{\kappa}}\rangle$ is by definition the eigenstate of $\hat{H}_{\boldsymbol{\kappa}}$ which is obtained by following $|\Psi_0\rangle$ adiabatically while the flux $\boldsymbol{\kappa}$ is turned on; owing to Eq. (10), its energy in insulators is E_0 ($\boldsymbol{\kappa}$-independent). Therefore in insulators—and in insulators *only*—$|\Psi_{0\boldsymbol{\kappa}1}\rangle$ is the ground eigenstate of $\hat{H}_{\boldsymbol{\kappa}_1}$; we fix its gauge by choosing $|\Psi_{0\boldsymbol{\kappa}_1}\rangle = \mathrm{e}^{-i\boldsymbol{\kappa}_1\cdot\hat{\mathbf{r}}}|\Psi_0\rangle$, in the same way as we did in the OBCs case:

$$P_x^{(\mathrm{el})} = \frac{e}{2\pi L^{d-1}}\mathrm{Im\ ln}\ \langle\Psi_0|\mathrm{e}^{-i\boldsymbol{\kappa}_1\cdot\hat{\mathbf{r}}}|\Psi_0\rangle = -\frac{e}{2\pi L^{d-1}}\mathrm{Im\ ln}\ \langle\Psi_0|\mathrm{e}^{i\frac{2\pi}{L}\sum_i x_i}|\Psi_0\rangle. \tag{18}$$

The polarization is intensive, ergo the logarithm scales like $N^{1-1/d}$, while the modulus of its argument tends to one from below. It is worth observing that the present gauge choice can be regarded as the many-body analogue of the periodic gauge in band-structure theory [1]: see Eq. (64) below, and the related footnote. Eq. (18) is the so-called single-point Berry-phase formula [2]; for a crystalline system of noninteracting electrons it yields the (by now famous) Berry-phase formula in band-structure theory [7], first obtained by King-Smith and Vanderbilt in 1993 [1,8] (see also the Appendix).

When the Hamiltonian is adiabatically varied, $|\Psi_0\rangle$ acquires an adiabatic time-dependence. It can be proved that $j_x^{(\mathrm{el})}$, defined as

$$j_x^{(el)} = \dot{P}_x^{(\mathrm{el})} = \frac{e}{2\pi L^{d-1}}\mathrm{Im}\ \left(\frac{\langle\dot{\Psi}_0|\mathrm{e}^{-i\boldsymbol{\kappa}_1\cdot\hat{\mathbf{r}}}|\Psi_0\rangle}{\langle\Psi_0|\mathrm{e}^{-i\boldsymbol{\kappa}_1\cdot\hat{\mathbf{r}}}|\Psi_0\rangle} + \frac{\langle\Psi_0|\mathrm{e}^{-i\boldsymbol{\kappa}_1\cdot\hat{\mathbf{r}}}|\dot{\Psi}_0\rangle}{\langle\Psi_0|\mathrm{e}^{-i\boldsymbol{\kappa}_1\cdot\hat{\mathbf{r}}}|\Psi_0\rangle}\right), \tag{19}$$

coincides indeed—to leading order in $1/L$—with the adiabatic current density which traverses the sample [2,7].

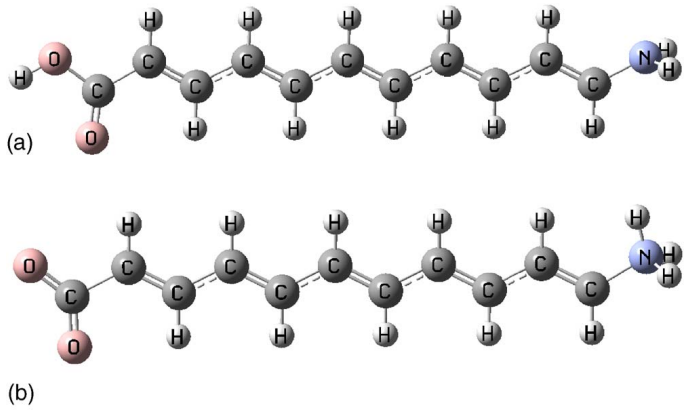

Fig. 1: *A centrosymmetric polymer with two different terminations: alternant trans-polyacetylene. Here the "bulk" is five-monomer long. After Ref. [9].*

The nuclear term can be elegantly included in Eq. (18). If X_ℓ is the x coordinate of the ℓ-th nucleus with charge eZ_ℓ, then

$$P_x = -\frac{e}{2\pi L^{d-1}} \mathrm{Im\ ln}\ \langle \Psi_0 | \mathrm{e}^{i\frac{2\pi}{L}\left(\sum_i x_i - \sum_\ell Z_\ell X_\ell\right)} | \Psi_0 \rangle, \tag{20}$$

clearly invariant under translation of the coordinate origin. This expression also applies if the quantum nature of the nuclei is considered, and $|\Psi_0\rangle$ includes the nuclear degrees of freedom.

4.3 Multivalued nature of polarization

We define the single-point Berry phase γ_x, including the nuclear contribution, as

$$\gamma_x = \mathrm{Im\ ln}\ \langle \Psi_0 | \mathrm{e}^{i\frac{2\pi}{L}\left(\sum_i x_i - \sum_\ell Z_\ell X_\ell\right)} | \Psi_0 \rangle, \qquad P_x = -\frac{e}{2\pi L^{d-1}}\,\gamma_x. \tag{21}$$

Following Eq. (16), the single-point Berry phase scales like $N^{1-1/d}$. Given that γ_x is arbitrary modulo 2π, bulk polarization within PBCs is a multivalued vector. This may appear a disturbing mathematical artifact, but is instead a key feature of the real world. In the following we analyze separately three different cases: $1d$ systems, $3d$ crystalline systems, and $3d$ noncrystalline systems at the independent-electron level.

4.3.1 One-dimensional polarization

The polarization P of a quasi-$1d$ system (e.g. a stereoregular polymer) has the dimensions of a pure charge; in the unbounded case within PBCs P is arbitrary modulo e. The modulo ambiguity is fixed only after the sample termination is specified: we are going to show this in detail on the paradigmatic example of polyacetylene, where the Berry phase yields $P{=}0$ mod e. We consider two differently terminated samples of trans-polyacetylene, as shown in Fig. 1: notice that in both cases the molecule as a whole is *not* inversion symmetric, although the bulk is. The dipoles of such molecules have been computed for several lengths from the Hartree-Fock ground state, as provided by a standard quantum-chemistry code [9]. The dipoles per monomer are plotted in Fig. 2: for small lengths both dipoles are nonzero, as expected, while in the large-chain limit they clearly converge to a quantized value. Since the lattice constant is $a = 4.67$ bohr, the dipole per unit length is $P = 0$ and $P = e$ for the two cases. The results in Fig. 2 are in perspicuous agreement with the Berry-phase theory: in the two bounded realizations of the

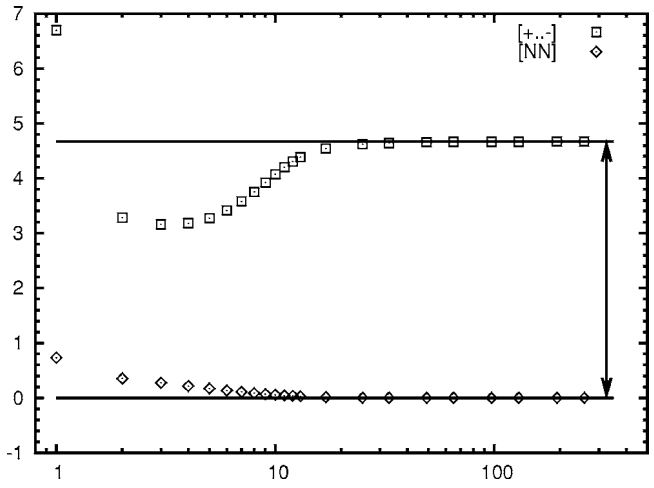

Fig. 2: *Quantization of polarization in polyacetylene: dipole per monomer (a.u.) as a function of the number of monomers in the chain, for the two different terminations. After Ref. [9].*

same quasi one-dimensional periodic system the dipole per unit length assumes—in the large-system limit—two of the values provided by the theory. Insofar as the system is unbounded the modulo e ambiguity in the P value cannot be removed.

4.3.2 Three-dimensional crystalline polarization

In the $3d$ case Eq. (21) yields

$$P_x = -\frac{e}{2\pi L^2}\,\gamma_x, \tag{22}$$

which clearly cannot be used as it stands in the $L \to \infty$ limit. Notwithstanding, polarization is a well defined multivalued observable whenever the system is *crystalline*: with this we mean that a uniquely defined lattice can be associated with the real sample. The lattice is an abstraction, which is uniquely defined even in cases with correlation, quantum nuclei, chemical disorder—i.e. crystalline alloys, a.k.a. solid solutions—where the actual wavefunction may require a supercell (multiple of the primitive lattice cell).

For the sake of simplicity we consider—without loss of generality—a simple cubic lattice of constant a. The supercell side L is an integer multiple of a: $L = Ma$. The integral is over a $3N$-dimensional hypercube of sides L:

$$\langle\Psi_0|\mathrm{e}^{i\frac{2\pi}{L}(\sum_i x_i - \sum_\ell Z_\ell X_\ell)}|\Psi_0\rangle = \int_{\mathrm{hcube}} \prod_{i=1}^{N} d\mathbf{r}_i\; \mathrm{e}^{i\frac{2\pi}{L}(\sum_i x_i - \sum_\ell Z_\ell X_\ell)} |\langle \mathbf{r}_1, \mathbf{r}_2 \ldots \mathbf{r}_N|\Psi_0\rangle|^2. \tag{23}$$

Owing to the crystalline hypothesis, the integral is equal the sum of M^2 identical integrals: see the Appendix for a proof. Therefore we may define a reduced matrix element and a reduced Berry phase

$$\tilde{\gamma}_x = \mathrm{Im}\,\ln \frac{1}{M^2} \int_{\mathrm{hcube}} \prod_{i=1}^{N} d\mathbf{r}_i\; \mathrm{e}^{i\frac{2\pi}{L}(\sum_i x_i - \sum_\ell Z_\ell X_\ell)} |\langle \mathbf{r}_1, \mathbf{r}_2 \ldots \mathbf{r}_N|\Psi_0\rangle|^2, \tag{24}$$

in terms of which

$$P_x = -\frac{e}{2\pi a^2}\,\tilde{\gamma}_x. \tag{25}$$

the polarization of a crystal is therefore a well defined multivalued crystalline observable, ambiguous modulo e/a^2 in each Cartesian component in the case of a simple cubic lattice.

A generic lattice is dealt with by means of a coordinate transformation [10]; the bulk value of $\mathbf{P}$ is then ambiguous modulo $e\mathbf{R}/V_{\rm cell}$, where $\mathbf{R}$ is a lattice vector and $V_{\rm cell}$ is the volume of a primitive cell. By definition a primitive cell is a minimum-volume one: this choice is mandatory in order to make $\mathbf{P}$ a well defined multivalued observable. As in the $1d$ case, the modulo ambiguity is resolved only after the sample termination is specified; there are some complications, though. The theory, owing to PBCs and to the hypothesis of macroscopic homogeneity, yields the polarization $\mathbf{P}$ in zero $\boldsymbol{\mathcal{E}}$ field; instead shape-dependent depolarization fields are generally present in a polarized $3d$ sample. The depolarization field is zero for a sample in the form of a slab, and with $\mathbf{P}$ parallel to the slab (transverse case) [11]. The second complication is the possible occurrence of metallic surfaces. Both complications are ruled out in the quasi-$1d$ case discussed above.

4.3.3 Infrared spectra of liquid and amorphous systems

Whenever a lattice cannot be defined, Eq. (22) shows that $\mathbf{P}$ itself is not a ground-state observable in the thermodynamic limit. Nonetheless the single-point Berry phase of Eq. (22), at finite size L, is instrumental for evaluating polarization *differences*, or macroscopic currents; the latter are the key entry in the theory of infrared spectra. It is enough to choose L larger than the relevant correlation lengths in the material; Eq. (22) can then be used to access polarization differences $\Delta\mathbf{P}$ much smaller than e/L^2.
For the sake of completeness we show here the form of Eq. (22) when $|\Psi_0\rangle$ is the Slater determinant of $N/2$ doubly occupied $\mathbf{k}=0$ (supercell-periodical) Kohn-Sham orbitals $|u_j\rangle = |\psi_j\rangle$. One defines the connection matrix

$$S_{jj'} = \langle u_j | \mathrm{e}^{i\frac{2\pi}{L}x} | u_{j'} \rangle; \tag{26}$$

by including the nuclei and accounting for double orbital occupancy the polarization, in terms of the instantaneous Kohn-Sham orbitals, is

$$P_x(t) = -\frac{e}{2\pi L^2}\,\gamma_x = -\frac{e}{2\pi L^2}\mathrm{Im\ ln}\,\left[\,(\det S)^2 \mathrm{e}^{-i\frac{2\pi}{L}\sum_\ell Z_\ell X_\ell}\,\right]. \tag{27}$$

The key quantity in the infrared spectra is the imaginary part of the isotropic dielectric response. The Kubo-Greenwood formula yields

$$\varepsilon"(\omega) = \frac{2\pi\omega}{3L^3 k_{\rm B}T}\int_{-\infty}^{\infty} dt\,\left\langle \mathbf{d}(t)\cdot\mathbf{d}(0)\right\rangle, \tag{28}$$

where $\mathbf{d}=L^3\mathbf{P}$ is the dipole of the simulation cell and the brackets indicate the thermal average. In a Car-Parrinello simulation the integrand is evaluated at discrete time steps, and only small polarization differences are needed: at any discretized time $n\Delta t$ the polarization is

$$\mathbf{P}(n\Delta t) = \mathbf{P}(0)+[\mathbf{P}(\Delta t)-\mathbf{P}(0)]+[\mathbf{P}(2\Delta t)-\mathbf{P}(\Delta t)]+\cdots+[\mathbf{P}(n\Delta t)-\mathbf{P}((n-1)\Delta t)]. \tag{29}$$

Not surprising, the material whose infrared spectrum has been most studied is liquid water. The very first Car-Parrinello infrared spectrum for liquid water appeared in 1997 [12]; many other followed over the years.

5 Topological polarization in one dimension

In presence of inversion symmetry $P = -P$, ergo either $P = 0$ or $P = e/2$, mod e. This feature has clearly a one-to-one mapping to $\mathbb{Z}_2$, the additive group of the integers modulo two. The polarization of a centrosymmetric polymer is in fact topological: one cannot continuously transform a $\mathbb{Z}_2$-even insulator into a $\mathbb{Z}_2$-odd—by enforcing inversion symmetry—without passing through a metallic state. Arguably, this is the simplest occurrence of a $\mathbb{Z}_2$ topological invariant in condensed matter physics. Similar arguments lead to the quantization of the soliton charge in polyacetylene, whose topological nature was discovered by Su, Schrieffer, and Heeger back in 1979 [13]; they also considered more generally non-singlet cases (here we always assume a nondegenerate singlet ground state).

Fig. 2 shows that quantization occurs in the large-L limit only: this is an OBCs feature. Within PBCs quantization occurs even at finite L: in all inversion symmetric cases, the matrix element in Eq. (20) is always real: either positive ($\mathbb{Z}_2$-even) or negative ($\mathbb{Z}_2$-odd).

The above results clearly demonstrate that polyacetylene is a $\mathbb{Z}_2$-even topological case. A paradigmatic $\mathbb{Z}_2$-odd case instead is a one-dimensional "ionic crystal": a linear chain of alternating equidistant anions and cations. In the long-chain limit $P = e/2$ mod e, independently of the ionicity of the two atoms; this happens, e.g., for the two-band Hubbard model discussed next, at low U values.

A topological quantum transition—occurring in a paradigmatic highly correlated system—was identified long ago in Refs. [14] and [15], although no topological jargon was in fashion at the time. Here I reinterpret topology-wise the original results.

The model system addressed was the two-band Hubbard model (at half filling):

$$H = \sum_{j\sigma} \Big[(-1)^j \Delta\, c^\dagger_{j\sigma} c_{j\sigma} - t\big(c^\dagger_{j\sigma} c_{j+1\sigma} + \text{H.c.}\big)\Big] + U \sum_j n_{j\uparrow} n_{j\downarrow}. \tag{30}$$

We assume $\Delta > 0$, and neutralizing classical charges equal to $+1$ on all sites; the system is clearly inversion-symmetric at any U.

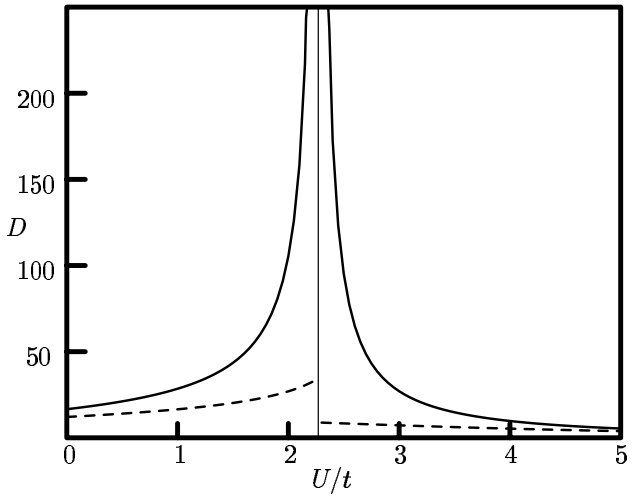

Fig. 3: *Squared localization length for the Hamiltonian in Eq. (30) at half filling for $t/\Delta = 1.75$: the plot shows the dimensionless quantity $D = (2\pi N/L)^2\lambda^2$. The system undergoes a quantum phase transition from band-like insulator ($\mathbb{Z}_2$-odd) to Mott-like insulator ($\mathbb{Z}_2$-even) at $U/t = 2.27$. After Ref. [15].*

Preliminarily, it is expedient to investigate the trivial $t = 0$ case. At small U the anion site (odd j) is doubly occupied, and the energy per cell is $-2\Delta+U$; at $U > 2\Delta$ single occupancy of each site is instead energetically favored. As for polarization, it is easily realized that the system is $\mathbb{Z}_2$-odd in the former case and $\mathbb{Z}_2$-even in the latter. At the transition point $U_c = 2\Delta$ the ground state is degenerate and the spectrum is gapless, ergo the system is "metallic". If the hopping t is then switched on adiabatically, the $\mathbb{Z}_2$ invariant in each of the two topological phases cannot flip unless a metallic state is crossed.

Finite t simulations have been performed in Ref. [15] for several U values, where the explicitly correlated ground-state wavefunction has been found by exact diagonalization, at fixed $t/\Delta = 1.75$. The insulating/metallic character of the system was monitored by means of the squared localization length

$$\lambda^2 = -\frac{L^2}{4\pi^2 N} \ln |\langle \Psi_0 | \mathrm{e}^{i\frac{2\pi}{L}\sum_i x_i} | \Psi_0 \rangle|^2, \tag{31}$$

which will be addressed in detail in Sect. 7.2.1 below. For the time being, suffices to say that in the large-N limit λ^2 stays finite in all kinds of insulators while it diverges in metals.

The results of the simulations are shown in Fig. 3. The t=0 arguments presented above guarantee that at low U values the system is a band-like insulator ($\mathbb{Z}_2$-odd) , while at high U values it is a Mott-like insulator ($\mathbb{Z}_2$-even). The sharp transition occurs at the singular point $U_c = 2.27t$; there is no metal-insulator transition, only an insulator-insulator transition, while the system is metallic at the transition point. If we start from the pure band insulator at $U = 0$, there is a single occupied band and a doubly occupied Wannier function, centered at the anion site: therefore $P = e/2$ mod e [1]. Suppose now we switch on the Hubbard U continuously: the Wannier function is no longer defined, while the polarization P, Eq. (20), is well defined at any U value (except U_c). At the transition point the gap closes and P flips to the 0 (mod e) value for $U>U_c$. Remarkably, it was found that the static ionic charges (on anion and cation) are continuous across the transition, while they are instead obviously discontinuous in the t=0 case. It was also found that the dynamical (Born) effective charge on a given site changes sign [14] at the transition; in retrospect, we now understand that such a sign change in a linear-response property was indeed the fingerprint of the flip of the topological $\mathbb{Z}_2$ index in the ground state.

6 Kubo formulæ for conductivity

Although this review only concerns ground-state properties, it is expedient to display the whole Kubo formulæ for the dynamical conductivity $\sigma_{\alpha\beta}(\omega)$. We define the $\boldsymbol{\kappa} = 0$ many-body velocity operator and its matrix elements:

$$\hat{\mathbf{v}} = \frac{1}{\hbar}\,\partial_{\boldsymbol{\kappa}} \hat{H} = \frac{1}{m}\sum_{i-1}^{N} \Big[\mathbf{p}_i + \frac{e}{c}\mathbf{A}(\mathbf{r}_i)\Big] \tag{32}$$

$$\mathcal{R}_{n,\alpha\beta} = \text{Re}\ \langle \Psi_0 | \hat{v}_\alpha | \Psi_n \rangle \langle \Psi_n | \hat{v}_\beta | \Psi_0 \rangle, \quad \mathcal{I}_{n,\alpha\beta} = \text{Im}\ \langle \Psi_0 | \hat{v}_\alpha | \Psi_n \rangle \langle \Psi_n | \hat{v}_\beta | \Psi_0 \rangle, \tag{33}$$

where $\mathcal{R}_{n,\alpha\beta}$ is symmetric and $\mathcal{I}_{n,\alpha\beta}$ antisymmetric; we further set $\omega_{0n} = (E_n - E_0)/\hbar$. The longitudinal (symmetric) conductivity is:

$$\sigma^{(+)}_{\alpha\beta}(\omega) = D_{\alpha\beta}\left[\delta(\omega) + \frac{i}{\pi\omega}\right] + \sigma^{(\mathrm{regular})}_{\alpha\beta}(\omega), \tag{34}$$

$$D_{\alpha\beta} = \frac{\pi e^2}{L^d}\left(\frac{N}{m}\delta_{\alpha\beta} - \frac{2}{\hbar}\sum_{n\neq 0}\frac{\mathcal{R}_{n,\alpha\beta}}{\omega_{0n}}\right), \tag{35}$$

$$\mathrm{Re}\ \sigma^{(\mathrm{regular})}_{\alpha\beta}(\omega) = \frac{\pi e^2}{\hbar L^d}\sum_{n\neq 0}\frac{\mathcal{R}_{n,\alpha\beta}}{\omega_{0n}}\big[\,\delta(\omega-\omega_{0n}) + \delta(\omega+\omega_{0n})\,\big], \tag{36}$$

$$\mathrm{Im}\ \sigma^{(\mathrm{regular})}_{\alpha\beta}(\omega) = \frac{2e^2}{\hbar L^d}\sum_{n\neq 0}\frac{\mathcal{R}_{n,\alpha\beta}}{\omega_{0n}}\,\frac{\omega}{\omega_{0n}^2-\omega^2}. \tag{37}$$

It will be shown below that the Drude weight $D_{\alpha\beta}$ can be regarded as a geometrical property of the many-electron ground state; it vanishes in insulators. The real part of the longitudinal conductivity obeys the f-sum rule

$$\int_0^\infty d\omega\ \mathrm{Re}\ \sigma_{\alpha\beta}(\omega) = \frac{D_{\alpha\beta}}{2} + \int_0^\infty d\omega\ \mathrm{Re}\ \sigma^{(\mathrm{regular})}_{\alpha\beta}(\omega) = \frac{\omega_{\mathrm{p}}^2}{8}\,\delta_{\alpha\beta} = \frac{\pi e^2 n}{2m}\,\delta_{\alpha\beta}, \tag{38}$$

where $n = N/L^d$ is the electron density and ω_{p} is the plasma frequency.
Dissipation can be included phenomenologically in the Drude term by adopting a single-relaxation-time approximation, exactly as in the classical textbook case [16, 17], i.e.

$$\sigma^{(\mathrm{Drude})}_{\alpha\beta}(\omega) = \frac{\tau}{\pi}\,\frac{D_{\alpha\beta}}{1-i\omega\tau}, \tag{39}$$

whose $\tau \to \infty$ limit coincides with the first term in Eq. (34).
In the special case of a band metal (i.e. a crystalline system of non interacting electrons) $\sigma^{(\mathrm{regular})}_{\alpha\beta}(\omega)$ is a linear-response property which accounts for interband transitions, and is non-vanishing only at frequencies higher than a finite threshold; the threshold also survives after the electron-electron interaction is turned on, owing to translational symmetry and the related selection rules. In absence of translational symmetry the selection rule breaks down: in disordered systems—and in disordered systems *only* [18]—$\sigma^{(\mathrm{regular})}_{\alpha\beta}(0)$ may be nonzero (and the Drude weight may vanish).
Transverse conductivity is nonzero only when T-symmetry is absent. The Kubo formulæ for the transverse (antisymmetric) conductivity are

$$\mathrm{Re}\ \sigma^{(-)}_{\alpha\beta}(\omega) = \frac{2e^2}{\hbar L^d}\sum_{n\neq 0}\frac{\mathcal{I}_{n,\alpha\beta}}{\omega_{0n}^2-\omega^2} \tag{40}$$

$$\mathrm{Im}\ \sigma^{(-)}_{\alpha\beta}(\omega) = \frac{\pi e^2}{\hbar L^d}\sum_{n\neq 0}\frac{\mathcal{I}_{n,\alpha\beta}}{\omega_{0n}}\big[\delta(\omega-\omega_{0n}) - \delta(\omega+\omega_{0n})\big]. \tag{41}$$

7 Time-reversal even geometrical observables

7.1 Drude weight

Electron transport in the diffusive regime is a balance between free acceleration and dissipation [17]; the Drude weight $D_{\alpha\beta}$ (also called adiabatic charge stiffness) is an intensive property of the pristine material, accounting for the former side of the phenomenon only.

In the case of a flat one-body potential (i.e. electron gas, either free or interacting) the velocity operator $\hat{\mathrm{v}}$ is diagonal over the energy eigenstates: the matrix elements $\mathcal{R}_{n,\alpha\beta}$ in Eq. (35) vanish and $D_{\alpha\beta}$ assumes the same value as in classical physics [19, 16], i.e., $D_{\alpha\beta} = \pi e^2 (n/m) \delta_{\alpha\beta}$. Given Eq. (38), switching on the potential (one-body and two-body) has the effect of transferring some spectral weight from the Drude peak into the regular term. For free electrons the acceleration induced by a constant $\boldsymbol{\mathcal{E}}$ field is $-e/m$, and the accelerating current is $-e$ times the mechanical acceleration. $D_{\alpha\beta}$ measures then the free acceleration of the many-electron system induced by a field $\boldsymbol{\mathcal{E}}$ constant in space, although in the adiabatic limit only (it is an $\omega = 0$ linear response) [20]; equivalently, it measures the (inverse) inertia of the electrons.

The form of Eq. (35) does not explicitly show that $D_{\alpha\beta}$ is a ground-state property. In order to show that, I adopt the symbol "$\doteq$" with the meaning "equal in the dc limit", and I define $\sigma^{(\mathrm{D})}_{\alpha\beta}(\omega) \doteq \partial j_\alpha(\omega)/\partial \mathcal{E}_\beta(\omega)$. Conductivity requires the vector-potential gauge: we consider the response to a vector potential $A(\omega)$ in the dc limit

$$\sigma^{(\mathrm{D})}_{\alpha\beta}(\omega) \doteq \frac{\partial j_\alpha}{\partial A_\beta} \frac{\partial A}{\partial \mathcal{E}}. \tag{42}$$

The $\boldsymbol{\kappa}$-dependent current was given above in Eq. (10); we notice that

$$\frac{\partial j_\alpha}{\partial A_\beta} = \frac{e}{\hbar c} \frac{\partial j_\alpha}{\partial \kappa_\beta} = -\frac{e^2}{\hbar^2 c L^d} \frac{\partial^2 E_0(\boldsymbol{\kappa})}{\partial \kappa_\alpha \partial \kappa_\beta}\bigg|_{\boldsymbol{\kappa}=0} \qquad \frac{dA}{d\mathcal{E}} \doteq -c \left[\pi \delta(\omega) + \frac{i}{\omega} \right], \tag{43}$$

where the second expression comes from the causal inversion of $\mathcal{E}(\omega) = i\omega A(\omega)/c$ [18]; we thus arrive at Kohn's famous expression [5]

$$D_{\alpha\beta} = \frac{\pi e^2}{\hbar^2 L^d} \frac{\partial^2 E_0}{\partial \kappa_\alpha \partial \kappa_\beta}, \qquad \sigma^{(\mathrm{D})}_{\alpha\beta}(\omega) = D_{\alpha\beta} \left[\delta(\omega) + \frac{i}{\pi\omega} \right] \tag{44}$$

where we remind that it is crucial to set $\boldsymbol{\kappa} = 0$ in the derivative before taking the large-L limit. From Eq. (10) it is obvious that $D_{\alpha\beta}$ vanishes in insulators.

The expression in Eq. (44) is not yet geometrical; we arrive at an equivalent geometrical form starting from the identity $\langle \Psi_{0\boldsymbol{\kappa}} | \, (\hat{H}_{\boldsymbol{\kappa}} - E_{0\boldsymbol{\kappa}}) \, | \Psi_{0\boldsymbol{\kappa}} \rangle \equiv 0$, taking two derivatives, and setting $\boldsymbol{\kappa}$=0:

$$\frac{\partial^2 E_{0\boldsymbol{\kappa}}}{\partial \kappa_\alpha \partial \kappa_\beta} = \frac{N\hbar^2}{m} \delta_{\alpha\beta} - 2 \, \mathrm{Re} \, \langle \partial_{\kappa_\alpha} \Psi_{0\boldsymbol{\kappa}} | \, (\hat{H}_{\boldsymbol{\kappa}} - E_{0\boldsymbol{\kappa}}) \, | \partial_{\kappa_\beta} \Psi_{0\boldsymbol{\kappa}} \rangle \tag{45}$$

$$D_{\alpha\beta} = \frac{\pi e^2 N}{m L^d} \delta_{\alpha\beta} - \frac{2\pi e^2}{\hbar^2 L^d} \mathrm{Re} \, \langle \partial_{\kappa_\alpha} \Psi_0 | \, (\hat{H} - E_0) \, | \partial_{\kappa_\beta} \Psi_0 \rangle, \tag{46}$$

The two terms in Eq. (46) have a very transparent meaning: the first one measures the free-electron acceleration; the geometrical term measures how much such acceleration is hindered

by the one-body and two-body potentials. As observed above, the geometrical term is zero even for the *interacting* electron gas; whenever instead the one-body potential is not flat, then both one-body and two-body terms in $\hat{V}$ concur in hindering the free acceleration.
The geometrical term in Eq. (46) can also be cast as a sum rule for longitudinal conductivity: from Eq. (38) we have

$$\frac{\pi e^2}{\hbar^2 L^d} \,\mathrm{Re}\, \langle \partial_{\kappa_\alpha} \Psi_0 | \, (\hat{H} - E_0) \, | \partial_{\kappa_\beta} \Psi_0 \rangle = \int_0^\infty d\omega \,\mathrm{Re}\, \sigma_{\alpha\beta}^{(\mathrm{regular})}(\omega). \tag{47}$$

On the experimental side, the partitioning of $\sigma_{\alpha\beta}^{(+)}(\omega)$ into a broadened Drude peak and a regular term $\sigma_{\alpha\beta}^{(\mathrm{regular})}(\omega)$ is not so clearcut as one might wish [17].

7.2 Souza-Wilkens-Martin sum rule and the theory of the insulating state

The insulating behavior of a generic material implies that $D_{\alpha\beta} = 0$ and that $\mathrm{Re}\, \sigma_{\alpha\beta}^{(\mathrm{regular})}(\omega)$ goes to zero for $\omega \to 0$ at zero temperature. For this reason Souza, Wilkens, and Martin (hereafter quoted as SWM) proposed to characterize the metallic/insulating behavior of a material by means of the integral [21]

$$I_{\alpha\beta}^{(\mathrm{SWM})} = \int_0^\infty \frac{d\omega}{\omega} \,\mathrm{Re}\, \sigma_{\alpha\beta}^{(+)}(\omega), \tag{48}$$

which diverges for all metals and converges for all insulators; in a gapped insulator the integrand is zero for $\omega < \epsilon_{\mathrm{gap}}/\hbar$. Owing to a fluctuation-dissipation theorem, the SWM integral is a geometrical property of the insulating ground state.

7.2.1 Periodic boundary conditions

Dealing with dc conductivity obviously requires PBCs; whenever the Drude weight is nonzero, the integral in Eq. (48) diverges because of the $\delta(\omega)/\omega$ integrand. Therefore determining whether $I_{\alpha\beta}^{(\mathrm{SWM})}$ converges or diverges is completely equivalent to determining whether $D_{\alpha\beta}$ is zero or finite; it will be shown that the PBCs metric is related to $\sigma_{\alpha\beta}^{(\mathrm{regular})}(\omega)$ only.
We insert a complete set of states into Eq. (6) at $\boldsymbol{\kappa} = 0$ to obtain the intensive quantity

$$\mathfrak{g}_{\alpha\beta} = \frac{1}{N} g_{\alpha\beta}(0) = \frac{1}{N} \,\mathrm{Re} \sum_{n \neq 0} \langle \partial_{\kappa_\alpha} \Psi_0 | \Psi_n \rangle \langle \Psi_n | \partial_{\kappa_\beta} \Psi_0 \rangle. \tag{49}$$

We then evaluate the $\boldsymbol{\kappa}$-derivatives via perturbation theory in the parallel transport gauge

$$|\partial_{\kappa_\alpha} \Psi_0 \rangle = - \sum_{n \neq 0} |\Psi_n\rangle \frac{\langle \Psi_n | \hat{v}_\alpha | \Psi_0 \rangle}{\omega_{0n}}, \qquad \mathfrak{g}_{\alpha\beta} = \frac{1}{N} \sum_{n \neq 0} \frac{\mathrm{Re} \langle \Psi_n | \hat{v}_\alpha | \Psi_0 \rangle \langle \Psi_n | \hat{v}_\beta | \Psi_0 \rangle}{\omega_{0n}^2} \tag{50}$$

From the Kubo formula, Eq. (36), we have

$$\int_0^\infty \frac{d\omega}{\omega} \,\mathrm{Re}\, \sigma_{\alpha\beta}^{(\mathrm{regular})}(\omega) = \frac{\pi e^2}{\hbar L^d} \sum_{n \neq 0} \frac{\mathcal{R}_{n,\alpha\beta}}{\omega_{0n}^2} = \frac{\pi e^2 N}{\hbar L^d} \, \mathfrak{g}_{\alpha\beta}, \tag{51}$$

where the $N \to \infty$ limit is understood. The intensive quantity $\mathfrak{g}_{\alpha\beta}$, having the dimensions of a squared length, in the case of a band insulator is related to the gauge-invariant quadratic spread $\Omega_{\rm I}$ of the Wannier functions [1]: for an isotropic solid

$$\mathfrak{g}_{xx} = \frac{\Omega_{\rm I}}{n_{\rm b} d}, \tag{52}$$

where $n_{\rm b}$ is the number of occupied bands. It is seen from Eq. (51) that $\mathfrak{g}_{\alpha\beta}$ does not discriminate between insulators and metals: it is finite in both cases. The story does not ends here, though.

In 1999 Resta and Sorella have defined a squared localization length λ^2 as a discriminant for the insulating state [15]: as a function of N, λ^2 converges to a finite value in all insulators, and diverges in all metals. In the original paper the approach was demonstrated for the two-band Hubbard model of Eq. (30) and its quantum transition. Many years after the divergence/convergence of λ^2 has been successfully adopted for investigating the Mott transition in the paradigmatic case of a linear chain of hydrogen atoms [22]. In insulators λ^2 is a finite-N approximant of $\mathfrak{g}_{xx}$, but when the same definition is applied to metals λ^2 has the virtue of diverging. We assume an isotropic system and we consider once more $\boldsymbol{\kappa}_1 = (2\pi/L, 0, 0)$; since the metric is by definition the infinitesimal distance, Eqs. (1) and (5) yield to leading order

$$N \mathfrak{g}_{xx} \left(\frac{2\pi}{L} \right)^2 \simeq - \ln |\langle \Psi_0 | \Psi_{0\boldsymbol{\kappa}_1} \rangle|^2, \qquad \mathfrak{g}_{xx} \simeq - \frac{L^2}{4\pi^2 N} \ln |\langle \Psi_0 | \Psi_{0\boldsymbol{\kappa}_1} \rangle|^2. \tag{53}$$

If the system is insulating, we may replace $|\Psi_{0\boldsymbol{\kappa}_1}\rangle = \mathrm{e}^{-i\boldsymbol{\kappa}_1 \cdot \hat{\mathbf{r}}} |\Psi_0\rangle$ as we did in Eq. (18) above:

$$\mathfrak{g}_{xx} \simeq - \frac{L^2}{4\pi^2 N} \ln |\langle \Psi_0 | \mathrm{e}^{i \frac{2\pi}{L} \sum_i x_i} | \Psi_0 \rangle|^2. \tag{54}$$

The right-hand side coincides indeed with λ^2, Eq. (31), originally introduced in Ref [15]. Given that $\mathfrak{g}_{xx}$ is intensive, the logarithm in Eq. (53) scales like $N^{1-2/d}$.

Next we address the metallic case. In a band metal $|\Psi_0\rangle$ is a Slater determinant of Bloch orbitals, and not all the $\mathbf{k}$ vectors in the Brillouin zone are occupied. A selection rule then guarantees that $\langle \Psi_0 | \mathrm{e}^{i \frac{2\pi}{L} \sum_i x_i} | \Psi_0 \rangle$ vanishes even at *finite* N [23, 24]; therefore λ^2 is formally infinite. In disordered or correlated materials the selection rule breaks down, and λ^2 diverges in the large-N limit only. This can be seen as follows: Whenever the Drude weight is nonzero, then Eq. (44) guarantees that $|\Psi_{0\boldsymbol{\kappa}_1}\rangle$ is an eigenstate of $\hat{H}_{\boldsymbol{\kappa}_1}$ orthogonal to $\mathrm{e}^{-i\boldsymbol{\kappa}_1 \cdot \hat{\mathbf{r}}} |\Psi_0\rangle$; to lowest order in $\boldsymbol{\kappa}_1$ we have

$$0 = \langle \Psi_0 | \mathrm{e}^{i\boldsymbol{\kappa}_1 \cdot \hat{\mathbf{r}}} | \Psi_{0\boldsymbol{\kappa}_1} \rangle \simeq \langle \Psi_0 | \mathrm{e}^{i\boldsymbol{\kappa}_1 \cdot \hat{\mathbf{r}}} | \Psi_0 \rangle, \tag{55}$$

which proves the divergence of λ^2. In the large-L limit the modulus of the matrix element $\left| \langle \Psi_0 | \mathrm{e}^{i\boldsymbol{\kappa}_1 \cdot \hat{\mathbf{r}}} | \Psi_0 \rangle \right|$ approaches one from below in insulators, while it approaches zero in metals.

7.2.2 Open boundary conditions

The SWM integral is more useful in practical computations within OBCs. A bounded sample does not support a dc current, and $D_{\alpha\beta} = 0$ at any finite size: this is consistent with the fact that

Eq. (10) vanishes within OBCs. An oscillating field $\boldsymbol{\mathcal{E}}(\omega)$ in a large sample linearly induces a macroscopic polarization $\mathbf{P}(\omega)$; since $\mathbf{j}(t) = d\mathbf{P}(t)/dt$, we define a "fake" conductivity by means of the relationship

$$\tilde{\sigma}_{\alpha\beta}(\omega) = -i\omega \, \frac{\partial P_\alpha(\omega)}{\partial \mathcal{E}_\beta(\omega)} \, . \tag{56}$$

The Kubo formulæ for this OBCs response function are

$$\text{Re } \tilde{\sigma}_{\alpha\beta}(\omega) = \frac{\pi e^2}{\hbar L^d} \sum_{n\neq 0} \frac{\mathcal{R}_{n,\alpha\beta}}{\omega_{0n}} \, \big[\, \delta(\omega - \omega_{0n}) + \delta(\omega + \omega_{0n}) \, \big] . \tag{57}$$

Despite the formal similarity with Eq. (36), $\tilde{\sigma}_{\alpha\beta}(\omega)$ is *very different*—at finite size—from $\sigma^{(\text{regular})}_{\alpha\beta}(\omega)$: different eigenvalues, different matrix elements and selection rules; also, $\tilde{\sigma}_{\alpha\beta}(\omega)$ saturates the f-sum rule, while $\sigma^{(\text{regular})}_{\alpha\beta}(\omega)$ by itself does not (in metals). Then it is easy to show that the SWM integral is related to the OBCs metric in the same way as in Eq. (51):

$$\int_0^\infty \frac{d\omega}{\omega} \, \text{Re } \tilde{\sigma}_{\alpha\beta}(\omega) = \frac{\pi e^2}{\hbar L^d} \sum_{n\neq 0} \frac{\mathcal{R}_{n,\alpha\beta}}{\omega_{0n}^2} = \frac{\pi e^2 N}{\hbar L^d} \, \tilde{\mathfrak{g}}_{\alpha\beta}, \tag{58}$$

where again the $N \to \infty$ limit is understood. The OBCs metric per electron $\tilde{\mathfrak{g}}_{\alpha\beta}$ coincides with that for PBCs in insulators, but has the virtue of diverging in metals [25]. What actually happens is that the low-frequency spectral weight in the OBCs $\tilde{\sigma}_{\alpha\beta}(\omega)$ is reminiscent of—and accounts for—the corresponding Drude peak within PBCs, thus leading to a diverging $I^{(\text{SWM})}_{\alpha\beta}$. Within OBCs one has $|\partial_{\boldsymbol{\kappa}} \Psi_0\rangle = -i\hat{\mathbf{r}}|\Psi_0\rangle$, hence Eq. (6) yields

$$\tilde{\mathfrak{g}}_{\alpha\beta} = \frac{1}{N} \Big(\, \langle \Psi_0 | \hat{r}_\alpha \hat{r}_\beta | \Psi_0 \rangle - \langle \Psi_0 | \hat{r}_\alpha | \Psi_0 \rangle \langle \Psi_0 | \hat{r}_\beta | \Psi_0 \rangle \, \Big), \tag{59}$$

and the "Re" is not needed. This is clearly a second cumulant moment of the dipole (per electron): the symbol $\langle r_\alpha r_\beta \rangle_{\text{c}}$ has been equivalently used in some previous literature. Alternatively, $\tilde{\mathfrak{g}}_{\alpha\beta}$ measures the quadratic quantum fluctuations of the polarization in the ground state [21]. An equivalent expression for $\tilde{\mathfrak{g}}_{\alpha\beta}$ is in terms of the one-body density $n(\mathbf{r})$ and the two-body density $n^{(2)}(\mathbf{r},\mathbf{r}')$ [25]

$$\begin{aligned} \tilde{\mathfrak{g}}_{\alpha\beta} \;\; &= \;\; \frac{1}{2N} \int d\mathbf{r} \, d\mathbf{r}' \; (\mathbf{r}-\mathbf{r}')_\alpha (\mathbf{r}-\mathbf{r}')_\beta \big[\, n(\mathbf{r}) n(\mathbf{r}') - n^{(2)}(\mathbf{r},\mathbf{r}') \, \big] . \\ &= \; -\frac{1}{2N} \int d\mathbf{r} \, d\mathbf{r}' \; (\mathbf{r}-\mathbf{r}')_\alpha (\mathbf{r}-\mathbf{r}')_\beta \;\; n(\mathbf{r}) \, n_{\text{xc}}(\mathbf{r},\mathbf{r}'), \end{aligned} \tag{60}$$

where $n_{\text{xc}}(\mathbf{r},\mathbf{r}')$ is by definition the exchange-correlation hole density. Therefore $\tilde{\mathfrak{g}}_{\alpha\beta}$ is a second moment of the exchange-correlation hole, averaged over the sample.

Finite-size model-Hamiltonian OBCs calculations have provided—by means of $\tilde{\mathfrak{g}}_{\alpha\beta}$—insight into the Anderson insulating state in $1d$ [26,27], and into the Anderson metal-insulator transition in $3d$ [28].

8 Time-reversal odd geometrical observables

8.1 Anomalous Hall conductivity and Chern invariant

Edwin Hall discovered the eponymous effect in 1879; two years later he discovered the anomalous Hall effect in ferromagnetic metals. The latter is, by definition, the Hall effect in absence of a macroscopic B field. Nonvanishing transverse conductivity requires breaking of T-symmetry: in the normal Hall effect the symmetry is broken by the applied B field; in the anomalous one it is spontaneously broken, for instance by the development of ferromagnetic order. The theory of anomalous Hall conductivity in metals has been controversial for many years; since the early 2000s it became clear that, besides extrinsic effects, there is also an intrinsic contribution, which can be expressed as a geometrical property of the electronic ground state in the pristine crystal. Without extrinsic mechanisms the longitudinal dc conductivity would be infinite; such mechanisms are necessary to warrant Ohm's law, and are accounted for by relaxation time(s) τ; in the absence of T-symmetry, extrinsic mechanisms affect the anomalous Hall conductivity (AHC) as well. Two distinct mechanisms have been identified: they go under the name of "side jump" and "skew scattering" [29]. The side-jump term is nondissipative (independent of τ). Since a crystal with impurities actually is a (very) dilute alloy, we argued that the sum of the intrinsic and side-jump terms can be regarded as the intrinsic term of the alloy [30]. As a matter of principle, such "intrinsic" AHE of the dirty sample can be addressed either in reciprocal space [30,31], or even in real space [32]. Finally the skew-scattering term is dissipative, proportional to τ in the single-relaxation-time approximation. Here we deal with the intrinsic geometrical term only.
As pointed out by Haldane in a milestone paper that appeared in 1988 [33], AHC is also allowed in insulators, and is topological in $2d$: therein extrinsic effects are ruled out. In fact in insulators the dc longitudinal conductivity is zero, and—as a basic tenet of topology—any impurity has no effect on the Hall conductivity insofar as the system remains insulating. The effect goes under the name of quantum anomalous Hall effect (QAHE); the synthesis of a $2d$ material where the QAHE occurs was only achieved from 2013 onwards [34,35].
The Kubo formula of Eq. (40) immediately gives the intrinsic AHC term as

$$\mathrm{Re}\ \sigma^{(-)}_{\alpha\beta}(0) = \frac{2e^2}{\hbar L^d} \sum_{n\neq 0}{}' \frac{\mathrm{Im}\ \langle\Psi_0|\hat{v}_\alpha|\Psi_n\rangle\langle\Psi_n|\hat{v}_\beta|\Psi_0\rangle}{\omega_{0n}^2}. \tag{61}$$

In a similar way as for Eqs. (50) and (51), we easily get the expression

$$\mathrm{Re}\ \sigma^{(-)}_{\alpha\beta}(0) = -\frac{e^2}{\hbar L^d}\,\Omega_{\alpha\beta}(0), \tag{62}$$

where $\Omega_{\alpha\beta}(0)$ is the many-body Berry curvature, Eq. (7). It holds for metals and insulators, in either $2d$ or $3d$; the large-system limit is understood. In the band-structure case $\Omega_{\alpha\beta}(0)/L^d$ is simply related to the Fermi-volume integral of the one-body Berry curvature [1,31].
Next we consider the $2d$ case: in any smooth gauge the curvature per unit area can be written as

$$\frac{1}{L^2}\Omega_{xy}(0) = \frac{1}{L^2}\left(\frac{L}{2\pi}\right)^2 \int_0^{\frac{2\pi}{L}} d\kappa_x \int_0^{\frac{2\pi}{L}} d\kappa_y\ \Omega_{xy}(\boldsymbol{\kappa}), \tag{63}$$

where the integral and the prefactor are both dimensionless. Even this formula holds for both insulators and metals, but we remind that $|\Psi_{0\boldsymbol{\kappa}}\rangle$ is obtained by following $|\Psi_0\rangle$ as the flux $\boldsymbol{\kappa}$ is adiabatically turned on; the behavior of the integrand in Eq. (63) is then *qualitatively* different in the insulating vs. metallic case.

From now on we deal with the insulating case only. Since the Drude weight is zero, the energy is $\boldsymbol{\kappa}$ independent; furthermore the integral in Eq. (63) is actually equivalent to the integral over a torus and is therefore quantized. In order to show this, we observe that whenever the components of $\boldsymbol{\kappa}-\boldsymbol{\kappa}'$ are integer multiples of $2\pi/L$, the state $\mathrm{e}^{i(\boldsymbol{\kappa}-\boldsymbol{\kappa}')\cdot\hat{\mathbf{r}}}|\Psi_{0\boldsymbol{\kappa}}\rangle$ is an eigenstate of $\hat{H}_{\boldsymbol{\kappa}'}$ with the same eigenvalue

$$|\Psi_{0\boldsymbol{\kappa}'}\rangle = \mathrm{e}^{i(\boldsymbol{\kappa}-\boldsymbol{\kappa}')\cdot\hat{\mathbf{r}}}|\Psi_{0\boldsymbol{\kappa}}\rangle. \tag{64}$$

Since $\Omega_{xy}(\boldsymbol{\kappa})$ is gauge-invariant, an arbitrary phase factor may relate the two members of Eq. (64). It is worth stressing that in the topological case a globally smooth gauge does not exist; in other words we can enforce Eq. (64) as it stands (with no extra phase factor) only locally, not globally.[2]

The integral in Eq. (63) is quantized (even at finite L) and is proportional to the many-body Chern number, as defined by Niu, Thouless and Wu (NTW) in a famous paper [6]

$$C_1 = \frac{1}{2\pi}\int_0^{\frac{2\pi}{L}} d\kappa_x \int_0^{\frac{2\pi}{L}} d\kappa_x \; \Omega_{xy}(\boldsymbol{\kappa}), \qquad \text{Re}\;\sigma_{xy}^{(-)}(0) = -\frac{e^2}{h}C_1. \tag{65}$$

In the present formulation we have assumed PBCs at any $\boldsymbol{\kappa}$, and—following Kohn [5]—we have "twisted" the Hamiltonian. The reverse is done by NTW: the Hamiltonian is kept fixed, and the boundary conditions are "twisted". It is easy to show that the two approaches are equivalent: within both of them the two components of $\boldsymbol{\kappa}$ become effectively angles, the integration is over a torus, and the integral is a topological invariant.

The AHC is therefore quantized in any $2d$ T-breaking insulator, thus yielding the QAHE. Originally, NTW were not addressing the QAHE; the phenomenon addressed was instead the fractional quantum Hall effect, where the electronic ground state is notoriously highly correlated [36]. While the topological invariant is by definition integer, the fractional conductance owes—according to NTW—to the degeneracy of the ground state in the large-L limit. Also, in presence of a macroscopic $\mathbf{B}$ field, gauge-covariant boundary conditions and magnetic translations must be adopted.

8.2 Magnetic circular dichroism sum rule

Since a very popular (and misleading) paper appeared in 1992 [37], magnetic circular dichroism (MCD) has been widely regarded among synchrotron experimentalists as an approximate probe of orbital magnetization $\mathbf{M}$ in bulk solids. It became clear over the years that this is an

[2]The gauge choice of Eq. (64) is the many-body analogue of the periodic gauge in band-structure theory. Therein it is well known that, in the topological case, it is impossible to adopt a gauge which is periodic and smooth on the whole Brillouin zone: an "obstruction" is necessarily present. See Ch. 3 in Ref. [1].

unjustified assumption, thanks particularly to Refs. [38], [39], and [40]. The differential absorption of right and left circularly polarized light by magnetic materials is known as magnetic circular dichroism; the object of interest is the frequency integral of the imaginary part of the antisymmetric term in the conductivity tensor

$$I_{\alpha\beta}^{(\mathrm{MCD})} = \mathrm{Im} \int_0^\infty d\omega \; \sigma_{\alpha\beta}^{(-)}(\omega); \tag{66}$$

a kind of fluctuation-dissipation theorem relates $I_{\alpha\beta}^{(\mathrm{MCD})}$ to a ground-state property. The Kubo formula, Eq. (41), immediately yields

$$I_{\alpha\beta}^{(\mathrm{MCD})} = \frac{\pi e^2}{\hbar L^d} \sum_{n\neq 0} \frac{\mathcal{I}_{n,\alpha\beta}}{\omega_{0n}} = \frac{\pi e^2}{\hbar L^3} \, \mathrm{Im} \sum_{n\neq 0} \frac{\langle \Psi_0 | \hat{v}_\alpha | \Psi_n \rangle \langle \Psi_n | \hat{v}_\beta | \Psi_0 \rangle}{\omega_{0n}}; \tag{67}$$

this expression holds both within OBCs and PBCs, although with different eigenvalues, different matrix elements, and different selection rules (at any finite size). In both cases, $I_{\alpha\beta}^{(\mathrm{MCD})}$ can be cast as a geometric property of the electronic ground state, via the substitution

$$|\partial_{\boldsymbol{\kappa}} \Psi_0\rangle = -\sum_{n\neq 0} |\Psi_n\rangle \frac{\langle \Psi_n | \hat{\mathbf{v}} | \Psi_0 \rangle}{\omega_{n0}} \tag{68}$$

$$(\hat{H} - E_0) |\partial_{\boldsymbol{\kappa}} \Psi_0\rangle = -\sum_{n\neq 0} |\Psi_n\rangle \langle \Psi_n | \hat{\mathbf{v}} | \Psi_0 \rangle. \tag{69}$$

By comparing the last expression to Eq. (67) the geometrical formula is

$$I_{\alpha\beta}^{(\mathrm{MCD})} = \frac{\pi e^2}{\hbar^2 L^3} \, \mathrm{Im} \, \langle \partial_{\kappa_\alpha} \Psi_0 | (\hat{H} - E_0) | \partial_{\kappa_\beta} \Psi_0 \rangle. \tag{70}$$

The PBCs many-body expression for $I_{\alpha\beta}^{(\mathrm{MCD})}$, Eq. (70), unfortunately cannot be compared with a corresponding formula for M. To this day such a formula does not exist: the orbital magnetization of a correlated many-body wavefunction within PBCs is currently an open (and challenging) problem. A thorough comparison has been done at the band-structure level only, where both $I_{\alpha\beta}^{(\mathrm{MCD})}$ and M have a known expression, as a Fermi-volume integral of a geometrical integrand [39, 40].

A direct comparison between $I_{\alpha\beta}^{(\mathrm{MCD})}$ and M was instead provided within OBCs as early as 2000 by Kunes and Oppeneer [38]; we are going to retrieve their outstanding result within the present formalism. As already observed, within OBCs one has $|\partial_{\boldsymbol{\kappa}} \Psi_0\rangle = -i\hat{\mathbf{r}} |\Psi_0\rangle$, ergo

$$\begin{aligned} I_{\alpha\beta}^{(\mathrm{MCD})} &= \frac{\pi e^2}{\hbar^2 L^3} \, \mathrm{Im} \, \langle \Psi_0 | \hat{r}_\alpha (\hat{H} - E_0) \hat{r}_\beta | \Psi_0 \rangle = -\frac{i\pi e^2}{2\hbar^2 L^3} \, \mathrm{Im} \, \langle \Psi_0 | \hat{r}_\alpha [\hat{H}, \hat{r}_\beta] | \Psi_0 \rangle \\ &= -\frac{\pi e^2}{2\hbar L^3} \langle \Psi_0 | (\hat{r}_\alpha \hat{v}_\beta - \hat{r}_\beta \hat{v}_\alpha) | \Psi_0 \rangle. \end{aligned} \tag{71}$$

The ground-state expectation value in Eq. (71) was originally dubbed "center of mass angular momentum". By expanding the many-body operators $\hat{\mathbf{r}}$ and $\hat{\mathbf{v}}$, the matrix element is the ground-state expectation value of $\sum_{ii'} \mathbf{r}_i \times \mathbf{v}_{i'}$, while the orbital moment of a bounded sample

is proportional to the expectation value of $\sum_i \mathbf{r}_i \times \mathbf{v}_i$. The two coincide only in the single-electron case; this is consistent with the band-structure findings. Indeed it has been proved that $I^{(\mathrm{MCD})}_{\alpha\beta}$ and $\mathbf{M}$ coincide *only* for an isolated flat band: a disconnected electron distribution with one electron per cell (and per spin channel) [40].
The MCD sum rule $I^{(\mathrm{MCD})}_{\alpha\beta}$ is an outstanding ground-state observable per se, because of reasons not to be explained here, and which are at the root if its enormous experimental success. Notwithstanding, there is no compelling reason for identifying it, even approximately, with some form of orbital magnetization. The two observables $I^{(\mathrm{MCD})}_{\alpha\beta}$ and $\mathbf{M}$ provide a quantitatively different measure of spontaneous T-breaking in the orbital degrees of freedom of a given material.

9 Conclusions

The known geometrical observables come in two very different classes: those in class (i) only make sense for insulators, and are defined modulo 2π (in dimensionless units), while those in class (ii) are defined for both insulators and metals, and are single-valued. Such outstanding difference owes—at the very fundamental level—to the fact that the observables in class (i) are expressed by means of gauge-dependent $(2n-1)$-forms, while those in class (ii) are expressed in terms of gauge-invariant $2n$-forms.
I have thoroughly discussed here the only observable in class (i) whose many-body formulation is known: macroscopic polarization [2]; it is rooted in the Berry connection, a gauge-dependent 1-form, called Chern-Simons 1-form in mathematical speak. The many-body connection, Eq. (5), may yield a physical observable only after the gauge is fixed: in the present case, I adopted the many-body analogue of the periodic gauge in band-structure theory. I have also discussed the multivalued nature of bulk polarization, whose features in either $1d$ or $3d$ are somewhat different.
Another class-(i) geometrical observable is known in band-structure theory, where it is expressed as the Brillouin-zone integral of a Chern-Simons 3-form: this is the so called "axion" term in magnetoelectric response [1]. The corresponding many-body expression is not known; it is even possible that it could not exist as a matter of principle [41]. In the presence of some protecting symmetry a class-(i) observable may only assume the values zero or π (mod 2π): the observable becomes then a topological $\mathbb{Z}_2$ index: a $\mathbb{Z}_2$-odd crystalline insulator cannot be "continuously deformed" into one $\mathbb{Z}_2$-even without passing through a metallic state and without breaking the protecting symmetry.
Four geometrical observables of class (ii), having a known many-body expression, have been discussed in the present Review. All are single valued, and all are rooted in gauge-invariant 2-forms; the following table summarizes them:

Time-reversal odd	**Time-reversal even**
Anomalous Hall conductivity	Souza-Wilkens-Martin sum rule
Magnetic circular dichroism sum rule	Drude weight

The four observables are expressed by means of the $\boldsymbol{\kappa} = 0$ values of the geometrical 2-forms $\mathcal{F}$ and $\mathcal{G}$, defined as

$$\mathcal{F} = [\,\langle\partial_{\kappa_\alpha}\Psi_{0\boldsymbol{\kappa}}|\partial_{\kappa_\beta}\Psi_{0\boldsymbol{\kappa}}\rangle - \langle\partial_{\kappa_\alpha}\Psi_{0\boldsymbol{\kappa}}|\Psi_{0\boldsymbol{\kappa}}\rangle\langle\Psi_{0\boldsymbol{\kappa}}|\partial_{\kappa_\beta}\Psi_{0\boldsymbol{\kappa}}\rangle\,]\,d\kappa_\alpha d\kappa_\beta, \tag{72}$$

$$\mathcal{G} = \langle\partial_{\kappa_\alpha}\Psi_{0\boldsymbol{\kappa}}|\,(\hat{H}_{\boldsymbol{\kappa}} - E_{0\boldsymbol{\kappa}})\,|\partial_{\kappa_\beta}\Psi_{0\boldsymbol{\kappa}}\rangle\,d\kappa_\alpha d\kappa_\beta. \tag{73}$$

Both forms are extensive; the real symmetric part of $\mathcal{F}$ coincides with the quantum metric, Eq. (6), while its imaginary part (times -2) coincides with the Berry curvature, Eq. (7).

The T-odd observables in the table are obtained from the antisymmetric imaginary part of $\mathcal{F}$ (AHC) and $\mathcal{G}$ (MCD sum rule); similarly, the T-even observables are obtained from the real symmetric part of $\mathcal{F}$ (SWM sum rule) and $\mathcal{G}$ (Drude weight). All of these observables have an elegant independent-electron crystalline counterpart: within band-structure theory they are expressed as Fermi volume integrals (Brillouin-zone integrals in insulators) of gauge-invariant geometrical 2-forms in Bloch space [42]. There is one very important T-odd geometrical observable missing from the above table: orbital magnetization. Its expression within band-structure theory is known since 2006, for both insulators and metals [1,3]. Very bafflingly, a corresponding expression in terms of the many-body ground state does not exist to this day.

The two T-even observables have an important meaning in the theory of the insulating state [24]. The Drude weight is zero in all insulators, and nonzero in all metals; to remain on the safe side, the statement applies to systems without disorder [18]. Instead the geometrical term in the SWM sum rule within PBCs does not discriminate between insulators and metals; nonetheless I have shown that a discretized formulation of the same observable—proposed by Resta and Sorella back in 1999 [15]—does discriminate. Furthermore it is expedient to alternatively cast the SWM sum rule in the OBCs Hilbert space: even in this case the geometrical observable acquires the virtue of discriminating between insulators and metals [24,28].

Among the five observables dealt with in this Review, only two may become topological. I have shown that the polarization of a $1d$ (or quasi-$1d$) inversion-symmetric insulator is a topological $\mathbb{Z}_2$ invariant (in electron-charge units): Fig. 2 perspicuously shows that polyacetylene is a $\mathbb{Z}_2$-even topological case. In modern jargon, the $\mathbb{Z}_2$ invariant is "protected" by inversion symmetry. Notably, the—closely related—topological nature of the soliton charge in polyacetylene was discovered long ago [13]. The second geometrical observable which may become topological is the AHC: this occurs in $2d$ insulators whenever T-symmetry is absent. Therein the AHC in natural conductance units[3] is a $\mathbb{Z}$ invariant (Chern number): the effect is known as QAHE (quantum anomalous Hall effect) [34,35]. The same $\mathbb{Z}$ invariant plays the key role in the theory of the fractional quantum Hall effect [6].

Acknowledgments

During several stays at the Donostia International Physics Center in San Sebastian (Spain) over the years, I have discussed thoroughly the topics in the present Review with Ivo Souza; his invaluable contribution is gratefully acknowledged. The hospitality by the Center is acknowledged as well. Work supported by the ONR Grant No. N00014-17-1-2803.

[3] In $2d$ conductivity and conductance have the same dimensions; their natural units are klitzing^{-1}. The klitzing (natural resistance unit) is defined as h/e^2.

Appendix

As in the main text we address a simple cubic lattice of constant a, with $L = Ma$; here we consider the electronic term only. We define $[\mathbf{r}] = (\mathbf{r}_1, \mathbf{r}_2 \ldots \mathbf{r}_N)$, and we indicate with the simple integral symbol $\int$ a multidimensional integral over the segment $(0, L)$ in each variable. Then the integral over the hypercube is

$$\langle \Psi_0 | \mathrm{e}^{i\frac{2\pi}{L}\sum_i x_i} | \Psi_0 \rangle = \int \prod_{i=1}^{N} d\mathbf{r}_i \; \mathrm{e}^{i\frac{2\pi}{L}\sum_i x_i} |\langle [\mathbf{r}] | \Psi_0 \rangle|^2 \tag{74}$$

$$= \int dy_1 dz_1 \int dx_1 \prod_{i=2}^{N} d\mathbf{r}_i \; \mathrm{e}^{i\frac{2\pi}{L}\sum_i x_i} |\langle [\mathbf{r}] | \Psi_0 \rangle|^2. \tag{75}$$

Under the crystalline hypothesis, the inner integral is a lattice-periodic function of (y_1, z_1), hence

$$\langle \Psi_0 | \mathrm{e}^{i\frac{2\pi}{L}\sum_i x_i} | \Psi_0 \rangle = M^2 \int_{\mathrm{cell}} dy_1 dz_1 \int dx_1 \prod_{i=2}^{N} d\mathbf{r}_i \; \mathrm{e}^{i\frac{2\pi}{L}\sum_i x_i} |\langle [\mathbf{r}] | \Psi_0 \rangle|^2. \tag{76}$$

As defined in the main text, the reduced Berry phase is then

$$\tilde{\gamma}_x^{(\mathrm{el})} = \mathrm{Im\ ln} \int_{\mathrm{cell}} dy_1 dz_1 \int dx_1 \prod_{i=2}^{N} d\mathbf{r}_i \; \mathrm{e}^{i\frac{2\pi}{L}\sum_i x_i} |\langle [\mathbf{r}] | \Psi_0 \rangle|^2. \tag{77}$$

This holds for a correlated wavefunction in a perfect lattice; in case of chemical disorder one instead averages over the disorder by evaluating Eq. (75) on the large supercell and then dividing it by M^2 before taking the "Im ln". A similar reasoning applies to the nuclear term as well: hence Eq. (24) in the main text.

At the independent-electron level $|\Psi_0\rangle$ is the Slater determinant of N Bloch orbitals. We get rid of trivial factors of 2 by addressing spinless electrons; furthermore we consider the contribution to $P_x^{(\mathrm{el})}$ of a single occupied band. The $\mathbf{k}_m$ Bloch vectors are

$$m \equiv (m_1, m_2, m_3), \qquad \mathbf{k}_m = 2\pi/L \;\; (m_1, m_2, m_3), \quad m_s = 0, 1, \ldots, M-1. \tag{78}$$

The Bloch orbitals $|\psi_{\mathbf{k}_m}\rangle = \mathrm{e}^{i\mathbf{k}_m \cdot \mathbf{r}} |u_{\mathbf{k}_m}\rangle$ are normalized over the crystal cell of volume a^3. It is expedient to define the auxiliary Bloch orbitals $|\tilde{\psi}_{\mathbf{k}_m}\rangle = \mathrm{e}^{i\frac{2\pi}{L}x} |\psi_{\mathbf{k}_m}\rangle$, and $|\tilde{\Psi}_0\rangle$ as their Slater determinant; we also define $\mathbf{q} = (2\pi/L, 0, 0)$. Then

$$\langle \Psi_0 | \mathrm{e}^{i\frac{2\pi}{L}\sum_i x_i} | \Psi_0 \rangle = \langle \Psi_0 | \mathrm{e}^{i\sum_i \mathbf{q}\cdot\mathbf{r}_i} | \Psi_0 \rangle = \langle \Psi_0 | \tilde{\Psi}_0 \rangle = \big(\det \mathcal{S}\big)/M^{3N}, \tag{79}$$

where $\mathcal{S}$ is the $N \times N$ overlap matrix, in a different normalization

$$\mathcal{S}_{mm'} = M^3 \langle \psi_{\mathbf{k}_m} | \tilde{\psi}_{\mathbf{k}_{m'}} \rangle = M^3 \langle u_{\mathbf{k}_m} | \mathrm{e}^{i(\mathbf{q}+\mathbf{k}_{m'}-\mathbf{k}_m)\cdot\mathbf{r}} | u_{\mathbf{k}_{m'}} \rangle$$

$$= M^3 \langle u_{\mathbf{k}_m} | u_{\mathbf{k}_{m'}} \rangle \, \delta_{\mathbf{q}+\mathbf{k}_{m'}-\mathbf{k}_m} = M^3 \langle u_{\mathbf{k}_m} | u_{\mathbf{k}_m - \mathbf{q}} \rangle \, \delta_{mm'}. \tag{80}$$

The normalization factors cancel: we have in fact

$$\langle \Psi_0 | \mathrm{e}^{i\frac{2\pi}{L}\sum_i x_i} | \Psi_0 \rangle = \frac{1}{M^{3N}} \det \mathcal{S} = \prod_{m_1,m_2,m_3=0}^{M-1} \langle u_{\mathbf{k}_m} | u_{\mathbf{k}_m - \mathbf{q}} \rangle, \tag{81}$$

$$\tilde{\gamma}_x^{(\mathrm{el})} = \frac{1}{M^2} \sum_{m_2,m_3=0}^{M-1} \mathrm{Im\ ln} \prod_{m_1=0}^{M-1} \langle u_{\mathbf{k}_m} | u_{\mathbf{k}_m - \mathbf{q}} \rangle; \tag{82}$$

the multi-band case is dealt with in detail in Ref. [11].

References

[1] D. Vanderbilt: *Berry Phases in Electronic Structure Theory* (Cambridge University Press, 2018)

[2] R. Resta, Phys. Rev. Lett. **80**, 1800 (1998)

[3] D. Ceresoli, T. Thonhauser, D. Vanderbilt, and R. Resta, Phys. Rev. B **74**, 024408 (2006)

[4] M.V. Berry, Proc. Roy. Soc. Lond. A **392**, 45 (1984)

[5] W. Kohn, Phys. Rev. **133**, A171 (1964)

[6] Q. Niu, D.J. Thouless, and Y.S. Wu, Phys. Rev. B **31**, 3372 (1985)

[7] R. Resta, Eur. Phys J. B **91**, 100 (2018)

[8] R.D. King-Smith and D. Vanderbilt, Phys. Rev. B **47**, 1651 (1993)

[9] K.N. Kudin, R. Car, and R. Resta, J. Chem. Phys. **127**, 194902 (2007)

[10] R. Resta, Rev. Mod. Phys. **66**, 899 (1994)

[11] R. Resta, J. Phys.: Condens. Matter **22** 123201 (2010)

[12] P.L. Silvestrelli, M. Bernasconi, and M. Parrinello, Chem. Phys. Lett. **277**, 478 (1997)

[13] W.P. Su, J.R. Schrieffer, and A.J. Heeger, Phys. Rev. Lett. **42**, 1698 (1979)

[14] R. Resta and S. Sorella, Phys. Rev. Lett. **87**, 4738 (1995)

[15] R. Resta and S. Sorella, Phys. Rev. Lett. **82**, 370 (1999)

[16] N.W. Ashcroft and N.D. Mermin, *Solid State Physics* (Saunders, Philadelphia, 1976), Ch. 1 and Ch. 13

[17] P.B. Allen, in: *Conceptual foundations of materials: A standard model for ground- and excited-state properties*, S.G. Louie and M.L. Cohen (eds.) (Elsevier, 2006), p. 139

[18] D.J. Scalapino, S.R. White, and S.C. Zhang, Phys. Rev. **47**, 7995 (1993)

[19] P. Drude, Annalen der Physik. **306**, 566 (1900)

[20] R. Resta, J. Phys. Condens. Matter **30**, 414001 (2018)

[21] I. Souza, T. Wilkens, and R.M. Martin, Phys. Rev. B **62**, 1666 (2000)

[22] L. Stella, C. Attaccalite, S. Sorella, and A. Rubio, Phys. Rev. B **84**, 245117 (2011)

[23] R. Resta, J. Phys.: Condens. Matter **14**, R625 (2002)

[24] R. Resta, Riv. Nuovo Cimento **41**, 463 (2018)

[25] R. Resta, J. Chem. Phys. **124**, 104104 (2006)

[26] G.L. Bendazzoli, S. Evangelisti, A. Monari, and R. Resta, J. Chem. Phys. **133**, 064703 (2010)

[27] A. Marrazzo and R. Resta, Phys. Rev. Lett. **122**, 166602 (2019)

[28] T. Olsen, R. Resta, and I. Souza, Phys. Rev. B **95**, 045109 (2017)

[29] N. Nagaosa, J. Sinova, S. Onoda, A.H. MacDonald, and N.P. Ong, Rev. Mod. Phys. **82**, 1539 (2010)

[30] R. Bianco, R. Resta, and I. Souza, Phys. Rev. B **90**, 125153 (2014)

[31] D. Ceresoli and R. Resta, Phys. Rev. B **76**, 012405 (2007)

[32] A. Marrazzo and R. Resta, Phys. Rev. B **95**, 121114(R) (2017)

[33] F.D.M. Haldane, Phys. Rev. Lett. **61**, 2015 (1988)

[34] C.-Z. Chang et al. Science **340**, 167 (2013)

[35] C.-Z. Chang et al. Nat. Mater. **14**, 473 (2015)

[36] R.B. Laughlin, Phys. Rev. Lett. **50**, 1395 (1983)

[37] B.T. Thole, P. Carra, F. Sette, and G. van der Laan, Phys. Rev. Lett. **68**, 1943 (1992)

[38] J. Kunes and P.M. Oppeneer, Phys. Rev. B **61**, 15774 (2000)

[39] I. Souza and D. Vanderbilt, Phys. Rev. B **77**, 054438 (2008)

[40] R. Resta. Phys. Rev. Research **2**, 023139 (2020)

[41] J.E. Moore, private communication

[42] R. Resta, 2018 (unpublished, rejected by Phys. Rev. X)

11 Topological Semimetals

Andreas P. Schnyder
Max-Planck-Institut für Festkörperforschung
Stuttgart

Contents

E. Pavarini and E. Koch (eds.)
Topology, Entanglement, and Strong Correlations
Modeling and Simulation Vol. 10
Forschungszentrum Jülich, 2020, ISBN 978-3-95806-466-9
http://www.cond-mat.de/events/correl20

1 Introduction

The last decade has witnessed tremendous progress in our understanding of topological band theory. Soon after the discovery of topological insulators [1], it has been realized that topology plays also a significant role in gapless systems, i.e., in topological semimetals [2–7]. Topological semimetals exhibit protected band crossings near the Fermi energy with nonzero topological charges. While the existence of these band crossings has been recognized early on during the development of band theory [8], their fundamental importance has been understood only recently. In the course of the last few years it has been shown that topological band crossing give rise to a variety of interesting phenomena, such as, intrinsic anomalous Hall effects [6], exotic surface states [5], large thermopower, and unusual responses related to quantum anomalies [9]. Because of these properties, topological semimetals could potentially be used for new device applications [10]. E.g., the helical nature of the surface states can be used for low-dissipation transport [11]. The spin-momentum locking of the surface states can be utilized for low-consumption spintronic devices and magnetic memory devices [12]. The high photosensitivity of topological semimetals is of importance for the construction of ultrafast photodetectors [13]. Moreover, many topological semimetals have large thermoelectric responses, which could be of use for high-efficiency energy converters or thermal detectors [14].

There are two different types of topological band crossings, namely, accidental band crossings and symmetry-enforced band crossings. Accidental band crossings are protected by *symmorphic* crystal symmetries and are only perturbatively stable [2]. That is, they can be adiabatically removed by large symmetry-preserving deformations of the Hamiltonian, for example, through pair annihilation. Dirac points and Dirac lines are examples of accidental band crossings, which are protected by parity-time inversion, reflection, or rotation symmetry [7, 15]. Another example is Weyl points, which can be stable even in the absence of symmetries [5, 6]. Accidental band crossings also occur in the Bogoliubov bands of superconductors [2]. Symmetry-enforced band crossings [16–22], however, arise in the presence of *nonsymmorphic* symmetries and are globally stable, i.e., they cannot be removed even by large deformations of the Hamiltonian. That is, these band crossings are required to exist due to nonsymmorphic symmetries alone, independent of material details, such as chemical composition or energetics of the bands.

In these lectures we will discuss both types of band crossings, first focusing on accidental band crossings in Sec. 2 and then studying symmetry-enforced band crossings in Sec. 3. A particular focus will be on nodal-line semimetals, where the band crossings occur along one-dimensional lines in the BZ, close to or at the Fermi energy. But we will also discuss Weyl semimetals, where the band crossings occur at isolated points in the Brillouin zone (BZ).

In the following we will focus on weakly interacting semimetals, which can be described within the single-particle picture. Using the band theory of solids [23], the electronic wavefunctions ψ in a crystal of a semimetal can be classified by their crystal momentum $\mathbf{k}$, which is defined in the periodic BZ. Bloch's theorem tells us that ψ can be expressed in terms of Bloch states $|u_m(\mathbf{k})\rangle$, which are defined in a single unit cell of the crystal. These Bloch states are eigenstates

of the Bloch Hamiltonian $H(\mathbf{k})$,[1]

$$H(\mathbf{k})\,|u_m(\mathbf{k})\rangle = E_m(\mathbf{k})\,|u_m(\mathbf{k})\rangle\,, \tag{1}$$

where m represents the band index. The eigenvalues $E_m(\mathbf{k})$ in the above equation are called Bloch bands and the set $\{E_m(\mathbf{k})\}$ is referred to as the band structure of the solid.
In this lecture we are interested in the crossings between two different bands, $E_m(\mathbf{k})$ and $E_{m'}(\mathbf{k})$, say. That is, we want to know under which conditions the two energies $E_m(\mathbf{k})$ and $E_{m'}(\mathbf{k})$ become degenerate at certain points or lines in the BZ. The main focus will be on electronic band structures of solids. However, the band crossings discussed here can also occur in different contexts, for example, for photonic bands of dielectric superlattices [24], for phonon bands in crystals, for magnon bands in ordered antiferromagnets [25], or for Bogoliubov bands in superconductors [1, 2].
The remainder of these notes are organized as follows. In Sec. 2.1 we will begin by deriving a classification of accidental band crossings protected by time-reversal symmetry, particle-hole symmetry, and/or chiral symmetry. As concrete examples of such accidental band crossings, we will consider, among others, Weyl and nodal-line semimetals (Secs. 2.2 and 2.3). For these examples we will discuss the bulk-boundary correspondence, which relates the nontrivial topology of the band crossing in the bulk to the appearance of surface states. We will also review the quantum anomalies that arise in the low-energy descriptions of these semimetals. Section 3 is devoted to the study of symmetry-enforced band crossings. We will first explain some general properties of nonsymmorphic symmetries and show how these can lead to symmetry-enforced band crossings. Subsequently, two examples of nonsymmorphic band crossings will be discussed: Weyl lines protected by glide reflection in Sec. 3.2 and Dirac lines protected by off-center symmetries in Sec. 3.3. For each of these examples, we present some material realizations and discuss implications for experiments.

2 Accidental band crossings

Accidental band crossings occur, for example, when a hole-like and an electron-like parabolic band in a two-dimensional material overlap, forming two band crossings, as shown in Fig. 1. This band crossing is stable if the two bands have a non-trivial topology and/or opposite symmetry. In general these accidental crossings share the following features:

- They are protected by *symmorphic* crystal symmetries and/or nonspatial symmetries. Here, symmorphic symmetry means a symmetry which leaves at least one point of the real-space crystal invariant. Symmorphic symmetries are point-group symmetries of the crystal, such as rotation or reflection. Nonspatial symmetry refers to a symmetry that dose not transform different lattice sites into each other. I.e., a symmetry that acts locally in real space, such as time-reversal or particle-hole symmetry.

[1] For superconductors the Bloch Hamiltonian should be replaced by a Bogoliubov-de Gennes Hamiltonian.

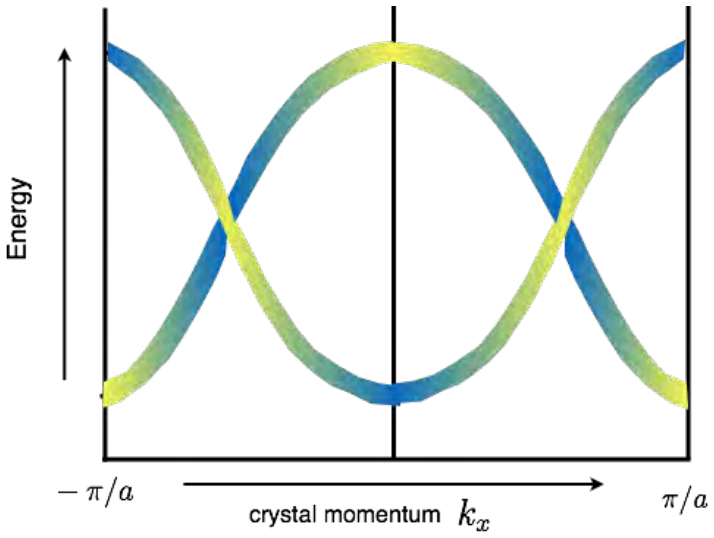

Fig. 1: *When an electron- and hole-like band of different symmetry overlap, they form two accidental band crossings. The color shading indicates some "pseudo-spin" degree of freedom of the Bloch states* $|u_n(\mathbf{k})\rangle$*, which depends on crystal momentum* $\mathbf{k}$*.*

- Accidental band crossings exhibit local topological charges n_{top}. These topological charges are defined in terms of contour integrals, e.g.,

$$n_{\text{top}} = \frac{1}{2\pi} \oint_{\mathcal{C}} \mathcal{F}(\mathbf{k})\, d\mathbf{k} \;\in\; \mathbb{Z}, \tag{2}$$

  where the integration is along the contour $\mathcal{C}$, which encloses the band crossing point or line. Here, $\mathcal{F}(\mathbf{k})$ represents a general curvature function, such as the Berry curvature or the winding number density. These topological charges are quantized to integer values, i.e., $n_{\text{top}} \in \mathbb{Z}$. For point crossings, the sum of the topological charges of all crossings formed by a given pair of bands needs to be zero, due to a fermion-doubling theorem [26].

- Accidental band crossings are only perturbatively stable. That is, small symmetry-preserving perturbations can move the band crossings in the BZ, but cannot remove them, by opening up a gap. However, large symmetry-preserving deformations can completely remove the band crossings. E.g., for point crossings one can pair annihilate two point crossings with opposite topological charge by a large symmetry-preserving deformation.

It follows from the last point above, that classifications of accidental band crossings based on symmetry and topology only tell us whether for a given set of symmetries a band crossing is *possible*. I.e., these classifications only tell us whether a given set of symmetries protect band crossings or not. They do not tell us whether these crossings actually occur, which depends on the detailed energetics of the bands (i.e., on how the bands disperse through the BZ).

2.1 Classification of band crossings

Topological band crossings of the accidental type can be classified using the Dirac-matrix Hamiltonian method [2, 27, 28]. This method relies on the fact that close to a band crossing the Bloch Hamiltonian $H(\mathbf{k})$, Eq. (1), can in general be approximated by a Dirac Hamiltonian, i.e., by

$$H_D(\mathbf{k}) = \sum_{j=1}^{d} k_j \gamma_j, \tag{3}$$

where d is the spatial dimension and γ_j are gamma matrices obeying the anti-commutation relations

$$\{\gamma_i, \gamma_j\} = 2\delta_{ij}\mathbb{1}, \qquad j = 0, 1, \ldots, d. \tag{4}$$

Using Eq. (4), we find that $H_D^2 = \sum_{j=1}^{d} k_j^2 \mathbb{1}$. Hence, the energy spectrum of $H_D(\mathbf{k})$ is given by

$$E = \pm\sqrt{\sum_{j=1}^{d} k_j^2}, \tag{5}$$

which exhibits a band crossing at $\mathbf{k} = \mathbf{0}$, where the bands become degenerate with $E = 0$. (I.e., the Dirac Hamiltonian has no gap.) The Dirac-matrix Hamiltonian method analyzes the stability of the gapless Dirac-Hamiltonian (3) against gap-opening deformations. That is, one studies whether there exists a gap-opening mass term $m\gamma_0$, i.e., an additional gamma matrix γ_0 with $\{\gamma_0, \gamma_j\} = 0$ ($j = 1, 2, \ldots, d$), with which $H_D(\mathbf{k})$ can be deformed. If such a mass term exists, then the band crossing can be removed. I.e., by adding $m\gamma_0$ to H_D the spectrum deforms into $E = \pm\sqrt{m^2 + \sum_{j=1}^{d} k_j^2}$, which has no band crossing anymore at $\mathbf{k} = 0$. This indicates that the band crossing is topologically trivial. However, if there does not exist an additional gamma matrix γ_0, then the band crossing is topologically nontrivial and stable against deformations.
The classification of band crossings is done in terms of the following three characteristics (cf. Table 1):

(i) Spatial and nonspatial symmetries of the Bloch Hamiltonian $H(\mathbf{k})$.

(ii) The co-dimension $p = d - d_{BC}$ of the band crossing, where d_{BC} is the dimension of the band crossing. (I.e., $d_{BC} = 0$ for point crossings, $d_{BC} = 1$ for line crossings, etc.)

(iii) How the band crossing transforms under the nonspatial (anti-unitary) symmetries, which map $\mathbf{k} \to -\mathbf{k}$. That is, we need to distinguish whether the band crossing is mapped onto itself under the nonspatial symmetries or not, see Fig. 2. For this reason we need to differentiate between band crossings at high-symmetry points and off high-symmetry points of the BZ.

Before performing the classification, let us first discuss how the spatial and nonspatial symmetries restrict the form of the Dirac Hamiltonian (3).

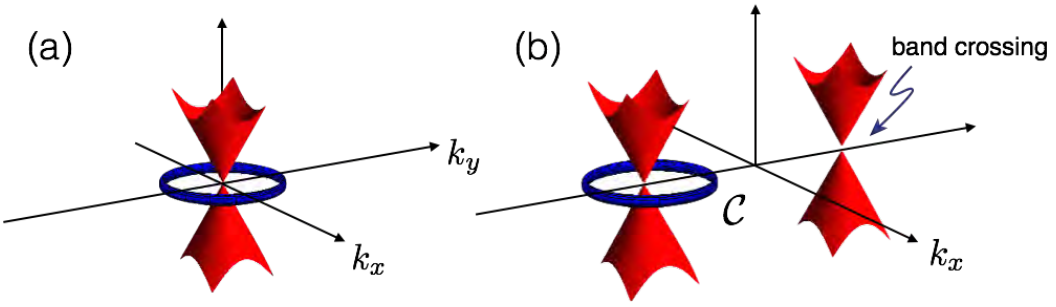

Fig. 2: *The classification of stable band crossings depends on how the band crossings transform under nonspatial (anti-unitary) symmetries. (a) The band crossing is left invariant under nonspatial symmetries. (b) Two band crossings are pairwise related by the nonspatial symmetries, which map* $\mathbf{k} \to -\mathbf{k}$.

2.1.1 Symmetry operations

We consider the classification in terms of both nonspatial and spatial symmetries.

Nonspatial symmetries. Nonspatial symmetries are symmetries that act locally in real space, i.e., they do not transform different lattice sites into each other. There are three different nonspatial symmetries that need to be considered: anti-unitary time-reversal symmetry (TRS) and particle-hole symmetry (PHS), as well as chiral (i.e., sublattice symmetry) [2, 29]. Here, "anti-unitary" refers to the fact that these symmetries can be written as a product of a unitary matrix U with the complex conjugation operator $\mathcal{K}$. In momentum space, time-reversal and particle-hole symmetry act on the Bloch (or Bogoliubov-de Gennes) Hamiltonian as

$$\mathcal{T}^{-1}H(-\mathbf{k})\mathcal{T} = +H(\mathbf{k}), \quad \text{and} \quad \mathcal{C}^{-1}H(-\mathbf{k})\mathcal{C} = -H(\mathbf{k}), \tag{6a}$$

respectively, where $\mathcal{T}$ and $\mathcal{C}$ are the anti-unitary operators for time-reversal and particle-hole symmetry. Both $\mathcal{T}$ and $\mathcal{C}$ can square either to $+1$ or -1, depending on the type of the symmetry (see last three columns of Table 1). Chiral symmetry, on the other hand, is implemented by[2]

$$\mathcal{S}^{-1}H(\mathbf{k})\mathcal{S} = -H(\mathbf{k}), \tag{6b}$$

where $\mathcal{S}$ is a unitary operator. Symmetries (6) define the ten Altland-Zirnbauer (AZ) symmetry classes (i.e., the "ten-fold way") [2, 30, 31], which are listed in Table 1. The first column in Table 1 gives the name of the ten AZ symmetry classes. The labels T, C, and S in the last three columns indicate the presence ("+", "−", and "1") or absence ("0") of time-reversal symmetry, particle-hole symmetry, and chiral symmetry, respectively, as well as the sign of the squared symmetry operators $\mathcal{T}^2$ and $\mathcal{C}^2$.
Combining Eqs. (6) with Eq. (3), we find that when the Dirac Hamiltonian obeys TRS, PHS, or chiral symmetry, the gamma matrices in Eq. (3) must satisfy

$$\{\gamma_i, \mathcal{T}\} = 0, \quad [\gamma_i, \mathcal{C}] = 0, \quad \{\gamma_i, \mathcal{S}\} = 0, \tag{7}$$

[2]Note that combining TRS with PHS yields a chiral symmetry.

Table 1: *Classification of stable band crossings in terms of the ten AZ symmetry classes [2], which are listed in the first column. The first and second rows give the co-dimensions $p = d - d_{BC}$ for band crossings at high-symmetry points [Fig. 2(a)] and away from high-symmetry points of the BZ [Fig. 2(b)], respectively.*

at high-sym. point off high-sym. point	p=8 p=2	p=1 p=3	p=2 p=4	p=3 p=5	p=4 p=6	p=5 p=7	p=6 p=8	p=7 p=1	T	C	S
A	0	$\mathbb{Z}$	0	$\mathbb{Z}$	0	$\mathbb{Z}$	0	$\mathbb{Z}$	0	0	0
AIII	$\mathbb{Z}$	0	$\mathbb{Z}$	0	$\mathbb{Z}$	0	$\mathbb{Z}$	0	0	0	1
AI	0	0[a]	0	$2\mathbb{Z}$	0	$\mathbb{Z}_2$[a,b]	$\mathbb{Z}_2$[b]	$\mathbb{Z}$	+	0	0
BDI	$\mathbb{Z}$	0	0[a]	0	$2\mathbb{Z}$	0	$\mathbb{Z}_2$[a,b]	$\mathbb{Z}_2$[b]	+	+	1
D	$\mathbb{Z}_2$[b]	$\mathbb{Z}$	0	0[a]	0	$2\mathbb{Z}$	0	$\mathbb{Z}_2$[a,b]	0	+	0
DIII	$\mathbb{Z}_2$[a,b]	$\mathbb{Z}_2$[b]	$\mathbb{Z}$	0	0[a]	0	$2\mathbb{Z}$	0	−	+	1
AII	0	$\mathbb{Z}_2$[a,b]	$\mathbb{Z}_2$[b]	$\mathbb{Z}$	0	0[a]	0	$2\mathbb{Z}$	−	0	0
CII	$2\mathbb{Z}$	0	$\mathbb{Z}_2$[a,b]	$\mathbb{Z}_2$[b]	$\mathbb{Z}$	0	0[a]	0	−	−	1
C	0	$2\mathbb{Z}$	0	$\mathbb{Z}_2$[a,b]	$\mathbb{Z}_2$[b]	$\mathbb{Z}$	0	0[a]	0	−	0
CI	0[a]	0	$2\mathbb{Z}$	0	$\mathbb{Z}_2$[a,b]	$\mathbb{Z}_2$[b]	$\mathbb{Z}$	0	+	−	1

[a] For these entries there can exist bulk band crossings away from high-symmetry points that are protected by $\mathbb{Z}$ invariants inherited from classes A and AIII. (TRS or PHS does not trivialize the $\mathbb{Z}$ invariants.)

[b] $\mathbb{Z}_2$ invariants protect only band crossings of dimension zero at high-symmetry points.

where $i = 1, 2, \ldots, d$. Similarly, any mass term $m\gamma_0$ that leads to the opening of a gap at the band crossing must satisfy

$$[\gamma_0, \mathcal{T}] = 0, \quad \{\gamma_0, \mathcal{C}\} = 0, \quad \{\gamma_0, \mathcal{S}\} = 0. \tag{8}$$

Spatial symmetries. Spatial symmetries are symmetries that act non-locally in position space, i.e., they transform different lattice sites into each other. Point-group symmetries are an example of spatial symmetries. Here, we shall focus on reflection symmetries with the unitary operator R. For concreteness we assume that R lets $x \to -x$. The invariance of the Bloch Hamiltonian (1) under this reflection implies

$$R^{-1} H(-k_1, \tilde{\mathbf{k}}) R = H(k_1, \tilde{\mathbf{k}}), \tag{9}$$

where $\tilde{\mathbf{k}} = (k_2, \ldots, k_d)$ and the unitary reflection operator R can only depend on k_1, since it is symmorphic [cf. Eq. (44)]. Note that for spin-$\frac{1}{2}$ particles (e.g., Bloch electrons with spin-orbit coupling) R transforms the spin degree of freedom as

$$R \hat{S}_x R^{-1} = \hat{S}_x \quad \text{and} \quad R \hat{S}_{y,z} R^{-1} = -\hat{S}_{y,z}, \tag{10}$$

where $\hat{S}_i = \frac{\hbar}{2}\hat{\sigma}_i$ is the spin operator. Hence, the spin part of R is given by $i\sigma_x$.[3] In general, R contains also an internal part which rearranges the positions of the atoms in the unit cell.

[3] The reason to include the factor i here is to ensure that $R^2 = -1$, since R^2 effectively corresponds to a spin rotation by 2π. However, in general, there is a phase ambiguity in the definition of R, since a phase can be absorbed in the electronic creation/annihilation operators.

Combining Eq. (9) with Eq. (3), we find that when the Dirac Hamiltonian obeys reflection symmetry, the gamma matrices in Eq. (3) must satisfy

$$\{\gamma_1, R\} = 0, \quad [\gamma_j, R] = 0, \quad \text{where } j = 2, 3, \ldots, d, \tag{11}$$

and the mass term must satisfy $[\gamma_0, R] = 0$.

2.1.2 Band crossings at high-symmetry points

We will now use the Dirac-matrix Hamiltonian method[4] to classify band crossings at high-symmetry points of the BZ, i.e., at time-reversal invariant momenta (TRIMs) of the BZ, e.g., the Γ point. This classification approach consists of the following steps:

1. Write down a d-dimensional gapless Dirac Hamiltonian H_D of the form of Eq. (3), that is invariant under all the considered symmetries. The matrix dimension of the gamma matrices should be minimal, i.e., large enough such that all symmetries can be implemented in a nontrivial way, but not larger.

2. Check whether there exists a symmetry-allowed mass term $m\gamma_0$, which anticommutes with H_D. If *yes*, then the band crossing can be gapped out. This indicates that the band crossing is topologically trivial, which is labeled by "0" in Table 1. If *no*, then the band crossing is topologically stable (i.e., protected by the symmetries), which is labeled by "$\mathbb{Z}$ or "$\mathbb{Z}_2$" in Table 1.

3. To determine whether there is a single or multiple band crossings protected by the symmetries, we have to consider multiple copies of the Dirac Hamiltonian H_D. Doubled versions of H_D can be obtained as

$$H_D^{\text{db}} = \sum_{i \in A} k_i \gamma_i \otimes \sigma_z + \sum_{i \in A^c} k_i \gamma_i \otimes \mathbb{1}, \tag{12}$$

   where the first summation is over an arbitrary subset $A \subseteq \{1, 2, ..., d\}$ and the second summation is over the complement of this subset A^c. We then have to check whether there exist gap-opening terms for these enlarged Dirac Hamiltonians. If there exists a mass term for all possible versions of H_D^{db}, then the band crossing is classified by a $\mathbb{Z}_2$ invariant. If the band crossing is stable for an arbitrary number of copies of H_D, then it is classified by a $\mathbb{Z}$ number, see Table 1.

To make this more explicit, let us discuss some specific cases.

[4] This approach is closely related to the problem of Clifford algebra extensions [2, 28], which puts it on a rigorous footing.

Class A in 2D. First, we consider a band crossing in a two-dimensional system without any symmetries, corresponding to class A in Table 1. The generic low-energy 2×2 Hamiltonian for such a band crossing at $\mathbf{k} = 0$ reads $\mathcal{H}^A_{2D} = \sum_{\mathbf{k}} \Psi^\dagger_{\mathbf{k}} H^A_{2D} \Psi_{\mathbf{k}}$, where

$$H^A_{2D} = k_x\sigma_x + k_y\sigma_y \tag{13}$$

and $\Psi_{\mathbf{k}} = (c_{1\mathbf{k}}, c_{2\mathbf{k}})^T$ is a spinor with two orbital degrees of freedom. Since this band crossing can be gapped out by the mass term $m\sigma_z$, it is topologically trivial and therefore unstable. This is indicated by a "0" in the fourth column of Table 1.

Class A in 3D. Next, we study a zero-dimensional band crossing in three-dimensions without any symmetries. This type of band crossing is realized in Weyl semimetals [2, 5, 6]. The low-energy 2×2 Hamiltonian takes the form $\mathcal{H}^A_{3D} = \sum_{\mathbf{k}} \Psi^\dagger_{\mathbf{k}} H^A_{3D} \Psi_{\mathbf{k}}$, with

$$H^A_{3D} = k_x\sigma_x + k_y\sigma_y + k_z\sigma_z. \tag{14}$$

It is impossible to find a mass term for this Hamiltonian, because there exist only three gamma matrices of rank 2. (There exists no "fourth Pauli matrix" that anticommutes with H^A_{3D}.) Therefore, the band-crossing is stable. To determine whether the Weyl crossing (14) has a $\mathbb{Z}$ or $\mathbb{Z}_2$ classification, we need to consider all possible doubled versions of H^A_{3D}, cf. Eq. (12). We can consider, for example, the following doubled version of H^A_{3D}

$$H^{A,\text{db1}}_{3D} = k_x\sigma_x \otimes \sigma_z + k_y\sigma_y \otimes \sigma_0 + k_z\sigma_z \otimes \sigma_0, \tag{15}$$

where $\otimes$ denotes the tensor product between two Pauli matrices. For this doubled version of H^A_{3D}, there exist two mass terms, e.g., $\sigma_x \otimes \sigma_x$ and $\sigma_x \otimes \sigma_y$, which gap out the band crossing. However, there exists another doubled version of H^A_{3D}, namely

$$H^{A,\text{db2}}_{3D} = k_x\sigma_x \otimes \sigma_0 + k_y\sigma_y \otimes \sigma_0 + k_z\sigma_z \otimes \sigma_0, \tag{16}$$

whose band crossing is stable. We find that there does not exist any mass term for $H^{A,\text{db2}}_{3D}$, which gaps out the band crossing. Since we have found one doubled version of H^A_{3D} which has a stable (four-fold degenerate) band crossing, we conclude that Weyl band crossings exhibit a $\mathbb{Z}$ classification. (One can show that there exist also multiple copies of H^A_{3D} with stable band crossings.) This is indicated by the label "$\mathbb{Z}$" in the fifth column of Table 1.
The Weyl points described by Eq. (14) are monopoles of Berry flux, i.e., they realize hedgehog defects of the Berry curvature (see Fig. 4). The stability of these Weyl points is guaranteed by a quantized Chern number (see Sec. 2.2).

Class A + R in 2D. Let us now add reflection symmetry to the game. We consider again a two-orbital system with the low-energy Hamiltonian $\mathcal{H}^{A+R}_{2D} = \sum_{\mathbf{k}} \Psi^\dagger_{\mathbf{k}} H^{A+R}_{2D} \Psi_{\mathbf{k}}$, where

$$H^{A+R}_{2D} = k_x\sigma_x + k_y\sigma_y, \tag{17}$$

which is symmetric under reflection symmetry $R^{-1}H_{2D}^{A+R}(-k_x,k_y)R = H_{2D}^{A+R}(k_x,k_y)$, with $R=\sigma_y$. This Hamiltonian describes the low-energy physics of a single Dirac cone of graphene. We observe that the only possible gap-opening mass term $m\sigma_z$, which anticommutes with H_{2D}^{A+R}, is symmetry forbidden, since it breaks reflections symmetry ($R^{-1}\sigma_z R=-\sigma_z$). Hence, the band-crossing of H_{2D}^{A+R} at $\mathbf{k}=0$ is stable and protected by reflection symmetry. We find that also the doubled version of H_{2D}^{A+R},

$$H_{2D}^{A+R,\text{db}} = k_x\sigma_x\otimes\sigma_0 + k_y\sigma_y\otimes\sigma_0, \tag{18}$$

is stable, since there exists no reflection-symmetric mass term. For example, $\hat{m}=\sigma_z\otimes\sigma_x$ breaks reflection, since $(\sigma_y\otimes\sigma_0)^{-1}\hat{m}(\sigma_y\otimes\sigma_0)\neq\hat{m}$. Therefore, the reflection-symmetric band crossing (17) has a $\mathbb{Z}$ classification. This is indicated by the label "$M\mathbb{Z}$" in the fifth column of Table VIII of Ref. [2].

Class AII in 2D. Next, we study a band crossing in two-dimensions with time-reversal symmetry ($\mathcal{T}^2=-1$), corresponding to class AII in Table 1. The low-energy Dirac Hamiltonian reads again

$$H_{2D}^{\text{AII}} = k_x\sigma_x + k_y\sigma_y. \tag{19}$$

But now we impose time-reversal symmetry (6a) with the operator $\mathcal{T}=i\sigma_y\mathcal{K}$, which squares to -1 (class AII). This type of time-reversal symmetric band crossing is realized at the surface of three-dimensional topological insulators with spin-orbit coupling. The only possible mass term, which anticommutes with H_{2D}^{AII}, is $m\sigma_z$. However, $m\sigma_z$ breaks time-reversal symmetry (since, $\mathcal{T}^{-1}m\sigma_z\mathcal{T}\neq m\sigma_z$) and is therefore forbidden by symmetry. Hence, Eq. (19) describes a topologically stable band crossing in class AII. Next, we examine different doubled versions of H_{2D}^{AII}, i.e.,

$$H_{2D}^{\text{AII,db}} = \begin{pmatrix} H_{2D}^{\text{AII}} & 0 \\ 0 & H_{2D}^{\text{AII}'} \end{pmatrix}, \tag{20}$$

where $H_{2D}^{\text{AII}'}\in\{\pm k_x\sigma_x\pm k_y\sigma_y, \pm k_x\sigma_x\mp k_y\sigma_y\}$, see Eq. (12). (The time-reversal operator for these double Hamiltonians is $\mathcal{T}=i\sigma_y\otimes\sigma_0\mathcal{K}$.) It is not difficult to show that for each of the four versions of $H_{2D}^{\text{AII,db}}$ there exists at least one symmetry-preserving mass term, which gaps out the band crossing. For example, for the first version of $H_{2D}^{\text{AII,db}}$ with $H_{2D}^{\text{AII}'}=+k_x\sigma_x+k_y\sigma_y$, the mass term is $\sigma_z\otimes\sigma_y$. Thus, the band crossings described by $H_{2D}^{\text{AII,db}}$ is unstable. Therefore, we conclude that Eq. (19) has a $\mathbb{Z}_2$ classification, see fourth column of Table 1.

2.1.3 Band crossings off high-symmetry points

In this section we classify band crossings that are located away from high-symmetry points, i.e., away from the TRIMs of the BZ, see Fig. 2(b). These band crossings can be moved around in the BZ, as they are not pinned at the TRIMs. They transform pairwise into each other by the

nonspatial anti-unitary symmetries (time-reversal and particle-hole symmetry). For this reason, we have to take into account the full momentum dependence of the Hamiltonian in the entire BZ. That is, within the Dirac-matrix Hamiltonian approach, we need to consider the following type of Hamiltonian [27]

$$H_D = \sum_{i=1}^{p-1} \sin k_i \gamma_i + \Big(p - 1 - \sum_{i=1}^{p} \cos k_i\Big)\tilde{\gamma}_0, \tag{21}$$

which contains the momentum-dependent mass term $\tilde{\gamma}_0$, cf. Eq. (3). The Dirac Hamiltonian (21) describes d_{BC}-dimensional band crossings (with $d_{BC} = d - p$), which are located at

$$\mathbf{k} = (0, \ldots, 0, \pm\pi/2, k_{p+1}, \ldots, k_d). \tag{22}$$

We observe that the band crossings (22) are located away from the high-symmetry points $(0, 0, 0, \ldots, 0)$, $(\pi, 0, 0, \ldots, 0)$, $(0, \pi, 0, \ldots, 0)$, etc. of the BZ. The classification of these band crossings proceeds in a similar way as in Sec. 2.1.2. It consists of the following steps:

1. Write down a d-dimensional Dirac Hamiltonian H_D of the form Eq. (21) with $p{=}d{-}d_{BC}$, which satisfies all the considered symmetries. The rank of the gamma matrices in Eq. (21) should be large enough, such that all symmetries can be implemented in a nontrivial way, but not larger.

2. Check, whether

   - there exists an additional momentum-independent mass term $\tilde{\Gamma}$, which anticommutes with H_D and which is invariant under all symmetries.
   - there exists an additional momentum-dependent kinetic term $\sin k_p \gamma_p$, which anticommutes with H_D and which respects all symmetries.

   If the answer is *yes* for either of the above two points, then the band crossing can be gapped out. Hence, the band crossing is topologically trivial (entries labeled by "0" in Table 1). If the answer is *no* for both of the above points, then the band crossing is topologically stable (entries labeled by "$\mathbb{Z}$" or "$\mathbb{Z}_2$" in Table 1).

3. To determine whether there is a single or multiple band crossings protected by the symmetries, consider multiple copies of H_D, similar to Eq. (12).

Using this approach it was shown that only $\mathbb{Z}$-type invariants can ensure the stability of band-crossings off high-symmetry points [2]. ($\mathbb{Z}_2$-type invariants do not give rise to stable band crossings off high-symmetry points.) To exemplify this, we discuss some specific cases.

2.2 Weyl semimetal

We study the band crossing points of a three-dimensional Weyl semimetal [2, 5, 6], which belongs to symmetry class A (cf. Sec. 2.1.2). The Hamiltonian is defined on the cubic lattice and is given by $\mathcal{H}^A_{3D} = \sum_{\mathbf{k}} \Psi_{\mathbf{k}} H^A_{3D} \Psi_{\mathbf{k}}$, with (cf. Eq. (21) with $p = 3$)[5]

$$H^A_{3D} = \sin k_x \sigma_x + \sin k_y \sigma_y + (2 - \cos k_x - \cos k_y - \cos k_z)\sigma_z, \tag{23}$$

and the spinor $\Psi_{\mathbf{k}} = (c_{1\mathbf{k}}, c_{2\mathbf{k}})$, which has two orbital degrees of freedom (e.g., s and p orbitals), but no spin-degree of freedom, since the semimetal is assumed to be magnetically ordered. The spectrum of Eq. (23) is given by

$$E_{\mathbf{k}} = \pm\sqrt{(\sin k_x)^2 + (\sin k_y)^2 + (2 - \cos k_x - \cos k_y - \cos k_z)^2}. \tag{24}$$

H^A_{3D} exhibits two band crossing points at $E = 0$ (called Weyl points), which are located at $(0, 0, \pm\pi/2)$. As in Sec. 2.1.2, we find that these Weyl nodes are topologically stable, since there does not exist any fourth gamma matrix of rank two. (I.e., there exist no additional mass or kinetic terms.) We also find that the doubled version $H^A_{3D} \otimes \sigma_0$ has stable band crossings. Hence, the classification is of $\mathbb{Z}$ type, see third column of Table 1.

The stability of the Weyl points is guaranteed by a quantized Chern number

$$C = \frac{1}{2\pi} \oint_{\mathcal{C}} \mathcal{F}(\mathbf{k}) d\mathbf{k}, \qquad \text{where} \qquad \mathcal{F}(\mathbf{k}) = \nabla_{\mathbf{k}} \times \mathbf{A}_{\mathbf{k}} \tag{25}$$

is the Berry curvature of the occupied band and $\mathcal{C}$ is a two-dimensional closed integration contour. The Berry connection $\mathbf{A}_{\mathbf{k}}$ is defined as $\mathbf{A}_{\mathbf{k}} = i\langle u_-(\mathbf{k})|\nabla_{\mathbf{k}}|u_-(\mathbf{k})\rangle$, with $|u_-(\mathbf{k})\rangle$ the Bloch state of the occupied band. The Weyl points act as sources and drains of Berry curvature, i.e., the vector field $\mathcal{F}(\mathbf{k})$ points inwards at one Weyl point and outwards at the other. The Chern number (25) measures how much Berry flux passes through the contour $\mathcal{C}$. For contours that enclose one of the two Weyl points the Chern number is $C = \pm 1$. For contours that do not enclose a Weyl point, the Chern number is zero $C = 0$.

For Hamiltonian (23) the Chern number can be rewritten in the simple form[6]

$$C(k_z) = \frac{1}{4\pi} \oint_{\mathcal{C}_{k_z}} dk_x dk_y \, \hat{\mathbf{d}}_{\mathbf{k}} \cdot \left[\partial_{k_x} \hat{\mathbf{d}}_{\mathbf{k}} \times \partial_{k_y} \hat{\mathbf{d}}_{\mathbf{k}}\right], \qquad \text{with} \quad \hat{\mathbf{d}}_{\mathbf{k}} = \frac{\mathbf{d}(\mathbf{k})}{|\mathbf{d}(\mathbf{k})|}, \tag{26}$$

and $d_x(\mathbf{k}) = \sin k_x$, $d_y(\mathbf{k}) = \sin k_y$, and $d_z(\mathbf{k}) = (2 - \cos k_x - \cos k_y - \cos k_z)$. Here, for simplicity, we choose $\mathcal{C}$ to be parallel to the $k_x k_y$-plane, see Fig. 4(a). The vector $\hat{\mathbf{d}}_{\mathbf{k}}$ in Eq. (26) defines a map from $\mathbf{k}$ to the unit sphere S^2, see Figs. 3(a) and 3(b). The Chern number $C(k_z)$, Eq. (26), measures how many times the $\hat{\mathbf{d}}_{\mathbf{k}}$-vector wraps around S^2 as $\mathbf{k}$ sweeps through the contour $\mathcal{C}_{k_z}$. (Note that for $\mathbf{k}$ restricted to a spherical contour $\mathcal{C}$, $\hat{\mathbf{d}}_{\mathbf{k}}$ represents a map from S^2 to S^2, whose topology is given by the second homotopy group $\pi_2(S^2) = \mathbb{Z}$ [32].) Let us now study how $C(k_z)$, Eq. (26), changes as a function of k_z. Two different regions of k_z can be distinguished:

[5]Note that this model has an inversion symmetry, i.e., $(\sigma_z)^{-1} H^A_{3D}(-\mathbf{k})\sigma_z = H^A_{3D}(\mathbf{k})$, which ensures that the two Weyl points are at the same energy.

[6]The fact that there is a non-zero Chern number can also be diagnosed from the parity eigenvalues at the TRIMs [5]. The parity eigenvalues at the Γ point are opposite to those at all the other TRIMs. From this it follows that the Chern number $C(k_z = 0)$ must be non-zero.

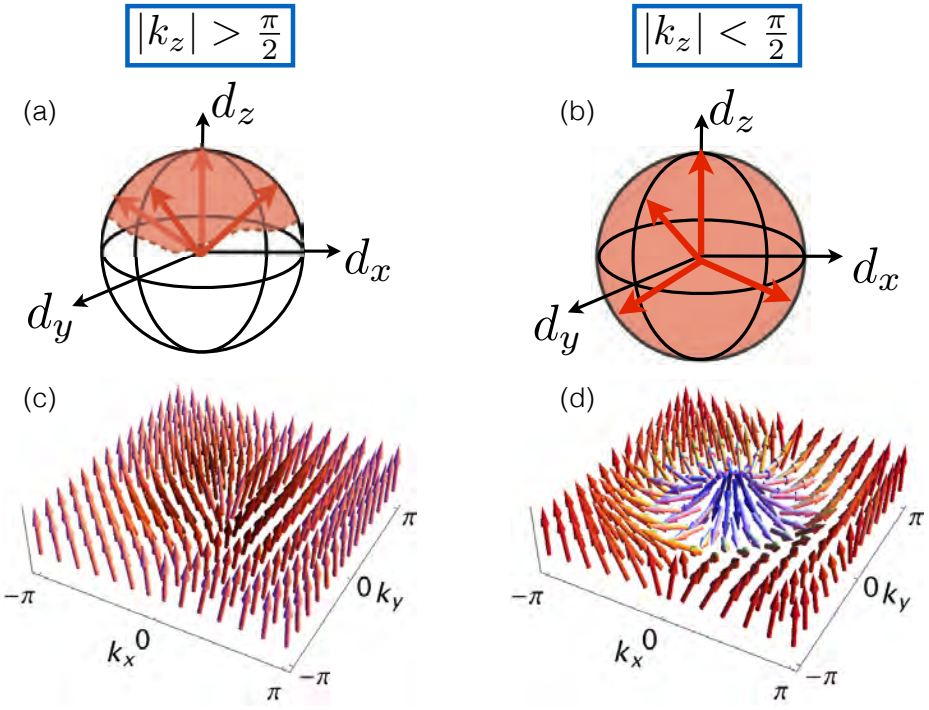

Fig. 3: *(a),(b) show the regions covered by the* $\mathbf{d_k}$*-vector, Eq.* (26)*, on the unit sphere. (c), (d) depict the textures of* $\mathbf{d_k}$ *in the* k_xk_y*-plane, i.e., in the contour* $\mathcal{C}_{k_z}$*. (a), (c) corresponds to* $C(k_z) = 0$*, while (b), (d) represents* $C(k_z) \neq 0$*.*

Trivial region. For $|k_z| > \pi/2$, the $\hat{\mathbf{d}}_\mathbf{k}$-vector covers only a small region around the north pole of S^2, i.e., it points mostly upwards. Hence, $\hat{\mathbf{d}}_\mathbf{k}$ does not wrap around S^2, leading to a zero Chern number $C(k_z) = 0$, see left-hand side of Fig. 3. This follows also from the fact that the contour $\mathcal{C}$ can be continuously shrunk to zero, without crossing through the singularities of the Weyl points. Thus, the integral (26) must vanish.

Topological region. For $|k_z| < \pi/2$, however, the $\hat{\mathbf{d}}_\mathbf{k}$-vector wraps once around the unit sphere S^2. That is, it points along all directions as $\mathbf{k}$ sweeps through $\mathcal{C}_{k_z}$, producing a Skyrmion texture in the k_xk_y-plane, see right-hand side of Fig. 3. As a consequence, the Chern number is nonzero, i.e., $C(k_z) = \pm 1$, which endows the Weyl points with a nonzero topological charge (also know as "chirality"). This agrees with the fact that the contour $\mathcal{C}$ cannot be continuously shrunk to zero, without crossing through the Weyl point singularities. Hence, the integral (26) must be nonzero.

Due to the periodicity of the BZ, we can consider the contour $\mathcal{C}_{k_z}$ to enclose either the upper or the lower part of the BZ, see Fig. 4(a). Both ways of closing the contour must give consistent results. A contour $\mathcal{C}_{k_z}$ with $|k_z| > \pi/2$, which can be shrunk to zero, can also be viewed as enclosing both Weyl points. Hence, the Chern numbers of the two Weyl points must add up to zero, i.e., they must have opposite topological charges, which is a manifestation of the fermion-doubling theorem [26].

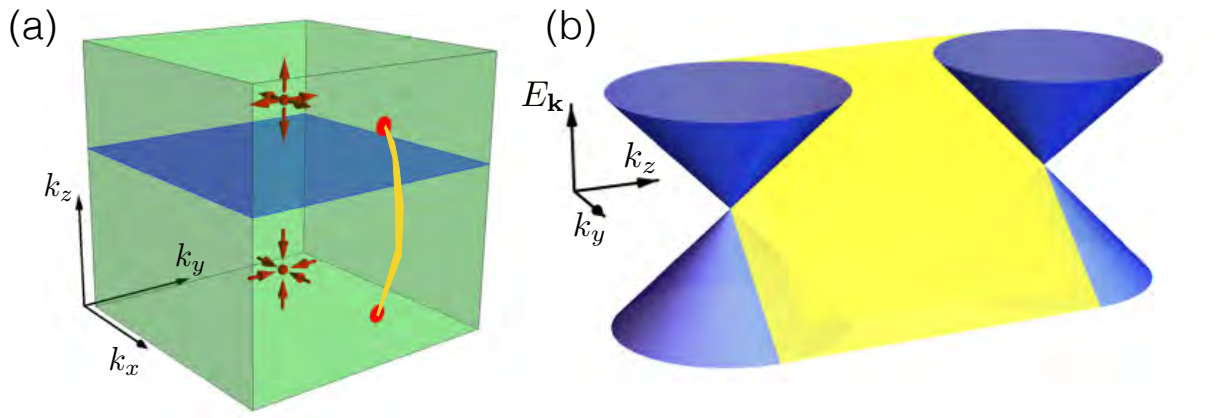

Fig. 4: *(a) The Weyl points (red spheres) are sources and drains of Berry flux (red arrows). In the surface BZ there exists a Fermi arc state (yellow), which connects the projection of the two Weyl points. The blue plane indicates the integration contour $\mathcal{C}_{k_z}$ of Eq.* (26)*. (b) Schematic energy dispersion of the Fermi arc state in the (100) surface BZ. The Fermi arc surface state (yellow) smoothly connects to the linearly dispersing bulk bands (blue) of the two Weyl points.*

2.2.1 Fermi arc surface states

We now discuss the surface states of Weyl semimetals, which arise due to the nontrivial topology of the Weyl points. For this we consider again Hamiltonian (23) restricted to a planar contour $\mathcal{C}_{k_z}$ which is perpendicular to the k_z axis [blue plane in Fig. 4(a)]. As we have seen above, for any contour $\mathcal{C}_{k_z}$ with $|k_z| < \pi/2$ the Chern number is $C = \pm 1$. Thus, each of the two-dimensional Hamiltonians $H^A_{3D,k_z}(k_x, k_y)$,with $|k_z| < \pi/2$, represents a two-dimensional Chern insulator. These Chern insulators all have chiral edge modes, which on the surface perpendicular to, e.g., the x direction, have a linear dispersion with $E \simeq vk_y$. Hence, there is a collection of chiral edge modes on the (100) surface, which all disperse in the same direction. They form an arc in the surface BZ, connecting the projection of the two Weyl points (yellow arc in Fig. 4). This arc smoothly connects to the bulk bands, as shown in Fig. 4(b). We note that these arc states cannot exist in purely two-dimensional systems, as they would contradict the continuity of the band structure (bands cannot terminate at a point). At surfaces, however, these arc states are allowed, since their end points smoothly connect with the bulk bands.

2.2.2 The chiral anomaly

Since the two Weyl points of opposite Chern number (i.e., opposite chirality) are separated by a large momentum in the BZ, one might naively expect that the number of electrons $n_\pm$ at each Weyl point with $C = \pm 1$ are separately conserved. In other words, one might think that besides the regular electric charge $e(n_+ + n_-)$, also the chiral charge $e(n_+ - n_-)$ is conserved. Indeed, within a classical low-energy description of Weyl semimetals the chiral charge is preserved. However, at the quantum level this symmetry is broken, giving rise to an anomaly, i.e., the chiral anomaly [5, 6]. That is, in the presence of electric fields $\mathbf{E}$ and magnetic fields $\mathbf{B}$ the

number of electrons $n_\pm$ at a given Weyl point is changed as

$$\frac{d}{dt}n_\pm = \pm\frac{e^2}{h^2}\mathbf{E}\cdot\mathbf{B}. \tag{27}$$

Therefore, an electric field together with a magnetic field can generate (or destroy) chiral charge, i.e., they can pump electric charges from one Weyl point to the other, leading to valley polarizations. The total electric charge, however, remains preserved in this process. The chiral anomaly has a number of experimental consequences, such as anomalous Hall effect and negative magnetoresistance [6].

2.3 Dirac nodal-line semimetal

As a second example, we study a nodal-line band crossing in a three-dimensional semimetal with time-reversal symmetry (class AI) and reflection symmetry [33, 35, 36]. The Hamiltonian is defined on the cubic lattice and is given by $\mathcal{H}_{3D}^{AI+R} = \sum_{\mathbf{k}} \Psi_{\mathbf{k}}^\dagger H_{3D}^{AI+R}\Psi_{\mathbf{k}}$, where the spinor $\Psi_{\mathbf{k}} = (c_{p\mathbf{k}}, c_{d\mathbf{k}})^T$ describes spinless Bloch electrons (no spin-orbit coupling) originating from p and d orbitals and H_{3D}^{AI+R} reads (cf. Eq. (21) with $p = 2$)[7]

$$H_{3D}^{AI+R} = \sin k_z\sigma_2 + [2 - \cos k_x - \cos k_y - \cos k_z]\,\sigma_3. \tag{28}$$

The spectrum of this Hamiltonian

$$E_{\mathbf{k}} = \pm\lambda_{\mathbf{k}} = \pm\sqrt{(2 - \cos k_x - \cos k_y - \cos k_z)^2 + (\sin k_z)^2}, \tag{29}$$

exhibits a band-crossing at $E = 0$, which is located along a nodal ring within the $k_z = 0$ plane, see Fig. 5(a). Such a nodal-line band crossing at the Fermi energy is realized in Ca_3P_2, CaAgP, and other materials [2,15,33]. Eq. (28) is time-reversal symmetric with the time-reversal operator $\mathcal{T} = \sigma_0\mathcal{K}$, and reflection symmetric, $R^{-1}H_{3D}^{AI+R}(k_x, k_y, -k_z)R = H_{3D}^{AI+R}(k_x, k_y, k_z)$, with the reflection operator $R = \sigma_z$. There is also an inversion symmetry, $\mathcal{P}^{-1}H_{3D}^{AI+R}(-\mathbf{k})\mathcal{P} = H_{3D}^{AI+R}(\mathbf{k})$, with the inversion operator $\mathcal{P} = \sigma_z$. We observe that the only possible mass term $m\tau_x$ that anticommutes with H_{3D}^{AI+R} is symmetry forbidden, since it breaks reflection symmetry ($R^{-1}m\sigma_x R = -m\sigma_x$) and space-time inversion symmetry [$(\mathcal{TP})^{-1}m\sigma_x(\mathcal{TP}) = -m\sigma_x$]. Hence, the nodal line band crossing is stable and protected by reflection symmetry and $\mathcal{PT}$ symmetry. However, the band crossing of the doubled version of H_{3D}^{AI+R}

$$H_{3D}^{AI+R,\mathrm{db}} = \sin k_z\sigma_2 \otimes \sigma_0 + [2 - \cos k_x - \cos k_y - \cos k_z]\,\sigma_3 \otimes \sigma_0. \tag{30}$$

is protected only by reflection but not by $\mathcal{PT}$ symmetry, since the mass term $\hat{m} = \sigma_x \otimes \sigma_y$ is symmetric under $\mathcal{PT}$ [$(\sigma_z\otimes\sigma_0\mathcal{K})^{-1}\hat{m}(\sigma_z\otimes\sigma_0\mathcal{K}) = \hat{m}$], but breaks R [$(\sigma_z\otimes\sigma_0)^{-1}\hat{m}(\sigma_z\otimes\sigma_0) \neq \hat{m}$]. From this we conclude that nodal rings of type (28) have a $\mathbb{Z}$ classification in the presence of reflection symmetry, but only a $\mathbb{Z}_2$ classification in the presence of $\mathcal{PT}$ symmetry.

[7] Here, we have included both $\cos k_x$ and $\cos k_y$ terms in order to deform the nodal line of Eq. (21) into a nodal ring.

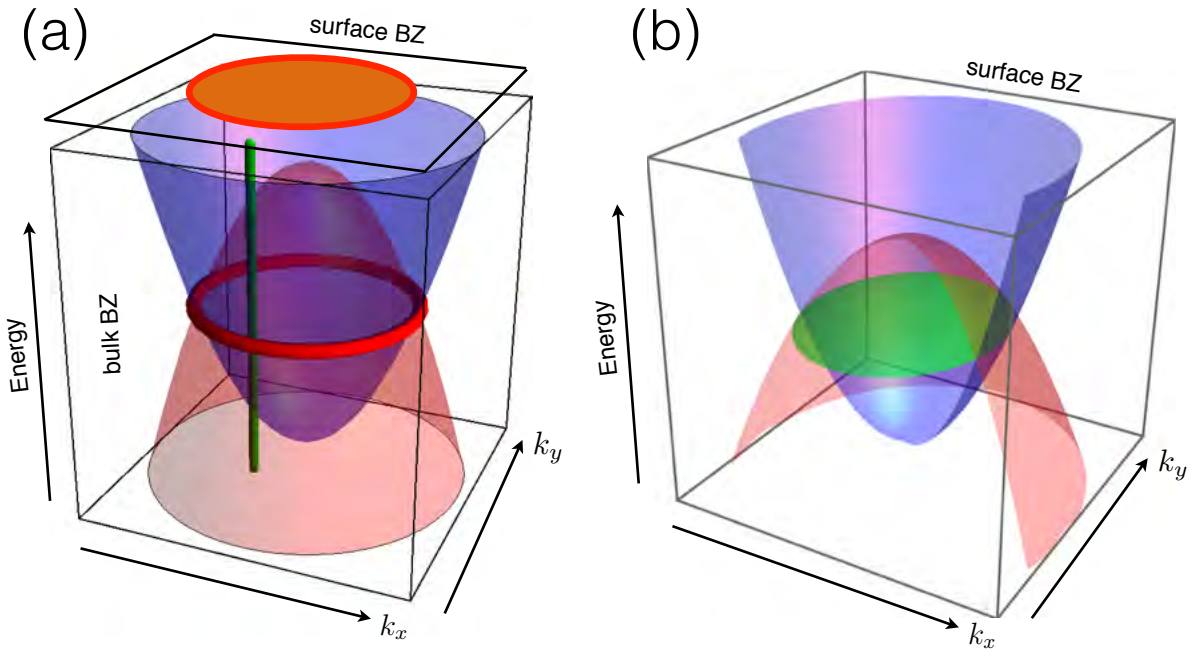

Fig. 5: *(a) Hamiltonian* (28) *describes an electron- and a hole-like band, which cross each other along a nodal loop (red ring). The green line represents the contour $\mathcal{L}$ of Eq.* (31)*. The red area in the surface BZ indicates the region where surface states exist. (b) Schematic energy dispersion of the drumhead surface state in the (001) surface BZ. The drumhead surface state (green) smoothly connects to the bulk bands (blue and red) of the nodal ring.*

The topological invariant, which guarantees the stability of the nodal ring, is the Berry phase. The Berry phase is defined as a one-dimensional contour integral over the Berry connection (for a related mirror invariant, see Ref. [33])

$$P_{\mathcal{L}} = -i \oint_{\mathcal{L}} dk_l \, \langle u_-(\mathbf{k})| \, \nabla_{k_l} \, |u_-(\mathbf{k})\rangle \, . \tag{31}$$

Here, $|u_-(\mathbf{k})\rangle$ is the filled Bloch eigenstate of Eq. (28), which is given by

$$|u_-(\mathbf{k})\rangle = \frac{1}{\sqrt{2\lambda_{\mathbf{k}}(\lambda_{\mathbf{k}} - M_{\mathbf{k}})}} \begin{pmatrix} \lambda_{\mathbf{k}} - M_{\mathbf{k}} \\ i \sin k_z \end{pmatrix} , \tag{32}$$

with $M_{\mathbf{k}} = 2 - \cos k_x - \cos k_y - \cos k_z$. Note that the Berry phase is only defined up to mod 2π. One can show that reflection symmetry R and space-time inversion $\mathcal{PT}$ lead to the quantization of the Berry phase, i.e., $P_{\mathcal{L}} \in \{0, \pi\}$ [33]. For contours $\mathcal{L}$ that do not interlink with the nodal ring, the Berry phase (31) is zero, since the contour can be continuously shrunk to a single point. For a contour $\mathcal{L}$ that does interlink with the nodal ring the Berry phase evaluates to $P_{\mathcal{L}} = \pi$. In this case, the contour cannot be continuously shrunk to zero without crossing the nodal ring. Hence, the nodal ring is stable to small changes in the parameters, as long as mirror or $\mathcal{PT}$ symmetry is not broken.

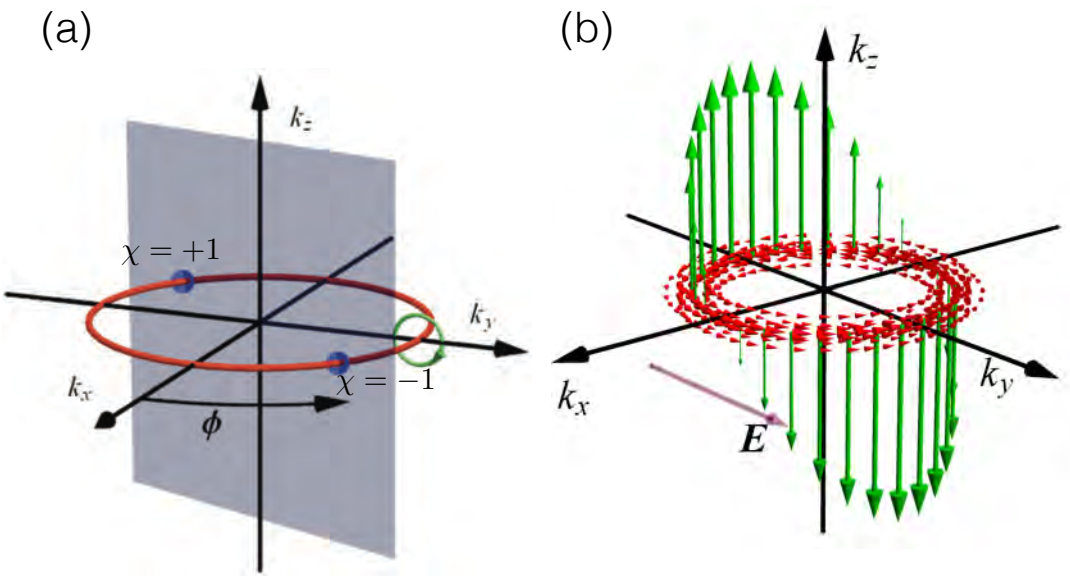

Fig. 6: *(a) The nodal-line semimetal is decomposed into a family of two-dimensional subsystems (blue plane) parametrized by the angle ϕ. (b) In the presence of an electric field (violet arrow), the nonzero Berry curvature (red arrows) leads to a transverse Hall current (green arrows). Figures adapted from Ref. [35].*

2.3.1 Drumhead surface state

We now discuss the surface states of nodal-line semimetals, that arise due to the nontrivial topology of the nodal ring. For this purpose we consider Hamiltonian (28) restricted to a line contour $\mathcal{L}_{k_x,k_y}$, which is perpendicular to the k_xk_y-plane, i.e., along the k_z direction [green line in Fig. 5(a)]. As we have seen above, for any contour $\mathcal{L}_{k_x,k_y}$, with $\cos k_x + \cos k_y > 1$, the Berry phase is $P = \pi$. Hence, each of the one-dimensional Hamiltonians $H^{AI+R}_{3D;k_x,k_y}(k_z)$, with $\cos k_x + \cos k_y > 1$, represents a one-dimensional topological insulator with non-zero Berry phase. These one-dimensional topological insulators all have midgap end states [34]. As a consequence, there is a collection of end states on the (001) surface, which form a drumhead that smoothly connects to the projected bulk bands [green area in Fig. 5(b)]. This drumhead state is not allowed to exist in purely two-dimensional systems, as it would violated the continuity of the band structure (bands cannot terminate at lines). At a surface, however, such drumhead states can exist, since their edges smoothly connect to the bulk bands.

2.3.2 The parity anomaly

To discuss the parity anomaly, we divide the nodal-line semimetal into a collection of two-dimensional subsystems parametrized by the angle $\phi \in [0, \pi)$, as shown in Fig. 6(a). Each of these subsystems contains two Dirac points with opposite sign of Berry phase $\chi = \mathrm{sgn}(P)$, which are related by time-reversal symmetry. The quantum field theory of a single Dirac point

of such a subsystem coupled to an electromagnetic field A_μ includes the term

$$S_{\text{CS}}^{\phi,\chi} = \chi \frac{e^2}{4\pi} \int d^2x dt\, \epsilon^{\mu\nu\lambda} A_\mu \partial_\nu A_\lambda. \tag{33}$$

This Chern-Simons term only arises at the quantum level and is a manifestation of the parity anomaly, since it breaks $\mathcal{PT}$ symmetry. Varying the Chern-Simons term with respect to A_μ, gives the anomalous transverse current

$$j_\mu^{\phi,\chi} = \chi \frac{e^2}{4\pi} \epsilon^{\mu\nu\lambda} \partial_\nu A_\lambda \tag{34}$$

for a single Dirac point in subsystem ϕ with chirality χ. Hence, electromagnetic fields generate a topological current, which flows perpendicular to the applied field. These transverse currents are depicted in green in Fig. 6. For a field along the k_y axis, the transverse currents flow downward on the side of the ring with $k_y > 0$, while they flow upward on the opposite side. This leads to an accumulation of charge on opposite surfaces of nodal-line semimetals. Since the contributions on opposite sides of the nodal ring cancel out, the topological currents can only be measured by a device that filters electrons based on their momenta [35]. Alternatively, the topological currents can be induced and probed by axial gauge fields, which couple oppositely to electrons with opposite momenta [36].

3 Symmetry-enforced band crossings

In this section we study symmetry-enforced band crossings that are *movable* (but not removable) [16–22]. These movable band crossings, which are required to exist by symmetry alone, exhibit the following properties:

- They are protected by nonsymmorphic crystal symmetries, possibly together with non-spatial symmetries. A nonsymmorphic symmetry is a symmetry $G = \{g, \mathbf{t}\}$, which combines a point-group symmetry g with a translation $\mathbf{t}$ by a fraction of a Bravais lattice vector (see Sec. 3.1).

- Symmetry-enforced band crossings are characterized by a global topological charge, which measures the winding of the eigenvalue of G as we go through the BZ. As shown in Fig. 7, one needs to go twice (or n times) through the BZ in order to get back to the same eigenvalue.

- Symmetry-enforced band crossings are globally stable. That is, they cannot be removed, even by large symmetry-preserving deformations. They are required to exist by symmetry alone, independent of any other material details (e.g, chemical composition or energetics of the bands).

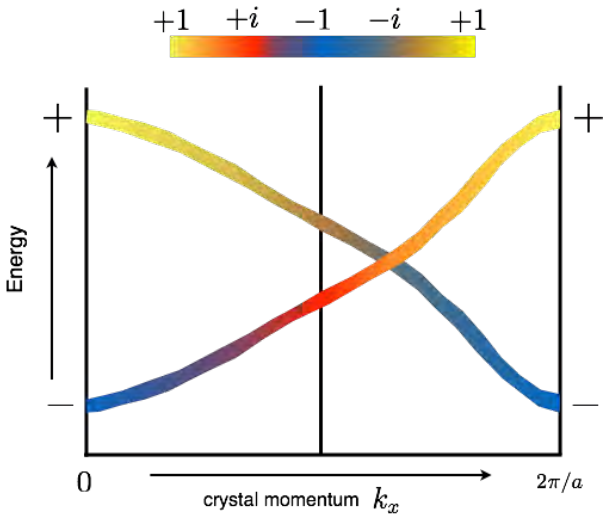

Fig. 7: *Nonsymmorphic symmetries lead to symmetry-enforced band crossings. The color shading indicates how the eigenvalue of the nonsymmorphic symmetry changes as a function of crystal momentum. Note that one needs to go through the BZ twice (or n times), in order to get back to the same eigenvalue.*

Strategy for materials discovery. The last point above allows us to construct the following strategy to discover new materials with topological band crossings [21, 22], which consists of three steps:

(i) First, we identify the space groups (SGs) whose nonsymmorphic symmetries enforce the desired band crossings. This can be done by either (i) computing the algebraic relations obeyed by the symmetry operators or (ii) by computing the compatibility relations between irreducible symmetry representations (irreps).

(ii) Second, we perform a database search for materials in these SGs. The most comprehensive database on inorganic crystals is the Inorganic Crystal Structure Database (ICSD) from the Leibniz Institute in Karlsruhe (https://icsd.fiz-karlsruhe.de). Other databases, which also contain band structures, are the AFLOW database (http://aflowlib.org), the Materials Project database (https://www.materialsproject.org), the database for material sciences at the IOP of the Chinese Academy of Science (http://materiae.iphy.ac.cn), and the Topological Materials Database (https://topologicalquantumchemistry.com).

(iii) Third, we compute the electronic band structure of these materials to check whether the band crossings are near the Fermi energy.

In Secs. 3.2.3 and 3.3.2 we will present two materials that have been found using the above strategy.

3.1 Nonsymmorphic symmetries lead to enforced band crossings

Nonsymmorphic symmetries $G = \{g|\mathbf{t}\}$ combine a point-group symmetry g with a translation $\mathbf{t}$ by a fraction of a Bravais lattice vector, see Fig. 8. Without loss of generality, we can assume

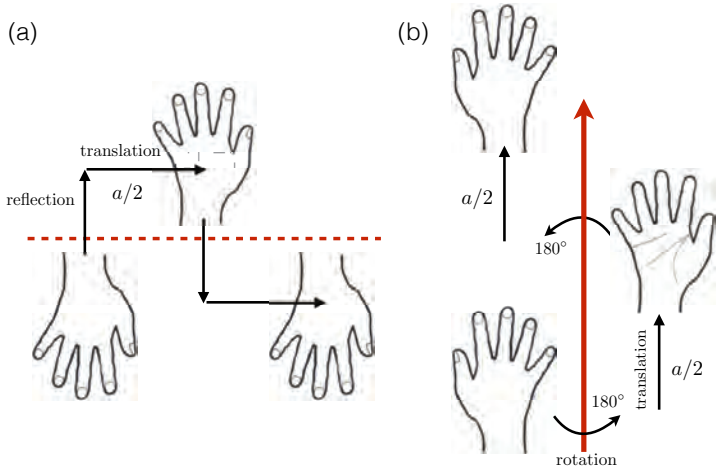

Fig. 8: *This figure illustrates two nonsymmorphic symmetries: A glide reflection in panel (a) and a two-fold screw rotation in panel (b).*

that the fractional translation $\mathbf{t}$ is parallel to the invariant space of g, i.e., that $g\mathbf{t} = \mathbf{t}$. The reason for this is that any component of $\mathbf{t}$ that is not invariant under g can be removed by a suitable choice of unit cell (i.e., a suitable choice of reference for g). (An exception to this rule will be discussed in Sec. 3.3.) Applying an n-fold nonsymmorphic symmetry n times yields a translation, i.e.,

$$G^n = \{g^n|n\mathbf{t}\} = \pm p\, T_{\mathbf{a}}, \quad p \in \{1, 2, \ldots, n-1\}, \tag{35}$$

where $T_{\mathbf{a}}$ is the translation operator for the Bravais lattice vector $\mathbf{a}$ and g is an n-fold point-group symmetry. The $\pm$ sign on the right-hand side of Eq. (35) originates from g^n, which equals -1 for spin-1/2 quasiparticles (Bloch electrons with spin-orbit coupling) and $+1$ for spinless quasiparticles (Bloch electrons without spin-orbit coupling). Two simple examples of nonsymmorphic symmetries are illustrated in Fig. 8:

- a glide reflection $M = \{m|\mathbf{t}\}$, with $M^2 = \pm T_{\mathbf{a}}$
- a two-fold screw rotation $C_2 = \{c_n|\mathbf{t}\}$, with $(C_2)^2 = \pm T_{\mathbf{a}}$

In the band structure of materials with nonsymmorphic symmetries, the operators $G = \{g|\mathbf{t}\}$ can enforce band degeneracies in the g-invariant space of the BZ, i.e., on lines or planes which satisfy $g\mathbf{k} = \mathbf{k}$. In these g-invariant spaces, the Bloch states $|u_m(\mathbf{k})\rangle$ can be constructed in such a way that they are simultaneous eigenfunctions of both G and the Hamiltonian. To derive the G-eigenvalues of the Bloch states $|u_m(\mathbf{k})\rangle$, we observe that

$$G^n = \pm e^{-ip\mathbf{k}\cdot\mathbf{a}}, \tag{36}$$

which follows from Eq. (35). Hence, the eigenvalues of G are

$$G\,|\psi_m(\mathbf{k})\rangle = \begin{cases} e^{i\pi(2m+1)/n} e^{-ip\mathbf{k}\cdot\mathbf{a}/n}\,|\psi_m(\mathbf{k})\rangle\,, & \text{for spin 1/2,} \\ e^{i2\pi m/n}\, e^{-ip\mathbf{k}\cdot\mathbf{a}/n}\,|\psi_m(\mathbf{k})\rangle\,, & \text{for spin 0,} \end{cases} \tag{37}$$

where $m \in \{0, 1, \ldots, n-1\}$. Because of the phase factor $e^{-ip\mathbf{k}\cdot\mathbf{a}/n}$ in Eq. (37) the eigensectors of G can switch, as $\mathbf{k}$ moves along the g-invariant space. From this it follows that pairs of bands must cross at least once within the invariant space.[8] With this we have found the basic mechanism that leads to symmetry-enforced band degeneracies [16–19],

Let us now explain in more detail how a screw rotation leads to a symmetry-enforced band crossing in a simple one-dimensional system with two atoms per unit cell. In momentum space such a system is described by a two-band Hamiltonian $\mathcal{H}(k)$. The screw rotation symmetry (π rotation, followed by half translation) takes the form [16]

$$G(k)\mathcal{H}(k)G^{-1}(k) = \mathcal{H}(k), \qquad G(k) = \begin{pmatrix} 0 & e^{-ik} \\ 1 & 0 \end{pmatrix}, \tag{38}$$

where the exponential factor e^{-ik} accounts for the fact that one of the two atoms is moved to the next unit cell. Here, we consider the case of spin-0 quasiparticles (Bloch electrons without spin-orbit coupling), hence $G(k)$ does not contain a spin part. Now, since $G^2(k) = \sigma_0 e^{-ik}$ the eigenvalues of G are $\pm e^{-ik/2}$, i.e., we can label the two bands of $H(k)$ by the eigenvalues of $G(k)$

$$G\,|\psi_\pm(\mathbf{k})\rangle = \pm e^{-ik/2}\,|\psi_\pm(\mathbf{k})\rangle\,, \tag{39}$$

cf. Eq. (37) with $n = 2$ and $p = 1$. We see that the eigenvalues are momentum dependent and change from $\pm$ at $k = 0$ to $\mp$ at $k = 2\pi$, as we go through the BZ. Hence, the two eigenspaces get interchanged and the bands must cross at least once, see Fig. 7.

It is also possible to mathematically prove that there needs to be at least one crossing [16]. The proof is by contradiction. First, we observe that $G(k)$ does not commute with σ_3 (it anti-commutes). Therefore, $\mathcal{H}(k)$ cannot contain a term proportional to σ_3, since it is symmetry forbidden. Moreover, we can drop terms proportional to the identity, since they only shift the energy of the eigenstates, but do not alter the band crossings. For this reason the Hamiltonian can be assumed to be off-diagonal and can be written as

$$H(k) = \begin{pmatrix} 0 & q(k) \\ q^*(k) & 0 \end{pmatrix}. \tag{40}$$

With this parametrization, the spectrum of $\mathcal{H}(k)$ is symmetric around $E = 0$ and is given by $E = \pm|q(k)|$. For this reason, any band crossing must occur at $E = 0$. Applying the symmetry constraint (38), we find that $q(k)$ must satisfy

$$q(k)e^{ik} = q^*(k). \tag{41}$$

We now need to show that any periodic function $q(k)$ satisfying the constraint (41) must have zeros, corresponding to a band crossing point. To see this, we introduce the complex variable

[8] Here we assume that here are no additional degeneracies due to other symmetries.

$z := e^{ik}$ and the complex function $f(z) := q(k)$. From Eq. (41) it follows that $zf(z) = f^*(z)$. Assuming that $f(z)$ is nonzero on the unit circle S^1, then

$$z = f^*(z)/f(z), \tag{42}$$

which, however, leads to a contradiction. This is because for $z \in S^1$ the two sides of Eq. (42) both define functions from S^1 to S^1. But the left hand side has winding number 1, while the right hand side has *even* winding number, since $f^*(z)/f(z) = e^{-2i\text{Arg}[f(z)]}$. Thus, $f(z)$ and $q(k)$ must vanish at some k by contradiction. Therefore, there must be a band crossing point somewhere in the BZ.

3.2 Weyl nodal-line semimetal

Next we discuss how a glide reflection symmetry can enforce two-fold degeneracies along a line. Materials with these line degeneracies are called Weyl nodal-line semimetals. For concreteness, we consider a system with spin-orbit coupling, which is invariant under the hexagonal SG 190 ($P\bar{6}2c$). This SG contains a glide reflection symmetry of the form

$$M_x \ : \ (x, y, z) \to (-x, y, z + \tfrac{1}{2})i\sigma_x, \tag{43}$$

where the Pauli matrix σ_x operates in spin space. Applying this glide reflection twice yields minus a unit translation in the x direction, i.e., $-\hat{T}_x$, where the minus sign is due to the spin part. The glide reflection (43) leaves two planes in the BZ invariant, namely the $k_x = 0$ plane and the $k_x = \pi$ plane, see Fig. 9(a).

3.2.1 Symmetry eigenvalues

We now use the arguments from Sec. 3.1 to show that the glide reflection M_x leads to symmetry-enforced degeneracies along a line within the $k_x = \pi$ plane. Within the $k_x = \pi$ plane, the Bloch bands can be chosen to be eigenstates of M_x with the eigenvalues

$$M_x \left|\psi_\pm(\mathbf{k})\right\rangle = \pm ie^{-ik_z/2} \left|\psi_\pm(\mathbf{k})\right\rangle, \tag{44}$$

which follows from Eq. (37) with $p = 1$ and $n = 2$. Next, we add time-reversal symmetry to the game, since we want to study nonmagnetic systems. Time-reversal symmetry sends the crystal momentum $\mathbf{k}$ to $-\mathbf{k}$ and acts on the Hamiltonian as (see Sec. 2.1.1)

$$\mathcal{T}^{-1} H(-\mathbf{k}) \mathcal{T} = +H(\mathbf{k}), \tag{45}$$

with the operator $\mathcal{T} = i\sigma_y \mathcal{K}$ and $\mathcal{K}$ the complex conjugation operator. Time-reversal symmetry leaves two points in the $k_x = \pi$ plane invariant [blue and red dots in Fig. 9(a)], which are called time-reversal invariant momenta (TRIMs). At these TRIMs the bands are two-fold degenerate due to Kramers theorem, i.e., they form Kramers pairs. Away from the TRIMs, however, the bands are in general non-degenerate. (Note that spin-orbit coupling lifts the spin degeneracy.) Since $\mathcal{T}$ contains the complex conjugation operator $\mathcal{K}$, the Kramers pairs at the TRIMs are

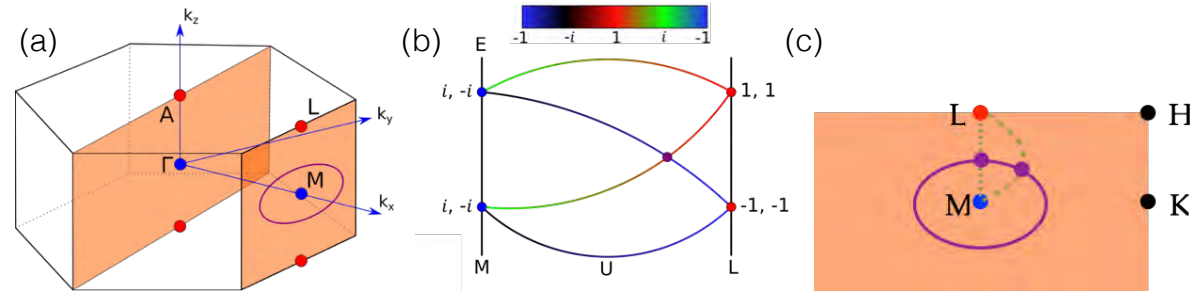

Fig. 9: *(a) Weyl nodal line in the $k_x = \pi$ plane protected by the glide mirror symmetry M_x, Eq.* (43)*. (b) Band connectivity diagram for a line connecting M and L within the $k_x = \pi$ plane, which is left invariant by M_x. The bands are Kramers degenerate at M and L. The color shading indicates the M_x eigenvalues* (44) *of the Bloch bands. (c) The Bloch bands along any path within the $k_x = \pi$ plane, connecting M to L, exhibit the band connectivity shown in (b). Figures adapted from Ref. [21].*

formed by bands whose M_x eigenvalues are complex conjugate pairs. Using Eq. (44), we find that at the L point of the $k_x = \pi$ plane the M_x eigenvalues are $+1$ and -1, while at the M point they are $+i$ and $-i$. (Similar arguments hold for the TRIMs in the $k_x = 0$ plane.) Hence, at M the Kramers pairs are formed by bands with opposite M_x eigenvalues [blue dot in Fig. 9(a)], while at L they are formed by bands with the same M_x eigenvalues [red dot in Fig. 9(a)]. This is shown in Fig. 9(b), where the M_x eigenvalues are indicated by the color shading. We see that since the Kramers pairs switch partners as we go from M to L, the bands must cross at least once forming a group of four connected bands with an *hourglass dispersion*. Because this holds for any one-dimensional path within the $k_x = \pi$ plane, connecting M to L, the $k_x = \pi$ plane must contain a Weyl line degeneracy, as shown in Fig. 9(c).

3.2.2 Compatibility relations

The existence of symmetry-enforced band crossings can also be inferred from the compatibility relations between irreducible representations (irreps) at different high-symmetry points of the BZ [37]. To show this we consider again a system in SG 190 with spin-orbit coupling. But before doing so, we first need to review some basic properties of double SGs and their double-valued irreps [38].

Band structures of nonmagnetic materials with spin-orbit coupling (i.e., materials with a time-reversal symmetry $\mathcal{T}^2 = -1$) are invariant under the symmetries of *double* SGs. Correspondingly, the symmetry operators under which these band structures transform are given by the *double-valued* irreps of the double SGs. If we consider the band structure at a particular high-symmetry point $\mathbf{k}$ (or high-symmetry line), then the symmetries are reduced to a subgroup of the double SG. This subgroup is denoted by $\mathcal{G}_\mathbf{k}$ and is called the little group at $\mathbf{k}$. Because the Bloch Hamiltonian restricted to $\mathbf{k}$ commutes with this little group $\mathcal{G}_\mathbf{k}$, the bands at $\mathbf{k}$ can be labeled by the double valued irreps of $\mathcal{G}_\mathbf{k}$, which are denoted by $\bar{\mathbf{D}}_\mathbf{k}$. If we move continuously away from a high-symmetry point $\mathbf{k}_1$ to a nearby point $\mathbf{k}_2$, then the symmetries are lowered. That is,

Irreps \Element	E	M_x
$\overline{M}_5$	$\begin{pmatrix}+1 & 0\\ 0 & +1\end{pmatrix}$	$\begin{pmatrix}+i & 0\\ 0 & -i\end{pmatrix}$
$\overline{L}_2$	$+1$	-1
$\overline{L}_3$	$+1$	-1
$\overline{L}_4$	$+1$	$+1$
$\overline{L}_5$	$+1$	$+1$
$\overline{C}'_3$	$+1$	$e^{\frac{i}{2}(\pi+k_z)}$
$\overline{C}'_4$	$+1$	$e^{-\frac{i}{2}(\pi-k_z)}$

Table 2: *Double valued irreps of SG 190 ($P\bar{6}2c$) without time-reversal at the TRIMs M and L and within the mirror plane $k_z = \pi$, denoted by C'. Due to the partial translation of M_x, the irreps for C' have momentum-dependent phases. For the labeling of the irreps we use the convention of Ref. [37].*

the little group $\mathcal{G}_{\mathbf{k}_2}$ is smaller than the little group $\mathcal{G}_{\mathbf{k}_1}$, and forms a subgroup $\mathcal{G}_{\mathbf{k}_2} \subset \mathcal{G}_{\mathbf{k}_1}$. As a consequence, representations $\widetilde{\mathbf{D}}_{\mathbf{k}_2}$ of $\mathcal{G}_{\mathbf{k}_2}$ can be inferred (i.e., subduced) from the little-group irreps $\bar{\mathbf{D}}_{\mathbf{k}_1}$, i.e., we have

$$\widetilde{\mathbf{D}}_{\mathbf{k}_2} = \bar{\mathbf{D}}_{\mathbf{k}_1} \downarrow \mathcal{G}_{\mathbf{k}_2}. \tag{46}$$

Decomposing the subduced representations $\widetilde{\mathbf{D}}_{\mathbf{k}_2}$ into irreps yields the compatibility relations between the irreps $\bar{\mathbf{D}}_{\mathbf{k}_1}$ and $\bar{\mathbf{D}}_{\mathbf{k}_2}$ [37–39]. From these compatibility relations one can deduce the connectivity of the Bloch bands in the BZ.

We will now show how this works for SG 190. We start be determining the little group irreps at the TRIMs M and L, and within the mirror plane $k_x = \pi$ (denoted by C'). Table 2 lists the double-valued irreps without time-reversal symmetry. We find that at the M point there is only one double-valued irrep, namely $\bar{M}_5$, which is two-dimensional and pseudoreal. At the L point there are four different irreps: $\bar{L}_2$, $\bar{L}_3$, $\bar{L}_4$, and $\bar{L}_5$, which are one-dimensional and complex. The irreps for C' are all one-dimensional and have $\mathbf{k}$-dependent phases, due to the translation part of the glide reflection M_x, Eq. (43). At the TRIMs M and L we need to construct time-reversal symmetric irreps (i.e., real irreps) using Table 2. We note that pseudoreal irreps are time-reversal symmetric by themselves. Complex irreps, on the other hand, must be paired up into complex-conjugate pairs to make them time-reversal symmetric [38, 39]. Hence, at the L point we need to pair $\bar{L}_2$ with $\bar{L}_3$ and $\bar{L}_4$ with $\bar{L}_5$, see Fig. 10(a). With this, all time-reversal symmetric irreps at the TRIMs are two dimensional, in agreement with the Kramers theorem, which leads to two-fold degeneracies. As we move away from the TRIMs to a point in C', these two-dimensional irreps decompose into one-dimensional irreps, in such a way that the compatibility relations are satisfied.

To figure out how the Kramers pairs split up, we therefore need to derive the compatibility relations between the irreps at M, L, and C'. For this purpose, we use the following relation

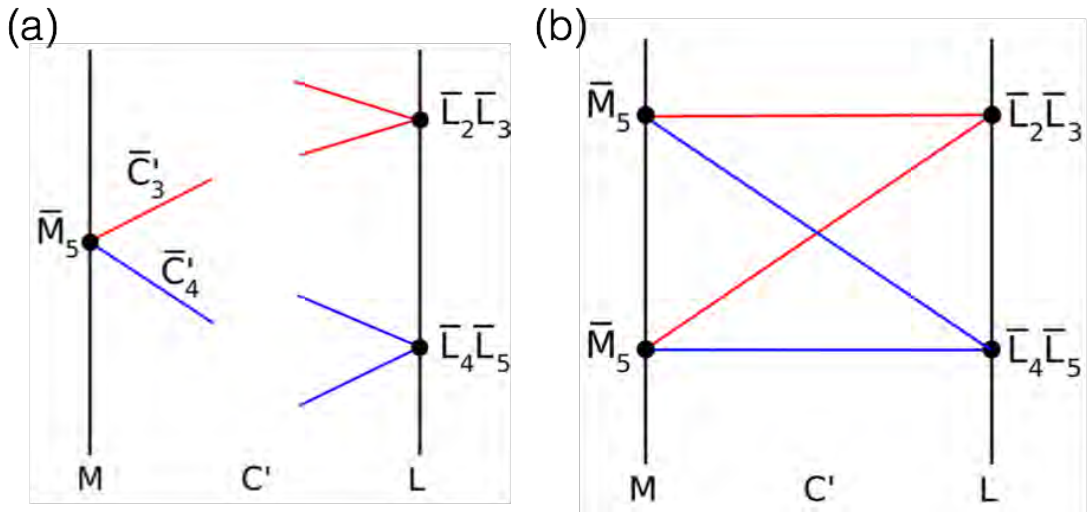

Fig. 10: *(a) Compatibility relations for SG 190 between the little-group irreps at M, L, and C' ($k_x = \pi$ plane). (b) Band connectivity diagram for SG 190 for a path within the $k_x = \pi$ plane connecting M to L. Figures adapted from Ref. [21].*

between the characters χ of the irreps[9]

$$\chi[\overline{D}_l(g)] = \sum_{i=1}^{2} \chi[\overline{C}'_{m_i}(g)], \tag{47}$$

for any group element g. Here, $\chi[\overline{D}_l(g)]$ is the character of the irrep $\overline{D}_l$ at the TRIM M or L, while $\{\overline{C}'_{m_1}, \overline{C}'_{m_2}\}$ is the set of irreps that $\overline{D}_l$ decomposes into, as we move away from the TRIMs to a point on C'. Relation (47) follows from continuity, which requires that the characters of the irreps are preserved, as we continuously move away from a TRIM to a point on C'. By use of Eq. (47), we infer that the time-reversal symmetric irrep at M (where $k_z = 0$) decomposes into

$$\overline{M}_5 \;\rightarrow\; \overline{C}'_3 + \overline{C}'_4, \tag{48a}$$

while for the real irreps at L (where $k_z = \pi$) we have

$$\begin{aligned} \overline{L}_2\overline{L}_3 &\;\rightarrow\; \overline{C}'_3 + \overline{C}'_3, \\ \overline{L}_4\overline{L}_5 &\;\rightarrow\; \overline{C}'_4 + \overline{C}'_4. \end{aligned} \tag{48b}$$

The above two relations represent the compatibility relations between the irreps at the TRIMs (M and L) and C'. They determine the connectivity of the bands on the path M–C'–L. That is, as we move from M to C' and then on to L, the Kramers pairs at M must split up and then pair up again, such that the compatibility relations (48) are satisfied. Therefore the bands must connect as shown in Fig. 10(b). That is, the irreps switch partners as we move within C' from M to L. As a consequence, the band connectivity is nontrivial with sets of four connected bands that show an hourglass dispersion, with at least one movable crossing between M and L. Hence, each quartet of bands within the C' plane forms at least one Weyl nodal line, which fully agrees with the results of Sec. 3.2.1, cf. Fig. 9(b).

[9]The character of a group irrep associates with each group element the trace of the corresponding irrep matrix.

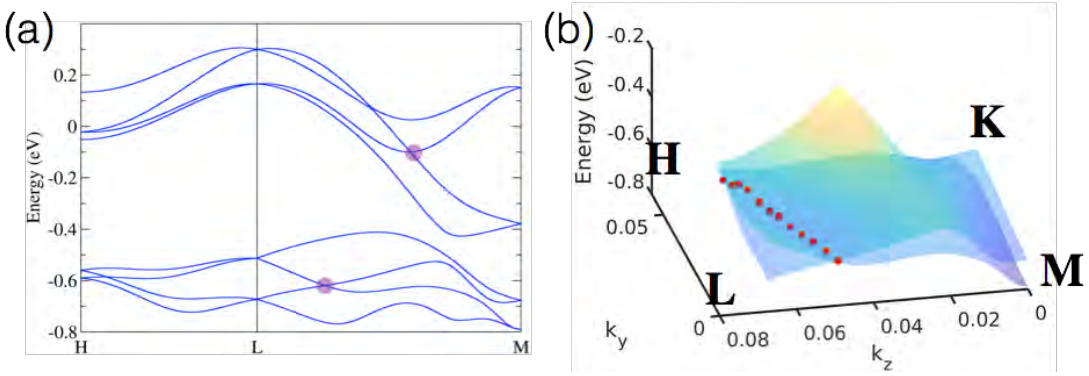

Fig. 11: *(a) Electronic band structure of ZrIrSn along the high-symmetry path H–L–M, cf. Fig 9. The band crossings along M–L (violet dots) are part of Weyl nodal lines within the $k_x = \pi$ plane. (b) Dispersion of the pair of bands that form the Weyl nodal line at $E \simeq -0.64$ eV. The nodal line (red dots) encloses the L point.*

3.2.3 Example material: ZrIrSn

Having found that all band structures with strong spin-orbit coupling in SG 190 exhibit Weyl nodal lines, we now apply the strategy of page 19 to find real materials that exhibit these line degeneracies. To do so, we consult the ICSD database (https://icsd.fiz-karlsruhe.de) to find materials with heavy elements (indicating strong spin-orbit coupling) that crystallize in SG 190. This was performed in Ref. [21] and it was found that ZrIrSn is a good example. ZrIrSn contains only heavy elements resulting in strong spin-orbit coupling. Indeed, the calculated band structure [Fig. 11(a)] shows that the spin-orbit coupling leads to a large band splitting away from the TRIMs, by about 100 meV. As predicted in the previous section, along the M–L path we observe groups of four connected bands with an hourglass dispersion and at least one crossing. As shown in Fig. 11(b), these crossings are part of Weyl nodal lines in the C' plane, i.e., two-fold degeneracies on rings which enclose one of the TRIMs.
Similar to the Dirac nodal-line semimetal of Sec. 2.3, the topology of this Weyl nodal ring is described by a π Berry phase [33], which leads to drumhead surface states. Furthermore, the bands that form nodal rings carry large Berry curvatures, which leads to anomalous transport properties, for example, anomalous magnetoelectric responses or large Hall effects.

3.3 Dirac nodal-line semimetal

As a second example, we study how off-center symmetries can enforce four-fold degeneracies along a line, i.e., how they can enforce the existence of Dirac nodal lines. In Sec. 2.3, we have already discussed a Dirac nodal-line semimetal with an *accidental* nodal ring, which is protected by symmorphic symmetries (i.e., reflection or $\mathcal{PT}$ symmetry). Here, however, we discuss Dirac nodal lines that are *symmetry enforced* by off-center symmetries. Moreover, we shall consider systems with strong spin-orbit coupling, which was neglected in Sec. 2.3. For concreteness, we consider spin-orbit coupled systems which are symmetric under the hexagonal SG 176 ($P6_3/m$). This SG contains the glide reflection

$$\widetilde{M}_z \;:\; (x, y, z) \to (x, y, -z + \tfrac{1}{2}) i\sigma_z, \tag{49a}$$

where σ_z acts in spin space, and the inversion symmetry

$$P \ : \ (x, y, z) \to (-x, -y, -z). \tag{49b}$$

These two symmetries form together a pair of so-called off-center symmetries [20, 21]. We observe hat the translation part $\mathbf{t} = \frac{1}{2}\hat{z}$ of the glide reflection (49a) is perpendicular to the $\widetilde{m}_z$ invariant space (i.e., the xy mirror plane). As mentioned on page 20, this type of glide reflection can be transformed into a symmorphic symmetry by a different choice of unit cell i.e., by shifting the origin by $\frac{1}{4}\hat{z}$. However, this shift in origin also affects P, leading to a translation part in P. Since $\widetilde{M}_z$ and P have different reference points, it is not possible to choose the origin such that both $\widetilde{M}_z$ and P are without translation parts. A pair of two such symmetries with different reference points are called *off-center symmetries*.

3.3.1 Commutation relations

We now show that the momentum dependence of the commutation relation between $\widetilde{M}_z$ and P enforces the existence of fourfold degenerate nodal-lines. The glide reflection $\widetilde{M}_z$ leaves two planes in the hexagonal BZ invariant, namely the $k_x = 0$ plane and the $k_x = \pi$ plane, see Fig. 12(a). Within these planes the Bloch states can be labeled by the $\widetilde{M}_z$ eigenvalues $\pm i$ (remember that $\widetilde{M}_z^2 = -1$). I.e., we have

$$\widetilde{M}_z \left|\psi_\pm(\mathbf{k})\right\rangle = \pm i \left|\psi_\pm(\mathbf{k})\right\rangle . \tag{50}$$

To derive the commutation relation between $\widetilde{M}_z$ and P, we apply the symmetry operators $\widetilde{M}_z$ and P in succession,

$$\begin{aligned}
&(x, y, z) \xrightarrow{P} (-x, -y, -z) \xrightarrow{\widetilde{M}_z} (-x, -y, +z + \tfrac{1}{2}) i\sigma_z, \\
&(x, y, z) \xrightarrow{\widetilde{M}_z} (x, y, -z + \tfrac{1}{2}) i\sigma_z \xrightarrow{P} (-x, -y, +z - \tfrac{1}{2}) i\sigma_z.
\end{aligned}$$

This tells us that $\widetilde{M}_z P$ and $P\widetilde{M}_z$ differ by a unit translation in the z direction. Hence, by letting $\widetilde{M}_z P$ and $P\widetilde{M}_z$ act on the Bloch states (50), we get the commutation relation in $\mathbf{k}$-space

$$\widetilde{M}_z P \left|\psi_\pm(\mathbf{k})\right\rangle = e^{ik_z} P \widetilde{M}_z \left|\psi_\pm(\mathbf{k})\right\rangle . \tag{51}$$

It follows that the two symmetry operators commute in the $k_z = 0$ plane, while they anticommute in the $k_z = \pi$ plane. Since we are interested in nonmagnetic systems, we now also need to study the commutation relation between the off-center symmetries (49) and the time-reversal operator $\mathcal{T} = i\sigma_y \mathcal{K}$. Because $\mathcal{T}$ commutes with both $\widetilde{M}_z$ and P, we have

$$\widetilde{M}_z P\mathcal{T} \left|\psi_\pm(\mathbf{k})\right\rangle = e^{ik_z} P\mathcal{T} \widetilde{M}_z \left|\psi_\pm(\mathbf{k})\right\rangle . \tag{52}$$

Thus, the Kramers pair $\left|\psi_\pm(\mathbf{k})\right\rangle$ and $P\mathcal{T}\left|\psi_\pm(\mathbf{k})\right\rangle$ have the same $\widetilde{M}_z$ eigenvalues for $k_z = \pi$ (since $\widetilde{M}_z \left[P\mathcal{T}\left|\psi_\pm(\mathbf{k})\right\rangle\right] = -P\mathcal{T}\left[\pm i\left|\psi_\pm(\mathbf{k})\right\rangle\right] = \pm iP\mathcal{T}\left|\psi_\pm(\mathbf{k})\right\rangle$), while for $k_z = 0$, they have opposite $\widetilde{M}_z$ eigenvalues. Hence, if two Kramers pairs of bands with opposite $\widetilde{M}_z$ eigenvalues

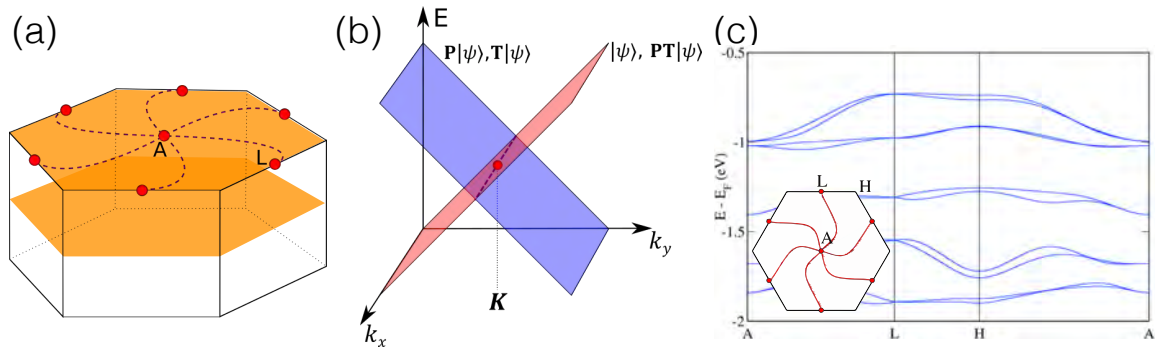

Fig. 12: *(a) Dirac nodal-lines in the $k_z = \pi$ plane, which connect the A and L points. (b) Two Kramers degenerate bands with opposite $\widetilde{M}_z$ eigenvalues cross each other to form a Dirac nodal line. (c) Electronic band structure of $LaBr_3$ along the high-symmetry path A–L–H–A. The band crossings along H–A are part of Dirac nodal lines within the $k_z = \pi$ plane. The inset shows the shape of the Dirac nodal line for the two top most bands in the main panel. Figures adapted from Ref. [21].*

cross within the $k_z = \pi$ plane, they form a Dirac nodal line. This Dirac nodal line cannot gap out, since the two Kramers pairs have opposite $\widetilde{M}_z$ eigenvalues. For $k_z = 0$, however, the crossing of two Kramers pairs of bands is not protected, since the two Kramers pairs have the same $\widetilde{M}_z$ eigenvalue.

Such a Dirac nodal line is in fact required to exist by symmetry alone, i.e., it occurs in any material with the off-center symmetries $(\widetilde{M}_z, P)$ and, in particular, in any material with spin-orbit coupling crystallizing in SG 176, irrespective of the chemical composition. To show that the Dirac nodal line is symmetry enforced, we consider the degeneracies at the TRIMs within the $k_z = \pi$ plane, i.e., at A and L [Fig. 12(a)]. At these two TRIMs the bands are four-fold degenerate, i.e., they form quartets of four degenerate states, which have the $\widetilde{M}_z$ eigenvalues

$$\widetilde{M}_z\,|\psi_\pm(\mathbf{K})\rangle = \pm i\,|\psi_\pm(\mathbf{K})\rangle\,, \tag{53a}$$
$$\widetilde{M}_z P\,|\psi_\pm(\mathbf{K})\rangle = \mp iP\,|\psi_\pm(\mathbf{K})\rangle\,, \tag{53b}$$
$$\widetilde{M}_z \mathcal{T}\,|\psi_\pm(\mathbf{K})\rangle = \mp i\mathcal{T}\,|\psi_\pm(\mathbf{K})\rangle\,, \tag{53c}$$
$$\widetilde{M}_z P\mathcal{T}\,|\psi_\pm(\mathbf{K})\rangle = \pm iP\mathcal{T}\,|\psi_\pm(\mathbf{K})\rangle\,, \tag{53d}$$

where $\mathbf{K} \in \{\mathrm{A}, \mathrm{L}\}$. These four Bloch states are mutually orthogonal to each other, because they are either Kramers partners or they have opposite $\widetilde{M}_z$ eigenvalues. Moving away from the TRIMs, the degenerate quartet splits, in general, into two Kramers pairs of bands. Due to inversion and time-reversal symmetry, the dispersion of the Kramers pairs of bands is symmetric with respect to the TRIMs. That is, the Kramers pairs of bands at $\mathbf{K}+\mathbf{k}$ and $\mathbf{K}-\mathbf{k}$ have the same energy, but opposite $\widetilde{M}_z$ eigenvalues, as shown in Fig. 12(b). It now follows from continuity, that each quartet of states at $\mathbf{K}$ cannot exist in isolation, but must be part of a Dirac nodal line connecting two TRIMs, see Fig. 12(a). This Dirac nodal line must be symmetric under inversion, time-reversal, and all other point-group symmetries of the SG, but is otherwise free to move within the $k_z = \pi$ plane. That is, the Dirac nodal line is movable, but not removable. For SG 176, which has a sixfold rotation symmetry, the Dirac nodal lines are shaped like stars, see Figs. 12(a) and 12(c).

3.3.2 Example material: $LaBr_3$

We have shown that all materials crystallizing in SG 176 have star-shaped nodal lines within the $k_z = \pi$ plane. In order to look for materials, we consult again the ICSD database and search for compounds with heavy elements crystallizing in SG 176. In Ref. [21] it was found that $LaBr_3$ is a good example. Figure 12(c) shows the first-principles band structure of $LaBr_3$ along the high-symmetry lines A–L–H–A . All bands are Kramers degenerate, due to the presence of $P\mathcal{T}$ symmetry. Along the H–A line we observe band crossings, which are part of Dirac nodal lines, whose shape resembles a star [inset of Fig. 12(c)].

4 Conclusions and future directions

In this chapter, we have reviewed accidental and symmetry-enforced band crossings. We have presented a classification of accidental band crossings in terms of symmetries and we have discussed how nonsymmorphic symmetries can lead to symmetry-enforced band crossings. We have presented a number of examples, ranging from Weyl semimetals with point nodes to Dirac semimetals with line nodes. From these discussions it is clear that symmetry together with topology fundamentally restricts the possible forms of band structures, i.e., in particular, their connectivity and their degeneracies. We have discussed this in terms of the momentum dependence of the symmetry eigenvalues, and in terms of compatibility relations between irreducible representations. An alternative approach is to study the properties of symmetric Wannier functions, which form space group representations. In this approach topological bands are identified as those, whose symmetric Wannier functions are not exponentially localized [40]. Combining this with symmetry based indicators, it is possible to perform high-throughput searches for topological materials [41–43].

While topological band structures of time-reversal invariant materials have been investigated extensively, topological band structures of magnetic systems still need to be understood better. Another avenue for future research is the study of how electron-electron correlations change the topology of materials. On the one hand, correlations can connect two topological band structures (or phases) that are distinct in the single-particle picture, on the other hand they can give rise to entirely new topological phenomena [2]. Finally, on the experimental front, there is a crucial need for better topological materials. In particular semimetals, where the Fermi energy is closer to the band crossing, and where there are no other bands close to the Fermi energy. The reader is invited to look for new topological semimetals by himself using the strategy detailed on page 19.

Acknowledgments. The material presented in this chapter is based upon works I did together with my students and collaborators, in particular, Ching-Kai Chiu, Yang-hao Chan, Yuxin Zhao, Jonathan Zhang, Wenbin Rui, Leslie Schoop, and Maia Vergniory. I thank them for sharing ideas and for their efforts. I also thank the organizers of the 10th Autumn School on Correlated Electrons for the invitation to contribute to this lecture series.

References

[1] M.Z. Hasan and C.L. Kane, Rev. Mod. Phys. **82**, 3045 (2010)

[2] C.-K. Chiu, J.C.Y. Teo, A.P. Schnyder, and S. Ryu, Rev. Mod. Phys. **88**, 035005 (2016)

[3] G.E. Volovik: *Topology of quantum vacuum*, *Lecture Notes in Physics*, Vol. 870 (Springer Berlin, 2013)

[4] G.E. Volovik, Lect. Notes Phys. **718**, 31 (2007)

[5] N.P. Armitage, E.J. Mele, and A. Vishwanath, Rev. Mod. Phys. **90**, 015001 (2018)

[6] A. Burkov, Annu. Rev. Condens. Matter Phys. **9**, 359 (2018)

[7] S.-Y. Yang, H. Yang, E. Derunova, S.S.P. Parkin, B. Yan, and M.N. Ali, Advances in Physics: X **3**, 1414631 (2018)

[8] C. Herring, Phys. Rev. **52**, 365 (1937)

[9] X. Huang, L. Zhao, Y. Long, P. Wang, D. Chen, Z. Yang, H. Liang, M. Xue, H. Weng, Z. Fang, X. Dai, and G. Chen, Phys. Rev. X **5**, 031023 (2015)

[10] P. Liu, J.R. Williams, and J.J. Cha, Nature Reviews Materials **4**, 479 (2019)

[11] A.A. Burkov, Nat. Mater. **15**, 1145 (2016)

[12] P. Li, W. Wu, Y. Wen, C. Zhang, J. Zhang, S. Zhang, Z. Yu, S.A. Yang, A. Manchon, and X.-x. Zhang, Nat. Commun. **9**, 3990 (2018)

[13] Q. Wang, C.-Z. Li, S. Ge, J.-G. Li, W. Lu, J. Lai, X. Liu, J. Ma, D.-P. Yu, Z.-M. Liao, and D. Sun, Nano Letters **17**, 834 (2017)

[14] R. Lundgren, P. Laurell, and G.A. Fiete, Phys. Rev. B **90**, 165115 (2014)

[15] A. Yamakage, Y. Yamakawa, Y. Tanaka, and Y. Okamoto, J. Phys. Soc. Jpn. **85**, 013708 (2016)

[16] Y.X. Zhao and A.P. Schnyder, Phys. Rev. B **94**, 195109 (2016)

[17] L. Michel and J. Zak, Phys. Rev. B **59**, 5998 (1999)

[18] S.M. Young and C.L. Kane, Phys. Rev. Lett. **115**, 126803 (2015)

[19] A. Furusaki, Science Bulletin **62**, 788 (2017)

[20] B.-J. Yang, T.A. Bojesen, T. Morimoto, and A. Furusaki, Phys. Rev. B **95**, 075135 (2017)

[21] J. Zhang, Y.-H. Chan, C.-K. Chiu, M.G. Vergniory, L.M. Schoop, and A.P. Schnyder, Phys. Rev. Materials **2**, 074201 (2018)

[22] Y.-H. Chan, B. Kilic, M.M. Hirschmann, C.-K. Chiu, L.M. Schoop, D.G. Joshi, and A.P. Schnyder, Phys. Rev. Materials **3**, 124204 (2019)

[23] J. Singleton: *Band Theory and Electronic Properties of Solids* Oxford Master Series in Condensed Matter Physics (Oxford University Press, 2001)

[24] T. Ozawa, H.M. Price, A. Amo, N. Goldman, M. Hafezi, L. Lu, M.C. Rechtsman, D. Schuster, J. Simon, O. Zilberberg, and I. Carusotto, Rev. Mod. Phys. **91**, 015006 (2019)

[25] K. Li, C. Li, J. Hu, Y. Li, and C. Fang, Phys. Rev. Lett. **119**, 247202 (2017)

[26] H. Nielsen and M. Ninomiya, Nuclear Physics B **185**, 20 (1981)

[27] C.-K. Chiu and A.P. Schnyder, Phys. Rev. B **90**, 205136 (2014)

[28] T. Morimoto and A. Furusaki, Phys. Rev. B **88**, 125129 (2013)

[29] A.P. Schnyder, S. Ryu, A. Furusaki, and A.W.W. Ludwig, Phys. Rev. B **78**, 195125 (2008)

[30] S. Ryu, A.P. Schnyder, A. Furusaki, and A.W.W. Ludwig, New J. Phys. **12**, 065010 (2010)

[31] A. Altland and M.R. Zirnbauer, Phys. Rev. B **55**, 1142 (1997)

[32] M. Nakahara: *Geometry, Topology and Physics* (Tailor & Francis, New York, 2003)

[33] Y.-H. Chan, C.-K. Chiu, M.Y. Chou, and A.P. Schnyder, Phys. Rev. B **93**, 205132 (2016)

[34] D. Vanderbilt and R.D. King-Smith, Phys. Rev. B **48**, 4442 (1993)

[35] W.B. Rui, Y.X. Zhao, and A.P. Schnyder, Phys. Rev. B **97**, 161113 (2018)

[36] T. Matsushita, S. Fujimoto, and A.P. Schnyder, arXiv:2002.11666 (2020)

[37] L. Elcoro, B. Bradlyn, Z. Wang, M.G. Vergniory, J. Cano, C. Felser, B.A. Bernevig, D. Orobengoa, G. de la Flor, and M.I. Aroyo, J. Appl. Crystallogr. **50**, 1457 (2017)

[38] C. Bradley and A.P. Cracknell: *The Mathematical Theory of Symmetry in Solids: Representation theory for point groups and space groups* (Clarendon Press, Oxford, 1972)

[39] S.C. Miller and W.F. Love: *Tables of Irreducible Representations of Space Groups and Co-representations of Magnetic Groups* (Pruett, Boulder, 1967)

[40] J. Cano and B. Bradlyn, arXiv e-prints arXiv:2006.04890 (2020)

[41] M.G. Vergniory, L. Elcoro, C. Felser, N. Regnault, B.A. Bernevig, and Z. Wang, Nature **566**, 480 (2019)

[42] T. Zhang, Y. Jiang, Z. Song, H. Huang, Y. He, Z. Fang, H. Weng, and C. Fang, Nature **566**, 475 (2019)

[43] F. Tang, H.C. Po, A. Vishwanath, and X. Wan, Nat. Phys. **15**, 470 (2019)

12 Aspects of Topological Superconductivity

Manfred Sigrist
Institute for Theoretical Physics
ETH Zürich, Switzerland

Contents

E. Pavarini and E. Koch (eds.)
Topology, Entanglement, and Strong Correlations
Modeling and Simulation Vol. 10
Forschungszentrum Jülich, 2020, ISBN 978-3-95806-466-9
http://www.cond-mat.de/events/correl20

1 Introduction

Superconductivity is undoubtedly one of the most remarkable and enigmatic ground states of electronic matter. At sufficiently low temperature electrons of a metal condense into a coherent state of Cooper pairs and open a single-quasiparticle excitation gap. This has been the notion of the BCS theory of 1957 which counts among the most comprehensive descriptions of many-electron properties in condensed matter physics. While the original BCS theory is based on the simplest intrinsic structure of Cooper pairs, superconductivity appearing in systems with strong electron correlation realizes more complex pair wave states whose internal structure expand the space of superconducting phases and phenomena tremendously. As we will discuss below, we distinguish between *conventional* and *unconventional* superconducting states [1–3]. The former are found in the standard textbook superconductors such as the elemental metals Pb, Al or Nb and many compounds. Unconventional superconductivity, on the other hand, occurs in materials classes like the cuprate high temperature superconductors such as $YBa_2Cu_3O_7$ and the heavy Fermion compounds represented by UBe_{13}, UPt_3 and $CeCoIn_5$, which all also show strong magnetic correlations [4–7]. An intensely studied case is Sr_2RuO_4 whose nature of superconductivity is debated at present [8, 9].

In this lecture we would like to address a special subclass among the unconventional superconductors which display topological properties. The first phases in this class where actually not superconductors, but the neutral superfluid ^{3}He whose phases rest on the same Cooper pairing paradigm as all known superconductors. ^{3}He has two phases in the absence of a magnetic field, the A-phase and the B-phase, which both have topological properties and distinguish themselves by their symmetry [10]. While the B-phase preserves maximal possible symmetries of the fluid, the A-phase spontaneously violates time reversal symmetry (TRS) and is know as a "chiral superfluid". Both phases can generate topologically protected edge states, a trade mark of topological insulators. In the following we will put our focus on chiral superconducting phases which break TRS and explain some of the important features and phenomena. We will also touch briefly upon TRS conserving topological superconductors. In this lecture it is expected that the basics of BCS superconductivity are known, but otherwise the technical level will be kept rather low. There are textbooks and numerous review articles which go deeper into technical details [11–14]. Early works by G. Volovik date back more than three decades [15].

2 Unconventional superconductivity

2.1 Pair wave function

We first address the nature of an unconventional superconductor by analyzing the structure of its ground state and at the same time introduce the standard notations. For simplicity we restrict ourselves here exclusively to systems with a single electronic band whose states are Bloch states $|\boldsymbol{k}, s\rangle$ created (annihilated) by the operators $\hat{c}^\dagger_{\boldsymbol{k}s}$ ($\hat{c}_{\boldsymbol{k}s}$). The BCS-like ground state is a coherent state of electron pairs (Cooper pairs) with vanishing total momentum, such that we can define a

pair wavefunction,

$$F_{ss'}(\boldsymbol{k}) = \left\langle \hat{c}_{-\boldsymbol{k}s'} \hat{c}_{\boldsymbol{k}s} \right\rangle \tag{1}$$

where $\langle \cdots \rangle$ denotes the expectation value for the ground state or a thermal average, in general. Obviously, the particle number is not conserved as is the essence of a coherent state. The wavefunction is 2×2-matrix in spin space and satisfies the relation $\hat{F}(\boldsymbol{k})=-\hat{F}(-\boldsymbol{k})^T$ due to the Pauli principle, i.e., the pair wave function is odd under exchange of the two electrons. If time reversal and inversion symmetry are preserved in the normal state, we distinguish the two cases

$$\hat{F}(\boldsymbol{k}) = \begin{cases} f_0(\boldsymbol{k})\, \hat{\sigma}^0 i\hat{\sigma}^y & \text{with} \quad f_0(\boldsymbol{k}) = \ f_0(-\boldsymbol{k}) \\ \boldsymbol{f}(\boldsymbol{k}) \cdot \hat{\boldsymbol{\sigma}} i\hat{\sigma}^y & \text{with} \quad \boldsymbol{f}(\boldsymbol{k}) = -\boldsymbol{f}(-\boldsymbol{k}) \end{cases} \tag{2}$$

where the upper stands for an even-parity spin-singlet and lower for an odd-parity spin-triplet pairing state, represented by a scalar ($f_0(\boldsymbol{k})$) and vector ($\boldsymbol{f}(\boldsymbol{k})$) wavefunction. Here $\hat{\boldsymbol{\sigma}}$ denotes the Pauli matrices and $\hat{\sigma}^0$ the two-dimensional unit matrix.

We distinguish conventional and unconventional Cooper pairing by the sum of $f_0(\boldsymbol{k})$ over the Brillouin zone (BZ)

$$I_0 = \sum_{\boldsymbol{k}\in \mathrm{BZ}} f_0(\boldsymbol{k}) \qquad \text{and} \qquad \boldsymbol{I} = \sum_{\boldsymbol{k}\in \mathrm{BZ}} \boldsymbol{f}(\boldsymbol{k}) \tag{3}$$

which is proportional to the real space on-site amplitude of the pair wavefunction.[1] The notion *conventional* only applies to even parity states with $I_0 \neq 0$. All states with $I_0 = 0$ or $\boldsymbol{I} = 0$ are called *unconventional*. Obviously, all odd-parity states are unconventional. The fact that paired electrons avoid to meet on the same position, gives these states an advantage over conventional pairs in systems with strong electron repulsion. In such a case, standard electron-phonon mediated pairing interaction, which is essentially a contact interaction, is ineffective in causing unconventional pairing states and other pairing mechanism yielding longer-ranged interactions are necessary, such as spin fluctuation exchange.

2.2 Symmetry properties

Within Landau theory of second-order phase transitions the low-temperature ordered phase is characterized by an order parameter describing the spontaneous symmetry breaking. This order parameter belongs to an irreducible representation of the normal state symmetry group, for superconductivity involving the crystal point group ($\mathcal{P}$), spin rotation ($SU(2)$), and TRS ($\mathcal{T}$) which can be broken in unconventional superconducting states beside $U(1)$-gauge symmetry (coherent state). The general pair wave function can be written as a superposition

$$\hat{F}(\boldsymbol{k}) = \sum_{n=1}^{N_\Gamma} \eta_n \hat{F}_{\Gamma,n}(\boldsymbol{k}) \tag{4}$$

[1] The real space pair wavefunction is given by the Fourier transform (with Ω as the volume)

$$\hat{\Phi}(\boldsymbol{r}-\boldsymbol{r}') = \frac{1}{\Omega} \sum_{\boldsymbol{k}\in \mathrm{BZ}} \hat{F}(\boldsymbol{k}) e^{i\boldsymbol{k}\cdot(\boldsymbol{r}-\boldsymbol{r}')}$$

where the $\{\hat{F}_{\Gamma,1}(\boldsymbol{k}), \cdots, \hat{F}_{\Gamma,N_\Gamma}(\boldsymbol{k})\}$ form the basis set of the irreducible representation Γ of dimension N_Γ, and η_n are complex coefficients. The symmetry operations are most conveniently performed within the notation introduced in Eq. (2), where rotation operations $g \in \mathcal{P}$ (spin and lattice are tied together through spin-orbit coupling) lead to

$$g \circ \hat{F}(\boldsymbol{k}) \quad \Rightarrow \quad \begin{cases} g \circ f_0(\boldsymbol{k}) = f_0(R_g \boldsymbol{k}) \\ g \circ \boldsymbol{f}(\boldsymbol{k}) = R_g \boldsymbol{f}(R_g \boldsymbol{k}) \end{cases} \tag{5}$$

with R_g is the corresponding real space rotation matrix. Inversion yields $\mathcal{I} \circ f_0(\boldsymbol{k}) = f_0(-\boldsymbol{k}) = f_0(\boldsymbol{k})$ and $\mathcal{I} \circ \boldsymbol{f}(\boldsymbol{k}) = \boldsymbol{f}(-\boldsymbol{k}) = -\boldsymbol{f}(\boldsymbol{k})$. Time reversal and $U(1)$-operation, $\mathcal{K}$ and Φ, respectively, give

$$\mathcal{K} \circ f_\mu(\boldsymbol{k}) = f_\mu(\boldsymbol{k})^* \quad \text{and} \quad \Phi \circ f_\mu(\boldsymbol{k}) = f_\mu(\boldsymbol{k}) e^{i\phi} \, . \tag{6}$$

Assuming that a given superconducting phase belongs to a single representation, we can associate its symmetry properties easily with the behavior of the corresponding basis functions. The conventional superconducting phase is in the non-degenerate trivial representation of even parity, constituting the state of highest possible symmetry – only $U(1)$-gauge symmetry is broken. Otherwise, in Eq. (3) the sum I_0 would vanish.

A particularly important feature is the *degeneracy*, connected with the dimension N_Γ, because it allows for intriguing phenomena which are not available in conventional superconductors. For a concrete and simple example, we consider here the case of $N_\Gamma = 2$ which is important for topologically non-trivial superconductors with chiral pairing. For this purpose we look at the tetragonal point group, D_{4h}, which has two-dimensional irreducible representations E_g and E_u, with even and odd parity, respectively. The basis functions reflecting the symmetry operations are in their most simple form

$$\begin{aligned} E_g: \quad & f_{0,\Gamma,x}(\boldsymbol{k}) = k_z k_x \qquad f_{0,\Gamma,y}(\boldsymbol{k}) = k_z k_y \\ E_u: \quad & \boldsymbol{f}_{\Gamma,x}(\boldsymbol{k}) = \hat{\boldsymbol{z}} k_x \qquad \boldsymbol{f}_{\Gamma,y}(\boldsymbol{k}) = \hat{\boldsymbol{z}} k_y \end{aligned} \tag{7}$$

where $\boldsymbol{f}$ of the odd parity state is oriented along the z-axis corresponding to the spin-triplet state with the spin state $(S, S_z) = (1, 0)$ corresponding to "equal spin" pairing.

Only a discrete set of superpositions of these basis states are stable. The possible superconducting phases for these degenerate pairing state basis can be found using the Landau free energy expansion in the order parameter. The complex coefficients η_n of Eq. (4), which has two components $\boldsymbol{\eta} = (\eta_x, \eta_y)$, can play the role of the order parameter. The free energy then contains the following terms,

$$F[\boldsymbol{\eta}] = a(T)|\boldsymbol{\eta}|^2 + b_1|\boldsymbol{\eta}|^4 + \frac{b_2}{2}\left\{\eta_x^{*2}\eta_y^2 + \eta_x^2\eta_y^{*2}\right\} + b_3|\eta_x|^2\,|\eta_y|^2 \tag{8}$$

which include all independent scalar combinations of $\boldsymbol{\eta}$ transforming under $E_{g,u}$ up to 4^{th} order. There are only three fourth-order terms. Here $a(T) = a'(T - T_c)$ (both components have the same critical temperature) and b_1, b_2 and b_3 are real coefficients. All coefficients constitute

material specific input to the theory. Under the constraint that the free energy is bound from below, we find the following three phases

$$\boldsymbol{\eta}_A \propto \left\{ \begin{array}{c} (1,+i) \\ (1,-i) \end{array} \right\}, \quad \boldsymbol{\eta}_B \propto \left\{ \begin{array}{c} (1,+1) \\ (1,-1) \end{array} \right\}, \quad \boldsymbol{\eta}_C \propto \left\{ \begin{array}{c} (1,0) \\ (0,1) \end{array} \right\}, \tag{9}$$

which all are two-fold degenerate. The phase A is *chiral* and breaks TRS, while the other two are *nematic* and break crystal rotational symmetry. Which of the three phases is realized depends on microscopic details not accessible to our symmetry arguments. A weak-coupling approach yield generally the A-phase as most stable as it has least zero nodes. In the following we will focus on this phase, because it includes the best known topologically non-trivial superconducting phase.

3 Topological properties of a two-dimensional chiral superconductor

In this section we start out with a superconductor within a two-dimensional or a quasi-two-dimensional metal, where the latter is characterized by having an essentially cylindrical Fermi surface (FS) as we will encounter also in Sect. 5. As mentioned above we restrict to a single band model and assume basic knowledge of the BCS theory.

3.1 Nambu space representation

In a first step we introduce the Nambu representation of the microscopic Hamiltonian in mean field form (up to added constant terms)

$$\mathcal{H}_{\rm mf} = \frac{1}{2} \sum_{\boldsymbol{k}} \hat{C}^\dagger_{\boldsymbol{k}} H_{\boldsymbol{k}} \hat{C}_{\boldsymbol{k}} \tag{10}$$

with the Nambu spinor $\hat{C}_{\boldsymbol{k}} = \left(\hat{c}_{\boldsymbol{k}\uparrow}, \hat{c}_{\boldsymbol{k}\downarrow}, \hat{c}^\dagger_{-\boldsymbol{k}\uparrow}, \hat{c}^\dagger_{-\boldsymbol{k}\downarrow}\right)^T$ and the Hamiltonian matrix

$$H_{\boldsymbol{k}} = \left(\begin{array}{cc} \xi_{\boldsymbol{k}} \hat{\sigma}^0 & \hat{\Delta}_{\boldsymbol{k}} \\ \hat{\Delta}^\dagger_{\boldsymbol{k}} & -\xi_{-\boldsymbol{k}} \hat{\sigma}^0 \end{array} \right) \tag{11}$$

with $\xi_{\boldsymbol{k}}$ as the band energy measured relative the chemical potential μ ($\xi_{\boldsymbol{k}} = 0$ defines the FS) and the gap function

$$\hat{\Delta}_{\boldsymbol{k}} = i\hat{\sigma}^y \left\{ \hat{\sigma}^0 d_0(\boldsymbol{k}) + \hat{\boldsymbol{\sigma}} \cdot \boldsymbol{d}(\boldsymbol{k}) \right\} = \left(\begin{array}{cc} -d_x(\boldsymbol{k}) + i d_y(\boldsymbol{k}) & d_z(\boldsymbol{k}) + d_0(\boldsymbol{k}) \\ d_z(\boldsymbol{k}) - d_0(\boldsymbol{k}) & d_x(\boldsymbol{k}) + i d_y(\boldsymbol{k}) \end{array} \right) \tag{12}$$

with $d_0(\boldsymbol{k})$ even and $\boldsymbol{d}(\boldsymbol{k})$ odd functions of $\boldsymbol{k}$. The Nambu representation doubles the electronic spectrum by adding the (redundant) hole spectrum. The coherent state corresponds to a hybridization of electrons and holes through the off-diagonal elements $\hat{\Delta}_{\boldsymbol{k}}$, which are connected with the pair wavefunction within mean field theory through the pairing interaction

$$\hat{V} = \frac{1}{2} \sum_{\boldsymbol{k},\boldsymbol{k}'} \sum_{s_1,s_2,s_3,s_4} V^{s_1 s_2 s_3 s_4}_{\boldsymbol{k},\boldsymbol{k}'} \, \hat{c}^\dagger_{\boldsymbol{k} s_1} \hat{c}^\dagger_{-\boldsymbol{k} s_2} \hat{c}_{-\boldsymbol{k}' s_3} \hat{c}_{\boldsymbol{k}' s_4} \, . \tag{13}$$

The relation is given by

$$\Delta_{\boldsymbol{k}ss'} = -\sum_{\boldsymbol{k}'}\sum_{\tilde{s},\tilde{s}'} V^{ss'\tilde{s}\tilde{s}'}_{\boldsymbol{k},\boldsymbol{k}'} F_{\tilde{s}'\tilde{s}}(\boldsymbol{k}) \tag{14}$$

such that the symmetry properties of the $\hat{\Delta}_{\boldsymbol{k}}$ and $\hat{F}(\boldsymbol{k})$ are identical.
The Hamiltonian in Eq. (10) with (11) yields the spectrum

$$E_{\boldsymbol{k}} = \sqrt{\xi^2_{\boldsymbol{k}} + |\Delta_{\boldsymbol{k}}|^2} \quad \text{with} \quad |\Delta_{\boldsymbol{k}}|^2 = \frac{1}{2}\,\mathrm{Tr}\,\hat{\Delta}^\dagger_{\boldsymbol{k}}\hat{\Delta}_{\boldsymbol{k}} \tag{15}$$

for the Bogoliubov quasiparticles $\hat{A}_{\boldsymbol{k}} = (\hat{a}_{\boldsymbol{k}\alpha}, \hat{a}_{\boldsymbol{k}\beta}, \hat{a}^\dagger_{-\boldsymbol{k}\alpha}, \hat{a}^\dagger_{-\boldsymbol{k}\beta})$ obtained by the unitary transformation

$$\hat{C}_{\boldsymbol{k}} = U_{\boldsymbol{k}}\hat{A}_{\boldsymbol{k}} \quad \text{with} \quad U_{\boldsymbol{k}} = \begin{pmatrix} \hat{u}_{\boldsymbol{k}} & \hat{v}_{\boldsymbol{k}} \\ \hat{v}^*_{-\boldsymbol{k}} & \hat{u}^*_{-\boldsymbol{k}} \end{pmatrix} \tag{16}$$

with $U_{\boldsymbol{k}}\,U^\dagger_{\boldsymbol{k}} = 1$. We derive $U_{\boldsymbol{k}}$ through the condition

$$U^\dagger_{\boldsymbol{k}} H_{\boldsymbol{k}} U_{\boldsymbol{k}} = \begin{pmatrix} E_{\boldsymbol{k}}\hat{\sigma}^0 & 0 \\ 0 & -E_{-\boldsymbol{k}}\hat{\sigma}^0 \end{pmatrix}. \tag{17}$$

Note that $\hat{u}_{\boldsymbol{k}}$ and $\hat{v}_{\boldsymbol{k}}$ constitute wave functions of the electron and the hole-like components of the quasiparticles, respectively, as can be seen from

$$\hat{u}_{\boldsymbol{k}} = \frac{1}{\sqrt{2}}\sqrt{1 + \frac{\xi_{\boldsymbol{k}}}{E_{\boldsymbol{k}}}}\,, \qquad \hat{v}_{\boldsymbol{k}} = -\frac{\hat{\Delta}_{\boldsymbol{k}}}{\sqrt{2|\Delta_{\boldsymbol{k}}|}}\sqrt{1 - \frac{\xi_{\boldsymbol{k}}}{E_{\boldsymbol{k}}}}\,. \tag{18}$$

3.2 Topological invariant – Chern number

We now turn to the chiral A-phase we introduced above and restrict ourselves to the odd parity case, because the even-parity state cannot be realized in a purely two-dimensional system as it involves k_z-dependence, indicating extensions of Cooper pairs along the z-axis. Because it will be useful later, we consider here a tight-binding model on a square lattice with a simple nearest-neighbor hopping dispersion

$$\xi_{\boldsymbol{k}} = -2t\big(\cos k_x + \cos k_y\big) - \mu \tag{19}$$

where t is the hopping matrix element and the lattice constant is unity. The Cooper pairs shall originate from a nearest-neighbor pairing interaction, which leads to the pair wave function and the gap function

$$\boldsymbol{f}^{\pm}(\boldsymbol{k}) = F_0\hat{\boldsymbol{z}}\big(\sin k_x \pm i\sin k_y\big) \quad \text{and} \quad \boldsymbol{d}^{\pm}(\boldsymbol{k}) = \Delta_0\hat{\boldsymbol{z}}\big(\sin k_x \pm i\sin k_y\big) \tag{20}$$

transforming within E_u of the tetragonal point group. It is easy to see that for this gap structure using Eq. (12) the gap matrix $H(\boldsymbol{k})$ in Eq. (11) can be decomposed into two disconnected parts with two-dimensional Hamiltonian matrices,

$$h(\boldsymbol{k}) = \begin{pmatrix} \xi_{\boldsymbol{k}} & d_z(\boldsymbol{k}) \\ d^*_z(\boldsymbol{k}) & -\xi_{\boldsymbol{k}} \end{pmatrix} = \boldsymbol{h}_{\boldsymbol{k}}\cdot\hat{\boldsymbol{\tau}} \tag{21}$$

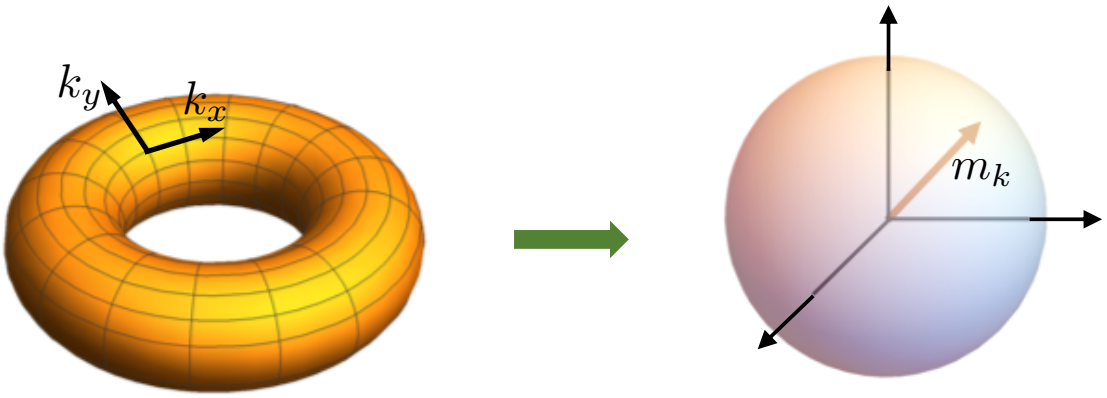

Fig. 1: *Mapping from the Brillouin zone to the unit sphere: The representation of the Hamiltonian $\boldsymbol{h_k}$ as a unit vector $\boldsymbol{m_k} = \boldsymbol{h_k}/|\boldsymbol{h_k}|$ allows us to map the two-dimensional BZ in $\boldsymbol{k}$-space to a unit sphere.*

corresponding to the spinors $\left(\hat{c}_{\boldsymbol{k}\uparrow}, \hat{c}^\dagger_{-\boldsymbol{k}\downarrow}\right)$ and $\left(\hat{c}_{\boldsymbol{k}\downarrow}, \hat{c}^\dagger_{-\boldsymbol{k}\uparrow}\right)$, where $\boldsymbol{\tau}$ are Pauli matrices for the particle-hole space. Note that this can be considered now a spinless subspaces. The three-dimensional vector

$$\boldsymbol{h_k} = \left[\mathrm{Im}\,(d_z(\boldsymbol{k}),\, \mathrm{Re}\,(d_z(\boldsymbol{k}),\, \xi_{\boldsymbol{k}}\right] \tag{22}$$

is a mapping of the two-dimensional BZ (torus) to a sphere with unit vector $\boldsymbol{m_k}$=$\boldsymbol{h_k}/|\boldsymbol{h_k}|$ (Fig. 1). With $\boldsymbol{m_k}$ we define

$$\Omega^z_{\boldsymbol{k}} = \frac{1}{2}\,\boldsymbol{m_k} \cdot \left[\partial_{k_x}\boldsymbol{m_k} \times \partial_{k_y}\boldsymbol{m_k}\right] \tag{23}$$

which is known as the z-component of the Berry curvature $\boldsymbol{\Omega_k}$. We use now $\Omega^z_{\boldsymbol{k}}$ to define a *topological invariant*, the *Chern number*, to characterize the chiral state. The Chern number C is obtained from $\Omega^z_{\boldsymbol{k}}$ by an integral over the BZ

$$N_{\mathrm{C}} = 2\pi \int_{\mathrm{BZ}} \frac{d^2k}{(2\pi)^2}\Omega^z_{\boldsymbol{k}} \tag{24}$$

and is an integer for a topologically non-trivial state. Geometrically this corresponds to (half of) the area element on the sphere, such that the integral (24) results in the number of times $\boldsymbol{m_k}$ wraps around the sphere when $\boldsymbol{k}$ covering the (torus of) the BZ.

The calculation of C in this way looks rather tedious. Fortunately, there is a considerably simpler way to determine the Chern number which relies on the knowledge of the gap function on the FS:

$$N_{\mathrm{C}} = \frac{1}{2\pi}\oint_{\mathrm{FS}} d\boldsymbol{k} \cdot \boldsymbol{\nabla}_{\boldsymbol{k}} \arg[d_z(\boldsymbol{k})] \tag{25}$$

which corresponds to the non-trivial phase winding of the gap function (analogous for the pair wavefunction) around the FS. It is rather easy to see that for $\mu < 0$ the FS is closed around the BZ center and the phase of $d_z(\boldsymbol{k})$ acquires a winding of 2π going around the FS in positive

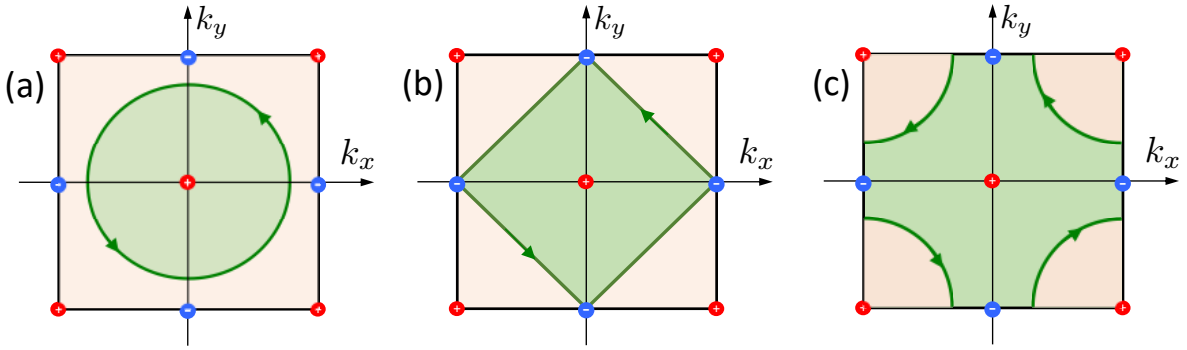

Fig. 2: *Charges of the gap function $d_z^+(\boldsymbol{k})$ in the first BZ. The Chern charges are $+1$ for the red circles and -1 for the blue points. The Chern number is obtained from Eq. (25) by counting the charge which is encircled by the Fermi surface as a path running in the positive orientation. (a) Below half filling: FS closed around center of the BZ and has $C = +1$; (b) At half filling: the gap function vanishes on the FS at the blue points on the BZ boundary, such that Eq. (25) is not defined; (c) Above half filling: the FS closes around a red corner point of the BZ, which leads to $C = -1$ when considering that effective path orientation is negative. Note that (b) is the point of a Lifshitz transition from an electron- to a hole-like FS, which is at the same time a topological transition between different Chern numbers, where the gap vanishes.*

direction for the gap function in Eq. (20), with $d_z^+(\boldsymbol{k}) = \Delta_0(\sin k_x + i \sin k_y)$. The gap function $d_z^-(\boldsymbol{k})$ yields a winding -2π. The sign of N_C indicates the sign of chirality.
A further convenient feature of the gap function is the appearance of zeros in the BZ or boundary. Because the gap function is periodic in $\boldsymbol{k}$-space we find for the odd-parity state

$$d_z(\boldsymbol{k}) = -d_z(-\boldsymbol{k}) = -d_z(-\boldsymbol{k}+\boldsymbol{G}) \tag{26}$$

where $\boldsymbol{G}$ is a reciprocal lattice vector. If the condition $\boldsymbol{k} = -\boldsymbol{k}+\boldsymbol{G}$ is satisfied, $d_z(\boldsymbol{k}) = 0$, which is in the give case true for the four inequivalent points $\boldsymbol{K}_{1,\dots,4} = (0,0), (\pi,0), (0,\pi), (\pi,\pi)$. We can attribute these zeros a charge corresponding to a winding number.

$$d_z(\boldsymbol{k} = \boldsymbol{K}_n+\boldsymbol{q}) = \Delta_0 q\, e^{iQ_n\theta_{\boldsymbol{q}}} \tag{27}$$

with $Q_1 = Q_4 = +1$ and $Q_2 = Q_3 = -1$ for $d_z^+(\boldsymbol{k})$ (see Fig. 2). The total charge vanishes, $\sum_{n=1}^4 Q_n = 0$. These "Chern charges" are very handy to determine the Chern number through Eq. (25) by examining which charges are encircled in which way. In Fig. 2 we consider three cases of band filling assuming a simple tight-binding model with nearest-neighbor hopping with $\xi_{\boldsymbol{k}}$ given in Eq. (19). The case (a) displays a simple electron-like FS ($\mu < 0$) which encircles the charge Q_1 at the BZ center in a positive orientation (arrows). Note we always define "positive orientation" with respect to BZ center. In case (c) the FS ($\mu > 0$) is hole-like, going around the charge Q_4 at the BZ corner. We can calculate C by shifting the BZ in a way to make $\boldsymbol{K}_4$ the center which, however, leaves the orientation of encircling negative and leads to $C = -1$. On the other hand, we may stick with Fig. 2(c) and follow the path around the BZ center, which consists of the disconnected green FS lines and join them by a path along the BZ boundary

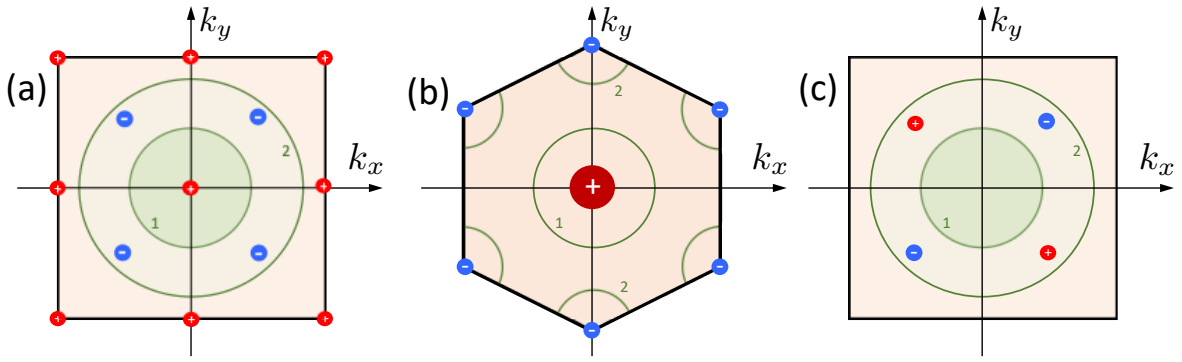

Fig. 3: *Charges of the various gap functions in the first BZ. (a) Next-nearest neighbor pairing with the gap function $d_z^+(\boldsymbol{k})$ of Eq. (29) has N_C=+1 for FS 1 and C=−3 for FS 2. (b) Chiral d-wave state, $d_0^\pm(\boldsymbol{k})$ of Eq. (30) in a hexagonal system has a charge Q_1=2 at the BZ center and $Q_{2,3}$=−1 at the BZ corners for positive chirality. (c) $s+id$-wave state of Eq. (31) which has four zeros whose charges cancel to zero for all Fermi surfaces of tetragonal crystal symmetry.*

passing through the (blue) charges at $\boldsymbol{K}_2$ and $\boldsymbol{K}_3$. In this way we get the Chern number by taking each of the four charge contributions at these BZ boundaries only half, as they are cut. This then yields a full contribution from the charge at the center and four halves from the BZ boundary

$$N_C = +1 + \frac{1}{2}(-4) = -1 \tag{28}$$

consistent with the other view point considering only the charge at $\boldsymbol{K}_4$. The case (b) of half filling (μ=0) corresponds to the Lifshitz transition between the electron- and hole-like FS and leads to a zero in the gap functions, $d_z(\boldsymbol{K}_{2,3})$=0. Here, the Chern number jumps discontinuously and we encounter a topological transition. In Fig. 2 we considered a state with one chirality, $d_z^+(\boldsymbol{k}) = \Delta_0(\sin k_x + i \sin k_y)$ which changes under time reversal operation to $d_z^-(\boldsymbol{k}) = \Delta_0(\sin k_x - i \sin k_y)$ with all the charges switching sign.

Larger Chern numbers can be obtained by alternative pairing states, e.g., for Cooper pairing of electrons on next-nearest neighbor sites in a square lattice, which lead to a gap function

$$d_z^\pm(\boldsymbol{k}) = \Delta_0\big(\cos k_y \sin k_x \pm i \cos k_x \sin k_y\big). \tag{29}$$

This state belongs to the same representation E_u as (20), but is different in terms of topology reflected by the Chern number. This gap functions has additional zeros in the BZ besides the ones found above, $\boldsymbol{K}_{1,\ldots,4}$. They lie at the four points $\boldsymbol{K}_{5,\ldots,8} = \frac{\pi}{2}(\pm1,\pm1), \frac{\pi}{2}(\pm1,\mp1)$. The charges rearrange: $Q_{1,\ldots,4}$=±1 and $Q_{5,\ldots,8}$=∓1 for $d_z^\pm$ in Eq. (29). Again the total charge vanishes. We encounter here also Chern numbers of N_C=∓3 for the electron-like FS 2 enclosing the inner five zeros (see Fig. 3(a)).

Another case is the so-called chiral d-wave state which is an even-parity spin singlet pairing state. The two necessary components of the basis functions, $k_x^2-k_y^2$ and k_xk_y, are not degenerate in the tetragonal system, but only in a lattice of hexagonal symmetry with point group D_{6h} where they belong to the two-dimensional representation E_{2u}, Considering here also a nearest-

neighbor type of pairing state (on a triangular lattice) we obtain a gap function of the form

$$d_0^{\pm}(\boldsymbol{k}) = \Delta_0 \sum_{n=1}^{3} e^{\pm i2\pi n/3} \cos(\boldsymbol{k}\cdot\boldsymbol{T}_n) \tag{30}$$

with $\boldsymbol{T}_1 = (0,1)$, $\boldsymbol{T}_2 = (\sqrt{3}/2, -1/2)$ and $\boldsymbol{T}_3 = (-\sqrt{3}/2, -1/2)$. We find zeros at the BZ center and corners, $\boldsymbol{K}_1 = (0,0)$ and $\boldsymbol{K}_{2,3} = (0,1), (\sqrt{3}/2, 1/2)$, respectively, as shown in Fig. 3(b). The corresponding charges are $Q_1 = \pm 2$ and $Q_{2,3} = \mp 1$ ensuring again that the total sum vanishes. The electron-like FS (1) as well as the hole-like FS (2) would, therefore, have $N_{\rm C} = \pm 2$. There is no topological phase transition possible at the Lifshitz transition, since the FS never passes through a gap zero going from FS 1 to FS 2.

Finally we would like to introduce an example of a superconducting phase with broken TRS which is not chiral. This is the well-known $s+id_{x^2-y^2}$-wave state. In the tetragonal crystal lattice the two constituents are not degenerate, as they belong to different one-dimensional representations, A_{1g} and B_{1g}. So we assume that for some coincidence both states are competitive, although they may have different strength and also different critical temperatures (superconducting double transition). We consider this state built up from nearest-neighbor pairing, $d_{0,s}(\boldsymbol{k}) = \cos k_x + \cos k_y$ also known as extended s-wave state, and $d_{0,d}(\boldsymbol{k}) = \cos k_x - \cos k_y$. This leads to

$$d_0(\boldsymbol{k}) = \Delta_s\big(\cos k_x + \cos k_y\big) \pm i\Delta_d\big(\cos k_x - \cos k_y\big) \tag{31}$$

which has zeros at $\boldsymbol{K}_{1,2} = \pm\frac{\pi}{2}(1,1)$ and $\boldsymbol{K}_{3,4} = \pm\frac{\pi}{2}(1,-1)$ whose charges are opposite, $Q_{1,2} = \pm 1$ and $Q_{3,4} = \mp 1$ such that the Chern number by symmetry vanishes always, as in Fig. 3(c) for both typical FS (1 and 2).

Note that due to the fact that we have used the reduced Hamiltonian in the discussion following Eq. (21) we should include the spin degeneracy in the Chern number, such that $N_{\rm C}$ is multiplied by a factor 2, in general.

3.3 Symmetry criterion

Whether an unconventional pairing state is chiral or not can be decided also simply by considering a rather simple symmetry property. As we mentioned before, the ideal condition to get a TRS breaking state is found when the pair wave function belongs to a degenerate irreducible representation of the crystal point group. The chiral superconducting state has a chiral axis which is in the case considered above the z-axis. Looking at the most simple form of a chiral state, $k_x \pm ik_y$, we recognize the spherical harmonic $Y_{1,\pm 1}(\boldsymbol{k})$ which corresponds to an angular momentum $L_z = \pm\hbar$. In any point group the angular momentum can be associated with irreducible representations Γ_L. In a chiral superconducting state we may attach a net "angular momentum" with the Cooper pair, e.g.,

$$\langle \boldsymbol{L}\rangle = \Big\langle \mathrm{Tr}\big(\hat{\Delta}_{\boldsymbol{k}}^{\dagger}(\boldsymbol{k}\times\boldsymbol{\nabla}_{\boldsymbol{k}})\hat{\Delta}_{\boldsymbol{k}}\big)\Big\rangle_{BZ} \tag{32}$$

where $\langle\cdots\rangle_{BZ}$ is an average over the BZ. The symmetry related criterion for a finite $\langle \boldsymbol{L}\rangle$ is that the decomposition of $\Gamma\otimes\Gamma_L\otimes\Gamma$ includes the trivial representation where Γ is the representation

of the pairing state. For the point group D_{4h} the angular momentum parallel to z-axis belongs to the A_{2g}, such that for the chiral p-wave order parameter in E_u follows

$$E_u \otimes A_{2g} \otimes E_u = A_{1g} \oplus A_{2g} \oplus B_{1g} \oplus B_{2g} \tag{33}$$

which includes the trivial representation A_{1g}. Thus, it is possible to construct a chiral pairing state within the representation E_u of D_{4h}. The same is true for the representation E_{2g} in D_{6h}. On the other hand, the $s{+}id$ state is composed of A_{1g} and B_{1g} in D_{4h} and

$$(A_{1g} \oplus B_{1g}) \otimes A_{2g} \otimes (A_{1g} \oplus B_{1g}) = A_{2g} \oplus A_{2g} \oplus B_{2g} \oplus B_{2g} \tag{34}$$

which does not contain A_{1g}. Thus we cannot form a chiral state from order parameters in these two representations. Interestingly, uniaxial deformation along the axis $[110]$ would change the condition, reducing the symmetry to D_{2h} with the corresponding representations A_{1g} and B_{1g}. But now the L_z is also in the representation B_{1g} and the decomposition within the point group D_{2h} includes the trivial representation. Returning back to the Chern number, we see in Fig. 3(c) the deformation may change the Fermi surface in way (elliptically elongated along $[1,1]$ and squeezed $[1,-1]$) such that only the zeros of charges of the same sign are encircled.

4 Edge states in chiral superconductors

In the context of topological phases often the concept of bulk-edge correspondence is mentioned [12, 13]. In chiral superconductors this manifests itself in the presence of chiral quasiparticle modes at the surface with energies below the bulk gap. There is a relation between the Chern number and the basic structure of the edge states as we will point out below, after discussing a specific case. In this section we will also analyze a few physical properties connected with these surface modes.

4.1 Edge states

One of the simplest cases to discuss the structure of edge states is a chiral p-wave state. For this purpose we consider the Bogoliubov-de Gennes equation which allows us to analyze inhomogeneous superconducting phases and local excitation spectra. We will work here with the reduced particle-hole space in the two-spinor representation as given in Eq. (21). To illustrate the edge states it is sufficient to use the Andreev approximation where we focus on the momentum range very close to the FS and separate the fast spatial dependence due to the Fermi wave vector from the slow ones: $\xi_{\boldsymbol{k}} \approx \hbar \boldsymbol{v}_F \cdot (\boldsymbol{k} - \boldsymbol{k}_F)$ (see for example Ref. [16]). In a real space formulation this leads to the differential equations

$$\begin{pmatrix} \hbar \boldsymbol{v}_F \cdot (i\boldsymbol{\nabla} - \boldsymbol{k}_F) & \Delta_{\boldsymbol{k}_F} \\ \Delta^*_{\boldsymbol{k}_F} & -\hbar \boldsymbol{v}_F \cdot (i\boldsymbol{\nabla} - \boldsymbol{k}_F) \end{pmatrix} \begin{pmatrix} u_{\boldsymbol{k}_F}(\boldsymbol{r}) \\ v_{\boldsymbol{k}_F}(\boldsymbol{r}) \end{pmatrix} = E \begin{pmatrix} u_{\boldsymbol{k}_F}(\boldsymbol{r}) \\ v_{\boldsymbol{k}_F}(\boldsymbol{r}) \end{pmatrix} \tag{35}$$

where $u_{\boldsymbol{k}_F}(\boldsymbol{r})$ and $v_{\boldsymbol{k}_F}(\boldsymbol{r})$ are the electron and hole component of the wave function, respectively, of the stationary eigenstates. These eigenstates are labeled by the Fermi momenta $\boldsymbol{k}_F$

indicating the direction of a quasi-classical trajectory of motion, characteristic to the Andreev approximation. With this we can introduce the field operators like

$$\hat{\Psi}(\boldsymbol{r}) = \sum_{\boldsymbol{k}_F} \Big(\hat{a}_{\boldsymbol{k}_F} u_{\boldsymbol{k}_F}(\boldsymbol{r}) + \hat{a}^\dagger_{-\boldsymbol{k}_F} v_{\boldsymbol{k}_F}(\boldsymbol{r}) \Big) \tag{36}$$

where $(\hat{a}_{\boldsymbol{k}_F}, \hat{a}^\dagger_{-\boldsymbol{k}_F})$ are (spinless) Bogoliubov quasi particle operators. We locate the surface at $x{=}0$ (normal vector parallel to x-axis) and assume specular scattering. Then we can take the ansatz for the wave function

$$\begin{pmatrix} u_{\boldsymbol{k}_F}(\boldsymbol{r}) \\ v_{\boldsymbol{k}_F}(\boldsymbol{r}) \end{pmatrix} = b_1 \begin{pmatrix} A^+_{\boldsymbol{k}_F+} \\ r_{\boldsymbol{k}_F+} A^-_{\boldsymbol{k}_F+} \end{pmatrix} e^{+iq_x x + i\boldsymbol{k}_{F+}\cdot\boldsymbol{r}} + b_2 \begin{pmatrix} r^*_{\boldsymbol{k}_F-} A^-_{\boldsymbol{k}_F-} \\ A^+_{\boldsymbol{k}_F-} \end{pmatrix} e^{-iq_x x + i\boldsymbol{k}_{F-}\cdot\boldsymbol{r}} \tag{37}$$

with the boundary condition that the wave function vanishes at the surface, $x{=}0$ as can be achieved with the proper choice of $b_{1,2}$. Moreover,

$$\int_0^\infty dx \int_0^L dy \Big(|u_{\boldsymbol{k}_F}(\boldsymbol{r})|^2 + |v_{\boldsymbol{k}_F}(\boldsymbol{r})|^2 \Big) = 1 \tag{38}$$

where periodic boundary condition can be assume along y-direction for a system of length L. The parameters in Eq. (37) are $A^\pm_{\boldsymbol{k}_F} = [E \pm \sqrt{E^2{-}|\Delta_{\boldsymbol{k}_F}|^2}]^{1/2}$, $\boldsymbol{k}_{F\pm} = k_F(\pm\cos\theta_{\boldsymbol{k}_F}, \sin\theta_{\boldsymbol{k}_F})$ $r_{\boldsymbol{k}_F} = \Delta^*_{\boldsymbol{k}_F}/|\Delta_{\boldsymbol{k}_F}|$, and $iq_x = \pm\sqrt{E^2{-}|\Delta_{\boldsymbol{k}_F}|^2}/\hbar v_{F_x}$ ($|q_x| \ll k_F$). Within the Andreev approximation the continuous energy spectrum of the extended quasiparticle state is given by $E = \pm\sqrt{(\hbar v_F q_x)^2{+}|\Delta_{\boldsymbol{k}_F}|^2}$. However, there are also states with subgap energies ($|E| < |\Delta_{\boldsymbol{k}_F}|$) which are bound states at the surface, called *Andreev bound states*. Their energy is obtained by solving the equation

$$r_{\boldsymbol{k}_F+} r^*_{\boldsymbol{k}_F-} = \frac{E + \sqrt{E^2{-}|\Delta_{\boldsymbol{k}_F}|^2}}{E - \sqrt{E^2{-}|\Delta_{\boldsymbol{k}_F}|^2}} \quad \Rightarrow \quad E = E_{k_y} = \mathrm{Im}\,[\Delta_{\boldsymbol{k}_F}]\Big|_{\boldsymbol{k}_F\cdot\hat{\boldsymbol{y}}=k_y} \tag{39}$$

where we use the momentum k_{F_y} parallel to the surface to label the dispersion as we assume translational invariance along y-direction. Note that the expression $E_{k_y}{=}\mathrm{Im}\,[\Delta_{\boldsymbol{k}_F}]$ has to be used with care and is only valid as such for states with $|N_C|{=}1$. For higher Chern numbers the solution of Eq. (39) has to take the winding of the gap function properly into account (see Fig. 4(c) for the example of $N_\mathrm{C}{=}-3$).

We introduce the electron operator $\hat{\phi}_{k_y}$ specifically for the edge state,

$$\hat{\gamma}_{k_y} = \int d^2r \left(\hat{\phi}_{k_y} u^*_{k_F}(\boldsymbol{r}) - \hat{\phi}^\dagger_{-k_y} v^*_{k_F}(\boldsymbol{r}) \right) \quad \text{and} \quad \hat{\gamma}^\dagger_{-k_y} = \int d^2r \left(\hat{\phi}^\dagger_{-k_y} u_{k_F}(\boldsymbol{r}) - \hat{\phi}_{k_y} v_{k_F}(\boldsymbol{r}) \right) \tag{40}$$

which then lead to the edge state Hamiltonian,

$$\mathcal{H}_\mathrm{sf} = \sum_{k_y} E_{k_y} \hat{\gamma}^\dagger_{k_y} \hat{\gamma}_{k_y} \ . \tag{41}$$

The same spectrum we obtain also for the other part of the original Hamiltonian, so that we could label $\hat{\gamma}_{k_y}$ additionally with a spin index. Note that for the zero-energy mode ($E_{k_y=0}{=}0$) we

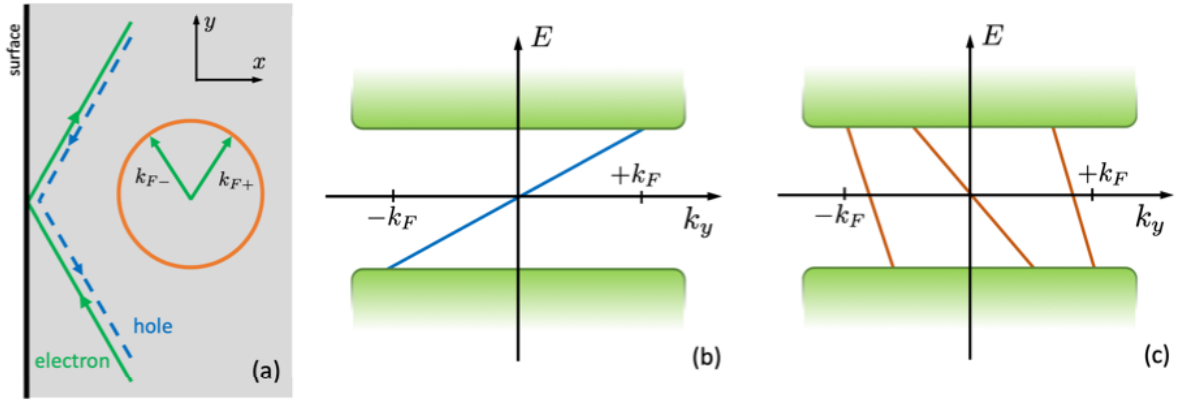

Fig. 4: *Chiral edge states: (a) Closed quasi-classical trajectories of electrons (green) and holes (blue) connected through Andreev reflections yield subgap bound states at the surface. Schematic structure of the quasiparticle spectrum: (b) Chiral edge mode with energies below the quasiparticle continuum (green) for* $N_{\mathrm{C}}=+1$ *[situation as in Fig. 2 (a) and 3 (a) FS 1]. (c) Chiral edge modes for* $N_{\mathrm{C}}=-3$ *[situation as shown in Fig. 3 (a) FS 2].*

find that $u_{\boldsymbol{k}_F}(\boldsymbol{r})=u_{\boldsymbol{k}_F}(\boldsymbol{r})^*=v_{\boldsymbol{k}_F}(\boldsymbol{r})=v_{\boldsymbol{k}_F}(\boldsymbol{r})^*$. Thus, the creation and annihilation operator are identical $\hat{\gamma}_0=\hat{\gamma}_0^\dagger$. This mode has no electrical charge as electron and hole compensate perfectly. This mode has then the property of a Majorana fermion [12, 13].
Taking $\Delta_{\boldsymbol{k}_F}=d_z(\boldsymbol{k}_F)$ from Eq. (20) we find for the subgap energies

$$E_{k_y} = \pm\Delta_0 \sin k_y \tag{42}$$

which yields a chiral mode whose orientation is connected directly with the chirality, i.e., the sign of the slope corresponds to sign of the Chern number N_{C} (see Fig. 4 (b)). The number of surface modes crossing zero energy in with a certain orientation is connected with $r_{\boldsymbol{k}_F} = \exp[-i\arg\{d_z(\boldsymbol{k}_F)\}]$ in Eq. (39) which provides a direct relation to the Chern number in Eq. (25). The Chern number as a winding number determines the number of chiral branches which connect the lower with the upper continuum of the spectrum of Bogoliubov quasiparticles as can be seen upon examination of Eq. (39) [17]. This means eventually,

$$N_{\mathrm{C}} = \sum_{k_y} \mathrm{sign}[v_y(k_y)]\,\delta(E_{k_y}) \tag{43}$$

where N_{C} corresponds to the net number of zero-energy crossings of given sign of velocity $\hbar v_y(k_y)=dE_{k_y}/dk_y$. The relation constitutes the concept *bulk-edge correspondence* and shows that the character of the surface bound states are related to the topological properties of the bulk state. This is analogous to the integer Quantum Hall state, for our chiral p-phase the $\nu=1$ case. It is instructive to look at the quasi-classical trajectories as displayed in Fig. 4 (a). An electron with given momentum bounces off specularly from the surface back towards the bulk superconductor and is through an Andreev reflection turned into hole which essentially retraces the original path of the electron. With the Andreev reflection of the hole the path is completed

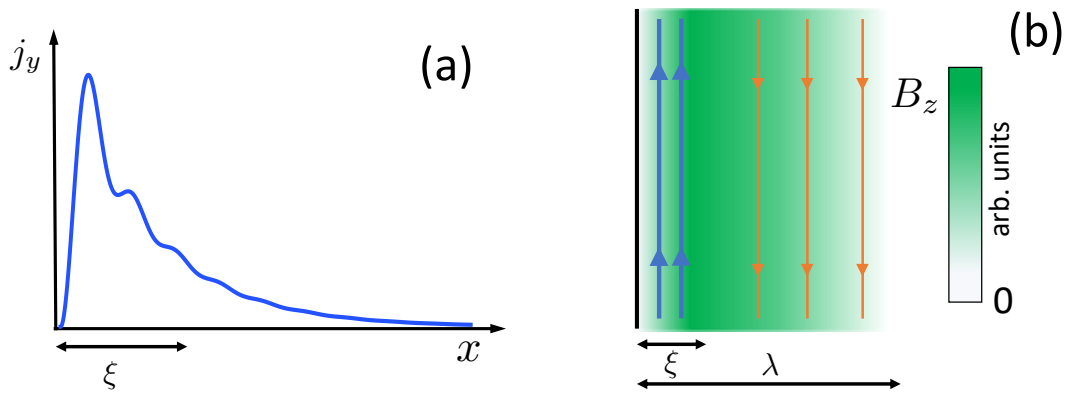

Fig. 5: *Spontaneous supercurrent at surface. (a) Charge currents induced by the chiral edge state extend on a length ξ (coherence length) into the bulk (oscillations are of Friedel-type with wave vector k_F. (b) The magnetic field (green shading) induced by the edge current (blue) is screened by counter currents (red) on a length scale λ, the London penetration depth.*

such that we can view this as closed orbit involving both an electron and a hole component, obviously as an electron-hole superposition constituting Bogoliubov quasiparticles as of the superconductor. The localization length along the x-axis is the order of the bulk coherence length $\xi \approx \hbar v_F/|\Delta_0|$ as obtained from the wave function in Eq. (37). In the following we will consider the phenomenological implications.

4.2 Surface currents

Fig. 4 (a) reveals a further property of the chiral edge state. The closed quasi-classical trajectory for a given k_{Fy} carries a net electrical current parallel to the surface, because electrons and holes move in opposite direction. Restricting to the Andreev bound states the expression for the current density is given by

$$\begin{aligned} J_y(x) &= -\frac{2e}{L}\sum_{k_y=\boldsymbol{k}_F\cdot\hat{\boldsymbol{y}}} v_{Fy}\Big(|u_{\boldsymbol{k}_F}(x)|^2 f(E_{k_y}) - |v_{\boldsymbol{k}_F}(x)|^2 f(-E_{k_y})\Big) \\ &= -\frac{2e}{L}\sum_{k_y} v_{Fy}\Big(|u_{\boldsymbol{k}_F}(x)|^2 + |v_{\boldsymbol{k}_F}(x)|^2\Big) f(E_{k_y}) \end{aligned} \tag{44}$$

with $\hbar\boldsymbol{v}_F = \boldsymbol{\nabla}_{\boldsymbol{k}}\xi_{\boldsymbol{k}}\big|_{\boldsymbol{k}=\boldsymbol{k}_F}$. By symmetry the current density has only a non-vanishing y-component. The relations $E_{k_y} = -E_{-k_y}$ and $v_{Fy}(k_y) = -v_{Fy}(-k_y)$ ensure that the electronic ($u_{\boldsymbol{k}}$) and hole ($v_{\boldsymbol{k}}$) part add up in the same direction. Like the bound state this current is confined to a coherence length ξ at the surface, as shown in Fig. 5. The magnetic field generated by this current is screened (Meissner-Ochsenfeld effect) by counter currents on a length scale of London penetration depth λ, such that the integrated current at the surface vanishes (see Fig. 5(b)). The current induced by the edge states depends on details of the band structure through $\boldsymbol{v}_F$. Moreover, it is important to note that also the quasiparticles of the continuum contribute to the current, which lead to some quantitative changes and are ignored in Eq. (44). Consequently, the magnitude of

the current is not uniquely connected with the topology of the chiral state. In contrast to the Quantum Hall state where the chiral edge mode is made up of electrons, here it is a part of the Bogoliubov quasiparticle spectrum. Bogoliubov quasiparticles are due to the hybridization of electrons and holes and, consequently, do not conserve charge [18–20]. As we will show below there is no connection to the Chern number sometimes even not on qualitative level.
It has been discussed whether the chirality would yield a spontaneous Hall effect, a transverse voltage as response to a supercurrent. The discussion of this phenomenon is rather complex and exceeds our analysis. The effect is very small and we refer to Ref. [21].

4.3 Quasiparticle current and thermal Hall effect

The analogy to the Quantum Hall effect, however, seems to hold for the Bogoliubov quasiparticles, whose spectrum and current is uniquely connected to the topology of the state. Unlike the charge, the energy of quasiparticles is conserved and we can consider the energy (heat) current carried by the edge states, as defined by

$$J_y^{(Q)}(x) = \frac{1}{L}\sum_{k_{Fy}} E_{k_{Fy}} v_{k_y}\Big(|u_{\boldsymbol{k}_F}(\boldsymbol{r})|^2 + |v_{\boldsymbol{k}_F}(\boldsymbol{r})|^2\Big) f(E_{\boldsymbol{k}_{Fy}}) \tag{45}$$

where the quasiparticle velocity is given by $\hbar v_y(k_y) = \partial E_{k_y}\partial k_y$. Integrating over x with the normalization condition (38) we obtain

$$I^{(Q)}(T) = \int \frac{dk_y}{2\pi} E_{k_y} v_y(k_y) f(E_{k_y}) \; . \tag{46}$$

In the low-temperature limit ($k_BT \ll \Delta_0 \sim k_BT_c$) we may use Sommerfeld expansion for the temperature dependence

$$\begin{aligned} I^{(Q)}(T) \;&= \int \frac{dk_y}{2\pi} v_y(k_y)\left(E_{k_y}\Theta(-E_{k_y}) - k_BT\frac{\beta^2E_{k_y}^2}{4\cosh^2(\beta E_{k_y}/2)} + \cdots\right) \\ &\approx I_0^{(Q)} - \frac{k_BT}{\hbar}\int\frac{dE}{2\pi}\frac{\beta^2E^2}{4\cosh^2(\beta E/2)} \;=\; I_0^{(Q)} - \frac{\pi}{6}\frac{(k_BT)^2}{\hbar} \; . \end{aligned} \tag{47}$$

Thus, the first correction to the (non-universal) zero-temperature current is universal, as it does not contain any material-dependent parameters.
Let us now consider a Hall-bar geometry, shown in Fig. 6, where the two edges have by symmetry opposite quasiparticle currents. Due the gap of the bulk state, the electronic heat current is carried only by the edge states. Therefore, the total heat current along the bar consists of the contribution of both surface which flow in opposite direction. A finite current only appears, if the temperature is different on the two surfaces and the leading contribution is

$$I_{tot}^{(Q)} = I_1^{(Q)} + I_2^{(Q)} = \frac{\pi}{6}\frac{k_B^2}{\hbar}\big(T_2^2 - T_1^2\big) = -\frac{\pi}{6}\frac{k_B^2T}{\hbar}\Delta T = \kappa_{yx}\Delta T \tag{48}$$

with $T_1 = T - \Delta T/2$ and $T_2 = T + \Delta T/2$. This is the Righi-Leduc effect, the heat current

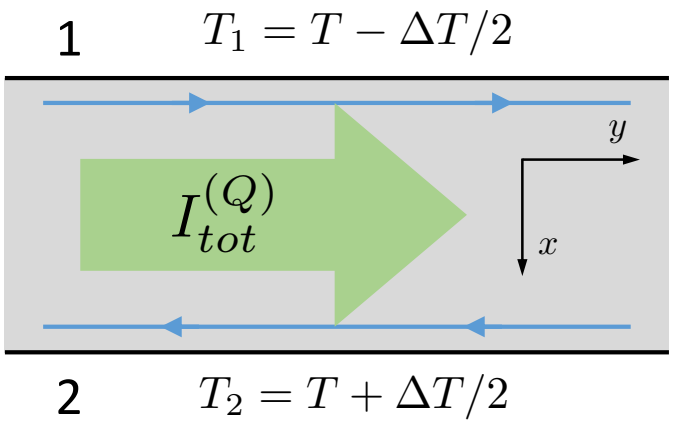

Fig. 6: *Hall bar for the Righi-Leduc effect or thermal Hall effect: Difference in temperature on the two edges induce a heat current along the bar. For chiral edge states this yields a quantum thermal Hall effect.*

induced by a transverse temperature difference is *quantized* with the same universal contribution for each chiral edge mode [14, 22–24], such that we can write

$$\kappa_{xy} = -\kappa_{yx} = \frac{\pi}{6}\frac{k_B^2 T}{\hbar} N_{\rm C} \ . \tag{49}$$

Thus, assuming positive chirality ($k_x + ik_y$) for the case in Fig. 3(a) the FS 1 and 2 would yield $N_{\rm C}$=2 and $N_{\rm C}$= − 6, respectively, including the spin. Note that the universal linear-T behavior is valid only in the limit of very small T and the leading correction $\sim e^{-\Delta_0/k_B T}(\Delta_0/k_B T)^2$ is due to thermally activated quasiparticles.

The thermal Hall effect reveals the topological nature of the superconducting phases while neither the spontaneous supercurrent at the surface nor the spontaneous Hall effect are universal and may even be too small to measure. An illustrative example for this discrepancy can be seen in the behavior when crossing the Lifshitz transition for the situation of Fig. 2 (a-c). The spectra of the surface bound states are shown in Fig. 7 (a) and (b) where the former corresponds to the electron-like and the latter to the hole-like Fermi surface. In both cases the Fermi velocity v_{Fy} entering the surface current expression in Eq. (44) has the same sign for negative energies E_{k_y}. Thus, in both cases the surface current I runs in the same direction despite the fact that the two situations correspond to Chern numbers of opposite sign. Thus, the Lifshitz transition between to two FS topologies upon rising μ leaves at most a slight anomaly in the supercurrent as function of μ. The surface current is not tied to the Chern number, but changes sign under the time reversal operation. In contrast, the thermal Hall conductance κ_{xy}/T changes from one universal value to the other, as the quasiparticle velocity v_y changes sign for the two kinds of edge states.

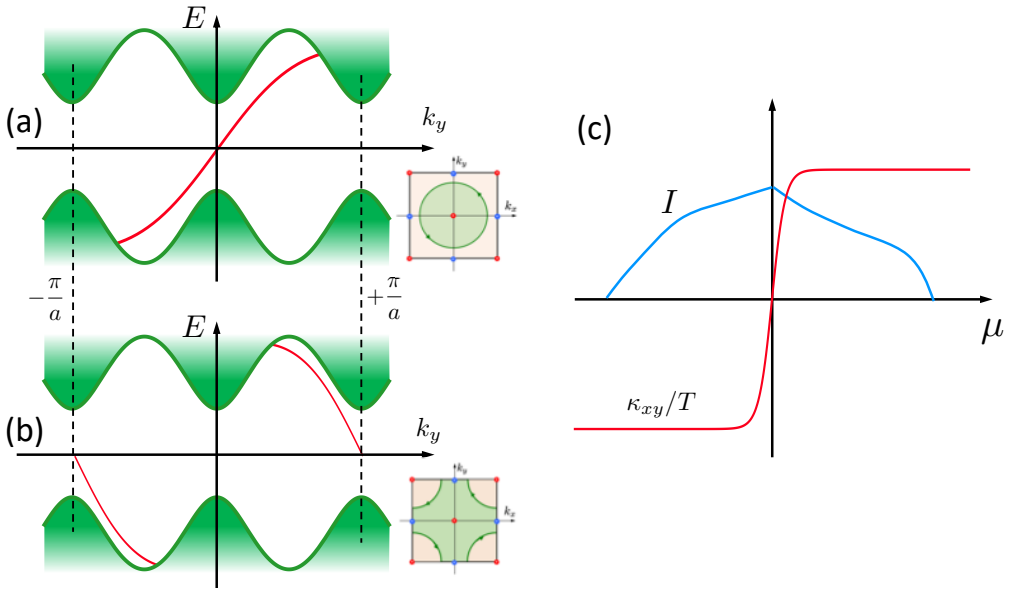

Fig. 7: *Topology versus currents: Chiral edge states for (a) electron-like and (b) hole-like FS have dispersions with opposite velocity. (c) The direction of the charge current (electron – hole flow) is unchanged (only small anomaly at the Lifshitz transition at $\mu = 0$), while the thermal Hall conductance κ_{xy}/T changes sign between two universal values (width of the transition shrinks with lowering T).*

5 Chiral superconductivity in three dimensions

In a genuinely three-dimensional material the generic case of a chiral superconductor is not topologically non-trivial because is has to have zero nodes in the gap. We would like to consider here in a simple way, how one can characterize the properties of such superconductors nevertheless, using some of the tools introduced above.

For our discussion we use again a system with simple tetragonal point group D_{4h} with a gap function of chiral p-wave state, $\boldsymbol{d}(\boldsymbol{k}) = \Delta_0 \hat{\boldsymbol{z}}(\sin k_x \pm i \sin k_y)$ without any k_z-dependence. The chiral axis is along the z-axis. We now define a sliced Chern number (SCN) by cutting through the three-dimensional BZ for fixed k_z. The cross section includes again 2D FS ($\mathrm{FS}(k_z)$) which allow us to determine a Chern number through the winding number

$$n_{\mathrm{C}}(k_z) = \frac{1}{2\pi} \oint_{\mathrm{FS}(k_z)} d\boldsymbol{k} \cdot \boldsymbol{\nabla}_{\boldsymbol{k}} \arg[d_z(\boldsymbol{k})] \tag{50}$$

which is an integer and depends on the charges of the encircled gap zero lines crossing the BZ (along z-direction). The overall "Chern number" is then obtained through the integration over k_z

$$N_{\mathrm{C}} = \frac{a}{2\pi} \int_{-\pi/a}^{+\pi/a} \frac{dk_z}{2\pi} n_{\mathrm{C}}(k_z) \; . \tag{51}$$

Now let us look at two generic examples, shown in Fig. 8. For a weak dispersion along the z-

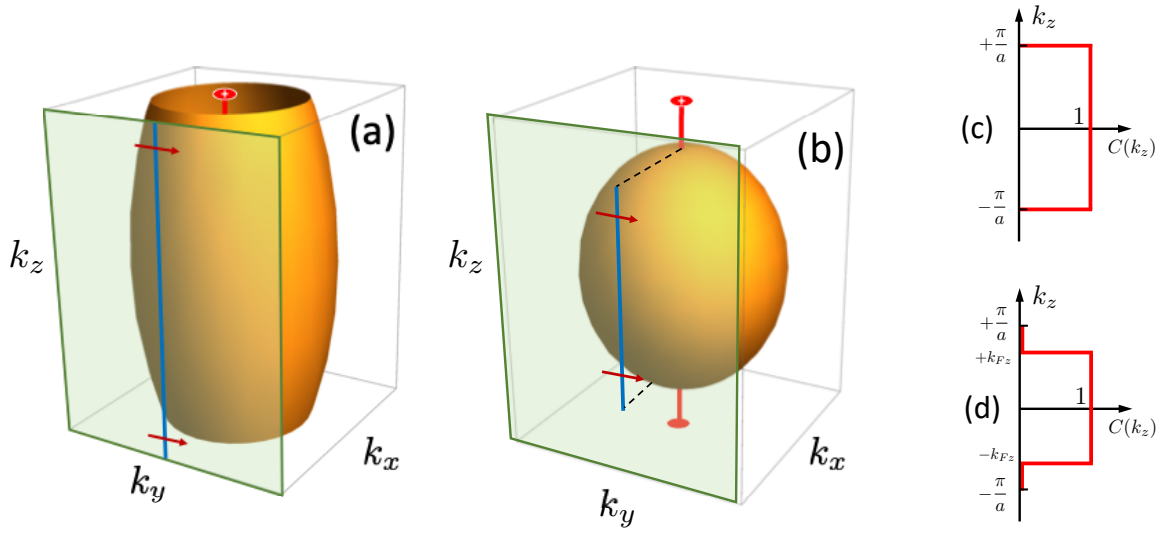

Fig. 8: *Fermi surfaces in three-dimensional systems: (a) Quasi-two-dimensional metal with open (cylindrical) FS and no gap zeros yields an integer Chern number with a Fermi arc (blue line) crossing the whole surface BZ (green k_y-k_z-plane). (b) Genuine three-dimensional metal with closed Fermi surface has point nodes at the poles. The Fermi arc is limited by the projection of the nodal points and the non-integer Chern number reflects the restricted length.*

axis the FS will be open and cylindrical (a) such that none of the zeros of the gap function $d_z(\boldsymbol{k})$ crosses the FS anywhere. This corresponds to a quasi-two-dimensional system. Thus, the bulk quasiparticle spectrum remains fully gapped and $n_{\rm C}(k_z) = \pm 1$ for all k_z in the BZ, as shown in Fig. 8 (c) leading to $N_{\rm C} = \pm 1$, an integer number indicating a topologically non-trivial state. On the other hand, a strong dispersion along the z-axis yields a closed Fermi surface (Fig. 8 (b)). There are only cross section of the Fermi surface for $-k_{Fz} < k_z < +k_{Fz}$ where $n_{\rm C}(k_z) = \pm 1$. Here the gap function $d_z(\boldsymbol{k})$ has point nodes in the gap at the two poles of the FS ($k_x = k_y = 0$). The Chern number is $N_{\rm C} = \pm k_{Fz} a/\pi$, i.e., non-integer.

What information does the Chern number $N_{\rm C}$ carry? These superconductors have chiral edge states connected with $n_{\rm C}(k_z)$, whose spectrum looks as depicted in Fig. 4(b), for a surface with normal vector along x-direction. For the standard chiral p-wave state we can find for all k_z with $n_{\rm C}(k_z) = \pm 1$ that there is one k_y value where $E_{k_y} = 0$ which we may call a Fermi point. The sign of the sliced Chern number $n_{\rm C}(k_z)$ gives these Fermi points an orientation. In the k_y-k_z-plane they form a so-called Fermi arc which in case (a) crosses the whole BZ while it has a finite length for case (b). The Chern number $N_{\rm C}$ is a measure for the length of the Fermi arc. The Chern number $N_{\rm C}$ appears again in the thermal Hall effect,

$$\kappa_{xy} = \frac{\pi}{6}\frac{k_B^2 T}{\hbar}\int \frac{dk_z}{2\pi} n_{\rm C}(k_z) = \frac{\pi}{6}\frac{k_B^2 T}{\hbar} N_{\rm C}\,. \tag{52}$$

A universally quantized value is only found for truly topological phases as for the quasi-two-dimensional case (a) in Fig. 8. Note that for the case (b) the presence of point nodes in the gap introduces stronger corrections to linear-T law of κ_{xy} which has a T^3 dependence.

6 Topological superconducting phases with TRS

Another class of topological superconductors conserves time reversal symmetry and belong to the odd-parity pairing states, as long as parity is a symmetry. In many aspects these superconductors are related to the B-phase of superfluid ^{3}He.

6.1 Two-dimensional systems

We return to two-dimensional superconductors and consider here as an example the spin-triplet superconducting phase belonging to one-dimensional representation of the tetragonal point group D_{4h}. These are given by the gap functions

$$\begin{aligned} \boldsymbol{d}_{A_{1u}}(\boldsymbol{k}) &= \Delta_0\big(\hat{\boldsymbol{x}}\sin k_x + \hat{\boldsymbol{y}}\sin k_y\big)\ , \qquad & \boldsymbol{d}_{A_{2u}}(\boldsymbol{k}) &= \Delta_0\big(\hat{\boldsymbol{x}}\sin k_y - \hat{\boldsymbol{y}}\sin k_x\big)\ , \\ \boldsymbol{d}_{B_{1u}}(\boldsymbol{k}) &= \Delta_0\big(\hat{\boldsymbol{x}}\sin k_x - \hat{\boldsymbol{y}}\sin k_y\big)\ , \qquad & \boldsymbol{d}_{B_{2u}}(\boldsymbol{k}) &= \Delta_0\big(\hat{\boldsymbol{x}}\sin k_y + \hat{\boldsymbol{y}}\sin k_x\big)\ . \end{aligned} \tag{53}$$

All four states (53) are equal-spin pairing states with spin parallel / antiparallel to the z-axis. We focus here on $\boldsymbol{d}_{A_{1u}}(\boldsymbol{k})$ which has the following gap matrix

$$\hat{\Delta}_{\boldsymbol{k}} = \begin{pmatrix} \Delta_{\boldsymbol{k}\uparrow\uparrow} & \Delta_{\boldsymbol{k}\uparrow\downarrow} \\ \Delta_{\boldsymbol{k}\downarrow\uparrow} & \Delta_{\boldsymbol{k}\downarrow\downarrow} \end{pmatrix} = \begin{pmatrix} -\Delta_0\big(\sin k_x - i\sin k_y\big) & 0 \\ 0 & \Delta_0\big(\sin k_x + i\sin k_y\big) \end{pmatrix} \tag{54}$$

such that the Nambu space can again be decomposed into two subspace with the spinors $(\hat{c}_{\boldsymbol{k}s}, \hat{c}_{-\boldsymbol{k}s})$ with $s = \pm 1$ for spin up and down, respectively. It is obvious that each subspace has a "chiral" gap function with a definite "Chern number"

$$N_{\mathrm{C},s} = \frac{1}{2\pi}\oint_F S d\boldsymbol{k}\cdot\boldsymbol{\nabla}_{\boldsymbol{k}}\arg[\Delta_{\boldsymbol{k}ss}] \tag{55}$$

which is spin dependent with $N_{\mathrm{C},+1}{=}{-}N_{\mathrm{C},-1}$. The net Chern number taking both spins together, $N_{\mathrm{C}}{=}\sum_s N_{\mathrm{C},s} = 0$, vanishes, since TRS is conserved. Nevertheless, bulk-edge correspondence is reflected by the presence of "spin chiral edge states" of opposite orientation for the two spin subspaces (see Fig. 9(a)): $E_{k_y,s} = \mathrm{Im}\,[\Delta_{\boldsymbol{k}_F,ss}]$. These edge states can be obtained again by means of the Bogoliubov-de Gennes equations used above. They are called *helical* as propagation direction and spin of the quasiparticles are tied together.

Analogous to Sect. 4.1 we introduce again quasiparticle operators for the edge state which have now a spin index, $\hat{\Gamma}_{k_y} = \big(\hat{\gamma}_{k_y\uparrow}, \hat{\gamma}_{k_y\downarrow}\big)$. The surface Hamiltonian reads,

$$\mathcal{H}_{\mathrm{sf}} = \sum_{k_y,s} E_{k_y,s}\,\hat{\gamma}^\dagger_{k_y,s}\hat{\gamma}_{k_y,s} = \sum_{k_y,s,s'} \mathcal{E}_{k_y,ss'}\,\hat{\gamma}^\dagger_{k_y,s}\hat{\gamma}_{k_y,s'}\ . \tag{56}$$

Here $\mathcal{E}_{k_y,ss'}$ follows from the symmetry general relation $(\hat{\boldsymbol{n}}\times\boldsymbol{k}_\parallel)\cdot\boldsymbol{\sigma}_{ss'} = k_y\sigma^z_{ss'}$ where $\hat{\boldsymbol{n}}{=}(100)$ is the surface normal vector and $\boldsymbol{k}_\parallel$ the momentum parallel to the surface.

For the time being we restrict here to the situation of an electron like FS closed around the BZ center, for simplicity.

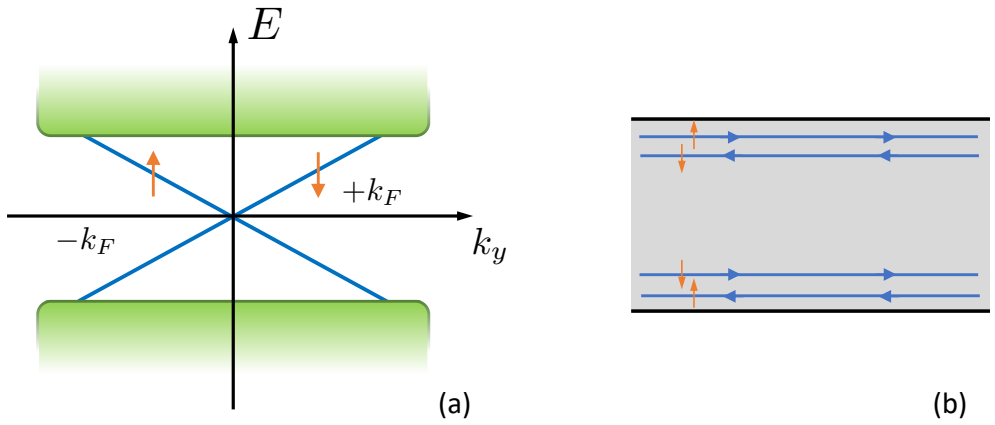

Fig. 9: *Helical edge states: (a) The energy dispersion is spin dependent with opposite quasiparticle velocity for up and down spin. (b) This yields spin currents at the surface.*

6.2 Surface currents and universal properties

Due to TRS conservation there is no spontaneous supercurrent along the surface unlike in the case of a chiral superconducting phase. The helical spectrum of the Andreev bound states results in a spin current in turn. Following the same way as in Eq. (44) we find that after the integration over x the total surface current for the spin s is given by

$$I_{y,s} = \frac{1}{L}\sum_{k_y} v_{Fy}(k_y) f(E_{k_y,s}) \ . \tag{57}$$

With the relations, $E_{k_y,s} = -E_{k_y,\bar{s}} = E_{-k_y,\bar{s}}$ and $v_{Fy}(k_y) = -v_{Fy}(-k_y)$ follows that $I_{y,s} = -I_{y,\bar{s}}$. Therefore obviously the supercurrent vanishes, i.e., $I_y = I_{y,\uparrow} + I_{y,\downarrow} = 0$. However, we obtain a net spin current along the edge

$$I_y^{(s)} = \frac{\hbar}{2}\big(I_{y,\uparrow} - I_{y,\downarrow}\big) = \frac{\hbar}{L}\sum_{k_y} v_{Fy}(k_y) f(E_{k_y,\uparrow}) \tag{58}$$

whereby this current runs in the opposite direction on the two edges of a bar as shown in Fig. 9(b). This current would also contain contributions from the continuum not included in Eq. (57). Like the chiral supercurrents these spin currents are not universal. Unlike the supercurrent, the spin current does not lead to screening currents.

On the other hand, there is an analog to the quantized thermal Hall effect for chiral superconductors. Very much in the same way as in Sect. 4.3 we can derive a relation like in Eq. (48),

$$\kappa_{xy}^{(s)} = -\kappa_{yx}^{(s)} = \frac{\pi}{3}\frac{k_B^2 T}{\hbar} \tag{59}$$

whereby the response to the transverse temperature difference in the Hall bar is a "spin heat current"

$$I_y^{(Q,s)} = \int \frac{dk_y}{2\pi} E_{k_y} v_y(k_y)\big(f(E_{k_y\uparrow}) - f(E_{k_y\downarrow})\big) \ . \tag{60}$$

Considering this in a Hall bar geometry again, this would constitute a quantized thermal spin Hall effect. An experimental verification would very likely be rather challenging.

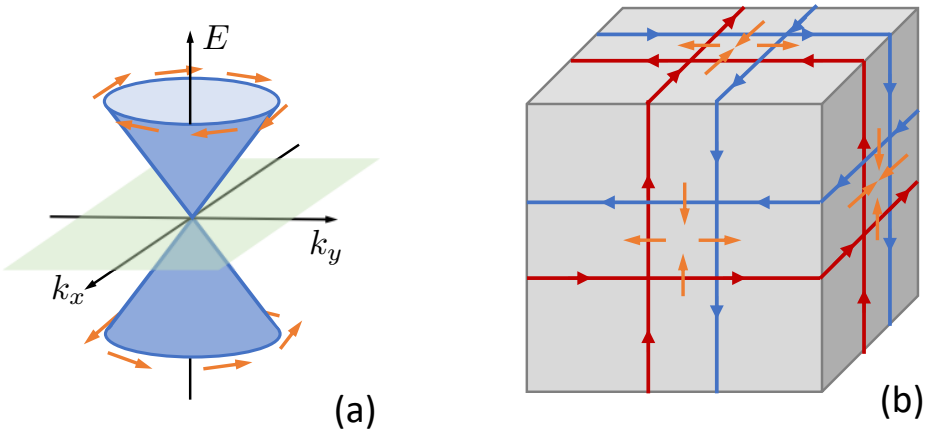

Fig. 10: *Edge states for the Balian-Werthammer state $\boldsymbol{d}(\boldsymbol{k}) = \Delta_0 \hat{\boldsymbol{\nu}} \cdot \boldsymbol{k}$: (a) The edge states are helical with Dirac-type cone dispersion on the two surface BZ (here k_x-k_y). The arrows (orange) show the spin texture. (b) These edge states yield spin currents with transverse spin orientation on all surfaces.*

6.3 Three-dimensional systems

The prime example of a topological phase in this category is the Balian-Werthammer (BW) state which corresponds to the B-phase of superfluid ^{3}He [3, 10]. It is an odd-parity state with a gap function

$$\boldsymbol{d}(\boldsymbol{k}) = \begin{cases} \Delta_0 \big(\hat{\boldsymbol{x}} k_x + \hat{\boldsymbol{y}} k_y + \hat{\boldsymbol{z}} k_z \big) & \text{(I)} \\ \Delta_0 \big(\hat{\boldsymbol{x}} \sin k_x + \hat{\boldsymbol{y}} \sin k_y + \hat{\boldsymbol{z}} \sin k_z \big) & \text{(II)} \end{cases} \tag{61}$$

where case (I) corresponds to a fully rotationally symmetrical system like ^{3}He and case (II) is the analogous state in a simple cubic lattice with nearest-neighbor pairing. Unlike all the other odd-parity states considered above this is not an equal-spin pairing state. The spin configuration is locked to the momentum space (like for the states in Eq. (53) which constitutes a dynamical "spin-orbit coupling"). The gap function has no zeros on a closed Fermi surface in case (I) and in case (II) there is a finite number of zero points in the BZ. The analysis of the topology by slicing the BZ reveals that "topological invariants" only exist for $\boldsymbol{k} \cdot \hat{\boldsymbol{\nu}} = 0$ ($\hat{\boldsymbol{\nu}}$ slicing normal vector) or at the BZ boundary for case (II). Thus, we do not have Fermi arcs unlike in the case of time reversal symmetry breaking chiral superconductors.

It is straightforward to derive the edge states from the corresponding Bogoliubov-de Gennes equations [25, 12]. The corresponding surface Hamiltonian for case (I) reads

$$\mathcal{H}_{\mathrm{sf}} = \sum_{\boldsymbol{k}_\parallel, s, s'} (\hat{\boldsymbol{n}} \times \boldsymbol{k}_\parallel) \cdot \boldsymbol{\sigma}_{ss'} \, \hat{\gamma}^\dagger_{\boldsymbol{k}_\parallel, s} \hat{\gamma}_{\boldsymbol{k}_\parallel, s'} \tag{62}$$

which shows a helical spectrum with a cone shaped dispersion around the center of the surface BZ. In Fig. 10(a) we show the momentum dependence of the subgap quasiparticle energy for the normal vector along the z-axis. This leads to surface spin currents as displayed in Fig. 10(b). In this case we have only a Fermi point in the surface BZ. In case (II) it is possible to have additional such cones at points of the BZ boundary some of which show a reversed spin pattern.

AZ class	$SU(2)$	TRS	parity	examples	edge states
D	$\times$	$\times$	odd	spinless chiral p-wave	chiral
DIII	$\times$	$\bigcirc$	odd	BW p-wave	helical
A	$\triangle$	$\times$	odd	spinful chiral p-wave	chiral
AIII	$\triangle$	$\bigcirc$	odd	nematic	zero-energy
C	$\bigcirc$	$\times$	even	chiral d-wave	chiral
CI	$\bigcirc$	$\bigcirc$	even	nematic	zero-energy

Table 1: *Six classes of Bogoliubov-de Gennes Hamiltonians: We distinguish behavior under spin $SU(2)$ and TRS operation – "$\bigcirc$" present, "$\times$" absent, "$\triangle$" restricted $SU(2)$ with S_z preserved. We use examples discussed in parts above.*

7 Symmetry classification

In the context of topological phases, in particular topological insulators, single-particle Hamiltonians have been categorized into ten symmetry classes and led to the so-called periodic table of topological matter. Among these we find also the classes to which superconductors belong, the subgroup of the Bogoliubov-de Gennes Hamiltonians [26,27]. In this section we would like briefly to locate the examples we have given above within this classification scheme, because it is often used in literature. The basis of the classification are properties of the Hamiltonian as given in Eq. (11) under the discrete symmetries of time-reversal, particle-hole, and sublattice (so-called chiral) symmetry. In Table 1 we give the list of the six relevant classes which are labeled according to the Altland-Zirnbauer (AZ) classes [28].

We will now consider briefly the different classes.

Classes without spin rotation symmetry $SU(2)$: Class D violating TRS is in 2D systems characterized by an integer Chern number. An example is a spinless chiral p-wave superconductor, e.g., the reduced Hamiltonian in Eq. (21) which possesses chiral edge states. The class DIII conserves TRS and includes the superconducting states discussed in Sect. 6 which generate helical edge states in two and three dimensions.

Classes with conserved spin S_z-component: We find the spinful chiral p-wave superconductor including both spin components in $H(\boldsymbol{k})$ possessing integer Chern numbers in 2D systems. This belongs to class A without TRS and has chiral edge states. Class AIII with TRS contains the odd-parity states like nematic phase B and C in Eq. (9). These states have zeros in the gap. They can develop zero-energy Andreev bound states for certain surfaces as can be seen from our analysis in Sect. 4.1. For all trajectories with $\Delta_{\boldsymbol{k}_{F+}}=-\Delta_{\boldsymbol{k}_{F-}}$ we find from Eq. (39) $E=0$.

Classes with full spin rotation symmetry: Here we find the even-parity spin-singlet superconductors where Cooper pairs do not have any spin dependence. The class C breaks TRS and incorporates the chiral d-wave state, $d_{x^2-y^2}+id_{xy}$-wave, which is characterized by a Chern number in 2D and possesses chiral edge states. An alternative chiral d-wave state in 3D systems has $d_{xz}+id_{yz}$-symmetry with a line node. Nematic d-wave states like $d_{x^2-y^2}$ and d_{xy} belong to class CI. Analogous to the nematic odd-parity states, they have zero-energy Andreev bound states for certain surface orientations.

8 Realizations of topological superconducting phases

As mentioned in the introduction unconventional superconductivity is most likely found in materials with strongly correlated electrons. While such superconductors are known since the late 1970's it is still a highly non-trivial task to identify the structure of Cooper pairs.

A few experimental methods are considered important in the context of topological superconductivity. For the detection of spontaneously broken TRS in superconductors there are two widely trusted methods. These are the zero-field muon spin relaxation (see, e.g., Ref. [29]) and the polar Kerr effect (see, e.g., Ref. [30]). The former measures the depolarization rate of the spins of injected muons. For numerous superconductors we find an increase of the depolarization rate indicating that the superconductor produces intrinsically a spontaneous magnetic field distribution associated with broken TRS. The polar Kerr effect observes the rotation of the polarization axis of reflected light relative to the incident polarization. By symmetry such an effect is possible for chiral superconductors for incident beams along the chiral axis. The estimate of the magnitude of the observed signals, however, is a complex theoretical problem [30].

Among the superconductors labeled as TRS breaking by these two methods, we find several which are candidates for chiral superconductivity. In this respect the most intensively investigated is Sr_2RuO_4 which has been suggested to be a chiral p-wave superconductor [8, 31]. During the last year, however, new experimental data led to a debate whether Sr_2RuO_4 is indeed an odd-parity superconductor. SrPtAs has been discussed as a candidate for chiral d-wave superconductivity of the $d_{x^2-y^2}+id_{xy}$-wave type [32, 33]. Chiral d-wave superconductivity of the $d_{zx}+id_{zy}$-wave type has been proposed for the heavy Fermion superconductor URu_2Si_2 [30, 34]. Chiral superconductivity may also be realized in UPt_3, another heavy Fermion compound, as a chiral f-wave channel, with a gap function, $\boldsymbol{d}(\boldsymbol{k}) = \hat{\boldsymbol{z}}k_z(k_x+ik_y)^2$ or $\boldsymbol{d}(\boldsymbol{k}) = \hat{\boldsymbol{z}}(k_x+ik_y)(5k_z^2-1)$ [35, 36].

While magnetic properties have been observed through μSR and polar Kerr effect in many of these superconductors, so far attempts, focussed mainly on Sr_2RuO_4, to directly detect the magnetic fields produced by surface currents, using scanning probes, have only delivered negative results [37, 38]. This may reflect the fact that the generated magnetic fields are not universal and too small for the conditions in the experiment [18–20]. On the other hand, quasiparticle tunnelling data for Sr_2RuO_4 show zero-bias anomalies indicating the presence of edge states [39, 40]. Note, however, that these experiments cannot distinguish chiral from helical edge states easily.

Since magnetism is considered adversary to superconductivity, the superconducting phases appearing in the ferromagnetic heavy Fermion systems, UGe_2, URhGe and UCoGe, have attracted also much attention [41, 42]. These systems break TRS even in the normal state and the Cooper pairs form in a spin polarized environment, most likely with odd-parity. This has been the basis of proposals of superconducting phases with topological properties (for a recent work see [43]). A most recent case of an U-based superconductors which possibly realizes chiral pairing is UTe_2, a heavy Fermion metal close to a ferromagnetic quantum critical point [44].

Unconventional superconductivity in materials without an inversion center in their crystal lattice

represent another intriguing class, because parity is not a symmetry for Cooper pairs anymore. Also here topological features have been discussed (see for example [45]). A brief overview of the many realizations of topological bulk superconductors can be found in Ref. [46].

9 Conclusion

This brief lecture notes give only a very selected insight into a very dynamical and fast evolving field. The very active subject of artificially structured systems designed to show topological superconductivity have been completely omitted. In particular, one-dimensional systems, so-called nano-wires, provide a way to generate Majorana edge modes in a controlled way and are considered as potential building blocks for so-called topological quantum computers [47, 48]. Also nodal structures of the pair wavefunction or the gap functions are a subject of topological matter [49, 50].

References

[1] M. Sigrist and K. Ueda, Rev. Mod. Phys. **63**, 239 (1991)

[2] V.P. Mineev and K.V. Samokhin: *Introduction to Unconventional Superconductivity* (Gordon and Breach, 1999)

[3] A.J. Leggett, Rev. Mod. Phys. **47**, 331 (1975)

[4] G.R. Stewart, Adv. Phys. **66**, 75 (2017)

[5] M.R. Norman, Science **332**, 196 (2011)

[6] C. Pfleiderer, Rev. Mod. Phys. **81**, 1551 (2009)

[7] B.D. White, J.D. Thompson, and M.B. Maple, Physica C **514**, 246 (2015)

[8] Y. Maeno, S. Kittaka, T. Nomura, S. Yonezawa, and K. Ishida, J. Phys. Soc. Jpn. **81**, 011009 (2012)

[9] A.P. Mackenzie, J. Supercond. Nov. Magn. **33**, 177 (2020)

[10] D. Vollhardt and P. Wölfle: *The Superfluid Phases of Helium 3* (Taylor & Francis, 1990)

[11] X.L. Qo and S.C. Zhang, Rev. Mod. Phys. **83**, 1057 (2011)

[12] B.A. Bernevig and T.L. Hughes: *Topological Insulators and Topological Superconductors* (Princeton University Press, 2013)

[13] M. Sato and Y. Ando, Rep. Prog. Phys. **80**, 076501 (2017)

[14] N. Read and D. Green, Phys. Rev. B **61**, 10267 (2000)

[15] G.E. Volovik, Sov. Phys. JETP **67**, 1804 (1988); JETP Lett. **66**, 522 (1997)

[16] J.B. Ketterson and S.N. Song: *Superconductivity* (Cambridge University Press, 1999)

[17] G.E. Volovik and V.M. Yakovenko, J. Phys.: Condens. Matter **1**, 5263 (1989)

[18] W. Huang, E. Taylor, and C. Kallin, Phys. Rev. B **90**, 224519 (2014)

[19] S. Lederer, W. Huang, E. Taylor, S. Raghu, and C. Kallin, Phys. Rev. B **90**, 134521 (2014)

[20] S.B. Etter, A. Bouhon, and M. Sigrist, Phys. Rev. B **97**, 064510 (2018)

[21] A. Furusaki, M. Matsumoto, and M. Sigrist, Phys. Rev. B **64**, 054514 (2001)

[22] T. Qin, Q. Niu and J. Shi, Phys. Rev. Lett. **107**, 236601 (2011)

[23] H. Sumiyoshi and S. Fujimoto, J. Phys. Soc. Jpn. **82**, 023602 (2013)

[24] Y. Imai, K. Wakabayashi, and M. Sigrist, Phys. Rev. B **93**, 024510 (2016)

[25] Y. Okuda and R. Nomura, J. Phys.: Condens. Matter **24**, 343201 (2012)

[26] A.P. Schnyder, S. Ryu, A. Furusaki, and A.W.W. Ludwig, Phys. Rev. B **78**, 195125 (2008)

[27] C.K. Chiu, J.C.Y. Teo, A.P. Schnyder, and S. Ryu, Rev. Mod. Phys. **88**, 035005 (2016)

[28] A. Altland und M.R. Zirnbauer, Phys. Rev. B **55**, 1142 (1997)

[29] G.M. Luke, Y. Fudamoto, K.M. Kojima, M.I. Larkin, J. Merrin, B. Nachumi, Y.J. Uemura, Y. Maeno, Z.Q. Mao, Y. Mori, H. Nakamura, and M. Sigrist, Nature **394**, 558 (1998)

[30] A. Kapitulnik, Physica B **460**, 151 (2015); E.R. Schemm, E.M. Levenson-Falk, and A. Kapitulnik, Physica C **535**, 13 (2017)

[31] Y. Liu and Z.Q. Mao, Physica C **514**, 339 (2015)

[32] P.K. Biswas, H. Luetkens, T. Neupert, T. Stürzer, C. Baines, G. Pascua, A.P. Schnyder, M.H. Fischer, J. Goryo, M.R. Lees, H. Maeter, F. Brückner, H.-H. Klauss, M. Nicklas, P.J. Baker, A.D. Hillier, M. Sigrist, A. Amato, and D. Johrendt Phys. Rev. B **87**, 180503 (2013)

[33] M.H. Fischer, T. Neupert, C. Platt, A.P. Schnyder, W. Hanke, J. Goryo, R. Thomale, and M. Sigrist, Phys. Rev. B **89**, 020509 (2014)

[34] Y. Kasahara, T. Iwasawa, H. Shishido, T. Shibauchi, K. Behnia, Y. Haga, T.D. Matsuda, Y. Onuki, M. Sigrist, and Y. Matsuda, Phys. Rev. Lett. **99**, 116402 (2007)

[35] E.R. Schemm, W.J. Gannon, C.M. Wishne, W.P. Halperin, and A. Kapitulnik, Science **345**, 190 (2014)

[36] P. Goswami and A.H. Nevidomskyy, Phys. Rev. B **92**, 214504 (2015)

[37] J.R. Kirtley, C. Kallin, C.W. Hicks, E.-A. Kim, Y. Liu, K.A. Moler, Y. Maeno, and K.D. Nelson, Phys. Rev. B **765**, 014526 (2007)

[38] P.J. Curran, S.J. Bending, W.M.Desoky, A.S. Gibbs, S.L. Lee, and A.P. Mackenzie, Phys. Rev. B **89**, 144504 (2014)

[39] Z.Q. Mao K.D. Nelson, R. Jin, Y. Liu, and Y. Maeno, Phys. Rev. Lett. **87**, 037003 (2001)

[40] S. Kashiwaya, H. Kashiwaya, H. Kambara, T. Furuta, H. Yaguchi, Y. Tanaka, and Y. Maeno, Phys. Rev. Lett. **107**, 077003 (2011)

[41] A.D. Huxley, Physica C **514**, 368 (2015)

[42] D. Aoki, K. Ishida, and J. Flouquet, J. Phys. Soc. Jpn. **88**, 022001 (2019)

[43] A.K.C. Cheung and S. Raghu, Phys. Rev. **93**, 134516 (2016)

[44] L. Jiao, S. Howard, S. Ran, Z. Wang, J. Olivares Rodriguez, M. Sigrist, Z. Wang, N.P. Butch, and V. Madhaven, Nature **579**, 523 (2020)

[45] M. Sato and S. Fujimoto, Phys. Rev. B **79**, 094504 (2009)

[46] S. Yonezawa, AAPPS Bulletin **26**, No. 3, 3 (2016)

[47] M. Franz, Nat. Nanotechnol. **8**, 149 (2013)

[48] H.M. Guo, Sci. China-Phys. Mech. Astron. **59**, 637401 (2016)

[49] S. Kobayashi, Y. Yanase, and M. Sato, Phys. Rev. B **94**, 134512 (2016)

[50] T. Bzdusek and M. Sigrist, Phys. Rev. B **96**, 155105 (2017)

13 Group-Theoretical Classification of Superconducting States

David Sénéchal

Département de Physique et Institut Quantique

Université de Sherbrooke, Québec, Canada

Contents

E. Pavarini and E. Koch (eds.)
Topology, Entanglement, and Strong Correlations
Modeling and Simulation Vol. 10
Forschungszentrum Jülich, 2020, ISBN 978-3-95806-466-9
http://www.cond-mat.de/events/correl20

1 Introduction

Superconductivity is understood as a condensation of pairs of electrons. As such, it is a rather subtle case of spontaneous symmetry breaking involving *off-diagonal long range order* (ODLRO), and is usually described in terms of spontaneously broken electromagnetic $U(1)$ gauge symmetry [1]. This chapter is about superconductors that break other symmetries, specifically point-group symmetries, in addition to $U(1)$ gauge symmetry. For lack of space and time, we focus on the theoretical classification of such states, not on experimental evidence or phenomenology.

1.1 Notation

Let us first establish the notation. We consider a crystalline solid with N_b "active" electron bands. Electron states are usually described in the Bloch-band basis, with wave functions $\varphi_{\mathbf{k},a}(\mathbf{x})$ for band a and wave vector $\mathbf{k}$, or in a Wannier-orbital basis, with wave functions $w_m(\mathbf{x}-\mathbf{r})$ for the Wannier orbital $m = 1,\ldots,N_b$ centered at the lattice site $\mathbf{r}$. We are used to the latter in the context of strongly correlated electrons. In second-quantized language, we express various physical observables in terms of creation and annihilation operators. In particular, the operator $\Psi_\sigma(\mathbf{x})$ annihilates an electron of spin projection σ ($\sigma = \uparrow, \downarrow$) at the continuous position $\mathbf{x}$ and obeys the anticommutation relations

$$\bigl\{\Psi_\sigma(\mathbf{x}),\, \Psi^\dagger_{\sigma'}(\mathbf{x}')\bigr\} = \delta_{\sigma\sigma'}\,\delta(\mathbf{x}-\mathbf{x}') \qquad \bigl\{\Psi_\sigma(\mathbf{x}),\, \Psi_{\sigma'}(\mathbf{x}')\bigr\} = 0\,. \tag{1}$$

The operator $\Psi_\sigma(\mathbf{x})$ can be expressed in the Bloch basis as

$$\Psi_\sigma(\mathbf{x}) = \sum_{\mathbf{k},a,\sigma} d_{a,\sigma}(\mathbf{k})\,\varphi_{\mathbf{k},a}(\mathbf{x}) \quad \text{where} \quad \{d_{a,\sigma}(\mathbf{k}),\, d^\dagger_{b,\sigma'}(\mathbf{k}')\} = (2\pi)^3\delta(\mathbf{k}-\mathbf{k}')\,\delta_{a,b}\,\delta_{\sigma,\sigma'}\,, \tag{2}$$

or in the Wannier basis as

$$\Psi_\sigma(\mathbf{x}) = \sum_{\mathbf{r},m,\sigma} c_{\mathbf{r},m,\sigma}\,w_{m,\sigma}(\mathbf{x}-\mathbf{r}) \quad \text{where} \quad \{c_{\mathbf{r},m,\sigma},\, c^\dagger_{\mathbf{r}',m',\sigma'}\} = \delta_{\mathbf{r},\mathbf{r}'}\,\delta_{m,m'}\,\delta_{\sigma,\sigma'}\,. \tag{3}$$

A non-interacting Hamiltonian for the free propagation of such electrons takes, in the Wannier basis, the general form

$$H_0 = \sum_{\mathbf{r},\mathbf{r}',m,m',\sigma} t^{m,m'}_{\mathbf{r},\mathbf{r}'}\,c^\dagger_{\mathbf{r},m,\sigma}\,c_{\mathbf{r}',m',\sigma} \tag{4}$$

(we ignore the spin-orbit (SO) interaction for the moment). If $c_{m,\sigma}(\mathbf{k})$ is the Fourier transform of $c_{\mathbf{r},m,\sigma}$, the above Hamiltonian may be written in a simpler form, diagonal in $\mathbf{k}$ because of translation invariance on the lattice

$$H_0 = \sum_{\mathbf{k},m,m',\sigma} t^{m,m'}(\mathbf{k})\,c^\dagger_{m,\sigma}(\mathbf{k})\,c_{m',\sigma}(\mathbf{k}) \tag{5}$$

(we will call this description the *orbital basis*). Finally, the $\mathbf{k}$-dependent $N_b\times N_b$ matrix $t^{m,m'}(\mathbf{k})$ may be diagonalized by a unitary matrix $V_{a,m}(\mathbf{k})$, which brings us to the annihilation operator

$d_{\mathbf{k},a}(\mathbf{k})$ in the Bloch basis

$$d_{a,\sigma}(\mathbf{k}) = \sum_m V_{a,m}(\mathbf{k})\, c_{m,\sigma}(\mathbf{k}) \tag{6}$$

in terms of which the non-interacting Hamiltonian becomes completely diagonal

$$H_0 = \sum_{\mathbf{k},a,\sigma} \varepsilon_a(\mathbf{k})\; d^\dagger_{a,\sigma}(\mathbf{k})\, d_{a,\sigma}(\mathbf{k})\;. \tag{7}$$

In practice, band structure calculations provide us with the band energies $\varepsilon_a(\mathbf{k})$ and the wave functions $\varphi_{\mathbf{k},a}(\mathbf{x})$, from which Wannier functions can be obtained with some degree of arbitrariness, although a maximal localization principle can be followed [2]. Alternatively, the Wannier basis can be the starting point, using a tight-binding approximation.

1.2 Pairing

The fundamental object of superconductivity is a pair of electrons, or Cooper pair. A generic annihilation operator for a Cooper pair takes the following form, in a translation invariant system[1]

$$\hat{\Delta} = \int d^3\mathbf{r}\; d^3\mathbf{r}'\; \Delta_{\sigma\sigma'}(\mathbf{r}-\mathbf{r}')\; \Psi_\sigma(\mathbf{r})\, \Psi_{\sigma'}(\mathbf{r}')\;. \tag{8}$$

Because of the Pauli principle, i.e., anticommutation relations (1), we can impose an antisymmetry condition on the amplitude

$$\Delta_{\sigma\sigma'}(\mathbf{r}-\mathbf{r}') = -\Delta_{\sigma'\sigma}(\mathbf{r}'-\mathbf{r})\;. \tag{9}$$

In the Bloch basis, this pairing operator and the antisymmetry condition are expressed as

$$\hat{\Delta} = \sum_{\mathbf{k},a,b,\sigma,\sigma'} \Delta_{a\sigma,b\sigma'}(\mathbf{k})\; d_{a\sigma}(\mathbf{k})\, d_{b\sigma'}(-\mathbf{k}) \qquad \Delta_{a\sigma,b\sigma'}(\mathbf{k}) = -\Delta_{b\sigma',a\sigma}(-\mathbf{k})\,. \tag{10}$$

Likewise, in the Wannier basis,

$$\hat{\Delta} = \sum_{\mathbf{r},\mathbf{r}',m,m',\sigma,\sigma'} \Delta_{\mathbf{r}m\sigma,\mathbf{r}'m'\sigma'}\; c_{\mathbf{r}m\sigma}\, c_{\mathbf{r}'m'\sigma'} \qquad \Delta_{\mathbf{r}m\sigma,\mathbf{r}'m'\sigma'} = -\Delta_{\mathbf{r}'m'\sigma',\mathbf{r}m\sigma} \tag{11}$$

and, in the orbital basis,

$$\hat{\Delta} = \sum_{\mathbf{k},m,m',\sigma,\sigma'} \Delta_{m\sigma,m'\sigma'}(\mathbf{k})\; c_{m\sigma}(\mathbf{k})\, c_{m'\sigma'}(-\mathbf{k}) \qquad \Delta_{m\sigma,m'\sigma'}(\mathbf{k}) = -\Delta_{m'\sigma',m\sigma}(-\mathbf{k})\,. \tag{12}$$

A general order parameter function (or pairing function) can be expressed as a linear combination of basis functions. We can use a basis made of products of $\mathbf{k}$-dependent, orbital-dependent and spin-dependent factors. In the orbital basis, this takes the form

$$\Delta_{m,\sigma;m',\sigma'}(\mathbf{k}) = \sum_{\alpha\beta\gamma} \psi_{\alpha\beta\gamma}\, f^\alpha(\mathbf{k})\, O^\beta_{mm'}\, S^\gamma_{\sigma\sigma'}\;. \tag{13}$$

[1] We ignore here the possibility of *pairing waves*, i.e., of Cooper pairs having a finite momentum. The Fulde-Ferrell-Larkin-Ovchinnikov state in an example where such pairing may occur. For another example, see Ref. [3].

where the amplitudes $\psi_{\alpha\beta\gamma}$ determine the precise form of pairing, given a suitable choice for the basis functions $f^\alpha(\mathbf{k})$ (momentum space), $O^\beta_{mm'}$ (orbital space) and $S^\gamma_{\sigma\sigma'}$ (spin space). In the Bloch basis, the expansion would be similar

$$\Delta_{a,\sigma;b,\sigma'}(\mathbf{k}) = \sum_{\alpha\beta\gamma} \chi_{\alpha\beta\gamma}\, f^\alpha(\mathbf{k})\, B^\beta_{ab}(\mathbf{k})\, S^\gamma_{\sigma\sigma'} \ , \tag{14}$$

with a different set of amplitudes $\chi_{\alpha\beta\gamma}$, and $\mathbf{k}$-dependent basis functions $B^\beta_{ab}(\mathbf{k})$ in "band space". The reason the basis functions $O^\beta_{mm'}$ do not depend on $\mathbf{k}$ is that Wannier functions can be chosen to have a clear "orbital character" in space, like atomic orbitals, which transform in a well-defined way under rotations and reflections (Section 4.2 will provide an example of this). Consequently, the band basis functions B^β_{ab} must depend on $\mathbf{k}$; this makes the discussion of inter-band superconductivity more complex in the Bloch basis than in the orbital basis.
Each of the spatial, orbital (or band) and spin parts can be either symmetric or antisymmetric under the exchange of quantum numbers, but he overall combination must be antisymmetric. For instance, in the absence of SO coupling, spin is conserved and pairing occurs either in the singlet (spin 0) channel or in the triplet (spin 1) channel. In the case of a single band, the spatial part $f(\mathbf{k})$ must then be even ($f(-\mathbf{k}) = f(\mathbf{k})$) for singlet pairing, and odd ($f(-\mathbf{k}) = -f(\mathbf{k})$) for triplet pairing. This remains so in the case of intra-orbital (or intra-band) pairing, i.e., when $O^\beta_{mm'} = 0$ for $m \neq m'$, but inter-orbital pairing brings other possibilities, and spin-orbit interactions complicate the matter further.

1.2.1 Spin part

The conventional way to describe the spin part is as follows

$$S_{\sigma\sigma'} = d_\gamma(\hat{\mathbf{d}}_\gamma)_{\sigma\sigma'} \qquad\qquad \hat{\mathbf{d}}_\gamma = i(\tau_\gamma\tau_2) \ , \tag{15}$$

where the set of Pauli matrices $\tau_{1,2,3}$ is augmented by the identity matrix τ_0. The three components $\gamma = 1, 2, 3$ form the symmetric, triplet part of the pairing function, whereas the antisymmetric, singlet part is represented by the component $\gamma = 0$.
Under a rotation in spin space, the 3-vector (d_x, d_y, d_z) (or (d_1, d_2, d_3)) transforms as a pseudo-vector (i.e., invariant under spatial inversion) and constitutes the triplet component, whereas d_0 behaves like a pseudo-scalar (it changes signs under inversion) and constitutes the singlet component. In the absence of SO coupling, the system being invariant under spin rotations, the pairing function fully factorizes into a spin part and the rest. In other words, all terms in the expansion (13) have the same spin part, and the pairing state can be characterized by a fixed vector (d_x, d_y, d_z) (triplet pairing) or by d_0 (singlet pairing).

1.2.2 Spatial part

The spatial part $f(\mathbf{k})$ of the pairing function could equally well be described in real space

$$f(\mathbf{k}) = \sum_{\mathbf{r}} f_{\mathbf{r}} e^{i\mathbf{k}\cdot\mathbf{r}} \tag{16}$$

where $f_{\mathbf{r}}$ is, so to speak, the pairing amplitude for electrons separated by a lattice vector $\mathbf{r}$. The spatial extent of the Cooper pair is called the *coherence length*, denoted ξ. This roughly means that $f_{\mathbf{r}}$ typically drops exponentially as a function of $\mathbf{r}$ with a characteristic length ξ. For short coherence lengths, $f_{\mathbf{r}}$ is dominated by the smallest values of $\mathbf{r}$: on-site ($\mathbf{r}$=$\mathbf{0}$) and nearest-neighbor amplitudes. Pure on-site pairing means $f_{\mathbf{r}} = \delta_{\mathbf{r},\mathbf{0}}$ and therefore a $\mathbf{k}$-independent amplitude. The celebrated d-wave pairing on a square lattice with unit lattice vectors $\hat{\mathbf{x}}$ and $\hat{\mathbf{y}}$ means $f_{\pm\hat{\mathbf{x}}} = -f_{\pm\hat{\mathbf{y}}}$, all other amplitudes being zero, and therefore $f(\mathbf{k}) = \cos k_x - \cos k_y$.

1.3 Mean-field approximation and nodal lines

In the mean-field approximation, a constant and uniform pairing field is assumed to pervade the system. The effective Hamiltonian for singlet superconductivity then takes the following form, in the Bloch basis

$$H_0 = \sum_{\mathbf{k},a,\sigma} \varepsilon_a(\mathbf{k})\; d^\dagger_{a,\sigma}(\mathbf{k})\, d_{a,\sigma}(\mathbf{k}) + \sum_{\mathbf{k},a,b} \Delta_{ab}(\mathbf{k}) \big[d_{a\uparrow}(\mathbf{k})\, d_{b\downarrow}(-\mathbf{k}) - d_{a\downarrow}(\mathbf{k})\, d_{b\uparrow}(-\mathbf{k}) \big] \tag{17}$$

(We assume that the chemical potential μ is included in the dispersion relation $\varepsilon_a(\mathbf{k})$ as an additive constant.) In order to diagonalize this Hamiltonian, one introduces an extended array of annihilation operators[2]

$$\Psi(\mathbf{k}) = \big(d_{1\uparrow}(\mathbf{k}), \ldots, d_{N_b\uparrow}(\mathbf{k}), d^\dagger_{1\downarrow}(-\mathbf{k}), \ldots, d^\dagger_{N_b\downarrow}(-\mathbf{k}) \big)\,. \tag{18}$$

The second half of the array $\Psi(\mathbf{k})$ is basically the particle-hole transformation of the first half; this procedure is attributed to Nambu. Because we are dealing with fermions, the components of $\Psi(\mathbf{k})$ still obey anticommutation relations and we can treat them as *bona fide* annihilation operators. One can then express H_0 as

$$H_0 = \sum_{\mathbf{k}} \Psi^\dagger(\mathbf{k}) \mathcal{H}(\mathbf{k}) \Psi(\mathbf{k}) \tag{19}$$

where $\mathcal{H}(\mathbf{k})$ is a $2N_b \times 2N_b$ matrix with the following block structure:

$$\mathcal{H}(\mathbf{k}) = \begin{pmatrix} \boldsymbol{\epsilon}(\mathbf{k}) & \boldsymbol{\Delta}^\dagger(\mathbf{k}) \\ \boldsymbol{\Delta}(\mathbf{k}) & -\boldsymbol{\epsilon}(-\mathbf{k}) \end{pmatrix} \tag{20}$$

where $\boldsymbol{\epsilon}(\mathbf{k})$ is the diagonal matrix with elements $\varepsilon_a(\mathbf{k})$ and $\boldsymbol{\Delta}(\mathbf{k})$ is the matrix of band components $\Delta_{ab}(\mathbf{k})$.

To complete the analysis, we need to diagonalize the Hermitian matrix $\mathcal{H}(\mathbf{k})$ via a *Bogoliubov transformation*. Because of the particular structure of the matrix $\mathcal{H}(\mathbf{k})$, its eigenvalues come in pairs of opposite signs and the ground state (the superconducting condensate) is obtained by

[2] This particular form works well when the $\mathbf{d}$-vector is d_0 or d_z. In other cases, or when spin is not conserved, one must proceed to a full Nambu doubling of the degrees of freedom,
i.e., $\Psi(\mathbf{k}) = \big(d_{1\uparrow}(\mathbf{k}), \ldots, d_{N_b\uparrow}(\mathbf{k}), d_{1\downarrow}(\mathbf{k}), \ldots, d_{N_b\downarrow}(\mathbf{k}), d^\dagger_{1\downarrow}(-\mathbf{k}), \ldots, d^\dagger_{N_b\downarrow}(-\mathbf{k}), d^\dagger_{1\uparrow}(-\mathbf{k}), \ldots, d^\dagger_{N_b\uparrow}(-\mathbf{k}) \big)$.

filling all the negative energy levels. The resulting new set of annihilation operators annihilate quasiparticles on top of the superconducting ground state.
As a simple example, let us consider a one-band model ($N_b = 1$). $\boldsymbol{\epsilon} \to \epsilon$ and $\boldsymbol{\Delta} \to \Delta$ are then scalar functions and the eigenvalues of Hamiltonian (20) are then easily computed to be

$$\xi(\mathbf{k}) = \pm\sqrt{\varepsilon^2(\mathbf{k}) + \Delta^2(\mathbf{k})} \tag{21}$$

Recall that the chemical potential is included in the function $\varepsilon(\mathbf{k})$, so that the Fermi surface is defined by the condition $\varepsilon(\mathbf{k}) = 0$. Low-energy quasiparticles will exist on top of the condensate if $\xi(\mathbf{k}) = 0$ for some values of $\mathbf{k}$ that we call *nodes*. In this simple, one-band case, nodes exist when both scalar functions $\varepsilon(\mathbf{k})$ and $\Delta(\mathbf{k})$ vanish. For instance, in the well-known case of d-wave superconductivity on a square lattice, $\Delta(\mathbf{k}) \propto \cos k_x - \cos k_y$ and the nodes are located along the diagonals of the Brillouin zone : $k_x = \pm k_y$. When more than one band is present, complications occur (see Sect. 4.3 below).

2 Elements of group theory

2.1 Groups

Since group theory is not necessarily familiar to all, we will review the basics in this section, with en emphasis on finite groups.[3]
A group G is a set $\{a, b, c, \ldots\}$ endowed with a multiplication law satisfying the following constraints:

1. Group multiplication is associative: $(ab)c = a(bc)$.
2. There is a neutral element e such that $ea = ae = a\ , \forall a \in G$.
3. Each element a has an inverse a^{-1} such that $aa^{-1} = a^{-1}a = e$.

It is implicit that if $a, b \in G$, then $ab \in G$ (closure under the group multiplication).
These rules are obeyed by the set of all nonsingular square matrices of order n, called $GL(n)$. A *subgroup* H of G is a subset of G that is also a group under the same multiplication law, i.e., that is closed under group multiplication. For instance, the group $O(n)$ is the subgroup of $GL(n)$ made of orthogonal matrices. A group is *continuous* if its elements form a topological space, i.e., a space with the notion of continuity. In particular, a *Lie group* is also a differentiable manifold ($O(n)$ is a Lie group). By contrast, a *discrete group* has well-separated elements, and a *finite group* has a finite number of such elements. In general group multiplication is not commutative; when it is, the group is said to be *Abelian*, otherwise it is *nonabelian*. A subset of elements of G are called *generators* if all elements of the group (with the exception of e) may be obtained by repeated products within the subset.
The point groups of solid-state physics are finite subgroups of $O(n)$, and as such are sets of rotations and reflections closed under repeated application. We will often refer to the elements

[3] There is a large selection of textbooks on group theory. Let us point out the classic Hamermesh text [4], as well as the more recent "nutshell" text by A. Zee [5].

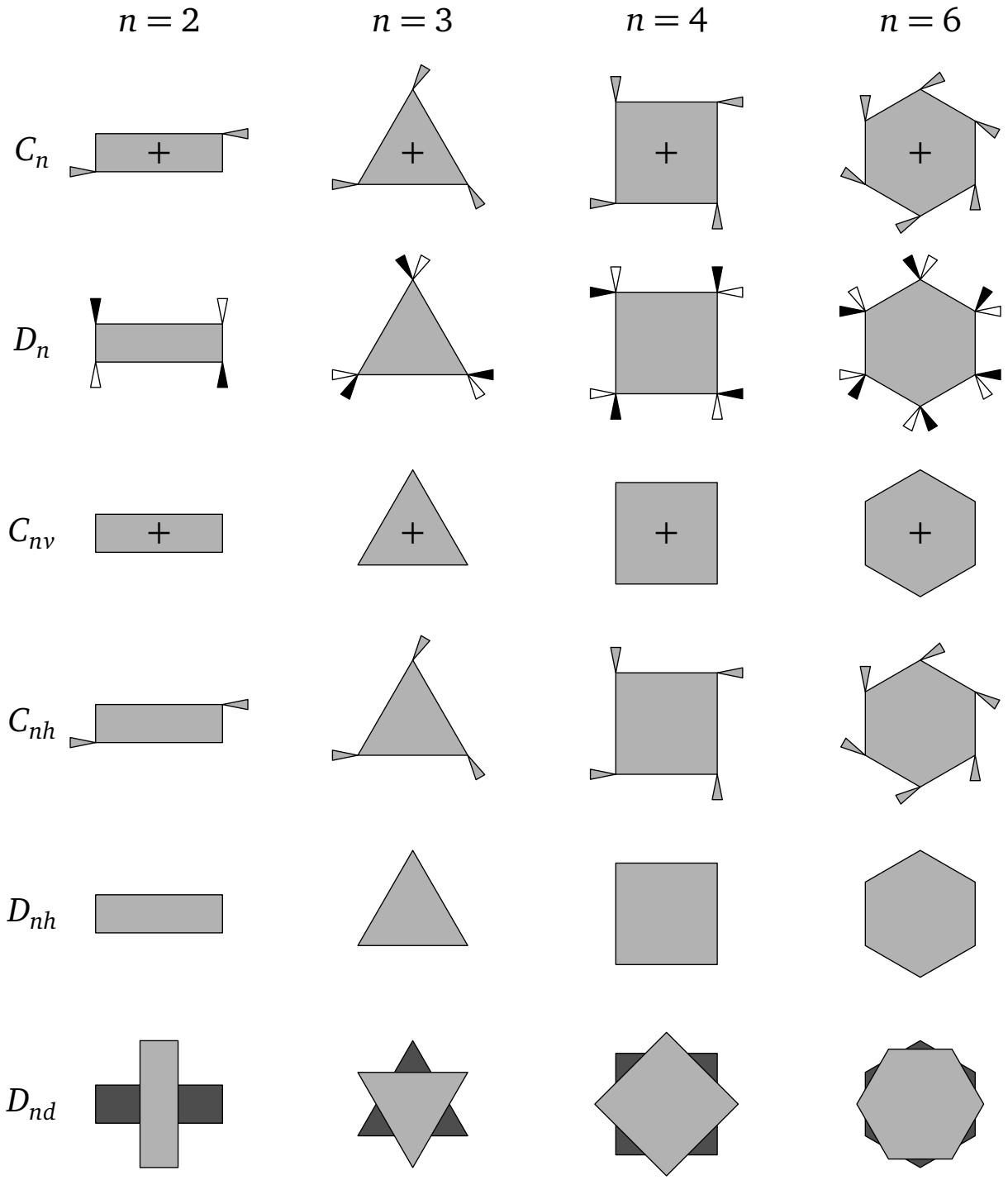

Fig. 1: *Graphical definition of the most common point groups. The group elements are those that leave each figure unchanged. Decorations added to vertices are geometrical features that rest on the plane of the page (gray), stick out of it (white) or into it (black). The darker colored objects are underneath the lighter ones. Objects marked with a + sign have a top face distinct from their bottom face and thus have no mirror symmetry about the plane or rotation axes lying in the plane.*

of these groups as *transformations*, as they can be viewed as acting on an object or physical configuration. The most common point groups can be defined as transformations on simple objects as illustrated on Fig. 1:[4]

1. C_n (cyclic group): the group elements are rotations by $2\pi/n$ about the z axis (perpendicular to the plane).
2. D_n (dihedral group): in addition to the rotations of C_n, the group contains n rotations of π about n axes lying on the xy plane.
3. C_{nv} (pyramidal group): in addition to the rotations of C_n, the group contains n reflections across n mirror planes perpendicular to the xy plane.
4. C_{nh} (reflection group): in addition to the rotations of C_n, the group contains a reflection across the xy plane.
5. D_{nh} (prismatic group): in addition to the $2n$ rotations of D_n, the group contains a reflection across the xy plane.
6. D_{nd} (antiprismatic group): Similar to D_{nh}, except that the n π-rotation axes lying on the xy plane are not the intersection of the xy plane with the n mirror planes perpendicular to the xy plane. Rather, these axes are alternating with these intersections.

2.2 Representations

In general, we are dealing with *group representations*, i.e., realizations of the group elements in terms of d-dimensional matrices acting on some space (that space V is called the *module* of the representation). A group element a is represented by a matrix $R(a)$ and that correspondence is a *homomorphism* with respect to the group operation: $R(ab) = R(a)R(b)$. Two representations R and R' are said to be *equivalent* if they are related by a change of basis, i.e., $R(a) = SR'(a)S^{-1}, \forall a \in G$. For a finite group, it can be shown that any representation is equivalent to a unitary representation, i.e., a representation made of unitary (or orthogonal) matrices, such that $R(a^{-1}) = R^{-1}(a) = R^{\dagger}(a)$. A simple example of a representation for the group C_{4v} is given in Table 1.

A representation is said to be *reducible* if a basis exists in the module V of the representation such that all elements $R(a)$ have the same block-diagonal structure. This means that the module can be seen as the direct sum of two submodules: $V = V_1 \oplus V_2$, each of $V_{1,2}$ being the support for a representation in its own right. In other words, the two submodules are not mixed with one another when acted upon by the group elements. Otherwise, the representation is said to be *irreducible*. One of the common tasks of group theory is the reduction of representations in terms of *irreps* (as irreducible representations are often called). The representation shown in Table 1 happens to be irreducible.

[4] In a crystalline solid, one should in principle consider the full *space group*, which contains translations as well as rotations and reflections. But translation invariance amounts to say that the gap function depends on a single wave vector $\mathbf{k}$, and the presence of the lattice implies that it should be unchanged when replacing $\mathbf{k}$ by $\mathbf{k} + \mathbf{Q}$, where $\mathbf{Q}$ is an element of the reciprocal lattice.

Table 1: *A simple example of group representation for C_{4v}: the matrices act on the coordinates (x, y). C_n is a rotation by $2\pi/n$ in the x-y plane. σ_x, σ_y, σ_d and $\sigma_{d'}$ are reflections across the planes $x = 0$, $y = 0$, $x = -y$ and $x = y$, respectively.*

g	$R(g)$	g	$R(g)$	g	$R(g)$	g	$R(g)$
e	$\begin{pmatrix} 1 & 0 \\ 0 & 1 \end{pmatrix}$	C_4	$\begin{pmatrix} 0 & 1 \\ -1 & 0 \end{pmatrix}$	C_4^{-1}	$\begin{pmatrix} 0 & -1 \\ 1 & 0 \end{pmatrix}$	C_2	$\begin{pmatrix} -1 & 0 \\ 0 & -1 \end{pmatrix}$
σ_x	$\begin{pmatrix} -1 & 0 \\ 0 & 1 \end{pmatrix}$	σ_y	$\begin{pmatrix} 1 & 0 \\ 0 & -1 \end{pmatrix}$	σ_d	$\begin{pmatrix} 0 & 1 \\ 1 & 0 \end{pmatrix}$	$\sigma_{d'}$	$\begin{pmatrix} 0 & -1 \\ -1 & 0 \end{pmatrix}$

A capital result of group theory are *Schur's lemmata*:

1. If R and R' are two irreps of different dimensions $d \neq d'$, then no nonzero rectangular matrix A exists such that $R(a)A = AR'(a)\ \ \forall a \in G$.
2. If R and R' are two irreps of the same dimension $d = d'$ and if a square matrix A exists such that $R(a)A = AR'(a)\ \ \forall a \in G$, then the two representations are equivalent.

The consequence of these two lemmata is the following. Consider a module V upon which a reducible representation acts. Then $V = V_1 \oplus V_2$ is a direct sum, and so is each element of the representation: $R(a) = R_1(a) \oplus R_2(a)$. Let H be a matrix acting on V that commutes with all the group elements, i.e., $HR(a) = R(a)H$. If the representations R_1 and R_2 are not equivalent, then H is necessarily block diagonal too, i.e., has no matrix elements between V_1 and V_2. Typically, in quantum mechanics, H is a Hamiltonian acting on a Hilbert space and G is a group of transformations that commute with H, i.e., that leave the Hamiltonian invariant. The construction of irreps then allows us to consider smaller spaces (the blocks) that are not mixed with one another under time evolution. Said otherwise, energy eigenstates and eigenvalues can be classified according to the irreps of the symmetry group of the problem.

2.3 Character tables

An important tool in identifying irreps of finite groups is the notion of *character*. Let us start by defining *conjugacy classes*. Two elements a and b of a group G are *conjugate* to one another if there is another element c such that $a = cbc^{-1}$. Intuitively, this means that the two transformations a and b are of the "same type", as c can be seen as a change of basis (or point of view), after which the two transformations a and b are equivalent. For instance, in the group C_{4v}, $a = \sigma_x$ and $b = \sigma_y$ are related by the rotation $c = C_4$: they are conjugate. Evidently, if a is conjugate to b and b is conjugate to a third element c, then a is also conjugate to c: conjugacy is an equivalence relation and therefore the group G can be split into separate *conjugacy classes*. Obviously, the identity e is a conjugacy class by itself. In C_{4v}, the two mirror reflections collectively denoted σ_v (σ_x and σ_y) form a class, as do the two reflections σ_d and $\sigma_{d'}$ and the two rotations C_4 and C_4^{-1}; finally, the single rotation by π (C_2) is a class by itself. Thus, C_{4v} has 5 conjugacy classes and 8 elements.

Table 2: *Character table of C_{4v}, with a list of the simplest (i.e., lowest degree) basis functions. The basis functions of the two-dimensional representation E form a doublet, written here and elsewhere in this chapter within square brackets $[\cdots,\cdots]$. The last column shows the gap basis functions derived in Sect. 3.1.*

	e	$2C_4$	C_2	$\sigma_{x,y}$	$\sigma_{d,d'}$	basis functions	gap functions
A_1	1	1	1	1	1	1	1
A_2	1	1	1	-1	-1	$\mathcal{R}_z\ ,\ xy(x^2-y^2)$	$\sin k_x\ \sin k_y(\cos k_x-\cos k_y)$
B_1	1	-1	1	1	-1	x^2-y^2	$\cos k_x-\cos k_y$
B_2	1	-1	1	-1	1	xy	$\sin k_x\ \sin k_y$
E	2	0	-2	0	0	$[\mathcal{R}_x,\mathcal{R}_y]\ ,\ [x,y]$	$[\sin k_x,\sin k_y]$

The *character* $\chi(a)$ of an element a in a representation R is the trace of that matrix: $\chi(a) = \operatorname{tr} R(a)$. Because of the cyclic property of the trace, two conjugate elements have the same character in a given representation, and therefore characters are properties of conjugacy classes, not of individual elements. We can therefore envisage a matrix-like table, called a *character table*, where the different irreps are laid out in rows and the different conjugacy classes in columns, each cell containing the character $\chi_i^{(\mu)}$ for the conjugacy class i within the irrep μ. See, for instance, Table 2 for C_{4v}, Table 3 for D_{4h} and Table 4 for C_{6v}. Note that the dimension of each irreducible representation is naturally given by the character of the identity class e.
Schur's lemma can be used to demonstrate the following orthogonality relation

$$\sum_i^K \frac{g_i}{g}\,\chi_i^{(\nu)*}\chi_i^{(\mu)} = \delta_{\mu\nu}\ , \tag{22}$$

where g stands for the number of elements of the group G, g_i is the number of elements in conjugacy class i, and K is the number of conjugacy classes. This relation states that the different rows of the character table are orthogonal (if weighted by g_i). This implies that there cannot be more than K rows in the table, as the rows are vectors of dimension K. Indeed, it can be shown that the number of non-equivalent irreps is precisely equal to K and that

$$\sum_\mu^K d_\mu^2 = g \tag{23}$$

where d_μ is the dimension of irrep μ. Finally, the orthogonality of the rows of the character table also applies to its columns:

$$\sum_\mu^K \frac{g_i}{g}\,\chi_i^{(\mu)*}\chi_j^{(\mu)} = \delta_{ij}\ . \tag{24}$$

These powerful orthogonality relations allow us to decompose any reducible representation R into a direct sum of irreps. Indeed, a general reducible representation can in principle be

Table 3: *Character table of D_{4h}, with a list of the lowest degree basis functions.*

	e	$2C_4$	C_2	$2C_2'$	$2C_2''$	i	$2S_4$	σ_z	$\sigma_{x,y}$	$\sigma_{d,d'}$	basis functions
A_{1g}	1	1	1	1	1	1	1	1	1	1	1
A_{2g}	1	1	1	-1	-1	1	1	1	-1	-1	$\mathcal{R}_z\ ,\ xy(x^2{-}y^2)$
B_{1g}	1	-1	1	1	-1	1	-1	1	1	-1	$x^2{-}y^2$
B_{2g}	1	-1	1	-1	1	1	-1	1	-1	1	xy
E_g	2	0	-2	0	0	2	0	-2	0	0	$[\mathcal{R}_x, \mathcal{R}_y]\ ,\ z[x,y]$
A_{1u}	1	1	1	1	1	-1	-1	-1	-1	-1	$xyz(x^2{-}y^2)$
A_{2u}	1	1	1	-1	-1	-1	-1	-1	1	1	z
B_{1u}	1	-1	1	1	-1	-1	1	-1	-1	1	xyz
B_{2u}	1	-1	1	-1	1	-1	1	-1	1	-1	$z(x^2{-}y^2)$
E_u	2	0	-2	0	0	-2	0	2	0	0	$[x,y]$

expressed as

$$R = \bigoplus_{\mu}^{K} a_\mu R^{(\mu)}\,. \tag{25}$$

The a priori unknown integer a_μ (the multiplicity of $R^{(\mu)}$ in R) can be determined by use of the orthogonality relation (22), using the known characters χ_i of the reducible representation R

$$a_\mu = \sum_{i}^{K} \frac{g_i}{g}\,\chi_i^{(\mu)*}\chi_i\,. \tag{26}$$

The reducible representation R acts on a module V which, likewise, is a direct sum of irreducible modules

$$V = \bigoplus_{\mu}^{K} V^{(\mu)}. \tag{27}$$

A vector ψ belonging to the module V will be affected by the transformation $a \in G$ as $\psi \to R(a)\psi$. It can be shown that the components of ψ along the submodule $V^{(\mu)}$ associated to the irrep μ can be obtained by applying on ψ the following *projection operator*

$$P^{(\mu)} = \sum_{a} \frac{d_\mu}{g}\,\chi^{(\mu)*}(a)R(a) \tag{28}$$

where $\chi^{(\mu)}(a)$ is the character of element a in representation μ. In other words, the vector $P^{(\mu)}\psi$ belongs to the submodule $V^{(\mu)}$ and, when acted upon by any transformation $a \in G$, will stay in this submodule. Projection operators are exceedingly useful in constructing basis functions (or, in superconductivity applications, gap functions) from tensor products.

2.4 Example: The D_{4h} character table

Let us illustrate the ideas behind character tables with a more complex example than C_{4v}: The point group D_{4h}. This group has the following $K = 10$ conjugacy classes:

1. The identity e
2. Two rotations C_4, i.e., of angle $\pi/2$, about the z axis.
3. A rotation C_2, i.e., of angle π, about the z axis.
4. Two rotations C_2' (π) about the x and y axes.
5. Two rotations C_2'' (π) about the diagonal axes $x \pm y$.
6. One space inversion i
7. Two pseudo-rotations S_4 of $\pi/4$ (rotations times inversion).
8. A reflection σ_z across the $z = 0$ plane.
9. 2 reflections $\sigma_{x,y}$ across the $x = 0$ and $y = 0$ planes.
10. 2 reflections $\sigma_{d,d'}$ across planes $y = -x$ and $y = x$.

Correspondingly, there are $K = 10$ irreps, divided into two groups: the g-type representations (first five rows on Table 3) that are even under the space inversion i, and the u-type representations, which are odd under i. For each representation, Table 3 gives an example of functions (homogeneous polynomials in x, y, z), or of rotations (R_x, R_y, R_z), that transform under that representation (in general, the elements of $O(n)$ acting on homogeneous polynomials in $\{x, y, z\}$ will produce another homogeneous polynomial of the same degree. Consequently, homogeneous polynomials of a given degree can be arranged into irreps. Likewise, an orthogonal matrix O will act on a rotation matrix $\mathcal{R}$ as $\mathcal{R} \to O\mathcal{R}O^{-1}$ and produce another rotation matrix about a different axis (equivalently, one could express infinitesimal rotations in terms of pseudo-vectors, and the group elements will act on these pseudo-vectors). Rotations therefore transform under the group and can also be arranged into irreps.
Let us go through some of these representations:

- A_{1g} is the trivial representation, of dimension 1. Each group element is represented by the number 1.
- A_{2g}, of dimension 1, is odd under π-rotations C_2' and C_2'', as well as under the reflections $\sigma_{x,y}$ and $\sigma_{d,d'}$. A rotation $\mathcal{R}_z$ about the z axis belongs to this representation; in particular, it changes sign when rotated by π with respect to a horizontal axis, but not when reflected across the xy plane. It also changes sign when reflected across a vertical mirror plane. The quartic polynomial $xy(x^2-y^2)$ behaves the same way; note that xy does not, because it is even under $\sigma_{d,d'}$.
- B_{1g} is odd under the $\pi/2$ rotations C_4, under the π-rotations C_2'' about the diagonals, under the $\pi/2$ pseudo-rotations S_4, and under the diagonal reflections $\sigma_{d,d'}$. It is well represented by the quadratic polynomial x^2-y^2 and by what we commonly call d-wave superconductivity on a square or cubic lattice.
- B_{2g} is similar, except that it is odd under the other set of reflections and $\pi/2$ rotations, as if rotated by 45° compared to B_{1g}. It is represented by the monomial xy and by d-wave superconductivity, this time with a d_{xy} form factor instead of $d_{x^2-y^2}$.

- E_g is a two-dimensional representation, represented by the doublet of pseudo-vectors $[\mathcal{R}_x, \mathcal{R}_y]$, or by the doublet of monomials $[zx, zy]$.
- The u-type representations have the same characters as the g-type representations for proper transformations (the first 5 columns), and opposite characters for the improper transformations (the last 5 columns). Proper transformations have determinant $+1$ and describe actual transformation that a rigid object may undergo, whereas improper transformation have determinant -1 and can always be viewed as a proper transformation times the inversion i.

2.5 Tensor products

Given two representations $R^{(1)}_{ij}(a)$ and $R^{(2)}_{ij}(a)$ of dimensions d_1 and d_2, acting respectively on modules V_1 et V_2, the product representation of dimension $d_1 d_2$ acts on the tensor product module $V_1 \otimes V_2$ and is made of the tensor products of the matrices of the two representations

$$R_{ik,jl}(a) = R^{(1)}_{ij}(a) R^{(2)}_{kl}(a) \text{ or } R(a) = R^{(1)}(a) \otimes R^{(2)}(a)\,. \tag{29}$$

A product representation is in general reducible, even if the two factors are irreducible. Reducing a product representation to its irreducible components is an important problem of group theory. The direct sum

$$R^{(\mu)} \otimes R^{(\nu)} = \bigoplus_{\rho} C^{\rho}_{\mu\nu}\, R^{(\rho)} \tag{30}$$

is called the *Clebsch-Gordan series*. For one-dimensional representations (including all representations of Abelian groups), this series is trivial since it contains a single term. For multidimensional representations, the series can be inferred from the character table, by noting that the character of a product representation is the product of the characters of its factors

$$\chi_i(R^{(\mu)} \otimes R^{(\nu)}) = \chi^{(\mu)}_i \chi^{(\nu)}_i = \sum_{\rho} C^{\rho}_{\mu\nu} \chi^{(\rho)}_i\,. \tag{31}$$

Applying the orthogonality relation (22) to this relation yields

$$C^{\rho}_{\mu\nu} = \sum_{i=1}^{K} \frac{g_i}{g}\, \chi^{*(\rho)}_i \chi^{(\mu)}_i \chi^{(\nu)}_i\,. \tag{32}$$

The states of the product module $V_1 \otimes V_2$ associated with each component of the Clebsch-Gordan series can be obtained by applying the projection operators (28). An example application of projection operators is given in Sect. 3.1.

2.6 Back to superconductivity: The Landau free energy

We will assume that Landau's theory of phase transitions qualitatively describes the superconducting transition as temperature is lowered. This theory assumes that the broken symmetry state is described by an order parameter ψ, which vanishes in the normal state and develops a

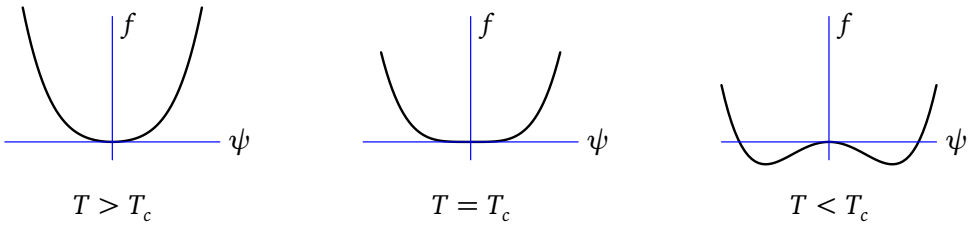

Fig. 2: *Behavior of the Landau free energy functional across a continuous (a.k.a. second order) phase transition.*

nonzero value in the broken symmetry state. It further assumes that a local free energy functional $f[\psi]$ may be defined and that the physical, uniform value of ψ corresponds to a minimum of f (see Fig. 2).

If the precise form of ψ, i.e., the precise pattern of symmetry breaking, is not known, then we may assume that ψ may be decomposed on a basis of possible pairing functions. Going back to Eq. (13), let us combine the three indices α, β, γ into a single index r:

$$\Delta_{m,\sigma;m',\sigma'}(\mathbf{k}) = \sum_r \psi_r \, \Delta^{(r)}_{m,\sigma;m',\sigma'}(\mathbf{k}) \tag{33}$$

The Landau free energy functional is then a power expansion in terms of the coefficients ψ_r:

$$f[\psi] = a_{rs}(T)\psi_r^*\psi_s + b_{rspq}(T)\,\psi_r^*\psi_s^*\psi_p\psi_q + \cdots \tag{34}$$

where the ellipsis stands for gradient- and higher-degree terms, and T is the temperature.

The Landau functional should have the same symmetries as the underlying Hamiltonian. If these symmetries form a group G of transformations, Schur's lemma tells us that organizing the basis functions $\boldsymbol{\Delta}^{(r)}$ according to irreps of G makes the matrix $a(T)$ block-diagonal: $a(T) = \bigoplus_\mu a^{(\mu)}(T)$, i.e., it has no matrix elements between functions belonging to different irreps. Within each representation, the matrix $a^{(\mu)}(T)$ may be diagonalized, and at some point upon lowering T one of its eigenvalues, initially all positive, may change sign, which signals the superconducting phase transition and a minimum of $f[\psi]$ at $\psi \neq 0$. This is going to first occur in one of the representations and will define the symmetry character of the superconducting state.[5]

For this reason it is important to arrange the possible gap functions into irreps of the symmetry group G. It amounts to a classification of possible superconducting states. Of course, a precise physical theory—a microscopic Hamiltonian—is needed in order to determine in which irrep superconductivity actually appears; but this is not the subject of this chapter.

Since the basis functions are products of spin, orbital and spatial factors, the group theoretical analysis can be done on each of these factors separately, followed by suitable tensor products. In the absence of SO coupling, the system is invariant under rotations in spin space; this leads to a clear separation between singlet and triplet gap functions, and only the combined orbital and spatial factors need to be classified according to the point group G.

[5] This is the simplest scenario, but nothing forbids competing minima, and hence additional phase transitions, to appear at lower temperatures.

3 Single-band superconductors

Let us continue our exploration by focusing first on single-band superconductors. In the absence of SO coupling, the classification of gap functions according to the point group is then limited to the spatial part. The exponentials $e^{i\mathbf{k}\cdot\mathbf{r}}$ form a set of basis functions $f^{\mathbf{r}}(\mathbf{k})$ for the spatial part. Under an element g of the point group, $\mathbf{k} \to g\mathbf{k}$ and $e^{i\mathbf{k}\cdot\mathbf{r}}$ is mapped into $e^{ig\mathbf{k}\cdot\mathbf{r}} = e^{i\mathbf{k}\cdot(g^{-1}\mathbf{r})}$. Given a lattice vector $\mathbf{r}$, the set of functions labeled by $S = \{g\mathbf{r}\},\ g \in G$ will transform amongst themselves and will form a (generally reducible) representation. The matrices associated with that representation simply perform permutations of the element of the set S and are obtained from the unit matrix by a permutation of the rows. Moreover, since the point groups are subgroups of $O(n)$, all the elements of S will have the same modulus.
In the one-band case, the Pauli principle forces the singlet pairing functions to be even in $\mathbf{k}$, whereas triplet functions are odd in $\mathbf{k}$. We will focus in what follows on a simple example. A more thorough discussion can be found in Ref. [6].

3.1 C_{4v} symmetry

Let us illustrate the situation of a two-dimensional system on a square lattice with C_{4v} symmetry. The character table is shown on Table 2. Let us consider in succession the representations generated from the vectors $\mathbf{r}=\mathbf{0}$ (on-site), $\mathbf{r}=\hat{\mathbf{x}}$ (first neighbor) and $\mathbf{r}=\hat{\mathbf{x}}+\hat{\mathbf{y}}$ (second neighbor). The representation generated from $\mathbf{r}=\mathbf{0}$ contains a single function, equal to 1, belonging to A_1. The one generated from $\mathbf{r}=\hat{\mathbf{x}}$ contains the four functions

$$\left(e^{ik_x}, e^{ik_y}, e^{-ik_x}, e^{-ik_y}\right) \tag{35}$$

in terms of which the group generators are

$$R(C_4) = \begin{pmatrix} 0 & 1 & 0 & 0 \\ 0 & 0 & 1 & 0 \\ 0 & 0 & 0 & 1 \\ 1 & 0 & 0 & 0 \end{pmatrix} \quad R(\sigma_x) = \begin{pmatrix} 0 & 0 & 1 & 0 \\ 0 & 1 & 0 & 0 \\ 1 & 0 & 0 & 0 \\ 0 & 0 & 0 & 1 \end{pmatrix} \tag{36}$$

The other elements of the representation are

$$R(C_2) = \begin{pmatrix} 0 & 0 & 1 & 0 \\ 0 & 0 & 0 & 1 \\ 1 & 0 & 0 & 0 \\ 0 & 1 & 0 & 0 \end{pmatrix} \quad R(\sigma_y) = \begin{pmatrix} 1 & 0 & 0 & 0 \\ 0 & 0 & 0 & 1 \\ 0 & 0 & 1 & 0 \\ 0 & 1 & 0 & 0 \end{pmatrix} \quad R(C_4^{-1}) = \begin{pmatrix} 0 & 0 & 0 & 1 \\ 1 & 0 & 0 & 0 \\ 0 & 1 & 0 & 0 \\ 0 & 0 & 1 & 0 \end{pmatrix}$$

$$R(\sigma_d) = \begin{pmatrix} 0 & 1 & 0 & 0 \\ 1 & 0 & 0 & 0 \\ 0 & 0 & 0 & 1 \\ 0 & 0 & 1 & 0 \end{pmatrix} \quad R(\sigma_{d'}) = \begin{pmatrix} 0 & 0 & 0 & 1 \\ 0 & 0 & 1 & 0 \\ 0 & 1 & 0 & 0 \\ 1 & 0 & 0 & 0 \end{pmatrix} \quad R(e) = \begin{pmatrix} 1 & 0 & 0 & 0 \\ 0 & 1 & 0 & 0 \\ 0 & 0 & 1 & 0 \\ 0 & 0 & 0 & 1 \end{pmatrix}$$

From these expression we can compute the projection operators (28). An explicit computation shows that

$$P^{(A_1)} = \frac{1}{4}\begin{pmatrix} 1 & 1 & 1 & 1 \\ 1 & 1 & 1 & 1 \\ 1 & 1 & 1 & 1 \\ 1 & 1 & 1 & 1 \end{pmatrix},\ P^{(B_1)} = \frac{1}{4}\begin{pmatrix} 1 & -1 & 1 & -1 \\ -1 & 1 & -1 & 1 \\ 1 & -1 & 1 & -1 \\ -1 & 1 & -1 & 1 \end{pmatrix},\ P^{(E)} = \frac{1}{2}\begin{pmatrix} 1 & 0 & -1 & 0 \\ 0 & 1 & 0 & -1 \\ -1 & 0 & 1 & 0 \\ 0 & -1 & 0 & 1 \end{pmatrix}$$

whereas $P^{(A_2)}$ and $P^{(B_2)}$ vanish. The basis functions we seek are the eigenvectors of these projectors with eigenvalue $+1$

$$A_1 \ :\ (1,1,1,1) \qquad B_1 \ :\ (1,-1,1,-1) \qquad E \ :\ (1,0,-1,0)\ \&\ (0,1,0,-1) \tag{37}$$

which, in terms of the basis (35), are

$$A_1 \ :\ \cos k_x + \cos k_y \qquad B_1 \ :\ \cos k_x - \cos k_y \qquad E \ :\ [\sin k_x, \sin k_y]\,. \tag{38}$$

The representation generated from $\mathbf{r} = \hat{\mathbf{x}} + \hat{\mathbf{y}}$ contains the four functions

$$\left(e^{i(k_x+k_y)}, e^{i(k_x-k_y)}, e^{-i(k_x+k_y)}, e^{-i(k_x-k_y)}\right)\,. \tag{39}$$

By repeating the same procedure, one finds following basis functions

$$A_1 \ :\ \cos k_x \cos k_y \qquad B_2 \ :\ \sin k_x \sin k_y \qquad E \ :\ [\sin(k_x+k_y), \sin(k_x-k_y)]\,. \tag{40}$$

We need to go to the fourth neighbor $\mathbf{r} = 2\hat{\mathbf{x}}+\hat{\mathbf{y}}$ in order to get a basis function belonging to A_2:

$$A_2 \ :\ \sin k_x \ \sin k_y(\cos k_x - \cos k_y) \tag{41}$$

The simplest basis functions for the spatial part of the gap function are shown in the last column of Table 2. Since we are dealing with a single band model, the nodes are solely determined by the structure of the gap function $\Delta(\mathbf{k})$ obtained directly from the functions of Table 2.
The A_1 representation corresponds to isotropic (or s-wave) pairing. The B_1 representation is the well-known d-wave pairing, and the B_2 representation is a variant, rotated by $45°$. The A_2 representation constitutes a more exotic case corresponding to g-wave pairing. Assuming a constant modulus $|\mathbf{k}|$, the gap functions associated to the one-dimensional representations of Table 2 have the following shape as a function of polar angle in the k_x-k_y plane:

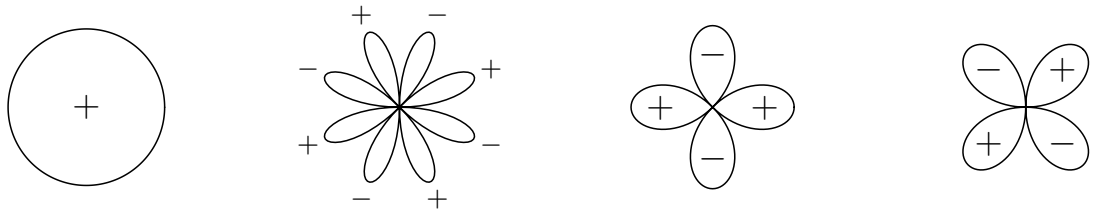

The gap functions associated with these representations have respectively 0, 8, 4, and 4 nodes (or zeros) as a function of angle from 0 to 2π. The sign of the function in each lobe is indicated. The E representation is odd under inversion and is therefore associated with triplet superconductivity. The gap function in that case is the doublet $[\sin k_x, \sin k_y]$. Each member of the doublet has two nodal directions. However, it is possible to combine them into complex functions $\sin k_x \pm i \sin k_y$, each behaving like an effective one-dimensional representation of C_{4v}, mapped onto one another by complex conjugation or, physically speaking, time reversal. These complex combinations have no nodes, as the real and imaginary parts do not vanish at the same angle. These gap symmetries are respectively called p_x, p_y and $p_x \pm i p_y$. The corresponding angular dependences are illustrated below, again assuming a constant modulus $|\mathbf{k}|$:

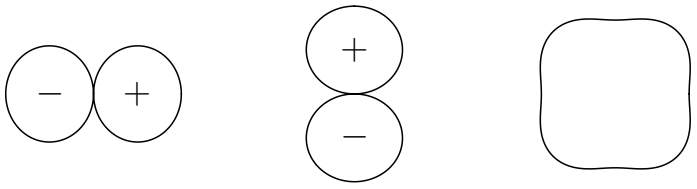

p_x p_y $|p_x \pm i p_y|$

3.2 C_∞ symmetry

In the continuum approximation, i.e., for very long coherence lengths, it is legitimate to assume that a two-dimensional model might have continuous rotation invariance about the z axis. The rotation symmetry, combined with a mirror symmetry across any vertical plane, is effectively the $n \to \infty$ limit of C_{nv}. The irreps of $C_{\infty v}$ are

1. A_1 : the character is 1 for every rotation and reflection.

2. A_2 : the character is 1 for every rotation and -1 for every reflection.

3. E_n ($n \in \mathbb{N}^*$) : the character is $2\cos(n\theta)$ for a rotation of angle θ and 0 for reflections. This is realized by the 2×2 rotation matrices $R(\theta)$ and reflection operators $\Sigma(\theta)$

$$R(\theta) = \begin{pmatrix} \cos\theta & \sin\theta \\ -\sin\theta & \cos\theta \end{pmatrix} \qquad \Sigma(\theta) = \begin{pmatrix} \cos\theta & \sin\theta \\ \sin\theta & -\cos\theta \end{pmatrix} \tag{42}$$

The basis functions corresponding to E_n are the pairs $[\cos n\varphi, \sin n\varphi]$, φ being the polar coordinate on the k_x-k_y plane. These functions have n nodal lines each. The spatially even representations (A_1 and E_{2m}) correspond to singlet superconductivity and the odd representations (A_2 and E_{2m+1}) to triplet superconductivity. The representations $n = 0, 1, 2, \ldots$ are traditionally labeled s, p, d, f, g, etc, like the orbital quantum number in atomic physics. The gap functions in many point groups are labeled likewise, according to the number of nodal lines (e.g., C_{4v} above).

4 Multi-band superconductors

4.1 Band vs orbital basis

Let g denote an element of the point group G. In the absence of SO coupling, its effect on the annihilation operator $c_{\mathbf{r},m,\sigma}$ (Wannier basis) is the following

$$c_{\mathbf{r},m,\sigma} \to c'_{\mathbf{r},m,\sigma} = \sum_{m'} U_{mm'}(g)\, c_{g\mathbf{r},m',\sigma} \tag{43}$$

where $g\mathbf{r}$ is the mapping of site $\mathbf{r}$ under g and $U(g)$ constitutes a N_b-dimensional representation of the group G acting on orbital space. The matrix $U(g)$ is independent of $\mathbf{r}$ by translation invariance, and therefore the same transformation applies in the orbital basis

$$c_{m,\sigma}(\mathbf{k}) \to c'_{m,\sigma}(\mathbf{k}) = \sum_{m'} U_{mm'}(g)\, c_{m',\sigma}(g\mathbf{k})\,. \tag{44}$$

The same symmetry operation is expressed differently in the band basis. From Eq. (6), we find

$$d'_a(\mathbf{k}) = \sum_b \tilde{U}_{ab}(g,\mathbf{k})\, d_b(g\mathbf{k}) \tag{45}$$

where $g\mathbf{k}$ is the image of $\mathbf{k}$ under g and

$$\tilde{U}_{ab}(g,\mathbf{k}) = \sum_{m,m'} V_{a,m}(\mathbf{k})\, V^*_{b,m'}(\mathbf{k})\, U_{mm'}(g)\,. \tag{46}$$

The matrix $\tilde{U}_{ab}(g,\mathbf{k})$ depends on $\mathbf{k}$. Hence the orbital basis makes the group-theoretical analysis much simpler, compared to the band basis, as mentioned above. This is therefore the basis we will use in the following. The physical relevance of the two bases is discussed in Sect. 6.

4.2 The case of Sr_2RuO_4

This formalism for inter-orbital superconductivity can be applied to a model for Sr_2RuO_4 [7–9], summarized in Fig. 3. It is defined on a square lattice, with three Ru t_{2g} orbitals per site. In the figure, these three orbitals (d_{yz}, d_{xz} and d_{xy}) have been drawn on separate planes for clarity. The main hopping terms are illustrated in the figure, but are not so important for our purpose, except for their defining a noninteracting Hamiltonian with D_{4h} symmetry (see Table 3). We use the group D_{4h} even though the model is two-dimensional because (i) we want to cover a three-dimensional extension of the model with weak inter-plane coupling and (ii) the orbitals themselves transform in a nontrivial way under the reflection σ_z across the xy plane. The treatment summarized here is taken from [10].

The group D_{4h} can be generated by successive applications of the elements C_4, σ_x, and σ_z. From Fig. 3 it is obvious that these operations have the following effect on the three orbitals

$$U(C_4) = \begin{pmatrix} 0 & 1 & 0 \\ -1 & 0 & 0 \\ 0 & 0 & -1 \end{pmatrix} \qquad U(\sigma_x) = \begin{pmatrix} 1 & 0 & 0 \\ 0 & -1 & 0 \\ 0 & 0 & -1 \end{pmatrix} \qquad U(\sigma_z) = \begin{pmatrix} -1 & 0 & 0 \\ 0 & -1 & 0 \\ 0 & 0 & 1 \end{pmatrix} \tag{47}$$

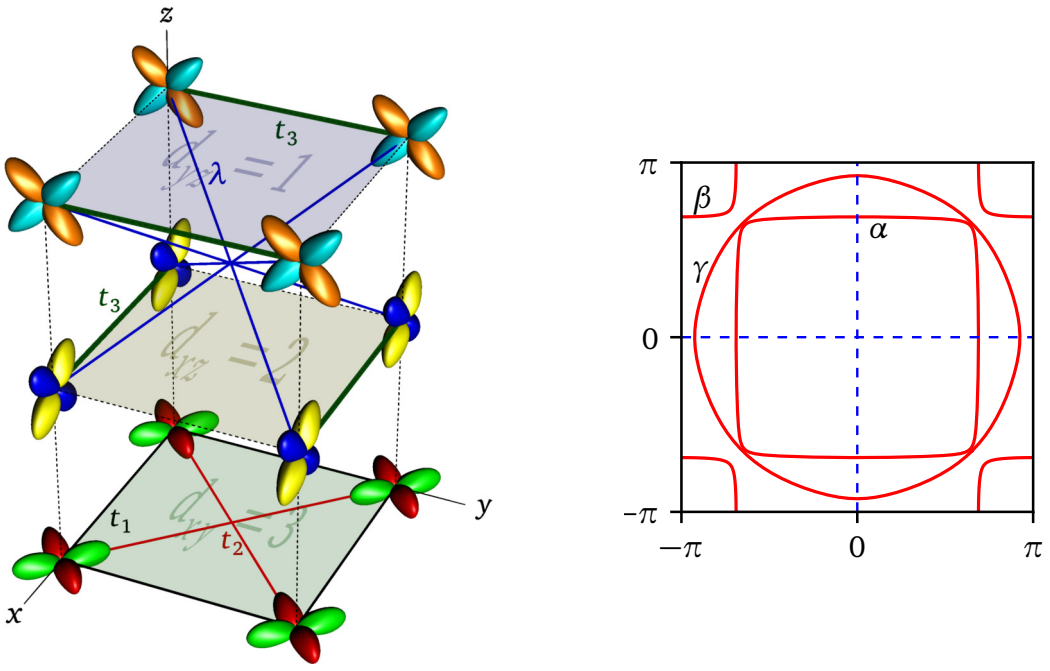

Fig. 3: *Left panel: Schematic view of the SRO unit cell. The three orbitals have been vertically separated for clarity (the model considered is purely two-dimensional). The labels 1,2,3 correspond, respectively, to the d_{yz}, d_{xz}, and d_{xy} orbitals. The different hopping terms ($t_{1,2,3}$ and λ) are illustrated. Right panel: Fermi surface of Sr_2RuO_4 in the simple model illustrated on the left. The α and β bands are a mixture of the d_{xz} and d_{yz} orbitals, whereas the γ band is pure d_{xy}.*

These matrices form, with the rest of the elements of the group, a reducible 3-dimensional representation. From the characters one infers it to be $B_{2g} \oplus E_g$.
The orbital part of the pairing function can be expanded in terms of the following 3×3 matrices

$$\hat{\mathbf{a}}_x = \begin{pmatrix} 1 & 0 & 0 \\ 0 & 0 & 0 \\ 0 & 0 & 0 \end{pmatrix} \quad \hat{\mathbf{b}}_x = \begin{pmatrix} 0 & 0 & 0 \\ 0 & 0 & 1 \\ 0 & 1 & 0 \end{pmatrix} \quad \hat{\mathbf{c}}_x = \begin{pmatrix} 0 & 0 & 0 \\ 0 & 0 & 1 \\ 0 & -1 & 0 \end{pmatrix}$$

$$\hat{\mathbf{a}}_y = \begin{pmatrix} 0 & 0 & 0 \\ 0 & 1 & 0 \\ 0 & 0 & 0 \end{pmatrix} \quad \hat{\mathbf{b}}_y = \begin{pmatrix} 0 & 0 & 1 \\ 0 & 0 & 0 \\ 1 & 0 & 0 \end{pmatrix} \quad \hat{\mathbf{c}}_y = \begin{pmatrix} 0 & 0 & 1 \\ 0 & 0 & 0 \\ -1 & 0 & 0 \end{pmatrix} \tag{48}$$

$$\hat{\mathbf{a}}_z = \begin{pmatrix} 0 & 0 & 0 \\ 0 & 0 & 0 \\ 0 & 0 & 1 \end{pmatrix} \quad \hat{\mathbf{b}}_z = \begin{pmatrix} 0 & 1 & 0 \\ 1 & 0 & 0 \\ 0 & 0 & 0 \end{pmatrix} \quad \hat{\mathbf{c}}_z = \begin{pmatrix} 0 & 1 & 0 \\ -1 & 0 & 0 \\ 0 & 0 & 0 \end{pmatrix}$$

A general basis state for pairing in orbital space may then be expressed via three vectors $\mathbf{a}$, $\mathbf{b}$,

and $\mathbf{c}$ as

$$O_{mn} = \mathbf{a} \cdot \hat{\mathbf{a}}_{mn} + \mathbf{b} \cdot \hat{\mathbf{b}}_{mn} + \mathbf{c} \cdot \hat{\mathbf{c}}_{mn} \,. \tag{49}$$

The orbital part $O_{mm'}$ transforms as follows under a group operation g

$$O_{mm'} \to \sum_{n,n'} U_{mn}(g)\, U_{m'n'}(g)\, O_{nn'} \quad \text{or} \quad O \to U(g)\, O\, U^T(g) \,. \tag{50}$$

These 9 matrices (48) belong to a 9-dimensional representation of D_{4h}, obtained by taking the tensor products of the matrices (47) with themselves. The content of this representation can easily be shown to be $2A_{1g} \oplus B_{1g} \oplus B_{2g} \oplus E_g$ for symmetric states (spin singlets), and $A_{2g} + E_g$ for antisymmetric states (spin triplets). Again, this classification ignores the spatial part (or rather, supposes that it is invariant).

We can combine these orbital gap functions with spatial functions classified according to Table 3, by taking tensor products and reducing them to irreps using projection operators. Ref. [10] provides tables of singlet and triplet states belonging to each representation, with and without inter-orbital pairing. These tables are too lengthy to reproduce here, but let us consider two examples:

1. Singlet pairing may occur in the constant ($\mathbf{k}$-independent) $\hat{\mathbf{b}}_z$ state, which belongs to the B_{2g} representation of D_{4h}, and is basically pairing between electrons belonging to the d_{xz} and d_{yz} orbitals. This admixture of orbitals occurs in bands α and β of Sr_2RuO_4 (see right panel of Fig. 3), mostly along the diagonals of the Brillouin zone. This pairing would lead to nodes at the intersection of the α and β branches of the Fermi surface with the k_x and k_y axes (dashed lines on the Fig. 3), as the pairing changes sign under C_4 rotations (from Table 3). It therefore has d-wave character.
2. The E_{2u} representation contains many simple triplet gap functions, including $\sin k_z[\hat{\mathbf{b}}_x, \hat{\mathbf{b}}_y]$ and $\hat{\mathbf{a}}_z[\sin k_x, \sin k_y]$. This corresponds to what is usually called $p \pm ip$ superconductivity in this context. The $\hat{\mathbf{a}}_z[\sin k_x, \sin k_y]$ function involves only the γ band and would vanish at two points along the γ band Fermi surface (hence the p-wave epithet). The $\sin k_z[\hat{\mathbf{b}}_x, \hat{\mathbf{b}}_y]$ function vanishes at the equator ($k_z = 0$) and involves admixtures of the d_{xy} and d_{xz} bands ($\hat{\mathbf{b}}_x$) and of the d_{xy} and d_{yz} bands ($\hat{\mathbf{b}}_y$).

4.3 Are nodes imposed by symmetry?

In the one-band case, a symmetry-imposed node occurs in a pairing function that vanishes in some direction because it is odd under certain symmetry operations in the irreducible representation it belongs to. For instance, in the representation B_{1g} of D_{4h} or C_{4v}, the pairing function must be odd under a diagonal reflection σ_d, and must accordingly vanish along the diagonals, which is indeed the case of the standard d-wave function $\cos k_x - \cos k_y$. The pairing function being a scalar, its zeros correspond to nodes. The one-band case is simple because translation invariance allows us to express the order parameter as a scalar function of the wave vector $\mathbf{k}$.

However, strictly speaking, the notion of symmetry-imposed nodes does not make sense in the case of multi-orbital models, with or without spin-orbit coupling.

In a multi-orbital model, the pairing function is a multi-component object: a matrix. That matrix may be odd under a certain symmetry operation, but that does not imply that it must vanish at a fixed point of that operation in momentum space, because the odd character can reside in the orbital part instead of the spatial part. Indeed, the odd character translates into the following transformation property for the pairing function, in the case of, say, the reflection σ_d

$$\Delta_\nu(k_x,k_y,k_z) \to \Delta'_\nu(k_x,k_y,k_z) = \mathcal{U}(\sigma_d)_{\nu\nu'}\,\Delta_{\nu'}(k_y,k_x,k_z) \tag{51}$$

where the index ν labels basis vectors in orbital space (i.e., not the same as the original orbital basis with indices m, m') and $\mathcal{U}$ the orbital part of the representation. In the B_{1g} representation, we therefore have the condition $\Delta'_\nu(k_x,k_y,k_z) = -\Delta_\nu(k_x,k_y,k_z)$, or $[\mathcal{U}(\sigma_d)\boldsymbol{\Delta}(k_y,k_x,k_z)]_\nu = -\Delta_\nu(k_x,k_y,k_z)$, which translates into $[\mathcal{U}(\sigma_d)\boldsymbol{\Delta}(k_x,k_x,k_z)]_\nu = -\Delta_\nu(k_x,k_x,k_z)$ along the diagonal. In the single-orbital case, $\mathcal{U}{=}1$ and that condition implies $\Delta(k_x,k_x,k_z) = 0$. In the multi-orbital case, the orbital part $\boldsymbol{\Delta}$ of the pairing function may be an eigenvector of $\mathcal{U}$ with eigenvalue -1, and this imposes no condition at all on $\Delta_\nu(k_x,k_x,k_z)$. For instance, in our model for Sr_2RuO_4, the pairing function $\hat{\mathbf{a}}_x{-}\hat{\mathbf{a}}_y$, which is wave vector independent, belongs to B_{1g}. The matrix $\mathcal{U}$ in that case exchanges a_x and a_y and is equivalent to -1 in orbital space, which leaves an even (here constant) spatial part.

Another example: the inter-orbital pairing function $\hat{\mathbf{c}}_x \sin k_x + \hat{\mathbf{c}}_y \sin k_y$ belongs to A_{1u} and describes a singlet state that is odd under the reflection σ_z across the xy-plane. Indeed, under this reflection, the orbitals d_{xz} and d_{yz} change sign, and so, according to Eq. (50), do the components $\hat{\mathbf{c}}_x$ and $\hat{\mathbf{c}}_y$, while the functions $\sin k_x$ and $\sin k_y$ are unaffected. The matrix-valued pairing function then takes the form

$$\boldsymbol{\Delta}(k_x,k_y,k_z) = \begin{pmatrix} 0 & 0 & \sin k_y \\ 0 & 0 & \sin k_x \\ -\sin k_y & -\sin k_x & 0 \end{pmatrix} \tag{52}$$

(we ignore spin, which is in a singlet state in this example). The transformation law of that pairing function under σ_z is $\boldsymbol{\Delta} \to \boldsymbol{\Delta}' = U(\sigma_z)\,\boldsymbol{\Delta}\,U^T(\sigma_z)$, where $U(\sigma_z)$ is given in Eq. (47). Therefore $\boldsymbol{\Delta}' = -\boldsymbol{\Delta}$, as it should be in representation A_{1u}. Accordingly, while that pairing function may have nodes, e.g., as a function of k_z, their precise shape or location is not imposed by symmetry.

4.4 The graphene lattice

As a different type of multiband system, let us consider the graphene lattice. It can be seen as a triangular Bravais lattice of elementary hexagons with a basis of two sites (A and B) and lattice basis vectors $\mathbf{e}_1$ and $\mathbf{e}_2$; see Fig. 4.

If the two atoms on sublattices A and B are identical, the point group of the lattice is C_{6v}, when considered from the middle of a hexagonal plaquette. This group has 12 elements in 6 conjugacy classes. All elements may be generated by a $\pi/3$ rotation C_6 and a reflexion σ_v with respect to the horizontal axis of Fig. 4. The character table is shown in Table 4. The particularity

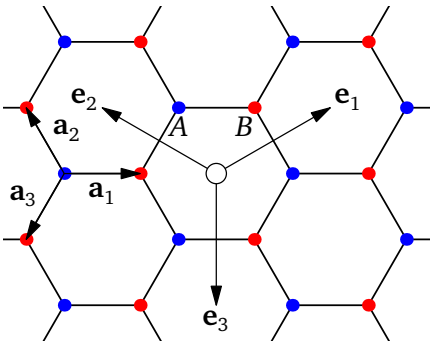

Fig. 4: *The graphene lattice, with two sites (A and B) per unit cell. The lattice basis vectors $\mathbf{e}_{1,2}$ are shown, as well as the elementary bond vectors $\mathbf{a}_i$. The lattice vector $\mathbf{e}_3$ is conveniently defined as $\mathbf{e}_3 = -\mathbf{e}_1 - \mathbf{e}_2$.*

Table 4: *Character table of C_{6v}, with a list of the nearest-neighbor pairing functions for each irrep, expressed as function of $k_i = \mathbf{k}\cdot\mathbf{e}_i$. Irreps A_2 and B_2 need longer-range pairing to appear.*

	e	$2C_6$	$2C_3$	C_2	$3\sigma_v$	$3\sigma_d$	basis functions
A_1	1	1	1	1	1	1	$1\ ,\ \cos k_1 + \cos k_2 + \cos k_3$
A_2	1	1	1	1	-1	-1	
B_1	1	-1	1	-1	1	-1	$\sin k_1 + \sin k_2 + \sin k_3$
B_2	1	-1	1	-1	-1	1	
E_1	2	1	-1	-2	0	0	$[\sin k_1 - \sin k_2\ ,\ \sin k_1 - \sin k_3]$
E_2	2	-1	-1	2	0	0	$[\cos k_1 - \cos k_2\ ,\ \cos k_1 - \cos k_3]$

of this system is that the group transformations do not leave the unit cell intact (a unit cell may be defined as a pair of neighboring A and B sites, and the ambiguity in defining these pairs breaks the C_{6v} symmetry). This makes the separation (13) into orbital and momentum variables awkward. In this case it is therefore preferable to work directly in real space and to incorporate orbital and Wannier indices into a single spatial index $\mathbf{r}$, belonging to the A or B sublattices (the sites $\mathbf{r}$ therefore do not form a Bravais lattice). If we ignore the spin part, the pairing amplitude is then simply a function $\Delta_{\mathbf{r},\mathbf{r}'}$. Translation invariance imposes the condition $\Delta_{\mathbf{r}+\mathbf{e}_i,\mathbf{r}'+\mathbf{e}_i} = \Delta_{\mathbf{r},\mathbf{r}'}$. We will define $\mathbf{b} = \mathbf{r}' - \mathbf{r}$ as the bond vector, and it turns out that this vector uniquely characterizes the pairing amplitude, even though the set of $\mathbf{b}$ vectors does not form a Bravais lattice. We can therefore express the pairing function as $\Delta_{\mathbf{b}}$ and the action of a group element $g \in G$ on such a function may be represented as

$$\Delta_{\mathbf{b}} \longrightarrow \sum_{\mathbf{b}'} R_{\mathbf{b},\mathbf{b}'}(g)\Delta_{\mathbf{b}'} \tag{53}$$

Because the point group preserves the norm of $\mathbf{b}$, we can restrict our analysis to sets of bond vectors of the same length.

The simplest possibility beyond the trivial one-site pairing $\mathbf{b} = 0$ is nearest-neighbor pairing, with $\mathbf{b} = \pm\mathbf{a}_i$ ($i = 1, 2, 3$) where the elementary bond vectors $\mathbf{a}_i$ are defined on Fig. 4. It is also

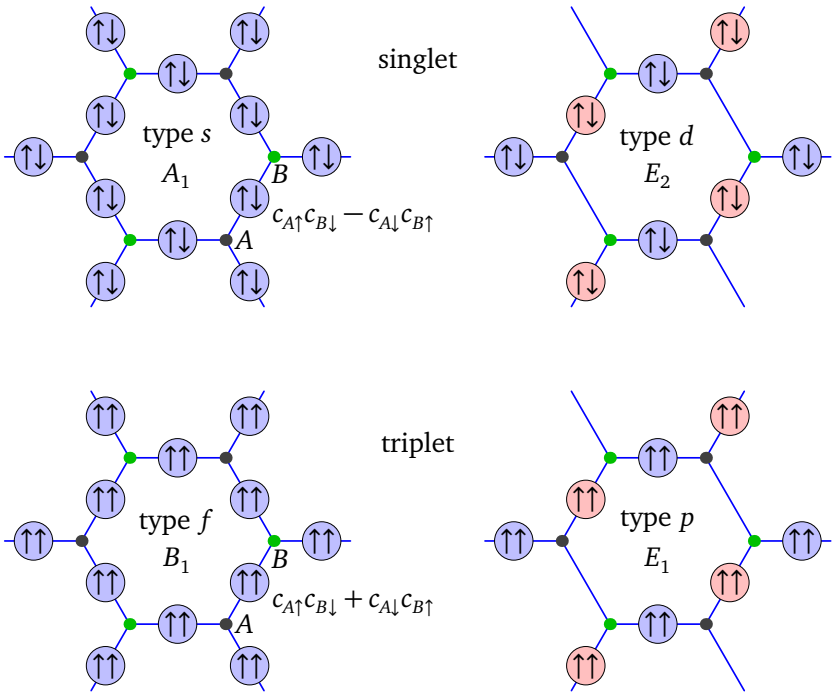

Fig. 5: *The simplest pairing functions on the graphene lattice. Each pairing (singlet or triplet) lives on nearest-neighbor bonds. The color (blue = +, red = −) represents the sign of the pairing amplitude. Note that rotating by $\pi/3$ exchanges the A and B sublattices, and therefore changes the sign of the triplet amplitude $c_{A\uparrow}c_{B\downarrow} + c_{A\downarrow}c_{B\uparrow}$, which justifies, in particular, the f-wave label.*

the predominant pairing to expect in a strongly correlated model with a large on-site repulsion U. These six bonds are associated with a multiplet of six pairing functions $\Delta_{\mathbf{b}} = \delta_{\mathbf{b},\pm\mathbf{a}_i}$ (i=1, . . . , 3). The explicit representation matrices $R(g)$ are simple to construct, and so are the projection operators $P^{(\mu)}$ associated with the 6 irreps of C_{6v}.

The mathematics are the same as for a one-band model defined on a triangular lattice. In that case, the pairing functions are written, in the usual language, in the last column of Table 4, as a function of the wavevector components $k_i = \mathbf{k} \cdot \mathbf{e}_i$. There is a simple correspondence between these functions and the graphene pairing functions $\Delta_{\mathbf{b}}$:

$$e^{\pm ik_j} \longleftrightarrow \delta_{\mathbf{b},\pm\mathbf{a}_j} \tag{54}$$

For instance, the nearest-neighbor graphene pairing function belonging to the B_1 representation would be

$$\Delta_{\mathbf{b}}(B_1) = \delta_{\mathbf{b},\mathbf{a}_1} - \delta_{\mathbf{b},-\mathbf{a}_1} + \delta_{\mathbf{b},\mathbf{a}_2} - \delta_{\mathbf{b},-\mathbf{a}_2} + \delta_{\mathbf{b},\mathbf{a}_3} - \delta_{\mathbf{b},-\mathbf{a}_3} \ . \tag{55}$$

The functions associated with A_1 and E_2 are even under a spatial inversion (here equivalent to the π-rotation C_2), and are therefore appropriate for singlet pairing, whereas those associated with B_1 and E_1 are odd and are appropriate for triplet pairing. These possibilities are illustrated schematically in Fig. 5, taken from Ref. [11]. Based on the number of times the bond amplitude changes sign as a function of angle, representations A_1, B_1, E_1, and E_2 can be labeled as s, f, p, and d-wave, respectively.

5 Superconductors with spin-orbit interaction

5.1 One-band model with Rashba coupling

Let us consider a simple one-band model on a square lattice with a Rashba SO coupling

$$H_0 = \sum_{\mathbf{k}} C_{\mathbf{k}}^\dagger \Big(\varepsilon(\mathbf{k}) + \kappa\big(\tau_y \sin k_x - \tau_x \sin k_y\big)\Big) C_{\mathbf{k}} \tag{56}$$

where $C_{\mathbf{k}} = (c_{\mathbf{k}\uparrow}, c_{\mathbf{k}\downarrow})$. Assuming nearest-neighbor hopping t, the dispersion relation is $\varepsilon(\mathbf{k}) = -2t(\cos k_x + \cos k_y)$. This model has C_{4v} symmetry and, without the SO interaction, the gap functions are classified in accordance with Sect. 3.1. Because of the κ term, under a point group transformation g, both the orbital and spin indices are affected

$$c_{\mathbf{r},\sigma} \to c'_{\mathbf{r},\sigma} = \sum_{\sigma'} S_{\sigma\sigma'}(g)\, c_{g\mathbf{r},\sigma'} \tag{57}$$

where $g\mathbf{r}$ is the image of $\mathbf{r}$ by g. Under the $\pi/2$ rotation C_4, we can apply the usual expression for $SU(2)$ spin rotations and

$$S(C_4) = \cos\frac{\pi}{4} + i\sigma_z \sin\frac{\pi}{4} = \frac{1}{\sqrt{2}} \begin{pmatrix} 1+i & 0 \\ 0 & 1-i \end{pmatrix} \tag{58}$$

As for the reflection σ_x, it maps (k_x, k_y) into $(-k_x, k_y)$ and therefore should have the following effect

$$S^\dagger\, \tau_x\, S = \tau_x \qquad S^\dagger\, \tau_y\, S = -\tau_y\ . \tag{59}$$

A solution is to set $S(\sigma_x) = i\tau_x$.

The matrices $S(g)$ generated from $S(C_4)$ and $S(\sigma_x)$ from a *spin representation* of C_{4v}. Such representations are not listed in the character table 2. In particular, within such a spin representation, the fourth power $S(C_4)^4$ is -1, not 1.[6] The tensor product of this spin representation with itself yields symmetric and antisymmetric unitary representations, characterized by the $\mathbf{d}$-vector basis (15), namely:

1. A_1, with gap function $\hat{\mathbf{d}}_0$ (singlet)
2. A_2, with gap function $\hat{\mathbf{d}}_z$ (triplet).
3. E, with gap function $[\hat{\mathbf{d}}_x, \hat{\mathbf{d}}_y]$ (triplet).

(the projection operator technique illustrated in Sect. 3.1 can be applied equally well to this situation.) The first (A_1) is antisymmetric under exchange of the quantum numbers of the two electrons, the other two (A_2 and E) are symmetric. These unitary representations can in turn be tensored with orbital and spatial representations, provided the overall pairing function is antisymmetric. Table 5 lists the simplest gap functions coming from this exercise. In particular, the usual singlet d-wave function belonging to B_1 would generically have a small triplet admixture with the function $\hat{\mathbf{d}}_x \sin k_y + \hat{\mathbf{d}}_y \sin k_x$. Would this affect the nodes? In general yes, if the strength of the Rashba SO coupling κ is large enough.

[6] This is the analog for point groups of the properties of spin rotations in the continuum. In some sense, such spin representations are the "square roots" of the usual representations: their tensor products with themselves are unitary representations. They are *projective* (or *ray*) representations.

Table 5: *On-site and first-neighbor gap functions for a square lattice with C_{4v} symmetry and spin-orbit coupling.*

Irrep	Basis functions
A_1	$\hat{\mathbf{d}}_0 \quad , \ (\hat{\mathbf{d}}_x \sin k_y - \hat{\mathbf{d}}_y \sin k_x)$
A_2	$\hat{\mathbf{d}}_x \sin k_x + \hat{\mathbf{d}}_y \sin k_y$
B_1	$\hat{\mathbf{d}}_0(\cos k_x - \cos k_y) \ , \ \hat{\mathbf{d}}_x \sin k_y + \hat{\mathbf{d}}_y \sin k_x$
B_2	$\hat{\mathbf{d}}_x \sin k_x - \hat{\mathbf{d}}_y \sin k_y$
E_1	$\hat{\mathbf{d}}_z[\sin k_x, \ \sin k_y]$

5.2 Sr_2RuO_4

The case of Sr_2RuO_4 provides us with a more complex application of the above ideas. The spin-orbit term appropriate for Sr_2RuO_4 is

$$H_{\rm SO} = i\,\frac{\kappa}{2} \sum_{\mathbf{r}} \sum_{l,m,n} \varepsilon_{lmn}\ c^\dagger_{\mathbf{r},l,\sigma}\, c_{\mathbf{r},m,\sigma'}\, \tau_{n,\sigma\sigma'} \tag{60}$$

where τ_n is the $n^{\rm th}$ Pauli matrix, acting on spin indices. Under a general D_{4h} transformation, the spin-orbit term becomes

$$i\frac{\kappa}{2} \sum_{\mathbf{r}} \sum_{l,m,n} \varepsilon_{l'm'n}\, U^*_{l'l}\, U_{m'm}\ c^\dagger_{\mathbf{r},l,\sigma}\, c_{\mathbf{r},m,\sigma'}\ S^*_{\alpha\sigma}\, S_{\alpha'\sigma'}\, \tau_{n,\alpha\alpha'}\ . \tag{61}$$

In order for the spin-orbit term to be invariant, the spin rotation matrix S must belong to a spin representation of the group such that

$$\begin{aligned} S^\dagger\, \tau_n\, S &= R_{nn'}\, \tau_{n'} \\ \varepsilon_{l'm'n}\, U^*_{l'l}\, U_{m'm} &= R^{-1}_{nn'}\, \varepsilon_{lmn'} \end{aligned} \tag{62}$$

It can be shown that, for the generators of D_{4h},

$$S(C_4) = \frac{1}{\sqrt{2}} \begin{pmatrix} 1{+}i & 0 \\ 0 & 1{-}i \end{pmatrix} \qquad S(\sigma_x) = \begin{pmatrix} 0 & i \\ i & 0 \end{pmatrix} \qquad S(\sigma_z) = \begin{pmatrix} i & 0 \\ 0 & -i \end{pmatrix} \tag{63}$$

We then proceed like in the previous section: we build tensor product representations for pairs of electrons, and tensor those with irreps for the spatial part of the gap function. The resulting gap functions are numerous. Singlet and triplet gap functions can coexist in the same irrep, and new ones arise. For instance, in the B_{1g} (a.k.a. d-wave) representation, we find the singlet gap function $\hat{\mathbf{a}}_z \hat{\mathbf{d}}_0(\cos k_x - \cos k_y)$ and the triplet gap function $\hat{\mathbf{c}}_z \hat{\mathbf{d}}_z(\cos k_x - \cos k_y)$. Since spin is not conserved separately, not only do singlet and triplet components coexist in the same irrep, but different directions of the $\mathbf{d}$-vector can also coexist. For instance, the function $\hat{\mathbf{c}}_x \hat{\mathbf{d}}_x + \hat{\mathbf{c}}_y \hat{\mathbf{d}}_y$ also belongs to the same representation. Details can be found in [10].

6 Final remarks

Group theory is a powerful tool for classifying superconducting pairing states, especially in the presence of many orbitals. However, it must be kept in mind that it makes no *dynamical* predictions. It does not inform us on which of the gap functions is preferred on the basis of a particular model; other tools are necessary. We can, however, venture in the following general considerations in the presence of many bands: For weakly correlated materials, the band description is more natural than the Wannier (orbital) description. We would then expect pairing to occur at weak energies, i.e., for wave vectors close to the Fermi surface. Since pairing occurs between opposite wave vectors, this nearly restricts it to occur within each band separately (assuming time reversal symmetry, i.e., that $-\mathbf{k}$ belongs to the Fermi surface if $\mathbf{k}$ does). What appears as inter-orbital pairing might then be merely intra-band pairing.
On the other hand, for strongly correlated materials, pairing may occur on a wider energy scale, in which case the relation to Fermi surfaces is less important and the Wannier description is more appropriate. In that case, we also expect pairing to have a shorter range and the short-range pairing functions found in the general method exposed here are more relevant. The case of Sr_2RuO_4 is particularly interesting: that material is undoubtedly strongly correlated. At the same time, its three bands (α, β, γ) have Fermi surfaces that almost touch along the diagonals (Fig. 3). In an intermediate-coupling situation, inter-orbital pairing would therefore be expected to occur in the vicinity of these diagonal areas where the three Fermi surfaces almost meet.

Acknowledgments

The author thanks M. Bélanger for critical reading of the manuscript. This work was supported by the Natural Sciences and Engineering Research Council of Canada (NSERC) under grant RGPIN-2015-05598.

References

[1] P.W. Anderson, Phys. Rev. **112**, 1900 (1958)

[2] N. Marzari, A.A. Mostofi, J.R. Yates, I. Souza, and D. Vanderbilt, Rev. Mod. Phys. **84**, 1419 (2012)

[3] B. Roy and I.F. Herbut, Phys. Rev. B **82**, 35429 (2010)

[4] M. Hamermesh: *Group Theory and Its Application to Physical Problems* (Dover publications, 1989)

[5] A. Zee: *Group Theory in a Nutshell for Physicists* (Princeton University Press, 2016)

[6] J.F. Annett, Advances in Physics **39**, 83 (1990)

[7] C. Bergemann, A.P. Mackenzie, S.R. Julian, D. Forsythe, and E. Ohmichi, Advances in Physics **52**, 639 (2003)

[8] C. Noce and T. Xiang, Physica C: Superconductivity **282-287**, 1713 (1997)

[9] Q.H. Wang, C. Platt, Y. Yang, C. Honerkamp, F.C. Zhang, W. Hanke, T.M. Rice and R. Thomale, EPL (Europhysics Letters) **104**, 17013 (2013)

[10] S.O. Kaba and D. Sénéchal, Phys. Rev. B **100**, 214507 (2019) See also the erratum: Phys. Rev. B **101**, 209901 (2020)

[11] J.P.L. Faye, P. Sahebsara, and D. Sénéchal, Physical Review B **92**, 085121 (2015)

14 Linear Response and Electron-Phonon Coupling

Rolf Heid
Institute for Quantum Materials and Technologies
Karlsruhe Institute of Technology

Contents

E. Pavarini and E. Koch (eds.)
Topology, Entanglement, and Strong Correlations
Modeling and Simulation Vol. 10
Forschungszentrum Jülich, 2020, ISBN 978-3-95806-466-9
http://www.cond-mat.de/events/correl20

1 Introduction

Electron and phonon quasiparticles are the fundamental constituents of solids. Knowledge of their interaction provides deeper insight in many physical properties. In metals, the electron-phonon coupling (EPC) profoundly alters low-energy electronic excitations, and gives important contributions to transport and thermodynamic properties. Coupling to phonons creates naturally an attractive interaction among electronic quasiparticles, triggering eventually the occurrence of a superconducting state. Recent decades have seen the rise of powerful computational tools to calculate these fundamental properties from first principles. In particular, density functional theory (DFT) and its extensions have been very successful in providing a deeper understanding of materials properties.

The purpose of this lecture is to introduce the modern linear-response technique within the DFT framework, which gives access to EPC properties on a microscopic level, and to establish the connections to derived physical quantities. In Section 2, we will present an overview of the linear-response scheme, which is called density functional perturbation theory (DFPT). In Section 3, this approach is applied to the case of a crystalline solid, and we show how EPC properties can be calculated. Applications to various physical observables related to the EPC will be presented in Section 4. Finally, in Section 5, we will take a brief look at more complex extensions of DFT and how they can be used for an improved description of the EPC.

Throughout this Chapter, Rydberg atomic units $\hbar{=}2m_e{=}e^2/2{=}1$ as well as $k_B{=}1$ are used.

2 Linear response in density functional theory

In this Section, we will develop the machinery of the linear response in the context of density functional theory. The description will be kept rather general, but with having in mind to apply it to the case of a crystalline solid, which will be addressed in more detail in the following Section.

2.1 Adiabatic perturbations

There often exists an intimate relationship between physical observables and changes of ground state properties under perturbations. To be specific, let us consider interacting electrons moving in the potential of a periodic arrangement of atoms. In its ground state it has the energy E_0. This system can be perturbed in various ways. Examples are the displacement of an atom out of its equilibrium position δR, or a distortion of the crystal by applying a homogeneous strain η. Application of a homogeneous electric field, $\mathbf{E}$ is a further example.

In all these cases, the perturbation can be arbitrarily small. The electronic system reacts adiabatically, if it remains in the ground state under a small perturbation λ. The ground state energy becomes a function of λ: $E_0 = E_0(\lambda)$. Many physical quantities are then linked directly to derivatives of this function,

$$Q_n = \left.\frac{d^n E}{d\lambda^n}\right|_{\lambda\to 0} . \tag{1}$$

type of perturbation λ	order n	physical property Q
displacements of atoms	1	atomic force
$\delta\mathbf{R}$	2	force constants
	≥ 3	anharmonic force constants
homogeneous strain η	1	stress
	2	elastic constants
	≥ 3	higher order elastic constants
homogeneous electric field $\mathbf{E}$	1	dipole moment
	2	polarizability
$\delta\mathbf{R} + \eta$	2+1	Grüneisen parameter
$\delta\mathbf{R} + \mathbf{E}$	1+2	Raman scattering cross section

Table 1: *Examples of external perturbations and physical quantities connected to derivatives of the ground-state energy.*

Table 1 lists examples of such relationships between perturbations and physical observables. Some physical quantities are connected to mixed derivatives of two different perturbations. A well known example is the Raman scattering cross section, which involves both atomic displacement and homogeneous electric field as perturbations.
Density functional theory is ideally suited to exploit this relationship between physical observables and derivatives of the ground-state energy, because it targets ground-state properties by design.

2.2 Basics of density functional theory

The foundations of density functional theory (DFT) have been laid in the seminal works by Hohenberg, Kohn, and Sham [1,2] in the mid 60's, and are outlined in numerous reviews [3–5]. Here we focus on the essential features which we need later.
Hohenberg and Kohn [1] proved, that the ground-state energy of a system of interacting electrons moving in an external potential $v_{\text{ext}}(\mathbf{r})$ is obtained by minimizing the functional

$$E[n] = F[n] + \int d^3r \, v_{\text{ext}}(\mathbf{r}) \, n(\mathbf{r}) \tag{2}$$

with respect to the electron density $n(\mathbf{r})$. At its minimum, $n(\mathbf{r})$ is the true electron density of the interacting system. The functional $F[n]$ is universal, i.e., independent of the external potential.
An important step for practical applications was done by Kohn and Sham [2]. By using the minimum principle they showed that one can define a fictitious system of non-interacting electrons, which in its ground state possesses the same inhomogeneous density as the interacting system [2]. The energy functional is expressed as

$$F[n] = T_s[n] + E_H[n] + E_{XC}[n] \,, \tag{3}$$

where T_s represents the kinetic energy of the non-interacting electrons

$$T_s[n] = \sum_i f_i \int d^3r \, \psi_i^*(\mathbf{r}) \left(-\nabla^2\right) \psi_i(\mathbf{r}) \tag{4}$$

and $E_H[n]$ the Hartree energy

$$E_H[n] = \int d^3r \int d^3r' \, \frac{n(\mathbf{r})n(\mathbf{r}')}{|\mathbf{r}-\mathbf{r}'|} \, . \tag{5}$$

The complexity of the original many-body problem is transferred to the exchange-correlation energy E_{XC}. It is also a functional of the density, and has the important property that it is universal and thus does not depend on the external potential. However, it functional form is in general unknown.

For the non-interacting electron system, the density can be expressed in terms of the single-particle wave functions ψ_i,

$$n(\mathbf{r}) = \sum_i f_i \left|\psi_i(\mathbf{r})\right|^2 , \tag{6}$$

where f_i denotes the occupation number of the state ψ_i.

From the variational property of the energy functional, one can derive the single-particle equation (Kohn-Sham equation)

$$\Big(-\nabla^2 + v_{\text{eff}}(\mathbf{r}) \Big) \psi_i(\mathbf{r}) = \varepsilon_i \, \psi_i(\mathbf{r}) \, . \tag{7}$$

Here, ε_i denotes the energy of the single-particle state ψ_i. The effective potential $v_{\text{eff}}(\mathbf{r})$ is a functional of the density and given as a sum of the external potential and a screening potential

$$v_{\text{eff}}[n] = v_{\text{ext}} + v_{\text{scr}}[n] = v_{\text{ext}} + v_H[n] + v_{XC}[n] \, . \tag{8}$$

The latter is obtained as functional derivatives of the last two terms in the total energy functional (3). It consists of the Hartree potential

$$v_H(\mathbf{r})[n] = \frac{\delta E_H}{\delta n(\mathbf{r})} = \int d^3r' \, \frac{2n(\mathbf{r}')}{|\mathbf{r}-\mathbf{r}'|} \, , \tag{9}$$

which describes an average electrostatic potential originating from the other electrons, and the exchange-correlation potential $v_{XC}(\mathbf{r}) = \delta E_{XC}/\delta n(\mathbf{r})$.

Essentially, the original complex many-body problem is mapped onto a much simpler non-interacting electron system. The remaining task is to solve a set of single-particle equations (6)–(8), which has to be done in a self-consistent manner.

The big success of DFT partly rests on the empirical fact that already simple approximations to v_{XC} often give very accurate results. One ansatz is the local-density approximation (LDA)

$$v_{XC}^{LDA}(\mathbf{r}) = \left. \frac{d\big(n \, \varepsilon_{XC}^{\text{hom}}(n)\big)}{dn} \right|_{n=n(\mathbf{r})} , \tag{10}$$

where $\varepsilon_{XC}^{\text{hom}}(n)$ represents the exchange-correlation energy density of the homogeneous interacting electron gas. Another is the generalized-gradient approximation (GGA), where a dependence of v_{XC} on both local density and local gradient of the density is considered. For both types of local approximations, various parameterizations derived from analytical and numerical studies exist [4, 6–8].

2.3 Linear-response formulation

Here we show how the perturbative approach is set up within the DFT framework. We will first present some general considerations before applying them to the more specific cases in the next Section.

2.3.1 Energy derivatives

Let us consider a situation where the external potential $v_{\rm ext}$ depends on a set of adiabatic perturbation parameters $\Lambda = \{\lambda_a, a = 1, \ldots, p\}$. Each $v^\Lambda_{\rm ext}$ determines an electronic ground state with density $n^\Lambda(\mathbf{r})$, for which the energy functional $E^\Lambda[n] = F[n] + \int d^3r\, v^\Lambda_{\rm ext}(\mathbf{r}) n(\mathbf{r})$ is minimal

$$\left.\frac{\delta E^\Lambda[n]}{\delta n(\mathbf{r})}\right|_{n=n^\Lambda} = 0\,. \tag{11}$$

The ground-state energy is then given by

$$E^\Lambda_0 = E^\Lambda[n^\Lambda] = F[n^\Lambda] + \int d^3r\, n^\Lambda(\mathbf{r}) v^\Lambda_{ext}(\mathbf{r})\,, \tag{12}$$

which depends on the perturbation via the external potential and implicitly via the density. Its derivative then contains two contributions

$$\begin{aligned}\frac{\partial E^\Lambda_0}{\partial \lambda_a} &= \int d^3r\, n^\Lambda(\mathbf{r}) \frac{\partial v^\Lambda_{\rm ext}(\mathbf{r})}{\partial \lambda_a} + \int d^3r\, \left.\frac{\delta E^\Lambda[n]}{\delta n(\mathbf{r})}\right|_{n=n^\Lambda} \frac{\partial n^\Lambda(\mathbf{r})}{\partial \lambda_a} \\ &= \int d^3r\, n^\Lambda(\mathbf{r}) \frac{\partial v^\Lambda_{\rm ext}(\mathbf{r})}{\partial \lambda_a}\,. \end{aligned} \tag{13}$$

The second term vanishes because of Eq. (11). Thus the first derivative depends on the ground-state density only. This represents the DFT equivalent of the well known Hellmann-Feynman-Theorem [9].

Because Eq. (13) is valid for each finite Λ, one can take the second-order derivatives

$$\frac{\partial^2 E^\Lambda_0}{\partial \lambda_a \partial \lambda_b} = \int d^3r\, \frac{\partial n^\Lambda(\mathbf{r})}{\partial \lambda_b} \frac{\partial v^\Lambda_{\rm ext}(\mathbf{r})}{\partial \lambda_a} + \int d^3r\, n^\Lambda(\mathbf{r}) \frac{\partial^2 v^\Lambda_{\rm ext}(\mathbf{r})}{\partial \lambda_a \partial \lambda_b}\,. \tag{14}$$

Usually, the parametric dependence of $v^\Lambda_{\rm ext}$ on Λ is known, and its derivatives can be obtained easily. The hard part is to calculate the derivatives of the electron density. Eq. (14) demonstrates, that knowledge of the first-order variation of n is sufficient to access the second-order derivatives of the total energy. This aspect is very important for practical purposes, as one has to consider merely the linear response of the electron system.

As shown above, the first derivative of the energy depends solely of the unperturbed ground-state density, while second-order derivatives require knowledge of the density and its first-order derivatives. Both results are special cases of the so-called $(2n+1)$ theorem, which states that all derivatives of the total energy up to $(2n+1)$-th order with respect to the adiabatic perturbation can be calculated from the knowledge of all derivatives of the Kohn-Sham eigenstates and density up to n-th order. The proof given by Gonze *et al.* [10–12] essentially rests on the variational property of the energy functional.

2.3.2 Linear response within the Kohn-Sham scheme

Let us now discuss how the linear response of the density is actually calculated with the DFT framework. It involves standard perturbation techniques under the condition that the effective potential entering the Kohn-Sham equations depends on the ground-state density. To this end we are interested in the linear response of the Kohn-Sham system

$$\Big(-\nabla^2 + v_{\rm eff}(\mathbf{r})\Big)\psi_i(\mathbf{r}) = \varepsilon_i\psi_i(\mathbf{r})\,. \tag{15}$$

A small perturbation in the effective potential, $\delta v_{\rm eff}$, gives rise to a first-order variation of the single-particle wave functions

$$\delta\psi_i(\mathbf{r}) = \sum_{j(\neq i)} \frac{\langle j|\delta v_{\rm eff}|i\rangle}{\varepsilon_i - \varepsilon_j}\psi_j(\mathbf{r})\,. \tag{16}$$

Using a similar expression for $\delta\psi_i^*(\mathbf{r})$ gives

$$\delta n(\mathbf{r}) = \sum_i f_i\left(\psi_i^*(\mathbf{r})\,\delta\psi_i(\mathbf{r}) + \delta\psi_i^*(\mathbf{r})\,\psi_i(\mathbf{r})\right) = \sum_{i\neq j}\frac{f_i - f_j}{\varepsilon_i - \varepsilon_j}\,\langle j|\delta v_{\rm eff}|i\rangle\,\psi_i^*(\mathbf{r})\,\psi_j(\mathbf{r})\,. \tag{17}$$

On the other hand, δn contributes to the variation of the effective potential

$$\begin{aligned}
\delta v_{\rm eff}(\mathbf{r}) &= \delta v_{\rm ext}(\mathbf{r}) + \delta v_{\rm scr}(\mathbf{r}) = \delta v_{\rm ext}(\mathbf{r}) + \int d^3r'\, I(\mathbf{r},\mathbf{r}')\,\delta n(\mathbf{r}') \\
I(\mathbf{r},\mathbf{r}') &\equiv \frac{\delta v_{\rm scr}(\mathbf{r})}{\delta n(\mathbf{r}')} = \frac{\delta v_{\rm H}(\mathbf{r})}{\delta n(\mathbf{r}')} + \frac{\delta v_{\rm XC}(\mathbf{r})}{\delta n(\mathbf{r}')} = \frac{2}{|\mathbf{r}-\mathbf{r}'|} + \frac{\delta^2 E_{XC}}{\delta n(\mathbf{r})\,\delta n(\mathbf{r}')}\,.
\end{aligned} \tag{18}$$

Eqs. (17) and (18) must be solved self-consistently to obtain the first-order variation of the density.

It is instructive to establish a relationship between δn and $\delta v_{\rm ext}$. It can be derived by first writing the linear relationship (17) between δn and $\delta v_{\rm eff}$ more explicitly

$$\delta n(\mathbf{r}) = \int d^3r'\,\chi_0(\mathbf{r},\mathbf{r}')\,\delta v_{\rm eff}(\mathbf{r}') \tag{19}$$

$$\chi_0(\mathbf{r},\mathbf{r}') = \sum_{i\neq j}\frac{f_i - f_j}{\varepsilon_i - \varepsilon_j}\,\psi_i^*(\mathbf{r})\,\psi_j(\mathbf{r})\,\psi_j^*(\mathbf{r}')\,\psi_i(\mathbf{r}')\,. \tag{20}$$

Here, χ_0 represents the charge susceptibility of the non-interacting Kohn-Sham system. It is expressed solely by ground-state quantities [13]. Although obtained by perturbation theory, Eq. (20) is exact because the Kohn-Sham equations describe non-interacting electrons.

In combination with Eq. (18) this leads to

$$\delta v_{\rm eff} = \delta v_{\rm ext} + I\,\chi_0\,\delta v_{\rm eff}\,, \tag{21}$$

which can be solved for $\delta v_{\rm eff}$

$$\delta v_{\rm eff} = \big(1 - I\,\chi_0\big)^{-1}\delta v_{\rm ext} = \epsilon^{-1}\,\delta v_{\rm ext}\,, \tag{22}$$

where $\epsilon = 1 - I\,\chi_0$ denotes the static dielectric matrix and describes the screening of the "bare" perturbation. Using Eq. (19), one finally arrives at

$$\delta n = \chi_0\,\epsilon^{-1}\,\delta v_{\text{ext}}\,, \tag{23}$$

which in principle allows the calculation of the second derivative, Eq. (14).
The problem is now reduced to a calculation of ϵ^{-1}. Direct evaluation of Eq. (23) has several caveats. Firstly, it involves inversion of the matrix $\epsilon(\mathbf{r}, \mathbf{r}')$, which for periodic systems is most conveniently done in Fourier space. It is, however, often numerically expensive, because a proper convergence requires a large number of Fourier components, and the size of the matrix becomes prohibitively large. Secondly, to obtain χ_0 via Eq. (20) involves summation also over unoccupied orbitals, which either converge slowly, or are not accessible at all, as in band-structure methods employing minimal basis sets (e.g. LMTO).

2.3.3 Modern formulation: Density functional perturbation theory

An important progress has been achieved by a new formulation of the linear-response approach, which avoids some of the aforementioned problems of the dielectric matrix approach. It is called density functional perturbation theory (DFPT) and has been proposed independently by Zein *et al.* [14–16] and Baroni *et al.* [17, 18]. A concise description can be found in [19]. We will give a short outline for the case of a non-metallic system.
In the expression (17) for the first-order density variation, the prefactor $(f_i - f_j)/(\varepsilon_i - \varepsilon_j)$ restricts the sum to combinations where one state comes from the valence space and the other from the conduction space. Using time-reversal symmetry, this can be rewritten as

$$\delta n(\mathbf{r}) = 2 \sum_{vc} \frac{1}{\varepsilon_v - \varepsilon_c}\,\langle c|\delta v_{\text{eff}}|v\rangle\,\psi_v^*(\mathbf{r})\,\psi_c(\mathbf{r})\,. \tag{24}$$

Now one defines the quantity

$$|\Delta_v\rangle = \sum_c \frac{1}{\varepsilon_v - \varepsilon_c}|c\rangle\,\langle c|\delta v_{\text{eff}}|v\rangle\,, \tag{25}$$

which collects the summation over the conduction bands. The linear response of the density is rewritten as

$$\delta n(\mathbf{r}) = 2 \sum_v \psi_v^*(\mathbf{r})\Delta_v(\mathbf{r})\,. \tag{26}$$

To avoid an explicit evaluation of the sum in Δ_v, one makes use of the following property

$$\big(H_{KS} - \varepsilon_v\big)|\Delta_v\rangle = -\sum_c |c\rangle\langle c|\delta v_{\text{eff}}|v\rangle = -P_c\,\delta v_{\text{eff}}|v\rangle = (P_v - 1)\delta v_{\text{eff}}|v\rangle\,. \tag{27}$$

Here, $H_{KS} = -\nabla^2 + v_{\text{eff}}$ is the KS Hamiltonian. $P_c = \sum_c |c\rangle\langle c|$ denotes the projector onto the conduction space, and $P_v = 1 - P_c$ the projector onto the valence space. Eq. (27) represents a linear equation for Δ_v, where only valence-state quantities enter. Solution of this linear equation turns out to be numerically much more efficient than the expensive summation over conduction states.
In practice, Eqs. (26), (27) together with (18) define a set of self-consistent equations which is typically solved in an iterative manner.

3 Electron-phonon coupling

The most common application of DFT linear response approaches addresses the calculation of lattice dynamical properties, i.e., phonons, and their interaction with electrons. Here we discuss the underlying concepts.

3.1 General considerations

Our starting point will be the adiabatic or Born-Oppenheimer approximation. The coupling between electrons and ions is governed by the large ratio of the ionic mass (M) and electronic mass (m). It allows a partial decoupling of the dynamics of the ions and the electrons by a systematic expansion in terms of the small parameter $\kappa = (m/M)^{1/4}$ [20, 21]. To lowest order, the total wave function of the coupled electron-ion system can be written as a product $\Psi(\underline{\mathbf{r}}, \underline{\mathbf{R}}) = \chi(\underline{\mathbf{R}})\psi(\underline{\mathbf{r}}; \underline{\mathbf{R}})$, where $\underline{\mathbf{r}}$ and $\underline{\mathbf{R}}$ denote the sets of electron and ion coordinates, respectively. The electronic wave function obeys the equation

$$\left(T_e + V_{ee} + V_{e\text{-}i}(\underline{\mathbf{R}})\right) \psi_n(\underline{\mathbf{r}}; \underline{\mathbf{R}}) = E_n(\underline{\mathbf{R}})\, \psi_n(\underline{\mathbf{r}}; \underline{\mathbf{R}})\,, \tag{28}$$

where T_e and V_{ee} denote the kinetic energy and Coulomb interaction of the electron system, respectively. $V_{e\text{-}i}$ represents the electron-ion interaction. Through this term, wave functions and energies depend parametrically on the ionic positions $\underline{\mathbf{R}}$, and as a consequence also the electronic ground-state energy $E_0(\underline{\mathbf{R}})$. The latter enters the effective potential

$$\Omega(\underline{\mathbf{R}}) = V_{ii}(\underline{\mathbf{R}}) + E_0(\underline{\mathbf{R}})\,, \tag{29}$$

which governs the statics and dynamics of the ions in adiabatic approximation. Here $V_{ii}(\underline{\mathbf{R}})$ denotes is the ion-ion (Coulomb) interaction. Ω is the starting point of the microscopic theory of lattice dynamics (see review articles [22–24]). Dynamical properties are derived by a systematic expansion of Ω in atom displacements $\mathbf{u}$ around a chosen reference configuration, $\mathbf{R}_i = \mathbf{R}_i^0 + \mathbf{u}_i$, leading to

$$\Omega(\underline{\mathbf{R}}) = \Omega(\underline{\mathbf{R}}^0) + \sum_{i\alpha} \Phi_a(i) u_{i\alpha} + \frac{1}{2} \sum_{i\alpha j\beta} \Phi_{\alpha\beta}(i,j) u_{i\alpha} u_{j\beta} + \dots\,. \tag{30}$$

Greek indices α and β denote Cartesian coordinates, while i and j are atom indices. The term of first order is the negative of the force acting on an atom in the reference configuration, i.e., $F_{i\alpha} = -\frac{\partial \Omega}{\partial R_{i\alpha}}\Big|_0 = -\Phi_\alpha(i)$. It vanishes if one chooses as reference the equilibrium configuration, which minimizes Ω. The second-order coefficients given by

$$\Phi_{\alpha\beta}(i,j) = \left.\frac{\partial^2 \Omega}{\partial R_{i\alpha} \partial R_{j\beta}}\right|_0 \tag{31}$$

are the so-called force constants.

To get a coupling of the dynamics of electrons and ions, one has to go beyond the adiabatic approximation. It is described by an electron-ion vertex and appears to first order in κ. One can

show that it results in off-diagonal matrix elements among the electronic eigenstates ψ_n and has the form

$$\langle n|\delta_{\mathbf{R}}V|n'\rangle\,. \tag{32}$$

The operator $\delta_{\mathbf{R}}V$ stands for the linear change of the potential felt by the electrons under a displacement of an atom from its rest position.
In the following, we will show how these general considerations come to life within a density functional theory context. To this end, we will do this specifically for the very important case of a solid, i.e., a periodic arrangement of atoms.

3.2 Density functional perturbation theory

3.2.1 Phonon properties from DFPT

In adiabatic approximation, Eq. (28) describes interacting electrons moving in the potential determined by the ionic positions. This can be (approximately) solved by the DFT approach. We now consider the case of a solid, and assume that ions in their rest positions are sitting on a periodic lattice. KS eigenstates are now Bloch states $|\mathbf{k}\nu\rangle$ characterized by momentum $\mathbf{k}$ and band index ν, respectively, and are solutions of $H_{KS}|\mathbf{k}\nu\rangle = \varepsilon_{\mathbf{k}\nu}\,|\mathbf{k}\nu\rangle$.
In a periodic crystal, ions are characterized by two indices $i{=}(ls)$, which denote the unit cell (l) and the ions inside a unit cell (s), respectively. For periodic boundary conditions, the Fourier transform of the force constant matrix is related to the dynamical matrix

$$D_{s\alpha s'\beta}(\mathbf{q}) = \frac{1}{\sqrt{M_s M_{s'}}}\sum_l \Phi_{\alpha\beta}(ls,0s')\,e^{-i\mathbf{q}(\mathbf{R}^0_{ls}-\mathbf{R}^0_{0s'})}\,, \tag{33}$$

which determines the equation for the normal modes or phonons

$$\sum_{s'\beta} D_{s\alpha s'\beta}(\mathbf{q})\,\eta_{s'\beta}(\mathbf{q}j) = \omega^2_{\mathbf{q}j}\,\eta_{s\alpha}(\mathbf{q}j)\,. \tag{34}$$

$\omega_{\mathbf{q}j}$ and $\eta_{s\alpha}(\mathbf{q}j)$ denote the energy and polarization of the normal mode determined by the wavevector $\mathbf{q}$ and the branch index j.
According to Eqs. (29) and (30), the force constants consist of two contributions, the ion-ion and the electronic contribution. The ion-ion part stems from the Coulomb interaction of ions positioned on a periodic lattice and can be evaluated with standard methods (Ewald summation). The second part comes from the second derivative of the electronic energy and is thus accessible by density functional perturbation theory. To this end we consider periodic displacements of the ions from their equilibrium positions, $\mathbf{R}_{ls} = \mathbf{R}^0_{ls} + \mathbf{u}_{ls}$, of the form

$$u_{ls\alpha} = d_{s\alpha}\,e^{i\mathbf{q}\mathbf{R}^0_{ls}} + d^*_{s\alpha}\,e^{-i\mathbf{q}\mathbf{R}^0_{ls}}\,, \tag{35}$$

The complex amplitudes $d_{s\alpha}$ allow to vary the relative phase of the displacement. It is convenient to denote the corresponding derivatives by $\delta^{\mathbf{q}}_{s\alpha} \equiv \frac{\partial}{\partial d_{s\alpha}}$ and $\delta^{-\mathbf{q}}_{s'\beta} \equiv \frac{\partial}{\partial d^*_{s\alpha}}$. The electronic contribution to the dynamical matrix can be then written as a mixed derivative

$$D_{s\alpha s'\beta}(\mathbf{q}) = \frac{1}{\sqrt{M_s M_{s'}}}\,\delta^{\mathbf{q}}_{s\alpha}\delta^{-\mathbf{q}}_{s'\beta}E\bigg|_{\mathbf{u}=0}\,. \tag{36}$$

Commonly, the external potential is expressed as a superposition of atomic potentials v_s centered at the instantaneous positions of the ions

$$v_{\rm ext}(\mathbf{r}) = \sum_{ls} v_s(\mathbf{r}-\mathbf{R}_{ls})\,. \tag{37}$$

Its first-order variation, evaluated at the equilibrium positions, is given by

$$\delta^{\mathbf{q}}_{s\alpha} v_{\rm ext}(\mathbf{r}) = -\sum_{l} \nabla^{\mathbf{r}}_{\alpha} v_s(\mathbf{r}-\mathbf{R}^0_{ls})\, e^{i\mathbf{q}\mathbf{R}^0_{ls}} = -e^{i\mathbf{q}\mathbf{r}} \sum_{l} e^{i\mathbf{q}(\mathbf{R}^0_{ls}-\mathbf{r})}\, \nabla^{\mathbf{r}}_{\alpha} v_s(\mathbf{r}-\mathbf{R}^0_{ls})\,. \tag{38}$$

The quantity defined by the lattice sum has the periodicity of the original lattice. Thus the derivative $\delta^{\mathbf{q}}_{s\alpha}$ can be considered to carry a momentum $\mathbf{q}$.
When using a Bloch representation for the electronic eigenstates, the variation of the effective potential, $\delta^{\mathbf{q}}_{s\alpha} v_{\rm eff}$, connects states of momentum $\mathbf{k}$ with those of momentum $\mathbf{k}+\mathbf{q}$. The Fourier transform of the first order density variation takes the form

$$\delta^{\mathbf{q}}_{s\alpha} n(\mathbf{q}+\mathbf{G}) = -\frac{4}{V} \sum_{\mathbf{k}v} \big\langle \mathbf{k}v \big| e^{-i(\mathbf{q}+\mathbf{G})\mathbf{r}} \big| \Delta^{\mathbf{q}}_{s\alpha}(\mathbf{k}v) \big\rangle\,, \tag{39}$$

where V denotes the crystal volume. The quantity appearing on the right hand side is closely related to the first-order variation of the valence state $|\mathbf{k}v\rangle$ and is defined by (see Eq. (25))

$$|\Delta^{\mathbf{q}}_{s\alpha}(\mathbf{k}v)\rangle = \sum_{c} \frac{|\mathbf{k}+\mathbf{q}c\rangle\langle \mathbf{k}+\mathbf{q}c|\delta^{\mathbf{q}}_{s\alpha} v_{\rm eff}|\mathbf{k}v\rangle}{\varepsilon_{\mathbf{k}+\mathbf{q}c}-\varepsilon_{\mathbf{k}v}}\,. \tag{40}$$

It is obtained by solving the inhomogeneous linear equations (see Eq. (27))

$$\big(H_{KS}-\varepsilon_{\mathbf{k}v}\big)|\Delta^{\mathbf{q}}_{s\alpha}(\mathbf{k}v)\rangle = \big(P_v^{\mathbf{k}+\mathbf{q}}-1\big)\,\delta^{\mathbf{q}}_{s\alpha} v_{\rm eff}|\mathbf{k}v\rangle\,. \tag{41}$$

Eqs. (39) and (41) together with (18) constitute a set of equations, which is solved self-consistently for a fixed $\mathbf{q}$ to obtain $\delta^{\mathbf{q}}_{s\alpha} n$. As a by-product, also $\delta^{\mathbf{q}}_{s\alpha} v_{\rm eff}$ is calculated.
The electronic contribution to the dynamical matrix takes the form

$$\delta^{\mathbf{q}}_{s\alpha}\delta^{-\mathbf{q}}_{s'\beta} E = \sum_{\mathbf{G}} \left[\delta^{\mathbf{q}}_{s\alpha} n(\mathbf{G}+\mathbf{q})\, \delta^{-\mathbf{q}}_{s'\beta} v_{\rm ext}(\mathbf{G}+\mathbf{q}) + \delta^{\mathbf{q}}_{s\alpha}\delta^{-\mathbf{q}}_{s'\beta} v_{\rm ext}(\mathbf{G})\right]\,. \tag{42}$$

3.2.2 Electron-phonon vertex from DFPT

We have seen that the lowest-order electron-ion interaction describes scattering of electronic states via the operator $\delta_{\mathbf{R}} V$ which denotes the change of the potential felt by the electrons due to an ionic displacement. If the potential V is the bare electron-ion potential V^0, then $\delta_{\mathbf{R}} V = \nabla V^0|_{\mathbf{R}_0}\mathbf{u}$. In the context of DFPT, Eq. (32) would then be identified with

$$g^{\mathbf{q}\lambda}_{\mathbf{k}+\mathbf{q}\nu',\mathbf{k}\nu} = \sum_{s\alpha} A^{\mathbf{q}j}_{s\alpha} \langle \mathbf{k}+\mathbf{q}\nu'|\delta^{\mathbf{q}}_{s\alpha} v_{\rm ext}|\mathbf{k}\nu\rangle \qquad \text{with} \qquad A^{\mathbf{q}j}_{s\alpha} = \frac{\eta_{s\alpha}(\mathbf{q}j)}{\sqrt{2M_s\omega_{\mathbf{q}j}}}\,, \tag{43}$$

where a transformation to the normal-mode coordinates is performed. Physically, g represents the probability amplitude of scattering a single electron by a simultaneous creation or annihilation of a single phonon. In the form given above this is called the bare vertex.

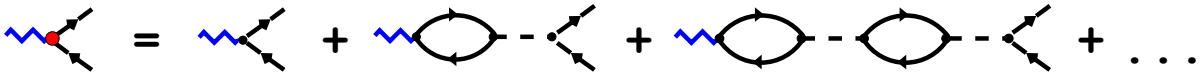

Fig. 1: *Diagrammatic representation of the screened electron-phonon vertex within the DFT framework. Blue zigzag lines represent phonons, black lines electron propagators, and the dashed lines the effective electron-electron interaction.*

However, in solids, and in particular in metals, the bare electron-ion potential is screened by the other electrons. Screening also alters the vertex significantly. Within linear response theory this operator takes the form

$$\delta_{\mathbf{R}} V = \epsilon^{-1} \nabla V^0|_{\mathbf{R}_0} \mathbf{u} \,. \tag{44}$$

ϵ^{-1} is the inverse dielectric matrix, which is a measure of the screening. Note that in Eq. (44), the screening operator does not commute with the gradient operation, and thus can not be written in terms of the gradient of a screened potential.
It is instructive to look at it from a many-body perturbation perspective. Fig. 1 shows a diagrammatic representation of the screened vertex. The bare vertex is given by the first graph on the right hand side, and is screened by virtual electron-hole excitations coupled via an effective interaction. From the relationship (21) between the external (bare) and effective (screened) perturbation, we can see that within the DFPT framework, the electron-hole bubble is represented by the charge-susceptibility of the non-interaction Kohn-Sham system (20). The effective interaction is given by the kernel I defined in Eq. (18) and incorporates besides the Coulomb interaction also contributions from exchange and correlation.
In essence this leads to a replacement of the external potential by the screened or effective one

$$g^{\mathbf{q}\lambda}_{\mathbf{k}+\mathbf{q}\nu',\mathbf{k}\nu} = \sum_{s\alpha} A^{\mathbf{q}j}_{s\alpha} \langle \mathbf{k}+\mathbf{q}\nu' | \delta^{\mathbf{q}}_{s\alpha} v_{\text{eff}} | \mathbf{k}\nu \rangle \,. \tag{45}$$

Applying the self-consistent procedure described above results in the linear response of the effective potential $\delta^{\mathbf{q}}_{s\alpha} v_{\text{eff}}$, which is then used to calculate the electron-phonon matrix elements. The self-consistency procedure automatically takes into account the important screening effects. Eq. (45) thus enables the calculation of the screened EPC matrix elements on a microscopic level, including their full momentum dependence and resolving the contributions from different electronic bands and phononic modes. For further details one can refer to the book of Grimvall [25].

4 Applications

4.1 Fröhlich Hamiltonian and many-body perturbation

When developing a perturbative treatment of the mutual influence of the electronic and phononic subsystems in a solid, the question arises, what are the proper noninteracting quasiparticles to start with. The correct answer requires to know the solution to some extent. As we will see, electronic states are significantly influenced by lattice vibrations mostly in close vicinity of the

Fermi energy. It is therefore appropriate to start with electrons moving in a static potential of a rigid ion lattice, without any renormalization by the lattice vibrations. On contrast, the bare vibrations of the ion lattice would be a bad starting point, because they are strongly altered by the screening of the electrons. This screening must be built into the description of the harmonic lattice vibrations which defines the noninteracting phonons.
Therefore, a good starting point is the *Fröhlich Hamiltonian*, which in second quantization reads

$$H = H_e + H_{ph} + H_{e\text{-}ph}\,. \tag{46}$$

The electron system is described by noninteracting quasi-particles with dispersion $\varepsilon_{\mathbf{k}\nu}$. These quasiparticles are considered to be the stationary solutions of band electrons in a perfect periodic lattice, and include already renormalization from Coulomb interaction.

$$H_e = \sum_{\mathbf{k}\nu\sigma} \varepsilon_{\mathbf{k}\nu}\, c^\dagger_{\mathbf{k}\nu\sigma} c_{\mathbf{k}\nu\sigma}\,. \tag{47}$$

Here $c_{\mathbf{k}\nu\sigma}$ ($c^\dagger_{\mathbf{k}\nu\sigma}$) are the annihilation (creation) operators for an electronic state with momentum $\mathbf{k}$, band index ν, spin σ, and band energy $\varepsilon_{\mathbf{k}\nu}$.
The lattice Hamiltonian is expressed in terms of quantized harmonic vibrations, and represents noninteracting phonons

$$H_{ph} = \sum_{\mathbf{q}j} \omega_{\mathbf{q}j} \left(b^\dagger_{\mathbf{q}j} b_{\mathbf{q}j} + \frac{1}{2} \right), \tag{48}$$

where $b_{\mathbf{q}j}$ ($b^\dagger_{\mathbf{q}j}$) are the annihilation (creation) operators for a phonon with momentum $\mathbf{q}$, branch index j, and energy $\omega_{\mathbf{q}j}$. Phonons are the quanta of the normal mode vibrations. The operator of atom displacements is expressed as $u_{ls\alpha} = e^{i\mathbf{q}\mathbf{R}^0_{ls}} 1/\sqrt{N_q} \sum_{\mathbf{q}j} A^{\mathbf{q}j}_{s\alpha} \big(b_{\mathbf{q}j} + b^\dagger_{-\mathbf{q}j} \big)$, where N_q is the number of points in the summation over $\mathbf{q}$.
The third term describes the lowest-order coupling between electrons and phonons,

$$H_{e\text{-}ph} = \sum_{\mathbf{k}\nu\nu'\sigma} \sum_{\mathbf{q}j} g^{\mathbf{q}j}_{\mathbf{k}+\mathbf{q}\nu',\mathbf{k}\nu}\, c^\dagger_{\mathbf{k}+\mathbf{q}\nu'\sigma} c_{\mathbf{k}\nu\sigma} \left(b_{\mathbf{q}j} + b^\dagger_{-\mathbf{q}j} \right)\,. \tag{49}$$

$g^{\mathbf{q}j}_{\mathbf{k}+\mathbf{q}\nu',\mathbf{k}\nu}$ is the electron-phonon matrix element, Eq. (45) and describes the probability amplitude for scattering an electron with momentum $\mathbf{k}$ from band ν to a state with momentum $\mathbf{k}+\mathbf{q}$ in band ν' under the simultaneous absorption (emission) of a phonon with momentum $\mathbf{q}$ ($-\mathbf{q}$) and branch index j.
To simplify the treatment, we will use a compact notation combining momentum and band or branch index into a single symbol: $k{=}(\mathbf{k}\nu)$, $k'{=}(\mathbf{k}'\nu')$, and $q{=}(\mathbf{q}j)$. The EPC matrix elements are then denoted as

$$g^q_{k',k} = g^{\mathbf{q}j}_{\mathbf{k}'\nu',\mathbf{k}\nu}\, \delta_{\mathbf{k}',\mathbf{k}+\mathbf{q}}\,, \tag{50}$$

which implicitly takes into account momentum conservation.
This general form of the Fröhlich Hamiltonian is the starting point for a many-body perturbation theory [26], where $H_0 = H_e + H_{ph}$ denotes the Hamiltonian of the unperturbed quasiparticles, and $H_{e\text{-}ph}$ represents the perturbational part.

The bare Green functions of the unperturbed Hamiltonian $H_0 = H_e + H_{ph}$ are

$$G_0(k, i\omega_n) = \frac{1}{i\omega_n - \varepsilon_k} \tag{51}$$

$$D_0(q, i\nu_m) = \frac{1}{i\nu_m - \omega_q} - \frac{1}{i\nu_m + \omega_q}\,. \tag{52}$$

where $\omega_n = (2n{+}1)\pi\, T$ and $\nu_m = 2m\pi\, T$, with n, m integer values, denote fermionic and bosonic Matsubara frequencies, respectively. Electronic energies are measured with respect to the chemical potential. The Dyson equations

$$G(k, i\omega_n)^{-1} = G_0(k, i\omega_n)^{-1} - \Sigma(k, i\omega_n) \tag{53}$$

$$D(q, i\nu_m)^{-1} = G_0(q, i\nu_m)^{-1} - \Pi(q, i\nu_m) \tag{54}$$

connect bare and renormalized Green functions via the electron and phonon self-energy, Σ and Π, respectively. In the following we will have a closer look at the leading contributions of EPC to these electron and phonon self-energies.

4.2 Renormalization of electronic properties

The lowest-order diagram of the electron self-energy represents a virtual exchange of a phonon

$$\Sigma_{ep}(k, i\omega_n) = -T \sum_m \frac{1}{N_q} \sum_{k',q} g^q_{k',k}\, G_0(k', i\omega_n{-}i\nu_m)(g^q_{k',k})^* D_0(q, i\nu_m)\,. \tag{55}$$

After performing the Matsubara sum over ν_m one obtains

$$\Sigma_{ep}(k, i\omega_n) = \frac{1}{N_q} \sum_{k',q} |g^q_{k',k}|^2 \left(\frac{b(\omega_q) + f(\varepsilon_{k'})}{i\omega_n{+}\omega_q{-}\varepsilon_{k'}} + \frac{b(\omega_q) + 1{-}f(\varepsilon_{k'})}{i\omega_n{-}\omega_q{-}\varepsilon_{k'}} \right). \tag{56}$$

Σ_{ep} depends on temperature T via the Fermi and Bose distribution functions, $f(\varepsilon) = (e^{\varepsilon/T}{+}1)^{-1}$ and $b(\omega) = (e^{\omega/T}{-}1)^{-1}$, respectively.

To discuss the quasiparticle renormalization, we consider the retarded Green function, which is obtained by analytic continuation of Eq. (53) to real axis via $i\omega_n \to \varepsilon + i\delta$ with an infinitesimal positive δ. It is connected to the analytic continuation of the self-energy via the Dyson equation

$$G(k, \varepsilon) = \big(\varepsilon - \varepsilon_k - \Sigma(k, \varepsilon)\big)^{-1}\,. \tag{57}$$

It is straightforward to perform the analytic continuation of $\Sigma_{ep}(k, i\omega_n \to \varepsilon{+}i\delta)$ in the form given in Eq. (56) and to derive the expression for the imaginary part

$$\mathrm{Im}\Sigma_{ep}(k, \varepsilon) = -\frac{\pi}{N_q} \sum_{k',q} |g^q_{k',k}|^2 \Big(\delta(\varepsilon{-}\varepsilon_{k'}{+}\omega_q)\big(b(\omega_q){+}f(\varepsilon_{k'})\big) + \delta(\varepsilon{-}\varepsilon_{k'}{-}\omega_q)\big(b(\omega_q){+}1{-}f(\varepsilon_{k'})\big) \Big) \tag{58}$$

It determines the quasiparticle linewidth (inverse lifetime) by

$$\Gamma_k = -2\mathrm{Im}\Sigma(k, \bar{\varepsilon}_k)\,, \tag{59}$$

while the shifted quasiparticle energy is determined by the real part via $\overline{\varepsilon}_k = \varepsilon_k - \mathrm{Re}\Sigma(k,\overline{\varepsilon}_k)$. $\mathrm{Re}\Sigma_{ep}$ is obtained via the Kramers-Kronig relation $\mathrm{Re}\Sigma_{ep}(k,\varepsilon)=1/\pi\int d\varepsilon'\,\mathrm{Im}\Sigma_{ep}(k,\varepsilon')/(\varepsilon-\varepsilon')$. This can be rewritten by introducing two spectral functions

$$\alpha^2F_k^{\pm}(\varepsilon,\omega) = \frac{1}{N_q}\sum_q \delta(\omega-\omega_q)\sum_{k'}|g^q_{k',k}|^2\delta(\varepsilon-\varepsilon_{k'}\pm\omega)\,. \tag{60}$$

They depend on the electronic state k via the EPC vertex. The imaginary part can then be cast in the form

$$\mathrm{Im}\Sigma_{ep}(k,\varepsilon) = -\pi\int_0^\infty d\omega\Big(\alpha^2F_k^+(\varepsilon,\omega)\big(b(\omega)+f(\omega+\varepsilon)\big)+\alpha^2F_k^-(\varepsilon,\omega)\big(b(\omega)+f(\omega-\varepsilon)\big)\Big)\,. \tag{61}$$

The physical interpretation of this expression is as follows. When a quasiparticle hole is created at the state k ($\varepsilon < \varepsilon_F$), electrons can scatter from states with higher or lower energies, respectively, accompanied by either emission or absorption of a phonon. The probabilities are given by $\alpha^2F_k^-$ and $\alpha^2F_k^+$, respectively, weighted with the appropriate bosonic and fermionic distribution functions. A similar description holds when a quasiparticle (electron) is created at energies above the Fermi level.
Due to the small scale of the phonon energies, emission and absorption spectra are often rather similar as one can ignore the phonon energy ω_q in the δ-function of (60). Then

$$\alpha^2F_k^{\pm} \approx \alpha^2F_k(\varepsilon,\omega) = \frac{1}{N_q}\sum_q \delta(\omega-\omega_q)\sum_{k'}|g^q_{k',k}|^2\delta(\varepsilon-\varepsilon_{k'})\,. \tag{62}$$

For this *quasielastic approximation* the expression for the EPC-induced linewidth simplifies to

$$\Gamma_k = \pi\int_0^\infty d\omega\Big(\alpha^2F_k(\overline{\varepsilon}_k,\omega)\big(2b(\omega)+f(\omega+\overline{\varepsilon}_k)+f(\omega-\overline{\varepsilon}_k)\big)\Big)\,. \tag{63}$$

The spectral function α^2F_k contains the essential information related to the electron-phonon coupling of the specific electronic state $k=(\mathbf{k}\nu)$. A convenient measure for the strength of the EPC is the dimensionless coupling parameter

$$\lambda_k = 2\int d\omega\,\frac{\alpha^2F_k(\varepsilon_k,\omega)}{\omega}\,. \tag{64}$$

It characterizes the strength of the coupling of a specific electronic state to the whole phonon spectrum, and depends both on the momentum and band character of the electronic state.
An example for a calculation of λ_k is given in Fig. 2. The topological insulator Bi_2Se_3 possesses at its (0001) surface a metallic surface state with a very characteristic dispersion, a so-called Dirac cone. Its origin lies in the topological nature of the bulk band structure, and has very unusual properties, in particular a peculiar spin polarization. The study showed that the EPC coupling constant increases linearly with energy for states in the upper cone, but remains

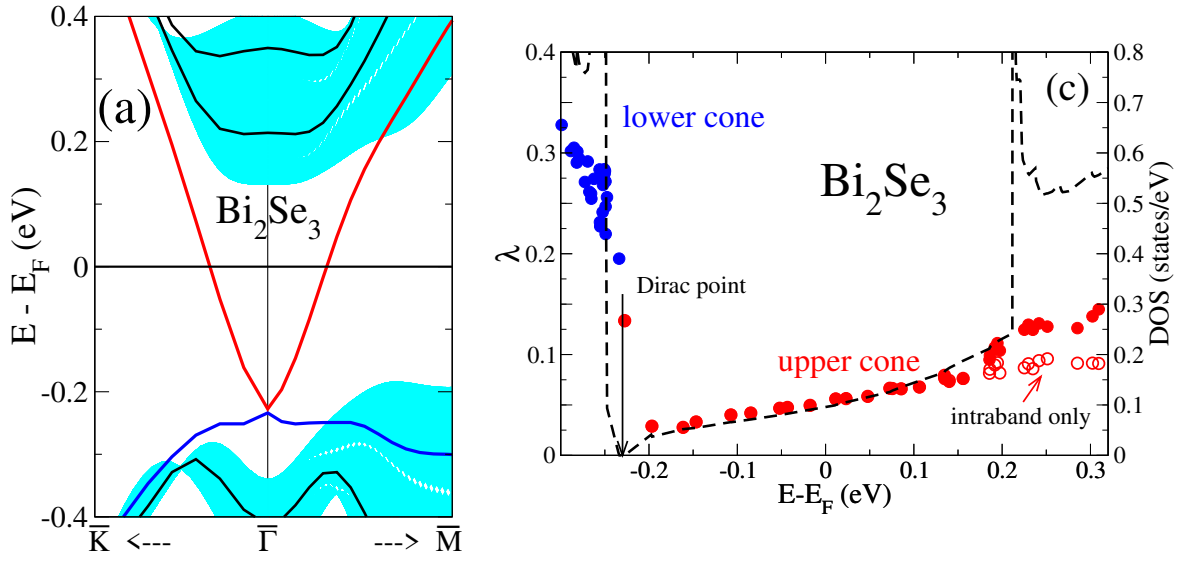

Fig. 2: *Renormalization of electronic states in the surface a Dirac cone of the topological insulator Bi_2Se_3. Calculations were done for a slab consisting of 3 quintuple layers (QL) separated by a large vacuum. (a) Bandstructure of the (0001) surface; shaded area indicated surface-projected bulk states. (b) Coupling constants of electronic states as function of binding energy. After [27].*

small enough ($\lambda < 0.15$), such that the electronic quasiparticles are not much disturbed by the coupling to phonons [27].

There are two relations which connect this parameter to experimentally accessible quantities. The first is related to the real part of the self-energy for an electronic band crossing the Fermi level

$$\lambda_k = \left.\frac{\partial \mathrm{Re}\Sigma_{ep}(k,\varepsilon)}{\partial \varepsilon}\right|_{\varepsilon=0_F,T=0} . \tag{65}$$

Thus the coupling constant is given by the slope of $\mathrm{Re}\Sigma_{ep}$ right at the Fermi energy in the limit $T \to 0$. λ_k is also called the mass-enhancement parameter, because the quasiparticle velocity is changed to $v_k^* = v_k/(1+\lambda_k)$ and can be interpreted as an enhanced effective mass $m_k^* = m_k(1+\lambda_k)$, where m_k denotes the unrenormalized mass. Eq. (65) is often utilized in ARPES measurements of bands crossing the Fermi level, which attempt to extract the energy dependence of the real part of the self-energy.

A second route to determine the coupling constant of an electronic state is via the temperature dependence of the linewidth. In Eq. (63), the T-dependence it contained solely in the Bose and Fermi distribution functions. For temperatures larger than the maximum phonon frequencies, it becomes almost linear in T, and its slope is determined by the average coupling parameter defined above

$$\Gamma_k \approx 2\pi\lambda_k T . \tag{66}$$

This relationship has been widely used to extract λ_k from measurements of $\Gamma_k(T)$, in particular for surface electronic states.

4.3 Phonon renormalization

The EPC also renormalizes the phononic quasiparticles. Measurement of the phonon linewidth provides another way to gain experimental information about the coupling strength. We will briefly sketch this approach here.

The finite linewidth γ_q (half-width at half maximum), or inverse lifetime of a phonon mode is connected to the imaginary part of the phonon self-energy by $\gamma_q = -2\mathrm{Im}\Pi_q(\omega_q)$. The leading contributing to $\Pi_q(\omega)$ is given by virtual electron-hole excitations expressed as

$$\begin{aligned} \Pi_q(i\nu_m) &= T\sum_n \frac{1}{N_k}\sum_{k,k'} |g^q_{k',k}|^2 G_0(k,i\omega_n)\, G_0(k'\nu', i\omega_n{+}i\nu_m) \\ &= \frac{1}{N_k}\sum_{k',k} |g^q_{k',k}|^2 \,\frac{f(\varepsilon_k)-f(\varepsilon_{k'})}{i\nu_m+\varepsilon_k-\varepsilon_{k'}}\,. \end{aligned} \tag{67}$$

Analytic continuation results in

$$\gamma_q = 2\pi\frac{1}{N_k}\sum_{k',k} |g^q_{k',k}|^2 \left(f(\varepsilon_k){-}f(\varepsilon_{k'})\right)\delta\big(\omega_q+(\varepsilon_k{-}\varepsilon_{k'})\big)\,. \tag{68}$$

This expression contains the T-dependence via the Fermi distribution functions f. Because phonon energies are typically small compared to electronic energies, the energy difference $\varepsilon_k{-}\varepsilon_{k'}$ is also small, and one can approximate

$$f(\varepsilon_k)-f(\varepsilon_{k'}) \approx f'(\varepsilon_k)\,(\varepsilon_k{-}\varepsilon_{k'}) \to -f'(\varepsilon_k)\omega_q \tag{69}$$

with $f' = df/d\varepsilon$. In the limit $T \to 0$, $f'(\varepsilon_k) \to -\delta(\varepsilon_k)$, and by neglecting ω_q inside the δ-function, the expression further simplifies to

$$\gamma_q = 2\pi\omega_q\frac{1}{N_k}\sum_{k',k} |g^q_{k',k}|^2\,\delta(\varepsilon_k)\,\delta(\varepsilon_{k'})\,. \tag{70}$$

This approximate formula for the linewidth, first derived by Allen [28], is widely used in numerical calculations. As will be discussed below, γ_q in the form of Eq. (70) enters directly the expression for the coupling strength of a phonon mode relevant for superconductivity. Thus measurements of the phonon linewidths, for example by inelastic neutron or x-ray scattering experiments, provide information about the importance of a phonon mode for the pairing. One has to keep in mind, however, that γ_q only represents the contribution from EPC, while the experimental linewidth also contains other contributions like those from anharmonic decay processes. Furthermore, approximation (70) does not hold in the limit $\mathbf{q} \to 0$ for metals, because the phonon frequency in Eq. (68) cannot be neglected anymore for intraband contributions, which involve arbitrarily small energy differences $\varepsilon_k{-}\varepsilon_{k'}$.

An example of a combined study of EPC by DFPT and neutron-scattering experiments is shown in Fig. 3 for YNi_2B_2C [29, 30]. This member of the nickelborocarbide family is a strong coupling superconductor (T_C=15.2 K), and exhibits pronounced phonon anomalies related to large and momentum dependent EPC. Good agreement for both renormalized phonon frequencies and linewidths as function of momentum indicates a good predictive power of the DFPT calculation for this compound.

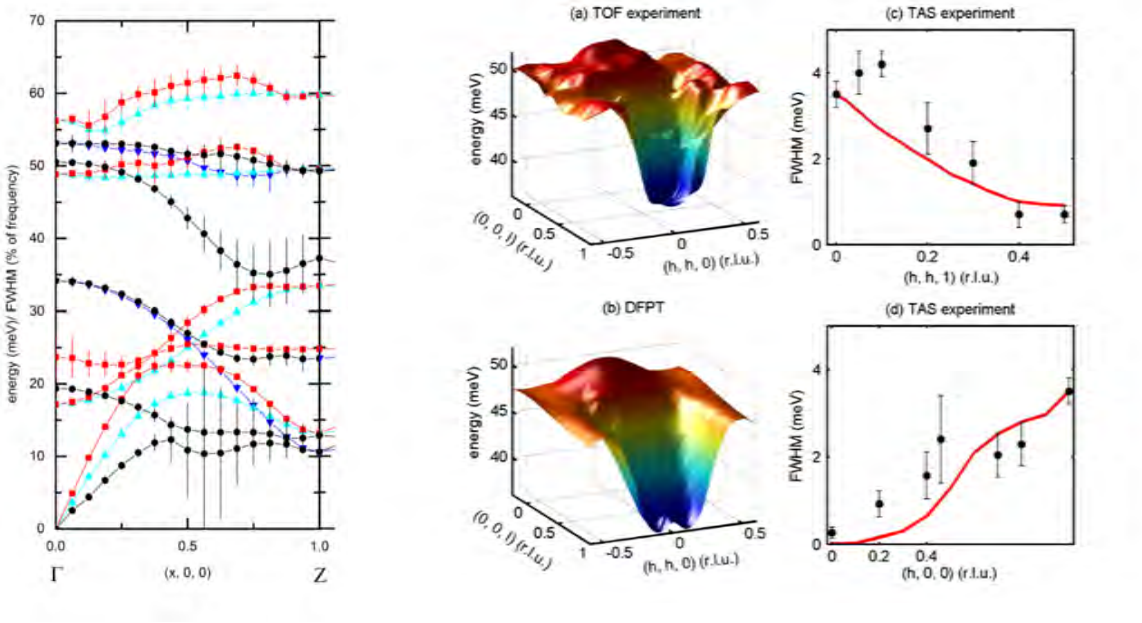

Fig. 3: *Lattice dynamics of YNi_2B_2C. Left panel: theoretical phonon dispersion and linewidths (vertical bars) from DFPT. Right panel: time-of-flight neutron scattering results for the dispersion (a) and linewidth (c) of a prominent phonon branch compared with predictions from DPFT in (b) and (d), respectively. After [29, 30].*

4.4 Transport

The electron-phonon interaction plays an important role for electronic transport properties. The general approach is based on Boltzmann transport theory (see, e.g., [25, 31–33]) and is briefly sketched in the following. To be specific, we discuss the contribution of the EPC to the case of electrical conductivity. In a semi-classical picture, when one applies an external electric field $\mathbf{E}$, electrons become accelerated. By collisions with other objects (like defects, phonons or other electrons) they are scattered, until finally a steady state is reached. It is characterized by a new distribution F_k which differs from the Fermi distribution $f_k = f(\varepsilon_k)$ in equilibrium. Knowledge of F_k allows to calculate the electronic current density via (for definiteness, we assume a field along x)

$$j_x = -\frac{2e}{V}\frac{1}{N_k}\sum_k F_k (v_k)_x \tag{71}$$

and the diagonal component of the electrical conductivity $\sigma_{xx} = j_x/E_x$
The new occupation F_k is determined using the well known Boltzmann transport equation

$$-eE\,\frac{\partial F_k}{\partial k_x} = \left(\frac{\partial F_k}{\partial t}\right)_{\text{coll}} . \tag{72}$$

The left-hand side describes the change in occupations induced by the electric field, which is balanced by the rate of change of the occupation due to collisions given on the right-hand side. Using Fermi golden rule the latter is expressed as

$$\left(\frac{\partial F_k}{\partial t}\right)_{\text{coll}} = \sum_{k'}\Big(P_{k'k}\,F_{k'}\,(1-F_k) - P_{kk'}\,F_k\,(1-F_{k'})\Big). \tag{73}$$

Here, $P_{kk'}$ denotes the probability of scattering an electron from state (k) to (k'). The first term ($\propto P_{k'k}$) describes events, where electrons are scattered into state (k), and the second those, where electrons are scattered out of that state. $P_{kk'}$ must satisfy a detailed balance condition

$$P_{k'k}\, f_{k'}\,(1-f_k) = P_{kk'}\, f_k\,(1-f_{k'}) \tag{74}$$

such that the RHS of Eq. (72) vanishes in equilibrium.
When the scattering process is due to the electron-phonon interaction, the probability depends on the EPC vertex and the availability of phonons

$$P_{kk'} = \frac{2\pi}{N}|g^q_{k'k}|^2\Big(b(\omega_q)\,\delta(\varepsilon_{k'}-\varepsilon_k-\omega_q) + \big(b(\omega_q)+1\big)\,\delta(\varepsilon_{k'}-\varepsilon_k+\omega_q)\Big) \tag{75}$$

The first term describes a phonon annihilation, the second a phonon creation process.
For small applied fields, it is sufficient to look at the first-order change of the occupation with the electric field E_x

$$F_k = f_k + f^1_k\,, \quad f^1_k \propto E_x \tag{76}$$

and to resort to the linearized Boltzmann equation, where the left-hand side is approximated by

$$-\,eE_x\frac{\partial F_k}{\partial k_x} \to -eE_x\frac{\partial f_k}{\partial k_x} = -eE_x\frac{\partial f_k}{\partial \varepsilon_k}\frac{\partial \varepsilon_k}{\partial k_x} = -eE_x\frac{\partial f_k}{\partial \varepsilon_k}(v_k)_x\,. \tag{77}$$

The right-hand side simplifies in $\mathcal{O}(E_x)$ to

$$\begin{aligned}\sum_{k'}\;&\Big(P_{k'k}\big(f^1_{k'}(1-f_k) - f_{k'}f^1_k\big) - P_{kk'}\big(f^1_k(1-f_{k'}) - f_k f^1_{k'}\big)\Big)\\ &= \sum_{k'}\Big(-\,f^1_k\big(P_{k'k}\,f_{k'} + P_{kk'}(1-f_{k'})\big) + f^1_{k'}\big(P_{k'k}(1-f_k) + P_{kk'}\,f_k\big)\Big)\\ &= \sum_{k'}P_{kk'}\Big(-\,f^1_k\frac{1-f_{k'}}{1-f_k} + f^1_{k'}\frac{f_k}{f_{k'}}\Big)\end{aligned} \tag{78}$$

In the last step, use of the detailed balance relation (74) was made.
To proceed further, one applies the so-called *energy relaxation time approximation*. It consists of neglecting the occupation changes of the in-scattered electrons: $f^1_{k'} = 0$. Then the RHS consists only of the first term, which using Eq. (75) just gives $-f^1_k/\tau_k$. Here $\tau_k = 1/\Gamma_k$ is the lifetime or inverse linewidth of the electronic state (k) as derived in Eq. (63). Now the linearized Boltzmann equations with (76) and (77) can be solved easily

$$f^1_k = eE_x\frac{\partial f_k}{\partial \varepsilon_k}(v_k)_x\tau_k \tag{79}$$

which finally gives for the conductivity

$$\sigma_{xx} = -\frac{2e}{VE_x}\frac{1}{N_k}\sum_k F_k(v_k)_x = -\frac{2e}{VE_x}\frac{1}{N_k}\sum_k f^1_k(v_k)_x = \frac{2e^2}{V}\frac{1}{N_k}\sum_k\Big(-\frac{\partial f_k}{\partial \varepsilon_k}\Big)(v_k)_x(v_k)_x\tau_k \tag{80}$$

Direct evaluation of this equation from first principles is quite demanding, as it requires the calculation of V_k and in particular τ_k for each relevant k. It has been used to assess the mobility of carriers in doped semiconductors [34, 35].

For metals, a simplified expression often works very well. Here, the k-dependent lifetime is replaced by an effective relaxation time τ, which is determined using a variational procedure to solve the Boltzmann equation [31]. In the case of pure electron-phonon scattering, it takes the form [36–38]

$$\frac{1}{\tau} = 2\pi \int dx \, \frac{x}{\sinh^2 x} \, \alpha^2_{\rm tr} F(\omega) \tag{81}$$

with $x = \omega/2T$. The properties of the electron-phonon scattering are encoded in the transport spectral function

$$\alpha^2_{\rm tr} F(\omega) = \frac{1}{N_q} \sum_q \delta(\omega - \omega_q) \frac{1}{N(0)} \frac{1}{N_k} \sum_{kk'} |g^q_{k'k}|^2 \, \eta_{k'k} \, \delta(\varepsilon_k) \, \delta(\varepsilon_{k'}) \, , \tag{82}$$

where $N(0) = 1/N_k \sum_k \delta(\varepsilon_k)$ is the electronic density of states per spin at the Fermi energy. $\alpha^2_{\rm tr} F(\omega)$ is very similar to the isotropic Eliashberg function $\alpha^2 F$ appearing in the theory of phonon-mediated superconductivity (see Eq. (87)). The only difference lies in the efficiency factor

$$\eta_{k'k} = 1 - \frac{\mathbf{v}_k \mathbf{v}_{k'}}{|\mathbf{v}_k|^2} \, , \tag{83}$$

which accounts for a dependence on the scattering direction. Then the conductivity becomes

$$\sigma_{xx} = \tau \, \frac{2e^2}{V} \frac{1}{N_k} \sum_k \Big(-\frac{\partial f_k}{\partial \varepsilon_k} \Big) (v_k)_x (v_k)_x = \tau \frac{2e^2 N(0)}{V} \big\langle v_x^2 \big\rangle \tag{84}$$

$\big\langle v_x^2 \big\rangle$ denotes the Fermi-surface average of $(v_k)_x^2$, and an isotropic average has been taken. Along these lines, first DFPT calculations for simple metals appeared already in 1998 [39].

4.5 Phonon-mediated pairing

Superconductivity is a macroscopic quantum phenomenon of the electron system. Its origin lies in an instability of the Fermi liquid state and leads to a new ground state of correlated paired electrons (Cooper pairs). The superconducting state has the important property that the quasiparticle spectrum is gapped. The size of the gap plays the role of an order parameter. In their seminal paper, Bardeen, Cooper, and Schrieffer (BCS) [40] have shown that this state is stabilized, whenever there exists an attractive interaction among two electrons. Such an attractive interaction is always provided by the electron-phonon coupling, which thus represents a natural source for pairing in any metal. EPC is known to be the pairing mechanism in most superconductors, which are commonly termed classical superconductors to distinguish them from more exotic materials where other types of pairing mechanism are suspected.

The BCS theory treated the EPC only in a simplified form appropriate for the weak coupling limit. A more complete theory has been soon after worked out applying many-body techniques (for a review see, e.g., Scalapino [41]) . The resulting Eliashberg theory [42] extends the framework of BCS into the strong coupling regime and allows quantitative predictions.

Central to the theoretical formulation is a set of coupled equations, the so-called Eliashberg equations. A detailed derivation and justification of the approximations involved is given in the

review of Allen and Mitrovic [43]. One of its simplest form are the so-called *isotropic gap equations*. They are obtained by taking Fermi-surface averages of relevant quantities, i.e., ignoring the explicit momentum dependence, but keeping their frequency dependence. The justification comes from the observation that superconducting properties like the gap function are often very isotropic. In real materials, defects are always present and tend to average anisotropic gaps.
On the imaginary axis the isotropic gap equations read

$$\begin{aligned} i\omega_n\big(1-Z(i\omega_n)\big) &= -\pi T\sum_{n'}\Lambda(\omega_n-\omega_{n'})\,\frac{\omega_{n'}}{\sqrt{\omega_{n'}^2+\Delta(i\omega_{n'})^2}} \\ \Delta(i\omega_n)\,Z(i\omega_n) &= \pi T\sum_{n'}\Lambda(\omega_n-\omega_{n'})\,\frac{\Delta(i\omega_{n'})}{\sqrt{\omega_{n'}^2+\Delta(i\omega_{n'})^2}}\,. \end{aligned} \tag{85}$$

Here, $\Delta(i\omega_n)$ is the frequency-dependent gap function and $Z(i\omega_n)$ the frequency-dependent quasiparticle renormalization factor. The pairing interaction is encoded in the kernel

$$\Lambda(\nu_m) = \int d\omega\,\frac{2\omega\alpha^2F(\omega)}{(\nu_m)^2+\omega^2}\,, \tag{86}$$

where the electron-phonon coupling properties are described by the isotropic Eliashberg function

$$\alpha^2F(\omega) = \frac{1}{N_q}\sum_q\delta(\omega-\omega_q)\frac{1}{N(0)}\frac{1}{N_k}\sum_{kk'}|g^q_{k'k}|^2\delta(\varepsilon_k)\,\delta(\varepsilon_{k'})\,, \tag{87}$$

The isotropic Eliashberg function has the structure of a phonon density of states, weighted with squared EPC matrix elements averaged over states at the Fermi surface.
The set of non-linear equations (85) must be solved self-consistently for a given temperature T and pairing function α^2F. The superconducting state is characterized by a solution with $\Delta(i\omega_n)\neq 0$. The largest T which still allows such a solution defines the critical temperature T_c.
The interaction kernel $\Lambda(\nu_m)$ entering both equations is an even function of ν_m. It takes its largest value at $\nu_m = 0$

$$\lambda = \Lambda(0) = 2\int d\omega\,\frac{\alpha^2F(\omega)}{\omega}\,. \tag{88}$$

λ is called the (isotropic) coupling constant and is a dimensionless measure of the average strength of the electron-phonon coupling. Depending on its value, materials are characterized as strong ($\lambda > 1$) or weak coupling ($\lambda < 1$) . Due to the factor $1/\omega$ in the integral, low-energy modes contribute more to the coupling strength than high-energy modes.
An important feature of the Eliashberg gap equations is that they only depend on normal-state properties, which specify a particular material. These comprise the electronic band structure, phonons, and the EPC vertex. Therefore, DFPT enables materials-specific predictions of superconducting properties from *first principles*.
One can establish a connection between α^2F and the phonon linewidths derived in the limit $T\to 0$, Eq. (70), namely

$$\alpha^2F(\omega) = \frac{1}{2\pi N(0)}\frac{1}{N_q}\sum_q\frac{\gamma_q}{\omega_q}\delta(\omega-\omega_q)\,, \tag{89}$$

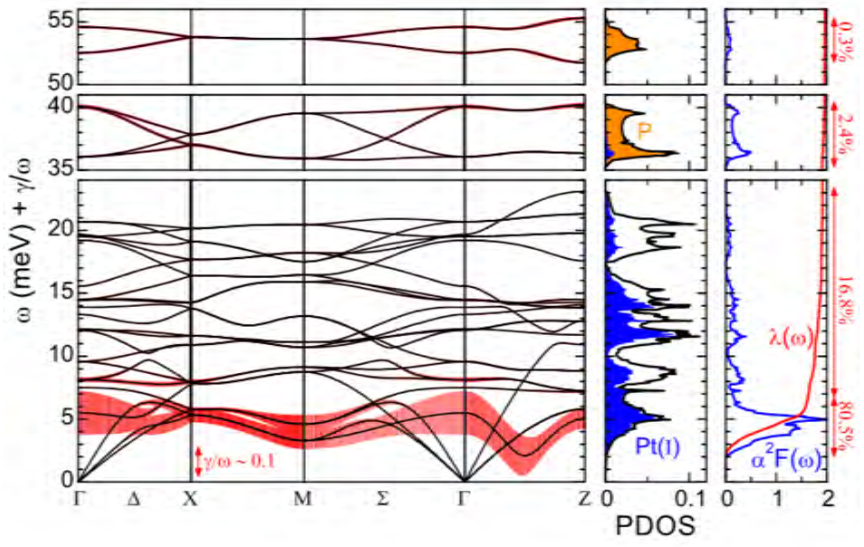

Fig. 4: *DFPT results for the superconductor $SrPt_3P$. Left: phonon dispersion and relative linewidths (vertical red bars); middle: phonon density of states; right: calculated isotropic α^2F. DFPT predicts a soft, but strong-coupling phonon branch, which is the origin of the large peak in α^2F at low energies, and of a large coupling constant of $\lambda \approx 2$. After [46].*

which leads to the formula for the isotropic coupling constant

$$\lambda = \frac{1}{\pi N(0)} \frac{1}{N_q} \sum_q \frac{\gamma_q}{\omega_q^2} \,. \tag{90}$$

The dimensionless prefactor γ_q/ω_q in (89) can be interpreted as a measure of the coupling due to an individual phonon mode. The Eliashberg function is then given as a sum over all phonon branches and averaged over phonon momenta.

The residual Coulomb interaction among the quasiparticles can, however, not be completely neglected in the discussion of phonon-mediated superconductivity. It has a repulsive character and tends to reduce or completely suppress the pairing. It was shown by Morel and Anderson [44], that the Coulomb repulsion can be taken into account by replacing in the equation for the gap function the kernel by

$$\Lambda(i\omega_n - i\omega_{n'}) \to \big(\Lambda(i\omega_n - i\omega_{n'}) - \mu^*(\omega_c)\big)\, \Theta(\omega_c - |\omega_{n'}|) \,. \tag{91}$$

A cutoff ω_c is introduced which must be chosen to be much larger than phononic energies. μ^* is called the effective Coulomb pseudopotential. In praxis, μ^* is commonly treated as a phenomenological parameter of the order of ≈ 0.1 for normal metals. A more satisfactory approach, which actually allows to incorporate the Coulomb effects from *first principles*, is the density-functional theory of superconductors [45].

As an example, Fig. 4 shows results for the non-centrosymmetric, strong-coupling superconductor $SrPt_3P$ ($T_C = 8.4$ K). DFPT predicts that the pairing is driven mainly by a low-frequency mode, which carries more than 80% of the coupling. The existence of the low-frequency mode was confirmed by high-resolution inelastic X-ray experiments [46].

5 Extensions: LDA+U and beyond

In the previous Sections, we have demonstrated how the linear response technique is applied to the calculation of lattice dynamical properties and the evaluation of the electron-phonon vertex. This technique has been implemented for various band structure techniques. They usually rely on local approximations to the exchange-correlation functional (either LDA of GGA variants), which allows a straightforward evaluation of derivatives of the exchange-correlation potential $v_{\rm xc}$. Yet, weaknesses of the local approximations are well known. Examples are an underestimation of band gaps in semiconductors, the failure to catch the long-range part of the van der Waals interaction, or the inadequate description of the Mott-Hubbard physics in strongly correlated materials. Various modifications have been proposed to improve these deficiencies. In many cases, they amount to a replacement of the local exchange-correlation potentials or functional by a more complex quantity, and thus has direct consequences for the evaluation of the linear response. In the following, we will use the DFT+U method, which is one of the simplest extension, as an example to discuss the type of complications arising in such schemes. At the end we will briefly touch more elaborate approaches.

The DFT+U method intends to improve the DFT description of electronic structures in the presence of pronounced local correlation. Examples are atoms with open d or f shells. The method has been introduced almost 30 years ago [47, 48] and is nowadays implemented in a variety of DFT codes. A more recent review can be found in [49].

Starting point is the definition of a correlated subspace, usually constructed from atom-like orbitals, $\Phi_a(\mathbf{r})$. The index $a = (lm\sigma)$ represents a collection of quantum numbers characterizing the orbital. The DFT+U functional is expressed as

$$E = E_{\rm local} + E_U \,. \tag{92}$$

$E_{\rm local}$ is the DFT energy functional in a local approximation, i.e., with E_{XC} approximated by the LDA or GGA exchange-correlation energy. E_U is a correction of the form

$$E_U = \frac{1}{2}\sum_{abcd}\langle ab|v_c|cd\rangle\left(\rho_{ac}\rho_{bd} - \rho_{ad}\rho_{bc}\right) - E_{\rm dc}[\{\rho_{ab}\}] \,. \tag{93}$$

E_U is a function of the orbital density matrix of the correlated orbitals, which is calculated from the Kohn-Sham eigenstates ψ_i as

$$\rho_{ab} = \sum_{i}^{\rm occ}\langle i|b\rangle\langle a|i\rangle \,. \tag{94}$$

$\langle ab|v_c|cd\rangle$ denotes the matrix elements of the Coulomb potential and thus encodes the local electron-electron interaction. There exists different variants of the functional form of this Coulomb kernel, but in all cases, it is expressed in terms of a few parameters only. The most common ones are U and J, which represent the effective Coulomb and exchange interactions, respectively.

The term E_{dc} is the famous *double counting* term which attempts to correct for the fact that $E_{\rm local}$ already contains part of the local electron-electron interaction. Different expressions for the *double counting* term exist, but it is always given by a quadratic polynomial in ρ_{ab}.
The Kohn-Sham equations are augmented by an additional potential

$$v_{\rm eff} = v_{\rm ext} + v_{\rm scr}[n(\mathbf{r})] + \hat{v}_U[\{\rho_{ab}\}] \tag{95}$$

given by

$$\hat{v}_U = \sum_{ab} v_{ab}|a\rangle\langle b| = \sum_{ab} v_{ab}\hat{Q}_{ab} \tag{96}$$

with

$$v_{ab} = \frac{\delta E_U}{\delta \rho_{ba}} = \sum_{cd} \big(\langle ac|v_c|bd\rangle - \langle ad|v_c|cb\rangle\big)\rho_{cd} - (v_{\rm dc})_{ab}\,. \tag{97}$$

$\hat{v}_U$ is a non-local operator containing the operator $\hat{Q}_{ab} = |a\rangle\langle b|$ of the local correlated subspace. When solving the self-consistent Kohn-Sham equations, ρ_{ab} can formally be considered as additional degrees of freedom besides the density $n(\mathbf{r})$. In each step, after solving the Kohn-Sham equation to obtain the KS wave functions, both the density and the orbital density matrix are updated, and finally a new effective potential is calculated with the help of Eqs. (96) and (97).
What are the consequences for the linear-response calculations? Let us first consider the linear change of the orbital density matrix under an external adiabatic perturbation. It consists of two parts

$$\delta\rho_{ab} = \delta\rho_{ab}^{(el)} + \delta\rho_{ab}^{(b)} \tag{98}$$

with

$$\begin{aligned}
\delta\rho_{ab}^{(el)} &= \sum_{i}^{\rm occ} \Big(\big\{\delta\langle i|\big\}\hat{Q}_{ba}|i\rangle + \langle i|\hat{Q}_{ba}\big\{\delta|i\rangle\big\} \Big) \\
\delta\rho_{ab}^{(b)} &= \sum_{i}^{\rm occ} \langle i|\delta\hat{Q}_{ba}|i\rangle\,.
\end{aligned} \tag{99}$$

$\delta\rho_{ab}^{(el)}$ results from the variation of the KS wave functions, while $\delta\rho_{ab}^{(b)}$ derives from a change of the local basis by the perturbation. The latter comes into play when a perturbation modifies the correlated subspace. This happens, for example, when an atom is displaced and the correlated subspace attached to this atom is moved along.
Derivatives of the total energy involve additional contributions from E_U. In first order it reads as

$$\frac{\partial E}{\partial \lambda} \to \sum_{ab} \frac{\delta E_U}{\delta \rho_{ab}} \left(\frac{\partial \rho_{ab}^{(b)}}{\partial \lambda} \right)\,. \tag{100}$$

This form is a consequence of the Hellmann-Feynman theorem, which ensures, that no contribution from the first-order variation of the wave functions enters. Only the explicit dependence of the correlated subspace on the perturbation plays a role. This is not true anymore for the second derivative of the energy

$$\frac{\partial^2 E}{\partial \lambda_1 \partial \lambda_2} \to \sum_{abcd} \frac{\delta^2 E_U}{\delta \rho_{ab}\delta \rho_{cd}} \left(\frac{\partial \rho_{ab}^{(b)}}{\partial \lambda_1} \right) \left(\frac{\partial \rho_{cd}}{\partial \lambda_2} \right) + \sum_{ab} \frac{\delta E_U}{\delta \rho_{ab}} \frac{\partial}{\partial \lambda_2} \left(\frac{\partial \rho_{ab}^{(b)}}{\partial \lambda_1} \right)\,. \tag{101}$$

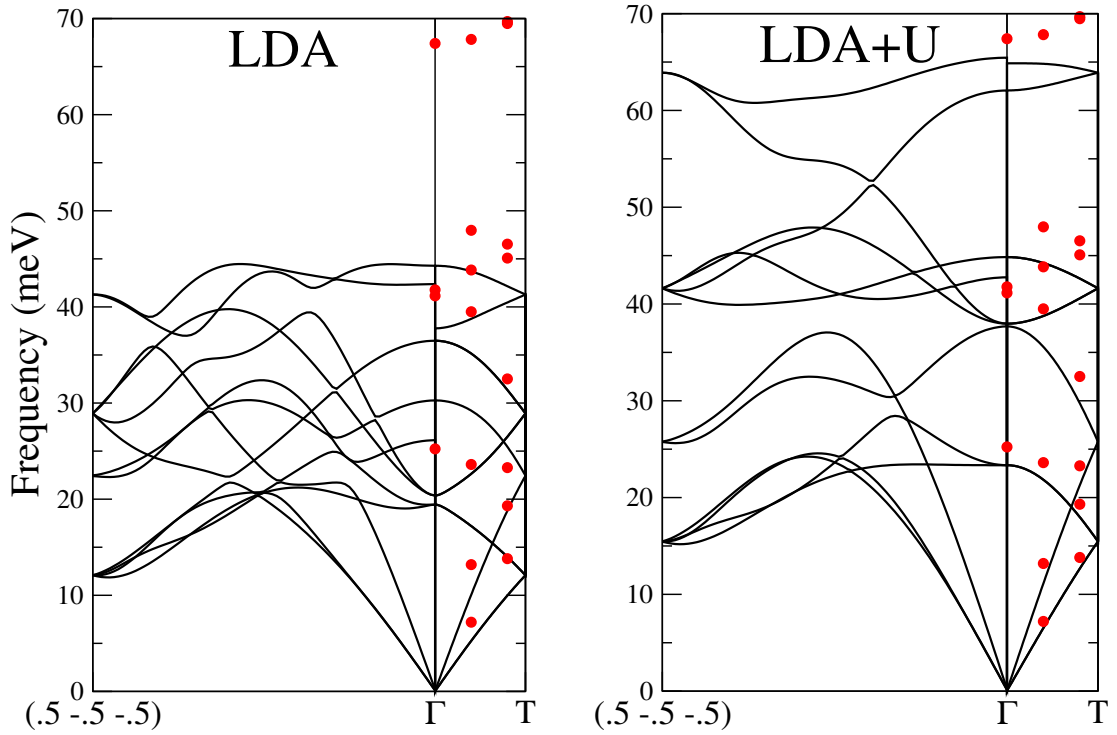

Fig. 5: *Phonon dispersion of NiO for LDA (left panel) and LDA+U (right panel) using U=5 eV. Experimental data (red circles) are taken from [51].*

Both terms now contain first-order variations of the KS wave functions. They are solutions of the linear Eq. (27), but with $\delta v_{\rm eff}$ augmented by an additive contribution from the orbital density matrix

$$\delta v_{\rm eff}(\mathbf{r}) = \delta v_{\rm ext}(\mathbf{r}) + \int d^3r'\, I(\mathbf{r},\mathbf{r}')\,\delta n(\mathbf{r}') + \sum_{abcd} I_{ab,cd}\,\delta\rho_{cd}\,\hat{Q}_{ab} + \sum_{ab} v_{ab}\,\delta\hat{Q}_{ab}\,, \qquad (102)$$

where

$$I_{ab,cd} = \frac{\partial v_{ab}}{\partial \rho_{cd}} = \frac{\partial^2 E_U}{\partial\rho_{ab}\partial\rho_{cd}}\,. \qquad (103)$$

Combined with Eq. (99) this closes the DFPT self-consistency cycle. The above expressions exhibit an increased complexity as compared to the standard DFPT. This is the reason why up to now, only one implementation has been reported [50].

Finally, the EPC vertex can be corrected by taking into account both the modified wave functions and the augmented change of the effective potential (102).

The effect of the +U correction can be quite dramatic not only for electronic structure, but also for derived quantities like the lattice dynamics. An example is given in Fig. 5, which compares the phonon spectrum of NiO obtained with LDA and LDA+U. NiO is a textbook example of a charge-transfer insulator, where local correlations in the open d shell of Ni are decisive. In its ground state, it orders antiferromagnetically along the cubic [111] direction of the rock-salt structure, and possesses a large optical gap of 3.1 eV. While LDA can reproduce the AF state, it severely underestimates the gap (0.4 eV). The gap is increased by adding the +U correction.

For a test calculation with $U = 5$ eV, the gap increases to 2.8 eV. At the same time, the phonon spectrum hardens significantly (see Fig. 5). Its origin lies in an effectively reduced screening when the LDA+U correction is applied. This significantly improves agreement with experiment. Similar trends were also found for MnO [50].
To conclude this Section, we will take a brief look at more advanced corrections to the local approximation in DFT, and discuss recent attempts to use them in linear response and electron-phonon interaction. Three classes will be considered:

1. Hybrid functionals: the local approximation to the exchange energy, $E_X(n)$, is replaced by the exact, non-local exchange. This corrects some deficiencies of the local approximations, and improves the description of wave functions and energies (e.g. gaps in semiconductors). The prize to pay is a drastically increased numerical effort in evaluating both exchange energy and potential, preventing up to now a full DFPT implementation. Phonons and EPC have been addressed using frozen phonon techniques [52–54], but they require the use of supercells and give only limited information on the momentum dependence.

2. GW approach: the KS equations describe a fictitious system of non-interacting electrons, and KS states differ in general from the true quasiparticle wave functions and energies. The latter are determined from a quasiparticle equation, which replaces v_{XC} in the KS equation by a self-energy operator $\hat{\Sigma}$. The GW method evaluates $\hat{\Sigma}$ based on the lowest-order term of the electron-electron interaction. $\hat{\Sigma}$ is expressed in terms of the Green function "G") and screened electron-electron interaction ("W"). This approach, too, is numerically very expensive, but improves the description of quasiparticle properties. It has been used to improve the EPC vertex in the context of frozen-phonon techniques [53]. Very recently a more elaborate linear-response formulation was developed [55]. It starts from a LDA/GGA self-consistent DFPT calculation to obtain the first-order change of the KS wave functions. This is subsequently used to calculate $\delta\hat{\Sigma}$ and to correct the EPC vertex via
$$\delta v_{\text{eff}}^{GW} = \delta v_{\text{eff}}^{DFT} - \delta v_{XC} + \delta\hat{\Sigma}\,. \tag{104}$$
This perturbative scheme has the advantage to get the EPC matrix elements for arbitrary momenta without the need of a supercell.

3. DFT + Dynamical mean-field theory (DMFT): local correlations are cast into a frequency-dependent self-energy $\Sigma(\omega)$ by solving a many-body impurity problem. The impurity system is embedded in a crystalline environment, whose electronic structure is described by DFT. Kotliar and coworkers developed a formulation based on a generating functional, from which both DFT and DMFT equations are derived in a unified framework [56]. Based on this description, a linear response approach has been formulated and applied to a lattice dynamical properties [57]. The method is, however, involved and numerically challenging.

6 Summary

The purpose of this tutorial was to give an introduction into modern linear-response techniques, give access to fundamental properties of electrons, phonons, and their interactions from first principles. In many respects, this approach has matured into a powerful tool, which is applied routinely to a large variety of material classes. We have also discussed examples of physical quantities, which are influenced or even determined by EPC in a direct way, thus providing experimental probes to critically assess theoretical predictions. While for many compounds DFPT predictions for the EPC strength turn out to be rather reliable, larger deviations are expected in cases, when standard DFT already fails to properly describe the electronic subsystem. First promising steps have been taken to incorporate more sophisticated treatments of electron correlations in order to improve the description of EPC in systems, where strong correlations play a crucial role.

References

[1] P. Hohenberg and W. Kohn, Phys. Rev. B**136**, 864 (1964)

[2] W. Kohn and L.J. Sham, Phys. Rev. A**140**, 1133 (1965)

[3] R.M. Dreizler and E.K.U. Gross: *Density Functional Theory: An Approach to the Quantum Many-Body Problem* (Springer, Berlin, 1990)

[4] R.O. Jones and O. Gunnarsson, Rev. Mod. Phys. **61**, 689 (1989)

[5] R.G. Parr and W. Yang: *Density-Functional Theory of Atoms and Molecules* (Oxford University Press, New York, 1989)

[6] D.C. Langreth and M.J. Mehl, Phys. Rev. B **28**, 1809 (1983)

[7] J.P. Perdew, K. Burke, and M. Ernzerhof, Phys. Rev. Lett. **77**, 3865 (1996)

[8] J.P. Perdew, K. Burke, and M. Ernzerhof, Phys. Rev. Lett. **78**, 1396 (1997)

[9] R.P. Feynman, Phys. Rev. **56**, 340 (1939)

[10] X. Gonze and J.-P. Vigneron, Phys. Rev. B **39**, 13120 (1989)

[11] X. Gonze, Phys. Rev. A **52**, 1086 (1995)

[12] X. Gonze, Phys. Rev. A **52**, 1096 (1995)

[13] M.S. Hybertsen and S.G. Louie, Phys. Rev. B **35**, 5585 (1987)

[14] N.E. Zein, Sov. Phys. Solid State **26**, 1825 (1984)

[15] D.K. Blat, N.E. Zein, and V.I. Zinenko, J. Phys. Condens. Matt. **3**, 5515 (1991)

[16] N.E. Zein, Phys. Lett. A **161**, 526 (1992)

[17] S. Baroni, P. Giannozzi, and A. Testa, Phys. Rev. Lett. **58**, 1861 (1987)

[18] P. Giannozzi, S. de Gironcoli, P. Pavone, and S. Baroni, Phys. Rev. B **43**, 7231 (1991)

[19] S. Baroni, S. de Gironcoli, A. Dal Corso, and P. Giannozzi, Rev. Mod. Phys. **73**, 515 (2001)

[20] M. Born and J.R. Oppenheimer, Ann. Physik **84**, 457 (1927)

[21] G.V. Chester and A. Houghton, Proc. Phys. Soc. **73**, 609 (1959)

[22] M. Born and K. Huang: *Dynamical Theory of Crystal Lattices* (Clarendon Press, Oxford, 1954)

[23] A.A. Maradudin, E.W. Montroll, G.H. Weiss, and I.P. Ipatova: *Solid State Physics, Supplement 3* (Academic Press, New York, 1971), p. 1

[24] H. Boettger: *Principles of the Theory of Lattice Dynamics* (Physik Verlag, Weinheim, 1983)

[25] G. Grimvall: *The Electron–Phonon Interaction in Metals* in E. Wohlfarth (ed.): *Selected Topics in Solid State Physics* (North-Holland, New York, 1981)

[26] G.D. Mahan: *Many-Particle Physics*, (Plenum Press, New York, 1990)

[27] R. Heid, I.Yu. Sklyadneva, and E.V. Chulkov, Sci. Rep. **7**, 1095 (2017)

[28] P.B. Allen, Phys. Rev. B **6**, 2577 (1972)

[29] F. Weber, S. Rosenkranz, L. Pintschovius, J.-P. Castellan, R. Osborn, W. Reichardt, R. Heid, K.-P. Bohnen, E.A. Goremychkin, A. Kreyssig, K. Hradil, and D. Abernathy, Phys. Rev. Lett. **109**, 057001 (2012)

[30] F. Weber, L. Pintschovius, W. Reichardt, R. Heid, K.-P. Bohnen, A. Kreyssig, D. Reznik, and K. Hradi, Phys. Rev. B **89**, 104503 (2014)

[31] J.M. Ziman: *Electrons and phonons: the theory of transport phenomena in solids* (Clarendon, Oxford, 1960)

[32] F. Giustino, Rev. Mod. Phys. **89**, 015003 (2017)

[33] T. Sohier, M. Calandra, C.-H. Park, N. Bonini, N. Marzari, and F. Mauri, Phys. Rev. B **90**, 125414 (2014)

[34] W. Li, Phys. Rev. B **92**, 075405 (2015)

[35] M. Fiorentini and N. Bonini, Phys. Rev. B **94**, 085204 (2016)

[36] P.B. Allen, Phys. Rev. B **3**, 305 (1971)

[37] P.B. Allen, Phys. Rev. B **13**, 1416 (1976)

[38] P.B. Allen, W.E. Pickett, and H. Krakauer, Phys. Rev. B **37**, 7482 (1988)

[39] R. Bauer, A. Schmid, P. Pavone, and D. Strauch, Phys. Rev. B **57**, 11276 (1998)

[40] J. Bardeen, L.N. Cooper, and J.R. Schrieffer, Phys. Rev. **108**, 1175 (1957)

[41] D.J. Scalapino: *The Electron-Phonon Interaction and Strong-Coupling* in R.D. Parks (ed.): *Superconductivity, Vol. 1* (Dekker, New York, 1969)

[42] G.M. Eliashberg, Zh. Eksp. Fiz. **38**, 966 (1960) [Sov. Phys. JETP **11**, 696 (1960)]

[43] P.B. Allen and B. Mitrović, Solid State Physics **37**, 1 (1982)

[44] P. Morel and P.W. Anderson, Phys. Rev. **125**, 1263 (1962)

[45] L.N. Oliveira, E.K.U. Gross, and W. Kohn, Phys. Rev. Lett. **50**, 2430 (1988)

[46] D.A. Zocco, S. Krannich, R. Heid, K.-P. Bohnen, T. Wolf, T. Forrest, A. Bosak, and F. Weber, Phys. Rev. B **92**, 220504 (2015)

[47] V.I. Anisimov and O. Gunnarsson, Phys. Rev. B **43**, 7570 (1991)

[48] V.I. Anisimov, J. Zaanen, and O.K. Andersen, Phys. Rev. B **44**, 943 (1991)

[49] B. Himmetoglu, A. Floris, S. de Gironcoli, and M. Cococcioni, Int. J. Quantum Chem. **114**, 14 (2014)

[50] A. Floris, S. de Gironcoli, E.K.U. Gross, and M. Cococcioni, Phys. Rev. B **84**, 161102(R) (2011)

[51] W. Reichardt, V. Wagner, and W. Kress, J. Phys. C**8**, 3955 (1975)

[52] C.H. Patterson, Phys. Rev. B **77**, 115111 (2008))

[53] Z.P. Yin, A. Kutepov, and G. Kotliar, Phys. Rev. X**3**, 021011 (2013)

[54] B. Pamuk, J. Baima, R. Dovesi, M. Calandra, and F. Mauri, Phys. Rev. B **94**, 035101 (2016)

[55] Z. Li, G. Antonius, M. Wu, F.H. da Jornada, and S.G. Louie, Phys. Rev. Lett.**122**, 186402 (2019)

[56] G. Kotliar, S.Y. Savrasov, K. Haule, V.S. Oudovenko, O. Parcollet, and C.A. Marianetti, Rev. Mod. Phys. **78**, 865 (2006)

[57] S.Y. Savrasov and G. Kotliar, Phys. Rev. Lett. **90**, 056401 (2003)

15 Entanglement in Many-Body Systems

Frank Pollmann
Technical University of Munich
Garching

Contents

E. Pavarini and E. Koch (eds.)
Topology, Entanglement, and Strong Correlations
Modeling and Simulation Vol. 10
Forschungszentrum Jülich, 2020, ISBN 978-3-95806-466-9
http://www.cond-mat.de/events/correl20

1 Introduction

The notion of quantum entanglement goes back to the early years of quantum mechanics and was subject of several papers by Schrödinger [1]. At the same time Einstein, Podolsky, and Rosen discussed their famous "Gedankenexperiment" that attempted to show that quantum mechanical theory was incomplete [2]. Quantum entanglement is a physical phenomenon that occurs when particles interact in a way such that the quantum state of each particle cannot be described independently of the state of the others—including when the particles are separated by a large distance. For a long time, it was a topic discussed mostly in quantum optics and for systems with few degrees of freedom. In the last decades, however, it has seen a revival with input from very different areas, including the theory of black holes, quantum information and communication, the numerical investigation of quantum-many body systems, as well as the characterization of topological quantum states and quantum phase transitions.
In this chapter, we will introduce some basics of many-body entanglement and focus on a few selected applications. We begin by introducing basic notions of entanglement in many-body systems and discuss the *area law*, which is commonly obeyed by ground states of local Hamiltonians [3]. We then discuss different concepts in which the area law and the resulting locality of the ground state turn out to be extremely helpful for the investigation of quantum-many body phenomena: First, we show that one-dimensional area law states can represented using matrix-product states (MPSs), allowing for efficient simulations of ground state properties and time-evolution [4,5]. Second, we investigate the entanglement properties of gapped ground states and how they transform under symmetries, providing a framework for the classification of SPT phases [6,7]. Third, we identify universal scaling properties of the entanglement entropies that allow us to characterize quantum phase transitions [8]. Finally we show how to apply all the concepts above to investigate the phase diagram of a spin-1 chain.

2 Many-body entanglement

In the following, we introduce the concept of entanglement entropy and entanglement spectra in many-body systems. Let us consider the bipartition of the Hilbert space $\mathcal{H} = \mathcal{H}_A \otimes \mathcal{H}_B$ of an N-body quantum system as illustrated in Fig. 1(a), where $\mathcal{H}_A$ ($\mathcal{H}_B$) describes all the states defined in subsystem A and B, respectively.
We perform a so-called *Schmidt decomposition*, in which we decompose a (pure) state $|\Psi\rangle \in \mathcal{H}$ as

$$|\Psi\rangle = \sum_\alpha \Lambda_\alpha |\alpha\rangle_A \otimes |\alpha\rangle_B , \quad |\alpha\rangle_{A(B)} \in \mathcal{H}_{A(B)}, \tag{1}$$

where the states $\{|\alpha\rangle_{A(B)}\}$ form an orthonormal basis of (the relevant subspace of) $\mathcal{H}_A$ ($\mathcal{H}_B$) and $\Lambda_\alpha \geq 0$. The Schmidt decomposition is unique up to degeneracies and for a normalized state $|\Psi\rangle$ we find that $\sum_\alpha \Lambda_\alpha^2 = 1$. Note that the Schmidt decomposition is equivalent to the singular-value decomposition of the coefficient matrix ψ_{ij} for chosen local bases $|i\rangle_A$ and $|i\rangle_B$, respectively. An important aspect of the Schmidt decomposition is that it gives direct insight

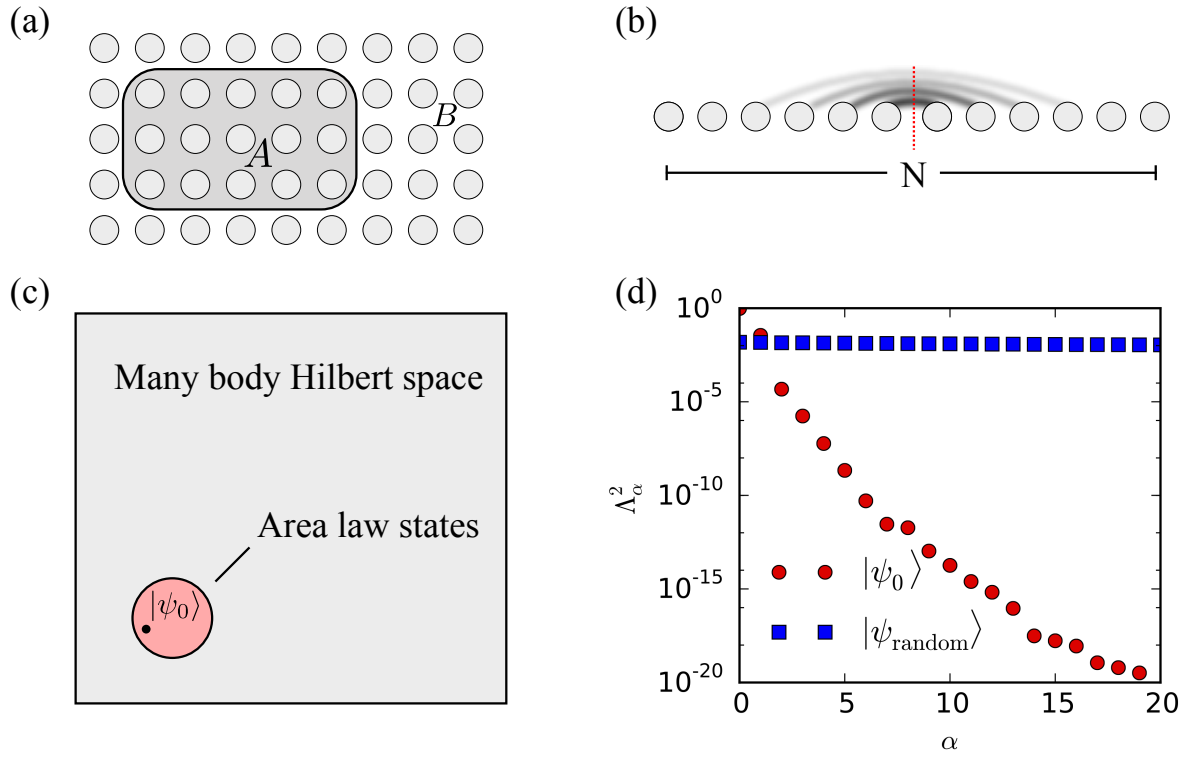

Fig. 1: *(a) Bipartition of a system into two parts A and B. The shaded area A has a boundary ∂A of with surface area $|\partial A|$. (b) Significant quantum fluctuations in gapped ground states occur only on short length scales. (c) 1D area law states make up a very small fraction of the many-body Hilbert space but contain all gapped ground states. (d) Comparison of the largest Schmidt values of the ground state of the transverse field Ising model ($g = 1.5$) and a random state for a system consisting of $N = 16$ spins. The index α labels different Schmidt values.*

into the *bipartite entanglement* (i.e., the quantum entanglement between degrees of freedom in $\mathcal{H}_A$ and $\mathcal{H}_B$) of a state: If no entanglement between the two subsystems is present, the state is a *product state* and the Schmidt decomposition has only one single non-zero Schmidt value ($\Lambda_1 = 1$ and $\Lambda_{\alpha>1} = 0$). If the degrees of freedom of the two subsystems are entangled, we necessarily have multiple non-zero Schmidt values in the decomposition.

A useful measure to quantify the amount of entanglement is the so-called *entanglement entropy*, which is defined as the von-Neumann entropy $S = -\operatorname{Tr}\left(\rho_A \log(\rho_A)\right)$ of the reduced density matrix ρ_A. The *reduced density matrix* of an entangled (pure) quantum state $|\psi\rangle$ is the density matrix of a mixed state defined on the subsystem,

$$\rho_A \equiv \operatorname{Tr}_B \left(|\psi\rangle \langle\psi|\right). \tag{2}$$

A simple calculation shows that it has the Schmidt states $|\alpha\rangle_A$ as eigenstates and the Schmidt coefficients are the square roots of the corresponding eigenvalues, i.e., $\rho_A = \sum_\alpha \Lambda_\alpha^2 |\alpha\rangle_A \langle\alpha|_A$ (equivalently for ρ_B). Hence, the entanglement entropy can be directly expressed in terms of the Schmidt values Λ_α,

$$S = -\operatorname{Tr}\left(\rho_A \log(\rho_A)\right) = -\sum_\alpha \Lambda_\alpha^2 \log \Lambda_\alpha^2. \tag{3}$$

Note that we would get the same entanglement entropy from the reduced density matrix ρ_B. If there is no entanglement between the two subsystems, we find $S = 0$; and $S > 0$ if there is any entanglement.
More generally, we can also consider Rényi entropies of the reduced density matrix

$$S_n = \frac{1}{1-n} \log \mathrm{Tr}\left((\rho_A)^n\right). \tag{4}$$

For the special case $n \to 1$, we recover the von-Neumann entropy. In analogy to the entanglement entropy, we find $S_n{>}0$ for an entangled and $S_n{=}0$ for an unentangled state for all n. Rényi entropies with integer n have the advantage that they can be evaluated by introducing n replicas—a tool that was originally introduced in analytical calculations [9]. This technique is also suitable to obtain Rényi entropies for Monte Carlo simulations [10] or even experimentally [11, 12]
Another useful quantity is the so-called *entanglement spectrum* $\{\varepsilon_\alpha\}$ [13], which is defined in terms of the spectrum $\{\Lambda_\alpha^2\}$ of the reduced density matrix by $\varepsilon_\alpha = -2 \log \Lambda_\alpha$.
To demonstrate the concepts above, we consider a simple system consisting of two spin-$1/2$ with a bipartition in which the first spin is in subsystem A and the second in subsystem B.
The first example is a wave function

$$|\psi\rangle \;=\; \frac{1}{2}\Big(|\uparrow\uparrow\rangle + |\uparrow\downarrow\rangle + |\downarrow\uparrow\rangle + |\downarrow\downarrow\rangle\Big) \tag{5}$$

with Schmidt decomposition

$$|\psi\rangle \;=\; 1 \cdot \tfrac{1}{\sqrt{2}}\big(|\uparrow\rangle + |\downarrow\rangle\big) \otimes \tfrac{1}{\sqrt{2}}\big(|\uparrow\rangle + |\downarrow\rangle\big), \tag{6}$$

representing a product state with entanglement entropy $S = 0$. The second example is a wave function

$$|\psi\rangle \;=\; \frac{1}{2}\Big(|\uparrow\downarrow\rangle + |\downarrow\uparrow\rangle\Big) \tag{7}$$

with Schmidt decomposition

$$|\psi\rangle \;=\; \frac{1}{\sqrt{2}} \cdot \Big(|\uparrow\rangle \otimes |\downarrow\rangle\Big) + \frac{1}{\sqrt{2}} \cdot \Big(|\uparrow\rangle \otimes |\downarrow\rangle\Big), \tag{8}$$

representing a maximally entangled state with entanglement entropy $S = \log 2$.

2.1 Area law

As we will discuss now, ground states of (gapped) local Hamiltonians are very special with respect to their entanglement properties—they fulfill an *area* law. It turns out that this allows on one hand for efficient numerical simulations and on the other hand provides the basis for the characterization of universal properties of quantum phases.
Let us first mention that a "typical" state in the Hilbert space has a *volume law*, i.e., the entanglement entropy grows proportionally with the volume of the partitions. In particular, it has

been shown in Ref. [14] that in a system of N sites with on-site Hilbert space dimension d, a randomly drawn state $|\psi_{\rm random}\rangle$ has an entanglement entropy of $S \approx N/2 \log d - 1/2$ for a bipartition into two parts of $N/2$ sites. Highly excited eigenstates of generic (ergodic) Hamiltonians typically show the same behavior.

In contrast, ground states $|\psi_0\rangle$ of gapped and local Hamiltonians follow an *area law*, i.e., the entanglement entropy grows proportionally to the area of the cut [3][1]

$$S = \alpha |\partial A| + \ldots, \tag{9}$$

where α in the leading term is a non-universal coefficient and $|\partial A|$ denotes the surface area of the cut.

For the special case of a one dimensional chain of length N that is cut into two equal halves as shown in Fig. 1(b) this implies that $S(N)$ is constant for $N \gtrsim \xi$ (with ξ being the correlation length). This can be intuitively understood from the fact that a gapped ground state contains only fluctuations within the correlation length ξ and thus only degrees of freedom near the cut are entangled. A rigorous proof of the area law for 1D gapped and local Hamiltonians is given in Ref. [15]. Since typical states have a volume law, ground states are very special states and can be found within a very small corner of the Hilbert space, as illustrated in Fig. 1(c).

An important observation is that in slightly entangled states, only a relatively small number of Schmidt states contribute significantly to the weight of the state. This is demonstrated in Fig. 1(d) by comparing the largest 20 Schmidt values of an area law state and a volume law state for a bipartition of an $N{=}16$ chain into two half-chains. As an example of an area law state, we considered here the ground state of the transverse field Ising model

$$H = -\sum_n \sigma_n^z \sigma_{n+1}^z + g\sigma_n^x, \tag{10}$$

with σ_n^x and σ_n^z being the Pauli operators and $g > 0$. This $\mathbb{Z}_2$ symmetric model has a quantum phase transition at $g_c = 1$. As shown in Fig. 1(d) for a representative example of $g = 1.5$, the entire weight of the ground state is essentially contained in a few Schmidt states. Generic states fulfilling the area law show a similar behavior and thus the above observation provides an extremely useful approach to compress quantum states by truncating the Schmidt decomposition. In particular, for all $\varepsilon > 0$ we can truncate the Schmidt decomposition at some *finite* χ (independent of the system size) such that

$$\Big\| \, |\psi\rangle - \underbrace{\sum_{\alpha=1}^{\chi} \Lambda_\alpha \, |\alpha\rangle_L \otimes |\alpha\rangle_R}_{|\psi^{\rm trunc}\rangle} \Big\| < \varepsilon \tag{11}$$

This particular property of area law states is intimately related to the matrix-product state (MPS) representation of 1D quantum states, as we will discuss in the next chapter. The situation is very different for a highly entangled (volume law) random state: All the Schmidt values are roughly constant for all $2^{N/2}$ states and thus the 20 dominant states contain a vanishing weight (assuming an equal weight of configurations, we find $\Lambda_\alpha^2 \approx 1/2^{N/2}$ per Schmidt state).

[1] The condition of a gap can in certain cases be released but generically leads to sub-leading $\log$ corrections. In systems with a Fermi surface, the area law breaks down.

2.2 Entanglement in free-particle models

While it is generically very hard to obtain the entanglement entropy in many-body systems, it can be easily obtained for free-particle models [16,17]. This is particularly useful as it allows us to study many interesting aspects of entanglement in various settings—for example, universal properties that might occur independently of the presence or absence of interactions.
For free-particle states, the reduced density matrix ρ_A of a bipartite system can be written as

$$\rho_A = \frac{1}{Z} e^{-\mathcal{H}_A} \text{ , with } \mathcal{H}_A = \sum_{i \in A} \varepsilon_i \, f_i^\dagger f_i, \tag{12}$$

where $f_i^\dagger$ (f_i) creates (annihilates) a single particle with energy ε_i with respect to the so-called "entanglement Hamiltonian" $\mathcal{H}_A$. The constant Z ensures the correct normalization $\mathrm{Tr}\, \rho_A = 1$. Note that $\mathcal{H}_A$ is not simply the physical Hamiltonian H restricted to the subsystem A and therefore Eq. (12) is not a true Boltzmann formula.
Let us now consider a non-interacting fermionic Hamiltonian of the form

$$H = \sum_{i,j} t_{i,j} \, c_i^\dagger c_j. \tag{13}$$

For a given filling factor, the ground state is a Slater determinant describing the filled Fermi sea. Following Wick's theorem, all many-particle correlation functions factorize into products of one-particle functions, for example

$$\left\langle c_i^\dagger c_j^\dagger c_k c_l \right\rangle = \left\langle c_i^\dagger c_l \right\rangle \left\langle c_j^\dagger c_k \right\rangle - \left\langle c_i^\dagger c_k \right\rangle \left\langle c_j^\dagger c_l \right\rangle. \tag{14}$$

We can thus write the reduced density matrix in the form

$$\rho_A = K \exp\Big(- \sum_{i,j \in A} h_{i,j} \, c_i^\dagger c_j \Big) \tag{15}$$

with some constant K. We now need to find a matrix $h_{i,j}$ chosen such that ρ_A reproduces the correct single-particle correlation function $C_{i,j} = \left\langle c_i^\dagger c_j \right\rangle$ for $i, j \in A$. This is done in a common diagonal representation of both matrices: We diagonalize $C_{i,j}$ in subsystem A with eigenvalues ζ_n and corresponding eigenstates $\varphi_n(i)$. The transformation

$$c_i = \sum_n \varphi_n(i) f_n \tag{16}$$

yields for the single-particle correlation function $\left\langle f_n^\dagger f_{n'} \right\rangle = \zeta_n \, \delta_{n,n'}$. To obtain this from the reduced density matrix ρ_A, the entanglement Hamiltonian $\mathcal{H}_A$ must have the diagonal form Eq. (12) with the single-particle entanglement spectrum

$$\varepsilon_n = \log\left(\frac{1 - \zeta_n}{\zeta_n} \right). \tag{17}$$

The many body entanglement entropy is then given by the sum of the contributions of each fermionic mode

$$S = - \sum_n \Big(\zeta_n \log \zeta_n + (1 - \zeta_n) \log(1 - \zeta_n) \Big). \tag{18}$$

To demonstrate the ideas, we consider a model of spinless fermions on a 1D chain of N sites with periodic boundary conditions described by the Hamiltonian

$$H = -t \sum_j \left(c_j^\dagger c_{j+1} + H.c \right). \tag{19}$$

The following simple Python script calculates the entanglement entropy for the ground state at half filling for a bipartition into two halves (i.e., $A \equiv 1 \ldots N/2$ and $B \equiv N/2{+}1 \ldots N$):

```
import numpy as np
N = 20
t = 1
H = np.zeros((N,N))
for i in range(N):
   H[i,np.mod(i+1,N)] = -t
   H[np.mod(i+1,N),i] = -t

E,U = np.linalg.eigh(H)
C = np.dot(U[:N//2,:N//2],np.conj(U[:N//2,:N//2].T))
z = np.linalg.eigvalsh(C)

print ("S = ",-np.sum(z*np.log(z) + (1-z)*np.log(1-z)))
```

3 Efficient representation and matrix-product states (MPSs)

We will now introduce MPSs, which allow for an efficient representation of area law states in 1D. When working with MPSs, it is very helpful to use a diagrammatic tensor representation, which is illustrated in Fig. 2 (a) and (b). In this notation, a tensor with n indices is represented by a symbol with n legs.

We consider a chain with N sites and label the local basis on site n by $|j_n\rangle$ with $j_n = 1, \ldots, d$, e.g., for a spin-1/2 we have $d = 2$ local states $|\uparrow\rangle, |\downarrow\rangle$. Using the tensor product of local basis states, a generic (pure) quantum state can then be expanded as

$$|\psi\rangle = \sum_{j_1, j_2, \ldots j_N} \psi_{j_1 j_2 \cdots j_N} |j_1, j_2, \ldots, j_N\rangle . \tag{20}$$

Note that the order-N tensor $\psi_{j_1,\ldots,j_n}$ has d^N complex entries which makes it prohibitively expensive to store or manipulate exactly even for moderate system sizes. For example, even on a large supercomputer, a simple $S{=}1/2$ system with $d{=}2$ can only be simulated exactly for up to $N{\approx}40$ sites. Since numerical investigations of quantum-many body systems often require much larger systems, it is important to find ways to "compress" the quantum states to a manageable size—this is exactly what we will be able to do using MPS!

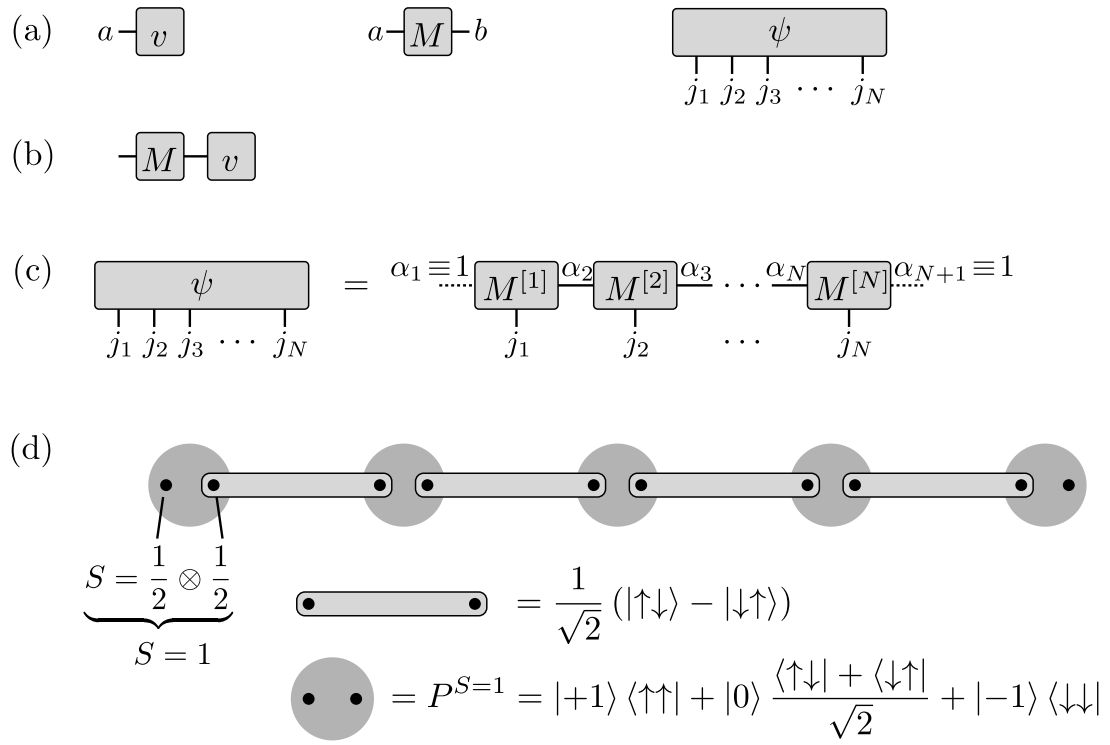

Fig. 2: *(a) Diagrammatic representations of a vector v, a matrix M, and the coefficients of a general many-body state $\psi_{j_1 j_2 \ldots j_n}$. (b) The connection of two legs symbolizes a tensor contraction, here $(Mv)_a = \sum_b M_{ab} v_b$, i.e., summing over the relevant indices. (c) The amplitude of the wave function is decomposed into a product of matrices $M^{[n]j_n}$. The indices α_1 and α_{N+1} are trivial, which we indicate by dashed lines. (d) Diagrammatic representation of the AKLT state. The $S = 1$ sites are decomposed into two $S = \frac{1}{2}$ that form singlets between neighboring sites. With open boundary conditions, the $S = \frac{1}{2}$ spins on the left and right are free edge modes leading to a four-fold degeneracy of the ground state.*

In an MPS, the coefficients $\psi_{j_1,\ldots,j_n}$ of a pure quantum state are decomposed into products of matrices of the form [18–20]

$$|\psi\rangle = \sum_{j_1,\ldots,j_N} \sum_{\alpha_2,\ldots\alpha_N} M^{[1]j_1}_{\alpha_1\alpha_2} M^{[2]j_2}_{\alpha_2\alpha_3} \ldots M^{[N]j_N}_{\alpha_N\alpha_{N+1}} |j_1, j_2, \ldots, j_N\rangle \tag{21}$$

$$\equiv \sum_{j_1,\ldots,j_N} M^{[1]j_1} M^{[2]j_2} \ldots M^{[N]j_N} |j_1, j_2, \ldots, j_N\rangle \,. \tag{22}$$

Here, each $M^{[n]j_n}$ is a $\chi_n \times \chi_{n+1}$ dimensional matrix, i.e., we have a set of d matrices for each site, which we usually group into a tensor of order 3 as shown in Fig. 2(b). The superscript $[n]$ denotes the fact that for a generic state we have a different set of matrices on each site. The indices α_n of the matrices are called "bond", "virtual", or "auxiliary" indices, to distinguish them from the "physical" indices j_n. The matrices at the boundary are vectors, that is $\chi_1 = \chi_{N+1} = 1$, such that the matrix product in Eq. (22) produces a 1×1 matrix, i.e., a single number $\psi_{j_1,\ldots,j_n}$.

3.1 Simple examples of MPS

To become more familiar with the MPS notation, let us consider a few examples.

Product state: The state $|\psi\rangle = |\varphi^{[1]}\rangle \otimes |\varphi^{[2]}\rangle \otimes \cdots \otimes |\varphi^{[n]}\rangle$ can easily be written in the form of Eq. (22); since it has no entanglement, the bond dimension is simply $\chi_n = 1$ on each bond and the 1×1 "matrices" are given by

$$M^{[n]j_n} = \left(\varphi^{[n]}_{j_n}\right). \tag{23}$$

Concretely, the ground state of the transverse field Ising model given in Eq. (10) at infinite field $g \to \infty$ is a product state $|\leftarrow \cdots \leftarrow\rangle \equiv \left(\frac{1}{\sqrt{2}}|\uparrow\rangle - \frac{1}{\sqrt{2}}|\downarrow\rangle\right) \otimes \cdots \otimes \left(\frac{1}{\sqrt{2}}|\uparrow\rangle - \frac{1}{\sqrt{2}}|\downarrow\rangle\right)$, which we write as an MPS using the same set of matrices on each site n,

$$M^{[n]\uparrow} = \left(\tfrac{1}{\sqrt{2}}\right) \qquad \text{and} \qquad M^{[n]\downarrow} = \left(\tfrac{-1}{\sqrt{2}}\right). \tag{24}$$

For the Néel state $|\uparrow\downarrow\uparrow\downarrow\ldots\rangle$, we need different sets of matrices on odd and even sites,

$$M^{[2n-1]\uparrow} = M^{[2n]\downarrow} = \left(1\right) \qquad \text{and} \qquad M^{[2n-1]\downarrow} = M^{[2n]\uparrow} = \left(0\right) \tag{25}$$

for $n = 1, \ldots, N/2$.

Dimerized state: A product of singlets $\frac{1}{\sqrt{2}}\Big(|\uparrow\downarrow\rangle - |\downarrow\uparrow\rangle\Big) \otimes \cdots \otimes \frac{1}{\sqrt{2}}\Big(|\uparrow\downarrow\rangle - |\downarrow\uparrow\rangle\Big)$ on neighboring sites can be written with 1×2 matrices on odd sites and 2×1 matrices on even sites given by

$$M^{[2n-1]\uparrow} = \begin{pmatrix} \frac{1}{\sqrt{2}} & 0 \end{pmatrix}, \quad M^{[2n-1]\downarrow} = \begin{pmatrix} 0 & \frac{-1}{\sqrt{2}} \end{pmatrix}, \quad M^{[2n]\uparrow} = \begin{pmatrix} 0 \\ 1 \end{pmatrix}, \quad M^{[2n]\downarrow} = \begin{pmatrix} 1 \\ 0 \end{pmatrix}. \tag{26}$$

Spin-1 AKLT state: Affleck, Kennedy, Lieb, and Tasaki (AKLT) [21] constructed a Hamiltonian for which the ground state is an exact MPS of bond dimension χ=2. The Hamiltonian reads

$$H = \sum_j \vec{S}_j \vec{S}_{j+1} + \frac{1}{3}\left(\vec{S}_j \vec{S}_{j+1}\right)^2 = 2\sum_j \left(P^{S=2}_{j,j+1} - \frac{1}{3}\right), \tag{27}$$

where $\vec{S}$ are spin $S = 1$ operators and $P^{S=2}_{j,j+1}$ is a projector onto the $S = 2$ sector of the spins on sites j and $j+1$. This model is in a topologically nontrivial phase with remarkable properties of the ground state—we will get into this later. To construct the ground state, we note that the projector $P^{S=2}_{j,j+1}$ does not give a contribution if we decompose the $S = 1$ spins on each site into two $S = \frac{1}{2}$ spins and form singlets between spins on neighboring sites, as illustrated in Fig. 2(d). While the ground state is unique on a ring with periodic boundary conditions, in a chain with open boundary conditions the $S = \frac{1}{2}$ spins on the edges do not contribute to the energy and thus lead to a 4-fold degeneracy of the ground state. Given the structure of the ground state, we can construct the corresponding MPS: We start by writing the product of singlets with the matrices of Eq. (26) and add arbitrary spin-$\frac{1}{2}$ states φ^L and φ^R on the left and right. We apply the projectors $P^{S=1}$ to map the two spin-$\frac{1}{2}$ onto the physical spin-1 site, and contract the three tensors on each site to obtain the MPS structure. For sites $1 < n < N$ in the bulk, we obtain

$$M^{[n]+1} = \sqrt{\frac{4}{3}}\begin{pmatrix} 0 & 0 \\ \frac{1}{\sqrt{2}} & 0 \end{pmatrix} \quad M^{[n]0} = \sqrt{\frac{4}{3}}\begin{pmatrix} \frac{1}{2} & 0 \\ 0 & -\frac{1}{2} \end{pmatrix} \quad M^{[n]-1} = \sqrt{\frac{4}{3}}\begin{pmatrix} 0 & -\frac{1}{\sqrt{2}} \\ 0 & 0 \end{pmatrix}. \tag{28}$$

Here, we included the factor $\sqrt{\frac{4}{3}}$ to normalize the MPS.

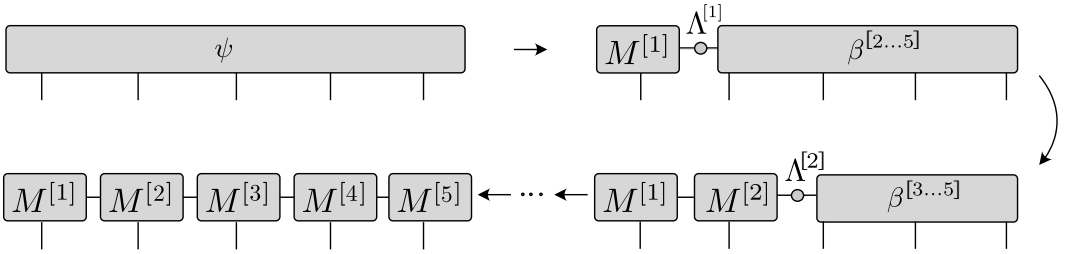

Fig. 3: *Iterative conversion of a state $|\psi\rangle$ given by a rank-N tensor $\psi_{i_1,\ldots,i_N}$ using successive Schmidt decompositions in a diagrammatic representation. The horizontal lines represent the bond (Schmidt indices) $\alpha, \beta, \gamma, \ldots$ and the vertical lines represent the physical indices $j_n \in \{1, \ldots, d\}$. Connected lines between tensors denote summation over the corresponding indices (see text for details).*

3.2 Area law and MPS

In general any state in a finite system can be decomposed *exactly* into the MPS form of Eq. (22). However, the caveat is that for a generic state (with a volume law entanglement), the required bond dimension $\chi_{\max} := \max_n \chi_n$ increases exponentially with the number of sites N. It turns out that all area law states can be very well approximated by MPS with a finite bond dimension $\chi_{\max}$ [22, 23].

For illustration, we will show now how a state can be brought into an MPS form starting from a full many-body state $|\psi\rangle$. For this, we perform successive Schmidt decompositions as shown diagrammatically in Fig. 3. We start by performing a Schmidt decomposition Eq. (1) of the state $|\psi\rangle$ into the first site and the rest such that

$$|\psi\rangle = \sum_{\alpha_1=1}^{d} \Lambda^{[1]}_{\alpha_1} |\alpha_1\rangle_{[1]} |\alpha_1\rangle_{[2,\ldots,N]}. \tag{29}$$

The states $|\alpha_1\rangle_{[1]}$ and $|\alpha_1\rangle_{[2,\ldots,N]}$ form an orthogonal basis for the left and right part, respectively. The first matrix $A^{[i]j_1}_{\alpha_1}$ in the MPS is the matrix relating the left Schmidt states $|\alpha_1\rangle_{[1]}$ with the local states $|j_1\rangle$ (describing the local states on the first site) and is given by $A^{[1]j_1}_{\alpha_1} = \langle j_1|\alpha_1\rangle_{[1]}$. The resulting mixed representation of the state reads

$$|\psi\rangle = \sum_{j_1=1}^{d} \sum_{\alpha_1=1}^{d} A^{[1]j_1}_{\alpha_1} \Lambda^{[1]}_{\alpha_1} |j_1\rangle |\alpha_1\rangle_{[2,\ldots N]}. \tag{30}$$

Next we proceed to the next bond and perform a Schmidt decomposition of the state such that

$$|\psi\rangle = \sum_{\alpha_2=1}^{d^2} \Lambda^{[2]}_{\alpha_2} |\alpha_2\rangle_{[1,2]} |\alpha_2\rangle_{[3,\ldots,N]}. \tag{31}$$

The second matrix $A^{[2]j_2}_{\alpha_1\alpha_2}$ then relates the mixed basis states $|\alpha_1\rangle_{[1]}|j_2\rangle$ with the left Schmidt states $|\alpha_2\rangle_{[1,2]}$ and is given by $A^{[2]j_2}_{\alpha_1\alpha_2} = \left[\langle\alpha_1|_{[1]}\langle j_2|\right] |\alpha_2\rangle_{[1,2]}$. The resulting mixed representation of the state reads

$$|\psi\rangle = \sum_{\alpha_1=1}^{d} \sum_{\alpha_2=1}^{d^2} \sum_{j_1,j_2=1}^{d} A^{[1]j_1}_{\alpha_1} A^{[2]j_2}_{\alpha_1\alpha_2} \Lambda^{[2]}_{\alpha_2} |j_1, j_2\rangle |\alpha_2\rangle_{[3,\ldots,N]}. \tag{32}$$

This procedure can now be continued until reaching the right end of the chain. We choose the last matrix $A^{[N]j_n}$ to relate the states $\Lambda_{\alpha_N}|\alpha_n\rangle_{[N]}$ to the local basis $|j_n\rangle$. Then it is easy to see that we finally arrive at a representation of the state that has exactly the form Eq. (22).
Generically, the matrix dimension increases exponentially as we proceed toward the center of the chain. However, for area law states, we can make an approximation by neglecting the Schmidt states that have a very small Schmidt values. For the ground state of the Ising model discussed above, we can find a very good approximation of the ground state as MPS by keeping only a maximal bond dimension of $\sim$20 with a truncation error that is of the order of the machine precision (independent of the system size).

3.3 Canonical form

The MPS representation Eq. (22) is not unique. Consider the bond between sites n and $n{+}1$, which defines a bipartition into $L = \{\,1,\ldots,n\,\}$ and $R = \{\,n{+}1,\ldots,N\,\}$. Given an invertible $\chi_{n+1}\times\chi_{n+1}$ matrix X, we can replace

$$M^{[n]j_n} \to \tilde{M}^{[n]j_n} := M^{[n]j_n}X^{-1}, \qquad M^{[n+1]j_{n+1}} \to \tilde{M}^{[n+1]j_{n+1}} := XM^{[n+1]j_{n+1}} \tag{33}$$

and still represent the same state $|\psi\rangle$. This freedom can be used to define a convenient "canonical form" of the MPS, following Ref. [24, 25]. Without loss of generality, we can decompose the matrices $\tilde{M}^{[n]j_n} = \tilde{\Gamma}^{[n]j_n}\tilde{\Lambda}^{[n+1]}$, where $\tilde{\Lambda}^{[n+1]}$ is a square, diagonal matrix with positive entries $\tilde{\Lambda}^{[n+1]}_{\alpha_{n+1}}$ on the diagonal. Performing partial contractions gives a representation looking very similar to the Schmidt decomposition (1)

$$\begin{aligned}|\psi\rangle &= \sum_{j_1,\ldots,j_N} M^{[1]j_1}\ldots M^{[n-1]j_{n-1}}\tilde{\Gamma}^{[n]j_n}\,\tilde{\Lambda}^{[n+1]}\,\tilde{M}^{[n+1]j_{n+1}}M^{[n+2]j_{n+2}}\ldots M^{[N]j_N}\,|j_1,\ldots,j_N\rangle \\ &= \sum_{\tilde{\alpha}_{n+1}} \tilde{\Lambda}^{[n+1]}_{\tilde{\alpha}_{n+1}}\,|\tilde{\alpha}_{n+1}\rangle_L \otimes |\tilde{\alpha}_{n+1}\rangle_R\,, \qquad \text{where}\end{aligned} \tag{34}$$

$$|\tilde{\alpha}_{n+1}\rangle_L = \sum_{j_1,\ldots,j_n} \left(M^{[1]j_1}\ldots M^{[n-1]j_{n-1}}\tilde{\Gamma}^{[n]j_n}\right)_{1,\tilde{\alpha}_{n+1}} |j_1,\ldots,j_n\rangle\,, \tag{35}$$

$$|\tilde{\alpha}_{n+1}\rangle_R = \sum_{j_{n+1},\ldots,j_N} \left(\tilde{M}^{[n+1]j_{n+1}}M^{[n+2]j_{n+2}}\ldots M^{[N]j_N}\right)_{\tilde{\alpha}_{n+1},1} |j_{n+1},\ldots,j_N\rangle\,. \tag{36}$$

However, for general M and $\tilde{\Gamma}^{[n]}$, the states $|\tilde{\alpha}_{n+1}\rangle_{L/R}$ will not be orthonormal. Note that we can interpret the X in Eq. (33) as a basis transformation of the states $|\tilde{\alpha}_{n+1}\rangle_R$ in Eq. (36). The idea of the canonical form is to choose the X in Eq. (33) such that it maps $|\tilde{\alpha}_{n+1}\rangle_R$ to the Schmidt states $|\alpha_{n+1}\rangle_R$. Using the Schmidt values $\Lambda^{[n+1]}_{\alpha_{n+1}}$ on the diagonal of $\tilde{\Lambda}^{[n+1]} \to \Lambda^{[n+1]}$, we find that Eq. (34) indeed gives the Schmidt decomposition. Repeating this on each bond yields the canonical form

$$|\Psi\rangle = \sum_{j_1,\ldots,j_N} \Gamma^{[1]j_1}\Lambda^{[2]}\Gamma^{[2]j_2}\Lambda^{[3]}\ldots\Lambda^{[N]}\Gamma^{[N]j_N}\,|j_1,\ldots,j_N\rangle\,. \tag{37}$$

It turns out that the canonical form of MPS is extremely useful for different purposes. First, fixing the gauge degree of freedom allows for a more efficient optimization of MPS in numerical algorithms. Second, it provides convenient analytical properties for exactly proving certain universal properties, which we will use later on in the context of symmetry protected phases.

3.4 Time Evolving Block Decimation (TEBD)

Now that we know how to represent quantum states as MPS, we would like to manipulate them and use them for studying microscopic models. A very useful algorithm is the Time Evolving Block Decimation (TEBD) algorithm [26], which allows evaluating the time evolution of a MPS

$$|\psi(t)\rangle = U(t)\,|\psi(0)\rangle\,. \tag{38}$$

The time evolution operator U can either be $U(t) = \exp(-\mathrm{i}tH)$, yielding a real time evolution, or an imaginary time evolution $U(\tau) = \exp(-\tau H)$. The latter can be used to evaluate (finite temperature) Green functions or as a first, conceptually simple way to find the ground state of the Hamiltonian H through the relation

$$|\psi_{\mathrm{GS}}\rangle = \lim_{\tau\to\infty} \frac{e^{-\tau H}\,|\psi_0\rangle}{\|e^{-\tau H}\,|\psi_0\rangle\|}. \tag{39}$$

The TEBD algorithm makes use of the Suzuki-Trotter decomposition [27], which approximates the exponent of a sum of operators with a product of exponents of the same operators. For example, the first and second order expansions read

$$e^{(X+Y)\delta} = e^{X\delta}e^{Y\delta} + \mathcal{O}(\delta^2), \tag{40}$$

$$e^{(X+Y)\delta} = e^{X\delta/2}e^{Y\delta}e^{X\delta/2} + \mathcal{O}(\delta^3). \tag{41}$$

Here X and Y are operators, and δ is a small parameter. To make use of these expressions, we assume that the Hamiltonian is a sum of two-site operators of the form $H = \sum_n h^{[n,n+1]}$, where $h^{[n,n+1]}$ acts only on sites n and $n+1$, and decompose it as a sum

$$H = \underbrace{\sum_{n\ \mathrm{odd}} h^{[n,n+1]}}_{H_{\mathrm{odd}}} + \underbrace{\sum_{n\ \mathrm{even}} h^{[n,n+1]}}_{H_{\mathrm{even}}}. \tag{42}$$

Each term H_{odd} and H_{even} consists of a sum of commuting operators, therefore $e^{H_{\mathrm{odd}}\delta} = \prod_{n\ \mathrm{odd}} e^{h^{[n,n+1]}\delta}$ and similar for H_{even}. We now divide the time into small time slices $\delta t \ll 1$ (the relevant time scale is in fact the inverse gap) and consider a time evolution operator $U(\delta t)$. Using, as an example, in the first order decomposition (40), the operator $U(\delta t)$ can be expanded into products of two-site unitary operators

$$U(\delta t) \approx \left[\prod_{n\ \mathrm{odd}} U^{[n,n+1]}(\delta t)\right]\left[\prod_{n\ \mathrm{even}} U^{[n,n+1]}(\delta t)\right], \tag{43}$$

where $U^{[n,n+1]}(\delta t) = e^{-\mathrm{i}\,\delta t\, h^{[n,n+1]}}$. The successive application of these two-site unitary operators to an MPS is the main part of the algorithm and explained in the following.

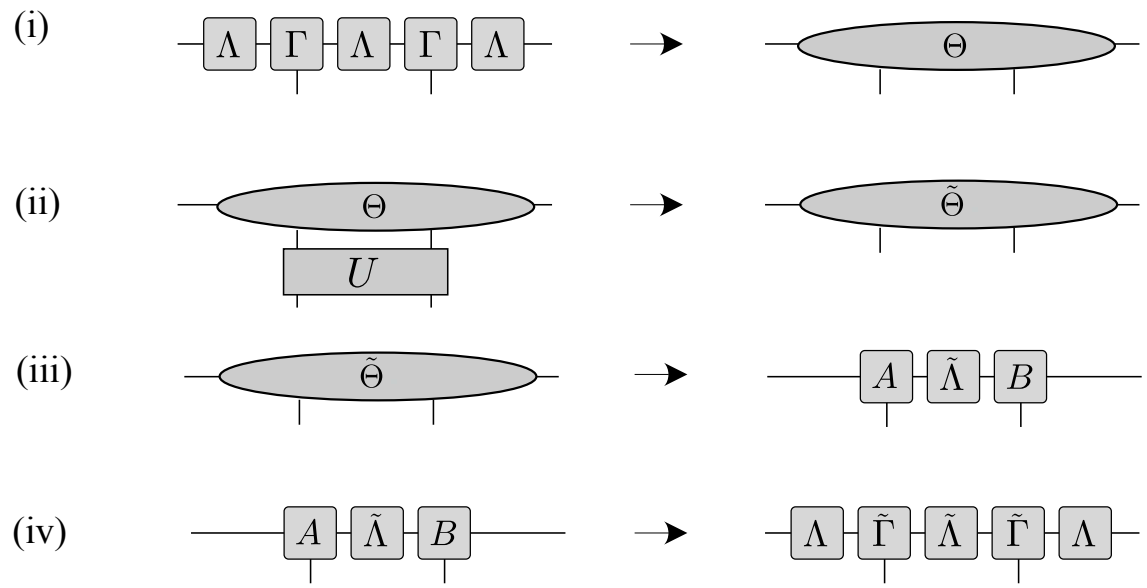

Fig. 4: *Update to apply a two-site unitary U and recover the canonical MPS form (see text for details). Note that we do not explicitly label the positions of the individual tensors in favor for a less cluttered presentation.*

Local unitary updates of an MPS. One of the advantages of the MPS representation is that local transformations can be performed efficiently. Moreover, the canonical form discussed above is preserved if the transformations are unitary [24].
A one-site unitary U simply transforms the tensors Γ of the MPS

$$\tilde{\Gamma}^{[n]j_n}_{\alpha_n\alpha_{n+1}} = \sum_{j'_n} U^{j_n}_{j'_n} \Gamma^{[n]j'_n}_{\alpha_n\alpha_{n+1}}. \tag{44}$$

In such a case the entanglement of the wave-function is not affected and thus the values of Λ do not change. The update procedure for a two-site unitary transformation acting on two neighboring sites n and $n+1$ is shown in Fig. 4. We first find the wave function in the basis spanned by the left Schmidt states $|\alpha_n\rangle_L$, the local basis $|j_n\rangle$ and $|j_{n+1}\rangle$ on sites n and $n+1$, and the right Schmidt states $|\alpha_{n+2}\rangle_R$, which together form an orthonormal basis $\{\ |\alpha_n\rangle_L \otimes\ |j_n\rangle \otimes\ |j_{n+1}\rangle \otimes\ |\alpha_{n+2}\rangle_R\}$. Calling the wave function coefficients Θ, the state is expressed in a mixed bases as

$$|\psi\rangle = \sum_{\alpha_n, j_n, j_{n+1}, \alpha_{n+2}} \Theta^{j_n j_{n+1}}_{\alpha_n\alpha_{n+2}} |\alpha_n\rangle_L |j_n\rangle |j_{n+1}\rangle |\alpha_{n+2}\rangle_R . \tag{45}$$

Using the definitions of the canonical form, Θ is given by

$$\Theta^{j_n j_{n+1}}_{\alpha_n\alpha_{n+2}} = \sum_{\alpha_{n+1}} \Lambda^{[n]}_{\alpha_n} \Gamma^{[n],j_n}_{\alpha_n\alpha_{n+1}} \Lambda^{[n+1]}_{\alpha_{n+1}} \Gamma^{[n+1],j_{n+1}}_{\alpha_{n+1}\alpha_{n+2}} \Lambda^{[n+2]}_{\alpha_{n+2}}. \tag{46}$$

Writing the wave function in this basis is useful because it is easy to apply the two-site unitary in step (ii) of the algorithm

$$\tilde{\Theta}^{j_n j_{n+1}}_{\alpha_n \alpha_{n+2}} = \sum_{j'_n j'_{n+1}} U^{j_n j_{n+1}}_{j'_n j'_{n+1}} \Theta^{j'_n j'_{n+1}}_{\alpha_n \alpha_{n+2}}. \tag{47}$$

Next we have to extract the new tensors $\tilde{B}^{[n]}, \tilde{B}^{[n+1]}$ and $\tilde{\Lambda}^{[n+1]}$ from the transformed tensor $\tilde{\Theta}$ in a manner that preserves the canonical form. We first "reshape" the tensor $\tilde{\Theta}$ by combining indices to obtain a $d\chi_n \times d\chi_{n+2}$ dimensional matrix $\tilde{\Theta}_{j_n \alpha_n; j_{n+1} \alpha_{n+2}}$. Because the basis $\{ \mid \alpha_n \rangle_L \otimes \mid j_n \rangle \}$ is orthonormal, as for the right, it is natural to decompose the matrix using the singular value decomposition (SVD) in step (iii) into

$$\tilde{\Theta}_{j_n \alpha_n; j_{n+1} \alpha_{n+2}} = \sum_{\alpha_{n+1}} \tilde{A}^{[n]}_{j_n \alpha_n; \alpha_{n+1}} \tilde{\Lambda}^{[n+1]}_{\alpha_{n+1} \alpha_{n+1}} \tilde{B}^{[n+1]}_{\alpha_{n+1}; j_{n+1} \alpha_{n+2}}, \tag{48}$$

where $\tilde{A}^{[n]}, \tilde{B}^{[n+1]}$ are isometries and $\tilde{\Lambda}^{[n+1]}$ is a diagonal matrix. Indeed, the suggestive notation that the new tensors are in mixed canonical form is justified, since the SVD yields a Schmidt decomposition of the wave function for a bipartition at the bond between sites n and $n+1$. The isometry $\tilde{A}^{[n]}$ relates the new Schmidt states $|\alpha_{n+1}\rangle_L$ to the combined bases $|\alpha_n\rangle_L \otimes |j_n\rangle$. Analogously, the Schmidt states for the right site are obtained from the matrix $B^{[n+1]}$. Thus the diagonal matrix $\tilde{\Lambda}^{[n+1]}$ contains precisely the Schmidt values of the transformed state. In a last step (iv), we reshape the obtained matrices $\tilde{A}^{[n]}, \tilde{B}^{[n+1]}$ back to tensors with 3 indices and recover the right canonical form by

$$\tilde{\Gamma}^{[n] j_n}_{\alpha_n \alpha_{n+1}} = (\Lambda^{[n]})^{-1}_{\alpha_n} \tilde{A}^{[n]}_{j_n \alpha_n; \alpha_{n+1}} \qquad \text{and} \qquad \tilde{\Gamma}^{[n+1] j_{n+1}}_{\alpha_{n+1} \alpha_{n+2}} = \tilde{B}^{[n+1]}_{\alpha_{n+1}; j_{n+1} \alpha_{n+2}} (\Lambda^{[n+2]})^{-1}_{\alpha_{n+2}}. \tag{49}$$

After the update, the new MPS is still in the canonical form. The entanglement at the bond between n and $n+1$ has changed and the bond dimension increased to $d\chi$. Thus the amount of information in the wave function grows exponentially if we successively apply unitaries to the state. To overcome this problem, we perform an approximation by fixing the maximal number of Schmidt terms to $\chi_{\max}$. In each update, only the $\chi_{\max}$ most important states are kept in step (iii), i.e., if we order the Schmidt states according to their size we simply truncate the range of the index α_{n+1} in Eq. (48) to be $1 \ldots \chi_{\max}$. This approximation limits the dimension of the MPS and the tensors B have at most a dimension of $\chi_{\max} \times d \times \chi_{\max}$. Given that the truncated weight is small, the normalization conditions for the canonical form will be fulfilled to a good approximation. In order to keep the wave function normalized, one should divide by the norm after the truncation, i.e., divide by $\mathcal{N} = \sqrt{\sum_{j_n, j_{n+1}, \alpha_n, \alpha_{n+2}} \left| \Theta^{j_n j_{n+1}}_{\alpha_n \alpha_{n+2}} \right|^2}$.
Using the TEBD algorithm, we can now perform real and imaginary time evolution of MPS. While the imaginary time evolution provides a tool to find ground states, it turns out that a variational optimization is often more efficient. This is done using the density-matrix renormalization group (DMRG) method [28]. The DMRG replaces step (ii) in the TEBD algorithm, in which the two site gate is applied, with a variational optimization of the local tensors. This can be done using for example the Lanczos algorithm. Instead we refer to the existing literature for further details [4, 5].

4 Symmetry-protected topological (SPT) phases

Symmetry and topology are cornerstones in the characterization of quantum phases of matter. The classification of phases in terms of spontaneously broken symmetries is well known, for example the ferro- and paramagnetic phase of the transverse field Ising model. Topological phases of matter are more subtle and require new frameworks for their theoretical understanding.

We consider a gapped one-dimensional system with bosonic degrees of freedom of length L that is invariant under a global symmetry group G. An example of such symmetry is the $\mathbb{Z}_2$ symmetry $\bigotimes_j \sigma_j^x$ of the transverse field Ising model Eq. (10). Note that the classification scheme needs the symmetries to be well-defined even when having open boundaries, which for a unitary symmetry $\bigotimes_j u_j(g)$ with $g \in G$ is guaranteed if it is a product over local symmetry operations $u_j(g)$ on sites (or unit cells), referred to as an on-site symmetry. More general symmetries (such as for example spatial inversion symmetry) will require a more general "entanglement based" approach which we will discuss below. If we assume that the symmetry is not spontaneously broken, then for periodic boundary conditions the ground state must be unique and hence invariant, i.e.,

$$|\psi\rangle = \left[\bigotimes_n u_n(g)\right] |\psi\rangle. \tag{50}$$

However, if we have open boundary conditions, then the absence of spontaneous symmetry breaking in the bulk still allows for the symmetry operation to act non-trivially near the edges. Since the bulk is invariant and thus not affected by the symmetry operation, we can formally write this as $\bigotimes_j u_j(g) = U_L(g)U_R(g)$—which is valid in the ground state subspace. These effective operators U_L and U_R are exponentially localized near the boundaries on a length-scale set by the correlation length. In the thermodynamic limit ($L \to \infty$) $U_L(g)$ and $U_R(g)$ have no overlap and since the Hamiltonian is local, this means that $U_L(g)$ and $U_R(g)$ do not change the energy of a state in the ground state subspace. We refer to this as symmetry fractionalization. The same holds for any other unbroken symmetry $h \in G$, so we can equivalently write $U_L(h)U_R(h)$. Any group relation between g and h then implies a relation between the edge symmetries. In particular, $\{U_L(g), U_L(h), \dots\}$ then obey the same group relations as G, possibly up to a phase factor. In the bosonic case, where U_L and U_R commute, both edges completely decouple and the physical symmetry is then *projectively* represented on each edge (see next section for details about projective representations). Such a projective representation has discrete labels that cannot change smoothly. Since any non-trivial projective representation has a minimal dimension > 1, it protects degenerate modes on the edge.

4.1 Projective representations

Let us consider a group G with group elements $g_i \in G$ and discuss how to classify different SPT phases. The matrices $U(g_i)$ form a *projective* representation of G if

$$U(g_i)U(g_j) = \omega(g_i, g_j)U(g_i g_j), \tag{51}$$

where $\omega(g_i, g_j) \in U(1)$ represent the so-called *factor set*. Thus a projective representation is a linear representation modulo a $U(1)$ phase factor. In the case that all phase factors are unity, the representation is a linear representation of the group. Because of the associativity of the group, i.e., the elements of G fulfill $g_i(g_j g_k) = (g_i g_j)g_k$, the factor set must satisfy

$$\omega(g_j, g_k)\omega(g_i, g_j g_k) = \omega(g_i g_j)\omega(g_i g_j, g_k). \tag{52}$$

Transforming the matrices as $\tilde{U}(g_i) = \beta(g_i)U(g_i),\ \beta(g_i) \in U(1)$ yields a new factor set

$$\tilde{\omega}(g_i, g_j) = \frac{\beta(g_i g_j)}{\beta(g_i)\beta(g_j)}\omega(g_i, g_j). \tag{53}$$

Two projective representations $\tilde{U}(g)$ and $U(g)$ that are related by such a transformation are considered to be equivalent and belong to the same class.
It was Isaac Schur who derived in 1904 a classification of different types of projective representation using so called "Schur multipliers" to label different classes. These correspond to the second cohomology group $H_2(G, U(1))$ of a group G. Instead of discussing the details of the proof, we refer for a general introduction to Ref. [29] and consider some simple examples.

(1) Group $\mathbb{Z}_\mathbf{N}$. The generators of the group are $\exp(i\pi/N)$ rotations and the group elements are $\{1, R, R^2, \ldots, R^N\}$. For a projective representation of the group we can assign an arbitrary phase such that $U^N(R) = \exp(i\varphi)$. However, a simple rescaling $U(R)$ by $\exp(i\varphi/N)$ can always transform the projective representation to a linear one. Thus this group has only one class and all projective representation can be transformed into a linear one.

(2) Group $\mathbb{Z}_\mathbf{2} \times \mathbb{Z}_\mathbf{2}$. This group is generated by π rotations R_x and R_z about two orthogonal axes. Clearly, $R_x^2 = R_z^2 = 1$ and $R_z R_x = R_x R_z$, thus the group elements are $\{1, R_x, R_z, R_x R_z\}$. The group $\mathbb{Z}_2 \times \mathbb{Z}_2$ has two different classes of projective representations which can be distinguished by the gauge invariant phase factor

$$U(R_x)U(R_z)U^{-1}(R_x)U^{-1}(R_z) = \exp(i\varphi)$$

with $\varphi = 0, \pi$. Clearly, as each element occurs with its inverse, the phase of the commutator cannot be change by rephasing the operators.
Both cases can be realized using a representation of the rotations in terms of spin operators by $U(R_x) = \exp(i\pi S^x)$ and $U(R_z) = \exp(i\pi S^z)$. The $S = 1$ representation with

$$S^x = \frac{1}{\sqrt{2}}\begin{pmatrix} 0 & 1 & 0 \\ 1 & 0 & 1 \\ 0 & 1 & 0 \end{pmatrix}, \quad S^z = \begin{pmatrix} -1 & 0 & 0 \\ 0 & 0 & 0 \\ 0 & 0 & 1 \end{pmatrix}. \tag{54}$$

is a linear ($\varphi = 0$) representation. The $S = 1/2$ spin matrices

$$S^x = \frac{1}{2}\begin{pmatrix} 0 & 1 \\ 1 & 0 \end{pmatrix}, \quad S^z = \frac{1}{2}\begin{pmatrix} 1 & 0 \\ 0 & -1 \end{pmatrix}. \tag{55}$$

form a projective ($\varphi = \pi$) representation. This can be seen easily as $U(R_x) = \sigma_x$ and $U(R_z) = \sigma_z$ anti-commute (σ_x, σ_z are the Pauli matrices).

4.2 MPS representations of SPT phases

For the study of SPT phases, it will be useful to derive how symmetry operations act on MPS in the canonical form. Let us consider an on-site symmetry operation which is applied to all sites

$$|\tilde{\psi}\rangle = \left[\bigotimes_n u_n(g)\right]|\psi\rangle, \tag{56}$$

where $u_n(g)$ is acting on site n with g being an element of the symmetry group G under which the state $|\psi\rangle$ is invariant. In the MPS formulation, the transformation corresponds to contracting the symmetry operation with all physical legs as shown in Fig. 5(a). In Ref. [30] it was shown that for an MPS in canonical form the matrices Γ^j transform under symmetry operations g as

$$\sum_{j'} u_{jj'}(g)\Gamma^{j'} = e^{i\theta_g}U^\dagger(g)\Gamma^j U(g), \tag{57}$$

with a diagrammatic representation as shown in Fig. 5(b). Here $U(g)$ is a unitary matrix which commutes with the Λ matrices, and $e^{i\theta(g)}$ is a phase.[2] It is clear that this is a sufficient condition for the MPS to be symmetric. To show that it is a necessary condition, one has to apply the Schwarz inequality and use conditions of the canonical form [30].

Equivalently to the discussion above, it can be shown that the matrices $U(g)$ form a χ-dimensional *linear* or *projective* representation of the symmetry group of the wave function and $e^{i\theta(g)}$ is a linear (1D) representation [6]. The matrices $U(g)$ are actually a representation of the symmetry operations in the basis of Schmidt states (this can be seen by going back to the definition of the canonical form). Note that we assumed a translationally invariant MPS but we can directly generalize the concept to the general case by allowing site dependent $U(g)$.

Similar relations can be derived for symmetries that are not on-site operations. For a time reversal transformation Γ^j is transformed to $(\Gamma^j)^*$ (complex conjugate) on the left hand side (including possible spin rotations). In the case of inversion symmetry Γ^j is transformed to $(\Gamma^j)^T$ (transpose) on the left hand side of Eq. (57). We refer to Refs. [6, 7] for further details.

4.3 Simple examples of different SPT phases

We will now consider two different MPSs for a spin-1 chain that belong to different symmetry protected phases protected by the $\mathbb{Z}_2 \times \mathbb{Z}_2$ symmetry, i.e, π rotations about the x and z axis. Clearly, the onsite representation of the $\mathbb{Z}_2 \times \mathbb{Z}_2$ in terms of the $S = 1$ degrees of freedom is a linear one. Let us now analyze how the MPS representation of two different states transforms under the $\mathbb{Z}_2 \times \mathbb{Z}_2$ symmetry.

Spin-1 AKLT state: The AKLT state has $SO(3)$ symmetry and $\mathbb{Z}_2 \times \mathbb{Z}_2$ is a subgroup thereof. Since the MPS representation Eq. (28) is very simple, we can directly extract the projective representation by applying the symmetry operations and find that

$$U(R_x) = \sigma_x,\ U(R_z) = \sigma_z$$

[2] As $U(g)$ commutes with Λ, it also commutes with the reduced density matrices ρ^L and ρ^R.

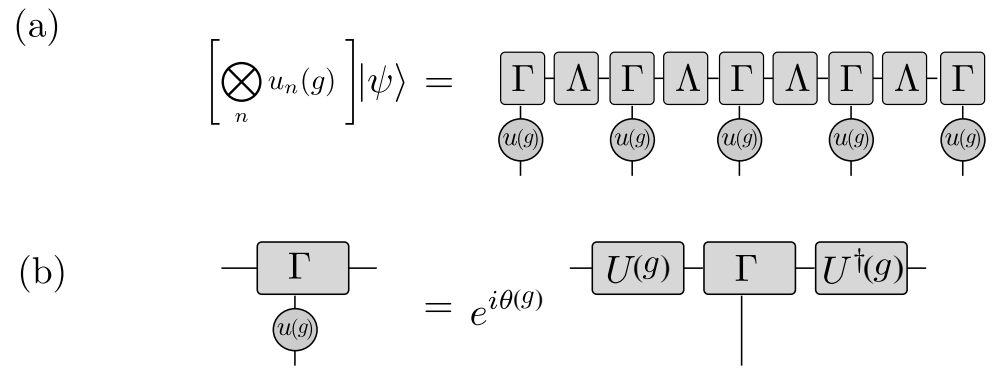

Fig. 5: *(a): Transformation of an MPS under an on-site symmetry g applied to all sites. (b): Representation of a symmetry operation in terms of the MPS.*

and $\theta = \pi$ (To arrive at this result, one can simply apply the on-site symmetry operations to the MPS). The representation of $\mathbb{Z}_2 \times \mathbb{Z}_2$ is a projective one with the gauge invariant phase factor $U(R_x)U(R_z)U^\dagger(R_x)U^\dagger(R_z) = -1$.

Spin-1 product state: A product state of $S^z = 0$ eigenstates of the form $|0\rangle \otimes |0\rangle \otimes \cdots \otimes |0\rangle$ is invariant under $\mathbb{Z}_2 \times \mathbb{Z}_2$ and the MPS transforms trivially under $\mathbb{Z}_2 \times \mathbb{Z}_2$ rotations

$$U(R_x) = 1,\ U(R_z) = 1$$

with $U(R_x)U(R_z)U^\dagger(R_x)U^\dagger(R_z) = 1$ and $\theta = 0$.

As argued above, these phase factors characterize the two phases as they cannot be changed unless the symmetry is broken or the system undergoes a phase transition. Thus we have identified two representatives of different SPT phases.

4.4 Degeneracies in the entanglement spectrum

Here we discuss some practical ideas of how to detect SPT in numerical simulations in terms of the entanglement spectrum. Topological phases with non-trivial projective representations necessarily have degeneracies in the entanglement spectrum. That is, *all* eigenvalues of the reduced density matrices ρ^L and ρ^R for the bipartition of the system into two half-chains are degenerate.

To see this, let us assume that the ground state is represented as a MPS and is symmetric under a symmetry group G. Using the Eq. (57), we find the symmetry representation $U(g)$ in terms of the auxiliary indices which commutes with the reduced density matrices. If the $U(g)$ for $g \in G$ form a projective representation of the symmetry group, we can find a set of non-commuting elements such that for example $U(g_i)U(g_j)U(g_i)^\dagger U(g_j)^\dagger = \exp(i\varphi)$. The non-trivial commutation relations require that the irreducible representations have dimensions larger than one, which yields degeneracies in the spectrum of ρ^L and (ρ^R). For example, if $\varphi = \pi$, the spectrum is doubly degenerate, since ρ^L and ρ^R commute with the two unitary matrices U_x, U_z which anti-commute among themselves.

5 Universal entanglement scaling at critical points

In the previous section, we mainly focused on local and gapped Hamiltonians for which we found an area law. We will now shift our attention to ground states at critical points where the correlation length diverges and the state becomes scale invariant. The microscopic details become irrelevant for the long wavelength physics and according to the universality hypothesis, certain quantities only depend on basic properties like the symmetry of the system.
Many critical points in one-dimensional systems can be described by *conformal field theories* (CFT). A CFT is a quantum field theory that is invariant under conformal transformations (i.e., transformations that locally preserve angles, but not necessarily lengths). The number of independent conformal transformations is infinite for $1{+}1$D, which makes conformal symmetry highly constraining in this case. As a result, conformally invariant critical points in $1{+}1$ dimensions can be described by a small number of parameters. One of the key quantities in this context is the *central charge* c, which is a universal quantity that quantifies the low energy degrees of freedom of the theory. For example, for free bosons $c = 1$, whereas the Ising universality class has $c = 1/2$.
We will now show that the central charge is intimately linked to the bipartite entanglement entropy [9,8]. Let us compute the entanglement entropy for the bipartition of a $1{+}1$ dimensional lattice model from the reduced density matrix ρ_A. Since the eigenvalues lie in the interval $[0, 1]$ and $\operatorname{Tr}\rho_A = 1$, $\operatorname{Tr}\rho_A^n$ is convergent and analytic for all $\operatorname{Re} n > 1$. Hence we can obtain the entanglement entropy using

$$S = -\lim_{n\to 1} \frac{\partial}{\partial n} \operatorname{Tr}\rho_A^n. \tag{58}$$

While calculating $\operatorname{Tr}\rho_A^n$ for a generic n is not feasible, it is possible for positive integer n using the replica trick and then analytically continuing it to a general complex value. In particular, the calculation for positive integer n reduces to that of a partition function on a Riemann surface that is analytically achievable in a quantum field theory. Using this approach, it is now possible to obtain the entanglement entropy for a $1{+}1$ dimensional CFT in different settings:
First, we consider the case in which we cut out ℓ consecutive sites from an infinite chain for which we find [9]

$$S = \frac{c}{3} \log\left(\frac{\ell}{a}\right) + \mathcal{O}(1). \tag{59}$$

Here c is the central charge and a is an ultraviolet cutoff, corresponding to a lattice spacing. Thus the entanglement entropy does not exhibit an area law but instead diverges logarithmically. Moreover, the Rényi entropies are given by

$$S_n = \frac{c}{6}\left(1 + \frac{1}{n}\right) \log\left(\frac{\ell}{a}\right) + \mathcal{O}(1). \tag{60}$$

Second, we consider the case in which we cut a finite chain of length L into two pieces of length ℓ and $L - \ell$ for which we obtain

$$S = \frac{c}{6} \log\left(\frac{2L}{\pi a} \sin\frac{\pi\ell}{L}\right) + \mathcal{O}(1), \tag{61}$$

with the special case for a bipartition into two equally sized halves,

$$S = \frac{c}{6} \log \left(\frac{\ell}{a} \right) + \mathcal{O}(1). \tag{62}$$

The coefficient in front of the logarithm is thus half of the one where we cut out a finite block from an infinite system. These above two formulas are particularly useful for extracting the central charge from finite size numerics.
Third, we consider an infinite system that is close to a critical point, where the correlation length is large but finite. In this case one can often still effectively describe the system by a conformal field theory. One then obtains for the entanglement entropy [31]

$$S = \frac{c}{6} \log \left(\frac{\xi}{a} \right) + \mathcal{O}(1). \tag{63}$$

The latter formula is very useful for infinite-system MPS based simulations of critical points, where a finite bond dimension induces a finite correlation length. In this *entanglement scaling* approach, a simulation at the critical point is performed with increasing bond dimension, which can be used to extract the central charge [32, 33].

6 Case study: Phase diagram of a spin-1 chain

We now demonstrate the usefulness of the entanglement based quantities we derived in the preceding sections to numerically study the phase diagram of a spin-1 chain. For this we will first use MPS based methods to obtain the ground state and then analyze its properties using entanglement spectroscopy and entanglement scaling.
We will investigate the phase diagram of the Hamiltonian

$$H = J \sum_j \vec{S}_j \cdot \vec{S}_{j+1} + D \sum_j (S_j^z)^2, \tag{64}$$

where the first term is the spin-1 Heisenberg coupling ($J > 0$) and the second term is a single ion anisotropy ($D > 0$). This model has various symmetries that can protect SPT phases, including time reversal, inversion symmetry, and $\mathbb{Z}_2 \times \mathbb{Z}_2$ spin rotation symmetry. The phase diagram of this model is well known (Ref. [34] and citations therein) and thus it serves as a good testing case.
In order to understand the phase diagram, let us first consider the limiting cases:

- For $D \ll J$, the model reduces to the antiferromagnetic spin-1 Heisenberg model and the ground state is in the Haldane phase [35], which also contains the AKLT state $|\psi_{\mathrm{AKLT}}\rangle$ [21]. Based on the consideration made in Section 4, we know that the ground state is in a non-trivial SPT phase.

- For $D \gg J$, the ground state is adiabatically connected to a simple product state $|\psi_{\text{large } D}\rangle = |0\rangle \otimes |0\rangle \otimes \cdots \otimes |0\rangle$, which is thus in a trivial phase.

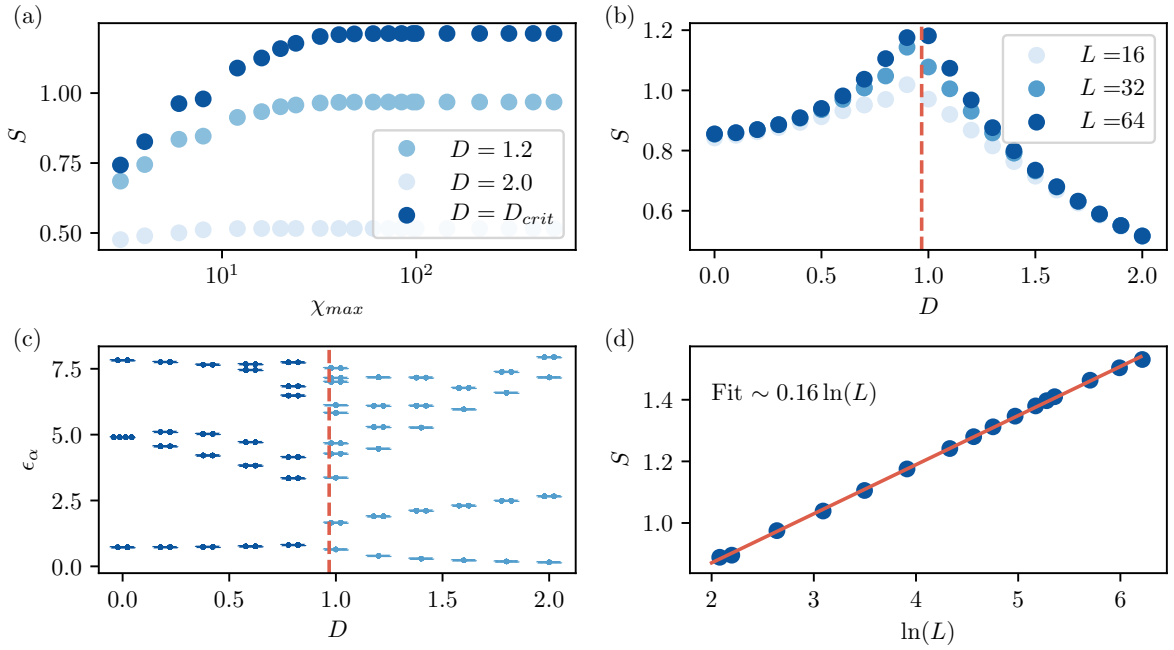

Fig. 6: *(a) Half-chain entanglement entropy for the spin-1 chain Eq. (64) of length* $L = 128$ *as function of the bond dimension* $\chi_{\max}$ *used for the MPS simulations for different* D*. (b) Half-chain entanglement entropy for different systems sizes as function of* D*. The dashed line indicates the location of the exact critical point [34]. (c) Entanglement spectrum as function of* D *with a characteristic degeneracy in the Haldane phase. (d) Scaling of the entanglement entropy at the critical point, allowing us to extract a central charge* $c = 1$*.*

Consequently, there has to be a phase transition between the two limiting cases.

We use the DMRG [28] method to variationally optimize an MPS ansatz for the ground state of the Hamiltonian and implement the code in Python with the TeNpy package [5]. A minimal code that finds the MPS representation for a spin-1 chain reads:

```
from tenpy.networks.mps import MPS
from tenpy.models.spins import SpinModel
from tenpy.algorithms import dmrg

M = SpinModel({"S":1,"L": 16,"bc_MPS": "finite",
               "Jx": 0,"Jy": 0,"Jz": 0,"D":2})
psi = MPS.from_product_state(M.lat.mps_sites(), [1]*16, "finite")
dmrg_params = {"trunc_params": {"chi_max": 30, "svd_min": 1.e-10}}
info = dmrg.run(psi, M, dmrg_params)
print("S[j] =", psi.entanglement_entropy())
```

For numerical stability, we add a small field at the first and last site to prevent the edge modes from coupling to each other. To test the convergence and figure out the required bond dimension $\chi_{\max}$, we plot the half-chain entanglement entropy S in Fig. 6(a). We find that S converges for relatively small $\chi_{\max}$ for the system sizes considered. Indeed, based on the area law, we expect that the required bond dimension is independent of system size in gapped phases. However, the

entanglement entropy diverges logarithmically at critical points and thus the bond dimension has to be increased as we increase the system size (typically $\chi_{\max} \sim L^{\kappa}$ for some model specific exponent $\kappa > 0$). The logarithmic divergence of the entanglement entropy provides a useful signature to determine critical points in phase diagrams as seen in Fig. 6(b). We can clearly distinguish the area law behavior in the gapped phases from the critical point. Similar techniques have been used in the literature to pinpoint the critical point at $D_C/J = 0.96845(8)$ [34]. The entanglement spectrum shown in Fig. 6(c) shows the characteristic degeneracy throughout the Haldane phase and only accidental degeneracies in the large D phase. Note that we could also use non-local order parameters to distinguish the two phases [36, 37]. Lastly we focus on the properties of the critical point and investigate the entanglement scaling in Fig. 6(d). Using Eq. (62), we extract a central charge of $c = 1$, compatible with the universality of a Gaussian transition [38].
The tools applied in this case study can (in principle) be applied to determine the phase diagram of any one-dimensional model Hamiltonian. The main obstacle is that the ground state might be highly entangled, preventing an accurate representation as an MPS. This is particularly the case when considering critical phases, especially if the central charge is large.

7 Conclusions and further developments

In these lecture notes, we discussed a few aspects of many-body entanglement. After a general introduction, we introduced the *area law* which is commonly obeyed by ground states of local Hamiltonians, i.e., the leading term of the entanglement entropy grows at most proportionally with the boundary between the two partitions. This is in contrast to the *volume* law which is found for random or highly excited states. The area law and resulting locality of the ground state are extremely helpful to investigate the intricate structure of quantum many-body states and their emergent quantum orders. To demonstrate this, we focused on three different applications to one-dimensional quantum spin systems: First, we showed that area law states can be efficiently represented using MPSs—which are the basis for several algorithms that allow to simulate large quantum systems. Second, we investigated the entanglement properties of ground states and how they transform under symmetries, providing a framework for the classification of SPT phases. Third, we identified universal scaling properties of the entanglement entropies.
We obviously only covered a small fraction of this fast moving and rich field. Let us close by briefly mentioning some exciting aspects that could not be covered in theses notes.

Topological entanglement. The entanglement entropy for a simply connected region for a two-dimensional system has the general form $S = \alpha|\partial A| - \gamma + \ldots$, where α in the leading term is a non-universal coefficient and $|\partial A|$ is the perimeter of the subsystem. The sub-leading term γ, also known as the topological entanglement entropy, is universal and reflects the anyonic content that characterizes the topological order [39, 40]. This is directly related to the total quantum dimension (D) of the underlying topological field theory as $\gamma = \log D$. The topological entanglement is a very useful quantity to detect topological orders.

Many-body localization. So far we only discussed entanglement of ground states but the concept is also very useful to characterize non-equilibrium properties. One of the most remarkable predictions of quantum mechanics is that an arbitrarily weak random potential is sufficient to localize all energy eigenstates of a single particle moving in one dimension. Recent work has proposed that, if there are electron-electron interactions but the electronic system is isolated from other degrees of freedom, there can be a many-body localization (MBL) transition even in a one-dimensional system for which all the single-particle states are localized [41]. Entanglement is useful to characterize MBL in different ways: First, while the highly excited eigenstates of generic Hamiltonians fulfill a volume law, the eigenstates of a fully MBL systems obey an area law [42]. Thus the entanglement of eigenstates serves as an "order parameter" to detect a transition from an extended to an MBL phase. Second, the dynamical properties of the entanglement entropy allow us to distinguish a non-interacting (Anderson) localized system from an MBL system. While the entanglement following a quantum quench saturates for the former, it shows a logarithmic growth as function of time for the latter [43].

Acknowledgement.

We would like to acknowledge Rohit Dilip for performing the DMRG simulations presented in the case study and for useful comments on the manuscript. We also want to thank Johannes Hauschild for coauthoring related lecture notes on tensor-network simulations [5] that are partly reproduced in the matrix-product state section.

References

[1] E. Schrödinger, Proceedings of the Cambridge Philosophical Society **31**, 555 (1935)

[2] A. Einstein, B. Podolsky, and N. Rosen, Phys. Rev. **47**, 777 (1935)

[3] J. Eisert, M. Cramer, and M.B. Plenio, Rev. Mod. Phys. **82**, 277 (2010)

[4] U. Schollwöck, Ann. Phys. (N. Y). **326**, 96 (2011)

[5] J. Hauschild and F. Pollmann, SciPost Phys. Lect. Notes p. 5 (2018)

[6] F. Pollmann, A.M. Turner, E. Berg, and M. Oshikawa, Phys. Rev. B **81**, 064439 (2010)

[7] X. Chen, Z.-C. Gu, and X.-G. Wen, Phys. Rev. B **83**, 035107 (2011)

[8] P. Calabrese and J. Cardy, J. Phys. A: Mathematical and Theoretical **42**, 504005 (2009)

[9] C. Holzhey, F. Larsen, and F. Wilczek, Nuclear Physics B **424**, 443 (1994)

[10] M.B. Hastings, I. González, A.B. Kallin, and R.G. Melko, Phys. Rev. Lett. **104**, 157201 (2010)

[11] A. Elben, B. Vermersch, M. Dalmonte, J.I. Cirac, and P. Zoller, Phys. Rev. Lett. **120**, 050406 (2018)

[12] D.A. Abanin and E. Demler, Phys. Rev. Lett. **109**, 020504 (2012)

[13] H. Li and F.D.M. Haldane, Phys. Rev. Lett. **101**, 010504 (2008)

[14] D.N. Page, Phys. Rev. Lett. **71**, 1291 (1993)

[15] M.B. Hastings, J. Stat. Mech. Theory Exp. **2007**, P08024 (2007)

[16] I. Peschel and M.-C. Chung, J. Phys. A: Mathematical and General **32**, 8419 (1999)

[17] I. Peschel, Journal of Physics A: Mathematical and General **36**, L205 (2003)

[18] M. Fannes, B. Nachtergaele, and R.F. Werner, Commun. Math. Phys. **144**, 443 (1992)

[19] S. Östlund and S. Rommer, Phys. Rev. Lett. **75**, 3537 (1995)

[20] S. Rommer and S. Östlund, Phys. Rev. B **55**, 2164 (1997)

[21] I. Affleck, T. Kennedy, E.H. Lieb, and H. Tasaki, Phys. Rev. Lett. **59**, 799 (1987)

[22] D. Gottesman and M.B. Hastings, New J. Phys. **12**, 025002 (2010)

[23] N. Schuch, M.M. Wolf, F. Verstraete, and J.I. Cirac, Phys. Rev. Lett. **100**, 030504 (2008)

[24] G. Vidal, J.I. Latorre, E. Rico, and A. Kitaev, Phys. Rev. Lett. **90**, 227902 (2003)

[25] G. Vidal, Phys. Rev. Lett. **98**, 070201 (2007)

[26] G. Vidal, Phys. Rev. Lett. **93**, 040502 (2004)

[27] M. Suzuki, J. Math. Phys. **32**, 400 (1991)

[28] S.R. White, Phys. Rev. Lett. **69**, 2863 (1992)

[29] G. Karpilovsky: *The Schur multiplier*. LMS monographs (Clarendon Press, 1987)

[30] D. Perez-Garcia, M.M. Wolf, M. Sanz, F. Verstraete, and J.I. Cirac, Phys. Rev. Lett. **100**, 167202 (2008)

[31] P. Calabrese and J. Cardy, J. Stat. Mech. **2004**, P06002 (2004)

[32] L. Tagliacozzo, T.R. de Oliveira, S. Iblisdir, and J.I. Latorre, Phys. Rev. B **78**, 024410 (2008)

[33] F. Pollmann, S. Mukerjee, A.M. Turner, and J.E. Moore, Phys. Rev. Lett. **102**, 255701 (2009)

[34] S. Hu, B. Normand, X. Wang, and L. Yu, Phys. Rev. B **84**, 220402 (2011)

[35] F.D.M. Haldane, Phys. Lett. A **93**, 464 (1983)

[36] M. den Nijs and K. Rommelse, Phys. Rev. B **40**, 4709 (1989)

[37] F. Pollmann and A.M. Turner, Phys. Rev. B **86**, 125441 (2012)

[38] A. Luther and D.J. Scalapino, Phys. Rev. B **16**, 1153 (1977)

[39] M. Levin and X.-G. Wen, Phys. Rev. Lett. **96**, 110405 (2006)

[40] A. Kitaev and J. Preskill, Phys. Rev. Lett. **96**, 110404 (2006)

[41] D.M. Basko, I.L. Aleiner, and B.L. Altshuler, Ann. Phys. (N.Y). **321**, 1126 (2006)

[42] B. Bauer and C. Nayak, Phys. Rev. X **4**, 041021 (2014)

[43] J.H. Bardarson, F. Pollmann, and J.E. Moore, Phys. Rev. Lett. **109**, 1 (2012)

16 Quantifying Spatial Correlations in General Quantum Dynamics

Markus Müller
Peter-Grünberg-Institut 2
Forschungszentrum Jülich

Contents

E. Pavarini and E. Koch (eds.)
Topology, Entanglement, and Strong Correlations
Modeling and Simulation Vol. 10
Forschungszentrum Jülich, 2020, ISBN 978-3-95806-466-9
http://www.cond-mat.de/events/correl20

1 Introduction

Correlated dynamics play a key role in many aspects of our world, ranging from collective behavior of swarms of animals, correlations in the fluctuations of share prices at the stock market, to dynamical processes determining our weather. In physics, correlations in the dynamics of interacting many-body systems lie at the heart of our understanding of collective dynamical phenomena. Understanding the role of correlations in quantum systems is both a fundamental challenge and of high practical relevance for the control of multi-particle quantum systems, for example in the context of the ongoing efforts to build large-scale quantum computers and quantum simulators [1, 2]. Whereas most research has been focusing on various types of correlations that can be present in the *states* of quantum systems, in this lecture, our main focus will be on correlations that can be present in the *dynamics* of quantum systems. In particular, we will be discussing some basics of quantum dynamics in closed and open quantum systems, and introduce and discuss a general and rigorous method to quantify the amount of correlations in general dynamics of quantum systems. We will then apply these methods to various physical examples, such as the correlated decay of excited atoms coupled to the radiation field, and to the characterization of noise characteristics in real experimental trapped-ion quantum computers.

1.1 Temporal vs spatial correlations

Between what types of correlations in the dynamics of quantum systems can we distinguish? Quantum systems can display a wide variety of dynamical behaviors, in particular in open quantum systems, which are systems that are coupled to the surrounding environment. One interesting feature which has attracted much attention is the presence of memory effects (non-Markovianity) in the time evolution. Such *temporal* effects typically arise for strong enough coupling between the system and its environment, or when the environment is structured [3–5]. Whereas memory effects (or time correlations) can be present in any quantum system exposed to noise, another extremely relevant feature, which we will focus on in this lecture, are correlations in the dynamics of different parts of composite, i.e., multi-partite quantum systems. Since different parties of a partition are often, though not always, identified with different places in space, we will in the following refer to these correlations between subsystems of a larger quantum system as *spatial* correlations.

Spatial correlations in the dynamics give rise to a wide plethora of interesting phenomena, such as super-radiance [6] and decoherence-free subspaces [7–9], which we will also discuss as part of this lecture, and other phenomena like super-decoherence [10] and sub-radiance [11].

Moreover, clarifying the role of spatial correlations in the performance of a large variety of quantum processes is a highly active area of research, e.g. in quantum computing. There, spatially correlated noise can substantially reduce the parameter regimes and lower the error thresholds below which errors can be successfully fought off by quantum error correction techniques [12–14]. Other areas of interest are understanding the role of spatial correlations in the quantum dynamics underlying photosynthesis and excitation transfer [15, 16], and applications in quantum metrology [17].

As already mentioned, numerous works have aimed at quantifying up to which extent quantum dynamics deviates from the Markovian behavior. However, much less attention has been paid to developing quantifiers of spatial correlations in the dynamics. This may be partially due to the well-known fact that under many, though not all practical circumstances, dynamical correlations can be detected by studying the time evolution of correlation functions of properly chosen observables $\mathcal{O}_A$ and $\mathcal{O}_B$, acting respectively on the two parties A and B of a composite system S of interest. Indeed, any correlation $C(\mathcal{O}_A, \mathcal{O}_B) = \langle \mathcal{O}_A \otimes \mathcal{O}_B \rangle - \langle \mathcal{O}_A \rangle \langle \mathcal{O}_B \rangle$ detected during the time evolution of an initial product state, $\rho = \rho_A \otimes \rho_B$, witnesses the correlated character of the dynamics. Here, ρ_A and ρ_B denote the initial density operators of the two subsystems. However, it is a priori not easy to guess suitable observables. Furthermore there exist highly correlated dynamics, which cannot be realized by a combination of local processes and which do not generate any such correlation, e.g. a swap process between two parties.

Thus, it is important to develop methods which allow one to detect the presence or absence of spatial correlations in the dynamics, without a priori knowledge of the underlying microscopic dynamics, and which do not require one to resort to adequately chosen "test" observables and initial "test" quantum states. Such methods should furthermore provide a rigorous ground to quantitatively compare the amount of spatial correlations in different dynamical processes. These characteristics are essential for a "good" correlation quantifier that can be used to study spatial correlations in quantum dynamics from a fundamental point of view, to clarify their role in physical processes, as well as to measure and quantify spatial correlations in the dynamics of experimental quantum systems.

In this lecture, we will introduce first basic concepts of correlations in quantum states and quantum dynamics, and then introduce methods to quantify the degree of correlation in general quantum dynamics.

1.2 Correlations in quantum states

Before discussing quantum dynamics, let us, however, take a step back and first consider correlations that can be present in quantum states: a famous example of quantum-mechanically perfectly correlated states are Bell states [12], also called EPR-pairs, named after Einstein, Podolsky and Rosen [18]. An example is the following state of two qubits A and B

$$\left|\Phi^+\right\rangle_{\mathrm{AB}} = \frac{1}{\sqrt{2}}\Big(\left|0\right\rangle_{\mathrm{A}} \otimes \left|0\right\rangle_{\mathrm{B}} + \left|1\right\rangle_{\mathrm{A}} \otimes \left|1\right\rangle_{\mathrm{B}} \Big) = \frac{1}{\sqrt{2}}\Big(\left|00\right\rangle_{\mathrm{AB}} + \left|11\right\rangle_{\mathrm{AB}} \Big), \tag{1}$$

where $|0\rangle$ and $|1\rangle$ denote the computational basis states of each qubit (or spin-1/2 particle). Here and in the following we will mostly suppress the tensor-product symbol, for simplicity and compactness of notation. If now, say, the first qubit is measured in the computational basis, i.e., the state is projected onto either $|0\rangle_1$ or $|1\rangle_1$ (the eigenstates of the Pauli matrix $Z = |0\rangle\langle 0| - |1\rangle\langle 1|$), each of the two possible measurement outcomes $+1$ (for $|0\rangle_1$) and -1 (for $|1\rangle_1$) will be obtained with probability $1/2$. If the second qubit is also measured, it will be found with certainty in the same state as the first qubit – the measurement outcomes will be perfectly correlated. Note that this measurement statistics could also be explained by purely

classical correlations: think of a machine that with probability of 50% prepares both qubits in $|00\rangle_{\rm AB}$, and with 50% in $|11\rangle_{\rm AB}$ – the resulting measurement statistics would be the same. But what happens if the qubits of the Bell state (1) are measured in the X-basis instead, i.e., the observable Pauli matrix $X = |0\rangle\langle 1| + |1\rangle\langle 0|$ is measured? The Bell state can be equally written as

$$|\Phi^+\rangle_{\rm AB} = \frac{1}{\sqrt{2}}\Big(|00\rangle_{\rm AB} + |11\rangle_{\rm AB} \Big) = \frac{1}{\sqrt{2}}\Big(|{+}{+}\rangle_{\rm AB} + |{-}{-}\rangle_{\rm AB} \Big) \tag{2}$$

with $|\pm\rangle = \big(|0\rangle \pm |1\rangle \big)/\sqrt{2}$ denoting the eigenstates of X, $X|\pm\rangle = \pm|\pm\rangle$. Thus, the measurement outcomes for measurements in this different basis are also perfectly correlated! This feature is a signature of the entangled nature of this two-qubit state: in fact, there exists no basis, in which $|\Phi^+\rangle_{\rm AB}$ can be written as a product of single-qubit states $|\psi_1\rangle_{\rm A}$ and $|\psi_2\rangle_{\rm B}$, $|\Phi^+\rangle \neq |\psi_1\rangle_{\rm A} \otimes |\psi_2\rangle_{\rm B}$ – therefore, the two qubits are entangled.

How can one then quantify the amount of correlations in a bi-partite quantum state? This can be done by means of the quantum mutual information, which is a generalization of the Shannon mutual information in the classical case [12], which quantifies the mutual dependence between two random variables. Let us start by considering the density matrix $\rho_{\rm S}$ describing the joint state of a system S, which is composed of two parts A and B. The von Neumann entropy $S(\rho_{\rm S})$ of the state $\rho_{\rm S}$ is defined by

$$S(\rho_{\rm S}) := -{\rm Tr}\rho_{\rm S}\log(\rho_{\rm S}) \tag{3}$$

The density operator $\rho_{\rm S}$ can be written in terms of its eigenstates $|\psi_i\rangle$, $\rho_{\rm S} = \sum_i p_i |\psi_i\rangle\langle\psi_i|$, with $p_i \geq 0$ and $\sum_i p_i = 1$. Then the expression for the von Neumann entropy reduces to $S(\rho_{\rm S}) = -\sum_i p_i \log p_i$. For the system S in a pure state $|\psi\rangle$, $\rho_{\rm S} = |\psi\rangle\langle\psi|$, and $S(\rho_{\rm S}) = 0$.

The reduced density operators, associated to parts A and B of the composite system, $\rho_{\rm S}|_{\rm A}$ and $\rho_{\rm S}|_{\rm B}$, are obtained by performing the partial trace [12] over the respective complementary parts

$$\rho_{\rm S}|_{\rm A} = {\rm Tr}_{\rm B}(\rho_{\rm S}), \qquad \rho_{\rm S}|_{\rm B} = {\rm Tr}_{\rm A}(\rho_{\rm S}). \tag{4}$$

For the Bell state of Eq. (1), the reduced density operators correspond to the fully mixed state

$$\rho_{\rm S}|_{\rm A} = \frac{1}{2}\Big(|0\rangle\langle 0|_{\rm A} + |1\rangle\langle 1|_{\rm A} \Big), \qquad \rho_{\rm S}|_{\rm A} = \frac{1}{2}\Big(|0\rangle\langle 0|_{\rm B} + |1\rangle\langle 1|_{\rm B} \Big), \tag{5}$$

and thus the von Neumann entropies evaluate to $S(\rho_{\rm S}|_{\rm A}) = S(\rho_{\rm S}|_{\rm B}) = \log 2$.

Now, the quantum mutual information of a state $\rho_{\rm S}$ is given by

$$I(\rho_{\rm S}) = S(\rho_{\rm S}|_{\rm A}) + S(\rho_{\rm S}|_{\rm B}) - S(\rho_{\rm S}). \tag{6}$$

For the Bell state of Eq. (1) the quantum mutual information assumes its maximum value for a two-qubit system, $I(\rho_{\rm S}) = 2\log 2$, indicating that the Bell states are indeed *maximally correlated* quantum states. On the other hand, for any product state, i.e., if $\rho_{\rm S} = \rho_{\rm S}|_{\rm A} \otimes \rho_{\rm S}|_{\rm B}$, the quantum mutual information vanishes, which indicates that the subsystems A and B are independent. In order words, outcomes of local measurements on subsystems A and B are in the latter case *completely uncorrelated*, and thus from measuring one subsystem no information

about the state of the other subsystem can be inferred. Thus, quantum mutual information, as its classical counterpart, indicates by how much knowing about one part of a larger system reduces the uncertainty about the other part.

Finally, how can correlations in quantum states be detected in practice, i.e., in an experiment? As discussed, they reveal themselves in correlations in the measurement statistics of suitably chosen observables: Non-vanishing values for correlation functions such as $C(\mathcal{O}_\mathrm{A}, \mathcal{O}_\mathrm{B}) = \langle \mathcal{O}_\mathrm{A} \otimes \mathcal{O}_\mathrm{B} \rangle - \langle \mathcal{O}_\mathrm{A} \rangle \langle \mathcal{O}_\mathrm{B} \rangle$ signal the presence of correlations. For the example of the Bell state of Eq. (1), the choice of, e.g., $\mathcal{O}_\mathrm{A} = Z_\mathrm{A}$ and $\mathcal{O}_\mathrm{B} = Z_\mathrm{B}$ is suitable, since $\langle Z_\mathrm{A} \rangle = \mathrm{Tr}_\mathrm{A}(Z_\mathrm{A} \rho_\mathrm{S}|_\mathrm{A}) = 0$, and similarly for qubit B, whereas $\langle Z_\mathrm{A} \otimes Z_\mathrm{B} \rangle = +1$. In contrast, for a product state such as e.g. $|0\rangle_\mathrm{A} \otimes |0\rangle_\mathrm{B}$, the correlator expectation value vanishes, $C(Z_\mathrm{A}, Z_\mathrm{B}) = 0$.

2 Quantum dynamics

2.1 Closed- and open-system quantum dynamics

After this brief discussion about correlations that can be present in quantum *states*, let us turn our attention to quantum *dynamics*. General time evolution of a quantum system S, which can be coupled to an environment, can be described by quantum operations $\mathcal{E}_\mathrm{S}$ [3]. Here, we will focus on completely positive and trace-preserving (CPT) maps, often also called Kraus maps, which map valid physical density matrices describing the state of the system S onto other physical density matrices

$$\mathcal{E}_\mathrm{S} : \rho_\mathrm{S} \mapsto \mathcal{E}_\mathrm{S}(\rho_\mathrm{S}) = \sum_i K_i \, \rho_\mathrm{S} \, K_i^\dagger. \tag{7}$$

Here, the set of so-called Kraus operators $\{K_i\}$ fulfill $\sum_i K_i^\dagger K_i = \mathbb{1}_\mathrm{S}$. Note that this includes the case of time evolution in closed quantum systems, where $\rho_\mathrm{S} \mapsto U_\mathrm{S} \, \rho_\mathrm{S} \, U_\mathrm{S}^\dagger$, i.e., one Kraus operator corresponds to the unitary time evolution operator U_S and all other Kraus operators vanish.

As an example for open-system dynamics let us briefly discuss dephasing dynamics of a single qubit or spin-1/2 system. This dynamics is present in many physical systems, and it is a limiting factor in almost all architectures that are being used for quantum processors. Such dynamics can be generated for instance by fluctuating fields (e.g. magnetic background fields) in the lab. We can thus describe the dephasing process using a single fluctuating variable $B(t)$, referred to in the following as effective magnetic field

$$H_G(t) = \frac{1}{2} \, B(t) \, Z. \tag{8}$$

For simplicity, we assume the random fluctuation in the values of the effective magnetic field to obey a Gaussian distribution $P(B)$, which implies that

$$\left\langle \exp\left[\pm \mathrm{i} \int_0^t B(t')dt' \right] \right\rangle = \exp\left[-\frac{1}{2} \left\langle \left(\int_0^t B(t')dt' \right)^2 \right\rangle \right]. \tag{9}$$

If one additionally assumes a stationary autocorrelation function of the noise source

$$\big\langle B(t+\tau)\, B(t)\big\rangle = \big\langle B(\tau)\, B(0)\big\rangle, \tag{10}$$

and furthermore a δ-correlation of the noise, one obtains that

$$\big\langle B(\tau)\, B(0)\big\rangle = \big\langle [B(0)]^2\big\rangle\, \delta(\tau). \tag{11}$$

Using these properties, one finds

$$\left\langle \left[\int_0^t B(t')dt'\right]^2 \right\rangle = \big\langle [B(0)]^2\big\rangle t = \gamma t, \tag{12}$$

where we have defined the dephasing rate $\gamma = \big\langle [B(0)]^2\big\rangle$.
For an arbitrary initial (pure) state, $\rho(0) = |\psi(0)\rangle\langle\psi(0)|$, with $|\psi(0)\rangle = \alpha\,|0\rangle + \beta\,|1\rangle$, the state at time t will be given by an average over the noise realizations

$$\rho(t) = \int |\psi(t)\rangle\langle\psi(t)|\, P(B)\, dB = |\alpha|^2\,|0\rangle\langle 0| + |\beta|^2\,|1\rangle\langle 1| + e^{-\frac{1}{2}\gamma t}\big(\alpha\beta^*\,|0\rangle\langle 1| + \alpha^*\beta\,|1\rangle\langle 0|\big). \tag{13}$$

This allows us to identify this process as the dephasing channel [12]

$$\mathcal{E}_{\rm S} : \rho_{\rm S} \mapsto (1-p)\rho_{\rm S} + pZ\rho_{\rm S}Z, \tag{14}$$

i.e., as a quantum operation with the two Kraus operators $K_0 = \sqrt{1-p}\,\mathbb{1}$ and $K_1 = \sqrt{p}Z$ and the identification $p = \frac{1}{2}(1 - e^{-\frac{1}{2}\gamma t})$. Thus, for long times ($t \to \infty$, $p \to 1/2$), the initial coherence (off-diagonal elements of the density matrix (13)) completely vanishes and the qubit ends in an incoherent mixture of the computational basis states.

2.2 Detection of correlated dynamics

Let us now generalize our previous discussions in Sec. 1.2 about two qubits and consider a general bipartite quantum system $\mathrm{S} = \mathrm{AB}$ undergoing some dynamics given by a completely positive and trace preserving (CPT) map $\mathcal{E}_{\rm S}$. Without loss of generality we will assume that the dimension of both subsystems A and B is the same, $\dim(\mathcal{H}_{\rm A}) = \dim(\mathcal{H}_{\rm B}) = d$, and therefore $d_{\rm S} := \dim(\mathcal{H}_{\rm S}) = d^2$. The dynamics $\mathcal{E}_{\rm S}$ is said to be uncorrelated with respect to the subsystems A and B if it can be decomposed as $\mathcal{E}_{\rm S} = \mathcal{E}_{\rm A} \otimes \mathcal{E}_{\rm B}$, with individual CPT maps $\mathcal{E}_{\rm A}$ and $\mathcal{E}_{\rm B}$ acting on the subsystems A and B, respectively. Otherwise we call it correlated.
Simple examples of correlated dynamics from the field of quantum information are, e.g., two-qubit entangling gates, such as the prototypical two-qubit controlled-NOT (or CNOT) gate [12]

$$\text{CNOT} = |0\rangle\langle 0|_{\rm A} \otimes \mathbb{1}_{\rm B} + |1\rangle\langle 1|_{\rm A} \otimes X_{\rm B} \tag{15}$$

which flips the state of the target qubit (B), $|0\rangle \leftrightarrow |1\rangle$, if and only if the control qubit (A) is in the $|1\rangle$ state. For suitably chosen input product states, e.g. $|\psi(0)\rangle = |+\rangle_1 \otimes |0\rangle_2$, this unitary

gate creates (maximally) correlated output states such as the Bell state of Eq. (1), therefore the CNOT gate is clearly a correlated quantum dynamics!
Similarly, spatially homogeneous or *global* (magnetic) field fluctuations, acting with the same strength on a register of two or more qubits, described by a Hamiltonian

$$H_G(t) = \frac{1}{2} B(t) \sum_k Z_k \tag{16}$$

result in spatially correlated dephasing dynamics. This dynamics $\mathcal{E}_{\rm S}$ on the qubit register cannot be described by a product of independent dephasing processes, $\mathcal{E}_{\rm S} \neq \otimes_k \mathcal{E}_k$, with $\mathcal{E}_k$ acting on the k-th qubit. It is left as an exercise to work out the generalization of Eq. (14) for this scenario of correlated dephasing dynamics. Again, working with suitably chosen input states, e.g. $|\psi(0)\rangle = \otimes_k |+\rangle_k$, should allow one to distinguish between spatially correlated and uncorrelated dephasing.
In fact, this idea holds true in general: any correlation $C(\mathcal{O}_{\rm A}, \mathcal{O}_{\rm B}) = \langle \mathcal{O}_{\rm A} \otimes \mathcal{O}_{\rm B} \rangle - \langle \mathcal{O}_{\rm A} \rangle \langle \mathcal{O}_{\rm B} \rangle$ detected during the time evolution of an initial product state, $\rho_{\rm S} = \rho_{\rm A} \otimes \rho_{\rm B}$, witnesses the correlated character of the dynamics. However, for this to work, one needs to be lucky or have a priory knowledge about the dynamics and thereby be able to choose suitable observables and input states, for which correlated dynamics generates non-vanishing correlations in the final quantum state generated by the dynamics. Furthermore, note that there exist highly correlated dynamics, which cannot be realized by a combination of local processes, which however do not generate any such correlation. A simple example is the swap process between two parties. Such dynamics can either act on internal degrees of freedom, induced, e.g., by the action of a swap gate acting on two qubits [12], or can correspond to (unwanted) external dynamics, caused, e.g., by correlated hopping of atoms in an optical lattice [19] or the melting of an ion Coulomb crystal and subsequent recooling dynamics with a possibly different rearrangement of particles in trapped-ion architectures [20].

3 Rigorous quantifier for correlations in quantum dynamics

In light of this discussion, let us therefore now discuss a systematic and rigorous method to capture and quantify spatial correlations in quantum dynamics, not requiring any a-priori knowledge or assumptions about the dynamics taking place on the composite quantum system.

3.1 Choi-Jamiołkowski isomorphism

The central tool of our construction is the Choi-Jamiołkowski isomorphism [21, 22, 12]. This is a one-to-one correspondence of a given quantum dynamics of a system to an equivalent representation in the form of a quantum state in an enlarged Hilbert space. As we will see, this mapping will allow us to use tools developed for the quantification of correlations in quantum *states*, as we discussed above in Sec. 1.2, for our purpose of quantifying correlations in the quantum *dynamics* taking place in the bi-partite system ${\rm S} = {\rm AB}$. For this mapping, consider a

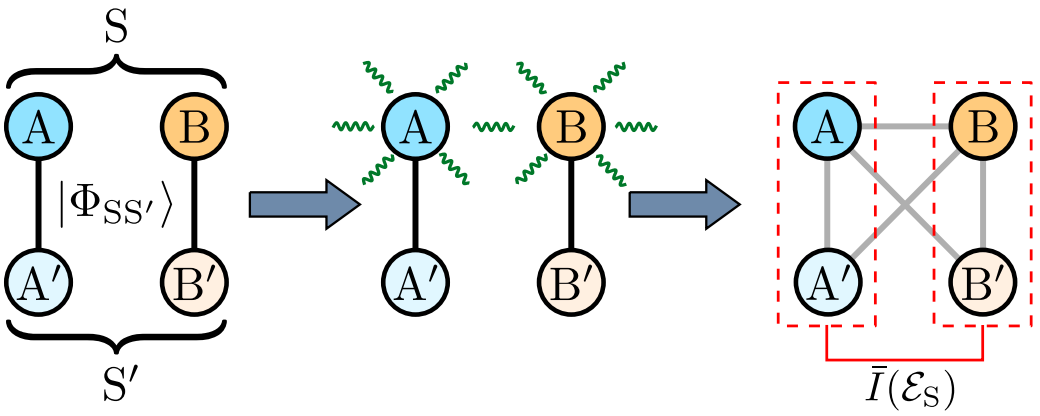

Fig. 1: *Schematics of the method. Left: the system S is prepared in a maximally entangled state* $|\Phi_{SS'}\rangle$ *with the auxiliary system* S′. *This state is just a product of maximally entangled states between* AA′ *and* BB′, *see Eq. (17). Middle: the system undergoes some dynamics* $\mathcal{E}_S$. *Right: if and only if this process is correlated with respect to* A *and* B, *the total system* SS′ *becomes correlated with respect to the bipartition* AA′|BB′. *The degree of correlation of the dynamics can then be measured by the normalized mutual information, see Eq. (20).*

second d^2-dimensional bipartite system $S' = A'B'$, essentially a "copy" of system S. Next, let $|\Phi_{SS'}\rangle$ be the maximally entangled state between S and S′,

$$|\Phi_{SS'}\rangle := \frac{1}{d}\sum_{j=1}^{d^2} |jj\rangle_{SS'} = \frac{1}{d}\sum_{k,\ell=1}^{d} |k\ell\rangle_{AB} \otimes |k\ell\rangle_{A'B'}\,. \tag{17}$$

Here, $|j\rangle$ denotes the state vector with 1 at the j-th position and zero elsewhere, i.e., the canonical basis in the d^2-dimensional Hilbert space of S and its "copy" S′. Similarly, $|k\rangle_A$ and $|l\rangle_B$ denote the canonical basis of the d-dimensional subsystems A, B, and A′, B′. The Choi-Jamiołkowki representation of some CPT map $\mathcal{E}_S$ on S is then given by the d^4-dimensional quantum state

$$\rho_S^{CJ} := \mathcal{E}_S \otimes \mathbb{1}_{S'}\big(\,|\Phi_{SS'}\rangle\langle\Phi_{SS'}|\,\big). \tag{18}$$

This means it is obtained by acting with the quantum operation $\mathcal{E}_S$ on S, and the identity operation $\mathbb{1}_{S'}$ on S′, as shown schematically in the middle part of Fig. 1. The entire information about the dynamical process $\mathcal{E}_S$ taking place in S is now contained in this unique state ρ_S^{CJ} in the enlarged d^4-dimensional space.

To become familiar with the Choi-Jamiołkowki representation of a quantum process, it is a useful exercise to show that for a system S consisting of a single qubit, which undergoes dephasing dynamics as described by Eq. (14), the Choi-Jamiołkowki state (18) reads

$$\rho_S^{CJ} = \frac{1}{2}\Big(\,|00\rangle\langle 00|_{SS'} + |11\rangle\langle 11|_{SS'}\,\Big) + \frac{1}{2}(1-2p)\Big(\,|00\rangle\langle 11|_{SS'} + |11\rangle\langle 00|_{SS'}\,\Big). \tag{19}$$

3.2 Construction of a correlation measure

In order to formulate a faithful measure of spatial correlations for dynamics, we adopt a resource theoretic approach (see, e.g., [23, 24] where this approach is used in the context of entanglement theory). The idea is that one may consider correlated dynamics as a resource to perform whatever task that cannot be implemented solely by (composing) uncorrelated evolutions $\mathcal{E}_{\mathrm{A}} \otimes \mathcal{E}_{\mathrm{B}}$. Then, suppose that the system S undergoes some dynamics given by the map $\mathcal{E}_{\mathrm{S}}$. Now, consider the (left and right) composition of $\mathcal{E}_{\mathrm{S}}$ with some uncorrelated maps $\mathcal{L}_{\mathrm{A}} \otimes \mathcal{L}_{\mathrm{B}}$ and $\mathcal{R}_{\mathrm{A}} \otimes \mathcal{R}_{\mathrm{B}}$, which act before and after $\mathcal{E}_{\mathrm{S}}$, so that the total dynamics is given by $\mathcal{E}'_{\mathrm{S}} = (\mathcal{L}_{\mathrm{A}} \otimes \mathcal{L}_{\mathrm{B}})\mathcal{E}_{\mathrm{S}}(\mathcal{R}_{\mathrm{A}} \otimes \mathcal{R}_{\mathrm{B}})$. It is clear that any task that we can do with $\mathcal{E}'_{\mathrm{S}}$ by composition with uncorrelated maps can also be achieved with $\mathcal{E}_{\mathrm{S}}$ by composition with uncorrelated maps. Hence, we assert that the amount of correlation in $\mathcal{E}_{\mathrm{S}}$ is at least as large as in $\mathcal{E}'_{\mathrm{S}}$. In other words, the amount of correlations of some dynamics does not increase under composition with uncorrelated dynamics. This is the fundamental law of this resource theory of spatial correlations for dynamics, and any faithful measure of correlations should satisfy it. For the sake of comparison, in the resource theory of entanglement, entanglement is the resource, and the fundamental law is that entanglement cannot increase under application of local operations and classical communication (LOCC) [23]. For example, the entangled state of Eq. (1) can be transformed via the local unitary X_B on qubit B into another Bell state $\frac{1}{\sqrt{2}}(|01\rangle_{\mathrm{AB}} + |10\rangle_{\mathrm{AB}})$, with the same amount of entanglement. However, a product state of two qubits, not having any entanglement, cannot be transformed into an entangled state by local operations such as single-qubit gate operations or local measurements on A and B, or classical communication between the two single-qubit subsystems A and B. In this spirit, we introduce a measure of correlations for dynamics [25] via the (normalized) quantum mutual information of the Choi-Jamiołkowski state $\rho_{\mathrm{S}}^{\mathrm{CJ}}$, Eq. (18),

$$\bar{I}(\mathcal{E}_{\mathrm{S}}) := \frac{I(\rho_{\mathrm{S}}^{\mathrm{CJ}})}{4\log d} := \frac{1}{4\log d}\Big(S\left(\rho_{\mathrm{S}}^{\mathrm{CJ}}|_{\mathrm{AA}'}\right) + S\left(\rho_{\mathrm{S}}^{\mathrm{CJ}}|_{\mathrm{BB}'}\right) - S\left(\rho_{\mathrm{S}}^{\mathrm{CJ}}\right)\Big). \tag{20}$$

Here, $S(\cdot) := -\mathrm{Tr}[(\cdot)\log(\cdot)]$ is again the von Neumann entropy, now evaluated for the reduced density operators $\rho_{\mathrm{S}}^{\mathrm{CJ}}|_{\mathrm{AA}'} := \mathrm{Tr}_{\mathrm{BB}'}(\rho_{\mathrm{S}}^{\mathrm{CJ}})$ and $\rho_{\mathrm{S}}^{\mathrm{CJ}}|_{\mathrm{BB}'} := \mathrm{Tr}_{\mathrm{AA}'}(\rho_{\mathrm{S}}^{\mathrm{CJ}})$; see Fig. 1. In essence, here we apply the quantum mutual information and von Neumann entropy we have seen in Sec. 1.2 for quantum states, now to the Choi-Jamiołkowski state, which is equivalent to the quantum dynamics taking place on system S.

But why is the quantity $\bar{I}(\mathcal{E}_{\mathrm{S}})$ a good and faithful measure of how correlated the dynamics given by $\mathcal{E}_{\mathrm{S}}$ is? The reason is that it satisfies the following desired properties:

i) The quantity $\bar{I}(\mathcal{E}_{\mathrm{S}}) = 0$ if and only if $\mathcal{E}_{\mathrm{S}}$ corresponds to uncorrelated dynamics, $\mathcal{E}_{\mathrm{S}} = \mathcal{E}_{\mathrm{A}} \otimes \mathcal{E}_{\mathrm{B}}$. This follows from the fact that the Choi-Jamiołkowski state of an uncorrelated map is a product state with respect to the bipartition $\mathrm{AA}'|\mathrm{BB}'$ (no proof given here).

ii) The quantity $\bar{I}(\mathcal{E}_{\mathrm{S}}) \in [0, 1]$. It is clear that $\bar{I}(\mathcal{E}_{\mathrm{S}}) \geq 0$, moreover it reaches its maximum value when $S(\rho_{\mathrm{S}}^{\mathrm{CJ}})$ is minimal and $S\left(\rho_{\mathrm{S}}^{\mathrm{CJ}}|_{\mathrm{AA}'}\right) + S\left(\rho_{\mathrm{S}}^{\mathrm{CJ}}|_{\mathrm{BB}'}\right)$ is maximal. Both conditions are met when $\rho_{\mathrm{S}}^{\mathrm{CJ}}$ is a maximally entangled state with respect to the bipartition $\mathrm{AA}'|\mathrm{BB}'$, leading to $I(\rho_{\mathrm{S}}^{\mathrm{CJ}}) = 2\log d^2$.

iii) The fundamental law of the resource theory for correlations in quantum dynamics is satisfied, namely that

$$\bar{I}(\mathcal{E}_{\mathrm{S}}) \geq \bar{I}\big((\mathcal{L}_{\mathrm{A}} \otimes \mathcal{L}_{\mathrm{B}})\mathcal{E}_{\mathrm{S}}(\mathcal{R}_{\mathrm{A}} \otimes \mathcal{R}_{\mathrm{B}})\big), \tag{21}$$

stating that the amount of correlations of the dynamics $\mathcal{E}_{\mathrm{S}}$ decreases or at most stays the same, if the dynamics is composed with uncorrelated dynamics. Stated differently, if a process is a composition of a correlated and an uncorrelated part, the amount of correlations in the composition has to be equal or smaller than the amount of correlation that is inherent to the correlated part. Here, equality in the above inequality is reached for composition with uncorrelated unitary dynamics, $\mathcal{L}_{\mathrm{A}}(\cdot) = U_{\mathrm{A}}(\cdot)U_{\mathrm{A}}^{\dagger}$, $\mathcal{L}_{\mathrm{B}}(\cdot) = U_{\mathrm{B}}(\cdot)U_{\mathrm{B}}^{\dagger}$, $\mathcal{R}_{\mathrm{A}}(\cdot) = V_{\mathrm{A}}(\cdot)V_{\mathrm{A}}^{\dagger}$, and $\mathcal{R}_{\mathrm{B}}(\cdot) = V_{\mathrm{B}}(\cdot)V_{\mathrm{B}}^{\dagger}$.

Leaving aside the normalization factor $1/(4\log d)$, the quantifier (20) can be intuitively understood as the amount of information that is needed to distinguish the actual dynamics $\mathcal{E}_{\mathrm{S}}$ from the individual dynamics of its parts $\mathcal{E}_{\mathrm{S}_1} \otimes \mathcal{E}_{\mathrm{S}_2}$ [12]. Namely, the information that is lost when $\mathcal{E}_{\mathrm{S}_1} \otimes \mathcal{E}_{\mathrm{S}_2}$ is taken as an approximation of $\mathcal{E}_{\mathrm{S}}$. The normalized quantity $\bar{I} \in [0,1]$ quantifies this information relative to the maximum value it can take on all possible processes.
For clarity, we remark that the use of an ancilla system S' is merely underlying the mathematical construction of the isomorphism. It is not required in an experimental determination of $\bar{I}$. Rather than reconstructing the Choi-Jamiołkowski state $\rho_{\mathrm{S}}^{\mathrm{CJ}}$ from quantum state tomography [12] on the enlarged system SS', one can equivalently determine $\rho_{\mathrm{S}}^{\mathrm{CJ}}$ by reconstructing the dynamics $\mathcal{E}_{\mathrm{S}}$ by means of quantum process tomography on the physical system S alone. For a system S of N qubits, due to the Choi-Jamiołkowski isomorphism the number of real parameters to determine, $4^N(4^N-1)$, is in both cases the same and grows exponentially with the number of qubits.

3.3 Maximally correlated quantum dynamics

Before computing $\bar{I}$ for some cases of physical interest it is worth studying which dynamics achieve the maximum value $\bar{I}_{\max} = 1$. From the resource theory point of view, these dynamics can be considered as maximally correlated since they cannot be constructed from other maps by composition with uncorrelated maps [because of Eq. (21)]. One can show the following property of maximally correlated dynamics:

Theorem 1. If for a map $\mathcal{E}_{\mathrm{S}}$ the property that $\bar{I}(\mathcal{E}_{\mathrm{S}}) = 1$ holds, it must be unitary $\mathcal{E}_{\mathrm{S}}(\cdot) = U_{\mathrm{S}}(\cdot)U_{\mathrm{S}}^{\dagger}$, $U_{\mathrm{S}}U_{\mathrm{S}}^{\dagger} = \mathbb{1}$.

Proof. As aforementioned, the maximum value, $\bar{I}(\mathcal{E}_{\mathrm{S}}) = 1$, is reached if and only if $\rho_{\mathrm{S}}^{\mathrm{CJ}}$ is a maximally entangled state with respect to the bipartition $\mathrm{AA}'|\mathrm{BB}'$, $|\Psi_{(\mathrm{AA}')|(\mathrm{BB}')}\rangle$. Then

$$\mathcal{E}_{\mathrm{S}} \otimes \mathbb{1}_{\mathrm{S}'}\big(\,|\Phi_{\mathrm{SS}'}\rangle\langle\Phi_{\mathrm{SS}'}|\,\big) = |\Psi_{(\mathrm{AA}')|(\mathrm{BB}')}\rangle\langle\Psi_{(\mathrm{AA}')|(\mathrm{BB}')}| \tag{22}$$

is a pure state. Therefore $\mathcal{E}_{\mathrm{S}}$ must be unitary as the Choi-Jamiołkowski state is pure if and only if it represents a unitary map. □

What are examples of maximally correlated dynamics? One example for such dynamics is the swap operation, exchanging the states of the two parties A and B, $U_{\mathrm{S}} = U_{\mathrm{A}\leftrightarrow\mathrm{B}}$, and thus also any unitary of the form of $(U_{\mathrm{A}} \otimes U_{\mathrm{B}})U_{\mathrm{A}\leftrightarrow\mathrm{B}}(V_{\mathrm{A}} \otimes V_{\mathrm{B}})$.

However, not every U_{S} that is maximally correlated falls into this class. For example, the unitary operation of two qubits $U'_{\mathrm{S}} = |21\rangle\langle 12| + \mathrm{i}\big(|11\rangle\langle 21| + |12\rangle\langle 11| + |22\rangle\langle 22|\big)$ is maximally correlated, however, it cannot be written as $(U_{\mathrm{A}} \otimes U_{\mathrm{B}})U_{\mathrm{A}\leftrightarrow\mathrm{B}}(V_{\mathrm{A}} \otimes V_{\mathrm{B}})$, since that would imply vanishing $\bar{I}(U'_{\mathrm{S}}U_{\mathrm{A}\leftrightarrow\mathrm{B}})$ whereas $\bar{I}(U'_{\mathrm{S}}U_{\mathrm{A}\leftrightarrow\mathrm{B}}) = 1/2 \neq 0$.

What about, e.g., the 2-qubit controlled-NOT (CNOT) gate? Interestingly, operations able to create highly correlated states such as the CNOT gate achieve a correlation value of 1/2 and thus do not correspond to maximally correlated dynamics. Note that whereas a CNOT gate creates, for appropriately chosen two-qubit initial states, maximally entangled states, there are other states which are left completely uncorrelated under its action. The measure $\bar{I}$ captures, completely independently of initial states and of whether possibly created correlations are quantum or classical, the fact that correlated dynamics cannot be realized by purely local dynamics.

This leads to the following question: Among the quantum processes of a given system which correspond to maximally correlated dynamics, is there one from which any other dynamics can be obtained – something like the mother of all dynamics?

In some resource theories, such as bipartite entanglement, this is the case: there the maximal element (e.g. a Bell state in a 2-qubit system) can generate any other element by applying the operations which fulfill its fundamental law, e.g. LOCC. This is not the case here, i.e., maximally correlated evolutions cannot generate any arbitrary dynamics by composition with uncorrelated operations. Indeed, if $\mathcal{E}_{\mathrm{S}}^{\max}$ were able to generate any other dynamics it would, in particular, be able to generate any unitary evolution U_{S}, $(\mathcal{L}_{\mathrm{A}} \otimes \mathcal{L}_{\mathrm{B}})\mathcal{E}_{\mathrm{S}}^{\max}(\mathcal{R}_{\mathrm{A}} \otimes \mathcal{R}_{\mathrm{B}})(\cdot) = U_{\mathrm{S}}(\cdot)U_{\mathrm{S}}^{\dagger}$. However, this would imply that $\mathcal{L}_{\mathrm{A}} \otimes \mathcal{L}_{\mathrm{B}}$, $\mathcal{E}_{\mathrm{S}}^{\max}$ and $(\mathcal{R}_{\mathrm{A}} \otimes \mathcal{R}_{\mathrm{B}})$ are unitary evolutions as well, so that $(U_{\mathrm{A}} \otimes U_{\mathrm{B}})U_{\mathrm{S}}^{\max}(V_{\mathrm{A}} \otimes V_{\mathrm{B}}) = U_{\mathrm{S}}$, with $\mathcal{E}_{\mathrm{S}}^{\max}(\cdot) = U_{\mathrm{S}}^{\max}(\cdot)U_{\mathrm{S}}^{\max\dagger}$. Since $\bar{I}(\mathcal{E}_{\mathrm{S}})$ is invariant under the composition of uncorrelated unitaries, this result would imply that for any correlated unitary U_{S}, $\bar{I}(U_{\mathrm{S}})$ would take the same value, $\bar{I}(U_{\mathrm{S}}^{\max})$, and this is not true, as we have seen for the examples of the swap operation and the CNOT gate.

4 Quantifying dynamical correlations in physical systems

4.1 Correlated dynamics of atoms in the electromagnetic vacuum

Let us now illustrate the behavior of $\bar{I}(\mathcal{E}_{\mathrm{S}})$ for the paradigmatic example of two identical two-level atoms interacting with the vacuum of the electromagnetic radiation field.

The free Hamiltonian of the atoms of transition frequency ω is

$$H_{\mathrm{S}} = \frac{\omega}{2}\big(Z_1 + Z_2\big) \tag{23}$$

with Z_j the Pauli-matrix for the j-th atom. In addition, the environmental free Hamiltonian

corresponds to the modes of the radiation field and is given by

$$H_{\rm E} = \sum_{\boldsymbol{k}} \sum_{\lambda=1,2} \omega_{\boldsymbol{k}} a_\lambda^\dagger(\boldsymbol{k}) a_\lambda(\boldsymbol{k}), \tag{24}$$

where $\boldsymbol{k}$ and λ stand for the wave vector and the two polarization degrees of freedom, respectively. We have taken natural units $\hbar = c = 1$. The dispersion relation in free space is $\omega_{\rm k} = |\boldsymbol{k}|$, and the field operators $a_\lambda^\dagger(\boldsymbol{k})$ and $a_\lambda(\boldsymbol{k})$ describe the creation and annihilation of photons with wave vector $\boldsymbol{k}$ and polarization vector $\boldsymbol{e}_\lambda$. These fulfill $\boldsymbol{k}\cdot\boldsymbol{e}_\lambda = 0$ and $\boldsymbol{e}_\lambda \cdot \boldsymbol{e}_{\lambda'} = \delta_{\lambda,\lambda'}$.
The atom-field interaction is described in dipole approximation by the Hamiltonian

$$H_{\rm SE} = -\sum_{j=1,2} \left[\sigma_j^- \boldsymbol{d}\cdot\boldsymbol{E}(\boldsymbol{r}_j) + \sigma_j^+ \boldsymbol{d}^*\cdot\boldsymbol{E}(\boldsymbol{r}_j)\right]. \tag{25}$$

Here, $\boldsymbol{d}$ is the dipole matrix element of the atomic transition, $\boldsymbol{r}_j$ denotes the position of the j-th atom, and the raising and lowering operators σ_j^+ and σ_j^- are defined as $\sigma_j^+ = (\sigma_j^-)^\dagger = |e\rangle_j\,{}_j\langle g|$ for its exited $|e\rangle_j$ and ground $|g\rangle_j$ states. Furthermore, the electric field operator is given (in Gaussian units)

$$\boldsymbol{E}(\boldsymbol{r}) = {\rm i}\sum_{\boldsymbol{k},\lambda} \sqrt{\frac{2\pi\omega_{\boldsymbol{k}}}{\mathcal{V}}}\boldsymbol{e}_\lambda(\boldsymbol{k})\left(a_\lambda(\boldsymbol{k}){\rm e}^{{\rm i}\boldsymbol{k}\cdot\boldsymbol{r}} - a_\lambda^\dagger(\boldsymbol{k}){\rm e}^{-{\rm i}\boldsymbol{k}\cdot\boldsymbol{r}}\right), \tag{26}$$

where $\mathcal{V}$ denotes the quantization volume. Under a series of standard assumptions known as the Markovian weak-coupling limit [3] the dynamics of the atoms is governed by a Lindblad master equation of the form

$$\frac{d\rho_{\rm S}}{dt} = \mathcal{L}(\rho_{\rm S}) = -{\rm i}\tfrac{\omega}{2}\big(Z_1 + Z_2, \rho_{\rm S}\big) + \sum_{i,j=1,2} a_{jk}\Big(\sigma_k^-\rho_{\rm S}\sigma_j^+ - \tfrac{1}{2}\{\sigma_j^+\sigma_k^-, \rho_{\rm S}\}\Big). \tag{27}$$

After taking the continuum limit ($\frac{1}{\mathcal{V}}\sum_{\boldsymbol{k}} \to \frac{1}{(2\pi)^3}\int d^3\boldsymbol{k}$) and performing the integrals, the coefficients a_{jk} are given by (see e.g. Sec. 3.7.5 of Ref. [3])

$$a_{jk} = \gamma_0\big(j_0(x_{jk}) + P_2(\cos\theta_{jk}) j_2(x_{jk})\big). \tag{28}$$

Here, $\gamma_0 = \frac{4}{3}\omega^3|\boldsymbol{d}|^2$, and $j_0(x)$ and $j_2(x)$ are spherical Bessel functions [26]

$$j_0(x) = \frac{\sin x}{x}, \quad j_2(x) = \left(\frac{3}{x^3} - \frac{1}{x}\right)\sin x - \frac{3}{x^2}\cos x, \tag{29}$$

and

$$P_2(\cos\theta) = \frac{1}{2}\big(3\cos^2\theta - 1\big) \tag{30}$$

is a Legendre polynomial, with

$$x_{jk} = \omega|\boldsymbol{r}_j - \boldsymbol{r}_k| \quad \text{and } \cos^2(\theta_{jk}) = \frac{|\boldsymbol{d}\cdot(\boldsymbol{r}_j - \boldsymbol{r}_k)|^2}{|\boldsymbol{d}|^2|\boldsymbol{r}_j - \boldsymbol{r}_k|^2}. \tag{31}$$

Notice that if the distance between atoms $r = |\boldsymbol{r}_1 - \boldsymbol{r}_2|$, is much larger than the wavelength associated with the atomic transition $r \gg 1/\omega$, we have $a_{jk} \simeq \gamma_0\delta_{ij}$ and only the diagonal

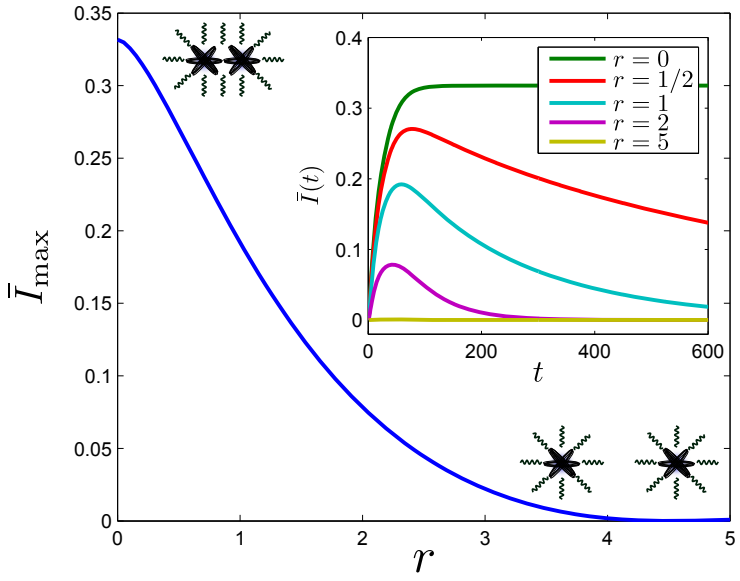

Fig. 2: *Maximum value of $\bar{I}$ as a function of the distance r for two two-level atoms radiating in the electromagnetic vacuum. As expected, the amount of correlations in the dynamics decreases with r. In the inset, $\bar{I}$ is represented as a function of time for different distances r between atoms ($\omega = |\boldsymbol{d}|/2 = 1$, θ=0). With increasing time, correlations in the dynamics build up, which for longer times decay to zero, except for the limit vanishing distance $r \to 0$ between the two atoms.*

terms $\gamma_0 = \frac{4}{3}\omega^3|\boldsymbol{d}|^2$ are relevant. Then, the master equation describes two-level atoms interacting with independent environments, and there are no correlations in the emission of photons by the first and the second atom. In the opposite case, when $r \ll 1/\omega$, every matrix element approaches the same value $a_{ij} \simeq \gamma_0$, in the master equation the atomic transitions can be approximately described by the collective jump operators $J_\pm = \sigma_1^\pm + \sigma_2^\pm$, and the pair of atoms becomes equivalent to a four-level system with Hamiltonian $\omega J_z = \frac{\omega}{2}(Z_1 + Z_2)$ at the mean position $(\boldsymbol{r}_1 - \boldsymbol{r}_2)/2$ interacting with the electromagnetic vacuum. This emission of photons in a collective way is known as super-radiance. It can be effectively described in terms of collective angular momentum operators and was first studied in the 1950s by Robert H. Dicke [6].

To quantitatively assess this behavior of uncorrelated/correlated dynamics as a function of the interatomic distance r, we can numerically compute the measure of correlations $\bar{I}$ according to Eq. (20). To this end, we consider a maximally entangled state $|\Phi_{\mathrm{SS}'}\rangle$ between two sets S and S′ of two qubits according to the maximally correlated state as given for the general case in Eq. (17). Namely, here S is the set of the two physical qubits, i.e., the two two-level atoms 1 and 2, and the "copy" system S′ is made up of two auxiliary qubits 1′ and 2′ as sketched in Fig. 1. Next, the part S of the maximally entangled state $|\Phi_{\mathrm{SS}'}\rangle\langle\Phi_{\mathrm{SS}'}|$ is evolved according to the master equation (27) while keeping the part S′ constant, to obtain $\rho_{\mathrm{S}}^{\mathrm{CJ}}(t)$. This can be done, for instance, by numerically integrating the master equation $\frac{d\rho_{\mathrm{S}}^{\mathrm{CJ}}(t)}{dt} = \mathcal{L} \otimes \mathbb{1}[\rho_{\mathrm{S}}^{\mathrm{CJ}}(t)]$, with the initial condition $\rho_{\mathrm{S}}^{\mathrm{CJ}}(0) = |\Psi_{\mathrm{SS}'}\rangle\langle\Psi_{\mathrm{SS}'}|$, where $\mathcal{L}$ is for the present example specified in Eq. (27). Tracing out qubits 2 and 2′ of $\rho_{\mathrm{S}}^{\mathrm{CJ}}(t)$ yields $\rho_{\mathrm{S}}^{\mathrm{CJ}}(t)|_{11'}$, and similarly tracing out qubits 1 and 1′ yields $\rho_{\mathrm{S}}^{\mathrm{CJ}}(t)|_{22'}$. Finally, this allows one to compute the von Neumann entropies of $\rho_{\mathrm{S}}^{\mathrm{CJ}}(t)|_{11'}$, $\rho_{\mathrm{S}}^{\mathrm{CJ}}(t)|_{22'}$ and $\rho_{\mathrm{S}}^{\mathrm{CJ}}(t)$ to calculate $\bar{I}(t)$ according to Eq. (20).

The results are shown in Fig. 2. Despite the fact that the value of $\bar{I}$ depends on time (the dynamical map is formally given by $\mathcal{E}_{\mathrm{S}} = \mathrm{e}^{t\mathcal{L}}$), the correlation quantifier $\bar{I}$ decreases as r increases, as expected. Furthermore, the value of $\bar{I}$ approaches zero for long times t (see inset plot), except in the limiting case of vanishing distance $r = 0$ between the two atoms. This is because for $r \neq 0$ the dynamics becomes uncorrelated in the asymptotic limit, $\lim_{t\to\infty} \mathrm{e}^{t\mathcal{L}} = \mathcal{E} \otimes \mathcal{E}$. Here, the single-qubit Kraus maps describing the dynamics of the composite two-atom system are given by $\mathcal{E}(\cdot) = K_1(\cdot)K_1^\dagger + K_2(\cdot)K_2^\dagger$ with Kraus operators $K_1 = \left(\begin{smallmatrix} 0 & 0 \\ 1 & 0 \end{smallmatrix}\right)$ and $K_2 = \left(\begin{smallmatrix} 0 & 0 \\ 0 & 1 \end{smallmatrix}\right)$. It can be checked from the form of this map that therefore for long times both atoms will eventually end up in the product state formed of both atoms in the ground state $|g\rangle$. However, for $r = 0$, $\lim_{t\to\infty} \mathrm{e}^{t\mathcal{L}}$ is a correlated map. Thus, we obtain perfect agreement between the rigorous measure of correlations $\bar{I}$ and the physically expected behavior of two distant atoms undergoing independent decay.

4.2 Noise characterization of an experimental quantum computer

In the following, we will apply the correlation quantifier to a second physical scenario. We will use it to study the dynamics of spatial correlations of noise processes that are present in a trapped ion quantum computer, which has been built by our collaborators in the experimental ion-trap group at Innsbruck, Austria [27], and for which we quantitatively characterized its spatial noise correlations in a recent joint project [28]. To date, trapped ions are one of most advanced platforms for quantum information processing, and a highly promising platform to build reliable and scalable quantum computers. Figure 3 shows the schematic of a linear-ion trap quantum processor.

Let us briefly describe the experimental platform used to implement the correlation characterization protocol. Each qubit is encoded in the $4S_{1/2}$ and $3D_{5/2}$ electronic states of a single $^{40}\mathrm{Ca}^+$ ion of a string of ions trapped in a macroscopic linear Paul trap [27]. Doppler cooling of the ion crystal is performed on a short-lived cycling transition between the $4S_{1/2}$ and the $4P_{1/2}$ levels, as illustrated in Fig. 4. The same transition is used to detect the qubit state via the electron shelving scheme. Two additional repumping lasers ensure that the ion does not get trapped in a dark state and enable resetting from the long-lived $3D_{5/2}$ state. A more detailed description of the tool-set and the experimental setup used can be found in [27].

To manipulate the state of the qubit, two different laser beams are used: A global beam effectively illuminates all ions in the chain with equal power and allows rotations of all qubits simultaneously. Therefore interactions of the following form are possible:

$$R_\phi(\theta) = \exp\left(-i\frac{\theta}{2}S_\phi\right), \tag{32}$$

where $S_\phi = \sum_{k=0}^{N}(X_k \cos\phi + Y_k \sin\phi)$ with X_k and Y_k being single-qubit Pauli matrices acting on qubit k.

To perform local operations on single qubits an addressed beam is available. This tightly focused beam is steered along the linear ion chain via an electro-optical deflector. By driving the

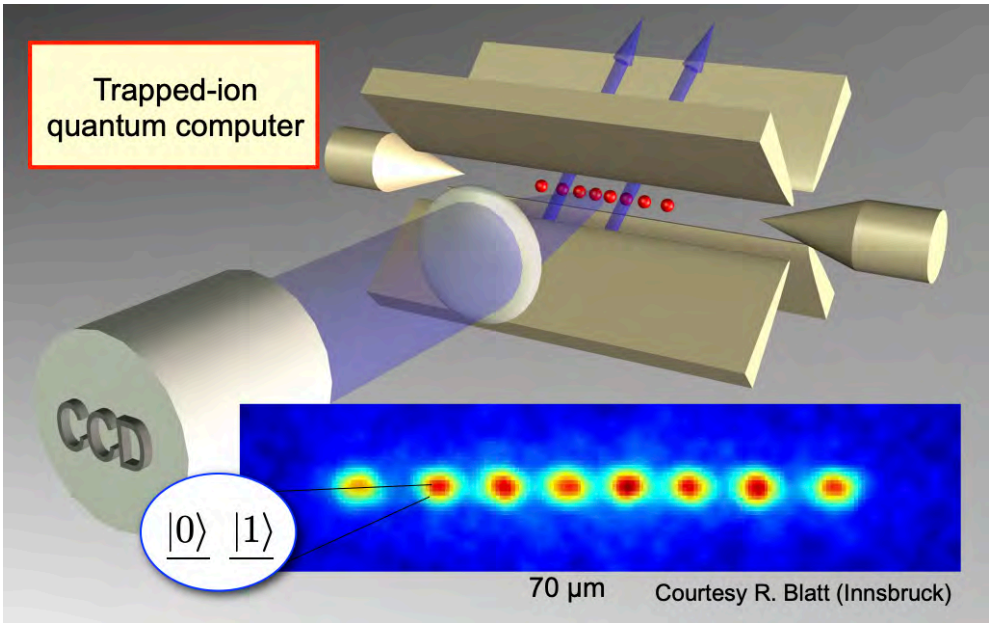

Fig. 3: *Schematics of a linear-ion-trap quantum computer. A linear Paul trap formed of metallic blades and endcap electrodes (at the left and right end of the trap) is used to apply a combination of static electric and oscillating radio-frequency fields, to create a confining potential in all three directions for the charged ions. Ions can be laser-cooled so that they form at sufficiently low temperatures self-assembled Coulomb crystals, such as shown in the fluorescence picture of a linear ion crystal. Here, the ion positions are determined by the interplay of mutual Coulomb repulsion between the ions and external confinement through the trapping fields. A pair of (meta-)stable electronic states is used to encode one qubit in each of the ions. Tightly focused as well as collectively applied laser beams are then be applied to the ions. These can be used to initialize the register of qubits to a well-defined initial state at the beginning of a quantum computation, to apply single-qubit gate operations and to read out the final state at the end of a quantum algorithm by collecting the light from state-dependent fluorescence imaging via a CCD camera. Two- or multi-qubit entangling gate operations can be implemented by coupling the electronic dynamics to the collective vibrational modes (phonons) of the ion crystal, which can thereby act as a quantum bus.*

qubit transition on resonance or in a detuned way, two types of rotations can be realized:

$$R_{\phi}^{(k)}(\theta) = \exp\left(-i\frac{\theta}{2}(X_k\cos\phi + Y_k\sin\phi)\right)$$

and

$$S_z^{(k)}(\theta) = \exp\left(-i\frac{\theta}{2}Z_k\right).$$

This control toolset allows one to prepare the qubits in the required initial state, encode them in different Zeeman sublevels and perform quantum process tomography. Entangling gates belong also to the gate set of the quantum processor [27], but are not needed for the noise correlation characterization protocol and therefore not discussed here.

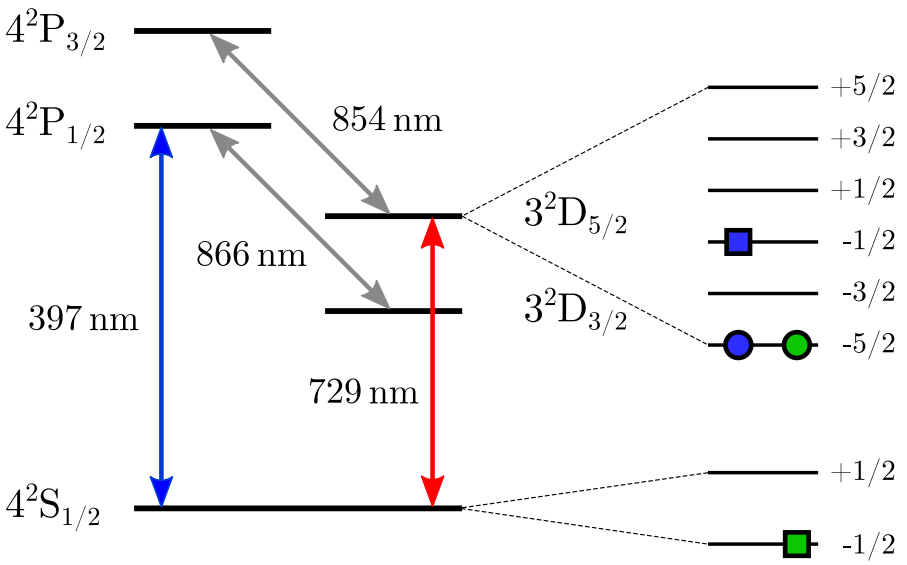

Fig. 4: *Electronic level scheme of $^{40}Ca^+$. The green and blue squares and circles indicate different qubit encodings, denoted **A** and **B**, respectively. Squares are marking the qubit state $|1\rangle$ whereas the state $|0\rangle$ is highlighted with circles. The corresponding frequency shifts of the transitions caused by the magnetic field are -2.80 MHz/G and $+3.36$ MHz/G for the qubits marked with green and blue symbols respectively. For configuration 1 described in the enumeration in the main text for both qubits the encoding marked in green is used. The asymmetry in scenario 2 is introduced by encoding one of the qubits in the states illustrated in blue. For the third configuration both qubits again use the encoding marked in green and the spontaneous decay from $|0\rangle$ to $|1\rangle$ is enhanced. Figure from [28].*

Let us now discuss how the temporal development of the spatial correlation estimator $\bar{I}$ can be used to determine the degree of spatial correlations in a two-qubit register. For this, we perform full quantum process tomography on qubit registers with varying degree of correlations. The electronic hyperfine level structure of the $^{40}Ca^+$ (see Fig. 4) is rich enough to allow the experimentalists to choose and investigate the noise characteristics for qubits encoded in various pairs of computational basis states. Here, the idea is that the degree of noise correlations between individual qubits can be tuned by encoding them in Zeeman states with differing magnetic field susceptibility. As a consequence, different sensitivities to noise from magnetic field fluctuations is expected. Concretely, there exist multiple possibilities to encode a qubit in the Zeeman levels of the $4S_{1/2}$ and $3D_{5/2}$ states as shown in Fig. 4. The susceptibility of the qubits to the magnetic field ranges from -2.80 MHz/G to $+3.36$ MHz/G, which allows the experimentalists to tune not only the coherence time of the individual qubits but also the *correlations* between qubits, when magnetic field fluctuations are the dominant source of noise.

Understanding the dephasing dynamics, and in particular noise correlations, in registers containing qubits in different encodings is essential in the context of error mitigation and quantum error correction: this understanding will be needed to determine the viability of an approach to build, e.g., functional logical qubits formed of entangled ensembles of physical qubits, which can be used to fight errors by means of quantum error correction techniques.

4.3 Experimental determination of spatial dynamical correlations

In the following we will consider dephasing dynamics that is caused by a magnetic field acting on a string of two ions. The various qubit-states have different susceptibilities to magnetic field fluctuations, given by the Landé g factors g_i of the involved Zeeman substates. The phase that qubit i accumulates during the time evolution is therefore given by

$$\phi_i(t) = \int_0^t d\tau B(\tau)\mu_b g_i$$

with the time-dependent magnitude of the magnetic field $B(\tau)$ and the Bohr magneton μ_b. The magnetic field fluctuations can be modeled by multiple random implementations of $B(t)$. The time evolution for a single implementation can then be expressed as

$$U(\phi_1) = \exp\left(-i\phi_1(\sigma_1^z + g\sigma_2^z)\right) \tag{33}$$

with the ratio of the Landé factors $g{=}g_2/g_1$. In order to estimate the dynamics under a dephasing decay, one needs to average the evolution over many noise realizations with random phases.
In the experiment we investigated the following qubit configurations that implement dephasing and spontaneous decay dynamics:

1. **Configuration 1:** For the realization of maximally correlated dephasing dynamics, both qubits are encoded in the $\left|4S_{1/2},\, m_S{=}{-}1/2\right\rangle$ and $\left|3D_{5/2},\, m_S{=}{-}5/2\right\rangle$ states. This encoding is referred to as encoding **A** hereinafter, and corresponds to the green markers in Fig. 4. Both qubits have a susceptibility to the magnetic field of -2.80 MHz/G, leading to identical susceptibility coefficients ($g = 1$) (see Eq. (33)).

2. **Configuration 2:** To introduce an asymmetric dephasing dynamics, one qubit is encoded in **A** and the second is encoded in the states $\left|3D_{1/2},\, m_S{=}{-}1/2\right\rangle$ and $\left|3D_{5/2},\, m_S{=}{-}5/2\right\rangle$ respectively. This encoding is referred to as encoding **B** hereinafter, and corresponds to the blue markers in Fig. 4. Their different susceptibilities to magnetic field noise of -2.80 MHz/G and $+3.36$ MHz/G introduce unequal dephasing and therefore are expected to affect correlations between the qubits, corresponding to the susceptibility coefficients ($g = -0.83$).

3. **Configuration 3:** Uncorrelated dynamics can be engineered in this experimental system by introducing spontaneous decay. In this scenario, both qubits are encoded in Encoding **A**. A laser pulse resonant with the $3D_{5/2} \leftrightarrow 4P_{3/2}$ transition at 854 nm shortens the effective lifetime of the exited state by inducing a spontaneous decay to the $4S_{1/2}, m_S = -1/2$ level via the short-lived $3P_{3/2}, m_S = -3/2$ level. Since spontaneous emission of visible photons by the ions at a distance of several micrometers corresponds to an uncorrelated noise process, as we have seen in Sec. 3, this controllable pump process implements an uncorrelated noise process that can be modeled as spontaneous decay. The effective lifetime depends on the laser power and is in our case set to be $T_{\text{spont}} = 7(1)\ \mu$s.

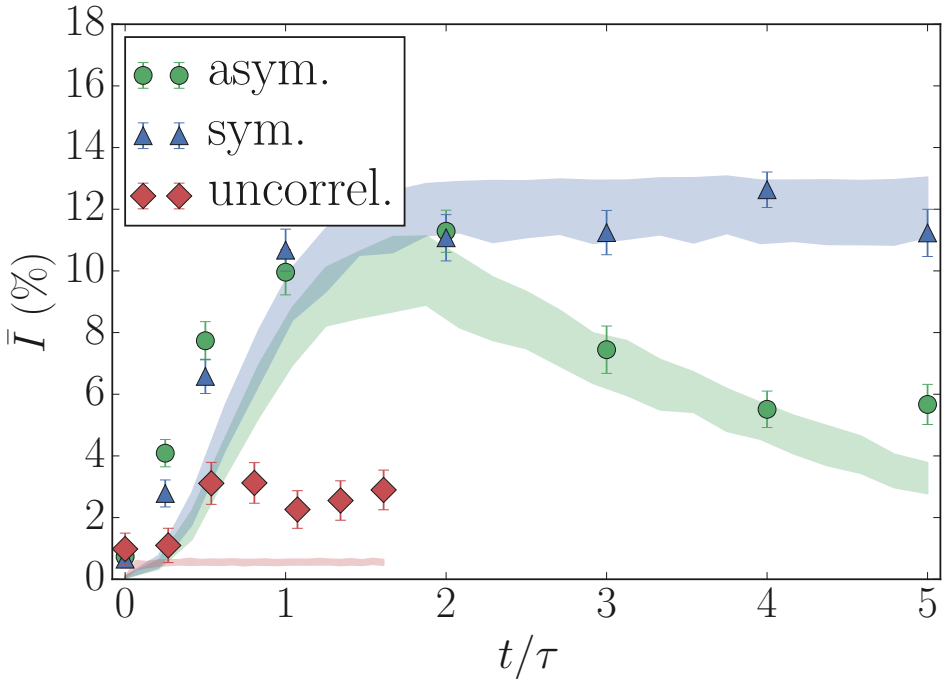

Fig. 5: *Dynamics of the spatial correlation quantifier $\bar{I}$ for different qubit encodings. Three cases are depicted: Both qubits encoded in $|4S_{1/2}, m_S{=}-1/2\rangle \leftrightarrow |3D_{5/2}, m_S{=}-5/2\rangle$ (blue triangles), one qubit encoded in $|4S_{1/2}, m_S{=}-1/2\rangle \leftrightarrow |3D_{5/2}, m_S{=}-5/2\rangle$ and $|3D_{1/2}, m_S{=}-1/2\rangle \leftrightarrow |3D_{5/2}, m_S{=}-5/2\rangle$ (green circles) and both qubits subject to uncorrelated dynamics via spontaneous decay (red diamonds). The horizontal axis is normalized to the coherence time for the first two cases and to the decay time for the third case. Results from a Monte Carlo based numerical simulations with 500 samples are depicted with shaded areas in the corresponding color. Figure from [28].*

The small quantum register consisting of only two qubits allows one to perform full process tomography [12] to fully reconstruct the dynamics $\mathcal{E}_{\mathrm{S}}$ in the two-qubit system. From this, the correlation measure $\bar{I}$ (see Eq. (20)) can be directly determined. In the present platform, the amplitude of the magnetic field fluctuations is non-stationary as it depends on the entire laboratory environment, e.g., due to fluctuating currents flowing through wires, which therefore cannot be controlled accurately. However, the apparatus allows one to engineer a stationary magnetic field noise as the dominating noise source (a situation where laser and magnetic field noise have to be taken into account is described in [28]). Thus we could control and tune the single qubit coherence time. The stationary magnetic field noise is engineered by our experimental colleagues by applying a white-noise current to the coils that generate the magnetic field at the ions' positions. The noise amplitude is set such that the coherence time of the qubit encoded in $\left|4S_{1/2}, m_S{=}-1/2\right\rangle$ and $\left|3D_{5/2}, m_S{=}-5/2\right\rangle$ is reduced from $59(3)$ ms to $1.98(7)$ ms. The increase of magnetic field noise by a factor of ≈ 30 ensures that laser phase-noise is negligible on these timescales. From the measured data, a process matrix fully describing $\mathcal{E}_{\mathrm{S}}$ was reconstructed using an iterative maximum likelihood method to ensure trace preservation and positivity of the process matrix.

The results for the estimated quantifier for spatial correlations as defined in Eq. (20) $\bar{I}$ are shown in Fig. 5 for the decoherence processes of the different configurations described above. These processes are described by an exponential decay and show different timescales. To compare the data from the different configurations we express the free evolution time in units of the respective decay times τ. The temporal development of $\bar{I}$ is studied for evolution times of up to 5 times the decoherence time for configurations 1 and 2 and up to 1.6 times the lifetime for configuration 3, as the differences in the dynamics of different correlation strength are most pronounced on those timescales.

It can be seen in Fig. 5 that **the symmetric configuration** (Configuration 1), depicted with blue triangles and labeled with *"sym."*, shows the highest degree of correlations that reaches a steady state for long evolution times. The correlations converge to a saturation value of 11.2(8) %, which is in agreement with the theoretical value of 12.5 % (as expected in the limit of perfectly correlated dephasing) within 2 standard deviations. It is left and suggested as an exercise to determine this value of $\bar{I} = 1/8$ for the case of perfectly correlated two-qubit dephasing dynamics, as we discussed above in Sec. 2.2 and described by the fluctuating field Hamiltonian Eq. (16).

Measurements using **the asymmetric configuration** (Configuration 2), depicted with green circles and labeled with *"asym."*, show similar dynamics to the symmetric setting for times up to twice the coherence time. For longer evolution times, however, a significant decrease in correlations is observed.

The third investigated scenario (Configuration 3) implementing engineered **uncorrelated** dynamics by adding spontaneous decay, is depicted with red diamonds. The correlations do not exceed a value of 3.1(6) % in this case. This is significantly lower than the maximum of $\bar{I}$ for fully and partially correlated dephasing dynamics.

The blue shaded area in the figure shows simulated results where random phase fluctuations are acting on a two-qubit system. Whereas there is qualitative agreement between simulations and measurements, there are still statistically significant deviations, especially in the case of uncorrelated dynamics, of up to approximately $4\,\sigma$. We assume that this overestimation of the spatial correlations in the system dynamics by the quantifier is due to mis-calibration and drifts of experimental parameters. For instance a mismatch between the actual and the calibrated Rabi frequency would lead to additional correlated errors during the process tomography. This effect is most pronounced for Configuration 3, where the dynamics are expected to show no correlations at all.

4.4 Decoherence-free subspaces and entanglement-based magnetometry

What can one learn from the build-up of strong correlations in the dynamics of qubits, as observed in particular for the symmetric encoding in Fig. 5 in the previous section? And can one use this information for useful applications? Can these correlations be harnessed to protect fragile qubit states from decoherence caused by correlated dephasing dynamics? The answer is yes!

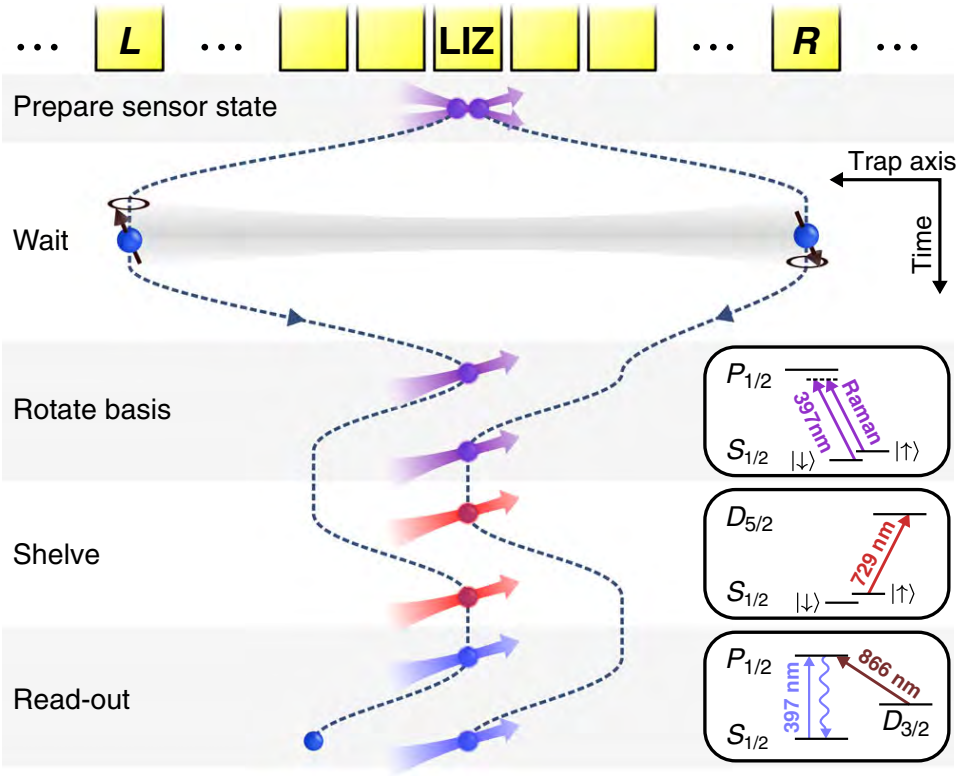

Fig. 6: *Experimental procedure implemented in [29] for measurements of inhomogenous magnetic fields in a segmented ion trap. After the creation of the sensor Bell state by means of single- and two-qubit gates in the laser interaction zone (LIZ), the two constituent ions are separated and shuttled to the desired trap segments L and R. In order to measure the accumulated phase during the interrogation time T, the ions are individually shuttled back to the LIZ to perform basis rotations that allow for state read-out via electron shelving and fluorescence detection in either the X_1X_2 or Y_1Y_2 measurement basis. For basis rotations, electron shelving, and fluorescence detection, the relevant energy levels are shown in the small inset figures at the right. Figure reproduced from [29].*

The key idea of how this works can be understood by considering a fluctuating magnetic field which acts with exactly the same magnitude, and thus *perfectly spatially correlated* on all qubits, as discussed above and described by Hamiltonian of Eq. (16). A single-qubit superposition state $|\psi\rangle_k = \alpha\,|0\rangle_k + \beta\,|1\rangle_k$ will under such noise dephase over time and end up in a classical mixture $|\rho\rangle_k = |\alpha|^2\,|0\rangle\langle 0|_k + |\beta|^2\,|1\rangle\langle 1|_k$. If we, however, consider instead a Bell state of two qubits,

$$|\psi\rangle_{12} = \alpha\,|01\rangle_{12} + \beta\,|10\rangle_{12}\,, \tag{34}$$

we find that under the time evolution generated by the collective dephasing Hamiltonian Eq. (16) such a superposition remains an eigenstate of the time evolution operator at all times. Or in other words, no relative phase in the superposition state (34) is accumulated. Therefore, under this correlated dephasing noise, the basis states $|01\rangle_{12}$ and $|10\rangle_{12}$ span a two-dimensional so-called decoherence-free subspace (DFS): this is a subspace of the two-qubit Hilbert space, within

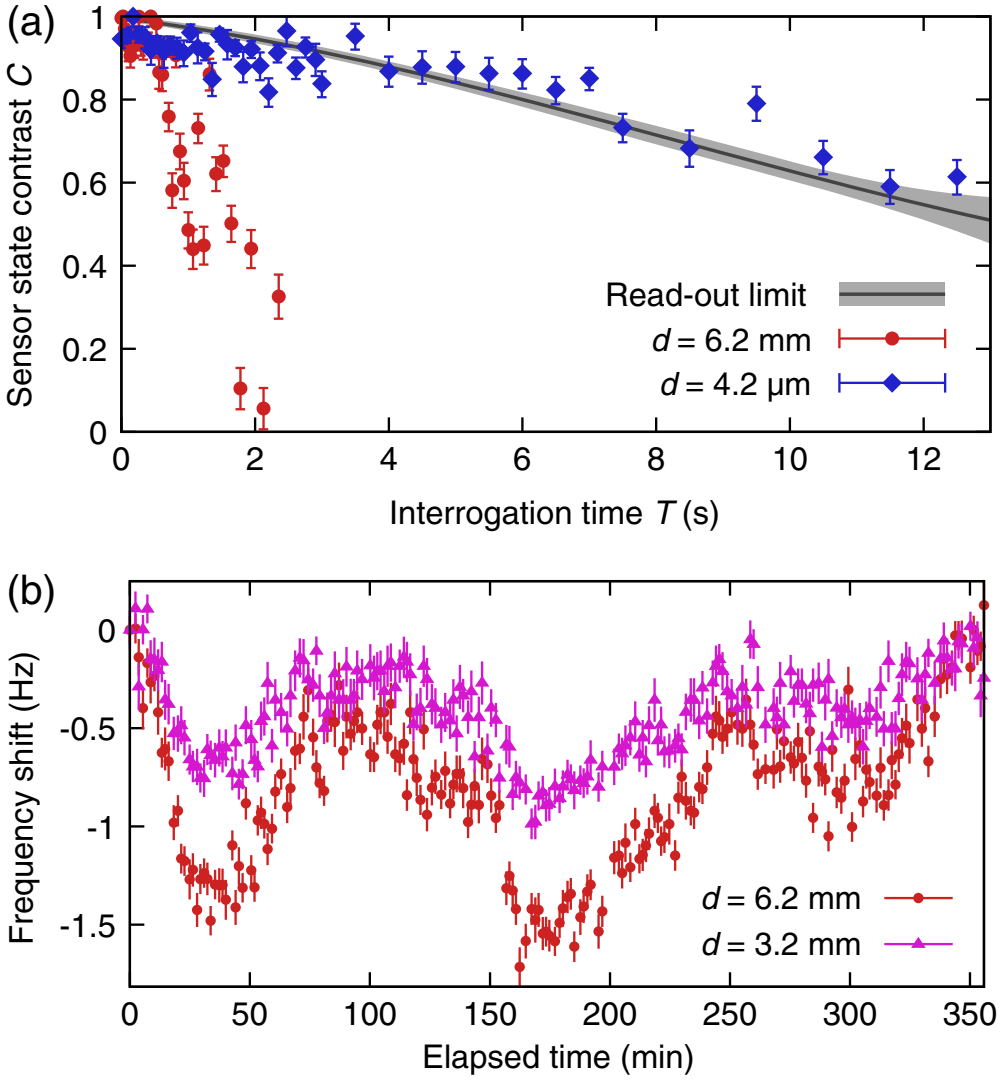

Fig. 7: *(a) Sensor state contrast C as a function of the interrogation time during which the two ions of the sensor Bell state (34) are exposed to the magnetic fields at their respective positions, spatially separated by a distance of $d = 6.2$ mm (red dots) and $d = 4.2$ µm (blue squares). For illustration, the black curve and gray region indicate a third-order polynomial fit to a separate read-out fidelity measurement and its confidence bands (see [29]). (b) Simultaneous drift of the measured frequency difference for ion distances $d = 6.2$ mm (blue circles) and $d = 3.2$ mm (purple triangles) over a duration of about 6 hours with an interrogation time of $T = 150$ ms. Figure reproduced from [29].*

which the noise acts trivially and quantum information can be stored and protected for longer times than in single physical qubits. Alternatively, one can view the state of Eq. (34) as a minimal "logical qubit" formed of two physical qubits, with effective logical basis states $|0\rangle_L = |01\rangle_{12}$ and $|1\rangle_L = |10\rangle_{12}$, and which offers protection against spatially correlated dephasing noise. Using such two-qubit DFS spaces in two ions, quantum information and entanglement can be preserved for timescales of minutes, as impressively demonstrated already in 2005 [9],

and which is to be contrasted to typical single-qubit coherence times of (tens) of milliseconds. What happens if the dephasing noise is spatially correlated, however, these correlations are not perfect? Can this be exploited as a measurement tool? In Ref. [29] it was shown that under these circumstances Bell states of the form (34) can be used as highly sensitive probe states to detect small spatially inhomogeneous dc magnetic fields. As discussed above, common-mode magnetic-field fluctuations are not seen by the entangled sensor state. In contrast, inhomogeneous components of the field can be detected! This gives rise to excellent sensitivity to small differences in local magnetic fields in different areas of the trap, separated by distances as large as 0.61mm. For comparison typical inter-ion distances in an ion Coulomb crystal are a few micrometer. The experimental setup and field gradient probing protocol is summarized in Fig. 6. Figure 7 shows experimental results of this technique, which allows to probe magnetic field differences over distances of several mm, and with spatial resolution as small as about 20 nm, and with accuracies down to 300 fT and sensitivities down to 12 pT/$\sqrt{\mathrm{Hz}}$.

5 Lower bounds, multi-partite systems, and outlook

The exact determination of the correlation quantifier $\bar{I}$ requires as input the process $\mathcal{E}_{\mathrm{S}}$, which can be reconstructed from quantum process tomography [12]. For small systems formed of only two qubits, this is feasible, it becomes, however, impractical for larger systems due to the exponential number of measurements required. The good news is that a lower estimate for $\bar{I}$ can be obtained by performing correlation measurements on the subsystems S_1 and S_2. Here, the central result is that the normalized quantity $\bar{I}(\mathcal{E}_{\mathrm{S}})$ is bounded from below by

$$\bar{I}(\mathcal{E}_{\mathrm{S}}) \geq \frac{1}{8 \ln d} \frac{C^2_{\rho'}(\mathcal{O}_1, \mathcal{O}_2)}{\|\mathcal{O}_1\|^2 \|\mathcal{O}_2\|^2}, \tag{35}$$

with two local quantum observables $\mathcal{O}_1$ and $\mathcal{O}_2$ and $C_{\rho'}(\mathcal{O}_1, \mathcal{O}_2) = \langle \mathcal{O}_1 \otimes \mathcal{O}_2 \rangle_{\rho'} - \langle \mathcal{O}_1 \rangle_{\rho'} \langle \mathcal{O}_2 \rangle_{\rho'}$. Here, $\rho' = \mathcal{E}_{\mathrm{S}}(\rho)$ is the evolution of an initial product state ρ according to the dynamical map $\mathcal{E}_{\mathrm{S}}$, while $\| \cdot \|$ denotes the operator norm (the absolute value of the maximum eigenvalue) and we have taken the logarithms inside $\bar{I}(\mathcal{E}_{\mathrm{S}})$ in Eq. (20) to be binary logarithms $\log_2$ (otherwise the natural logarithm $\ln d$ on the right hand side becomes multiplied by a different factor).

So far, we have focused our discussion on the characterization of correlations in the dynamics of bipartite quantum systems. The approach to measure and estimate bipartite correlations can be extended to the multi-partite case. In this situation, one has to specify what kind of correlations are the matter of interest. For instance, one may be interested in the amount of correlations shared between two parties of the system or between all parties. Figure 8 illustrates a generic situation where correlations among all systems are investigated. For example, suppose we consider the total amount of correlations, i.e., the amount of correlations shared by all parties. In that case, if the system S has M parties $\mathrm{S}_1, \mathrm{S}_2, \ldots, \mathrm{S}_M$, we can introduce respective ancillary systems $\mathrm{S}'_1, \mathrm{S}'_2, \ldots, \mathrm{S}'_M$ as we did in the bipartite case, and prepare a collection of M maximally entangled states between S_1 and S'_1, S_2 and S'_2, etc. [see Fig. 8(A)]. The dynamics is then applied on the system S we want to study. The amount of total (normalized) correlations in the

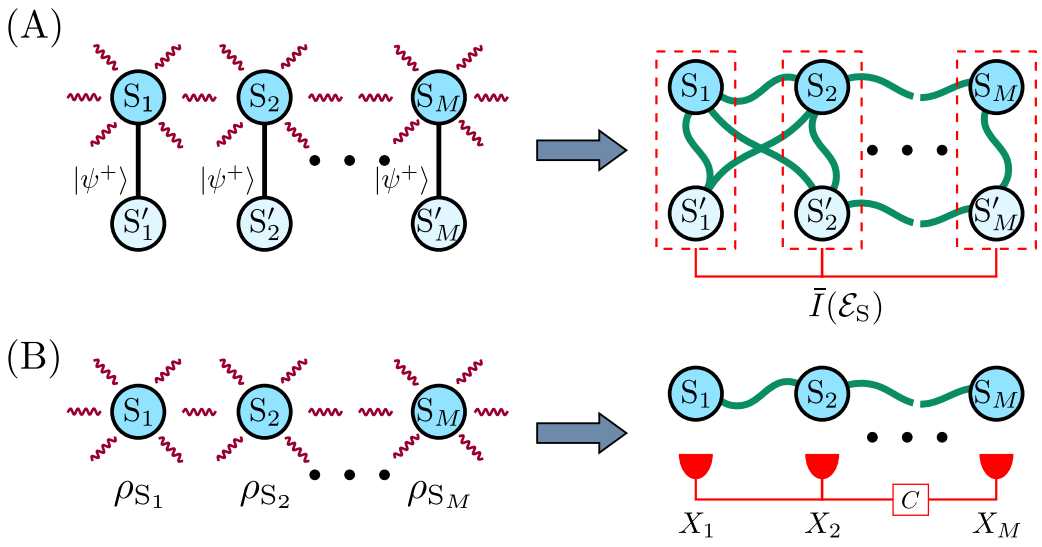

Fig. 8: *Schematic illustration of the multipartite correlation measure. (A) Choi-Jamiołkowski representation of the dynamics. The system is prepared in a product of maximally entangled states of $2M$ parties $\{S_j|S'_j\}$ and the dynamics affects only the subsystems S_j. If and only if the dynamics are correlated, the bipartitions $\{S_iS'_i|S_jS'_j\}$ will be entangled, yielding a nonzero correlation measure $\bar{I}$. (B) Schematic depiction of the procedure to estimate a lower bound of $\bar{I}$. There, the system is initially prepared in a separable state $\rho_{S_1} \otimes \rho_{S_2} \cdots \otimes \rho_{S_M}$ and correlations in the dynamics show up as correlations C (see Eq. (38)) in the measurement of suitably chosen observables $\mathcal{O}_j$. Figure reproduced from [28].*

dynamics can then be assessed by

$$\begin{aligned}\bar{I}(\mathcal{E}_S) &:= \frac{1}{2M\log d} S\left(\rho_S^{CJ} \middle\| \rho_S^{CJ}|_{S_1S'_1} \otimes \ldots \otimes \rho_S^{CJ}|_{S_MS'_M}\right) \\ &:= \frac{1}{2M\log d}\left\{\left[\sum_{i=1}^{M} S\left(\rho_S^{CJ}|_{S_iS'_i}\right)\right] - S\left(\rho_S^{CJ}\right)\right\}, \end{aligned} \tag{36}$$

where $\rho_S^{CJ}|_{S_iS'_i} = \mathrm{Tr}_{\{\forall S_{j\neq i}S'_{j\neq i}\}}(\rho_S^{CJ})$.
A lower bound for the multipartite setting can be applied as shown in Fig. 8(B), by measuring correlations. Mathematically the same steps as in the bipartite case [see Eq. (35)] can be applied, resulting in

$$\bar{I}(\mathcal{E}) \geq \frac{1}{4M\ln d} \frac{C^2_{\rho'}(\mathcal{O}_1,\ldots,\mathcal{O}_M)}{\|\mathcal{O}_1\|^2\ldots\|\mathcal{O}_M\|^2}. \tag{37}$$

Here, $\rho(t)$ is the joint state after the evolution of an initial product state, $\mathcal{O}_1,\ldots,\mathcal{O}_M$ are local observables for the parties $S_1,\ldots,S_M$, respectively, and the correlation function is

$$C_{\rho(t)}(\mathcal{O}_1,\ldots,\mathcal{O}_M) = \langle \mathcal{O}_1\ldots\mathcal{O}_M\rangle_{\rho(t)} - \langle\mathcal{O}_1\rangle_{\rho(t)}\ldots\langle\mathcal{O}_M\rangle_{\rho(t)}. \tag{38}$$

This multipartite bound makes investigating correlation dynamics accessible in systems that are too large for full quantum process tomography, as here the number of measurements increases only linearly compared to the exponential scaling for full quantum process tomography.

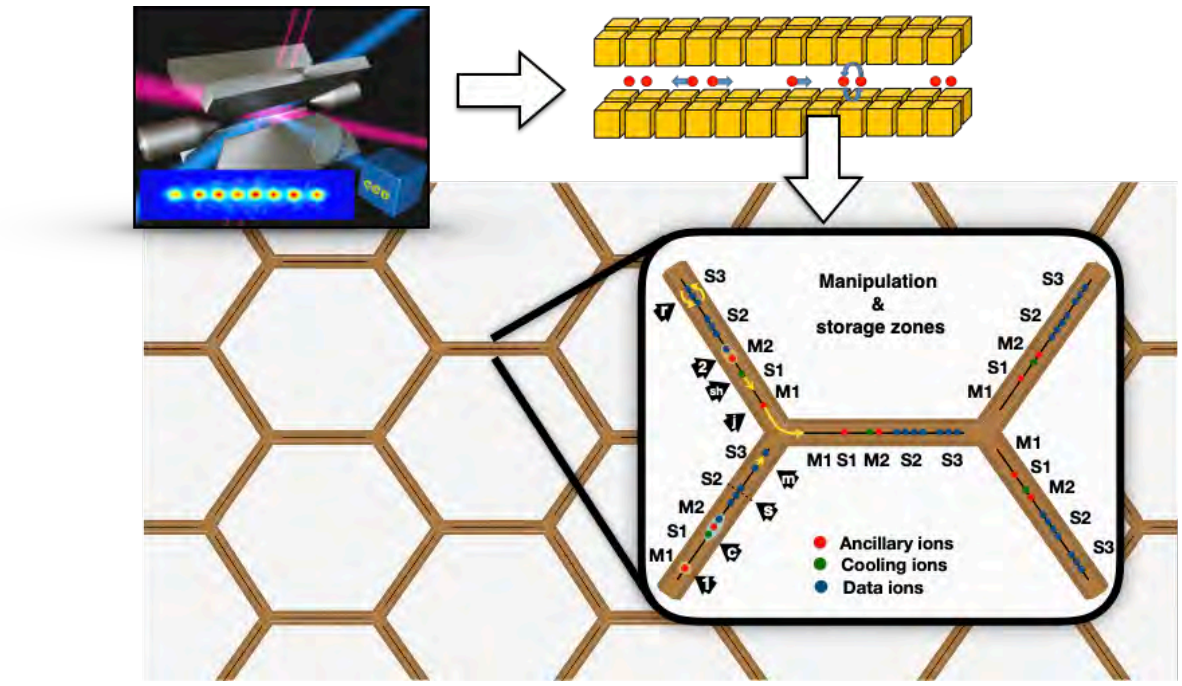

Fig. 9: *Illustration of one scalable route from macroscopic linear Paul traps (upper left) towards large-scale ion-trap quantum processors. Ions can be stored in segmented traps (upper right), where ion crystals can be controlled locally, and ions can be split, moved around and merged with ion-crystals in different trapping regions. This allows one to control increasingly larger qubit registers with high flexibility. Such linear traps can be coupled via junctions, along which ions can be moved from one trap into neighboring zones, where they can be stored (S) or manipulated (M). This will allow one to assemble traps into larger two-dimensional trap arrays, which can be used to host and control large registers of qubits for quantum error correction and eventually large-scale fault-tolerant quantum computation.*

In summary, based on the mapping of quantum dynamics to quantum states in an enlarged Hilbert space via the Choi-Jamiołkowski isomorphism, in this lecture we have discussed a rigorous and systematic method to quantify the amount of spatial correlations in general quantum dynamics. Furthermore, we have applied the theoretical concepts developed to paradigmatic physical models and demonstrated their usefulness for the characterization of noise in experimental quantum processors. We expect that noise characterization techniques such as the ones discussed in this lecture will be of fundamental importance for the study of dynamics in a large variety of quantum systems. From a practical and more applied standpoint, such tools are likely to be essential to make further progress in developing and characterizing increasingly larger and scalable qubits registers, as shown for trapped ions in Fig. 9, to make the dream of large-scale quantum computers and simulators become a reality.

Acknowledgments. I would like to thank my collaborators, Angel Rivas from the Complutense University in Madrid, for the joint theory work of Refs. [25, 28], as well as my colleagues from Rainer Blatt's experimental ion-trapping group at the University of Innsbruck for the joint and joyful collaboration that gave rise to the results of Ref. [28].

References

[1] M. Kjaergaard et al., Annu. Rev. Condens. Matter Phys. **11**, 369 (2020)

[2] C.D. Bruzewicza et al., Appl. Phys. Rev. **6**, 021314 (2019)

[3] H.P. Breuer and F. Petruccione: *The Theory of Open Quantum Systems* (Oxford University Press, 2002)

[4] C.W. Gardiner and P. Zoller: *Quantum Noise* (Springer, Berlin, 2004)

[5] A. Rivas and S.F. Huelga: *Open Quantum Systems. An Introduction* (Springer, Heidelberg, 2011)

[6] R.H. Dicke, Phys. Rev. **93**, 99 (1954)

[7] P. Zanardi and M. Rasetti, Phys. Rev. Lett. **79**, 3306 (1997)

[8] D. Kielpinski, et al., Science **291**, 1013 (2001)

[9] H. Haeffner, et al., Appl. Phys. B **81**, 151 (2005)

[10] T. Monz, et al., Phys. Rev. Lett. **106**, 130506 (2011)

[11] A. Crubellier, et al., J. Phys. B: At. Mol. Phys. **18**, 3811 (1985)

[12] M.A. Nielsen and I.L. Chuang: *Quantum Computation and Quantum Information* (Cambridge University Press, 2010)

[13] D. Aharonov, A. Kitaev and J. Preskill, Phys. Rev. Lett. **96**, 050504 (2006)

[14] J. Preskill, Quant. Inf. Comput. **13**, 181 (2013)

[15] F. Caruso, et al., J. Chem. Phys. **131**, 105106 (2009)

[16] P. Rebentrost, M. Mohseni and A. Aspuru-Guzik, J. Phys. Chem. B. **113**, 9942 (2009)

[17] J. Jeske, J.H. Cole and S.F. Huelga, New J. Phys. **16**, 073039 (2014)

[18] A. Einstein, B. Podolsky and N. Rosen, Phys. Rev. **47**, 777 (1935)

[19] M. Lewenstein, A. Sanpera, and V. Ahufinger: *Ultracold Atoms in Optical Lattices. Simulating quantum many-body systems* (Oxford University Press, 2012)

[20] H.C. Nägerl, et al., Appl. Phys. B **66**, 603 (1998)

[21] M.-D. Choi, Linear Algebra Appl. **10**, 285 (1975)

[22] A. Jamiołkowski, Rep. Math. Phys. **3**, 275 (1972)

[23] M.B. Plenio and S. Virmani, Quant. Inf. Comp. **7**, 1 (2007)

[24] F.G.S.L. Brandão and M.B. Plenio, Nat. Phys. **4**, 873 (2008)

[25] A. Rivas and M. Müller, New J. Phys. **17**, 062001 (2015)

[26] M. Abramowitz and I.A. Stegun: *Handbook of Mathematical Functions* (Dover Publications, New York, 1972)

[27] P. Schindler, et al., New J. Phys. **15**, 123012 (2013)

[28] L. Postler, et al., Quantum **2**, 90 (2018)

[29] T. Ruster, et al., Phys. Rev. X **7**, 031050 (2017)

Index